Lecture Notes in Electrical Engineering 862

Anshuman Tripathi · Amit Soni ·
Ashish Shrivastava · Anil Swarnkar ·
Jagrati Sahariya *Editors*

Intelligent Computing Techniques for Smart Energy Systems

Proceedings of ICTSES 2021

Springer

Lecture Notes in Electrical Engineering

Volume 862

Series Editors

Leopoldo Angrisani, Department of Electrical and Information Technologies Engineering, University of Napoli Federico II, Naples, Italy
Marco Arteaga, Departament de Control y Robótica, Universidad Nacional Autónoma de México, Coyoacán, Mexico
Bijaya Ketan Panigrahi, Electrical Engineering, Indian Institute of Technology Delhi, New Delhi, Delhi, India
Samarjit Chakraborty, Fakultät für Elektrotechnik und Informationstechnik, TU München, Munich, Germany
Jiming Chen, Zhejiang University, Hangzhou, Zhejiang, China
Shanben Chen, Materials Science and Engineering, Shanghai Jiao Tong University, Shanghai, China
Tan Kay Chen, Department of Electrical and Computer Engineering, National University of Singapore, Singapore, Singapore
Rüdiger Dillmann, Humanoids and Intelligent Systems Laboratory, Karlsruhe Institute for Technology, Karlsruhe, Germany
Haibin Duan, Beijing University of Aeronautics and Astronautics, Beijing, China
Gianluigi Ferrari, Università di Parma, Parma, Italy
Manuel Ferre, Centre for Automation and Robotics CAR (UPM-CSIC), Universidad Politécnica de Madrid, Madrid, Spain
Sandra Hirche, Department of Electrical Engineering and Information Science, Technische Universität München, Munich, Germany
Faryar Jabbari, Department of Mechanical and Aerospace Engineering, University of California, Irvine, CA, USA
Limin Jia, State Key Laboratory of Rail Traffic Control and Safety, Beijing Jiaotong University, Beijing, China
Janusz Kacprzyk, Systems Research Institute, Polish Academy of Sciences, Warsaw, Poland
Alaa Khamis, German University in Egypt El Tagamoa El Khames, New Cairo City, Egypt
Torsten Kroeger, Stanford University, Stanford, CA, USA
Yong Li, Hunan University, Changsha, Hunan, China
Qilian Liang, Department of Electrical Engineering, University of Texas at Arlington, Arlington, TX, USA
Ferran Martín, Departament d'Enginyeria Electrònica, Universitat Autònoma de Barcelona, Bellaterra, Barcelona, Spain
Tan Cher Ming, College of Engineering, Nanyang Technological University, Singapore, Singapore
Wolfgang Minker, Institute of Information Technology, University of Ulm, Ulm, Germany
Pradeep Misra, Department of Electrical Engineering, Wright State University, Dayton, OH, USA
Sebastian Möller, Quality and Usability Laboratory, TU Berlin, Berlin, Germany
Subhas Mukhopadhyay, School of Engineering & Advanced Technology, Massey University, Palmerston North, Manawatu-Wanganui, New Zealand
Cun-Zheng Ning, Electrical Engineering, Arizona State University, Tempe, AZ, USA
Toyoaki Nishida, Graduate School of Informatics, Kyoto University, Kyoto, Japan
Federica Pascucci, Dipartimento di Ingegneria, Università degli Studi "Roma Tre", Rome, Italy
Yong Qin, State Key Laboratory of Rail Traffic Control and Safety, Beijing Jiaotong University, Beijing, China
Gan Woon Seng, School of Electrical & Electronic Engineering, Nanyang Technological University, Singapore, Singapore
Joachim Speidel, Institute of Telecommunications, Universität Stuttgart, Stuttgart, Germany
Germano Veiga, Campus da FEUP, INESC Porto, Porto, Portugal
Haitao Wu, Academy of Opto-electronics, Chinese Academy of Sciences, Beijing, China
Walter Zamboni, DIEM - Università degli studi di Salerno, Fisciano, Salerno, Italy
Junjie James Zhang, Charlotte, NC, USA

The book series *Lecture Notes in Electrical Engineering* (LNEE) publishes the latest developments in Electrical Engineering - quickly, informally and in high quality. While original research reported in proceedings and monographs has traditionally formed the core of LNEE, we also encourage authors to submit books devoted to supporting student education and professional training in the various fields and applications areas of electrical engineering. The series cover classical and emerging topics concerning:

- Communication Engineering, Information Theory and Networks
- Electronics Engineering and Microelectronics
- Signal, Image and Speech Processing
- Wireless and Mobile Communication
- Circuits and Systems
- Energy Systems, Power Electronics and Electrical Machines
- Electro-optical Engineering
- Instrumentation Engineering
- Avionics Engineering
- Control Systems
- Internet-of-Things and Cybersecurity
- Biomedical Devices, MEMS and NEMS

For general information about this book series, comments or suggestions, please contact leontina.dicecco@springer.com.

To submit a proposal or request further information, please contact the Publishing Editor in your country:

China

Jasmine Dou, Editor (jasmine.dou@springer.com)

India, Japan, Rest of Asia

Swati Meherishi, Editorial Director (Swati.Meherishi@springer.com)

Southeast Asia, Australia, New Zealand

Ramesh Nath Premnath, Editor (ramesh.premnath@springernature.com)

USA, Canada:

Michael Luby, Senior Editor (michael.luby@springer.com)

All other Countries:

Leontina Di Cecco, Senior Editor (leontina.dicecco@springer.com)

**** This series is indexed by EI Compendex and Scopus databases. ****

More information about this series at https://link.springer.com/bookseries/7818

Anshuman Tripathi · Amit Soni ·
Ashish Shrivastava · Anil Swarnkar ·
Jagrati Sahariya
Editors

Intelligent Computing Techniques for Smart Energy Systems

Proceedings of ICTSES 2021

Springer

Editors
Anshuman Tripathi
Nanyang Technological University
Singapore, Singapore

Ashish Shrivastava
Manipal University Jaipur
Jaipur, India

Skill Faculty of Engineering
and Technology
Shri Vishwakarma Skill University
Haryana, India

Jagrati Sahariya
National Institute of Technology
Uttarakhand
Srinagar, India

Amit Soni
Manipal University Jaipur
Jaipur, India

Anil Swarnkar
Malaviya National Institute of Technology
Jaipur
Jaipur, India

ISSN 1876-1100 ISSN 1876-1119 (electronic)
Lecture Notes in Electrical Engineering
ISBN 978-981-19-0251-2 ISBN 978-981-19-0252-9 (eBook)
https://doi.org/10.1007/978-981-19-0252-9

© The Editor(s) (if applicable) and The Author(s), under exclusive license to Springer Nature Singapore Pte Ltd. 2022
This work is subject to copyright. All rights are solely and exclusively licensed by the Publisher, whether the whole or part of the material is concerned, specifically the rights of translation, reprinting, reuse of illustrations, recitation, broadcasting, reproduction on microfilms or in any other physical way, and transmission or information storage and retrieval, electronic adaptation, computer software, or by similar or dissimilar methodology now known or hereafter developed.
The use of general descriptive names, registered names, trademarks, service marks, etc. in this publication does not imply, even in the absence of a specific statement, that such names are exempt from the relevant protective laws and regulations and therefore free for general use.
The publisher, the authors, and the editors are safe to assume that the advice and information in this book are believed to be true and accurate at the date of publication. Neither the publisher nor the authors or the editors give a warranty, expressed or implied, with respect to the material contained herein or for any errors or omissions that may have been made. The publisher remains neutral with regard to jurisdictional claims in published maps and institutional affiliations.

This Springer imprint is published by the registered company Springer Nature Singapore Pte Ltd.
The registered company address is: 152 Beach Road, #21-01/04 Gateway East, Singapore 189721, Singapore

Preface

In today's world, intelligent computing has found applications in almost every research domain. So, keeping in view the needs and demand of the intelligent computing, First International Conference on **Intelligent Computing Techniques for Smart Energy Systems (ICTSES-2018)** was successfully organized during December 22–23, 2018, at Manipal University Jaipur, Rajasthan, India. The proceedings of the conference was published in the Scopus Indexed Lecture Notes on Electrical Engineering, Springer, with 104 papers. Moving forward, the second version of ICTSES-2021 was organized during September 1–3, 2021, by the School of Electrical, Electronics and Communication Engineering (SEEC), at Manipal University Jaipur, Rajasthan, India, in association with Malaviya National Institute of Technology (MNIT), Jaipur, and National Institute of Technology, Uttarakhand.

Due to ongoing COVID pandemic situation, the conference was organized in online mode. It received interest from various countries with 185 paper submissions through the Easy Chair Conference Management System. Seventy papers were accepted for presentation during the conference after thorough review process under four tracks, viz. electrical engineering, electronics engineering, communication technologies and computing techniques.

The conference focussed on the recent areas in the field of electrical, electronics, computer engineering and computational techniques along with interdisciplinary research, to serve the modern society. It was aimed to bring together the leading academic scientists, researchers and research scholars to exchange and share their experiences and research results to an international forum with the aim of creating, replacing, improving, or understanding the recent areas in the intelligent computing.

We extend our heartfelt thanks to the conveners and the organizing committee for making the event a success. We also express our sincere regards to the management of Manipal University Jaipur, Malaviya National Institute of Technology, and National Institute of Technology Uttarakhand for their continuous support and cooperation for the event. We extend our gratitude to all authors and reviewers, speakers, advisory committee members from various academic institutes and industries

We take this opportunity to thank Prof. Udaykumar R. Yaragatti, chief guest for the conference with Dr. Anshuman Tripathi from NTU Singapore, Prof. K. R. Niazi

from MNIT Jaipur, Dr. Surya Prakash from IIT Indore, Dr. Anand Nayyar from Duy Tan University, Da Nang, Vietnam, and industry speaker Mr. Rajesh Nimare from Secure Meters Ltd., Udaipur, for their informative and interesting invited talks during the conference.

We extend our sincere thanks to team Springer for accepting our proposal and providing valuable support for publishing conference proceedings in Lecture Notes of Electrical Engineering, Springer.

Editors

Singapore — Anshuman Tripathi
Jaipur, India — Amit Soni
Jaipur, India — Ashish Shrivastava
Jaipur, India — Anil Swarnkar
Srinagar, India — Jagrati Sahariya

Contents

About the Editors

Dr. Anshuman Tripathi joined NTU in November 2012 and leads the electromobility and grid connectivity areas of RD&D in the Energy Research Institute at NTU (ERI@N). Before joining ERI@N, he has spent close to 10 years in the industry. From July 2004 to August 2007 at GE, he formed electrical machine design competence in GE-global research delivering machine-converter solutions to GE transportation and GE healthcare systems. He also worked on wireless power transfer solutions for GE health care and GE-NBC. He then joined Vestas Wind Power Systems in September-2007 where he was instrumental in creating a 2 and 3 MW converter design group comprising of hardware, software and control groups. This group delivered solutions for V-90, V-112 and V-164 turbine platforms of Vestas. He has research interests in grid connection of large and remote wind and solar farms, grid codes and compliance, power hardware in the loop simulations for power network designs, electrical drive train designs and hybrid energy storage for stationary and mobile applications. He has 35 patents in the areas of power systems, control, electrical machines and 22 IEEE publications.

Prof. (Dr.) Amit Soni has done his graduation in Electrical (Electronics and Power) Engineering from SRTMU, Maharashtra, in the year 2001 and was awarded 'Gold Medal' for his outstanding academic performance. He has done M.Tech. (Power System) in the year 2005 and Ph.D. (Power System) in 2012 both from Malaviya National Institute of Technology (MNIT), Jaipur. He has joined Manipal University, Jaipur, on August 20, 2014, and is currently working as Director (International Collaborations) from 1st October 2021. Earlier he has served as Director (Quality and Compliance) for period of one year and has successfully contributed in University NIRF, AQAR, NBA and Media rankings. He has rich experience of 20 years while working with various institutions, which includes 3 years of industrial experience in RRVPNL, Jaipur. Before joining Manipal University, Jaipur, he has performed various administrative roles such as Director, Asians Institute of Technology, Rajasthan, Head, Electrical Department, Coordinator and Chairman for various Academic Committees at both undergraduate and postgraduate levels. He has served as Professor and Head, Department of Electrical Engineering from

December 18, 2015, for a span of 4.5 years and during this tenure had successfully organized several national and international workshops, Scopus indexed international conferences, initiated MoUs and also developed research laboratories. He is currently working in interdisciplinary research areas which includes solar photovoltaic materials, optoelectronics, thin film technology, renewable energy systems and power system. He has published 6 book chapters and 60 research papers in repute SCI indexed international journals and Scopus indexed conferences which includes high-impact Q1 and Q2 journals of repute. He has delivered several invited talks, keynote addresses and chaired/co-chaired sessions in various repute indexed conferences. He is regular reviewer of research articles for many high-impact journals. He has successfully supervised three Ph.D.s, and currently, 6 research scholars are working under his supervision. He is currently working as PI for DST SERB funded research project in collaboration with MLSU, Udaipur, and NIT Uttarakhand. He is a life member of Solar Energy Society of India, Member ISTE, India, and IEEE, USA.

Dr. Ashish Shrivastava is currently working as Professor and Head of Department of Electrical Engineering, School of Electrical, Electronics and Communication, Manipal University, Jaipur, since July 2017. He did his B.E. and M.Tech. degrees with honors in Electrical Engineering from the Govt. Engineering College, Rewa (MP), and NIT Bhopal, (MP), respectively. He did his Ph.D. in Electrical Engineering Department from Indian Institute of Technology Delhi (IITD), New Delhi. He was conferred with prestigious POSOCO Power System Award (PPSA-2014) in the doctoral category for significant contribution in research work at IITD. He is Senior Member of IEEE and Life Member of ISTE. He comes with the rich and diversified experience of 20 years in various fields including teaching, research and administration as well. He is currently supervising eight Ph.D. scholars and is a regular reviewer of research articles for many high-impact journals including *IEEE transactions on Industrial Electronics*, *Industrial Informatics*, *Power Electronics*, *IET Power Electronics*, Elsevier, etc. He has strong flair for writing and research and has authored 4 book chapters and published 60 research articles in international journals/conferences of high repute, including IEEE Transactions. He has delivered more than 20 expert lectures at different platforms. He was instrumental in organizing many conferences/workshops/seminars/symposia at various capacities and has chaired/co-chaired sessions in a number of national/international conferences.

Dr. Anil Swarnkar is presently working as Associate Professor in the Department of Electrical Engineering at MNIT, Jaipur. He has been associated with the institute for around 21 years. He is also serving as Associate Dean (Academics) at MNIT Jaipur. He has received POSOCO Power System Award 2013 in Ph.D. category for innovative research in the area of power systems. The award is given by Power System Operation Corporation (POSOCO), Power Grid Corporation of India Ltd, in partnership with the Foundation for Innovation and Technology Transfer, IIT Delhi. He has a patent to his credit in 2015. He did his B.E. and M.Tech.

degrees with honors in Electrical Engineering from the Rani Durgavati University, Jabalpur, MP, and MNIT, Jaipur (Rajasthan), respectively. He did his Ph.D. in Electrical Engineering Department from MNIT, Jaipur. He is Senior Member of IEEE and Member of Power and Energy Society, and Grid Community, IEEE. He has a rich teaching experience of 21 years with 3 successful doctoral degree completion under his guidance. He is currently supervising one Ph.D. scholar. He has delivered many invited talks at different platforms. He has successfully organized many conferences/workshops/seminars/symposia at various capacities and has chaired/co-chaired sessions in number of national/international conferences.

Dr. Jagrati Sahariya Assistant Professor—I, Department of Physics, National Institute of Technology, Uttarakhand, is working in the field of γ-ray scattering and band structure calculations since last 10 years. She has received her Ph.D. degree in 2012 in the field of electronic structure calculation and Compton scattering. She has studied electronic and magnetic properties of a variety of technological important materials. She has sufficient expertise in using different band structure methods like full potential linearized augmented plane wave, linear combinations of atomic orbitals and spin-polarized relativistic Korringa–Kohn–Rostoker to compute electronic structure, optical and magnetic properties and Compton profiles of variety of materials. She has published more than 70 papers in peer-reviewed international journals of high-impact factor and repute conferences both at national and at international levels. She has also executed a research project funded by SERB under Fast Track Scheme.

Fault Analysis and Protection Scheme for DC Microgrid

Shreya Nagaraja, Sankarshan Durgaprasad, N. Sumanth, and Sangeeta Modi

Abstract DC microgrids (DCMG) have gained attention in recent years because of their superiority over their counterpart AC microgrid in terms of efficiency, controllability, integration of distributed energy resources (DER's), and system installation in remote locations. Due to the infancy of the topic, the major challenge faced in DCMG is the lack of suitable protection schemes. Therefore, this work intends to depict the implementation of a protection scheme for a 96 V grounded DC microgrid of ring nature and fault analysis on the selected system. Main reason for the stated protection challenge in DC microgrid is unavailability of zero-level crossing (natural). A preliminary load flow analysis on DC microgrid is discussed and performed to establish the steady-state power flow conditions. This is followed by the EMTP to determine selected microgrid behavior during transient conditions and decide on protection schemes. A hardware-in-loop (HIL) environment is developed and discussed to verify the effectiveness of the protection scheme.

Keywords Microgrid · Protection · HIL · Fault · Overload · Overcurrent · Protection scheme

1 Introduction

Globally, due to the increasing levels of demand for energy and entrance of DERs, the electrical distribution network is experiencing changes in the arrangement of power clusters, which are known as microgrids. Coupled with the environmental advantages provided by sustainable sources, according to various cross-over algorithms, it is now cheaper to replace existing fossil fuel-based energy sources with wind and solar [1].

Broadly, microgrids can be divided into two: ACMG and DCMG. As the name suggests, the dispersal in an ACMG is through AC, and in a DCMG, it is DC.

S. Nagaraja (✉) · S. Durgaprasad · N. Sumanth · S. Modi
Department of Electrical and Electronics, PES University, Bangalore, India
e-mail: shreya.nagaraja@gmail.com

S. Durgaprasad
e-mail: sankarshandurgaprasad@pesu.pes.edu

© The Author(s), under exclusive license to Springer Nature Singapore Pte Ltd. 2022

A. Tripathi et al. (eds.), *Intelligent Computing Techniques for Smart Energy Systems*, Lecture Notes in Electrical Engineering 862,
https://doi.org/10.1007/978-981-19-0252-9_1

Microgrids are known to be reliable due to their ability to function in both grids and islanded mode. The reliability is increased of the power network. Due to the partial dependency on the grid, the customers are considered as "prosumers," thus lowering energy costs for consumers and business. Microgrids also strengthen the central grid, by contributing to the network during peak demands.

It is expected that microgrids and smart grids have the following features [2–4]:

- High penetration of RES, energy efficiency,
- Reliability, ESS, resilience, distributed generation (DG) units,
- Advanced control methods,
- Sensing measurements,
- Advanced loads, real-time energy management systems, and
- Cyber security, IT.

The purpose of this work is to implement local and centralized protection algorithms on an LVDC system. The protection algorithm must be selective, effective, and fast. This is done so by verifying the protection algorithm in a hardware-in-loop environment.

Section 2 will briefly explain the overview of protection in DC microgrids. Section 3 will discuss the methods used for digitally simulating the grid for load flow analysis and transient (EMTP) analysis and the results of the same. Section 4 explains the methodology, conduction, and results of the hardware-in-loop system developed.

2 Overview of Protection in DC Microgrid

2.1 Challenges of DC Protection

Lack of zero crossing possesses a fundamental challenge in protection of DC systems as this makes it harder for circuit breakers and fuses to interrupt current. Other challenges can be categorized into (1) arcing and fault clearing time, (2) multi-terminal protection, (3) stability, (4) communication challenges, and (5) ground fault challenges. Arcing and fault clearing time issues arise due to usage of conventional DC circuit breakers. Absence of controllability of power converters and lack of physical inertia cause instability issue. The presence of capacitive filters poses great threat to the system at the time of fault. They discharge rapidly, and depending on the fault location, design of filter, and the converter capacity, surges in current can be between 10,000 A and 50,000 A [5].

2.2 DC Grid Configurations

Depending on the required application and design, the DC microgrid can have various architectures and thus can be categorized as follows:

1. Radial (single) bus,
2. Multi-bus,
3. Loop or ring, and
4. Interconnected configuration.

For radial configurations, feeders create power flow only in one direction. For such a system, single bus topology is popular. Ring or so-called loop type configuration is used to provide a sustainable supply of power after the permanent fault isolation. Interconnected configuration of DC microgrid is proposed, in order to have a bidirectional flow of power. This is achieved by connecting DC microgrids via AC/DC/AC converter interface to an AC network as shown in Fig. 5. The conversion stage in between AC systems, i.e., conversion, helps to propagate the fault through regulation from one side of AC to the other. This also enhances the power supply reliability [6].

2.3 Faults in DC Microgrid

DCMG faults can be majorly divided into two types: (1) short-circuit fault and (2) arc fault. Arc fault can be series or in parallel arc fault. Short-circuit (SC) fault is further classified into (a) L-to-L and (b) L-to-G. When a forward line and a return line are shorted by a path created in between them, the resulting fault is a line-to-line fault. However, when either of the two lines are shorted with the ground, then the fault is a line-to-ground fault.

A pole–pole (P–P) fault is very rare but is a possible event, if the poles are side by side. A P–P fault is followed by a very severe and high magnitude fault current. This can also result in discharging of a high transient fault current in the microgrid. A pole–ground faults are very common and frequent, but its severity is less. The fault impedance is dependent on the earthing configuration.

2.4 Protection Methods in DC Microgrids

Details of the comparative analysis between various protection algorithms for DC systems are provided in [7, 8]. Faults are categorized into two types: (1) non-unit protection and (2) unit type protection.

Non-unit protection schemes do not have a fixed boundary of protection. While protecting their own designated areas, non-unit protection schemes have zones that overlap. Unit protection schemes have a specific area of protection and are usually communication based as discussed in [8].

Table 1 Comparison between various protection schemes

Method of protection	Speed	Selectivity	Reliability	Price
Over current	M	L	H	M
Distance	H	M	M	M
Differential	VH	H	H	H
Event based	H	M	M	L
Hand-shaking	M	L	M	L
Wavelet	H	H	VH	M
ANN	M	H	H	L
Communication based	VH	H	L	H

Bayati et al. [7] categorize various types of protection algorithms based on speed, selectivity, reliability, and price of implementation as given in Table 1. Bayati et al. [7] propose a slope impedance technique that has been implemented in the hardware-in-loop setup developed. This method is compared with over current and directional overcurrent methods of protection: V: very; M: medium; L: low; H: high.

3 Simulation Methodology

3.1 Load Flow Studies

Determining the steady-state behavior of the system serves as a prerequisite for any studies which can subsequently be performed on it. Load flow technique is a numerical application tool which helps to establish the current and power flow at each bus in the system under inspection. With developments recently in power electronics technologies, DERs with DC output type at distribution voltage levels have enforced the need for DC load flow analysis tools. In DC load flow application, only active power and magnitude of voltage, current, and impedance are considered. Figure 1 represents a flowchart illustrating the course of load flow analysis. With

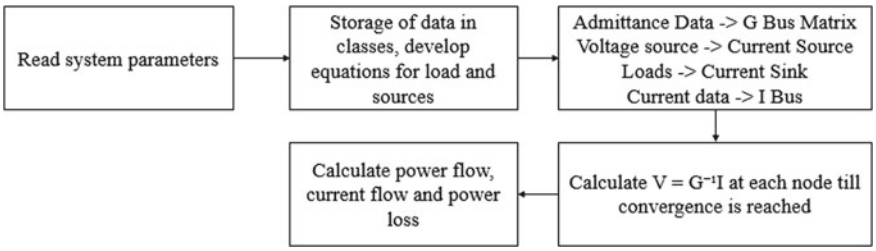

Fig. 1 Flowchart for load flow analysis

information obtained from this application, relay threshold, feeder line ratings, losses in the systems, and required power compensation can be determined.

Load flow analysis has been performed to estimate the steady-state behavior of the MG chosen. Impedance values of the feeder lines and the loads available from the grid data are used to build the impedance matrix. The bus impedance matrix is essentially an entity which indicates the interconnection of the buses. The voltage sources are converted into current sources, and the constant current loads are modeled as current sinks. These models combine with the actual current sources have been used to found the I bus matrix. The I bus matrix serves to provide information regarding the current injected or drawn from the load.

Buses are classified into three types

- Slack bus,
- Generator bus, and
- Load bus.

The next step in the process of load flow studies is to calculate the steady-state voltage at each bus. Each bus is rated at some nominal operating voltage. However, the intrinsic impedance associated with the loads and feeder lines results in the drop or rise in the bus voltage.

3.2 EMTP Studies

When a normally operational power system encounters a fault, the behavior shifts from steady state to transient state. At steady state, the inductor in a DC circuit behaves as a short circuit, whereas a capacitor functions as an open circuit, hence providing infinite impedance to the current. In the transient state, the components of the circuit display electromagnetic activities. The effect of the transmission line inductance and capacitance is to be considered in order to determine the time-varying characteristics of current at the buses. The transient characteristics of the system ascertain the severity of the fault and also initiate the appropriate relay action. Figure 2 represents a flowchart illustrating the course of electromagnetic transient program.

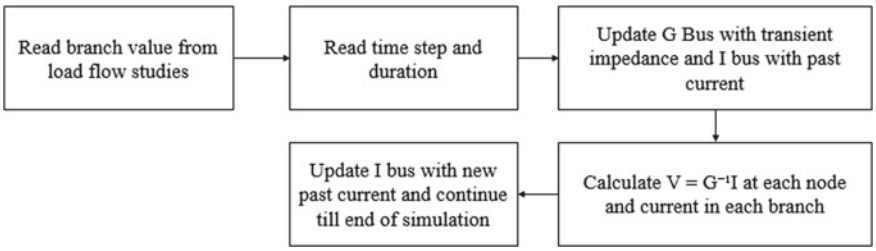

Fig. 2 Flowchart for EMTP studies

With information obtained from this application, a post-fault analysis of the system can be performed to determine the cause and preventive methods.

Digital computers have played a significant role in solving electromagnetic transient problem. These methods of solution can be classified in two ways: frequency domain and domain related to time methods. At present, popularly used way of transient analysis is dependent on the implementation of the rule based on trapezoidal and the "Bergeron's" method. Dommel played a key role in the extension of the Bergeron's method [8]. The scheme belonging to Dommel's combined the method of Bergeron's and the rule of trapezoidal giving rise to a capable algorithm for solving 1 and many phase systems networks transients involving lumped parameters that are distributed. The differential equations encountered in these types of problems are approximated into equations that are algebraic involving V, I, and past history values using the trapezoidal rule. This rule is applicable when we consider a very small timestep [9]. In power systems, a detailed modeling is required for the part of the system to be studied under the influence of transient phenomena. The elements are therefore converted to their network equivalents. This reduces the computation time and complexity, while the accuracy of simulation is retained. The network equivalents of an inductor and capacitor are illustrated below. This method is further extended to model a feeder line conductor which contains intrinsic inductance in the series and capacitance in the shunt [10].

Inductor equations are listed below

$$V = L\frac{\mathrm{d}i}{\mathrm{d}t} \tag{1}$$

$$\frac{V1(t) - V2(t) + V1(t-\Delta t) - V2(t-\Delta t)}{2} = L\frac{i(t) - i(t-\Delta t)}{\Delta t} \tag{2}$$

$$i(t) = (V1(t) - V2(t)) * \frac{\Delta t}{2L} + (V1(t+\Delta t) - V2(t-\Delta t)) * \frac{\Delta t}{2L} + (i(t-\Delta t)) \tag{3}$$

Capacitor equations are listed below

$$i = C\frac{\mathrm{d}v}{\mathrm{d}t} \tag{4}$$

$$C * \frac{V1(t) - V2(t) - V1(t-\Delta t) + V2(t-\Delta t)}{\Delta t} = \frac{i(t) - i(t-\Delta t)}{2} \tag{5}$$

$$i(t) = (V1(t) - V2(t)) * \frac{2C}{\Delta t} - (V1(t+\Delta t) - V2(t-\Delta t)) * \frac{2C}{\Delta t} + (i(t-\Delta t)) \tag{6}$$

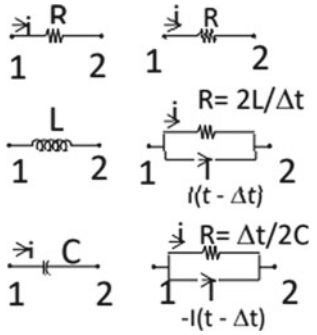

Fig. 3 Circuit equivalent of different parameters

Figure 3 shows the equivalent circuits of resistors, capacitors, and inductors during EMTP studies.

3.3 Program Results

An 11-bus ring system (Fig. 4) with a nominal voltage of 96 V has been simulated to study the level of fault currents when fault occurs at different buses. The system is first studied for steady-state power flow. This is followed by the simulation of the fault to find the maximum current due to fault when a line-to-ground fault occurs at a bus. The first bus is modeled to simulate a PV model. The 11th bus is simulated to behave as a battery.

Figure 5 shows the level of fault current when a fault occurs at the second bus from the left most source. The curve in red is of higher magnitude as it is closer to the source. The green curve represents current coming from the battery bus. Figure 6 distinguishes the fault levels as a function of the distance from the source. The relay at different buses is to be coordinated in order to avoid redundant tripping.

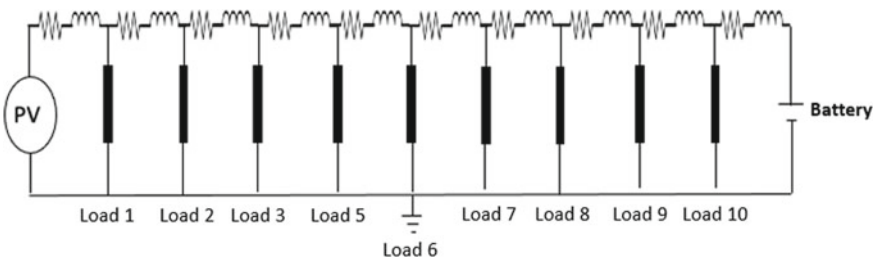

Fig. 4 Equivalent circuit of simulated system

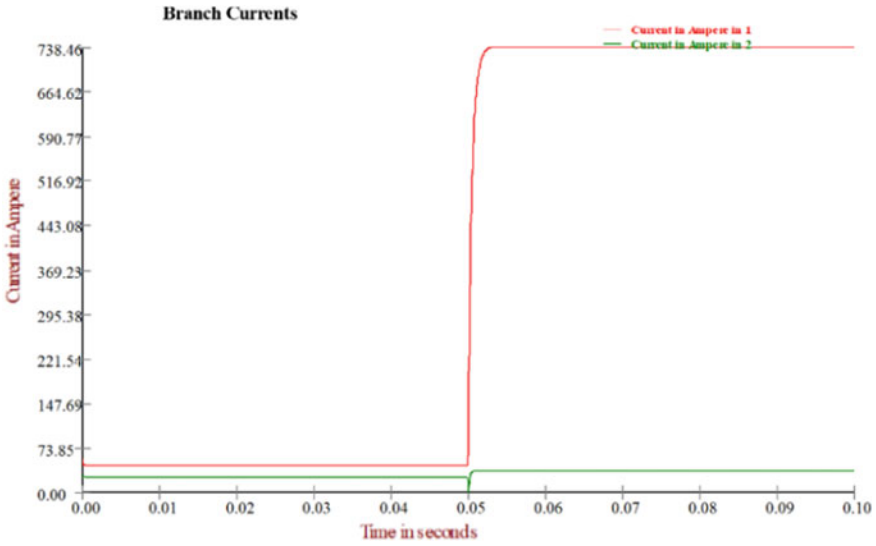

Fig. 5 Branch current at fault bus 2

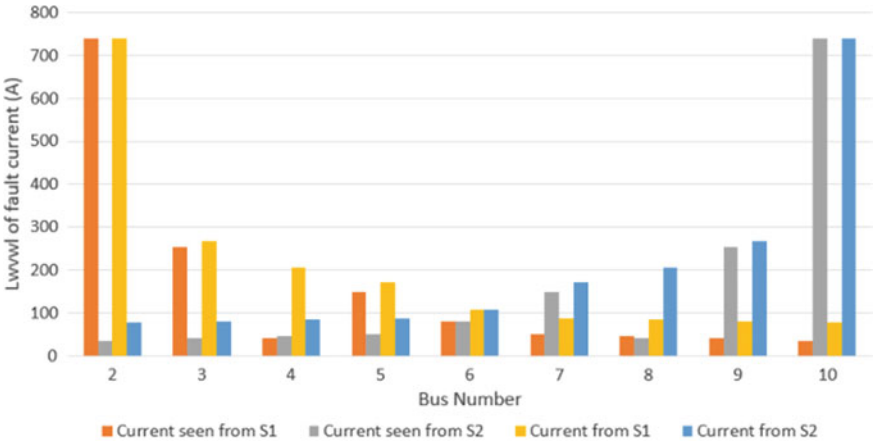

Fig. 6 Fault current levels

4 Hardware-in-Loop

4.1 Overview

Microgrids can function in harmony with the utility grid and also function as a resilient independent entity capable of supplying power to essential loads only when

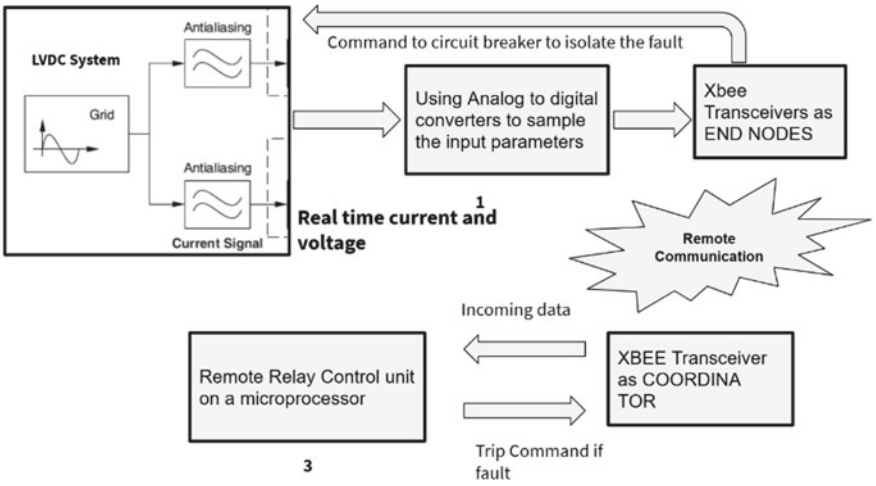

Fig. 7 Hardware-in-loop overview

supported by multiple tiers of protection and control. The Python simulation developed is used to model the behavior of microgrids in real time which allowed real microgrid protection and control. Combination of hardware-in-loop testing with digital signal processors is capable of physically connecting the simulated network, controllers requiring low-level or RF-based signals, protection requiring secondary-level signals, and real power hardware exchanging real power with the simulated environment. This results in an extremely powerful microgrid testbed. Figure 7 shows the hardware-in-loop overview.

4.2 Circuit Diagram

Figure 8 shows the overall circuit diagram of the hardware-in-loop system implemented. The system comprises the grid side that have four Xbees and four Nanos. Each Nano and Xbee corresponds to one bus. However, this system is flexible. More than one DAC can be connected to a single Nano, imitating the output readings of more than one sensor at the bus. The Mega represents the remote coordinator that is in charge of detecting the location of faults in case of line faults. Local protection is implemented at each bus with the help of the Nano.

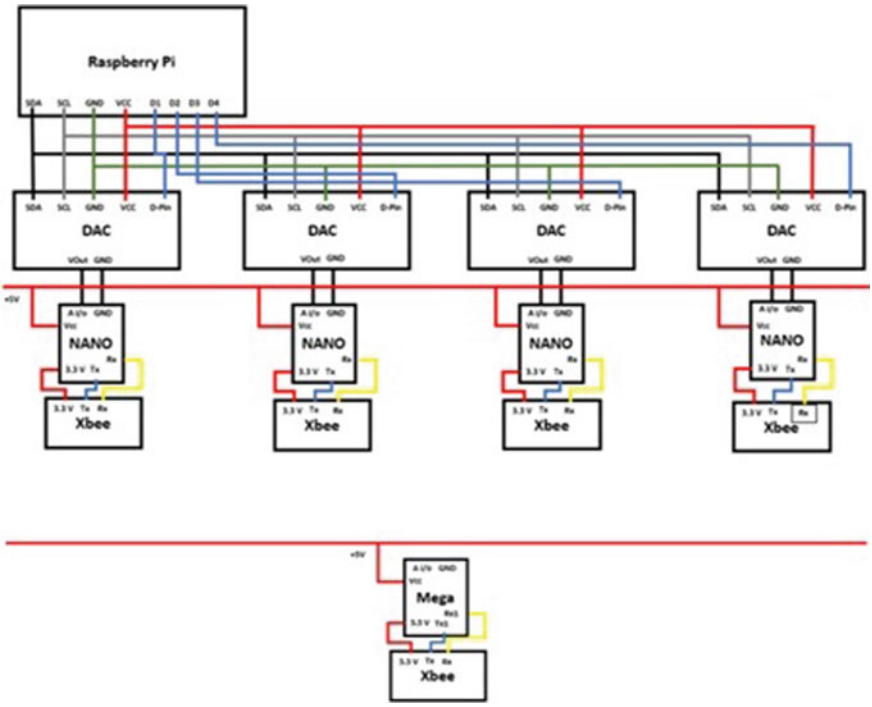

Fig. 8 HIL circuit diagram

4.3 Protection Algorithm

The scope of this project focuses on the implementation of three types of protection algorithms, namely bus fault protection, overloading protection, and line fault protection.

A bus fault can be a result of various scenarios which include failure of support insulators, failure of circuit breakers, foreign object accidentally falling across the bus bar, etc. The algorithm illustrated in Fig. 9 depicts the sequence of events adopted to detect and isolate a bus fault from the rest of the supply to avoid complete power interruption.

Differential protection scheme is adopted for the protection of the bus bar to which various loads are connected. The implementation procedure has three steps: monitoring the system, detection of fault or abnormal conditions, and classification of the fault and finally initiating the appropriate tripping sequence. The current was monitored using current sensors at either side of the bus bar and also at the feeder line connecting the loads. The sampled analog signals were then converted into digital data by the ADC present in the signal processor. The sum of the three currents at each bus was computed and compared against the threshold to determine fault condition.

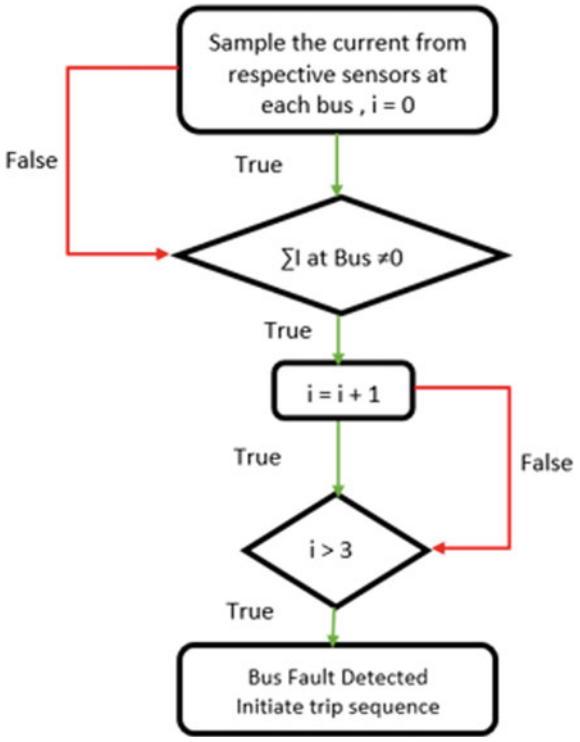

Fig. 9 Overcurrent bus fault protection

Once the fault condition was identified, the microprocessor checks for consistency in the system currents and triggers the circuit breakers involved to isolate the fault.

An overloading condition is usually a result of fault which occurs when the load draws an abnormally high current. This can lead to overheating and degradation of the system wiring. The algorithm illustrated in Fig. 10 depicts the sequence of events adopted to detect and isolate the fault to protect the load from overcurrent condition. Overcurrent protection scheme is adopted for the protection of the feeder line to which various loads are connected during an overloading condition. The implementation procedure has three steps: monitoring the system, detection of fault or abnormal conditions, and classification of the fault and finally initiating the appropriate tripping sequence. The current was monitored using current sensors between the bus and the loads. The sampled analog signal was then converted into digital data by the ADC present in the signal processor. The value of the load current was compared against the threshold to determine fault condition. Once the fault condition was identified, the microprocessor checks for consistency in the system currents and triggers the circuit breakers involved to isolate the fault.

A transmission line fault is usually a result of fault which occurs when there is an accidental shorting between the line and the ground of the system. The algorithm illustrated in Fig. 11 depicts the sequence of events adopted to detect and isolate a line fault from the rest of the supply. Directional overcurrent-based protection

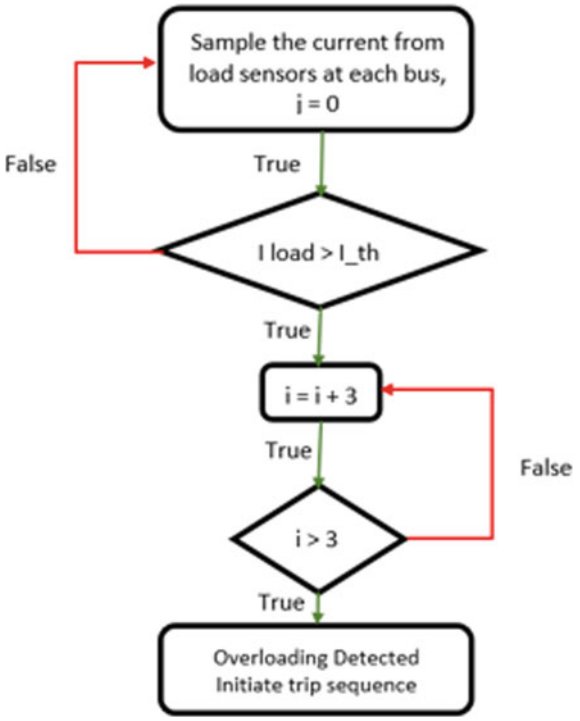

Fig. 10 Overloading condition protection

scheme combined with RF communication is adopted for the protection of the line to which various loads are connected at either end. The implementation procedure has three steps: monitoring the system, detection of fault or abnormal conditions, and classification of the fault and finally initiating the appropriate tripping sequence. The currents entering and leaving the transmission line were monitored using current sensors. The sampled analog signal was then converted into digital data by the ADC present in the signal processor. The current values at the either end of the transmission lines are communicated to a central control unit where the data is processed. The value of the currents is compared against each other and a threshold to determine the fault condition. Once the fault condition was identified, the microprocessor checks for consistency in the system currents and triggers the circuit breakers involved to isolate the fault.

Figure 12 shows the slope impedance protection algorithm implemented that includes the calculation of the impedance across the line between two busses. Based on the impedance calculated and the direction of the slope, this method can be used to detect, locate, and isolate the faults.

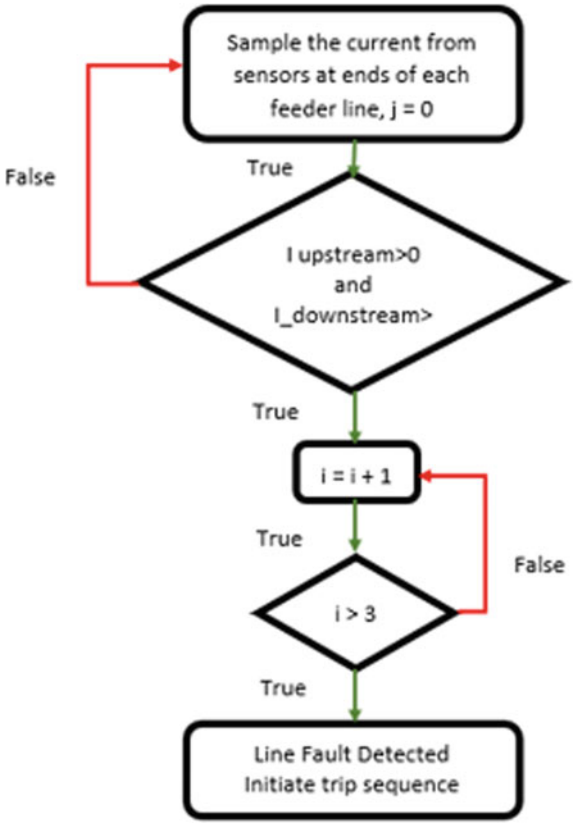

Fig. 11 Directional overcurrent line fault protection

4.4 Comparative Analysis of Protection Algorithm Performed

Table 2 shows the comparative analysis of the protections algorithms performed in the hardware-in-loop system developed using a mixed signal microprocessor. The protection schemes under consideration are as follows:

1. Overcurrent protection scheme,
2. Directional overcurrent protection scheme, and
3. Slope impedance method protection scheme.

Based on the results obtained, overcurrent and directional overcurrent protection can be chosen due to its effectiveness and simplicity. Overcurrent protection is used for detecting bus fault and overloading conditions at the local level. Directional overcurrent protection algorithm has been implanted at the remote control location for detecting line faults in the grid.

Thus, from the results obtained from protection algorithms implemented, overcurrent and directional overcurrent protection algorithms can be implemented on hardware systems.

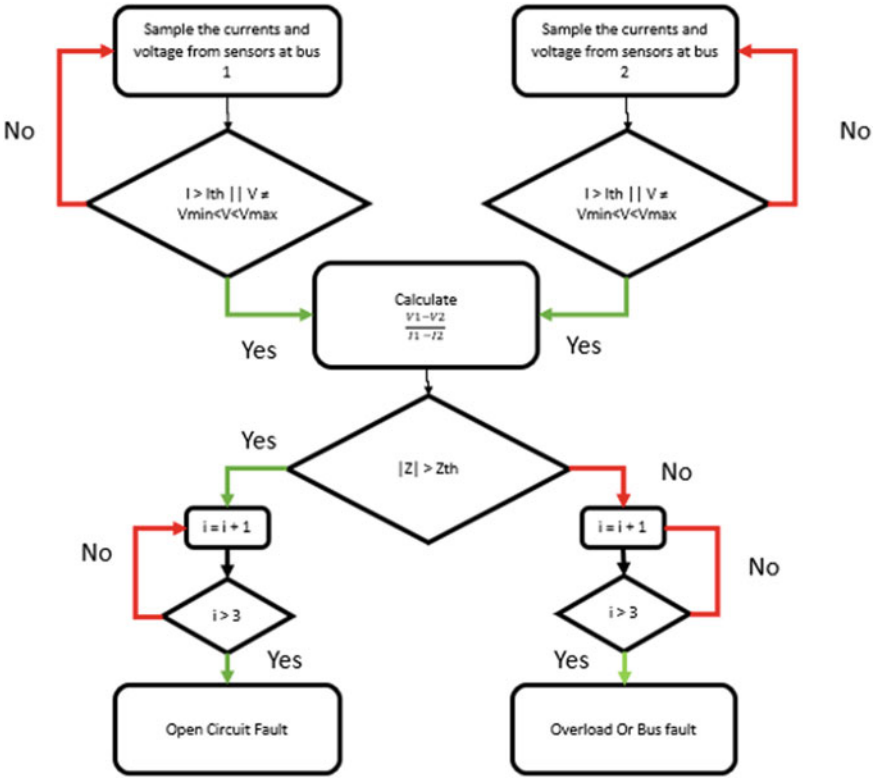

Fig. 12 Slope impedance protection algorithm

Table 2 Experimental results and comparative analysis

Protection algorithm name	Type of protection	Measuring parameters	Application	Detection and tripe signal time (five readings average) (ms)
Overcurrent	Local	Current	Fault	<10
Directional overcurrent	Central	Current and direction	Fault and location	50
Slope impedance	Central	Current, voltage, and direction	Fault, location, type of fault	12

5 Conclusion

This work focusses on design and simulation modeling of a 96 V DC using a Python script accompanied by load flow analysis, short-circuit study, and EMTP applications. Fault analysis has been carried out on the selected microgrid system and presented.

The results obtained for fault analysis are considered for the development of the relay co-ordination algorithm. The software simulation setup provides a suitable platform for the modeling, development, implementation, and testing of protection algorithms. Overcurrent protection, differential overcurrent protection, and slope impedance method were some of the protection algorithms developed and tested using the digitally simulated environment. The digital data computed by the EMTP application is converted into analog signals using DAC which are then fed as inputs to the relay processing unit. The response of the relay unit for different algorithms was observed.

This methodology for developing relay protection algorithm provides a suitable environment to test, modify and study multiple protective schemes, and finally choose the one which is best suited for the system under consideration.

References

1. Gimon E, O'Boyle M, Clack CTM, Mckee S (2019) The coal cost crossover: economic viability of existing coal compared to new local wind and solar resources. Vibrant Clean Energy Energy Innov Policy Technol
2. Smart grid: reinventing the electric power system. In: IEEE power and energy society (2012)
3. Lund H, Munster E (2006) Integrated energy systems and local energy markets. Energy Policy 34:1152–1160
4. Baran ME, Mahajan NRDC (2003) Distribution for industrial system: opportunities and challenges. IEEE Trans Ind Appl 39(6):1596–1601
5. Cuzner RM, Venkataramanan G (2008) The status of DC micro-grid protection. In IEEE industry applications society annual meeting, pp 1–8
6. Javed W, Chen D, Farrag ME, Xu Y (2019) System configuration, fault detection, location, isolation and restoration: a review on LVDC microgrid protections. Energies 12(6):1001. https://doi.org/10.3390/en12061001
7. Bayati N, Hajizadeh A, Soltani M (2018) Protection in DC microgrids: a comparative review. IET Smart Grid 1. https://doi.org/10.1049/iet-stg.2018.0035
8. Dommel HW (1969) Digital computer solution of electromagnetic transients in single- and multiphase networks. IEEE Trans Power Apparatus Syst 88(2):34–741
9. Martinez-Velasco JA., Elèctrica DDE (1998) Digital computation of electromagnetic transients in power systems: current status. IEEE PES Working Group, 15(09),1–1
10. Meyer WS, Liu TH (1987) Electromagnetic Transient Program Theory Book. Branch of System Engineering Bonneville Power Administration Portland, Oregon

A Case Study on Electric Vehicle Conversion from an Internal Combustion Engine Vehicle

Shopan Dey, Aniruddha Mukherjee, and Amit Soni

Abstract This paper discusses the conversion process of an internal combustion engine vehicle (ICEV) into an electric vehicle (EV). During the research, a 10 kW BLDC motor with a 400 A motor controller is used to replace the IC engine of a vehicle. The shaft of the electric motor is directly connected with the existing gearbox. So, the driver can use the existing gearbox with a foot throttle of an electronic speed controller. The foot throttle is connected with the motor controller. In this system, a 96 V/130 A lead–acid battery pack is used as the power source of the electric vehicle. An external 96 V/15 A charger is used to charge the onboard battery pack. During the conversion, an android-based digital dashboard system is developed to replace the existing vehicle dashboard. This digital dashboard collects real-time vehicle data like real-time data like car speed, rev, brake, battery voltage, current and power consumption, motor and controller temperature, and error from motor controller using the CAN port. Then, process the data and send it to an android device. And an android application is developed to show that real-time data into a GUI. The driver can also control the electrical peripherals of the vehicle from the android application. In this conversion process, a Maruti 800 car was successfully converted into an electrical vehicle.

Keywords Electric vehicle (EV) · Brushless DC motor (BLDC) · Electric dashboard · Electronics control unit (ECU)

1 Introduction

Due to high vehicular pollution, the electric vehicle is getting popular day by day. Lots of electric vehicles are invented for the high market demand. But, there is also a huge amount of conventional fuel vehicle are existed; these are needed to convert into

S. Dey · A. Mukherjee (✉)
University of Engineering and Management, Jaipur, Rajasthan, India
e-mail: mukherjeeanirudh73@gmail.com

A. Soni
Manipal University Jaipur, Jaipur, Rajasthan, India

© The Author(s), under exclusive license to Springer Nature Singapore Pte Ltd. 2022

A. Tripathi et al. (eds.), *Intelligent Computing Techniques for Smart Energy Systems*,
Lecture Notes in Electrical Engineering 862,
https://doi.org/10.1007/978-981-19-0252-9_2

an electric vehicle. The step-by-step conversion process is presented in this paper. There are also lots of research are available related to electric vehicle conversion but not the same. In a paper, Vražić et al. convert an internal combustion engine vehicle into an electric drive vehicle. And they have analyzed costs and benefits including conversion cost and running cost. They have also done a comparison between an EV and a diesel ICE vehicle [1]. Yiangkamolsing et al. done an electric Tuk-Tuk conversion in Thailand. During their research, they convert the Tuk-Tuk from internal combustion engine vehicle to an electric power vehicle. For the conversion process, they used a 5 kW electric motor and controller, 72 V 150 A LiFePo4 battery. As the result, they got maximum speed for the electric vehicle is 71 km/h. and maximum range of 110 km [2]. Kato et al. have done a quantitative analysis of eco-driving effect for EV with newly developed "Eco-driving test mode." Three ICEVs, two EVs, and one HEV were tested during the research. The eco-driving effects from an averaged drive as usual to average eco-driving in the eco-driving test ride were estimated. And the effects of 660 cc CTV ICEV, 1300 cc CVT ICEV, 1800 cc 4AT ICEV, 1500 cc HEV, EV type A, and EV type B were 12.0%, 12.2%, 10.9%, 12.6%, 18.4%, and 11.7%, respectively [3]. In another paper, Nikam and Fernandes developed a low-cost electric drive train. They converted an internal combustion engine vehicle into an electric vehicle. They replaced the IC engine with the electric motor and kept the existing gearbox and transmission as it is [4]. Pedrosa et al. done a case study on electric vehicle conversion. They present the conversion process of an internal combustion engine vehicle into an electric vehicle using a three-phase inverter [5]. Karki et al. converted a Maruti 800 into an electric vehicle for within cost of USD 6000. In their paper, they focus on the necessity of match and optimization parameters related to the required speed, road gradient, and diving range. And electric motor, drive, and battery pack should choose from the reference data mentioned above [6]. Another research was done by Fathabadi for the conversion of electric vehicles with clean and renewable energy. He proposed a conversion system with battery/PV/wind hybrid power source to be utilized in PHEVs [7]. Baghdadi et al. have done an electric vehicle performance and consumption evolution on two electric vehicles. One is an electric Peugeot iOn and an AGV electric version of the Ford Transit Connect. In the result, they got the observed driving range, and consumption from these tests is more realistic than the overestimated NEDC values and is very well in line with, e.g., more accurate US EPA values [8]. In a paper, Mansuri et al. present the feasibility of CO_2 emission reduction in Kota, India by replacing the present fossil fuel-based internal combustion engine vehicles with hydrogen-fueled fuel cell electric vehicles [9]. Sneha Angeline and Newlin Rajkumar discuss the impacts of electric vehicles on the environment. They focused on the charging infostructure for EVs [10]. In another paper, Ghorbani et al. present a study on the retrofit conversion of hybrid electric vehicles (HEVs) to plug-in HEVS (PHEVs) with powertrain system analysis toolkits (PSATs). They have also done some research on battery management strategies and got the result about improvement in fuel economy [11]. In a paper, García et al. investigated the potential of different online supervisory control strategies to operate a P2 parallel full hybrid electric vehicle equipped with an internal combustion engine running under dual-mode reactivity controlled compression ignition-conventional

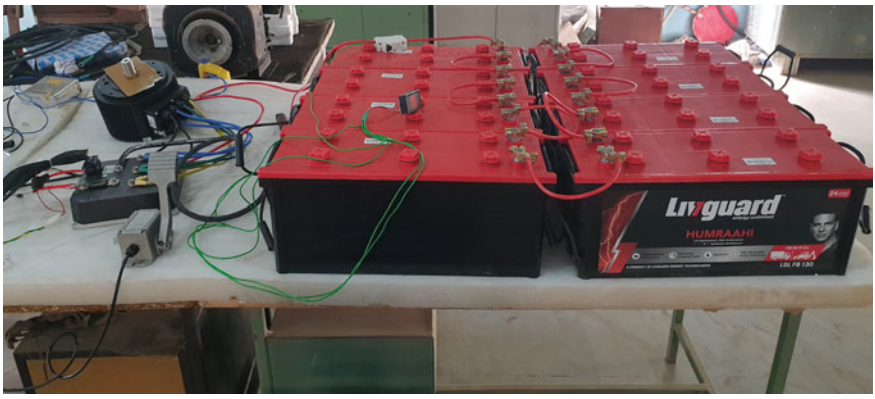

Fig. 1 Experimental setup for connection testing of electric car modules

diesel combustion strategy. Two case scenarios were analyzed: a fuel economy-oriented strategy and a nitrogen oxides emissions-oriented strategy [12]. Krawiec has researched the achievement of a fully electric bus fleet in a transit company. An outline of the decision support tool for the deployment of electric buses using the energy consumption model to calculate the total cost of ownership is presented in his paper [13]. In a paper, Liu et al. proposed an electric drive-reconstructed onboard converter for power factor improvement [14]. Another paper Praneeth et al. developed a universal onboard charger to charge the EV battery. The proposed charger is with household power sockets and can provide voltage range of 200–450, 48–72, and 96–150 V [15]. Janabi and Wang used a switched capacitor (SC) voltage boost converter for EV conversion [16]. In another paper pertaining to power conversion in EV a new technique was proposed. The proposed inverter has two parts: One is control part and other one power conversion part [17].

Based on the literature survey, in this paper, we present the step-by-step conversion process of an internal combustion engine vehicle to an electrical vehicle. In this conversion process, we select a used Maruti 800 to convert into electrical vehicle. We use a 10 kW BLCD motor, 96 V/400 A motor controller, and 12.48 kWh battery to replace the IC engine showed in Fig. 1. A linear variable resistance-based root throttle was suggested to replace the acceleration paddle. And a self-developed electronics control unit (ECU) alongside a digital dashboard for the old dashboard and ECU was also suggested. After the conversion, the EV is tested in the laboratory environment and on-road testing. And output result is closely observed.

2 Methodology and Setup

In our study, we select a Maruti 800 car to convert an electric vehicle from internal combustion engine vehicle as in Fig. 2a. We have done the conversion process in

Fig. 2 Different steps of EV conversion process. **a** Old Maruti 800, **b** removing of different engine parts, **c** motor and controller placement, **d** battery placement and charger

three steps: (1) Mechanical modification, (2) Insertion of electrical items, and (3) Android app development. During the first step, we remove all the engine parts except the engine block and crankshaft as in Fig. 2b. We also keep the gearbox and transmission system as it is. In the second step, we place the electric motor on the top of the engine block and connect the motor shaft and crankshaft with the belt. We use a 10 kW BLDC motor to drive the Maruti 800 car. We place the motor controller behind the motor and top of the engine block as in Fig. 2c. For the power source, we use eight 12 V 130 Ah lead–acid batteries in series. We place all the batteries in the back of the car as in Fig. 2d. And we replace the acceleration paddle with a foot throttle paddle. As we do not want to replace the gearbox and transmission system so clutch paddle, gear handle and braking system will remain same. To replace the old dashboard of Maruti 800, we develop an android-based digital dashboard and CAN-based EV electronics control unit (ECU) as in Fig. 3. ECU controls the motor controller and other electrical peripherals of the vehicle according to the user input.

In the final step, to display and receive the user input, an android application is developed. This application communicates with ECU through Bluetooth communication. A graphical user interface (GUI) is available in the android application to display real-time vehicle information, i.e., vehicle speed, battery voltage, battery current, power, consume energy, electricity costing, motor and controller temperature, battery label, and error. We develop this application on android studio with Java programming language. This application uses mobile Bluetooth to communicate with ECU. After connection establishment, it sends the data request to ECU.

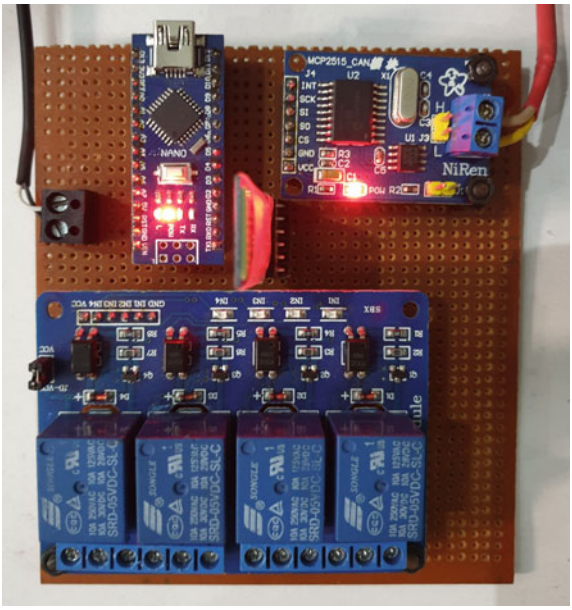

Fig. 3 Electronic control unit (ECU) of android-based digital dashboard for electric car

Then, ECU sends the raw data to the android application. Finally, android application processes the data and show it on GUI. The developed android application worked as touch dashboard and accept the user interaction then send it to ECU.

There is also a different button to control the electrical peripherals of the car, shown in Fig. 4a. Android dashboard application communicates with ECU through Bluetooth, and ECU communicates with the motor controller the switching relay board through CAN port.

3 Results and Discussion

Once completing the setup, the electric car can be powered on by the ignition key. Then, ECU will turn on the main power contactor for battery supply. The next step is to open the android application (My CAR) and connect the android device with the electric car through Bluetooth. After completing the connection establishment, all vehicle information will be visible on the android device like Fig. 4a. The other screenshot of android dashboard is presented on Fig. 4. This electric car can be drive as same as old fuel car. This electric car is tested on both controlled environment and on-road testing. In both testing, it has performed well. Maximum 70 km/h speed and 100 km electric range are achieved during the testing. The ECU also performed very well on it testing. All the features like low battery speed limit, critical battery shutdown, and over temperature power limit have performed smoothly on different power and temperature condition.

Fig. 4 Screenshot of android application: **a** Dashboard, **b** electricity costing, **c** battery consumption, **d** motor speed

4 Conclusion

The step-by-step process of electric vehicle conversion from an internal combustion engine vehicle was presented in this paper. During this process, a Maruti 800 card was successfully converted into an electric vehicle and observed the different parameters on indoor and on-road testing. For the electric vehicle conversion, the existing gearbox and transmission system keep as it is. For the EV conversion, 10 kW BLDC motor, 96 V/400 A motor controller, and 9.6 kW/h lead–acid battery are used. An EV controller was also developed for the digital dashboard of electric vehicle. Using this dashboard, user can monitor all the real-time vehicle information on an android device. Users can also control the electrical peripherals from this dashboard. The EV controller also has an on-board diagnostic (OBD) system to check real-time information and error. The mentioned controller is tested on EV in different power conditions also. The converted electric vehicle has few useful features like a regenerative braking system, cruise speed controller, low battery speed limit, and critical battery shutdown.

References

1. Vražić M, Vuljaj D, Pavasović A, Pauković H (2014) Study of a vehicle conversion from internal combustion engine to electric drive. In: 2014 IEEE international energy conference (ENERGYCON), pp 1544–1548. https://doi.org/10.1109/ENERGYCON.2014.6850628
2. Yiangkamolsing C, Laoonual Y, Channarong S, Katikawong W, Sasawat P, Yaotanee B (2019) A development of electric Tuk Tuk conversion in Thailand. In: 2019 IEEE transportation

electrification conference and expo, Asia-Pacific (ITEC Asia-Pacific), pp 1–8. https://doi.org/10.1109/ITEC-AP.2019.8903895
3. Kato H, Ando R, Kondo Y, Suzuki T, Matsuhashi K, Kobayashi S (2013) Comparative measurements of the eco-driving effect between electric and internal combustion engine vehicles. In: 2013 World electric vehicle symposium and exhibition (EVS27), pp 1–5. https://doi.org/10.1109/EVS.2013.6914843
4. Nikam SP, Fernandes BG (2014) Low cost electric drivetrain for conversion of ICE vehicle into an electric vehicle. In: 2014 IEEE international conference on power electronics, drives and energy systems (PEDES), pp 1–4. https://doi.org/10.1109/PEDES.2014.7042131
5. Pedrosa D, Monteiro V, Goncalves H, Martins JS, Afonso JL (2014) A case study on the conversion of an internal combustion engine vehicle into an electric vehicle. IEEE Veh Power Propul Conf (VPPC) 2014:1–5. https://doi.org/10.1109/VPPC.2014.7006994
6. Karki A, Shrestha BP, Tuladhar D, Basnet S, Phuyal S, Baral B (2019) Parameters matching for electric vehicle conversion. In: 2019 IEEE transportation electrification conference (ITEC-India), pp 1–5. https://doi.org/10.1109/ITEC-India48457.2019.ITECINDIA2019-133
7. Fathabadi H (2018) Plug-in hybrid electric vehicles: replacing internal combustion engine with clean and renewable energy based auxiliary power sources. IEEE Trans Power Electron 33(11):9611–9618. https://doi.org/10.1109/TPEL.2018.2797250
8. Baghdadi ME, De Vroey L, Coosemans T, Van Mierlo J, Foubert W, Jahn R (2013) Electric vehicle performance and consumption evaluation. In: 2013 World electric vehicle symposium and exhibition (EVS27), pp 1–8. https://doi.org/10.1109/EVS.2013.6914988
9. Mansuri MF, Saxena BK, Mishra S (2020) Shifting from carbon to hydrogen economy: a case study of Rajasthan state in India. In: 2020 international conference on computational intelligence for smart power system and sustainable energy (CISPSSE), pp 1–6. https://doi.org/10.1109/CISPSSE49931.2020.9212292
10. Sneha Angeline PM, Newlin Rajkumar M (2020) Evolution of electric vehicle and its future scope. Mater Today Proc 33(7):3930–3936. https://doi.org/10.1016/j.matpr.2020.06.266
11. Ghorbani R, Bibeau E, Filizadeh S (2010) On conversion of hybrid electric vehicles to plug-in. IEEE Trans Veh Technol 59(4):2016–2020. https://doi.org/10.1109/TVT.2010.2041563
12. García A, Carlucci P, Monsalve-Serrano J, Valletta A, Martínez-Boggio S (2020) Energy management strategies comparison for a parallel full hybrid electric vehicle using reactivity controlled compression ignition combustion. Appl Energy 272:115191. https://doi.org/10.1016/j.apenergy.2020.115191
13. Krawiec K (2020) A concept of conventional or mixed bus fleet conversion with electric vehicles a planning process. Int J Electr Electron Eng Telecommun 9(1)
14. Liu S, Xin D, Yang L (2020) A novel single-phase bidirectional electric-drive-reconstructed on-board converter for electric vehicles. IEEE Access 8:44739–44747. https://doi.org/10.1109/ACCESS.2020.2970201
15. Praneeth AVJS, Vincent D, Williamson SS (2019) An universal on-board battery charger with wide output voltage range for electric transportation. IEEE Energy Convers Congr Exposition (ECCE) 2019:1159–1165. https://doi.org/10.1109/ECCE.2019.8912749
16. Janabi A, Wang B (2020) Switched-capacitor voltage boost converter for electric and hybrid electric vehicle drives. IEEE Trans Power Electron 35(6):5615–5624. https://doi.org/10.1109/TPEL.2019.2949574
17. Bindu R, Patil S, Thale S (2017) Design and control of power conversion system for electric vehicle application. In: 2017 international conference on technological advancements in power and energy (TAP Energy), pp 1–6. https://doi.org/10.1109/TAPENERGY.2017.8397264

Image Processing Using Elephant Herding Optimization: A Review

Vishnu Soni, Abhay Sharma, and Jitendra Rajpurohit

Abstract Nature-inspired algorithms (NIAs) are very well defined for intuitive image processing operations. Among various nature-inspired algorithms, elephant herding optimization (EHO) is most preferably used as its application in image segmentation due to its high accuracy, efficient and optimized output, optimal to high speed, excellent performance, and ability of solve multi-objective optimization problems. This paper presents a review of various articles on EHO for image segmentation. For this purpose, recent development in the field of image segmentation and optimized results has been studied, and their outcomes have been presented. Image segmentation, edge-based segmentation, thresholding, region-based segmentation, and morphological segmentation by mean of EHO are studied and presented with optimized outcomes.

Keywords Image segmentation · EHO · NIA · Thresholding · Morphology · Optimization

1 Introduction

Image segmentation [1] is a process of subdividing any image into its constituent regions and/or objects. Segmentation is characteristically accomplished to establish object regions and boundaries [2]. It is based on two basic NIA [3] characteristics of intensity values, i.e., discontinuity and similarity. In the discontinuity (boundary approach), the hasty transforms in gray-level image [4] is completed on separation basis, while in the similarity (region approach), the separation is completed on identical or consistent region basis. The process is classified into local segmentation

V. Soni (✉) · A. Sharma
Amity University Rajasthan, Jaipur, India
e-mail: vishnusoni2221991@gmail.com

J. Rajpurohit
University of Petroleum and Energy Studies, Dehradun, India

© The Author(s), under exclusive license to Springer Nature Singapore Pte Ltd. 2022

A. Tripathi et al. (eds.), *Intelligent Computing Techniques for Smart Energy Systems*,
Lecture Notes in Electrical Engineering 862,
https://doi.org/10.1007/978-981-19-0252-9_3

process [5] and global segmentation process [6]. The local segmentation is accomplished with some specified region of given image, while the global segmentation is accomplished with large pixel of complete image.

Edge-based segmentation: In image segmentation, three primary gray discontinuities are presented, which are defined as edge-based segmentation [7]. It includes point detection, line detection, and edge detection. Let's consider response of mask is given as

$$R = W_1 Z_1 + W_2 Z_2 + W_3 Z_3 + W_4 Z_4 + \cdots + W_n Z_n \tag{1}$$

$$R = \sum_{i=1}^{n} W_i Z_i \tag{2}$$

W is the coefficients of $m \times n$ filter, and Z is pixel of image filter.

$W(-1, -1)$	$W(-1, 0)$	$W(-1, 1)$
$W(0, -1)$	$W(0, 0)$	$W(0, 1)$
$W(1, -1)$	$W(1, 0)$	$W(1, -1)$

Point can be detected when mask is centered; line detection is similar to point detection by keeping mask at horizontal, and in the edge detection, digital derivatives [8] of first and second order implementation approach are used.

Thresholding: Thresholding [9] is a point of critical line defined as T. After deciding the value of T, image is divided into two gray-level image is called thresholding. Thresholding is given as

$$g(x, y) = \begin{cases} 1, \text{ if } f(x, y) > T \\ 0, \text{ if } f(x, y) \leq T \end{cases} \tag{3}$$

Basic global, basic adaptive and optimal global, and adaptive thresholding [10] are various classes of thresholding which can be used according to required segmentation.

Region-based segmentation: This approach is used to grow "seed points" [11] or to grow regions be mean of appending each seed of neighborhood pixels similar to seed point. Image splitting and merging [12] as part of image growing provide more sharp images as compared to thresholding. Various region growing algorithms like unseeded region growing (USRG), mean shift algorithm (MSA), and fast scanning algorithm (FSA) can be performed to obtain region-based segmentation [13].

Morphological segmentation: Morphological segmentation [14] is a process of segmenting any size of grayscale image. Number of morphological operations can be performed to improve the outcomes of fast scanning algorithm. It includes erosion

(subtracting), dilation (adding or combining), thinning, opening (dilation of the erosion), and closing (erosion of the dilation) operations [15].

2 Elephant Herding Optimization

One of the most utilized nature-inspired algorithm for segmenting, restoring, and optimization [16] is known as elephant herding optimization (EHO) algorithm. EHO was proposed by Wang [17] to solve real-life problems and providing their optimal solutions. It is basically a metaheuristic search method [18], works under the herding behavior of elephant's group and predicts the state-of-the-art approach in high-level segmentation. EHO is used to model by mean of two operators: the *Clan updating operator* and the *separation operator* [19]. Variety of key constraints like localization error, complexity analysis, continuous optimization, root mean square error (RMSE), combinatorial optimization, discrepancy between source position and fittest point, constrained optimization, convergence rate and multi-objective optimization can be tested by mean of EHO algorithm [20] (Fig. 1).

The concept behind elephant herding is the herding nature of male elephants. When they are calves, they love to live with their family and female elephants, but as they turned into young, they leave their family and tend to live some other places.

Flow graph of elephant herding optimization algorithm: Among the two operators (clan update and separation operator), the population iteration, maximum population, and fittest points [21] are used in terms of algorithm flow graph. It indicates the optimized outcomes by mean of EHO (Fig. 2).

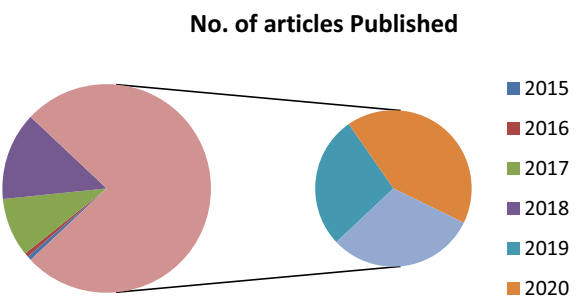

Fig. 1 EHO popularity among researchers

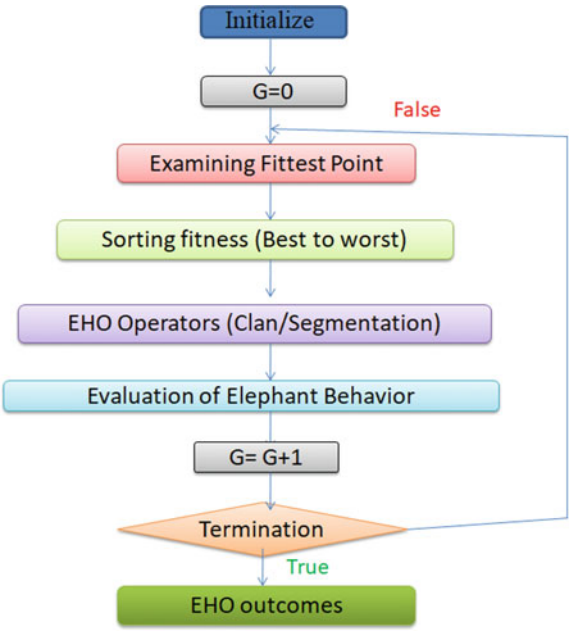

Fig. 2 EHO algorithm flow graph

3 Image Segmentation Using Elephant Herding Optimization Algorithm

Review Articles

Xu et al. proposed feature selection by mean of improved elephant herding optimization (IEHO). It was proposed to reduce the running time while maintaining the classification accuracy. It significantly outperforms the efficiency and sensitivity in optimized manner [22].

Tuba et al. used "*Kapur and Otsu's criteria*" to provide a solution of multilevel image thresholding problem. They concluded and successfully provided a solution to multilevel thresholding problems by mean of small variance value [23].

Avudaiappan et al. used medical images by mean of dual encryption procedure. They utilized the local and global parameters. The performance of the proposed algorithm was measured in terms of mean square error (MSE), peak signal-to-noise ratio (PSNR), and correlation coefficient (CC) [24].

Chibani et al. proposed EHO to explain Web service composition by mean of quality of services. They offered excellent performances by mean of convergence speed, scalability, and fitness evaluations [25].

Jino et al. offered image processing techniques including image segmentation by using various nature-inspired algorithms (NIAs) like EHO, BA, FA, and PSO. They summarized and presented their different values and accuracy levels [26].

Shankar et al. identified EHO algorithm as an image safety during segmentation. It was optimized by means of hybrid optimization technique. The confidentiality level of the received segmented image was eventually increased [27].

Tahani et al. proposed a combined technique for optimization of outcomes of vertical axis wind turbine connected with straight blades by mean of flower pollination algorithm (FPA), gray wolf optimizer (GWO), and EHO algorithm [28].

Jayanth et al. proposed multispectral image classification along with spatial resolution by mean of EHO algorithm. Fitness function, accuracy, convergence were observed for multi-spectral pixel by use of SVM method [29].

Elhosseini et al. proposed different class of EHO algorithm to show the effect of controlled parameters. Benchmark to verify the performance proposed different classes of benchmark functions was used [30].

Cardoso et al. proposed maximum correlation point implementation using EHO to improve search process. They concluded that proposed NIA performance is best as compare to PSO and ES [31].

Sathesh Kumar et al. proposed distinctive encryption strategies by means of security model. Different encryption techniques were used to store sensitive data to cloud server [32].

Juan Li et al. used EHO by mean of clan operator. An inclusive assessment has been presented by them. They provide a solution to various image segmentation problems. Subsequent attribute has been proposed in this article [33].

Metkar identified an essential attribute by mean of EHO. Segmentation algorithm is classified by mean of gloom (gray texture of an image). She presented different segmentation algorithms and concluded that quadtree and merger algorithms are essentially used for segmented images [34].

Outcomes of muscle fiber image by mean of EHO are presented in Fig. 3. It indicates that edge-based segmentation, thresholding, region-based segmentation, and morphological segmentation of a muscle fiber image are obtained and optimized by mean of EHO [35].

By using EHO, accuracy and sensitivity are measured for the various segmentation as mentioned above which is presented in Table 1.

With these above mentioned outcomes, a graph is plotted indicating accuracy and sensitivity for image segmentation of muscle fiber image by use of EHO. It is shown in Fig. 4.

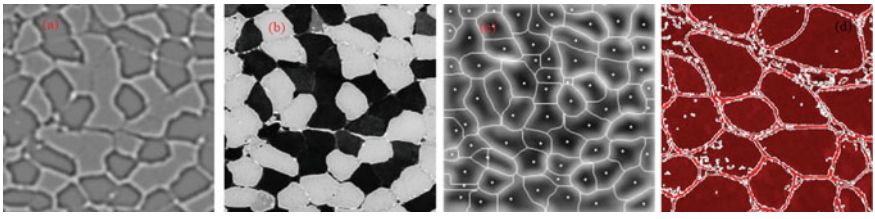

Fig. 3 Muscle fiber image, **a** edge-based segmentation, **b** thresholding, **c** region-based segmentation, **d** morphological segmentation

Table 1 Accuracy and sensitivity obtained by mean of EHO

Image segmentation process	Accuracy	Sensitivity
Edge-based segmentation	95.73	98.22
Thresholding	96.66	98.37
Region-based segmentation	97.60	98.57
Morphological segmentation	98.37	99.12

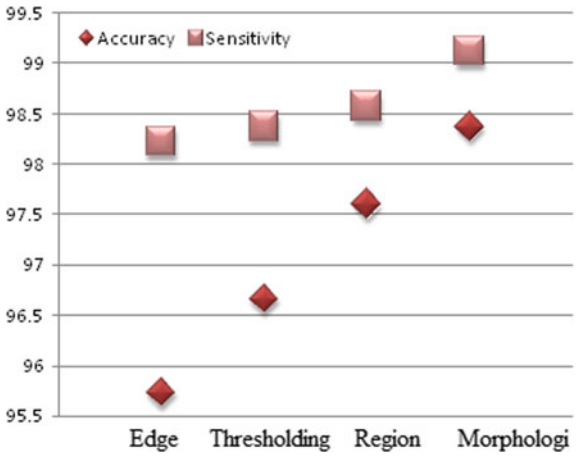

Fig. 4 Variation of accuracy and sensitivity by use of EHO

4 Conclusion

Nature-inspired algorithms are showing significant role in the field of image processing and imaging. Image segmentation is also showing importance in medical imaging. Here, in this paper, image segmentation and its classifications by mean of elephant herding optimization algorithm are proposed to optimize the outcomes. This metaheuristic search method is based on herding behavior of elephants. The *clan updating operator* and the *separation operator* are used to optimize segmentation outcomes. The clan updating operator sets the value of a field to current date, either as a date or a timestamp, while a separator is one or two tokens that separate some features from other features; muscle fiber images are segmented by mean of edge-based segmentation, thresholding, region-based segmentation, and morphological segmentation. After successful implementation of presented algorithm, the accuracy and sensitivity are optimized as 98.37 and 99.12, respectively, for morphological segmentation. Finally, it is concluded that by using EHO, image segmentation is optimized, and in future, this can be used for segmentation and identification of various cancers like breast, lung, and cervical cancer.

Acknowledgements I would like to thank all the direct and indirect resources for this work.

Conflict of Interest Author declares No conflict of interest for this manuscript.

References

1. Sharma A, Chaturvedi R, Bhargava A (2022) A novel opposition based improved firefly algorithm for multilevel image segmentation. Multimedia Tools Appl 1–24
2. Ghamisi P, Couceiro MS, Martins FM, Benediktsson JA (2013) Multilevel image segmentation based on fractional-order Darwinian particle swarm optimization. IEEE Trans Geosci Remote Sens 52(5):2382–2394
3. Horng MH (2011) Multilevel thresholding selection based on the artificial bee colony algorithm for image segmentation. Expert Syst Appl 38(11):13785–13791
4. Tuba E, Alihodzic A, Tuba M (2017) Multilevel image thresholding using elephant herding optimization algorithm. In: Proceedings of the 2017 14th international conference on engineering of modern electric systems (EMES), Oradea, Romania
5. Felzenszwalb PF, Huttenlocher DP (1998, June) Image segmentation using local variation. In: Proceedings 1998 IEEE computer society conference on computer vision and pattern recognition (Cat. No. 98CB36231) (pp 98–104), IEEE
6. Wang X, Tang Y, Masnou S, Chen L (2015) A global/local affinity graph for image segmentation. IEEE Trans Image Process 24(4):1399–1411
7. Farag AA (1992) Edge-based image segmentation. Remote Sens Rev 6(1):95–121
8. Brejl M, Sonka M (2000) Object localization and border detection criteria design in edge-based image segmentation: automated learning from examples. IEEE Trans Med imaging 19(10):973–985
9. Sharma A, Chaturvedi R, Kumar S, Dwivedi UK (2020) Multi-level image thresholding based on Kapur and Tsallis entropy using firefly algorithm. J Interdisc Math 23(2):563–571
10. Cheriet M, Said JN, Suen CY (1998) A recursive thresholding technique for image segmentation. IEEE Trans Image Process 7(6):918–921
11. Gould S, Gao T, Koller D (2009) Region-based segmentation and object detection. Adv Neural Inf Process Syst 22
12. Soni V et al (2021) A critical review on nature inspired optimization algorithms. IOP Conf Ser Mater Sci Eng 1099:012055
13. Xiansheng C (2011) An edge detection new algorithm based on Laplacian operator. In: IEEE library 2011
14. Anand A, Tripathy SS, Sukesh Kumar R (2015) An improved edge detection using morphological Laplacian of Gaussian operator. In: 2nd international conference on signal processing and integrated networks (SPIN)
15. DHIEB M, FRIKHA M (2016) A multilevel thresholding algorithm for image segmentation based on particle swarm optimization. In: IEEE library 2016
16. Li J, Lei H, Alavi AH, Wang GG (2020) Elephant herding optimization: variants, hybrids, and applications. Math 8(9):1415
17. Wang GG, Deb S, Coelho LDS (2015, December) Elephant herding optimization. In: 2015 3rd international symposium on computational and business intelligence (ISCBI) (pp 1–5), IEEE
18. Elhosseini MA, El Sehiemy RA, Rashwan YI, Gao XZ (2019) On the performance improvement of elephant herding optimization algorithm. Knowl-Based Syst 166:58–70
19. Li W, Wang GG, Alavi AH (2020) Learning-based elephant herding optimization algorithm for solving numerical optimization problems. Knowl-Based Syst 195:105675
20. Li J, Lei H, Alavi AH, Wang GG (2020) Elephant herding optimization: variants, hybrids, and applications. Mathematics 8(9):1415
21. Almufti S, Asaad R, Salim B (2018) Review on elephant herding optimization algorithm performance in solving optimization problems. Int J Eng Technol 7:6109–6114
22. Xu H, Cao Q, Fu H, Chen H (2019) Applying an improved elephant herding optimization algorithm with spark-based parallelization to feature selection for intrusion detection. Int J Performability Eng 15(6):1600
23. Tuba M (2014) Multilevel image thresholding by nature-inspired algorithms: A short review. Comput Sci J Moldova 66(3):318–338

24. Avudaiappan T, Balasubramanian R, Pandiyan SS, Saravanan M, Lakshmanaprabu SK, Shankar K (2018) Medical image security using dual encryption with oppositional based optimization algorithm. J Med Syst 42(11):1–11
25. Chibani SS, Tari A (2017) Elephant herding optimization for service selection in qos-aware web service composition. Int J Comput Inform Eng 11(10):1124–1128
26. Jino Ramson SR, Lova Raju K, Vishnu S, Anagnostopoulos T (2019) Nature inspired optimization techniques for image processing—A short review. Nat Inspired Optim Technol Image Process Appl 113–145
27. Shankar K, Elhoseny M, Perumal E, Ilayaraja M, Sathesh Kumar K (2019) An efficient image encryption scheme based on signcryption technique with adaptive elephant herding optimization. In: cybersecurity and secure information systems (pp 31–42). Springer, Cham
28. Tahani M, Babayan N, Mehrnia S, Shadmehri M (2016) A novel heuristic method for optimization of straight blade vertical axis wind turbine. Energy Convers Manage 127:461–476
29. Jayanth J, Shalini VS, Ashok Kumar T, Koliwad S (2019) Land-use/land-cover classification using elephant herding algorithm. J Indian Soc Remote Sens 47(2):223–232
30. Elhosseini MA, El Sehiemy RA, Rashwan YI, Gao XZ (2019) On the performance improvement of elephant herding optimization algorithm. Know-Based Syst 166:58–70
31. de Vasconcelos Cardoso A, Nedjah N, de Macedo Mourelle L, Tavares YM (2018, February) Co-design system for template matching using dedicated co-processor and modified elephant herding optimization. In: 2018 IEEE 9th latin american symposium on circuits & systems (LASCAS) (pp 1–4), IEEE
32. Kumar S, Velliangiri S, Karthikeyan P, Kumari S, Kumar S, Khan MK (2021) A survey on the blockchain techniques for the Internet of Vehicles security. Trans Emerg Telecommun Technol e4317
33. Li J, Lei H, Alavi AH, Wang GG (2020) Elephant herding optimization: variants, hybrids, and applications. Math 8(9):1415
34. Metkar A, Maroo M, Sawant A, Singh V, Mhatre S (2020, April) Hardware implementation of image processing algorithms on FPGA. In: Proceedings of the 3rd international conference on advances in science & technology (ICAST)
35. Standard test images. http://www.imageprocessingplace.com/rootfilesV3/imagedatabases.htm. Accessed 5 May 2017

A Review on IoT-Based Efficient Energy Management System for Smart Homes

Ganesh Shirsat, Aniruddha Mukherjee, and Amit Soni

Abstract Electrical energy demand dramatically increases in quickly developing world population. In smart cities, Internet of Things (IoT) is implemented with smart devices which will be incorporated into smart homes and effectively take an interest in power market through demand response (DR) programs for efficient management of electrical energy to fulfill this expanding energy need. In terms of cost of electricity, energy consumption, and peak average ratio (PAR), a price-based DR program for energy management strategy, buildings genetic algorithm (GA), binary particle swarm optimization (BPSO) algorithm, genetic binary particle swarm optimization (GBPSO) algorithm, and genetic wind driven optimization (GWDO) algorithm has been developed for IoT-enabled smart homes. In this context, we interested to develop combination of genetic and gravitational search algorithm method for managing the energy use of IoT-enabled smart equipment in smart homes by scheduling PAR, which lowers power costs and improves user comfort (UC). This will improve the efficiency and long-term viability of IoT-enabled smart homes.

Keywords Internet of Things · Energy management · Smart homes · Smart devices · Demand response programs

1 Introduction

With a populace of 1.3 billion, India is the second most crowded country and the third biggest economy, estimated by purchasing power equality (PPP). India has seen solid financial execution in ongoing many years, empowering a critical abatement in destitution levels, more prominent energy access for its residents, and developing entrance of cleaner energy across the economy. India has set an objective development pace of 9%, which would put it on a direction toward turning into a USD 5 trillion economy by 2024–2025, making it the quickest developing economy on the planet. India's supported monetary development is putting a colossal interest on

G. Shirsat · A. Mukherjee (✉) · A. Soni
University of Engineering and Management, Jaipur, Rajasthan, India
e-mail: mukherjeeanirudh73@gmail.com

© The Author(s), under exclusive license to Springer Nature Singapore Pte Ltd. 2022

A. Tripathi et al. (eds.), *Intelligent Computing Techniques for Smart Energy Systems*,
Lecture Notes in Electrical Engineering 862,
https://doi.org/10.1007/978-981-19-0252-9_4

its energy assets, energy frameworks, and foundation. Population density is high through the vast majority of the country, with the exemptions of the deserts in the west and the Himalayan Mountains in the north. Around 45% of the land region is agrarian, and more than 24% is forest. 66% of the populace lives in provincial zones. Notwithstanding, the urban areas are developing quickly, and the urbanization rate is around 2.4% of each year [1]. Over the previous many years, energy demand has consistently expanded across all areas, including farming, industry, business and residential, and is required to keep on developing. Regardless, India's per capita energy utilization remains at 30% of the normal worldwide.

DR programs are the SGs' major initiatives that provide incentives that encourage customers to take part in the energy market by using advanced metering equipment. There are two types of DR programs: (a) price-based DR programs and (b) incentive-based DR programs. Distribution system operators (DSOs) are agents with Internet of Things capabilities who may operate consumer devices remotely when it is required with minimal warning in the incentive-based manner. Price-based incentives allow IoT-enabled consumers to control their power use on their own in the price-based technique [1, 2]. The residential buildings utilize more than 80% of total energy; price-based DR program method is a critical programed that delivers positive outcomes for both DSOs and customers while undertaking energy management.

A pragmatic optimization model is figured for effective energy management in the execution of private structure by energy utilization scheduling of IoT-empowered appliances using advanced metering and diverse DR programs like day ahead valuing plan (DAPS), time of use pricing schemes (ToUPS) and real time pricing scheme (RTPS) of the smart grid [3].

In this study, in addition to PAR and electricity cost, the user comfort (UC) in terms of delay is estimated and examined in order to address the energy management issue by power use management of smart home devices utilizing DR programs in an IoT-enabled system of smart homes.

2 Related Work or Methodology

2.1 Optimization Techniques

A lot of work to satisfy increased energy need in smart grid for energy has been completed. This is arranged into following types:

2.1.1 Mathematical Models-Based Energy Management

A programmed and ideal private energy utilization scheduling strategy which attempts to accomplish a good compromise between limiting the energy costs just as the burden for the activity of both electrical and thermal in a smart home is produced

for effective energy management [4]. The proposed scheduling technique prompts huge decrease in energy costs for assorted burden situations with the power demand from the grid.

The emerging mixed integer nonlinear optimization issue is settled in Reference [5], while data are refreshed in an iterative manner for the duration of the day to follow the changes in the expected price signals and the variations in the controller inputs. The outcomes from various reasonable contextual investigations show the adequacy of the proposed controller in limiting the consumer's day by day power bill while safeguarding solace level, as well as preventing future least-price peaks from forming.

2.1.2 Metaheuristic and Heuristic-Based Energy Management Methods

The focal controller operates on teh principle of particle swarm optimization (PSO) to optimize the up to require temperature of TCLs based on open air natural data and customer preferences [6]. The interior temperature required for human environment was calculated using the fuzzy controller.

The advancement model was developed using a genetic algorithm. With client behavior learning, a price enhancement model has been developed for customer benefit augmentation in Ref. [7]. Then again, battery activity advancement under powerful estimating plans has been done in Ref. [8]. The effects of value estimate mistake and smart grid limits have been investigated experimentally based on actual data from Spain's electricity industry.

The primary benefits of metaheuristic procedures are their ease of use, their ability to handle non-direct or irregular goals and limits, and their ability to handle high-computational complicated challenges. However, one of the drawbacks of using metaheuristic algorithms is that they can meet rashly and stall out in the near future, especially for complex problems. For problems with a large number of variables, these approaches are time-consuming.

2.1.3 Artificial Intelligence-Based Energy Management Methods

To reduce the energy consumption of TCLs in smart homes while considering demand response, a reinforcement learning approach was used [9]. The reinforcement learning-based unique estimation energy utilization algorithm has been proposed in refereed paper [10]. Clients have used the post-decision state (PDS) learning algorithm to learn the difference in retail prices and make informed decisions. In addition, reinforcement learning was used to familiarize the client with their displeasure [11].

Artificial intelligence has the ability to operate with incomplete data, parallel processing, learning, pattern recognition, and dealing with nonlinear functions. It, too, encounters certain roadblocks. To run AI models, you will need equipment with a lot of processing power. It is solely capable of working with numbers. The approval and confirmation of the AI model necessitate a wide range of tests.

2.1.4 Hybrid Method-Based Energy Management

The authors use price-based DR programs to schedule thermostatically controlled, uninterruptible, and interruptible smart home loads using the binary particle swarm optimization (BPSO) algorithm and integer linear programming (ILP) [12]. The researchers' main goal is to reduce the expense as well as the discomfort. The cost of power is reduced at the expense of increased PAR, disrupting the power system's stability.

3 Problem Statement and Formulation of Energy Management

3.1 Problem Identification

Energy management in smart home by power usage is challenging due to nonlinear and random behavior of users. As a result, energy management in a smart home with the help of scheduling smart appliances is regarded in terms of power usage.

Efficient energy management system for smart home lies under the umbrella of demand side management; it permits consumers to regulate and deal with the minimum utilization of power to minimize their electricity bills. In recent days, power utilization is around 30% of the worldwide energy utilization [13]. As per the US private energy consumption review, an investigation led in [6] shows that 15% of energy consumption reduced by scheduling the appliances of smart homes. Because home customers are more concerned about their energy bills as well as their comfort, energy advancement through a variety of approaches and creative use of electricity is necessary. Hence, the electricity utilization awareness and scheduling the load alone have capacity to minimize the consumption by 15% in smart homes.

Other regular dynamic tactics include stimulated annealing, genetic algorithm, and genetic annealing methods that using genetic and temperature as the main rules for scheduling smart home appliances. Swarm-based algorithms, on the other end, are flexible, stochastic, intelligent, de-incorporated, and non-traditional in structure.

The scheduling of loads is done in such a way that the execution time, reaction time, and overall cost of consumption are reduced. The load of smart houses is scheduled using swarm optimization-based metaheuristic methods. A swarm is a group of things that includes ants, molecules, honey bees, and other insects. It describes how a swarm of particles locates a food hotspot and schedules the responsibility of the load. Particle swarm optimization, genetic algorithms, and gravitational search algorithms are all effective load scheduling methods that work on the concepts of genes in chromosomes, Newton's law of gravitational attraction and velocity, respectively [14]. These standards enable in the determination of the next suitable particle for the load. In terms of processing time and cost, the gravitational search algorithm is perhaps the best optimization tool for load scheduling than PSO.

To identify the next best fit location of the load in smart homes, the combination of genetic and gravitational search algorithm combines the talents of both hereditary and gravitational search algorithms. This may be done utilizing a hybrid approach, mutation, preserving the best locations, novel cost estimation, and a recollection idea in a gravitational search algorithm. The objective of this method is to lower the total cost of usage for smart home devices.

4 Proposed Energy Management Model

The suggested energy management system's aim is to manage and analyze the energy usage of smart home appliances in order to control energy utilizing demand response programs without human interaction. The followings are the goals of the proposed energy management system:

- Effective energy utilization
- Electricity cost minimization
- UC maximization
- PAR alleviation

These objectives are achieved through the use of algorithms based on a combination of genetic and gravitational search energy management controller (EMC), which organizes electricity usage of smart home appliances in the smart grid using price-based demand response programs, resulting in efficient energy utilization in the IoT-enabled environment. This section explains the planned project. The proposed work consists of IoT-enabled DSOs that use enhanced SG metering. Home gateway, EMC, smart appliances, smart meter, indoor display, remote control, and wireless home area network are all included in the smart house. Smart appliances such as power adjustable devices, essential devices, and time adjustable devices are included in this study's smart home. The rated power of the gadgets with customizable power is flexible, and they follow a timetable set in stone. The IoT-enabled EMC is used in smart homes and is programmed to react to DR price indications in real time, overcoming the constraint of consumers' lack of understanding, which is a barrier to DR program implementation. The used EMC integrated with IoT accepts price-based DR programs, smart gadgets power rating, duration of time operation, and in the presence of target function and restrictions, available power grid energy as inputs to plan power use of smart homes smart devices. The IoT-enabled EMC in a smart homes can connect with smart devices via a variety of communication links like HomePlug, Z-Wave, ZigBee, and Wi-Fi in order to divulge the created power usage schedule. In a residential building, the energy management procedure is monitored on-site or remotely via computers or mobile phones via the Internet of Things. The working flow depicted in Fig. 1 displays all of the procedures.

The smart home's smart devices follow the schedule set by the combination of genetic and gravitational search algorithm-based EMC to save money, reduce PAR, and increase UC through efficient energy use. The suggested effort will result in an

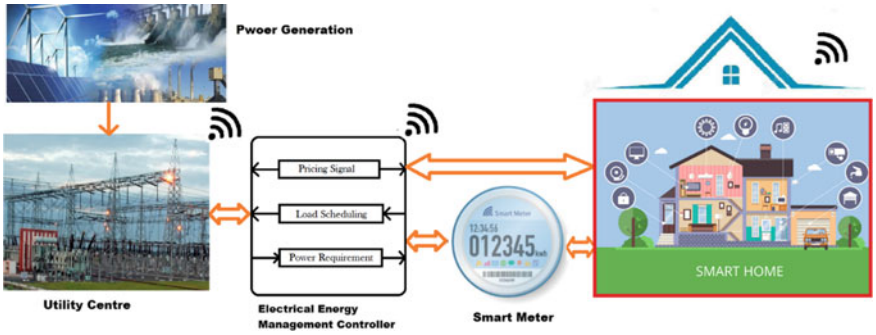

Fig. 1 IoT-enabled smart home energy management system

optimized power usage plan for smart home appliances that actively participate in the SG's energy management sector.

5 Discussion

To identify the next best fit location of the load in smart homes, the combination of genetic and gravitational search algorithm combines the talents of both hereditary and gravitational search algorithms. This may be done utilizing a hybrid approach, mutation, preserving the best locations, novel cost estimation, and a memory-based idea in a gravitational search algorithm. In this perspective, the technique described [4], defines the lowest cost scheduling of accessible energy assets and controlled machines while meeting occupant's comfort index including a specialized criteria.

Furthermore, when the ADR approach [5] is applied to a single residence, it demonstrates the importance of incorporating extensive demonstrations of home machines in order to use the adaptability within each equipment class. Finally, the findings reveal the importance of the suggested regulator's moving activity throughout the day in order to track price signal and outdoor temperature changes. This outcomes in limiting the power bill while staying away from infringement of the indoor temperature inclination. These outcomes show the viability of the controller to lessen the electricity payment and peak demand under different conditions, just as the significance of demonstrating basic machines.

In wise multi-specialist control framework [6] with heuristic enhancement, it is seen that the framework is fit for accomplishing the control objectives by organizing the numerous specialists and the analyzer. A GUI-based reenactment stage is likewise evolved to give the adaptability to clients to control the coordinated structure framework dependent on their own inclinations.

An interval number advancement [12] dependent on resilience degree for limitation infringement is developed to deal with the unpredictability of household load scheduling, when both hot water demand and ambient temperature are unknown

and shown as stretch numbers The simulation findings show that the proposed interval number advancement can produce plans that are resilient to fluctuating hot water demand and ambient temperature while also being flexible to a wide range of consumer requests.

6 Conclusion

DR algorithms can be used to achieve efficient electricity usage, optimal electricity consumption, and cost minimization. In this work, expected HG-GSA algorithm, which is a combination of the genetic and gravitational search algorithm. The energy management controller programmed with our suggested HG-GSA algorithm in IoT-enabled environment which automatically responds to demand side in compliance with the energy management requirements of smart homes. Under these DR programs, the suggested HG-GSA-based technique schedules power usage of smart equipment in smart homes. The purpose of our proposed HG-GSA-based strategy is to reduce electricity costs, reduce PAR, and improve UC.

References

1. International Energy Agency (2020) India 2020 energy policy review. Int Energy Agency 1–304. [Online]. Available: https://niti.gov.in/sites/default/files/2020-01/IEA-India2020-In-depth-EnergyPolicy_0.pdf.
2. Hafeez G, Javaid N, Iqbal S, Khan FA (2018) Optimal residential load scheduling under utility and rooftop photovoltaic units. Energies 11(3):1–27. https://doi.org/10.3390/en11030611
3. Zhao Z, Lee WC, Shin Y, Bin Song K (2013) An optimal power scheduling method for demand response in home energy management system. IEEE Trans Smart Grid 4(3):1391–1400. https://doi.org/10.1109/TSG.2013.2251018
4. Shirazi E, Jadid S (2015) Optimal residential appliance scheduling under dynamic pricing scheme via HEMDAS. Energy Build 93:40–49. https://doi.org/10.1016/j.enbuild.2015.01.061
5. Althaher S, Mancarella P, Mutale J (2015) Automated demand response from home energy management system under dynamic pricing and power and comfort constraints. IEEE Trans Smart Grid 6(4):1874–1883. https://doi.org/10.1109/TSG.2014.2388357
6. Wang L, Wang Z, Yang R (2012) Intelligent multiagent control system for energy and comfort management in smart and sustainable buildings. IEEE Trans Smart Grid 3(2):605–617. https://doi.org/10.1109/TSG.2011.2178044
7. Meng FL, Zeng XJ (2016) A profit maximization approach to demand response management with customers behavior learning in smart grid. IEEE Trans Smart Grid 7(3):1516–1529. https://doi.org/10.1109/TSG.2015.2462083
8. Lujano-Rojas JM, Dufo-López R, Bernal-Agustín JL, Catalão JPS (2017) Optimizing daily operation of battery energy storage systems under real-time pricing schemes. IEEE Trans Smart Grid 8(1):316–330. https://doi.org/10.1109/TSG.2016.2602268
9. Ruelens F, Claessens BJ, Vandael S, De Schutter B, Babuska R, Belmans R (2017) Residential demand response of thermostatically controlled loads using batch reinforcement learning. IEEE Trans Smart Grid 8(5):2149–2159. https://doi.org/10.1109/TSG.2016.2517211
10. Kim B, Zhang Y, Member S, Van Der Schaar M, Lee J, Member S (2016) Scheduling with reinforcement learning. IEEE Trans Smart Grid 7(5):2187–2198

11. Wen Z, O'Neill D, Maei H (2015) Optimal demand response using device-based reinforcement learning. IEEE Trans Smart Grid 6(5):2312–2324. https://doi.org/10.1109/TSG.2015.2396993
12. Wang J, Li Y, Zhou Y (2016) Interval number optimization for household load scheduling with uncertainty. Energy Build 130:613–624. https://doi.org/10.1016/j.enbuild.2016.08.082
13. Nesmachnow S (2014) An overview of metaheuristics: accurate and efficient methods for optimisation. Int J Metaheuristics 3(4):320. https://doi.org/10.1504/ijmheur.2014.068914
14. Rashedi E, Nezamabadi-pour H, Saryazdi S (2009) GSA: a gravitational search algorithm. Inf Sci (Ny) 179(13):2232–2248. https://doi.org/10.1016/j.ins.2009.03.004

Minimization of Tie-Line Power Fluctuations using GCSC with Gas-Thermal-EV System for LFC Considering Time-Delay Effect

Siddhant Gudhe and Hiramani Shukla

Abstract Power system stability, frequency deviation, or power mismatch issues are managed by electrical vehicles (EV) as an energy storage element. Gate-controlled-series-capacitor (GCSC) is used to control power flow across tie-lines. To achieve high power quality, management of automatic generation control (AGC) at generation side is used. Along with the preexisting energy sources like thermal and gas, EV and series GCSC are used for load frequency control (LFC). The system under investigation includes thermal and gas with EV in both area with GCSC is connected in series between two areas. Area 1 includes thermal with EV integration, and Area 2 has gas system with EV penetration. An aggregate model of EV is used in both the areas. The system is analyzed for step load and random load disruptions. To control the frequency, proportional-integral-derivative (PID) controller is used. Firefly algorithm (FF-A) optimization techniques are implemented to find the control variables. Time-delay effect is also taken into consideration, and the system under study is demonstrated in MATLAB/Simulink environment. The simulation results show that FF-A has low oscillation, very small undershoot, and have huge improvement in delay margin.

Keywords Load frequency control · Electric vehicles · PID controller · GCSC · Time-delay · Firefly algorithm

1 Introduction

Power system is considered as large-scale complex multi-source multi-variable system. Penetration of electric vehicles (EV) into power system has been increasing at an exponential rate. The EV along with the conventional power sources possess more stability concerns. Electric vehicles in a large quantity connected to the grid have the effect on the system frequency, power, and stability. If such fleets of EV charging and discharging are not managed, which may lead to power quality issues

S. Gudhe · H. Shukla (✉)
Electrical Engineering Department, Maulana Azad National Institute of Technology, Bhopal, India
e-mail: hiramanishukla143@gmail.com

© The Author(s), under exclusive license to Springer Nature Singapore Pte Ltd. 2022

A. Tripathi et al. (eds.), *Intelligent Computing Techniques for Smart Energy Systems*,
Lecture Notes in Electrical Engineering 862,
https://doi.org/10.1007/978-981-19-0252-9_5

and also the transformer may overload. There is rapid technological advancement in the battery. EV battery is used to drive the traction motor via inverter control. Therefore, the driving range for EV depends on the stored energy of the battery. Efficient control of the EV is essential for the efficiency improvement. The model developed for the analysis contains the conventional energy sources which includes thermal and gas turbine. Gas turbine transfer function contains the effects of speed governor, valve position, combustion, fuel compressor, and turbine. Thermal transfer function considers the effects of steam turbine.

Gate-controlled-series-capacitor (GCSC) connection makes power flow efficient between tie-lines. GCSC has the power electronics converters with considerable inertia. AGC is coordinated with the various system devices which includes HVDC and FACTS devices. The effect of HVDC link on LFC is beyond the scope of this paper. This paper focuses the importance of GCSC for the frequency control of the system by controlling tie-line power flow. GCSC integration for the multi-area system has been carried out by Oshnoei et al. [1] by using robust model predictive control. The implementation of thermal and gas along with EV is studied by Debbarma et al. [2] without time-delay effect consideration. The FF-A has been successfully implemented for the thermal power system by Jagatheesan et al. [3], but the integration of EV and time-delay effects has not been considered. AGC of multi-area gas turbine and thermal system has been carried out by Saikia et al. [4] with integral (I) controller and by Patel et al. [5] with PI controller. Implementation using PI controller has been also conducted by Bhadoria et al. [6] using firefly algorithm (FF-A). A new model of EV has been proposed by Izadkhast et al. [7]. The same aggregate model of EV is used along with the conventional sources by Debbarma et al. [8]. The effect of the time-delay on the load frequency control has been very beautifully studied by Macana et al. [3] and Hua et al. [9]. The decentralized optimal EV control approach is introduced by Kariminejad et al. [10].

The proposed model in the paper contains thermal and gas with aggregated model of EV. Also the interconnection of GCSC between Area 1 and Area 2 is under study. Section 2 describes the system under study, and Sect. 3 discusses FF-A. Simulation performance and conclusion are discussed in Sects. 4 and 5.

2 System Under Investigation

For the analysis for the system using controllers, two areas system model are considered. PID controller is used, and their variables are calculated by using FF-A optimization technique. Electric vehicle model is introduced in both the areas, and the analysis is completed. System undergoes through step load as well as random load variation. The time-delay effect is also taken into account.

2.1 Time-Delay Effect

Large-scale integration of conventional energy sources along with HVDC and FACTS devices increases the inertia of overall system with low frequency variation. There are delays in power system which are not intentional, but the delay is provided to receive signals at the control unit. For the large power system, time-delays are usually not considered. This time-delays are usually taken into account for isolated smart grids, while considering the time-delay factor, the calculation of time-delay margin is beyond the scope of this paper. Various methodologies are used in literature to calculate time-delay margin [3].

2.2 Model of Overall System

The overall system model consist of two areas system. The block diagram of overall system under study is shown in Fig. 1. Area 1 includes gas turbine with EV integration, and Area 2 has gas turbine with EV penetration. An aggregate model of EV is used in both the areas. Gas turbine contains governor, compressor, combustion, and turbine. GCSC as a power flow control device is connected between both the areas. Both the areas are applied with time-delay for communication with the command center. Both step load disruption (SLD) and random load disruption (RLD)

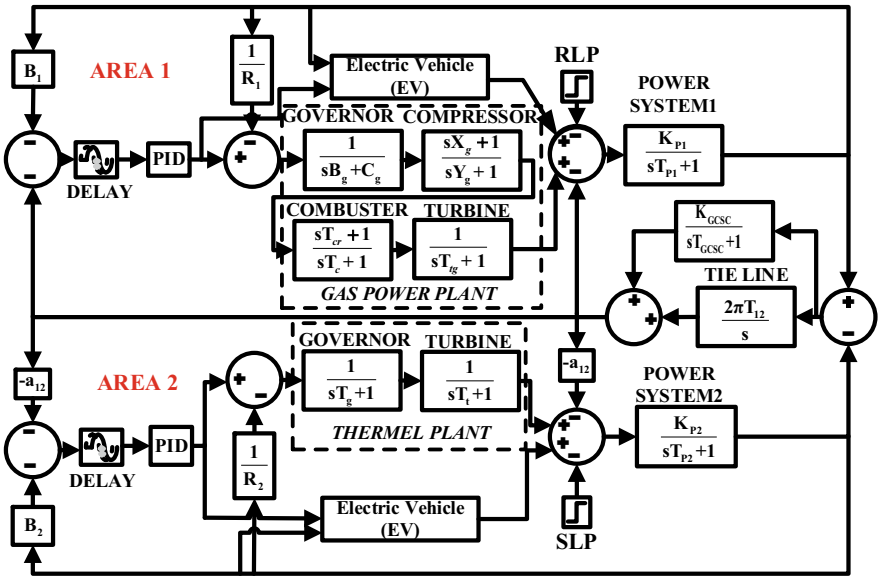

Fig. 1 Block diagram of overall system under investigation

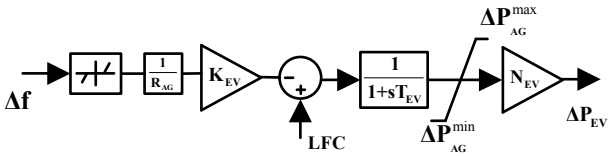

Fig. 2 Block diagram of aggregated model of EV

are applied and tested in both the areas. The system is studied for the change in frequency in both the areas and change in tie-line power.

2.3 Model of Electric Vehicle (EV)

The aggregated model of EV [8] gives the generalized model for the frequency control of the overall system which is shown in Fig. 2. The changed frequency is passed through the dead-band which limits the change in frequency within the particular band which is nearly +10 and −10 MHz of the rated frequency. N_{EV} is the number of EV connected. For the analysis purpose, all the EV connected are assumed to be of same battery rating. The battery charger is denoted by the transfer function of first order with a small time constant T_{EV}. Upper limit and lower limit of the battery reserve are represented by (1) and (2). Charging power is directly proportional to the droop coefficient R_{AG}, it is also dependent upon the participation factor K_{EV}. The participation of every EV for frequency control is said to be participation factor of that particular EV [8].

$$\Delta P_{\mathrm{AG}}^{\max} = +[\Delta P_{\mathrm{EV}i}/N_{\mathrm{EV}}] \tag{1}$$

$$\Delta P_{\mathrm{AG}}^{\min} = -[\Delta P_{\mathrm{EV}i}/N_{\mathrm{EV}}] \tag{2}$$

where $\Delta P_{\mathrm{AG}}^{\max}$ is the maximum power output for particular group of EV and $\Delta P_{\mathrm{AG}}^{\min}$ is the minimum power output for same group of EV. N_{EV} is total number of EV which is assumed to be 1800 number of EV for Area 1 and 1600 number for Area 2 for the system under study.

2.4 Controller Design

The PI controller and PID controller equations are given by $G(s)_{\mathrm{PI}} = K_{\mathrm{Pk}} + \frac{K_{\mathrm{Ik}}}{s}$ and $G(s)_{\mathrm{PID}} = K_{\mathrm{Pk}} + \frac{K_{\mathrm{Ik}}}{s} + K_{\mathrm{Dk}} \cdot s$, respectively. By optimally tuning the control variables proportional gain K_{Pk}, integral gain K_{Ik}, and derivative gain K_{Dk}. The performance is improved for the kth area, where k represents the area number for multi-area system.

K_{Pk} controls the overshoots, rise time, and steady state error with minimum effect on settling time. K_{Ik} affects the overshoots and rise time, but effect on settling time is still negligible. K_{Dk} is used to control settling time along with overshoot. The cost function to compare system with and without GCSC is shown in Eq. (3)

$$J = \int_0^T \left(\Delta f_{\text{area-1}}^2 + \Delta f_{\text{area-2}}^2 + \Delta P_{\text{tie}}^2\right) \mathrm{d}t \tag{3}$$

3 Firefly Algorithm (FF-A) Flowchart

Population-based algorithm where flashing patterns and behavior of tropical fireflies is analyzed called as firefly algorithm (FF-A). This is good optimization technique. FF-A has been proposed by Yang in 2008 at the University of Cambridge. This algorithm was further developed for multimodal optimization by Yang 2009 [11]. The objective function is formulated by the magnitude of light of a firefly. The brightness of firefly I at selected position x is given by as $I(x)/f(x)$ for minimization of the objective function. The equation of light brightness is given by equation

$$I = I_0 \mathrm{e}^{-\gamma r} \tag{4}$$

where

I_0 = original intensity of light and

γ = coefficient of light absorption which varies with distance r.

β is called as attractiveness which is defined by other fireflies. As the distance between sources and light decreases, media absorb light, therefore, degree of absorption changes the attractiveness which is given by $\beta = \beta_0 \mathrm{e}^{-\gamma r^2}$ for r_i considered as zero (Fig. 3).

The motion of a firefly i is allured to another, more enchanted firefly j is determined by Eq. (5)

$$x_i^{k+1} = x_i^k + \beta_0 \mathrm{e}^{-\gamma r_{ij}^2}\left(x_j^k - x_i^k\right) + \alpha \varepsilon_i^k \tag{5}$$

where α = randomization parameter and vector of random numbers is given by ε_i^k.

For FF-A optimization used in this study, tuned values are: number of fireflies = 10, maximum iterations = 100, $\beta = 0.2$, $\alpha = 0.5$, and $\gamma = 0.5$.

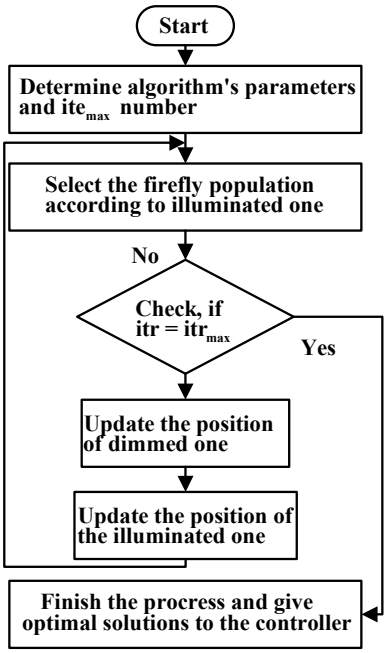

Fig. 3 Flowchart of firefly algorithm

4 Simulation Performance

Simulation is performed in two parts. In first part, the system is simulated using GCSC and without GCSC with PID controller using FF-A. In second part, simulation results are shown for RPD and is tested for the time-delay. All the results are verified with aggregate model of EV connected. The parameters for the simulation are shown in Table 1. Variable load applied to the system under investigation is shown in Fig. 4.

The results with and without GCSC for step loading disruption (SLD) are shown in Figs. 5 and 6 shows the random loading disruption (RLD) results in case of with and without application of GCSC with time-delay effect of 1.5 s. Results are verified using PID controller.

Table 1 Simulation parameters for system under investigation

Parameters	Values
f (frequency), B_i (damping constant), R (regulation)	60 Hz, 0.425 pu/Hz, 2.4 Hz/pu
B_g (valve position), C_g (valve position), X_g (leas time constant), Y_g (lag time constant), T_{cr} (combustion reaction time-delay), T_c (fuel time-delay), T_{tg} (compressor discharge time constant)	0.05, 1, 0.6 s, 1 s, 0.01, 0.23, 0.2 s
K_g, T_g, K_t, T_t, K_{GCHC}, T_{GCHC}	1, 0.3 s, 1, 0.08 s, 1, 0.015 s
T_{12}, a_{12}	0.0867, −1

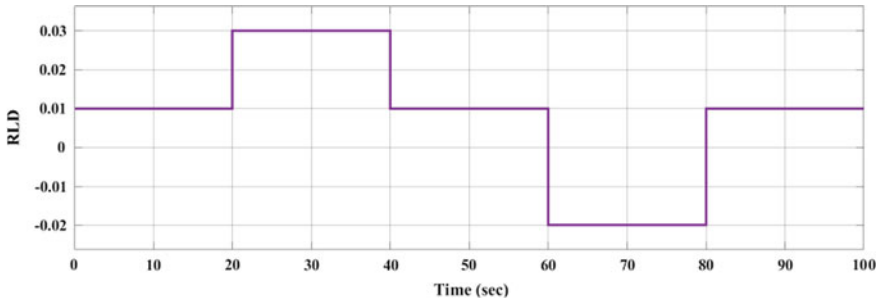

Fig. 4 Variable load applied to the system under study

Fig. 5 SLD with and without GCSC

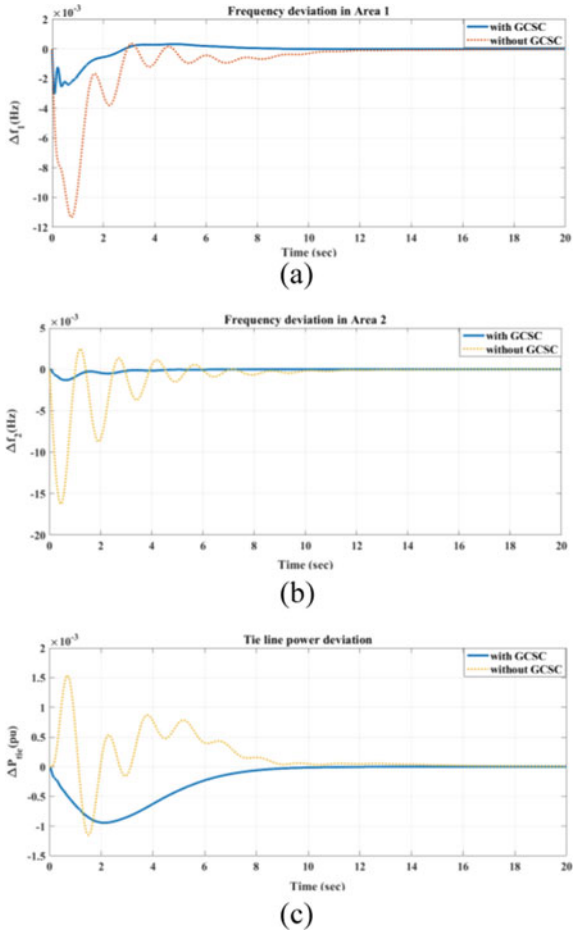

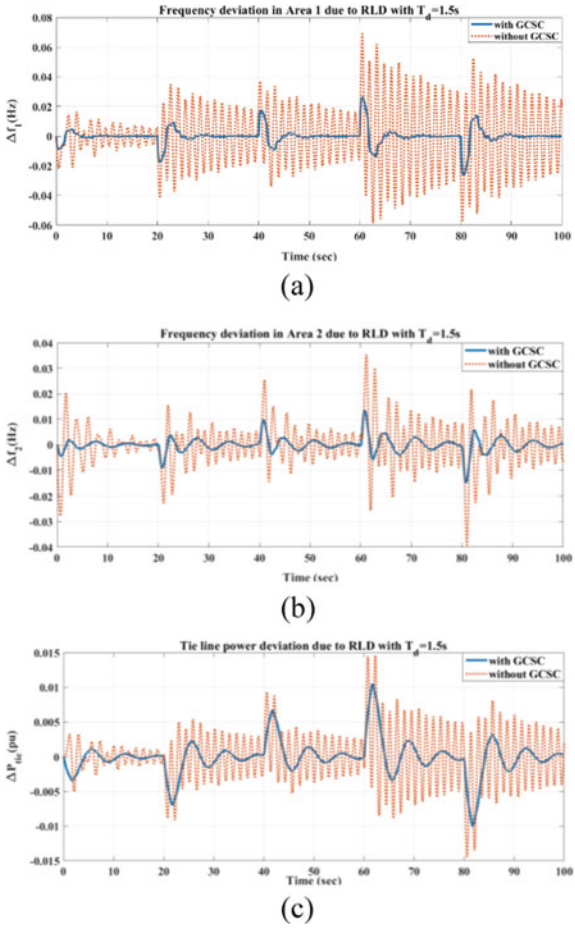

Fig. 6 RLD with and without GCSC. **a** Frequency fluctuations in area 1, **b** frequency fluctuations in area 2, and **c** tie-line power variation

At exact 1.5 s, FF-A variables make system marginally stable. Beyond 1.5 s, FF-A gives control variables for PID which makes system unstable. So, time-delay margin FF-A based controller is less than 1.5 s. The calculation of time-delay margin has tedious mathematical calculations depending on the system. Exact time-delay margin is not shown as delay in simulation is based on Pade approximation [3]. Figure 7 gives the convergence curve for PID controller, and Fig. 8 gives cost function curve with and without GCSC using Eq. (3).

Tables 2 and 3 show the controller limitations found from both the techniques. Table 4 shows the magnitude of peak overshoot, undershoot as well as settling time using PID controller with and without GCSC, respectively.

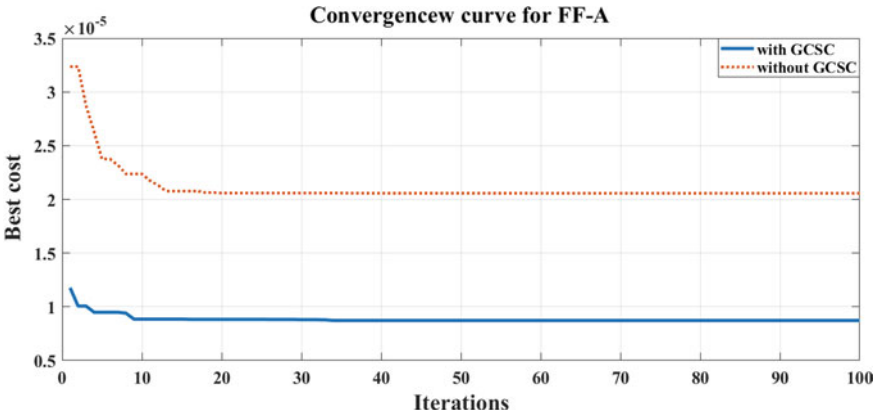

Fig. 7 Convergence curve with and without GCSC

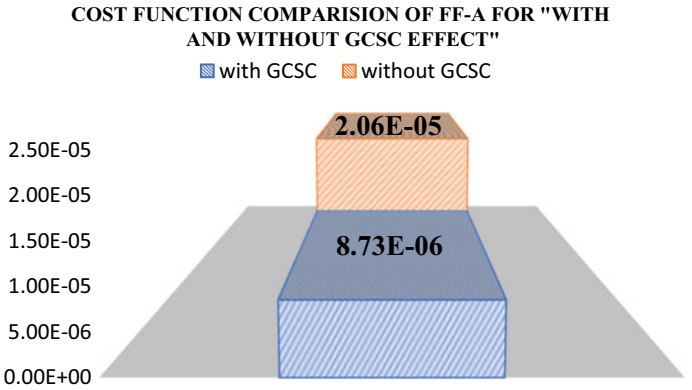

Fig. 8 Cost function with and without GCSC

Table 2 PID control variables with GCSC

Parameters (FF-A)	K_P, K_I, and K_D
Area 1	1, 0.9679, and 0.8997
Area 2	0.9388, 0.4352, and 0.1273

Table 3 PID control variables without GCSC

Parameters (FF-A)	K_P, K_I, and K_D
Area 1	0.1265, 0.9907, and 0.8956
Area 2	0.9587, 0.4352, and 0.1973

Table 4 Comparison of control system parameters for PID controller

Parameters		Δf_1 (Hz)	Δf_2 (Hz)	ΔP_{tie} (pu)
Without GCSC	Peak overshoot (ms)	0.36	2.45	1.55
	Peak undershoot (ms)	11.3	16.3	1.15
	Settling time (s)	17.2	14.6	16.3
With GCSC	Peak overshoot (ms)	0.3	–	–
	Peak undershoot (ms)	3	1.3	0.95
	Settling time (s)	9.1	7.12	10.2

5 Conclusion and Discussion

In this paper, system having two areas is used to compare system stability using GCSC. Area 1 has thermal, and Area 2 contains gas turbine. Aggregated model of EV is penetrated in both the areas. The simulation results show that GCSC with PID controller outperforms system without GCSC in terms of settling time and oscillations. Time-delay effects are considered, and time-delay margin is approximated. Even delayed system using GCSC shows good performance as compared to system not having GCSC. For the system under study, delay margin obtained is 1.5 s, but system becomes marginally stable at 1.5 without GCSC. More stability margin indicate that the system is robust and reliable. Also the verification of GCSC system superiority can be concluded from peak overshoot, undershoot as well as settling time. Cost function using GCSC is lesser than without GCSC system. Low value of convergence curve and cost function gives optimized controller parameters [10]. Therefore, it is easily concluded that system having GCSC gives much optimized parameters.

Simulation results can be generalized for the multi-area multi-source system. As a future research, different controller can be tested using both the techniques. For the calculation of the time-delay margins, different methodologies for the large-scale power system can be explore.

References

1. Oshnoei A, Kheradmandi M, Khezri R, Mahmoudi A (2021) Robust model predictive control of gate-controlled series capacitor for LFC of power systems. IEEE Trans Ind Inform 17(7):4766–4776
2. Rakhshani E, Remon D, Cantarellas AM, Garcia JM, Rodriguez P (2017) Virtual synchronous power strategy for multiple HVDC interconnections of multi-area AGC power systems. IEEE Trans Power Syst 32(3):1665–1677
3. Debbarma S, Dutta A (2017) Utilizing electric vehicles for LFC in restructured power systems using fractional order controller. IEEE Trans Smart Grid 8(6):2554–2564
4. Jagatheesan K, Anand B, Samanta S, Dey N, Ashour AS, Balas VE (2019) Design of a proportional-integral-derivative controller for an automatic generation control of multi-area

power thermal systems using firefly algorithm. IEEE/CAA J Autom Sin 6(2):503–515
5. Saikia LC, Chowdhury A, Shakya N, Shukla, S, Soni PK (2013) AGC of a multi area gas-thermal system using firefly optimized IDF controller. In: 2013 annual IEEE India conference (INDICON), pp 1–6
6. Patel A, Bhongade S (2019) Designing of load frequency controller for two-area interconnected power system using grey wolf optimization. In: 2019 international conference on computing, power and communication technologies (GUCON), pp 318–325
7. Bhadoria VS, Jaiswal SP, Tayal A, Singh J (2019) Firefly algorithm for frequency controller of autonomous hybrid energy system. In: 2019 2nd international conference on power energy, environment and intelligent control (PEEIC), pp 150–155
8. Izadkhast S, Garcia-Gonzalez P, Frías P (2015) An aggregate model of plug-in electric vehicles for primary frequency control. IEEE Trans Power Syst 30(3):1475–1482
9. Macana CA, Mojica-Nava E, Quijano N (2013) Time-delay effect on load frequency control for microgrids. In: 2013 10th IEEE international conference on networking, sensing and control (ICNSC), pp 544–549
10. Hua C, Wang Y (2020) Delay-dependent stability for load frequency control system via linear operator inequality. IEEE Trans Cybern 1–9
11. Yang XS (2009) Firefly algorithms for multimodal optimization. In: Watanabe O, Zeugmann T (eds) Stochastic algorithms: foundations and applications. SAGA 2009. Lecture notes in computer science, vol 5792. Springer, Berlin, Heidelberg

Investigation of Timing Issues of True Single-Phase Clock Circuits for Nanodevices

Asirbad Mishra, Harshita Rai, Shilpi Birla, Neha Singh, and Neeraj Kumar Shukla

Abstract With the advent of microelectronics, the scaling of a transistor had become challenging due to the several factors out of which dynamic power is one of the important factors to be dealt with. With the reduction in chip area need of low power circuits increased, these circuits would consume less dynamic power. Static CMOS logic implementation is a widely used technology for VLSI circuits as it offers high noise immunity and low static power consumption. However, there are certain limitations for CMOS circuits having a fan-in of N requires a $2N$ number of transistors for logic implementation, resulting in increased area consumption as compared to that of Dynamic logic structures. Dynamic logic implementation requires only $(N + 2)$ transistors for a circuit with a fan-in of N. Moreover, these circuits are ratio-less and have faster switching speeds. This paper is focused on True Single-Phase Clock (TSPC) logic as an appropriate choice of logic that can lead to high performance as compared to dynamic and domino logic circuits. In this paper, we have compared the basic logic circuits (AND, NAND, OR, NOR) over other circuits like Dynamic and Domino techniques with TSPC logic. The results show that a NOR logic TSPC showed a significant 72% reduction in dynamic power than that of Domino circuit and Dynamic circuit and in the case of OR TSPC logic there was 57% power reduction for Domino circuit and 35% power reduction for Dynamic circuit. Similarly, in the case of NAND logic, TSPC has 79% dynamic power reduction over the domino Circuit and 35% over the dynamic circuit and in the case of AND TSPC logic, it gives a 57% power reduction for domino circuit and 35%, respectively. A full bit adder has been implemented using the TSPC logic gates and compared it with the conventional adder.

Keywords Domino circuit · Dynamic power · Propagation delay · TSPC · Dynamic circuit

A. Mishra · H. Rai · S. Birla (✉) · N. Singh
Department of Electronics and Communication Engineering, Manipal University Jaipur, Jaipur, Rajasthan 303007, India
e-mail: shilpi.birla@jaipur.manipal.edu

N. K. Shukla
Department of Electrical Engineering, King Khalid University, Abha, Saudi Arabia

© The Author(s), under exclusive license to Springer Nature Singapore Pte Ltd. 2022

A. Tripathi et al. (eds.), *Intelligent Computing Techniques for Smart Energy Systems*, Lecture Notes in Electrical Engineering 862,
https://doi.org/10.1007/978-981-19-0252-9_6

1 Introduction

For more than 20 years, the primary focus in the semiconductor industry was downsizing the area of the chip keeping the functional parameters of an integrated circuit intact. According to Moore's law, the number of transistors per silicon chip doubles about every 18 months. The continuous scaling of the devices leads to overrule the Moore's Law and predicted the More than Moore (MTM) which states that in every 12 months the number of the transistor count will be double on a chip. In simple words, this law meant to imply that number of transistors would have exponential growth and to do so several transistors were densely packed to form an Integrated Circuit (IC) which later paved its way toward FET technology. The scaling of MOS has various constraints in terms of speed, transistors count per unit area, and power consumption. The continuous scaling of the MOSFET devices and the increase in components on a single chip result in more complex technology. As the gate length is reduced there is a change in the MOSFET characteristics due to short channel effects such as threshold voltage shift, increased leakage current, increased output conductance. Other than this scaling down also leads to excessive process variation and reliability issues which eventually lead to power and performance degradation. Therefore, it is of great importance to develop technologies that will enable continued implementation of increasingly higher performance devices at nanoscale regime.

2 Background Work

In paper [1], two high-speed full adder cells have been designed using NP-CMOS and Multi-Output Dynamic Logic Style which has been able to achieve better performance as compared to static and dynamic cells and consume less power at different voltages. The problem of charge sharing is resolved and there is a good enhancement in the voltage levels.

The focus discussed in [2] is mainly on the optimization of different performance parameters like power, delay, and power delay product for a CMOS-based full adder. The proposed design, i.e., 22*T* domino-based full adder was able to achieve minimum value in terms of the above parameters and performed better than the other full adder circuits. In [3], proposed the usage of the Adders exploitation FTL and MT-CMOS logic technique to efficiently reduce power and increase the speed of dynamic logic circuit which lead to the removal of charge sharing problems related to dynamic and domino families. The above-proposed technique was able to shrivel the power consumption and area of the circuit simultaneously. A detailed view of designing circuits using dynamic logic family has been discussed in [4]. The scaling of MOS devices results in high density of transistor per unit area but at the same time speed and power issues becomes the matter of concern. Various logic families have been discussed with reference to power consumption area and charge sharing issues.

The brief idea about True Single-Phase Clock (TSPC) logic is given in [5] and discusses the various properties of this logic family. It shares the advantages of TSPC, i.e., requires less hardware power and has lower phase noise. It also talks about the design consideration of TSPC as these circuits fail at sufficiently low clock frequencies. The primary aim was the implementation of a charge steering technique for Discrete-time charge steering circuits on 65 nm CMOS technology [6] as it has low power consumption than that of Continuous-time current-steering counterpart even at high switching activity. Besides having low power consumption this technique has got other advantages like digital latching and allowing unstable multistage op-amps to perform well in complex circuits due to its discrete-time nature. The main aim was to meet multiple parametric goals in terms of area, power, speed, and noise margin and was achieved by using six different domino-based techniques that were implemented on a 4 input and six input OR and AND gate [7].

3 Proposed Work

Logic circuits play an important role in building the circuital for designing any hardware where electrical quantity like the voltage, is used to represent the ON state or OFF state of the circuit. These circuits can be single input–single output or can have multiple inputs and multiple outputs depending on the requirement of the hardware design. These logic circuits can be categorized broadly into two types, i.e., combinational circuit and static circuit.

There are various techniques to represent the logic circuits using Static CMOS logic family or Dynamic logic family, the Static logic family has Pull up and Pull down network to design any circuit which counts to total $2N$ number of transistors, where N is the number of inputs while the Dynamic logic settles at $N + 2$ transistor count. Firstly, the Dynamic logic technique for CMOS circuit design is shown in Fig. 1. It is better as compared to static circuits as this technique is faster and requires less surface area. In practical designs, there is always a tradeoff between speed and dynamic power consumption. One of the major drawbacks of such circuits is their high toggling activity which affects the power consumption of the circuit.

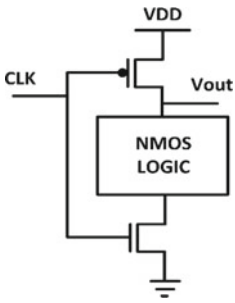

Fig. 1 Dynamic logic circuit

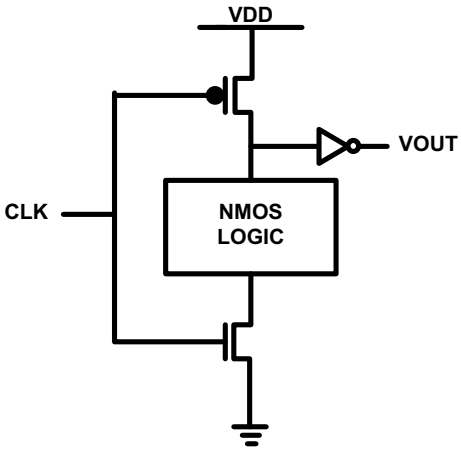

Fig. 2 Domino logic circuit

The other limitation of dynamic circuits is cascading, to avoid the cascading problem one of the solution is to use a more effective technique known as Domino logic circuit as shown in Fig. 2 where a single clock is used for pre-charge and evaluation of the cascaded blocks of logic circuits, these circuits are used mainly for designing non-complemented circuits but this circuit had its setbacks like charge sharing which was resolved by use of bleeding transistor but practically it did not give 100% inverted clock and had some clock skews.

Due to the above-mentioned design issues in clock distribution which lead to slow transitions in domino logic. In this paper, True Single-Phase Clock (TSPC) logic which had virtually evolved from NORA Dynamic logic is discussed and the advantage of using this circuit is its high-speed topology which consumes less power and occupies less area than other methods. TSPC logic is categorized into four configurations: Pre-charged high, Pre-charged low, Non-Pre-charged low, and Non-Pre-charged high. In this paper the proposed design involves the use of Non-Pre-charged high configuration implemented using basic logic gates to reduce the dynamic power consumption. In this type of configuration when the clock is low, the circuit evaluates the output and when the clock is high it holds the value of the previous output and hence its value depends on the input. In Fig. 3a–d, the proposed TSPC designs are shown. We have used a clocked CMOS Inverter to get the desired outputs of AND TSPC logic and OR TSPC logic.

4 Results and Simulation

To simulate the circuits HSPICE from Synopsys has been used. We have used 16 nm PDK to simulate the circuits. The simulation has been done for the logic gates using Dynamic logic, Domino logic, and TSPC logic. Dynamic power and propagation

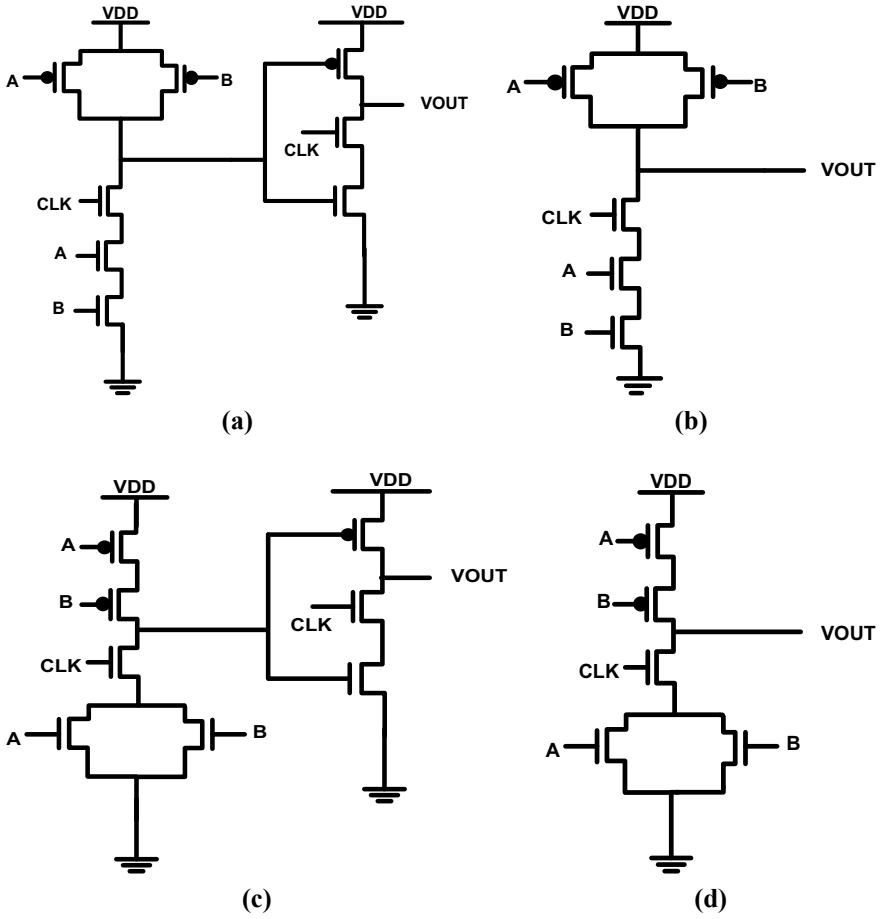

Fig. 3 **a** Proposed TSPC AND logic. **b** Proposed TSPC NAND logic. **c** Proposed TSPC OR logic. **d** Proposed TSPC NOR logic

delay has been calculated for various logic gates based on the various design topologies. The simulation has been done at three different voltages 0.8, 0.9, and 1 V. Table 1 shows the propagation delay for NOR, AND, NAND, and OR gates. From Table 1, we can conclude that all the proposed TSPC logic gates are having the least propagation delay.

Figures 4, 5, 6, and 7 shows that Dynamic power of NOR, NAND, OR, and AND gate, respectively. The graph shows the comparison between the Domino, Dynamic, and Proposed TSPC logic gates. The four figures show that the dynamic power is minimum in TSPC logic circuits.

Since we found that the TSPC NAND gate with minimum power dissipation and delay. A full adder has been designed using conventional CMOS NAND gate and NAND gate using proposed TSPC logic. The block diagram of full adder is as shown

Table 1 Propagation delay for different circuits

Logic circuit propagation delay (in ns)		Supply voltage in volts (V)		
		0.8	0.9	1.0
Dynamic	NOR	1.25	1.15	1.05
	NAND	1.24	1.11	1.05
	OR	0.64	0.56	0.49
	AND	6.10	6.01	5.94
Domino	NOR	1.38	1.25	1.15
	NAND	1.38	1.25	1.16
	OR	1.32	1.19	1.13
	AND	1.33	1.23	1.14
TSPC (proposed)	NOR	1.18	1.1	1.01
	NAND	0.173	0.15	0.073
	OR	0.146	0.145	0.075
	AND	0.195	0.177	0.167

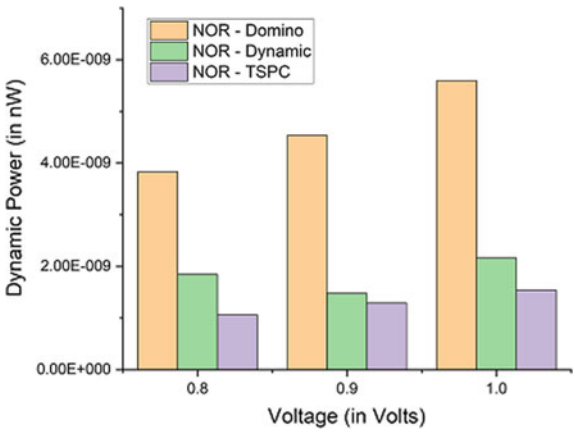

Fig. 4 Dynamic power for NOR gates for various logic families

in Fig 8. The full adder has two outputs SUM and Carry as shown in Fig. 8. The circuit has been designed using Microwind Software.

The simulation of the two full adders has been done at 16 nm technology at three different voltages 0.8, 0.9, and 1 V. The results are being shown in Table 2. The adder which is designed using proposed TSPC logic using Fig. 8. As it is shown in Table 2 various parameters like Power Dissipation, Average Power Dissipation, Propagation Delays, Worst Case Delay, and Leakage Current. The various parameters show the performance of the two circuits designed using NAND CMOS and NAND TSPC logic circuits. The simulation has been done at three different voltages at 0.8, 0.9, and 1 V and it is clearly visible that the TSPC full adder is having minimum power dissipation, minimum average power, the propagation delay is reduced by 3× time

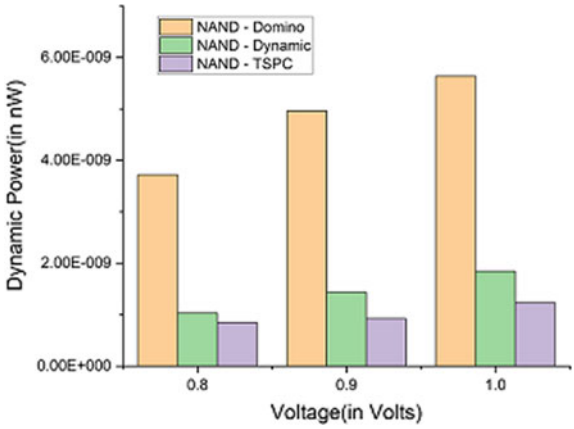

Fig. 5 Dynamic power for NAND gates for various logic families

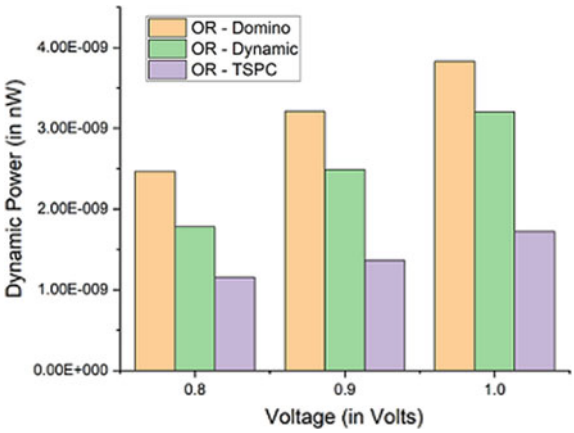

Fig. 6 Dynamic power for OR gates for various logic family

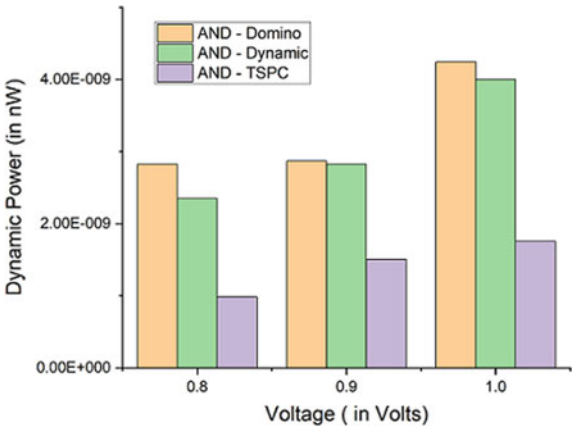

Fig. 7 Dynamic power for AND gates for various logic families

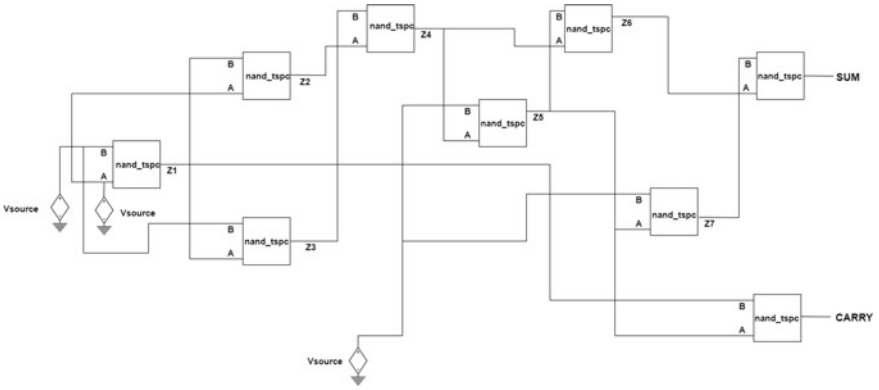

Fig. 8 Block diagram of NAND based full adder

Table 2 Full adder simulation

Parameters/voltage	1 V		0.9 V		0.8 V	
	TSPC FA	NAND FA (SIMPLE CMOS)	TSPC FA	NAND FA (SIMPLE CMOS)	TSPC FA	NAND FA (SIMPLE CMOS)
Power dissipation (W)	2.77E−09	2.90E−09	1.19E−09	1.28E−09	4.06E−10	4.45E−10
Avg power (W)	1.87E−07	7.32E−07	1.48E−07	5.93E−07	1.13E−07	4.67E−07
Prop delay (S)	2.58E−09	7.56E−09	3.59E−09	7.58E−09	3.71E−09	7.62E−09
Worst case delay (S)	3.99E−09	1.12E−08	5.98E−09	1.12E−08	6.15E−09	1.12E−08
Leakage current (A)	1.98E−07	2.55E−07	1.75E−07	2.15E−07	1.51E−07	1.77E−07

at 1 V for TSPC full adder. Minimum delay is most attractive feature of this TSPC based full adder. This adder can be considered as one of the fast speed adder. A layout the TSPC full adder has also been designed as shown in Fig. 9.

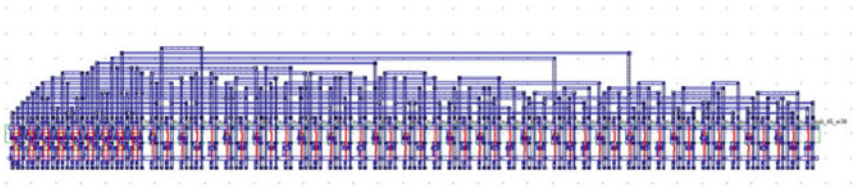

Fig. 9 Layout of the adder circuit

5 Conclusion

As the Domino logic consumes power in the inverters while the TSPC topology which is drawn from the NORA logic has removed one of the clocked transistors which helps in the reduction of the Dynamic power and the propagation delay. From the above simulation results from Table 1 and the graphs are shown in this paper, it has been observed that TSPC Non-Pre-charged high logic has been able to achieve better performance due to low power consumption and a better switching activity (speed) as compared to that of Domino and Dynamic logic designs. The adder circuits show drastic improvement in terms of all the performance parameters like Power Dissipation and Propagation Delays.

References

1. Mirzaee RF, Moaiyeri MH, Navi K (2010) High-speed NP-CMOS and multi-output dynamic full adder cells. Int J Electr Electron Eng 4:304–310
2. Verma S, Kumar D, Marwah GK (2014) New high-performance 1-bit full adder using domino logic. In: Proceedings of 2014 international conference on computational intelligence and communication networks, pp 961–965
3. Rathor VS, Khandelwal S, Akashe S (2014) Performance analysis of high-speed domino CMOS logic circuits. Int J Comput Appl 99(5)
4. Roy K, Prasad SC (2009) Low-power CMOS VLSI circuit design. Wiley Publications
5. Razavi B (2016) TSPC logic [a circuit for all seasons]. IEEE Solid-State Circuits Mag 8(4):10–13
6. Razavi B (2013) Charge steering: a low-power design paradigm. In Proceedings of 2013 IEEE 2013 custom integrated circuits conference, pp 1–8
7. Kamde S, Badjate S, Hajare P (2014) Comparative analysis of improved domino logic based techniques for VLSI circuits. Int J Eng Res Gen Sci 2(3):43–50

Comparative Analysis of Machine Learning Techniques for Software Effort Estimation

Somya Goyal

Abstract Software Effort Estimation (SEE) is paramount task in software development life cycle. It estimates the future effort which would be needed for the successful completion of project. The accuracy of estimation controls the project success. This paper conducts an empirical comparison among the most popular machine learning techniques for SEE to figure out the most accurate one. Three models namely ANN_SG, SVR_SG, and GLR_SG are developed using artificial neural network, support vector regression, and generalized linear regression techniques, respectively. Five datasets from PROMISE repository are used and accuracy measures for comparison are MAR (Mean Absolute Error) and MMRE (Mean Magnitude of Relative Error). It is found that ANN_SG outperforms the other models with better prediction accuracy, and it reduces the error rate for SVR_SG and GLR_SG by 58.4%, and 48.2% respectively. It can be concluded from the experimental results that the ANN_SG is best performer among the candidate models for SEE statistically.

Keywords Software effort estimation (SEE) · Neural network · MMRE · Support vector regression (SVR) · Generalized linear regression (GLR) · Promise dataset

1 Introduction

Software effort estimation (SEE) is highly challenging software management task due to the constantly changing scenario of software industry. Early project planning is essential for successful completion of projects. It includes accurate in-prior prediction of resources (or efforts) needed to accomplish the project. As per the Standish Group report, out of total number of commenced projects, only 31% are completed successfully [1]. One of the major causes of this poor success rate is poor software management which involves inaccurate estimation of the requirements. More the accurate estimation of the required resources (or efforts), more are the chances of completion of project within the constraints. In past 30 years, numerous Machine

S. Goyal (✉)
Manipal University Jaipur, Jaipur, Rajasthan 303007, India
e-mail: somyagoyal1988@gmail.com

© The Author(s), under exclusive license to Springer Nature Singapore Pte Ltd. 2022

A. Tripathi et al. (eds.), *Intelligent Computing Techniques for Smart Energy Systems*,
Lecture Notes in Electrical Engineering 862,
https://doi.org/10.1007/978-981-19-0252-9_7

Learning (ML) based SEE models have been devised in literature [2]. It is observed that 68.7% of total research in SEE domain is solely contributed by ML techniques majorly regression analysis, artificial neural networks, and support vector machines [3]. The research trends suggest that ML estimator works consistently under diverse environment [4]. Hence, advancement is desirable for better results [5–8]. Literature advocates that the best effort estimators from the ML literature in SEE domain [9, 10] are Artificial Neural Network (ANN) [11–13], Support Vector Regression (SVR) [14, 15], and Generalized Linear Model (GLM) [16]. The performance of these three popular models is compared. For this agenda, three models (ANN_SG, SVR_SG, GLR_SG) are developed and compared. The study utilizes the PROMISE repository based five datasets—Desharnais, COCOMO81, China, Maxwell, and Miyazaki94 for the experimentation [17].

The contribution of this study is to find out the best ML technique for SEE after conducting an empirical comparison among the most popular techniques. The research questions to carry out this study are as follows

- **RQ1**—Which is the best SEE model in terms of error values and prediction accuracy?
- **RQ2**—Does the answer to above RQ bear the statistical proof for validation?

The organization of paper is as follows: Sect. 2 brings the highlights to the related literature work. Section 3 elaborates the methodology with the description to the datasets and evaluation criteria used for the conduction of this study. Section 4 discusses the experimental results and analytical inferences drawn. In Sect. 5, the concluding remarks are stated with reference to the future work.

2 Related Works

In SEE field, ML based models have captured the industry attention for accurate estimation as the software industry is continuously growing and changing. Nowadays, ML techniques are proven to be more accurate and effective rather than traditional estimation models. Goyal et al. [11] deployed multilayer perceptrons for effort estimation over desharnais dataset. Pospieszny et al. [16] implemented ANN, SVM, and GLM as an ensemble model and evaluated performance using MAE, MMRE, and PRED. They advocated that the ensemble model outperforms the single models for accurate SEE prediction. Sehra et al. [17] extended the SVM method with fuzzy approach to enhance the accuracy of the model. Shukla et al. [18] advocated ANN model over nearest neighbor and linear regression model. Idri et al. [19] did experimentation with SVMs and introduced imputation technique for performance improvement of SVMs.

The author makes following observations from the literature work—(1) ANN, SVR, and GLM are the most popular ML models; (2) PROMISE is most widely

accepted dataset being publicly available; And (3) the MAR (mean absolute residuals), MMRE (mean magnitude of relative error) are the most popular evaluation criteria.

In next section, the proposed methodology with the set-up model has been explained in detail.

3 Proposed Methodology

This section discusses the proposed methodology for this study. The proposed model with workflow is depicted as Fig. 1. The training subset of data is used in building the three models namely ANN_SG (artificial neural network algorithm), SVR_SG (support vector regression), and GLR_SG (generalized linear model) [20]. All three learners are *k*-fold cross validated with 10 as a value of *k*. In this way, the proposed model has been set-up for comparing the accuracy of models recorded empirically.

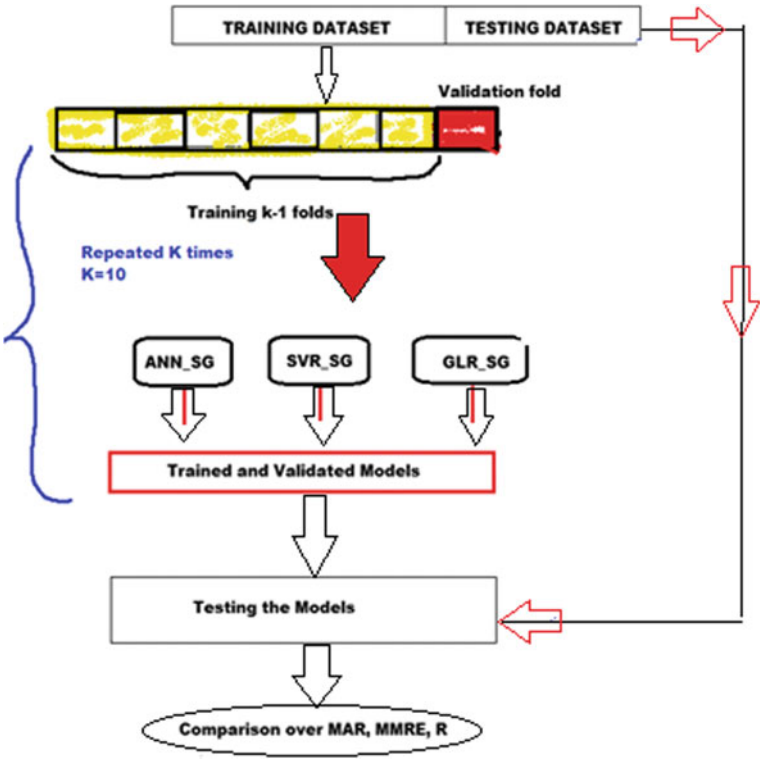

Fig. 1 Proposed model: comparison among three models (ANN_SG, SVR_SG, and GLR_SG)

Table 1 Parameter settings for the candidate models

Learner	Property: value pair
ANN_SG	Algorithm: backpropagation; Training function: trainlm; No. of hidden layer: 01; Hidden layer size:10 neurons; Input size: variable; Learning rate: 0.01
SVR_SG	Kernel: linear; CV with $k = 10$
GLR_SG	CV with $k = 10$; Stopping criteria: MAR

Table 2 Description: PROMISE dataset

Dataset	Features #	Instances #
Desharnais	11	81
COCOMO81	18	63
China	14	499
Maxwell	27	62
Miyazaki94	8	48

All the experiments are performed on MATLAB R2019 platform. The parameter settings for models are given as Table 1.

3.1 Description to Datasets

The PROMISE Dataset is utilized to conduct this study [21]. The reason is the popularity and free of cost availability of the datasets. For this study, five datasets from the repository are selected namely—Desharnais, COCOCMO81, China, Maxwell, and Miyazaki94. The description of the datasets is tabulated as Table 2.

3.2 Evaluation Criteria

The performance of proposed models is measured using three evaluation metrics—MAR, MRE, and MMRE. The reason of selecting these criteria is the suitability and popularity of these measures among the researchers [4, 16, 18, 19]. For the validation purpose, coefficient of correlation (R) is also computed [22, 23]. Table 3 gives the definition to evaluation criteria.

Table 3 Definition; MAR, MRE, MMRE, and *R*

Criteria name	Criteria definition
Mean absolute residual (MAR)	$1/N * \sum_{i=1}^{N} \lvert E(\text{Observed}) - E(\text{Predicted}) \rvert$
Magnitude of relative error (MRE)	$\frac{\lvert E(\text{Observed}) - E(\text{Predicted}) \rvert}{E(\text{Observed})}$
Mean magnitude of relative error (MMRE)	$1/N * \sum_{i=1}^{N} \text{MRE} * 100$ where N denotes the total number of instances
Coefficient of correlation (R)	$\sum_{i=1}^{N}(T - \text{mean}(T))(Y - \text{mean}(Y)) \div \sqrt{\left(\sum_{i=1}^{N}(T - \text{mean}(T)(T - \text{mean}(T))) \times \left(\sum_{i=1}^{N}(Y - \text{mean}(Y))(Y - \text{mean}(Y))\right)\right)}$ where N, T, Y denotes the number of instances, target effort ant, predicted effort for specific say "i" instance

4 Reporting Results

This section reports the results obtained from the study along with the drawn inferences to find answers to Research Questions (RQs).

4.1 Reporting Answer to RQ1

To answer RQ1, the performance of all three learners is recorded over all five datasets using MAR, MMRE, and *R* criteria. Tables 4, 5, and 6 report the results over MAR,

Table 4 Comparison of three learners over MAR criteria

MAR	Desharnais	Cocomo81	China	Maxwell	Miyazaki94
ANN_SG	**1645.89**	**271.82**	**171.4**	**3301.19**	**18.15**
SVR_SG	2312.99	493.99	1908.88	4746.41	48.21
GLR_SG	1865.98	661.3	1891.62	3826.74	22.91

Table 5 Comparison of three learners over MMRE criteria

MMRE	Desharnais	Cocomo81	China	Maxwell	Miyazaki94
ANN_SG	**0.41**	**7.32**	**0.11**	**0.92**	**0.67**
SVR_SG	0.7	1.24	0.7	0.96	0.76
GLR_SG	0.49	14.73	0.97	0.95	0.7

Table 6 Comparison of three learners over *R* criteria

Coefficient of correlation (*R*)	Desharnais	Cocomo81	China	Maxwell	Miyazaki94
ANN_SG	**0.88**	**0.99**	**0.99**	**0.94**	**1.0**
SVR_SG	0.64	0.69	0.75	0.64	0.87
GLR_SG	0.79	0.8	0.83	0.84	0.9

MMRE, and *R* criteria respectively. The columns of table represent the dataset and rows represent the regression model. The best values of metrics are highlighted as bold face.

It is observed that ANN_SG shows lowest values for MRE and MMRE and highest values of *R* over all five datasets. Further, boxplots are plotted for graphical analysis of results are shown as Figs. 2, 3, and 4. It is clear from the plots that ANN_SG has lowest median for MAR and MMRE and highest median for *R* along with low variance.

The validation of the best performance exhibited by ANN_SG model is done with the computation of *R*-value as the coefficient of correlation between the actual values of effort and the predicted values of the effort over all five datasets at *p*-value of 0.05. The observation is made that the model gives high values of *R*: 0.88, 0.99,

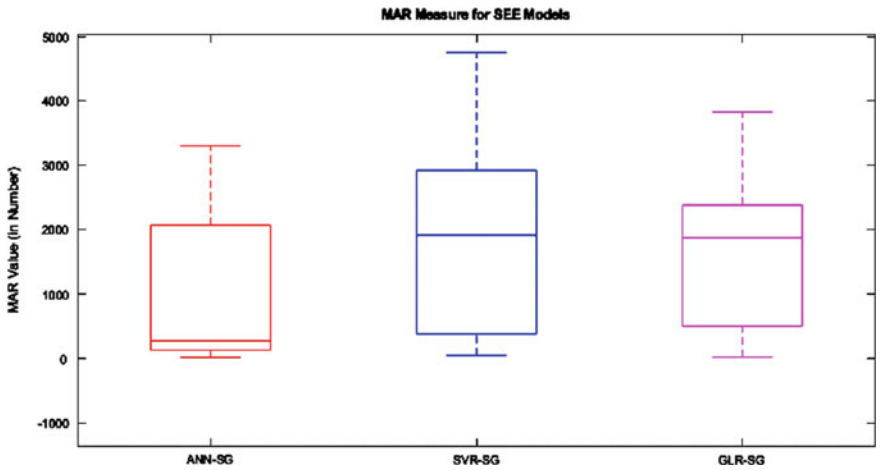

Fig. 2 Plot for MAR values

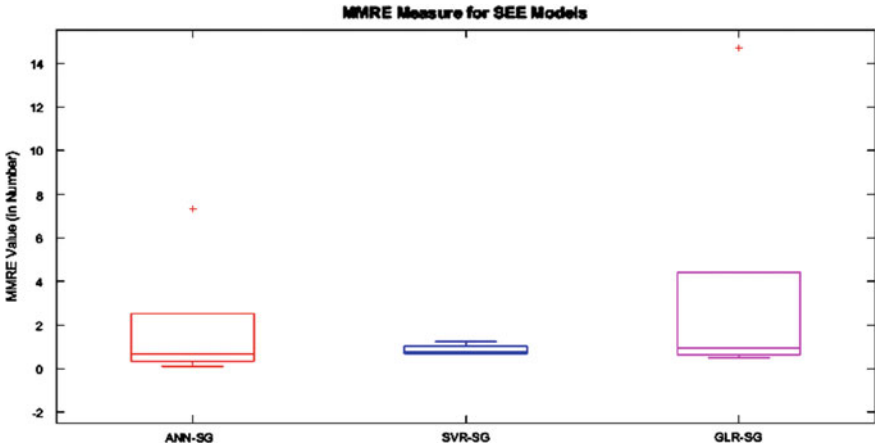

Fig. 3 Plot for MMRE values

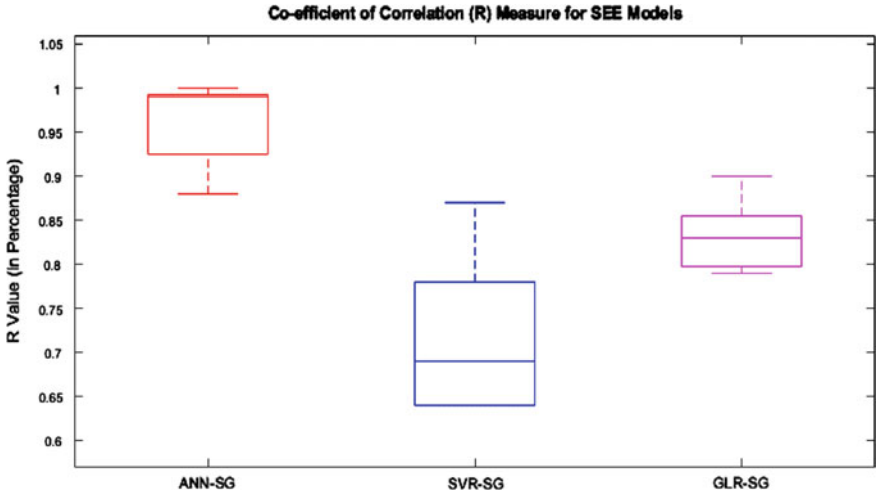

Fig. 4 Plot for *R* value

0.99, 0.94, and 1.0 at p-value < 0.05 for Desharnais, Cocomo81, China, Maxwell, and Miyazaki94 datasets respectively [22, 23] (see Fig. 5a–e).

Answer to RQ1—From the results, it can be inferred that the model ANN_SG performs better than SVR_SG, and GLR_SG in terms of all three evaluation criteria over all five datasets with an average improvement of 51.4% in MAR and 48.2% in MMRE of base models.

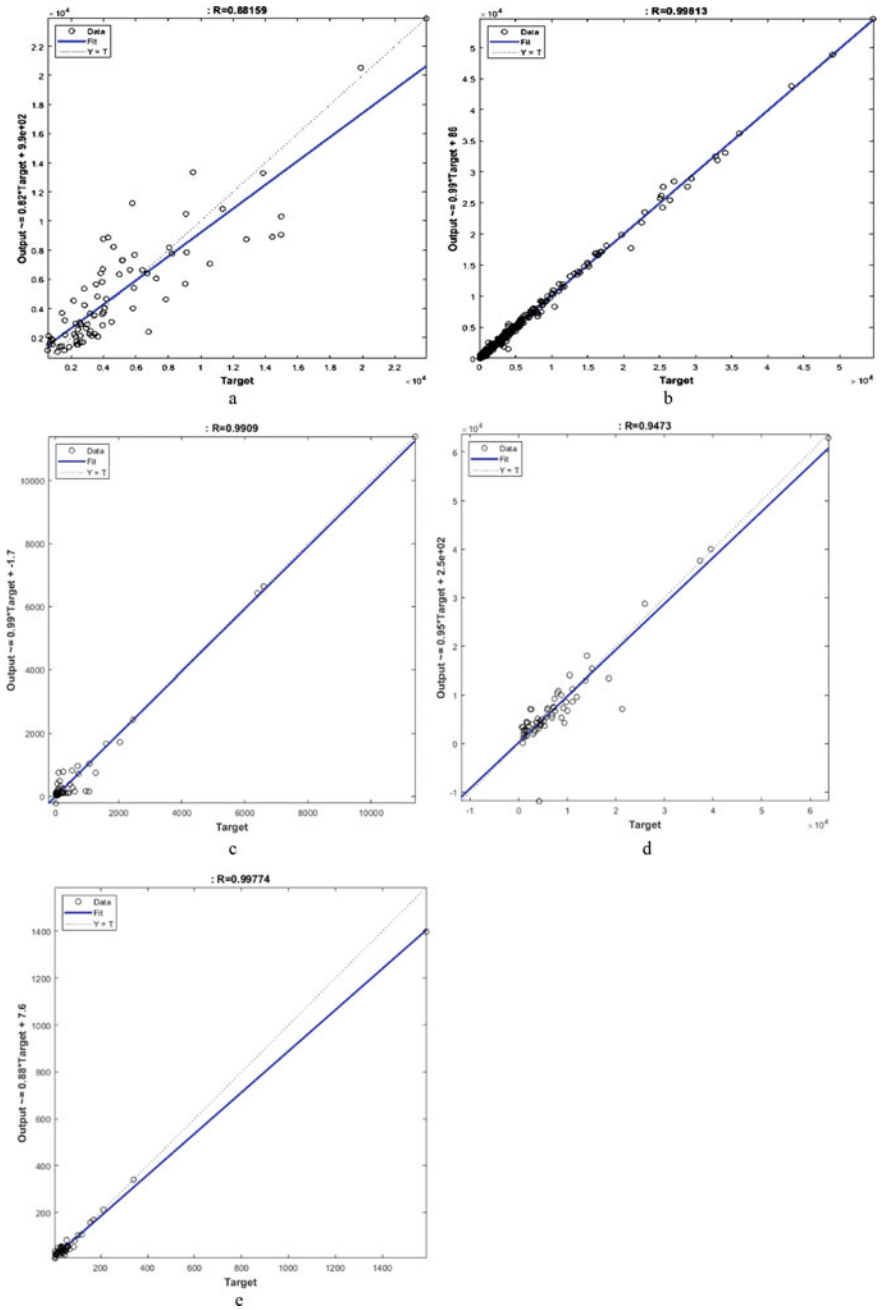

Fig. 5 **a** Plot over Desharnais dataset. **b** Plot over COCOMO81 dataset. **c** Plot over China dataset. **d** Plot over Maxwell dataset. **e** Plot over Miyazaki94 dataset. **a**–**e** Coefficient of correlation *R*-between actual effort and predicted effort by ANN_SG

Table 7 Result of Friedman test for comparison of three models

p-static at 95% confidence level	Desharnais	Cocomo81	China	Maxwell	Miyazaki94
p-value	0.0012	0.0001	0.0012	0.001	0.0021

4.2 Reporting Answer to RQ2

It is the most crucial question to answer before reporting this entire study. It needs the confirmation of above answer in statistical aspect. In order to validate the answer to RQ1 statistically, non-parametric statistical test—Friedman's test is selected [24]. The test is conducted at the confidence level of 95%. The null hypothesis is assumed as H_0: "The MRE reported by models ANN_SG, SVR_SG, and GLR_SG are same."

The Friedman test is conducted for SEE models over all five datasets individually. The value of test statistic is reported in Table 7. It is observed that the *p*-statistic is very small than 0.05 for all five datasets and hence, the hypothesis H_0 is rejected. It is significant to conclude that the ANN_SG significantly improves the performance over other SEE models. It is clear that ANN_SG is best performer with minimum MRE values.

Answer to RQ2—It is significant to conclude that the answer reported to RQ1 (under Sect. 4.1) is statistically validated. Hence, the ANN based SEE model ANN_SG is the best SEE model over all the competing models statistically.

5 Conclusions and Future Scope

Software effort estimation is paramount in software development process. This study makes a comparative analysis of the performance of three most popular SEE models to find out which has the best prediction power. The results state that—Artificial Neural Network based SEE model ANN_SG is statistically better than other two models (SVR_SG and GLM_SG). The Friedman test for multiple comparisons is conducted for statistical validation. Hence, the work is being concluded with the results that ANN_SG based SEE prediction model is better than other methods from the literature. In future, the work is proposed to be extended utilizing more SEE models and deep learning algorithms. The study can also be replicated with real-time industry datasets.

References

1. Chaos Report (2020) The Standish Group. https://hennyportman.files.wordpress.com/2021/01/project-success-qrc-standish-group-chaos-report-2020.pdf. Accessed 12 June 2021
2. Goyal S, Bhatia PK (2021) Empirical software measurements with machine learning. In: Bansal A, Jain A, Jain S, Jain V, Choudhary A (eds) Computational intelligence techniques and their applications to software engineering problems. CRC Press, Boca Raton, pp 49–64. https://doi.org/10.1201/9781003079996
3. Goyal S (2021) Handling class-imbalance with KNN (neighbourhood) under-sampling for software defect prediction. Artif Intell Rev. https://doi.org/10.1007/s10462-021-10044-w
4. Sehra SK, Brar YS, Kaur N, Sehra SS (2017) Research patterns and trends in software effort estimation. Inf Softw Technol 91:1–21
5. Goyal S (2021) Predicting the defects using stacked ensemble learner with filtered dataset. Autom Softw Eng 28:14. https://doi.org/10.1007/s10515-021-00285-y
6. Goyal S (2020) Heterogeneous stacked ensemble classifier for software defect prediction. In: 2020 sixth international conference on parallel, distributed and grid computing (PDGC), Waknaghat, pp 126–130. https://doi.org/10.1109/PDGC50313.2020.9315754
7. Goyal S, Bhatia PK (2021) Heterogeneous stacked ensemble classifier for software defect prediction. Multimed Tools Appl. https://doi.org/10.1007/s11042-021-11488-6
8. Goyal S, Bhatia PK (2021) Software fault prediction using lion optimization algorithm. Int J Inf Technol. https://doi.org/10.1007/s41870-021-00804-w
9. Goyal S, Bhatia PK (2020) Comparison of machine learning techniques for software quality prediction. Int J Knowl Syst Sci (IJKSS) 11(2):21–40. IGI Global. https://doi.org/10.4018/IJKSS.2020040102
10. Goyal S, Bhatia PK (2021) Software quality prediction using machine learning techniques. In: Sharma MK, Dhaka VS, Perumal T, Dey N, Tavares JMRS (eds) Innovations in computational intelligence and computer vision. Advances in intelligent systems and computing, vol 1189. Springer, Singapore, pp 551–560. https://doi.org/10.1007/978-981-15-6067-5_62
11. Goyal S, Bhatia PK (2020) Feature selection technique for effective software effort estimation using multi-layer perceptrons. In: Proceedings of ICETIT 2019. Lecture notes in electrical engineering, vol 605. Springer, Cham, pp 183–194. https://doi.org/10.1007/978-3-030-30577-2_15
12. Goyal S, Bhatia PK (2019) GA based dimensionality reduction for effective software effort estimation using ANN. Adv Appl Math Sci 18(8):637–649
13. Goyal S, Bhatia PK (2019) A non-linear technique for effective software effort estimation using multi-layer perceptrons. In: 2019 international conference on machine learning, big data, cloud and parallel computing (COMITCon), Faridabad, pp 1–4. https://doi.org/10.1109/COMITCon.2019.8862256
14. García-Floriano A, López-Martín C, Yáñez-Márquez C, Abran A (2018) Support vector regression for predicting software enhancement effort. Inf Softw Technol 97:99–109
15. Goyal S (2021) Effective software defect prediction using support vector machines (SVMs). Int J Syst Assur Eng Manag. https://doi.org/10.1007/s13198-021-01326-1
16. Pospieszny P, Czarnacka-Chrobot B, Kobylinski A (2018) An effective approach for software project effort and duration estimation with machine learning algorithms. J Syst Softw 137:184–196
17. Sehra SK, Brar YS, Kaur N, Sehra SS (2019) Software effort estimation using FAHP and weighted kernel LSSVM machine. Soft Comput 23(21):10881–10900
18. Shukla S, Kumar S (2019) Applicability of neural network based models for software effort estimation. In: 2019 IEEE world congress on services (SERVICES), Milan, pp 339–342. https://doi.org/10.1109/SERVICES.2019.00094
19. Idri A, Abnane I, Abran A (2018) Support vector regression-based imputation in analogy-based software development effort estimation. J Softw Evol Proc 30(12):e2114. JSME-18-0052.R2. ISSN 2047-7473. https://doi.org/10.1002/smr.2114

20. Bishop C (2006) Pattern recognition and machine learning. Springer, Singapore
21. Shirabad JS, Menzies TJ (2005) The PROMISE repository of software engineering databases. School of Information Technology and Engineering, University of Ottawa, Canada
22. Ewins DJ (2000) Modal testing: theory, practice and application, 2nd edn. Research Studies Press, Baldock
23. Ewins DJ (2000) Model validation: correlation for updating. Sadhana 25(3):221–234
24. Field A. Discovering statistics using SPSS, 3rd edn. Sage, London

A Review of Factors Affecting the Sensitivity of Piezoresistive Microcantilever Based MEMS Force Sensor

Monica Lamba, Sivasubramanian Ananthi, Himanshu Chaudhary, and Kulwant Singh

Abstract The performance of the MEMS sensor depends upon different parameters such as sensitivity, dynamic range, accuracy, hysteresis, linearity, resolution, bandwidth, repeatability, and response time. Among all, sensitivity is one of the important parameter which not only defines the relationship between physical signal and output electrical signal but also a decisive parameter to select a sensor for specific range of applications. In this paper, different factors are identified from the existing work which are affecting the sensitivity of piezoresistive microcantilever based force sensor. The main finding of the paper revealed that sensitivity depends upon the dimension of microcantilever (length, width, and thickness), dimension of piezoresistors (length, width, and thickness), placement of piezoresistors, material of microcantilever and piezoresistors, and stress concentrated region on microcantilever with appropriate shape and placement. The main conclusion of this study is that by varying these factors, the sensitivity of the piezoresistive microcantilever based force sensor can be enhanced and the designed sensor could be used for some specific range of application in the field of microbotics.

Keywords MEMS · Force sensor · Sensitivity · Microbotics · Microcantilever · Piezoresistors

1 Introduction

In this electronics era, the requirement of MEMS technology is increasing at a very faster pace because of its applicability in various area of application such as electronic, automotive, medical, communication, and defense. MEMS technology is the miniaturized of mechanical and electro-mechanical devices and structures that are prepared by the process of microfabrication. MEMS mainly consists of microsensors, microactuators, microelectronics, and microstructures. It has been decades that researchers and developers are constantly designing, simulating, and fabricating

M. Lamba (✉) · S. Ananthi · H. Chaudhary · K. Singh
Manipal University Jaipur, Jaipur, India
e-mail: lambamonica346@gmail.com

© The Author(s), under exclusive license to Springer Nature Singapore Pte Ltd. 2022

A. Tripathi et al. (eds.), *Intelligent Computing Techniques for Smart Energy Systems*,
Lecture Notes in Electrical Engineering 862,
https://doi.org/10.1007/978-981-19-0252-9_8

microsensors for almost every physical quantity including temperature [1], pressure [2], force [3–7], intensity [8], acceleration [9], magnetic field [10], radiation [11], chemical [12], etc. Recently researchers community also start developing on microactuators which includes microvalves [13], optical switches [14], micromirror arrays [15], micropumps [16], and many others. Fundamentally the dimensions of microsensors and microactuators are in the range of microns, but these microstructures control is upto macroscale level. Though a lot of research is still awaited in the field of MEMS sensors, especially for sensing a physical quantity namely force. MEMS force sensor is gaining popularity because of its wide range of application in the field of material characterization, microgrippers, drug delivery, minimal invasive surgery, and microbotic application [3–7]. The designed sensor is able to sense low magnitude forces in micro and nano Newton range. To sense these low magnitude forces, the sensor requirements to have high sensitivity, dynamic range, accuracy, hysteresis, linearity, resolution, bandwidth, repeatability, and response time. For developing a sensor different mechanical mechanisms were available such as diaphragm, beams, cantilevers, and membranes, but for sensing forces cantilevers are most suitable due to its high sensitivity, versatility, and low cost [17]. Among different sensing mechanism available in MEMS piezoresistive sensing mechanism are preferred for sensing low magnitude forces [3–7]. In this paper, different factors are identified from the existing literature which are affecting the sensitivity of piezoresistive microcantilever based force sensor some of them are worth mentioning here. Harley and Kenny demonstrated in their study that improvement in displacement, force sensitivity, and bandwidth is achievable by thinning the piezoresistive cantilevers [18]. Loui et al. revealed through the observed results that cantilevers having length greater than width are the most favorable shape for point loading applications, for example, force measurements and microscopy whereas shorter and wider cantilevers are suitable for surface loading and useful for application in biological and chemical sensor [19]. Lim et al. reported in their study that effects of design parameters viz. material and of cantilever beam, length, and thickness, on sensitivity. Observed results indicated that increase in the length, reduction in the thickness of cantilever beam and material of the beam having lower Young's modulus of elasticity enhanced the sensitivity of cantilever beam whereas the shape of the cantilever beam does not notably impact upon its sensitivity [20]. The dimensions of piezoresistors as discussed by Madhavi et al. [21] can greatly influence the performance parameters of the sensor. Nachippan et al. reported in their study that sensitivity of biosensors is improved by increasing the deflection of microcantilever beam. Further, deflection in cantilever beam is increased by increasing the length or by reducing the beam thickness but it leads to reduction in resonant frequency of the cantilever beam [22]. By changing the dimension and doping concentration of piezoresistors, the sensitivity and noise immunity of the designed sensor are affected as brought out by Suja et al. [23]. Sosa et al. fabricated and optimized a blood pressure sensor ideal for biomedical applications [24]. Tahani et al. demonstrated the effect of different geometries, dimensions, position, and number of holes on cantilevers on sensitivity of a sensor. Study revealed that an octagonal hole placed close to the root possesses the highest sensitivity [25]. Muhammad et al. proposed that paddle type cantilever

with stress concentrated regions has displacement sensitivity enhanced by 1.55 times in comparison with an ordinary cantilever [26]. Firdaus et al. in their research work has mentioned that a half cut stress concentrated region on the piezoresistive microcantilever increases stress by more than 100% and also enhances the sensitivity of the designed sensor [27]. Rahim et al. conducted a study to analyze the effects of incorporating various stress concentrated region (SCR) on the cantilevers. Observed results revealed that rectangular shaped SCR improves sensitivity in comparison with other shapes [28].

Pandya et al. fabricated a micro-force sensor using laboratory made SU-8 tip and silicon on insulator as substrate material with piezoresistive sensing mechanisms. The reported spring constant is 0.1488 N/m and sensitivity 2.7 mV/N [29]. A microforce plate array was developed by Takahashi et al. in their research for synchronized measurement of anterior and vertical components of Ground Reaction Forces generated by the legs movement of an ant. The reported maximum GRF using the designed sensor is 10 μN and 5 μN along z-axis and x-axis respectively [30]. A polycrystalline silicon based piezoresistive cantilever is fabricated by Villanueva et al. having width and thickness of the order of submicron useful for measurement of static force with reported force sensitivity and resolution as 97 μV/pN and 30 pN respectively [31]. A silicon diaphragm based MEMS force sensor developed by Rab et al. which reported sensitivity as 35–0.40 mV/V/N in the range 10–50 N [32]. MEMS technology based force sensor is fabricated using H-free (a-C) amorphous carbon developed by Ma et al. having force measuring range from 0 to 1.16 N having sensitivity 80.71 V/V/N and nonlinearity at 1.3% full scale with good quality of repeatability [33]. Kwoka et al. demonstrated in their study that micromechanical cantilevers are one of the attractive methods for force measurement. In addition of this Kwoka et al. reported that Soft MetMol MEMS silicon cantilever developed using silicon on insulator (SOI) as the substrate material with piezoresistive sensing mechanism and evaluated the stiffness which is much less than traditional piezoresistive silicon cantilever. The designed sensor achieved deflection sensitivity and force sensitivity of 11 Vm^{-1} and 263 VN^{-1} at an applied bias of 2 V.

In this manuscripts factors affecting the sensitivity of piezoresistive microcantilever based force sensor are identified from the existing literature.

2 Analytical Analysis of Different Factors Affecting Sensitivity

For developing a MEMS force sensor, the mechanical structure used for this study is the microcantilever. Microcantilever is a beam like structure which is fixed at one end and free at another end. The force to be sensed by the sensor is applied at the tip of the free end in response to that microcantilever displaces from its original position. This displacement will cause stress to be induced at the fixed of the cantilever beam. Higher the deflection, higher will be the induced stress. Then comes the role of

sensing mechanism, for this study the sensing mechanism used is the piezoresistive sensing mechanism. The stress developed at the fixed end of the cantilever beam is sensing by this sensing mechanism and output is indicated in form of electrical signal. Input quantity applied to the sensor is force and the output is in the form of electrical signal. The sensitivity is defined as the ratio of change in output (voltage) with respect to change in input (force). Here, different factors affecting sensitivity of piezoresistive microcantilever based force sensor has proven with analytical analysis.

2.1 Factor Affecting with Microcantilever Mechanism

The applied force at the tip of the microcantilever is responded in form of displacement as indicated in Fig. 1a, b.

The equation of the displacement of rectangular cantilever is given by the relation indicated in Eq. (1)

$$\delta = \frac{4(1-\nu)\sigma L}{2ET^2} \tag{1}$$

where δ is the deflection of the cantilever, ν is the Poisson's ratio, σ is the applied stress, L is length of the microcantilever, E is the Young's modulus of elasticity, and T is the thickness of microcantilever. Equation (1) clearly indicates that deflection of the microcantilever mainly depends on the applied stress (σ), geometrical parameters (L, T), and material properties (ν, E). From Eq. (1) it can be perceived that deflection of the cantilever is directly proportional to the applied stress (force per unit area), to length but inversely proportional to Young's modulus of elasticity and thickness of the cantilever.

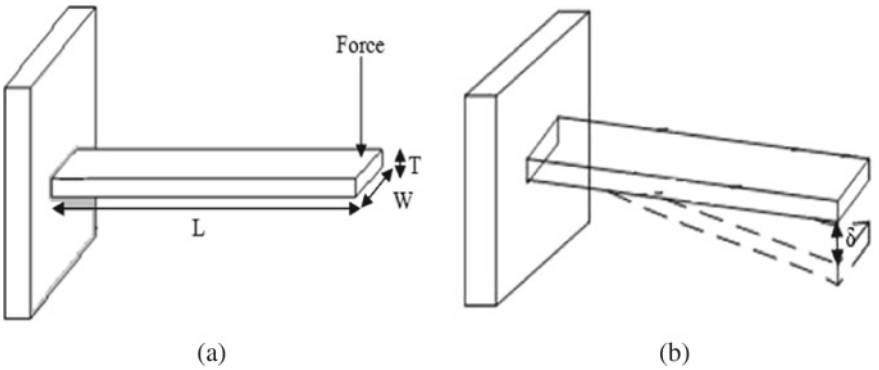

Fig. 1 **a** Rectangular cantilever, **b** deflection in rectangular cantilever

2.2 Factor Affecting with Sensing Mechanism

In piezoresistive sensing mechanism, piezoresistors are arranged on the microcantilever in Wheatstone bridge configuration as indicated in Fig. 2a, b.

When null force is applied on the cantilever, the length of each resistor has equal length.

The mathematical expression of resistance is given by the relation as indicated by Eq. (2).

$$R = \frac{\rho l}{A} = \frac{\rho l}{wt} \tag{2}$$

Here R is the resistance, A is the cross-sectional area, l is the length, w is the width, t is the thickness, and ρ is the resistivity of the piezoresistors. Equation (2) clearly indicates that resistance is directly proportional to piezoresistors length, resistivity of the material selected for piezoresistors, and inversely proportional to their width and thickness of the piezoresistors.

Further equation of change in resistance ΔR with respect to original resistance is given by the relation indicated in Eq. (3).

$$\frac{\Delta R}{R} = \pi_l \sigma_l + \pi_t \sigma_t \tag{3}$$

Here, π_l and π_t are the longitudinal and transverse piezoresistive coefficient whereas σ_l and σ_t are the longitudinal and transverse stress respectively.

Resistance change will cause output voltage to vary as indicated by Eq. (4)

$$V_{\text{out}} = V_{\text{in}}\left(\frac{\Delta R}{R}\right) \tag{4}$$

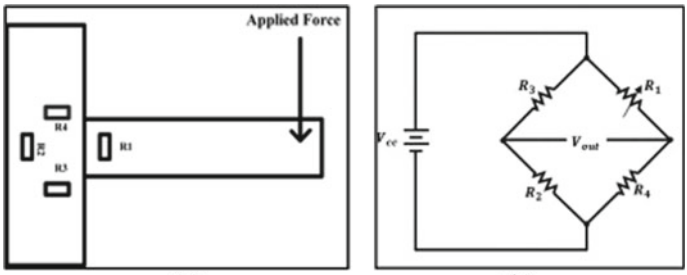

Fig. 2 **a** Top view of piezoresistive microcantilever, **b** quarter Wheatstone bridge configuration [3]

Here, V_{out} is the output voltage, V_{in} is the input voltage, ΔR is the change in resistance whereas R is the resistance. The output voltage is directly proportional to resistance change and the applied input voltage whereas inversely proportional to resistance.

2.3 Factors Affecting Sensitivity

It is the ratio of change in output with respect to the change in input. Here for piezoresistive microcantilever based force sensor, input quantity is the applied force and output is the voltage. So the equation for sensitivity is given by the relation indicated in Eq. (5)

$$S = \frac{\Delta V}{\Delta F} \tag{5}$$

3 Conclusion

From the literature reviewed and analytical analysis, it has been released that sensitivity of the piezoresistive microcantilever based force sensor depends upon the various factors which mainly includes the dimensions of microcantilever, piezoresistors dimensions, material of microcantilever and piezoresistors. As far as the dimension of microcantilever is concern, with the increase in length and decreasing thickness, Young's modulus of elasticity sensitivity increases. In respect with the piezoresistors increasing length and reduction in width and thickness enhances the sensitivity of the sensor. As the change in resistance increases the output voltage developed across the Wheatstone bridge increases which further increases the sensitivity of the sensor. The appropriate selection of all these factors leads to the development of high sensitive piezoresistive microcantilever based force sensor.

4 Future Prospective

The optimized design of piezoresistive microcantilever based force sensor is useful for sensing low magnitude forces in the range of micro and nano Newton range. The designed sensor can be useful for micromanipulation application specially in the field of microbotics.

References

1. Jackson T, Mansfield K, Saafi M, Colman T, Romine P (2008) Measuring soil temperature and moisture using wireless MEMS sensors. Measurement 41(4):381–390
2. Singh K, Joyce R, Varghese S, Akhtar J (2015) Fabrication of electron beam physical vapor deposited polysilicon piezoresistive MEMS pressure sensor. Sens Actuators A Phys 223:151–158
3. Lamba M, Mittal N, Singh K, Chaudhary H (2020) Design analysis of polysilicon piezoresistors PDMS (polydimethylsiloxane) microcantilever based MEMS force sensor. Int J Mod Phys B 34(09):2050072
4. Lamba M, Chaudhary H, Singh K (2020) Optimized analysis of sensitivity and non-linearity for PDMS–graphene MEMS force sensor. IETE J Res 1–15
5. Lamba M, Chaudhary H, Singh K (2019) Analytical study of MEMS/NEMS force sensor for microbotics applications. IOP Conf Ser Mater Sci Eng 594(1):012021. IOP Publishing
6. Lamba M, Nag M, Chaudhary H, Singh K (2020) Model prediction of microcantilever using DOE for stress and eigen frequency analysis for force measurement. IOP Conf Ser Mater Sci Eng 748(1):012025. IOP Publishing
7. Lamba M, Chaudhary H, Singh K (2020) Graphene piezoresistive flexible force sensor for harsh condition. AIP Conf Proc 2294(1):020008. AIP Publishing LLC
8. Zhou N, Jia P, Liu J, Ren Q, An G, Liang T, Xiong J (2020) MEMS-based reflective intensity modulated fiber-optic sensor for pressure measurements. Sensors 20(8):2233
9. Hulsing R (1998) MEMS inertial rate and acceleration sensor. IEEE Aerosp Electron Syst Mag 13(11):17–23
10. Marauska S, Jahns R, Greve H, Quandt E, Knöchel R, Wagner B (2012) MEMS magnetic field sensor based on magnetoelectric composites. J Micromech Microeng 22(6):065024
11. Augustyniak I, Dziuban J, Knapkiewicz P, Matusiak M, Olszacki M, Pons P (2013) MEMS high-doses radiation sensor. In: 2013 transducers & eurosensors XXVII: the 17th international conference on solid-state sensors, actuators and microsystems (TRANSDUCERS & EUROSENSORS XXVII), June 2013. IEEE, pp 1503–1506
12. Holthoff EL, Heaps DA, Pellegrino PM (2010) Development of a MEMS-scale photoacoustic chemical sensor using a quantum cascade laser. IEEE Sens J 10(3):572–577
13. Takao H, Miyamura K, Ebi H, Ashiki M, Sawada K, Ishida M (2005) A MEMS microvalve with PDMS diaphragm and two-chamber configuration of thermo-pneumatic actuator for integrated blood test system on silicon. Sens Actuators A Phys 119(2):468–475
14. Yeow TW, Law KE, Goldenberg A (2001) MEMS optical switches. IEEE Commun Mag 39(11):158–163
15. Guan S, Nelson BJ (2005) Pulse-reverse electrodeposited nanograinsized CoNiP thin films and microarrays for MEMS actuators. J Electrochem Soc 152(4):C190
16. Nguyen NT, Huang X, Chuan TK (2002) MEMS-micropumps: a review. J Fluids Eng 124(2):384–392
17. Duc TC, Creemer JF, Sarro PM (2006) Piezoresistive cantilever beam for force sensing in two dimensions. IEEE Sens J 7(1):96–104
18. Harley JA, Kenny TW (1999) High-sensitivity piezoresistive cantilevers under 1000 Å thick. Appl Phys Lett 75(2):289–291
19. Loui A, Goericke FT, Ratto TV, Lee J, Hart BR, King WP (2008) The effect of piezoresistive microcantilever geometry on cantilever sensitivity during surface stress chemical sensing. Sens Actuators A Phys 147(2):516–521
20. Lim YC, Kouzani AZ, Duan W, Kaynak A (2010) Effects of design parameters on sensitivity of microcantilever biosensors. In: IEEE/ICME international conference on complex medical engineering, July 2010. IEEE, pp 177–181
21. Madhavi KY, Krishna M, Murthy CC (2013) Effect of diaphragm geometry and piezoresistor dimensions on the sensitivity of a piezoresistive micropressure sensor using finite element analysis. IJESE 1(9)

22. Nachippan NM, Balaji V, Reddy SVS, Logesh K (2015) Enhancement of deflection of microcantilever beam for improving the sensitivity of biosensor. Int J ChemTech Res 8(8):349–356
23. Suja KJ, Kumar GS, Nisanth A, Komaragiri R (2015) Dimension and doping concentration based noise and performance optimization of a piezoresistive MEMS pressure sensor. Microsyst Technol 21(4):831–839
24. Sosa J, Montiel-Nelson JA, Pulido R, Garcia-Montesdeoca JC (2015) Design and optimization of a low power pressure sensor for wireless biomedical applications. J Sens 2015
25. He JH, Li YF (2006) High sensitivity piezoresistive cantilever sensor for biomolecular detection. J Phys Conf Ser 34(1):429–435
26. Bhatti MA, Xi LC, Zhong LY, Abdalla AN (2007) Design and finite element analysis of piezoresistive cantilever with stress concentration holes. In: 2007 2nd IEEE conference on industrial electronics and applications, May 2007. IEEE, pp 1171–1174
27. Firdaus SM, Azid IA, Sidek O, Ibrahim K, Hussien M (2008) Half cut stress concentration (HCSC) region design on MEMS piezoresistive cantilever for sensitivity enhancement. In: 2008 33rd IEEE/CPMT international electronics manufacturing technology conference (IEMT), Nov 2008. IEEE, pp 1–6
28. Rahim RA, Bais B, Majlis BY (2008) Design and analysis of MEMS piezoresistive SiO_2 cantilever-based sensor with stress concentration region for biosensing applications. In: 2008 IEEE international conference on semiconductor electronics, Nov 2008. IEEE, pp 211–215
29. Pandya HJ, Kim HT, Roy R, Desai JP (2014) MEMS based low cost piezoresistive microcantilever force sensor and sensor module. Mater Sci Semicond Process 163–173
30. Takahashi H, Thanh-Vinh N, Jung UG, Matsumoto K, Shimoyama I (2014) MEMS two-axis force plate array used to measure the ground reaction forces during the running motion of an ant. J Micromech Microeng 24(6):065014
31. Villanueva LG, Rius G, Pérez-Murano F, Bausells J (2015) Piezoresistive cantilever force sensors based on polycrystalline silicon. In: 2015 10th Spanish conference on electron devices (CDE), Feb 2015, pp 1–4
32. Kumar R, Rab S, Pant BD, Maji S (2018) Design, development and characterization of MEMS silicon diaphragm force sensor. Vacuum 153:211–216
33. Ma X, Guo P, Tong X, Zhao Y, Zhang Q, Ke P, Wang A (2019) Piezoresistive behavior of amorphous carbon films for high performance MEMS force sensors. Appl Phys Lett 114(25):253502

Dynamics Modeling and Motion Simulation of a Segway Robotic Transportation System

Izzat Aldarraji, Ayad A. Kakei, Ayad Ghany Ismaeel, Georgios Tsaramirsis, and Akshet Patel

Abstract Simulation is an essential interactive computer tool that can be applied to monitor systems graphically. A simulation of motion is presented in this study to support the control of Segway Robot Transportation Platform (SRTP). The introduced system provides simulation of the SRTP using MATLAB. The nonlinear dynamic equations of the motion for the Segway system are determined using the Lagrange approach. The derived nonlinear equations are then arranged in state space model format. The SRTP is simulated using the derived state space model using MATLAB. The introduced modeling and simulation processes have shown their ability to produce and plot the motion of the Segway parts with monitoring the effect of the Segway physical parameters such as mass of cart.

Keywords Segway robotic · Transportation system · Dynamics analysis · Lagrange approach · Nonlinear dynamics equations · State space · Segway motion · Modeling · Simulation

I. Aldarraji
Department of Automated Manufacturing, University of Baghdad, Baghdad, Iraq

I. Aldarraji · A. A. Kakei
Department of Mechanical Engineering, University of Kirkuk, Kirkuk, Iraq
e-mail: ayad.kakei@uokirkuk.edu.iq

A. G. Ismaeel
Department of Computer Technical Engineering, Al-Kitab University, Kirkuk, Iraq
e-mail: ayad.ghany@uoalkitab.edu.iq

G. Tsaramirsis
Higher Colleges of Technology, Abu Dhabi Women's College, Abu Dhabi, UAE
e-mail: gtsaramirsis@hct.ac.ae

A. Patel (✉)
Department of Mechatronics, Manipal University, Jaipur, India
e-mail: akshet.189403031@muj.manipal.edu

© The Author(s), under exclusive license to Springer Nature Singapore Pte Ltd. 2022

A. Tripathi et al. (eds.), *Intelligent Computing Techniques for Smart Energy Systems*,
Lecture Notes in Electrical Engineering 862,
https://doi.org/10.1007/978-981-19-0252-9_9

1 Introduction

The requirement of a new transport platform that can move easily in an intelligent way has been raised recently. The Segway robot is a motorized platform that can transport the rider efficiently by balancing him [1]. In this balancing process, when the person leans forward, the Segway will push itself right to the ground and keep its alignment upright [2]. The Segway robots have been built based on the principle of inverted pendulum [3]. In [4], a Segway electric vehicle is designed to transport persons, using a control algorithm that is implemented to the designed platform and can balance the persons standing on it in less than two second. In addition, this Segway is designed in a way that it can absorb shocks on rough roads. Generally, the Segway is a nonlinear time-varying system. In [5], a robust controller is designed for Segway to manipulate the issues of both the unknown coefficients and model errors. In [6], the authors focused on stabilization of the Segway in their project. The Segway platform is linearized as a first step [7]. Then, the technique of Linear-Quadratic Regulator is implemented to stabilize the Segway platform. Moreover, the Segway system is stabilized at a desired velocity in a straight path. However, simulation of the Segway Robotic Transportation platform (SRTP) is an essential computer graphic tool that is applied for monitoring the motion of these platforms [8]. The simulation process assists in saving time in modeling of Segway robotics. Furthermore, simulation of the motion of Segway robotics can be applied in planning the motion and design of Segway robotics. Manufacturing SRTP is an expensive process which includes hardware and software tasks that need a long time. Simulation systems can test SRTPs before building in the design stage which in turn help to check the features of Segway robotics graphically. Hence, modification of the SRTP parameters until reaching the best ones in the design stage can be implemented before the manufacturing process. In this study, a computer simulation and modeling are produced to monitor the motion of a SRTP. The nonlinear dynamic equations for the Segway system are derived based on the Lagrange approach. The derived nonlinear equations are then arranged in state space equations format. The SRTP is simulated using the derived state space equations using MATLAB. The rest of the paper is organized as follows. In Sect. 2, the dynamic equations and state space model of the SRTP model are derived in detail. In Sect. 3, simulation results are presented and discussed. In Sect. 4, the conclusions of this study are summarized.

2 Model

Modeling is an essential step that should be taken into consideration at the early stage of the design and control process [9–11]. The SRTP is a two wheeled vehicle that should have the ability of self-balancing [12]. The presented SRTP model is shown in Fig. 1. In the modeling process of this study, as shown in Fig. 2a, b, the following concepts are assumed: the mass of the LeanSteer Frame (m_1) is centered

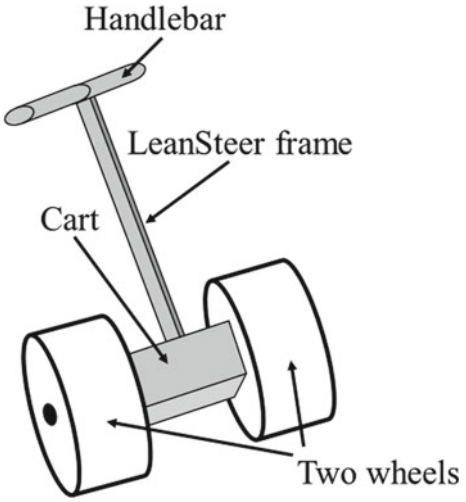

Fig. 1 Segway robotic platform

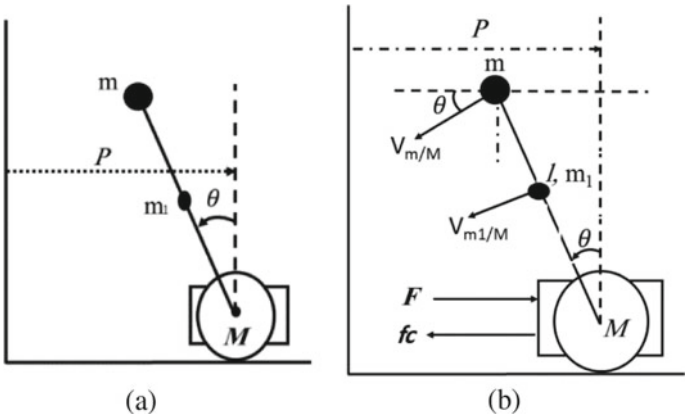

Fig. 2 Segway robotic model **a** diagram of platform, **b** dynamic model

at the middle of its length l; the mass of the rider m is centered at the Handlebar; the mass of the cart (M) is located at the center of the wheel axis; the friction force of the cart is f_c; the input force to the SRTP is F; the linear velocity of the rider with respect to the cart is $V_{m/M}$; and the linear velocity of the LeanSteer frame with respect to the cart is $V_{m1/M}$.

The kinetic energy of the SRTP is:

$$T = \frac{1}{2}mV_m^2 + \frac{1}{2}m_1V_{m1}^2 + \frac{1}{2}I\dot{\theta}^2 + \frac{1}{2}MV_M^2 \tag{1}$$

The inertia of the LeanSteer frame (I) is calculated as: $I = \frac{m_1l^2}{12}$.

Fig. 3 Linear velocity directions

Where V_m, V_{m1}, and V_M are the linear velocity of the rider, LeanSteer frame, and cart, respectively [13]. These velocities are calculated according to their directions shown in Fig. 3.

According to Fig. 3, the linear velocity of the rider is obtained as the following:

$$V_m^2 = V_M^2 + V_{m/M}^2 - 2V_{m/M}V_M\cos\theta$$

$$V_m^2 = \dot{P}^2 + \left(l\dot{\theta}\right)^2 - 2l\dot{\theta}\,\dot{P}\cos\theta \tag{2}$$

where $\dot{P}$ denotes the linear velocity of the cart. The linear velocity of the LeanSteer frame is obtained as:

$$V_{m1}^2 = V_M^2 + V_{\frac{m1}{M}}^2 - 2V_{\frac{m1}{M}}V_M\cos\theta$$

$$V_{m1}^2 = \dot{P}^2 + \left(\frac{l}{2}\dot{\theta}\right)^2 - l\dot{\theta}\,\dot{P}\cos\theta \tag{3}$$

Inserting Eqs. (2) and (3) into Eq. (1), yields

$$\begin{aligned} T = {} & \frac{1}{2}m\dot{P}^2 + \frac{1}{2}ml^2\dot{\theta}^2 - ml\dot{\theta}\,\dot{P}\cos(\theta) + \frac{1}{2}m_1\dot{P}^2 \\ & + \frac{1}{2}\frac{1}{4}m_1l^2\dot{\theta}^2 - \frac{1}{2}m_1l\dot{\theta}\,\dot{P}\cos\theta + \frac{1}{2}\frac{m_1l^2}{12}\dot{\theta}^2 + \frac{1}{2}M\dot{P}^2 \end{aligned}$$

$$T = \frac{1}{2}(m + m_1 + M)\dot{P}^2 + \frac{1}{2}\left(m + \frac{1}{3}m_1\right)l^2\dot{\theta}^2 - \left(m + \frac{1}{2}m_1\right)l\dot{\theta}\,\dot{P}\cos\theta \tag{4}$$

On the other side, the potential energy of the SRTP is obtained as

$$U = mgl\cos\theta + m_1g\frac{l}{2}\cos\theta \tag{5}$$

where g represents the gravitational acceleration. By inserting Eqs. (4) and (5) into the following Lagrange formula:

$$L = T - U \tag{6}$$

Results:

$$L = \frac{1}{2}(m + m_1 + M)\dot{P}^2 + \frac{1}{2}\left(m + \frac{1}{3}m_1\right)l^2\dot{\theta}^2 - \left(m + \frac{1}{2}m_1\right)l\dot{\theta}\dot{P}\cos\theta - mgl\cos\theta - m_1 g\frac{l}{2}\cos\theta \tag{7}$$

Now, the dynamic equations of the SRTP model are derived based on the following general form of the Lagrange equation:

$$\frac{\mathrm{d}}{\mathrm{d}t}\left(\frac{\partial L}{\partial \dot{q}_i}\right) - \frac{\partial L}{\partial q_i} = Q_i \tag{8}$$

For coordinate *P*:

$$\frac{\partial L}{\partial \dot{P}} = (m + m_1 + M)\dot{P} - \left(m + \frac{1}{2}m_1\right)l\dot{\theta}\cos\theta$$

$$\frac{\mathrm{d}}{\mathrm{d}t}\left(\frac{\partial L}{\partial \dot{P}}\right) = (m + m_1 + M)\ddot{P} - \left(m + \frac{1}{2}m_1\right)l\left[\ddot{\theta}\cos\theta - \dot{\theta}^2\sin\theta\right]$$

$$\frac{\mathrm{d}}{\mathrm{d}t}\left(\frac{\partial L}{\partial \dot{P}}\right) = (m + m_1 + M)\ddot{P} - \left(m + \frac{1}{2}m_1\right)l\ddot{\theta}\cos\theta + \left(m + \frac{1}{2}m_1\right)l\dot{\theta}^2\sin\theta$$

$$\frac{\partial L}{\partial P} = 0$$

$$Q_1 = F - b\dot{P}$$

Referring to Eq. (8), by substituting $\left(\frac{\partial L}{\partial \dot{P}}\right)$, $\frac{\partial L}{\partial P}$, and Q_1, results

$$(m + m_1 + M)\ddot{P} - \left(m + \frac{1}{2}m_1\right)l\ddot{\theta}\cos\theta + \left(m + \frac{1}{2}m_1\right)l\dot{\theta}^2\sin\theta = F - b\dot{P} \tag{9}$$

where b represents the coefficient of friction of the friction force f_c.

For coordinate θ:

$$\frac{\partial L}{\partial \dot{\theta}} = \left(m + \frac{1}{3}m_1\right)l^2\dot{\theta} - \left(m + \frac{1}{2}m_1\right)l\dot{P}\cos\theta$$

$$\frac{\mathrm{d}}{\mathrm{d}t}\left(\frac{\partial L}{\partial \dot{\theta}}\right) = \left(m + \frac{1}{3}m_1\right)l^2\ddot{\theta} - \left(m + \frac{1}{2}m_1\right)l\ddot{P}\cos\theta + \left(m + \frac{1}{2}m_1\right)l\dot{P}\dot{\theta}\sin\theta$$

$$\frac{\partial L}{\partial \theta} = \left(m + \frac{1}{2}m_1\right)l\dot{\theta}\dot{P}\sin\theta + mgl\sin\theta + m_1 g\frac{l}{2}\sin\theta$$

$$Q_2 = 0$$

Referring to Eq. (8), by substituting $\frac{\mathrm{d}}{\mathrm{d}t}\left(\frac{\partial L}{\partial \dot{\theta}}\right)$, $\frac{\partial L}{\partial \theta}$, and Q_2, results

$$\left(m + \frac{1}{3}m_1\right)l^2\ddot{\theta} - \left(m + \frac{1}{2}m_1\right)l\ddot{P}\cos\theta - \left(m + \frac{m_1}{2}\right)gl\sin\theta = 0 \tag{10}$$

The dynamic equations of the system are represented by Eqs. (9) and (10). In matrix form, the system can be represented as:

$$\begin{bmatrix} (m + m_1 + M) & -\left(m + \frac{1}{2}m_1\right)l\cos\theta \\ -\left(m + \frac{1}{2}m_1\right)l\cos\theta & \left(m + \frac{1}{3}m_1\right)l^2 \end{bmatrix}\begin{bmatrix} \ddot{P} \\ \ddot{\theta} \end{bmatrix} + \begin{bmatrix} b & \left(m + \frac{1}{2}m_1\right)l\dot{\theta}\sin\theta \\ 0 & 0 \end{bmatrix}\begin{bmatrix} \dot{P} \\ \dot{\theta} \end{bmatrix} = \begin{bmatrix} F \\ \left(m + \frac{m_1}{2}\right)gl\sin\theta \end{bmatrix} \tag{11}$$

Next, the state space model of the derived system in Eqs. (9) and (10) is developed. Assume the following state variables: $P = y_1$, $\dot{P} = y_2$, $\theta = y_3$, $\dot{\theta} = y_4$. Then, Eqs. (9) and (10) is represented as:

$$(m + m_1 + M)\dot{y}_2 - \left(m + \frac{1}{2}m_1\right)l\dot{y}_4\cos y_3 + \left(m + \frac{1}{2}m_1\right)ly_4^2\sin y_3 + by_2 = F \tag{12}$$

$$\left(m + \frac{1}{3}m_1\right)l^2\dot{y}_4 - \left(m + \frac{1}{2}m_1\right)l\dot{y}_2\cos y_3 - \left(m + \frac{m_1}{2}\right)gl\sin y_3 = 0 \tag{13}$$

Assuming $\dot{y}_1 = y_2$, $\dot{y}_3 = y_4$, the state space model according to Eqs. (12) and (13) is obtained as:

$$\begin{bmatrix} 1 & 0 & 0 & 0 \\ 0 & (m + m_1 + M) & 0 & -\left(m + \frac{1}{2}m_1\right)l\cos y_3 \\ 0 & 0 & 1 & 0 \\ 0 & -\left(m + \frac{1}{2}m_1\right)l\cos y_3 & 0 & \left(m + \frac{1}{3}m_1\right)l^2 \end{bmatrix}\begin{bmatrix} \dot{y}_1 \\ \dot{y}_2 \\ \dot{y}_3 \\ \dot{y}_4 \end{bmatrix} = \begin{bmatrix} y_2 \\ F - \left(m + \frac{1}{2}m_1\right)ly_4^2\sin y_3 - by_2 \\ y_4 \\ \left(m + \frac{m_1}{2}\right)gl\sin y_3 \end{bmatrix} \tag{14}$$

This State space model is represented in MATLAB to simulate the SRTP [14, 15].

3 Simulation Results

The derived state space model was applied in MATLAB with the following code to monitor the motion of the SRTP [16]:

```
function ydot=segway(t,y)
% define physical parameters of SRTP M;m;m1;B;L;J;g;F
G=[1 0 0 0;0 m+m1+M 0 -(m+(m1/2))*L*cos(y(3));0 0 1 0;0 -
(m+(m1/2))*L*cos(y(3)) 0 (m+(m1/3))*L*L];
F1=[y(2);-(m+(m1/2))*L*y(4)^2*sin(y(3))+F-
B*y(2);y(4);(m+(m1/2))*g*L*sin(y(3))];
ydot=inv(G)*F1;
%%%%%%%%%%%%%%%%%
close all
clear all
clc
t0=0;tf=50;y0=[0 0 0.261 0];
[t,y]=ode45('segway',[t0 tf],y0);
plot(t,y(:,1))
xlabel('time/s')
ylabel('distance/ m')
figure
plot(t,y(:,2))
xlabel('time/s')
ylabel(' velocity dp/dt:m/s')
figure
plot(t,y(:,3))
xlabel('time/ s')
ylabel('theta/ Radian')
figure
plot(t,y(:,4))
xlabel('time')
ylabel('angular velocity dtheta/dt:Radian/s')
```

The SRTP is implemented within two tests [17]. In the first test, the SRTP is simulated with the following physical parameters: $M = 0.6\,\text{kg}$; $m_1 = 0.3\,\text{kg}$, $b = 1.03\,\text{Ns/m}$; $l = 0.4\,\text{m}$, $I = 0.007\,\text{kgm}^2$, the input force is of step input type of unit value $F = 1\,\text{N}$. The Segway LeanSteer frame is assumed at initial position $\theta = 15°$. The simulation result of this test is shown in Fig. 4 [18].

In test 2, all the physical parameters of test 1 were the same except the mass of the cart. The cart is assumed of a heavy mass $M = 50\,\text{kg}$ i.e., approximately doesn't move [19]. The system was critically unstable with respect to theta as shown in Fig. 5. In contrast, in test 1, the SRTP had two degree of freedom and it was stable after approximately 15 s: [20].

4 Conclusions

This paper introduces a procedure to model and simulate motion of SRTP. Modeling process of the dynamic behavior is implemented based on the Lagrangian approach.

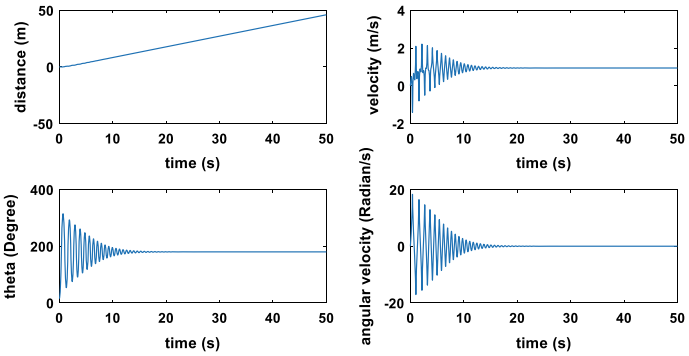

Fig. 4 Simulation result of test 1

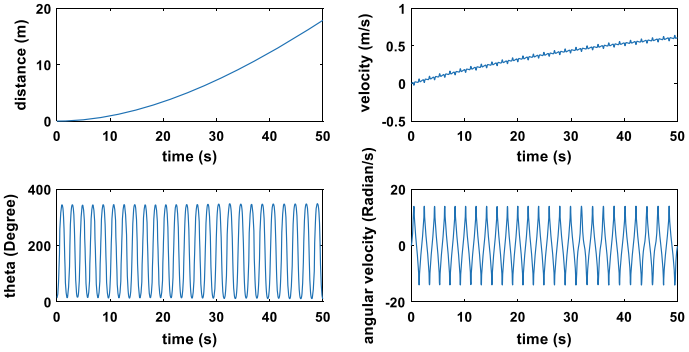

Fig. 5 Simulation result of test

The developed nonlinear model is represented in state space equations format. These state space equations are solved using MATLAB to simulate the motion of the SRTP. The simulation process showed its ability to monitor the linear motion of the SRTP and the angular motion of the LeanSteer frame for any physical parameters. It is indicated that the SRTP can be stable for moderate cart weight. The main limitation was that in the case of heavy cart weight, the system was critically unstable. This is something that will be addressed in future work by using genetic algorithms to find out the optimal parameters.

References

1. Pinto LJ, Kim D, Lee JY, Han C (2012) Development of a Segway robot for an intelligent transport system. In: 2012 IEEE/SICE international symposium on system integration (SII), pp 710–715. https://doi.org/10.1109/SII.2012.6427308
2. Castro A, Adams C, Singhose W (2013) Dynamic response characteristics of a two-wheeled

inverted-pendulum transporter. In: 52nd IEEE conference on decision and control, pp 1532–1537. https://doi.org/10.1109/CDC.2013.6760100
3. Younis W, Abdelati M (2009) Design and implementation of an experimental Segway model. AIP Conf Proc 350–354
4. Draz MU, Ali MS, Majeed M, Ejaz U, Izhar U (2012) Segway electric vehicle. In: 2012 international conference of robotics and artificial intelligence, pp 34–39. https://doi.org/10.1109/ICRAI.2012.6413423
5. Kim BW, Park BS (2016) Robust control for the Segway with unknown control coefficient and model uncertainties. Sensors (Basel) 16(7):1000. https://doi.org/10.3390/s16071000
6. Veen JA (2018) Stabilization and trajectory tracking of a Segway. Bachelor integration project IE&M, University of Groningen, Faculty of Science and Engineering
7. Jarvis R (2004) A 'do-it-yourself' Segway mobile robot platform. In: Proceedings of the Australasian conference on robotics & automation
8. Steiner M (2018) ROS navigation stack on a Loomo Segway robot. Dissertation BSc thesis, Vienna University, Munich
9. Al-Darraji I, Derbali M, Tsaramirsis G (2021) Tilting-rotors quadcopters: a new dynamics modelling and simulation based on the Newton-Euler method with lead compensator control. In: 2021 8th international conference on computing for sustainable global development (INDIACom), pp 363–369. https://doi.org/10.1109/INDIACom51348.2021.00063
10. Al-Darraji I, Piromalis D, Kakei AA, Khan FQ, Stojmenovic M, Tsaramirsis G, Papageorgas PG (2021) Adaptive robust controller design-based RBF neural network for aerial robot arm model. Electronics 10:831. https://doi.org/10.3390/electronics10070831
11. Al-Darraji I, Derbali M, Jerbi H, Khan FQ, Jan S et al (2021) A technical framework for selection of autonomous UAV navigation technologies and sensors. Comput Mater Contin 68(2):2771–2790
12. Gong Y et al (2019) Feedback control of a Cassie bipedal robot: walking, standing, and riding a Segway. In: 2019 American control conference (ACC). IEEE
13. Nguyen HG et al (2004) Segway robotic mobility platform. In: Mobile robots XVII, vol 5609. International Society for Optics and Photonics
14. Kulshreshtha M, Chandra SS, Randhawa P, Tsaramirsis G, Khadidos A, Khadidos AO (2021) Oatcr: outdoor autonomous trash-collecting robot design using YOLOv4-tiny. Electronics 10(18). https://doi.org/10.3390/electronics10182292
15. Tsaramirsis K et al (2021) Bio-virus spread simulation in real 3D space using augmented reality. Eng Sci 16(18):319–330. https://doi.org/10.30919/es8d592
16. Dunkers CM et al (2014) Indoor navigation and manipulation using a Segway RMP
17. Randhawa P, Basakhatre TP (2021) Design of pitch attitude hold mode for commercial aircraft using extended state observer. In: Goyal D, Chaturvedi P, Nagar AK, Purohit S (eds) Proceedings of second international conference on smart energy and communication. Algorithms for intelligent systems. Springer, Singapore. https://doi.org/10.1007/978-981-15-6707-0_26
18. Khanzode AS, Masne AG. Design and development of mechanical Segway
19. Randhawa P, Shanthagiri V (2015) Concept of operations to system design and development—an integrated system for aircraft mission feasibility analysis using STK engine, Matlab and Labview. Int J Instrum Control Syst 5(4):01–12. https://doi.org/10.5121/ijics.2015.5401
20. Simon C, Clarke D, Knoll A (2014) Modular multi sensor data fusion architecture for autonomous vehicles: using the RACE system on a Segway RMP 440. In: 2014 international conference on multisensor fusion and information integration for intelligent systems (MFI). IEEE

Microgrid Energy Management Strategy for Low Dynamics Load Applications Using Simulink

Jai Kumar Maherchandani, Ritesh Tirole, and Raju Kumar Swami

Abstract This paper presents an energy management strategy for microgrid consisting of photovoltaic, wind energy conversion system, battery, fuel cell, and electrolyzer system. Rule-based energy management strategy is designed to meet efficiently the slow varying residential load demand of rural households within the individual source limits. Simulation is carried out using MATLAB. Simulation results show that the developed energy management strategy is able to meet the instantaneous load demand in varying irradiance, wind speed, and load conditions keeping the battery state of charge and electrolyzer hydrogen pressure in allowable limits.

Keywords Battery · Fuel cell · Photovoltaic · Wind energy conversion system · Energy management strategy

1 Introduction

Increasing environment pollution and rapid depletion of fossil fuel are the two major concern of present world. Although a lot of efforts are being made at various level by the national and international agencies to address these issues, like environment pollution, etc. The tremendous increase in the percentage of renewable energy share is observed in the total electrical energy installed capacity of the developing countries, which is definitely a positive indication toward resolutions of environment pollution and fossil fuel depletion problem. In country like India, renewable energy share increased to 23%, which includes 33,713 MW from solar, 37,505 MW from wind, and 14,690 MW from other renewables [1].

J. K. Maherchandani
College of Technology and Engineering, Udaipur, Rajasthan, India

R. Tirole (✉)
Sir Padampat Singhania University, Udaipur, Rajasthan 313001, India
e-mail: ritesh.tirole@spsu.ac.in

R. K. Swami
Pacific University, Udaipur, Rajasthan 313001, India

© The Author(s), under exclusive license to Springer Nature Singapore Pte Ltd. 2022

A. Tripathi et al. (eds.), *Intelligent Computing Techniques for Smart Energy Systems*,
Lecture Notes in Electrical Engineering 862,
https://doi.org/10.1007/978-981-19-0252-9_10

With the help of renewable energy sources, installed capacity of electrical energy generation is continuously increasing worldwide. Still, a large number of populations living in isolated area are having no access to grid electricity, and approximately, 1.2 billion people have no access for domestic use [2–4]. Microgrid (MG) consisting of renewable and clean energy sources may be a potential solution to meet the electricity requirement of these areas such MG may integrate solar, wind as a primary source, and fuel cell (FC), battery as a backup source to increase the reliability of the system.

An energy management strategy (EMS) is always required to decide the proper energy share among the various source components of MG considering the individual limits and operational conditions.

Different EMSs [5–10] are presented in the literature for various configurations of MG with different objectives. These may be broadly classified as rule-based EMS and optimization-based EMS. Rule-based EMS is easy to implement and computationally more efficient. The present work focuses on the rule-based EMS for a microgrid consisting of photovoltaic (PV), wind energy conversion system (WECS), FC, battery, and electrolyzer system.

The rest of the paper is arranged as follows. Section 2 presents the modeling of MG source components. Section 3 gives the details of developed EMS. Simulation results and conclusion are presented in Sects. 4 and 5, respectively.

2 Modeling of Microgrid Components

2.1 Types of Grid-Connected Solar PV Configuration

MG configuration consisting of PV, WECS, FC, battery, and electrolyzer is shown in Fig. 1. The modeling of the MG source components is discussed below:

PV System

Solar cells show a nonlinear current–voltage characteristic that depends on temperature and solar radiation as shown in Eq. (1) [11]:

$$I = I_{\text{ph}} - I_{\text{o}}\left(\text{e}^{\frac{q(V+IR_{\text{s}})}{nkT}} - 1\right) - \frac{V + IR_{\text{s}}}{R_{\text{sh}}} \tag{1}$$

where I_{ph}, I_{o}, R_{s}, R_{sh}, q, K, and T are photocurrent, saturation current of the diode, series resistance, shunt resistance, diode ideality factor, Boltzmann's constant, electron charge, and absolute temperature in Kelvin.

Wind Energy Conversion System

Permanent magnet synchronous generator (PMSG) has better efficiency, reliability, and low maintenance for output of the wind power. The wind power output can be given by:

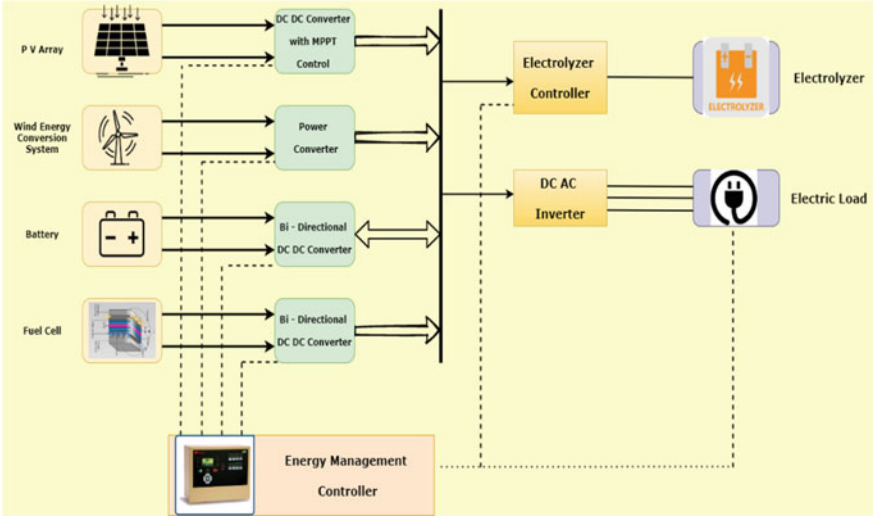

Fig. 1 Microgrid configuration

$$P = \frac{1}{2}\rho A V^3 C_P \tag{2}$$

Here, ρ is air density; V is wind speed; C_P is power coefficient of the wind turbine; A is area swept by the rotor blades of the wind turbine.

Battery System

A storage system is an essential component to operate in the case of an emergency. The battery size storage is significant, and modeling should be done to calculate the demand in case of emergency. The modeling equations as per below mentioned [12].

$$B_{\text{size}} = \frac{E_{\text{load}} \times \text{Days}_{\text{off}}}{\text{DoD}_{\max} \times \eta_{\text{temp}}} \tag{3}$$

where E_{load} load is in ampere hour delivered for the period of unavailability of power, Days_{off}: storage days (the days that power from the electric grid is unavailable), $\text{DOD}_{\max}$: maximum depth of discharge of the battery, and η_{temp}: temperature corrector factor.

$$E_B(t) = E_B(t-1) \cdot (1-\zeta) + \left(\frac{E_{GA}(t) - E_L(t)}{\eta_{\text{inv}}}\right) \cdot \eta_{\text{Batt}} \tag{4}$$

here ζ, η_{inv}, and η_{Batt} are self-discharge factor measured hourly, inverter efficiency, and battery efficiency, respectively; $E_B(t)$ and $E_B(t-1)$ are the charge quantity of storage system at time t and $t-1$, respectively, and E_L and E_{GA} are the load demand and renewable energy power, respectively.

Fuel Cell

It is used to increase the performance of the microgrid system. The modeling Eq. (5) is given here [13].

$$V_{\text{out}} = E - T[a + b\ln(I)] - (R_{\text{ohm0}} + k_{\text{RI}}I - k_{\text{RT}}I)I + \frac{RT}{zF}\ln\left(1 - \frac{I}{I_{\text{limit}}}\right) \quad (5)$$

where E: reversible potential of each cell, T: temperature, a and b are constant terms, I: current, R_{ohm0}: is the constant part of the ohmic resistance, k_{RI} and k_{RT}: empirical constants, R: gas constant, z: number of electrons participating, F: Faraday constant, and I_{limit}: limitation current.

Electrolyzer

Electrolyzer stacks are used in hybrid system in series or parallel to get the required rating. The modeling Eq. (6) is used [13].

$$V = V_{\text{rev}} + \frac{r}{A}I + s\log\left(\frac{t}{A}I + 1\right) \quad (6)$$

where V: terminal voltage, V_{rev}: reversible cell voltage, r: parameter related to ohmic resistance of the electrolyte, A: surface area of the electrode, I: current, s and t are coefficients related to overvoltage on electrodes.

3 Energy Management Strategy

EMS for the MG shown in Fig. 1 is discussed here. The MG is capable to meet the energy requirement of a small slow varying residential load. Operating points of individual MG source components are decided on the basis of available PV power, wind power, battery state of charge (SOC) level, pressure of hydrogen tank, load demand, and other operating conditions. The power rating of source components is given in Table 1.

Let P_{D} is load demand, P_{PV} and P_{Wind} are the available photovoltaic power and wind power, respectively. $P_{\text{FC\_min}}$ and $P_{\text{FC\_max}}$ are the minimum and maximum fuel

Table 1 Rating of MG source components

MG source component	Rating
Photovoltaic system	1 kW
Wind energy conversion system	1.5 kW
Fuel cell stack	1.2 kW
Battery	20 A-h
Electrolyzer	0.5 kW

cell power. SOC_{max} and $P_{H_{2\_max}}$ are the battery maximum SOC level and hydrogen tank maximum pressure, respectively. EMS is design considering PV and WECS as a primary energy sources and FC and battery as secondary energy sources. Deficit load demand P_{def} is given by:

$$P_{def} = P_D - (P_{PV} + P_{wind}) \tag{7}$$

Electrolyzer is used to consume the excess power or charge the battery, depending on the operating conditions. PV system is given higher priority than WECS to supply the load demand. Different possible cases and rules are given as follows:

Case I: Sufficient PV power (P_{PV}) available

- Load demand is fulfilled by PV system alone.
- Excess power is used to charge the battery if battery SOC $<$ SOC_{max}.
- If battery SOC $\cong$ SOC_{max}, excess power is supplied to electrolyzer for hydrogen production till $P_{H_2} \cong P_{H_{2\_max}}$.

Case II: Low PV power ($P_{PV} < P_D$) and sufficient wind power ($P_{PV} + P_{wind} > P_D$)

- Maximum power extracted from PV system.
- Wind power is regulated depending on load demand, battery SOC level and hydrogen tank pressure level (P_{H_2}).
  - (a) If $P_{H_2} \cong P_{H_{2\_max}}$ and (SOC $\cong$ SOC_{max}), only optimum power extracted from WECS so that PV and WECS can fulfill the load demand.
  - (b) If SOC $<$ SOC_{max} or $P_{H_2} < P_{H_{2\_max}}$,depending on the hydrogen tank pressure level and battery SOC level power extracted from WECS.

Case III: Insufficient PV and WECS power ($P_{PV} + P_{wind} < P_D$) and $P_{FC\_min} < P_{def} < P_{FC\_max}$

- Maximum power extracted from PV and WECS.
- Deficit load power demand P_{def} supplied by FC.

Case IV: Insufficient PV and WECS power ($P_{PV} + P_{wind} < P_D$) and $P_{FC\_max} < P_{def} < P_{FC\_max} + P_{B\_max}$ and 60 $<$ SOC $\leq$ SOC_{max}

- Maximum power extracted from PV and WECS.
- Deficit power drawn from FC and battery.

Case V: Insufficient PV and WECS power ($P_{PV} + P_{wind} < P_D$) and $P_{def} < P_{FC\_min}$ and 60% $<$ SOC $\leq$ SOC_{max}

- Maximum power extracted from PV and WECS.
- Deficit power drawn from battery.

Case VI: Insufficient PV and WECS power ($P_{PV} + P_{wind} < P_D$) and $P_{def} < P_{FC\_min}$ and SOC $<$ 60%

- Maximum power extracted from PV and WECS.

- FC supply the deficit power and charge the battery.

Case VII: Unfavorable PV and wind conditions

- FC and battery will be used to supply critical load on priority basis.

4 Result

The simulation results of the EMS described in previous section for the MG consists of PV, WECS, FC, battery, and electrolyzer shown in Fig. 1 are presented. Figures 2, 3, and 4 present the hypothetical wind speed, solar irradiance, and slow varying residential load demand, respectively. Energy management controller using the EMS and considering the operating conditions decide the power share from each individual MG source component.

PV, WECS, FC, battery power output, and electrolyzer power consumption are given in Figs. 5, 6, 7, 8, and 9, respectively.

Figures 10 and 11 show the status of the hydrogen storage and the SOC of the

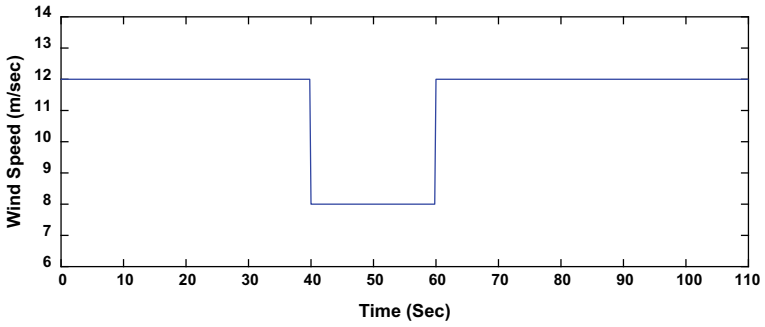

Fig. 2 Wind profile

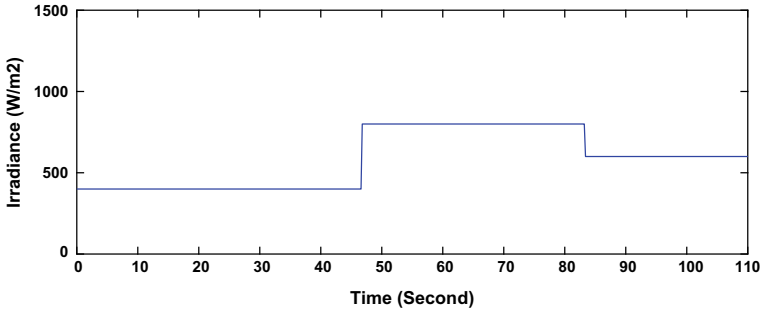

Fig. 3 PV irradiance

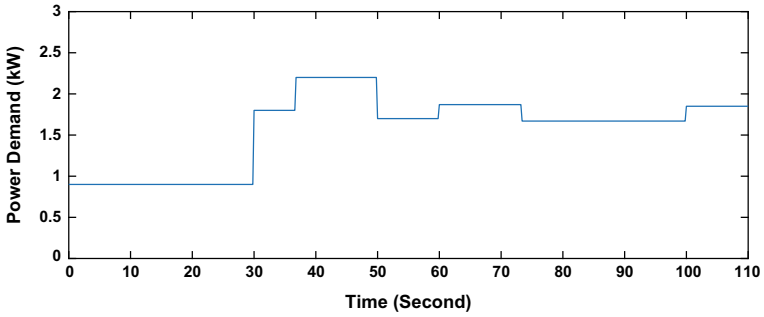

Fig. 4 Load power demand

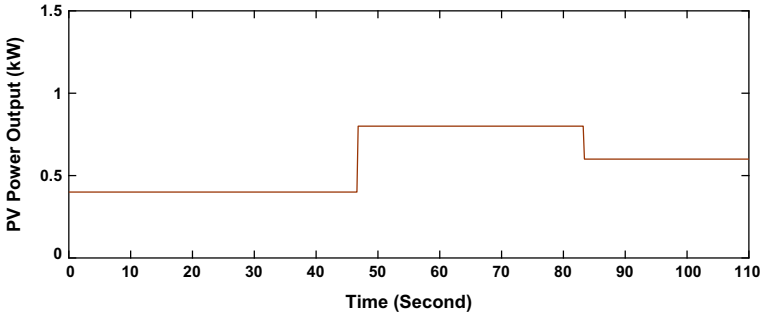

Fig. 5 Photovoltaic power output

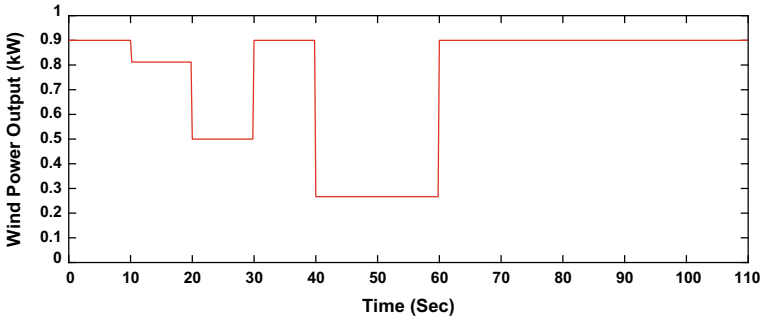

Fig. 6 Wind energy power output

battery, respectively.

At $t = 0$, the initial load demand is 0.9 kW; PV (0.4 kW) alone cannot fulfill the load demand. Battery SOC and hydrogen pressure are less than the maximum allowable limit. Maximum power (0.9 kW after considering losses) is extracted from WECS. After fulfilling the load demand, excess power is utilized to charge the battery and

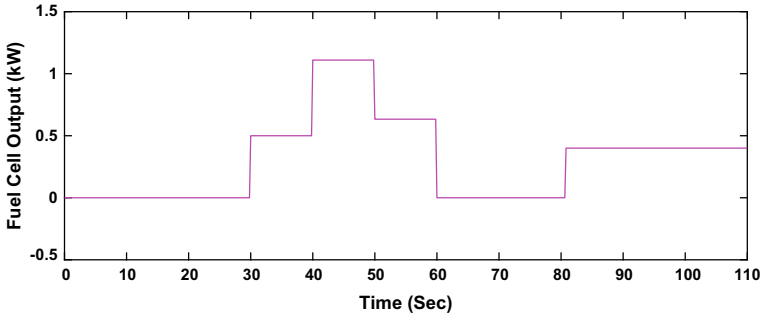

Fig. 7 Fuel cell power output

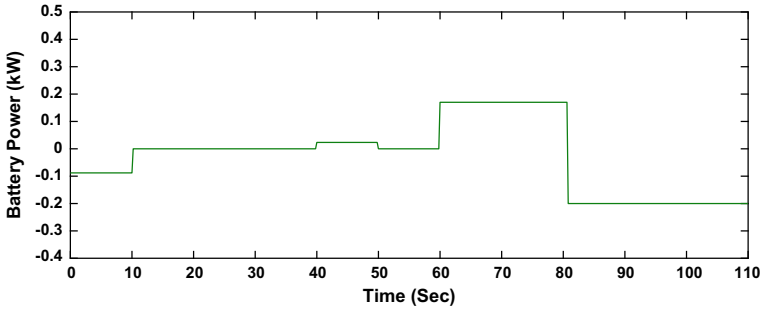

Fig. 8 Battery power output

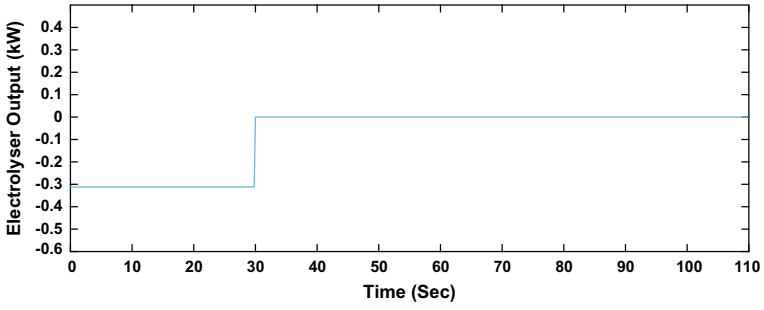

Fig. 9 Electrolyzer power output

consumed by electrolyzer for the production of hydrogen. Figures 10 and 11 show the corresponding rise in hydrogen pressure and battery SOC level, respectively. Battery SOC reaches at its maximum limit at $t = 10$ s and stops consuming power; in such case, wind energy conversion system starts to extract optimum power by controlling the rotor speed, and excess wind power is consumed by the electrolyzer. Hydrogen tank pressure reaches to maximum value at $t = 20$ s; at this instant, battery SOC

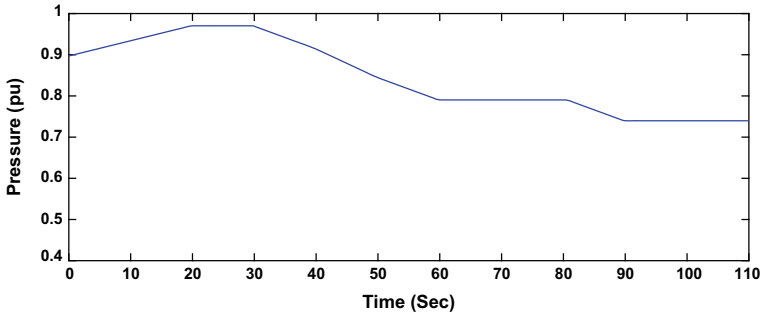

Fig. 10 Hydrogen pressure

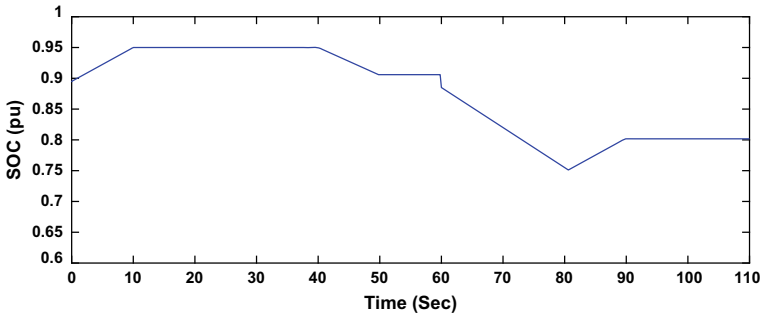

Fig. 11 Battery state of charge

level is also at the maximum value, so WECS will extract the deficit load power demand only. Load demand further increases at $t = 30$ s; PV and WECS deliver the maximum power, and deficit load power demand is supplied by FC. At $t = 40$ s, wind power generation reduces because of drop in wind speed, and deficit load demand is supplied by both FC and battery. Again, at $t = 50$ s, load demand decreases, and deficit load power demand is supplied by FC only. Deficit load power demand is less than the fuel cell minimum limit at $t = 60$ s, so it is supplied by battery.

Similar to the above described cases, energy management controller decides the power sharing among the different source components of MG to meet load power demand effectively for the rest of the simulation period.

Simulation results reveal that the overall coordination of the PV system, WECS, FC, battery, electrolyzer, and load is done by the developed EMS.

5 Conclusion

The energy management strategy for a microgrid consisting of PV, WECS, FC, battery, electrolyzer is presented. Performance of developed EMS is evaluated by carrying simulation for varying solar irradiance, wind speed, and load conditions. Results reveal that developed EMS is able to divide the load demand among various source components of MG and manage the battery SOC level and hydrogen tank pressure. Developed EMS is able to efficiently manage the slow varying residential load demand of an isolated area supplied by MG with different renewable and clean energy source.

References

1. Central Electricity Authority (2019) CEA annual report 2018–19. Annu Rep 248
2. Kumari J, Subathra P, Edwin Moses J, Shruthi D (2017) Economic analysis of hybrid energy system for rural electrification using homer. In: Proceedings of IEEE international conference on innovations in electrical, electronics, instrumentation and media technology, ICIEEIMT 2017. https://doi.org/10.1109/ICIEEIMT.2017.8116824
3. Muh E, Tabet F (2019) Comparative analysis of hybrid renewable energy systems for off-grid applications in Southern Cameroons. Renew Energy. https://doi.org/10.1016/j.renene.2018.11.105
4. Krishan O, Suhag S (2019) Techno-economic analysis of a hybrid renewable energy system for an energy poor rural community. J Energy Storage. https://doi.org/10.1016/j.est.2019.04.002
5. Singh N, Tirole R, Almas SK, Sood D (2021) Renewable power generation using asynchronous generator: a review. In: Gupta OH, Sood VK (eds) Recent advances in power systems. Lecture notes in electrical engineering, vol 699. Springer, Singapore. https://doi.org/10.1007/978-981-15-7994-3_18
6. Wang C, Nehrir MH (2008) Power management of a stand-alone wind/photovoltaic/fuel cell energy system. IEEE Trans Energy Convers. https://doi.org/10.1109/TEC.2007.914200
7. Thale SS, Wandhare RG, Agarwal V (2015) A novel reconfigurable microgrid architecture with renewable energy sources and storage. IEEE Trans Ind Appl. https://doi.org/10.1109/TIA.2014.2350083
8. Swarnkar A, Maherchandani JK (2018) Performance analysis of hybrid fuel cell/battery/supercapacitor electric vehicle for different battery state of charge levels. In: 2018 international conference on recent innovations in electrical, electronics & communication engineering (ICRIEECE), pp 2306–2311. https://doi.org/10.1109/ICRIEECE44171.2018.9008909
9. Sharma RK, Mishra S (2018) Dynamic power management and control of a PV PEM fuel-cell-based standalone ac/dc microgrid using hybrid energy storage. IEEE Trans Ind Appl 54(1):526–538. https://doi.org/10.1109/TIA.2017.2756032
10. Cingoz F, Elrayyah A, Sozer Y (2016) Optimized resource management for PV-fuel-cell-based microgrids using load characterizations. IEEE Trans Ind Appl. https://doi.org/10.1109/TIA.2015.2499287
11. Osman Haruni A, Negnevitsky M, Haque ME, Gargoom A (2013) A novel operation and control strategy for a standalone hybrid renewable power system. IEEE Trans Sustain Energy. https://doi.org/10.1109/TSTE.2012.2225455

12. Yuan C, Haj-Ahmed MA, Illindala MS (2015) Protection strategies for medium-voltage direct-current microgrid at a remote area mine site. IEEE Trans Ind Appl. https://doi.org/10.1109/TIA.2015.2391441
13. AbdelHady R (2017) Modeling and simulation of a micro grid-connected solar PV system. Water Sci. https://doi.org/10.1016/j.wsj.2017.04.001

Comparative Analysis of Traditional and Cloud-Based Disaster Recovery Methods

Prajwal Bhardwaj, Kaustubh Lohani, Ravi Tomar, and Rohit Srivastava

Abstract Regardless of size or function, every organization requires a disaster recovery plan (DRP) to ensure business continuity in case of a service interruption due to a cyber-attack or a natural calamity like a flood and fire. In addition, these plans should achieve target recovery requirements of recovery time. Earlier disaster recovery was done via storing backups at a data center. However, this required the organization to maintain every aspect of the data center. This maintenance can quickly increase the operational cost, leading to smaller organizations not implementing their disaster recovery plan. Then in the 2000s, cloud computing came along and brought an entirely new way to implement DRP. This technological leap came with its pros and cons. Traditional DR has kept the data protected for a long time, but we must evaluate the differences with the advent of novel technologies like cloud DR. This paper compares and contrasts conventional DR techniques and the newer cloud-based approach. Furthermore, we also look at current cloud-based DR solutions along with their pros and cons.

Keywords Disaster recovery · Cloud-based disaster recovery · Traditional disaster recovery · RPO · RTO · Disaster recovery solutions

1 Introduction

Disaster recovery methods are essential in this day and age where a service interruption can hugely offset organization revenue and reputation, making business continuity and disaster recovery plans extremely crucial. These interruptions can be caused by various reasons ranging from natural reasons like floods or man-made reasons like short circuits in the server farm.

To offset the possibility of loss to business in case of a disaster, organizations create a disaster recovery plan. Among other things, the main objective of this plan is to clearly define the assets crucial for business continuity in case of a disaster, disaster

P. Bhardwaj · K. Lohani (✉) · R. Tomar · R. Srivastava
School of Computer Science, University of Petroleum and Energy Studies, Dehradun 248007, India
e-mail: kaustubhlohani25@gmail.com

© The Author(s), under exclusive license to Springer Nature Singapore Pte Ltd. 2022

A. Tripathi et al. (eds.), *Intelligent Computing Techniques for Smart Energy Systems*, Lecture Notes in Electrical Engineering 862,
https://doi.org/10.1007/978-981-19-0252-9_11

recovery objectives such as recovery time, and dictate the amount of resources (cost and human resources) needed to implement the plan. Next, based on the disaster recovery plan, a disaster recovery methodology is selected. Popular disaster recovery methodologies include traditional DR and cloud-based DR.

The concept of a traditional disaster recovery solution involves replicating the primary site and creating a secondary site that could function as a backup in case a disaster strikes the primary site. Traditional disaster recovery solutions are generally expensive because of their mandate of having primary and secondary sites. This two-site design prompted many smaller organizations to rethink if they want to invest substantial resources in planning and implementing something that might or might not happen. Further, including the functionality of Business Continuity (BC) and DRP results in increased cost in the already expensive service.

Thankfully, cloud-based DR methods evolved as an alternative that introduced the "pay-as-you-go" subscription model, which enabled smaller organizations to consider having a DRP in place. Cloud-based solutions offer organizations the choice to outsource their setup and maintenance of the disaster recovery site to a cloud vendor for which the vendor charges a fee. Moreover, cloud-based DR solutions offer more flexibility, meaning the organizations can generally scale their services up or down whenever needed. This technological leap came with advantages and disadvantages. One significant advantage is the cost-effectiveness and scalability to increase or decrease the allocated resources; in contrast, many argue that the data is less secure and less private in the cloud as cloud DR solutions is a setup that is not in complete control of the organization using it as a backup site.

We describe both these disaster recovery approaches in detail and discuss their pros and cons in other sections. Furthermore, we provide insights on how exactly an organization should decide between them. Additionally, we list out some of the popular cloud-based solutions along with their advantages and disadvantages.

2 Terminologies

2.1 Disaster Recovery Plan (DRP)

A DRP is a set of policies and procedures created by an organization detailing the response to unplanned service failures due to natural or fabricated disasters and cyber-attacks.

2.2 Business Continuity (BC)

The area focuses on allowing applications and services to quickly come back online after an unexpected failure or service interruption due to disaster.

2.3 Failover

The process of activating the backup site in a disaster is called a failover procedure. Initiating the failover process activates the replicated modules in the DR site and shifts the day-to-day operations on the activated site in case of a disaster at the primary location.

2.4 Failback

The procedure of reverting the operations to the primary site from the backup site once the disaster is contained is called a failback procedure.

3 Critical Parameters to Measure the Effectiveness of the DRP

Before comparing and contrasting the traditional DR and cloud-based DR, we need to understand the parameters that define the ideal DR solution. Five key parameters can be used to measure the effectiveness of a DR solution [1].

3.1 Recovery Time Objective (RTO)

RTO defines the maximum acceptable time between unexpected system failure and the resumption of normal operations and service levels. RTO enables the organization to plan for its DRP.

- *Lower the better*

3.2 Recovery Point Objective (RPO)

RPO is a parameter to measure the maximum acceptable amount of data loss measured in time in a disaster. If the RPO is set to 50 min, the data should be backed up every 50 min. RTO, RPO combined helps the organization to define DRP policies and procedures effectively.

- *Lower the better*

3.3 Performance Impact

The DR methodology employed should have little to no impact on typical operation performance before and after recovery.

- *Lower the performance impact on day-to-day operations, the better*

3.4 Consistency

DR solution used should ensure that the accuracy of the systems operations remains after switching to the backup server. Inconsistency between the regular and backup server operations can cause further disruption in the organization's activities.

- *Higher the consistency, the better*

3.5 Geographical Separation

Ensuring that the same disaster should not impact the DR site as the primary site, there should be a reasonable geographical separation between the two sites.

- *A reasonable separation is ideal rather than much higher as higher separation will increase the latency and directly impact the application response time* (Fig. 1).

4 Disaster Recovery Site Mechanism

A disaster recovery site is a secondary backup location where the organization can temporarily shift its operations in a security breach or a natural disaster.

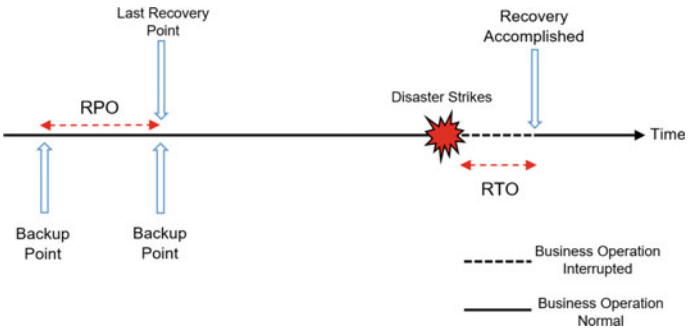

Fig. 1 Highlighting the timeline for RPO and RTO

For an organization, the DR site is one of the areas that they need to cover for ensuring BC in case of a disaster. Before opting for a DR site mechanism, several factors like disaster recovery objectives, cost, location, time frame, and resources needed should be considered for implementing an effective DRP.

There are three different DR site mechanisms: hot site, cold site, and warm site [1].

4.1 Hot Site

A hot site typically provides the organization with mirrored backup servers ready to run in an adverse event. This mechanism aims to provide the least RPO and RTO.

Further, this DR mechanism uses mirroring to ensure the highest consistency. Moreover, this mechanism aims to deliver the least RTO, which mandates ready servers on standby at all times. These reasons lead hot site mechanisms to incur higher costs.

4.2 Cold Site

In the concept of a cold site, data is backed up periodically in a matter of hours or days, increasing the RPO. Furthermore, servers are not readily available for transitioning operations in case of a disaster.

Cold servers generally take hours or days to transition to a ready state for shifting operations, making the RPO highest among the three mechanisms. Effectively, this mechanism has the highest RPO and RTO, making it the most cost-effective with the most negligible performance impact on the primary site.

4.3 Warm Site

This approach is the most balanced among the three. This mechanism may use the synchronous approach like the hot site or the asynchronous approach like the cold site for data replication. The replication methodology can be changed according to the target RPO. Servers in this mechanism are kept in a semi-ready state which may take some minutes to get them online.

The “semi-ready” or “warm” state slows the recovery process but at the same time also reduces cost. Recovery time or RTO for warm site is more than hot site but less than cold site.

5 Traditional Disaster Recovery

Traditionally disaster recovery uses data and application replication techniques on dedicated servers. These servers can be located on-premises or in remote locations around the world.

The simplest traditional DR solution is the offline backup to disks. Superficially, this might seem reasonable enough since no specialized equipment or IT team is required to implement this. However, many things can go wrong here. For example, the person maintaining the backups can commit a mistake, the cost of disks can quickly add up if the quantity of data is more, transporting the backup to a secure location can be a tedious task. Further, any secure location can be costly to set up and maintain. Finally, restoring this becomes a tedious task as data is scattered between disks and not present at a single storage location. Furthermore, this approach only replicated data but ignores applications and system configurations necessary for ensuring quick business continuity in case of a disaster [1].

The more complex approach involves replicating the primary site and creating a secondary site. The backup server where data is replicated is called a secondary site. Unfortunately, this additional site demands the same resources as the primary site, making this approach very costly.

Traditional DR sites come to action only in case of data replication or in a disaster scenario. Setting up this site live can take unavoidably long, which can hamper BC goals. Furthermore, manual operations are often needed if the connection between the DR site and the primary site gets interrupted, increasing the RTO.

5.1 Advantages of Traditional DR

Control

Traditional DR solutions offer more control over the server infrastructure as they are generally set up and maintained by the parent organization rather than outsourcing to a cloud vendor.

This control can come in many forms, such as kernel or operating system control, freedom over hardware configuration, and choice of DR implementation tools and technologies.

Privacy

Traditional DR solutions are by definition maintained by the organization itself; this limits the involvement of a third party, decreasing the potential nodes and eyes the data needs to travel to, offering more privacy when compared with cloud-based DR solutions.

Accessibility

Data replicated using traditional DR is generally accessible without the Internet as the servers are set up to ensure this, increasing data accessibility.

5.2 Disadvantages of Traditional DR

Scalability

Traditional DR offers limited scalability with the growth of the organization. In contrast, cloud-based solutions can be scaled up or down as per the need of the organization.

Essentially, with cloud-based solutions, the organizations can start implementing DRP with limited computational resources; however, they can increase the computational capabilities once they feel comfortable or their requirements increase. However, this is not the case with the traditional DR solutions, as increasing computational capabilities sometimes means upgrading existing hardware or software due to compatibility issues. For example, if the storage drive technology needs to be changed from Hard Disk Drive (HDD—older technology) to Solid State Drive (SSD—newer technology), other hardware changes might also be required to ensure that every hardware is compatible with the newer SSD technology.

Cost

Even when not in use, traditional DR consumes power in the form of electricity and cooling. Apart from power usage, other resources like human capital, infrastructure are also required at both places. These redundant costs add to the whole investment, increasing the overall cost of the implementation [2].

Recovery Time

Usually, recovery time in the traditional approach is very high compared to the cloud-based approach. In case of failure, organizations need to restore replicated data in the primary server. In the cloud-based approach, they can activate the virtualized applications in the cloud server and shift their operations on the cloud.

Downtime

Even if the backups are online in traditional DR, the system must go down for some time while switching to the secondary site. In most cases, this downtime is unpredictable, hampering business continuity [2].

Most of these drawbacks like cost, recovery time, downtime, and scalability of traditional DR can be solved using a cloud-based DR solution. However, there are caveats in the cloud-based model (discussed in the further sections) that must be considered while choosing one over the other.

6 Cloud-Based Disaster Recovery

Cloud-based DR is typically offered with a "pay-as-you-go" subscription model, which minimizes the capital required to set up a DR service. Furthermore, the server paired with operating system (OS), applications, and data is contained in the same virtualized instance, making investing in hardware on-site and off-site unnecessary. Since the organization does not maintain hardware, other hardware-related expenses such as power and cooling are non-existent. The reason due to which cloud DR trumps the traditional DR methodology is cloud redundancy. Cloud DR service providers back up data to geographically diverse locations, ensuring business continuity even in the worst cases [3].

In recent years cloud computing is seen as an alternative to expensive traditional DR methodology. Commonly in this model, instances of a virtualized physical server are offered as a recovery site. Sites on cloud DR is automated and can go live within seconds, minimizing the risk of data loss and upholding business continuity [4].

Cloud-based DR solutions come under the umbrella of Disaster Recovery as a Service (DRaaS). DRaaS is delivered through one of the three cloud service models Infrastructure as a Service (IaaS), Platform as a Service (PaaS), and Software as a Service (SaaS).

6.1 Advantages of Cloud-Based DR Over Traditional DR Solutions

Maintenance Cost

In contrast with the traditional solution cloud-based DR, infrastructure is set up and maintained by the Cloud Service Provider (CSP). Infrastructure encapsulates additional requirements like power and cooling costs, human capital for maintenance.

Pay-as-you-go subscription model

According to the National Institute of Standards and Technology (NIST—Body that formally defined cloud in 2011) [5],—one of the critical features of cloud computing solutions is that the client needs to pay only for what they use. As cloud-based DR solutions are an extension of cloud computing, they generally operate on a "pay-as-you-go" subscription model, according to which an organization needs to pay only for the resources they use and only for the time they use it. In contrast with the traditional model, where the organization must bear the entire cost of the DR setup even if it sits idle. This subscription model further reduces the DR operational cost.

Scalability

In contrast with traditional DR solutions, a cloud-based model is more flexible and provides an easy switch to powerful servers, more storage when needed. It also

provides the option to scale down to less storage and less computational resources, saving cost.

Automatic Failover

Detecting a disaster and performing automatic failover can be complex, as temporary network failures can cause false disaster alarms. For this reason, traditional DR relies on manual disaster detection to perform failover. Cloud-based DR solves this problem by monitoring the primary site using cloud nodes located at different geographical locations. These cloud nodes monitor several network parameters for potential network failure and react intelligently. This quick and accurate disaster detection helps the cloud-based solution automate failover [1].

Recovery Time

Traditional DR systems take much time to set up due to connection interruption between primary and secondary sites. Further, if offline backups are also used, then recovery time increases further. In contrast, cloud-based solutions take less time due to advantages like automatic failover, failback, and the inclusion of other automated virtualized platforms [6].

6.2 Challenges of Cloud-Based DR Over Traditional DR

Data Privacy and Security

Since a third party is involved in data transfer and storage, data privacy and security risk increases. The concern for data privacy and security is one of the significant reasons for critical sectors such as banking and finance hesitate to opt for cloud-based DR solutions; instead, they prefer to spend more money and use a traditional system.

Accessibility

Data is only accessible over a stable Internet connection. Any failure of this connection can lead to no backup data accessibility. However, moving vast amounts of data in or out of the DR site can take more time when compared with the traditional DR method, where data transfers are generally done over a local network providing faster speed and execution.

Control

The CSP manages the underlying cloud infrastructure in a cloud-based solution, including networks, storage, and operating system. Consequently, the client organization generally gets very little control over these elements; instead, the client controls and manages the deployment environment on which the applications and data from the primary site reside (Fig. 2).

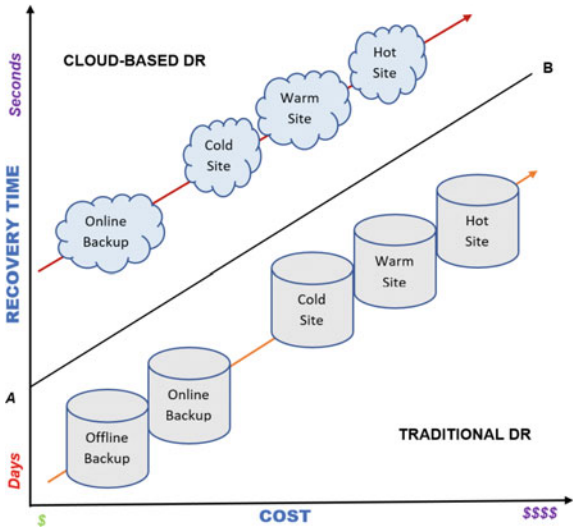

Fig. 2 A pictorial representation comparing traditional and cloud-based DR based on recovery time and cost. (Area above line AB corresponds to cloud-based DR, and below AB denotes traditional DR)

6.3 Popular DRaaS Providers

There are several cloud-based DR (also known as DRaaS—Disaster Recovery as a Service) providers; some of the popular ones include:

- Microsoft—Azure Site Recovery
- Quorum onQ
- Zerto Virtual Replication
- Acronis
- Axcient x360
- Expedient
- Zetta.net—Zetta Backup and Recovery
- Carbonite Cloud Backup

6.4 Multi-cloud DR Strategy

Using a cloud-based DR ensures business continuity until the cloud provider being used faces a disaster. In that case, the organization is only left with the primary site and no backup or secondary site, so if there is a service interruption for the organization when the cloud provider is down, it can result in catastrophic harm to their business. So, to offset this risk and increase the number of DR sites or ensure enough geographical separation, multi-cloud DR is used.

Essentially, the multi-cloud DR strategy involves backing up data using more than one cloud vendor to ensure business continuity (BC) in a disaster when the cloud provider is facing downtime. Using multi-cloud means that the organization

Table 1 Summarizing the features of traditional and cloud-based disaster recovery solutions

Parameter	Traditional DR	Cloud-Based DR
Overall Cost	High	Low due to the pay-as-you-go subscription model
Control	High	Low
Scalability	Difficult and expensive	Easy and cheap
Accessibility	Easily accessible with or without an Internet connection, unless a disaster strikes the secondary site or the connection issues arise	Easily accessible only with a stable Internet connection, however, the speed of data transfer might be significantly less
Automatic Failover	Challenging to achieve thus generally this feature is Absent	Present
Recovery Time	High	Low
Data Privacy	Higher level of data privacy due to negligible third party involvement	Data is less private due to the involvement of parties other than the client organization
Downtime	Generally High and unpredictable	Generally Low and predictable

has more than one secondary site, which can be a backup to the primary site or the other secondary sites [7, 8].

However, this strategy to implement more than one cloud for backup can be very tedious for several reasons. One principal concern is making sure that the geographical location of every DRaaS provider is different. If this is not the case, then the purpose of having multi-cloud DR gets defeated. Furthermore, working with several cloud vendors can get complicated quickly; thus, the organization needs an expert IT team to integrate different cloud systems. Moreover, having multiple secondary cloud sites can increase the overall cost of implementing the DRP [7].

Additionally, using multiple clouds provides the organization with the flexibility to break down the components of their primary site and handle each of these parts with a different DR approach (Table 1).

7 Choosing Between Traditional and Cloud-Based DR Methodologies

Having a DRP is essential for any organization. There is no right or wrong approach for selecting the DR model. Having a DRP in place is the crucial part. However, organizations can look at some parameters to zero in on one of the approaches.

First and foremost, the organization should evaluate its business requirements and potential risks. For example, a cloud-based hot site can be suited if the business requirement demands mission criticality like medical operations. However, more

straightforward cases like the backup of surveillance data can be accomplished using traditional offline DR [9, 10].

Secondly, the IT stack implemented on the primary site should also be looked at. This should be done to ensure the availability of the same IT stack on both models.

Furthermore, data security and privacy requirements should be considered. Keeping data private and secure is the utmost priority, then a traditional DR solution should be preferred because of no third party involvement in the data transfer and storage [11, 12].

Moreover, RTO and RPO needs should also be considered based on mission criticality.

Finally, the most crucial factor is cost. Therefore, the organization should consider their available budget for DR. Cloud-based DR is generally a cheaper alternative among the two [13].

There are positives and negatives in both traditional and cloud-based approaches. Nevertheless, it is what works the best for a particular organization according to their business needs [14, 15].

8 Conclusion

This paper has discussed the pros and cons of traditional and cloud-based DR methodologies, further comparing the two leading methodologies from the perspective of an organization looking to adopt one of them.

We have argued in the above section that the cloud-based approach is an excellent match or even better in some cases when compared with the traditional DR model. Both of these approaches have their pros and cons. If data security and privacy are a concern, then the traditional model trumps the cloud-based approach. If lower cost is paramount, then a cloud-based system is better suited. Furthermore, to ensure business continuity even in the worst cases, the multi-cloud approach can be beneficial. Moreover, as discussed above, there are advantages and disadvantages to both traditional and cloud-based DR approaches. It finally rests with the organization to choose between them based on their requirements.

References

1. Wood T, Cecchet E, Ramakrishnan KK, Shenoy PJ, van der Merwe JE, Venkataramani A (2010) Disaster recovery as a cloud service: economic benefits & deployment challenges. HotCloud 10:8–15
2. Pokharel M, Lee S, Park JS (2010) Disaster recovery for system architecture using cloud computing. In: 2010 10th IEEE/IPSJ international symposium on applications and the internet. IEEE, pp 304–307
3. US Signal (2020) Traditional or CLOUD-BASED Disaster recovery: Does it matter? US Signal. https://ussignal.com/blog/traditional-or-cloud-based-dr. Accessed 23 June 2021

4. Tamimi AA, Dawood R, Sadaqa L (2019) Disaster recovery techniques in cloud computing. In: 2019 IEEE Jordan international joint conference on electrical engineering and information technology (JEEIT). IEEE, pp 845–850
5. Mell P, Grance T (2011) The NIST definition of cloud computing. NIST. https://doi.org/10.6028/nist.sp.800-145
6. Wikimedia Foundation (n.d.) Disaster recovery. Wikipedia. https://en.wikipedia.org/wiki/Disaster_recovery. Accessed 23 June 2021
7. Goel S (2020) Why is multi-cloud strategy the best disaster recovery strategy. Cloud Management Insider. https://www.cloudmanagementinsider.com/why-is-multi-cloud-strategy-the-best-disaster-recovery-strategy/. Accessed 23 June 2021
8. Khoshkholghi MA, Abdullah A, Latip R, Subramaniam S (2014) Disaster recovery in cloud computing: a survey
9. Lenk A, Tai S (2014) Cloud standby: disaster recovery of distributed systems in the cloud. In: European conference on service-oriented and cloud computing. Springer, Berlin, pp 32–46
10. Alhazmi OH, Malaiya YK (2013) Evaluating disaster recovery plans using the cloud. In: 2013 Proceedings annual reliability and maintainability symposium (rams). IEEE, pp 1–6
11. Javaraiah V (2011) Backup for cloud and disaster recovery for consumers and SMBs. In: 2011 Fifth IEEE international conference on advanced telecommunication systems and networks (ANTS). IEEE, pp 1–3
12. Yadav AK, Tomar R, Kumar D, Gupta H (2012) Security and privacy concerns in cloud computing. Comput Sci Softw Eng 2(5)
13. Moşteanu D, Roxana N (2020) Management of disaster and business continuity in a digital world. Int J Manage 11(4)
14. Arean O (2013) Disaster recovery in the cloud. Netw Secur 2013(9):5–7
15. Jian-Hua Z, Nan Z (2011) Cloud computing-based data storage and disaster recovery. In: 2011 International conference on future computer science and education. IEEE, pp 629–632

Voltage Profile Enhancement Using FACTS Devices

Akash Sharma and Rajive Tiwari

Abstract 'Flexible AC Transmission Systems' (FACTS) is a feasible option for offering reactive power support at local load centers while keeping voltages within safe operating limits. Because FACTS devices are expensive, their suitable locations in the system must be determined. The main goal of this paper is to enhance the voltage level by lowering the systems' active and reactive power losses. Using the FACTS device 'Static VAR Compensator' (SVC), the voltage profile in the system is enhanced. SVC technology is investigated in this work for voltage increase, system loss reduction, and minimization of fluctuations.

Keywords FACTS · SVC · STATCOM · VSC · FC-TCR · Matpower · MATLAB/Simulink

1 Introduction

The loads are increasing day by day at very fast rate. When we talk about the industrialization, modernization, and the concept of smart cities, in all these cases, power demand is a common thing. As a power engineer, it is our responsibility to meet the load demand. To do so, we can create, establish, or introduce a new power plant; it may be solar, wind, thermal, nuclear etc. But here, we focused on how can we increase the transmittable power from sending side to receiving side in existing transmission system. Voltage profile is also affected due to rapid disturbance in load demand. An important concern on a power system engineer is the instability in the power system because of the voltage collapse [1]. To avoid such type of issues, we are going to use high power electronics-based devices or FACTS devices. In present time, the use of FACTS devices is increasing exponentially to tackle the issue of voltage collapse.

A. Sharma (✉) · R. Tiwari
Department of Electrical Engineering, NIT Jaipur, Jaipur, India
e-mail: 2019pes5345@mnit.ac.in

R. Tiwari
e-mail: rtiwari.ee@mnit.ac.in

© The Author(s), under exclusive license to Springer Nature Singapore Pte Ltd. 2022

A. Tripathi et al. (eds.), *Intelligent Computing Techniques for Smart Energy Systems*,
Lecture Notes in Electrical Engineering 862,
https://doi.org/10.1007/978-981-19-0252-9_12

The operation and control of the electric power system is becoming significantly more complex as power demand increases. The control of the present network is primarily mechanical. These mechanical devices cannot be regulated on a regular basis due to their sluggish response time. For these reasons, FACTS technology were developed. The introduction of FACTS controllers around three decades ago revolutionized electric power flow improvement in a transmission network. To provide smooth power transfer across locations, Flexible alternate current transmission system (FACTS) devices are utilized to increase the controllability of power network in transmission line structure. As a result, the operation of the power network is improved, and the power transmission capacity is raised.

With the help of FACTS devices, steady-state power flow through transmission line will increase, stability limits will also be improved, and the overall dynamic behavior and performance of the system will also improve [2].

2 Literature Review

Static var controller can be used to enhance voltage profile when subjected to different loading conditions [3]. The reactive load demand was increased and analyze to voltage profile for each and every bus. In this work, he explained that when reactive load is increased, then magnitude of voltages of buses are reduced and voltage angles are also changed. After finding the critical bus, we can install FACTS devices on it.

Satish Kumar (2015) in this paper, he introduce a wind generation in IEEE 14 bus system. He analyzed the performance of the transmission system using 'PSAT' power system analysis toolbox [4]. In this work, he explained about the transient behavior of power system network. He has done the time domain analysis and optimum power flow and continuation power flow.

Manjiri Chiddarwar [5] Electrical power systems are a huge interconnected network that needs careful design in order to sustain the system's steady-state operations and continuous power flow operation without limits. New technology, like as the FACTS device, is employed in load flow analysis to meet this criterion. 'Flexible Alternating Current Transmission System' (FACTS) is a power electronics device that is used to manage power flow and increase system stability in a power system. STATCOM is a versatile controller of the FACTS family of controllers that can manage all transmission parameters of power systems at the same time, such as voltage, impedance, and phase angle, which influence the power flow of a transmission line. This study is primarily concerned with the application of STATCOM's steady-state model in the Newton-Raphson approach. The effectiveness and performance of the model will be tested using the IEEE bus system. The simulations are run in a MATLAB environment using a common IEEE bus test system such as the 30 bus system.

2.1 Contribution of Paper

In this paper, FC-TCR is introduced in MATLAB R2016a Simulink environment to analyze the impact of compensation on single machine system. After this, 'FACTS' controllers such as SVC is incorporated in the electric power system for the improvement of voltage level and minimization of losses with the help of 'NRLF' method. The graphical comparison of results is also presented in this paper. The effectiveness of proposed technique has been tested on standard IEEE-14 and IEEE-9 bus systems using MATPOWER 7.1. Optimal size and optimal location have been found with analytical approach.

3 Simulink Model

An uncompensated system's fundamental transmission (11 kV) model is shown in this diagram. The block of current measurement, voltage measurement block, actual and reactive power block, and scopes are all included in this model. The system receives 11 kV voltage from the AC voltage source. For the below transmission line model, line impedance (1 + j1) and load are held constant at 10 MW and 15MVAR. MATLAB/Simulink is used for simulation. The instantaneous source and load currents flowing through the transmission line are measured by the current measurement block, while the source and load voltages are measured by the voltage measurement block. The active and reactive power measuring blocks are used to measure real and reactive power on the load side. After the simulation, the scopes show the results. This model provides four scopes: one display the source voltage (Vs) and source current (Is), second one displays receiving end voltage (Vr) and current (Ir), third one displays sending end real (Ps) and reactive (Qs) power, and fourth one displays receiving side real (Pr) and reactive (Qr) power after simulation (Figs. 1 and 2).

A fixed capacitor is connected in parallel with the thyristor-controlled reactor in FC-TCR. The FC-TCR circuit has three currents: system current, reactor current, and capacitor current. The FC-TCR can supply the system with constant lagging and leading vars. The firing angle of back-to-back thyristor valves linked in series with the reactor is used to control the flow of current through the reactor. The capacitor provides the system with leading var. TCR is usually rated higher than the capacitor for delivering lagging vars to the system.

In Fig. 3, multiple compensating devices are used. Here, α is the firing angle of thyristors. With the help of varying firing angles, we can control the output parameters of our Simulink model. Firing angle of first unit = 180, second unit = 180, third unit = 180, and fourth unit = 144.1 (in degree) see Table 1.

Mode 1: Inductive mode, i.e., absorbing reactive power from transmission line, 90 $\leq$ firing angle < 110.

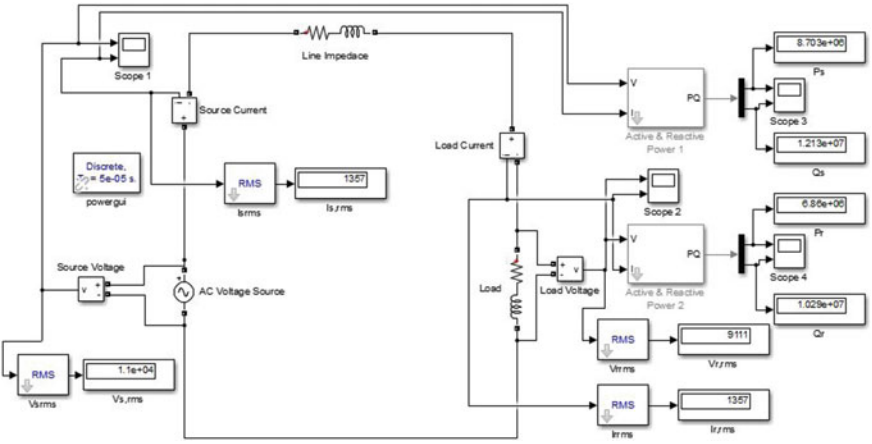

Fig. 1 MATLAB circuit of uncompensated system

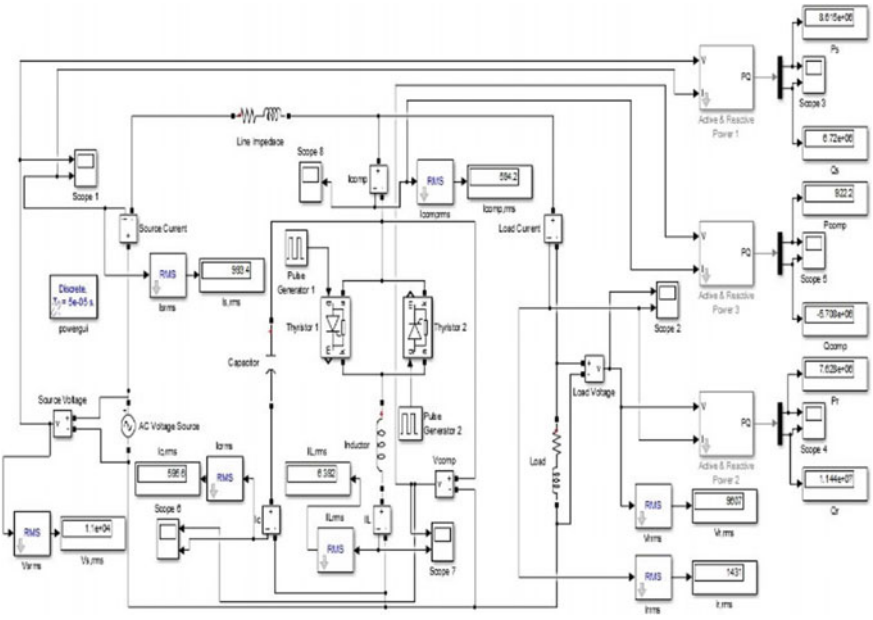

Fig. 2 Compensated system by using FC-TCR

Mode 2: floating mode, i.e., neither absorb nor supply reactive power from/to transmission line, firing angle = 110.

Mode 3: Capacitive mode, i.e., supply reactive power to transmission line, 110 < firing angle ≤ 180 (Fig. 4).

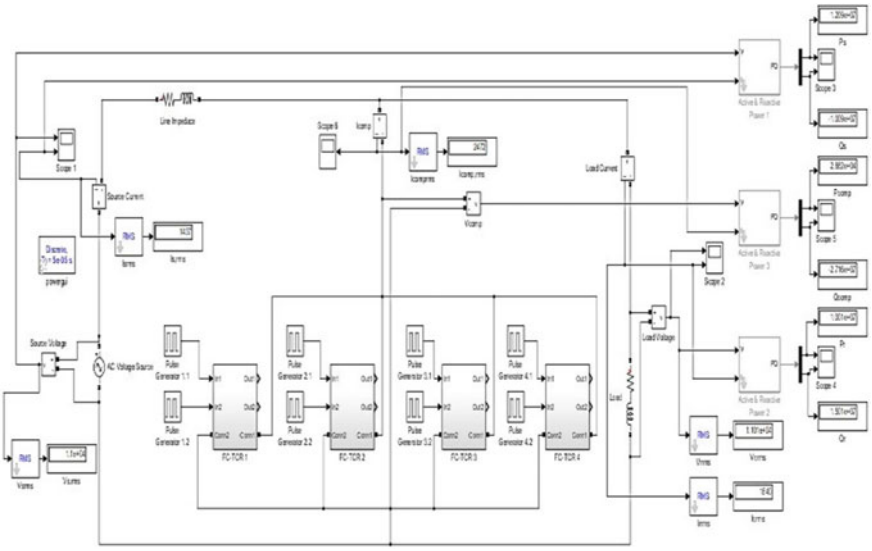

Fig. 3 Compensated system by using multiple units of FC-TCR

The fundamental goal of using reactive shunt compensation in a transmission system is to enhance the amount of power that can be transmitted. This may be necessary to improvise the system's steady-state transmission characteristics and stability. VAR compensation is thus employed for voltage regulation at the transmission line's midpoint (or some intermediate) to segment it and at the line's end (radial) to prevent voltage instability, as well as for dynamic voltage management to improve transient stability and 'damp power oscillations' [6]. There are lots of facts devices are available as follows.

Shunt devices—'SCV,' 'STATCOM'

Series devices—'TCSC,' 'GCSC', 'SSSC' [7]

Shunt-Series devices—'UPFC,' 'IPFC'

Table 1 shows that uncompensated system is not capable to fulfill the load demands so FC-TCR is placed in between load and source. It works into three modes inductive, capacitive, and floating mode. In inductive mode, it will absorb reactive power from system, and in capacitive mode, it will deliver reactive power to the system, but in case of floating mode, there is no power exchange between them. Eventually, all the parameters are quite similar in floating mode and without compensation.

It is a graphical representation of results. Figure 5 shows that uncompensated system where receiving end active power is 6.86 MW, and reactive power is 10.29 Mvar. Figure 6 shows that after compensation, we get 10 MW active power and 15 Mvar reactive power which is equal to load demand.

Sending end voltage is 11 kV and the receiving end voltage is only 9.11 kV in case of without compensation. Voltage drop is approx. 17.18%. But after incorporation

Table 1 Parameters for uncompensated and compensated line under different mode of operations

Mode		Inductive mode		Floating mode	Capacitive mode		2nd unit	3rd unit	4th unit
Firing angle		90°	100°	110°	120°	180°	180°	180°	144.1°
Line parameters	Without any compensation								
Ps (MW)	8.703	9.127	8.924	8.775	8.674	8.616	9.189	10.63	12.09
Qs (MVAR)	12.13	15.98	14.1	12.13	10.31	6.693	6.718	−5.857	−10.09
Pr (MW)	6.86	6.312	6.575	6.851	7.11	7.632	8.486	9.412	10.01
Qr (MVAR)	10.29	9.468	9.862	10.28	10.66	11.45	12.73	14.12	15.01
P_{comp} (MW)	–	0.015	0.049	0.072	0.063	0.0005	0.0013	0.0026	0.0286
Q_{comp} (MVAR)	–	3.714	1.934	0	−1.85	−5.73	−12.76	−21.19	−27.16
Vs (KV)	11	11	11	11	11	11	11	11	11
Is (KA)	1.357	1.675	1.529	1.382	1.245	0.991	0.8376	1.104	1.437
Vr (KV)	9.111	8.745	8.957	9.153	9.306	9.610	10.13	10.67	11.01
Ir (KA)	1.357	1.302	1.329	1.357	1.383	1.432	1.510	1.590	1.640

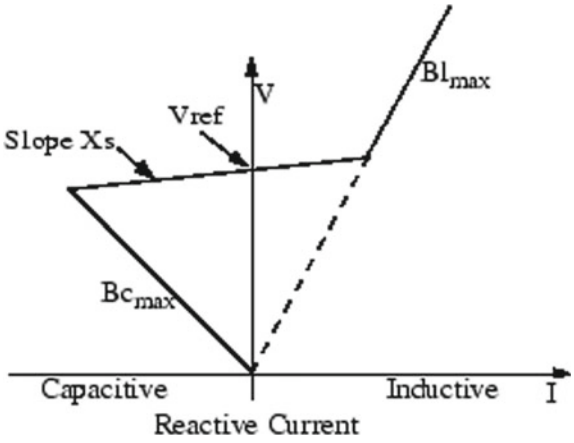

Fig. 4 VI characteristics of SVC

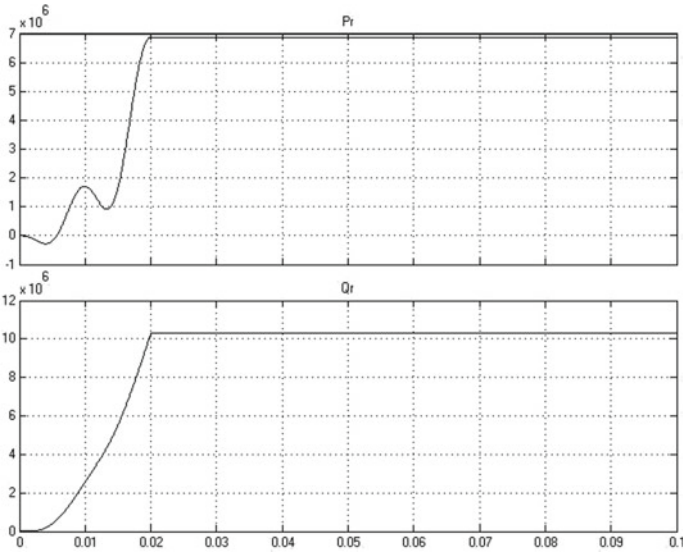

Fig. 5 Uncompensated system

of FC-TCR sending end and receiving end voltages both are same. See Table 1. This situation is called flat voltage profile of the system [8].

As the transmittable power is increased, the area margin given by equal area criteria is also increased, so that the stability of the system is also improved. The concept of FACTS implies the use of high power electronics devices in order to control power flow in a transmission network, thereby allowing transmission lines to be loaded to their full capacity.

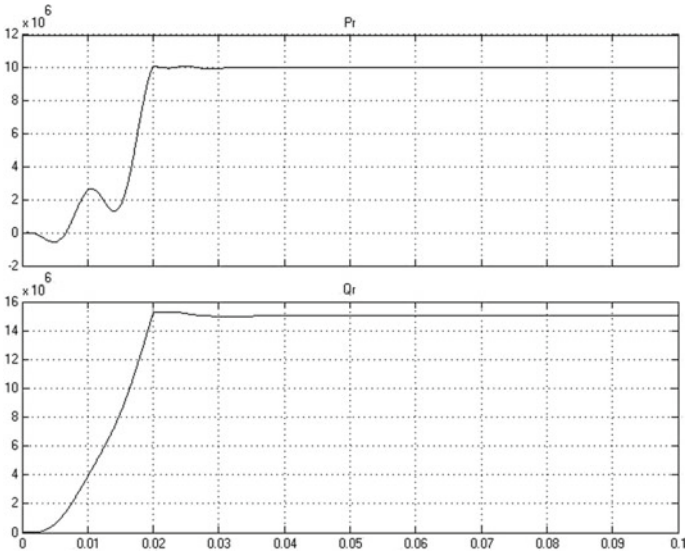

Fig. 6 Compensated system

3.1 Equations

In this paper, the firing angle model of SVC is used. The following are the differential and algebraic equations that can be used to create the model with respect to a sinusoidal voltage:

$$I_{\mathrm{SVC}} = -jB_{\mathrm{SVC}}V_k$$

The fundamental frequency of TCR equivalent reactance X_{TCR} is given below:

$$X_{\mathrm{TCR}} = \frac{\Pi X L}{\sigma - \sin\sigma}$$

where $\sigma = 2(\Pi - \alpha)$, $X_L = \omega L$.

In term of firing angle

$$X_{\mathrm{TCR}} = \frac{\Pi X L}{[2(\Pi - \alpha) + \sin 2\alpha]}$$

where 'α' and 'σ' is firing angle and conduction, respectively. At $\alpha = 90°$, TCR conducts fully and the equivalent reactance X_{TCR} becomes X_{L} while at $\alpha = 180°$, TCR is blocked and its equivalent reactance becomes infinite. The SVC effective reactance X_{SVC} is determined with the help of parallel combinations of X_{C} and X_{TCR} [9].

$$X_{\mathrm{SVC}} = \frac{\Pi X_L X_C}{X_L\{2(\Pi - \alpha) + \sin 2\alpha\} - \Pi X_L}$$

where $X_C = \frac{1}{\omega C}$.

$$Q_k = -V^2 k\left\{\frac{Xc2(\Pi - \alpha) + \sin 2\alpha}{\Pi X c X_L}\right\}$$

The SVC equivalent susceptibility ($B_{SVC} = 1/X_{SVC}$) profile as a function of firing angle has no discontinuities, i.e., B_{svc} varies in both operative regions in a continuous, smooth manner. As a result, linearization of the SVC power flow equations based on B_{SVC} will have superior numerical behavior than the linearized model based on X_{SVC} with regard to firing angle [10].

4 Results and Discussion

In this paper, IEEE 9 and IEEE 14 bus system have been used to analyze the incorporation of SVC. The comparable study has been done with and without injection of reactive power to the system. In this work, analytical approach is used to find out the optimal or suboptimal location and size as well.

4.1 Case 1 IEEE 9 Bus System

It has been observed that the voltage level of the system has been improved after the injection of reactive power to the system. The overall voltage profile of the standard system has been improved when the SVC placed at different buses, but the improvement in voltage profile with maximum deviation is observed only at bus no. 9. The overall voltage level is shown in figure, after injection of 40 Mvar huge increment in voltage level can be observed at bus no. 9 (Fig. 7).

Real and reactive power losses in IEEE9 bus system with and without compensation shown in Figs. 8 and 9, respectively. As we can see, 40 Mvar is an optimal size for injection of reactive power to the system because at this time, losses are minimum in comparison to others.

See Tables 2 and 3. After incorporating SVC in case of IEEE 9 system, power system performance improved, with real power losses reduced from 4.641 MW (without SVC) to 4.495 MW (with SVC) and reactive power losses reduced from 48.38 MVAR (without SVC) to 46.98 MVAR (with SVC). After implementing SVC to bus no. 9, the voltage level of the 'IEEE 9' bus system is improved from 0.9956 p.u. to 1.0306 p.u. As a result, real and reactive power losses are reduced, and the voltages profile of the system is boosted with the addition of SVC.

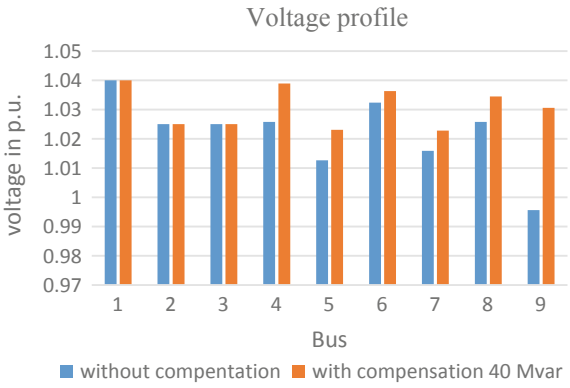

Fig. 7 Voltage profile of IEEE9 bus system

Fig. 8 Real power losses for ieee9 bus system

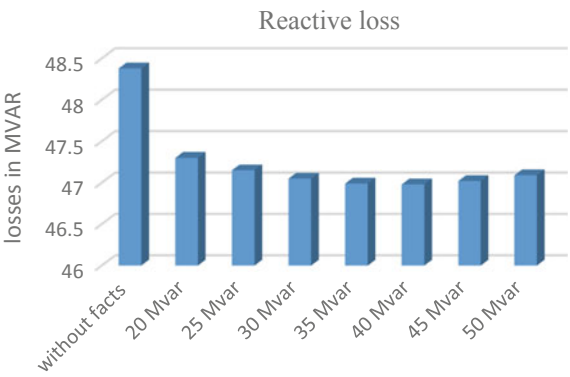

Fig. 9 Reactive power losses for ieee9 bus

IEEE 9 bus system

Load demands P_d is 315 MW and Q_d is 115 MVAR. It has three loads at bus no. 5, 7, and 9. It has three generators, nine buses, and nine branches.

Table 2 Voltages in p.u. with and without compensation for IEEE9 bus system

Bus	Without facts	20 Mvar	25 Mvar	30 Mvar	35 Mvar	40 Mvar	45 Mvar	50 Mvar
1	1.04	1.04	1.04	1.04	1.04	1.04	1.04	1.04
2	1.025	1.025	1.025	1.025	1.025	1.025	1.025	1.025
3	1.025	1.025	1.025	1.025	1.025	1.025	1.025	1.025
4	1.0258	1.0325	1.0341	1.0357	1.0373	1.0389	1.0405	1.0421
5	1.0127	1.0179	1.0192	1.0205	1.0218	1.0230	1.0243	1.0255
6	1.0324	1.0344	1.0349	1.0353	1.0358	1.0363	1.0368	1.0373
7	1.0159	1.0194	1.0203	1.0211	1.0220	1.0228	1.0236	1.0245
8	1.0258	1.0302	1.0313	1.0323	1.0334	1.0345	1.0355	1.0365
9	0.9956	1.0134	1.0178	1.0221	1.0264	1.0306	1.0348	1.0390

Table 3 Active and reactive power losses for IEEE9 bus system

	Without facts	20 Mvar	25 Mvar	30 Mvar	35 Mvar	40 Mvar	45 Mvar	50 Mvar
MW	4.641	4.527	4.512	4.501	4.496	4.495	4.499	4.507
MVAR	48.38	47.3	47.15	47.05	46.99	46.98	47.02	47.09

IEEE 14 bus system

Load demands P_d is 259 MW and Q_d is 83.7 MVAR. It has fourteen buses, five generators, eleven loads, and twenty branches.

4.2 Case 2 IEEE-14 Bus System

The voltage profile of the standard system has been noted that it improved after the installation of SVC. When the SVC is placed at different bus numbers [11], the overall voltage profile of the system improves, but the improvement in voltage profile with largest changes is only seen at bus number 14. Take a look at Fig. 10.

In this study, voltage level is observed for each and every bus for IEEE14 bus system. With the help of Table 5, we can see the highest deviation (1.036–1.060) observed at 14 bus system. So bus no. 14 is suitable place for FACTS devices. In this case, analytical approach is taken into account for optimal size of devices. The optimal size is 8 Mvar because the real and reactive losses are minimum that is 13.341 MW and 54.35 MVAR. Graphical representation of active and reactive losses are shown in Figs. 11 and 12.

Voltage level in per unit at each and every bus of IEEE 14 bus system is shown in Table 4. Parameter shows that voltage level is increasing after injection of reactive power to the system. Table 5 shows that active and reactive power loss with different size of compensation.

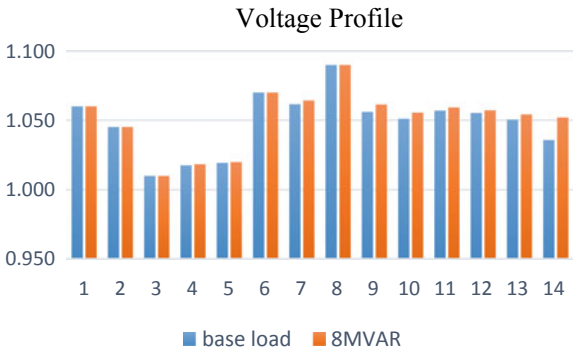

Fig. 10 Voltage profile of IEEE14 bus system

Fig. 11 Real power losses for ieee14 bus system

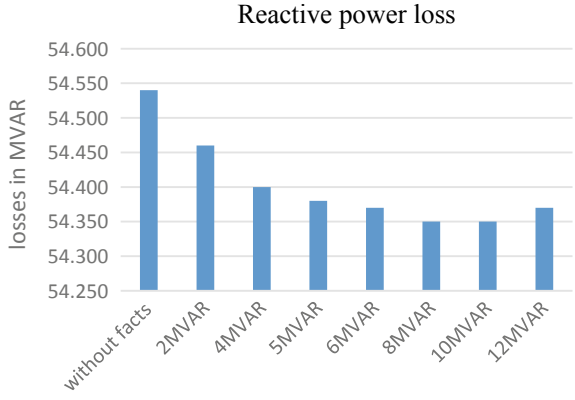

Fig. 12 Reactive power losses for ieee14 bus

Active and reactive power losses in IEEE14 bus system with and without compensation is reduced to 52 KW and 190 KVAR, respectively, shown in Figs. 11 and 12. As we can see, 8 Mvar is an optimal size for injection of reactive power to the system [12].

Table 4 Voltage in p.u. with and without compensation for IEEE 14 bus system

Bus no.	Base case	2MVAR	4MVAR	5MVAR	6MVAR	8MVAR	10MVAR	12MVAR
1	1.060	1.060	1.060	1.060	1.060	1.060	1.060	1.060
2	1.045	1.045	1.045	1.045	1.045	1.045	1.045	1.045
3	1.010	1.010	1.010	1.010	1.010	1.010	1.010	1.010
4	1.018	1.018	1.018	1.018	1.018	1.019	1.019	1.019
5	1.020	1.020	1.020	1.020	1.020	1.020	1.020	1.020
6	1.070	1.070	1.070	1.070	1.070	1.070	1.070	1.070
7	1.062	1.062	1.063	1.063	1.064	1.064	1.065	1.066
8	1.090	1.090	1.090	1.090	1.090	1.090	1.090	1.090
9	1.056	1.057	1.059	1.059	1.060	1.061	1.063	1.064
10	1.051	1.052	1.053	1.054	1.054	1.055	1.057	1.058
11	1.057	1.057	1.058	1.058	1.059	1.059	1.060	1.060
12	1.055	1.056	1.056	1.056	1.057	1.057	1.058	1.058
13	1.050	1.051	1.052	1.053	1.053	1.054	1.055	1.056
14	1.036	1.040	1.044	1.046	1.048	1.052	1.056	1.060

Table 5 Active and reactive power losses in IEEE 14 bus system

	Without facts	2MVAR	4MVAR	5MVAR	6MVAR	8MVAR	10MVAR	12MVAR
MW loss	13.393	13.369	13.352	13.347	13.343	13.341	13.346	13.359
Mvar loss	54.540	54.46	54.4	54.38	54.37	54.35	54.35	54.37

5 Conclusion

The voltage profile of the system should be between permissible limits; failing to do so will result in voltage sag/swell, which must be avoided in order to keep the power system stable. In this work, the use of a Static Var Compensator (SVC) is proposed for improving the voltage profile and lowering system power losses with the help of Simulink model. A Newton-Raphson load flow problem with the required objective has been formulated to determine the optimal size and location of SVC in an IEEE 9 and IEEE 14 bus system. It is concluded that the best location for SVC is bus number 9, and the best size is 40 MVAR in case of IEEE 9 bus system. Similarly, best location of SVC is bus no. 14 and best size is 8 MVAR in case of IEEE 14 bus system [13, 14, 15].

References

1. Kundur P (1994) Power system stability and control. McGraw-Hill
2. Khanmohammadi S, Tarafdar Hagh M, Abapour M (2007) Fuzzy logic based SVC for reactive power compensation and power factor correction. In: Power engineering conference, 2007 IPEC 2007 International. IEEE, pp 1241–1246
3. Srivastava SK (2012) Enhancement in voltage stability and reactive power compensation using D-STATCOM. Int J Eng Res Technol (IJERT) 1(7)
4. Kumar S, Kumar A, Sharma NK (2015) Analysis of power flow, continuous power flow and transient stability of IEEE-14 bus integrated wind farm using PSAT
5. Chiddarwar M (2018) Load Flow Analysis Using Facts Device
6. Jmii H, Meddeb A, Chebbi S (2016) Efficiency limits of SVC in improving voltage stability. In: 3rd International conference on GEEE, Apr 2016, Hammamet, Tunisie
7. Garg L, Agarwal SK, Kumar V, Improvement of power system transient stability using TCSC, SSSC and UPFC. International
8. Hingorani NG, Gyugyi L (2000) "Understanding FACTS", Concepts and technology of flexible AC transmission system. Ins Elect Electron Eng Inc., New York
9. Bhole S, Nigam P (2015) Improvement of voltage stability in power system by using SVC and STATCOM. Int J Innov Sci Eng Technol 2(4)
10. Singh B, Agarwal G (2018) Enhancement of voltage profile by incorporation of SVC in power system networks by using optimal load flow method in MATLAB/Simulink environments. Int J
11. Gerbex S, Cherkaoui R, Germond AJ (2001) Optimal location of multi types FACTs devices in power system by means of genetic algorithms. IEEE Trans Power Syst 16(3):537–544
12. Acha E, Kazemtabrizi B (2013) A new STATCOM model for power flows using the Newton-Raphson method. IEEE Trans Power Syst 28(3):2455–2465
13. Singh JG, Singh SN, Srivastava SC (2006) Placement of FACTS controllers for enhancing power system loadability. In: Power India conference. IEEE
14. Akter S et al (2012) Modelling, simulation and comparison of various FACTS devices in power system. Int J Eng Res Technol
15. Huang GM, Yan P (2002) The impacts of TCSC and SVC on power system load curtailments. In: Power engineering society summer meeting-2001, Available IEEE Xplore06

Akash Sharma was born in Jaipur, Rajasthan, India. He received the B.Tech. Degree in electrical engineering from the Arya College of Engineering & information Technology (ACEIT), Jaipur, Rajasthan, India. He worked in IRB Company as a GET in 2018. He is currently pursuing the M.Tech. Degree in electrical engineering (Power Systems) from the Malaviya National Institute of Technology (MNIT) Jaipur, Rajasthan, India. His research interests are in Power system Eng., assessment of FACTS controllers.

Comparative Analysis of 10T SRAM Cell using Nanodevices

Deepika Sharma, Shilpi Birla, and Neha Mathur

Abstract Most of the high-speed circuits use static random access memory (SRAM) to store electronics data on-chip. The necessity of designing low-area and high-speed integrated circuits (ICs) leads to scaling the CMOS devices. The limitation of MOSFET scaling introduced the new transistor technology. The paper introduced the comparative analysis of 10T SRAM cell design using CMOS, FinFET, and CNTFET. Performance analysis is carried out by using power consumption and static noise margin of the cells. Among all the cells, FinFET cell offers least static power of 5.2967 nW while CMOS and CNTFET offer 2.4194 μW and 0.5001 μW. The CNTFET cell has 42%, 43%, and 41% improved values of HSNM, RSNM, and WSNM, respectively, from the FinFET cell. The FinFET schemes yield substantially lower leakage power compared to CMOS and CNTFET-based cells.

Keywords CNTFET · SNM · CMOS · 10T SRAM · FinFET

1 Introduction

SRAMs are the pinnacle to store electronics data on chips to meet the performance needs of high-performance VLSI chips. In most microelectronic devices, SRAMs covered a wide range of areas. SRAMs are the most important parts of microelectronic devices [1]. Consumer's demands needed the reduction in the size of memory devices. Scaling of MOSFETs in the subthreshold region leads to increase in the threshold voltage which indirectly affects the "ON" and "OFF" currents of the transistor [2]. It also creates a lot of unwanted effects which reduces the performance analysis of the cells. It is became challenging to maintain large ON currents while keeping the low OFF currents below 45 nm technology nodes. This problem is solved by the invention of multiple gates controlling transistor. FinFET and CNTFET devices are the best solutions for implementing nanoscale CMOS devices [3].

D. Sharma · S. Birla (✉) · N. Mathur
Manipal University Jaipur, Jaipur, India
e-mail: shilpi.birla@jaipur.manipal.edu

© The Author(s), under exclusive license to Springer Nature Singapore Pte Ltd. 2022

A. Tripathi et al. (eds.), *Intelligent Computing Techniques for Smart Energy Systems*,
Lecture Notes in Electrical Engineering 862,
https://doi.org/10.1007/978-981-19-0252-9_13

The double gate structure of FinFET helps in controlling the currents and threshold voltage of the transistor. The ability of both front and back gates to control threshold voltage reduces the standby power dissipation. The feature of FinFET having high performance, low standby power, and high speed makes it a strong candidate to act as a bridge between bulk CMOS and non-silicon devices [4]. FinFET is the best candidate to design memory cells.

In the CNTFET structure, the channel is formed by using the carbon nanotube (CNT). Compared to MOSFET, the CNTFET has excellent features. CNTFET has a lower value of propagation delay, hence it is 15–20 times faster than MOSFET [5]. The chiral vector is one of the dominating parameters in CNTFET for deciding the value of threshold voltage and behavior of the channel. It has a direct relation with CNT diameter and an inverse relation with the threshold voltage. CNTs are made up of sheets of graphene rolled [6]. CNTFET works with the same principle as traditional silicon devices. It is a 3- or 4-terminal device in which a semiconducting tube behaves as a conducting channel to separate the source and drain contacts. It can be ON or OFF by using a gate terminal. According to the device operation mechanism, CNTFET can be of different types. The channel region of CNT is undoped, while the other regions such as drain or gate are heavily doped. Now in all CNTFETs, both source and drain contacts are made up of metal carbide [7]. The basic structure of SRAM cell is conventional 6T SRAM cell having 6 transistors in which 4 transistors store the values from the 2 access transistors. Figure 1 shows the conventional 6T SRAM cell design.

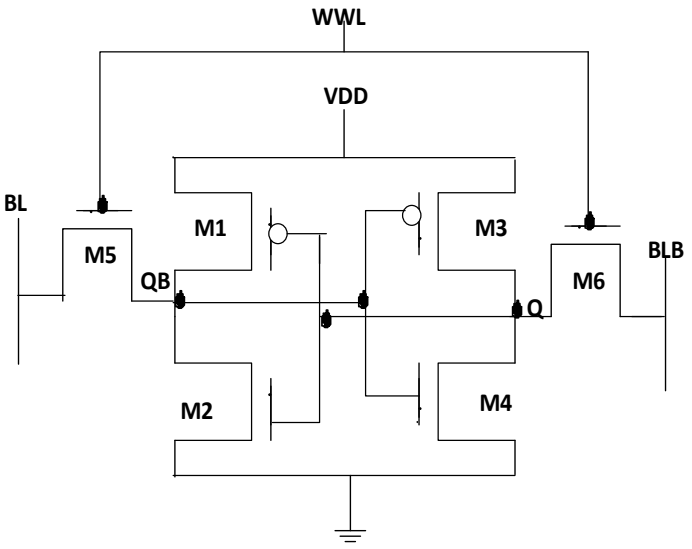

Fig. 1 6T SRAM cell [4]

2 10T CMOS, FinFET, and CNTFET SRAM Cells

Figure 2 shows the 10T CMOS-based SRAM cell in which 10 transistors are connected in such a fashion 6 transistors behave as conventional cell and the remaining 4 used for enhancing read and write operations. Both the word lines and bit lines are turned ON to read and write data from the cells [8].

Figure 3 represents the 10T FinFET-based SRAM cell. Cell structure consists of two inverter pairs and one transmission gate. Different types of word lines and bit lines are used to read and write data into the cell. Hold operation is initiates by holding the signal WWLA, RBL, and BB to "1" and the remaining signal to "0". Read operation is started by charging the signals read bit line (RBL), RWL WWLA, and BB and discharges the remaining signals. In write operation signals, WL, WWL, and RBL are charged to supply while signals WWLB and RWL are connected to ground.

Figure 4 shows the schematic of the conventional 10T CNTFET SRAM cell [5]. The cell has four transistors that behave as cross-coupled inverters to form the storage. The other transistor from T5 to T10 helps in reading and writing the data from the cell.

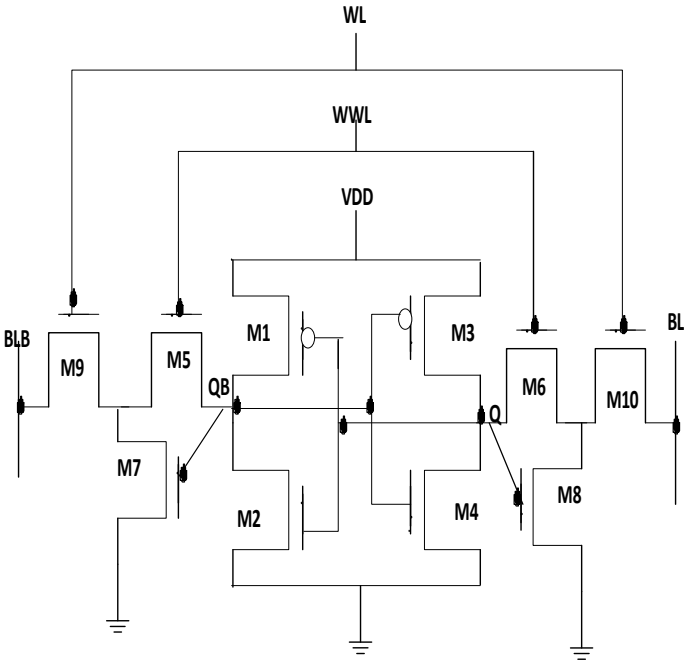

Fig. 2 10T CMOS-based cell [8]

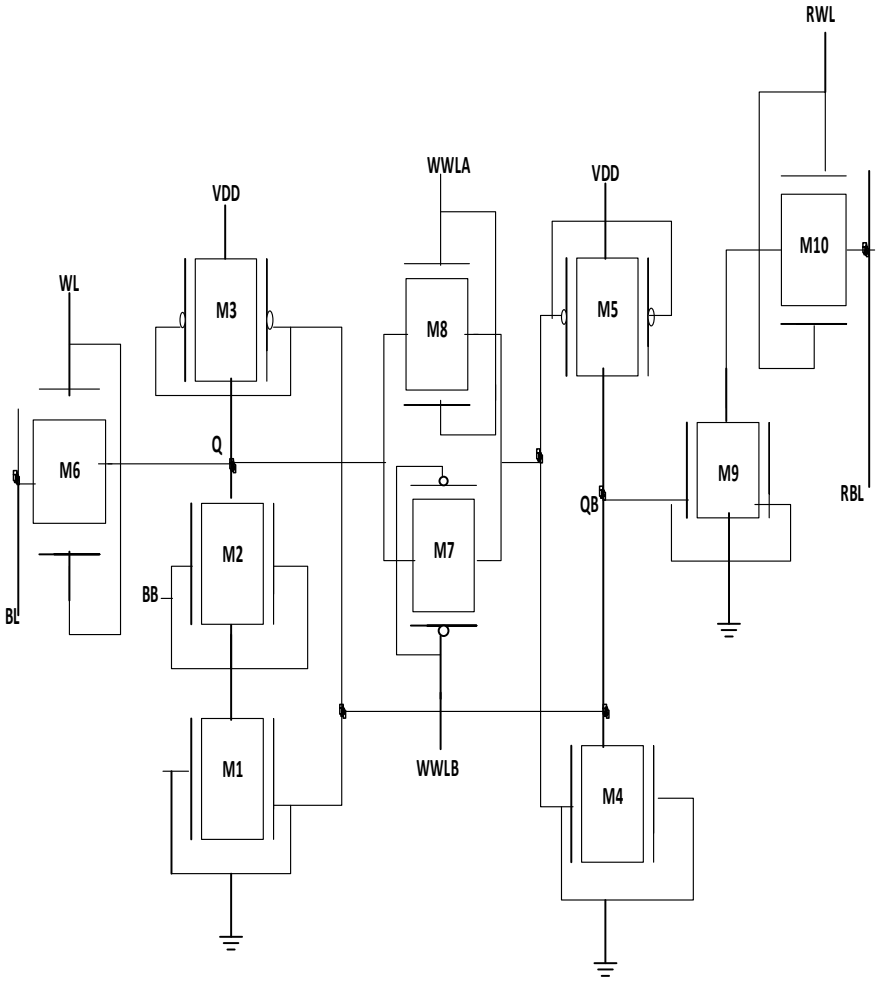

Fig. 3 10T FinFET-based SRAM cell [9]

In the write mode of the cell, the original value of data is assigned to BL and its complement to BLB. The data from bit lines to nodes are transfer through the access transistors by turning ON the word lines WWL and RWL.

In the read mode of the cell, WWL is kept low to disabled the access transistors (T5, T6) and decoupled the storage nodes from the bit lines. Both the bit lines are precharged to supply voltage for a while. The word line RWL is charged to VDD to turn ON the transistors T8 and T10. Transistors T7 and T9 are ON or OFF by the value stored at the storage node. By measuring the potential difference between the bit lines, the data stored in the cell are read using a sense amplifier. In the hold state, all bit lines and word lines are set to zero to turn OFF the access transistors to

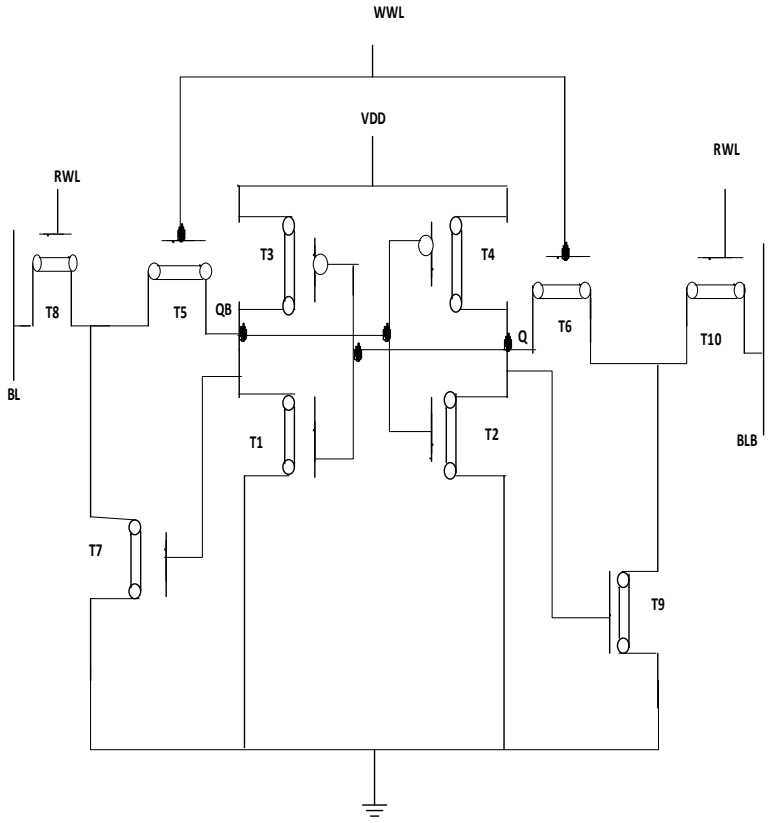

Fig. 4 Conventional CNTFET-based 10T SRAM cell [5]

disconnect the storage node from bit lines, and the storage nodes remain the same as they are.

3 Simulation Results

3.1 Stability

Stability plays an important role in the designing of SRAM cells. SNM helps in evaluating the stability of cell. SNM is the maximum amount of noise that can be tolerated by the cell without changing its data [10]. While reading the data, read stability should be high so that can be read easily without any interference. In a write operation, write stability is important to factor [11]. The graphical method is preferred to calculate SNM of the cell [12]. In this method, the VTC curve of one

inverter is superimposed on another inverted VTC curve [13]. The side length of smallest square in the lobe of butterfly curve shows the value of SNM.

Butterfly curves of all the CNTFET cell are shown in Figs. 5, 6, and 7 in which the CNTFET-based cell has the largest value of SNM, and FinFET has the second largest value of SNM. Furthermore, the conventional CMOS-based cell has the least value of SNM. All cells are simulated using the tool at 32 nm technology for a supply of 0.5 V. Hold SNM of CMOS is improved by 1.83x and 1.41x, while the read SNM is improved by 1.95x and 1.43x over FinFET and CNTFET cells, respectively. Whereas the write SNM has an improvement of 1.41x and 1.21x over FinFET and CNTFET cell, respectively. Table 1 shows the values of HSNM, RSNM, and WSNM of cells.

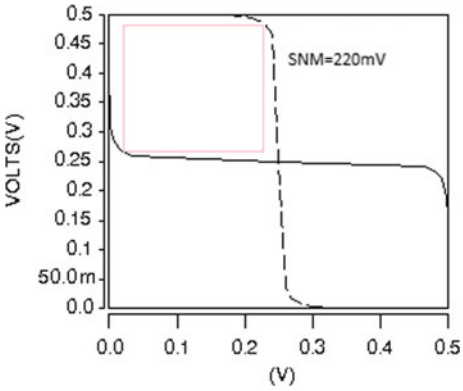

Fig. 5 Hold SNM for CNTFET

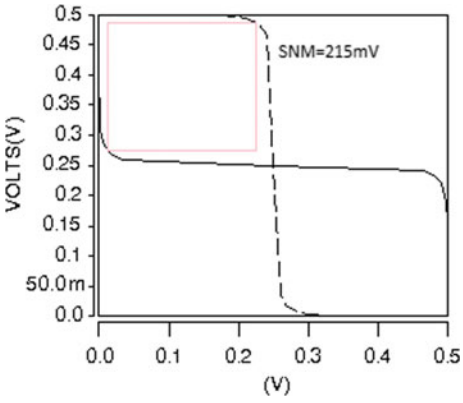

Fig. 6 Read SNM for CNTFET

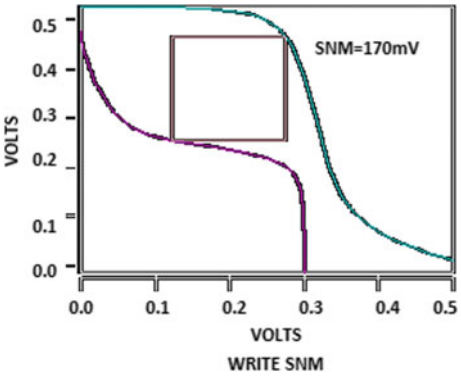

Fig. 7 Write SNM for CNTFET

Table 1 SNM values of cells

Type of cell	HSNM (mV)	RSNM (mV)	WSNM (mV)
10T CMOS	110	100	90
10T SG FinFET	155	150	120
10T CNTFET	220	215	170

Table 2 Leakage power analysis

Supply (V)	10T CMOS	10T SG FinFET	10T CNTFET (μW)
0.6	72.7817 μW	7.5442 nW	0.7202
0.5	2.4194 μW	5.2967 nW	0.5001
0.4	262.1833 nW	3.6087 nW	0.3201
0.3	70.7828 nW	1.4145 nW	0.1801
0.2	5.6341 nW	563.797 pW	0.08006

3.2 Leakage Power Dissipation

Power dissipation plays an important role in memory design. FinFET technique helps us in reducing the power consumption in SRAM circuits [14]. Most of the time SRAM remains idle in the circuit. The flow of currents in the idle portion of SRAM causes leakage power [15–18]. Table 2 compares the leakage power for all the cells.

4 Conclusion

In this paper, we compared leakage currents and SNM in 32 nm CMOS, FinFET, and CNTFET-based SRAM cells. Leakage power becomes a dominant factor in large memory array consumption. All designs are simulated by using HSPICE tool.

Performance is carried out by comparing SNM and leakage power of all designs. Both FinFET and CNTFET show better results compared to CMOS. FinFET-based SRAM cell has improved SNM by 29%, 36.36%, and 16% in the hold, read, and write modes, respectively, than the CMOS-based cell. While CNTFET has improved values of HSNM, RSNM, and WSNM by 83%, 95%, and 41%, respectively, than CMOS cell.

References

1. Bharadwaj AA, Soares IK, Madan HR, Ravish Aradhya HV (2015) Design and performance comparison of FinFET, CNFET and GNRFET based 6T SRAM . In: National conference on knowledge, innovation in technology and engineering (NCKITE), 10–11 Apr 2015
2. Doorn TS, Ter Maten EJ, Croon JA, Di Bucchianico A, Wittich O (2008) Importance sampling Monte Carlo simulations for accurate estimation of SRAM yield. In: Proceedings 34th European solid state circuits conference (ESSCIRC), pp 230–233
3. Parimala Devi M, Sharmila D, Meenakshi K (2013) Comparative study of 8T SRAM Cell using CMOS, FinFET and CNTFET in nanoscale technologies. Int J Electron Commun Technol IJECT 4(2)
4. Boopathi Raja G, Madheswaran M (2013) Design and performance comparison of 6-T SRAM cell in 32 nm CMOS, FinFET and CNTFET technologies. Int J Comput Appl (0975-8887) 70(21)
5. Elangovan M, Gunavathi K (2020) High stable and low power 10T CNTFET SRAM cell. J Circuits Syst Comput 29(10)
6. Kim YB (2011) Design methodology based on carbon nanotube field effect transistor (CNFET). Computer Engineering Dissertations
7. Geethumol TS, Sreekala KS, Dhanusha PB (2017) Power and area efficient 10T SRAM with improved read stability. Ictact J Microelectron 03(01)
8. Hosseini-Salekdeh S-R (2016) A comparative analysis of 6T and 10T SRAM cells for sub-threshold operation in 65 nm CMOS technology. M.Sc. thesis, Waterloo, Ontario, Canada
9. Sharma D, Birla S (2021) Design and analysis of 10T SRAM cell with stability characterizations. In: 2021 First international conference on advances in electrical, computing, communications and sustainable technologies (ICAECT 2021)
10. Lorenzo R, Paily R (2019) Low power 10T SRAM cell with improved stability solving soft error issue. In: IEEE Region 10 conference TENCON
11. Mohammed MU, Nizam A, Ali L, Chowdhury MH (2019) A low leakage SRAM bitcell design based on MOS-type graphene nano-ribbon FET. In: Proceedings of the IEEE international symposium on circuits and systems (ISCAS), Sapporo Japan, May 2019, pp 1–4
12. Kumar AA, Chalil A (2019) Analysis of 6T SRAM cell on planar and FinFET technology. In: International conference on communication and signal processing, 4–6 Apr 2019
13. Natarajamoorthy M, Subbiah J (2020) Stability improvement of an efficient graphene nanoribbon field-effect transistor-based SRAM design. Hindawi J Nanotechnol
14. Dani LM, Singh G (2015) FinFET based 6T SRAM cell for nanoscaled technologies. Int J Comput Appl 127(13)
15. Akashe S, Bhushan S, Sharma S (2012) Modeling and simulation of high level leakage power reduction techniques for 7T SRAM cell design. J Microelectron Electr Comp Mater 42(2):83–87

16. Kumar NR (2018) A review of low-power VLSI technology developments. In: Innovations in electronics and communication engineering, pp 17–27
17. Grossar E et al (2016) Read stability and Write-ability analysis of SRAM cells for nanometer technologies. IEEE J Solid-State Circuits 41:2577–2588
18. Maute JM, Puebla VK, Nericua RT, Gerasta OJ, Hora JA (2018) Design implementation of 10T static random access memory cell using stacked transistors for power dissipation reduction. In: IEEE 10th international conference on humanoid, nanotechnology, information technology, communication and control, environment and management (HNICEM) IEEE conference

Integration of Community Solar PV and DG Set for EV Charging Station

Shashi Kant Jatav and Praveen Kumar Agrawal

Abstract The trend of installing energy storage like batteries in residential areas is increasing. However, the cost of the battery and complementary electronic hardware is higher. Also, since there may not be enough power generation from the rooftop photovoltaic (RPV) system to charge the battery to its full capacity in winter, batteries installed in a single home may not be used optimally for most of the time of the year. On the other hand, if community solar power is optimally designed, the battery can be used to its full capacity. Renewable energy powered charging stations (CS) are essential for the sustainability of electric vehicles (EV). Therefore, using community solar photovoltaic energy as the main energy source for electric vehicle charging stations is a cost-effective method. In addition, diesel generator sets (DG) and local power station or grid are also used as backup power sources to provide continuous power for the EV charging station. The charging station can provide local home load in islanded mode or grid connected mode or DG connected mode as well. So, when we merge the idea of community solar with geography and electric power system infrastructure with scenario of rural India and its importance to establish a robust EV charging station infrastructure across country it becomes very achievable. This paper discusses a feasible strategy to effectively implement the community solar scheme in the low load areas to make a lucrative scenario which can be explored by corporate entities to set up an EV charging station while keeping it beneficial for the participating community also. To achieve this kind of capital intensive scheme few suggestions are proposed, since the India is the very economically diverse country and capital cannot be available for such projects everywhere from single identity itself be it the people, the state or the privet sector in such scenarios the suggested way forward is to incline the privet EV project with the government subsidized schemes and rope in the local people to form a coalition such that not a single partner has to bear the project alone.

Keywords Community solar · EV charging station · Bidirectional DC-DC converter · Battery charging · Grid connected · PV array

S. K. Jatav (✉) · P. K. Agrawal
Malaviya National Institute of Technology, Jaipur, India
e-mail: 2019pes5042@mnit.ac.in

© The Author(s), under exclusive license to Springer Nature Singapore Pte Ltd. 2022

A. Tripathi et al. (eds.), *Intelligent Computing Techniques for Smart Energy Systems*,
Lecture Notes in Electrical Engineering 862,
https://doi.org/10.1007/978-981-19-0252-9_14

1 Introduction

In a community-owned solar business model, a group of homes (customers) opt to buy a portion of their electricity from a solar facility off-site, typically because they lack adequate on-site solar resources or property ownership rights. Other alternative is to buy a solar rooftop photovoltaic (RPV) system from a community solar rooftop photovoltaic (RPV) system installed on houses with appropriate space and suitable orientation [1], which makes RPV installation in some places more appealing than in others. The majority of RPVs are placed by individual homeowners, which export power to the grid between non-peak hours, culminating in a 'duck curve' demand profile, according to the utility.

Additionally, in order to enhance the adoption of RPVs, several authorities have begun to permit their energy infrastructure to be utilized for exchanging electricity supplied by RPVs among surrounding customers [2]. A time-varying Feed in Tariff (FiT), as outlined in [3–5], can promote grid integration by delivering a low FiT during times of high RPV production and a high FiT during peak hours. Another option is to use energy storage devices, such as battery energy storage systems, in residential buildings or in the feeder that supplies them battery energy storages (BESs). Many research publications have explored using and integrating BESs in distribution systems, particularly at the home level. For example, improving the voltage profile [6], managing the quick variations in the electrical output of RPVs [7, 8], and using an auxiliary power source to regulate frequency [9, 10].

A scheme to deliver electrical power to the community load demand employing PV array and Diesel Generator set in islanded and utility grid connected modes. All these modes are tried while charging electric vehicle (EV) battery and delivering to community electricity demand [11]. This type of arrangement requires a battery energy storage, however we can realize that the key parameters in battery design are its charge and discharge rate and the overall capacity. Research presents a technical analysis of battery energy storages in achieving the desired objectives of self-consumption, self-sufficiency and peak shaving [12]. Integration of this establishment is the more inclusive approach and it increases the reliability and stability of the utility grid. A grid interfaced solar photovoltaic (SPV) power generating system consisting of a SPV, DC-DC boost converter, voltage source converter (VSC), interfacing inductors, ripple filter and a three-phase grid feeding variety of linear and nonlinear loads [13].

1.1 Proposed System

Figure 1 shown below is the schematic diagram of proposed scheme of electric vehicle charging station (EVCS). The EVCS incorporates the community solar photo voltaic (PV) and a diesel generator (DG) set as backup power supply for establishing the EV charging station, which is used for charging the EV and provide the backup

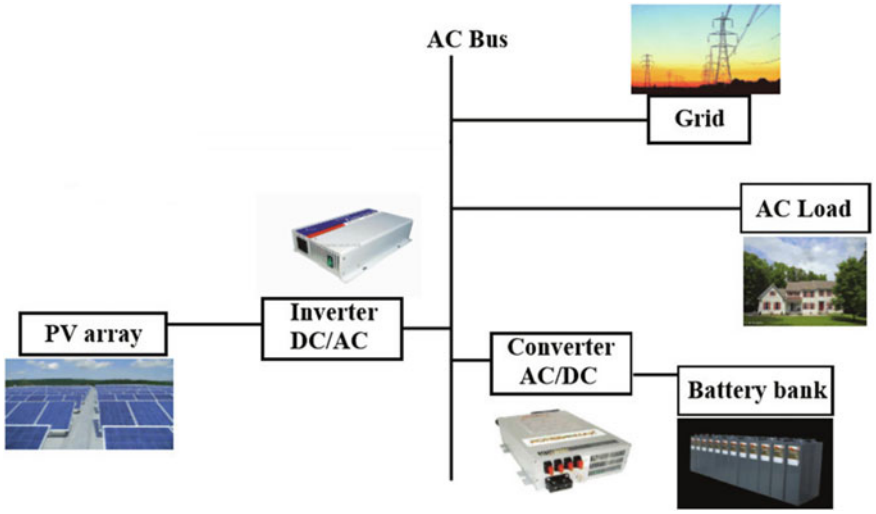

Fig. 1 Scheme of proposed system [14]

supply to the associated community which is participating in community solar. An insulated gate bipolar transistor (IGBT) switches-based boost converter works as an intermediate between the DC bus and the point of common coupling (PCC) or the point of the EV Charging Station. The Community Solar Photo Voltaic assembly supplies electricity at the DC bus using a DC-DC boost converter, and the DG and utility grid supply electricity at the Point of Common Coupling. The EV connected as CS withdraw electricity from the DC bus using a bidirectional DC to DC converter. This bidirectional DC to DC converter can be used for the EV-to-grid power transfer as well as EV to community power transfer. Local households belonging to solar community also take power from the PCC. An RC filter is installed on either sides of the bidirectional switches, this arrangement is installed to limit the noise generated due switching which are generated when the EV charging station is running in standalone and DG connected mode or the utility grid connected mode.

2 Design of the Proposed System

The designed system is a three-phase grid connected 100 kW PV array system with a 3-leg VSC having 6 IGBTs with antiparallel diode connected across each, three inductors and one capacitor.

2.1 Design of the Community Photovoltaic Array

The PV power generation system is rated at 100 KW peak power and will be used to power an EV charging station. As per design considerations solar module consists of 96 cells connected in series. Also as per rating for the given model of PV each cell has a 0.5–0.66 V open circuit voltage and a 5.96 A short circuit current (I_{sc}). As a result, each module has a 64.2 V open circuit voltage (V_{sc}) and a 5.96 A short circuit current. The generalized equation for maximum active power at MPPT in a PV array is the product of voltage at MPPT and current at MPPT which is as follows:

$$P_{\max M} = V_{\text{mpp}M} * I_{\text{mpp}M} \tag{1}$$

For this system of EV charging station power is supplied via community solar PV module which will have parallel and series strings as following.

Parallel strings = 66.

Series strings = 5.

Maximum power occurs in a general condition at 85% of the open circuit voltage and short circuit current rating

$$P_{\max M} = (85\% \text{ of } V_{\text{oc}} * 85\% \, of \, I_{\text{sc}}$$

Thus $I_{\text{mpp}M}$ is 5.58 A and $V_{\text{mpp}M}$ is 54.7 V of each module.

$$P_{\max M} = (54.7 * 5) * (5.58 * 66) \approx 100\,\text{kW}$$

2.2 Designing of DC-DC Boost Converter

The generated voltage as the terminals of PV is 274 V which is needed to be boost as level of 500 V, this is achieved with the help of DC-DC boost converter. The design components of the DC-DC boost converter are as following.

L_b is the input inductor and the value is given by,

$$L_b = \frac{V_{\text{pv}} D}{2\Delta i_1 f_{\text{sh}}}$$

Here, D is Duty cycle expressed as (D) = $1 - (V_{\text{in}}/V_b)$. This DC-DC converter boosts the voltage of PV array from $V_{\text{in}} = V_{\text{pv}} = 274\,\text{V}$ to $V_{\text{dc}} = 500$ V. The calculated value of duty cycle D is 0.453 and $V_{\text{in}} = V_{\text{pv}}$ which is the output voltage of PV array. The input current ripple denoted as Δi_1 and for this DC-DC converter design, the value of Δi_1 is considered 10% of input current, the value of this ripple current can be calculated as follows

$$i_1 = (P/V_{\text{in}}) = 368.28\,\text{A}.$$

The calculated value of Δi_1 is 36.828A. f_{sh} is switching frequency and its value considered for this case is $f_{\text{sh}} = 100$ kHz. The value of inductance (L_b) on calculating with the above mentioned parameters is 5 mH.

2.3 Designing of VSC

2.3.1 Design and Selection of DC Link Capacitor

The calculation of DC link capacitor for proposed scheme has been calculated on the principal of energy conservation. In this method the design of DC link capacitor (C_d) of voltage source converter (VSC) depends on the instantaneous energy available to the VSC at the time of transients. By using the principle of energy conservation the value of DC capacitor is given as

$$\frac{1}{2}C_d\left[V_{\text{dc}}^2 - V_{\text{dc1}}^2\right] = 3\alpha I V t_s$$

On solving the above equation we get the value of capacitor 6000 μF.

VSC takes input from grid voltage grid current and DC bus voltage and generate pulses in unison of MPPT control block pulse.

2.3.2 Design of AC Inductor

The ripple current Δi, switching frequency f_s and DC bus voltage (V_{dc}) are all factors in determining the AC inductance L_f of VSC.

$$L_f = \frac{\sqrt{3}mV_{\text{dc}}}{12hf_s\Delta i}$$

where *h and m* are the overload factor and the modulation index, respectively. Now taking, $\Delta i = 5\%$, $f_s = 100$ kHz, $m = 0.9$, $V_{\text{dc}} = 500$ V, $h = 1.2$, and solving the above equation for value of inductor, we get the approximate value of L_f, 5 mH.

3 Control Algorithm

The proposed EVCS consists of various electric power generating sources and the CS works in different configuration for charging the EVCS battery according to the

charging station's working plan (see Figs. 2 and 3) As a result, the control must be configured in such a way that all electric power sources are efficiently exploited without interfering with the charging of EVCS battery storage or the community electricity demand. Furthermore, EV charging station must support multimode operation and a variety of power quality requirements. As a result, the control architecture for standalone/island, utility grid connected, and auxiliary DG set connected mode is discussed here.

In island/standalone condition, Fig. 2 illustrate the control scheme for the DC bus voltage managing in standalone mode, this employs 2 back to back connected PI controllers. This DC connection voltage is controlled by the outer PI controller, which also produces the reference current for the current loop. This cascaded PI controller reduces error in the current signal and thus generates the required duty cycle for the bidirectional DC to DC converter.

The controller's goal while operating in utility grid or when in DG connected scheme is to draw just real power while taking in considering that it does not breaches the pre-set quality standards, this state achieved by delivering the demand of the reactive power for EV battery charger, harmonics current and community load, locally. Figure 3 shows the control scheme for the utility grid or DG employed mode.

The MPPT is attained applying the Perturb and Observe (P&O) dependent MPPT algorithm [11]. In this procedure, the controller changes the voltage from the array by a small amount and tests power; if increase in power is observed, the controller applies further corrections in that direction until increment in power stops.

The VSC control system uses an external control loop to adjust the DC bus voltage and an internal control loop to regulate direct and quadrature components of grid currents. Direct axis or active component of current (I_d) as reference is the output of the DC voltage external controller. Quadrature axis or reactive component of current (I_q) reference is kept zero to keep power factor unity. Active component (V_d) and reactive component (V_q) of voltage outputs of the current controller are changed to three modulating signals V^*_{abc} and are used by the PWM Generator.

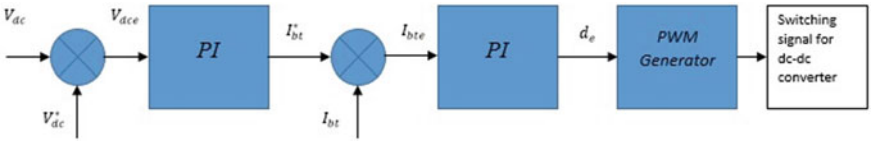

Fig. 2 DC bus voltage regulation in standalone/island operation mode

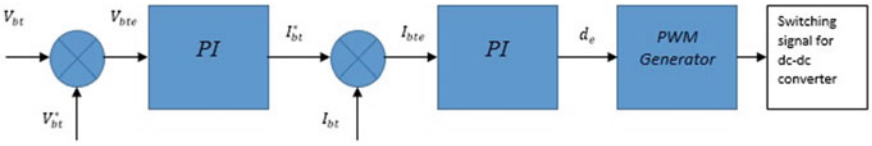

Fig. 3 EV charger control scheme in utility grid interfaced system

4 MATLAB-Based Modeling

Model of the community solar EV charging station having DG set as backup is designed on Simulink (MATLAB). The utility grid of 25 kV is interfaced with the designed system using VSC for exchange of power between EV battery and utility grid. The voltage outer-loop, and current inner-loop double PI control are applied operation of VSC. The designed simulation is run on the MATLAB version 9.7.0.1190202 (R2019b) using Simulink toolbox and 1e−6 discrete solver.

5 Results and Discussion

The envisioned EV Charging Station is designed in SIMULINK realizing the community solar scheme as 66 parallel-connected PV modules, VSC has been realized employing the insulated gate bipolar junction transistor (IGBT) with antiparallel diodes connected across them bidirectional DC to DC converter (BDDC) and boost converter also been realized using IGBT's. The designed EVCS functions in both island/standalone and utility grid connected mode. The results are derived for steady state condition in utility grid interfaced or DG connected mode.

5.1 PV Array Scope

The designed PV array is subjected to variable irradiance which ranges from to and constant temperature of 25, PV coupled DC to DC converter takes bus voltage as reference and boosts the output to provide desired voltage output, during day time PV module is generating the electrical energy and delivering the load and charging the battery storage having the charging control govern by PWM of the converter.

As the irradiance starts to reduce the power output also starts to deplete so the power delivered to the load and battery charging also starts to reduce (Fig. 4).

5.2 Power Fed to the Grid

Power generated by the CSPV is first delivered to the community load and the charger/DC-DC converter for battery storage charging, remaining power is then transferred to the grid, the designed model perform accordingly (Fig. 5).

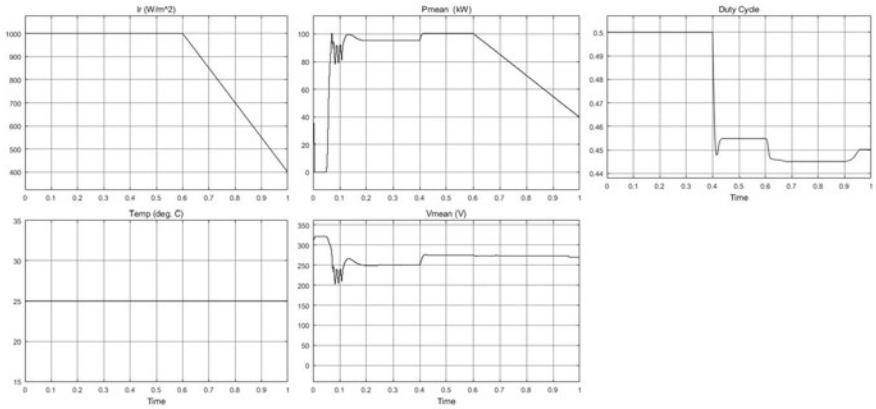

Fig. 4 PV array irradiance, temperature, voltage, current and duty cycle at standalone mode

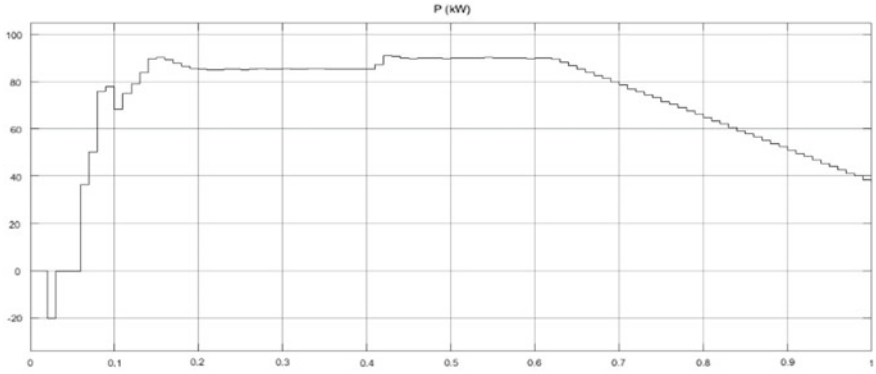

Fig. 5 Power fed to the grid in grid connected mode

5.3 Battery Charging

5.3.1 In Islanded Mode

See Fig. 6.

5.3.2 Grid Connected Mode

The proposed model has been tested in three modes of operation namely, standalone mode DG connected mode and grid connected mode (Fig. 7).

To take real world scenario in context where load will vary at any given time the model is tested for a range of KVAr loads and the system is found to be

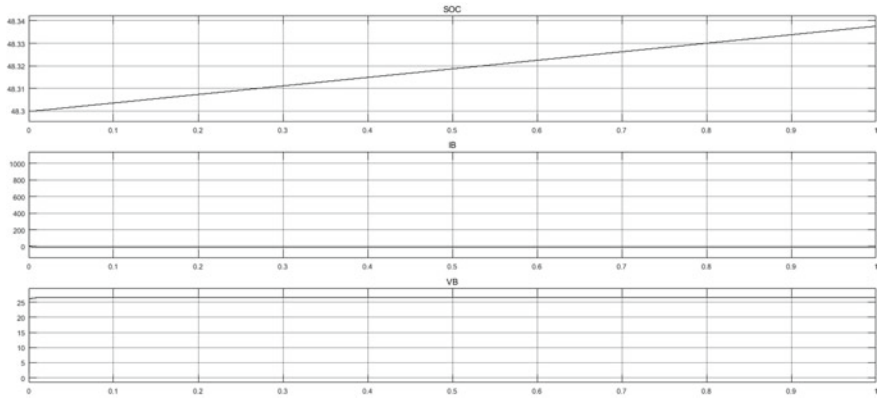

Fig. 6 Battery SoC, current I and voltage in standalone mode

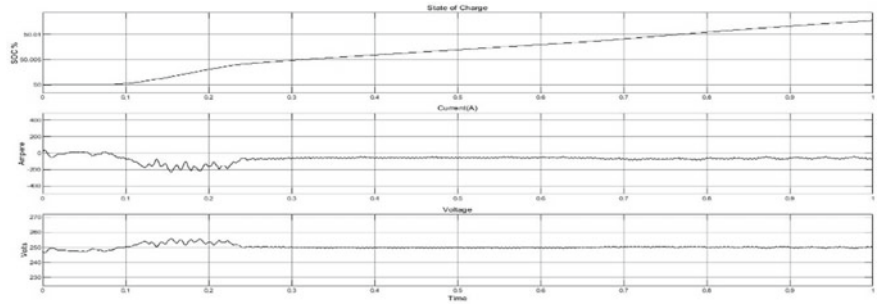

Fig. 7 Battery SoC, current I and voltage in grid connected mode

charging/discharging the battery to balance the power at the DC bus, below is the tabulated data of the test in various modes (Fig. 8).

6 Conclusion

The designed community solar EV charging station connected to utility grid performed as desired in all three modes of operation and the control algorithms P&O and double loop control scheme performed as desired for unity power factor. The total harmonic distortion (THD) in voltage and current are found to be satisfactory.

Standalone mode						
Load	Battery				PV duty cycle(avg.)	
kvar	SOC	I(Amp.)	V(volts)		1000(Ir)	400(Ir)
50	50.013	-85.49	244.5	Charging	0.4852	0.5144
100	50.011	-81.15	244.4	Charging	0.4888	0.5262
150	49.872	90.22	244.4	Discharging	0.4936	0.5364
200	49.443	92.13	244.3	Discharging	0.4947	0.5547
250	48.536	95.77	244.1	Discharging	0.5653	0.5743
DG connected mode						
100	50.123	-140.8	242.4	Charging	0.5086	0.5094
150	49.975	138.6	242.5	Discharging	0.5119	0.5171
200	49.981	140.5	242.5	Discharging	0.5116	0.5084
250	49.975	141.7	243.1	Discharging	0.5117	0.5061
Grid connected mode						
100	50.116	139.6	242.5	Charging	0.4653	0.4423
150	50.104	150.3	242.1	Charging	0.4911	0.4703
200	50.073	157.8	242.2	Charging	0.4856	0.468
250	50.064	169.1	241.4	Charging	0.4715	0.4431

Fig. 8 Battery charging/discharging in various modes at different loads

References

1. Tongsopit S, Moungchareon S, Aksornkij A, Potisat T (2016) Business models and financing options for a rapid scale-up of rooftop solar power systems in Thailand. Energy Policy 95:447–457
2. Illinois blazes new trail for private microgrids using utility wires, News, Retrieved 24/04/18
3. Hayat MA, Shahnia F, Shafiullah G (2018) A novel dynamic feed-in tariff for residential rooftop PVs. In: 45th IEEE photovoltaic specialists conference (PVSC), Hawaii, pp 1–6
4. Hayat MA, Shahnia F, Arefi A (2017) Efficient seasonal time of use feed-in tariff for residential rooftop PVs in Australian electricity market. World renewable energy congress XVI, Perth, pp 1–4
5. Hayat MA, Shahnia F, Arefi A (2018) Efficient seasonal time of use feed-in tariff for residential rooftop PVs. In: Sayigh A (ed) Australian electricity market, in transition towards 100% renewable energy. Springer, Berlin, pp 171–175
6. Shahnia F, Wishart MT, Ghosh A (2013) Voltage regulation, power balancing and battery storage discharge control by smart demand side management and multi-objective decision making. In: 23rd Australasian universities power engineering conference (AUPEC), Hobart
7. Jabalameli N, Deilami S, Masoum MAS, Shahnia F (2013) Rooftop PV with battery storage for constant output power production considering load characteristics. In: 8th International conference on electrical and electronics engineering (ELECO), Bursa
8. Jabalameli N, Masoum MAS, Shahnia F, Mehr TH (2013) Impact of battery rating on performance of rooftop PV supporting household loads, regulating PCC voltage and providing constant output power to grid. In: 23rd Australasian universities power engineering conference (AUPEC), Hobart
9. Goyal M, Ghosh A, Shahnia F (2014) Distributed battery storage units for overload prevention in an islanded microgrid. In: 24th Australasian universities power engineering conference (AUPEC), Perth, Australia, Sept 2014, pp 1–6
10. Goyal M, Ghosh A, Shahnia F (2014) Overload prevention in an autonomous microgrid using battery storage units. IEEE power and energy society general meeting, Washington DC, pp 1–5
11. Femia N, Petrone G, Spagnuolo G, Vitelli M (2005) Optimization of perturb and observe maximum power point tracking method. IEEE Trans Power Electron 20(4):963–973

12. Chaudhari K, Ukil A, Kumar KN, Manandhar U, Kollimalla SK (2018) Hybrid optimization for economic deployment of ESS in PV-integrated EV charging stations. IEEE Trans Ind Inf 14(1):106–116
13. Luthander R et al (2016) Self-consumption enhancement and peak shaving of residential photovoltaics using storage and curtailment. Energy 112:221–231
14. https://www.researchgate.net/figure-configuration-of-grid-connected-hybrid-renewable-energy-system_fig1_316743161
15. Hayat MA, Shahnia F, Arefi A (2016) Comparison of the electricity tariffs and bills across the zones of Australian power distribution companies. In: 26th Australasian universities power engineering conference (AUPEC), Brisbane, Australia, pp 1–5
16. Hayat MA, Shahnia F, Shafiullah G (2018) Replacing flat rate feed-in tariff for rooftop photovoltaic system with a dynamic one to consider technical, environmental, social and geographical factors. IEEE Trans Ind Inform. https://doi.org/10.1109/TII.2018.2887281
17. Solar Panel rebate to be phased out from 1st of January 2017, Website, Retrieved 15/05/18
18. Mehr TH, Ghosh A, Shahnia F (2017) Cooperative control of battery energy storage systems in microgrids. Int J Electr Power Energy Syst 87:109–120
19. Hayat MA, Shahnia F, Arefi A (2017) Comparison of the economic benefits and the payback periods of rooftop solar panels in Australia. In: IEEE 3rd international conference on power generation systems and renewable energy technologies (PGSRET), Johor Bahru
20. Schram W et al (2018) Photovoltaic systems coupled with batteries that are optimally sized for household self-consumption: assessment of peak shaving potential. Appl Energy 223:69–81
21. Klingler A (2017) Self-consumption with PV+Battery systems: a market diffusion model considering individual consumer behaviour and preferences. Appl Energy 205:1560–1570
22. Yu H (2018) A prospective economic assessment of residential PV self consumption with batteries and its systemic effects: the French case in 2030. Energy Policy 113:673–687
23. Dongol D et al (2018) A model predictive control based peak shaving application of battery for a household with photovoltaic system in a rural distribution grid. Sustain Energy Grids Netw 16:1–13
24. Verma A, Singh B (2019) Integration of Solar PV-WECS and DG set for EV charging station. IEEE Access 7
25. Hayat MA, Shahnia F, Shafiullah GM (2019) Technical analysis of the charge/discharge rate and the capacity of batteries in meeting the residential peak demand within a community solar. IEEE PES Innovative Smart Grid Technologies Asia
26. Singh B, Shahani DT, Verma AK, Power balance theory based control of grid interfaced solar photovoltaic power generating system with improved power quality
27. Yang Y, Jia Q, Deconinck G, Guan X, Qiu Z, Hu Z (2018) Distributed coordination of EV charging with renewable energy in a microgrid of buildings. IEEE Trans Smart Grid 9(6):6253–6264
28. Alam M et al (2013) Mitigation of rooftop solar PV impacts and evening peak support by managing the available capacity of distributed energy storage systems. IEEE Trans Power Syst 28(4):3874–3884
29. Habib S, Khan MM, Abbas F, Sang L, Shahid MU, Tang H (2018) A comprehensive study of implemented international standards, technical challenges, impacts and prospects for electric vehicles. IEEE Access 6:13866–13890
30. Esther S, Singh SK, Goswami AK et al (2018) Recent challenges in vehicle to grid integrated renewable energy system: a review. In: Proceedings of the 2018 second international conference on intelligent computing and control systems (ICICCS), Madurai, India, pp 427–435
31. Joseph PK, Devaraj E, Gopal A (2019) Overview of wireless charging and vehicle-to-grid integration of electric vehicles using renewable energy for sustainable transportation. IET Power Electron 12(4):627–638
32. Masrur MA, Skowronska AG, Hancock J et al (2018) Militarybased vehicle-to-grid and vehicle-to-vehicle microgrid-system architecture and implementation. IEEE Trans Transp Electrif 4(1):157–171

33. Noureldeen O, Hamdan I, Hassanin B (2019) Design of advanced artificial intelligence protection technique based on low voltage ride-through grid code for large-scale wind farm generators: a case study in Egypt. SN Appl Sci 1(6):1–19
34. Noureldeen O, Hamdan I (2018) Design of robust intelligent protection technique for large-scale grid-connected wind farm. Protect Control Mod Power Syst 3(1):1–13
35. Qian K, Gao G, Sheng Z (2018) A maximum current control method for three-phase PWM rectifier for the ITER in-vessel vertical stability coil power supply. IEEE Trans Plasma Sci 46(5):1689–1693

Impact of Variation of Performance Parameters on the Efficiency of CNTFET Based 7T SRAM Cells

Neha Mathur, Shilpi Birla, and Deepika Sharma

Abstract Technology node modification is the demand of the present era of the IC industry. Conventional CMOS to FINFET and now CNTFET is playing a major role to fulfill this demand because beyond the 7 nm technology node CNTFET shows the same performance and is not affected by the issues coming from the short channel effect. Meanwhile, memory cells are also a backbone of sequential circuits of digital systems. Among all memory cells, SRAM is a major building block of digital systems. IC designing of SRAM cells are started with CMOS and now with increasing technology nodes, its design is saturated with FINFET also. In this paper CNTFET is taken for SRAM designing which includes all technology nodes for their designing. Now the task is select the number of CNTFETs for the designing of SRAM. CNTFET based SRAMs are available with 6T, 7T, 8T, 9T, and many more. This paper includes a conventional 7T SRAM cell and a new SRAM cell is also proposed that is also designed using 7T. Both cells are compared in terms of their efficiency with the variation of performance parameters of CNTFET.

Keywords CNTFET · CMOS · FET · SNM · SRAM

1 Introduction

SRAMs are the pinnacle to store electronics data on chips to meet the performance with the scaling of technology nodes or enhancement of functionality of systems, the demand for highly efficient systems in terms of power consumption, delay speed, etc. is also at the peak of consideration. All these requirements of the systems are prominently followed by conventional CMOS with 32 nm technology nodes. Beyond this limit, major issues like excess leakage current and short channel effect cannot be neglected [1, 2]. In this situation, the most efficient alternative is CNTFETs because it reduces the limitations coming from conventional CMOS.

N. Mathur · S. Birla (✉) · D. Sharma
Department of Electronics and Communication Engineering, Manipal University Jaipur, Jaipur, India
e-mail: Shilpi.birla@jaipur.manipal.edu

© The Author(s), under exclusive license to Springer Nature Singapore Pte Ltd. 2022

A. Tripathi et al. (eds.), *Intelligent Computing Techniques for Smart Energy Systems*, Lecture Notes in Electrical Engineering 862,
https://doi.org/10.1007/978-981-19-0252-9_15

CNTFET is more dominant than conventional CMOS when compared to their performance parameters even beyond 32 nm channel length. Some prominent properties of CNTFET can be expressed in terms of high value of gate dielectric, low voltage operated quasi ballistic transport, higher drive current, higher transconductance, lower heat dissipation, higher average carrier velocity, and the higher ON–OFF current ratio [3, 4]. Memory cells are a fundamental source of Dynamic digital systems which include SRAM in front this. Thus the performance of digital systems is majorly dependent on the efficiency of memory cells. The researchers investigated and then proposed CNTFETs based memory cells and their performance results are fulfilling the expectation of dynamic digital systems in recent years. In this paper, static style and dynamic style 7T SRAM cells are simulated. HSPICE tool is used to design and simulate both conventional 7T and proposed 7T SRAM cells with Stanford CNTFET model file.

2 CNTFET Based Conventional 7T SRAM Cell with Static Style

7T-1 SRAM Cell: This structure is a mirror image of a conventional 6T-based SRAM cell with one extra transistor namely, M7, at the bottom of the circuit. M7 is working to provide feedback connection between the cross-coupling structure of both the inverters [5, 6]. Gate terminals of access transistors M5 and M6 are controlled by write select and read select signals (Fig. 1).

Hold Operation is executed by setting write select, read select and write bar at ‘0’ while supply VDD is applied at both read and write a bit. Meanwhile, the read and write operation can only be performed by exerting the written bar at ‘1’ because

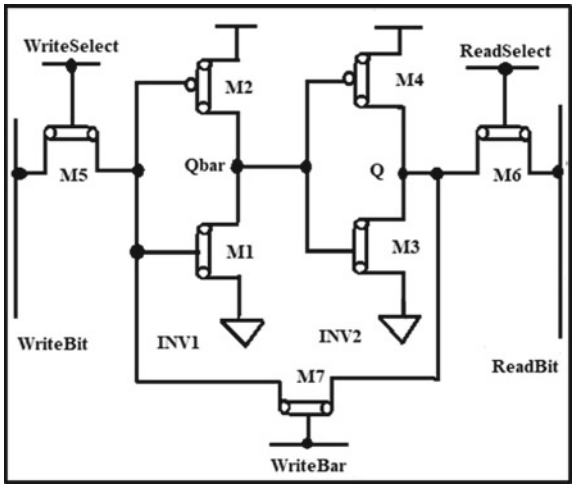

Fig. 1 Conventional CNTFET based 7T SRAM cell (7T-1) [7]

now only M7 will be turned on. Consequently, to perform read operation both write and read select is need to be set at '1' while the read and write bit is adjusted with VDD. Similarly, the write operation is executed but also depends on the value want to write. If the cell is written with '0' then write bit is set with '0' and read bit is set with '1' and similar to write '1', need to set write a bit with '1' and read bit is set with '0' [8].

3 CNTFET Based Proposed 7T SRAM Cell

7T-2 SRAM Cell: This proposed structure includes one more PMOS transistor T7 which is connected with VDD and the gate terminal is grounded. This structure also consists of two inverters designed using T1, T2, T3, and T4 with cross-coupling way of connection acts as storage cell while T5 and T6 are access transistors, controlled by a word line (WL). Values are stored at Q and QB outputs of the inverter [9, 10] (Fig. 2).

Hold operation is accomplished by setting WL is at '0'. Which controls the access transistors by turning them off. Thus Q and QB are completely disconnected, from bit lines and hold the previously stored values.

Read operation can only be executed by disconnecting Q and QB from the bit lines but these should be precharged at VDD. Now discontinuation of both storage nodes can be achieved by turning off the access transistors.

Write operation is executed by setting the data to be stored in a bit line (BL) and the complement of BL is at the bit line bar (BLB), while the word line is set at '1' [11].

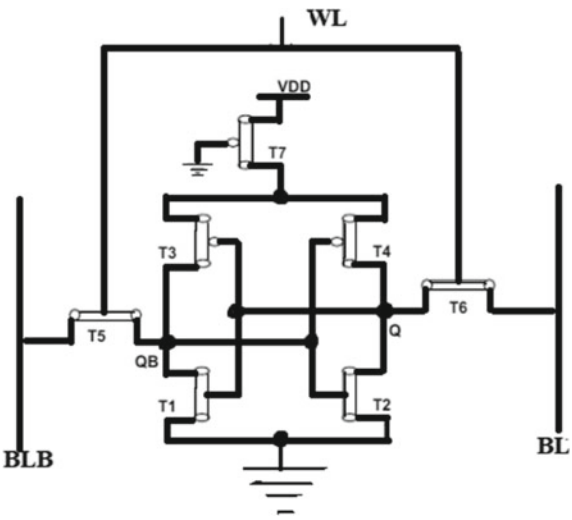

Fig. 2 Proposed CNTFET based 7T SRAM cell (7T-2)

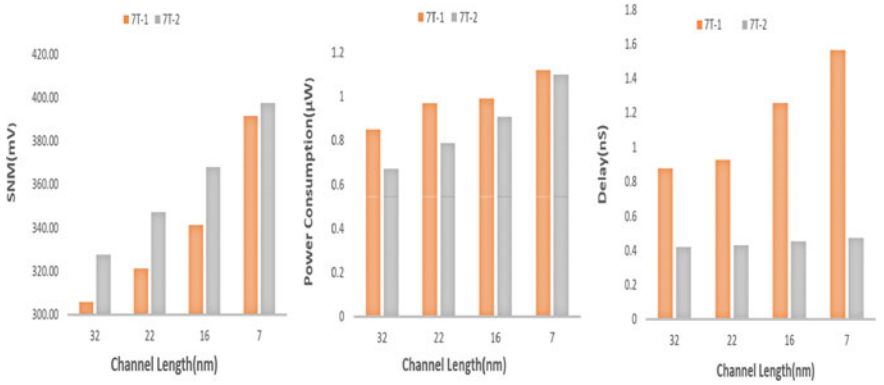

Fig. 3 Variations of SNM, power consumption and delay with the variation of Channel Length (nm)

4 Results and Discussion

4.1 Impact of Variation of Channel Length

Impact of variation of channel length has been observed with the simulation of conventional 7T SRAM (7T-1) and proposed 7T SRAM (7T-2) to evaluate the efficiency of both the structures. SNM, power consumption, and delay are evaluated for 32 nm, 22 nm, 16 nm, and 7 nm technology node.

As the channel length decreases, both the structures 7T-1 and 7T-2 SRAM cell shows increased static noise margin [12, 13]. Consequently, 7T-2 is more stable because of the high value of SNM. This stability demands less power consumption as well as less delay from their execution. The 7T-2 structure shows almost 10% more stability for 32 nm, 22 nm, and 16 nm while for 7 nm it is just approx. 2% more stable in terms of performance parameters. Thus 7T-2 structure of SRAM cell is more prominent with the variation of channel length (Fig. 3).

4.2 Impact of Variation of Dielectric Material

Dielectric constant with high k values are the prominent solution to overcome the gate leakage issue produced because of high power dissipation with the demand of technology scaling. Meanwhile, silicon dioxide having 3.9 its dielectric constant value, is treated as an ideal interface but shrinking of technology node creates excess power dissipation [14, 15]. Some most frequently available and used dielectrics are Silicon dioxide (3.9), Aluminum oxide (9), Hafnium oxide (15), Zirconium oxide (25), Lanthanum oxide (30), and Titanium oxide (80).

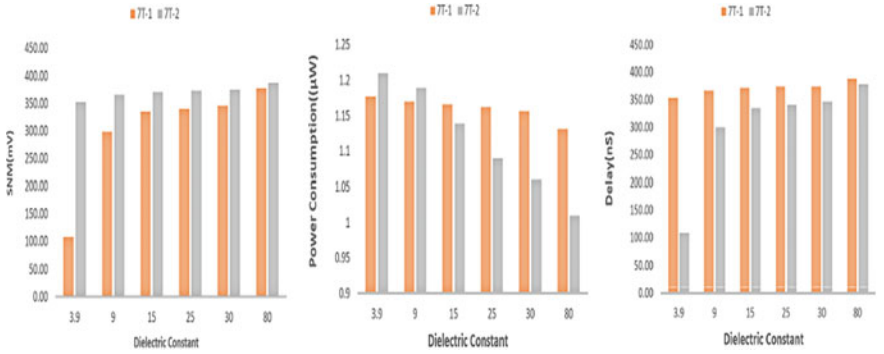

Fig. 4 Variations of SNM, power consumption and delay with the variation of dielectric constant

Now the next task is to check the impact of variation of dielectric constant for their performance parameters. This can be accomplished by taking different dielectrics with its thickness of 1 nm.

It is observed that SNM is going to be increased for the high value of the dielectric constant in both structures. 7T-2 is showing more SNM than 7T-1 but for the 7T-2 structure, its increasing value is almost 1% from 39 to 80 as shown in Fig. 4. It is also noted that power consumption is also more for the 7T-1 structure because of less stability but for two dielectrics Silicon dioxide (3.9), Aluminum oxide (9) 7T-2 structure shows more power consumption. Now more stability and less power consumption reduce the delay of this 7T-2 structure. Thus, 7T-2 structure of SRAM cell is more efficient with the variation of dielectric constants (Fig. 4).

4.3 Impact of Variation of Oxide Thickness

Output characteristics of CNTFET depends on the thickness of the oxide layer in an inversely proportional manner. Thus by reducing the oxide thickness, conductivity can be increased. To avoid the tunneling effect, the minimum limit of the oxide thickness is 1.5 nm. In this paper a full range of oxide thickness is used, to observe the overall efficiency of SRAM cells. This range includes 1.5 nm, 3 nm, 6 nm, 9 nm, and 15 nm thickness of oxide layer [12, 16].

Both 7T-1 and 7T-2 structure of SRAM cell is simulated with the variation of oxide thickness and it has been noted that the stability of the cell is decreasing with the increasing value of oxide thickness in terms of SNM. Consequently, more power is also required thus power consumption increases for both structures. The 7T-2 structure requires almost 50% reduced power for its execution. Furthermore, a delay is also increased because of less stability of the cells. When compare both the structures for the variation of oxide thickness, 7T-2 is more efficient (Fig. 5).

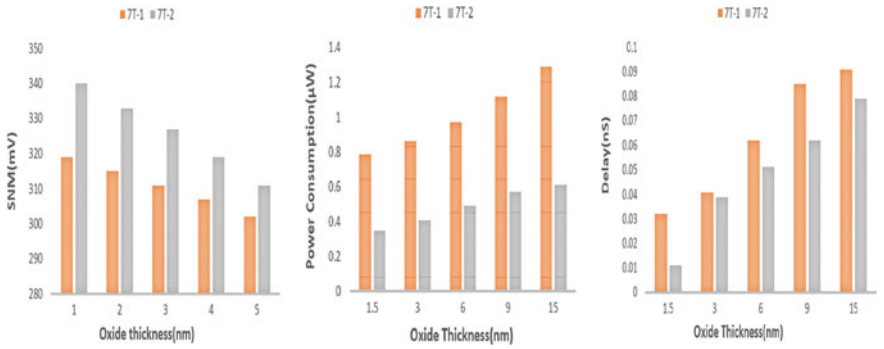

Fig. 5 Variations of SNM, power consumption and delay with the variation of oxide thickness

4.4 Impact of Variation of Fermi Level

In this paper, both structures of SRAM cell are simulated for different values of Fermi level in the range of 0.4 eV, 0.5 eV, 0.6 eV, and 0.7 eV. The optimum value of the Fermi level provides excellent efficiency to the cell. In CNTFET, the value of the Fermi level is decided by its level of doping [17, 18]. Analyzed results show that SNM is almost saturated for 7T-1 structure and 7T-2 structure but approximately 15% more for 7T-2. Power consumption is more for the 7T-1 structure when compare with 7T-2. Thus the 7T-2 structure of SRAM cell is faster than 7T-1 because of less delay.

Again 7T-2 SRAM cell is more efficient when compared with the 7T-1 SRAM cell (Fig. 6).

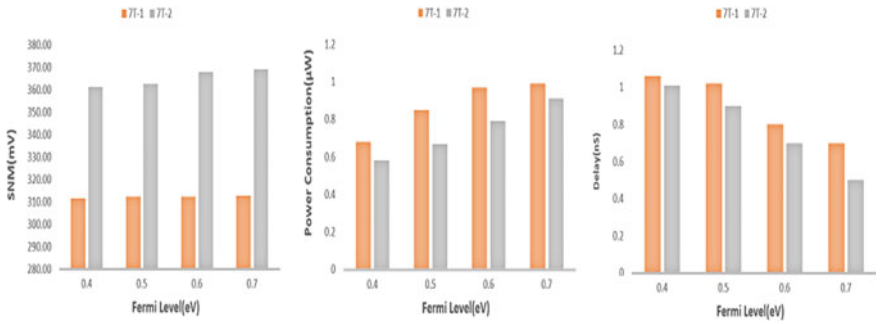

Fig. 6 Variations of SNM, power consumption and delay with the variation of Fermi Level

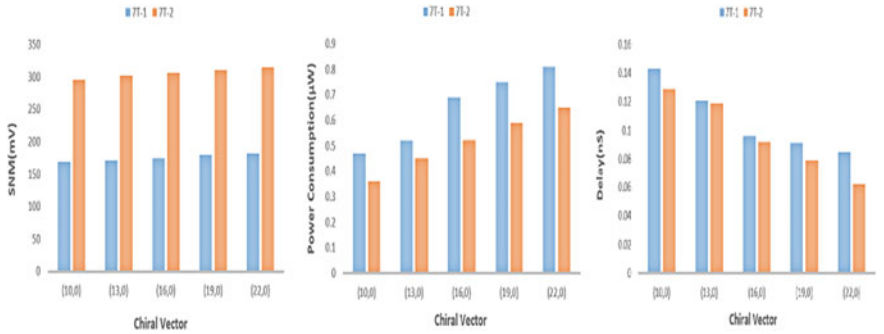

Fig. 7 Variations of SNM, power consumption and delay with the variation of chiral vector

4.5 Impact of Variation of Chiral Vector

Chiral vector is the most important design parameter of CNTFET because several parameters of CNTFET depend on it. Chiral vector also decides the nature of CNT, whether it will metal or semiconductor [19, 20]. In this paper both 7T-1 and 7T-2 SRAM cell is analyzed with this range of chiral vector (10, 0), (13, 0), (16, 0), (19, 0), (22, 0). Simulation shows that SNM is almost saturated for both structures, individually. But 7T-2 is almost 50% more stable than 7T-1 in terms of SNM. Meanwhile, power consumption is increasing for the structure with the variation of the chiral vector. In fact, structure 2 requires more power for their execution and power consumption is increasing with the variation of the chiral vector. But delay is decreasing for both the cells. The graph of delay variation is not uniform for all the values of the chiral vector.7T-2 SRAM cell is more stable than 7T-1 SRAM cell in performance metric (Fig. 7).

5 Conclusion

In this paper, two structures of CNTFET based 7T SRAM cells are taken. In which 7T-1 is a conventional structure while the 7T-2 structure is proposed. The objective of this paper is to simulate both the structures has completed. Simulation is achieved using the HSPICE tool and Stanford CNTFET model file. Simulation of both the structures is executed in terms of SNM, power consumption, and delay such that their efficiency can be measured. The complete execution is represented using different-different graphs for SNM, power consumption, and delay.

Initially, simulation is accomplished with standard values of all design parameters of CNTFET. Later as per the objective, variation of all design parameters is introduced. To achieve this, all design parameters like channel length, dielectric constant, oxide thickness, Fermi level, and chiral vector are taken. Each parameter is varied with their range of availability which includes channel length variation from 32 to

7 nm, different dielectrics, oxide thickness from 1.5 to 9 nm, Fermi level from 0.4 to 0.7 eV, and different available range of chiral vectors.

Consequently, simulation has done with the variation of all design parameters and values of SNM, power consumption, and delay are noted and represented in graphs with their values. After their proper comparison, it is found that the 7T-2 cell is more stable and efficient and providing almost 10% more stability than the 7T-1 SRAM cell.

References

1. Zhang Z, Delgado-Frias JG (2011) Low power and metallic CNT tolerant CNTFET SRAM design. In: 11th IEEE international conference on nanotechnology Portland Marriott, vol A247, pp 1177–1182
2. Patel PK, Malik M, Gupta TK (2018) Design of an ultralow power CNTFET based 9T SRAM with shared BL and half select free techniques. wileyonlinelibrary.com/journal/jnm, vol 4, pp 1–9
3. Murotiya Sl, Matta A, Gupta A (2012) Performance evaluation of CNTFET-based SRAM cell design. Int J Electr Electron Eng (IJEEE) 2:78–83
4. Prakasha P, Mohana Sundarama K, Anto Bennetb M (2018) A review on carbon nanotube field effect transistors (CNTFETs) for ultra-low power applications. Renew Sustain Energy Rev 89:194–203
5. Mohita, Newar T, Roy T (2016) Design and stability analysis of CNTFET based SRAM cell. In: IEEE Students' conference on electrical, electronics and computer science, vol 2, pp 77–81
6. Divya, Kaur M, Singh G (2018) Performance analysis of CNFET based 6T SRAM. COJ Electron Commun 1:1–9
7. Tamil Selvan S, Sundararajan M (2018) Performance evaluation of 3 value logic 7t And 8t CNTFET based SRAM cell design. Int J Pure Appl Math 120:33–47
8. Sayed SI, Abutaleb MM, Nossair ZB (2016) Optimization of CNFET parameters for high performance digital circuits. Hindawi Publ Corp Adv Mater Sci Eng 2016:1001–1009
9. Das S, Das D, Rahaman H (2016) Design of content addressable memory cell using carbon nanotube field effect transistors. In: Proceedings of the 2016 IEEE students' technology symposium, vol 2, pp 131–135
10. Spasova M, Nikolov D, Angelov G, Radonov R, Hristov M (2017) SRAM design based on carbon nanotube field effect transistor's model with modified parameters. IEEE 2:1–4
11. Elangovan M, Gunavathi K (2020) High stable and low power 8T CNTFET SRAM cell. J Circuits Syat Comput 29:2050080-1–18
12. Parimala Devi M, Sharmila D, Meenakshi K (2013) Comparative study of 8T SRAM cell using CMOS, FinFET and CNTFET in nanoscale technologies. Int J Electron Commun Technol 4:7–10
13. Joshi S, Alabawi U (2017) Comparative analysis of 6T, 7T, 8T, 9T, and 10T realistic CNTFET Based SRAM. Hindawi J Nanotechnol 2017:177–185
14. Prasad R, Madhavi BK, Lal Kishore K (v) Low leakage-power SRAM cell design using CNTFETs at 32nm Technology. LNICST 108:165–171
15. Bhavar Sonali R, Khule RS (2017) Design and analysis on the performance of CNTFET based inverter in nanometer regime. IJARIIE 3:1779–1784
16. Maheswar Y, Raju BL, Soundara Rajan K (2019) 256K Memory bank design with 9T SRAM bit cell and 22nm CNTFET optimizing for low power and area. Int J Innov Technol Explor Eng (IJITEE) 8:675–681
17. Ahmed SS, Makdey S, Bhoir D (2015) Performance enhancement of VLSI circuits using CNTFETs. Int J Eng Trends Technol (IJETT) 23:1–6

18. Jaiswal M, Singh AR (2015) Design and analysis of CNTFET-based SRAM. Int Res J Eng Technol (IRJET) 2:11–15
19. Rizvi A, Jaiswal P (2016) Study of CNTFET performance over MOSFET using digital logic circuits. IJVDCS 4:363–375
20. Singh A, Khosla M, Raj B (2016) CNTFET modeling and low power SRAM cell design. In: IEEE 5th global conference on consumer electronics, vol 2, pp 5090–5094

Performance Analysis of Oxide Capacitance at Gate-Dielectric Variation in Surrounding-Gate MOSFET Structure

Shashi Kant Dargar, Jitendra Kaushal Srivastava, Shilpi Birla, and Prabhat Kumar Panda

Abstract This work presents gate-oxide variation effect on the performance of cylindrical surrounding double-gate (CSDG) MOSFET, particularly the device saturation operation. The analysis is based upon the resemblance of the device oxide capacitance in the device pinch-off. The capacitance formation at pinch-off cannot be considered a cylindrical parallel plate; therefore, the capacitance results differently from conventional computing of capacitance depending on the device dimensions, oxide thickness, and the material properties of the device structure. In this work, the authors compare the results of the device with different oxide materials such as SiO_2, Si_3N_4, Al_2O_3, Ta_2O_5, and HfO_2 using numerical simulation. The parameter comparison results are insightful, which show that a high drain current is attained with HfO_2 gate-oxide material. Moreover, performance degradation has been observed with decreasing k value of the gate-oxide materials. The analysis results are promising for enhancing switching characteristics using different gate-dielectric materials. The device simulation results in DIBL for $k = 25$, i.e., HfO_2 ~ 35.56 mV/V (for $k = 3.9$, i.e., SiO_2 ~ 97.23 mV/V), subthreshold swing (SS) for HfO_2 ~ 0.056 V/decade (for SiO_2 ~ 0.080 V/decade). The presented research work helps to evaluate the ON capacitance of the device, which is appropriate for guiding the improved switching of CSDG MOSFET.

Keywords MOSFET · Double-gate MOSFET · Cylindrical oxide capacitance · Microelectronics · Nanotechnology · VLSI

S. K. Dargar (✉) · P. K. Panda
Department of Electronic Engineering, Kalasalingam Academy of Research and Education, Virudhunagar, Tamil Nadu, India
e-mail: drshashikant.dargar@ieee.org

J. K. Srivastava
Department of Electronic Engineering, RML Awadh University, Faizabad, Uttar Pradesh, India

S. Birla
Department of Electronic Engineering, Manipal University Jaipur, Jaipur, Rajasthan, India
e-mail: shilpi.birla@manipal.edu

© The Author(s), under exclusive license to Springer Nature Singapore Pte Ltd. 2022

A. Tripathi et al. (eds.), *Intelligent Computing Techniques for Smart Energy Systems*, Lecture Notes in Electrical Engineering 862,
https://doi.org/10.1007/978-981-19-0252-9_16

1 Introduction

The oxide capacitance of a MOSFET is an essential parameter on which the electrical characteristics primarily depend. Furthermore, in RF and high-frequency applications, the device capacitance highly influences the switching performance [1, 2]. The oxide layer capacitance is the principal constituent of the overall capacitance, and therefore, switching can be best controlled by optimizing oxide capacitances. However, Shockley [3] introduced the channel structure outside the gradual channel approximation [4]; the channel structure is not the same in pinch-off or saturation. So, the channels bring capacitance variation since the semiconductor channel serves as one of the device's electrodes of the capacitive system. Based on this fact, the cylindrical surrounding double-gate (CSDG) MOSFET has been an interesting RF switch [5–7], which can also be analyzed in saturation condition at which the channel does not follow uniformity. In its place, the channel proceeds in a conical shape that precisely describes the device's gate capacitance. The effect of the capacitance of an ON switch, i.e., saturation, is followed in this proposed work. In their previous research, the authors have discussed the origin and derived the mathematical analysis of oxide capacitance of the CSDG MOSFET structure. In this paper, the authors have done the numerical analysis of gate-oxide capacitance at the pinch-off condition in the CSDG MOSFET to present insulating material variation's effect on the device's performance.

The paper is organized as follows: Sect. 2 presents the CSDG capacitance structure of internal and external gate assembly. Section 3 describes the results of CSDG MOSFET performance with oxide material variation. Finally, Sect. 4 provides the conclusion and recommends future work.

2 CSDG Oxide Capacitance at Saturation

A cylindrical surrounding fouble-gate (CSDG) MOSFET structure is conceptualized from a rotational orientation of planar double-gate MOSFET [8]. However, due to the cylindrical shape, the analysis of the structure differs from a planar MOSFET. Figure 1 shows the sketch of the structural representation and the cross section of a typical CSDG MOSFET. The two cylindrical outer and inner metallic gates serve as the electrode surrounded by respective gate oxides of thickness (t_{ox}) forms oxide capacitances (C_{ox1} and C_{ox2}) in a CSDG MOSFET [9].

It is known that in a 2-dimensional view of a MOSFET device pinch-off, the channel presumes a shape of a triangular region, depleting the transfer of current that occurs when the drain to source bias increases above an overdrive voltage [10]. Similarly, CSDG has a conical depletion region at the device pinch-off condition due to its cylindrical shape. However, from the theory of depletion width analysis [11, 12], it is notable that past pinch-off, the CSDG structure channel adopts a shape of a truncated cone separately for inner and outer gate cylinder, as shown in Fig. 2.

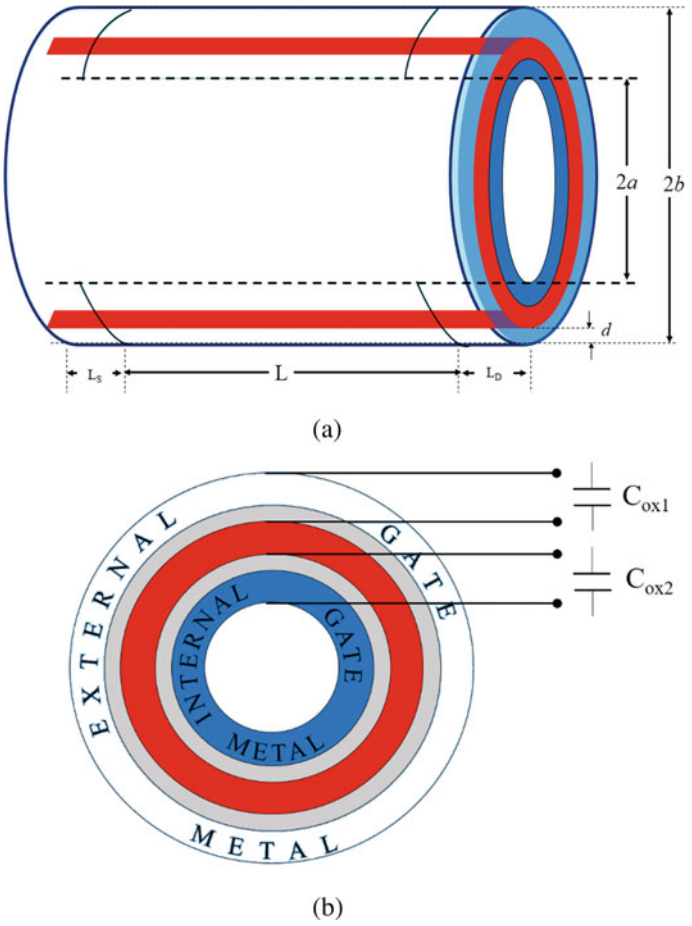

Fig. 1 **a** A typical CSDG structure and **b** cross section [9]

Therefore, instead of capacitance calculation using a cylindrical parallel plate, the capacitance of truncated conical shape should be used at pinch-off operation.

The oxide capacitive structure of the device, considering the internal gate of radius 'a' with an insulator thickness 't_{ox}', is shown in Fig. 2a. The figure depicts the truncated cone-shaped capacitive structure formed of semiconductor, oxide, and internal gate cylinder. Similarly, Fig. 2b shows the gate-oxide capacitor involving the external gate structure at the pinch-off condition that has radius 'b'. As the structure is hollow from the inner side, the cylindrical semiconductor channel forms residual truncated cone (RTC) shape [9, 12]. Hence, the oxide capacitance of the conical external assembly is the removal of the virtual truncated cone (VTC) capacitor from a cylindrical capacitor of radius 'b'. The resultant is the gate capacitance for the part at pinch-off. Now, if the external assembly's capacitive structure, as shown in Fig. 2 that having outer and inner radius of b and $a + t_{si} + t_{ox}$, respectively, the oxide

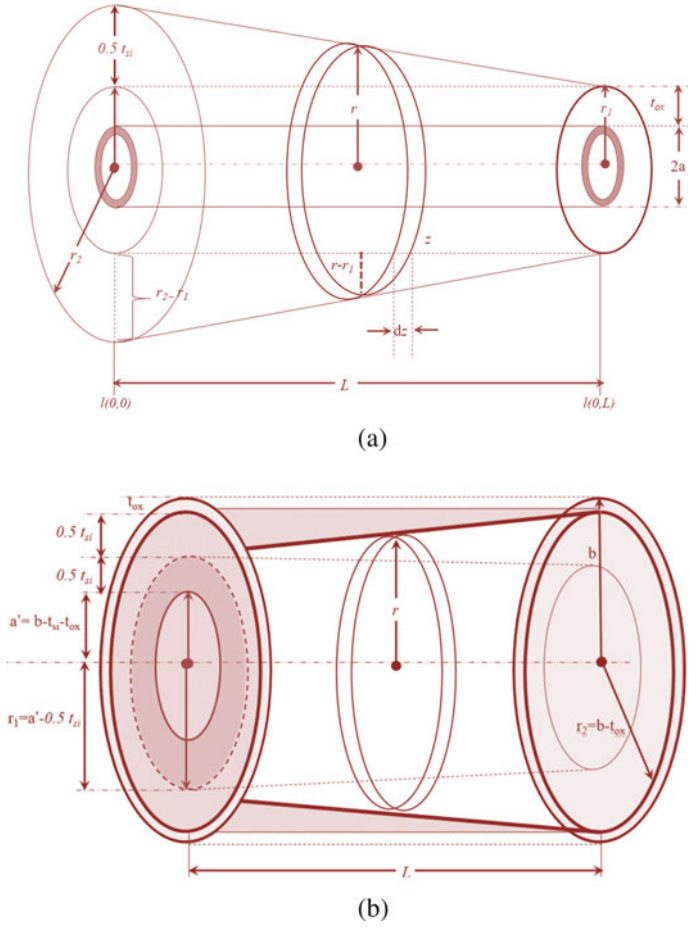

Fig. 2 Schematic of CSDG oxide capacitance structure at pinch-off: **a** internal gate assembly, **b** external gate

capacitance can be written as:

$$C_{\text{ox(ext)}} = C_{\text{RTC}} = C_{\text{exterior}} - C_{\text{VTC}} \tag{1}$$

C_{exterior} is $2\pi\varepsilon_o L/\ln(b/a + t_{\text{si}} + t_{\text{ox}})$, and C_{VTC} has been derived by the authors using the integration of annuli rings of the truncated cone structure in their previous work [9]. Considering the dielectric constant of the oxide material ε_{ox}, the overall oxide capacitance of CSDG MOSFET at a pinch-off condition would result in:

$$C_{\mathrm{ox}(CSDG)} = \frac{\frac{a\pi\varepsilon_{\mathrm{ox}}t_{\mathrm{si}}}{L.\ln\left\{\left(\frac{t_{\mathrm{ox}}+0.5t_{\mathrm{si}}}{2a+t_{\mathrm{ox}}+0.5t_{\mathrm{si}}}\right)\left(1+\frac{2a}{t_{\mathrm{ox}}}\right)\right\}}\left[\frac{2\pi\varepsilon_{\mathrm{ox}}L}{\ln\left(\frac{b}{a+t_{\mathrm{si}}}\right)} - \frac{\pi\varepsilon_{\mathrm{ox}}(b-t_{\mathrm{si}}-t_{\mathrm{ox}})t_{\mathrm{si}}}{L\ln\left(\frac{2b-1.5t_{\mathrm{si}}-2t_{\mathrm{ox}}}{b-0.5t_{\mathrm{si}}-t_{\mathrm{ox}}}\right)}\right]}{\frac{a\pi\varepsilon_{\mathrm{ox}}t_{\mathrm{si}}}{L.\ln\left\{\left(\frac{t_{\mathrm{ox}}+0.5t_{\mathrm{si}}}{2a+t_{\mathrm{ox}}+0.5t_{\mathrm{si}}}\right)\left(1+\frac{2a}{t_{\mathrm{ox}}}\right)\right\}} + \left[\frac{2\pi\varepsilon_{\mathrm{ox}}L}{\ln\left(\frac{b}{a+t_{\mathrm{ox}}}\right)} - \frac{\pi\varepsilon_{\mathrm{ox}}(b-t_{\mathrm{si}}-t_{\mathrm{ox}})t_{\mathrm{si}}}{L\ln\left(\frac{2b-1.5t_{\mathrm{si}}-2t_{\mathrm{ox}}}{b-0.5t_{\mathrm{si}}-t_{\mathrm{ox}}}\right)}\right]} \quad (2)$$

For a CSDG MOSFET structure, an ultra-thin MOS structure [11] is appropriately relevant. Consequently, the threshold voltage of the CSDG device, which accounts for the oxide capacitance of a CSDG structure, would result as:

$$V_{\mathrm{TH}} = 2\phi_f + \frac{qN_{\mathrm{sub}}\left(2\varepsilon_{\mathrm{si}}\varepsilon_0\left(2\phi_f\right)^{1/2}+1\right)}{C_{\mathrm{ox}(CSDG)}} + \left(\phi_m - (\chi + \frac{E_g}{2q} + \phi_f)\right) \quad (3)$$

where ϕ_m, χ, E_g, and ϕ_f are the metal work function, electron affinity for semiconductor, bandgap, and the Fermi potential, respectively. Now, using the charge sheet approximation method [13], the charge under source is $Q_s = -\left(\gamma q C_{\mathrm{ox}}/2k\mathrm{T}\phi_s^{1/2}\right)e^{(\phi_s-2\phi_B-V_{DB})k\mathrm{T}/\mathrm{q}}$, and accordingly, the subthreshold current for a CSDG MOSFET can be determined by:

$$I_{\mathrm{sub}} = \frac{W}{L}\mu\left(\frac{q}{k\mathrm{T}}\right)\left(\gamma q C_{\mathrm{ox(CSDG)}}/2k\mathrm{T}\sqrt{\phi_s}\right)\mathrm{e}^{(\phi_s-2\phi_B-V_{\mathrm{DS}})k\mathrm{T}/q}(1-\mathrm{e}^{-k\mathrm{T}V_{\mathrm{DS}}/q}) \quad (4)$$

The equation includes the internal and external capacitor structure of a CSDG MOSFET. The resulting capacitance depends upon the channel length (L), both the gate radii (a, b), the thickness of the semiconductor, and oxides (t_{si}, t_{ox}) of the device. The given relation assumes free space as a gate dielectric of the capacitor assembly with dielectric constant ε_o. In the typical CSDG MOSFET operation, the type of dielectric material affects the overall results. Therefore, we have used the various values of the gate oxide to evaluate the effect of the device performance.

3 Results and Comparison

The device characteristics and transconductance have been computed each time using the electronic simulator, with various oxide materials $\varepsilon_{\mathrm{ox}}$, $k = 3.9$ (SiO_2), $k = 7$ (Si_3N_4), $k = 9$ (Al_2O_3), $k = 22$ (Ta_2O_5), and $k = 25$ (HfO_2) at VD = 0.5 V and 1 V. The mathematical relations established in the saturation region of the device have been considered. The authors have drawn the electrical characteristics and the different parameters that describe device performances from the simulation run to compare performance.

3.1 Extraction of Threshold Voltage

The threshold is an essential value to turn a transistor into saturation. Therefore, it is desirable to have a low $V_{\text{th,}}$ which means switching at low voltage. Threshold voltage can be attained from the region $V_D \geq V_g - V_{\text{th}}$. The threshold voltage is determined by extrapolating graphically in a $\sqrt{I\,D}$ versus gate bias relation of the device.

3.2 Extraction of Subthreshold Swing (SS)

Another critical parameter defines the amount of gate bias required for diminution of drain current (I_D) to 0. It is given by $\mathrm{d}V_G/d\log I_D$. The value of SS should be as minimum as possible to obtain a high ON–OFF current ratio for switching. At low SS, a slight gate voltage variation can lead to radical fall of the drain current values by decades. Conversely, the subthreshold is also an operational region in which the device current increases exponentially from a pA OFF current to a high μA ON current. Therefore, the SS defines the current incremental rate beneath the device threshold for the applied gate bias [11, 14].

3.3 Extraction of Drain-Induced Barrier Lowering (DIBL)

The DIBL value in an ultra-scaled MOS device [14, 15] can be given by:

$$\frac{V_T|V_{\text{DS=0.1V}} - V_T|V_{\text{DS=0.5V}}}{0.5 - 0.1} \tag{5}$$

The results of the extracted parameters for the device with various gate-oxide materials have been obtained. The effect on performance parameters for the transconductance, the subthreshold swing (SS), and the drain-induced barrier lowering (DIBL) resulting from variation in gate-oxide materials is shown in Figs. 3, 4, and 5, respectively.

The transconductance plot of the device for various gate insulators is shown in Fig. 3. At the low gate voltage, the charge densities do not affect the conductance significantly; therefore, almost similar values of the device transconductance have been observed. However, further, increasing gate bias increases carrier charge density. A higher the value of dielectric constant k of insulator, the lager is the transconductance; nevertheless, the linearity at increasing gate bias has not been followed in the behavior.

The calculated parameters of threshold voltage and SS from the device characteristics at different gate-oxide materials are listed in Table 1. The device HfO_2 as the gate insulator results in the lowest V_{th} of 0.49 V and 0.43 V for drain voltage values

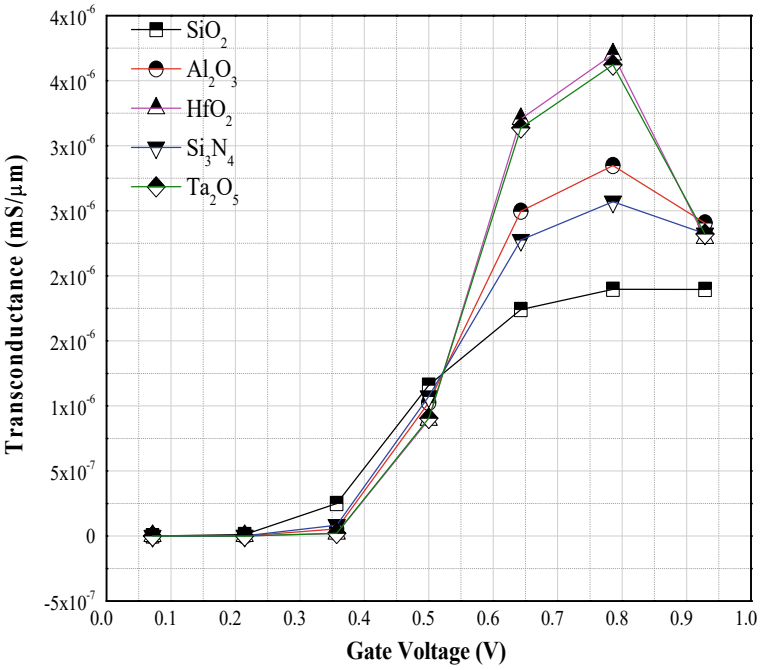

Fig. 3 Transconductance versus gate voltage characteristics for various oxide material

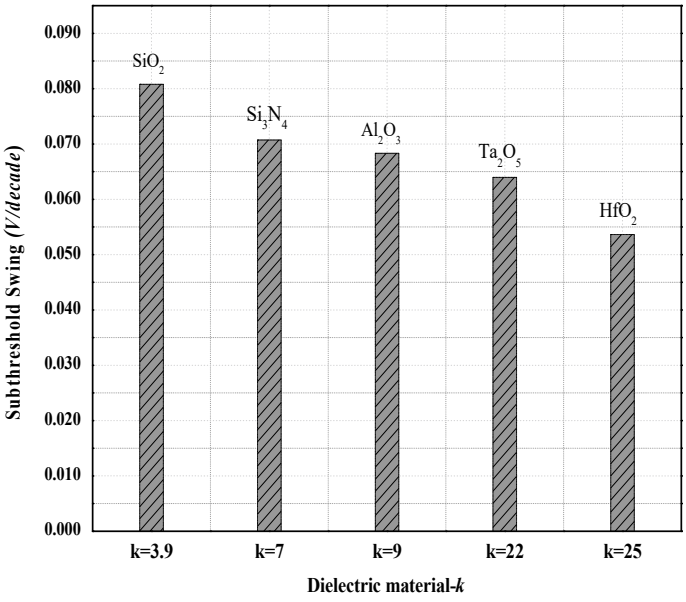

Fig. 4 Subthreshold swing of the simulated device at different oxide materials

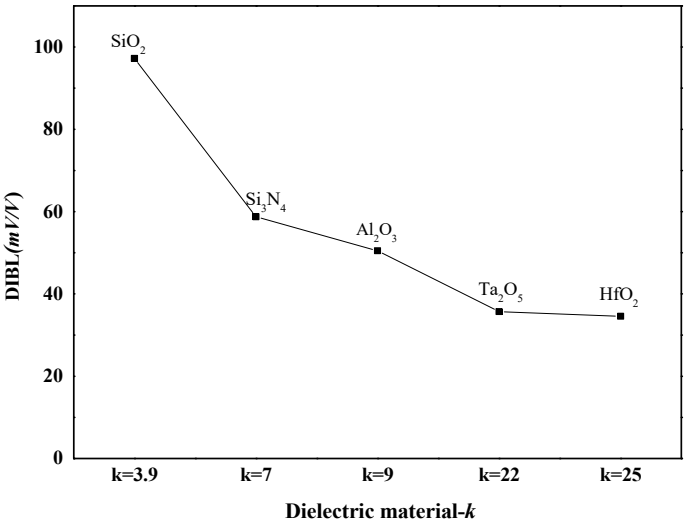

Fig. 5 Drain-induced barrier lowering (DIBL) at different oxide materials

Table 1 Parameters at different gate insulators

Oxide material	Threshold voltage at V_D 0.5 V	Threshold voltage at V_D 1 V	Subthreshold swing (V/decade)
SiO_2	0.60	0.51	0.080
Si_3N_4	0.63	0.54	0.077
Al_2O_3	0.58	0.55	0.067
Ta_2O_5	0.52	0.46	0.063
HfO_2	0.49	0.43	0.056

of 0.5 V and 1 V, respectively. The obtained value of SS is also represented in Fig. 4, which depicts that, based on the material's dielectric constant, desirable low SS can be achieved for faster switching applications [16].

It has been observed that the high-k gate-oxide material results in a comparatively larger drain current. The device structure with similar dimensions and gate-oxide thickness using SiO_2 material is inadequate to reduce leakage current due to direct electron tunneling, while alternative high-k materials can lessen the subthreshold swing. Figure 5 shows the comparison of the DIBL parameter at different high-k gate-oxide materials. For the case of HfO_2 and Ta_2O_5 gate dielectric of CSDG, the DIBL values are pretty close and comparable, yet the device SS is 16.03% larger for Ta_2O_5 than with a HfO_2. Therefore, HfO_2 could be preferable for device switching with steeper SS oscillation.

4 Conclusion and Future Aspects

The analysis in this work with various gate-oxide materials shows the effect of the gate insulator on the device's characteristics, and the switching behavior of the device can be improved using different dielectric materials at increasing k values. The basis of this analysis is a distinct form of the oxide capacitance at the pinch-off in the CSDG structure. The device simulation results in DIBL for $k = 25$, i.e., HfO_2 ~ 35.56 mV/V (for $k = 3.9$, i.e., SiO_2 ~ 97.23 mV/V), subthreshold swing (SS) for HfO_2 ~ 0.056 V/decade (for SiO_2 ~ 0.080 V/decade). The equivalent insulator thickness reduces in the case of high-k materials due to increased permittivity. Therefore, channel isolation effect is more influential in the high-k gate dielectrics of the device.

Similarly, a low DIBL is obtainable with the high-k material as the effective insulator thicknesses affect. In conclusion, device characteristics can be improved using an appropriate choice of a high-k dielectric gate insulator for suitable logic and switching circuits. Furthermore, several applications of CSDG MOSFETs have been reported, such as high frequency for high speed, data transmission, antenna, sensor networks, and RF circuits [17, 18] based on the switching phenomenon. Therefore, the analysis presented in this work is very significant in deeper understanding the oxide capacitance in a CSDG MOSFET to incorporate in the future applications. Moreover, the effect of oxide capacitance in saturation can be compared with the one obtained from the traditional cylindrical capacitor theory to distinguish the impact as future work.

References

1. Dargar SK, Srivastava VM (2019) Design and analysis of IGZO thin film transistor for AMOLED pixel circuit using double-gate tri active layer channel. Heliyon. 5(4):e01452. https://doi.org/10.1016/j.heliyon.2019.e01452
2. Srivastava VM, Singh G (2014) MOSFET technologies for a double-pole-four-throw radio-frequency switch, 1st edn. Springer, Switzerland
3. Sze SM (ed) (1991) Semiconductor devices: pioneering papers. World Scientific, Singapore
4. Taur Y, Lin HH (2018) Modeling of DG MOSFET I-V characteristics in the saturation region. IEEE Trans Electron Devices 65(5):1714–1720. https://doi.org/10.1109/TED.2018.2818943
5. Srivastava VM, Yadav KS, Singh G (2011) Design and performance analysis of double-gate MOSFET over single-gate MOSFET for RF switch. Microelectron J 42(3):527–534
6. Jung H (2020) SPICE model of drain induced barrier lowering in sub-10 nm junctionless cylindrical surrounding gate MOSFET. Int J Electr Comput Eng. 10(2):2088–8708. https://doi.org/10.11591/ijece.v10i2.pp1288-1295
7. Maduagwu UA, Srivastava VM (2019) Analytical performance of the threshold voltage and subthreshold swing of CSDG MOSFET. J Low Power Electron Appl 9(1):10. https://doi.org/10.3390/jlpea9010010
8. Sedra AS, Smith KC (2016) Microelectronic circuits. Oxford University Press
9. Dargar A, Srivastava VM (2019) Capacitive model of CSDG MOSFET at pinch-off for switching characteristics. In: Proceedings of 2019 international conference on computing, communication and networking technologies. https://doi.org/10.1109/ICCCNT45670.2019.8944904

10. Tsividis Y, McAndrew C (2011) Operation and modeling of the MOS transistor, 3rd edn. Oxford University Press, New York
11. Li Q (2011) A threshold voltage modeling for ultra-deep sub-micron MOSFETs. In: Proceedings of international conference on electronics and optoelectronics, Dalian, pp 468–471. https://doi.org/10.1109/ICEOE.2011.6015566
12. Dargar A, Srivastava VM (2020) Thickness modeling of short-channel cylindrical surrounding double-gate MOSFET at strong inversion using depletion depth analysis. Micro and Nanosystems 12(1):319–325. https://doi.org/10.2174/1876402912666200831175936
13. Sze SM, Li Y, Ng KK (2021) Physics of semiconductor devices. Wiley
14. Kumar PP, Malik MM, Gupta TK (2018) Reliable high-yield CNTFET-based 9T SRAM operating near threshold voltage region. J Comput Electron 17(2):774–783. https://doi.org/10.1007/s10825-017-1127-z
15. Dargar SK, Srivastava VM (2019) Analysis of short channel effects in multiple-gate (n, 0) carbon nanotube FETs. J Eng Sci Technol 14(6):3282–3293
16. Dargar SK, Srivastava VM (2019) Performance analysis of high-k dielectric based silicon nanowire gate-all-around tunneling FET. Int J Electr Electron Eng Telecommun
17. Kang L, Onishi K, Jeon Y, Lee BH, Kang C, Qi WJ, Lee JC (2000) MOSFET devices with polysilicon on single-layer HfO/sub 2/high-K dielectrics. In: International electron devices meeting 2000. Technical Digest. IEDM, Dec 2000, pp 35–38
18. Sharma A, Jain A, Pratap Y, Gupta RS (2016) Effect of high-k and vacuum dielectrics as gate stack on a junctionless cylindrical surrounding gate (JL-CSG) MOSFET. Solid-State Electron 123:26–32. https://doi.org/10.1016/j.sse.2016.05.016

Solution of Fractional Kinetic Equations by using Generalized Galue Type Struve Function

Garima Agarwal and Jayati Agnihotri

Abstract Subject of this paper is to compute the more generalized solution of fractional kinetic equations in terms of generalized Galue type Struve function. To solve this equation, the author used the Laplace transform. Some special cases are also discussed which shows that the concluded results are more accurate.

Keywords Fractional kinetic equations · Struve function · Gauss hypergeometric functions · Generalized Galue type Struve function · Thermonuclear reactions

Mathematics Subject Classification (2010) 26A33 · 33C20 · 35A22

1 Introduction

1.1 Fractional Kinetic Equations

There are two major types of nuclear reactions: one is nuclear fission in which nucleus splits into two or more smaller nuclei, and another one is nuclear fusion in which two or more smaller nuclei are combined to form one big nucleus. Energy involved in these reactions produces various forms of radiations. Such fusion reactions are also called thermonuclear reactions because of huge amount of heat energy involved. Energy produced in these reactions is so high that these reactions cannot be controlled. Stars keep on shining for trillion of years because of these reactions. All the reactions in the sun is due to these thermonuclear reactions. According to astronomer's model, sun is a hot ball of boiling gases with assumed thermal equilibrium and its chemical composition are non-uniform throughout its area. On the other

G. Agarwal · J. Agnihotri (✉)
Department of Department of Mathematics and Statistics School of Basic Sciences, Manipal University Jaipur, Jaipur, India
e-mail: jayati.202505028@muj.manipal.edu

G. Agarwal
e-mail: garima.agarwal@jaipur.manipal.edu

© The Author(s), under exclusive license to Springer Nature Singapore Pte Ltd. 2022

A. Tripathi et al. (eds.), *Intelligent Computing Techniques for Smart Energy Systems*, Lecture Notes in Electrical Engineering 862,
https://doi.org/10.1007/978-981-19-0252-9_17

hand, star can be defined by basic characteristic like brightness, colour, surface temperature, size and mass. The star structures and their models are studied on the basis of these characteristics and more information regarding state equation and lack of transparency. These models explain varying of pressure, luminous intensity and mass from centre of sun. Thermal equilibrium and hydrostatic equilibrium assumptions show that there is no time dependency of mathematical equations in mathematical model which explains about interior structure of stars. For further details, we suggest references [6, 9, 16]. Applied science, such as viscoelasticity, electrochemistry, signal processing and neuron model in biology [1, 5, 7, 8, 10, 12, 17], has wide use of fractional calculus. According to recent survey, real-life situations can be better handled by fractional-order differential equations solution. Many papers have shown solution of generalized fractional kinetic equation with involvement of special functions. Generalized fractional kinetic equation with involvement of generalized Bessel's function of first kind is given by Kumar et.al. [11] and generalized Struve function of first kind is given by Nisar et.al. [13]. Random reaction is shown by time-dependent quantity $N = N(t)$, and then it is easy to calculate rate of change by following equation:

$$dN/dt = -a + f \tag{1}$$

where a and f are destruction and production rate of N, respectively.
Eq. 1 can be written as

$$dN_i/dt = -aN_t + fN_t \tag{2}$$

where the function $N_t$is explained by $N_t(t^*) = N(t - t^*), t^* > 0$

$$dN_i/dt = -c_i N_i(t) \tag{3}$$

with the initial condition $N_i(t = 0) = n_0$ is the number species at time t=0 is given by [10]:

$$N_i(t) = N_0 e^{-c_i t} \tag{4}$$

or

$$N(t) - N_0 = c_0 {D_t}^{-1} N(t) \tag{5}$$

1.2 Struve Functions

Generalized Bessel function of order p is defined as [11]

$$ {}_aJ_p(x) = \sum_{k=0}^{\infty} \frac{(-1)^k}{\Gamma(ak+p+1)k!} \left(\frac{x}{2}\right)^{2k+p}, x \in R, a \in N = 1, 2, 3, \ldots \quad (6) $$

Galue type generalized modified Bessel function is defined as [9]

$$ {}_aI_p(x) = \sum_{k=0}^{\infty} \frac{(1)}{\Gamma(ak+p+1)k!} \left(\frac{x}{2}\right)^{2k+p}, x \in R, a \in N \quad (7) $$

Struve function of order ω is given by

$$ H_{\omega}(x) = \sum_{k=0}^{\infty} \frac{(-1)^k}{\Gamma(k+\frac{3}{2})\Gamma(k+\omega+\frac{3}{2})} \left(\frac{x}{2}\right)^{2k+\omega+1} \quad (8) $$

it is the particular solution of non-homogeneous Bessel differential equation

$$ x^2 y^{"}(x) + xy'(x) + (x^2 + p^2)y(x) = \frac{4\left(\frac{x}{2}\right)^{p+1}}{\sqrt{\pi}\Gamma(p+\frac{1}{2})} $$

where Γ is the classical gamma function whose Euler integral is given by

$$ \Gamma(z) = \int_o^{\infty} e^{-t} t^{z-1} dt, Re(z) > 0 $$

Remark 1 Struve function and its more generalization are defined as follows: [2–4, 11, 14, 15, 18–22]

(i) $H_{\omega}^{\psi}(t) = \sum_{n=0}^{\infty} \frac{(-1)^n \left(\frac{t}{2}\right)^{2n+\omega+1}}{\Gamma(\psi n+\omega+\frac{3}{2})\Gamma(n+\frac{3}{2})}, \psi > 0$

(ii) $H_{\omega}^{\psi,\mu}(t) = \sum_{n=0}^{\infty} \frac{(-1)^n \left(\frac{t}{2}\right)^{2n+\omega+1}}{\Gamma(\psi n+\omega+\frac{3}{2})\Gamma(\mu n+\frac{3}{2})}, \psi > 0, \mu > 0$

(iii) $H_{\omega,\phi}^{\psi}(t) = \sum_{n=0}^{\infty} \frac{(-1)^n \left(\frac{t}{2}\right)^{2n+\omega+1}}{\Gamma(\psi k+\frac{\omega}{\phi}+\frac{3}{2})\Gamma(n+\frac{3}{2})}, \psi > 0, \phi > 0$

(iv) $H_{\omega,\phi}^{\psi,\mu}(t) = \sum_{n=0}^{\infty} \frac{(-1)^n}{\Gamma(\mu n+\phi)\Gamma(\psi n+\omega+\frac{3}{2})} \left(\frac{t}{2}\right)^{2n+\omega+1}, \omega, \psi \in C$

(v) $H_{\omega,\phi,\rho}(t) = \sum_{n=0}^{\infty} \frac{(-\rho)^n \left(\frac{t}{2}\right)^{2n+\omega+1}}{\Gamma(n+\frac{3}{2})\Gamma(n+\omega+\frac{\phi}{2}+1)}, \omega, \psi, \rho \in C$

where $\omega > 0$, $\mu > 0$, and ϕ is an arbitrary constant.

Also **generalized Galue type Struve function** is defined as [9]

$$ {}_aW_{\omega,\phi,\rho,\chi}^{\psi,\mu}(t) = \sum_{n=0}^{\infty} \frac{(-\rho)^n}{\Gamma(\psi n+\mu)\Gamma(\psi n+\frac{\omega}{\chi}+\frac{\phi+2}{2})} \left(\frac{t}{2}\right)^{2n+\omega+1}, a \in N, \omega, \phi, \rho \in C \quad (9) $$

1.3 Main Result

Theorem 1 *If $a \in C, \omega, \phi, \rho \in C$, where $\phi > 0, \chi > 0$, and μ is an arbitrary parameter, then solution of kinetic equation*

$$N(t) - N_0 \left[{}_a W^{\psi,\mu}_{\omega,\phi,\rho,\chi}(t) \right] = -\delta^{\nu}{}_0 D_{\tau}{}^{-\nu} N(t) \tag{10}$$

where $\left[{}_a W^{\psi,\mu}_{\omega,\phi,\rho,\chi}(t) \right]$ is defined by equation 9 and $\delta^{\nu}{}_0 D_{\tau}{}^{-\nu} N(t)$ is Riemann–Liouville integral operator holds for

$$N(t) = N_0 \left[{}_a W^{\psi,\mu}_{\omega,\phi,\rho,\chi}(t) \sum_{r=0}^{\infty} (-1)^r \frac{t^{\nu r}}{(2n+\omega+1)_{\nu r}} \right] \tag{11}$$

Proof By substituting value of ${}_a W^{\psi,\mu}_{\omega,\phi,\rho,\chi}(t)$ by Eq. 9 in Eq. 10

$$N(t) + \delta^{\nu}{}_0 D_{\tau}{}^{-\nu} N(t) = N_0 \left[\sum_{n=0}^{\infty} \frac{(-\rho)^n}{\Gamma(\psi n + \mu)\Gamma(\psi n + \frac{\omega}{\chi} + \frac{\phi+2}{2})} \left(\frac{t}{2} \right)^{2n+\omega+1} \right]$$

$$N(t) + \delta^{\nu}{}_0 D_{\tau}{}^{-\nu} N(t) = N_0 \left[\sum_{n=0}^{\infty} \frac{(-\rho)^n}{\Gamma(\psi n + \mu)\Gamma(\psi n + \frac{\omega}{\chi} + \frac{\phi+2}{2})} \frac{(t)^{2n+\omega+1}}{(2)^{2n+\omega+1}} \right] \tag{12}$$

by taking Laplace transform on both sides of Eq. 12

$$N(s) + \delta^{\nu}{}_0 D_{\tau}{}^{-\nu} N(s) = N_0 \left[\sum_{n=0}^{\infty} \frac{(-\rho)^n}{\Gamma(\psi n + \mu)\Gamma(\psi n + \frac{\omega}{\chi} + \frac{\phi+2}{2})} \frac{L[(t)^{2n+\omega+1}]}{(2)^{2n+\omega+1}} \right]$$

$$N(s) + [1 + \delta^{\nu}{}_0 D_{\tau}{}^{-\nu}]$$
$$= N_0 \left[\sum_{n=0}^{\infty} \frac{(-\rho)^n}{\Gamma(\psi n + \mu)\Gamma(\psi n + \frac{\omega}{\chi} + \frac{\phi+2}{2})(2)^{2n+\omega+1}} \frac{\Gamma(2n+\omega+1}{S^{2n+\omega+1}} \right]$$

$$N(s) \left[1 + \left(\frac{s}{\delta} \right)^{\nu} \right] = N_0 \left[\sum_{n=0}^{\infty} \frac{(-\rho)^n \Gamma(2n+\omega+1) S^{-2n+\omega+1}}{\Gamma(\psi n + \mu)\Gamma(\psi n + \frac{\omega}{\chi} + \frac{\phi+2}{2})(2)^{2n+\omega+1}} \right]$$

$$N(s) = N_0 \sum_{n=0}^{\infty} \frac{(-\rho)^n \Gamma(2n+\omega+1) S^{-2n+\omega+1}}{\Gamma(\psi n + \mu)\Gamma(\psi n + \frac{\omega}{\chi} + \frac{\phi+2}{2})(2)^{2n+\omega+1}} \sum_{r=0}^{\infty} \left[- \left(\frac{s}{\delta} \right)^{-\nu r} \right] \tag{13}$$

Now on taking inverse Laplace transform of equation13

$$N(t) = N_0 \left[\sum_{n=0}^{\infty} \frac{(-\rho)^n \Gamma(2n+\omega+1)}{\Gamma(\psi n+\mu)\Gamma(\psi n+\frac{\omega}{\chi}+\frac{\phi+2}{2})2^{2n+\omega+1}} L^{-1} \right.$$
$$\left. \sum_{n=0}^{\infty} (-1)^r \delta^{\nu r} s^{2n+\omega+2+\nu r} \right]$$

$$N(t) = N_0 \left[\sum_{n=0}^{\infty} \frac{(-\rho)^n \Gamma(2n+\omega+1)}{\Gamma(\psi n+\mu)\Gamma(\psi n+\frac{\omega}{\chi}+\frac{\phi+2}{2})2^{2n+\omega+1}} L^{-1} \right.$$
$$\left. \sum_{n=0}^{\infty} (-1)^r \delta^{\nu r} \frac{t^{2n+\omega+2+\nu r}}{\Gamma(2n+\omega+1+\nu r)} \right]$$

$$N(t) = N_0 \left[{}_a W^{\psi,\mu}_{\omega,\phi,\rho,\chi} \sum_{n=0}^{\infty} (-1)^r \frac{t^{\nu r}}{(2n+\omega+1)_{\nu r}} \right]$$

Hence, the theorem is completely proved.

Theorem 2 *If $a \in C, \omega, \phi, \rho \in C$, where $\phi > 0, \chi > 0, d \neq \delta$, and μ is an arbitrary parameter, then solution of kinetic equation*

$$N(t) - N_0 \left[{}_a W^{\psi,\mu}_{\omega,\phi,\rho,\chi} (d^\nu t^\nu) \right] = -{\delta^\nu}_0 D_\tau{}^{-\nu} N(t) \tag{14}$$

where $\left[{}_a W^{\psi,\mu}_{\omega,\phi,\rho,\chi}(t) \right]$ is defined by Eq. 9 and ${\delta^\nu}_0 D_\tau{}^{-\nu} N(t)$ is Riemann–Liouville Integral Operator holds for

$$N(t) = N_0 \left[{}_a W^{\psi,\mu}_{\omega,\phi,\rho,\chi}(t) \sum_{r=0}^{\infty} (-1)^r \frac{\delta^{\nu r} t^{\nu r}}{(2n+\omega+1)_{\nu r}} \right] \tag{15}$$

Proof By substituting value of $\left[{}_a W^{\psi,\mu}_{\omega,\phi,\rho,\chi}(t) \right]$ by Eq. 9 in Eq. 14

$$N(t) + {\delta^\nu}_0 D_\tau{}^{-\nu} N(t) = N_0 \left[\sum_{n=0}^{\infty} \frac{(-\rho)^n}{\Gamma(\psi n+\mu)\Gamma(\psi n+\frac{\omega}{\chi}+\frac{\phi+2}{2})} \left(\frac{d^\nu t^\nu}{2} \right)^{2n+\omega+1} \right]$$

$$N(t) + {\delta^\nu}_0 D_\tau{}^{-\nu} N(t) = N_0 \left[\sum_{n=0}^{\infty} \frac{(-\rho)^n}{\Gamma(\psi n+\mu)\Gamma(\psi n+\frac{\omega}{\chi}+\frac{\phi+2}{2})} \frac{(d^\nu t^\nu)^{2n+\omega+1}}{(2)^{\nu(2n+\omega+1)}} \right]$$

$$N(t) + \delta^{\nu}{}_0D_\tau{}^{-\nu}N(t) = N_0\left[\sum_{n=0}^{\infty}\frac{(-\rho)^n}{\Gamma(\psi n+\mu)\Gamma(\psi n+\frac{\omega}{\chi}+\frac{\phi+2}{2})}\frac{(d^{\nu}t^{\nu})^{2n+\omega+1}}{(2)^{\nu(2n+\omega+1)}}\right] \tag{16}$$

Now on taking Laplace transform on both sides of Eq. 16

$$N(s) + \delta^{\nu}{}_0D_\tau{}^{-\nu}N(s) = N_0\left[\sum_{n=0}^{\infty}\frac{(-\rho)^n}{\Gamma(\psi n+\mu)\Gamma(\psi n+\frac{\omega}{\chi}+\frac{\phi+2}{2})}\frac{L(d^{\nu}t^{\nu})^{2n+\omega+1}}{(2)^{\nu(2n+\omega+1)}}\right]$$

$$N(s) + [1 + \delta^{\nu}{}_0D_\tau{}^{-\nu}]$$
$$= N_0\left[\sum_{n=0}^{\infty}\frac{(-\rho)^n(d^{\nu})^{2n+\omega+1}}{\Gamma(\psi n+\mu)\Gamma(\psi n+\frac{\omega}{\chi}+\frac{\phi+2}{2})(2)^{\nu(2n+\omega+1)}}\frac{\Gamma\nu(2n+\omega+1)}{S^{\nu(2n+\omega+1)}}\right]$$

$$N(s)\left[1+\left(\frac{s}{\delta}\right)^{\nu}\right] = N_0\left[\sum_{n=0}^{\infty}\frac{(-\rho)^n\Gamma\nu(2n+\omega+1)S^{\nu(-2n+\omega+1)}}{\Gamma(\psi n+\mu)\Gamma(\psi n+\frac{\omega}{\chi}+\frac{\phi+2}{2})(2)^{\nu(2n+\omega+1)}}\right]$$

$$N(s) = N_0\sum_{n=0}^{\infty}\frac{(-\rho)^n\Gamma\nu(2n+\omega+1)S^{-\nu(2n+\omega+1)}}{\Gamma(\psi n+\mu)\Gamma(\psi n+\frac{\omega}{\chi}+\frac{\phi+2}{2})(2)^{\nu(2n+\omega+1)}}\sum_{r=0}^{\infty}\left[-\left(\frac{s}{\delta}\right)^{-\nu r}\right] \tag{17}$$

now on taking inverse Laplace transform on both sides of Eq. 17

$$N(t) = N_0\left[\sum_{n=0}^{\infty}\frac{(-\rho)^n(d^{\nu})^{2n+\omega+1}\Gamma\nu(2n+\omega+1)}{\Gamma(\psi n+\mu)\Gamma(\psi n+\frac{\omega}{\chi}+\frac{\phi+2}{2})2^{\nu(2n+\omega+1)}}L^{-1}\right.$$
$$\left.\sum_{n=0}^{\infty}(-1)^r\delta^{-\nu r}s^{-\nu(2n+\omega+2+\nu r)}\right]$$

$$N(t) = N_0\left[\sum_{n=0}^{\infty}\frac{(-\rho)^n(d^{\nu})^{2n+\omega+1}\Gamma\nu(2n+\omega+1)}{\Gamma(\psi n+\mu)\Gamma(\psi n+\frac{\omega}{\chi}+\frac{\phi+2}{2})(2)^{\nu(2n+\omega+1)}}\right.$$
$$\left.\sum_{n=0}^{\infty}(-1)^r\delta^{\nu r}\frac{t^{\nu(2n+\omega+2+\nu r)}}{\Gamma\nu(2n+\omega+1+\nu r)}\right]$$

$$N(t) = N_0\left[\sum_{n=0}^{\infty}\frac{(-\rho)^n(d^{\nu})^{2n+\omega+1}}{\Gamma(\psi n+\mu)\Gamma(\psi n+\frac{\omega}{\chi}+\frac{\phi+2}{2})(2)^{\nu(2n+\omega+1)}}\right.$$
$$\left.\sum_{n=0}^{\infty}(-1)^r\frac{t^{\nu(2n+\omega+2+\nu r)}}{\Gamma\nu(2n+\omega+1+\nu r)_{\nu r}}\right]$$

$$N(t) = N_0 \left[{}_aW^{\psi,\mu}_{\omega,\phi,\rho,\chi}(d^\nu t^\nu) \sum_{n=0}^{\infty} (-1)^r \frac{t^{\nu r} \delta^{\nu r}}{(2n+\omega+1)_{\nu r}} \right]$$

Hence, the theorem is completely proved.

Theorem 3 *If $a \in C, \omega, \phi, \rho \in C$, where $\phi > 0, \chi > 0, d \neq \delta$, and μ is an arbitrary parameter, then solution of kinetic equation*

$$N(t) - N_0 \left[{}_aW^{\psi,\mu}_{\omega,\phi,\rho,\chi}(d^\nu t^\nu) \right] = -d^\nu {}_0D_\tau{}^{-\nu} N(t) \tag{18}$$

where $\left[{}_aW^{\psi,\mu}_{\omega,\phi,\rho,\chi}(t) \right]$ is defined by Eq. 9 and $\delta^\nu {}_0D_\tau{}^{-\nu} N(t)$ is Riemann–Liouville Integral Operator holds for

$$N(t) = N_0 \left[{}_aW^{\psi,\mu}_{\omega,\phi,\rho,\chi}(d^\nu t^\nu) \sum_{r=0}^{\infty} (-1)^r \frac{d^{\nu r} t^{\nu r}}{(2n+\omega+1)_{\nu r}} \right] \tag{19}$$

Proof By substituting value of $\left[{}_aW^{\psi,\mu}_{\omega,\phi,\rho,\chi}(t) \right]$ by Eq. 9 in Eq. 18

$$N(t) + d^\nu {}_0D_\tau{}^{-\nu} N(t) = N_0 \left[\sum_{n=0}^{\infty} \frac{(-\rho)^n}{\Gamma(\psi n + \mu)\Gamma(\psi n + \frac{\omega}{\chi} + \frac{\phi+2}{2})} \left(\frac{d^\nu t^\nu}{2} \right)^{2n+\omega+1} \right]$$

$$N(t) + d^\nu {}_0D_\tau{}^{-\nu} N(t) = N_0 \left[\sum_{n=0}^{\infty} \frac{(-\rho)^n}{\Gamma(\psi n + \mu)\Gamma(\psi n + \frac{\omega}{\chi} + \frac{\phi+2}{2})} \frac{(d^\nu t^\nu)^{2n+\omega+1}}{(2)^{\nu(2n+\omega+1)}} \right] \tag{20}$$

Now on taking Laplace transform on both sides of Eq. 20

$$N(s) + d^\nu {}_0D_\tau{}^{-\nu} N(s) = N_0 \left[\sum_{n=0}^{\infty} \frac{(-\rho)^n}{\Gamma(\psi n + \mu)\Gamma(\psi n + \frac{\omega}{\chi} + \frac{\phi+2}{2})} \frac{L(d^\nu t^\nu)^{2n+\omega+1}}{(2)^{\nu(2n+\omega+1)}} \right]$$

$$N(s) + [1 + d^\nu {}_0D_\tau{}^{-\nu}]$$
$$= N_0 \left[\sum_{n=0}^{\infty} \frac{(-\rho)^n (d^\nu)^{2n+\omega+1}}{\Gamma(\psi n + \mu)\Gamma(\psi n + \frac{\omega}{\chi} + \frac{\phi+2}{2})(2)^{\nu(2n+\omega+1)}} \frac{\Gamma\nu(2n+\omega+1)}{S^{\nu(2n+\omega+1)}} \right]$$

$$N(s) \left[1 + \left(\frac{s}{d} \right)^\nu \right] = N_0 \left[\sum_{n=0}^{\infty} \frac{(-\rho)^n \Gamma\nu(2n+\omega+1) S^{-\nu(-2n+\omega+1)}}{\Gamma(\psi n + \mu)\Gamma(\psi n + \frac{\omega}{\chi} + \frac{\phi+2}{2})(2)^{\nu(2n+\omega+1)}} \right]$$

$$N(s) = N_0 \sum_{n=0}^{\infty} \frac{(-\rho)^n \Gamma\nu(2n+\omega+1) S^{-\nu(2n+\omega+1)}}{\Gamma(\psi n + \mu)\Gamma(\psi n + \frac{\omega}{\chi} + \frac{\phi+2}{2})(2)^{\nu(2n+\omega+1)}} \sum_{r=0}^{\infty} \left[- \left(\frac{s}{d} \right)^{-\nu r} \right] \tag{21}$$

now on taking inverse Laplace transform on both sides of Eq. 21

$$N(t) = N_0 \left[\sum_{n=0}^{\infty} \frac{(-\rho)^n (d^{\nu})^{2n+\omega+1} \Gamma\nu(2n+\omega+1)}{\Gamma(\psi n+\mu)\Gamma(\psi n+\frac{\omega}{\chi}+\frac{\phi+2}{2}) 2^{\nu(2n+\omega+1)}} L^{-1} \right.$$
$$\left. \sum_{n=0}^{\infty} (-1)^r d^{-\nu r} s^{-\nu(2n+\omega+2+\nu r)} \right]$$

$$N(t) = N_0 \left[\sum_{n=0}^{\infty} \frac{(-\rho)^n (d^{\nu})^{2n+\omega+1} \Gamma\nu(2n+\omega+1)}{\Gamma(\psi n+\mu)\Gamma(\psi n+\frac{\omega}{\chi}+\frac{\phi+2}{2})(2)^{\nu(2n+\omega+1)}} \right.$$
$$\left. \sum_{n=0}^{\infty} (-1)^r d^{\nu r} \frac{t^{\nu(2n+\omega+2+\nu r)}}{\Gamma\nu(2n+\omega+1+\nu r)} \right]$$

$$N(t) = N_0 \left[\sum_{n=0}^{\infty} \frac{(-\rho)^n (d^{\nu r})^{2n+\omega+1}}{\Gamma(\psi n+\mu)\Gamma(\psi n+\frac{\omega}{\chi}+\frac{\phi+2}{2})(2)^{\nu(2n+\omega+1)}} \right.$$
$$\left. \sum_{n=0}^{\infty} (-1)^r \frac{t^{\nu(2n+\omega+2+\nu r)}}{\Gamma\nu(2n+\omega+1+\nu r)_{\nu r}} \right]$$

$$N(t) = N_0 \left[{}_a W^{\psi,\mu}_{\omega,\phi,\rho,\chi}(d^{\nu} t^{\nu}) \sum_{n=0}^{\infty} (-1)^r \frac{(dt)^{\nu r}}{(2n+\omega+1)_{\nu r}} \right]$$

Hence, the theorem is completely proved.

2 Conclusion

In view of the effectiveness and a great importance of fractional kinetic equation in various fields of applied sciences and engineering as well, a significant amount of research in this area has been carried out so far. The theorem established in the present paper contains solution to a generalized form of fractional kinetic equations involving generalized Galue type Struve function by application of Laplace transform. On account of being general in nature, our main findings under suitable parametric constraints yield numerous known and new results in terms of simple functions which may prove to be very useful in applications to various fields of science and technology.

Conflict of Interest Authors declare that there is no conflict of interests.

References

1. Adjabi Y, Jarad F, Baleanu D et al (2016) On Cauchy problems with Caputo Hadamard fractional derivative. J Comput Anal Appl 21(4):661–681
2. Baleanu D, Moghaddam M, Mohammadi H et al (2016) Afractional derivative inclusion problem via an integral boundary condition. J Comput Anal Appl 21(3):504–514
3. Bariz A (2010) Generalized bessels function of first kind, lecture notes in mathematics 1994. Springer, Berlin
4. Bhowmick KN (1962) Some relation between generalized struve function and hypergeometric functions. Vijana Parishad Anusandhan Patrika 5:93–99
5. Bhowmick KN (1963) A generalized struve function and its recurrence formula. Vijana Parishad Anusandhan Patrika 6:1–11
6. Chaurasia VBL, Kumar D (2010) On the solution of generalized fractional kinetic equation. Adv Stud Theor Phy 4:773–780
7. Galue L (2003) A generalized bessels functions int transform spec function 14:395–401
8. Humbert P, Agarwal RP (1953) Sur la fonction de Mittag- Leffleretquelquesunes de ses generalization. Bull Sci Math SerII 77:180–185
9. Kanth BN (1981) Integrals involving generalized struve function. Nepali Math Sci Rep 6:61–64
10. Kilbas AA, Srivastava HM, Trujilo JJ (2006) Theory and application of fractional differential equation. North-Holland Mathematics Studies, Elsevier, Amsterdam, p 204
11. Kumar D, Purohit SD, Secer A, Atangana A (2015) On generalized fractional kinetic equations involving generalized Bessel function of the first kind. Math Probl Eng. https://doi.org/10.1155/2015/289387
12. Mittag-Leffler GM (1905) Sur la representation analytique d' unefonctionmonogene (cinquieme note). Acta Math 29 (1):101–181. https://doi.org/10.1007/BFO2403200
13. Nisar KS, Baleanu D, Qurashi MM (2016) Fractional Calculus and application of generalized Struv function. Springer Plus, pp 1–13
14. Orhan H, Yagmur N (2013) Starlikeness and convexity of generalized Struve functions. AbstrAppl Anal
15. Orhan H, Yagmur N (2014) Geometric properties of generalized Struve functions. Ann Alexandru loan CuzaUniv-Math, 2478/aicu-2014-0007
16. Perdang J (1976) Lecturer notes in stellar stability parts I and II. Institutodiastronomia, Padova
17. Prabhakar TR (1971) A singular integral equation with generalized Mittag-Leffler function in the kernel. Yokohama Math J 19:7–15
18. Salim TO, Faraj AW (2012) A generalization of Mittag-Leffler function and integral operator associated with integral calculus. J Fract Appl 3(5):1–13
19. Singh RP (1974) Generalized Struve's function and its recurrence relation. Ranchi Univ Math J 5:65–67
20. Singh RP (1985) Generalized Struve's function and its recurrence equation. Vijnana Parishad Anusandhan Patrika 28:287–292
21. Singh RP (1988) Some integral representation of generalized Struve's function. Math Ed Siwan 22:91–94
22. Singh RP (1988) On definite integral involving generalized Struve's function. Math Ed Siwan 22:62–66

Current Status of Renewable Energy Sources in India and Its Utilization in Hybrid Energy System

Sunny Vaish, Naveen Kumar Sharma, and Gagandeep Kaur

Abstract The utilization of Renewable Energy Sources (RESs) is the best solution to overcome the bad impacts obtained from conventional power plants in the environment. RES has potential to generate enough power to support modern power sector and simultaneously reduces the greenhouse gases. India is a country that rich in RES. The current status of RES in India is presented in this paper. RESs like solar and wind energy relies on weather condition. They are intermittent in nature and varied throughout the whole year. Due to this, a single RES connected system are not more stable. A hybrid renewable energy source system is capable to efficiently utilizing and extracting the maximum possible power from the available RES in the environment. A collaboration of two or more RESs join to form hybrid renewable energy source (HRES) system. Various configuration of HRES system based on selection of type of bus is discussed in this paper. This type of system supports the power system and cost-effective operation. Some upcoming Wind-Solar Park projects which can contribute to the targets of RES programme in a country are also mentioned.

Keywords Renewable energy sources · Hybrid renewable energy sources · Configuration of HRES

1 Introduction

The population of world increased day by day which responsible for rapidly growing in demand of electricity. The generation of electricity is necessary to enhancing the living status of human beings and economy of any country [1]. The deficiency of energy is arising due to larger rate of consumption of energy around the world. The generation of power through conventional energy sources are now become more costly and incapable to serve the load demand effectively due to shortage of fossil fuels. The conventional energy sources (fossil fuels) are limited and also imperfectly disseminated on the earth. The excessive usage of fossil fuels (for example gas, oil,

S. Vaish (✉) · N. K. Sharma · G. Kaur
I. K. Gujral Punjab Technical University, Jalandhar, Punjab, India
e-mail: sunnyvaish3@gmail.com

© The Author(s), under exclusive license to Springer Nature Singapore Pte Ltd. 2022

A. Tripathi et al. (eds.), *Intelligent Computing Techniques for Smart Energy Systems*,
Lecture Notes in Electrical Engineering 862,
https://doi.org/10.1007/978-981-19-0252-9_18

coal) to generate power causes its depletion. This process continuously increases the bad impacts on the atmosphere which responsible for the rising of CO_2 levels that causes the global warming. Hence, this is very crucial to usage of Renewable Energy Sources (RES) to overcome these types of issues in the environment [2]. The RESs are sustainable resources that includes various sources such as solar energy, wind energy, biomass, geothermal energy and hydro, generated by nature. The potential of RES can be defined by changeability and availability of sources in the nature. The energy generated by solar and wind is utmost effective solution for issues raised through conventional fuels to generate power [2, 3]. The significance role of RESs in the markets of electricity and economy in the world [3]. The introduction of RESs delivers emission free power generation and reduces CO_2 levels. But RESs are dependent on environmental conditions and intermittent in nature. The maximize utilization and extraction of power from RES system can be achieved by hybrid renewable energy sources (HRES) system and Energy Storage System (ESS). The amalgamation system of HRES (solar photovoltaics, wind turbines, diesel engine system) and ESS (battery storage system) can minimize the cost of power [4]. The HRES system can be a promising solution of utilization of erratic nature of RES in the environment [5]. The utilization of ESS with HRES system in power system is more beneficiary than the single RES system. The sizing of HRES system for photovoltaic-based Micro grid (MG) by design space approach [6]. The ESS play key role in the Hybrid Energy System (HES). The reason behind is that the integration of ESS in the power generation sector provides surplus power in peak demand period at low cost and help to extract the maximum power from the RES system connected with it [7].

This paper consists of four sections. The first section presents the overall introduction and second section presents the current scenario of RES. A utilization of RES in hybrid renewable energy source (HRES) system explain in third section. The last fourth section presents the conclusion of the paper.

2 Current Scenario of Renewable Energy Source

According to International Energy Agency (IEA), the estimation of increment in demand of renewable energy is near about 1% from 2019 as compared to other energy resources. The delays in construction and supply chain arisen through pandemic of COVID-19 but still renewable electricity generation raises by approximately 5%. The annual growth (in percentage) for renewable electricity generation by source is shown in Fig. 1.

The RES system provides 30% of electricity around the world. The hydro power generation system is reached more than half of all RES power generation which is near about 60%. The speed of addition of RES could reduce in 2020 because of disturbances and constructions caused by shortage of labour [8]. It is expected that 60% of all RES capacity addition can be obtained from SPV in 2025 and wind

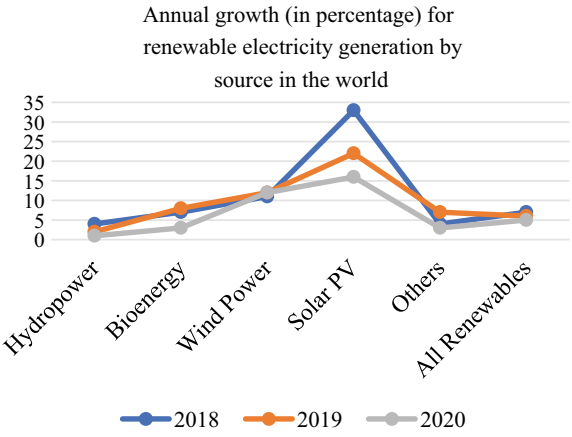

Fig. 1 Annual growth (in percentage) for renewable electricity generation by source in the world, 2018–2020 [8]

supports near about another 30%. RES would become a largest source of electricity generation and left behind the electricity generation from the coal by the 2025 [9].

2.1 Installed Capacity of India

The ranked of India in electricity consumption is reached at 3rd position in the world [10]. Figure 2 shows the total installed capacity in India (As on 30/04/2021). India is a country which has secured the position of third largest consumer and producer of electricity in the world [11]. According to Central Electricity Authority (CEA), the total installed capacity of India is about 382,730 MW. Thermal (coal, lignite, gas, diesel), nuclear, hydro and renewable energy sources are the main contributor in the total installed capacity of India [12].

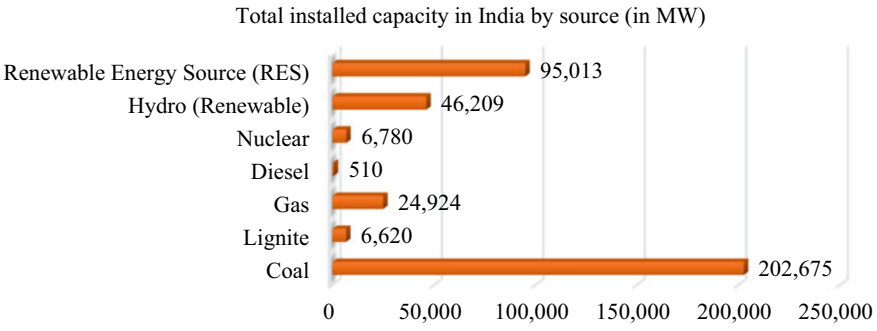

Fig. 2 Total installed capacity in India by source (as on 30/04/2021) [12]

India has got 3rd rank in power production and consumption, but it also contributes to the harmful gases in the environment. The coal is the main source of energy which contribute near about 53% of total installed capacity. The generation of power from coal is more than 50% in India. The RES contributes near about 36% of total power installed capacity in India [12].

2.2 Status of Renewable Energy Source in India

India is a one of the countries which generate large amount of power from renewable energy sources. The Table 1 presents the status of installed capacity of grid integrated renewable energy sources in India. The India has ranked 4th largest renewable power capacity around the world. It is near about the 136 GW which contribute 36% of total capacity of renewable energy in India and increasing continuously [13]. The total grid integrated RES power is approximately 94,433.79 MW in India [14].

The potential of solar renewable energy is the highest amongst the various RES in the country. The ground mounted and roof top solar power is near about 35,645 MW and 4439 MW, respectively. India has 250 to 300 clear sunny days in some states. The annual solar irradiance varies from 2200 to 1600 kWh/m^2.

The waste to energy and Solar Photovoltaic (SPV) are contribute to off-grid RES in India. The power contribution of waste to energy and SPV is approximately 218 MW and 1149 MW, respectively. The total contribution is 1368 MW in off-grid RES [14]. The set target of other RES technologies is 0.60 (in lakh) in which 0.11 is achieved in April–March 2021. The total contribution of other RES technologies is 51.65 (in lakh). There are some off-grid RES system or devices which also contribute to the

Table 1 Status of installed capacity of grid integrated renewable energy sources in India (in MW) [14]

Renewable energy source (RES)	Target (in MW)	Achievements (April–March 2021) (in MW)	Cumulative achievements (as on 31.03.2021) (in MW)
Wind power	3000.00	1503.30	39,247.05
Solar power—ground mounted	9000.00	3533.14	35,645.63
Solar power—roof top	2000.00	1924.44	4439.74
Small hydro power	100.00	103.64	4786.81
Biomass (bagasse, cogeneration)	200.00	173.37	9373.87
Biomass (non-bagasse, cogeneration)	50.00	97.24	772.05
Waste to power	30.00	21.00	168.64
Total	14,380.00	7356.13	94,433.79

Table 2 Status of off-grid renewable energy sources in India (in MW) [14]

Renewable energy source (RES)	Target (in MW)	Achievements (April–March 2021)	Cumulative achievements (as on 31.03.2021)
Waste to energy	10.00	20.76	218.95
SPV systems	500.00	171.11	1149.49
Total	**510.00**	191.87	**1368.44**

RES in India. The total number of SPV Street Lighting System (SLS), Home Lighting System (HLS), Solar Lanterns (SL), pumps are 830,373, 1,723,479, 7,948,219 and 286,830 installed, respectively. There are 218.95 MW waste to energy and 216,407.67 kWp (kiloWatt peak) power plants are also contribute to RES system India [15]. The status of off-grid renewable energy sources in India is depicted in Table 2.

India power system has capable to enhanced the power quality, access of continuous electricity at urban, rural and remote areas and fulfil power demand through its RES system. From the last 5.5 years, the installed solar capacity is increased around 2.6 GW to more than 34 GW. The country has also launched the world's largest RES expansion programme of 175 GW till 2022. India got globally 5th position for overall installation of RES capacity.

2.3 Upcoming Hybrid Renewable Energy Sources in India

India is country that blessed with enormous amount of RES such as solar energy and wind energy. They both RES can utilize as the alternative energy source to the conventional source of energy to accomplish the requirement of energy in the country. The potential of solar power and wind power of the country is 749 and 695 GW (at 120 m above from ground level), respectively. The National Institute of Wind Energy (NIWE) recognizes the best possible sites for the development of the wind/wind-solar hybrid power projects. The sites or location for project selected on the basis of availability of wind RES and adequate suitable land for wind power plants. If the site or location has found to be suitable for solar power plant also, the authority can consider to developing the Wind-Solar Power Park [16].

The introduction of Wind-Solar Power Park in the country has several benefits. These types of projects help to finish the target of 175 GW RES programme, support to transmission and distribution systems and also help to reduce the CO_2 emissions, etc. There are some planned locations for development of Wind Parks/ Wind-Solar Hybrid Park in India depicted in Table 3 [16].

Table 3 Planned locations for development of Wind Parks/ Wind-Solar Hybrid Park in India [16]

State	District	Area (km^2) available	Average wind speed (m/s)	Average wind power density (W/m^2)	Installable potential (MW) (assuming 5 MW/km^2)
Tamil Nadu	Tirunelveli	68	7.326	572.730	340
	Tuticorin	169	6.998	305.284	845
	Coimbatore and partially Palakkad (Kerala)	351	8.588	558.989	1755
	Tiruchirappalli and Perambalur	547	7.093	444.8000	2735
Andhra Pradesh	Tumakuru and Anantapur	1055	7.307	334.628	5275
Karnataka	Chitradurga and Davangere	640	7.132	369.945	3200
	Bellary and Davangere	924	7.139	335.037	4620
	Chitrdurga	269	7.153	309.581	1345
	Chitrdurga and Davangere	380	7.194	335.889	1900
Gujarat	Junagadh and Porbandar	2900	7.017	385.530	14,500
	Kutch	771	7.329	337.750	3855
	Kutch	680	7.510	371.885	3400
	Kutch	590	7.434	372.130	2950
	Kutch	308	7.297	358.508	1540
Rajasthan	Barmer	265	6.50	289.84	1325
	Barmer	109	6.52	286.69	545
Madhya Pradesh	West Nimar	220	6.91	400.90	1100
Telangana	Ranga Reddy	346	7.14	299.65	1730
	Ranga Reddy	197	6.61	268.43	985
	Total (MW)				53,945

3 Utilization of RES in Hybrid Renewable Energy Source (HRES) System

3.1 Hybrid Renewable Energy Source (HRES)

The RES such as solar energy and wind energy are natural resources which provides emission free environment but depends on environmental conditions. The power generation from solar and wind energy system depends upon the availability of intensity and irradiance level of sunlight and high cut-in wind speed, respectively. They are not uniformly distributed and not constant at every place. A Fig. 3 depicts the typical hybrid renewable energy source system. The system which consists of non-renewable energy source and two or more renewable energy source known as HRES systems [17]. Due to this, HRES system are now becoming more popular for power

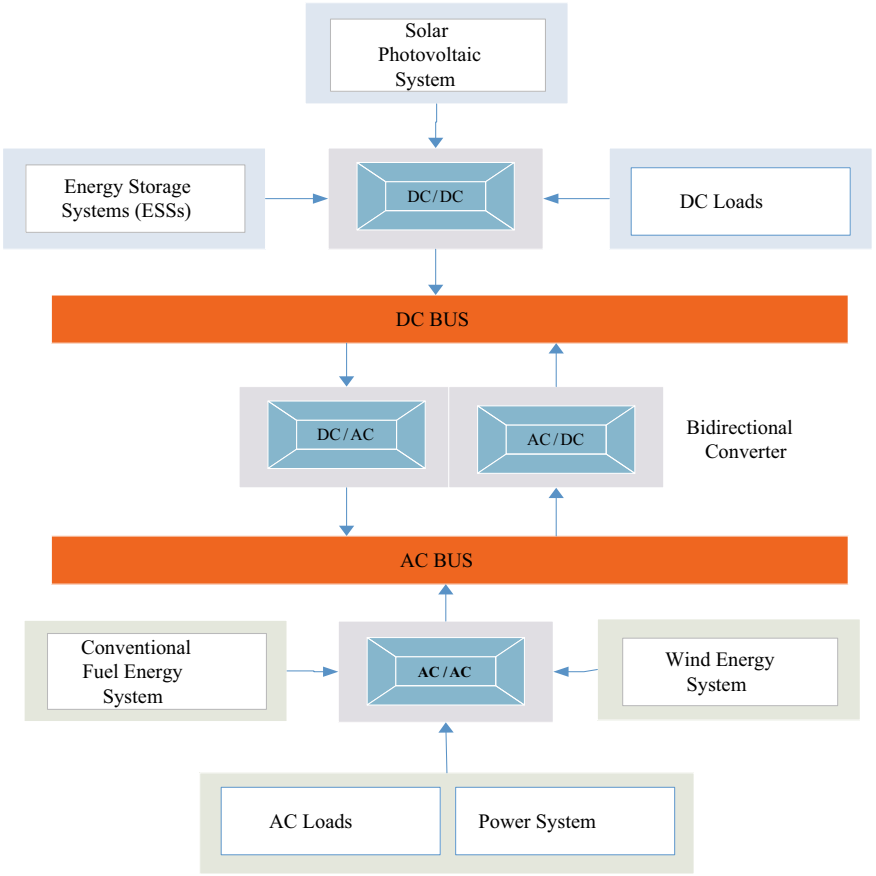

Fig. 3 A typical hybrid renewable energy source system [3]

generation at modern power sector as well as remote areas where access of centralized power is difficult. A study of current status and features of 19 software [18]. For hybrid energy system, a study of optimum sizing, management of energy, strategy for operation and controlling, various RES integration [3]. The issues of perfect sizing of hybrid energy system to supply sufficient energy to accomplish the necessities of loads and minimizing the investment and operational cost [19]. HRES system can operate off-grid mode (stand-alone) and on-grid mode (grid connected). The off-grid HRES system has lower cost and higher flexibility that of Solar Photovoltaic (SPV) or wind energy system. The utmost common HRES system constitute from SPV, wind, storage system (batteries) and SPV, (non-RES) diesel, storage system (batteries). The simulation and optimization of off-grid HRES system [20]. The ESS plays a crucial role in the stand-alone as well as grid tied HRES system. They store energy during the availability of solar energy and wind energy and delivers this stored energy when a useful work is to be carried out in the future. The RES system suffered from intermittency due to the variation in availability of sources.

This intermittency can be diminished from the HRES system through development of the energy management strategies. A review of energy management techniques in HRES systems [21].

3.2 Configuration of Hybrid Energy System with RES

Selection of Common-Bus Type—In the hybrid energy system, a various RES and non-RES, ESS, AC/DC loads and grid is connected with the DC or AC bus depending on the type of bus configuration is to be selected (AC/DC bus type) [22].

3.2.1 AC Common-Bus Type [22, 23]

AC common-bus type is a configuration in hybrid energy system which consists of various RES and non-RES, ESS, AC/DC loads and grid connected with common AC bus. All the power generating units are connected to AC bus through the power converters. The power delivered to AC bus by the sources. AC common-bus type system is more flexible than DC common-bus system because it can supply power directly to the grid as well as their consumers (AC loads). This type of system more advantageous for AC loads type consumers. Figure 4 presented the AC common-bus type configuration of HRES.

3.2.2 DC Common-Bus Type [22, 23]

DC common-bus type is a configuration in hybrid energy system which consists of various RES and non-RES.

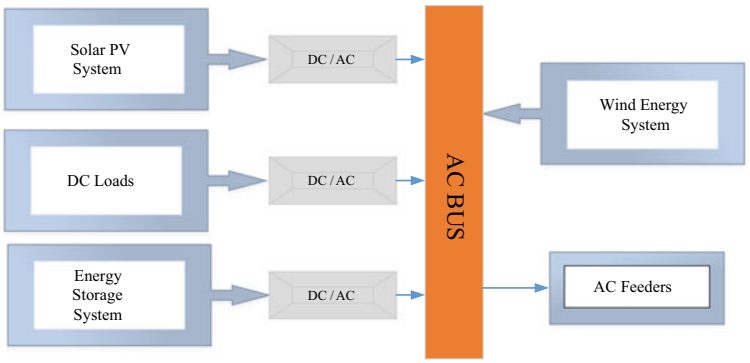

Fig. 4 AC common-bus type configuration of HRES [3]

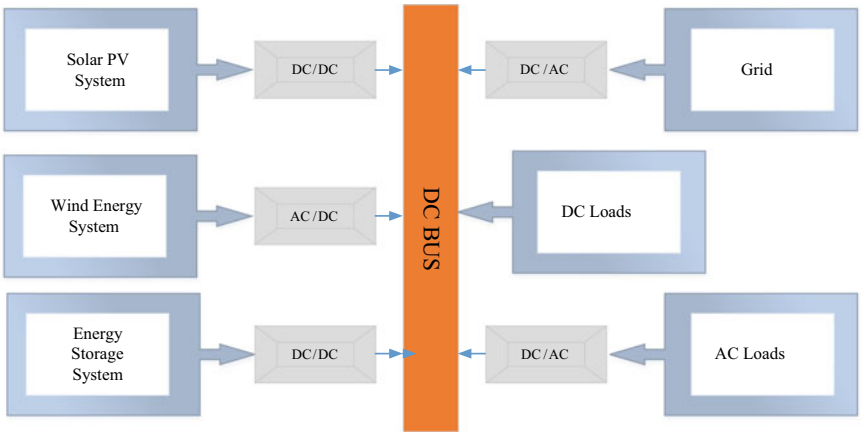

Fig. 5 DC common-bus type configuration of HRES [3, 22]

ESS, AC/DC loads and grid connected with common DC bus. A DC common-bus type configuration of HRES depicted in Fig. 5. The all-crucial power generator units are integrated with DC common-bus. The AC power generators have to first rectify their power by the power converters and then connected with the DC bus system. There is requirement of inverter to supply the power to utility grid and AC.

3.2.3 Hybrid AC-DC Type [22, 23]

Hybrid AC-DC type is a configuration in hybrid energy system which consists of various RES and non-RES, ESS, AC/DC loads and grid connected with common DC bus as well as common AC bus. A Fig. 6 shows hybrid AC-DC type configuration of HRES. The hybrid AC-DC type configuration better than both AC common-bus and

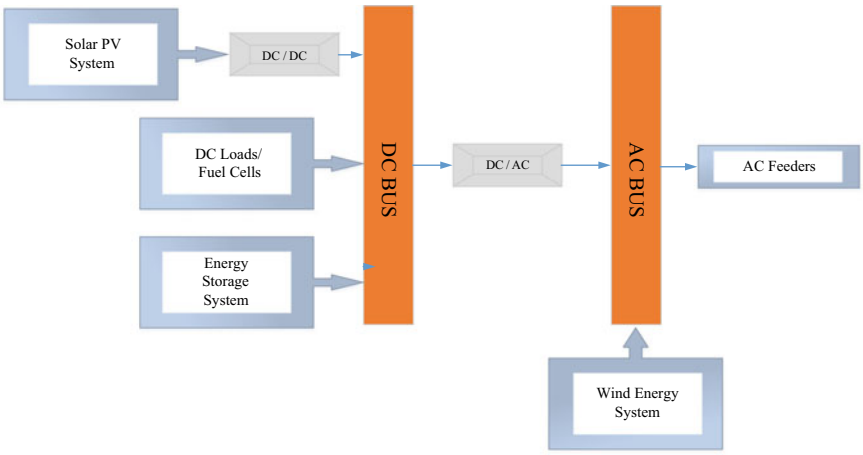

Fig. 6 Hybrid AC-DC type configuration of HRES [22]

DC common-bus type configuration because it has both the features of aforementioned configurations. In this type of configurations, RES and non-RES can directly supply a power to the AC loads consumer and increase system performance. The converter connected between the AC bus and DC bus can be replaced by bidirectional converters. The bidirectional converter can supply surplus power in the peak demand period.

The entry of various types of technologies of RES and storage system has lower costs which delivers power to the small communities. The investigation of modelling tools of HRES to create the emergent prospects that include social indicators to optimize systems in small communities [24]. The introduction of volatile RES in HRES system is very difficult. To develop economically and technically practicable HRES configuration is very crucial for the system. The feasible sizing of a HRES and significance of selection of data with erratic RES [5]. Due to changeability and randomness property of one RES system (for example wind and solar RES) are mostly stand-alone systems. To design the HRES system more effective and reasonable, the sizing of every component should be known. The methodologies for sizing, current classification and various evaluation indicators [25].

3.3 Cost-Effective Operation of HRES

Hybrid renewable energy system provides optimal and performs cost-effective operation. This paper presents the various configuration of hybrid energy system connected with RES systems (Solar and Wind energy system). But these RESs depend upon environmental conditions. The energy produced by RESs is variable and highly weather dependent. Therefore, an ESS can be installed to storing charge (electric

power) when RESs are available and discharge when there is demand of power. The integration of solar and wind energy system (HRES) in conventional power system can reducing the excess usage of fossil fuels as well as help to reduce the problems arising from pollutions.

3.3.1 SPV System

RES, such as sun and wind energy have volatile behaviour. The dilemma of complications in integration of RES with power system can be avoided by introducing the HRES in which various energy sources (conventional or non-conventional) are interconnected. An algorithm for optimal sizing of HRES is proposed on the basis of selection of data of extremely inconstant RESs in [5]. The aim of design and installation of SPV system is to utilize it minimum of 20–30 years and its monitoring and controlling unit functioning long lasting. The SPV power system required less maintenance than any other type of power generation equipment in running. The necessary condition for optimal maintenance operation is [26]:

1. Cleanliness of module surface by removing dust particles, snow, soil, etc.
2. Controlling of growing of vegetation nearby modules.
3. Examination of wires and all electrical contacts.
4. Inspection of inverter operation carefully.
5. Check mechanical mounting system.
6. Replacing the cracked or broken component (e.g. panels or its frame, etc.).

The Levelized Cost of Energy (LCOE) method takes into account the investment cost, the operating cost and recycling costs and the total energy produced during the system service life. In a simplified form, the LCOE can be expressed as:

$$\mathrm{LCOE} = \frac{\mathrm{IC} + \sum_{k=1}^{n} \mathrm{OC}_k}{\sum_{k=1}^{n} \mathrm{EP}_k} \tag{1}$$

where the IC, OC_k, EP_k and n represents the cost of investment, operating costs (such as maintenance) in the specific year, the production of electrical energy in specific year and number of production year, respectively. The LCOE method is very useful to know the economics practicability of PV plan developments for comparing the other technologies of electricity generation [27].

3.3.2 Wind Energy System

Wind energy available at free of cost and relies on environmental condition. The cost of installation for the wind turbine can be governed by initial capital cost of wind turbines (towers and installation) which is equal to approximately 84% of total installation cost of wind plant. The higher installation cost is one of the key barriers

to their uptake. Once the wind power plant installed, there is no need to investment for fuels. The capital costs of wind power plant can be divided into the following major groups:

1. Costs of turbine costs—This cost includes the blades, tower and transformer.
2. Costs of civil work—This includes whole construction cost to for preparation of site and foundations for the towers.
3. Costs of grid connection—This consists of transformers, sub-stations, connections with the transmission networks and local distributions and
4. Other Capital Costs—This includes the construction of buildings, system for controlling, costs of project consultants, etc.

The main key cost components of for off-shore and on-shore wind power plants are project planning and development, wind turbines, installations, connection of grid and cabling and foundations. These key components also play a very crucial role for overall cost reduction of wind power plant installations [28]. The different materials (such as, copper, fibreglass and iron), workers, legal and financial costs contributed approximately 30% of the cost reduction of wind turbines prices over the period 2005–2017. The finding of gap of acquaintance by quantitatively inspecting the drivers behind the cost reductions of on-shore wind turbines from 2005 to 2017 [29]. The minimization of cost depends upon performance of wind turbines. The size of wind turbine installation can be estimated by not only statistics of wind at a specific site but as well as infrastructure of turbine and costs of maintenance. The analysis study of six different standard wind turbines (GE 1.5 SLE, Enercon E44, Enercon E53, FD21-100, EWT DW54 and Hummer H25.0–200 kW) for comparison on account of the cost of energy and performance [30].

The solar and wind energy are available at free of cost and can generate enough power without polluting environment. The introduction of these RESs in the power system can help to reduce the generating cost of power from fossil fuels. The capital cost of installation of wind and solar power plant is required at starting stage. Then there is no investment is required to buy fuel. Simultaneously utilization of HRES in power system is help to reduce the GHG emissions developed by fossils fuels. When grid is at peak demand stage, ESS connected HRESs can utilized to accomplish the power demand and help to stable the system as well as performs cost-effective operations. HRES are also utilized in the condition of power events such as power cuts, faults and also in the condition when supply of power from the grid end is very high.

4 Conclusion

The conventional power sector relies on the fossil fuels to generate the power. A large amount of power is generated from a coal in the entire world and also depend on oils for producing energy. A conventional fuel is the key source of greenhouse gases in the atmosphere. The flexibility and performance of conventional power system can

be enhanced by penetration of RES. The RES is sustainable energy sources that can supports the green environment and reduces the dependency on conventional fuels in modern power sector. But RESs are not available at all the time in adequate form. They are non-uniformly distributed on the atmosphere of earth. By using HRES system with energy storage system, a RES can utilize in better manner. India became a 3rd largest producer and consumer of electricity plays a key role in reducing the CO_2 levels in the world. India can contribute in the targets for initiatives to installed more RES systems and reducing CO_2 emissions in the world. A discussed HRES configuration based on the selection of type of bus are beneficial for optimal designing of system. A system become a cost-effective if significant configuration is to be selected. HRES system can support grid in peak demand and power outages/fault events and provide power at reasonable cost. They can also provide power to remote areas where access of centralized power is not possible.

References

1. Jing W, Lai CH, Wong WSH, Wong MLD (2018) A comprehensive study of battery: supercapacitor hybrid energy storage system for standalone PV power system in rural electrification. Appl Energy 224:340–356
2. Strielkowski W (2020) Chapter 4: Renewable energy sources, power markets, and smart grid. Social impacts of smart grids, pp 97–151
3. Krishna KS, Kumar KS (2015) A review on hybrid renewable energy systems. Renew Sustain Energy Rev 52:907–916
4. Dawoud SM (2021) Developing different hybrid renewable sources of residential loads as a reliable method to realize energy sustainability. Alex Eng J 60(2):2435–2445
5. Alberizzi JC, Frigola JM, Rossi M, Renzi M (2020) Optimal sizing of a hybrid renewable energy system: importance of data selection with highly variable renewable energy sources. Energy Convers Manage 223
6. Jacob AS, Banerjee R, Ghosh PC (2018) Sizing of hybrid energy storage system for a PV based microgrid through design space approach. Appl Energy 212:640–653
7. Abdi H, Mohammadi-Ivatloo B, Javadi S, Khodaei AR, Dehnavi E (2017) Chapter 7: Energy storage systems. In: Distributed generation systems, pp 333–368
8. Annual growth for renewable electricity generation by source, 2018–2020. International Energy Agency, Paris. Available at: https://www.iea.org/data-and-statistics/charts/annual-growth-for-renewable-electricity-generation-by-source-2018-(2020). Accessed on 07 July 2021
9. Bahar H (2020) Renewables 2020: Analysis and forecast to 2025. International Energy Agency. Available at: https://iea.blob.core.windows.net/assets/1a24f1fe-c971-4c25-964a-57d0f31eb97b/Renewables_2020-PDF.pdf
10. Tayal M (2021) India among top 10 power consuming countries globally. Available at: https://www.saurenergy.com/solar-energy-news/india-among-top-10-power-consuming-countries-globally. Accessed on 07 July 2021
11. Tripathi B (2021) Now, India is the third largest electricity producer ahead of Russia, Japan. Available at: https://www.business-standard.com/article/economy-policy/now-india-is-the-third-largest-electricity-producer-ahead-of-russia-japan-118032600086_1.html. Accessed on 07 July 2021
12. Total installed capacity: power sector at a glance All India. Available at - https://powermin.gov.in/en/content/power-sector-glance-all-india. Accessed on 07 July 2021
13. Koundal A (2021) India's renewable power capacity is the fourth largest in the world, says PM Modi. ETEnergy World. Available at: https://energy.economictimes.indiatimes.com/news/ren

ewable/indias-renewable-power-capacity-is-the-fourth-largest-in-the-world-says-pm-modi/79430910. Accessed on 07 July 2021
14. Physical Progress in 2020–21: Ministry of New and Renewable Energy (MNRE). Available at: https://mnre.gov.in/the-ministry/physical-progress. Accessed on 07 July 2021
15. State wise details of decentralized/off-grid renewable energy systems/devices 31.03.2021, Ministry of New and Renewable Energy (MNRE). Available at: https://mnre.gov.in/the-ministry/physical-progress. Accessed on 07 July 2021
16. Concept note on development of wind parks/wind-solar Hybrid Park. Ministry of new and renewable energy (MNRE). Available at: https://mnre.gov.in/img/documents/uploads/file_f-1605265655087.PDF
17. Deshmukh MK, Deshmukh SS (2008) Modelling of hybrid renewable energy systems. Renew Sustain Energy Rev 12(1):235–249
18. Sinha S, Chandel SS (2014) Review of software tools for hybrid renewable energy systems. Renew Sustain Energy Rev 32:192–205
19. Erdinc O, Uzunoglu M (2012) Optimum design of hybrid renewable energy systems: overview of different approaches. Renew Sustain Energy Rev 16(3):1412–1425
20. Bernal-Agustin JL, Dufo-Lopez R (2009) Simulation and optimization of stand-alone hybrid renewable energy systems. Renew Sustain Energy Rev 13(8):2111–2118
21. Olatomiwa L, Mekhilef S, Ismail MS, Moghavvemi M (2016) Energy management strategies in hybrid renewable energy systems: a review. Renew Sustain Energy Rev 62:821–835
22. Lawan SM, Abidin WAWZ (2020) A review of hybrid renewable energy systems based on wind and solar energy—modelling, design and optimization. Wind solar hybrid renewable energy system. Available at: https://doi.org/10.5772/intechopen.85838
23. Rekioua D (2020) Hybrid renewable energy systems. Optimization and power management control. Available at: https://www.springer.com/gp/book/9783030340209
24. Cuesta MA, Castillo-Calzadilla T, Borges CE (2020) A critical analysis on hybrid renewable energy modelling tools: an emerging opportunity to optimise systems in small communities. Renew Sustain Energy Rev 122
25. Lian J, Zhang Y, Ma C, Yang Y, Chaima E (2019) A review on recent sizing methodologies of hybrid renewable energy systems. Energy Convers Manage 199
26. Benda V (2020) 18: Photovoltaics, including new technologies (Thin Film) and a discussion on module efficiency. Future Energy 375–412
27. Branker K, Pathak MJM, Pearce JM (2011) A review of solar photovoltaic levelized cost of electricity. Renew Sustain Energy Rev 15(9):4470–4482
28. Gielen D (2012) Renewable energy technologies: cost analysis. Wind Power Int Renew Energy Agency (IRENA) 1(5). Available at: https://www.irena.org/-/media/Files/IRENA/Agency/Publication/2012/RE_Technologies_Cost_Analysis-WIND_POWER.pdf
29. Elia A, Taylor M, Gallachoir BO, Rogan F (2020) Wind turbine cost reduction: a detailed bottom–up analysis of innovation drivers. Energy Policy 147
30. Charabi Y, Abdul-Wahab S (2020) Wind turbine performance analysis for energy cost minimization. Renew Wind Water Solar 7(5)

Comparative Sentiment Analysis on Stock Market News Using Machine Learning

Devansh Sachar, Hemlata Goyal, and Vijay Kumar Sharma

Abstract The forecasting of the stock market values particularly the multi-national firms is a truly intriguing and thought provoking task. Sentiment Analysis instigates many companies to conduct market survey, competitive analysis and gain an edge in their respective industry along with expedite the process to understand the future trends of stock news data. In the context of sentiment analysis, top 25 economic news and reddit reviews are taken for sentiment analysis using natural language processing for this work. The dataset is taken downfallen stock range (2000–2008) and uplifting stock range (2009–2016), in two slots. We examine machine learning classifiers of Random Forest, Multi Binomial Naïve Bayes, Passive Aggressive and Linear Regression individually for training–testing with accuracy measures of the sentimental data. Sentimental data is extracted with the N-gram and TF-IDF vectorization to evaluate the sentiment accuracy in changing the stock of the particular period. On the basis of Performance Measures for Random Forest, Multi Binomial Naïve Bayes, Passive Aggressive and Linear Regression machine learning models, a very less considerable difference is measured. Among all the machine learning models, Random Forest classifier is selected as best classifier with 85.97% accuracy and ± 1.0 error in terms of the effect of emotional values with respect to stock market values by the performance matrices. The obtained performance accuracy of all the applied models is more than 83% in all.

Keywords Machine learning · Stock news · n-grams · Tf-idf · Natural language processing

D. Sachar · H. Goyal (✉) · V. K. Sharma
Department of Computer and Communication Engineering, School of Computing and Information Technology, Manipal University Jaipur, Jaipur, Rajasthan, India
e-mail: singhalhem@gmail.com

© The Author(s), under exclusive license to Springer Nature Singapore Pte Ltd. 2022

A. Tripathi et al. (eds.), *Intelligent Computing Techniques for Smart Energy Systems*, Lecture Notes in Electrical Engineering 862,
https://doi.org/10.1007/978-981-19-0252-9_19

1 Introduction

In the field of engineering as well as finance, stock news analysis is a challenging problem. The aim of this work is to develop a sentiment analysis prediction model on the basis of connecting words and assigning positive or negative sentiment accordingly.

The stock market plays one of the most centric roles in an economy. The financial industry is expanding its horizons toward finance and business analytics sectors to fully understand the stock market movement. In this work, primarily focus is given on the economic news after the infamous 2008 stock market crash to fully understand the correlation between sentiment analysis and stock movement. Our generation consumes news articles on a daily basis through many mediums primarily economic headlines of newspapers through different news apps. Therefore, the news headlines play a humongous role in changing consumer sentiment. The fact of the matter still remains that what is the extent of the impact of these headlines. We found that the impact is far greater than expectation. We will use sentiment analysis on these headlines to carry out satisfactory results. This approach will help users gain the maximum clarity whether to trust these headlines or not.

Sentiment evaluation has been the leading application to extract sentiment and determine the values from online platform. Subjectivity evaluation aims at dividing language devices into categories: objective and subjective, while sentiment evaluation tries to divide the language devices into categories; negative and positive [1, 2]. Sentiment evaluation is the procedure of figuring out people attitudes, opinions, evaluations, value determinations and feelings toward entities [3].

The headline of financial information is required for sentiment analysis. Text pre-processing [4, 5] is an intricate pillar in textual mining, NLP and gathering statistics. It is used for obtaining ready unstructured records for understanding extraction. These are just some of the things which can be done by text pre-processing. Tokens are small stream of words or units which are created by splitting text into words by the process of tokenization. Stop words are basically a set of common words which are used in any language. Stop-word-elimination is the procedure of removing the often repeated phrases that don't add any significant relevance to the data record. On removal of stop words, dataset size decreases and the time to train the model also decreases. Removing stop words can potentially help improve the performance as there are lesser and only meaningful tokens left. Stemming is the process of returning the variation of the word into common representation by removing suffixes [4].

The proposed model uses Random Forest, Multi Binomial Naïve Bayes, Passive Aggressive and Linear Regression machine learning models for training–testing-validation of sentimental stock news dataset.

This is achieved by selecting news articles about companies, world economies, financial reports and text analysis for handling unstructured message data. Sentiment analysis can help new age investors in maximizing profits, minimizing costs and risks and improving investors' understanding of the stock market, leading to accurate investment decisions.

2 Related Work

In recent times these have been a tremendous upsurge in field of sentiment analysis and financial technology which has instigated many researchers to carry out data driven results to improve accuracy of different models. Many studies aim at improving accuracy by using twitter dataset as well as prices from different stock exchanges such as S&P 500 and NSE. The accumulation of both has given satisfactory results [6].

In order to integrate word association and lexical resources for analyzing stock market news, various integrative text extraction approaches are used in analyzing sentiments for financial markets, focus on price prediction with different time frames [7] and increase the accuracy of the prediction [8, 9]. To deal with unstructured data, all of the above studies are challenging.

Text mining approaches are used to forecast the trend analysis of the stock values on the basis of text information versus closing prices and price chart [10].

Bing et al. [11] planned an algorithmic rule to predict stock worth movements with 76.12% accuracy to analyze the social media public information contained within the tweet dataset. NLP techniques are employed in conjunction with data-processing approaches to reveal relationship patterns between public sentiment and numerical stock prices. A model for predicting stock prices supported the mix of a self-organizing-map (SOM) and supporting-fuzzy-vector-machines (FSVM) was proposed. This contribution suggested the idea to extract the fuzzy rules by the mixing of applied mathematics models of Machine learning [12].

The perfect accumulation of sentiment analysis into machine learning approach implementing upon the basics of SVM which will help attain empirical results and affect the investor's decision and the companies risk factor [13].

Stock Twits accompanied with sentiment analysis for constructing an optimum model of stock price movement prediction. Basically classifying each tweet as bullish or bearing which essentially means positive or negative [14].

The review structure is domain oriented for many sentiment analysis documents as one needs to be oriented of the topic and the keywords to find fitting tools to perform sentiment analysis. The author also mentions that negation is a key challenge in this process whether there is any form of structured data [15].

A sentence level summary model is introduced into the daily summaries of stock values forecasting by news articles. This paper discusses a general framework for forecasting stock prices that uses text document as input and generate predicted price movement as output [16].

The Stock Sonar (TSS) is primarily a sentiment analysis tool on the basis of hybrid technique that combines various sentiment dictionaries and various compositional patterns [17]. One of the most ground breaking features of TSS is that it provides to the point sentiment extraction i.e., only highlighting the polar attributes namely positive and negative leaving out the un-useful content of the article. This paper mainly aims at showing how it can enhance the process of document level sentiment

classifiers. The insights from this paper mainly focus on saving the time of daily investors which is utmost necessary in this digital age.

The aim of this paper is to minimize loss and get high accuracy prediction of sentiment analysis of stock news resulting returns to confirm a financially secure future.

3 Methodology

The proposed architecture of the model starts off by selecting a relevant data set which has a future scope and gives insightful results with high accuracy of sentiment analysis by using the most optimum combination and order of tools.

In this work, we will help users to determine which is the best way to maximize accuracy in order to make the perfect model on the basis of the top 25 headlines from 2000 to 2008 downfallen stock range and 2009–2016 uplifting stock range, in two slots. Text pre-processing is required for sentiment analysis [18] of stock news dataset. We used both 'n-gram' and 'tf-idf vectorizer' to convert text into vectors and applied Random Forest, Multi Binomial Naïve Bayes, Passive Aggressive and Linear Regression machine learning classifier for training–testing-validation and select the best model on the basis of performance measure.

The detailed methodology is given in Fig. 1 which essentially consists with three key components. Phase-1 is cleaning the data using pre-processing of the text and applying n-grams. The result of phase-1 is given as input to phase-2.

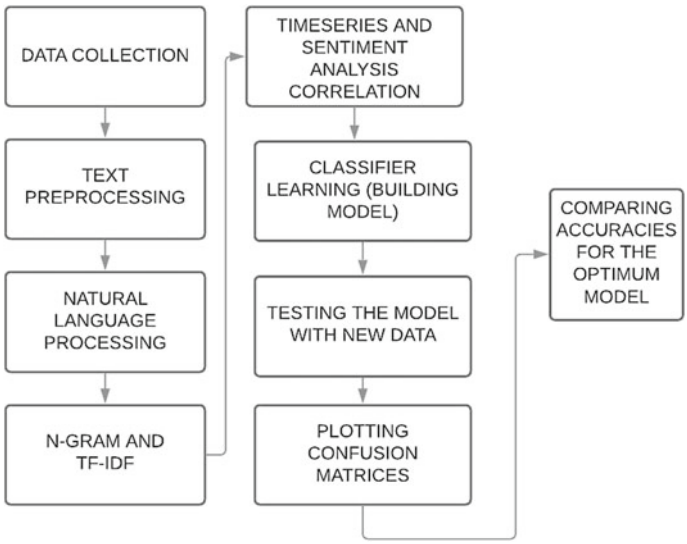

Fig. 1 Methodology of sentiment analysis for stock news

In phase-2, the text is converted into the vectors using tf-idf. Now time-series dataset of 2000–2008–2016 and sentiment analysis correlation above that 70% is sent to machine learning classifiers for training–testing.

In the last phase-3, we evaluate the performance measure matrices of Random Forest, Multi Binomial Naïve Bayes, Passive Aggressive and Linear Regression machine learning classifier for better understanding. All these processes are key to obtain the effective results and understand the usefulness of Machine learning in Sentiment analysis. Each design block is explained in the following sections.

3.1 Data Description

Stock news dataset is acquired from Kaggle repository from 2000 to 2008 and 2009 to 2016 in which headlines related to economics from the Reddit World Channel are taken. They're ranked based on the votes of Reddit users and selection of top 25 headlines are taken for a single date.

The main driving force which led to the division of the dataset in two slots was the 2008 Stock Market crash which was an abrupt moment in the stocks which led to the stock market coming at all time low very fast speed. The division of the dataset has been done to create a comprehensive contrast between values before and after the crash to increase the variance dimensionality for comparative sentiment analysis.

The dataset under consideration is a combination of world news and stock price changes. Date is taken in the first column while news headlines are in second column. All stock news is taken in sorted order from top to bottom ranking according to relevance. Hence, each date row having 25 lines. There are approximately 2000 rows of data for comprehensive analysis.

3.2 Classification Description

The main aim is to classify the stock news dataset into positive or negative sentiments. For this purpose, the data in the message text is pre-processed, followed by the classification of the messages using the Naive Bayes classifier. The following pre-processing processes are applied on various classification models on the basis of their input data specifications. Following is the text pre-processing steps that are carried out as given.

Tokenization. Tokenization is considered the building block of any text related task in a NLP related project. Tokenization is a way of separating a piece of text into smaller units called tokens. In our project we used tokenization to top news headlines into small streams of words which were later processed upon by N-gram.

Conversion in lowercase. To convert all the data to lowercase as during the training of the models it may consider same words as different as its case sensitive.

Removing of Stop words, Tags, Special Character. Stop words are not important in news text so removing them will help us bringing down the dimensionality of the model thus making it fast and better.

No need of tags and punctuations in news text as of no use to understand the sentiment of the news text and will just end up increasing the dimensionality and latency of the model. So, removal of these common punctuations and tags is done.

Stemming. To make similar words to their base word or in short removing the abbreviations used. At times these words will be treated differently even though they mean same such as 'doesn't' and 'does not' to increase dimensionality.

N-Gram. It is a probabilistic model for training the corpus typically word sequences occur in corpus text and so estimating the probabilities.

Term Frequency Inverse Document Frequency (TF-IDF). Term Frequency refers to the occurrence of a word pops up in a text and word occurrence in a document corpus is known as Inverse Document Frequency. In tf-idf, words are weighted according to their significance. Capital letter, non-alphanumeric characters, special characters and not necessary punctuations are eliminated first. After it, we gathered terms that were similar.

There are multiple methods to convert words to vectors. Here we use tf-idf, mathematical formulation is shown in Eq. (1–3) that allots each words a specific value on basis of their repetitions in each news text.

$$tf(t, d) = \frac{f_d(t)}{\max\limits_{w \epsilon d} f_d(w)} \tag{1}$$

$$idf(t, D) = \ln\left(\frac{|D|}{|\{d \in D : t \in d\}|}\right) \tag{2}$$

$$tfidf(t, d, D) = tf(t, d).idf(t, D) \tag{3}$$

Afterward, we used sklearn's *tf-idf* Vectorizer to convert the scanned text to *tf-idf* features, to construct a bag of terms, a count vector, and a *tf-idf* matrix.

How sentiment shifts over time, what was the sentiment of the general public that day with the package 'sentimentr' in order to pertain conclusive results, and plot the stock values versus the dates as shown in Fig. 4.

3.3 Machine Learning Classifiers

Random Forest Classifier. It belongs to the supervised ensemble technique and may be used for each Classification and Regression issues in Machine Learning. It

is a system of mixing a couple of classifiers to clear up a complicated hassle and to enhance the overall performance of the model.

Multi Binomial Naïve Bayes classifier. Naive Bayes is usually used in text classification with issues pertaining to numerous classes. Bayes theorem calculates likelihood $P(c|d)$ wherever c is that the class of the potential outcomes and d is the given instance that needs to be classified, representing some sure feature as shown in Eq. (4). Naive Bayes combines both Prior Probability and Likelihood measures to perform Posterior probability which is shown in Eq. (4). Naïve Bayes classifier is used to divide the input to positive and negative sentiment primarily by using tf-idf values.

$$PNB(C|d) = \frac{P(c).(\prod_{i=1}^{m} P(f_i|c)^{ni(d)}}{P(d)} \tag{4}$$

Passive Aggressive Classifier. It is underrated in the field of machine learning. It works by reporting as passive for correct classifications and agressive in any miscalculations. It is used to diversify the range of classifiers used in NLP field.

Logistic Regression. The primary reason for choosing Logistic Regression model is because it is widely implemented in the Financial Sector and makes utmost sense. It predicts the category dependent variable using the predefined independent variables. The result is a discrete value like 0 or 1. Logistical Regression is primarily used in classification problems as it optimum in determining the variables for classification.

4 Results

Stock news dataset is acquired from Kaggle repository from 2000 to 2008 downfallen stock range and 2009–2016 uplifting stock range, in two slots, in which headlines are ranked based on the votes of Reddit users and selection of top 25 headlines are taken for a single date as shown in Fig. 2.

To classify the stock news dataset into positive or negative sentiments, the data in the message text is pre-processed, followed by the classification of the messages using the Naive Bayes classifier and prediction model on the basis of connecting words and assigning positive or negative sentiment accordingly, shown in Fig. 3.

Year 2008, in which the greatest stock market crash took place, therefore, studying and analyzing the sentiments of general public after the crash will prove utmost insightful as shown in Fig. 4.

Figure 5 depicts the test results accomplished to forecast and analyze the stock marketplace behavior by the usage of sentiment evaluation. In the sentiment evaluation, the information statistics are split into training and testing sets. The results for the same have been depicted in Fig. 6. The results display that highest accuracy executed for sentiment evaluation version is as much as 85.97% for Random

A	B	C	D	E	F	G	H	I	J	K	L	M	N	O	P
Date	SENTIMENT	PREDICTED SENT.	Top1	Top2	Top3	Top4	Top5	Top6	Top7	Top8	Top9	Top10	Top11	Top12	Top13
03-01-2000		0	0	A 'hind	Scorec	Hughes' in	Jack gets h	Chaos as M	Depleted L	Hungry Spe	Gunners sc	Derby rais	Southgate	Hammers	Saints part	Wear w
04-01-2000		0	0	Scorec	The be	Leader: Ge	Cheerio, b	The main r	Has Cubie	Has Cubie	Has Cubie	Hopkins 'fi	Has Cubie	A tale of th	I say what	Elbows,
05-01-2000		0	0	Covent	United	Thatcher i	Police help	Tale of Tra	England or	Pakistan re	Cullinan cc	McGrath p	Blair Witch	Pele turns	Party divid	Manche
06-01-2000		1	1	Pilgrim	Thatch	McIlroy ca	Leicester b	United bra	Auntie bac	Shoaib app	Hussain hu	England's c	Revenge is	Our choice	Profile of t	New evi
07-01-2000		1	1	Hitcher	Beckha	Breast can	Alan Parke	Guardian r	Hollywooc	Ashes and	Whingers -	Alan Parke	Thuggery,	'Met faces	Everton fa	Our brea
10-01-2000		1	1	Fifth rc	BBC ur	Second Di	European	Third Divis	Welfare cc	Ferguson p	Southgate	Second bit	Scallywags	England m	Radio just	Faith in t
11-01-2000		1	1	Man U	How N	Buoyant B	Tranmere	United sit	Queen's Pa	Waugh hit	Knight mal	Scoreboar	Bond is no	You just ca	Blake blast	German
12-01-2000		0	0	Newca	Liverpc	Highlander	Edwards' p	Chelsea ga	Taylor sett	Tenth top-	Charlton c	German pa	The Beach	'Pariah' Irv	Jack Straw	Batty bu
13-01-2000		1	1	Bunglir	And in	United put	England ag	Donald po	Adams sta	Money mc	Tyson to e	Gas chamt	Union take	Win ticket	Irving deni	Gallant F
14-01-2000		1	1	Pompe	Roma	Prenton Pa	OK, I didn't	Chelsea tu	Top storey	West Indie	Donald's k	Cronje low	Counties t	Final to tel	TV rivals jc	Blatter:
18-01-2000		1	1	Englan	Robsor	Old Firm Ic	Babbel to	For Murali	All padded	Individuals	The best o	The patent	German oi	A high not	Just you w	The one
19-01-2000		0	0	No apc	One-of	Old Traffo	Draper set	Forest giar	Adams sta	The young	Indian out	At last the	Housing: T	Hick and tl	Defiant Ba	Why Str
20-01-2000		0	0	Homes	Wemb	Keegan ca	Backing fo	Leboeuf ri	South Afric	Wasim los	Swann ask	Rousing fir	Lords back	Hollywooc	Lords refo	Britain's
21-01-2000		0	0	Never I	Keegar	Magpies s	Investors c	All Wright	Under-19s	England lin	Scoreboar	England fu	South Afric	The empty	Leader: W	Reforme
24-01-2000		0	0	Lee pu	Jim Sw	Wilson prc	Wigan helc	Weah war	Town rise	Taylor rag	Robson tu	Owen's m	Leicester c	Jones rallie	John adds	Hunt hat
25-01-2000		0	0	Dazzler	Rivaldc	Stealthy Sc	Fans talk v	Gregory is	Double vis	Dalglish gi	Harry Pott	Berlioz: Se	White City	Music and	Beowulf b	Useful li
26-01-2000		1	1	Best gc	Wright	Dream scr	Bradford s	Villa stall c	Ganguly gi	Town plan	Caddick at	Atherton c	Labour set	Student di	Blunkett t	No poisc
27-01-2000		1	1	Lancas	Early si	Atherton i	Valiant En	Tranmere	Liverpool r	Hillsborou	Flying Scot	Ferguson t	Crocked pl	The man fi	Work in pr	The Russ
28-01-2000		0	0	Carlton	United	Svensson	Running sc	Bradford b	Robson ca	Dismal Eng	Abject Eng	Through th	Tim Roth a	National T	Hatching C	Marketir
31-01-2000		0	0	Nation	Nation	Nationwid	Birminghar	Rangers m	Computer	Nasa clear	Inquiry ani	More murc	Pressure fi	I'd like to t	Reaction t	How the
01-02-2000		1	1	Double	Even F	Owen in di	New spon	Claridge in	World Cup	Hussain ba	William Hu	'In plain sp	Blunt Blair	Portillo ba	Computer	Doctor's
02-02-2000		1	1	Hospit	English	Kick flicks	Italy order	Specialist c	Leboeuf bi	Debts forc	Housing: V	Zimbabwe	Bates blas	The farme	PM tells fa	Hague's
03-02-2000		0	0	Scoreb	Flower	Stricken Sv	Hot stuff f	Euro-fring	Chairman'	Vidmar set	Electric Ell	Sheringhar	Mandelsor	President a	Blair hits o	Blair's ru
04-02-2000		1	1	Vialli w	Safety-	Bold Pollo	Leicester r	Hussain pr	Atherton's	Rear Wind	A Room fc	The Big Te	Football 1,	Toy Story :	Toy Story :	England

Fig. 2 Data description for stock news

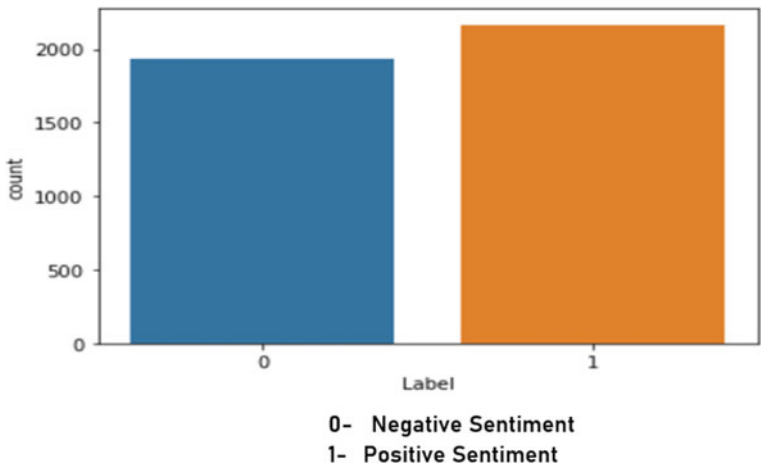

Fig. 3 Sentiment analysis dataset (0—negative, 1—positive)

Forest Classifier, 84.65% accuracy for Multi Binomial Naïve Bayes, 85.44% for Passive Aggressive and 83.20% for Linear Regression. Random Forest set of rules offers precise performance, excessive accuracy and accomplished nicely with textual statistics.

Figure 7 shows confusion matrix for Random Forest, Multi Binomial Naïve Bayes, Passive Aggressive and Linear Regression machine learning classifier, applied on sentimental stock news dataset. Random Forest is selected as best classifier with high precision, high recall and high accuracy of 85.97%.

Table 1 depicts the accuracy of Random Forest, Multi Binomial Naïve Bayes, Passive Aggressive and Linear Regression machine learning classifier, applied on sentimental stock news dataset.

Fig. 4 Stock values downfall view (2000–2008)

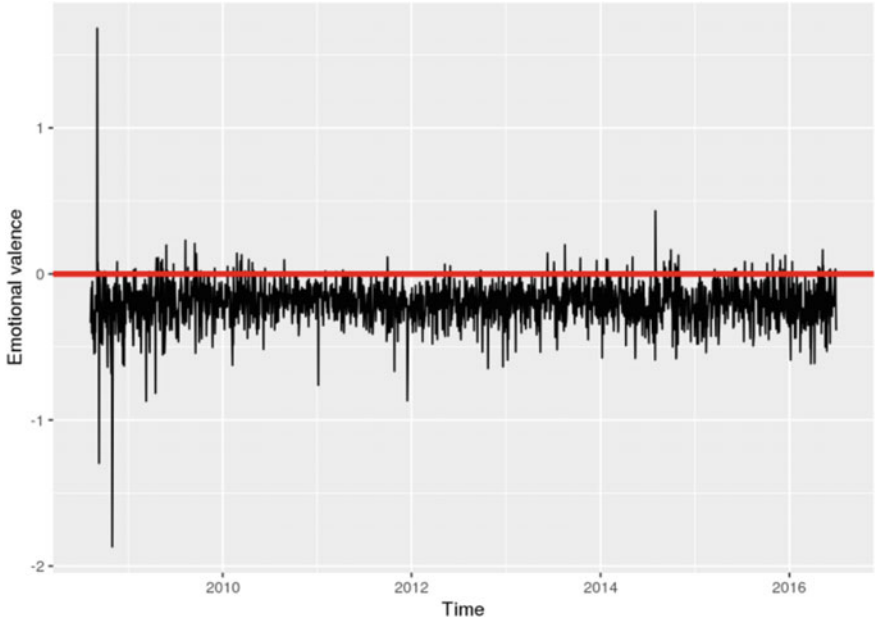

Fig. 5 Sentiment analysis of positive, negative (2008–2016)

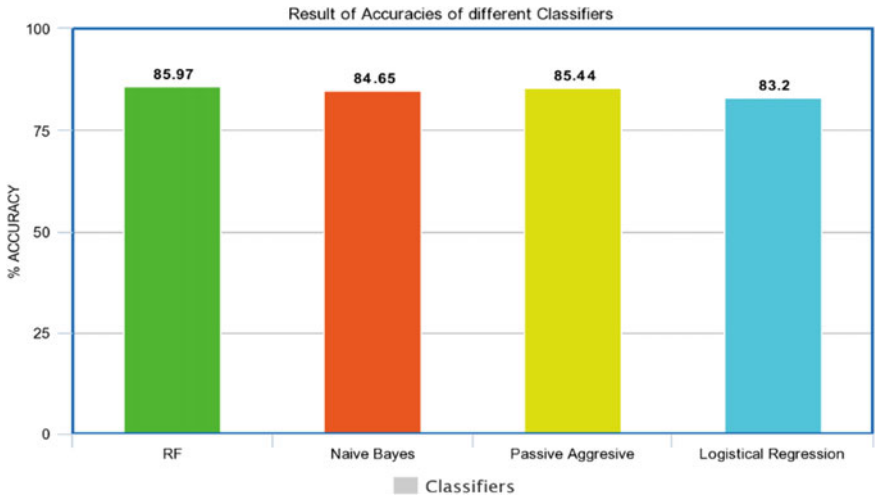

Fig. 6 Performance accuracies of machine learning models

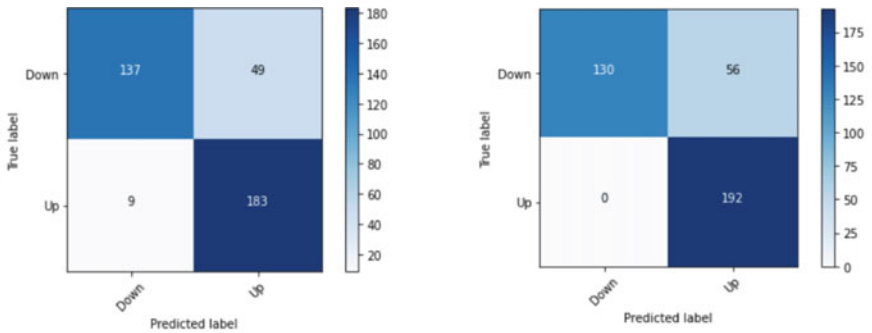

(a) Random Forest

(b) Multinomial Naïve Bayes

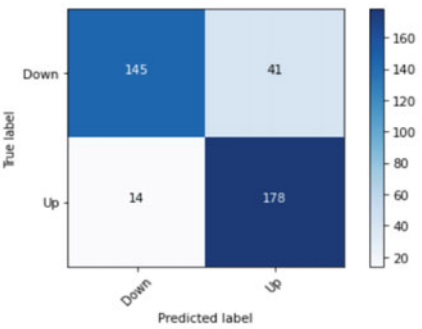

(c) Passive Aggressive

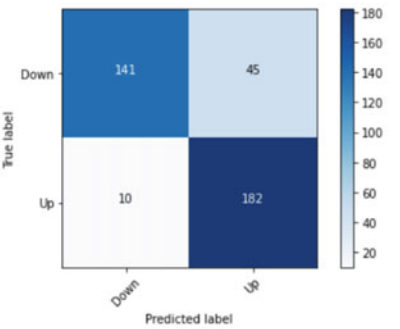

(d) Logical Regression

Fig. 7 Confusion matrices of applied machine learning model

Table 1 Training–testing accuracy of models

Machine learning classifier	Accuracy (%)
Multi binomial Naïve Bayes	84.65
Random Forest	85.97
Passive Aggressive	85.44
Logical Regression	83.20

5 Conclusion

In retrospect to the standard stock market prediction systems, our unique approach combines the sentiments of news feed ranked by reddit users which are quintessentially common people to understand the conduct of the equity related markets and in particular the stock market.

The proposed study investigated impact of reading extraordinary varieties of classifiers for expertise inventory marketplace conduct. The proposed version advanced helped in choosing the correct classifier for analysis of inventory marketplace, via way of means of thinking about extraordinary varieties of each day information at some point of a selected day. Highest accuracy executed for sentiment evaluation version is as much as 85.97% for Random Forest Classifier, 84.65% accuracy for Multi Binomial Naïve Bayes Classifier, 85.44% for Passive Aggressive and 83.20% for Linear Regression, in which Random Forest classifier is selected as best classifier for stock sentimental news dataset.

6 Future Work

This work is not analyzing the sentiments of audience emotions, twitter talks that are misspelled or double meaning, SMS messages. The future work to add above said text types in the current work to predict the accuracy with text analytics and machine learning algorithms. This model can be visually interpreted by making a 'Sentiment Analysis Web App' to help the user to evaluate the sentiment of his/her data in real time. Like RoBERTa which is a part of Facebook's ongoing commitment to develop with less reliance on time- and resource-intensive data labeling can also be implemented in this work.

References

1. Walter W, Ho K, Liu WR, Tracy K (2013) The relation between news events and stock price jump: an analysis based on neural network. In: 20th International Congress on Modelling and Simulation, Adelaide, Australia, 1–6 Dec 2013, pp 1–6. www.mssanz.org.au/modsim2013

2. Bharathi SS, Geetha A (2017) Sentiment analysis for effective stock market prediction. Int J Intell Eng Syst 10:146–154
3. Søgaard A (2013) Sentiment analysis and opinion mining. Lang. Comput. Group, Microsoft Res. Asia
4. Paper C (2016) Preprocessing techniques for text mining preprocessing techniques for text mining. J Emerg Technol Web Intell
5. Khedr AE, Yaseen N (2017) Predicting stock market behavior using data mining technique and news sentiment analysis. Int J Intell Syst Appl 9(7):22
6. Hana Alostad HD (2015) Directional prediction of stock prices using breaking news on Twitter. In: IEEE/WIC/ACM International Conference on Web Intelligence and Intelligent Agent Technology, pp 0–7
7. Patrick Uhr MF, Zenkert J (2014) Sentiment analysis in financial markets. IEEE International Conference on Systems, Man, and Cybernetics, pp 912–917
8. Hoang Thanh PM (2014) Stock market trend prediction based on text mining of corporate web and time series data. J Adv Comput Intell Intell Informatics 18(1)
9. Price SM, Shriwas J, Farzana S (2014) Using text mining and rule based technique for prediction of stock market price. Int J Emerg Technol Adv Eng 4(1)
10. Sahil Zubair KJC (2015) Extracting news sentiment and establishing its relationship with the S & P 500 Index. In: 48th Hawaii International Conference on System Sciences. Extr.
11. Bing I, Ou C (2014) Public sentiment analysis in twitter data for prediction of a company's stock price movements. In: IEEE 11th IEEE international conference on e-bus engineering public
12. Nguyen D, Le M (2014) A two-stage architecture for stock price forecasting by combining SOM and fuzzy-SVM. Int J Comput Sci Inf Secur 12(8):1–6
13. Wu DD, Zheng L, Olson DL (2014) A decision support approach for online stock forum sentiment analysis. IEEE Trans Syst Man Cybern Syst 44(8):1077–1087
14. Batra R, Daudpota SM (2018). Integrating StockTwits with sentiment analysis for better prediction of stock price movement. In: 2018 International conference on computing, mathematics and engineering technologies (iCoMET), pp 1–5. IEEE, Mar 2018
15. Hussein DMEDM (2018) A survey on sentiment analysis challenges. J King Saud Univ-Eng Sci 30(4):330–338
16. Li X, Xie H, Song Y, Zhu S, Li Q, Wang FL (2015) Does summarization help stock prediction? a news impact analysis. IEEE Intell Syst 30(3):26–34
17. Feldman R et al (2011) The stock sonar—sentiment analysis of stocks based on a hybrid approach. In: Twenty-third IAAI conference
18. Arora R, Singh P, Goyal H, Singhal S, Vijayvargiya S (2021) Comparative question answering system based on natural language processing and machine learning. In: 2021 International conference on artificial intelligence and smart systems (ICAIS). IEEE, March, pp 373–378

A New Hybrid Chaotic Map-Based Image Steganography Using Spectral Graph Wavelet

Shikha Chaudhary, Saroj Hiranwal, and C. P. Gupta

Abstract This paper proposes a new hybrid chaotic map-based image steganography using spectral graph wavelet (SGWT). A new hybrid chaotic map method is proposed using the composition of two existing chaotic maps: Hénon map and Duffing map. Using the proposed hybrid chaotic map, the secret image is scrambled. The SGWT transform using graph signal processing (GSP) is performed on cover and secret image, where each image is generated as a 2D grid graph and each pixel is displayed as a vertex of a graph. To hide the secret image in a cover image, the alpha blending operation is performed. Furthermore, the inverse graph wavelet is applied to bring forth the stego image. The experimental analysis and outcomes show that the suggested technique gives improved PSNR and NCC.

Keywords Steganography · Spectral graph wavelet · Graph signal processing · Chaotic map · Information hiding

1 Introduction

The term Steganography is originated from Greek that signifies "Covert Writing." It is the technique of hiding data without arising suspicion [1, 2]. In ancient era, secret messages were hidden by some physical means such as pigeons and head of a man was shaved to write the secret message, and women's earrings, etc. The invisible ink, drawings were also used to hide information by varying the length of a line, the colors, or other features of the picture. It is proved that great artists, such as Leonardo Da Vinci, Rafael, and Michelangelo, have concealed messages in their paintings [3]. The contemporary microdot, which consists of printed-period size images, also called Microdots started being popular in 1941, during the World

S. Chaudhary (✉) · S. Hiranwal
Rajasthan Institute of Engineering and Technology, Jaipur, India
e-mail: shikha.chaudhary18@gmail.com

C. P. Gupta
Rajasthan Technical University, Kota, India

© The Author(s), under exclusive license to Springer Nature Singapore Pte Ltd. 2022

A. Tripathi et al. (eds.), *Intelligent Computing Techniques for Smart Energy Systems*,
Lecture Notes in Electrical Engineering 862,
https://doi.org/10.1007/978-981-19-0252-9_20

War II [4]. The scientific study of digital steganography started in 1983 when the cryptographer Gustavus Simmons [5] published the first steganography work.

These days, steganography is primarily used to protect confidential data. The use of digital communication has effectually increased by which the internet has come up as a fastest way of communication [6]. Simultaneously, data through the internet is more vulnerable to various attacks like copyright violation, snooping, and goofing therefore the necessity of secret, reliable, and secure communication is required. Steganography is one of the techniques used for information hiding likewise fingerprinting and watermarking. It is reflected as a cutting-edge technique for hiding information which has secretiveness as its ultimate goal.

Steganography can be classified into two prime categories, (1) spatial domain: where the surreptitious message is straightly embedded into the pixel intensity of cover media, also known as substitution method [7]. It extracts some bits of secret image conating major information about the image and embeds it inside a cover image by altering covers' bits, example of spatial domain steganography approach is the Least Significant Bit (LSB) Substitution [8]. (2) Transform domain or Frequency domain technique: in this, data is inserted in the transform coefficients of the cover media after applying transformation on cover and secret media. This steganography scheme provides high level of security and could conceal huge data. It also provides the better invisibility of the hidden data as well as no loss of extracted secret information. The Discrete Cosine Transform (DCT), Discrete Fourier Transform (DFT), and Discrete Wavelet Transform (DWT) are examples of transfer domain technique [9–11].

2 Related Work

Various steganography schemes are showed in this section, to hide the information securely in a cover media. The most familiar steganography method is least significant bit substitution [12], where LSB of pixel is reformed by inserting the secret message which results in lesser PSNR and poor extracted image. Abdelwahab and Hassan [13] used DWT to transform cover and secret images. Kumar and Kumar [14] presented a steganography scheme using DCT and DWT but the information was lost in this scheme because of rounding. The DWT-based robust data hiding scheme was presented by Al-Ataby and Al-Naima [15], where the high-capacity insertion method is used to insert secret data in a cover data however the computation time was high. Masaebi and Moghaddam [16] proposed a steganography method using Contourlet transform; it is a robust scheme against common image processing attacks. Narasimmalou and Joseph [17] suggested a data hiding scheme where the cover image is decomposed using the DWT transform and its transform coefficients are modified. Raftari and Moghadam [18] designed a steganography approach by combining the integer wavelet transform (IWT) and DCT, the secret data is inserted in transfer domain by the use of Munkres' assignment algorithm. Ioannidou et al. [19] suggested an information hiding technique to conceal the secret data in the edges

of the image. However, this method has less payload capacity. Hemalatha et al. [20] developed a technique by hiding dual secret images inside a cover image to generate a good visibility of stego image. A new steganography method was proposed by El-Emam and Al-Zubidy [21] to insert a huge quantity of secret data inside a cover image by means of four security layers using an adaptive neural network. However, the computational time is high. Singh et al. [22] developed image steganography using SVD and IWT and generates good quality of stego image but, more persuade to image processing attacks. Sujarani et al. [23] presented chaotic map-based steganography technique, where the chaotic logistic map is applied to choose the pixel location of the cover image to insert the secret image. Sharma et al. [24] suggested a technique where steganography is combined with cryptography and neural network to make the technique more secure. Sahu and Swain [25] proposed a technique where rightmost n bits are used to hide the secret information which results in a better quality of stego image and good embedding capacity. Kiruba et al. [26] proposed a data hiding technique where the optimal pixels from each block is selected using Fruit fly optimization improved hybridized seeker algorithm to conceal the secret data. Muhuri et al. [27] suggested an IWT- and PSO-based steganography technique to discover a substitution matrix of secret data. Sharma et al. [28] proposed a Daubechies DWT-based steganography approach to hide secret data scrambled using Arnold transform. The smoothening operation using genetic algorithm was performed to denoise the generated stego image.

3 Background

Spectral graph wavelet transform (SGWT) [29] describes various wavelet transforms applied on data which can be presented in the form of graph. The graphs offer an exceptionally supple way to model the data of the applications whose data can be represented as vertices like connectivity networks, social networks, brain point clouds, and images, etc. It is the spectral decomposition of NXN size image, where N denotes the number of nodes of the graph and L is the Laplacian matrix of the graph [30]. A kernel function g is applied on L as a filter and s is a scaling function of wavelet. SGWT is centered on Chebyshev polynomial approximation that reduces the computational time by reducing the calculation of all sets of eigenvalues as well as eigenvectors of L.

A new hybrid chaotic map in discrete dynamic system is designed by compositing the two discrete classic chaotic maps: Hénon map and Duffing map. The Hénon map was presented by Michel Hénon [31]. The map is two-dimensional and maps the coordinates (x_i, y_i) to new points using following equation:

$$\begin{cases} x_{i+1} = 1 - ax_i^2 + y_i \\ y_{i+1} = bx_i \end{cases} \tag{1}$$

Equation (1) contains the parameters a and b having values $a = 1.4$, $b = 0.3$, on the given values of a and b the map shows chaotic behavior.

The Duffing map [32] is a discrete-time dynamic system which maps points (x_i, y_i) to new points using the following equation:

$$\begin{cases} x_{i+1} = y_i \\ y_{i+1} = -bx_i + ay_i - y_i^3 \end{cases} \tag{2}$$

The map's behavior depends on the parameters a and b, for the value of $a = 2.75$ and $b = 0.2$, it shows chaotic behavior.

4 Proposed Hybrid Chaotic Map

To design a new composite mapping scheme, Eq. (1) and (2) are combined with some modification to map the points (p_i, q_i) to new points (x_{i+1}, y_{i+1}). The new mapping scheme is derived as follows:

$$\begin{aligned} p_{i+1} &= 1 - up_i^2 + q_i \\ q_{i+1} &= vp_i \\ x_{i+1} &= q_{i+1} \\ y_{i+1} &= -bp_{i+1} + aq_{i+1} - q_{i+1}^3 \end{aligned} \tag{3}$$

In Eq. (3) the parameters $a \in [0, 2.75]$, $b \in [0, 0.2]$ and $u \in [0, 1.4]$, $v \in [0, 0.3]$ the chaotic behavior of new hybrid mapping system is analyzed on aforesaid parameters for the initial value of points $(p_i, q_i) = (1, 1)$. It is observed that the system shows chaotic behavior for the value of $a = 2.75$, $b = 0.15$, $u = 1.4$, $v = 0.3$, p_i, $=$ 1, and $q_i = 1$ as shown in Fig. 1.

5 Proposed Chaotic Map-Based Steganography Technique

The steganography mainly involves two steps: embedding process and extracting process. In embedding process, a secret image is first scrambled using a novel hybrid chaotic Henon Duffing map as shown in Eq. (3) and a secret key. Scrambling is a process to shuffle the position of image pixels so that it would not be identified. Spectral Graph Wavelet transform (SGWT) is performed on cover image and scrambled

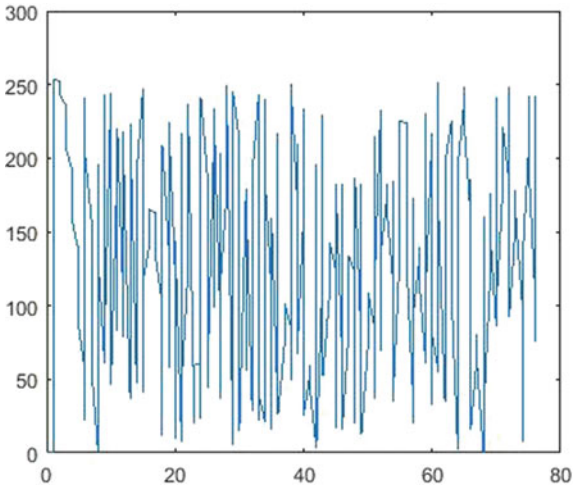

Fig. 1 Chaotic behavior of proposed hybrid chaotic map $a = 2.75$, $b = 0.15$, $u = 1.4$, $v = 0.3$, $p_i, = 1$, $q_i = 1$, and $i = [0, 255]$

secret image. The alpha blending operation is now performed on transformed images to embed the secret data in cover image. Alpha blending is an operation to generate a new image by mixing of two images [33]. The blending factor $\propto$ controls the visibility and quality of generated stego image where $0 \leq \propto \leq 1$ and 1, lower value of $\propto$ generates good quality of stego image whereas higher value of $\propto$ provides good visibility of extracted image but poor stego image.

$$C_B = (1 - \propto) C_{GW} + \propto SI_{GW} \tag{4}$$

Here C_B represents the blended image; C_{GW} is cover image and SI_{GW} is scrambled secret image. Afterward, inverse wavelet transform is performed to generate the stego image.

5.1 Embedding Phase

The embedding process includes various operations such as Graph wavelet analysis (SGWT), hybrid chaotic map for scrambling, alpha blending and graph wavelet synthesis (Inverse SGWT) to form stego image. The algorithmic steps of embedding process are shown in the following way:

Embedding Algorithm:

Step 1 Input cover image C of size $M\ X\ N$ and secret image I of size PXQ.
Step 2 Resize the secret image of size $M\ X\ N$.
Step 3 Apply Hybrid Chaotic map using Eq. (3) to scramble secret image and/or generate a scrambled image SI using a secret key K.

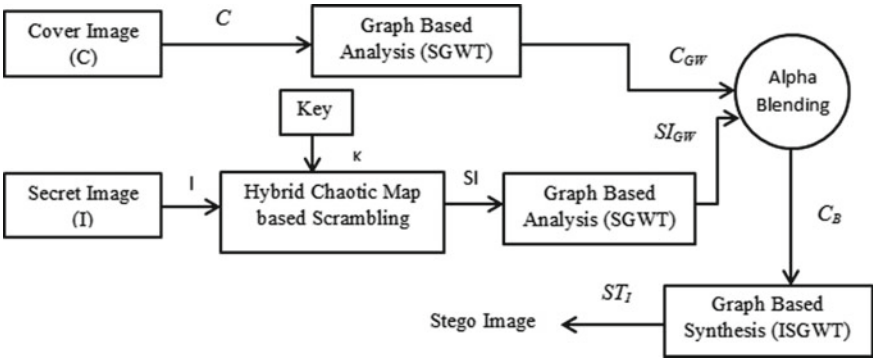

Fig. 2 Flowchart of embedding process for hiding secret image in a cover image

Step 4 Apply Spectral Graph wavelet on C and SI to get the transformed images C_{GW} and SI_{GW}.

Step 5 Perform Alpha Blending operation on CGW and SIGW and get blended image CB using Eq. (4).

Step 6 Apply Inverse Graph wavelet on C_B to generate stego image ST_I.

To send the secret information I to the receiver, first the secret image is scrambled using the hybrid chaotic map represented in Eq. (3) and a secret key so that in case of identification of presence of some noise in the transmitted image, the presence of secret image would not be identified; as an output the scrambled secret image SI is generated. The SGWT is performed on the cover image C and the scrambled image SI. In this approach, a 2D grid graph is used to present the images using graph signal processing. The Itersine single filter is used from the filter banks of graph signals. Both images C_{GW} and SI_{GW} are blended together to hide primary feature of secret image in cover image. Inverse graph wavelet is performed on blended image to generate the stego image. The flowchart of whole embedding process is presented in Fig. 2

5.2 Extracting Phase

The extracting process is the reverse of the embedding process, where spectral graph wavelet is applied on the stego image and cover image to build the 2D grid graphs of the images. The difference of both the generated graphs of stego and cover is carried out through alpha blending operation to extract the hidden scrambled secret image information. Inverse SGWT is applied to generate the hidden scrambled image through the extracted graph of hidden scrambled secret image. Finally, inverse hybrid chaotic map is applied on the scrambled secret image to extract the hidden secret image. The flowchart of the extracting process is shown in Fig. 3 and algorithm to extract the hidden secret image is as follows:

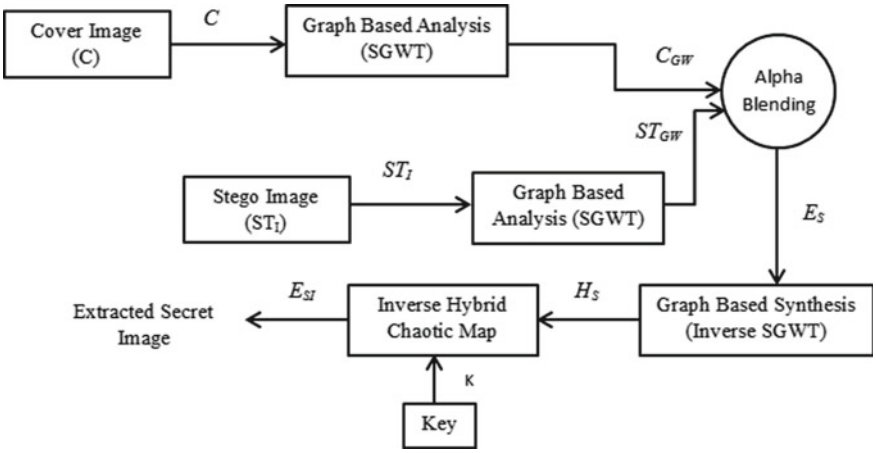

Fig. 3 Flowchart of extracting process for extracting secret image from stego image

Extracting Algorithm:

Step 1 Receive stego image ST_I and secret Key K.

Step 2 Apply Spectral Graph wavelet on C and ST_I to get the transformed images C_{GW} and ST_{GW}.

Step 3 Perform Alpha Blending operation on C_{GW} and ST_{GW} to extract encrypted information of secret image E_i.

$$E_{\mathrm{S}} = ST_{\mathrm{GW}} - C_{\mathrm{GW}}$$

Step 4 Apply Inverse Graph wavelet on E_{S} using a secret key K to get hidden scrambled image H_{S}.

Step 5 Apply inverse Hybrid Chaotic map on H_{S} to extracted secret image E_{SI}.

6 Experimental Analysis

To assess the performance of the suggested chaotic map-based image steganography scheme, MATLAB R2018a is used. The images Lenna.tif (256 × 256), Pepper.tif (256 × 256) are used as cover and secret image respectively for the evaluation of the performance of proposed method. We tested our approach on different values of $\propto$ between the ranges 0.001–0.30.

The performance of the suggested steganography scheme is measured by some performance parameters such as Mean Square Error (MSE), Peak Signal to Noise Ratio (PSNR), and Normalized Cross Correlation (NCC) [34, 35]. The MSE is used to calculate the variance between cover and stego image whereas PSNR is used to measure the alteration between the cover image and generated stego image as presented in Eqs. (5) and (6).

$$\mathrm{MSE} = \frac{1}{\mathrm{MN}} \sum_{k=1}^{M} \sum_{l=1}^{N} \left(C_{k,l} - ST_{I_{k,l}}\right)^2 \tag{5}$$

$$\mathrm{PSNR} = 10 \log_{10} \frac{\mathrm{Max}S^2}{\mathrm{MSE}} \mathrm{dB} \tag{6}$$

Here *MXN* is the size of cover and stego image, $C_{k,l}$, $ST_{I\,k,l}$ is the pixel value located at *k*th row and *l*th column and Max*S* is the maximum intensity of the pixel of a cover image. The low value of MSE and high value of PSNR signifies the good quality and better visibility of stego image. The value of PSNR greater than 30 dB is good because it is hard to discriminate the difference between cover image and stego image by human eyes.

NCC represents the correlation among the cover image and stego image, the value of NCC lies between [0, 1]; greater value of NCC signifies higher similarity. NCC is calculated using following equation:

$$\mathrm{NCC} = \sum_{k=1}^{M} \sum_{l=1}^{N} \left(C_{k,l} * ST_{I_{k,l}}\right) \frac{1}{\sum_{k=1}^{M} \sum_{l=1}^{N} C_{k,l}^2} \tag{7}$$

6.1 Experimental Performance Analysis

To assess the performance of the suggested hybrid chaotic map-based steganography scheme, different gray-scale images Lenna.tiff, Baboon.jpeg, and Airplane.jpeg of size (256X256) are taken as cover media and Boat.jpeg (256 × 256) as secret image as shown in Fig. 4.

The algorithm is tested on various values of alpha (α) ranging from 0.010 to 0.050 as mentioned in Table 1, this can be noticed from the table that the lower value of α gives good PSNR and NCC and lower MSE, but the quality of extracted image is poor. The higher value of α improves the quality of extracted image but degrades the

Fig. 4 Cover images of size (256 × 256) **a** lenna **b** baboon **c** airplane **d** flower

Table 1 PSNR, MSE, and NCC on different values of α, cover image Lenna and secret image Boat

α	PSNR	MSE	NCC	Quality of extracted image
0.001	64.3296	1.3706e + 03	0.9990	Poor
0.002	58.3090	5.4825e + 03	0.9980	Poor
0.003	54.7871	1.2336e + 04	0.9971	Poor
0.004	52.2884	2.1930e + 04	0.9961	Poor
0.005	50.3502	3.2466e + 04	0.9951	Poor
0.006	48.7665	4.9343e + 04	0.9941	Average
0.007	47.4276	6.7161e + 04	0.9932	Average
0.008	46.2678	8.7720e + 04	0.9922	Average
0.009	45.2447	1.1102e + 05	0.9912	Average
0.010	**44.8296**	**1.37E + 05**	**0.9902**	**Good**
0.020	38.3090	5.4825e + 05	0.9806	Good
0.030	34.7871	1.2336e + 06	0.9712	Good
0.040	32.2884	2.1930e + 06	0.9619	Good
0.050	30.3502	3.4266e + 06	0.9527	good

quality of stego image. For the value of $\alpha = 0.010$ and $\alpha = 0.020$, the PSNR and NCC between cover and stego image is good, quality of extracted secret image is good as well.

The secret image Boat Fig. 5a is scrambled using proposed hybrid chaotic map and the output of the scrambled secret image is shown in Fig. 5b. SGWT is applied on cover and secret image and both images are blended using alpha blending operation for $\alpha = 0.010$, generated stego image is shown in Fig. 5c.

The performance of the proposed technique is also evaluated and compared using the existing chaotic map-based technique [23] for different cover image and secret image as shown in Table 2. It can be observed from the table that the proposed hybrid chaotic map-based technique gives better PSNR than the existing chaotic map-based steganography technique. The NCC ≈ 1 shows that the generated stego image and

Fig. 5 **a** Secret image boat **b** hybrid chaotic map scrambled secret image boat **c** stego image

Table 2 PSNR and NCC of different cover image and Boat.jpeg as secret image on alpha = 0.010

Cover image	PSNR			NCC		
	Chaotic map [23]	DDWT [28]	Proposed technique	Chaotic map [23]	DDWT [28]	Proposed technique
Baboon	44.53	43.32	44.9402	–	0.9902	0.9910
Flower	43.98	44.15	44.2384	–	0.9913	0.9901
Lena	44.54	43.82	44.8296	–	0.9906	0.9902
Airplane	44.42	43.69	44.6328	–	0.9904	0.9927

cover image are almost similar. The performance comparison of PSNR and NCC of different stego images is drawn in Figs. 6 and 7, where Fig. 7 is representing the graph between the PSNR value of existing and proposed techniques and NCC plot between existing technique and proposed technique is shown in Fig. 7.

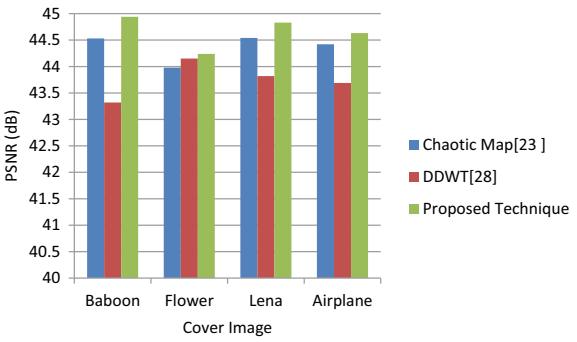

Fig. 6 PSNR of different cover images and Boat as secret image

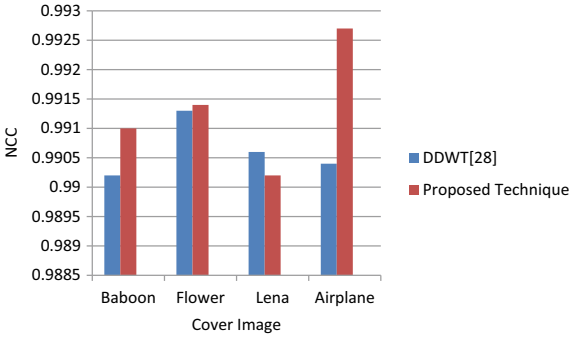

Fig. 7 NCC of different cover images and Boat as secret image

6.2 Computational Time Complexity Analysis

The time complexity of the proposed technique depends upon the time complexities of all the sub-processes involved in the algorithm. The time complexity of the embedding process on the input image of size $(m \times n)$ can be calculated as follows.

$$T_{\mathrm{S}}(m,n) \leq T_{\mathrm{Hybrid}}(m,n) + T_{\mathrm{SGWT}}(m,n) + T_{\mathrm{Alpha}B}(m,n) + T_{\mathrm{ISGWT}}(m,n)$$

$$T_S(m,n) \leq O(m*n) + O(\max(m,n)) + O(m*n) + O(\max(m,n))$$

Let $m = n$

$$T_S(n) \leq n*n + n + n*n + n$$

$$T_S(n) \leq 2n^2 + 2n$$

$$T_S \leq 2n^2 + 2n$$

$$T_S(n) \leq 3n^2$$

$$\text{For } n \geq 1, \quad C = 3$$

$$T_S(n) \leq Cn^2$$

$$T_S(n) = O(n^2)$$

From above derivation, it is proved that the total time taken by the algorithm is $O(n^2)$. The time complexity to compute various wavelet transforms are described in [35].

7 Conclusion

Steganography offers a way to hide the information. In this paper, we proposed a hybrid chaotic map-based steganography technique using spectral graph wavelet. In this technique, first hybrid chaotic map-based scrambling technique is generated, the method is the composition of Henon and Duffing map; then, the secret message is first scrambled using the proposed chaotic approach. The cover and scrambled secret image is transformed using spectral graph wavelet (SGWT). The transformed images are blended using alpha blending to mix the images and inverse SGWT is

performed to generate the stego image. The process is just reversed to extract the hidden secret image. The investigation is carried out on different cover images and observation is made that the proposed method gives good PSNR and NCC than the existing technique.

References

1. De Leeuw K, Bergstra J (2007) The history of information security. Elsevier, Burlington
2. Mielikainen J (2006) LSB matching revisited. IEEE Signal Process Lett 13(5):285–287
3. Kuhn M (1996) Information hiding. In Proceedings of the First International Workshop on Information Hiding
4. Johnson N, Duric Z, Jajodia S (2003) Information hiding. Kluwer Academic, Boston
5. Simmons G (1983) The prisoners' problem and the subliminal channel. In Proceedings of CRYPTO: advances in Cryptology, pp 51–67
6. Morkel T, Eloff JHP, Olivier MS (2015) An overview of image steganography. In: Proceedings of fifth annual information security South Africa Conference, June
7. Kumar V, Kumar D (2010) Performance evaluation of DWT based image steganography. In: IEEE 2nd International Advance Computing Conference, pp 223–228, Feb 2010
8. Mahajan P, Gupta H (2016) Improvisation of security in image steganography using DWT, huffman encoding & RC4 based LSB embedding. In: IEEE International conference on computing for sustainable global development (INDIACom), pp 523–529, Feb 2016
9. Shejul AA, Kulkarni UL (2010) A DWT based approach for steganography using biometrics. IEEE international conference on data storage and data engineering, pp 39–43, Feb 2010
10. Patel H, Dave P (2012) Steganography technique based on DCT coefficients. Int J Eng Res Appl 2(1):713–717
11. Rabie T (2012) Digital image steganography, an FFT approach. In: Proceedings of networked digital technologies: 4th international conference, pp 217–230, Dubai, Apr 2012
12. Chan CK, Chang LM (2003) Hiding data in image by simple LSB substitution. Pattern Recogn 37:469–474
13. Abdelwahab AA, Hassan LA (2008) A discrete wavelet transform based technique for image hiding. In: Proceedings of 25th national radio science conference, pp 1–9, Egypt
14. Kumar V, Kumar D (2010) Digital image steganography based on combination of DCT and DWT. In: Das VV, Vijaykumar R (eds) Information and communication technologies, Kochi
15. Al-Ataby A, Al-Naima F : A modified high capacity image steganography technique based on wavelet transform. Int Arab J Info Technol 7(4):358–364 (2010)
16. Masaebi S, Moghaddam AME (2012) A new approach for image hiding based on contourlet transform. Int J Electric Comput Eng 2(5):699–708
17. Narasimmalou T, Joseph AR (2012) Optimized discrete wavelet transform based steganography. In: Proceedings of IEEE international conference on advanced communication control and computing technologies, pp 88–89, Ramanathapuram
18. Raftari N, Moghadam AME (2012) Digital image steganography based on assignment algorithm and combination of DCT-IWT. In: Proceedings of international conference on computational intelligence, communication systems and networks, pp 295–300, Phuket
19. Ioannidou A, Halkidis ST, Stephanides G (2012) A novel technique for image steganography based on high payload method and edge detection. Expert Syst Appl 39:11517–11524
20. Hemalatha S, Acharya UD, Renuka A, Kamath PR (2013) A secure and high capacity image steganography technique. Sign Image Proc 4:83–89
21. El-Emam N, Al-Zubidy R (2013) New steganography algorithm to conceal a large amount of secret message using hybrid adaptive neural networks with modified adaptive genetic algorithm. J Syst Softw 86:1465–1481

22. Singh S, Singh R, Siddiqui TJ (2015) Singular value decomposition based image steganography using integer wavelet transform. In: Proceedings of international symposium on signal processing and intelligent recognition systems, pp 593–601, Trivandrum
23. Rajendran S, Doraipandian M (2017) Chaotic map based random image steganography using LSB technique. Int J Netw Secur 19(4), 593–598
24. Kartik S, Ashutosh A, Tanay S, Deepak G, Ashish K (2019) Hiding data in images using cryptography and deep neural network. J Artif Intell Syst 1:143–162 (2019). https://doi.org/10.33969/AIS.2019.11009
25. Sahu AK, Swain G (2019) A novel n-rightmost bit replacement image steganography technique. 3D Res 10:2. https://doi.org/10.1007/s13319-018-0211-x
26. Roselin Kiruba R, Sree Sharmila T (2021) Secure data hiding by fruit fly optimization improved hybridized seeker algorithm. Multidim Syst Sign Process 32:405–430
27. Muhuri PK, Ashraf Z, Goel S (2020) A novel image steganographic method based on integer wavelet transformation and particle swarm optimization. Appl Soft Comput J. https://doi.org/10.1016/j.asoc.2020.106257
28. Vijay S, Srivastava D, Pratistha M (2020) A Daubechies DWT based image steganography using smoothing operation. Int Arab J Inf Technol 17:154–161
29. Hammond DK, Vandergheynst P, Gribonval R (2019) The spectral graph wavelet transform: fundamental theory and fast computation. Ljubisa Stanković, Ervin Sejdić. In: Vertex-frequency analysis of graph signals, signals and communication technology. 978-3-030-03574-7. Springer International Publishing, pp 141–175
30. Ortega A, Frossard P, Kovačević J, José M, Moura F, Vandergheynst P (2018) Graph signal processing: overview, challenges, and applications. Proc IEEE 106(5)
31. Hénon M (1976) A two-dimensional mapping with a strange attractor. Commun Math Phys 50(1):69–77
32. Mishra M, Mankar VH (2012) Chaotic cipher using arnolds and duffings map. In: Wyld JZ, Nagamalai D (eds) Advances in computer science, engineering & applications, Dvol. 167 of Advances in intelligent systems and computing, pp 529–539. Springer, Berlin
33. Khalili M, Asatryan D (2013) Colour spaces effects on improved discrete wavelet transform-based digital image watermarking using Arnold transform map. IET Signal Process 7:177–187
34. Cheddad A, Condell J, Curran K, Kevitt PM (2010) Digital image steganography: survey and analysis of current methods. Signal Process 90:727–752
35. Jebamalar Leavline E, Sutha S, Asir Antony Gnana Singh D (2013) An analysis of computtional complexity of multiscale image representation schemes. In: National conference on emerging trends in electrical and electronics engineering, At University College of Engineering Panruti, Tamilnadu, India, Mar 2013

A Comprehensive Review on Fast Charging Stations Deployment for Electric Vehicles

Shakti Vashisth, Praveen Kumar Agrawal, Nikhil Gupta, K. R. Niazi, and Anil Swarnkar

Abstract The depletion of fossil fuels, strict environmental laws, and advancements in electric motors and storage technologies envisages the global acceptance of electric vehicles (EVs). The high growth in EVs may be expected in near future on account of fast and smooth acceleration, pollution-free operation, low running, and maintenance costs. The growing market of EVs imposes challenges behind the integration of fast charging stations (FCSs) in present distribution systems. Since EVs poses significant loading on the distribution systems, their integration alters distribution flows. This may reflect a negative impact on efficiency, node voltage, load profiles, reliability, protection, and security of the distribution system unless FCSs being allocated by considering these vital issues related to the system operation. A lot of work has been reported in the literature about the allocation of FCSs while addressing a variety of objectives and is successfully solved using different optimization techniques. This paper attempts to provide a brief literature review and an overview of recent research directions about the allocation of FCSs in primary distribution systems. The paper also throws some light on the impacts and issues of EVs integration which may be commonly confronted during system operation and also presents some futuristic directions for further research in this area.

Keywords Distribution systems · Electric vehicles · Fast charging stations

1 Introduction

In recent years, transportation sector is having a major shift from conventional vehicles to electric vehicles (EVs). One of the significant reasons for this is the deterioration in the air quality index due to the pollution caused by the combustion of the fossil fuels [1–3]. Moreover, most of the countries such as India need to import crude oil from other countries at higher prices. Therefore, the use of gasoline for

S. Vashisth (✉) · P. K. Agrawal · N. Gupta · K. R. Niazi · A. Swarnkar
Malaviya National Institute of Technology, Jaipur, India
e-mail: shaktivashistha@gmail.com

© The Author(s), under exclusive license to Springer Nature Singapore Pte Ltd. 2022

A. Tripathi et al. (eds.), *Intelligent Computing Techniques for Smart Energy Systems*,
Lecture Notes in Electrical Engineering 862,
https://doi.org/10.1007/978-981-19-0252-9_21

conventional vehicles is not only having adverse effects on environment but also have considerable running cost [4]. EVs on the other hand are the optimal solution for the above problems posed by the conventional vehicles. In addition, they are capable of delivering, sometimes, stored power to the grid. With the introduction of net metering, the EV owner can gain significant financial gains against the power sold to the grid. Since EVs usually employ highly efficient lithium-ion batteries, their running cost is low and distance covered in a single charge is noteworthy [5]. The other important benefit of EVs is that it has fewer moving parts in comparison to the conventional vehicles. This is due to the absence of internal combustion engines. Fewer moving parts results in lower maintenance cost. Hence, from the above discussion, it can be stated that EVs will be the main contributor for road transportation on account of economy, robustness, and environmental concerns. Due to the rapid growth of EVs, there is an urgent need for extensively distributed publicly accessible charging stations (CSs) that supplies electrical energy for recharging an EV battery [6].

Though EVs can be charged at residential or official parking bays from low voltage (LV), charging time is substantial. Moreover, the secondary distribution should be adequately designed to allow such operations. On the other hand, charging time is considerably reduced if EVs are charged through fast charging stations (FCSs) as it provide charging at medium voltage (MV). Such FCSs refer to direct current charging station (DC-CS) with nominal power greater or equal to 50 kW [7]. The time necessary for fast charging is about 20 min for charging up 80% capacity of the EV battery [8]. Thus, the total traveling distance of EVs can be greatly extended. Moreover, to reduced charging time, FCS can also assist EV owners during contingencies in the midway [6].

In many countries, FCS infrastructure is developing rapidly. To promote manufacturing of FCSs and adoption of EVs, the Government of India has taken several initiatives for ensuring safe, reliable, and affordable charging infrastructure including the subsidies on the purchase of EVs, which is a major step toward the promotion of these vehicles [9]. Also, charging reasonable tariff from the CS owners is another step toward motivating the businessmen and entrepreneurs to set up CSs at diverse locations of the country.

Plenty of research work has been reported in the area of planning and allocation of FCS, considering several issues and concerns while optimizing a variety of objectives using different optimization techniques. This paper presents a comprehensive literature review pertaining to FCS allocation, highlighting its impact on contemporary distribution systems, and discusses the challenges to be faced by distribution systems owning to installation of FCS. The paper also throws some light on the future excursions of the current research while considering more realistic issues of distribution systems with FCSs.

2 Planning of Fast Charging Station

Appropriate planning of FCS plays most significant role to enable large-scale EV penetration. Primary step for planning is site selection for developing infrastructure. A proper site selection improves the service quality and operational efficiency of FCS. It basically depends upon social, technical, economic, and environmental perspectives [2, 10]. One of the major social perspective, for FCS planning is population density which ought to be determined before selection of site, i.e., number of EVs should be known passing through that area which can be calculated by using closed-circuit television (CCTV) cameras and global positioning system (GPS) [11]. Population density helps to determine the most suitable location and FCS capacity. Generally, more dense areas and highways are preferable places for locating FCSs. Also, service level, traffic convenience, and location safety are the other important social aspects to be considered.

Technical perspectives consider the capacity of distribution system [12] that includes capacity of lines, transformers, switchgears, and protective devices. The site selection of FCS affects line losses, node voltage profile, and line flows. Furthermore, the coordination of existing distributed energy resources (DERs) and expected grid power transactions should be taken into account while planning infrastructure for FCSs.

Economic perspectives also play an important role in FCS planning; therefore, analysis of the total investment cost becomes significant. Investment cost for deploying FCS includes initial investment cost, operating cost, and maintenance cost. Initial cost can further be categorized into land acquisition cost, infrastructure cost etc. Operating cost includes energy and switching loss cost while maintenance cost incorporates converters, batteries, and other infrastructural maintenance expenses [6].

Environmental impacts consist of the waste disposal problem, ground water destruction, and greenhouse gas emission issues [2, 10] which if not addressed appropriately may lead to environmental hazards. It has been broadly projected that by the current degree of acceptance, most of conventional vehicles in India would be replaced by EVs in the near future. Therefore, in order to assist EV charging during the long road trips, government has proposed to construct a FCS at every 100 km on each side of the highway [9].

3 Impact of EVS on Distribution Systems

Recent studies have shown that EVs have significant impact on existing power distribution systems.

- As EVs are increasing rapidly, significant additional load is subjected to the distribution system. This surplus load leads to a substantial variation in load profile and may increase the peak demand of the system which can cause threat to the security of the power system [12, 13].

- EVs also can create reverse power flow in distribution systems. The bi-directional flow of power has some significant impacts on the following characteristics of distribution system, viz. load profile, load factor, and uncontrolled peak demand, change in voltage levels, violation of statutory limits, and voltage imbalance [14, 15].
- As load increases, the corresponding load factor, defined as the ratio of average load to the peak load, gets reduced [13]. Load factor is a measure of utilization rate of electrical energy usage, and that is why, reduced load factor indicates that load is not using electric system efficiently.
- As the mathematical perspective, EV charging systems are non-linear in nature which creates harmonic pollutions in the grid, and consequently, RMS value of current gets increased leading to the power losses in the distribution feeders [16].
- The deviation in voltage at the bus affects the reliability of the network which may deteriorate the system performance [10, 17, 18].
- Uncoordinated charging of EVs plays significant role to raise peak demand of the system which can be vulnerable for the security of the system.

4 Issues with Deployment of Fast Charging Stations

Deployment of FCSs at a particular location shall motivate EV procurement, convenient vehicle charging, employment opportunities to the individuals etc. However, their installation requires a huge investment. Moreover, FCS installation poses certain issues, which need to be resolved for their successful operation. Few of the major concerns have been discussed below.

- The projected high penetration levels of EVs and the necessity for wide deployment of fast charging facilities will introduce large loads on the distribution system [19]. Moreover, uncontrolled EV charging may increase stress on the system which if not addressed in time may lead to grid failure [11].
- In order to satisfy the increased load demand, further expansion or up gradation of network will be required [7], which demands a huge investment cost.
- Determination of charge scheduling policies in order to mitigate the negative impacts of the additional EV load on the grid, such as deterioration of power quality, transformer overloads, and peak load increment could be a major challenge [20].
- Lithium ion battery takes approximate 15 min to charge 80% of its capacity if battery is not over loaded, whereas gasoline vehicles takes 5 min to charge completely thus charging time is still higher than conventional vehicles [21].
- Since, EVs' fast charging duration is long in comparison to the duration of refilling conventional vehicles. This may lead to the formation of queues and long delays to the EV owners [22].
- In order to reduce waiting time of EVs drivers, FCS should have multiple outlets [22] which makes the FCS expensive to install initially.

- Charging infrastructure highly depends on electricity prices and battery sizes which will possibly rise in the future [23]. Higher running cost may adversely affect the popularity of EVs in the market.
- For installing a FCS, service providers must go through a proper procedure. The FCS owner needs to take the permission of the utility, local government, and business owners, which may take considerable amount of time. Therefore, FCS installation is a time-consuming process and can frustrate the FCS owner [21].

5 Recent Trends

In previous works, diverse objectives in context of FCS installation have been reported, such as minimization of the FCSs deployment cost [6, 16, 19, 24, 25], energy loss cost [6, 16, 19], maximization of flexibility of distribution system [18], voltage profile improvement [19], minimization of customer's waiting time [22, 26], minimization of social cost by reducing the distance traveled for charging EVs [24], enhancement of fast charging service capacity [27], maximization of convenience of EVs owners [6, 16], peak load minimization using battery energy storage (BESS) [5], convenience of FCS planner [8], improvement in the economics, and flexibility of EV charging station using BESS and demand response program [28]. The planning problem of FCS is solved by suggesting suitable single or multiple objectives and is solved using a variety of potential metaheuristic techniques, e.g., genetic algorithm (GA) [14], binary lighting search algorithm (BLSA) [16], cooperative co-evolutionary genetic algorithm [19], binary particle swarm optimization(BPSO) [20, 29], and binary firefly algorithm (BFA) [6].

From the discussions in the previous sections, it can be concluded that planning of FCS requires an appropriate location that can be determined by various factors like traffic density, distribution system capacity, cost of the appropriate location etc. Various methodologies have been proposed for solving issues related to these factors such as in [10], the authors proposed Bayesian network model for FCS site selection considering uncertainties, risks, qualitative, and quantitative factors. Moreover, a sensitivity analysis was performed regarding environmental, social, economic, and technical criteria, and it was concluded that technical and environmental criteria have the largest and lowest impacts, respectively, on the probability of site selection. In [11], a spatial and temporal model EV charging demand for a rapid CS located near highway exit is developed. The model is based on fluid dynamics traffic model and M/M/s queuing theory considering EVs charging demand which varies in space and time. Therefore, this model provides the coordination among neighboring utilities and may help distribution utility planners to identify charging demand for a specific charging location. Rural planner can also identify location and size of FCS on a highway. In [16], binary lightning search algorithm has been used to optimize the location and sizing of the FCS while considering build up cost, battery state of charge, road traffic density, transmission loss, and grid power losses. In [25], the modeling of a fast DC charging EV station with vehicle to grid (V2G) capability

has been presented and a strategy for charging station placement in a distribution system without hindering the reliability, and quality of the power is proposed. The FCS planning is a very complex and combinatorial problem due to having various techno-economic objectives. In [8], they proposed a simplified analytical approach which provides a few set of alternative attributes to the FCS planner so that an appropriate decision can be made while planning of FCS deployment. The proposed analytical approach eliminates the need of optimization techniques.

The other important parameter for the FCS installation is the estimation of the investment cost. The FCS owner will definitely try to minimize the investment cost of the charging station. Many research works focused in the direction of minimizing the various costs in order to set up a charging station with greater economy. Several researchers worked on minimizing the initial investment, energy loss, maintenance, operating costs etc. In [14], a day-ahead optimal network reconfiguration has been utilized to reduce the operation cost of the distribution system by alleviating the negative impact of EV integration, i.e., power and switching losses. GA has been utilized to optimize the performance of the distribution system. In [18], it has been observed that energy storage capability of electric vehicle mobility (EVM) fleets could mitigate the intermittency of wind generation and enhance system reliability as well as to reduce operation costs and increase the system flexibility by providing energy and ancillary services to the grid. In [19], a scenario-based planning of FCS has been developed while considering network reconfiguration for reducing the energy loss cost and improving the voltage profile using cooperative co-evolutionary genetic algorithm (CCGA). After establishment of FCS, the basic problem faced by most of the countries is the congestion in traffic due to queuing of vehicles at the charging stations. Due to this, waiting time gets increases which leads to frustration in EV drivers. Therefore, it becomes important to identify the means to reduce the waiting time of the EV owners. A few of the works addressed this problem by increasing the mobility of vehicle's charging. In [7], a specific study is performed to quantify the impact of the FCS and to identify the most suitable planning solutions needed to boost electric mobility and allow the effective integration of EVs on a real MV distribution system of the A2A utility situated in Italy. In [22], authors proposed a FCS model which provides multiple outlets (AC or DC) for charging EVs' according to their design. This is done in order to reduce the density of EVs waiting in a single queue. This paper also proposes new pricing policy with an aim to increase the operator's financial benefit and reducing the customers' waiting time simultaneously. According to this policy, FCS operator sets a threshold level of energy and increases the price for per obtained kWh if customers request to charge their batteries more than the threshold level. This scheduling mobile charging station (MCSs) to service the additional EVs during increased demand is proposed. MCS is a vehicle which carries large number of batteries for energy storage and can charge a number of EVs. Hence, MCS can be helpful to reduce the waiting time of EVs at fixed CS and can provide assistance to various EV owners at different spots while driving on highways.

A forthcoming technology to reduce customer waiting time is battery swapping. Battery swapping station (BSS) charges the batteries at off peak time and prepares them to be swapped in a considerably less time. They can potentially provide unique

benefits to the power system. In [26], a model for the scheduling of battery charging from the CS owner perspective is proposed. This paper also investigates the benefits of building the BSS from various perspectives. A concept of queuing theory for determining the arrival rates of EVs is becoming more popular and is a commonly used method. Certain research works focus on reducing the waiting time of EVs by enhancing their technical capabilities. The more profound use of digital technology can aid to the significant reduction in the waiting period of EVs. In [30], application of mobile Internet in identifying the parking space for the EVs in FCS has been introduced. The methodology suggests the generation of QR code for each vehicle which is scanned at the FCS and thereby assists dynamic parking space, routing guidance, orderly parking, vehicle charging, and card-free billing on the basis of time-of-use (TOU) strategy which increases the comfort of EV's driver. In [31], two types of algorithms have been proposed for selecting FCS while driving on the highway. First algorithm exploits local information of an EV, and second algorithm exploits the global information. Global information can be obtained through interactions between the EVs and a global CS selection server over the mobile telecommunications network. It has been concluded that the global information-based algorithm provides better solution to identify the workload status of each FCS, and therefore, drivers can reduce their waiting time while charging EVs. In [5], authors addressed the additional load demand of EV fast charging loads by integrating BESS within the FCS. This integration improves the operation of power system, relieves power congestion, and reduces the peak demand. On the other hand, implementation of demand response programs are also most effective solutions to reduce the peak load [32, 33]. In [28], an optimal decision-making model has been proposed coordinated with BESS. Moreover, participation of EV charging station in emergency demand response is also incorporated in order to improve the flexibility and economics of the charging station.

6 Conclusions and Future Directions

Deployment of FCS requires smart infrastructure for its smooth operation. The major infrastructural modifications are required in the existing distribution systems such as setting up new substations and reinforcement of feeders. Also, a suitable location for FCS installation is crucial considering the population density or traffic density. Upgradation of distribution system and land acquisition demands an enormous investment cost which becomes a major concern for the FCS owner. Moreover, few other important factors such as customers' convenience and owner's benefits cannot be ignored. In this work, a comprehensive literature review has been performed in order to bring insights of the upcoming challenges and concerns while planning the installation of a FCS.

Moreover, the paper also addresses few operational issues while setting up a FCS. FCSs poses significant fast varying loading which may adversely affect efficiency, power quality, reliability, and security of the distribution system besides their smooth

functioning and operations. The coordinated operation and planning of available energy resources may provide help in system operation but practically increases complexity and additional cost on control equipment, communication infrastructure, etc. However, price-based demand response programs may provide amicable means as they can diversify loading of FCSs which may be explored in future research. Moreover, new tariff structures may be evolved for FCSs as being one of the highly commercial activities with the aim of better network operations. On the other hand, conventional operational strategies such as network reconfiguration and on-load tap changers may also be explored. In this context, the distribution system expansion planning may also be investigated by erecting new tie-lines, new transformers, or the capacity enhancements of lines and transformers. Finally, new strategies may be developed and investigated to reduce the waiting period of EVs up to the convenience of customers.

References

1. Yang Q, Sun S, Deng S, Zhao Q, Zhou M (2018) Optimal sizing of PEV fast charging stations with Markovian demand characterization. IEEE Trans Smart Grid 10(4):4457–4466
2. Guo S, Zhao H (2015) Optimal site selection of electric vehicle charging station by using fuzzy topsis based on sustainability perspective. Appli Energy 158:390–402
3. Pal R, Chavhan S, Padmanaban S, Sayeed S (2021) A comprehensive analysis of electric vehicle charging station infrastructure in an urban area
4. Tie SF, Tan CW (2013) A review of energy sources and energy management system in electric vehicles. Renew Sustain Energy Rev 20:82–102
5. Gjelaj M, Arias NB, Traeholt C, Hashemi S (2019) Multifunctional applications of batteries within fast-charging stations based on EV demand-prediction of the users' behaviour. J Eng 18:4869–4873
6. Islam MM, Mohamed A, Shareef H (2015) Optimal allocation of rapid charging stations for electric vehicles. In: 2015 IEEE student conference on research and development (SCOReD), pp 378–383. IEEE
7. Celli, G, Mocci S, Pilo F, Soma GG, Cicoria R, Mauri G, Fasciolo E, Fogliata G (2013) Distribution network planning in presence of fast charging stations for EV
8. Vashisth S, Agrawal PK, Gupta N, Naizi K, Swarnkar A (2020) PEV traffic-based planning attributes for fast charging stations. In: 2020 IEEE 17th India Council International Conference (INDICON). IEEE, pp 1–7
9. Amendments in model building bye-laws (MBBL—2016) for electric vehicle charging infrastructure. Retrieved 14 Sept 2019. [Online Available]. http://mohua.gov.in/upload/whatsnew/5c6e472b20d0aGuidelines
10. Hosseini S, Sarder M (2019) Development of a Bayesian network model for optimal site selection of electric vehicle charging station. Int J Electr Power Energy Syst 105:110–122
11. Bae S, Kwasinski A (2011) Spatial and temporal model of electric vehicle charging demand. IEEE Trans Smart Grid 3(1):394–403
12. Jin X, Yu T, Wang X, Li S, Pu T (2016) A reconfiguration strategy for active distribution network with electric vehicles. In: 2016 International conference on smart grid and clean energy technologies (ICSGCE). IEEE, pp 155–160
13. Chang RF, Chang YC, Lu CN (2012) Loss minimization of distribution systems with electric vehicles by network reconfiguration. In: 2012 International conference on control engineering and communication technology. IEEE, pp 551–555

14. Melo DFR, Leguizamon W, Massier T, Gooi HB (2017) Optimal distribution feeder reconfiguration for integration of electric vehicles. In: 2017 IEEE PES innovative smart grid technologies conference-Latin America (ISGT Latin America). IEEE, pp 1–6
15. Putrus G, Suwanapingkarl P, Johnston D, Bentley E, Narayana M (2009) Impact of electric vehicles on power distribution networks. In: 2009 IEEE vehicle power and propulsion conference. IEEE, pp 827–831
16. Islam MM, Shareef H, Mohamed A (2018) Optimal location and sizing of fast charging stations for electric vehicles by incorporating traffic and power networks. IET Intell Transp Syst 12(8):947–957
17. Clement-Nyns K, Haesen E, Driesen J (2009) The impact of charging plug-in hybrid electric vehicles on a residential distribution grid. IEEE Trans Power Syst 25(1):371–380
18. Nikoobakht A, Aghaei J, Niknam T, Farahmand H, Korpås M (2019) Electric vehicle mobility and optimal grid reconfiguration as flexibility tools in wind integrated power systems. Int J Electr Power Energy Syst 110:83–94
19. Pahlavanhoseini A, Sepasian MS (2019) Scenario-based planning of fast charging stations considering network reconfiguration using cooperative coevolutionary approach. J Energy Storage 23:544–557
20. Paudel A, Supingklad W, Ongsakul W (2016) Distribution network reconfiguration to support electric vehicles integration. In: 2016 International conference on cogeneration, small power plants and district energy (ICUE). IEEE, pp 1–6
21. The challenges of EV charging: 10 things to know. Retrieved 14 Sept 2019. [Online Available]: https://www.techrepublic.com/article/the-challenges-of-ev-charging-10-things-to-know/
22. Zenginis I, Vardakas J, Zorba N, Verikoukis C (2017) Performance evaluation of a multi-standard fast charging station for electric vehicles. IEEE Trans Smart Grid 9(5):4480–4489
23. Gnann T, Funke S, Jakobsson N, Plötz P, Sprei F, Bennehag A (2018) Fast charging infrastructure for electric vehicles: today's situation and future needs. Transp Res Part D Transp Environ 62:314–329
24. Xiong Y, Gan J, An B, Miao C, Bazzan AL (2017) Optimal electric vehicle fast charging station placement based on game theoretical framework. IEEE Trans Intell Transp Syst 19(8):2493–2504
25. Archana A, Rajeev T (2020) Reliability index based approach for allocating EV charging station in a distribution system. In: 2020 IEEE international conference on power electronics, smart grid and renewable energy (PESGRE2020). IEEE, pp 1–6
26. Mahoor M, Hosseini ZS, Khodaei A, Kushner D (2017) Electric vehicle battery swapping station. arXiv preprint arXiv:1710.06895
27. Chauhan V, Gupta A (2018) Scheduling mobile charging stations for electric vehicle charging. In: 2018 14th International conference on wireless and mobile computing, networking and communications (WiMob), pp 131–136. IEEE
28. Wang J, Wu D, Zhao W, Shi S, Upadhaya B, Shi Y (2020) Queueing theory-based optimal decision-making model of battery energy storage-assisted fast charging station participating in emergency demand response. In: 2020 IEEE sustainable power and energy conference (iSPEC). IEEE, pp 2110–2115
29. Singh G, Swarnkar A, Gupta N, Niazi K (2020) A review of scheduling techniques and communication protocols for smart homes capable of implementing demand response. Intell Comput Tech Smart Energy Syst 505–513
30. Liu J (2017) Research and implementation of electric vehicle fast charging station parking guidance system based on mobile terminal. In: 2017 9th International conference on intelligent human-machine systems and cybernetics (IHMSC), vol 1. IEEE, pp 230–233
31. Yang SN, Cheng WS, Hsu YC, Gan CH, Lin YB (2013) Charge scheduling of electric vehicles in highways. Math Comput Model 57(11–12):2873–2882
32. Sharma B, Gupta N, Niazi K, Swarnkar A, Vashisth S (2019) Demand response in the global arena: Challenges and future trends. In: 2019 8th International conference on power systems (ICPS). IEEE, pp 1–5
33. Sharma B, Gupta N, Niazi K, Swarnkar A (2020) Demand response in distribution systems: a comprehensive review, pp 565–572

Effect of Noise on Concurrence of Compact Photonic CNOT Gate Designed Using Universal Cloner

Amit Kumar Sharma, Shishir Kumar Sharma, and Ritu Sharma

Abstract In this paper a two Qubit deterministic compact photonic CNOT gate is analyzed under noisy conditions. Concurrence of the designed compact photonic CNOT gate has been calculated with and without noise parameter. The behavior of this gate is universal. The feasibility of the scheme by observing variation in concurrence with different system parameters are assessed and reported. In strong ($g/k = 2.4$ and $k_s/k = 0.05$) and weak ($g/k = 0.1$ and $k_s/k = 0.01$) coupling condition the concurrence calculated is 0.01441 and 0.753, respectively. Under noisy environment the computed concurrence in strong ($g/k = 2.4$ and $k_s/k = 0.05$) and weak ($g/k = 0.3$ and $k_s/k = 1$) coupling condition is 0.1231 and 0.5265, respectively.

Keywords CNOT gate · Photonic qubits · Concurrence · Linear optics quantum computing (LOQC) · Quantum dot (QD)

1 Introduction

In the mid 1980s Richard Feynman and Yuri Manin coined the term quantum computing and communicated the possibility that a quantum computer can simulate the things that a classical computer proved unable. Recently, quantum phenomena's (Uncertainty, superposition and entanglement, etc.) have been investigated for computing and addressed significant computing problems such as quantum key distributions, quantum teleportation, Grover's algorithm (data base search) and Shor's algorithm (integer factorization). Nuclear magnetic resonance (NMR), Trapped ion, linear optics quantum computing (LOQC) and Quantum electrodynamics (QED) are the approaches which have been reported in literature for realizing quantum algorithms physically. LOQC can be employed for the designing of scalable quantum

A. K. Sharma (✉) · R. Sharma
ECE Department, MNIT, Jaipur, India
e-mail: amit250791@gmail.com

S. K. Sharma
B.S. Computer Engineering, Penn State University, University Park, Pennsylvania, USA

© The Author(s), under exclusive license to Springer Nature Singapore Pte Ltd. 2022

A. Tripathi et al. (eds.), *Intelligent Computing Techniques for Smart Energy Systems*, Lecture Notes in Electrical Engineering 862,
https://doi.org/10.1007/978-981-19-0252-9_22

computer utilizing linear optical elements. Photons are used as Qubits in the LOQC approach so that faster quantum communication and decoherence can be achieved [1–9]. In 2019 Aankur Saharia et al. presented a review article on linear optics quantum computing and established an elementary optical logic circuit [10]. In 2020 Min-Sung Kang et al. proposed a deterministic Fredkin gate using QD cavity unit, which can perform controlled swap operation between three Qubits [11]. It is difficult to design two Qubit quantum gates employing LOQC, as photon interaction is extremely challenging. The research presented in this paper will help researchers in exploring quantum circuits designed using QD cavity unit. A promising circuit (QD embedded inside a double sided optical cavity) as shown in Fig. 1, is explained and established as key component for all optical-based quantum computing, networking and memory. QD cavity acts as a spin-dependent beam splitter. It resolves the problem of photon interaction which is the main challenge in implementing two Qubit deterministic quantum circuits for photonic Qubits [13–19].

Two Qubit CNOT gate is universal gate that can be used to design any quantum circuit with help of one Qubit gates. Two Qubit CNOT gate is depicted in Fig. 2 'x' is control Qubit and 'y' is target Qubit. A 'NOT' operation will be performed on target Qubit only if control Qubit 'x' is 1, else it will remain unchanged [12].

The unitary matrix representation for ideal CNOT gate U is [12].

$$\text{CNOT}\,[U] = \begin{bmatrix} 1 & 0 & 0 & 0 \\ 0 & 1 & 0 & 0 \\ 0 & 0 & 0 & 1 \\ 0 & 0 & 1 & 0 \end{bmatrix} \tag{1}$$

In this paper analytical investigation of two Qubit photonic compact CNOT gate has been done under noisy condition and optimized parameters are calculated.

The CNOT gate is designed using QD within the double sided cavity depicted in Fig. 3. In this paper to describe the designed system the Heisenberg equations of

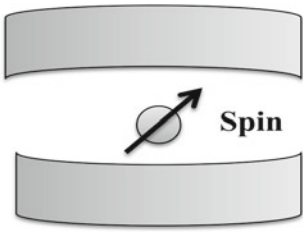

Fig. 1 QD within the double sided cavity [13]

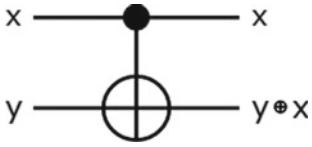

Fig. 2 CNOT [12]

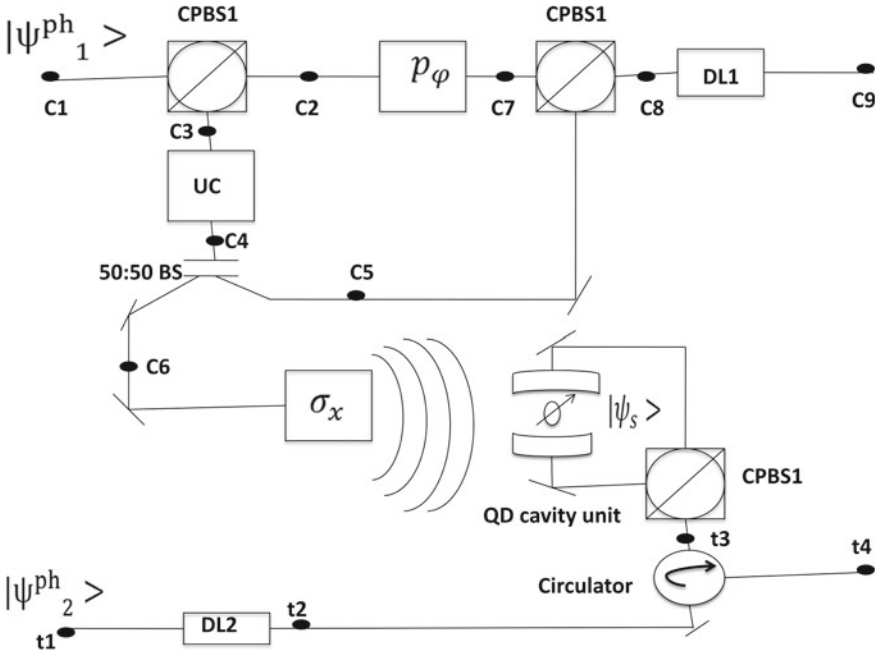

Fig. 3 CNOT gate designed using quantum dot inside double sided optical cavity [20]

motions are used. The Heisenberg equations of motions are expressed from Eq. (2–5) [13]

$$\frac{\mathrm{d}\hat{a}}{\mathrm{d}t} = -\left[i(w_c - w) + \frac{k}{2} + \frac{k_s}{2}\right]\hat{a} - g\sigma_- - \sqrt{k}\hat{a}_{\text{in}} \tag{2}$$

$$\frac{\mathrm{d}\sigma_-}{\mathrm{d}t} = -\left[i(w_X - w) + \frac{\gamma}{2}\right]\sigma_- - g\sigma_z\hat{a} \tag{3}$$

$$\frac{\mathrm{d}\sigma_z}{\mathrm{d}t} = 2g\left(\sigma_+\hat{a} + \hat{a}^+\sigma_-\right) - \gamma_{//}(1 + \sigma_z) \tag{4}$$

$$\hat{a}_{\text{out}} = \hat{a}_{\text{in}} + \sqrt{k}\hat{a} \tag{5}$$

where w, w_c, w_X are the frequencies of incoming photon, cavity and the transition, respectively. g is the coupling strength, k is the cavity field decay rate and k_s is the side leakage rate of the cavity field. $\gamma/2$ is the total QD dipole decay rate and $\gamma_{//}/2$ is the spontaneous emission rate. Dynamics of CNOT gate designed using cavity system can be found by solving master equation. Although, analytical solution of master equation is very difficult, quantum optics toolbox in MATLAB can be used to found density matrix of cavity Qubit system.

$$\frac{d\rho}{dt} = -i[H_{JC}, \rho] + (K + K_S)\left(\hat{a}\rho\hat{a}^{+} - \frac{1}{2}\hat{a}^{+}\hat{a}\rho - \frac{1}{2}\rho\hat{a}^{+}\hat{a}\right) + \gamma_{\prime\prime}\left(\hat{\sigma}_{-}\rho\hat{\sigma}_{+} - \frac{1}{2}\hat{\sigma}_{+}\hat{\sigma}_{-}\rho - \frac{1}{2}\rho\hat{\sigma}_{+}\hat{\sigma}_{-}\right) + \gamma^{*}\left(\hat{\sigma}_{z}\rho\hat{\sigma}_{z} - \rho\right) \tag{6}$$

Parameters are same as in Eq. (1)–(4). H_{JC} is the driven Jaynes—Cummings Hamiltonian.

$$H_{\mathrm{JC}} = (w_c - w)\hat{a}^{+}\hat{a} + (w_X - w)\sigma_{+}\sigma_{-} + ig\left(\sigma_{+}\hat{a} - \hat{a}^{+}\sigma_{-}\right) + i\sqrt{k}\hat{a}_{\mathrm{in}}\left(\hat{a} - \hat{a}^{+}\right) \tag{7}$$

Reflection ($R(\omega)$), transmission ($T(\omega)$), side and leakage ($S(\omega)$) and noise ($N(\omega)$) of QD cavity unit for hot cavity condition ($g \neq 0$) are expressed by Eq. (8)–(11) [13]

$$R(\omega) = \frac{i(\omega_c - \omega) + \frac{k_s}{2} + \frac{g^2}{i(\omega_{X^-} - \omega) + \frac{\gamma}{2}}}{i(\omega_c - \omega) + k + \frac{k_s}{2} + \frac{g^2}{i(\omega_{X^-} - \omega) + \frac{\gamma}{2}}} \tag{8}$$

$$T(\omega) = \frac{-k}{i(\omega_c - \omega) + k + \frac{k_s}{2} + \frac{g^2}{i(\omega_{X^-} - \omega) + \frac{\gamma}{2}}} \tag{9}$$

$$S(\omega) = \frac{\sqrt{k_s k}}{i(\omega_c - \omega) + k + \frac{k_s}{2} + \frac{g^2}{i(\omega_{X^-} - \omega) + \frac{\gamma}{2}}} \tag{10}$$

$$N(\omega) = \frac{\frac{ig\sqrt{\gamma k}}{i(\omega_{X^-} - \omega) + \frac{\gamma}{2}}}{i(\omega_c - \omega) + k + \frac{k_s}{2} + \frac{g^2}{i(\omega_{X^-} - \omega) + \frac{\gamma}{2}}} \tag{11}$$

Similarly these coefficients can be calculated for cold cavity case by putting g = 0.

2 Photonic Compact CNOT Gate

Schematic of compact CNOT gate designed using linear optical component, universal cloner and QD cavity system is shown in Fig. 3 [20]. Initially two photons 1 and 2 are prepared in states $\left|\psi_1^{ph}\right\rangle = \cos\theta_1|R_1\rangle + \sin\theta_1|L_1\rangle$ and $\left|\psi_2^{ph}\right\rangle = \cos\theta_2|R_2\rangle + \sin\theta_2|L_2\rangle$, and QD electron spin is initialized in state $|\psi^s\rangle = (|\uparrow_s\rangle$. Photon 1 is control photon (applied at $c1$ port) and photon 2 is target photon (applied at t1 port). Half wave plate (HWP) will work as Hadamard gate for right and left circular polarized quantum states. c-PBS is polarizing beam splitter which transmit right circular polarized photon ($|R\rangle$) and reflect left circular polarized photon ($|L\rangle$). σ_x transformation (apply only when control Qubit is in $|L\rangle$ state) is performed exactly

twice before and after target Qubit interact with QD cavity system and its action is to transform $|\uparrow_s\rangle \rightarrow |\downarrow_s\rangle$ $|\downarrow_s\rangle \rightarrow |\uparrow_s\rangle$. p_φ is applied to add negative sign to the input Qubit. Delay line, DL1 and DL2 are used to provide required delay to control and target Qubit. Circulator is used to separate input and output target quit from QD cavity. Universal cloner copies the input control Qubit.

The final output state $|\psi_t\rangle$ (photon 1 at c9 port and photon 2 at t4 port) of Compact CNOT gate under noisy conditions is given as

$$|\psi_t\rangle = n_1|R_1R_2> + n_2|R_1L_2> + n_3|L_1L_2> + n_4|L_1R_2> \tag{12}$$

The coefficients n_1, n_2, n_3 ad n_4 are expressed by Eq. (13)–(16)

$$n_1 = \cos\theta_1(\cos\theta_2 t_0 + \sin\theta_2 r_0) \tag{13}$$

$$n_2 = \cos\theta_1(\sin\theta_2 t_0 + \cos\theta_2 r_0) \tag{14}$$

$$n_3 = \sqrt{f_{uc}}\sin\theta_1(\sin\theta_2 t + \cos\theta_2 r) \tag{15}$$

$$n_4 = \sqrt{f_{uc}}\sin\theta_1(\cos\theta_2 t + \sin\theta_2 r) \tag{16}$$

3 Results and Discussion

For perfect CNOT gate operation, hot cavity must provide $R(\omega) = 1$ and $T(\omega) = 0$, and cold cavity must provide $R(\omega) = 0$ and $T(\omega) = 1$. But in practical case reflection and transmission coefficient depends on QD cavity parameters and input Qubits. Thus the performance and efficiency of the quantum gate will depend on input Qubits as well on cavity parameters. Amplitude and phase of reflection $R(\omega)$, transmission $T(\omega)$, leakage $S(\omega)$ and noise $N(\omega)$ coefficients are plotted (as shown from Figs. 4, 5, 6 and 7) with detuning $(\omega - \omega_c)/k$ parameter with $\gamma/k = 0.1$ for hot and cold cavity.

To measure the performance of the CNOT gate, the concurrence has been introduced]. The concurrence is used to quantify entanglement and indicates synchronization of output Qubits of CNOT gate and can be calculated by Eq. (17) [21]:

$$\text{Concurrence } (|\psi_t\rangle) = \left|\langle\psi_t|\,\tilde{\psi}_t\rangle\right| \tag{17}$$

here $|\psi t\rangle$ is the final state of the designed CNOT gate and $|\psi\tilde{}t\rangle$ is expressed by Eq. (18)

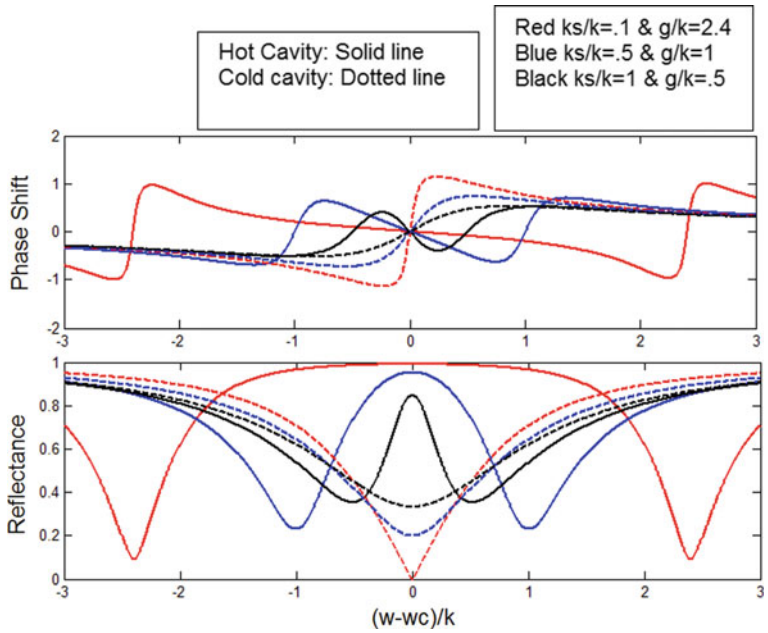

Fig. 4 Reflection coefficient $R(\omega)$ versus detuning $(\omega - \omega_c)/k$ with $\gamma/k = 0.1$ for hot and cold cavity

$$|\psi\tilde{}t\rangle = \sigma_y \otimes \sigma_y |\psi_t^*\rangle \tag{18}$$

Here σ_y is Pauli operator $\begin{bmatrix} 0 & -i \\ i & 0 \end{bmatrix}$ and $|\psi * t\rangle$ is $|\psi t\rangle$ with its amplitude complex conjugated.

It has been observed from Fig. 8 that concurrence is strongly correlated with coupling strength 'g' and cavity field decay rate 'k'. In strong ($g/k = 2.4$ and $k_s/k = 0.05$) and weak ($g/k = 0.1$ and $k_s/k = 0.01$) coupling condition concurrence calculated are 0.01441 and 0.53, respectively.

It can be seen form Fig. 9 that concurrence also depends on both normalized coupling strength 'g' and cavity field decay rate 'k'. In strong ($g/k = 2.4$ and $k_s/k = 0.05$) and weak ($g/k = 0.3$ and $k_s/k = 1$) coupling condition concurrence calculated are 0.1231 and 0.5265, respectively. Table 1 summarizes concurrence of Photonic Compact CNOT gate with and without noise under weak and strong coupling regime. Concurrence is strongly depending on noise parameter. Concurrence is achieving highest value in weak coupling condition for both noisy and without noisy cases.

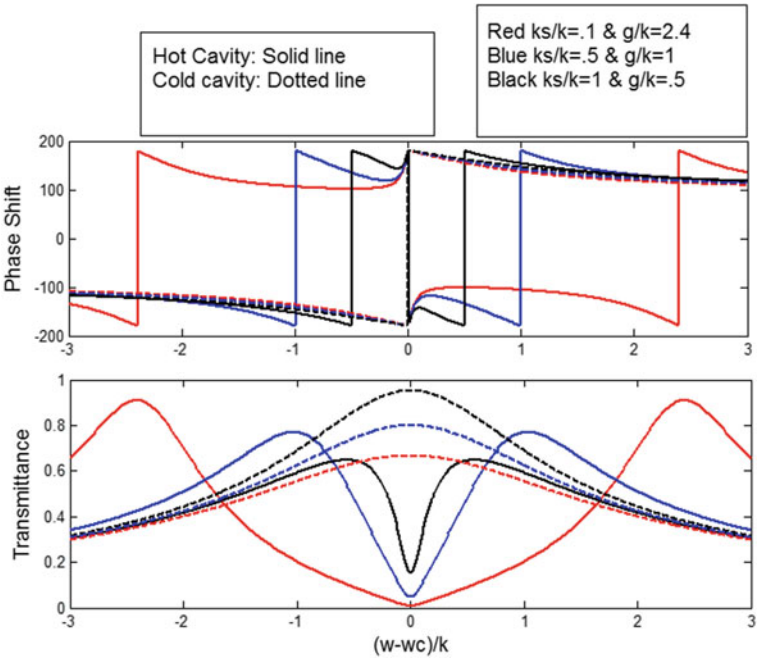

Fig. 5 Transmission coefficient $T(\omega)$ versus detuning $(\omega - \omega_c)/k$ with $\gamma/k = 0.1$ for hot and cold cavity

4 Conclusion

The result reported in this paper shows that coupling strength 'g' and cavity field decay rate 'k' greatly affects the concurrence of Photonic Compact CNOT gate. The desired concurrence can be achieved by optimizing the system parameters. The computed maximum concurrence is 0.753 at $g/k = 0.1$ and $k_s/k = 0.01$ without considering noise. The computed maximum concurrence is 0.5265 at ($g/k = 0.3$ and $k_s/k = 1$ with noise, which shows that noise greatly affect the performance of Compact CNOT gate. Compact CNOT gate is providing maximum concurrence only in weak coupling regime for both (with and without noise) the cases.

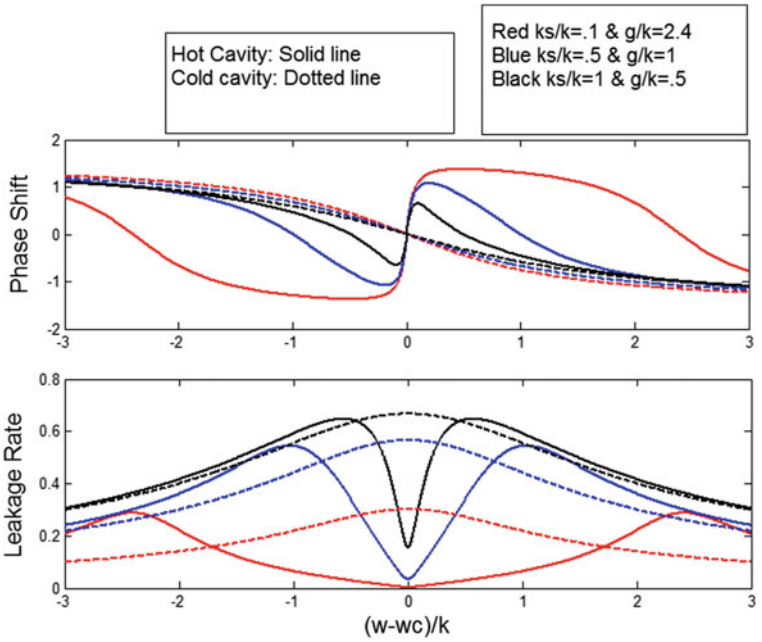

Fig. 6 Sideband leakage coefficient $S(\omega)$ versus detuning $(\omega - \omega_c)/k$ with for hot and cold cavity

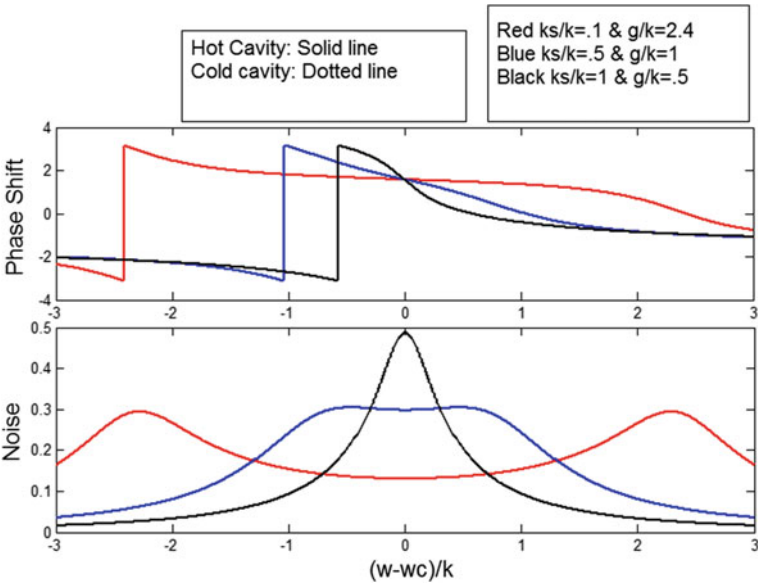

Fig. 7 Noise coefficient $N(\omega)$ versus detuning $(\omega - \omega_c)/k$ with $\gamma/k = 0.1$ for hot and cold cavity

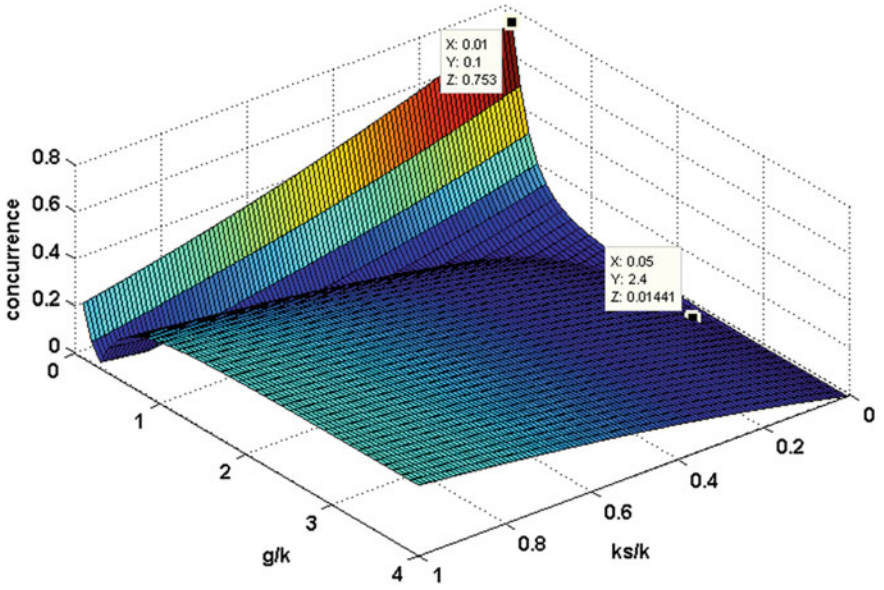

Fig. 8 Concurrence of photonic compact CNOT gate versus the coupling strength 'g' and cavity field decay rate 'k'

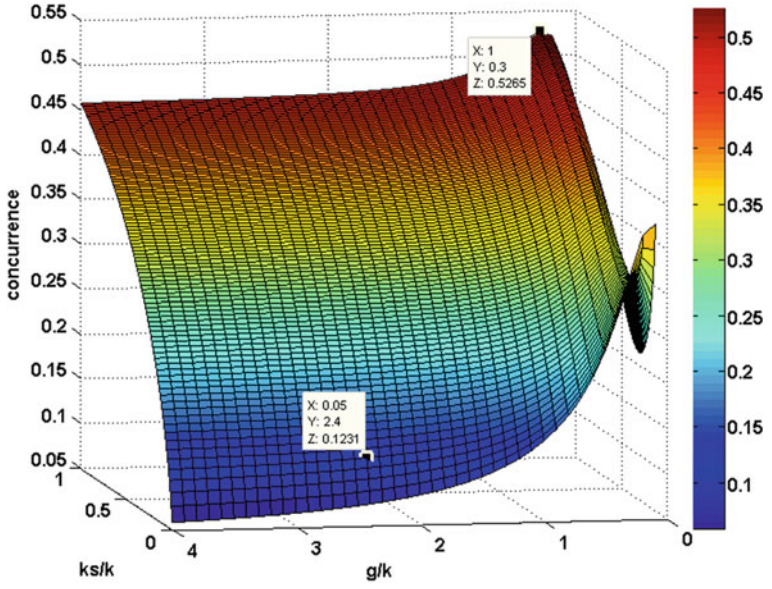

Fig. 9 Concurrence of Photonic Compact CNOT gate versus the coupling strength 'g' and cavity field decay rate 'k' under noisy conditions

Table 1 Concurrence of photonic compact CNOT gate with and without noise under weak and strong coupling regime

$\omega_c = \omega_{X^-}$ $\gamma/k = 0.1$				
Quantum circuit	Coupling condition	k_s/k	g/k	Concurrence
Photonic compact CNOT gate under noisy condition [reported in this paper]	Weak	1	0.3	52.65
Photonic compact CNOT gate under noisy condition [reported in this paper]	Strong	0.05	2.4	12.31
Photonic compact CNOT gate without noise [reported in this paper]	Weak	0.01	0.1	75.3
Photonic compact CNOT gate without noise [reported in this paper]	Strong	0.05	2.4	1.441
Photonic *I*swap gate using quantum hot cavity [22]	Weak	0	0.02	47.4

References

1. Bennett C, Brassard G (1984) Quantum cryptography: public key distribution and coin tossing. In: Proceeding of IEEE International Conference on computers, systems, and signal processing, p 175
2. Deutsch D, Jozsa R (1992) Rapid solutions of problems by quantum computation. In Proceedings of the Royal Society of London, vol 439, pp 553–558
3. Bennett C, Brassard G, Crepeau C, Jozsa R, Peres A, Wotters W (1993) Teleporting an unknown quantum state via dual classical and EPR channels. Phys Rev Lett 70:1895–1899
4. Shor PW (1994) Algorithms for quantum computation: discrete logarithms and factoring. In: Proceeding of 35th Annual IEEE symposium on fundamentals of computer sciences, pp 124–134
5. Grover LK (1996) A fast quantum mechanical algorithm for database search. In: Proceedings of 28th annual ACM symposium on the theory of computing, pp 212–219
6. Cerf NJ, Adami C, Kwiat PG (1998) Optical simulation of quantum logic. Phys Rev A 57:R1477-1480
7. Knill L, Milburn (2001) A scheme for efficient quantum computation with linear optics. Nature 409:46–52
8. Glancy S, LoSecco JM, Vasconcelos HM, Tanner CE (2002) Imperfect detectors in linear optical quantum computers. Phys Rev A 65:062317
9. Kok P, Munro WJ, Nemoto K, Ralph TC, Dowling JP, Milburn GJ (2007) Linear optical quantum computing with photonic qubits. Rev Mod Phys 79:135–174
10. Saharia A, Maddila RK, Ali J et al (2019) An elementary optical logic circuit for quantum computing: a review. Opt Quant Electron 51:224. https://doi.org/10.1007/s11082-019-1944-3
11. Kang M-S, Heo J, Choi S-G, Moon S, Han S-W (2020) Optical Fredkin gate assisted by quantum dot within optical cavity under vacuum noise and sideband leakage. Sci Rep 10:5123
12. Barenco CHB, Cleve R, DiVincenzo DP, Margolus N, Shor P, Sleator T, Smolin JA, Weinfurter H (1995) Elementary gates for quantum computation. Phys Rev A 52:3457–3467
13. Wang H-F, Wen J-J, Zhu A-D, Zhang S, Yeon K-H (2013) Deterministic cnot gate and entanglement swapping for photonic qubits using a quantum-dot spin in a double-sided optical microcavity. Phys Lett A 377(40):2870–2876
14. Wang HF, Zhu A-D, Zhang S, Yeon K-H (2013) Optically controlled phase gate and teleportation of a controlled-NOT gate for spin qubits in a quantum-dot–microcavity coupled system. Phys Rev A 87:062337

15. Kang M, Heo J, Choi S et al (2020) Optical Fredkin gate assisted by quantum dot within optical cavity under vacuum noise and sideband leakage. Sci Rep 10:5123
16. Gueddana A, Gholami P, Lakshminarayanan (2019) Can a universal quantum cloner be used to design an experimentally feasible near-deterministic CNOT gate? Quant Inf Process 18:221
17. Wei H-R, Deng F-G (2014) Universal quantum gates on electron-spin qubits with quantum dots inside single-side optical microcavities. Opt Express 22:593–607
18. Hu CY, Munro WJ, O'Brien JL, Rarity JG (2009) Proposed entanglement beam splitter using a quantum-dot spin in a double-sided optical microcavity. Phys Rev B 80:205326
19. Wei H-R, Deng F-G (2013) Scalable photonic quantum computing assisted by quantum-dot spin in double sided optical microcavity. Opt Express 21:17671–17685
20. Gueddana A, Lakshminarayanan V (2019) Toward the universal quantum cloner limit for designing compact photonic CNOT gate. arXiv: Quantum Physics}, (2019). https://arxiv.org/abs/1906.06547
21. Zhou L, Sheng Y-B (2015) Concurrence measurement for the two-qubit optical and atomic states. Entropy 17(6):4293–4322
22. Sharma AK, Sharma R (2020) Deterministic two Qubit iSWAP gate Using a resonator as coupler. In: Proceedings of 4th international conference on optical & wireless technologies (OWT 2020)

PSO and Firefly Algorithm Application for AGC Thermal-EV Integrated System with Nonlinearities

Hiramani Shukla and Siddhant Gudhe

Abstract System stability, frequency deviation, or power mismatch issues are due to the large-scale integration of electric vehicles (EV) to the preexisting power grid. EV acts as an energy storage system that not only acts as the load but also as a source. The quality of power is defined by the power flow and minimum frequency deviation for a particular area. Automatic generation control (AGC) on the generation side acts as a key component to achieve high-power quality. The variation of supply frequency and its stability along with its automatic control when the load fluctuates is called automatic load frequency control (ALFC). A time-delayed system with nonlinearities such as GDB and GRC has a very poor dynamic response of the system. So, the system optimization problem becomes complex by adding nonlinearities. EV as an energy storage source acts as an excellent candidate for frequency management by selecting optimum controller values. In this paper, two area systems have been taken for study. Both the areas include thermal and EV integration. The system is analyzed for step load disruption as well as random load disruption. To control the frequency, a proportional-integral-derivative (PID) controller is applied. Particle swarm optimization (PSO) and firefly algorithm (FF-A) optimization techniques are implemented to find the control variables and compared them. The time delay effect is also considered, and the system under study is verified in MATLAB/Simulink environment. The simulation results show that FF-A has low oscillation, reduced settling time, and a huge delay margin improvement.

Keywords Load frequency control · Electric vehicles · Time delay · GDB · GRC · PSO · Firefly algorithm

1 Introduction

Electric vehicles (EVs) have also been increasing at an exponential rate. The penetration of EV along with the renewable sources possesses more stability concerns.

H. Shukla (✉) · S. Gudhe
Electrical Engineering Department, Maulana Azad National Institute of Technology, Bhopal, India
e-mail: hiramanishukla143@gmail.com

© The Author(s), under exclusive license to Springer Nature Singapore Pte Ltd. 2022

A. Tripathi et al. (eds.), *Intelligent Computing Techniques for Smart Energy Systems*,
Lecture Notes in Electrical Engineering 862,
https://doi.org/10.1007/978-981-19-0252-9_23

Electric vehicles in a large quantity connected to the grid have an effect on the system frequency, power, and stability. If such fleets of EV charging and discharging are not managed, which may lead to power quality issues and also the transformer may overload.

The variation of supply frequency and its stability along with its automatic control when the load varies is called automatic load frequency control (ALFC). The area of research nowadays is the intelligent communication between EV and the grid. Bidirectional power flow in the EV can solve the problems with additional merits. EV can not only act as a load but also as an energy storage system. The owners of EVs could also benefit from the bidirectional mode. There is rapid technological advancement in the battery. There are various modes for EV charging. EV charging with no coordination or with one-way charging is called grid to vehicle (G2V) mode. EV also offers a vehicle to grid (V2G) with a bidirectional charger such that power flow is reversed. The bidirectional charger must be coordinated, regulated as well as smart to optimally use for grid load frequency control. Numerous optimization methods have been used for controllers for the tuning of the parameters.

Generator dead band (GDB) and generator rate constrain (GRC) are system nonlinearities that deteriorate system performance by large overshoots and large settling times. There have been over implications of the mathematical model of the system by ignoring the simultaneous presence of GDB and GRC. A small disturbance in the system with GRC and GDB can results in large nonlinearly. So, the selection of proper controllers is important using optimization techniques.

PID controller has been researched extensively as an appropriate controller for ALFC. Particle swarm optimization (PSO) is the most used optimization technique to find control parameters for the controller. Firefly algorithm (FF-A) optimization techniques have been proven efficient for the ALFC. In fact, FA outperforms PSO in all aspects of the control system.

The FF-A has been successfully implemented for the thermal power system [1], but the integration of EV and time delay effects has not been considered. Study [2] shows that FF-A used to find control variables for two area systems using integral controller, but implementation for proportional-integral (PI) or PID controller has not been discussed. Implementation using PI controller has been conducted [3]. Both PI and PID controllers have been investigated [4, 5] for FF-A, but time delays have not been taken into consideration. Fuzzy-PID using FF-A has been shown [6], and PID for hybrid energy sources is studied [7], but the time delay factor has not been discussed substantially.

The effect of EV on LFC is a prime area of research. The EV effect on the multi-area system has been carried out in detail [8–13]. The system with nonlinearities have been studied extensively [14], but the effect of communication time delays is not considered for this research.

The proposed model in the paper contains a thermal model, and aggregated model of EV [14] is under study. Section 2 describes the system under study, and Section 3 discusses the particle swarm optimization (PSO) technique and firefly algorithm (FF-A). Simulation performance and conclusion are discussed in Sects. 4 and 5.

2 System under Investigation

In order to analysis for the system using controllers, two area system models are considered. Two controllers are used, and their variables are calculated by using optimization technique. The electric vehicle model is introduced in both areas, and the analysis is completed. The system undergoes through step load as well as random load variation. The time delay effect is also taken into account.

2.1 Time Delay Effect

Large integration of various power sources increases the inertia, and frequency variation is very low. There are delays in the power system which is not intentional, but the delay is provided to receive at the control unit. For the large power system, time delays are usually not considered. A delayed linear system is marginally stable with all the roots lying on the left side of the s-plane. There is an infinite number of roots or time delays available for the same system [15]. The impact of the time delay factor is also considered, but the calculation of time delay margin is beyond the scope of this paper. Various methodologies are used in literature to calculate time delay margin [15, 16].

2.2 Model of Overall System

The overall system model consists of two area systems. The block diagram of the system under study is shown in Fig. 1. Area 1 and Area 2 contain the thermal plant model along with the aggregate EV model. Both the areas are applied with time delay for communication with the command centre. System nonlinearity such as GDB and GRC is added to the thermal power plant. Both step load disruption (SLD) and random load disruption (RLD) are applied and tested in both areas. The system is studied for the change in frequency in both the areas and the change in tie-line power.

2.3 Model of Electric Vehicle (EV)

The frequency regulation using EV and large fleets of EV are used to penetrate into the power system. The control centre for EV is called an EV aggregator which controls the charging-discharging of every EV. The dynamic model of the EV is defined by the first-order transfer function containing time constant TEV and gain KEV. The transfer function for the first EV is given by Eq. (1).

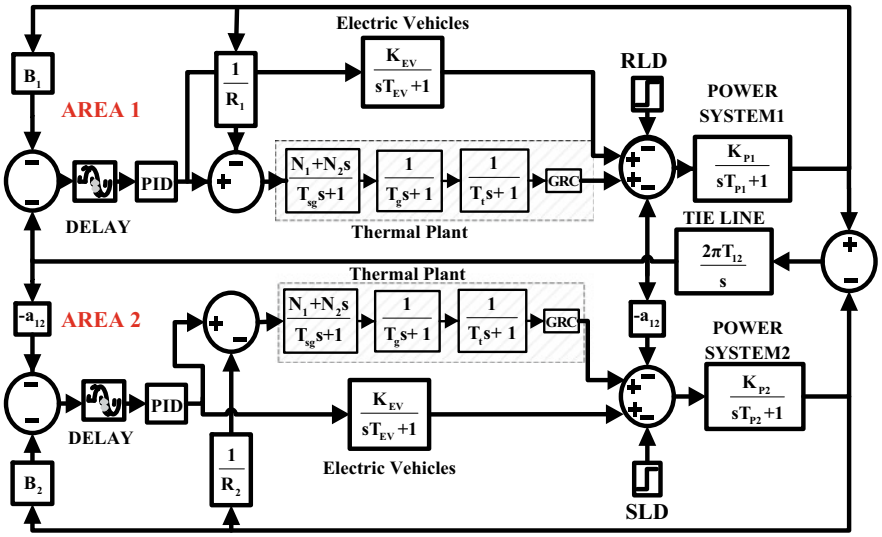

Fig. 1 Block diagram of the overall system under investigation

$$\frac{K_{\mathrm{EV}}}{sT_{EV}+1} \tag{1}$$

2.4 *Model of Thermal Power Plant*

The generator dead band (GDB) and generator rate constrain (GRC) are considered system nonlinearities that increase overshoot and oscillation and also results in poor dynamic response. Governor in the thermal power plant has mechanical friction, valve overlaps in hydraulic relays, backlash, etc., as dead bands. The specified maximum rate at which the power generation is changed is called a generator rate constrain. This is made by adding a limiter to the control system. Figure 2 shows the block diagram for GRC. Equation (2) shows the GDB where $N1$ and $N2$ are the second and third constant-coefficient, respectively, of the Fourier series.

$$\frac{N_1+N_2 s}{T_{sg}s+1} \tag{2}$$

Fig. 2 Block diagram of generator rate constrain

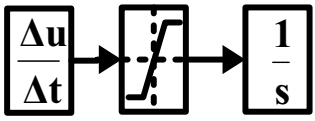

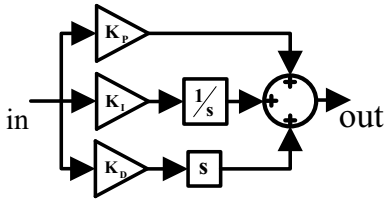

Fig. 3 Block diagram of PID controller design

2.5 Controller Design

PID controller has been well known and widely used controller for several years. Figure 3 shows the block diagram, and Eq. (3) defines the PID controller. By optimally tuning the control variables proportional gain, integral gain, and derivative gain, the performance is improved for the kth area controls the overshoots, rise time, and steady-state error with minimum effect on settling time affects the overshoots and rise time, but the effect on settling time is still negligible. The cost function to compare PSO and FF-A is shown in Eq. (3)

$$G(s)_{PID} = K_{Pk} + \frac{K_{Ik}}{s} + K_{Dk} \cdot s \tag{3}$$

3 System under Investigation Optimization Techniques used for Analysis

3.1 Particle Swarm Optimization

PSO is a meta-heuristics most popular optimization method. It is based on the concept of swarm intelligence observed in nature in animals who live in swarms, like fishes and birds. PSO has gained popularity in recent times in various applications in diverse fields. The PSO algorithm was brought up by Dr Kennedy and Dr Eberhart in 1995 [17]. The approach of PSO involves an involvement of all particles in the whole search space. Each particle plays a significant role in having an influence on all other existing particles also in the neighbourhood. In its formulation, it follows the movement pattern towards optimal value based on the self-experience and experience of nearby particles (Fig. 4).

The PSO technique is applied to extract the various controllers' parameters. The PSO parameters considered are learning rates $c_1 = c_2 = 1.496$, damping factor (ω_{damp}) = 0.729, inertia weight (ω) = 1, population size (n) = 10, and iterations (iter) = 100.

The governing equations update the velocity vector and position vector of the particles. Every particle represents a potential solution. They are bound to travel in

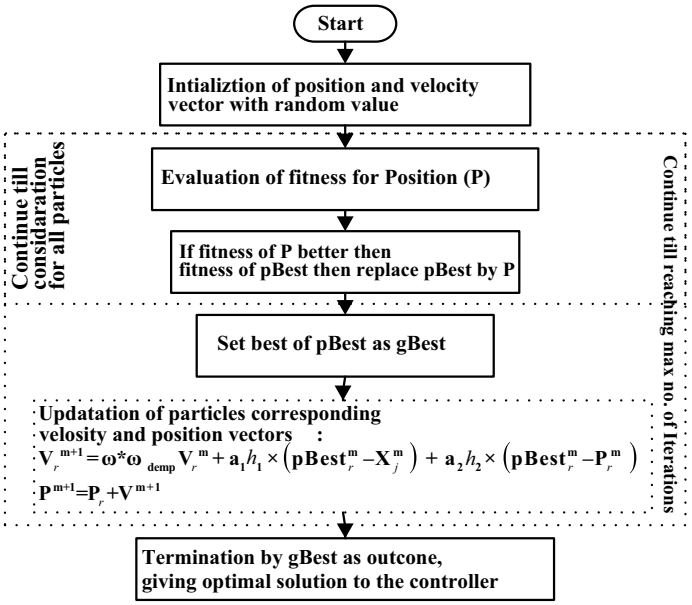

Fig. 4 Flowchart of particle swarm optimization. Where $r = 1, \ldots Z$, Z is total number of particles, m is the current iteration number, a_1 and a_2 are acceleration constants, h_1 and h_2 are random numbers between 0 and 1, ${V_r}^m$ is particle j velocity for mth iteration, (ω) is inertia weight and (ω_{damp}) is damping factor, ${P_r}^m$ is current position of the particle r of iteration m, $\text{pBest}_r{}^m$ is the previous best position of particle r, $\text{gBest}_r{}^m$ is global best position of particles

discrete time steps defined by the algorithm and update their new position. In the search space, the velocity vector corresponding to the particle has an influence on its own social behaviour along with the social behaviours of all other particles. The next task of the algorithm is to find the best value as per individual particle and also with respect to the whole swarm called personal best and global best values, respectively. Similarly, the velocity vector is also updated in subsequent iterations. The iterative process is stopped when it meets the pre-defined criteria by the algorithm. The iterations count is kept high to ensure efficient convergence and enhancing the reliability of derived optimization values.

3.2 Firefly Algorithm

Population-based algorithm where flashing patterns and behaviour of tropical fireflies is analyzed called as firefly algorithm (FF-A). This is a good optimization technique. FF-A has been proposed by Yang in 2008 at the University of Cambridge. This algorithm was further developed for multimodal optimization by Yang XS in 2009. The objective function is formulated by the magnitude of light of a firefly. The

brightness of firefly I at selected position x is given by as $I(x)/f(x)$ for minimization of the objective function. The equation of light brightness is given by Eq. (4) (Fig. 5)

$$I = I_o \mathrm{e}^{-\gamma r} \tag{4}$$

Where

I_0 = original intensity of light,

γ = coefficient of light absorption which varies with distance r.

β is called as attractiveness which is defined by other fireflies. As the distance between sources and light decreases, media absorbs light, therefore degree of absorption changes the attractiveness which is given by $\beta = \beta_o e^{-\gamma r^2}$ for r i considered as zero.

The motion of a firefly I is allured to another, and more enchanted firefly j [18, 19] is determined by Eq. (5)

$$x_i^{k+1} = x_i^k + \beta_o e^{-\gamma r_{ij}^2}(x_j^k - x_i^k) + \alpha \varepsilon_i^k \tag{5}$$

where

α = Randomization parameter and vector of random numbers are given by ε_i^k.

For FF-A optimization used in this study, tuned values are number of fireflies = 10, maximum iterations = 100, $\beta = 0.2$, $\alpha = 0.5$, and $\gamma = 0.5$.

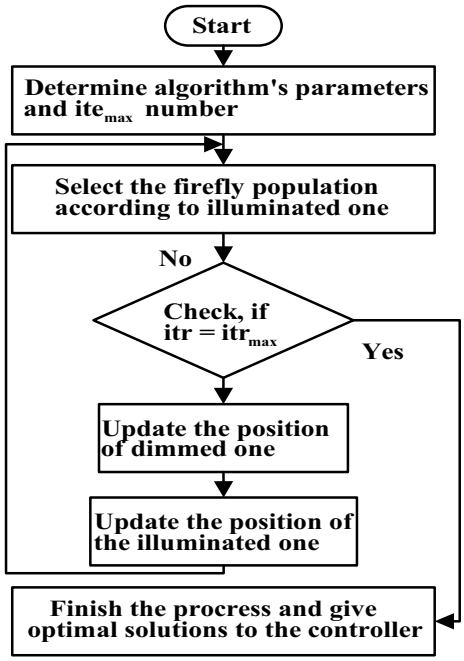

Fig. 5 Flowchart of firefly algorithm

4 Simulation Performance

Simulation is performed in three parts. In the first part, the comparison of PID controller parameters using PSO and FF-A is performed. In the second part, simulation results are shown for various loadings, and in the last part, the system is tested for the time delays. All the results are verified with the aggregate model of EV connected. The parameters for the simulation are shown in Table 1. The variable load applied to the system under study is shown in Fig. 6. The results for the PSO and FF-A comparison for step load disruption (SRD) are shown in Figs. 7 and 8 and show the random load disruption (RLD) comparing PSO and FF-A.

Figure 8 also shows the time delay of 0.5 s applied to the system along with RLD. At exact 0.5 s, PSO variables make the system marginally stable. Beyond 0.5 s, PSO gives variables for PID which makes the system unstable. So, the time delay margin for PSO-based controller is less than 0.5 s. The calculation of time delay margin has tedious mathematical calculations depending on the system. The exact time delay margin is not shown as delay in simulation is based on Pade approximation [15]. Figure 9 gives the convergence curve for PSO and FF-A. Figure 10 shows the bar chart for the cost function for Eq. (3).

Table 1 Simulation parameters for system under investigation

Parameters	Values
f (frequency), B_i (damping constant), R (regulation)	60 Hz, 0.425 pu/Hz, 2.4 Hz/pu
Thermal power plant	
T_g, T_t, N_1, N_2, T_{sg}	0.3 s, 0.08 s, 0.8, $-0.2/\pi$, 0.1 s
Electric vehicle	
K_{EV}, T_{EV}	1, 1 s
Power system	
K_{Pi}, T_{Pi}	120, 20 s
Tie line	
T_{12}, a_{12}	0.0867, -1

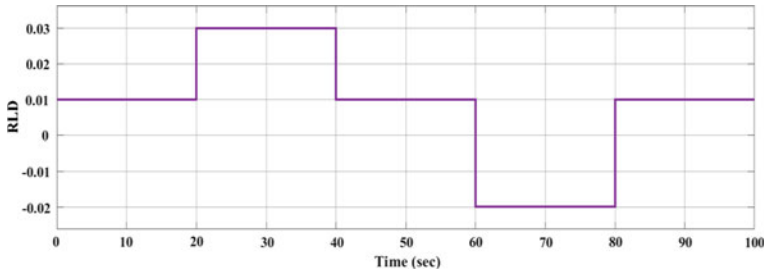

Fig. 6 Variable load applied to the system under study

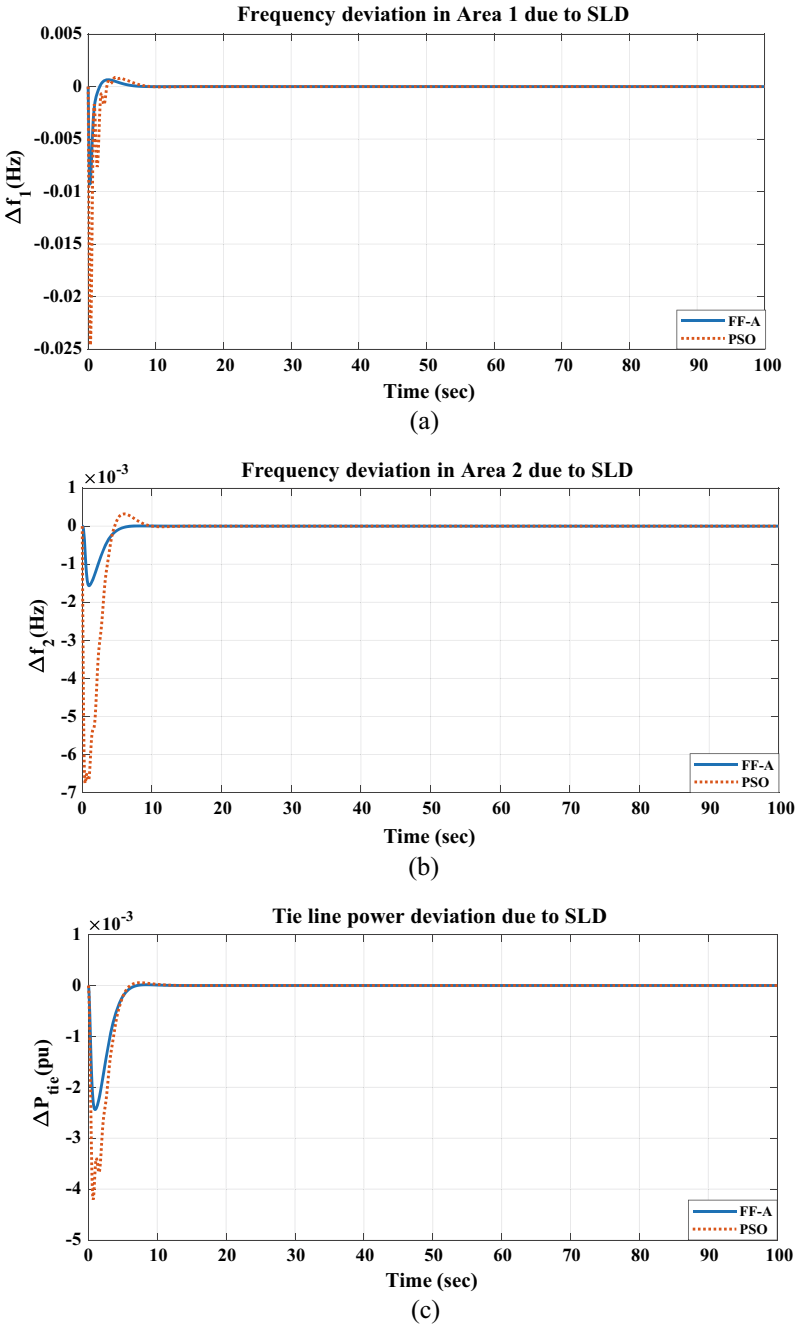

Fig. 7 Comparison of PSO and FF-A for SLD **a** frequency fluctuations in Area 1, **b** frequency fluctuations in Area 2, **c** tie-line power variation

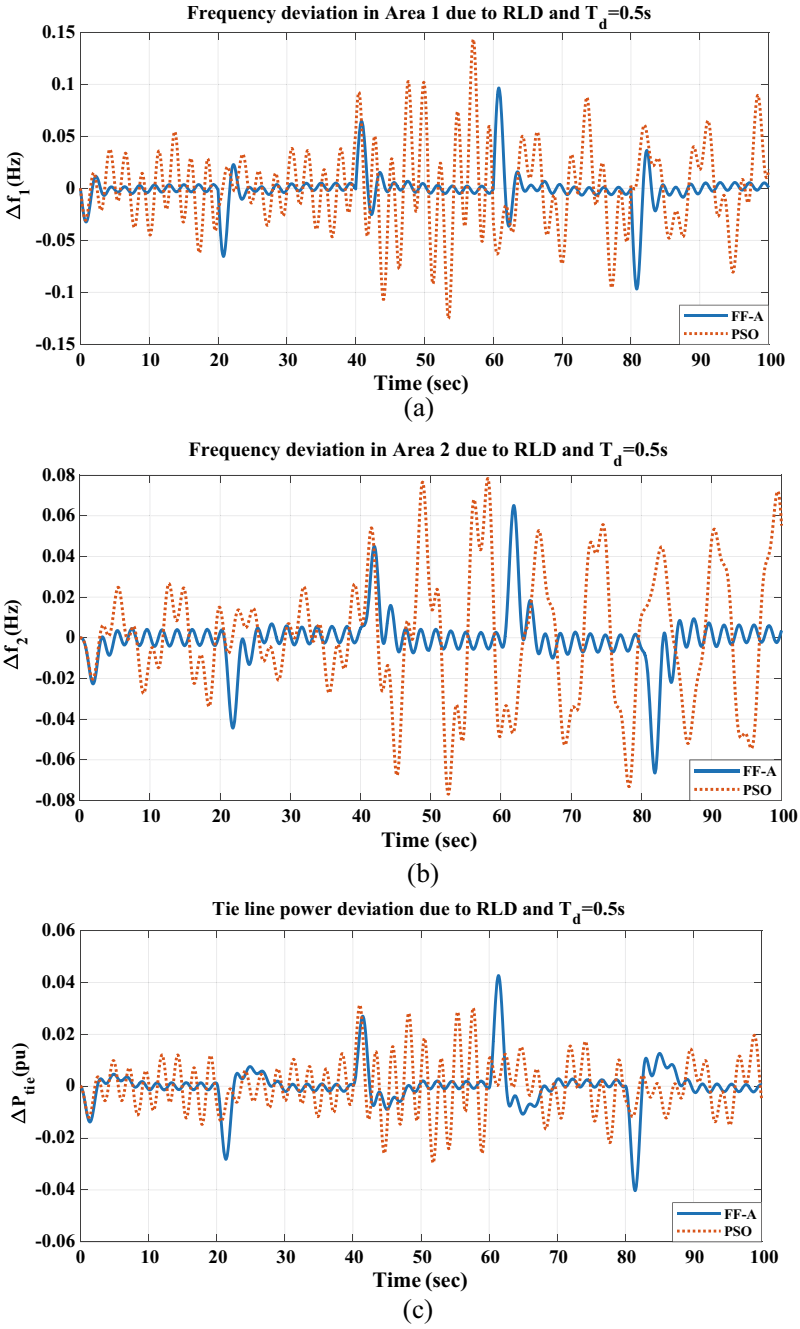

Fig. 8 Comparison of PSO and FF-A for RLD **a** frequency fluctuations in Area 1, **b** frequency fluctuations in Area 2, **c** tie-line power variation

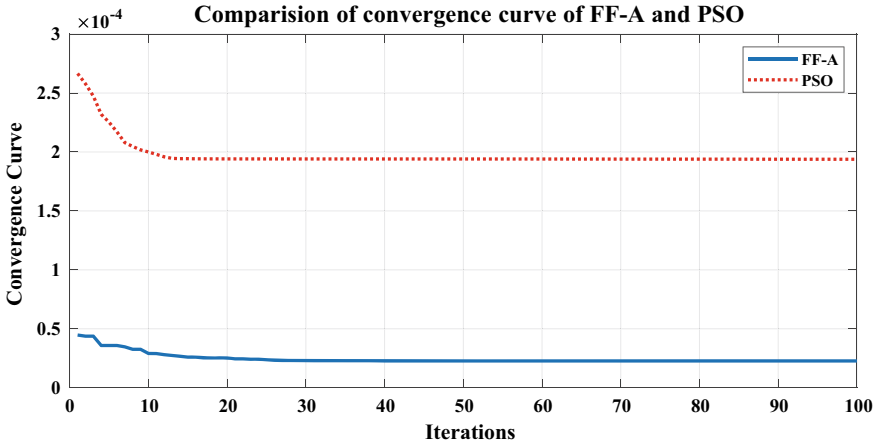

Fig. 9 Convergence curve for PSO and FF-A

Fig. 10 Bar chart for the cost function of Eq. (4)

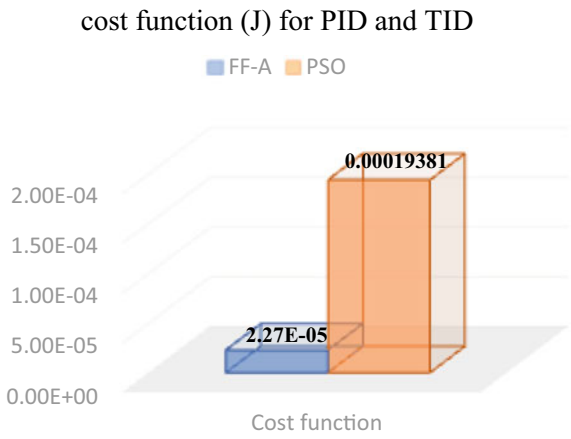

Tables 2 and 3 show the controller parameters obtained from the two optimization techniques. Table 4 shows the magnitude of peak overshoot, peak undershoots, and settling time for PSO and FF-A for TID controller, respectively. The cost function using FF-A is lesser than PSO. The low value of the convergence curve and cost

Table 2 PID control variables using PSO algorithm

Parameters (PSO)		KP	KI	KD	N
PID	Area 1	0.5733	0.6135	0.4727	65.16
	Area 2	0.5264	0.6534	0.6805	66.9

Table 3 PID control variables using firefly algorithm

Parameters (FF-A)		KP	KI	KD	N
PID	Area 1	1	0.6303	0.9989	55.67
	Area 2	0.8566	0.9485	0.5436	49.71

Table 4 Control system parameters using PSO and FF-A

Parameters		Δf_1 (Hz)	Δf_2 (Hz)	ΔPtie (pu)
PSO	Peak overshoot (ms)	0.9	0.32	0.05
	Peak undershoot (ms)	24.6	6.75	4.2
	Settling time (s)	12.4	13.2	12.3
FF-A	Peak overshoot (ms)	0.66	–	0.01
	Peak undershoot (ms)	9.26		2.44
	Settling time (s)	7.8	6.7	10.1

function gives optimized controller parameters. Therefore, it can be easily concluded that FF-A gives very optimized parameters compared to the PSO algorithm.

5 Conclusion and Discussion

In this paper, two area systems are analyzed to find PID controller control variables using PSO and FF-A optimization techniques. Both the time-delayed areas are operated with generator dead band (GDB) and generator rate constrains (GRC) nonlinearities. The simulation results show that system dynamics using the FF-A system outperforms the PSO system for settling time and oscillations. Both the techniques are tested for under step load and random load disruption. Time delay effects are considered, and the time delay margin is approximated. For the system under study, the delay margin for FF-A-based system is 0.5 s, but the system becomes marginally stable at exact 0.5 s for PSO-based system. Therefore, a system with a PSO stability margin is less than 0.5 s. More stability margin indicates that the system is robust and reliable. Also, the verification of FF-A superiority can be concluded from peak overshoot, undershoot, as well as settling time. Peak overshoot for FF-A is considerably improved compared to PSO. The cost function using FF-A is lesser than PSO. The low value of the convergence curve and cost function gives optimized controller parameters. Therefore, it can be easily concluded that FF-A gives very optimized controller parameters compared to the PSO algorithm.

The simulation results can be generalized for the multi-area system. In the future research, the different controllers can be tested using both techniques. For the calculation of the time delay margins, different methodologies for the large-scale power system can be explored.

References

1. Jagatheesan K, Anand B, Samanta S, Dey N, Ashour AS, Balas VE (2019) Design of a proportional-integral-derivative controller for an automatic generation control of multi-area power thermal systems using firefly algorithm. IEEE/CAA J Autom Sinica 6(2):503–515
2. Roshin KR, Bindumol EK (2020) Firefly algorithm based tuning of integral controller for frequency regulation of hybrid two area power system with nonlinearities and electric vehicles. In: 2020 International conference on power electronics and renewable energy applications (PEREA), pp 1–6
3. Bhadoria VS, Jaiswal SP, Tayal A, Singh J (2019) Firefly algorithm for frequency controller of autonomous hybrid energy system. In: 2019 2nd International conference on power energy, environment and intelligent control (PEEIC), pp 150–155
4. Khan R, Gogoi N, Barman J, Latif A, Das DC (2019) Virtual power plant enabled co-ordinated frequency control of a grid connected independent hybrid microgrid using Firefly algorithm. In: *2019 IEEE Region 10 Symposium (TENSYMP)*, pp 795–800
5. Boddepalli MK, Navuri PK (2018) Design and analysis of firefly algorithm based PID controller for automatic load frequency control problem. In: 2018 Technologies for smart-city energy security and power (ICSESP), pp 1–5
6. Debnath MK, Padhi JR, Satapathy P, Mallick RK (2017) Design of fuzzy-PID controller with derivative filter and its application using firefly algorithm to automatic generation control. In: 2017 6th International conference on computer applications in electrical engineering-recent advances (CERA), pp 353–358
7. Datta A, Konar S, Singha LJ, Singh KM, Lalfakzuala A (2017) A study on load frequency control for a hybrid power plant. In: 2017 second international conference on electrical, computer and communication technologies (ICECCT), pp 1–5
8. Ko KS, Sung DK (2018) The effect of EV aggregators with time-varying delays on the stability of a load frequency control system. IEEE Trans Power Syst 33(1):669–680
9. Naveed A, Sönmez Ş, Ayasun S (2021) Impact of electric vehicle aggregator with communication time delay on stability regions and stability delay margins in load frequency control system. J Mod Power Syst Clean Energy 9(3):595–601
10. Khooban M (2018) Secondary load frequency control of time-delay stand-alone microgrids with electric vehicles. IEEE Trans Ind Electron 65(9), 7416–7422
11. Pham TN, Trinh H, Hien LV (2016) Load frequency control of power systems with electric vehicles and diverse transmission links using distributed functional observers. IEEE Trans Smart Grid 7(1):238–252
12. Nguyen HNT, Zhang C, Zhang J (2016) Dynamic demand control of electric vehicles to support power grid with high penetration level of renewable energy. IEEE Trans Transp Electrificat 2(1):66–75
13. Debbarma S, Dutta A (2017) Utilizing electric vehicles for LFC in restructured power systems using fractional order controller. IEEE Trans Smart Grid 8(6):2554–2564
14. Yousef HA, Al-Kharusi K, Albadi MH, Hosseinzadeh N (2014) Load frequency control of a multi-area power system: an adaptive fuzzy logic approach. IEEE Trans Power Syst 29(4):1822–1830
15. Hua C, Wang Y (2020) Delay-dependent stability for load frequency control system via linear operator inequality. IEEE Trans Cybern 1–9
16. Cao Y, Li C, He T, Chen Y-P, Li S (2021) A novel Rekasius substitution based exact method for delay margin analysis of multi-area load frequency control systems. IEEE Trans Power Syst Early Access
17. Eberhart R, Kennedy J (1995) A new optimizer using particle swarm theory. In: MHS'95. Proceedings of the sixth international symposium on micro machine and human science, pp 39–43
18. Yang XS (2009) Firefly algorithms for multimodal optimization. In: Watanabe O, Zeugmann T (eds) Stochastic algorithms: foundations and applications. Lecture notes in computer science, vol 5792. Springer, Berlin

19. Yanga X, Zhaob Y (2020) Firefly algorithm and flower pollination algorithm. In: Nature-Inspired Computation and Swarm Intelligence Algorithms, Theory and Applications, pp 35–48

(γ, δ)-Fuzzy Hyperideals of Γ-Hypernear Rings

Neha Gahlot and Nagaraju Dasari

Abstract In this chapter, we study about a new idea (γ, δ)-fuzzy hyperideals in Γ-hypernear rings also study some different topics (γ, δ)-Cut set, on direct product (γ, δ)-fuzzy hyperideals.

Keywords Γ-hypernear ring · Fuzzy Γ-hypernear ring · (γ, δ)-fuzzy hyperideals in Γ-hypernear rings · (γ, δ)-Cut set · On direct product (γ,δ)-fuzzy hyperideals

2010 Mathematics Subject Classification 16Y30 · 16Y99 · 03E72

1 Introduction

Dr. Zadeh introduced fuzzy set in 1965 [1]. Since then many researchers applied the fuzzy concept in many branches of algebra like in group theory introduced by Rosenfeld [2] and in ring theory introduced by Mukherjee and Sen [3]. T. K. Dutta and T. Chanda introduced fuzzy ideal of Γ-Ring and fuzzy ideals in near-rings studied by Abou-Zaid [4].

Hypersystem is well-established algebraic structure in classical algebraic theory. Hypersystem has many applications in branch of mathematics, computer applications, information science and many more. Nowadays, hypersystem is studying in large number of countries of the whole world. In general, hyperstructure is an extension of classical algebraic structure. An idea about hyperstructure was firstly introduced by Marty in 1934 [5], and he introduced hypergroup after that Marty was started their results with fraction function, applications of group and many more algebraic structures. Recently, the two authors in a monograph of Leoreanu and corsini have collected last fifteen years many applications of algebraic hyperstructure mainly from the following topics: lattices, fuzzy sets, binary relation, rough set, geometry, hypergraph, automata, artificial intelligence, probabilities, codes, algebra, cryptography, relation algebra and median [6] and important relationships between

N. Gahlot (✉) · N. Dasari
Department of Mathematics and Statistics, Manipal University Jaipur, Jaipur, Rajasthan 303007, India
e-mail: gahlotneha1995@gmail.com

© The Author(s), under exclusive license to Springer Nature Singapore Pte Ltd. 2022

A. Tripathi et al. (eds.), *Intelligent Computing Techniques for Smart Energy Systems*, Lecture Notes in Electrical Engineering 862,
https://doi.org/10.1007/978-981-19-0252-9_24

algebraic structures and hyperstructures were studied by Ameri, Davvaz, Cristea, Leoreanu, Corsini, Zhan and many more researchers [7, 8, 9]. Sen et al. introduced the concept of fuzzy hypersemigroups in [10]. Leoreanu Foteaa and Davvazb studied about fuzzy hyperrings in [8], and characterization properties of fuzzy hyperideals in hyperrings with respect to a triangular norm introduced by Hila, Naka in [11] and characterization properties of fuzzy hyperideals in hyperrings with respect to a triangular norm introduced by Hila and Naka in [11]. Fuzzy hyperideals in hypernear rings studied by Zhan et al. in [12]. An algebraic structure hypernear ring was introduced by Dasic in [13]. Yamak et al. introduced normal fuzzy hyperideals in hypernear ring [14].

Firstly, a concept $(\in, \in \vee q)$ in a subnear ring and ring theory is introduced by Narayana and Manikantan [15], and in hypernear ring, it is introduced by Davvaz et al. [12] and a concept which based on of $(\in, \in \vee q)$ studied by many research's like Yao introduced (λ, τ)-fuzzy groups in [16] and (λ, τ)-fuzzy ideals in subring in [17]. Direct sum of (λ, τ)-fuzzy sub-ring introduced by Selvaraj and Sivakumar [9]. (λ, τ) an important role in fuzzy algebraic structures the reader refer to [18, 19, 20].

In this paper, first introduction and some basic definitions are related to this chapter, and in second section, we give definition, properties, example of (γ, δ)-fuzzy hyperideals in hypernear ring; in Sects. 3 and 4, we study about (γ, δ)-cut and direct product of (γ, δ)-fuzzy hyperideals in hypernear ring, respectively.

Now we introduced the some basic concepts which is necessary for this chapter.

An algebraic structure $(\mathcal{N}^*, +, \Gamma^*)$ is a near-ring which satisfy:

(1) $(\mathcal{N}^*, +)$ is a satisfy all properties of group (not necessarily commutative),
(2) $(\mathcal{N}^*, \Gamma^*)$ is semigroup,
(3) satisfy one of distributive properties, i.e. $i\rho\,(j+k) = i\rho j + i\rho k \,\forall\, i,\ j,\ k \in \mathcal{N}^*$ and $rho \in \Gamma^*$.

A subset $\mathcal{R}^*$ of a near-ring $\mathcal{N}^*$ is ideal where

(i) $(\mathcal{R}^*, +, \Gamma^*)$ is a Γ-near-ring,
(ii) $(j\rho k)\Upsilon k = i\rho(j\Upsilon k) \,\forall\, i,\ j,\ k \in \mathcal{R}^*$ and $\rho, \Upsilon \in \Gamma^*$,
(iii) $(\mathcal{R}^*, +, \Gamma^*)$ normal subgroup of $\mathcal{N}^*$,
(iv) $i\rho\,(j+k) - i\rho k \in \mathcal{R}^*$ (resp $i\rho j \in \mathcal{R}^*$) $\forall\, j \in \mathcal{R}^*,\ i,\ k \in \mathcal{N}^*$.

A subset $\mathcal{R}^*$ of $\mathcal{N}^*$ is ideal of $\mathcal{N}^*$ if it satisfies all the conditions.

Definition 1 [4] A fuzzy collection τ is a fuzzy ideal of Γ-near-ring $\mathcal{N}^*$ if it satisfies the following axioms:

(i) $min\{\tau(i), \tau(j)\} \leq \tau(i-j)$, for $i, j \in \mathcal{N}^*$.
(ii) $\tau(j) \leq \tau(i+j-i)$ for $i, j \in \mathcal{N}^*$.
(iii) $\tau(j) \leq \tau(i\rho(j+k) - i\rho k)$ for $i, j, k \in \mathcal{N}^*$ and $\rho \in \Gamma^*$.
(iv) $\tau(i) \leq \tau\,(i\rho j)$ for $i, j \in \mathcal{N}^*$.

A non-vacant set ϱ^* is an hyperstructure exist a map "$\circ$": $\varrho^* \times \varrho^* \to \wp^*(\varrho^*)$ here $\wp^*(\varrho^*)$ is power set of ϱ^*. An algebraic structure $(\varrho^*, +)$ is canonical hypergroup (not necessarily abelian) if it satisfies these properties:

(i) $\forall\, j, k, l \in \varrho^*,\ j + (k + l) = (j + k) + l$
(ii) $\exists\, 0 \in \varrho^*$ such that $0 + j = j + 0$ for each $j \in \varrho^*$.
(iii) For each $j \in \varrho^*$, a single element $\exists\, j' \in \varrho^*$ as for $0 \in (j + j') \cap (j' + j)$ (here j' is inverse of j);
(iv) $l \in j + k$ implies $k \in -j + l$ and $j \in l - k$.

Definition 2 [12] An algebraic structure $(\mathcal{N}^*, +, \Gamma^*)$ is Γ-hypernear ring if it varifies the following properties:

(i) $(\mathcal{N}^*, +)$ be an canonical hypergroup;
(ii) Semigroup with respect to the operation Γ^*.
(iii) verify one of distributive properties, i.e.
$i\rho\,(j + k) = i\rho j + i\rho k\ \forall\, i, j, k \in \mathcal{N}^*$ and $\rho \in \Gamma^*$.

Note: If $j \in \mathcal{N}^*$ and let two non-vacant subsets $J^*,\ K^*$ of $\mathcal{N}^*$, then by these $J^* + K^*$, $J^* + j$ and $j + K^*$ consequently $\bigcup_{j \in J^*, k \in K^*} j + k$, $J^* + \{j\}$ and $\{j\} + K^*$, respectively. Also, $\forall\, j, k \in \mathcal{N}^*$, we have $-(-j) = j$ and $0 = -0$ where $-(j + k) = -k - j$ and 0 is an only element. A subhypergroup $J^* \subseteq \mathcal{N}^*$ is an normal if for each $j \in \mathcal{N}^*$, it satisfies $j + J^* - j \subseteq J^*$. A normal subhypergroup J^* is referred to as a hyperideal of the hypergroup $\mathcal{N}^*$ if $i\rho\,(j + k) - i\rho k \cup i\rho j \in J^*\ \forall\, i, j, k \in \mathcal{N}^*$ and $\rho \in \Gamma^*$.

Definition 3 [21] Let a fuzzy set τ of an structure $(\mathcal{N}^*, +, \Gamma^*)$ is called fuzzy Γ-hypernear ring of $\mathcal{N}^*$ if it satisfies the following inequalities:

(i) $\min\{\tau(i), \tau(j)\} \leq \inf_{\flat \in i - j} \tau(\flat)\ \forall\, i,\ j \in \mathcal{N}^*$.
(ii) $\tau(i) \leq \tau(-i)\ \forall\, i \in \mathcal{N}^*$,
(iii) $\min\{\tau(i),\ \tau(j)\} \leq \tau(ij)\ \forall\, i,\ j \in \mathcal{N}^*$.
(iv) $\tau(j) \leq \inf_{\flat \in i + j - i} \tau(\flat), \forall\, i,\ j \in \mathcal{N}^*$,
(v) $\tau(i) \leq \tau(i\rho j),\ \forall\, i,\ j \in \mathcal{N}^*$.
(vi) $\tau(j) \leq \inf_{\flat \in i\rho\,(j+k) - i\rho k} \tau(\flat),\ \forall,\ i,\ j, k \in \mathcal{N}^*$ and $\rho \in \Gamma^*$.

2 (γ, δ)-Fuzzy Hyperideals in Γ-Hypernear Rings

In this section, we discuss $(\gamma,\ \delta)$-fuzzy right or left hyperideals and give some properties and examples related to $(\gamma,\ \delta)$-fuzzy hyperideals in Γ-hypernear rings.

Definition 4 A fuzzy collection $\mathcal{R}^*$ of hypernear ring $\mathcal{N}^*$ is a $(\gamma,\ \delta)$-fuzzy hyperideals of $\mathcal{N}^*$ if it is satisfying the following axiom:

(i) $\tau(i) \wedge \tau(j) \wedge \delta \leq \inf_{\flat \in i - j} \tau(\flat) \vee \gamma\ \forall\, i,\ i \in \mathcal{N}^*$
(ii) $\tau(j) \wedge \delta \leq \inf_{\flat \in i + j - i} \tau(\flat) \vee \gamma\ \forall\, i \in \mathcal{N}^*$ and $j \in \mathcal{R}^*$.
(iii) $\tau(j) \wedge \delta \leq \inf_{\flat \in i\rho\,(j+k) - i\rho k} \tau(\flat) \vee \gamma\ \forall,\ i,\ k \in \mathcal{N}^*,\ j \in \mathcal{R}^*$ and $\rho \in \Gamma^*$.
(iv) $\tau(i) \wedge \delta \leq \tau(i\rho j) \vee \gamma\ \forall\, i,\ k \in \mathcal{N}^*,\ j \in \mathcal{R}^*$ and $\rho \in \Gamma^*$.

Here γ, δ are two real numbers lying between 0 and 1 with $\gamma < \delta$ and also min $(\mathfrak{p}, \mathfrak{q})$ and max $(\mathfrak{p}, \mathfrak{q})$ is represented by $(\mathfrak{p} \wedge \mathfrak{q})$ and $(\mathfrak{p} \vee \mathfrak{q})$, respectively.

Obviously, an (γ, δ)-fuzzy hyperideal is $(\epsilon, \epsilon \vee q)$-fuzzy hyperideals of $\mathcal{N}^*$ if $\gamma = 0$ and $\delta = 0.5$.

Example 5 Let $\mathcal{N}^* = \{0^*, i^*, j^*, k^*\}$ and hyperoperation (+) and another operation $\rho \in \Gamma^*$ define on $\mathcal{N}^*$ is by the following tables:

$+$	0^*	i^*	j^*	k^*
0^*	$\{0^*\}$	$\{i^*\}$	$\{j^*\}$	$\{k^*\}$
i^*	$\{i^*\}$	$\{0^*, i^*\}$	$\{j^*\}$	$\{k^*\}$
j^*	$\{j^*\}$	$\{j^*\}$	$\{0^*, i^*, k^*\}$	$\{j^*, k^*\}$
k^*	$\{k^*\}$	$\{k^*\}$	$\{j^*, k^*\}$	$\{0^*, i^*, j^*\}$

ρ	0^*	i^*	j^*	k^*
0^*	0^*	i^*	j^*	k^*
i^*	0^*	i^*	j^*	k^*
j^*	0^*	i^*	j^*	k^*
j^*	0^*	i^*	j^*	k^*

Clearly $(\mathcal{N}^*, +, \Gamma^*)$ is a Γ-hypernear ring, define mapping $\tau: \mathcal{N}^* \to [0, 1]$ by $\tau(0^*) = 0.8$, $\tau(i^*) = 0.6$, $\tau(j^*) = 0.5$, $\tau(k^*) = 0.2$ and γ and δ is 0.3 and 0.7, respectively.

Then, a simple calculation reveals that τ is a (γ, δ)-fuzzy hyperideal of $\mathcal{N}^*$.

Lemma 6 Let τ be a (γ, δ)-fuzzy hyperideal of a Γ-hypernear ring $\mathcal{N}^*$, so $\tau(0) \vee \gamma \geq \tau(i^*) \wedge \delta \, \forall \, i^* \in \mathcal{N}^*$ where 0 is additive identity of $\mathcal{N}^*$.

Theorem 7 If τ is a fuzzy subcollection of a Γ-hypernear ring $\mathcal{N}^*$, then following conditions are equivalent:

(i) τ is a (γ, δ)-fuzzy hyperideal of $\mathcal{N}^*$.
(ii) τ_e is an hyperideal of $\mathcal{N}^*$ for any $e \in (\gamma, \delta]$.

Proof (i) $\Rightarrow$ (ii)

For any $e \in (\gamma, \delta]$ since τ is a fuzzy hyperideal of $\mathcal{N}^*$ clearly $\tau_e \neq \phi$. Now we want to show that τ_e is an hyperideal of $\mathcal{N}^*$. (i) for every $i, \ j \in \tau_e$, $\inf_{\flat \in i-j} \tau(\flat) \vee \gamma \geq (\tau(i) \wedge \tau(j)) \wedge \delta \geq e \wedge \delta = e$. Thus, $\flat \in i - j \in \tau_e$. (ii) Let for every $i \in \tau_e$, $j \in \mathcal{N}^*$, Now $\inf_{\flat \in j+i-j} \tau(\flat) \vee \gamma \geq \tau(i) \wedge \delta \geq e \wedge \delta = e$. Thus, $\flat \in j + i - j \in \tau_e$. (iii) Let for every $j \in \tau_e, i, \ k \in \mathcal{N}^*$ and $\rho \in \Gamma^*$ Now $\inf_{\flat \in i\rho(j+k)-i\rho k} \tau(\flat) \vee \gamma \geq \tau(j) \wedge \delta \geq e \wedge \delta = e$. Thus, $\flat \in i\rho(j + k) - i\rho k \in \tau_e$. Hence, τ_e is an hyperideal of $\mathcal{N}^*$.

(ii) ⇒ (i)

Suppose that τ_e is a hyperideal of $\mathcal{N}^*$ for any $e \in (\gamma, \delta]$. Now we have to prove that τ is an (γ, δ) fuzzy hyperideal of Γ-hypernear ring $\mathcal{N}^*$. We can prove this by contradiction, (i) Let for any $i, j \in \tau_e$ suppose $\inf_{\flat \in i-j} \tau(\flat) \vee \gamma < (\tau(i) \wedge \tau(j)) \wedge \delta = e$, thus $\inf_{\flat \in i-j} \tau(\flat) \vee \gamma < e$ (since $e \in (\gamma, \delta]$) so, $\flat \in i - j \notin \tau_e$ which is contradiction. Therefore $\inf_{\flat \in i-j} \tau(\flat) \vee \gamma \geq (\tau(i) \wedge \tau(j)) \wedge \delta$. (ii) Let for any $i \in \tau_e$ and $j \in \mathcal{N}^*$ suppose $\inf_{\flat \in j+i-j} \tau(\flat) \vee \gamma < \tau(i) \wedge \delta = e$, thus $\inf_{\flat \in j+i-j} \tau(\flat) \vee \gamma < e$ (since $e \in (\gamma, \delta]$) so, $\flat \in j + i - j \notin \tau_e$ which is contradiction therefore $\inf_{\flat \in j+i-j} \tau(\flat) \vee \gamma \geq \tau(i) \wedge \delta$. (iii) Let for any $j \in \tau_e$, $i, k \in \mathcal{N}^*$ and $\rho \in \Gamma^*$ then suppose $\inf_{\flat \in i\rho(j+k)-i\rho k} \tau(\flat) \vee \gamma < \tau(j) \wedge \delta = e$, thus $\inf_{\flat \in i\rho(j+k)-i\rho k} \tau(\flat) \vee \gamma < e$ (since $e \in (\gamma, \delta]$) so, $\flat \in i\rho(j + k) - i\rho k \notin \tau_e$ which is contradiction therefore $\inf_{\flat \in i\rho(j+k)-i\rho k} \tau(\flat) \vee \delta \geq \tau(j) \wedge \delta$. Hence τ is a (γ, δ)-fuzzy hyperideal of $\mathcal{N}^*$.

Corollary 8 *If τ is a fuzzy subcollection of a Γ-hypernear ring $\mathcal{N}^*$, then the following conditions are equivalent*:

(i) τ is a (γ, δ)-fuzzy hyperideal of $\mathcal{N}^*$.
(ii) τ_e is an hyperideal of $\mathcal{N}^*$ for any $e \in (\gamma, \delta)$.

Theorem 9 Let Q be any non-vacant subcollection of an Γ-hypernear ring $\mathcal{N}^*$ and τ_Q be an (γ, δ) fuzzy collection in $\mathcal{N}^*$ characterized by,

$$\tau_Q(i) = \begin{cases} d \text{ if } \ i \in Q \\ e \text{ if } \ i \notin Q \end{cases}$$

$\forall\, i \in \mathcal{N}^*$ and d, $e \in (\gamma, \delta]$ with $d > e$. Then τ_Q is an (γ, δ)-fuzzy hyperideal of $\mathcal{N}^*$ iff Q is a hyperideal of Γ-hypernear ring $\mathcal{N}^*$. Also, $\mathcal{N}^*_{\tau_Q} = Q$.

Proof Let consider τ_Q be an (γ, δ)-fuzzy hyperideal of hypernear-ring $\mathcal{N}^*$ and let $i, j \in Q$. then $\inf_{\flat \in i-j} \tau_Q(\flat) \vee \gamma \geq \min\{\tau_Q(i), \tau_Q(j)\} \wedge \delta = d \wedge \delta = d$ that implies $\flat \in i - j \in Q$. For each $i \in Q, j \in \mathcal{N}^*$. $\inf_{\flat \in j+i-j} \tau_Q(\flat) \vee \gamma \geq \tau_Q(i) \wedge \delta = d \wedge \delta = d$ that implies $\flat \in j + i - j \in Q$. For each $j \in Q, i, k \in \mathcal{N}^*$ $\inf_{\flat \in i\rho(j+k)-i\rho k} \tau_Q(\flat) \vee \gamma \geq \tau_Q(i) \wedge \delta = d \wedge \delta = d$ that implies $\flat \in i\rho(j + k) - i\rho k \in Q$. Therefore, Q is hyperideal of hypernear ring $\mathcal{N}^*$.

Conversely, let Q be an hyperideal of hypernear ring $\mathcal{N}^*$ and let $i, j \in \mathcal{N}^*$.

(i) (a) For $i, j \in Q$, then $\flat \in i - j \in Q$ and so $\inf_{\flat \in i-j} \tau_Q(\flat) \vee \gamma = d = d \wedge \delta \geq \min\{\tau_Q(i), \tau_Q(j)\} \wedge \delta$. (b) If atleast one of i or j is not in Q, then $\flat \in i - j \notin Q$ and so $\inf_{\flat \in i-j} \tau_Q(\flat) \vee \gamma = e = e \wedge \delta \geq \min\{\tau_Q(i), \tau_Q(j)\} \wedge \delta$. (c) If both $i, j \notin Q$, then $\flat \in i - j \notin Q$ and so $\inf_{\flat \in i-j} \tau_Q(\flat) \vee \gamma = e = e \wedge \delta \geq \min\{\tau_Q(i), \tau_Q(j)\} \wedge \delta$.

(ii) (a) Let $i,\ j \in \mathcal{N}^*$ and if $i \in Q$ then $\flat \in j+i-j \in Q$ then $\inf_{\flat \in j+i-j} \tau_Q(\flat) \vee \gamma = d = d \wedge \delta \geq \tau_Q(i) \wedge \delta$. (b) If i not in Q, then $\flat \in j+i-j \notin Q$, and so $\inf_{\flat \in j+i-j} \tau_Q(\flat) \vee \gamma = e = e \wedge \delta \geq \tau_Q(i) \wedge \delta$.

(iii) (a) Now let $i,\ j,\ k \in \mathcal{N}^*$, $\rho \in \Gamma^*$ and if $i \in Q$, then $\flat \in i\rho(j+k) - i\rho k \in Q$ and so $\inf_{\flat \in i\rho(j+k)-i\rho k} \tau_Q(\flat) \vee \gamma = d = d \wedge \delta \geq \tau_Q(j) \wedge \delta$. (b) If j not in Q, then $\flat \in i\rho(j+k) - i\rho j \notin Q$, and so, $\inf_{\flat \in i\rho(j+k)-i\rho k} \tau_Q(\flat) \vee \gamma = e = e \wedge \delta \geq \tau_Q(j) \wedge \delta$.

Thus, τ_Q is an $(\gamma,\ \delta)$-fuzzy hyperideal of Γ-hypernear ring $\mathcal{N}^*$. Now $\mathcal{N}^*_{\tau_Q} = \{i \in \mathcal{N}^* | \tau_Q(i) = \tau_Q(0)\} = \{i \in \mathcal{N}^* | \tau_Q(i) = d\} = \{i \in \mathcal{N}^* | i \in Q\} = Q$.

Corollary 10 Let $\mathcal{R}$ be a non-vacant subcollection of a Γ-hypernear ring $\mathcal{N}^*$, $\mathcal{R}$ is hyperideal of $\mathcal{N}^*$ if and only if $\psi_{\mathcal{R}}$ is a $(\gamma,\ \delta)$-fuzzy hyperideal of $\mathcal{N}^*$. (Here $\psi_{\mathcal{R}}$ represent characteristic function of $\mathcal{R}$).

Theorem 11 Let $\tau,\ \sigma$ be $(\gamma,\ \delta)$-fuzzy hyperideals of Γ-hypernear ring $\mathcal{N}^*$. Then $\tau + \sigma$ is also a $(\gamma,\ \delta)$-fuzzy hyperideals of $\mathcal{N}^*$ where

$$(\tau + \sigma)(i) = \sup\{\tau(i_1) \wedge \sigma(i_2) | i = i_1 + i_2\},\ \forall\, i \in \mathcal{N}^*$$

Proof Let $\forall\, i,\ j \in \mathcal{N}^*$ and $\rho \in \Gamma^*$, we have

(i) $\inf_{\flat \in i-j}(\tau + \sigma)(\flat) \vee \gamma$
$\geq \sup\{\inf_{\flat \in i_1 - i_2} \tau(\flat) \wedge \inf_{\flat \in j_1 - j_2} \sigma(\flat) | i = i_1 + j_1,\ j = i_2 + j_2\}$
$\vee\ \gamma \geq \sup\{\tau(i_1) \wedge \tau(i_2) \wedge \sigma(j_1) \wedge \sigma(j_2) \wedge \delta | i = i_1 + j_1,\ j = i_2 + j_2\}$
$= \sup\{\tau(i_1) \wedge \sigma(j_1) | i = i_1 + i_1\} \wedge \sup\{\tau(i_2) \wedge \sigma(j_2) | j = i_2 + j_2\} \wedge \delta$
$= (\tau + \sigma)(i) \wedge (\tau + \sigma)(j) \wedge \delta.$

(ii) $\inf_{\flat \in j+i-j}(\tau + \sigma)(\flat) \vee \gamma$
$\geq \sup\{\inf_{\flat \in j+i_1-j} \tau(\flat) \wedge \inf_{\flat \in j+i_2-j} \sigma(\flat) | i = i_1 + i_2\}$
$\vee\ \gamma \geq \sup\{\tau(i_1) \wedge \sigma(i_2) \wedge \delta | i = i_1 + i_2\}$
$= \sup\{\tau(i_1) \wedge \sigma(i_2) | i = i_1 + i_2\} \wedge \delta = (\tau + \sigma)(i) \wedge \delta.$

(iii) $\inf_{\flat \in i\rho(j+k)-i\rho k}(\tau + \sigma)(\flat) \vee \gamma$
$\geq \sup\{\inf_{\flat \in i\rho(j_1+k)-i\rho k} \tau(\flat) \wedge \inf_{\flat \in i\rho(j_2+k)-i\rho k} \sigma(\flat) | j = j_1 + j_2\} \vee\ \gamma$
$\geq \sup\{\tau(j_1) \wedge \sigma(j_2) \wedge \delta | j = j_1 + j_2\}$
$= \sup\{\tau(j_1) \wedge \sigma(j_2) | j = j_1 + j_2\} \wedge \delta$
$= (\tau + \sigma)(j) \wedge \delta.$

So, $\tau + \sigma$ is a $(\gamma,\ \delta)$-fuzzy hyperideals of $\mathcal{N}^*$.

Definition 12 Let $\mathcal{N}^*$ and $\mathcal{M}^*$ be Γ-hypernear rings. A map $\eta : \mathcal{N}^* \to \mathcal{M}^*$ is homomorphism if $\eta(i + j) = \eta(i) + \eta(j)$ and $\eta(i\rho j) = \eta(i)\,\rho\eta(j) \forall\, i,\ j \in \mathcal{N}^*$ and $\rho \in \Gamma^*$.

Theorem 13 Let $\eta : \mathcal{N}^* \to \mathcal{M}^*$ be a homomorphism and τ be an $(\gamma,\ \delta)$-fuzzy hyperrideal of Γ-hypernear ring $\mathcal{N}^*$ then $\eta(\tau)$ is also an $(\gamma,\ \delta)$-fuzzy hyperideal of a Γ-hypernear ring $\mathcal{M}^*$. where

$$\eta(\tau)(j) = \inf_{j \in \mathcal{M}^*} \{\tau(i) | \eta(i) = j\} \forall\, j \in \mathcal{M}^*.$$

Proof Let τ be an (γ, δ)-fuzzy hyperideal of hypernear ring $\mathcal{N}^*$. Now (i) Let for any $i_1, i_2 \in \mathcal{N}^*$ and $j_1, j_2 \in \mathcal{M}^*$ then we have

$$\begin{aligned}
&\inf_{\flat \in j_1 - j_2} \eta(\tau)(\flat) \vee \gamma \\
&= \inf_{i_1, i_2 \in \mathcal{N}^*} \{\inf_{\flat \in i_1 - i_2} \tau(\flat) | \eta(i_1 - i_2) = j_1 - j_2\} \vee \gamma \\
&= \inf_{i_1, i_2 \in \mathcal{N}^*} \{\inf_{\flat \in i_1 - i_2} \tau(\flat) \vee \gamma | \eta(i_1 - i_2) = j_1 - j_2\} \\
&\geq \inf_{i_1, i_2 \in \mathcal{N}^*} \{(\tau(i_1) \wedge \tau(i_2)) \wedge \delta | \eta(i_1) = j_1,\ \eta(i_2) = j_2\} \\
&= \inf_{i_1 \in \mathcal{N}^*} \{\tau(i_1) \wedge \delta | \eta(i_1) = j_1\} \wedge \inf_{i_2 \in \mathcal{N}^*} \{\tau(i_2) \wedge \delta | \eta(i_2) = j_2 \\
&= \eta(\tau)(j_1) \wedge \eta(\tau)(j_2) \wedge \delta.
\end{aligned}$$

(ii) Let for any $i_1, i_2 \in \mathcal{N}^*$, $j_1, j_2 \in \mathcal{M}^*$ then we have

$$\begin{aligned}
&\inf_{\flat \in j_2 + j_1 - j_2} \eta(\tau)(\flat) \vee \gamma \\
&= \inf_{i_1, i_2 \in \mathcal{N}^*} \{\inf_{\flat \in i_2 + i_1 - i_2} \tau(\flat) | \eta(i_2 + i_1 - i_2) = j_2 + j_1 - j_2\} \vee \gamma \\
&= \inf_{i_1, i_2 \in \mathcal{N}^*} \{\inf_{\flat \in i_2 + i_1 - i_2} \tau(\flat) \vee \gamma | \eta(i_2 + i_1 - i_2) = j_2 + j_1 - j_2\} \\
&\geq \inf_{i_1 \in \mathcal{N}^*} \{\tau(i_1) \wedge \delta | \eta(i_1) = j_1\} \\
&= \inf_{i_1 \in \mathcal{N}^*} \{\tau(i_1) \wedge \delta | \eta(i_1) = j_1\} \wedge \delta \\
&= \eta(\tau)(j_1) \wedge \delta.
\end{aligned}$$

(iii) Let for any $j, i_1, i_2 \in \mathcal{N}^*$, $j', k_1, k_2 \in \mathcal{M}^*$ and $\rho \in \Gamma^*$, $\rho \in \Gamma^*$ then

$$\begin{aligned}
&\inf_{\flat \in k_1 \rho (j' + k_2) - k_1 \rho k_2} \eta(\tau)(\flat) \vee \gamma \\
&= inf_{j, i_1, i_2 \in \mathcal{N}^*} \{\inf_{\flat \in i_1 \rho (j + i_2) - i_1 \rho i_2} \tau(\flat) | \eta(i_1 \rho (j + i_2) - i_1 \rho\, i_2) \\
&= k_1 \rho (j' + k_2) - k_1 \rho k_2\} \vee \gamma \\
&= inf_{j, i_1, i_2 \in \mathcal{N}^*} \{\inf_{\flat \in i_1 \rho (j + i_2) - i_1 \rho i_2} \tau(\flat) \vee \gamma | \eta(i_1 \rho (j + i_2) - i_1 \rho i_2) \\
&= k_1 \rho (j' + k_2) - k_1 \rho k_2\} \\
&\geq \inf_{j \in \mathcal{N}^*} \{\tau(j) \wedge \delta | \eta(j) = j')\} \\
&= \eta(\tau)(j') \wedge \delta.
\end{aligned}$$

Hence proof is completed.

Theorem 14 *If $\omega : \mathcal{N}^* \to \mathcal{M}^*$ is a homomorphism and $\mathfrak{D}$ is a (γ, δ)-fuzzy hyperideal of a Γ-hypernear ring $\mathcal{M}^*$, then $\omega^{-1}(\mathfrak{D})$ is a (γ, δ)-fuzzy hyperideal of a $\mathcal{N}^*$ where*

$$\omega^{-1}(\mathfrak{D})(i) = \mathfrak{D}(\omega(i))$$

Proof Let $\mathfrak{D}$ be an (γ, δ)-fuzzy hyperideal of Γ-hypernear ring M. Now we want show that $\omega^{-1}(\mathfrak{D})$ is a (γ, δ) fuzzy hyperideal of $\mathcal{N}^*$.

(i) For any $i, j \in \mathcal{N}^*$ then we have

$$\begin{aligned}&\inf_{\flat\in i-j}\omega^{-1}(\mathfrak{D})(\flat) \vee \gamma\\ &= \inf_{\flat\in i-j}\mathfrak{D}(\omega(\flat)) \vee \gamma \geq \mathfrak{D}(\omega(i)) \wedge \mathfrak{D}(\omega(j)) \wedge \delta\\ &= \omega^{-1}(\mathfrak{D})(i) \wedge \omega^{-1}(\mathfrak{D})(j) \wedge \delta.\end{aligned}$$

(ii) For any $i, j \in \mathcal{N}^*$ then we have

$$\begin{aligned}&\inf_{\flat\in j+i-j}\omega^{-1}(\mathfrak{D})(\flat) \vee \gamma\\ &= \inf_{\flat\in j+i-j}\mathfrak{D}(\omega(\flat)) \vee \gamma \geq \mathfrak{D}(\omega(i)) \wedge \delta\\ &= \omega^{-1}(\mathfrak{D})(i) \wedge \delta.\end{aligned}$$

(iii) For any $i, j, i \in \mathcal{N}^*$ and $\rho \in \Gamma^*$. We have

$$\begin{aligned}&\inf_{\flat\in i\rho(j+k)-i\rho k}\omega^{-1}(\mathfrak{D})(\flat) \vee \gamma\\ &= \inf_{\flat\in i\rho(j+k)-i\rho k}\mathfrak{D}(\omega(\flat)) \vee \gamma \geq \mathfrak{D}(\omega(j)) \wedge \delta\\ &= \omega^{-1}(\mathfrak{D})(j) \wedge \delta.\end{aligned}$$

Hence, $\omega^{-1}(\mathfrak{D})$ is a (γ, δ)-fuzzy hyperideal of $\mathcal{N}^*$.

Theorem 15 If $\{\tau_p(i)|p \in P\}$ be a family of (γ, δ)-fuzzy hyperideals of Γ-hypernear ring $\mathcal{N}^*$, then $\underset{p\in P}{\vee}\tau_p$ is also (γ, δ)-fuzzy hyperideal of $\mathcal{N}^*$.

Proof Let consider a family $\{\tau_p(i)|p \in P\}$ of (γ, δ)-fuzzy hyperideal of Γ-hypernear ring of $\mathcal{N}^*$. For $i, j, k \in \mathcal{N}^*$ we have,

$$\begin{aligned}&\inf_{\flat\in i-j}(\underset{p\in P}{\vee})\tau_p(\flat) \vee \gamma\\ &= \inf_{\flat\in i-j}\sup\{\tau_p(\flat)|p \in P\} \vee \gamma\\ &\geq \sup\{\min\{\tau_p(i), \tau_p(i)|p \in P\} \wedge \delta\\ &= \min\{\underset{p\in P}{sup}\,\tau_p(i) \wedge \delta, \underset{p\in P}{sup}\,\tau_p(j) \wedge \delta\}\\ &= \min\{\underset{p\in P}{\vee}\tau_p(i) \wedge \delta, \underset{p\in P}{\vee}\tau_p(j) \wedge \delta\}.\end{aligned}$$

$$\begin{aligned}\inf_{\flat\in j+i-j}\underset{p\in P}{\vee}\tau_p(\flat) \vee \gamma &= \inf_{\flat\in j+i-j}\sup\{\tau_p(\flat)|p \in P\} \vee \gamma\\ \geq \sup\{\tau_p(i)|p \in P\} \wedge \delta &= \underset{p\in P}{sup}\,\tau_p(i) \wedge \delta = \underset{p\in P}{\vee}\tau_p(i) \wedge \delta.\end{aligned}$$

$$\begin{aligned}
&\inf_{\flat\in i\rho(j+k)-i\rho k} \bigvee_{p\in P} \tau_p(\flat) \vee \gamma \\
&= \inf_{\flat\in i\rho(j+k)-i\rho k} \sup\{\tau_p(\flat) | p \in P\}. \vee \gamma \\
&\geq \sup\{\tau_p(j) | p \in P\} \wedge \delta \\
&= \sup_{p\in P} \tau_p(j) \wedge \delta = \bigvee_{p\in P} \tau_p(j) \wedge \delta.
\end{aligned}$$

Hence, $\bigvee_{p\in P} \tau_p$ is an (γ, δ)-fuzzy hyperideal of $\mathcal{N}^*$.

Theorem 16 If $\{\tau_p(i) | p \in P\}$ be a family of an (γ, δ)-fuzzy of Γ-hypernear ring $\mathcal{N}^*$ then $\bigwedge_{p\in P} \tau_p$ is also a (γ, δ)-fuzzy hyperideal of $\mathcal{N}^*$.

Proof Proof is straightforward.

Corollary 20 If τ and σ be two (γ, δ)-fuzzy hyperideals of Γ-hypernear ring $\mathcal{N}^*$, then $\tau \cup \sigma$ is also (γ, δ)-fuzzy hyperideal of $\mathcal{N}^*$.

3 Normal (γ, δ)-Fuzzy Hyperideals

Definition 17 An τ of Γ-hypernear ring $\mathcal{N}^*$ is normal fuzzy hyperideal (NFH) if $\tau(0) = 1$.

Theorem 22 Given a (γ, δ)-fuzzy hyperideal τ of an Γ-hypernear ring $\mathcal{N}^*$, and suppose τ^* is a fuzzy collection in $\mathcal{N}^*$ by defining $\tau^*(i) = \tau(i) + 1 - \tau(0) \forall i \in \mathcal{N}^*$. Then τ^* is a (γ, δ)-fuzzy hyperideal $\mathcal{N}^*$.

Proof Note that $\tau^*(0) = \tau(0) + 1 - \tau(0) = 1$ and for $i, j, k \in \mathcal{N}^*$ and $\rho \in \Gamma^*$,

$$\begin{aligned}
\inf_{\flat\in i-j} \tau^*(\flat) \vee \gamma &= (\inf_{\flat\in i-j} \tau(\flat) + 1 - \tau(0)) \vee \gamma \\
&\geq (\min\{\tau(i), \tau(i)\} \wedge \delta) + (1 \wedge \delta) - (\tau(0) \wedge \delta) \\
&= \min\{(\tau(i) + 1 - \tau(0)) \wedge \delta, (\tau(j)) + 1 - \tau(0)) \wedge \delta\} \\
&= \min\{\tau^*(i) \wedge \delta, \tau^*(j) \wedge \delta\} \\
&= \min\{\tau^*(i), \tau^*(j)\} \wedge \delta.
\end{aligned}$$

$$\begin{aligned}
&\inf_{\flat\in j+i-j} \tau^*(\flat) \vee \gamma \\
&= (\inf_{\flat\in j+i-j} \tau(\flat) + 1 - \tau(0)) \vee \gamma \geq (\tau(i) \wedge \delta) + (1 \wedge \delta) - (\tau(0) \wedge \delta) \\
&= (\tau(i) + 1 - \tau(0)) \wedge \delta = \tau^*(i) \wedge \delta
\end{aligned}$$

and

$$\begin{aligned}&\inf_{\flat\in i\rho(j+k)-i\rho k}\tau^*(\flat)\vee\gamma\\&\quad=\inf_{\flat\in i\rho(j+k)-i\rho k}\tau(\flat)+1-\tau(0)\vee\gamma\geq(\tau(j)\wedge\delta)\\&\qquad+(1\wedge\delta)-(\tau(0)\wedge\delta)=(\tau(j)+1-\tau(0))\wedge\delta\\&\quad=\tau^*(j)\wedge\delta.\end{aligned}$$

Hence, τ^* is a $(\gamma,\ \delta)$-fuzzy hyperideal of $\mathcal{M}^*$.

Definition 18 A function from $\mathcal{X}$ into [0, 1] is referred to as a $(\gamma,\ \delta)$-fuzzy subset of a set $\mathcal{X}$. The set of all $(\gamma,\ \delta)$-fuzzy subsets of $\mathcal{X}$ is $(\gamma,\ \delta)$-fuzzy power set of $\mathcal{X}$ and is represented by $I^{\mathcal{X}}_{\gamma,\delta}=[0,\ 1]^{\mathcal{X}}$.

Lemma 19 *Let $\tau\in I^{\mathcal{M}^*}_{\gamma,\delta}$. Then τ is a $(\gamma,\ \delta)$-fuzzy hyperideal of Γ-hypernear ring $\mathcal{N}^*$ iff upper level subset τ_d is $\mathcal{N}^*\forall d\in Im\,(\tau)$.*

Proof Proof is straightforward.

4 (γ, δ)-Cut Set

We introduce the concept of a $(\gamma,\ \delta)$-cut set of a fuzzy subset based on the notion of a $(\epsilon,\ \epsilon\vee q)$-level subset described in.

Definition 20 [5] Let τ be a fuzzy subset of the set $\mathcal{X}$ with $d\ in$ [0, 1] then there is the subset $\tau_d^{(\gamma,\delta)}$ of $\mathcal{X}$ as defined by

$$\tau_d^{(\gamma,\delta)}=\{i\in\mathcal{X}|\tau(i)\vee\gamma\geq d\wedge\delta\text{ or }\tau(i)>2\delta-d\vee\gamma\}$$

is known as $(\gamma,\ \delta)$-cut set of τ. We represented by $i_d\in(\gamma,\ \delta)$ if $i\in\tau_d^{(\gamma,\delta)}$. if τ is a fuzzy subset of $\mathcal{X}$ and $d\in[0,\ 1]$, then

$$\tau_d^{(\gamma,\delta)}=\begin{cases}\mathcal{X} & if\quad d\leq\gamma\\ \tau_D & if\quad\gamma<d\leq\delta\\ \tau_{(2\delta-d)}\vee\gamma & if\quad d>\delta\end{cases}$$

is a $(\gamma,\ \delta)$-cut set of τ.

Theorem 21. Let τ be a $(\gamma,\ \delta)$-fuzzy Γ-hypernear ring (fuzzy hyperideal) of $\mathcal{N}^*$, $\forall\, d\in[0,\ 1]$ if and only if $\tau_d^{(\gamma,\delta)}$ is a fuzzy Γ-hypernear ring (fuzzy hyperideal) of $\mathcal{N}^*$ or $\tau_d^{(\gamma,\delta)}=\phi$.

Proof We only prove the case of a $(\gamma,\ \delta)$-fuzzy Γ-hypernear ring (fuzzy hyperideal) of N. If $d\geq\gamma$, then $\tau_d^{(\gamma,\delta)}=\mathcal{N}^*$. If $\gamma<d\leq\delta$, then $\tau_d^{(\gamma,\delta)}=\tau_d$ and τ_d is a $\mathcal{N}^*$ from Theorem 7. If $d>\delta$, then $\tau_d^{(\gamma,\delta)}=\tau_{(2\delta-d)}\wedge\gamma$ and $(2\delta-d)\wedge\gamma\in[\gamma,\ \delta)$. So, $\tau_d^{(\gamma,\delta)}$ is a Γ-hypernear ring (hyperideal) $\mathcal{N}^*$.

5 On Direct Product of (γ, δ)-Fuzzy Hyperdeals

Let $\mathcal{N}^*$ and $\mathcal{M}^*$ be two Γ-hypernear rings with identity 0 and $0'$, respectively, then Γ-hypernear ring $\mathcal{N}^* \times \mathcal{M}^*$ is a identity $(0,\ 0')$ if we define $(i_1,\ j_1)\ (\rho_1,\ \rho_2)\ (i_2,\ j_2) = (i_1\rho_1 i_2,\ j_1\rho_2 j_2) \forall\ (i_1,\ j_1),\ (i_2,\ j_2) \in \mathcal{N}^* \times \mathcal{M}^*$ and $\rho_1,\ \rho_2 \in \Gamma_1^* \times \Gamma_2^*$ Moreover, the inverse element of any $(i,\ j) \in \mathcal{N}^* \times \mathcal{M}^*$ is $(x,\ y) \in \mathcal{N}^* \times \mathcal{M}^*$ if and only if x and y are inverse elements of i and j in $\mathcal{N}^*$ and $\mathcal{M}^*$, respectively.

Definition 22 [20] Let τ and σ be any two $(\gamma,\ \delta)$-fuzzy subset of $\mathcal{X}$ and $\mathcal{Y}$, respectively. Then their product of τ and σ represented by $(\tau \times \sigma) \vee$ is a $(\gamma,\ \delta)$-fuzzy subset of $(X \times Y) \vee \gamma$ defined as follows: $(\tau \times \sigma)\ (i,\ j) \vee \gamma = (\tau(i) \wedge \sigma(j)) \wedge \delta$. Where sum, multiplication, inverse of $(\gamma,\ \delta)$ as follows:

$$((\boldsymbol{a}_1,\ \boldsymbol{b}_1) + (\boldsymbol{a}_2,\ \boldsymbol{b}_2)) \vee \gamma = (\boldsymbol{a}_1 + \boldsymbol{a}_2,\ \boldsymbol{b}_1 + \boldsymbol{b}_2) \wedge \delta$$

$$((\boldsymbol{a}_1,\ \boldsymbol{b}_1) + (\boldsymbol{a}_2,\ \boldsymbol{b}_2)) \vee \gamma = (\boldsymbol{a}_1\boldsymbol{a}_2,\ \boldsymbol{b}_1\boldsymbol{b}_2) \wedge \delta$$

$$-(\boldsymbol{a},\ \boldsymbol{b}) \vee \gamma = (-\boldsymbol{a},\ -\boldsymbol{b}) \wedge \delta$$

Theorem 23 If τ and σ be two $(\gamma,\ \delta)$-fuzzy hyperideals of Γ-hypernear rings $\mathcal{M}^*$ and $\mathcal{N}^*$, respectively, then $\tau \times \sigma$ is also $(\gamma,\ \delta)$-fuzzy hyperideal of $\mathcal{M}^* \times \mathcal{N}^*$.

Proof Let $(i_1,\ i_2),\ (j_1,\ j_2),\ (k_1,\ k_2) \in \mathcal{M}^* \times \mathcal{N}^*$ and $\rho_1,\ \rho_2 \in \Gamma_1^* \times \Gamma_2^*$. Now,

(i) $\inf_{\flat \in (i_1, j_1) - (i_2, j_2)} (\tau \times \sigma)\ (\flat) \vee \gamma$
$= \inf_{\flat \in (i_1 - i_2), (j_1 - j_2)} (\tau \times \sigma)\ (\flat) \vee \gamma$
$\geq (\tau(i_1) \wedge \tau(i_2) \wedge \delta) \wedge (\sigma(j_1) \wedge \sigma(j_2) \wedge \delta) \wedge \delta$
$= \{(\tau(i_1) \wedge \sigma(j_1)) \wedge (\tau(i_2) \wedge \sigma(j_2))\} \wedge \delta$
$= \{(\tau \times \sigma)\ (i_1,\ j_1) \wedge (\tau \times \sigma)\ (i_2,\ j_2)\} \wedge \delta.$

(ii) $\inf_{\flat \in (i_2, j_2) + (i_1, j_1) - (i_2, j_2)} (\tau \times \sigma)\ (\flat) \vee \gamma$
$= \inf_{\flat \in (i_2 + i_1 - i_2), (j_2 + j_1 - j_2)} (\tau \times \sigma)\ (\flat) \vee \gamma$
$\geq (\tau(i_1) \wedge \delta) \wedge (\sigma(i_1) \wedge \delta) \wedge \delta$
$= (\tau(i_1) \wedge \sigma(i_1)) \wedge \delta$
$= (\tau \times \sigma)\ (i_1,\ j_1) \wedge \delta.$

(iii) $\inf_{\flat \in (i_1, i_2)(\rho_1, \rho_2)((j_1, j_2) + (k_1, k_2)) - (i_1, i_2)(\rho_1, \rho_2)(k_1, k_2)} (\tau \times \sigma)\ (\flat) \vee \gamma$
$= \inf_{\flat \in i_1\rho_1(j_1 + k_1) - i_1\rho_1 k_1, i_2\rho_2(j_2 + k_2) - i_2\rho_2 k_2} (\tau \times \sigma)\ (\flat) \vee \gamma$
$\geq (\tau(i_1) \wedge \delta) \wedge (\sigma(i_2) \wedge \delta) \wedge \delta$
$= (\tau(i_1) \wedge \sigma(i_2)) \wedge \delta$
$= (\tau \times \sigma)\ (i_1,\ i_2) \wedge \delta.$

Hence $\tau \times \sigma$ is a (γ, δ)-fuzzy hyperideal of $\mathcal{M}^* \times \mathcal{N}^*$.

Lemma 24 Let τ and σ be any two fuzzy subsets of Γ-hypernear rings $\mathcal{M}^*$ and $\mathcal{N}^*$, respectively, if $\tau \times \sigma$ is (γ, δ)-fuzzy hyperideal of $\mathcal{M}^* \times \mathcal{N}^*$ then.

(i) $(\tau \times \sigma)(0, 0') \vee \gamma \geq (\tau \times \sigma)(i, j) \wedge \delta$.
(ii) $(\tau_1 \times \tau_2 \ldots \times \tau_n)(0_1, 0_2 \ldots 0_n) \vee \gamma \geq (\tau_1 \times \tau_2 \ldots \times \tau_n)(i_1, i_2 \ldots i_n) \wedge \delta$.

Theorem 25 Let τ and σ be a two fuzzy subsets of Γ-hypernear rings $\mathcal{M}^*$ and $\mathcal{N}^*$, respectively. If $\tau \times \sigma$ is a (γ, δ)-fuzzy hyperideal of Γ-hypernear ring $\mathcal{M}^* \times \mathcal{N}^*$, then atleast one of the following must be true.

(i) $\tau(0) \vee \gamma \geq \sigma(j) \wedge \delta \, \forall \, j \in \mathcal{N}^*$
(ii) $\sigma(0') \vee \gamma \geq \tau(i) \wedge \delta \, \forall \, i \in \mathcal{M}^*$

Proof Let $\tau \times \sigma$ is the (γ, δ)-fuzzy hyperideal of $\mathcal{M}^* \times \mathcal{N}^*$. By contradiction suppose that there exist $i \in \mathcal{M}^*$ and $v \in \mathcal{N}^*$ such that $\sigma(0') \vee \gamma < \tau(i) \wedge \delta$ and $\tau(0) \vee \gamma < \tau(j) \wedge \delta$.

Now

$$\begin{aligned}
&(\tau \times \sigma)(i, j) \vee \gamma \\
&\quad = (\tau(i) \wedge \sigma(j)) \wedge \delta \\
&\quad = (\tau(i) \wedge \delta) \wedge (\sigma(j) \wedge \delta) \\
&\quad > (\tau(0) \vee \gamma) \wedge (\sigma(0') \vee \gamma) \\
&\quad = (\tau(0) \wedge \sigma(0')) \vee \gamma = (\tau \times \sigma)(0, 0') \vee \gamma.
\end{aligned}$$

Thus, $\tau \times \sigma$ is a (γ, δ)-fuzzy hyperideals of the $\mathcal{M}^* \times \mathcal{N}^*$ satisfying $(\tau \times \sigma)(i, j) \wedge \delta > (\tau \times \sigma)(0, 0') \vee \gamma$ This is a contradict to Lemma (29).

Theorem 26 Suppose τ and σ be a two fuzzy subset of Γ-hypernear rings $\mathcal{M}^*$ and $\mathcal{N}^*$, respectively, if $\tau \times \sigma$ is a (γ, δ)-fuzzy hyperideal of Γ-hypernear ring $\mathcal{M}^* \times \mathcal{N}^*$, then either τ is a (γ, δ)-fuzzy hyperideal $\mathcal{M}^*$ or σ is a (γ, δ)-fuzzy hyperideal $\mathcal{N}^*$.

Proof Suppose $\tau \times \sigma$ is a (γ, δ)-fuzzy hyperideal $\mathcal{M}^* \times \mathcal{N}^*$. By using the property $\sigma(0') \vee \gamma \geq \tau(i) \wedge \delta \, \forall \, i, j, k, \in \mathcal{M}^*$ then two cases are possible $\gamma \geq \tau(i) \wedge \delta$ or $\sigma(0') \geq \tau(i) \wedge \delta$.

Case (i)

If $\gamma \geq \tau(i) \wedge \delta \, \forall \, i \in \mathcal{M}^*$ then for $i, j \in \mathcal{M}^*$ and $\rho \in \Gamma^*$,

$$\begin{aligned}
&\inf_{\flat \in i-j} \tau(\flat) \vee \gamma \geq \gamma \geq \tau(i) \wedge \tau(j) \wedge \delta \\
&\quad \geq (\tau(i) \wedge \tau(j))\delta \inf_{\flat \in j+i-j} \tau(\flat) \vee \gamma \geq \gamma \geq \tau(i) \wedge \delta.
\end{aligned}$$

$\inf_{\flat \in i\rho(j+k)-i\rho k} \tau(\flat) \vee \gamma \geq \gamma \geq \tau(j) \wedge \delta$. Hence, in this case τ is a (γ, δ)-fuzzy hyperideal $\mathcal{M}^*$.

Case (ii)

If $\sigma(0') \geq \tau(i) \wedge \delta$ then

(i) for $i,\ j \in \mathcal{M}^*$,

$$\begin{aligned}\inf_{\flat \in i-j}\tau(\flat) \vee \gamma &\geq [\inf_{\flat \in i-j}\tau(\flat) \wedge \sigma(0')] \vee \gamma \\ &= [\inf_{\flat \in i-j}\tau(\flat) \wedge \sigma(0'-0')] \vee \gamma \\ &= [\inf_{\flat \in (i,0')-(j,0')}(\tau \times \sigma)(\flat)] \vee \gamma \geq \\ &= [(\tau(i) \wedge \sigma(0')) \wedge (\tau(j) \wedge \sigma(0'))] \wedge \delta \\ &= (\tau(i) \wedge (\tau(j)) \wedge \delta.\end{aligned}$$

(ii) For $i,\ j \in \mathcal{M}^*$,

$$\begin{aligned}\inf_{\flat \in j+i-j}\tau(\flat) \vee \gamma &\geq [\inf_{\flat \in j+i-j}\tau(\flat) \wedge \sigma(0')] \vee \gamma \\ &= [\inf_{\flat \in j+i-j}\tau(\flat) \wedge \inf_{\flat \in 0'+0'-0'}\sigma(\flat)] \vee \gamma \\ &= [\inf_{\flat \in (j,0')+(i,0')-(j,0')}(\tau \times \sigma)(\flat)] \vee \gamma \\ &\geq (\tau \times \sigma)(i,\ 0') \wedge \delta \\ &= (\tau(i) \wedge \sigma(0')) \wedge \delta \\ &= \tau(i) \wedge \delta.\end{aligned}$$

(iii) For $i,\ j,\ k \in \mathcal{M}^*$ and $\rho \in \Gamma^*$,

$$\begin{aligned}\inf_{\flat \in i\rho(j+k)-i\rho k}\tau(\flat) \vee \gamma &\geq [\inf_{\flat \in i\rho(j+k)-i\rho k}\tau(\flat) \wedge \sigma(0')] \vee \gamma \\ &= [\inf_{\flat \in i\rho(j+k)-i\rho k}\tau(\flat) \wedge inf_{\flat \in 0'\rho(0'+0')-0'\rho 0'}\sigma(\flat)] \vee \gamma \\ &= [\inf_{\flat \in (i,0')\rho((j,0')+(k,0'))-(i,0')\rho(k,0')}(\tau \times \sigma)(\flat)] \vee \gamma \geq (\tau \times \sigma)(j,\ 0') \wedge \delta \\ &= (\tau(j) \wedge \sigma(0')) \wedge \delta = \tau(j) \wedge \delta.\end{aligned}$$

Hence, in this case τ is a $(\gamma,\ \delta)$-fuzzy hyperideal $\mathcal{M}^*$.

Theorem 27 Let τ and σ be fuzzy subsets of Γ-hypernear rings $\mathcal{M}^*$ and $\mathcal{N}^*$, respectively, such that $\tau(0) \vee \gamma \geq \tau(j) \wedge \delta$, $\forall\ j \in \mathcal{N}^*$ and $\tau \times \sigma$ is a $(\gamma,\ \delta)$-fuzzy hyperideal of $\mathcal{M}^* \times \mathcal{N}^*$ then, σ is a $(\gamma,\ \delta)$-fuzzy hyperideal of $\mathcal{N}^*$.

Corollary 28 Let $\tau_1,\ \tau_2, \ldots \tau_n$ be a $(\gamma,\ \delta)$-fuzzy subset of Γ-hypernear rings $\mathcal{N}_1^*,\ \mathcal{N}_2^* \ldots \mathcal{N}_n^*$, respectively, if $\tau_1 \times \tau_2 \times \ldots \times \tau_n$ is a $(\gamma,\ \delta)$-fuzzy hyperideal of Γ-hypernear ring $\mathcal{N}_1^* \times \mathcal{N}_2^* \times \ldots \times \mathcal{N}_n^*$, then atleast for one p, $\tau_p(0_p) \vee \gamma \geq \tau_k(p_k) \wedge \delta\ \forall\ p \in \mathcal{N}_k^*$, for $k = 1, 2, \ldots n$ where 0_p is an identity of $\mathcal{N}_p^*$ must be true.

Corollary 30 Let $\tau_1,\ \tau_2, \ldots \tau_n$ be a $(\gamma,\ \delta)$-fuzzy hyperideal of Γ-hypernear rings $\mathcal{N}_1^*,\ \mathcal{N}_2^* \ldots \mathcal{N}_n^*$, respectively, if $\tau_1 \times \tau_2 \times \ldots \times \tau_n$ is a $(\gamma,\ \delta)$-fuzzy hyperideal of $\mathcal{N}_1^* \times \mathcal{N}_2^* \times \ldots \times \mathcal{N}_n^*$, then atleast for one of $p,\ \tau_p$ is a $(\gamma,\ \delta)$-fuzzy hyperideal of $\mathcal{N}_p^*$.

Proof Suppose that τ_1 be a $(\gamma,\ \delta)$-fuzzy hyperideal of hypernear ring $\mathcal{N}_1^*$ then by using $\tau_p(0_p) \vee \gamma \geq \tau_1(i_1) \wedge \delta \, \forall \, i_1 \in \mathcal{N}_1^*$.

(i) For $i_1,\ j_1 \in \mathcal{N}_1^*$ then

$$\begin{aligned}
&\inf_{\flat \in i_1 - j_1} \tau_1(\flat) \vee \gamma \\
&= [\inf_{\flat \in i_1 - j_1} \tau_1(\flat) \wedge \tau_2(0_2) \wedge \ldots \wedge \tau_n(0_n)] \vee \gamma \\
&= [\inf_{\flat \in i_1 - j_1} \tau_1(\flat) \wedge \inf_{\flat \in 0_2 - 0_2} \tau_2(\flat) \wedge \ldots \wedge \inf_{\flat \in 0_n - 0_n} \tau_n(\flat)] \vee \\
&= [\inf_{\flat \in i_1 - j_1, 0_2 - 0_2 \ldots, 0_n - 0_n} (\tau_1 \times \tau_2 \times \ldots \times \tau_n)(\flat)] \vee \gamma \\
&= [\inf_{\flat \in (i_1, 0_2 \ldots, 0_n) - (j_1, 0_2 \ldots, 0_n)} (\tau_1 \times \tau_2 \times \ldots \times \tau_n)(\flat)] \vee \gamma \\
&\geq [(\tau_1 \times \tau_2 \times \ldots \times \tau_n)(i_1,\ 0_2 \ldots, 0_n) \wedge (\tau_1 \times \tau_2 \times \ldots \times \tau_n) \\
&\quad (j_1,\ 0_2 \ldots, 0_n)] \wedge \delta \\
&= [(\tau_1)\,(i_1) \wedge (\tau_2)(0_2) \wedge \ldots (\tau_n)(0_n) \wedge (\tau_1)\,(j_1) \\
&\quad \wedge (\tau_2)(0_2) \wedge \ldots (\tau_n)(0_n)] \wedge \delta \\
&= [\tau_1(i_1) \wedge \tau_1(j_1)] \wedge \delta.
\end{aligned}$$

(ii) For $i_1,\ j_1 \in \mathcal{N}_1^*$ then

$$\begin{aligned}
&\inf_{\flat \in j_1 + i_1 - j_1} \tau_1(\flat) \vee \gamma \\
&= [inf_{\flat \in j_1 + i_1 - j_1} \tau_1(\flat) \wedge \tau_2(0_2) \wedge \ldots \wedge \tau_n(0_n)] \vee \gamma \\
&= [inf_{\flat \in j_1 + i_1 - j_1} \tau_1(\flat) \wedge \inf_{\flat \in 0_2 + 0_2 - 0_2} \tau_2(\flat) \wedge \ldots \wedge \inf_{\flat \in 0_n + 0_n - 0_n} \tau_n(\flat)] \vee \gamma \\
&= [inf_{\flat \in j_1 + i_1 - j_1, 0_2 + 0_2 - 0_2 \ldots, 0_n + 0_n - 0_n} (\tau_1 \times \tau_2 \times \ldots \times \tau_n)(\flat)] \vee \gamma \\
&= [inf_{\flat (\in j_1, 0_2 \ldots, 0_n) + (i_1, 0_2 \ldots, 0_n) - (j_1, 0_2 \ldots, 0_n))} (\tau_1 \times \tau_2 \times \ldots \times \tau_n)(\flat)] \vee \gamma \\
&\geq [(\tau_1 \times \tau_2 \times \ldots \times \tau_n)\,(i_1,\ 0_2 \ldots 0_n)] \wedge \delta \\
&= [(\tau_1)\,(i_1) \wedge (\tau_2)(0_2) \wedge \ldots (\tau_n)(0_n)] \wedge \delta \\
&= \tau_1(i_1) \wedge \delta.
\end{aligned}$$

(iii) For $i_1,\ j_1,\ k_1 \in \mathcal{N}_1^*$ and $\rho_1 \in \Gamma_1^*$ then

$$\begin{aligned}
&\inf_{\flat \in i_1 \rho_1 (j_1 + k_1) - i_1 \rho_1 k_1} \tau_1(\flat) \vee \gamma \\
&= [inf_{\flat \in i_1 \rho_1 (j_1 + k_1) - i_1 \rho_1 k_1} \tau_1(\flat) \wedge \tau_2(0_2) \wedge \ldots \wedge \tau_n(0_n)] \vee \gamma \\
&= [inf_{\flat \in i_1 \rho_1 (j_1 + k_1) - i_1 \rho_1 k_1} \tau_1(\flat) \\
&\quad \wedge inf_{\flat \in 0_2 \rho_2 (0_2 + 0_2) - 0_2 \rho_2 0_2} \tau_2(\flat) \wedge \ldots \wedge \inf_{\flat \in 0_n \rho_n (0_n + 0_n) - 0_n \rho_n 0_n} \tau_n(\flat)] \vee \gamma \\
&= [inf_{\flat \in i_1 \rho_1 (j_1 + k_1) - i_1 \rho_1 k_1, 0_2 \rho_2 (0_2 + 0_2) - 0_2 \rho_2 0_2 \ldots, 0_n \rho_n (0_n + 0_n) - 0_n \rho_n 0_n} \\
&\quad (\tau_1 \times \tau_2 \times \ldots \times \tau_n)(\flat)] \vee \gamma \\
&= [inf_{\flat \in (i_1, 0_2 \ldots, 0_n)(\rho_1, \rho_2 \ldots \rho_n)((j_1, 0_2 \ldots 0_n) + (k_1, 0_2 \ldots, 0_n)) - (i_1, 0_2 \ldots, 0_n)(\rho_1, \rho_2 \ldots \rho_n)(k_1, 0_2 \ldots, 0_n)} \\
&\quad (\tau_1 \times \tau_2 \times \ldots \times \tau_n)(\flat)] \vee \gamma \\
&\geq [(\tau_1 \times \tau_2 \times \ldots \times \tau_n)\,(j_1,\ 0_2 \ldots 0_n)] \wedge \delta \\
&= [(\tau_1)(j_1) \wedge (\tau_2)(0_2) \wedge \ldots (\tau_n)(0_n)] \wedge \delta \\
&= \tau_1(j_1) \wedge \delta.
\end{aligned}$$

Hence τ_1 is $(\gamma,\ \delta)$-fuzzy hyperideal of a Γ-hypernear ring $\mathcal{N}_1^*$. Similarly, we can show that using property $\tau_p(0_p) \vee \gamma \geq \tau_k(i_k) \wedge \delta \, \forall \, i_k \in \mathcal{N}_k^*$, all τ_k for k = 2, 3,…n, is $(\gamma,\ \delta)$-fuzzy hyperideal of $\mathcal{N}_k^*$.

References

1. Zadeh LA (1996) Fuzzy sets. Inf Control 8:338–353
2. Rosenfeld A (1971) Fuzzy groups. J Math Anal Appl 35(3):512–517
3. Mukherjee TK, Sen MK (1987) On fuzzy ideals of a ring. Fuzzy Set Syst 21(1), 99–104
4. Zaid SA (2008) On fuzzy subnear-rings and ideals. Fuzzy Sets Syst 44:139–146
5. Marty F, Surune (1934) Generalisation de la notion de group. In: 4th Congress Math. Scandinaves, Stockholm, vol 8, pp 45–49
6. Corsini P, Leoreanu V (2003) Applications of hyperstructure theory. In: Advances in mathematics (Dordrecht). Kluwer Academic Publishers, Dordrecht
7. Davvaz B (2004) Isomorphism theorems on hyperrings. Indian J Pure Appl Math 35(3):321–331
8. Davvaz B, Leoreanu-Fotea V (2007) Hyperrings Theory and Applications. International Academic Press, USA
9. Cristea I, Davvaz B (2010) Atanassov's intuitionistic fuzzy grade of hypergroups. Inf Sci 180(8):1506–1517
10. Sen MK, Ameri R, Chawdhury G (2007) Fuzzy hypersemi groups. Soft Comput 12:891–900
11. Hila K, Naka K (2017) Characterization of hyperrings by fuzzy hyperideals with respect to a t-norm. Fuzzy Inf Eng 9(4):437–454
12. Zhan J, Davvaz B, Shum KP (2008) A new view of fuzzy hypernear-rings. Inf Sci 178:425–438
13. Dasic V (1990) Hypernear-rings. In: Proceedings of the Fourth International Congress, algebraic hyperstructures and applications, World Sci 19:75–85
14. Yamak S, Kazanc O, Davvaz B (2011) Normal fuzzy hyperideals in hypernear-rings. Neural Comput Appl 20(1):25–30
15. Narayana A, Manikantan T, $(\epsilon, \epsilon \text{Vq})$-fuzzy subnear-rings and $(\epsilon, \epsilon \text{Vq})$- fuzzy ideals of near-rings. J Appl Math Comput 18, 419–430 (2005)
16. Yao B (2005) (λ, μ)-fuzzy normal subgroups and (λ, μ)-fuzzy quotients subgroups. J Fuzzy Math 13(3), 695–705
17. Yao B (2007) (λ, μ)- fuzzy subrings and (λ, μ)-fuzzy ideals. J Fuzzy Math 15(4):981–987
18. Anitha B, Sivakumar D (2013) On (λ, μ)-anti-fuzzy subrings. Int J Comput Appl 75(8):0975–8887
19. Bhakat SK, Das P (1996) $(\in, \in \vee \text{q})$-fuzzy subgroup. Fuzzy Sets Syst 80(3):359–393
20. Arul selvaraj X, Sivakumar D (2011) On direct product of (λ, τ)-fuzzy subring. Int Math Form 6(41):2037– 2044
21. Davvaz B (1999) On hypernear-rings and fuzzy hyperideals. J Fuzzy Math 7(3):745–753

A Review on Multi-Input DC-DC Converter and Its Controlling for Hybrid Power System

Amogh Narwaria, Pankaj Swarnkar, and Sushma Gupta

Abstract The paper presented here gives a detailed insight on the multi-input DC-DC converter and its controlling methods. Multi-input DC-DC converters have been found of eminent importance in the field of non-conventional energy integration. Multi-input converters are being used to interface different non-conventional sources like photovoltaic cells, wind, fuel cells, etc. and energy storage. These converters are classified mainly under two categories—isolated and non-isolated topologies—and the most preferred is isolated topologies because it is best suited for high-power applications. The key focus of this paper is on controlling methods used for the multi-input DC-DC converter with conventional control scheme as well as intelligent control schemes; hence, a broad review is performed for the following mentioned above.

Keyword Multi-input DC-DC converter non-conventional energy sources hybrid power systems

1 Introduction

Non-conventional energy sources like solar, wind, fuel cells, etc. have become very popular and seen as the alternative to conventional energy sources which are depleting at a tremendous rate owing to the unprecedented growth in demand, and moreover, the environmental [1] concerns are also significant. As we know that non-conventional energy sources are unreliable due to its dependency on environmental conditions. The conventional converter scheme is presented in Fig. 1. To overcome this issue, integration of non-conventional sources is increasing in the recent days, the general structure of which is depicted in Fig. 2 [2]. By nature, intermittency and unpredictability of non-conventional sources and load highly demand the inclusion of energy storage like battery, etc. to meet the load demand and to improve the dynamic and steady-state performance of the system [3–10]. Thus, the multi-input DC-DC converters

A. Narwaria (✉) · P. Swarnkar · S. Gupta
Department of Electrical Engineering, Maulana Azad National Institute of Technology, Bhopal, Madhya Pradesh, India
e-mail: iamogh.narwaria@gmail.com

© The Author(s), under exclusive license to Springer Nature Singapore Pte Ltd. 2022

A. Tripathi et al. (eds.), *Intelligent Computing Techniques for Smart Energy Systems*, Lecture Notes in Electrical Engineering 862,
https://doi.org/10.1007/978-981-19-0252-9_25

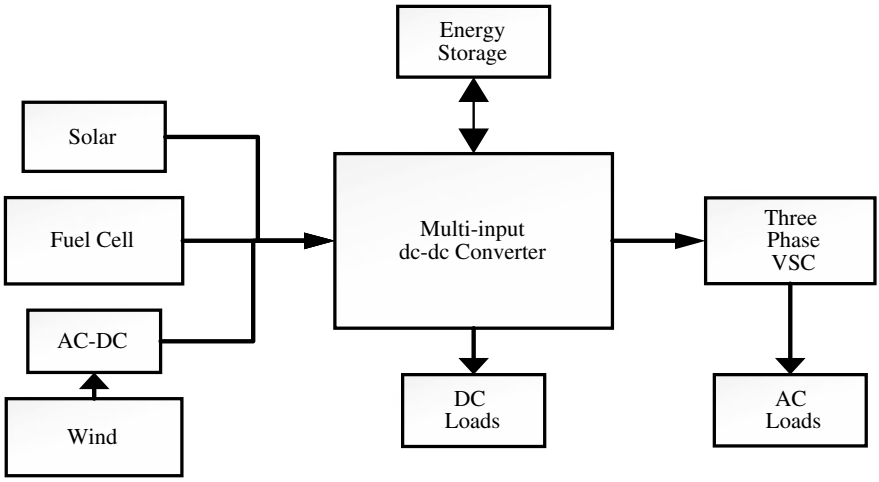

Fig. 1 Schematic diagram of multi-input converter structure

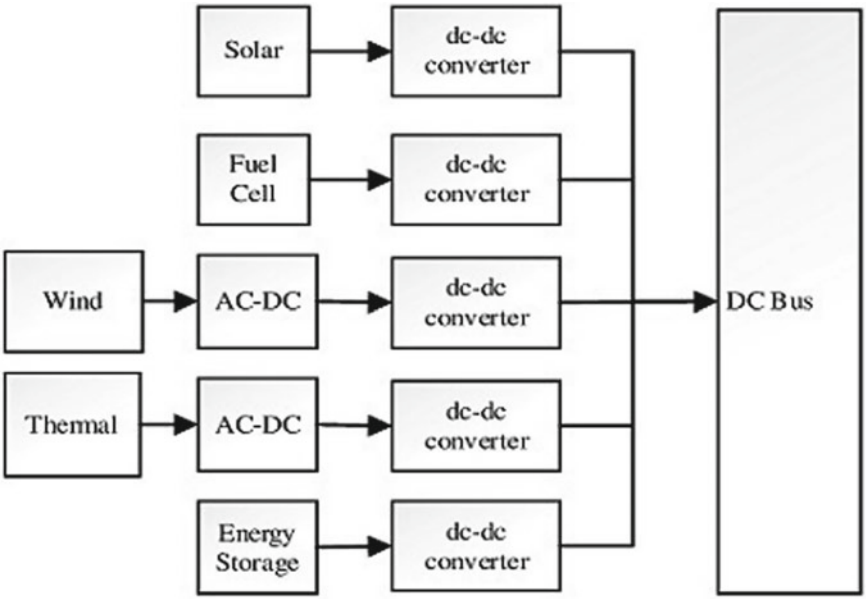

Fig. 2 Schematic diagram of conventional single-port structure

are employed to combine the sources, energy storage and load. Unlike conventional converters where for each source we require a separate converter, thereby increasing the number of switches as well as the complexity of the system. A comparison has been made given in Table 1 [9]. The biggest advantage of using the bidirectional

Table 1 Comparison of conventional structure and multi-input structure

	Conventional structure	Multi-input structure
Requirement of common DC bus	Yes	No
Conversion stages	More than one	Single-stage conversion
Control scheme	Separate control	Centralized control
Power flow management	Complicated, slow	Simple, fast
Transformer requirement	Required	Not required
Efficiency	Low	Improved

multi-input DC-DC converter is that power conversion takes place in a single stage and also it provides more flexibility to the system [11–15].

The two main categories of topologies used are isolated and non-isolated ones. Isolated topologies incorporate galvanic isolation as well as DC-DC converter functionalities to the power stage using the turn-ratio method of transformer. Further isolated topologies offer wide ranges of voltage operation, higher power flexibility between all ports but have higher device count too. The key motivation behind using non-isolated topologies is to achieve lesser number of active switches, and parasitic losses are also minimized because transformers are not used thereby increasing overall efficiency. The other advantages of non-isolated topology are its lower cost as compared to isolated topology; also it can achieve high power density [16].

Hybrid power system has come into existence as the need for reliable and continuous power supply has become the need of the present as well as for the bright future and since cannot rely on single source entirely so the idea of combining more than one power source [17–19].

The three-input DC-DC bidirectional converters were analyzed for integration of different non-conventional energy sources with energy storage into a single converter with three inputs [20]. A three-input port DC-DC converter can have two inputs as: one for PV input and other for wind or any other non-conventional energy input, and third port will be having the energy storing device, which has to be a bidirectional port, that is for discharging and charging [21, 22]. Output of the three-input port DC-DC converter can be connected to the DC load directly or to the grid or AC load by an inverter through a DC link capacitor [23].

Using three-input DC-DC non-isolated converters can end up in using lesser number of components as well as a solid structure [24–26]. Moreover, a methodical process of the origin of non-isolated three-input DC-DC converters has been explained in [26]. Some other shortcomings of the non-isolated three-input converters are that the voltage gain of most such converter is limited since the conversion ratio of voltage can only be changed or modified using the duty cycle. Some of the papers

mentioned show the use of coupled inductor for increasing the voltage conversion ratio to eliminate this problem [26–30].

However, the battery in this type of converters remains operating in every operating mode, resulting in shortening of the lifetime of the storage system and lessening the dependability of the complete scheme [31–33]. Just like the partially isolated topologies, the isolated topologies employ a high-frequency transformer, in order to properly equalize the diverse voltage levels among every port [13–15]. However, the components' total number employed in this type of topology is quite huge because the sharing of these elements is rare [26]. While the two types are partially isolated, and isolated converter topology may function using soft switching of the power electronic switches with suitable controlling [34–36].

2 Hybrid Power System

According to the literature, based on the category mentioned above apart from that the hybrid power system can also be classified grid connected and standalone system. The system connected to grid exhibits quality in equivalent to the network connection. In the independent basis, the procedure is centered on the isolated structure from the setup and this classification is shown using Fig. 3 [2].

Conventional power system is included with hybrid integrated with the grid having enhanced storing ability. In self-sufficient storage energy system for inadequate

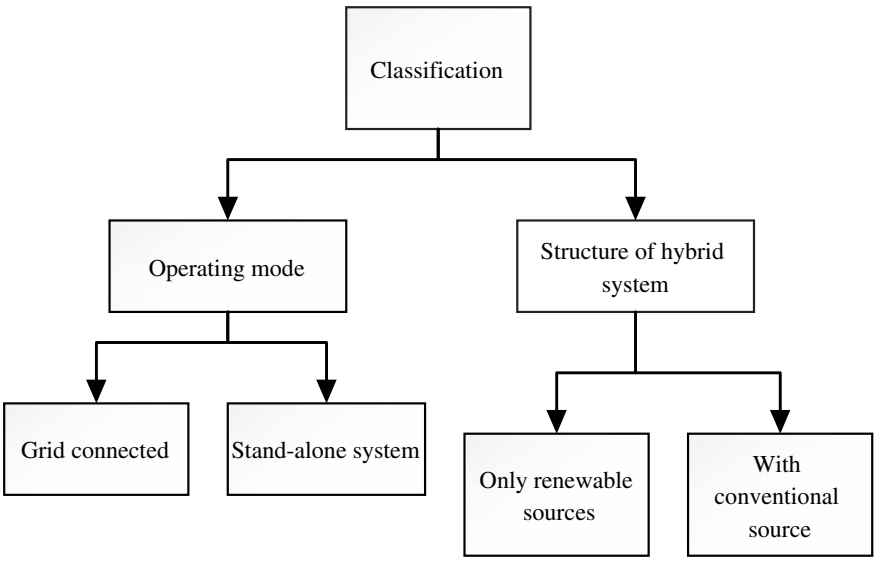

Fig. 3 Classification of hybrid power system

primary source, it needs to endure load. This hybrid power system includes non-conventional energy sources like photovoltaic generator, wind turbine or grouping of other non-conventional system. For hybrid power system, optimization of the sizing is essential and performed for matching demand of load with minimal cost. The main function of hybrid power system is cost cutting for power developed. Regarding the size of the hybrid power system, it is better and very much favorable to bring as much improvement as possible for satisfying the load demand with nominal cost. Various criteria being considered into consideration. The furthermost essentials are: (a) the expense of power created and (b) possibility of loss [35].

3 Multi-input DC-DC Converters

Multi-port conversion topologies proposed for the reduction of the switching devices and the number of components used. Multi-port converters are available in both isolated and non-isolated topologies [3–5], and the isolation is provided using the high-frequency transformer. The multi-input boost topology is a nonlinear multiple-input and multiple-output type having a many of the intermingling variables. Every output variable is affected by more than one control variables. Due to quite many connections between the control loops, the designing of controllers such as proportional–integral–derivative (PID) is complex. Decoupling network is an apt technique of controlling that allows designing of a controller for such type of multiple-input boost converter, and thereby, developing of these is one of the main aims of this work. An appraisal of hybrid energy systems, multi-port converters and control using different controllers like PI, fuzzy and neuro-fuzzy systems, etc. is discussed here (Fig. 4, [8]).

3.1 Buck and Boost-Type Bidirectional Converter

The most basic DC-DC topology was designed taking reference of the original boost and buck converter. The DC-DC converter, being illustrated in Fig. 5 [8], is mainly understood by making changes in the novel boost and buck converter. To be specific as the switches of the conventional converter being used here are replaced by bidirectional power switches, the new converter will be bidirectional boost and buck derivative converter. This converter functions giving a voltage value higher than the input voltage which is the similar operation as boost converter, and the converse will be as a buck converter.

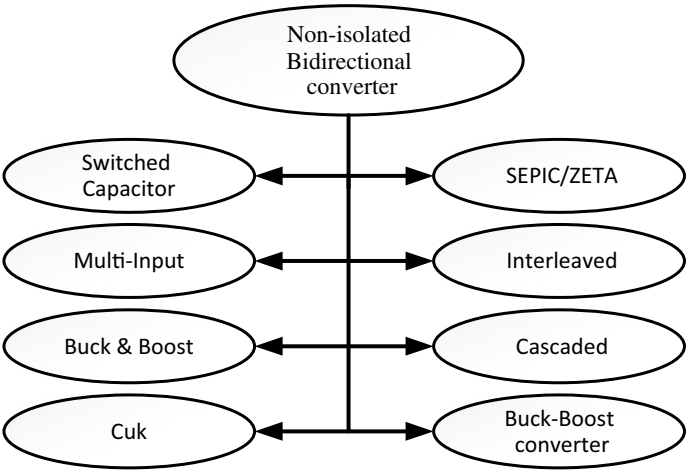

Fig. 4 Classification of non-isolated converter

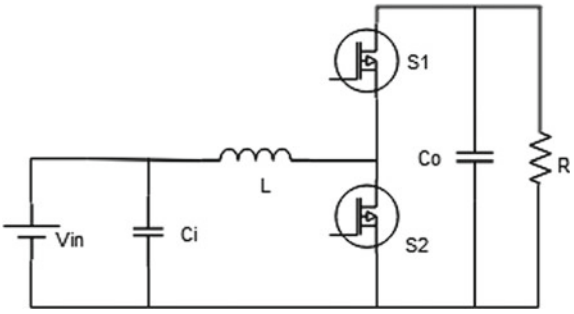

Fig. 5 Buck and boost derived

3.2 Boost and Buck-Inspired Bidirectional Converter

Built on the very much alike method which was being used to develop a bidirectional DC-DC structure, the buck and boost converter may be imitative, that is simply the usage of a dual-side switch as a substitute of using the one-directional switch in the given topology will be a way to a DC-DC topology as shown in Fig. 6 [8]. Moreover,

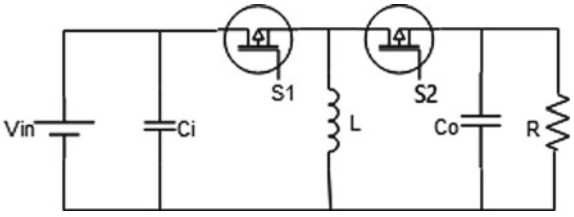

Fig. 6 Buck–boost derived

the very essence of the basic buck–boost converter is its capability to boost or buck the voltage level, and this bidirectional buck–boost converter provides this characteristic in both directions with a negative voltage.

3.3 Zeta-SEPIC-Inspired Converter

Zeta and single-ended primary inductor (SEPIC) are yet other kinds of converters; these are recognized by adjustment of the Ćuk converter components to get a voltage positive output. The Zeta/SEPIC DC-DC converter is shown in Fig. 7 [8]. Here the configuration acts like Zeta type when power is flowing to Vin terminal from the load side, and now if flow of power is from Vin terminal toward the load, it acts as a SEPIC-type converter. Moreover, ancillary branch whose connection is shown in Fig. 7 [8] has been suggested to make a novel straight power transfer route between the output and input in order to get ripples minimized in current [11] (Table 2, [21]).

4 Control Strategy

Selecting an appropriate control scheme for multi-input DC-DC converters is subject to its different structure also on control difficulties that occur. Thus, this portion

Fig. 7 Zeta-SEPIC derived

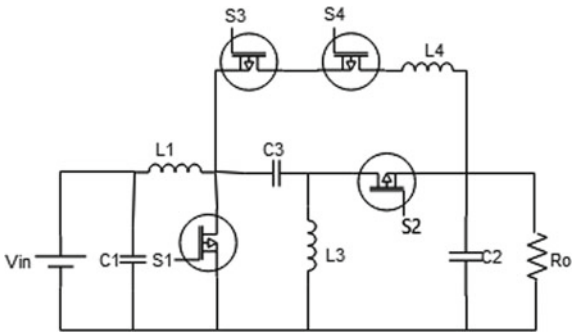

Table 2 Comparison between different converters

Topology	Cost	Reliability	Efficiency
Buck	++	++	+++
Boost	+++	+++	++++
Buck–boost	+	+	+
SEPIC-Zeta	+	+	++
Cuk	+	+	+

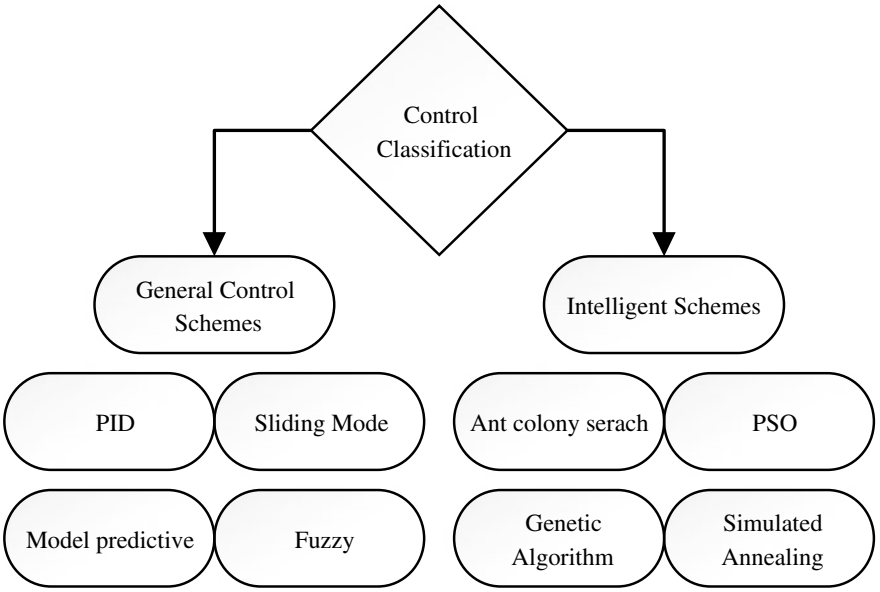

Fig. 8 Flowchart of the control techniques

explores the probable control strategies that can be used in isolated and non-isolated topologies [20]. Non-isolated structures are less expensive and less complicated also because it requires no transformer. Though any application is in needful of high power, in that case separation between load and sources is essential, and isolated topologies give some advantages, such as good reliability, electrical isolation, bidirectional energy flow, easy understanding of soft switching control and guarding the apparatus and operatives for reasons of safety.

Thus, the use of transformers is only beneficial if operating at high frequencies. On the other hand, the type of selection for converters, a higher efficacy and combined controlling tactics are necessary for such converters. The controlling schemes are suggested for diverse uses for solving several controlling difficulties that happened in isolated and non-isolated topologies [8] (Fig. 8, [8] and Table 3, [21]).

4.1 Basic Simulation Result

See Figs. 9 and 10 [37].

Table 3 Comparison of different control methods

S. No.	Control techniques	Benefits	Limitations
1	PID	Low cost High reliability	Low efficiency Not robust
2	Sliding mode	Reference tracking Fast and finite response	More state information and accuracy needed
3	Model predictive	Simple implementation Fast dynamic response	Only for linear model
4	Fuzzy	Fast response Robust response Nonlinear system	Sensitive to expert knowledge
5	ACO	Reduced components size	Computational complexity
6	PSO	Ease of calculation	High uncertainty
7	Simulated annealing	No local constraints	Reduced accuracy
8	Genetic algorithm	Higher accuracy	Longer computation time and higher complexity

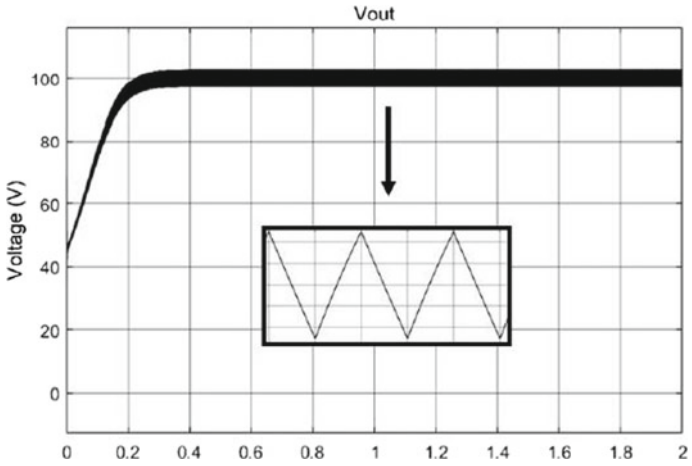

Fig. 9 Output voltage of basic simulation model

5 Conclusion

This paper presents a superficial review on hybrid power systems, bidirectional DC-DC converter topologies as well as different control strategies from the different configurations and the controlling strategies. In accordance with the circuit configuration consideration, similar to else converters, the main investigation is being centered to lessen the capacity, cost, loss, weight, and to increase the power density and reliability [36]. This paper also inspects the controlling structures and switching schemes applied to both isolated and non-isolated types of converters. Different

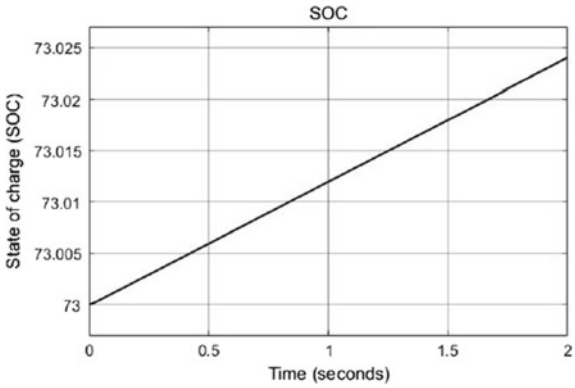

Fig. 10 %SOC of battery

control methods have been pointed out, its benefits as well as its limitations are also being discussed, and the controlling perspective of designing a switching control scheme having a higher efficacy and reliability is required. The recent developments in control designing went by the ease of control circuitry by reducing the additional components and varying the frequency.

References

1. Liu AD, Li H (2006) A ZVS bi-directional DC-DC converter for multiple energy storage elements. IEEE Trans Power Electron 21(5):1513–1517
2. Peng FZ, Li H, Su G-J, Lawler J (2004) A new ZVS bidirectional DC-DC converter for fuel cell and battery application. IEEE Trans Power Electron 19(1):54–65
3. Ohnishi H, Hagiwara M (2017) Experimental verification of a bidirectional chopper for battery energy storage systems capable of reduction in size and weight of an inductor. In: 2017 IEEE energy conversion congress and exposition (ECCE), Cincinnati, OH, pp 197–204
4. Lakshmi M, Hemamalini S (2017) Non isolated high gain dc-dc converter for dc-dc microgrids. IEEE Trans Ind Electron
5. Ajami A, Ardi H, Farakhor A (2015) A novel high step up DC DC converter based on integrating coupled inductors and switched capacitor techniques for renewable resource applications. IEEE Trans Power Electron
6. Park KB, Moon GW, Youn MJ (2010) Non isolated high step up boost converter integrated W\with SEPIC converter. IEEE Trans Power Electron
7. Elankurisil SA, Dash SS (2011) Comparison of isolated and non-isolated bi-directional dc-dc converters. J Eng 21:2341–2347
8. Gorji SA, Sahebi HG, Ektesabi M, Rad AB (2019) Topologies and control schemes of bidirectional DC–DC power converters: an overview. IEEE Access 7:117997–118019
9. Tao H, Kotsopoulos A, Duarte JL, Hendrix MAM (2006) Family of multiport bidirectional DC-DC converters. IEEE Proc Electr Power Appl 153(3):451–458
10. Ciccarelli F, Lauria D (2010) Sliding-mode control of bidirectional DCDC converter for super-capacitor energy storage applications. SPEEDAM 2010:1119–1122. https://doi.org/10.1109/SPEEDAM.2010.5542087
11. Agarwal, Deekshitha K, Singh S, Fulwani D (2015) Sliding mode control of a bidirectional DC/DC converter with constant power load. In: Proceedings of the ICDCM, Atlanta, GA, USA, pp 287–292

12. Dominguez X, Camacho O, Leica P, Rosales A (2016) A fixed frequency sliding-mode control in a cascade scheme for the half-bridge bidirectional DC-DC converter. In: Proceedings of the IEEE ETCM, Guayaquil, Ecuador, pp 1–6
13. Torreglosa JP, García P, Fernández LM, Jurado F (2014) Predictive control for the energy management of a fuel cell battery supercapacitor tramway. IEEE Trans Ind Inform 10(1):276–285
14. Pirooz A, Noroozian R (2016) Model predictive control of classic bidirectional DC-DC converter for battery applications. In: Proceedings of the PEDSTC, Tehran, Iran, 517–522
15. Ebad M, Song B (2012) Accurate model predictive control of bidirectional DC-DC converters for DC distributed power systems. In: Proceedings of the IEEE power energy meeting San Diego, CA, USA
16. Tuballa ML, Abundo ML (2016) A review of the development of smart grid technologies. Non-conventional Sustain Energy Rev 59:710–725
17. Khatib T, Mohamed A, Sopian K (2013) A review of photovoltaic systems size optimization techniques. Non-conventional Sustain Energy Rev 22:454–465
18. Lee JH, Yu DH, Kim JG, Kim YH, Shin SC, Jung DY, Jung YC, Won CY (2013) Auxiliary switch control of a bidirectional soft-switching DC/DC converter. IEEE Trans Power Electron 28(12):5446–5457
19. Onar, Kobayashi J, Erb DC, Khaligh A (2012) A bidirectional high-power-quality grid interface with a novel bidirectional non inverted buck boost converter for PHEVs. IEEE Trans Veh Technol 61(5):2018–2032
20. Jin K, Yang M, Ruan X, Xu M (2010) Three-level bidirectional converter for fuel-cell/battery hybrid power system. IEEE Trans Ind Electron 57(6):1976–1986
21. Mohapatra A, Mohapatra S, Bora SN (2020) Hybrid renewable energy system for real-time power management techniques - a review. In: 2020 IEEE international symposium on sustainable energy, signal processing and cyber security (iSSSC), pp 1–6
22. Forouzesh M, Siwakoti YP, Gorji SA, Blaabjerg F, Lehman B (2017) Step-up DC_DC converters: a comprehensive review of voltage boosting techniques, topologies, and applications. IEEE Trans Power Electron 32(12):9143–9178
23. Tytelmaier K, Husev O, Veligorskyi O, Yershov R (2016) A review of non-isolated bidirectional DC-DC converters for energy storage systems. In: Proceedings of the YSF, Kharkiv, Ukraine, pp 22–28
24. Du Y, Zhou X, Bai S, Lukic S, Huang A (2010) Review of non-isolated bi-directional DC-DC converters for plug-in hybrid electric vehicle charge station application at municipal parking decks. In: Proceedings of the IEEE APEC, Palm Springs, CA, USA, pp 1145–1151
25. Martinez-Salamero L, Calvente J, Giral R, Poveda A, Fossas E (1998) Analysis of a bidirectional coupled-inductor Cuk converter operating In sliding mode. IEEE Trans Circ Syst I Fundam Theory Appl 45(4):355–363
26. Wu T-F, Chang C-H, Chen Y-K (1999) A fuzzy logic controlled single stage converter for PV powered lighting system applications. In: Proceedings of IEEE IAS, Phoenix, AZ, USA, pp 1685–1
27. Jabbour, Mademlis C, Kioskeridis I (2014) Improved performance in a supercapacitor-based energy storage control system with bidirectional DC-DC converter for elevator motor drives. In: Proceeding of the PEMD Manchester, UK, 2014, pp 1–6
28. Gomariz S, Alarcon E, Martinez JA, Poveda A, Madrenas J, Guinjoan F (1998) Minimum time control of a buck converter by means of fuzzy logic approximation. In: Proceedings of the IEEE IECON, Aachen, Germany, pp 1060–1065
29. Yahyaoui I, Atieh A, Serna A, Tadeo F (2017) Sensitivity analysis for photovoltaic water pumping systems: energetic and economic studies. Energy Convers Manage 135:402–415
30. Hamasaki S, Mukai R, Tsuji M (2012) Control of power leveling unit with super capacitor using bidirectional buck/boost DC/DC converter. In: Proceedings of the ICRERA, Nagasaki, pp 1–6
31. Ciccarelli F, Lauria D (2010) Sliding-mode control of bidirectional DC-DC converter for supercapacitor energy storage applications. In: Proceedings of the SPEEDAM, Pisa, Italy, pp 1119–1122

32. Naayagi RT, Forsyth AJ, Shuttleworth R (2012) High-power bidirectional DC_DC converter for aerospace applications. IEEE Trans Power Electron 27(11):4366–4379
33. Kisacikoglu MC, Uzunoglu M, Alam MS (2007) Fuzzy logic control of a fuel cell/battery/ultra-capacitor hybrid vehicular power system. In: Proceedings of the IEEE vehicle power propulsion conference, Arlington, TX, USA, pp 591–596
34. Khanh LN, Seo JJ, Kim YS, Won DJ (2010) Power-management strategies for a grid-connected PV-FC hybrid system. IEEE Trans Ind Electron 25(3):1874–1882
35. Iqbal M, Azam M, Naeem M, Khwaja AS, Anpalagan A (2014) Optimization classification, algorithms and tools for non-conventional energy: a review. Non-conventional Sustain Energy Rev 39:640–654
36. Siddaiah R, Saini RP (2016) A review on planning, configurations, modeling and optimization techniques of hybrid non-conventional energy systems for off grid applications. Non-conventional Sustain Energy Rev 58:376–396
37. AboReada H, Williamson SS, Sood V (2019) Analysis and control of multi-input, single-output, non-isolated DC/DC converter for effective renewable energy management. In: 2019 IEEE transportation electrification conference and expo (ITEC), pp 1–6. https://doi.org/10.1109/ITEC.2019.8790542

Performance Analysis of 3-D Parallel Gated Junctionless Field Effect Nanowire Transistor

N. Bora, A. Sureka, C. Deka, and S. Mipun

Abstract A junctionless transistor is a uniformly doped nanowire-based transistor that has no gate junction. As the distance between junctions in modern devices approaches 10 nm, the formation of ultra-shallow junctions with extraordinarily high doping concentration gradients becomes essential. Junctionless transistors therefore could aid in the production of smaller devices and thus have drawn much attention for good scaling capability and technology compatibility. The present work demonstrates a simulation study performed using the Cogenda Visual TCAD 2-D 1.9.2 device simulator to analyse the optimised parameters for studying characteristics of a parallel gated MOSFET.

Keywords Parallel gated · TCAD · Junctionless transistor · Simulation

1 Introduction

The rapid advancement in semiconductor technology has reached to a certain point where circuits are just a few atoms wide, which prevent them from becoming smaller junctionless nanowire metal–oxide–semiconductor field effect transistor (JNT) is a novel device with significant promise for extending scalability; an alternative device for sub-20 nm nodes. The junctionless nanowire metal–oxide–semiconductor filled-effect junctionless transistor. In contrast to conventional MOSFET, JLFET does not require steep junction for source and drain, resulting in simplified processing and competitive electrical characteristics. Also, they exhibit a near-ideal saturation slope, exceptionally low leakage currents, and reduced carrier mobility with gate voltage and temperature than classical transistors.

A nanoscaled 3-D parallel gated MOSFET is designed using the Visual TCAD 1.9.2. Instead of junctions, the proposed structure divides a gate into two parallel sections. The gate is split to bring it closer to the source and drain regions, lowering

N. Bora (✉) · A. Sureka · C. Deka · S. Mipun
Nanoelectronics and VLSI Design Laboratory, Department of ECE, North Eastern Hill University, Shillong 793022, India
e-mail: nbora@nehu.ac.in

© The Author(s), under exclusive license to Springer Nature Singapore Pte Ltd. 2022

A. Tripathi et al. (eds.), *Intelligent Computing Techniques for Smart Energy Systems*, Lecture Notes in Electrical Engineering 862,
https://doi.org/10.1007/978-981-19-0252-9_26

DIBL (Drain Induced Barrier Lowering). Another advantage of splitting the gate is that it reduces the resulting electric field in the centre of the device, which improves the carrier mobility. The characteristic graphs obtained from the simulation methods are used to perform the work analysis of the designed device.

2 Device Model

Figure 1 is a 3-D constructed parallel gated Transistor. The dimensions of the designed 3-D transistor are, X-axis = 70 nm, Y-axis = 16 nm and Z-axis = 30 nm with applied uniform doping concentration of 1×10^{19} cm^{-3} (N_d). Hafnium dioxide (HfO_2) is used as an insulator instead of the traditional Silicon Dioxide (SiO2) between the gates and the silicon substrate. The oxide is applied on both the top and bottom of the transistor. A total of four parallel gates were constructed on the transistor. The gates were constructed parallely to the X-axis and perpendicularly to the Z-axis. The parallel gates are separated with the same oxide layer, i.e. HfO_2 with a gap of 6 nm. The Designing and simulation are done using the Visual TCAD device simulator platform.

The parallel gated junctionless field effect nanowire transistor results were compared and validated using TCAD software numerical results (PG JLFENT). The PG JLFENT's 3D TCAD simulation schematic is presented in Fig. 1, and the device was designed using SOI technology. To gain more in-depth results, simulations included drain driven barrier lowering effects, charge carrier trapping, and the Lombardi mobility model, among other things. In order to investigate the leakage currents difficulties of the PG JLFENT, the Shockley–Read–Hall recombination model was applied. The Fermi–Dirac statistics with impact ionisation model are also used in the simulations.

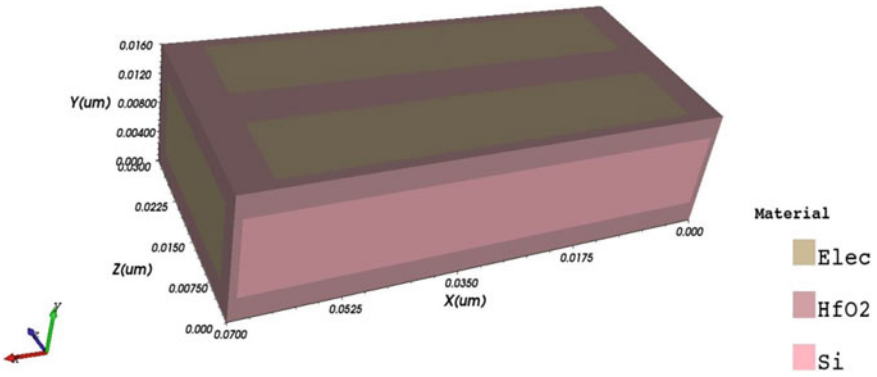

Fig. 1 Structure of the parallel gated MOSFET

3 Result and Discussions

To validate the analytical model for surface potential, drain current, and transconductance, the results were compared to those produced using TCAD software. The simulated Designed Transistor gadget used SOI technology. The entire Si area is thought to have a doping concentration of 1×10^{19} cm^{-3}.

In Fig. 2, we have plotted a graph between position along the Channel and Surface Potential (V). We have separated the silicon substrate towards the *X*-axis, 10 nm to 60 nm out of 69 nm silicon substrate, from the rest of the components of the transistor. This was produced while applying a constant voltage through Gate and a variable voltage through the drain. Four different gate voltages were applied.

In Fig. 3, plotted a graph between gate voltage and drain current. We have applied a constant voltage of 0.1 V, 0.25 V and 0.5 V at the drain, a variable voltage of 0–1 V (Table 1).

With a step of 0.05 V and doping concentration of 1×10^{19} cm^{-3} for the Linear scale and a variable voltage of −0.5–0.5 V with a step of 0.05 V and doping concentration of $5^{\times} 10^{19}$ cm^{-3} for the Logarithmic scale, at the gates of the transistor. As we keep on increasing the gate voltage the drain current for linear scale increases after the threshold voltage is passed.

In Fig. 4, we have shown a graph between drain voltage and drain current (with doping concentration 5×10^{19} cm^{-3}). We have introduced a variable Drain Voltage (0–1 V) and a constant gate voltage of 0.5 V, 0.75 V, 1 V was supplied at the gates of the transistor. In Fig. 5, we have plotted a graph between gate voltage and

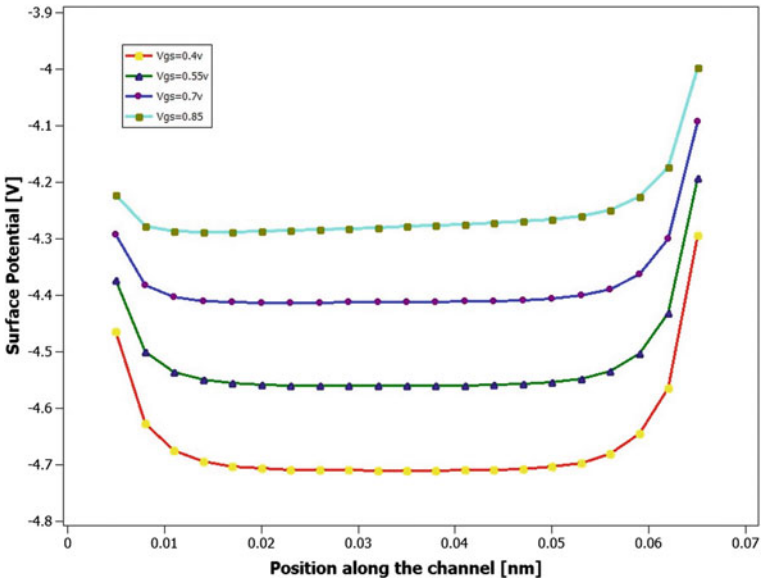

Fig. 2 Surface potential [V] versus position along the channel [nm]

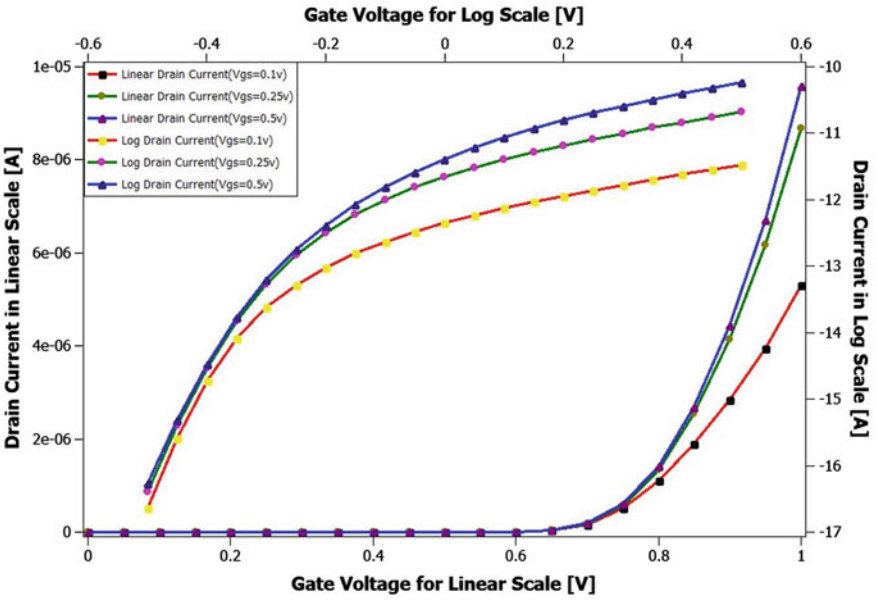

Fig. 3 Drain current [A] versus gate voltage [V]

Table 1 List of different parameters used during simulation

Dimensions	Abbreviation	Parameters
Gate length	L_g	60 nm
Gate width	W_g	1 nm
Channel thickness	T_{Si}	10 nm
Doping of channel	N_d	1×10^{19}
Oxide thickness (top)	T_{ox1}	2 nm
Oxide thickness (bottom)	T_{ox2}	2 nm

transconductance (with doping concentration 5×10^{19} cm^{-3}) with a constant drain voltage of 0.1 V, 0.25 V, and 0.5 V. The transconductance was calculated using the ratio of Differential Drain Current and Differential Drain Voltage, i.e.

$$g_m = \partial i_d / \partial v_g$$

where, g_m is Transconductance, ∂i_d is Differential Drain Current and ∂v_g Differential Gate Voltage.

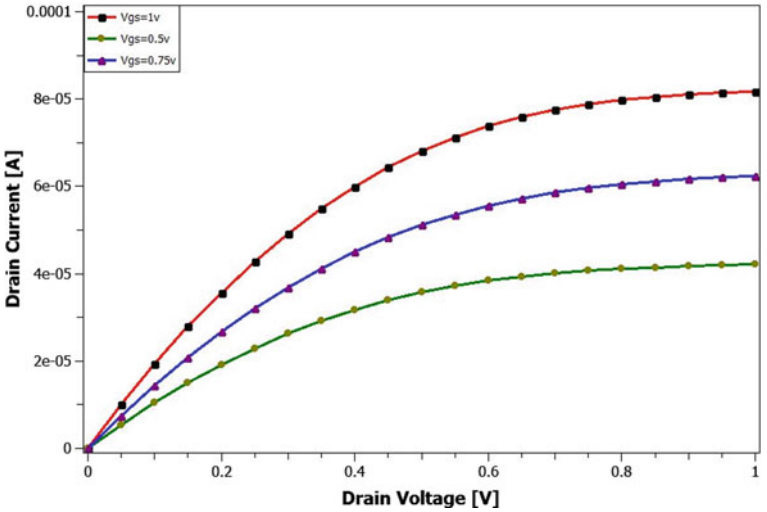

Fig. 4 Drain current [A] versus drain voltage [V]

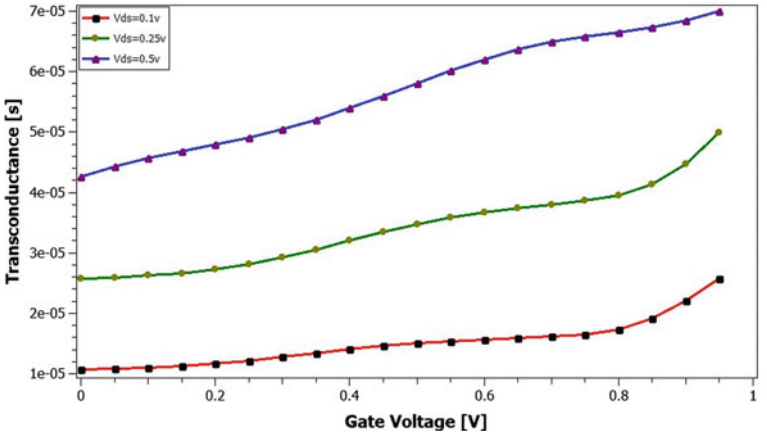

Fig. 5 Transconductance (S) versus gate voltage [V]

The gate voltage was increased from 0 to 1 V with a step of 0.05 V. The graph was increasing linearly as the gate voltage was slowly increased and after reaching a certain gate voltage, the graph stretches till it reaches the final gate voltage value (1 V).

4 Conclusion

In this work, we provide brief simulation research in which we designed and simulated the parallel gated junctionless transistor using Visual TCAD, and the resulting data is presented in the form of various graphs. Capacitance design based on physics is reprised for a TG FinFET bearing in mind for small geometry effects. The characteristics of capacitance-voltages operational in all regions are designed and displayed. The capacitance tool is appropriate for analysing transistor properties.

3D GENIUS VTCAD simulations were used to support the accuracy.

References

1. Ferain I, Colinge CA, Colinge JP (2011) Multigate transistors as the future of classical metal-oxide-semiconductor field-effect transistors. Nature 479:310–316. https://doi.org/10.1038/nature10676
2. Colinge JP, Kranti A, Yan R, Lee CW, Ferain I, Yu R, Akhavan ND, Razavi P (2011) Junctionless nanowire transistor (JNT): properties and design guidelines. Solid State Electron 65–66:33–37. https://doi.org/10.1016/j.sse.2011.06.004
3. Colinge JP, Lee CW, Afzalian A, Akhavan ND, Yan R, Ferain I, Razavi P, O'Neill B, Blake A, White M, Kelleher AM, McCarthy B, Murphy R (2010) Nanowire transistors without junctions. Nat Nanotechnol 5:225–229. https://doi.org/10.1038/nnano.2010.15
4. Bora N, Das P, Subadar R (2003) An analytical universal model for symmetric double gate junctionless transistors. J Nano Electron Phys 8. https://doi.org/10.21272/jnep.8(2).02003
5. Bora N, Subadar R (2019) A complete analytical model of surface potential and drain current for an ultra short channel double gate asymmetric junctionless transistor. J Nanoelectron Optoelectron 14:1283–1289. https://doi.org/10.1166/jno.2019.2643
6. Trevisoli R, Pavanello MA, Capovilla CE, Barraud S, Doria RT (2020) Analytical model for low-frequency noise in junctionless nanowire transistors. IEEE Trans Electron Devices. https://doi.org/10.1109/ted.2020.2986141
7. Charles Pravin J, Nirmal D, Prajoon P, Ajayan J (2016) Implementation of nanoscale circuits using dual metal gate engineered nanowire MOSFET with high-k dielectrics for low power applications. Phys E Low-Dimension Syst Nanostruct 83:95–100. https://doi.org/10.1016/j.physe.2016.04.017
8. Bora N, Deka N, Subadar R (2020) Quantum mechanical analysis on modeling of surface potential and drain current for nanowire JLFET. J Nano Res 64. https://doi.org/10.4028/www.scientific.net/JNanoR.64.123
9. Bora N, Baruah RK (2011) Quantum mechanical treatment on modeling of drain current, capacitances and transconductances for thin film undoped symmetric DG MOSFETs. In: IEEE 2011 International conference on nanoscience, technology and societal implications (NSTSI11), pp 1–6. https://doi.org/10.1109/NSTSI.2011.6111994
10. Mosfets S, Yu B, Member S, Lu H, Liu M, Taur Y, Mosfets S, Yu B, Member S, Lu H, Liu M, Taur Y (2007) Explicit continuous models for double-gate and surrounding-gate MOSFETs. IEEE Trans Electron Devices 54:2715–2722. https://doi.org/10.1109/TED.2007.904410
11. Bora N, Deka N, Subadar R (2020) A drain current and transconductance analytical model for symmetric double gate junctionless FENT. J Nano Res 65. https://doi.org/10.4028/www.scientific.net/JNanoR.65.39
12. Sarma KCD, Sharma S (2019) A method for reduction of off state leakage current in symmetric DG JLT. Eng Res Express 1. https://doi.org/10.1088/2631-8695/ab4083

13. Hazarika MR, Bora N (2018) Performance analysis of 3-D asymmetric junctionless double gate MOSFET. In: IEEE International conference on energy, communication, data analytics and soft computing, ICECDS. IEEE, pp 1391–1395. https://doi.org/10.1109/ICECDS.2017.8389672
14. Raibaruah AK, Sarma KCD (2020) Parallel gated junctionless field effect transistor. In: 2020 International conference on computational performance evaluation (ComPE). pp 178–181. https://doi.org/10.1109/ComPE49325.2020.9200029
15. Raibaruah AK, Sarma KCD (2021) A potential model for parallel gated junctionless field effect transistor. SILICON. https://doi.org/10.1007/s12633-020-00890-8
16. Cogenda Pte Ltd. (2014) Genius, 3-D device simulator, reference manual. Singapore

Design of MAC Unit for an Artificial Neural Network Using Reversible Logic Gates

B. S. Apoorva, Mohamed Arhaan Amjad, O. Bharatha, Pullagura Sai Surya, and S. Nagendra Prasad

Abstract The processing unit is the most essential part in an artificial neural network. The processing unit performs the complex parallel computations that are important for the efficient working of the neuron which along with the activation unit makes up an artificial neural network. In our work, we have proposed an efficient MAC (Multiplication and Accumulation) unit which can be implemented as the processing unit in an ANN. It makes use of Vedic Multiplier, Carry Select Adder (CSLA) and Ripple Carry Adder (RCA) using reversible logic gates. Our design attempts to be superior than the current implementations as far as area and delay are concerned. An efficient MAC processing unit can improve the speed of ANN to a larger extent. The Verilog HDL design language was used to create and implement our proposed MAC unit, and the results were analyzed.

Keywords MAC unit · Artificial neural network (ANN) · Carry select adder (CSLA) · Ripple carry adder · Reversible logic gates · Verilog HDL language

1 Introduction

ANN resembles the neural networks that exist in the human body. It has the ability to adapt by changing its structure according to the network's learning phase and has the ability to learn complex input and output relationships to solve linear and non-linear issues arising from various fields. This ANN can be trained and modeled accordingly to be able to solve particular issues that humans or conventional computational algorithm face difficulty in. The ANN is known for its speed and processing ability [1].

Artificial neural network (ANN) is comprising of basic processing elements. The processing unit is essentially the MAC (Multiplication and Accumulation) Unit. It plays a key role in the computation process. The performance of the ANN depends majorly on the efficiency of the processing unit. There are two types of ANN which

B. S. Apoorva · M. A. Amjad · O. Bharatha · P. S. Surya · S. Nagendra Prasad (✉)
PES Institute of Technology, Hosur Road, Electronic City, Bangalore, India
e-mail: apoorvabsappi26@gmail.com

© The Author(s), under exclusive license to Springer Nature Singapore Pte Ltd. 2022

A. Tripathi et al. (eds.), *Intelligent Computing Techniques for Smart Energy Systems*, Lecture Notes in Electrical Engineering 862,
https://doi.org/10.1007/978-981-19-0252-9_27

are characterized as Feed Forward and Feed Back Networks. Feed Forward networks are composed of a single multi-layer perception and a radial basis function [2].

MAC unit is an important element for the purpose of generation of essential signals in real time. It is used in various areas like digital signal processors, filters and convolution applications. They contribute to an important function in ANNs as well [3].

In today's world, massive amounts of energy are dissipated from the electronic systems leading to one of the major issues in the field of technology in present day. We need to cater to this issue as early as possible. During the computation, few bits are erased which directly affects the amount of energy that is dissipated from the particular system. There are certain circuits which resist the depletion of data. These are known as reversible circuits. These gates are used to generate outputs as well as inputs from the obtained outputs. In this way, it integrates bidirectional functionality and minimizes the energy dissipation resulting in overall efficiency of the system [4].

In this paper, we have implemented MAC unit by using Urdhva Tiryakbhyam technique from Vedic Mathematics by using Carry Select and Ripple carry adders. This implementation is done by using reversible logic gates to achieve better performance parameters.

2 Related Works

Ravali et al. [5] have proposed that any processor's important element is "multiplier." The architecture of any multiplier element is structured in a way that efficiency and speed of the multiplier block to be increased. "Vedic multiplication" is a multiplication technique which has better performance. "Vedic multiplication" is performed by the sutra called "Urdhva Tiryakbhyam" (UT) Sutra. This technique is better suited for speed related applications.

The authors [3] have proposed a solution for the MAC unit in digital signal processors by utilizing effective power and area occupying components. The multipliers delay is more when compared to other calculations, which results in the reduced speed of the circuit. The designed MAC Unit reduces power and delay, which reduces overall design space.

Ramkumar and Kittur [6] have proposed a Carry Select Adder (CSLA). It is utilized in various processors for speed and computational ability. Their work uses a gate-level modification which lessens power along with area. Their design has shown improvement from the regular SQRT CSLA.

Mamataj et al. [7] have proposed that the reversible logic is quite possibly the most propitious domain of research over decades and applied across various technologies. The goal of reversible logic is to reduce quantum cost, circuit profundity and the number of unnecessary outputs. Their work serves as a guideline while also providing insight into these gates.

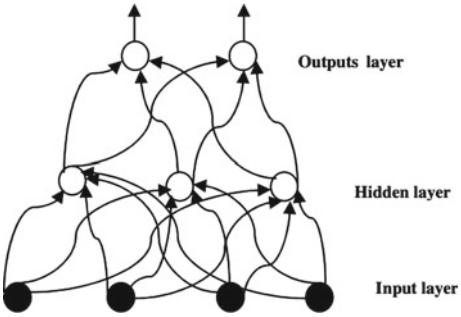

Fig. 1 Artificial neural network

The authors [8] have put forward an area and power efficient CSLA model, increasing the overall system efficiency.

The authors [9] have performed an analysis of reversible logic in terms of the gate level on the basis of power, delay and area by using sequential and combinational circuits with respect to the circuits that follow conventional basis.

The authors [10] have proposed an area and delay efficient MAC unit. Their work incorporates a 32-bit MAC using 32-bit array multiplier and RCA adder along with an additional MAC utilizing Vedic multiplier and RCA. Their work provides an insight for the various modifications that can be performed on the MAC unit.

3 Artificial Neural Networks (ANN)

ANN consists of processing units and deals with large amount of data, which is difficult to analyze and provides a better performance compared to other existing technologies. Simple Neural Network comprises three different layers which are input, hidden and output layers. The processing unit performs multiplication and accumulation operations in between the input and the output layers. Once processing is completed, final result is computed by utilizing the values of activation unit from the network [1] (Fig. 1).

4 Reversible Logic Gates

There must be *n*-inputs and *n*-outputs for a Reversible Logic Gate. A coordinated correspondence on a one-to-one basis exists between the vector of inputs and the vector of outputs. We can obtain the output result from inputs, as well as recuperate the inputs from the obtained output [7, 11].

Garbage outputs: To achieve reversibility, additional inputs or outputs are summed to match the number of inputs and outputs when necessary. These additional inputs or outputs are referred to as unnecessary outputs [7].

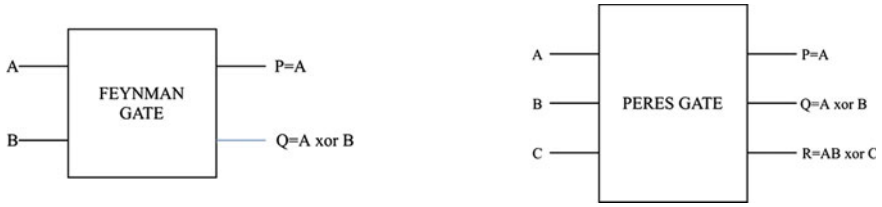

Fig. 2 Feynman gate and Peres gate

$$\text{Input} + \text{constantinput} = \text{output} + \text{garbageoutput}. \quad (1)$$

Constant inputs: To synthesize the logical function we need to maintain the number of inputs constant as either 0 or 1 [7, 11].

Quantum Cost: It is used to represent the ultimate cost of the designed circuitry. This is determined by the number of primary reversible logic gates required to realize and design the circuit. It is calculated as the smallest number of unitary gates required for circuit representation without changing the outputs [4, 7].

Feynman Gate This is a two-by-two gate. It is also termed as a Controlled NOT gate. These gates serve the purpose of fanning out. A and B are the inputs which give outputs $P = A$ and $Q =$ (A XOR B). This gate has a corresponding quantum cost of one [3, 4, 7, 11] (Fig. 2).

Peres Gate: This is a three-by-three gate. They have three inputs: A, B, C, and their outputs are $P = A$, $Q =$ (A XOR B), $R =$ (AB XOR C). It has quantum cost 4 [3, 4, 7, 11].

Fredkin Gate: It has three-by-three configuration. They have A, B, C as inputs and $P = A$, $Q =$ (A'B XOR AC), $R =$ (A'C XOR AB) are outputs. This has a quantum cost of five [4, 7, 11] (Fig. 3).

BVPPG gate: The BVPPG gate has a five-by-five configuration. It is typically used for multiplication. The two partial products are created concurrently. It has a quantum cost of ten [5].

HNG gate: It is a four-by-four configuration. This functions as a reversible full adder. If the inputs are (A, B, C, D) then $P = A$, $Q = B$, $R =$ (A XOR B XOR C), and $D =$ (A XOR B)C XOR AB XOR D. The HNG has quantum cost of six [5, 11].

5 Implementation

5.1 MAC (Multiplication and Accumulation Unit)

A MAC unit comprises of an multiplier block, an adder block and an accumulator block. A MAC unit requires fast adder and multiplier circuits for swift computations.

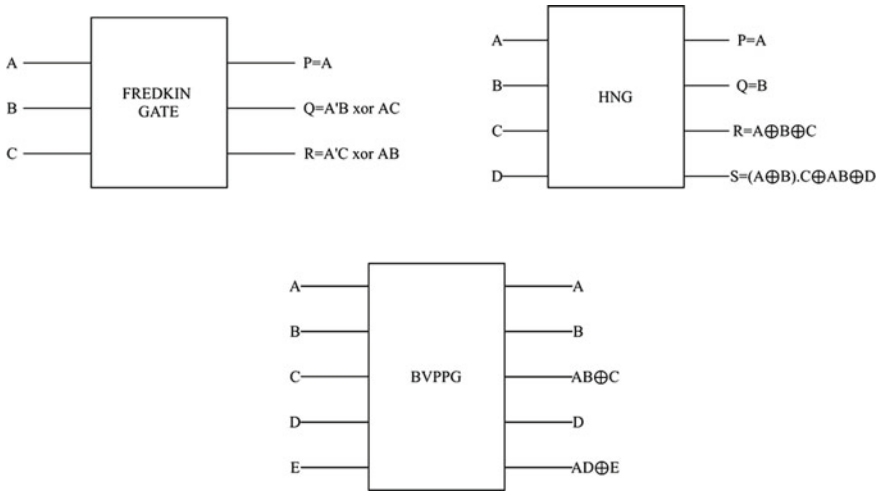

Fig. 3 Fredkin HNG and BVPPG gate

A standard MAC unit comprises of an multiplier and a accumulator which stores the accumulated sum from previous products that have been computed [12].

Here we will discuss about the execution of MAC unit in two different manners: The MAC unit that employs a Vedic multiplier, while the SQRT CSLA employs reversible logic gates and is based on a BEC and another MAC unit that employs a Vedic multiplier, and the ripple carry adder that employs reversible logic gates (Fig. 4).

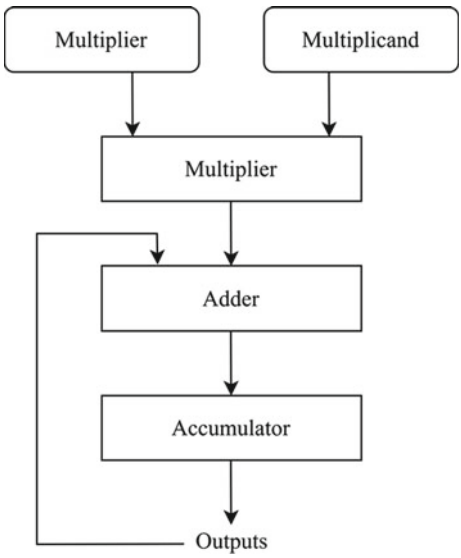

Fig. 4 Structure of MAC unit

5.2 *Vedic Multiplier Using SQRT CSLA*

For any application using multiplication process, the important factors are speed, efficiency and accuracy. The Vedic multiplication process can reduce the computation delay and provides accurate results [2].

The Vedic mathematics has different sutras for various applications. The sutra that is suitable for multiplication purpose is Urdhva Tiryakbhyam and Nikhilam Sutra. The latter sutra is suitable for multiplication of numbers that are increasing order of 10's power. The term Urdhva Tiryakbhyam in Sanskrit mean "Vertically and Crosswise." In this process, the intermediate products will be generated along with the corresponding summation of these generated products. In this multiplier as the total number of bits increase the factors such as area occupied and the gate delay rises in a slow phase, when compared to other multipliers [5].

Figure 5 depicts an 8-bit Vedic multiplier made up of 4 × 4 Vedic multipliers and an 8-bit SQRT CSLA. The 4 × 4 Vedic multipliers are implemented using 2 × 2 Vedic multipliers. The summation of intermediate partial products will be performed by 8-bit SQRT CSLA [13].

The dual eight-bit sequences of input are partitioned into dual four-bit sequences which are fed into the 4 × 4 Vedic multipliers. The 4-bit sequences that are given as input are *a*[3:0] & *b*[3:0], *a*[3:0] & *b*[7:4], *a*[7:4] & *b*[3:0] and *a*[7:4] & *b*[7:4] (Fig. 6).

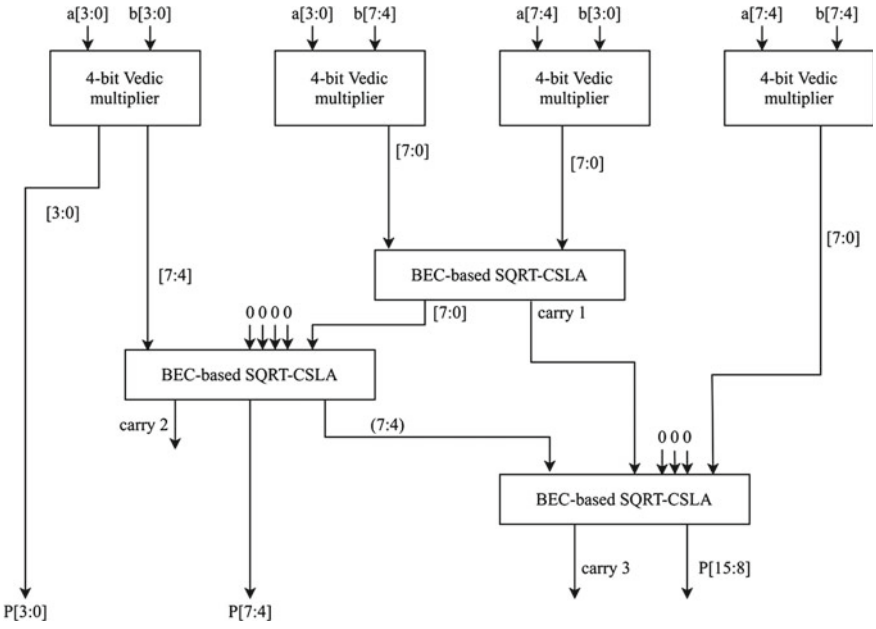

Fig. 5 Vedic multiplier using SQRT CSLA

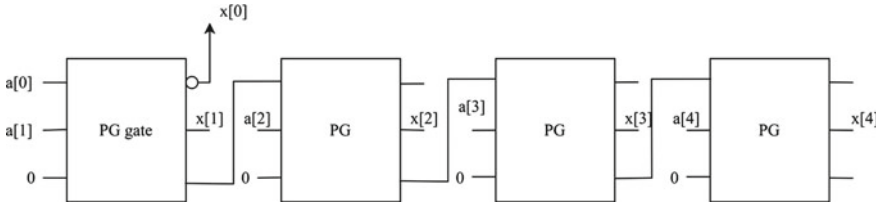

Fig. 6 BEC using reversible gates

5.3 BEC Based SQRT CSLA Using Reversible Logic Gates

Figure 7 depicts a SQRT CSLA based on BEC consisting of a BEC block, RCA block and multiplexer. The multiplexer here is used to toggle between the outputs of the RCA and the BEC depending on the incoming carry bit. The reversible logic gates used for the implementation of BEC based SQRT CSLA are Peres gate and Fredkin gate. SQRT CSLA has been designed for obtaining efficient output.

Full adder is implemented using Peres gate and multiplexers are implemented using Fredkin gate. Binary to excess-1 conversion block as shown in Fig. 6 is implemented in the SQRT CSLA to reduce the propagation delay.

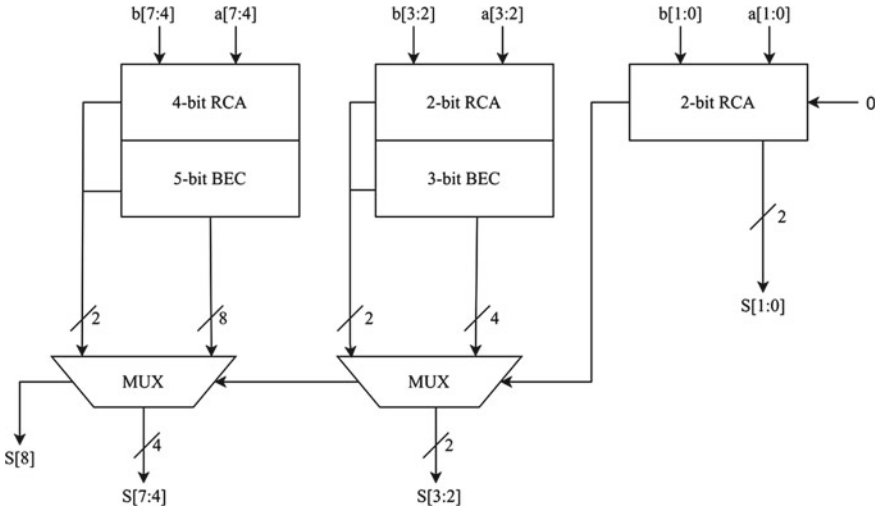

Fig. 7 BEC based SQRT CSLA

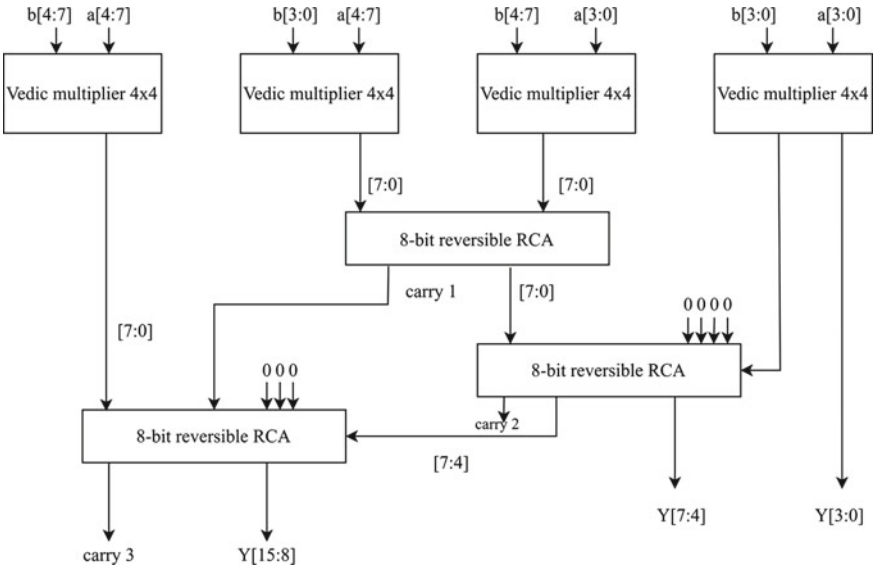

Fig. 8 Vedic multiplier using reversible RCA

5.4 *Vedic Multiplier Using Reversible RCA*

This section's 8 × 8 Vedic multiplier is made up of a 4 × 4 Vedic multiplier and an 8-bit reversible Ripple carry Adder is shown in Fig. 8. The main function block for the 4 × 4 vedic multiplier will be a 2 × 2 Vedic multiplier, and the 8-bit reversible ripple carry adders are built with reversible logic gates [14].

The inputs to the 4 × 4 Vedic multipliers are provided by a combination of 4-bit inputs for *a* and *b* respectively. These 4-bit sequences are given as input as *a*[3:0] & *b*[3:0], *a*[3:0] & *b*[7:4], *a*[7:4] & *b*[3:0] and *a*[7:4] & *b*[7:4]. The output of the multiplier is in 16-bit format.

5.5 *Reversible RCA Using Peres Gate and HNG Gate*

The Reversible RCA is shown in Fig. 9. It simplifies the adder operation by keeping it down to a simple two-level logic. To create our Ripple Carry Adder, we use Peres

Fig. 9 Reversible RCA using Peres and HNG gates

and HNG reversible logic gates. We use these gates to reduce the inherent delay of the adder.

In this 8-bit adder, we make use of one Peres gate and seven HNG gates. For the initial addition to take place, the carry is initially considered as zero. Each gate produces a carry-out bit which then propagates from the Peres gate to the subsequent gates to ultimately produce the sum and the final carry bit [5, 14].

6 Simulation and Results

The implementation of MAC unit using Vedic multiplier has been done by utilizing SQRT CSLA designed using BEC and RCA using reversible gates and the results are obtained with the help of ISim simulation tool and synthesized by utilizing the Xilinx ISE 14.7 tool. We generated the simulation results and the RTL schematics for both the implementations. Table 1 contains the comparison of area and delay parameters for both the implementations along with comparison with existing MAC implementation [2]. An LUT is a table that arbitrates what the output is for any provided input(s). It is a truth table within the frame of reference of combinatorial logic that actually defines its behavior. Slices occupied is a metric that indicates the area coverage of the design whereas delay determines its computational speed (Figs. 10, 11, 12 and 13).

Table 1 Result Comparison of both the implementations

Implementation	Slices LUTs	Slices occupied	Delay (ns)
Implementation 1 (using BEC based CSLA)	196	73	10.452
Implementation 2 (using reversible RCA)	127	55	8.906
Existing MAC implementation	717	397	19.100

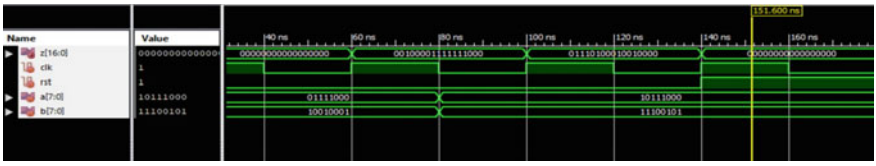

Fig. 10 Simulation result for implementation 1: A and B are the 8-bit inputs. Clk signal controls the incoming values and output results of the MAC unit. Reset signal is used to reset the accumulator

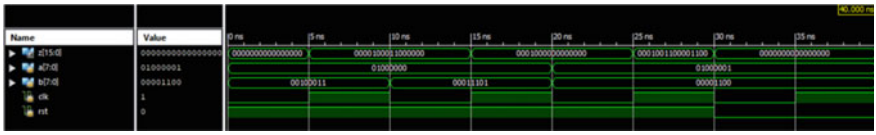

Fig. 11 Simulation result for implementation 2: A and B are given as the inputs. The value of the MAC is stored in the accumulator register. Reset signal is used to clear the accumulator value

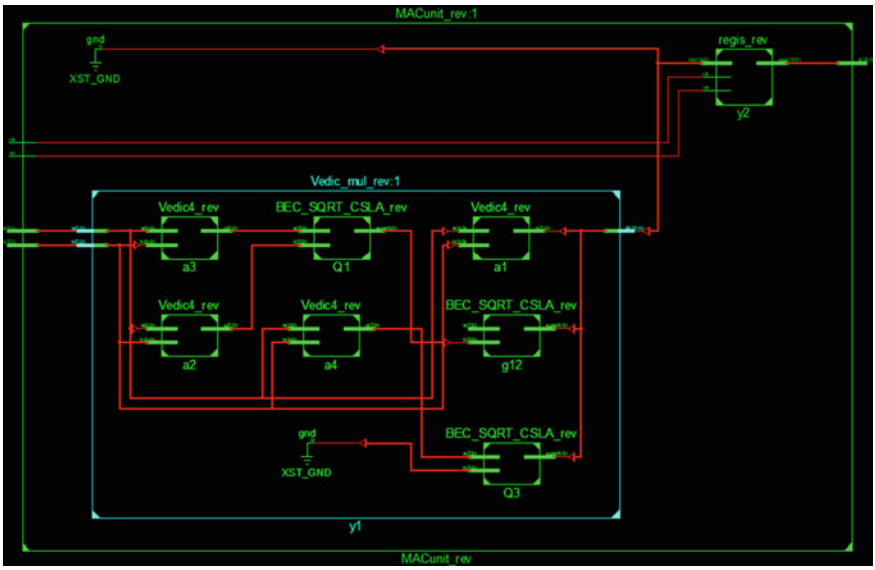

Fig. 12 RTL schematic for implementation 1: It represents our implementation in terms of the adders, multipliers that we have implemented and provides the schematic for the same

7 Conclusion

In conclusion, the proposed MAC unit has been designed using two different implementations, first of which is designed by a SQRT CSLA utilizing BEC and another using a Reversible RCA. Both designs are simulated, synthesized and compared based on result parameters such as area and delay. This proposed MAC unit can be implemented in a neuron as the processing unit for an Artificial Neural Network to improve its speed and efficiency.

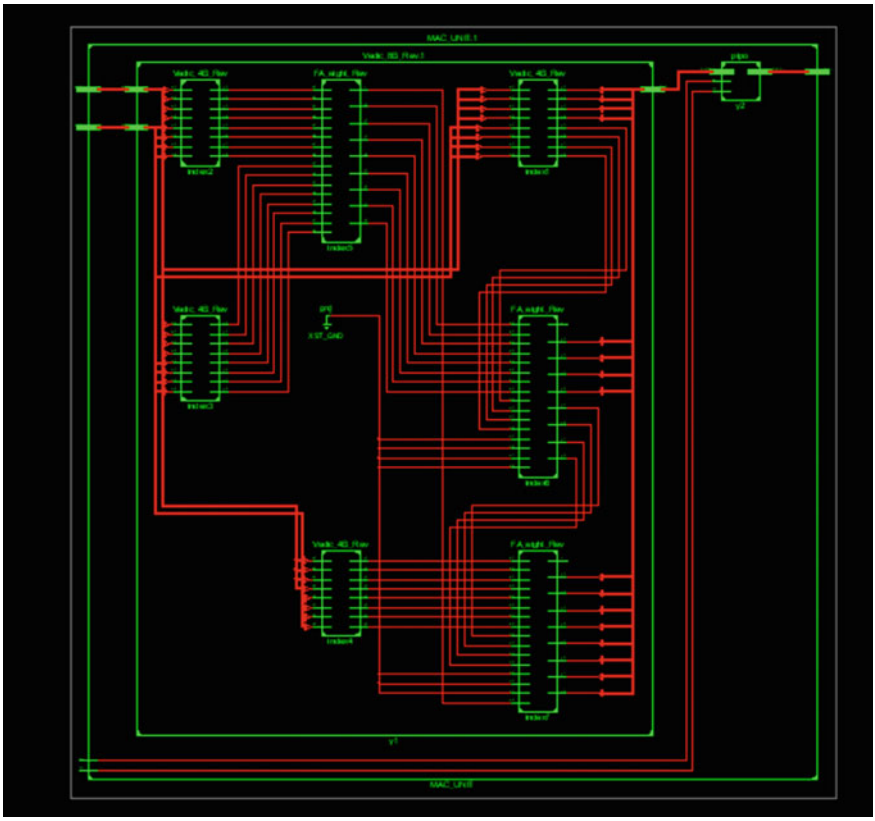

Fig. 13 RTL schematic for implementation 2: It represents our implementation in terms of the adders, multipliers that we have implemented and provides the schematic for the same

References

1. Dongare A, Kharde RR, Kachare AD (2012) Introduction to artificial neural network. Int J Eng Innov Technol (IJEIT) 2:189–194
2. Ranganath L, Kumar DJ, Reddy PSN (2016) Design of MAC unit in artificial neural network architecture using Verilog HDL. In: 2016 International conference on signal processing, communication, power and embedded system (SCOPES), pp 607–612
3. Sajad Shawl M, Singh A, Gaur N, Bathla S, Mehra A(2018) Implementation of area and power efficient components of a MAC unit for DSP processors. In: 2018 Second international conference on inventive communication and computational technologies (ICICCT). https://doi.org/10.1109/icicct.2018.8473065
4. Bhandari AS, Sharma P (2016) Introduction to reversible logic and mathematical derivation for V and V+ gates. Int J Comput Appl 153:14–18
5. Ravali B, Micheal Priyanka M, Ravi T (2015) Optimized reversible logic design for Vedic multiplier. In: 2015 International conference on control, instrumentation, communication and computational technologies (ICCICCT). https://doi.org/10.1109/iccicct.2015.7475262
6. Ramkumar B, Kittur HM (2012) Low-power and area-efficient carry select adder. IEEE Trans Very Large Scale Integr (VLSI) Syst 20:371–375. https://doi.org/10.1109/tvlsi.2010.2101621

7. Mamtaj S, Saha D, Banu N (2014) A review of reversible gates and its application in logic design. Am J Eng Res 3:151–161
8. Srinivasaperumal M, Pavithra S, Kavya Lekshmi VS, Mohammad Arshad K (2017) 128 bit modified carry select adder using binary to excess-one converter. Int J Adv Res Sci Eng (IJARSE) 6
9. Kalavakolanu SS (2018) Implementation of reversible logic at gate level. In: International conference on inventive systems and control (ICISC) 959–963
10. Lilly K, Nagaraj S, Manvitha B, Lekhya K (2020) Analysis of 32-Bit multiply and accumulate unit (MAC) using Vedic multiplier. In: 2020 International conference on emerging trends in information technology and engineering (ic-ETITE). https://doi.org/10.1109/ic-etite47903.2020.413
11. Garipelly R, Kiran PM, Kumar AS (2013) A review on reversible logic gates and their implementation. Int J Emerg Technol Adv Eng 3:417–423
12. Kokhila SM, Arasi MM (2016) Efficient design of MAC carry select adder using reversible logic gates. IJESC 6. https://doi.org/10.4010/2016.1128
13. Naik RN, Reddy PSN, Mohan KM (2013) Design of Vedic multiplier for digital signal processing applications. Int J Eng Trends Technol 4
14. Premananda BS, Pai SS, Shashank B, Bhat SS (2013) Design and implementation of 8-Bit Vedic multiplier. Int J Adv Res Electr Electron Instrum Eng 2

Biosensor Based on Bioreceptor: A Potential Biomedical Device Toward Early Detection of Bone Cancer

Seema Rani, Sanchita Bandyopadhyay-Ghosh, Subrata Bandhu Ghosh, and Guozhen Liu

Abstract Bone cancer primarily found in children and young adults occurs due to abnormal mass of tissue formation in bone. Presently practiced bone cancer detection methods, however, are not always efficient in terms of diagnosis at the early stage. There is an urgent need therefore toward early detection of bone cancer using biosensor with high analytical performance capabilities. Most of the available biomedical devices relying on biosensing technologies have limitations including high cost, slow response time, and requirement of expert skills. Bioreceptor based biosensors, in this regard, can provide crucial bone health information, owing to good selectivity, high sensitivity, and capabilities to detect specific bone turnover markers. In this article, various types of bone cancer and detection methods using different biomarkers are discussed with special emphasis on mechanisms, benefits, and challenges of various bone biosensors based on bioreceptors.

Keywords Bone · Bone cancer · Bone biomarkers · Bone remodeling · Bone metastasis · Bioreceptors · Biosensors

1 Introduction

Bone is a metabolically active connective tissue that protects the various organs of a body and provides structural support with movements. Bone is mostly made up of compact and spongy tissues. Compact bone is dense (only 10% porous) and provides support, while spongy bone is 50–90% porous with honeycombed appearance that makes it more flexible. Bone tissue is made up of four types of cells: osteoblasts, osteocytes, osteoclasts, and undifferentiated mesenchymal cells or osteogenic cells

S. Rani · S. Bandyopadhyay-Ghosh (✉) · S. B. Ghosh
Engineered Biomedical Materials Research and Innovation Centre (EnBioMatRIC), School of Automobile, Mechanical and Mechatronics Engineering (SAMM), Manipal University Jaipur, Jaipur, Rajasthan 303007, India
e-mail: sanchitab.ghosh@jaipur.manipal.edu

G. Liu
Graduate School of Biomedical Engineering, Faculty of Engineering, The University of New South Wales, Sydney, NSW 2052, Australia

© The Author(s), under exclusive license to Springer Nature Singapore Pte Ltd. 2022

A. Tripathi et al. (eds.), *Intelligent Computing Techniques for Smart Energy Systems*, Lecture Notes in Electrical Engineering 862,
https://doi.org/10.1007/978-981-19-0252-9_28

[1]. Osteoblast is responsible for bone formation and deposition of protein matrix on bone surface; bone resorption is done by osteoclast; osteogenic cell is a stem cell found in connective tissue and capable of producing cells of connective tissue lineages (bone, cartilage, and muscle); osteocytes behave as mechanosensory. Osteoclast, bone is degraded and released into circulation, and these degraded particles (enzymes or proteins) of bone behave as biomarkers of bone loss [2]. These proteins and enzymes are found in blood and urine by which we can measure bone metabolism. The timely identification of these bone markers is important for diagnosis of various bone diseases. It is important to note that bone grows continuously throughout the life with two processes: growth and remodeling [3]. Imbalance in bone formation and resorption during bone remodeling may cause bone cancer. In bone cancer, the cell growth goes out of control, forming a mass known as tumor and destroys the normal bone tissues. A bone tumor can be benign (non-cancerous) or malignant (cancerous). Malignant tumor can grow and spread to other parts of body. Cancer can be recognized based on the type of cell they originate from. Cancer spreading through the supporting tissues (bone, cartilage, fibrous tissue, and tendons) is known as sarcoma or soft tissue sarcoma. Sarcoma can further be classified as: osteosarcoma—derived from osteoblastic cells, chondrosarcoma—developed from cartilage cells, whereas chordoma—can occur in lower back of the spine or the base of skull, Ewing sarcoma—forms in soft bone tissue, fibrosarcoma—tumor of mesenchymal cell, multiple myeloma—cancerous plasma cells accumulated in bone marrow which mob out healthy blood cells. Bone cancer is the second most life-threatening disease in the world. Despite advances in recent technology and knowledge base, late diagnosis is the main cause of low survival rate of bone cancer patients. Biomarkers can play a very important role in early diagnosis of bone cancer and can be integrated within a biomedical device such as biosensor. The biomarkers can be proteins, deoxyribonucleic acid (DNA), or ribonucleic acid (RNA). Biomarkers can be categorized according to their intended application, staging, and predictive approach. Diagnostic biomarkers can be used as a tool to identify bone diseases. These biomarkers can be detected through bioreceptor based biosensors. Advantages of bioreceptor based biosensor are high specificity, good selectivity, fast response time, very less usage of reagents, interact with a specific analyte, small size, and ability to measure non-polar molecules. Bioreceptors contain biologically derived components that can recognize a biological analyte. A bioreceptor can be an enzyme, antibody, nucleic acid, RNA, or DNA in a cell.

In this article, diagnosis and treatment challenges associated with various types of bone cancer are discussed. Based on the importance of early detection, various detection methods are also discussed. Available biomarkers and their roles in identifying the bone cancer at early stage are explained. Further, this article has focused on various types of biosensors based on bioreceptors, considering that such bioreceptor based biosensors for bone cancer detection are identified as an emerging and promising area of research which needs to be explored further.

2 Bone Cancer

Based on cell type, from which the tumor originates, bone cancer can be classified as follows:

2.1 Primary Bone Cancer

Primary bone cancer initiates in bone and may cultivate on the outer layer or can propagate from the center of the bone. If there is a growth in tumor, the cancer cells multiply and may destroy the bone. If left untreated, such bone cancer may spread to other parts of the body as well. In this category, osteosarcoma, the most common form of bone cancer usually develops in osteoblast cells (immature bone tissue) and affects the outer hard layer of bone tissue. It usually occurs in pediatric and young adults [4, 5]. In this type of cancer, excess cells are produced in the long bones of the arms or the legs. However, it may affect hips, shoulder, or any other bones too [6]. The second most common type of bone cancer is chondrosarcoma which primarily affects the people of around 40 years of age and occurs in the cells of cartilage of hips, thigh area, shoulders, and pelvis [7]. It affects subchondral tissue that is found at the end of bone and covered with another tissue that is cartilage of bone. Ewing sarcoma is a type of bone cancer that generally affects pelvis, chest wall, legs, ribs, but can form in any bone. This rare form of bone cancer can begin either in soft tissues surrounding the bones or can directly occur in the bones. Children and young adults are at high risk of Ewing sarcoma [8]. Chordoma is an aggressive, locally invasive type of cancer that forms in bone of the spine and skull with poor prognosis (Fig. 1).

2.2 Secondary Bone Cancer

The cancer, that occurs in an organ, such as breast, lungs, or prostate and then spread (metastasizes) to the bone is known as metastatic bone diseases (MBD) or secondary bone cancer. This cancer can spread in the spine, ribs, upper arms, pelvis, and legs. Although half of the different types of cancer can spread to the bone and destroy particular area of the bone. This process of destruction of bone is also known as osteolytic bone destruction [9]. Another form of secondary bone cancer is osteoblastic. When a new bone has formed abnormally which weakens the bone [10]. Any cancer can spread to the bone, but the most common are breast, lung, prostate, myeloma, and thyroid.

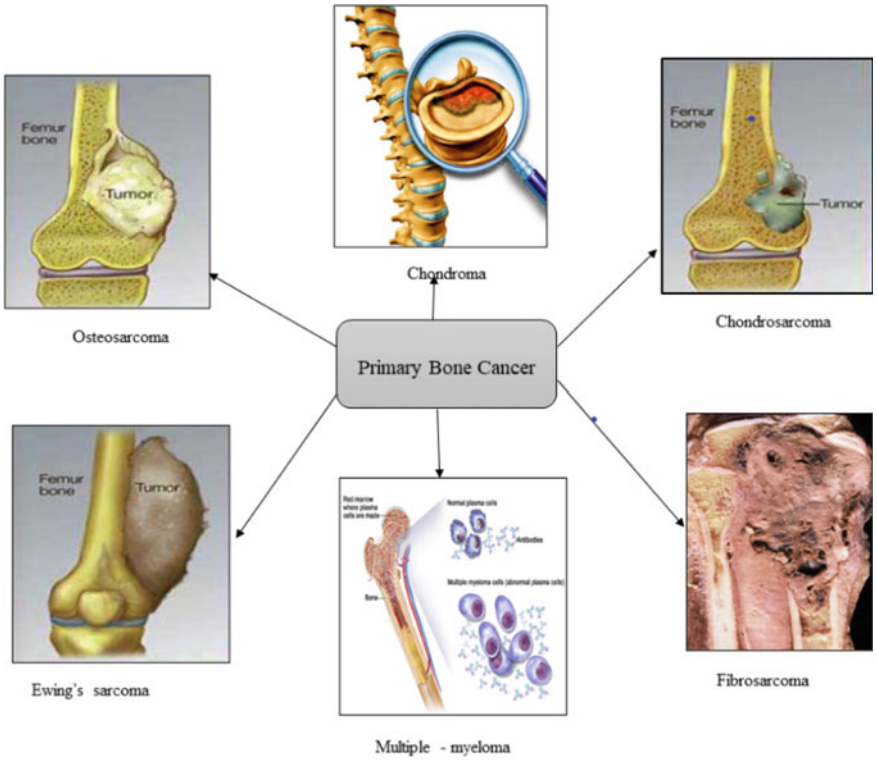

Fig. 1 Schematic representation of primary bone cancer

3 Biosensing Methods of Bone Cancer Detection

In the process of cancer treatment, various therapies, surgeries, scans, biopsy, radiography techniques, and blood test are performed. These mentioned techniques have their special features for analysis. However, all these techniques come in use after occurrence of diseases. A biosensor based biomedical devices, on the other hand can be used as a potential tool which can detect early occurrence of bone cancer.

3.1 Traditional Methods

The diagnosis process usually starts when patients turn up with pain, swelling, and complaints of spontaneous fracture in some cases. Based on symptoms doctor initially recommends X-ray that can be followed by costlier examinations such as bone densitometry, computed tomography (CT) scan, and magnetic resonance imaging (MRI). To investigate tumor grade and stage, bone biopsy can give accurate diagnosis for

further treatment. The traditional bone cancer monitoring techniques, however, have several limitations. Bone scan is limited to identify only some forms of cancer. Besides, such imaging devices are costlier, bigger in size, and require specialized lab assessment. Additionally, the information obtained from bone biopsy is limited to the infection zone under investigation and cannot make early detection of bone cancer.

3.2 Advanced Methods Based on Biomarkers

The advanced methods involve investigation of cancer cell at the level of gene and protein. In these, the biomarkers play an important role in prior detection of cancer and its treatment. Based on the state of disease, bone biomarkers can be divided as diagnostic, prognostic, and predictive detection in cancer research [11]. Nowadays, genomics and proteomics technologies are mostly used in biomarker detection strategies [12]. In genomics technology, the study of entire genome of an organism takes place. There are several other approaches also including RNA expression, DNA sequencing and micro-RNA profiling, etc. DNA sequencing can find genetic mutation in candidate genes and is also analyzes chromosomal rearrangement [13]. Proteomics technologies investigate functional role of key protein in bone cancer formation [14]. In this approach, various types of samples are used including blood, tear, urine, saliva, tissues, and cerebrospinal fluid samples.

Biomarkers for osteosarcoma: Multigene classifiers and series of miRNA fingerprints are proposed as signature in a biomarker study for osteosarcoma [15, 16]. Single-gene miRNA biomarkers are C7 or f24, miR-21, miRNA-214, and tenascin-C protein [17]. Recent study [18] has reported the regulatory function of circular RNAs (circRNAs) in osteosarcoma. Ghafouri-Fard and co-workers [19] reported abnormal regulation of long non-coding RNAs (lncRNAs) in osteosarcoma. Liu et al. [20] demonstrated that long non-coding RNA (MALAT1) is an important biomarker in osteosarcoma. Huang et al. [21] reported that miRNA-663a potential biomarker can diagnose osteosarcoma. Shi et al. [22] demonstrated that serum miR-194 might be a novel and promising biomarker that can detect osteosarcoma.

Biomarkers for chondrosarcoma: This bone cancer usually starts in cartilage cells but also spreads in soft tissues nearby bones sometimes. It mostly occurs in adults having more than 40 years of age with the most affected areas as thigh bone, shoulders, upper arm bone, ribs, or pelvis. The differential diagnosis biomarkers of chondrosarcoma's are IDH1 and IDH2 [23, 24]. The protein based markers are leptin, S100, VEGF-A, VEGF-C, and adiponectin [25].

Biomarkers of multiple myeloma: Multiple myeloma usually occurs in plasma cells and these plasma cells accumulate in bone marrow. They also activate other cells by releasing chemicals to degrade the bone. The biomarkers of multiple myeloma are cell free DNA, microRNAs, copy number variations (CNVs), telomeres and telomerase, ECM proteins, and angiogenic markers [26, 27].

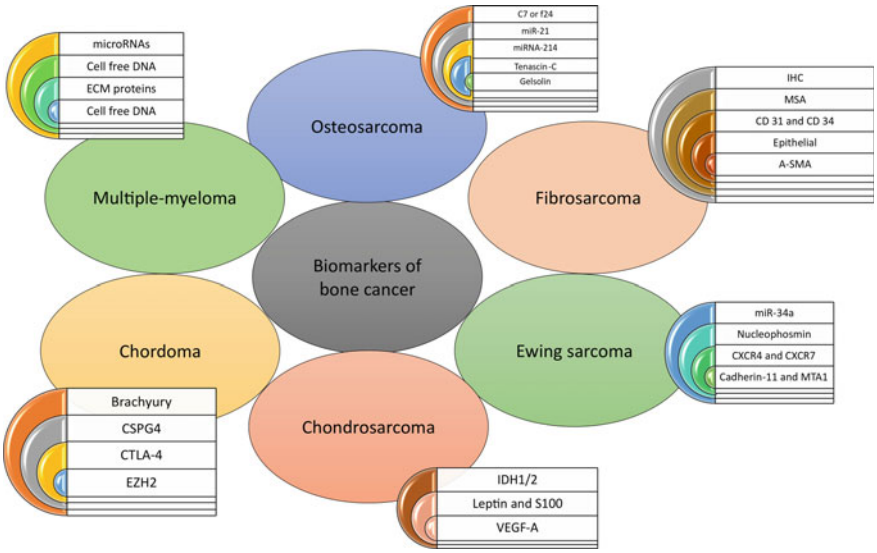

Fig. 2 Schematic representation of bone cancer biomarkers

Biomarkers of fibrosarcoma: Fibrosarcoma is a tumor of osteogenic cells that can start in fibrous tissue and spread in tendons, ligaments, and muscles. Biomarkers of fibrosarcoma are immunohistochemic (IHC), muscle specific actin (MSA), alpha smooth muscle actin (α-SMA), positive CD 31, CD 34, and epithelial [28, 29].

Biomarkers of Ewing sarcoma: Ewing sarcoma is a malignant tumor that affects adolescents from age 10–15 years of age and grows within marrow cavity of bone. Biomarkers of Ewing sarcoma are CXCR4, CXCR7 gene [30], miRNA-34a, miRNA, cadherin-11, MTA1 [31], nucleophosmin, ccf mtDNA [32].

Biomarkers of chordoma: Chordoma are very rare, and the tumors usually develop in cartilage, sinuses, bone of skull and rarely in lower back of spine [33]. Biomarkers of chondroma are CTLA-4, EZH2, CSPG4, and brachyury [34] (Fig. 2).

4 Biosensors: Basic Principles

Biosensors are a short form for biological sensor, wherein bio elements interact with analytes and produce biological response, which is converted to electrical signal by transducers [35, 36]. It is a device having combination of a sensitive component that can biologically recognize the analytes of interest along with a physical transducer which is used to detect those analytes. The biological reaction is transformed into a measurable signal and the analyzed results are displayed, which can further be used

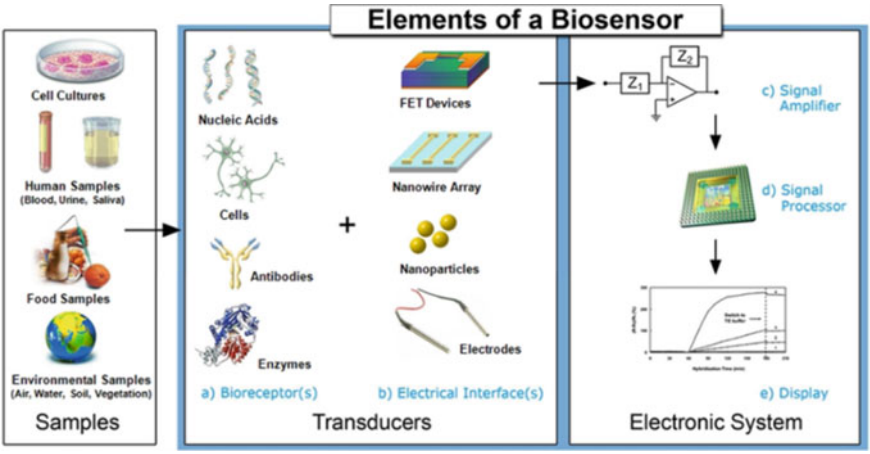

Fig. 3 Schematic representation of basic principle of biosensors [37] (Reproduced under the terms of the 'creative commons attribution' for open access content)

for quantitative and qualitative determinations. In biosensors, biological recognition usually includes nucleic acids, antibodies, enzymes, microorganisms, receptors, cells, and tissues (Fig. 3).

5 Classification of Bone Biosensors on the Basis of Bioreceptors

Bioreceptor is a molecule that precisely identifies the analytes (e.g., lactose glucose, ammonia, and alcohol, etc.). The bone biosensors can also be classified based on different bioreceptors like aptamer, antibody, enzymes, and whole cell. These bioreceptors recognize the analytes and generate signals in the form of charge, heat, light, pH, or mass change. Biosensors can also be classified based on bioreceptor utilization as catalytic biosensors and non-catalytic biosensors. In catalytic biosensor, new biochemical reaction products are found during analyte-bioreceptor interaction. Some of them use enzymes, tissues, and whole cells. However, in non-catalytic biosensors, no new product of biochemical reaction is found during interaction of analyte and bioreceptors. These sensors use cell receptors, antibodies, and nucleic acids [38].

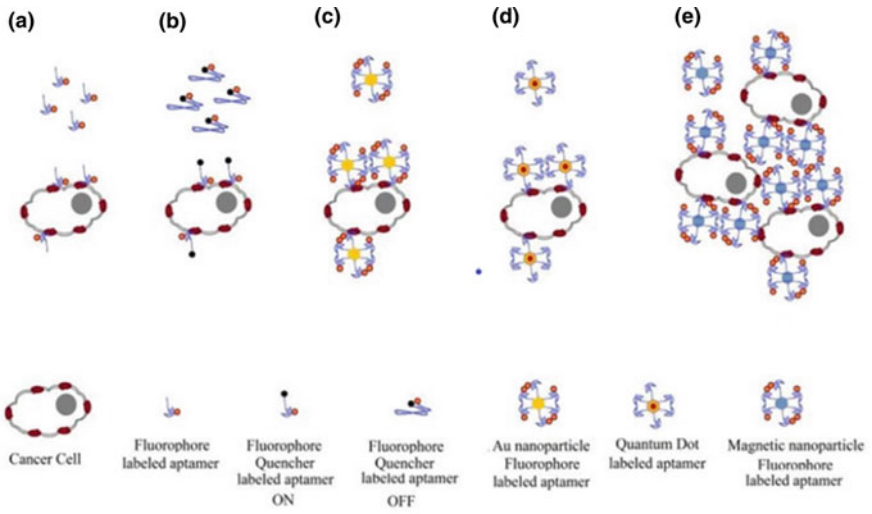

Fig. 4 Schematic representation of fluorescence biosensing. **a** Simple fluorophore-labeled aptasensor; **b** fluorophore/quenchere-based aptasensors; **c** gold nanoparticles/fluorophore-labeled aptasensors; **d** quantum dot aptasensors; and e magnetic nanoparticle/fluorophore-labeled aptasensors [43] (Reproduced under the terms of the 'creative commons attribution' for open access content)

5.1 Biosensors Based on Aptamer

Aptamers are single stranded synthetic nucleic acids (RNA or DNA) that selectively bind to target molecules and can be folded into two-dimensional as well as three-dimensional structures. Aptamers can be modified chemically and they are stable within pH range of 2–12 with wide range of temperature for storage [39]. Raghav and Srivastava [40] reported cancer antigen-125 (CA 125) detection by using gold–silver core–shell nanoparticles through using label free and reagent less immunosensors that can detect antigen in 20 min. Palmini and Brandi reported presence of miRNA-24 in osteosarcoma cells and tissues [41]. In 2019, Chen et al. developed an electrochemical aptasensor for cancer antigen 125 (CA-125) detection based on the use of flower like gold nanostructure deposited on screen printed carbon electrode with response in range of 0.05–50 ng mL^{-1} and detection limit of 5.0 pg mL^{-1} [42]. Bakhtiari et al. reported various approaches for aptamer based detection of cancer molecules [43] (Fig. 4).

5.2 Biosensors Based on Antibody

Antibodies are biorecognition elements and are used because of their strong antibody-antigen interactions with wide application range, producing analytical signals. Such

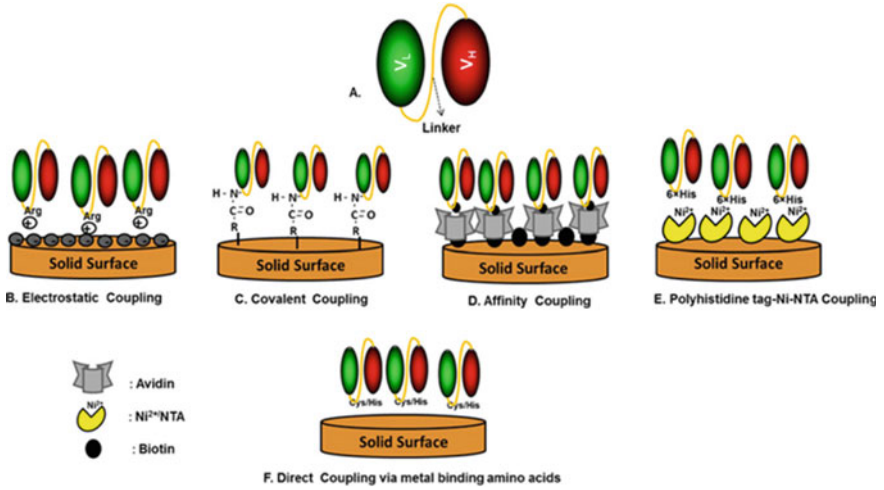

Fig. 5 Various types of immobilization techniques of antibodies in designing of biosensors [44] (Reproduced under the terms of the 'creative commons attribution' for open access content)

types of biosensors are also known as immunosensors. Immunosensors are categorized as labeled and non-labeled. In case of non-labeled type, antibody-antigen interactions produce physical change (charge, current, and ions). However, in labeled type, a noticeable label is involved in detection of antigen–antibody interactions. Sharma et al., demonstrated that antibodies and antibody derived analytical biosensors with various immobilization approaches are useful in biosensor designing [44] (Fig. 5).

5.3 Biosensors Based on Enzyme

Enzymes are biocatalysts, that can increase the biological reaction rate. Enzymes based biosensors rely on enzyme catalytic reactions that can generate or consume detectable compound like O_2, CO_2, H_2O_2, NH_3, and H^+ Based on enzyme specificity, various biosensors are designed. However, the structure of enzyme is very sensitive that makes it complicated and expensive. Electrochemical transducer is mostly used for these biosensors [45].

5.4 Biosensors Based on Whole Cell

Whole cell-based biosensors are made up of the unit on which cells are immobilized and use bacterial, viruses, algae, and protozoa [46]. These biosensors can be used

in cancer research for detection of various cancerous cell. Pan et al., demonstrated a 3D cell-based biosensors for anti-cancer drug screening [47]. Whole cell-based biosensor has great potential in bone cancer research, cell size and shape can easily identify a bone cancer.

5.5 Biosensors Based on Nucleic Acids

Nucleic acid-based biosensors use oligonucleotide as a sensing element with a known sequence of DNA or RNA. Nucleic acid-based biosensors are time consuming because of polymer chain reaction (PCR). Micro RNA (miRNA) based biosensors act as ultrasensitive tool to detect bone cancer [48]. In 2020, Sun et al. demonstrated that miRNA-615 acts as tumor suppressor and used as a target for osteosarcoma treatments [49]. Moccia et al. developed a paper-based biosensor with electrochemical peptide nucleic acid (PNA) that can detect a cancer biomarker miRNA-492 up to a linear range of 100 nm, with a detection limit of 6 nm [50].

6 Conclusion

Bone cancer is a life-threatening disease for which early diagnosis can significantly contribute to its treatment. In this article, we have discussed various types of bone cancers with traditional and advanced detection methods of bone cancer. We have also reviewed various biomarkers related to detection of primary bone cancers including osteosarcoma, Ewing sarcoma, chondrosarcoma, chordoma, multiple myeloma, and fibrosarcoma. The basic principles of biosensor designs for bone cancer detection have also been reviewed with special emphasis on bioreceptor based biosensors. Various bioreceptors including aptamer, antibody, enzymes, or whole cell that can be used for analysis of bone cancer, have been highlighted with their potential applications in bone biosensing devices. Finally, various mechanisms, advantages, and challenges of such biosensors have been reviewed in this article, establishing their promising potential in early detection of bone cancer.

References

1. Rodan GA (1992) Introduction to bone biology. Bone 13:S3–S6
2. Chapurlat RD, Confavreux CB (2016) Novel biological markers of bone: from bone metabolism to bone physiologya. Rheumatol (United Kingdom) 55(10):1714–1725
3. Brunetti G, Di Benedetto A, Mori G (2014) Bone remodelling. Imag Prosthet Joints A Comb Radiol Clin Perspect 27–37
4. Zhao X, Wu Q, Gong X, Liu J, Ma Y (2021) Osteosarcoma: a review of current and future therapeutic approaches. Biomed Eng Online 20(1):1–14

5. Rejniak KA, Lloyd MC, Reed DR, Bui MM (2015) Diagnostic assessment of osteosarcoma chemoresistance based on virtual clinical trials. Med Hypotheses 85(3):348–354
6. Evola FR et al (2017) Biomarkers of osteosarcoma, chondrosarcoma, and Ewing sarcoma. Front Pharmacol 8:1–14
7. Nugent M (2015) MicroRNA and bone cancer. Adv Exp Med Biol 889:201–230
8. Desai KI, Nadkarni TD, Goel A, Muzumdar DP, Naresh KN, Nair CN (2000) Primary Ewing's sarcoma of the cranium. Neurosurgery 46(1):62–69
9. Weber K (2018) Metastatic bone disease. AAOS Compr Orthop Rev 2 1:581–594
10. Ibrahim T, Flamini E, Mercatali L, Sacanna E, Serra P, Amadori D (2010) Pathogenesis of osteoblastic bone metastases from prostate cancer. Cancer 116(6):1406–1418
11. Joshi Garish KH, Rajandeep K (2016) Biomarkers in cancer. Int Res J Pharm Biosci 3(3):845–856
12. Wan-Ibrahim WI, Singh VA, Hashim OH, Abdul-Rahman PS (2015) Biomarkers for bone tumors: discovery from genomics and proteomics studies and their challenges. Mol Med 21(3):861–872
13. Ong M et al (2014) Validation and utilisation of high-coverage next-generation sequencing to deliver the pharmacological audit trail. Br J Cancer 111(5):828–836
14. Belczacka I et al (2018) Proteomics biomarkers for solid tumors: current status and future prospects. Mass Spectrom Rev 38(1):49–78
15. Han X, Wang W, He J, Jiang L, Li X (2019) Osteopontin as a biomarker for osteosarcoma therapy and prognosis (review). Oncol Lett 17(3):2592–2598
16. Gougelet A et al (2011) Micro-RNA profiles in osteosarcoma as a predictive tool for ifosfamide response. Int J Cancer 129(3):680–690
17. Lin Z, Xie X, Lu S, Liu T (2020) Noncoding RNAs in osteosarcoma: implications for drug resistance. Cancer Lett 504:91–103
18. Soghli N, Qujeq D, Yousefi T, Soghli N (2020) The regulatory functions of circular RNAs in osteosarcoma. Genomics 112(4):2845–2856
19. Ghafouri-Fard S, Shirvani-Farsani Z, Hussen BM, Taheri M (2021) The critical roles of lncRNAs in the development of osteosarcoma. Biomed Pharmacother 135:111217
20. Liu M et al (2019) Long non-coding RNA MALAT1 as a valuable biomarker for prognosis in osteosarcoma: a systematic review and meta-analysis. Int J Surg 72(July):206–213
21. Huang C, Sun Y, Ma S, Vadamootoo AS, Wang L, Jin C (2019) Identification of circulating miR-663a as a potential biomarker for diagnosing osteosarcoma. Pathol Res Pract 215(6):152411
22. Shi L, Xie C, Zhu J, Chen X (2020) Downregulation of serum miR-194 predicts poor prognosis in osteosarcoma patients. Ann Diagn Pathol 46(10):151488
23. Chen S et al (2017) Diagnostic utility of IDH1/2 mutations to distinguish dedifferentiated chondrosarcoma from undifferentiated pleomorphic sarcoma of bone. Hum Pathol 65:239–246
24. Flanagan AM, Lindsay D (2017) A diagnostic approach to bone tumours. Pathology 49(7):675–687
25. Jeong W, Kim HJ (2018) Biomarkers of chondrosarcoma. J Clin Pathol 579–583
26. Gupta N, Sharma A, Sharma A (2019) Emerging biomarkers in multiple myeloma: a review. Clin Chim Acta 503:45–53
27. Bustoros M, Mouhieddine TH, Detappe A, Ghobrial IM (2017) Established and novel prognostic biomarkers in multiple myeloma. Am Soc Clin Oncol Educ B 37:548–560
28. Augsburger D et al (2017) Current diagnostics and treatment of fibrosarcoma—perspectives for future therapeutic targets and strategies. Oncotarget 8(61):104638–104653
29. Folpe AL (2020) 'Hey! Whatever happened to hemangiopericytoma and fibrosarcoma?' An update on selected conceptual advances in soft tissue pathology which have occurred over the past 50 years. Hum Pathol 95:113–136
30. Bennani-Baiti IM et al (2010) Intercohort gene expression co-analysis reveals chemokine receptors as prognostic indicators in Ewing's sarcoma. Clin Cancer Res 16(14):3769–3778
31. Ohali A et al (2004) Prediction of high risk Ewing's sarcoma by gene expression profiling. Oncogene 23(55):8997–9006

32. Yu M, Wan YF, Zou QH (2012) Cell-free circulating mitochondrial DNA in the serum: a potential non-invasive biomarker for Ewing's sarcoma. Arch Med Res 43(5):389–394
33. Somers J, Faber LP (1999) Chondroma and chondrosarcoma. Semin Thorac Cardiovasc Surg 11(3):270–277
34. Traylor JI, Pernik MN, Plitt AR, Lim M, Garzon-Muvdi T (2021) Immunotherapy for chordoma and chondrosarcoma: current evidence. Cancers (Basel) 13(10):1–15
35. Rani S, Bandyopadhyay-Ghosh S, Ghosh SB, Liu G (2020) Advances in sensing technologies for monitoring of bone health. Biosensors 10(4):1–21
36. Garg V et al (2021) A hierarchically designed nanocomposite hydrogel with multisensory capabilities towards wearable devices for human-body motion and glucose concentration detection. Compos Sci Technol 213:108894
37. Grieshaber D, MacKenzie R, Os JV, Reimhult E (2008) Electrochemical biosensors—sensor principles and architectures. Sensors 8:1400–1458
38. Naresh V, Lee N (2021) A review on biosensors and recent development of nanostructured materials-enabled biosensors. Sensors (Switzerland) 21(4):1–35
39. Wang RE, Zhang Y, Cai J, Cai W, Gao T (2011) Aptamer-based fluorescent biosensors. Curr Med Chem 18(27):4175–4184
40. Raghav R, Srivastava S (2015) Core-shell gold-silver nanoparticles based impedimetric immunosensor for cancer antigen CA125. Sens Actuators, B Chem 220:557–564
41. Palmini G, Brandi ML (2021) microRNAs and bone tumours: role of tiny molecules in the development and progression of chondrosarcoma, of giant cell tumour of bone and of Ewing's sarcoma. Bone 149:115968
42. Chen J et al (2019) An electrochemical aptasensing platform for carbohydrate antigen 125 based on the use of flower-like gold nanostructures and target-triggered strand displacement amplification. Microchim Acta 186(6):2–9
43. Bakhtiari H, Palizban AA, Khanahmad H, Reza M (2020) Aptamer-based approaches for in vitro molecular detection of cancer. Res Pharm Sci 107–122
44. Sharma S, Byrne H, O'Kennedy RJ (2016) Antibodies and antibody-derived analytical biosensors. Essays Biochem 60(1):9–18
45. Liu H, Ge J, Ma E, Yang L (2018) Advanced biomaterials for biosensor and theranostics. Elsevier Inc.
46. Gupta N, Renugopalakrishnan V, Liepmann D, Paulmurugan R, Malhotra BD (2019) Cell-based biosensors: recent trends, challenges and future perspectives. Biosens Bioelectron 141:111435
47. Pan Y et al (2019) 3D cell-based biosensor for cell viability and drug assessment by 3D electric cell/matrigel-substrate impedance sensing. Biosens Bioelectron 130:344–351
48. Hong CY et al (2013) Ultrasensitive electrochemical detection of cancer-associated circulating microRNA in serum samples based on DNA concatamers. Biosens Bioelectron 50:132–136
49. Sun L et al (2020) MicroRNA-615 functions as a tumor suppressor in osteosarcoma through the suppression of HK2. Oncol Lett 20(5):1–8
50. Moccia M et al (2020) Paper-based electrochemical peptide nucleic acid (PNA) biosensor for detection of miRNA-492: a pancreatic ductal adenocarcinoma biomarker. Biosens Bioelectron 165:112371

A New Tool of Construction Project Decision-Making Under Refined Simplified Neutrosophic Similarity Measure

Sapna Gahlot and R. N. Saraswat

Abstract Refined simplified neutrosophic sets (RSNSs) are properly utilized in decision-making issues through sub-characteristics as their truth, indeterminacy, and falsity parts freely. This article defines the some measures of RSNSs dependent on Euclidian measure. We introduced the weighted similarity measure for RSNSs and their various MADM technique with RSNS data. In MADM procedure, the created technique provides the positioning order and the best choice of options with the help of similarity measure values among options and the ideal solution as indicated by the given characteristics and sub-characteristics weights. At that point, a MADM model in a development project by RSNS data is introduced to show the viability and achievability of the proposed MADM technique. This investigation broadens existing techniques and gives another route to RSN MADM issues.

Keywords Refined simplified neutrosophic set · Similarity measure · Multiple attribute decision-making · Construction project

Mathematics Subject Classification 94A15 · 62B10 · 62B86

1 Introduction

There are two types of decision-making procedures: group decision-making techniques and individual decision-making strategies. A group can frequently use individual decision-making procedures.

The act of establishing, organizing, executing, controlling, and closing a project constructed by a group to achieve specific objectives and meet explicit achievement models at a predetermined period is known as project management. The most important test for project managers is to complete all of the project objectives within the time restrictions. This information is usually depicted in project documentation, which is created at the outset of the development process. Degree, time, quality, and

S. Gahlot (✉) · R. N. Saraswat
Department of Mathematics and Statistics, Manipal University Jaipur, Jaipur, Rajasthan 303007, India
e-mail: sapna1994gahlot@gmail.com

© The Author(s), under exclusive license to Springer Nature Singapore Pte Ltd. 2022

A. Tripathi et al. (eds.), *Intelligent Computing Techniques for Smart Energy Systems*, Lecture Notes in Electrical Engineering 862,
https://doi.org/10.1007/978-981-19-0252-9_29

budget are the most important prerequisites. The goal of project management is to produce a complete assignment that adheres to the customer's wishes. The purpose of many project executives is to modify or change the customer's brief in order to possibly meet the customer's objectives.

Localization project management incorporates numerous standard project management rehearses despite the fact that many believe this sort of the board to be a totally different control. It centers around three significant objectives: time, quality, and spending plan.

Group decision-making is a circumstance confronted when people altogether settle on a decision from the options before them. The choice is then not, at this point owing to any single person who is an individual from the gathering. This is on the grounds that all the people and social gathering procedures, for example social impact, add to the result. The choices made by bunches are frequently unique in relation to those made by people. In work environment settings, communitarian dynamic is one of the best models to produce purchase in from different partners, fabricate accord, and support innovativeness. As indicated by the possibility of collaboration, choices made all in all additionally will in general be more viable than choices made by a solitary person. In this vein, certain community oriented plans can possibly create preferable net execution results over people following up on their own. Under typical regular conditions, cooperative or collective choice creation would frequently be liked and would produce a bigger number of advantages than singular dynamic when there is the ideal opportunity for appropriate consultation, conversation, and dialogue. This can be accomplished using board of trustees, groups, gatherings, associations, or other communitarian social procedures.

The FSs (fuzzy set) [1] is spoken to by the membership degree (MD) but in some cases, the FSs cannot be depicted through the non-membership degree (N-MD). As the speculation of FS, Atanassov [2] introduced an IFS (intuitionistic fuzzy set), which is described by the MD as well as N-MD. Be that as it may, IFS can just deal with inadequate and dubious data however not conflicting and vague data. Along these lines, a neutrosophic set (NS) was presented via Smarandache [3]. In NS, the truth, indeterminacy, and falsity are meant as T, I, F from the interval [0, 1] or $]^{-}0, 1^{+}[$. From that point onward, Simplified NSs (SNSs) defined via Ye [4], which is a subclasses of NSs and define the ideas of single valued neutrosophic sets (SVNSs) and INSs with the help of this they defined the many decision-making problems. Despite the fact that they have been applied in genuine MADM issues. Smarandache [3] first characterized n valued/refined NS, which is made out of its n sub-components spoke to by p truth sub-MD, r indeterminacy sub-MD, and s falsity sub-MD fulfilling $p + r + s = n$. Additionally, Ye and Smarandache [3] defined the refined NS (RNSs) to a refined single valued NS (RSVNSs), Here, its sub-components $T_1, T_2, \ldots, T_q$ and $I_1, I_2, \ldots, I_q$, and $F_1, F_2, \ldots, F_q$ are developed as a RSVNS, and afterward, they presented the closeness measure utilizing the union and intersection of RSVNSs to manage MADM issues through the characteristics and sub-characteristics.

The remainder of this paper is built as the accompanying. In Sect. 2, we define the all-inclusive measure for SNSs, RSNSs. We present the MADM technique utilizing the measure for RSNSs in Sect. 3 and, in Sect. 4, a model on DM of a development

project through characteristics and sub-characteristics by RSNS (RSVNS and RINS) and a few concluding comments in Sect. 5.

2 Preliminaries

Right now, we briefly describe some essential ideas and fundamental operational laws identified with INs, INSs, SVNS, and RSNSs.

NS [3] is defined through the parts T, I, F, which are characterized independently as the MD of the T, I, and F from interval [0, 1] or $]^{-}0, 1^{+}[$. In this manner, Ye [4] introduced the idea of SNS. A SNS A in a universe of discourse X by the element x, $A = \{\langle x, T_A(x), I_A(x), F_A(x)\rangle / x \in X\}$ s.t. $T_A(x), I_A(x), F_A(x) \in [0,1]$ for SVNS or $T_A(x), I_A(x), F_A(x) \subseteq [0,1]$ for INS and $\langle x, T_A(x), I_A(x), F_A(x)\rangle$ is known as SNN, simply denoted as $A = \langle t_a, i_a, f_a\rangle$ and includes SV as well as INN. Suppose two SNSs in X are $A = \{a_1, \ldots, a_n\}$ for $a_j \in A\{j = 1, \ldots, n\}$ and $B = \{b_1, \ldots b_n\}$ for $b_j \in B\{j = 1, \ldots, n\}$ s.t. $a_j = \langle t_{aj}, i_{aj}, f_{aj}\rangle$ and $b_j = \langle t_{bj}, i_{bj}, f_{bj}\rangle$. Then, the some measures among two SVNSs A and B are defined as [3]:

$$S_1(A, B) = \sqrt{\sum_{j=1}^{n} \left(\left(t_{aj} - t_{bj}\right)^2 + \left(i_{aj} - i_{bj}\right)^2 + \left(f_{aj} - f_{bj}\right)^2\right)} \tag{2.1}$$

For INSs, similarity measures among INSs A and B are defined as

$$\sqrt{\sum_{j=1}^{n} \begin{pmatrix} \left(\inf t_{aj} - \inf t_{bj}\right)^2 + \left(\sup t_{aj} - \sup t_{bj}\right)^2 + \left(\inf i_{aj} - \inf i_{bj}\right)^2 \\ + \left(\sup i_{aj} - \sup i_{bj}\right)^2 + \left(\inf f_{aj} - \inf f_{bj}\right)^2 + \left(\sup f_{aj} - \sup f_{bj}\right)^2 \end{pmatrix}} \tag{2.2}$$

According to the some properties of measures from [5, 6], measures $S_1(A, B)$ among two SNSs A and B also have these properties:

(R_1) $0 \leq S_1(A, B) \leq 1$;
(R_2) $S_1(A, B) = S_1(B, A)$;
(R_3) $S_1(A, B) = 1$ iff $A = B$;
(R_4) Assume S is also a SNS in X, If $A \subseteq B \subseteq S$, then $S_1(A, S) \leq S_1(A, B)$ and $S_1(A, S) \leq S_1(B, S)$.

2.1 Similarity Measures of RSNSs

Here, we define the some measures and weighted measures among RSNSs. These measures increasingly appropriate for taking care of MADM issues with sub-characteristics.

If a simplified NS $A = \{a_1, \ldots a_n\}$ for $a_j \in A(j = 1, 2, \ldots, n)$ is refined, $a_j = \langle t_j, i_j, f_j \rangle$ consists of the sub-components such as $a_{ji} = (t_{j1}, t_{j2} \ldots, i_{j1}, i_{j2}, \ldots f_{j1}, f_{j2}, \ldots)$. Then RSNS contains RSVNS with the components $t_{j1}, t_{j2} \ldots \in [0, 1], i_{j1}, i_{j2} \ldots \in [0, 1], f_{j1}, f_{j2} \ldots \in [0, 1]$, and $0 \leq t_{ji} + i_{ji} + f_{ji} \leq 3$ and RINS with $t_{j1}, t_{j2} \ldots \in [0, 1], i_{j1}, i_{j2} \ldots \in [0, 1], f_{j1}, f_{j2} \ldots \in [0, 1]$, and $0 \leq Ut_{ji} + Ui_{ji} + Uf_{ji} \leq 3$. We consider two RSNS $A = \{a_1,\ldots,a_n\}$ and $B = \{b_1,\ldots,b_n\}$ for $a_j \in A$ and $bj \in B$ $(j = 1, 2, \ldots, n)$, where $aji = \langle (taj1, taj2,\ldots, tajr(j)), (iaj1, iaj2,\ldots, iajr(j)), (faj1, faj2,\ldots, fajr(j))\}$ and $bji = \langle (tbj1, tbj2,\ldots, tbjr(j)), (ibj1, ibj2,\ldots, ibjr(j)), (fbj1, f_{bj2},\ldots, f_{bjr(j)})\}$ for $a_{ji} \in a_j$ and $b_{ji} \in b_j$ $(i = 1, 2,\ldots., r(j); j = 1, 2,\ldots, n)$. Hence, the measures among RSVNSs and RINSs are known as:-

(i) Similarity measures of RSVNSs

$$S_1(A, B) = \sqrt{\sum_{j=1}^{n} \frac{1}{r_j} \sum_{i=1}^{r(j)} \left(\left(t_{aj_{r(j)}} - t_{bj_{r(j)}}\right)^2 + \left(i_{aj_{r(j)}} - i_{bj_{r(j)}}\right)^2 + \left(f_{aj_{r(j)}} - f_{bj_{r(j)}}\right)^2 \right)} \tag{2.3}$$

(ii) Similarity measures of RINSs

$$S_1(A, B) = \sqrt{\sum_{j=1}^{n} \frac{1}{r_j} \sum_{i=1}^{r(j)} \begin{pmatrix} \left(\left(\inf t_{aj_{r(j)}} - \inf t_{bj_{r(j)}}\right)^2 + \left(\sup t_{aj_{r(j)}} - \sup t_{bj_{r(j)}}\right)^2 \\ + \left(\inf i_{aj_{r(j)}} - \inf i_{bj_{r(j)}}\right)^2 + \left(\sup i_{aj_{r(j)}} - \sup i_{bj_{r(j)}}\right)^2 \\ + \left(\inf f_{aj_{r(j)}} - \inf f_{bj_{r(j)}}\right)^2 + \left(\sup f_{aj_{r(j)}} - \sup f_{bj_{r(j)}}\right)^2 \end{pmatrix}} \tag{2.4}$$

Hence, $w = (w_1, w_2, \ldots w_n)$ and $w_j = \left(w_{11}, w_{22}, \ldots, w_{nr(j)}\right)$ $(i = 1, 2, \ldots, r(j); j = 1, 2, \ldots, n)$ are the weights of elements and sub-elements in RSNS, respectively. Therefore, weighted measures are defined as given below:

(i) Weighted similarity measures of RSVNSs

$W_1(A, B)$

$$= \sqrt{\sum_{j=1}^{n} w_j \sum_{i=1}^{r(j)} \left(\left(t_{aj_{r(j)}} - t_{bj_{r(j)}}\right)^2 + \left(i_{aj_{r(j)}} - i_{bj_{r(j)}}\right)^2 + \left(f_{aj_{r(j)}} - f_{bj_{r(j)}}\right)^2 \right)} \tag{2.5}$$

(ii) Similarity measures of RINSs

$$S_1(A, B) = \sqrt{\sum_{j=1}^{n} w_j \sum_{i=1}^{r(j)} \begin{pmatrix} \left(\inf t_{aj_{r(j)}} - \inf t_{bj_{r(j)}}\right)^2 + \left(\sup t_{aj_{r(j)}} - \sup t_{bj_{r(j)}}\right)^2 \\ + \left(\inf i_{aj_{r(j)}} - \inf i_{bj_{r(j)}}\right)^2 + \left(\sup i_{aj_{r(j)}} - \sup i_{bj_{r(j)}}\right)^2 \\ + \left(\inf f_{aj_{r(j)}} - \inf f_{bj_{r(j)}}\right)^2 + \left(\sup f_{aj_{r(j)}} - \sup f_{bj_{r(j)}}\right)^2 \end{pmatrix}} \tag{2.6}$$

The above weighted similarity measures $W_1(A, B)$ based on similarity measure also follow the above properties (R_1)–(R_4).

3 Application

This area is presenting a MADM strategy utilizing the developed measure of RSNSs.

How about we consider a m choices $A = \{A_1,\ldots A_m\}$ to be decided under attributes $K = \{k_1,\ldots k_n\}$ with their sub-qualities $K_j = \left\{k_{j1}, \ldots k_{jr(j)}\right\}$ $(j = 1, 2, \ldots, n)$. At that point, we give the assessment of the choices under the characteristics and sub-characteristics by RSNN.

Table 1 shows the relative assessment values among choices, DM $D = (A_{sji})_{m.n}$, A_{sji} $(i = 1, 2,\ldots, r(j); j = 1, 2,\ldots, n; s = 1, 2,\ldots, m)$define the value A_j with respect to each sub-characteristics $k_{jr(j)}$.

In Table 1, each alternative A_s in $A = \{A_1,\ldots, A_m\}$ is evaluated under all attributes $K = \{k_1,\ldots, k_n\}$ and sub-attributes $K_j = \left\{k_{j1}, \ldots, k_{jr(j)}\right\}$ by RSNN $A_{sji} = \langle(t_{sj}1, t_{sj}2,\ldots,t_{sjr}(j)), (i_{sj}1, i_{sj}2,\ldots, i_{sjr}(j)), (f_{sj}1, f_{sj}2,\ldots, f_{sjr}(j))\rangle$.

Table 1 Decision matrix

A_1	$k11, k12, \ldots, k1r(1),$	$k_{21}, k_{22},\ldots, k_2r(2)$	…	$kn1, kn2,\ldots, k_{nr}(n)$
A_1	$A11r(1)$	$A12r(2)$	…	$A1nr(n)$
A_2	$A21r(1)$	$A22r(2)$	…	$A2nr(n)$
A_3	$A31r(1)$	$A32r(2)$	…	$A3nr(n)$
…	…	…	…	…
A_m	$Am1r(1)$	$Am2r(2)$	…	$Amnr(n)$

Now, weight vectors $w = (w_1,\ldots, w_n)$ for the set $K = \{k_1,\ldots, k_n\}$ and $w_j = (w_1,\ldots, w_{jr(j)})$ for the set of sub-attributes such that $\sum_{j=1}^{n} w_j = 1$ and $\sum_{i=1}^{r(j)} w_{ji} = 1$ with $w_j, w_{ji} \in [0, 1]$.

The ideal solution from the RSNS DM $D = (A_{sji})_{m.n}$ as given below:

$$\begin{aligned} A_{aji} &= \langle (t_{aj1}, t_{aj2}, \ldots, t_{ajr(j)}), (i_{aj1}, i_{aj2}, \ldots, i_{ajr(j)}), (f_{aj1}, f_{aj2}, \ldots, f_{ajr(j)}) \rangle \\ &= \left\langle \left(\max_s (t_{sj1}), \max_s (t_{sj2}), \ldots, \max_s (t_{sjr(j)}) \right), \right. \\ &\quad \left(\min_s (i_{sj1}), \min_s (i_{sj2}), \ldots \min_s (i_{sjr(j)}) \right), \\ &\quad \left. \left(\min_s (f_{sj1}), \min_s (f_{sj2}), \ldots \min_s (f_{sjr(j)}) \right) \right\rangle \text{ For RSVNNs.} \end{aligned}$$

or

$$\begin{aligned} A_{aji} &= \langle (t_{aj1}, t_{aj2}, \ldots, t_{ajr(j)}), (i_{aj1}, i_{aj2}, \ldots, i_{ajr(j)}), (f_{aj1}, f_{aj2}, \ldots, f_{ajr(j)}) \rangle \\ &= \left\{ \left\langle \left[\max_s (Lt_{sj1}), \max_s (Ut_{sj1}) \right], \left[\max_s (Lt_{sj2}), \max_s (Ut_{sj2}) \right], \ldots, \right. \right. \\ &\quad \left. \left[\max_s (Lt_{sjr(j)}), \max_s (Ut_{sjr(j)}) \right] \right\rangle, \\ &\quad \left\langle \left[\min_s (Li_{sj1}), \min_s (Ui_{sj1}) \right], \left[\min_s (Li_{sj2}), \min_s (Ui_{sj2}) \right], \ldots, \right. \\ &\quad \left. \left[\min_s (Li_{sjr(j)}), \min_s (Ui_{sjr(j)}) \right] \right\rangle, \ldots, \\ &\quad \left\langle \left[\min_s (Lf_{sj1}), \min_s (Uf_{sj1}) \right], \left[\min_s (Lf_{sj2}), \min_s (Uf_{sj2}) \right], \ldots, \right. \\ &\quad \left. \left. \left[\min_s (Lf_{sjr(j)}), \min_s (Uf_{sjr(j)}) \right] \right\rangle \right\} \text{ For RINNs.} \end{aligned}$$

And ideal solution is shown as $A^* = \{A^*_1,\ldots, A^*_n\}$ where $A^* = (A_{aj1},\ldots, A_{ajr(j)})$ for $(j = 1, 2, \ldots, n)$.

Thus, by the 2.6, we obtain the values of $W_1(A_s, A^*)$ $(s = 1, 2,\ldots, m)$, all the choices are positioned, and the greatest one is resolved.

4 Case Study

An effective project can be accomplished by many cooperated factors as introduced in past written works [7, 8], which primarily relies upon the decision-making technique. Consequently, the decision makers need to viably settle on exact and solid choice as per the introduced prerequisites or target properties with their profoundly emotional critical components to choose the best option for some undertaking.

In a development project, the decision makers need to pic the greatest option in the choice arrangement of the choices $A = \{A_1, A_2, A_3, A_4\}$ recommended by various characters or offices like organization office, specialized division, money office, and so on to meet the necessities and the destinations of the task from the contractual worker organization. The accompanying two cases made out of the recommended choices by attributes set $K = k_1, k_2, k_3$ and sub-characteristic set

Table 2 Attributes and sub-attributes

k_1 budget	k_2 quality	k_3 delivery
k_{11} human resource cost	k_{21} experience or performance	k_{31} schedule
k_{12} materials and equipment cost	Technology k_{22}	k_{32} communication
k_{13} facilities		k_{33} risk and uncertainties

$K_j = \{k_{j1}, k_{j2}, k_{jr(j)}\}$ $(j = 1, 2, 3)$ in a development project are introduced to portray the appropriateness of the developed strategy (Table 2).

In RSVNS condition, the estimate values of technique arrangement of the choices $A = \{A_1, A_2, A_3, A_4\}$ over the characteristic and sub-characteristic must have a place from [0, 1]. The weight vector $K = \{k_1, k_2, k_3\}$ is $w = (0.3, 0.4, 0.3)$, and the weight vectors of the sub-characteristic sets $\{k_{11}, k_{12}, k_{13}\}$, $\{k_{21}, k_{22}\}$, and $\{k_{31}, k_{32}, k_{33}\}$ are given individually as $w_1 = (0.5, 0.3, 0.2)$, $w_2 = (0.6, 0.4)$, and $w_3 = (0.4, 0.2, 0.4)$. In this way, the RSVNS decision matrix $D = (A_{sji})_{4.3}$ relating to the options as for the three characteristic by given sub-characteristic is shown in Table 3.

To get the value of RSVNS for A^*, to get the some ideal solution:

$A^* = \{\langle(0.8, 0.7, 0.8),\ (0, 0.2, 0.1),\ (0.1, 0.1, 0.1)\rangle,$

$\langle(0.9, 0.8), (0.1, 0.1), (0.1, 0)\rangle, \langle(0.9, 0.8, 0.8),$

$(0.1, 0.1, 0.1),\ (0, 0, 0.1)\rangle\}.$

By Eq. 2.6 we obtain the outcome of measure among the choices A_s $(s = 1, 2, 3, 4)$ and A^* in Table 4.

Table 3 RSVNS decision matrix

	$k11, k12, k13$	$k21, k22$	$k31, k32, k33$
A_1	(0.5, 0.5, 0.6), (0.3, 0.4, 0.2), (0.2, 0.1, 0.2)	(0.7, 0.8), (0.1, 0.2), (0.1, 0.2)	(0.9, 0.8, 0.5), (0.1, 0.1, 0.3), (0, 0.1, 0.2)
A_2	(0.7, 0.6, 0.5), (0.2, 0.2, 0.3), (0.1, 0.2, 0.2)	(0.9, 0.5), (0.1, 0.3), (0.2, 0.2)	(0.7, 0.6, 0.8), (0.1, 0.3, 0.1), (0.2, 0.1, 0.1)
A_3	(0.8, 0.6, 0.8), (0, 0.3, 0.1), (0.2, 0.1, 0.1)	(0.7, 0.6), (0.2, 0.1), (0.3, 0.1)	(0.5, 0.6, 0.6), (0.2, 0.2, 0.3), (0.3, 0.2, 0.1)
A_4	(0.6, 0.7, 0.7), (0.2, 0.2, 0.1), (0.2, 0.1, 0.2)	(0.5, 0.8), (0.3, 0.1), (0.1, 0)	(0.8, 0.8, 0.6), (0.1, 0.2, 0.2), (0.1, 0, 0.2)

Table 4 Similarity measures between A_s and A^*

Measure	Value	Order	Best choice
$W_1(A_1, A^*)$	1.2618	$A1 > A2 > A3 > A4$	A_1
$W_1(A_2, A^*)$	1.2568		
$W_1(A_3, A^*)$	1.2031		
$W_1(A_4, A^*)$	1.0789		

Table 4 shows that the characteristic A_1 is the best alternative in the RSVNS environment.

5 Conclusion

This examination introduced the similarity measure based on RSNS, afterward introduced technique, which is increasingly reasonable for the issues that have different properties alongside the attribute and the sub-attribute weights.

Through the measure value, we can rank other options and pick the greatest one. At that point, descriptive model on the decision creating issue of a development project was given so as to show the possibility and adequacy of the defined technique. Clearly, this investigation broadens present techniques and gives another route to RSNS issues. For the upcoming examination, the introduced strategy will be stretched out to the measure for collective choice making.

References

1. Zadeh LA (1965) Fuzzy sets. Inf Control 8:338–353
2. Atanassov KT (1986) Intuitionistic fuzzy sets. Fuzzy Sets Syst 20(1):87–96
3. Smarandache F (1999) A unifying field in logics: neutrosophic logic. Multiple Valued Logic 8(3):489–503
4. Ye J (2013) Multicriteria decision-making method using the correlation coefficient under single-valued neutrosophic environment. Int J Gen Syst 42(4):386–394
5. Wang J, Li X (2015) Todim method with multi-valued neutrosophic sets. Control Decis 30(6):1139–1142
6. Broumi S, Deli I (2014) Correlation measure for neutrosophic refined sets and its application in medical diagnosis. Palestine J Math 3(1):11–19
7. Xu DS, Wei C, Wei GW (2017) TODIM method for single-valued neutrosophic multiple attribute decision making. Information 8:125
8. Broumi S, Smarandache F (2005) New distance and similarity measures of interval neutrosophic sets. In: International conference on information fusion, pp 1–7
9. Fan CX, Ye J (2017) The cosine measure of refined-single valued neutrosophic sets and refined-interval neutrosophic sets for multiple attribute decisionmaking. J Intell Fuzzy Syst 33(4):2281–2289
10. Song D (2017) Fault diagnosis of steam turbine based on single-valued neutrosophic rough set. Colliery Mech Electr Technol 2(1):36–38
11. Zavadskas EK, Bauˇsys R, Lazauskas M (2015) Sustainable assessment of alternative sites for the construction of a waste incineration plant by applying WASPAS method with single-valued neutrosophic set. Sustainability 7(12):15923–15936
12. Smarandache F (2013) n-Valued refined neutrosophic logic and its applications in physics. Prog Phys 4:143–146
13. Wang H, Smarandache F, Zhang Y, Sunderraman R (2010) Single valued neutrosophic sets. Rev Air Force Acad 10:410–413
14. Zhang H, Wang J, Chen X (2016) An outranking approach for multicriteria decision-making problems with interval-valued neutrosophic sets. Springer Verlag

15. Chen JQ, Ye J, Du SG (2017) Vector similarity measures between refined simplified neutrosophic sets and their multiple attribute decision-making method. Symmetry 9(8):153
16. Peng J, Wang J, Zhang H, Chen X (2014) An outranking approach for multi-criteria decision-making problems with simplified neutrosophic sets. Appl Soft Comput 25(c):336–346
17. Peng JJ, Wang JQ, Wang J, Zhang HY, Chen XH (2016) Simplified neutrosophic sets and their applications in multi-criteria group decision-making problems. Int J Syst Sci 47(10):2342–2358
18. Ye J (2016) The generalized dice measures for multiple attribute decision making under simplified neutrosophic environments. J Intell Fuzzy Syst 31:663–671
19. Ye J (2014) A multicriteria decision-making method using aggregation operators for simplified neutrosophic sets. J Intell Fuzzy Syst 26(5):2459–2466
20. Ye J (2014) Vector similarity measures of simplified neutrosophic sets and their application in multicriteria decision making. Int J Fuzzy Syst 16(2):204–211
21. Wang L, Zheng X, Zhang L, Yue Q (2016) Notes on distance and similarity measures of dual hesitant fuzzy sets. IAENG Int J Appl Math 46(4):488–494
22. Liu PD, Wang Y (2014) Multiple attribute decision-making method based on single-valued neutrosophic normalized weighted Bonferroni mean. Neural Comput Appl 25(7–8):2001–2010
23. Tan R, Zhang W, Chen L (2017) Study on emergency group decision making method based on vikor with single valued neutrosophic sets. J Saf Sci Technol 13(2):79–84
24. Broumi S, Deli I, Smarandache F (2015) N-Valued interval neutrosophic sets and their application in medical diagnosis. Crit Rev 45–68

Evaluation of Electromagnetic Fields between HV Cables of Electric Vehicle

Mahipal Bukya and Rajesh Kumar

Abstract In recent years, the electric vehicle (EV) has significantly changed the automobile industry globally. EVs are the prompt solution to reduce pollution, and they contribute to balancing energy demand in the transport sector. The level of voltage introduced in present EVs is far higher than the level that people can endure. With this high voltage, safety is one of the greatest challenges in high-voltage vehicles. Insulation plays a very major role in the electrical safety of the battery, high-voltage cable, motors, and other electrical components associated with different forces in EVs. In an electric vehicle, the insulation of the HV cable is an indicator of EV's safety performance. As part of the preliminary work on the safety of EV components, the evaluation of electromagnetic forces is very important. This paper used the comsol multiphysics software to evaluate the electromagnetic fields between the high-voltage cables in EV.

1 Introduction

In the world, conventional vehicles are dominant in the transportation sector. The energy needed for the transportation sector will grow strongly in the coming decades. In India, the energy consumed by the transportation sector is reported at around 18%. This demand is an estimated 94 million tonnes of oil equivalent energy (MTOE). If India continues on its current energy consumption trajectory, it will require approximately 200 MTOE of energy supply annually by 2030 to meet the demand of this transport sector. Present energy demand for the transportation sector is fulfilled by petroleum and other liquid fuels. Crude oil prices are increasing drastically, and the use of crude oil in the transportation sector also produces around 142 million tonnes

M. Bukya (✉)
Department of Electrical Engineering, Manipal University Jaipur, Jaipur, India
e-mail: mahipalbhukya@gmail.com

R. Kumar
Department of Electrical Engineering, MNIT Jaipur, Jaipur, India
e-mail: rkumar.ee@mnit.ac.in

© The Author(s), under exclusive license to Springer Nature Singapore Pte Ltd. 2022

A. Tripathi et al. (eds.), *Intelligent Computing Techniques for Smart Energy Systems*,
Lecture Notes in Electrical Engineering 862,
https://doi.org/10.1007/978-981-19-0252-9_30

of CO_2 emissions yearly, out of which the contribution of the road vehicle segment alone is around 123 million [1, 2]. Environmental and energy concerns create a strong demand for a transition from conventional vehicles to electric vehicles.

The change from conventional vehicles to electric vehicles faces new challenges. In EVs, the level of voltage introduced is far higher than the level that people can endure. With this high voltage, safety is one of the greatest challenges in high-voltage vehicles. Insulation plays a very important role in the electrical safety of the battery, HV cable, motors, and other electrical components associated with different forces in EVs. In an electric vehicle, the insulation of the high-voltage cable is an indicator of the electric vehicle's safety performance. The insulation depends on the voltage, temperature, mechanical stress, moisture, etc. [2, 3]. In the automotive industry, high voltage refers to voltages above 60V. Thus, the battery voltages in the range of DC 120 V to DC 1000 V are far away from protective extra-low voltage. Based on the voltage level, the EVs are classified as:

Low-Voltage Vehicle:

- <60 V (e.g. light electric vehicles like micro cars, electric auto rickshaw, electric scooters).

High-Voltage Electric Vehicle:

- 60 V to 600 V (e.g. electric cars).
- 600 V to 1 000 V (e.g. electric cars, sports car and some heavy duty vehicles).
- >1000 V (e.g. heavy duty electric vehicles, electric buses, and electric trucks).

These high voltage and current levels are sufficient to cause an electrical hazard in high-voltage electric vehicles. For this reason, research on the electrical insulation of electric vehicles is very important. Among these components, the function of the HV cable is to ensure the safer transmission of electrical energy without harming any failure of cable insulation. A simple EV cable wire is shown in Fig. 1. As features increase in EVs, the complexity of the electrical circuits of the EVs might also increase, so the evaluation of different fields is considerable to ensure high-voltage safety in electric vehicles. As part of the preliminary work on the safety of EV components, the evaluation of electromagnetic forces is very important. This paper used the comsol multiphysics software to evaluate the electromagnetic fields between the high-voltage cables in EV [3–6].

2 Problem Statement

The overall EV electrical system temperature rises as a result of high voltage and currents in EV electrical circuits and overload in EV, which may cause insulation breakdown in the EV electrical system [7, 8]. The dielectric and copper losses within a cable will create heat. These losses (and heat produced) are dependent on the amount of current flowing in the high-voltage cable. The operating temperature of any

Fig. 1 High-voltage EV cable[7]

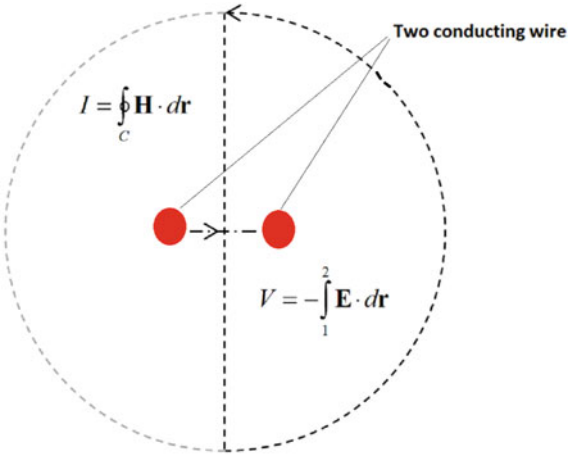

Fig. 2 Two conducting wire

electrical components is an important parameter in determining the peak allowable current. The real temperature of the cable depends on the material and wire exposed to direct heat produced by the battery and other electric components in an EV will be subject to more thermal loads and extra heating. The life of the insulation of the cable also depends on the operating temperature. Based on the Arrhenius equation of chemical reaction time vs. temperature, it says that for every 10 °C rise in temperature, the life of the insulation is cut in half. Inversely, a 10 °C decrease in temperature will double the life of the insulation. This extra heating needs to be considered in the evaluation of the electromagnetic fields (Fig. 2).

When selecting an EV cable, the consideration of fault conditions and the performance of the cable are also important. The analysis will be conducted to ensure that any cable can survive the impact of mechanical or electrical defects. Other factors should be considered when designing the cable in addition to the direct heating effect of fault currents.

Large amount of electromechanical stress and faults induces the breakdowns in the cable. The temperature and impact of different forces, like electromagnetic and mechanical, affect EV cable insulation. By considering all the factors, we evaluated the electromagnetic fields between the high-voltage cables of EVs and studied the importance of the heat conduction equation at the design level of the wire.

The electrical resistivity increases with increasing temperature. The resistivity of cable insulation (in common with all organic insulation) decreases with increasing temperature . Alternatively stated, the electrical conductivity increases with temperature:

The conductivity (σ) = ($1/\rho$)

3 Design Methodology

The electric field distribution is governed by the permittivity of the insulation materials, the geometry of the cable, and the voltage applied to the AC cable. The electric field distribution at DC depends on conductivity cable geometry, loading, and applied voltage. The high-voltage cable is necessary for components like motors, batteries, charging connectors, and HVAC components. The main requirement for a vehicle's HV system is the transmission of electrical energy without causing any insulation failure in EVs.

Considering the more general case of a cable, we used the below equation to compute the electric field, magnetic field, and temperature distribution in the cable. The temperature gradient $\nabla \cdot T$ in thermally influenced conductor leads to a flux of thermal energy that is given by the below equation [9, 10].

$$q = -K\nabla T \tag{1}$$

where q-local heat flux density in $\mathrm{w/m^2}$ and k-thermal conductivity in $\mathrm{w/m \cdot k}$. And also, the divergence criteria states that heat flux should be conserved $\nabla \cdot q = 0$. For a given volume, if the average divergence of q is not zero, it means the sum of all heat entering or leaving that volume is not zero; in that case, there is a heat source or sink in a given volume.

$$\nabla.(-K\nabla T) = Q \tag{2}$$

where K is the thermal coductivity ($\mathrm{w/m \cdot K}$), T is Temperature(K), and Q is heat source $\mathrm{w/m^3}$)

Considered the conducting wires in a dielectric medium with the electromagnetic fields around cable and demonstrated the evaluation Â of the fields between parallel conductors.

$$V = V2 - V1 = -\int_{r_1}^{r_2} E \cdot \mathrm{d}r \tag{3}$$

$$I = \int_{c} H \cdot \mathrm{d}r \tag{4}$$

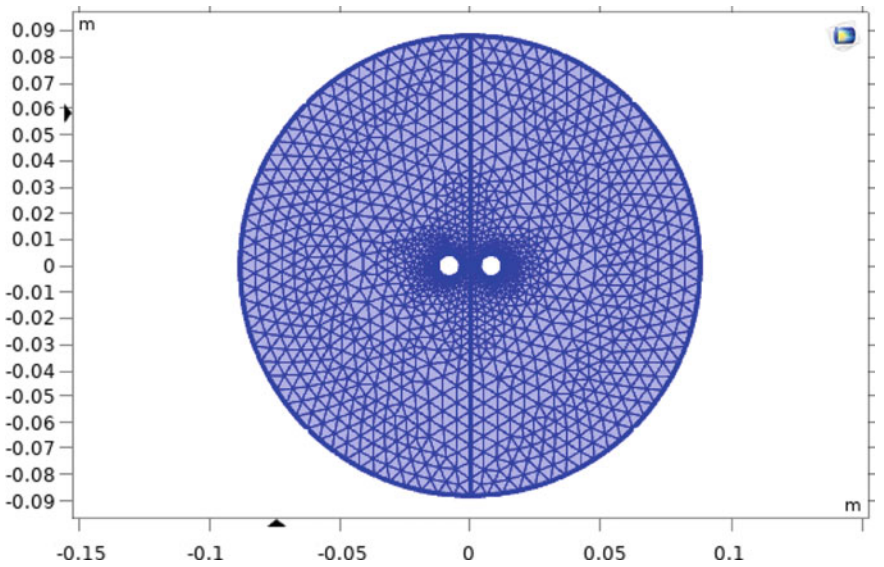

Fig. 3 Finite element meshes—Finer

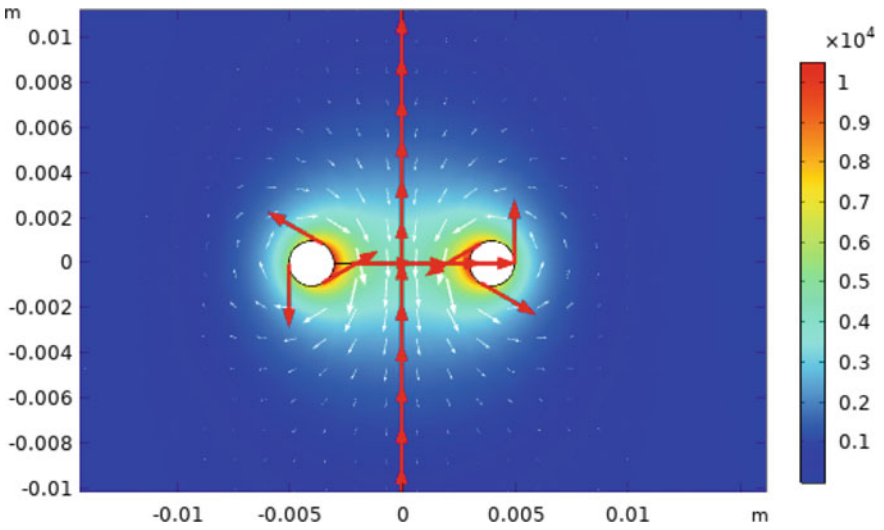

Fig. 4 Electric field and magnetic field distribution between two parallel wire

4 Simulation Results

The geometry is formulated in the comsol software and suitable material properties are selected, and we simulate the results here with respect to radial distance and in between the cables. Figure 3 shows the finite element meshes for the model geometry of the conducting wire. From Fig. 4, which shows the electromagnetic field variation around the cable and with respect to other conductors under no load and load, we conclude the electrical field is more on the surface of the conductor.

5 Conclusion

In this paper studied a suitable geometry of the cables in comsol multi-physics software and selected material properties for the evaluation of the electromagnetic field distribution of EV cables. Due to the heat produced by the battery and other electrical circuit components in the EV, the overall heat of the EV's electrical system increases, and it will affect the insulation of the cables. The permitivity and conductivity (σ) of cable insulation depend on temperature, geometry, and applied voltage. The electromagnetic filed distribution of high-voltage EV cable was evaluated using the comsol multi-physics module and studied the temperature distribution. The scope of this work can be expanded in future to include a few other parameters such as mechanical stress and vibration in the vehicle cable, as well as a precise evaluation of the comparable field and temperature distribution.

References

1. Pareek S, Sujil A, Ratra S, Kumar R (2020) Electric vehicle charging station challenges and opportunities: a future perspective. In 2020 International conference on emerging trends in communication, control and computing (ICONC3), Lakshmangarh, India, 2020, pp 1-6. https://doi.org/10.1109/ICONC345789.2020.9117473
2. https://beeindia.gov.in/content/e-mobility
3. Bukya M, Kumar R (2020) Safety consideration and design of high voltage cable for electric vehicle. In: 2020 International conference on power electronics & IoT applications in renewable energy and its control (PARC), Mathura, India, 2020, pp 485–490. https://doi.org/10.1109/PARC49193.2020.236661
4. Bukya M, Kumar R, Gupta RK (2020) A study on safety issues and analytical evaluation of stresses for HVDC cable in electrical vehicle. In AIP conference proceedings, vol 2294, 040001. https://doi.org/10.1063/5.0031351
5. Kjosevski S, Kostikj A, Kochov A (2017) Risks and safety issues related to use of electric and hybrid vehicles. V: G. Popov (ur.): XIV International congress machine, technolgies, materials. Borovets, Bulgaria, 2017, str. 169-172. https://doi.org/10.1109/ISGT-Asia.2019.8881809
6. Fischer HM (2013) Voltage classes for electric mobility. Published by: ZVEI-German Electrical and Electronic Manufacturers' Association Centre of Excellence Electric Mobility, Dec 2013. www.zvei.org

7. Potdevin H (2009) Insulation monitoring in high voltage systems for hybrid and electric vehicles. ATZ Elektron Worldw 4:28–31. https://doi.org/10.1007/BF03242246
8. Lian Y, Zeng D, Ye S et al (2018) High-voltage safety improvement design for electric vehicle in rear impact. Automot Innov 1:211–225. https://doi.org/10.1007/s42154-018-0030-z
9. https://www.coroplast-group.com/de/wireandcablescompleteproduct
10. https://www.comsol.co.in/model/electromagnetic-forces-on-parallel-current-carrying-wires-131

A Review on Biosynthesis of Nanoparticles and Their Applications

Rukshar and Nitu Bhatnagar

Abstract Synthesis of nanoparticles (NPs) by conventional techniques produces large amount of harmful and toxic byproducts. Thus, to resolve this problem, greener ways to develop metallic nanoparticles are needed which is eco-friendly, clean, and less toxic as compared to the conventional methods. Gold, silver, alloy, and magnetic nanoparticles are some basic type of NPs which can be produce by these methods. Plant-mediated biosynthesis of NPs is a new emerging green nanoparticle-based technology which have application in various field like water treatment, agriculture, industries, and biomedical field. Therefore, this review article emphasizes on synthesis of nanoparticles from naturally available resources and their application in various fields.

Keywords Biosynthesis · Nanoparticle · Wastewater treatment

1 Introduction

Nanotechnology is new emerging technology which has applications in agriculture field, wastewater treatment, biomedical field, industries, etc. Synthesis of nanoparticle done by chemical methods includes reduction in solution, chemical reactions in reverse micelles in the presence of light, while physical methods involve processes like thermal decay, radiation-based synthesis, and microwave-mediated synthesis [1]. Synthesis of nanoparticles from eco-friendly and non-toxic matters such as plant extract and microorganism makes it to utilize in different areas [2].

Biological methods with the capacity to control the size and shape of NPs have found exciting roles in various fields. In order to generate cost-effective and environment-friendly method, many researchers have synthesized various metallic

Rukshar
Department of Chemistry, Kanoria PG Mahila Mahavidyalaya Jaipur, Jaipur, Rajasthan, India

Rukshar · N. Bhatnagar (✉)
Department of Chemistry, Manipal University Jaipur, Jaipur, Rajasthan, India
e-mail: nitu.bhatnagar@jaipur.manipal.edu

© The Author(s), under exclusive license to Springer Nature Singapore Pte Ltd. 2022

A. Tripathi et al. (eds.), *Intelligent Computing Techniques for Smart Energy Systems*,
Lecture Notes in Electrical Engineering 862,
https://doi.org/10.1007/978-981-19-0252-9_31

NPs from biologically available materials [3]. In biosynthesis of metallic NPs, biomaterial works as a reductant which reduces metal ions in plant extract and extracellularly or intracellularly in microbes. One of the advantages of nanoparticle synthesis by biological method over physical process and chemical process that it can catalyze reaction more effectively at normal pressure and temperature [4]. Reduction of metal ions occurs by the components of biomolecules, and the reaction is generally activated by various groups like phenolic group, amide group, carbonyl group, proteins, amino acids, pigments, terpenoids, flavanoids, and other constituents present in the biomass or plant extract [5]. Various microorganisms like viruses, yeasts, bacteria, micro- and macro-algae, and plant extracts are the main biomaterials for the synthesis of various metallic NPs [6].

2 Biosynthesis of Nanoparticle

2.1 Microorganism-Based Nanoparticle Synthesis

Various microorganisms such as microalgae, yeast, macro-algae, bacteria, and fungi have biological materials which are capable to synthesize nanoparticle. The basic mechanism involves the metal ions reduction step by which metal ion is converted into nanoparticles [7]. Various microbes are able to synthesize different kind of nanoparticles like silver NPs, magnetite NPs, gold NPs, cadmium sulfide NPs, etc. out of which Ag NPs and Au NPs have received considerable attention of researchers [8] (Fig. 1).

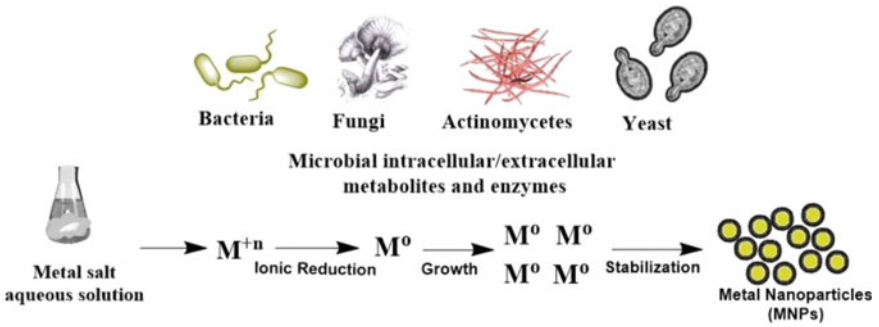

Fig. 1 Mechanism of synthesis of nanoparticle from microorganism [8] Some of the microorganisms-based biosynthesized nanoparticles are listed in Table 1

Table 1 Biosynthesized nanoparticles from microorganisms

S. No	Type of microorganism	Species	Nanoparticles and size of NPs (nm)	References
1	Bacteria	*Brevibacterium casei*	Ag; 50	[9]
2	Fungi	*Aspergillus clavatus*	Ag; 10–25	[9]
3	Bacteria	*Proteus mirabilis*	Ag; 10–20	[10]
4	Fungi	*Verticillium sp.*	Ag; 25	[10]
5	Bacteria	*Pseudomonas stutzeri*	Cu; 50–150	[11]
6	Fungi	*oxysporum*	CdS; 5–20	[12]
7	Fungi	*Colletotrichum sp.*	Au; 20–40	[12]
8	Fungi	*Fusarium oxysporum*	Zr; 3–11	[12]
9	Yeast	*Candida glabrata*	CdS; 2	[12]
10	Yeast	*Schizosaccharomyces pombe*	CdS; 1–1.5	[12]
11	Fungi	*MKY-3*	Ag; 2–5	[12]
12	Algae	*Plectonema boryanum*	Ag; 1–200 Au; 25–100	[13]
13	Fungi	*Yarrowiali polytica*	Au; 15	[13]
14	Fungi	*Phaenerochaete chrysosporium*	Ag; 50–200	[13]
15	Bacteria	*Ureibacillus thermosphaericus*	Au; 50–70	[13]
16	Fungi	*Neurospora crassa*	Au; 32	[13]
17	Algae	*Shewanella algae*	Au; 10–20	[13]
18	Bacteria	*Nocardia farcinica*	Au; 15–20	[14]

2.2 Plant-Based Nanoparticle Synthesis

Plant-based synthesis of metallic nanoparticles have also attracted attention of many researchers because of their simple synthesis methods and fast rate of synthesis reaction. Salt of metal ions firstly reduced in its atomic form by reducing agents which are present in the plant extract [15]. Then modified metal ion is converted into small clusters after the nucleation process, and after that, these small clusters are converted into particles. Various biomolecules such as terpenoids, chlorophyll pigment, and proteins work as a reducing agent in the synthesis of silver NPs, gold NPs, and gold NPs, respectively [16] (Fig. 2).

Some of the plant-based biosynthesized nanoparticles are listed in Table 2.

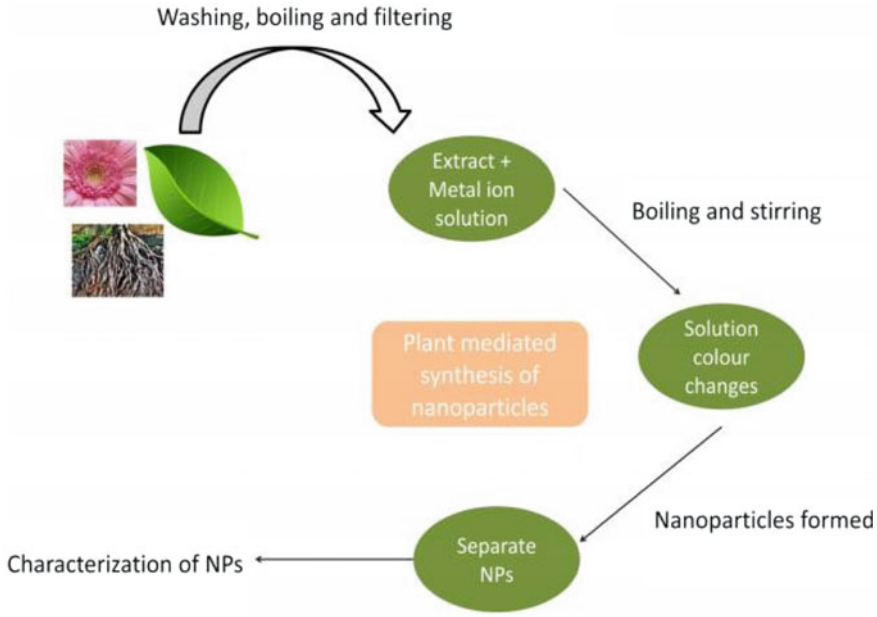

Fig. 2 Mechanism of synthesis of nanoparticles from plant extracts [16]

Table 2 Biosynthesized nanoparticles from plant extract

S. No	Plant name	Plant parts	Nanoparticles and size (nm)	References
1	Argemone maxicana	Leaves	Ag; 30	[17]
2	Emblica officinalis	Fruit	Ag and Au; 10–20 and 15–25	[18]
3	Nyctanthes arbortristis	Flower	Au; 19.8	[19]
4	Carica papaya	Fruit	Ag; 15	[20]
5	Mangifera indica	Leaves	Ag; 20	[21]
6	Pinus resinosa	Bark	Pd and Pt; 16–20 and 6–8	[22]
7	Jatropha curcas	Seed	Ag; 15–50	[23]
8	Doipyros kaki	Leaves	Pt; 2–12	[24]
9	Glycine max	Leaves	Pd; 15	[25]
10	Camellia sinensis	Leaves	Au; 40	[26]
11	Cuminum cyminum	Seed	Au; 1–10	[27]
12	Gardenia jasminoides	Leaves	Pd; 3–5	[28]

3 Application of Biosynthesized NPs

Biosynthesized NPs have applications in various fields such as biomedical field, wastewater treatment, and agriculture field and in environmental sensor technology due to these unique properties.

3.1 In Biomedical Field

Metallic nanoparticles exhibit antimicrobial nature which makes them a better candidate for application in the field of biomedical. Various kind of metallic nanoparticles such as Ti, Cu, Mg, and specially Ag and Au have antifungal, antiviral, and antimicrobial capabilities [29]. Silver nanoparticles have been used in wound dressings, implants, and bone cements [30]. Gold nanoparticles have been used in optical related treatment and have anticancer nature [31]. Magnetic nanoparticles show potential in drug delivery and hyperthermia. These metallic nanoparticles actively work as disinfectants and also find wide applications in food processing, etc. [32]. Green synthesized nanoparticles are also having important role in medicine in the diagnostics and sensing fields [33]. Biosynthesized metallic NPs also show optical properties which include low- or high-refractive index, transparency, photonic crystals, and photoluminescence nature [34].

3.2 In Environment Remediation

Biosynthesized metallic nanoparticles have vast application in various environmental treatment processes. Metallic nanoparticles are used in metal biosorption process, bioremediation process and biorecovery of metals. The biomass of microbes, along with some biopolymers and biological waste materials, has the nature to tie up and recover precious metals [35, 36]. Biosorption method is low-cost method in comparison of chemical method to recover the precious soluble metals in aqueous medium.

Due to their very specific large surface area, metallic nanoparticles are extensively used for catalysis process and especially in heterogeneous catalysis. Generally biosynthesized Pd NPs catalyst is used for the remediation process [37]. Pd NPs-based catalysts are used for dechlorination of chlorophenol (CP), dechlorination of polychlorinated biphenyl's (PCB), dechlorination of perchlorate, etc. These NPs are able to reduce various organic compounds effectively. Fe NPs and Au NPs effectively remove dyes such as methylene blue and methyl orange from waste water. Ag NPs stop biofouling of polyethersulfone membranes which are used for the removal of organophosphate pesticide [38].

3.3 In Industries

Biosynthesized NPs such as Pd, Au, and Pt are used as catalysts in different kind of organic synthesis reactions. They are widely used to catalyze cross coupling reactions, i.e., formation of C–C bond. They are also used as effective catalysts in the organic dyes synthesis. Various organisms have the capability to reduce and recover metal ions from metal salt solution [39]. Many biosynthesized NPs have the ability to elevate the performance of fuel cells. Biosynthesized NPs are also used in H_2 fuel production which catalyze the chemical oxidation process of the fuel and enhance the power recovery. Biosynthesized Au NPs are used in direct electrochemical sensing of Hb [37]. Biosynthesized cadmium sulfide NPs are used to produce hetero-junction with asymmetric electronic transfer [40].

They have also been found to exhibit optical property, due to which they found their applications in chemical sensing technology. Gold and Silver NPs are used for the detection of Fe^{+3} and Cu^{+4} in water [41].

4 Conclusion

The incredible properties of the nanoparticles have made them better candidate for application in many areas such as health care, agriculture, and environment remediation energy. Metallic NPs with different shapes and synthesized by chemical process and physical process involve multiple steps and cause environmental pollution because of the use of toxic chemical compounds. A huge number of biological materials are available for NPs biosynthesis; it can be predicted that synthesis of NPs from biological materials will be used at a large scale in future. Many researchers are trying to develop simple and eco-friendly methods for the synthesis of NPs. Therefore, the use of eco-friendly matters like plant extract, microorganisms like bacteria, virus, fungi, yeast, and enzymes for the production of metallic NPs offers various benefits of environment friendliness and compatibility for applications of NPs in various fields as they involve use of non-toxic chemicals for the synthesis process.

References

1. Mittal AK, Chisti Y, Banerjee UC (2013) Synthesis of metallic nanoparticles using plant extracts. Biotechnol Adv 31(2):346–356. https://doi.org/10.1016/j.biotechadv.2013.01.003
2. Anu K, Singaravelu G, Murugan K, Benelli G (2017) Green-synthesis of selenium nanoparticles using garlic cloves (Allium sativum): biophysical characterization and cytotoxicity on vero cells. J Clust Sci 28(1):551–563. https://doi.org/10.1007/s10876-016-1123-7
3. Ariga K, Nishikawa M, Mori T, Takeya J, Shrestha LK, Hill JP (2019) Self-assembly as a key player for materials nanoarchitectonics. Sci Technol Adv Mater 20:51–95. https://doi.org/10.1080/14686996.2018.1553108

4. Singh A, Dubey S, Dubey HK (2019) Nanotechnology: the future engineering. Int J Adv Innov Res 6:230–233
5. Slavin YN, Asnis J, Häfeli UO, Bach H (2017) Metal nanoparticles: understanding the mechanisms behind antibacterial activity. J Nanobiotechnol 15:65
6. Khan I, Saeed K, Khan I (2017) Nanoparticles: properties, applications and toxicities. Arab J Chem
7. FutureMarketInsights Global Market for Metal and Metal Oxide Nanoparticles to Surge at More Than 10% CAGR. Available Online: http://markets.businessinsider.com/news/stocks/Global-Market-forMetal-MetalOxide-Nanoparticles-to-Surge-at-More-Than-10CAGR-1001862836. Accessed on 21 Nov 2018
8. Ovais M, Khalil A, Ayaz M, Ahmad I, Nethi S, Mukherjee S (2018) Biosynthesis of metal nanoparticles via microbial enzymes: a mechanistic approach. Int J Mol Sci 19(12):4100. https://doi.org/10.3390/ijms19124100
9. Venkataraman D, Kalimuthu K, Sureshbabu RKP, Sangiliyandi G (2011) Metal nanoparticles in microbiology. In: Rai M, Duran N, vol 11, Springer, pp 17–35
10. Sukumaran P, Eldho KP (2012) Silver nanoparticles: mechanism of antimicrobial action, synthesis, medical applications, and toxicity effects. Int Nano Lett 2(32):2–10
11. Ratnika V, Bhadauria S, Gaur MS, Renu P (2011) Copper Nanoparticles Synthesis from electroplating industry effluent. Nano Biomed. Eng. 3(2):115–119
12. Abhilash, Revati K, Pandey BD (2011) Microbial synthesis of iron-based nanomaterial's—a review. Bull Mater Sci 34(2):191–198
13. Xiangqian L, Huizhong X, Chen Z, Chen G (2011) Biosynthesis of nanoparticles by microorganisms and their applications. J Nanomater 2011:1–16
14. Oza G, Pandey S, Gupta A, Kesarkar R, Sharon M (2012) Biosynthetic reduction of gold ions to gold nanoparticles by Nocardia farcinica. J Microbiol Biotechnol Res 2(4):511–515
15. Gopinath V, Priyadarshini S, Loke MF, Arunkumar J, Marsili E, Mubarakali D, Velusamy P, Vadivelu J (2017) Biogenic synthesis, characterization of antibacterial silver nanoparticles and its cell cytotoxicity. Arab J Chem 10:1107–1117. https://doi.org/10.1016/j.arabjc.2015.11.011
16. Shyam A, Smitha CS, George B, Sreelekha E (2020) Plant mediated synthesis of AgNPs and its applications: an overview. Inorg Nano-Metal Chem. https://doi.org/10.1080/24701556.2020.1852254
17. Singh A, Jain D, Upadhyay MK, Khandelwal N, Verma HN (2010) Green synthesis of silver nanoparticles using Argemone Mexicana leaf extract and evaluation of their antimicrobial activity. Dig J Nanomater Biostruct 5(2):483–489
18. Ankamwar B, Damle C, Ahmad A, Satry M (2005) Biosynthesis of gold and silver nanoparticles using Emblica officinalis fruit extract, their phase transfer and transmetallation in an organic solution. J Nanosci Nanotechnol B 5(10):1665–1671
19. Das RK, Gogoi N, Bora U (2011) Green synthesis of gold nanoparticles using Nyctanthes arbortristis flower extract. Bioprocess Biosyst Eng 34(5):615–619
20. Jain D, Daima HK, Kachhwala S, Kothari SL (2009) Synthesis of plantmediated silver nanoparticles using Papaya fruit extract and evaluation of their antimicrobial activities. Dig J Nanomater Biostruct 4(3):557–563
21. Phillip D (2011) Mangifera indica leaf-assisted biosynthesis of welldispersed silver nanoparticles. Spectrochim Acta Part A 78(1):327–331
22. Shenton W, Douglas T, Young M, Stubbs G, Mann S (1999) Inorganic—organic nanotube composites from template mineralization of tobacco mosaic virus. Adv Mater 11(3):253–256
23. Bar H, Bhui DK, Sahoo GP, Sarkar P, Pyne S, Misra A (2009) Green synthesis of silver nanoparticles using seed extract of Jatropha curcas. Colloids Surf A 348(1):212−216
24. Song JY, Kwon EY, Kim BS (2010) Biological synthesis of platinum nanoparticles using Diopyros kaki leaf extract. Bioprocess Biosyst Eng 33(1):159–164
25. Petla RK, Vivekanandhan S, Misra M, Mohanty AK, Satyanarayana N (2012) Soybean (Glycine max) leaf extract based green synthesis of palladium nanoparticles. J Biomater Nanobiotechnol 3(1):14–19

26. Sharma NC, Sahi SV, Nath S, Parsons JG, Gardea T, Pal T (2007) Synthesis of plant-mediated gold nanoparticles and catalytic role of biomatrix-embedded nanomaterials. Environ Sci Technol 41(14):5137–5142
27. Krishnamurthy S, Sathishkumar M, Lee SY, Bae MA, Yun YS (2011) Biosynthesis of Au nanoparticles using cumin seed powder extract. J Nanosci Nanotechnol 11(2):1811–1814
28. Jia L, Zhang Q, Li Q, Song H (2009) The biosynthesis of palladium nanoparticles by antioxidants in Gardenia Jasminoides Ellis: long life time nanocatalysts for p-nitrotoluene hydrogenation. Nanotechnology 20:385601
29. Alam H, Khatoon N, Raza M, Ghosh PC, Sardar M (2019) Synthesis and characterization of nano selenium using plant biomolecules and their potential applications. Bionanoscience 9(1):96–104. https://doi.org/10.1007/s12668-018-0569-5
30. Rajkumar R, Ezhumalai G, Gnanadesigan M (2020) A green approach for the synthesis of silver nanoparticles by Chlorella vulgaris and its application in photocatalytic dye degradation activity. Environ Technol Innov 101282. https://doi.org/10.1016/j.eti.2020.101282
31. Zhang Q, Li M, Luo B, Luo Y, Jiang H, Chen C, Wang S, Min D (2020) In situ growth gold nanoparticles in three-dimensional sugarcane membrane for flow catalytical and antibacterial application. J Hazard Mater 123445. https://doi.org/10.1016/j.jhazmat.2020.123445
32. Du L, Jiang H, Liu X, Wang E (2007) Biosynthesis of gold nanoparticles assisted by escherichia coli DH5 and its application on direct electrochemistry of hemoglobin. Electrochem Commun 9:1165–1170
33. Ju H, Zhang X, Wang J (2011) Nanobiosensing for clinical diagnosis. NanoBiosensing 535– 67. https://doi.org/10.1007/978-1-4419-9622-0_18
34. Kowshik M, Deshmukh N, Vogel W, Urban J, Kulkarni SK, Paknikar KM (2002) Microbial synthesis of semiconductor CdS nanoparticles, their characterization, and their use in the fabrication of an ideal diode. Biotechnol Bioeng 78:583–588
35. Chung KT, Cerniglia CE (1992) Mutagenicity of azo dyes: structure-activity relationships. Mutat Res 277:201–220. https://doi.org/10.1016/0165-1110(92)90044-a
36. Zhang Z, Shao C, Sun Y, Mu J, Zhang M, Zhang P, Guo Z, Liang P, Wang C, Liu Y (2012) Tubular nanocomposite catalysts based on size-controlled and highly dispersed silver nanoparticles assembled on electrospun silicananotubes for catalytic reduction of 4-nitrophenol. J Mater Chem 22:1387–1395. https://doi.org/10.1039/C1JM13421C
37. Vidhu VK, Philip D (2014) Catalytic degradation of organic dyes using biosynthesized silver nanoparticles. Micron 56:54–62. https://doi.org/10.1016/j.micron.2013.10.006
38. Yang M, Pan X, Zhang N, Xu Y (2013) A facile one-step way to anchor noble metal (Au, Ag, Pd) nanoparticles on a reduced graphene oxide mat with catalytic activity for selective reduction of nitroaromatic compounds. CrystEngComm 15:6819–6828. https://doi.org/10.1039/c3ce40694f
39. Kwon T, Woo HJ, Kim YH, Lee HJ, Park KH, Park S, Youn B (2012) Optimizing hemocompatibility of surfactant-coated silver nanoparticles in human erythrocytes. J Nanosci Nanotechnol 12:6168–6175. https://doi.org/10.1166/jnn.2012.6433
40. Simbine EO, Rodrigues LDC, Lapa-Guimaraes J, Kamimura ES, Corassin CH, Oliveira CAFD (2019) Application of silver nanoparticles in food packages: a review. Food Sci Technol 39:793–802. https://doi.org/10.1590/fst.36318
41. Bindhu MR, Umadevi M (2014) Silver and gold nanoparticles for sensor and antibacterial applications. Spectrochim Acta Part A Mol Biomol Spectrosc 128:37–45

Cost-Efficient Low-Profile MIMO Antenna for 5G Communications

Tapan Nahar and Sanyog Rawat

Abstract A wideband spatial diversity multiple input multiple output (MIMO) antenna is presented in this communication for 5G applications. Rectangular patch with rectangle-shaped slot and partial ground layer is used as individual antenna element, and two-elements MIMO configuration is designed which provides 27 GHz of bandwidth from 10.77 to 37.77 GHz which satisfies the bandwidth requirements of millimeter-wave ultra-high speed low latency communication of future 5G communications. Low mutual coupling is required over wide range of frequencies for effective wideband MIMO operation. Isolation layer is used in ground plane and on top layer to obtain wide frequency range of 25.297 GHz where isolation is greater than 15 dB. All the MIMO parameters are under acceptable limit over whole operating bandwidth which suggests the excellent performance of proposed antenna for wideband MIMO communications and improves the signal-to-noise ratio in multipath fading environment. Proposed antenna is simulated on CST Microwave studio.

Keywords Fifth generation (5G) · Mm-wave · MIMO antenna · Spatial diversity · Microstrip antenna · Ultra-high speed low latency communication

1 Introduction

5G is upcoming wireless technology which will provide ultra-high speed, low latency, and highly reliable communication which will be used in the applications such as wireless industrial automation, tele-surgery and tele-health services, ultra-high speed video broadcasting, machine-to-machine communication, driverless car, virtual reality, augmented reality, and unbelievable communication experience [1–7]. It will increase the capacity of networks. Millimeter (mm) wave spectrum will be used to support wide bandwidth requirements [2, 3]. Federal Communication Commission of United States has decided to allot 28, 37, and 39 GHz of license band for 5G communication [2–5]. To improve network capacity and suppress noise in multipath

T. Nahar · S. Rawat (✉)
Department of Electronics and Communication Engineering, Manipal University Jaipur, Jaipur, India
e-mail: sanyog.rawat@jaipur.manipal.edu

© The Author(s), under exclusive license to Springer Nature Singapore Pte Ltd. 2022

A. Tripathi et al. (eds.), *Intelligent Computing Techniques for Smart Energy Systems*, Lecture Notes in Electrical Engineering 862,
https://doi.org/10.1007/978-981-19-0252-9_32

environment, MIMO technology and antenna beamforming will be used [2–7]. In order to provide multiple simultaneous links in communication, MIMO technology will be utilized. MIMO antenna consists of multiple inputs multiple output antennas which should have minimum mutual coupling between antennas. Mutual coupling between antennas is due to surface waves and high amount of surface current generation from the port excitation. Large mutual coupling increases error rate and reduces channel capacity; to obtain wideband MIMO operations, wide isolation bandwidth is required which is very challenging [6, 8–21].

Various decoupling methods have been reported in literature to improve the isolation between adjacent elements. Neutralization lines can be used which consists of metallic slit or lumped elements. It passes electromagnetic waves between elements and reduces mutual coupling. Position of neutralization line is very important because it alters the impedance. Proper positioning of neutralization line may improve the bandwidth by matching the impedance [17, 18]. Advantages of using neutralization line are compact size, high efficiency, and wide bandwidth, but limitation is its complex analysis [22]. Decoupling network can be preferred to enhance isolation [23]. Decoupling network consists of discrete components or transmission lines which convert crossed admittance to the purely imaginary value. Dummy loads or coupled resonators may be used to decrease mutual coupling. Decoupling network affects the gain and increases complexity of antenna structure [18]. Electromagnetic band gap (EBG) structure also may be used to reduce the size and improve isolation. EBG consists of periodic arrangement of dielectric and metallic elements which produces band gap and block-specific frequencies [17, 18]. Major benefits of using EBG structure are wide range of impedance matching, size miniaturization, and high front-to-back ratio. Defected ground structure (DGS) and slot elements can also be used to reduce mutual coupling. Analysis of DGS is challenging, but it increases bandwidth, efficiency, and isolation. *S*-shaped periodic slots are etched from the ground between antennas in [19]. It resists electromagnetic waves and also induces the current between adjacent elements, and surface current is suppressed. Coupling can be controlled by adjusting alignments of these periodic slots. Isolation is improved by −40 dB using S-shaped periodic slots [19]. Similarly, square ring slots, *T*-shaped stub-based structure also effectively improve isolation [18]. Slot in ground layer provides wide impedance matching range. Metamaterials and complementary split ring resonators (CSRRs) can also be used. It increases the diversity gain and reduce size but increases the complexity in structure [17, 18]. CSRR consists of periodic metallic ring-shaped slots which provides filtering operation and improves the isolation. CSRR acts as inductor-capacitor tank circuit [8]. It stores energy at low frequencies and reduces current flow between antenna elements [19]. Capacitive-coupled loop is used in [15] to improve the isolation, but complexity is increased. Unsymmetrical ground plane is used in [6] to improve isolation. Proposed MIMO antenna provides isolation less than −40 dB in whole operating bandwidth.

In this communication, spatial diversity MIMO configuration of slotted rectangular patch antenna is designed on Computer Simulation Technology Microwave studio simulation software [24]. Wideband millimeter-wave antenna was presented in [1] which consists of rectangular ring-shaped patch antenna with defected ground

structure whose MIMO configuration is constructed and analyzed in this paper. Two-element MIMO configuration provides high mutual coupling and low isolation bandwidth. Various methods have been adopted to improve the isolation. Firstly, a slot is designed in the ground plane between two patches. It suppresses higher order modes and improves isolation and isolation frequency range, but it reduces impedance bandwidth. Metallic stub is introduced in ground plane between two antennas. It acts as parasitic-loaded resonating element and provides additional resonance at 31.9 GHz. It improves isolation frequency range as well as impedance bandwidth. Isolation layer (thin metallic layer) is used in both top and bottom layer to improve the isolation frequency range as well as impedance bandwidth. Isolation frequency range is improved from 4.373 GHz (of ANT1) to 25.297 GHz (of ANT5).

This paper consists of six major parts. 5G antenna's introduction and literature survey is discussed in Sect. 1. Section 2 presents evolution of proposed antenna design. Performance comparisons of simulated MIMO antennas are elaborated in Sect. 3. MIMO parameters of proposed antenna are discussed in another Sect. 4. Comparative analysis of various parameters of presented final design with various reported antennas by researchers is explained in Sect. 5. Section 6 contains the conclusion.

2 Evolution of Proposed Antenna Design

Wideband rectangular-slotted rectangular patch antenna has been designed and presented in our paper [1] for 5G applications. Antenna structure is shown in Fig. 1a which consists of a patch of $3.47 \times 4.23\ mm^2$ with rectangular slot of $1.47 \times 2.2\ mm^2$. Proposed antenna is designed on Roggers RT 5880 substrate which has relative permittivity, loss tangent, and thickness as 2.2, 0.0009 and 0.254 mm, respectively. Patch is fed by 50 Ω microstrip line with 0.78 mm width. Rectangular slot creates capacitive reactance which decreases the inductive part of impedance of feed line and improves impedance matching at broad range of frequencies [1]. For more bandwidth enhancement, partial ground plane of 3.218 mm length is used. Partial ground plane minimizes inductive effect of radiator by adding capacitive reactance [1]. In this way, broader impedance bandwidth of 94.02% is obtained at resonant frequency of 23.94 GHz. Benefits of this method are improvement of bandwidth without changing the size of antenna. Proposed antenna provides bidirectional radiation pattern which is very equivalent to figure of eight-type pattern of quarter wave monopole-type planar antenna. Reflection coefficient versus frequency plot and radiation plot are shown in Fig. 1b, c, respectively.

Spatial diversity multiple input multiple output (MIMO) antenna is designed by placing two antennas at distance of half wavelength. This configuration is termed as ANT1. Top side and bottom side view of proposed ANT1 is represented in Fig. 2a, b, respectively. For effective MIMO operation, isolation between adjacent elements should be high, and mutual coupling should be low [11–17]. To improve the isolation, various techniques have been applied and optimized. Firstly, a slot is eliminated

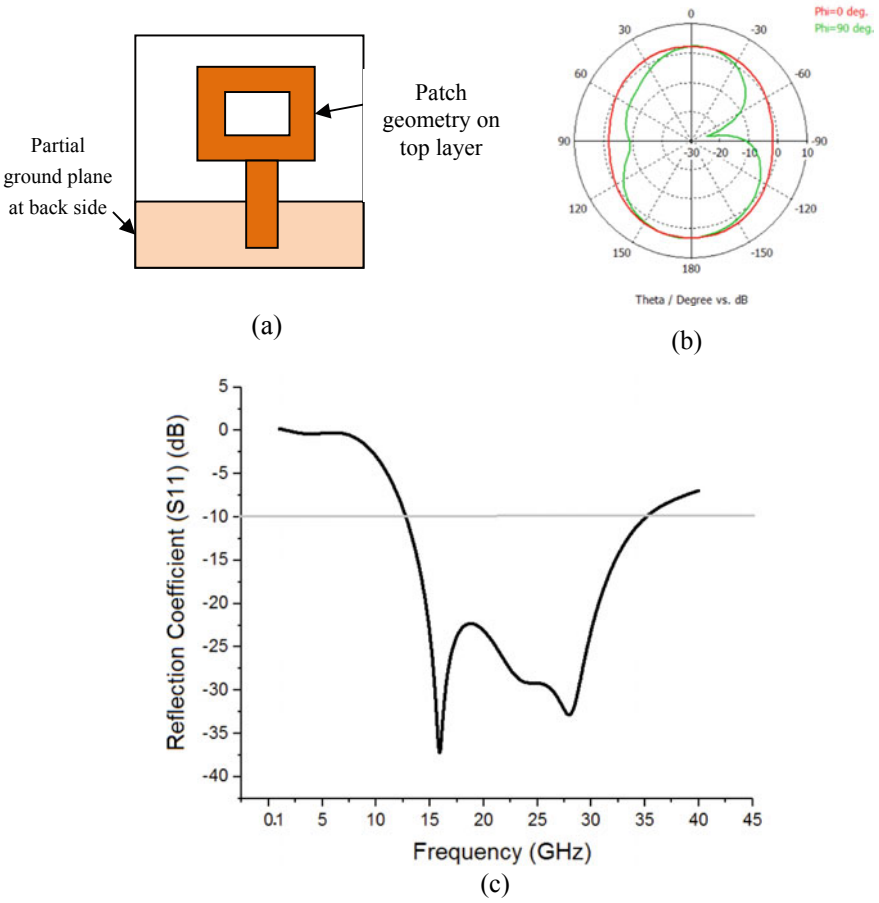

Fig. 1 **a** Structure of rectangular patch antenna with rectangle-shaped slot and partial ground plane, **b** radiation pattern, **c** reflection coefficient versus frequency plot [1]

from the ground at mid of common ground plane, and this configuration is termed as ANT2. Back view of ANT2 is shown in Fig. 2c. In next step, isolation layer (metallic element) is created in ground plane at the mid of antennas to reduce the mutual coupling. Gap between slot and isolation layer is optimized. Back view of this antenna termed ANT3 is presented in Fig. 2d. ANT4 consists of no gap between ground slot and isolation layer. Isolation layer is inserted between two patches on top layer also, and this configuration is termed as ANT5.

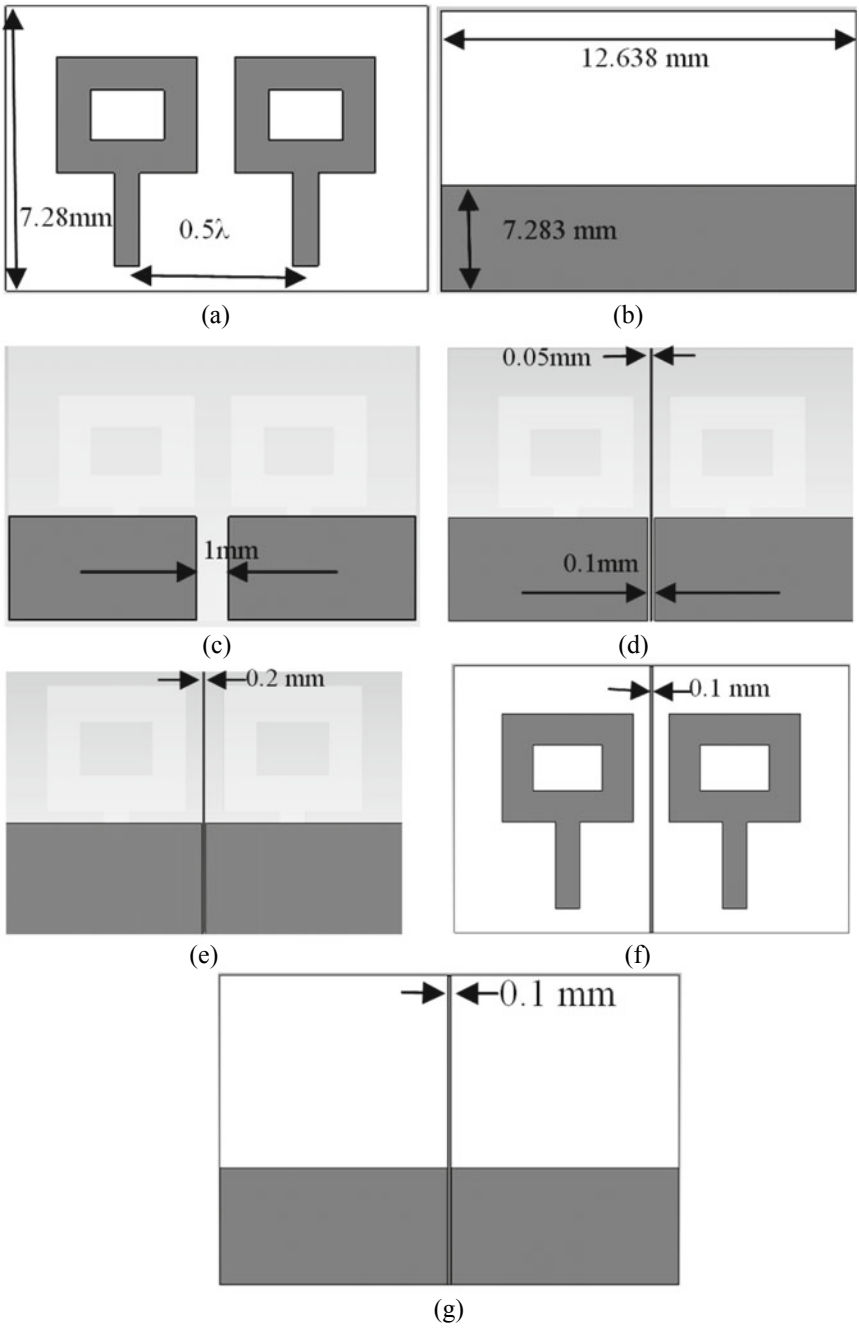

Fig. 2 Proposed antennas geometries, **a** front view of ANT1, **b** back view of ANT1, **c** back view of ANT2, **d** back view of ANT3, **e** back view of ANT4, **f** front view of ANT5, **g** back view of ANT5

3 Performance Comparisons of Proposed MIMO Antennas

3.1 Reflection Coefficient Versus Frequency Plot

Reflection coefficient (S_{11}) versus frequency plot provides information about the impedance matching performance, amount of reflected power, and bandwidth. It may be noted from Table 1 and Fig. 3a that bandwidth increases from ANT1 to ANT5. ANT5 provides maximum bandwidth of 27.004 GHz and has less than 10% reflected power from 10.773 to 37.77 GHz, but return loss is increased. Resonant frequency is shifted to higher values by cutting slots and inserting isolation layer. Consolidated reflection coefficient graph is shown in Fig. 3a. It may be noted from Fig. 3a that ANT1 is resonated from 11.06 to 38.4 GHz. When slot is introduced in the ground plane in ANT2, higher order modes are getting suppressed which results in slightly reduction in bandwidth, but isolation frequency range is increased. Neutralization slot acts as band-stop filter and reduces surface currents and mutual coupling. To improve further isolation frequency range, a metallic stub is used in ground in ANT3. It provides additional resonances at 32.5 GHz and increase the bandwidth as well as isolation range and acts as parasitic resonating elements. In ANT4, parasitic metallic stub is added between two patches. It acts as isolation layer and reduces the mutual coupling between adjacent elements. It improves isolation frequency range by around 6 GHz in comparison to ANT3, but it reduces bandwidth and increases the return loss. After optimizing dimension of isolation layer in patch and ground in ANT6, both bandwidth and isolation frequency range are increased, and gain is also increased. Multiple resonances have been obtained at 12, 30, and 37.5 GHz and overlapped beautifully from 10.773 GHz to 37.7 GHz within reflection coefficient $\leq$10 dB.

Table 1 Performance comparisons of proposed antennas

Performance parameter	ANT1	ANT2	ANT3	ANT4	ANT5
Bandwidth (S11 $\leq$ 10 dB)	11.068–34.844 (23.776 GHz)	11.581–31.637 (20.053 GHz)	12.632–34.014 (21.382 GHz)	13.983–32.997 (19.014 GHz)	10.773–37.77 (27.004 GHz)
S11(dB)	−28.191	−26.544	−27.051	−19.802	−21.815
Freq. Range (S21 $\leq$ 15 dB)	30.467–34.84 (4.373 GHz)	16.60–25.28 (8.67 GHz) 30.22–31.63 (1.411 GHz) Total (10.083 GHz)	15.28–24.96 (9.68 GHz) 30.71–34.01 (3.301 GHz) Total (12.986 GHz)	13.983–32.997 (19.014 GHz)	10.77–36.07 (25.297 GHz)
Gain (dB)	5.44	5	4.8	4.2	5.4
SLL (dB)	−7.4	−1.6	−9.5	–	−13.44

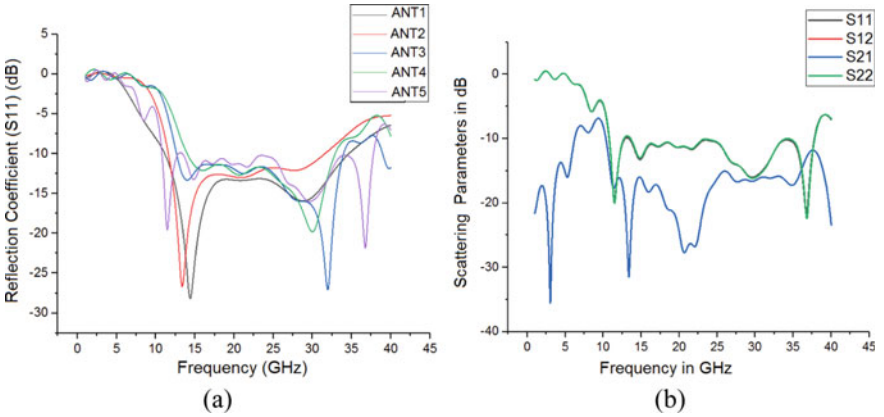

Fig. 3 **a** consolidated graph between reflection coefficient (S_{11}) and frequency, **b** scattering parameters versus frequency plot of ANT5

Scattering parameters of ANT 5 is presented in Fig. 3b. It may be seen that S_{11} and S_{22} parameters are exactly matched with each other, and similarly, S_{12} and S_{21} are also exactly same which indicates identical operations of two antennas in MIMO antenna. Figure 3b presents that for wide range of frequencies S_{11} is less than -10 dB, and S_{21} is less than -15 dB.

3.2 Mutual Coupling Versus Frequency Plot

S_{21}/S_{12} parameters represent the mutual coupling between antennas. S_{21} represents the power coupled to antenna 2 from antenna 1. S_{12} gives the mutual coupling from antenna 2 to antenna 1. For all the proposed antennas, S_{12} is much closer to S_{21} for the whole operating frequency range. For effective MIMO operations, mutual coupling should be low, or isolation should be high for operating bandwidth. Figure 4 represents the S_{21} versus frequency plot. Initially, ANT1 provides less than -15 dB mutual coupling for frequency range of 4.373 GHz (30.467–34.84 GHz). This range is improved up to 10.083 GHz (16.60–25.28 GHz and 30.22–31.63 GHz) by ANT2 by introducing the slot between common overlapping regions in the ground. Isolation range is further increased to 12.986 GHz by ANT3 when a thin metallic layer (isolation layer) is used in the ground plane. By optimizing the back-slot dimension in ANT4, isolation range is enhanced to 19.014 GHz. A thin metallic isolation layer is introduced between two patches in ANT5 to improve isolation between inter-elements. It may be clearly observed from Fig. 4 that ANT5 provides less than -15 dB of mutual coupling and less than 10% of reflected power from 10.77 to 36.07 GHz. Impedance bandwidth of 90.35% is obtained at 28 GHz for ANT5. ANT5 is very suitable for ultra-high speed MIMO operations.

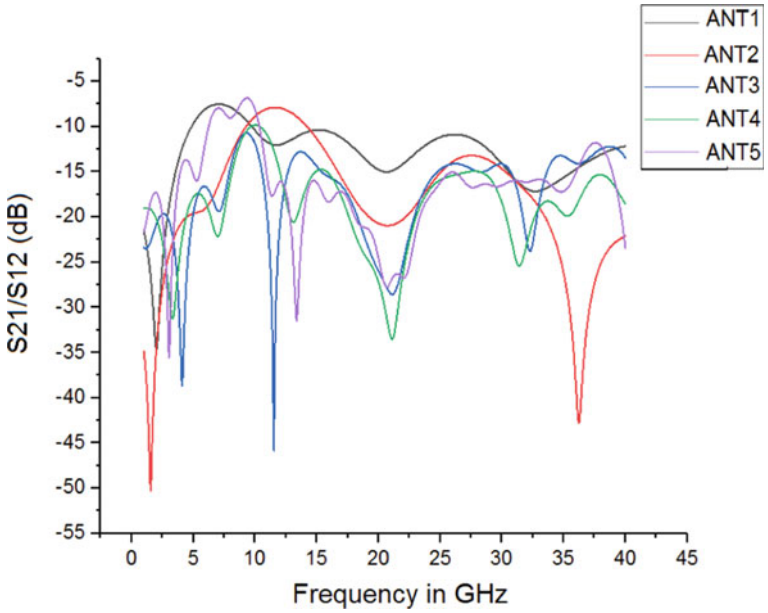

Fig. 4 Consolidated S_{21} versus frequency plot

3.3 Radiation Pattern

Radiation pattern represents the angular plot of received power or radiated power to or from antenna. Consolidated angular radiation plot of proposed antennas at Phi = 0 and 90° are represented in Fig. 5a, b, respectively. It is noted from Table 1 and Fig. 5a that peak side-lobe levels are reduced from −7.4 to −13.44 dB from ANT1 to ANT5. Reduction in mutual coupling between adjacent antennas can be also verified by decreased side-lobe levels for ANT 5. There are not many variations in gain of antenna. It may be observed from Fig. 5b that pattern is very similar to figure of eight of monopole antenna.

Performance parameters of MIMO configuration are dependent on scattering parameters. Low mutual coupling and small return loss will lead to effective MIMO operations over wide range of frequencies. It can be concluded from the comparative analysis of S_{11}, S_{21} and radiation pattern of the proposed geometries that ANT5 provides wide bandwidth where less than 10% of reflected power and isolation is greater than 15 dB. ANT5 is suitable for ultra-high speed low latency MIMO operations. MIMO performance of proposed ANT5 is discussed in detail.

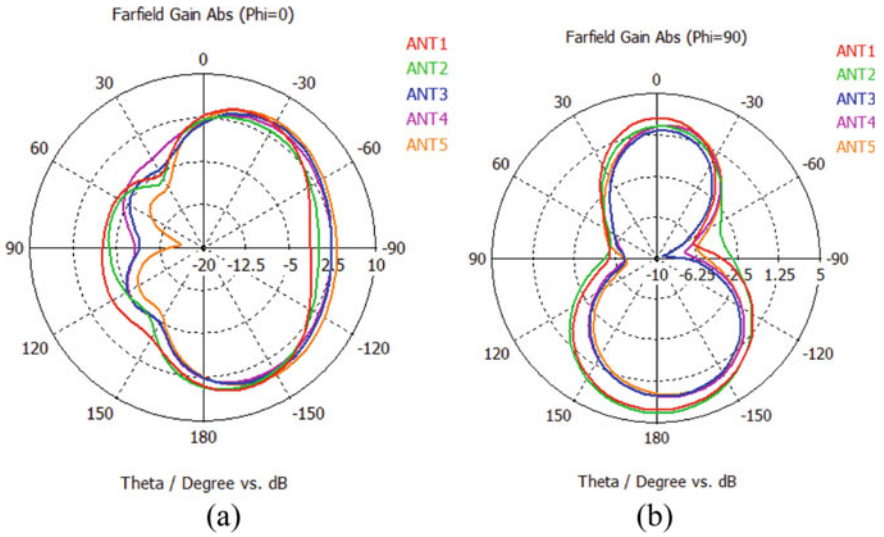

Fig. 5 Consolidated radiation plot of proposed structures, **a** at Phi = 0°, **b** at Phi = 90°

4 MIMO Results of Proposed Antenna

Analysis of performance of MIMO configuration can be done by calculating various MIMO parameters such as ECC, TARC, DG, MEG, and CCL. Envelope correlation coefficient (ECC) represents the independency in operation of two adjacent antennas. It may be observed from Fig. 6a that ECC of ANT5 is less than 0.3 at whole operating frequencies and very close to 0 at resonant frequency which shows effective MIMO operation. Diversity gain (DG) tells about enhancement in signal-to-noise ratio performance using multiple antenna configuration in comparison to single antenna. Figure 6b shows that DG is much closer to 10 for whole operating range which indicates good signal-to-noise ratio performance. Channel capacity loss (CCL) provides the information about the range up to which lossless communication can be possible. It may be noted from Fig. 6c that ANT5 provides less than 0.5 bit/sec/Hz throughout the operating range which represents minimum transmission losses. Mean effective gain (MEG) tells about effective operation of MIMO antenna in multipath fading environment. It may be noted from Fig. 6d that MEG1 and MEG2 is same which indicates identical operations of adjacent antennas. MEG of ANT5 is very closed to zero over operating range. Total active reflection coefficient (TARC) represents about the information about the range of frequencies where reflection is minimum and effective radiation takes place. It may be seen from Fig. 6e that TARC is less than 0 dB over whole operating bandwidth.

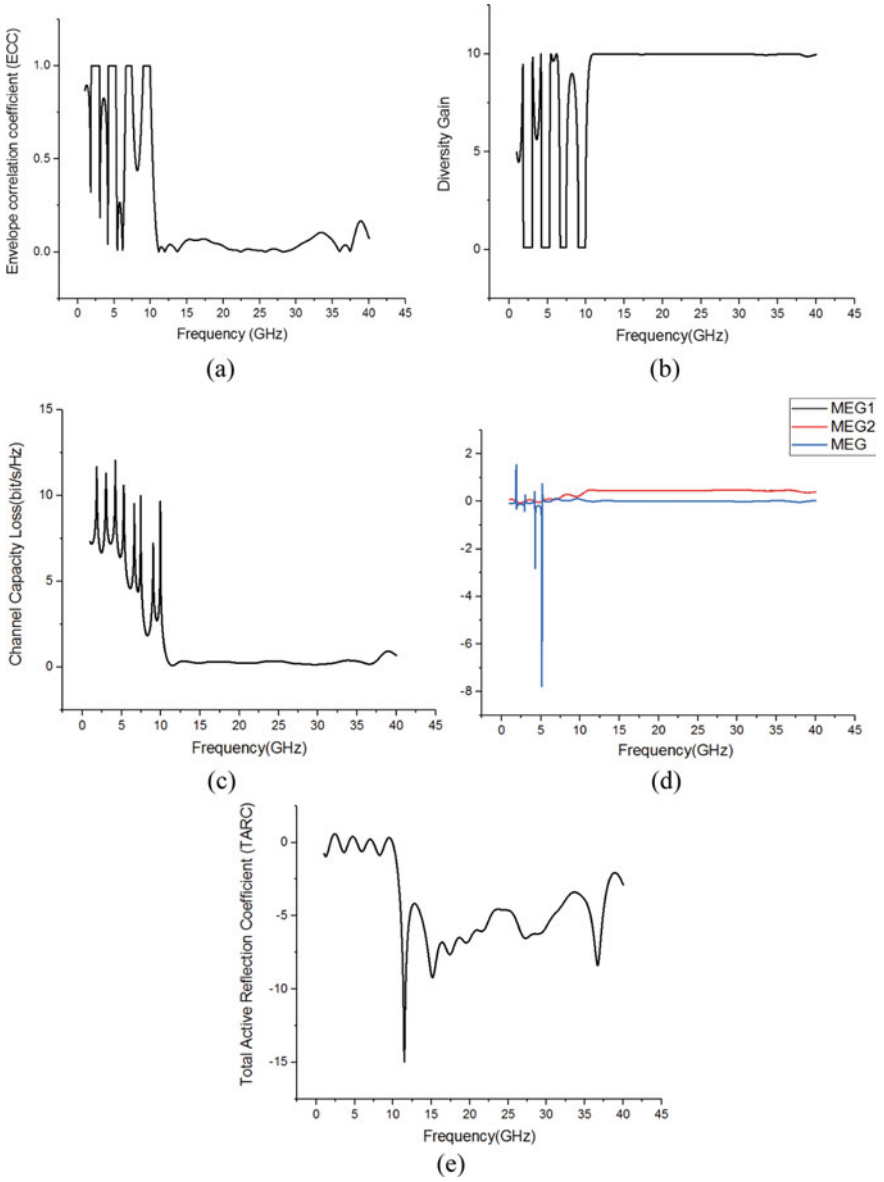

Fig. 6 MIMO parameters, **a** ECC, **b** DG, **c** CCL, **d** MEG, **e** TARC

5 Comparative Analysis of Performance of Proposed Antenna with Reported MIMO Antennas for 5G Communications

Presented spatial diversity MIMO antenna (ANT5) provides wide bandwidth of 25.297 GHz where isolation is better than 15 dB, and return loss is smaller than 10 dB which makes it suitable for 5G communication and ultra-high speed low latency communication. Proposed antenna provides all the parameters within acceptable range for wide range of frequencies. All the parameters of proposed antenna and reported 5G MIMO antenna are listed in Table 2.

6 Conclusion

Spatial diversity wideband MIMO antenna is proposed in this paper. Various techniques have been applied to improve the isolation over wide band of frequencies. Frequency range where isolation is greater than 15 dB is enhanced from 4.373 GHz to 25.297 GHz using various decoupling techniques. Proposed antenna provides less than 10% reflected power from 10.7 to 37.7 GHz which covers the mm-wave 5G spectrum allotted for in different countries and regions such as United States, Asia, and Europe. Wide bandwidth is achieved using partial ground plane and rectangular slots. Proposed antenna is planar, single layer, and has thickness of only 0.254 mm. So, it may be easily integrated with radio frequency-integrated circuits of mobile phone. Various MIMO parameters such as diversity gain, total active reflection coefficient, envelope correlation coefficient, mean effective gain, and channel capacity loss have been calculated, and result shows that antenna provides excellent performance for MIMO operations.

Table 2 Performance comparisons with reported MIMO antennas

Works	Size (mm^3)	Operating frequency range (GHz)	Bandwidth (GHz)	S21 (dB)	Diversity Gain	ECC	CCL (bit/sec/Hz)	TARC	MEG
Proposed	12.638*7.28*0.254	10.7–37.7	27	−31.316	9.99	0.003	0.2	−8.23	0
[11]	61.975*17.1666*0.8	26.69–30.29	3.53	≤ 40	–	0	–	–	–
[12]	16.5 × 26 × 0.7	25.5–41	14.5	≤ 40	–	0.0001	–	–	–
[13]	48*31*10	26–31	5	≤ 21	–	0.00015	–	–	–
[14]	30*30*0.787	27–29	2	≤ 27	–	< 0.16	–	–	−4.1
[15]	10*12*0.38	28.2–30.7	2.5	–	–	0.0001	–	–	–

References

1. Nahar T, Rawat S (2020) Low cost planar millimeter wave antenna array for 5G mobile applications. In: 2020 2nd International Conference on Advances in Computing, Communication Control and Networking (ICACCCN), Delhi, India (2020)
2. Qiao J, Shen XS, Mark JW, Shen Q, He Y, Lei L (2015) Enabling device-to-device communications in millimeter-wave 5G cellular networks. IEEE Commun Mag
3. Andrews JG, Buzzi S, Choi W, Hanly SV, Lozano A, Soong AC, Zhang JC (2014) What will 5G be? IEEE Jsac Special Issue On 5G Wirel Commun Syst
4. Roh W et al (2014) Millimeter-wave beamforming as an enabling technology for 5G cellular communications: theoretical feasibility and prototype results. IEEE Commun Mag 52(2):106–113
5. A White Paper on Enabling 5G in India. TRAI (2019)
6. Sarthak S (2019) Tetradecagonal ring shaped terahertz super wideband MIMO Antenna. Optik
7. Singhal S, Budania J (2019) Hexagonal fractal antenna for super wideband terahertz applications. Optik
8. Bonache J, Gil I, García-García J, Martín F (2016) Complementary split rings resonators (CSRRs): towards the miniaturization of microwave device design. J Comput Electron 5(2–3):193–197
9. Rubani Q, Gupta SH, Rajawat A (2020) A compact MIMO antenna for WBAN operating at Terahertz frequency. Optik 207:164447
10. Trinh-Van S, Lee JM, Yang Y, Lee KY, Hwang KC (2019) A side lobe-reduced, four-beam array antenna fed by a modified 4*4 butler matrix for 5G applications. IEEE Trans Antennas Propag 67(7)
11. Jose MC, Radha S, Sreeja BS, Kumar P (2019) Design of 28 GHz high gain 5G MIMO antenna array systems. In: TENCON 2019—2019 IEEE region 10 conference (TENCON)
12. Ejaz A, Mehak S, Anwer W, Amin Y, Loo J, Tenhunen H (2019) Investigating a 28 GHz wide-band antenna and its MIMO configuration. In: 2019 2nd international conference on communication, computing and digital systems (C-CODE), pp 7–10
13. Wani Z, Abegaonkar MP, Koul SK (2018) A 28-GHz antenna for 5G MIMO applications. Progress Electromagnet Res Lett 78:73–79
14. Kamal MM, Yang S, Ren X-C, Altaf A, Kiani SH, Anjum MR, Iqbal A, Asif M, Saeed SI (2021) Infinity shell shaped MIMO antenna array for mm-wave 5G applications. Electronics 10:165
15. Hasan MN, Seo M (2018) Compact omnidirectional 28 GHz 2×2 MIMO antenna array for 5G communications. In: 2018 international symposium on antennas and propagation (ISAP), pp 1–2
16. Goyal RK, Modani US (2021) A compact MIMO microsrip patch antenna design at 28 GHz for 5G smart phones. Int J Eng Res Technol (IJERT) NREST 09(4)
17. Kumar S, Dixit AS, Malekar RR, Raut HD, Shevada LK (2020) Fifth generation antennas: a comprehensive review of design and performance enhancement techniques. IEEE Access 8:163568–163593
18. Nadeem I, Choi D-Y (2019) Study on mutual coupling reduction technique for MIMO antennas. IEEE Access 7:563–586
19. Wei K, Li J, Wang L, Xing Z, Xu R (2016) S-shaped periodic defected ground structures to reduce microstrip antenna array mutual coupling. Electron Lett 52(15):1288–1290
20. Chen X, Zhang S, Li Q (2016) A review of mutual coupling in MIMO systems. IEEE Access 6:24706–24719
21. Savy L, Lesturgie M (2016) Coupling effects in MIMO phased array. In: Proceedings of the IEEE radar conference (RadarConf), pp 1–6
22. Ali WAE, Ibrahim AA (2017) A compact double-sided MIMO antenna with an improved isolation for UWB applications. AEU-Int J Electron Commun 82:7–13

23. Kuwabara N, Hiroshima Y (1997) Development of coupling and decoupling networks below 150 kHz. In: Proceedings of the international symposium on electromagnetic compatibility, pp 17–20
24. https://academy.3ds.com/en/software/cst-studio-suite-student-edition

Cable Faults Identifying Review and Procedure for New Instrument

G. Babu Naik and Sanjay Lakshminarayanan

Abstract Existences of underground cable faults like power transmission and distribution system are inevitable situations due to plentiful reasons. Power distributors to the consumer side will be placed very far distance of power supply and will cause the heavy loss of economic and uneasiness of power utilization. Hence, the faults should be detected quickly and rectified is a major concern of the power distributors. This paper states about the high-voltage underground cable fault locating methods that are present in practice and highly technical methods proposed by researchers.

Keywords Power cable · Fault detection and instrument techniques

1 Introduction

Identifying underground cable and overhead transmission line faults and locating the site of the fault for the power system is a crucial task in electrical technology. Engineering skills and technologies are heavily involved in locating fault locations. As a result, power distributors always prepare a team of highly skilled engineers and tools for the fault-finding mission. In today's world, there are a variety of methods for locating the fault location. However, each method has its own set of benefits and drawbacks. However, among all the other ways available, there are no good procedures that may provide the best fault location [1]. Users, on the other hand, are constantly considering new instruments that can provide the finest performance of technology. Due to industry growth, new construction buildings, commercial purposes, population density, and other factors, electricity distribution systems are pumped through underground cables to metropolitan areas [2–6].

Until the fault areas are repaired, the power distribution networks are fed back to other alternate sources. As a result, a rapid instrument is necessary to locate the problem, and power distribution networks must constantly prioritize correcting. The cost of the present underground cable fault locating gadget is comparatively higher.

G. Babu Naik (✉) · S. Lakshminarayanan
Department of Electrical and Electronics Engineering, BMS Institute of Technology and Management, Bengaluru, Karnataka, India
e-mail: babunaikg@bmsit.in

© The Author(s), under exclusive license to Springer Nature Singapore Pte Ltd. 2022

A. Tripathi et al. (eds.), *Intelligent Computing Techniques for Smart Energy Systems*, Lecture Notes in Electrical Engineering 862,
https://doi.org/10.1007/978-981-19-0252-9_33

As a result, in many cases, one method is insufficient to detect the issue, and another way is necessary to provide precise results with proper location. Organizing many tests with an instrument and locating the ultimate pinpointing flaw, on the other hand, takes more time [7, 8]. As a result, a good design instrument and a lightweight building machine would make detecting cable defects and pinpointing fault location easier for engineers. This document examines the many underground cable fault detection systems that are currently in use, as well as highly technical methods proposed by researchers.

Underground cables are progressively being employed in more electrical distribution networks due to their advantages over overhead lines. In bad weather, they are more reliable than overhead lines, and they are not influenced by trees. They are also less expensive and require less maintenance over short distances [9]. Underground cables, on the other hand, have a number of disadvantages, including the fact that they are more prone to long-term troubles after a flashover and are more difficult to find faults. The majority of faults in underground cable networks are permanent and can be classified as core to sheath to ground fault, core to ground fault, or core to sheath fault. Accurate identification of the fault location in the case of permanent failures in cables is crucial for power distribution networks for higher reliability, power quality, a faster restoration procedure, reduced outage time, and cheaper repair costs. It is crucial to keep the electrical system running smoothly. As a result, it is essential to limit the amount of defects in the power system and to resolve them quickly. As a result, it is vital to accurately detect and clear the issue in order to restore power in a timely manner. An overhead system is significantly easier to discover a broken location than a subterranean system for a variety of obvious reasons. The overhead system offers numerous tools, such as the phasor measurement unit that can detect the exact location and nature of a fault. Fourier analysis, artificial neural networks, Murray loop methodology, and Ohm's law method are only a few of the methods for finding problems in subterranean power cables. None of the preceding approaches will determine the exact location of the problem. Furthermore, none of these systems took into account the intensity of sheath currents or grounding modes, resulting in inefficient and erroneous fault location.

2 Literature Review

In the literature, various cable fault location methods have been discussed.

The process of sheath earth current and the link among sheath earth current and load current are investigated in research [10]. The EM-transient simulation model of cable sheath is created using PSCAD/EMTDC simulation software, which is capable of simulating a variety of sheath grounding system issues. The phase current and ground fault occur between two phases, according to the simulation results. Ground fault and phase fault were not explicitly addressed in three phases, and fault localization in underground cables was not well discussed.

The methodology to construct and verify the CZST model using the experimental properties of CZST was described in research [11]. It used a model of cable zero sequence current transformers to create fault location for single-phase ground faults (CZST); to construct and verify the CZST model, we used the magnetization reversal dynamics equation and the methods for taking the experimental properties of CZST. The CZST model was discussed in detail. The model developed allows researchers to investigate the static and dynamic modes of operation of SPGF safeguards in 6–10 kV electrical networks. It also ignores the numerous grounding modes as well as three phases that have yet to be established.

In an experiment described in Reference [12], with an artificial ground fault point stored in a cryostat pipe, the alternating current simulated a ground fault that flowed in the 275 kV HTS cable core. Insulation sheets were used as a protective covering on the investigated materials in this experiment. The effect of the core protective layer was not confirmed. It was considered since the inner pipe's core had been destroyed. However, this procedure did not provide an accurate location for the experimental work's problem.

[13] is a citation. Single-phase ground faults on the cable line side of short combination overhead-cable lines can be discovered utilizing comparisons of the currents circulating in the shields' rms values and their angles, according to simulation and laboratory test results. Underground cable faults were not included in this study, and line-to-line faults were not assessed.

Pandey [14] spoke on utilizing Fourier analysis on voltage readings to discover faults in underground cables. Because multiple grounding modes and sheath currents were not taken into account in the work, the produced cable model isn't particularly durable and accurate.

Filomena et al. [15] devised a fault location algorithm that is an improvement over the old method. The apparent impedance of cables for single phase to ground fault and three-phase fault is calculated using this method. The proposed approach compensates for subterranean cable capacitive currents. The model, on the other hand, ignores sheath currents and multiple grounding modes in the cable system.

For underground cable networks, Jamali et al. developed a defect location algorithm. Sequence impedance models were used to represent the taps and other cable sections. To achieve an optimum outcome, the principal causes of inaccuracy in traditional impedance-based approaches are taken into account by incorporating cable capacitance effects. Sheath currents are not taken into account by this algorithm [16, 17].

Aziz et al. [18] introduced a multi-terminal based on input fault location technique that is highly suited to older cables. The aging of the cables has a significant impact on their relative permeability and sequence capacitances. The method for fault localization is based on phasor measurements from several cable terminals. The multiple grounding modes in cable, as well as the influence of sheath currents, haven't been taken into account.

Wang et al. [19] presented a system for fault monitoring in cable lines based on the sheath grounding current. The fault phase and sound phase sheath grounding currents have different characteristics, according to the investigation. It can determine

the problematic location and detect the faulty phase using these differences. When fault resistance is high, this method has limitations in assessing the problem since the characteristics of a grounding fault become less visible as fault resistance grows.

Hans et al. [1] provided simulation and prototype model results, which were found to be consistent. The fault locating solution was found up to a distance of ten kilometers. This is not feasible over large distances. The measurements for safety and compactness were not considered.

For analysis purposes, Long et al. [20] coupled CWT with complex wavelets to estimate the impedance in the wavelet domain. The magnitude and phase fingerprints retrieved were shown to be useful in discriminating between the various cable kinds. Sheath current and grounding modes, however, were not taken into account.

Cheung et al. [21] addressed the environmental factors that influence cable fault situations, such as soil conditions, weather conditions, road conditions, and so on. Also noted, by employing the proper equipment, the time it takes to locate the cable issue will be significantly reduced.

Zhang et al. [22] proposed a multi-cycle incipient fault detection and location method for medium voltage subterranean cable based on arcing faults. For various fault durations, noise levels, and system parameters, the distance estimation method is determined. This approach was not designed for high-voltage subterranean cables, and single-end sheath currents and sheath grounding fault detection were not taken into account.

Based on the presence of the fault breakdown resistance, it was advised that only the reactance part be examined. The difficulty in dealing with grid uncertainties is a shortcoming of this type of technique. Zhu et al. [23] investigated the impact of uncertainty and devised a method for estimating the fault position range. The performance index of different impedance-based fault location algorithms was compared by Mora-Flrez et al. [24].

Apart from impedance-based approaches, Choi et al. [25, 26] reported a direct circuit analysis method that improved its robustness to load impedance uncertainty by using impedance compensation with voltage and current measurements. Furthermore, Nouri et al. [27] and Thomas et al. [28] used wavelet transform to solve the problem. The time difference between the traveling waves during the fault has been proposed to be measured. Lotfifard et al. [29] devised a systematic strategy to score fault location methods qualitatively and statistically in order to compare different methodologies.

To properly account for the uncertainties, statistical methods have been developed in addition to deterministic ones. Cormane et al. [30] proposed a method based on data clustering. To find single-phase faults, Mora-Flórez et al. [31] devised a statistical classification approach based on fuzzy probability functions.

By including measured locations and/or electrical values, Yu et al. [32] argued that the Bayesian approach method could integrate various measured data and increase accuracy. This method was not recommended for integrating non-rms measurement values such traveling wave timing and/or transient component frequency.

3 Types of Cable Fault Detection

There are four main functions of faults happening system in power distributions lies and cable classified the following categories: short circuit condition, high impedance to earthing short-circuit to earthing and open-circuit conditions. These faults did not meet the requirements of identifying the fault locations. Four categories are used mostly to finding the fault points.

- A bride-type method (Murray loop)
- Ohm's law method
- Identifying faults in underground cable using software tools.
- Identifying faults in underground cable using Bayesian inference.

These methods are providing the detection of fault location for various characteristics of power lines.

3.1 A Bridge-Type Method (Murray Loop)

A bridge-type method is used to find the location of cable fault. By considering this, test is performed in underground cable either by earth or the short-circuit faults. This method follows on basic principle of Wheatstone bridge for medium resistance calculation. This Wheatstone bride is used for finding the fault position in underground cables. The connection of a bridge-type method (Murray loop) test is shown in Fig. 1

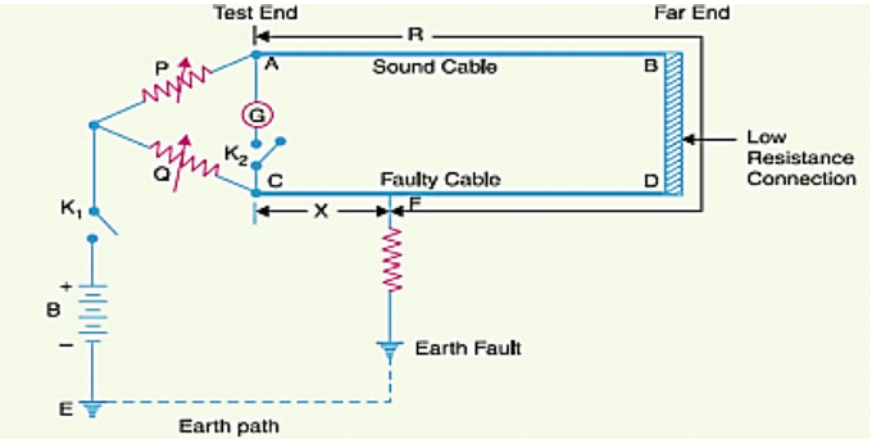

Fig. 1 Murray loop circuit connection test for cable fault

Using Wheatstone bridge under balance condition, equation can be written as;

$$LX = Q/(P + Q)L$$

Using above, LX is the length between fault end and test fault of the faulty cable, and L is the both cable of total length. Under this method, development is done for wide range of cable fault length not been considered.

3.2 Ohm's Law Method

The Ohm's law is used to find the short circuit fault using the basic principle. A direct DC voltage is applied to feeder end through a resistor based on the length of the cable fault changing in current. Across the series resistor, voltage drop will changes accordingly and will give the detection of fault location. However, this procedure is used to gather a lot of resistors indicates the cable length is measured in KMs, and identifying the cable fault point is done by collecting switches at each recognised KMs [1]. This method is collected with a bunch of resistors denoted by considering the cable length in terms of KMs and should be made at every fault location a bunch of switches to known KMs for exact fault identifying. This method also did not give the fault location for wide-rage cables.

3.3 Identifying Faults in Underground Cable Using Software Tools

In this method, they followed three steps, first step by creating a fault in the system for the transmission network model using MATLAB/SIMULINK. The second method is using of Fourier analysis fault voltages and currents with the SIMULIK model a set of artificial neural network [33]. The third method is using of OrCad fault locating at a distance from the either end of the position by considering the underground distribution system in a time domain analysis. Hence, by considering, these methods give the different variations of times of voltages and currents and array of faults.

3.4 Identifying Faults in Underground Cable Using Bayesian Inference

To identify fault location, proper procedure is calculated in the paper and block diagram shown in Fig. 2. The fault site for the preceding distribution system is determined using the components of comparisons of the currents circulating in the

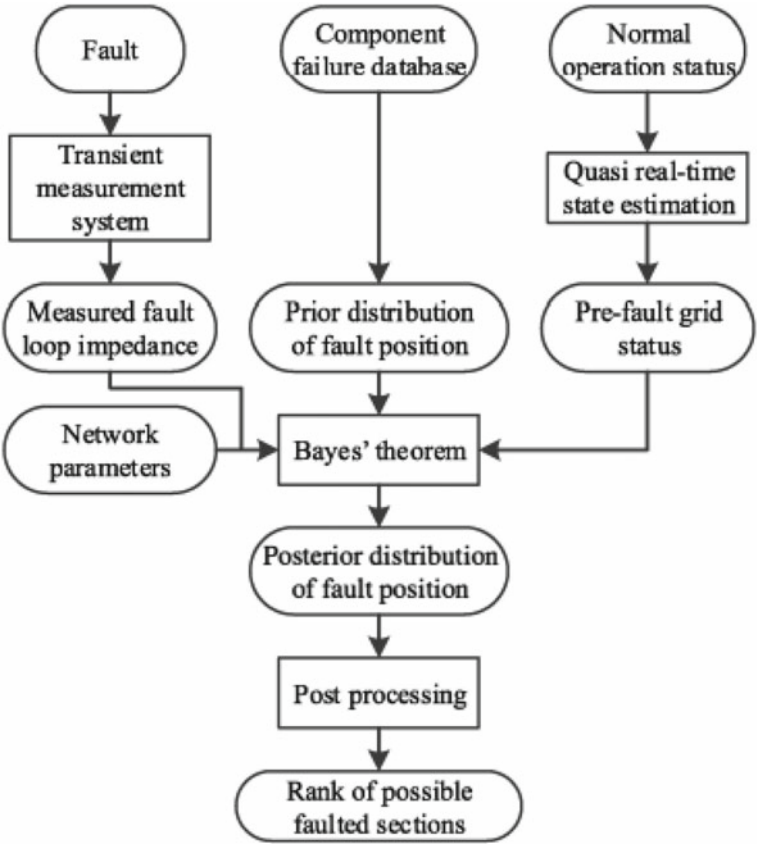

Fig. 2 Procedure for designed fault location

shields' rms values and angles failure rate data. Including this from the quasi-real time of state estimation, the status of the pre-fault grid connected system is obtained during normal condition when fault was occurred and transient is measured and recorded the faults pinpointing [34]. The fault loop impedance, network parameters, and state of the pre-fault grid system for the distribution power system were computed using the Bayes' theorem approach. It measures the ranking of faulted levels in each section.

This method represents a section-based fault identifying approach of medium-voltage underground cable's fault using Bayesian inference. This method did not consider the fault currents underground cables.

4 Few Proposed Cables Faults Locating Methods

Some few faults locating techniques were used by current researcher that shows a number of proposals which need to be tested yet practical in the field area.

Chrysochos [35] projected a fault location method using the ATP and EMTP simulation tool. In this method, sheath voltages induced and distribution current in three-phase along the cable of sheaths is considered for a medium-voltage cable (MVC). In single phase of short circuits, the transposition techniques are not effective since, due to asymmetrical fault currents for the three-phase short circuits, the voltage and current power distributions along the sheath earth are not so affective in this method.

Kulkarni [36] developed algorithm of robust practical incipient locating fault considering the fault arc-voltage. This software is implemented using a time domain function algorithm model, which was utilized by P-Q monitors to determine the cable fault distance is applied to the single line to ground fault. They tested the planned algorithm for underground failure analyzed below 10% of cable fault.

Zhang [9] proposed a system for fault cable using PSCAD and EMTDC indicating the fault detection and used algorithm to provide the accurate faults under various sector conditions. By adding sheath currents and detecting the signal, high signal sensitivity and currents may be easily detected through line grounding of sheaths, and this can be employed for wide-area applications.

Naidu et al. [2] proposed for underground cable in power distribution with fault location by considering PSCAD EMTP simulation tool. They have developed cable modeling for different grounding modes, shunt capacitance, and sheath currents taken into account. This method measured the voltage–current and also record it at the terminal end of cable fault locator. This method tested with software simulation results and get the accurate output.

These methods are computational in nature and are used to locate the defect. There is no evidence that the authors of this research employed a realistic approach to locating subterranean cable failures. However, these methods are considered for distant/impedance relay for their accuracy maintenance.

5 Purpose of Cable Fault Exposure and Investigations

The main purpose of this paper is to obtain a simple instrument to detect the fault and clear the automatic fault detection with injecting high pulse currents via high-voltage cable. In this, high-voltage DC pulse can be used for improving techniques with making test machine and easy to use.

The most commonly used for high-voltage cables are insulation, voltage resistivity, and lead sheath. Examples: (i) Mass impregnated paper (PILC), (ii)

polyvinylchloride (PVC), (iii) cross-linked-polyethylene (X-L-P-E), (iv) ethylene-propylene-rubber (E-P-R), (v)paper with oil and gas. Some other types of cables are also available, and those materials can be used for various type of isolations.

The pulsed high-voltage DC is applied through the above displayed materials, its start changing the behavior of capacitive current, insulation current, leakage current, and the current at the fault conditions. These currents should be analyzed for types of cables and to be determine the mini current needed for injecting the machine so that fault identifying is easy.

A DC pulsed current will be transferred through the cable, and it will be reflected at the faulty location or else discontinue the connection. It is important that DC pulsed current, how long it can withstand the cable strength, and a proper investigation is necessarily to find the current. Some few points should consider at the receiver-side design. They are minimum i/p signal needed, transmitter side and receiver side, the complexity circuits, protection circuit, machine capacity, assemble tools, and safety measurements. The basic infrastructure is required for designing the lightweight fault locating instrument used by field engineers.

6 Conclusion

This paper measures the fault detection in the power distribution network and also reviews the methods of locating the cable fault that been done experimental work on the field side. Few points of about sheath currents at the cable side have been studied. This paper also says to the authors to develop a machine to detect the cable fault faster and with light-weight instrument can be used by the technician. This document verifies the primary required investigation and the development of equipment.

References

1. Hans MR, Kor SC, Patil AS (2017) Identification of underground cable Fault location and development. In: 2017 international conference on data management, analytics and innovation (ICDMAI) zeal education society, Pune, India, Feb 24–26, 2017. 978-1-5090-4083-4/17/$31.00 ©2017 IEEE
2. Naidu OD, George N, Pradhan D (2016) A new fault location method for underground cables in distribution systems, 978-1-5090-3498-7/16/$31.00 ©2016 IEEE
3. Koep D (1999) Locating that underground cable fault. Available: http://www.ecmweb.com/mag/electric_locating_underground_cable/index.html
4. Siew WH et al (2003) Automatic fault location for underground distribution network. In: 17th international conference on electricity distribution, Barcelona, 2003, pp 1–3
5. Komoda M et al (1991) Development of a current detection type cable fault locator. Power Deliv IEEE Trans 6:541–545
6. Parker CETG (2012) Cable and cable fault locating—part 2. Available: http://www.tracerelectronicsllc.com/resources/Applications/Cable-Fault-Locating/FaultLocating-part2.pdf

7. Bukya M, Kumar R (2020) Safety consideration and design of high voltage cable for electric vehicle. Int Conf Power Electron IoT Appl Renew Energy Control (PARC) 2020:485–490. https://doi.org/10.1109/PARC49193.2020.236661
8. Bukya M, Kumar R, Gupta RK (2020) A study on safety issues and analytical evaluation of stresses for HVDC cable in electrical vehicle. In: AIP conference proceedings 2294, 040001 (2020). https://doi.org/10.1063/5.0031351
9. Zhang C, Kang X, Ma X, Jiang S, Qu X (2016) Shaanxi Key Laboratory of Smart Grid (Xi'an Jiaotong University) On-line incipient faults detection in underground cables based on single-end sheath currents. In: IEEE PES Asia-Pacific power and energy conference—Xi'an—China, pp 978–1–5090–5417
10. He B, Zhou Y, Li H, Ye T, Fan S, Wang X (202) Fault identification of high-voltage cable sheath grounding system based on ground current analysis. In: 2020 IEEE 4th conference on energy internet and energy system integration (EI2), 2020, pp 3248–3251. https://doi.org/10.1109/EI250167.2020.9347380
11. Shuin V, Evdakov A, Filatova G, Batmanov M (202) Simulation of cable current transformers for protection against single-phase ground fault in 6–10 kV networks. In: 2020 international youth conference on radio electronics, electrical and power engineering (REEPE), 2020, pp 1–4. https://doi.org/10.1109/REEPE49198.2020.9059187
12. Takagi T et al (2018) Protection against ground faults for a 275-kV HTS cable: an experiment. IEEE Trans Appl Supercond 28(4), 1–4. Art no. 5401304. https://doi.org/10.1109/TASC.2018.2807488
13. Granizo R, Alvarez F, Platero CA, Redondo M (2017) Novel protection method for ground faults detection in cables used in combined overhead-cable lines in power systems. In: 2017 IEEE international conference on environment and electrical engineering and 2017 IEEE industrial and commercial power systems Europe (EEEIC/I&CPS Europe), 2017, pp 1–6. https://doi.org/10.1109/EEEIC.2017.7977492
14. Pandey A (2010) Underground cable fault detection and identification via Fourier analysis. In: 2010 International Conference on High Voltage Engineering and Application (ICHVE), April 2010
15. Filomena AD, Resener M, Salim RH, Bretas AS (2009) Fault location for underground distribution feeders: an extended impedance-based formulation with capacitive current compensation. Electr Power Energy Syst 31:489–496
16. Jamali S, Talavat V (2004) Fault location method for distribution networks using 37-buses distributed parameter line model. In: Proceedings of the 8th IEE international conference on developments in power system protection, Apr. 5–8, 2004, pp 216–219
17. Takagi T, Yamakoshi YA, Yamaura M, Kondow R, Matsushima T (1982) Development of a new type fault locator using the one-terminal voltage and current data. IEEE Trans Power Apparatus Syst PAS-101(8):2892–2898
18. Aziz MMA, El Din EST, Ibrahim DK, Gilany M (2006) A phasor-based double ended fault location scheme for aged power cables. Electr Power Compon Syst 34:417–432
19. Wang K, Li Z, Zhang B (2016) A novel method of power cable fault monitoring. In: 2016 IEEE PES Asia-Pacific power and energy conference—Xi'an—China, 978-1-5090-5417-6/16/$ 3l.00 ©2016 IEEE
20. Long Z, Younan NH, Bialek TO (2012) Underground power cable fault detection using complex wavelet analysis. In: Proceedings of IEEE international conference on high voltage engineering and application, 2012, pp 59–62
21. Cheung G, Tian Y, Neier T (2016) Technics of locating underground cable faults inside conduits. In: Proceedings of IEEE international conference on condition monitoring and diagnosis (CMD), 2016, pp 619–622
22. Zhang W, Xiao X, Zhou K, Xu W, Jing Y (2017) Multicycle incipient fault detection and location for medium voltage underground cable. IEEE Trans Power Deliv 32(3):0885–8977
23. Zhu J, Lubkeman DL, Girgis AA (1997) Automated fault location and diagnosis on electric power distribution feeders. IEEE Trans Power Del 12(2):801–809

24. Mora-Florez J, Meléndez J, Carrillo-Caicedo G (2008) Comparison of impedance based fault location methods for power distribution systems. Electr Power Syst Res 78(4):657–666
25. Choi M-S, Lee S-J, Lee D-S, Jin B-G (2004) A new fault location algorithm using direct circuit analysis for distribution systems. IEEE Trans Power Del 19(1):35–41
26. Choi M-S, Lee S-J, Lim S-I, Lee D-S, Yang X (2007) A direct three-phase circuit analysis-based fault location for line-to-line fault. IEEE Trans Power Del 22(4):2541–2547
27. Nouri H, Wang C, Davies T (2001) An accurate fault location technique for distribution lines with tapped loads using wavelet transform. In: Proceedings of the IEEE Porto Power Tech, vol 3, pp 1–4
28. Thomas DWP, Carvalho RJO, Pereira ET (2003) Fault location in distribution systems based on traveling waves. In: Proceedings of the IEEE Bologna Power Tech Conference, vol 2, pp 1–5
29. Lotfifard S, Kezunovic M, Mousavi MJ (2013) A systematic approach for ranking distribution systems fault location algorithms and eliminating false estimates. IEEE Trans Power Del 28(1):285–293
30. Cormane JA, Vargas HR, Ordonez G, Carrillo G (2006) Fault location in distribution systems by means of a statistical model. In: Proceedings of the IEEE/PES transmission and distribution conference and exposition: Latin Amer. (TDC), Aug. 2006, pp 1–7
31. Mora-Flórez J, Estrada-Cardona N, Perez-Londono S (2008) Fault location in radial power systems based on statistical analysis. In: Proceedings of the 10th international conference on probablistic methods applied to power systems (PMAPS), May 2008, pp 1–6
32. Xiang Y, Cobben JF (2015) A Bayesian approach for fault location in medium voltage grids with underground cables. IEEE Power Energy Technol Syst J 2(4):116–124
33. Hasija K, Kumar A (2014) Detection and location of faults in underground cable using Matlab/Simulink/ANN and OrCad. 978-1-4799-6042-2/14/$31.00 ©2014 IEEE
34. Yu X (2015) Fault location for medium voltage underground cables using Bayesian inference. Power Tech, 2015 IEEE Eindhoven, July 2015, pp 1–5
35. Chrysochos AI, Makri ET, Dimou AC (2012) An investigation of the performance of underground cable installations in operational and fault conditions. In: 8th Mediterranean conference on power generation, transmission, distribution and energy conversion MEDPOWER 2012
36. Kulkarni S, Santoso S, Short TA (2014) Incipient fault location algorithm for underground cables. IEEE Trans Smart Grid 5(3):1165–1174

Simulation and Analysis of Single-Stage Grid-Connected Solar PV System Using ANN

Mukul Singh, Omveer Singh, M.A.Ansari, and Vishwamitra Singh

Abstract The research paper presents a single-stage solar photovoltaic battery grid-tied system with a simple phase-locked loop which needs less control to operate. The system losses are decreased because of the exclusion of boost converter and addition of a storage battery. Earlier, many other techniques were implemented to extract maximum power from the solar panels such as incremental conductance (InCond) and perturb and observe (P and O). Now, the maximum power is being tried to be extracted by using the artificial intelligence's artificial neural network (ANN) technique. Tests results for the system operations are studied from doing the simulations of the proposed model. The operation conducts on two modes, i.e., fixed power and variable power in compliance with IEEE-519 standards. The power given as input to the grid is fixed during mode 1 and varies during mode 2. It is very essential to extract maximum power from the solar panels by increasing the efficiency, reducing the losses, and evading any possible faults. Hence, Simulink model of solar PV system using the artificial neural network is being built and simulated. The obtained results are observed and analyzed in the research paper.

Keywords Stand-alone PV system · Solar power · Maximum power point tracking · Artificial neural network · Voltage source converter · MATLAB Simulink · Etc

M. Singh (✉) · O. Singh · M.A.Ansari
Department of Electrical Engineering, Gautam Buddha University, Gr. Noida, India
e-mail: gbubuddhams@gmail.com

V. Singh
Department of Electronics Engineering, Delhi Technological University, Delhi, India

© The Author(s), under exclusive license to Springer Nature Singapore Pte Ltd. 2022

A. Tripathi et al. (eds.), *Intelligent Computing Techniques for Smart Energy Systems*,
Lecture Notes in Electrical Engineering 862,
https://doi.org/10.1007/978-981-19-0252-9_34

1 Introduction

After the development of solar cell, there is a new era comes in the field of harnessing electricity from the solar energy. Many researchers start their research in the field of photovoltaics systems. In present, there are more than a lakh of research paper present. Different techniques and topologies have been developed, and new research work is continuingly being in progress. The demand for clean energy and improving power quality is so high that power filtering is now being introduced by my researcher, but it has constraints of reactive power being inserted into the system [1].

$$vd = ed + L(\mathrm{did}/\mathrm{d}t) - \omega.\mathrm{Liq} \tag{1}$$

$$vq = eq + L(diq/\mathrm{d}t) + \omega.\mathrm{Lid} \tag{2}$$

The PI controller is used by the system to calculate and minimize the error between reference current and actual current by implementing the calculation algorithm which include proportional gain and integral gain as K_p and K_i [2]. The lightning may cause serious damage to the installed solar panels. Hence, the areas near the solar PV should be properly fenced to have minimal injuries and avoid any damage to humans or animals [3]. The disconnection of PV by any reason, whether lightening or anything else, causes power loss and hence not economically preferential for PV systems connected to the grid or microgrid [4]. Single-phase inverter converts DC to AC and is used frequently because the appliances connected to AC grid are AC type [5]. FFT can be performed on the grid currents to satisfy IEEE-519 standards. Power quality can be improved by using SPV system to provide alleviation in harmonics and correction in power factor [6]. Input given by the use of only one inductor provides symmetric operation during two consecutive half cycles of microgrid thus producing less switching losses [7]. When operating point changes, the performance of PI controller is ensured by feed-forward neural network which renews the PI parameters [8]. The efficiency of the system is decreased due to the involvement of transformers because of the losses incurred by them when isolating and protecting the system from the leakage current produced between the PV panel and the earth. This can be avoided by the transformer-less operation which will increase the efficiency while decreasing the size and cost of operation. But, this will remove the galvanic isolation provided by the transformer, and leakage current may increase the harmonic distortion in voltage and current of inverter. Hence, limit is set on the value of leakage current to avoid any major harmonic distortion or disconnection [9]. More than one conversion stage of inverter maybe required depending upon the voltage level of the string terminal of the PV [10]. Two-stage converter is shown in Fig. 1a, and single-stage converter is shown in Fig. 1b. It is best to use single-stage converter preferably as it will make the system compact [11].

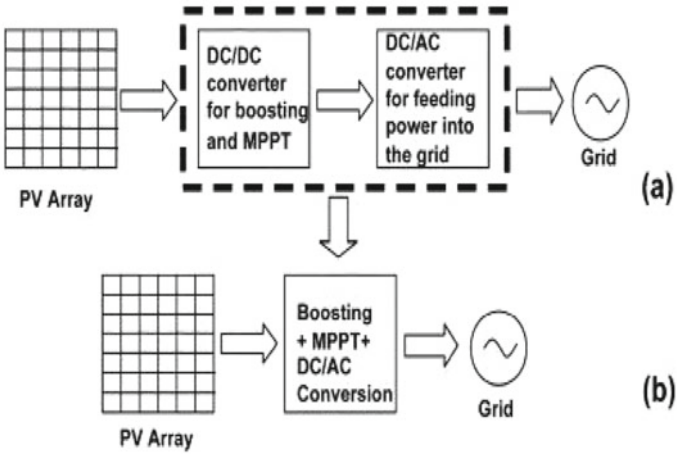

Fig. 1 Solar PV topologies of grid-connected system: **a** two-stage converter and **b** single-stage converter

2 Literature Review

PV system is also classified on the basis of connection with the grid. The systems connected with the grid are called grid-connected PV systems, whereas those which are working in the isolated environment are referred as stand-alone PV system. Stand-alone PV systems are mainly used with isolated microgrid [12]. The new LCL filter-based controllers boost the performance and robustness of the systems connected to the grid by reducing the grid disturbance associated with 5th and 7th harmonics and improving the power quality [13]. To synchronize the PV system when direct current component is rejected and supply is distorted because of transfer function which is mainly dependent on input signal, enhanced LTI-EPLL algorithm is can be used [14].

With the passage of time, there has been an advancement in harvesting approaches of solar energy as shown in Fig. 2. Initially, a central inverter was used as a more distributed approach with multiple PV array connected in series and parallel as shown in Fig. 2a. After that string inverter was used to be connected only with particular set of strings of PV array as shown in Fig. 2b. Later inverters were used alongside with DC optimizer as shown in Fig. 2c. Finally, micro-inverters are designed to be built into the individual panels at the back to make system more compact, efficient, and reliable as shown in Fig. 2d. This also eliminated the requirement of any low frequency-based power transformers [15]. To achieve optimized operation of power supply to residential load, linear quadratic regulator integral (LQRI) is used for multi-functional work associated with single-stage PV system. Nonlinear currents along with unbalanced loads cause harmonic currents at PCC. These harmonics can be eliminated by using adaptive feed-forward harmonic cancellation technique which also inserts active power into the grid or microgrid when control over grid current

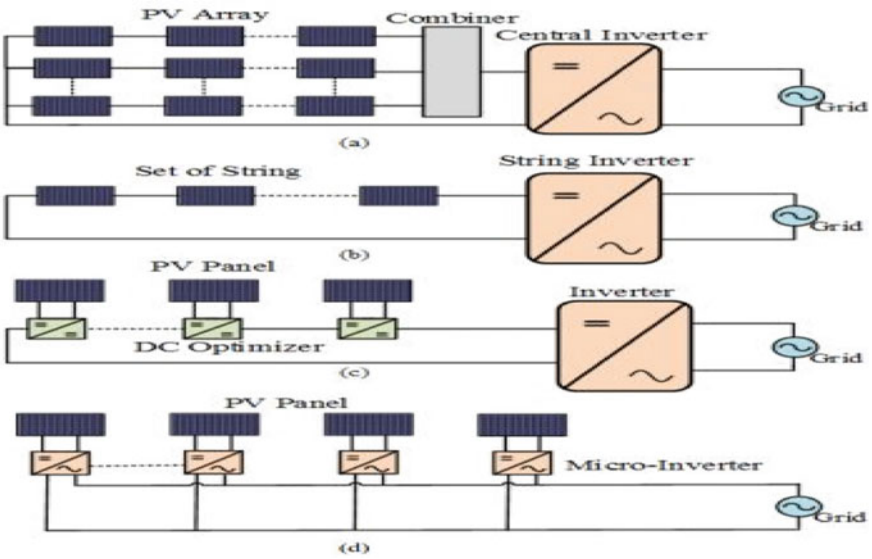

Fig. 2 Energy harvesting methods from PV grid-connected system

is required by the PV system connected to the grid [16]. During voltage unbalance or distortion, the amplitude of the fundamental part of current associated with the load can be extracted by the (MINF) multiple improved notch filter scheme as it decreases the harmonic components by DC offset rejection which under abnormal circumstances enhance power quality of the PV system connected to the grid [17].

$$I_{\mathrm{c}} = I_{\mathrm{ph}} - I_{\mathrm{d}} - I_{\mathrm{p}} \tag{3}$$

$$I_{\mathrm{ph}} = G/1000(I_{\mathrm{sc}} + k_{\mathrm{sc}}(T - T_{\mathrm{a}})) \tag{4}$$

A single-diode solar PV cell used around the globe is shown in Fig. 3 where I_{c} is

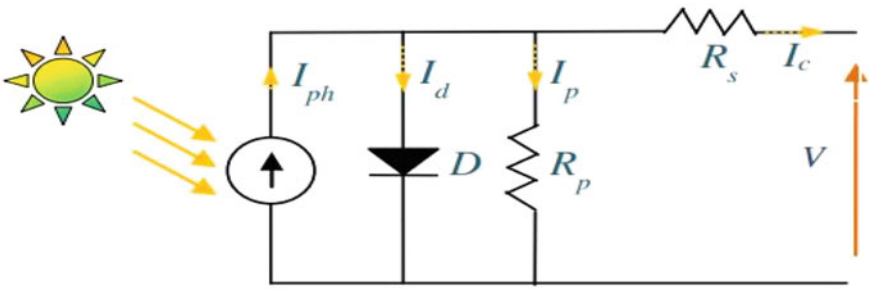

Fig. 3 Solar PV cell equivalent circuit of one diode

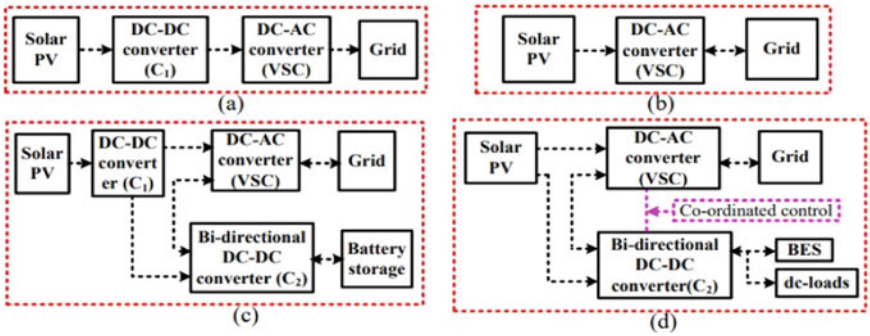

Fig. 4 Grid-connected solar PV stage advancement

the output current obtained from the solar cell, I_{ph} is the photonic current, Ip is the current passing through the shunt resistance, Id is the diode current passing through the $p-n$ junction, G is the solar irradiance [18]. Cascaded two-level inverter (CTLI) uses $p-q$ theory to generate the reference currents for the purpose of synchronization using hysteresis current controller to generate reference power which is inserted into the grid [19]. To maintain grid current free from harmonics and balanced, least mean square control algorithm is proposed to be used along with DC-DC buck-boost converter. Figure 4 shows the advancement in grid-connected solar PV connected with battery energy storage system over a period of time that is from two-stage to single-stage grid connected with VSC, later with BES, and finally single-stage connected with BES [20].

The grounded pole topology is used to mitigate the leakage current problem using the impedance source inverter which applies three-switch three-state technique to get the required AC voltage as output [21].

During disturbed grid voltage, INC algorithm along with modified proportional resonant (MPR) controller is used for fast tracking and reduction of harmonics by applying α-β reference frame linked with d-q reference frame for voltage control using controller. Amplification is not required except for AC modules and AC cells, so there is no need for centralized single-stage inverters [22]. SPWM voltage controller along with hysteresis current control can be used while operating with microgrid integrated with RES like solar PV, wind farm, diesel engine, and BES. The flowchart of management of power for PV and battery system connected to the grid is shown in Fig. 5. The flowchart signifies the two conditions when generated and measured PV power is more or less than the power needed by the load integrated to the grid. Both conditions are subdivided into two separate conditions such that whether the operating condition of the grid and the PV system is during peak hours or during off-peak hours of the day and night. During peak hours, the battery is discharged to supply desired amount of energy to the grid to meet the necessity of the grid due to high energy utilization by the loads attached. During off-peak hours, when PV and other energy sources successfully meet the requirement of the energy of the loads integrated, the battery is charged during daytime using the surplus of the energy

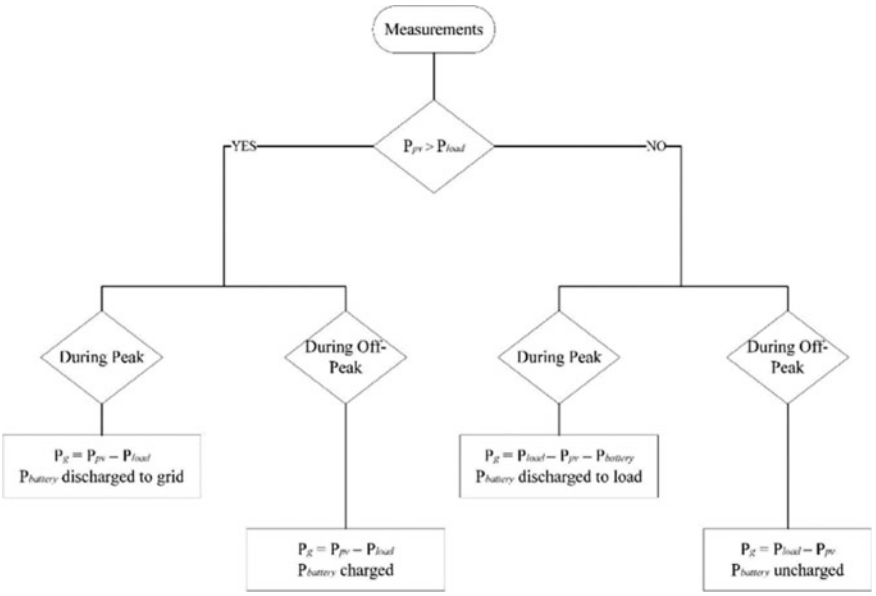

Fig. 5 Flowchart for power management of PV system

generated by the PV system. This is achieved by using the bidirectional DC-DC converter. Independently, separate PI, fuzzy, and ANN controllers can be integrated and used together successfully to reduce THD and voltage regulation using CHB [23]. The single-phase transformer-less inverter using PI and fuzzy logic scheme is used to operate serially connected PV panels connected to the grid or microgrid working under distinct irradiance and temperature conditions [24]. The circuits became more compact, and burden of control is decreased by using one bidirectional switch along with six unidirectional switches which provides a seven-level output to achieve steady state. The non-iterative scheme is implemented to generate maximum power using fill factor available through the PV datasheet parameters [25].

3 Simulation Models and Blocks

The Simulink MATLAB model of solar PV system connected to grid along with BES and nonlinear load via bidirectional converter and voltage source converter is shown in Fig. 6. Figure 7 shows PV system and MPPT block used in the MATLAB Simulink. Figure 8 shows the MPPT controller block based on artificial neural network connected with integral regulator implemented in above shown Simulink model.

Figure 9 shows the VSC used for conversion of energy transmitted on grid. Figure 10 shows the bidirectional DC-DC converter used before battery subsystem

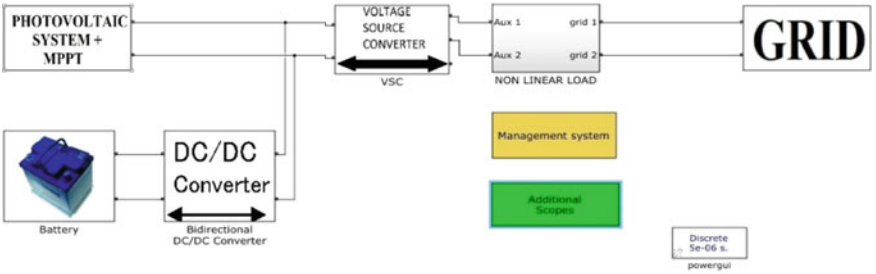

Fig. 6 Simplified model of single-stage grid-connected solar PV-battery grid-tied system

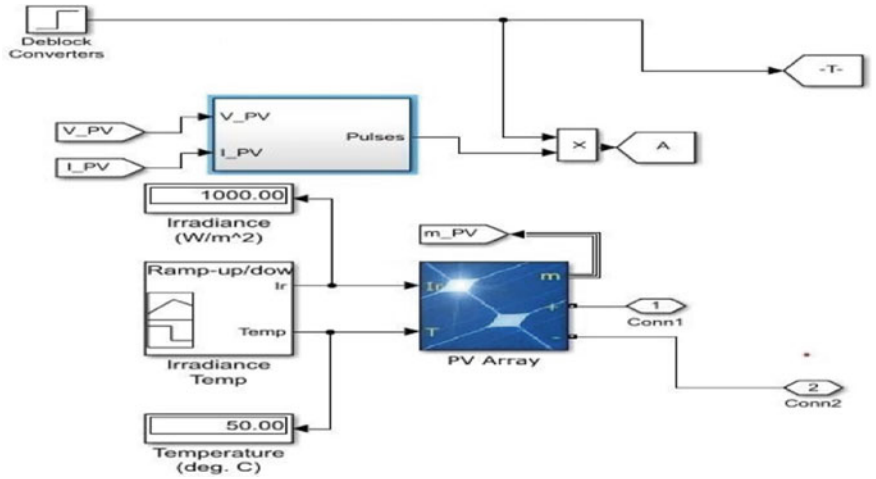

Fig. 7 PV system with MPPT block

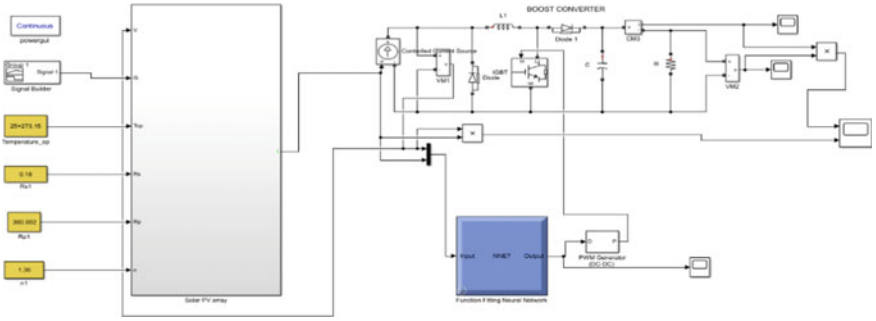

Fig. 8 ANN-based MPPT controller with integral regulator

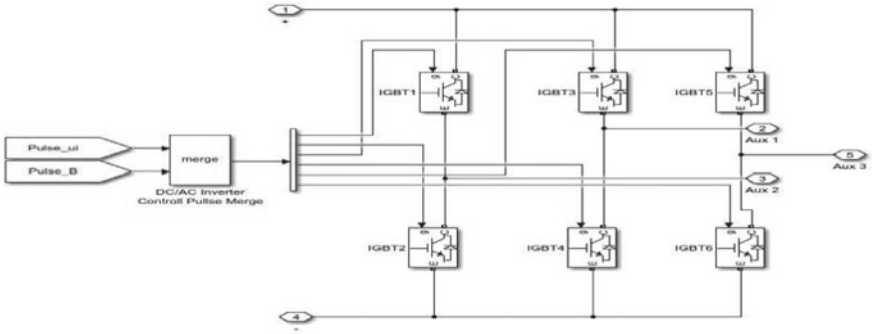

Fig. 9 Voltage source converter used in MATLAB Simulink

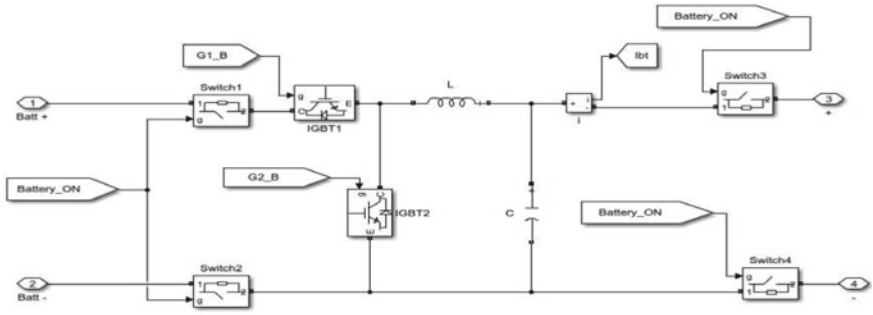

Fig. 10 Bidirectional DC-DC converter used in MATLAB Simulink

to provide DC input of energy to the battery for charging at 50 Hz frequency supplied directly by the PV system to the battery. Also, during discharging condition, fixed DC output is provided at 50 Hz with the help of DC-DC converter. Figure 11 shows the expanded battery subsystem used for charging and discharging as per requirement is integrated in the Simulink model into the grid after the PV system as shown in Fig. 6. Charging occurs during surplus energy generation, while discharging occurs when

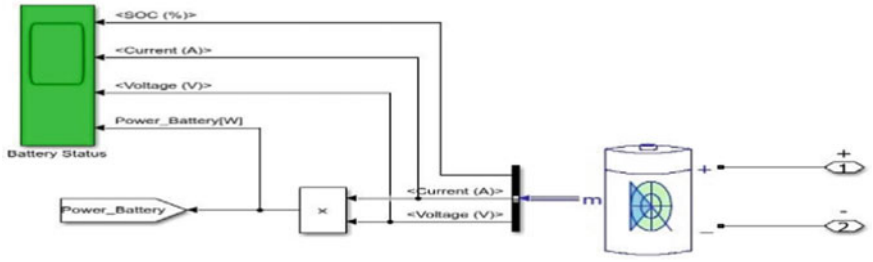

Fig. 11 Battery subsystem used in MATLAB Simulink

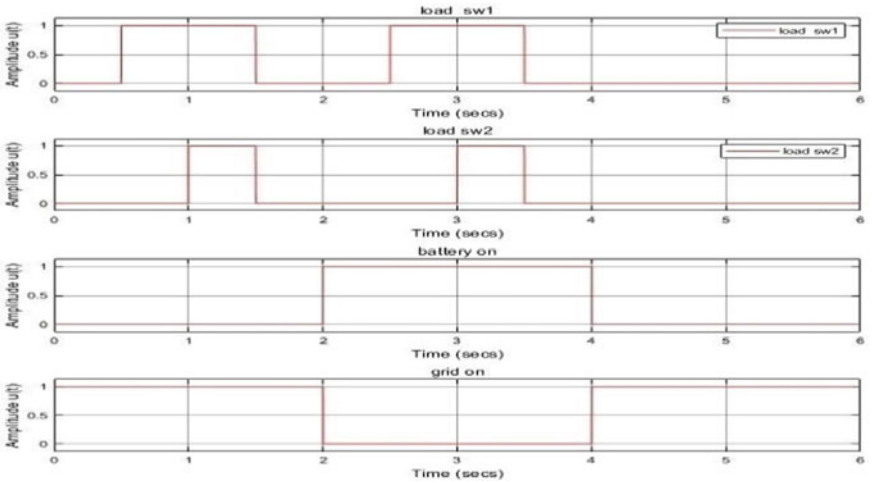

Fig. 12 Results for switching of load 1, load 2, battery, grid in simulation

demand is more than supply. Simulink blocks of VSC controller, battery controller, voltage source controller, nonlinear load block, bidirectional converter were also used during the simulation, but they are not shown in this research paper of the above presented Simulink model [26, 27].

4 Simulation Results

Figure 12 shows the various results of amplitude variation with respect to time for load 1, load 2, battery, and grid during switch ON condition. Variation of power with time when solar PV is connected to the grid along with load 1, load 2, and battery is shown in Fig. 13. Variation of primary and secondary voltage and current with respect to time during grid-connected condition is shown in Fig. 14. PV voltage, current, and DC voltage associated with the panel are plotted with respect to time is shown in Fig. 15.

5 Discussion and Conclusion

The research paper successfully implemented the artificial neural network technique for extracting the maximum power from the photovoltaic system connected to the grid under normal conditions but varying irradiation using a DC-DC boost converter. The best dynamic performance is given by ANN as compared to other MPPT techniques like P and O and InCond even under varying atmospheric conditions. During

nonuniform shading, the duty cycle modification method is used for changing the power while using ANN. The performance of ANN is far superior because of its training and prior input information about the possible maximum power point for tracking rather than tracking the variation in MPP while using other techniques. It has been observed that the maximum power tracked by the artificial neural network-based maximum power point tracker is 474.7 Watts with an efficiency of 94.4%.

The ripples obtained in the ANN model for current and voltage associated with the PV are very much less as compared to other MPP techniques. The variation of amplitude, power, voltage, and current with respect to time is observed in the research paper. It can be confidently concluded that the ANN technique, as compared to other techniques, is the best technique which provides highest efficiency and power generation because of its ability to track the maximum power point of a solar PV accurately even when the entire system is connected to the grid.

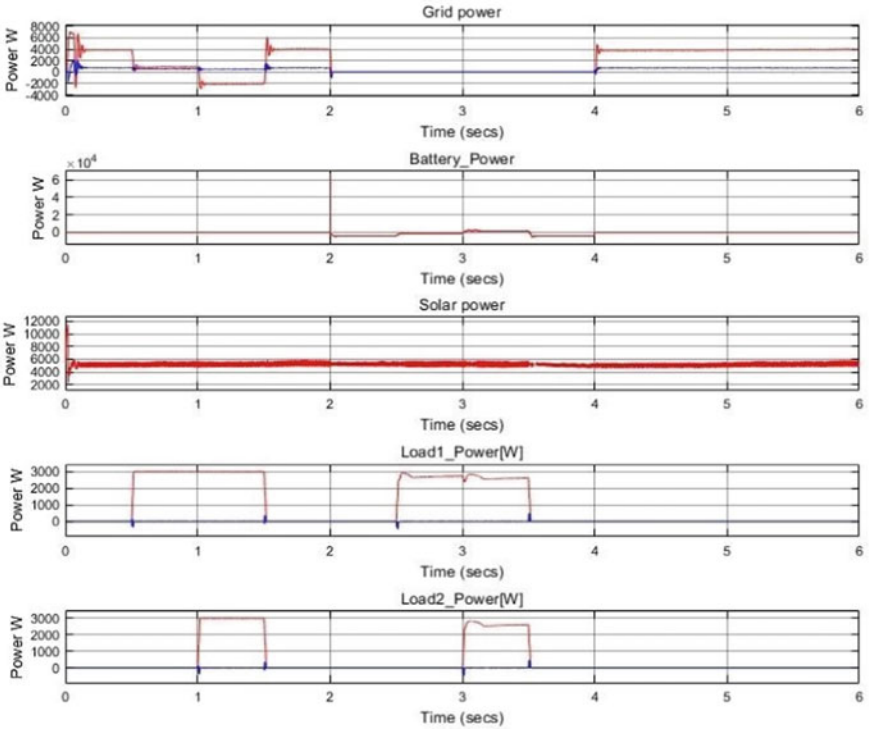

Fig. 13 Result for grid power, solar power, battery power, load-1 power, load-2 power

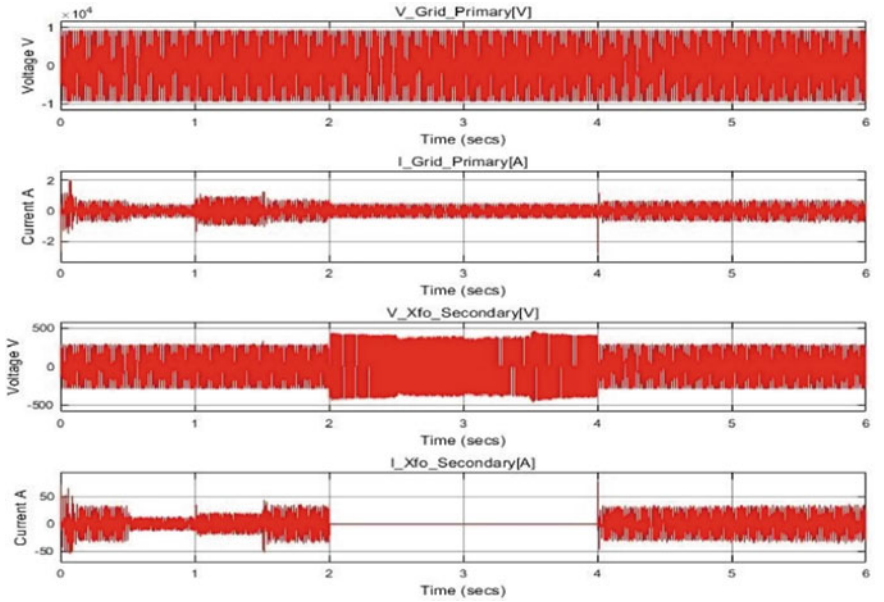

Fig. 14 Grid condition

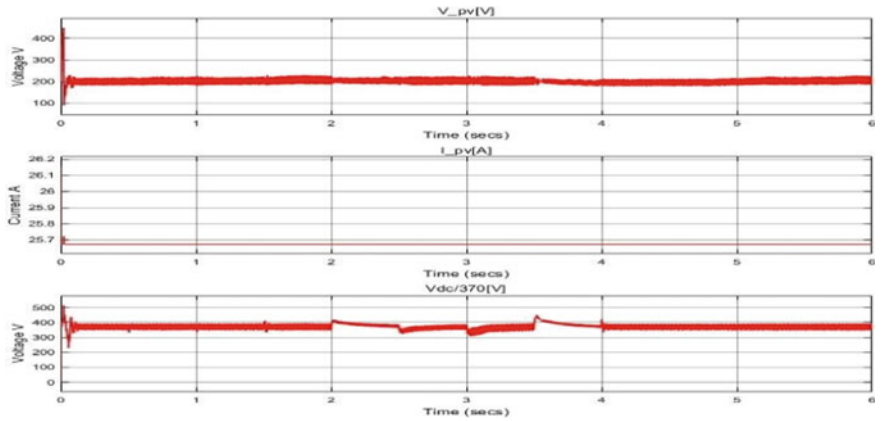

Fig. 15 Grid condition (b) PV panel condition

References

1. Andrews A, Scaria R (2019) Three-phase single stage solar PV integrated UPQC. In: 2nd international conference on intelligent computing, instrumentation and control technologies (ICICICT), pp 1130–1135. https://doi.org/10.1109/ICICICT46008.2019.8993163
2. Abu-Zaher M, Atia Y, Abo-Elyousr FK, El-Zohri E (2019) Experimental realization for P&O maximum power point tracking applied for single-stage three-phase grid-connected photovoltaic system. In: 21st international Middle East power systems conference (MEPCON), pp 704–709. https://doi.org/10.1109/MEPCON47431.2019.9008070
3. Bouzguenda M, Shwehdi MH, Mohamedi R, Aldoghan QM (2019) Performance of the 10-kW KFU Grid connected solar photovoltaic station9 Al Hasa9 KSA. In: IEEE international conference on intelligent techniques in control, optimization and signal processing (INCOS), pp 1–4. https://doi.org/10.1109/INCOS45849.2019.8951383
4. Chandran P, Madhura RS, Roselyn JP, Devaraj D, Gopal V, Ravi A (2019) Development of intelligent fuzzy PQ-FRT control strategy for grid-connected solar PV system. In: IEEE international conference on intelligent techniques in control, optimization and signal processing (INCOS), pp 1–5. https://doi.org/10.1109/INCOS45849.2019.8951347
5. Hinsui T, Sangtungtong W (2019) Voltage observer-based control for single-phase grid-connected PV inverter. In: 7th international electrical engineering congress (iEECON), pp 1–4. https://doi.org/10.1109/iEECON45304.2019.8938957
6. Das MSK, Sathyan S (2018) Comparison of control methods for single stage 3-phase grid connected PV system. In: International conference on inventive research in computing applications (ICIRCA), pp 1004–1007. https://doi.org/10.1109/ICIRCA.2018.8597330
7. Chigane K, Ouassaid M (2018) Online control using ANN-PI controller for single stage transformerless grid tied PV system. In: International symposium on advanced electrical and communication technologies (ISAECT), pp 1–6. https://doi.org/10.1109/ISAECT.2018.8618843
8. Gangavarapu S, Verma M, Rathore AK (2020) A novel transformerless single-stage grid-connected solar inverter. IEEE J Emerg Sel Top Power Electron. https://doi.org/10.1109/JESTPE.2020.3007556
9. Chaudhary S, Ahmad Z, Singh SN (2018) Single phase grid interactive solar photovoltaic inverters: a review. In: National power engineering conference (NPEC), pp 1–6. https://doi.org/10.1109/NPEC.2018.8476767
10. Jain S, Agarwal V (2007) A single-stage grid connected inverter topology for solar PV systems with maximum power point tracking. IEEE Trans Power Electron 22(5):1928–1940. https://doi.org/10.1109/TPEL.2007.904202
11. Sampaio LP, Silva SAO, Costa PJS (2019) Integrated zeta inverter applied in a single-phase grid-connected photovoltaic system. In: IEEE 15th Brazilian power electronics conference and 5th IEEE southern power electronics conference (COBEP/SPEC), pp 1–6. https://doi.org/10.1109/COBEP/SPEC44138.2019.9065295
12. Sharma RK, Mishra S, Mudliyar S (2018) Robust state feedback current controller with harmonic compensation for single stage grid connected PV inverter with LCL filter. In: IEEMA engineer infinite conference (eTechNxT), pp 1–6. https://doi.org/10.1109/ETECHNXT.2018.8385280
13. Kumar A, Gupta V, Gupta N, Babu BC (2019) Active power coefficient based control for grid-connected PV systems. In: IEEE 1st international conference on energy, systems and information processing (ICESIP), pp 1–7. https://doi.org/10.1109/ICESIP46348.2019.8938264
14. Alluhaybi K, Batarseh I, Hu H (2020) Comprehensive review and comparison of single-phase grid-tied photovoltaic microinverters. IEEE J Emerg Sel Top Power Electron 8(2):1310–1329. https://doi.org/10.1109/JESTPE.2019.2900413
15. Arab N, Kedjar B, Javadi A, Al-Haddad K (2019) A Multifunctional single-phase grid-integrated residential solar PV systems based on LQR control. IEEE Trans Ind Appl 55(2):2099–2109. https://doi.org/10.1109/TIA.2018.2883551

16. Jain V, Singh B (2019) A multiple improved notch filter-based control for a single-stage PV system tied to a weak grid. IEEE Trans Sustain Energy 10(1):238–247. https://doi.org/10.1109/TSTE.2018.2831704
17. Shah N (2018) Multilevel inverter based single-stage grid connected photovoltaic system using cascaded two-level inverter. In: IEEE international conference on power electronics, drives and energy systems (PEDES), pp 1–6. https://doi.org/10.1109/PEDES.2018.8707445
18. Singh B, Mishra S (2018) Dual mode operational control of single stage PV-battery based microgrid. In: IEEMA engineer infinite conference (eTechNxT), pp 1–5. https://doi.org/10.1109/ETECHNXT.2018.8385379
19. Myneni H, Ganjikunta SK (2020) Energy management and control of single-stage grid-connected solar PV and BES system. IEEE Trans Sustain Energy 11(3):1739–1749. https://doi.org/10.1109/TSTE.2019.2938864
20. Siriwattanasit C, Sangswang A, Naetiladdanon S, Mujjalinvimut E (2018) Single-phase transformerless grid-connected impedance source inverter. In: International electrical engineering congress (iEECON), pp 1–4. https://doi.org/10.1109/IEECON.2018.8712223
21. Singh M, Singh O, Kumar A (2019) Renewable energy sources integration in micro-grid including load patterns. In: 3rd international conference on recent developments in control, automation and power engineering (RDCAPE), pp 88–93. https://doi.org/10.1109/RDCAPE47089.2019.8979036
22. Singh M, Rana V, Ansari MA, Saini B, Singh P (2018) Power quality enhancement to sensitive loads with PV based microgrid system. In: International conference on sustainable energy, electronics, and computing systems (SEEMS), pp 1–6. https://doi.org/10.1109/SEEMS.2018.8687334
23. Kumar TS, Shanrnugam J (2020) Design and anlaysis of CHB inverter by using Pi fuzzy and ANN techniques with grid connected PV system. In: IEEE international conference for innovation in technology (INOCON), pp 1–7. https://doi.org/10.1109/INOCON50539.2020.9298260
24. Bhatia D, Singh A, Arora A (2020) PI and fuzzy logic control of single phase grid connected inverter serving two PV panels. In: IEEE 17th India council international conference (INDICON), pp 1–6. https://doi.org/10.1109/INDICON49873.2020.9342393
25. Chaicharoenaudomrung K, Boontawee T, Pakdeeto J, Areerak K, Areerak K (2021) Single phase grid connected PV system with a non—iterative MPPT. In: 9th international electrical engineering congress (iEECON), pp 57–60. https://doi.org/10.1109/iEECON51072.2021.9440067
26. Singh M, Singh O (2019) Phasor solution of a microgrid to accelerate simulation speed. In: 2nd international conference on advanced computing and software engineering (ICACSE). https://doi.org/10.2139/ssrn.3351025
27. Singh M, Ansari MA, Tripathi P, Wadhwani A (2018) VSC-HVDC transmission system and its dynamic stability analysis. In: International conference on computational and characterization techniques in engineering sciences (CCTES), doi: https://doi.org/10.1109/CCTES.2018.8674095

Linear Regression for Insolation Prediction

Himanshu Priyadarshi, Kulwant Singh, and Ashish Shrivastava

Abstract Solar energy is abundantly available in Jaipur, and one can harvest dividends by building smart energy storage systems based on solar energy. Government and energy utility authorities encourage the citizens as well as organizations for harnessing of solar energy through multiple initiatives and incentives. However, gaining competitive advantage in the domain of energy storage market can be done only when the delivery of energy services is reliable. Commercialization of solar energy cannot be realized to its optimum potential unless the reliability can be matched with the competing energy technologies. Hence, dependable machine learning models are very useful for the prognoses associated with the availability of solar radiation so that the associated energy storage management system can take appropriate corrective actions in wake of insolation variation. The prediction of available solar radiation provides resiliency to the energy storage system. In this work, weather data has been exploratorily correlated with solar radiation, and linear regression has been used as an instance of the multiple prognosis algorithms available, owing to its simplicity for this particular use case. The linear regression tool gives the coefficient of various stochastic weather factors, and with the currently available dataset and tool, mean absolute error of approximately 18% has been reported.

Keywords Insolation · Regression · Energy storage · Machine learning

1 Introduction

Sun is the preeminent source of heat and light and is in fact the primeval source of energy for many types of conventional as well as non-conventional sources of energy. With the focus shifting on the efforts to harness cleaner sources of energy, solar energy has been rediscovered by the modern scientists as a viable source of energy to substitute the rapidly depleting fossil fuels [1, 2]. Fossil fuels like petroleum

H. Priyadarshi · K. Singh · A. Shrivastava (✉)
School of Electrical and Electronics Engineering, Manipal University Jaipur, Jaipur, India
e-mail: rewa.ashish@gmail.com

© The Author(s), under exclusive license to Springer Nature Singapore Pte Ltd. 2022

A. Tripathi et al. (eds.), *Intelligent Computing Techniques for Smart Energy Systems*,
Lecture Notes in Electrical Engineering 862,
https://doi.org/10.1007/978-981-19-0252-9_35

Table 1 Insolation features and prognostics

Factors	Specifications	Nature
Geographic location	Latitudinal, longitudinal, and diurnal changes, altitude with mean sea level as the reference—affects the attenuation	Deterministic
Collector plate	Collector tilt angle or the orientation taking horizontal as the reference	Deterministic
Time of day	Hour angle—represents temporal variation	Deterministic
Time of year	Declination—represents the effect of seasons on insolation	Deterministic
Atmosphere and weather	Ozone layer status, dust, humidity, cloud cover	Non-deterministic

promised nearly instant gratification of the demand with its well-developed supply chain and availability at retail outlets.

In order to match the speed of gratification available with the petroleum sources, renewable solar energy is supported by energy storage technologies. It is by dint of these energy storage technologies that distributed generation is coming closer to its potential. Reliability is an important criterion for any energy technology, and in order to effectively tap the solar energy for energy storage devices, energy storage system designers have to have certain degree of cognizance regarding the predictability of the insolation being harnessed, which also ensures better coordination with power conditioners [3–5].

The factors like latitude and longitude can be considered constant. Altitude over the mean sea level can also be treated as deterministic, although it is subject to variation due to climatic changes stemming from environmental insensitivity of modern civilization. Weather conditions at the locality of reference play a very important role in determining the insolation part of the solar radiation. Expecting a universal mathematical model for mapping the weather conditions with insolation is against common sense, as weather conditions are flickering in nature, because of being governed by the fact how environment responds to the sensitivity or insensitivity of the human civilization. Hence, the requirement for a data-driven approach for insolation prognostics can hardly be overemphasized [6–8]. In this work, linear regression technique [9, 10] has been implemented for predicting the solar radiation (Table 1).

2 Methodology

The data utilized for this work is openly available by dint of Centre for Energy and Environment, Malaviya National Institute of Technology, Jaipur. The first stage of this functional prototype is an android-based application, programmed to capture the message sent by the weather data system through its dedicated module, followed by it the message being archived on Internet-based server, which is finally synchronized

with the cloud database, in a readable format, amenable of being downloaded in comma-separated variable format.

Exploratory data analysis is essential step for data visualization, and this includes data-preprocessing, correlation mapping, and then graphical representation. This could be done either by using MATLAB coding or that of Python. We have used Python coding for the exploratory data analysis. Python follows the philosophy of open-source sharing, and being easy to interpret, it is easy to implementation of application.

Figure 1 illustrates that the solar radiation has increased if the terminal points are compared. The isolation received depends on multiple factors like efficiency of the solar photovoltaic panels and cleanliness levels to name a few. With global awareness regarding harnessing of solar energy, it is but obvious that steps be taken to improve this efficiency at the panel level, as the solar cell efficiency depends on the material technology used, which cannot be altered once the panel is procured. Figure 2 complements Fig. 1 by supplying the wind speed patter over the same span; one could intuitively verify that solar radiation and wind pattern are complementary in nature meaning thereby that a local minima in the solar radiation graph corresponds with the local maxima in the graph of wind pattern.

The mapping of solar radiation with respect to the air temperature, depicted in Fig. 3, shatters the myth that higher temperature accompanies more solar radiation; in fact, the solar radiation is quite normally distributed peaking at nearly 300 K. The mean solar radiation on a monthly basis has been depicted in Fig. 4, which confirms that maximum solar radiation is received in the fourth month of the solar year, whereas it is minimum in August, which witnesses maximum cloud cover during monsoons. The variation of relative humidity on an hourly basis is depicted in Fig. 5.

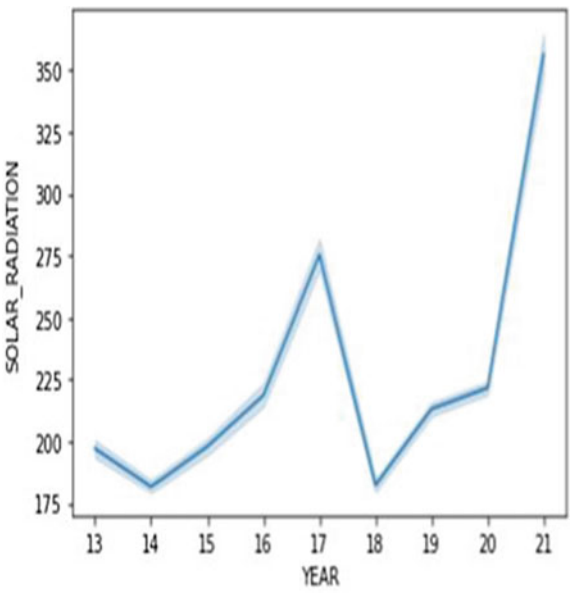

Fig. 1 Variation of insolation at the locality of reference in Jaipur from 2013 to 2021

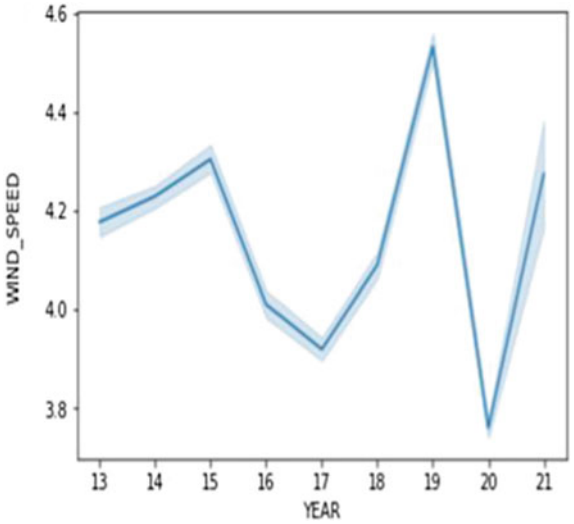

Fig. 2 Variation of wind speed at a locality of reference in Jaipur from 2013 to 2021

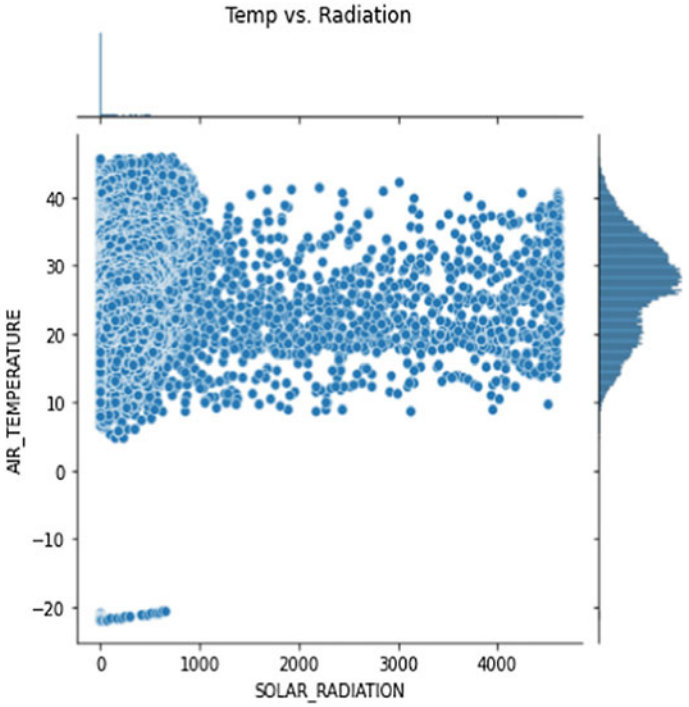

Fig. 3 Mapping of air temperature versus solar radiation received

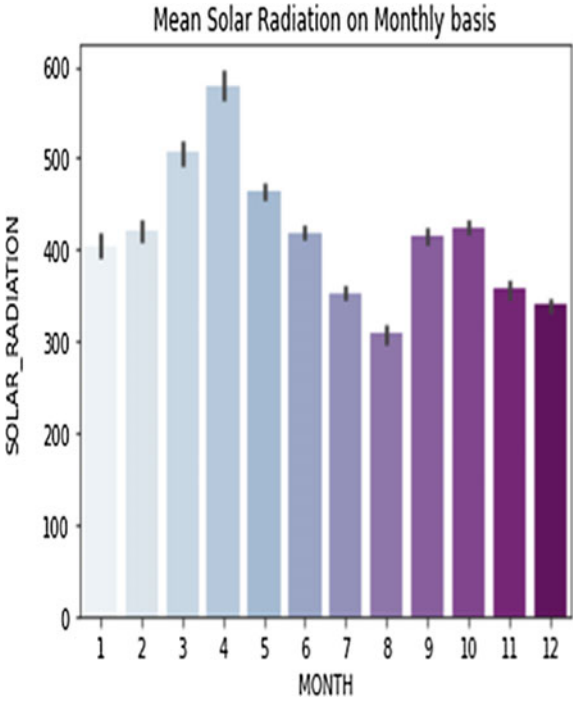

Fig. 4 Variation of average solar radiation received on a monthly basis

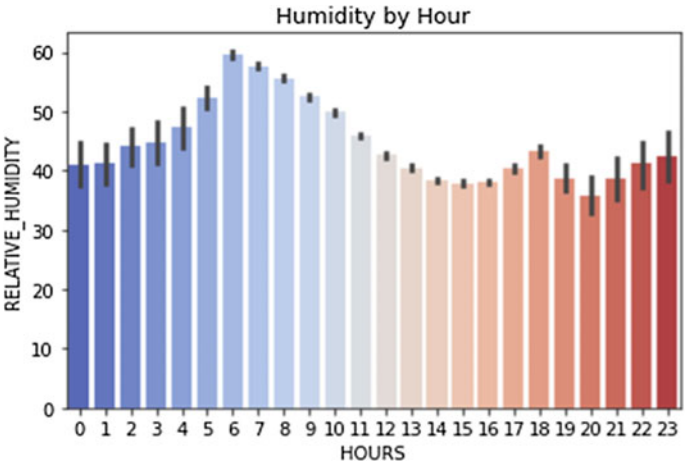

Fig. 5 Variation of relative humidity on an hourly basis

3 Results and Discussion

Machine learning is often projected as a sub-field of artificial intelligence; however, machine learning can arguably be treated as the enabling technology for building models based on data. In our approach, we have tried to build a simple linear model for prognosing solar radiation with the available weather data. In regression, we try to do continuous curve fitting with the given data. The general tendency of conventional procedures is to find the output based on the inputs with a given algorithm; however, with machine learning procedures, the algorithm is learnt by dint of the inputs as well as the output.

The problem of predicting the solar radiation received based on the available data comes under the regression category of supervised machine learning. Linear regression is a simple to implement algorithm, where the available data is trained to find the parameter of the linearized model, which is iteratively updated for getting the optimum value of the loss function using back-propagation. Linear regression has been implemented using appropriate machine learning packages of Python. The various coefficients associated with the linear curve fitting obtained based on a train and test split of 1:3 have been summarized in Table 2. While air temperature has the maximum value of the coefficient, wind direction has the minimum value of the coefficient in the linear regression curve fitting. The extrema of the air temperature exhibit negative coefficient with respect to the target variable, and so do relative humidity as well as minimum relative humidity. Wind speed has a positive coefficient, whereas the direction of the wind has nearly insignificant coefficient.

This linear regression machine learning algorithm gives a mean absolute error of 18.3%, whereas the root mean square error of 35.7% (Fig. 6).

Table 2 Value of coefficients in the linear regression machine learning model

Parameter	Value of the associated coefficient
Air temperature	140.820229
Maximum air temperature	−26.455553
Minimum air temperature	−108.022509
Relative humidity	−7.645195
Maximum relative humidity	9.330326
Minimum relative humidity	−3.464522
Wind speed	9.224988
Wind direction	−0.051011
Rain	−22.598859

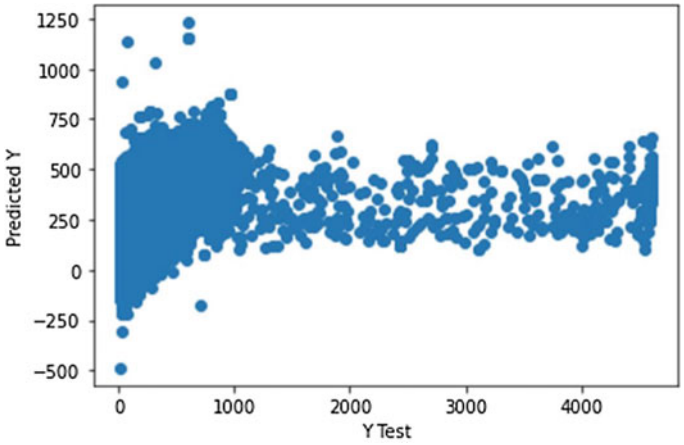

Fig. 6 Comparison of the predicted data with the actual data

4 Conclusion

The need of predictability in energy storage and utilization of insolation to strengthen the marketability of solar energy has been underscored. Weather data obtained from the source mentioned in the foregoing has been explored and visualized to validate the insights available in the literature. This has been followed by a curve-fitting problem in the continuous domain using linear regression. The entire work has been done using openly available resources. By making judicious utilization of resources, one can extend this work further to improve the accuracy of prediction.

Acknowledgements It would be impossible to list the various people who have directly or indirectly contributed to our motivation for contributing in the domain of solar energy. In order to express the essence, we are grateful to our teachers, for it is only by dint of their relentless support that we have developed some motivation for continuous learning. We also take the opportunity to appreciate the broad-mindedness of Centre for Energy and Environment, Malaviya National Institute of Technology, Jaipur, for making the weather data publicly available, and easily accessible in comma-separated variable format.

References

1. Rabl V et al (2020) Energy storage primer. IEEE Power and Energy Society
2. Solanki CS (2015) Solar photovoltaics: fundamentals, technologies and applications, 3rd edn. Prentice Hall India, India
3. Yadav AK, Chnadel SS (2014) Solar radiation prediction using artificial neural network techniques: a review. Renew Sustain Energy Rev 33:772–781. https://doi.org/10.1016/j.rser.2013.08.055

4. Patel RN, Sinha SK (2019) Performance analysis of PV system integrated with boost converter for low power applications. In: Advances in interdisciplinary engineering. Lecture notes in mechanical engineering. Springer, Singapore. https://doi.org/10.1007/978-981-13-6577-5_85
5. Ruchira R, Patel RN, Sinha SK (2021) Optimal sizing of microinverter based PV system for EWS houses. In: 2021 international conference on advances in electrical, computing, communication and sustainable technologies (ICAECT), pp 1–5. https://doi.org/10.1109/ICAECT49130.2021.9392551
6. Patel RN, Mittal A (2014) Programming in MATLAB—a problem solving approach, Pearson India
7. Khodayar M, Mohammadi S, Khodayar ME, Wang J, Liu G (2020) Convolutional graph autoencoder: a generative deep neural network for probabilistic spatio-temporal solar irradiance forecasting. IEEE Trans Sustain Energy 11(2):571–583
8. Boubaker S, Benghanem M, Mellit A, Lefza A, Kahouli O, Kolsi L (2021) Deep neural networks for predicting solar radiation at hail region, Saudi Arabia. IEEE Access 9:36719–36729. https://doi.org/10.1109/ACCESS.2021.3062205
9. Cao Z, Liu L, Markowitch O (2019) Comment on highly efficient linear regression outsourcing to a cloud. IEEE Trans Cloud Comput 7(3):893–893. https://doi.org/10.1109/TCC.2017.2709299
10. Tsakiris MC, Peng L, Conca A, Kneip L, Shi Y, Choi H (2020) An algebraic-geometric approach for linear regression without correspondences. IEEE Trans Inf Theory 66(8):5130–5144. https://doi.org/10.1109/TIT.2020.2977166

A Content-Based Music Recommendation System Using RapidMiner

Neha Sheth, Rohan Agrawal, and Santosh Kumar Vishwakarma

Abstract With the evolution of music information retrieval methods and music exploration technologies, there is enormous data generated on musical structure as well as users' listening habits which can support new applications and innovations in this domain. This paper presents an overview of music recommender systems and explains the various state-of-the-art methodologies used to develop accurate music recommenders that regard both the objective and subjective effects of music on users. It also presents an application of music recommendation, particularly rating prediction and genre-based song recommendation which is implemented in RapidMiner. As a comparative study, we have analyzed user KNN, matrix factorization, and a combined model using user KNN and global average algorithms and evaluated their respective performances. We have found that hybrid recommender systems using combined models perform better than most single model variants. The song recommendation model is further demonstrated, and the ten most similar songs (based on the artist name specified by the user) are returned. Hence, our paper is focused on two central tasks—a brief review of existing methods as well the application of music recommender systems using the data science platform, RapidMiner which provides automation of machine learning tasks, portability, and functionality.

Keywords Recommend system · RapidMiner · Term based model · Supervised learning

1 Introduction

What began as arbitrary vibrations and hymns created without much structure has now evolved through millennia to be finally defined as music, a cultural phenomenon dominating the lives of modern human beings. Music has been imperative since the times of the ancient Greeks who laid the foundations of acoustic theory to modern

N. Sheth · R. Agrawal · S. K. Vishwakarma (✉)
Manipal University Jaipur, Jaipur, India
e-mail: santoshk@jaipur.manipal.edu

© The Author(s), under exclusive license to Springer Nature Singapore Pte Ltd. 2022

A. Tripathi et al. (eds.), *Intelligent Computing Techniques for Smart Energy Systems*,
Lecture Notes in Electrical Engineering 862,
https://doi.org/10.1007/978-981-19-0252-9_36

humans who still continue to analyze the structure of music; it is power to express the complexities of cultural emotion and intricacies of music esthetics.

According to the popular music streaming service Spotify, there are more than 1300 music genres in the world today [1]. Even though the number of popular music genres is limited, the vast variety of arcane genres often highlights a need for relevant music recommendation to users. As online music streaming becomes the most customary method for people to discover new music, streaming services like Spotify, Apple Music, Pandora, and so on are able to collect enormous amounts of data about their users' listening habits and popular cultural trends in music.

This huge amount of data can facilitate a multitude of research and applications, like leveraging machine learning algorithms such as random forest, support vector machines and neural networks, and applications that support development of smart and automatic music recommenders capable of handling this enormous data and connecting all the various components of the system such as the user, the song item, and the various cultural parameters like demographics, diversity of subjective preferences, language, song popularity, and so on. Various notable data science platforms are being used for the purpose of assisting with the data operationalization and optimization cycle, such as XPlenty, DataRobot, RapidMiner, and so on.

Some of the remarkable developments in music recommendation include musical genre classification based on the tone, pitch, rhythm and overall structure of music, automatic playlist creation, fast music discovery, and automatic lyric generation, which are all popular features on music streaming services like Spotify, Apple Music, and Pandora. These developments are a result of intensive research and experimentation with the three main methods of music recommendation, namely content-based recommendation, collaborative filtering methods, and hybrid methods.

There are several challenges faced by music recommendation systems, such as tailoring music recommendations based on user-specific factors such as location, context and intent [2, 3], the cold start problem where the system has insufficient data about a new song item/user registered in the system [4], and data sparsity in terms of ratings and user inputs [5] as well as the intrinsic problem of objectively understanding the abstract effect of music which highly varies from person to person.

A substantial direction to improve upon is to explore the various inherent characteristics associated with music, such as melody, harmony, timbre, and form and to also pay equal attention to the user-subjective psychological, cognitive, and cultural impact of musical preferences. This also includes considering various applications and features that could be included in music recommendations such as playlist continuation, next track recommendation, and song discovery as well as trend-based recommendations [3].

In this paper, we elaborate the various techniques which have been used in the domain of music recommendation, reviewing the state-of-the-art mechanisms and the advantages and disadvantages of the respective methods in order to furnish an equally objective as well as subjective point of view which is proposed to be used while developing music recommenders. Further, we demonstrate content based as well as collaborative filtering models, in the domains of rating prediction and item

recommendation. Our project is intended as an application of music recommender systems using the innovative and automated capabilities of the RapidMiner software.

We perform prediction of ratings for users based on memory-based collaborative systems, wherein user ratings data from the LastFM's API [6] are used to find similarity between user preferences. Various methods such as user-based KNN, matrix factorization, and ensemble of methods are employed, and their respective performance vectors are compared. We deploy our model on RapidMiner and predict the ratings. Further, we have used Python to demonstrate a song and artist recommendation based on genre similarity.

The rest of the paper is organized as follows: Sect. 2 presents the literature review and various state-of-the-art mechanisms related to the present work in all the three types of recommendation techniques. Section 3 explains the methodology adopted to build the rating prediction and item recommendation models with a comparative study of algorithms used. Section 4 describes the results obtained with the comparison of performances of the various methods used. Finally, Sect. 5 concludes our paper with a brief summary.

2 Literature Review

The task of music recommendation can be distributed into three major parts—users, items, and user-item matching. User profiling, which includes data like geographic region, age, life style, interests, and gender can help perform user modeling in order to efficiently differentiate user's music tastes. The preferences in music of users is the main aim of performing user modeling; differences in user profiles can be found. Item profiling has three kinds of metadata—cultural, acoustic, and editorial. A matching algorithm is generally used to recommend personalized music to the listeners automatically. Broadly speaking, these algorithms can be collaborative, content based or hybrid. Artist similarity is one of the central themes around algorithms.

Content-Based Music Recommendation—information used in content-based MRs describes musical items/features and encompasses metadata as well as information that may be extracted from sources such as metadata and audio content. Metadata come in many forms, existing research such as [7] use social tags, created by users who provide text annotations for an item-tags. They use tags from Last.fm in order to assess similarity using weight vectors, allowing them to successfully resolve the vector sparsity problem, with the help of latent semantic analysis. Manual annotation provides in depth summaries pertaining to the content though limited in its structure despite the quality of products [8].

Web content mining uses text processing techniques, keyword annotations found on Web pages, lyrical database, RSS feeds [9] related to music. Artist similarity is the common thread connecting the existing approaches; [10, 11] use limited but high quality information from Web sites like Last.fm, Wikipedia to retrieve keywords and social tags; extracted keywords are used to predict the similarity ratings between various artists. Audio content includes features like (tonal, timbral, and temporal) and

auto-semantic annotations. Analysis of such data is acclaimed because it reveals the music consumption without being vulnerable to popularity bias. The user satisfaction of models based on such approaches was, at best, average [12]. Later, approaches adopted binary classification, using algorithms like KNN [13] and SVMs as well several Gaussian models [14]. In order to tackle discrepancies like overlooking user's information, high-level semantic concepts or abstraction (moods, genres) has proven to be useful, often deploying machine learning in order to predict annotation audio [15].

Collaborative Filtering—collaborative filtering methods predict users' preferences depending on the variety of items they have liked so far as well as depending on what users with similar taste liked/disliked. CF is broadly segregated as item based and user based. Item-based approach works on the notion that certain items are frequently put together; users who bought '*A*' also bought '*B*'. User-based approach adopts the fact that recommendations user is given are derived from the ratings provided to them from similar users. A key addition to the approach of using item-user matrix as done usually with the collaborative filtering techniques is to use context information, which essentially encompasses information that plays a role in affecting the user-system interaction such as mood, time, and location.

Existing approaches such as [16] explore the impact of attributes such as location and weather on user's preferences. An initial stage of classification and recommendation centers around using genre data. One major problem with the existing methods is the heavy computing process. [17] analyzed the issue using KNN and Naïve Bayes algorithms and found the classification performance by KNN to be 77.18% and NB 76% proposing better extraction and results with better managed data. As common as collaborative filtering approaches are, they do suffer from certain problems, such as cold start, sparsity, and scalability, which restrict the effectiveness of the models. However, the new proposed methods and approaches are circumventing the prevalent, aforementioned, and widespread obstacles. [18] focuses on solving some of the most prominent problems—sparsity and cold start. Cold start problem is improved upon by finding similarity among rated songs by registered users and using hash maps. The Sparsity problem is handled by finding correlation between items, using implicit as well as explicit data of rated songs. The proposed approach improved the precision value by 37%, recall by 10%, and F-measure by as much as 17% when juxtaposed with previous approaches. Categorization of artist and user is done in order to determine the extent to which a user falls in the gray sheep category. The clusters are intentionally created as fuzzy so as to not isolate the gray sheep users. This method significantly outperforms the other collaborative filtering approaches. Metadata are often considered to be a better model when dealing with cold start scenarios [19]. Some of the most efficient models, unsurprisingly, are found to be the ones which combine the prowess of the aforementioned collaborative and content-based models, known as hybrid models.

Hybrid Models—these models combine multiple recommender techniques, often collaborative filtering and content-based recommendation techniques, which enhance the features of collaborative filtering by taking into account the ratings of users and the features of content-based models by taking into account the item

attributes. There are several methods which can be used to achieve hybridization that can be categorized in switching, mixed, weighted, cascade, meta-level methods to name a few. [20] proposed a music recommender that puts into use a latent factor model for content-based recommendations and uses the implementation of CNN. In order to obtain 50-dimensional latest vectors, weighted matrix factorization was implemented on The Million Song Dataset [21]. Netflix, albeit not a music recommender, is a paragon of how efficient hybrid recommenders can be. It recommends the searching habits of users in a similar category (collaborative filtering) with their watching history as well as the movies which tend to share the same characteristics (content based).

The approach adopted by [22] centers around running and walking; the system proposed by the authors can adapt the music by matching the user's steps per minute to beats per minute of the music track. Wang et al. Baltrunas et al. [23] propose that driving music exploits ratings specifically assigned to contextual conditions such as—traffic and weather. Matrix factorization is extended to collaborative filtering by adding parameters for every pairwise combination and musical genre to model. This helps to incorporate user-related factors (mood, sleepiness) and environmental factors (weather, traffic) for rating prediction. Using stochastic gradient descent, they were able to decrease the mean absolute error because of contextual factors.

3 Methodology

We have implemented various approaches and utilized the data processing features of RapidMiner as well as Python to compare the performance vectors of various recommendation methods. We particularly focus on collaborative filtering and genre-based recommendation methods. For collaborative filtering, we use data provided by the LastFM API's user.getRecentTracks() method [6]. For content-based filtering using genres, we use data scraped from Every Noise at Once [7].

3.1 Collaborative Filtering—Rating Prediction

The recommendations extension in RapidMiner has three main capabilities for process development—item recommendation, rating prediction, and recommender performance.

Data Preprocessing—our original dataset consists of ratings for about a 1000 users' listening habits. We use a sample dataset of 50 users to build our model. Further, we use two other test cases of 50 users each to test our model performances.

Firstly, data preprocessing is done in order to normalize the value of play counts, which is the number of times an artist's song is played by a user. We make a data frame with a ratings attribute which is calculated by normalizing the play counts to a value between 0 and 5, which is the range of the respective ratings. Then,

we use RapidMiner and retrieve our preprocessed dataset. The data roles like user identification, item identification and rating as label of the data are set using the set role operator.

Splitting Data—we split our data using the split data operator with training size of 80% and testing size of 20%. The partition parameter is set for this purpose, the ratio being 0.8 and 0.2.

Model and Evaluation—the training set is modeled using three methods— KNN, matrix factorization as well as a combined model using user KNN and global average. We use the testing set to apply to our pretrained model using the apply model (Ratings Prediction) operator and evaluate the performance of our predictions. The performance vector computes the rating prediction error methods, namely root mean square error (RMSE), mean absolute error (MAE) as well as normalized mean absolute error (NMAE).

A. ***User KNN model***—the user KNN model is built with the number of neighbors as 10. The minimal rating is 0, and the range of our ratings is specified as 5. We use Pearson correlation to compute the similarity. The user KNN method finds the k ($k = 10$) most similar users who rated an artist to find the mean similarity score. We deploy this model on our training set of 50 user samples. Further, we use 2 test cases of 50 users each to test the model. The error rates of each respective testing set are observed and found to be in a common range of values.
B. ***Matrix Factorization***—we also use matrix factorization with ratings range parameter as 5. This method factorizes the observed rating values using a factor matrix for users and items as well. It expresses the users and artists as combinations of different amounts of each other. The learning rate used is 0.01.
C. ***Combined Model***—finally, we investigate different variants of methods in order to compute their respective errors. We have particularly explored an ensemble of methods, wherein we have multiplied the training data using the multiply operator in order to make independent copies of the data to train it using the models user KNN and global average. The global average operator computes the average rating value over all the ratings for accurate prediction. The models are combined using the model combiner operator and finally applied on the test data. The result obtained is a minor improvement to the previous models. The workflow of the process is shown in Fig. 1.

3.2 Content-Based Song Recommendation

We have used Python to develop a genre similarity-based recommender system and demonstrated the functioning in a single-page Web application using the Python's open-source data app framework, streamlit. Using the machine learning capabilities of sklearn, we are able to provide suitable recommendations to users after they select a song or an artist from a corpus of about 10,000 song-artist pairs obtained from

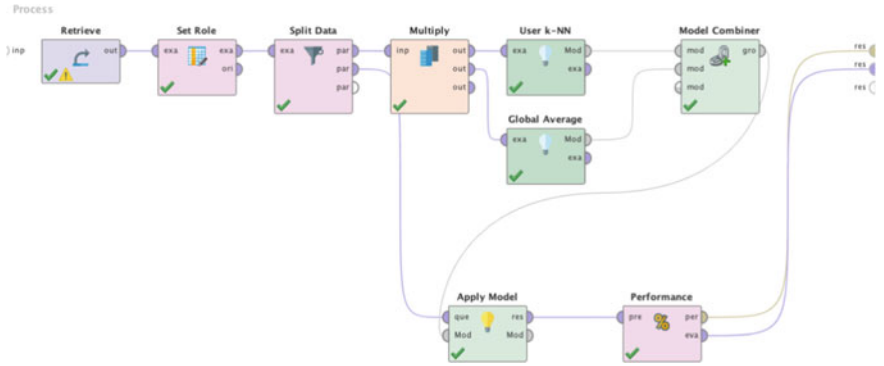

Fig. 1 Workflow of combined model

Every Noise at Once Web site. The user can get up to 10 song recommendations based on the song name or artist name they type.

The music genres dataset used has 1494 genres, with each genre containing 200 songs each. We have filtered the genres to include about 120 popular genres. The genre list is alterable as per the need. The workflow is divided into several steps as described below:

Data Preprocessing—we clean and preprocess the dataset in order to fill the missing values, removing noisy data, and also reducing the size of the dataset to remove redundant parts. Then, we combine the useful features like artist name, song name, and genre in order to make a new column, 'combined features'. This column is used to find similarity between genres.

Feature Extraction—in order to perform feature extraction, we use CountVectorizer() to convert the words to a vector of token counts. This produces a sparse representation of the counts as a matrix which can be further processed. It helps us tokenize our words as well as create a kind of vocabulary of known words.

Computing similarity—we then compute the similarity between the token vectors/matrices of the respective combined features using cosine similarity. This method computes the similarity as a normalized dot product of the respective song and its combined genre features. This matrix is saved as a data frame which is to be used by our streamlit app in order to query the required recommendations.

Interactive streamlit demonstration—we use the capabilities of streamlit to create a single-page interactive application. The main challenge here was the fast access of recommendations from the huge similarity matrix saved. We cache the data frames in streamlit in order to make this happen so that we don't have to load them every time we want to query an item. Finally, we allow the user to select a song or artist name from the corpus of song-artist pairs. Based on the selection, a list of ten most similar songs is produced.

The flowchart of our model is illustrated in Fig. 2

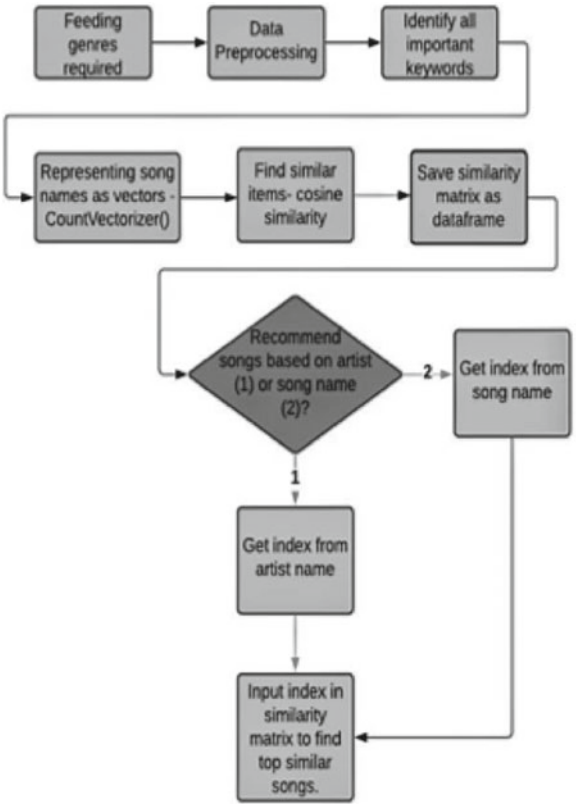

Fig. 2 Flowchart of genre-based music recommender

4 Results and Discussions

Our project comprises two main parts—rating prediction and item recommendation. We have performed rating prediction using the collaborative filtering methods in RapidMiner. The results are obtained as respective error rates in three cases. We can compare the results as follows (Table 1).

We have used several test cases to compare the error rates in order to evaluate the performance of our model. We have found that the error rates in testing data are quite similar to that of training data, which shows that there is no overfitting in the model.

Table 1 Comparison of models for rating prediction

Algorithm	RMSE	MAE	NMAE
User KNN	0.392	0.165	0.041
Matrix factorization	0.760	0.610	0.153
Combined—User KNN and global average	0.354	0.156	0.031

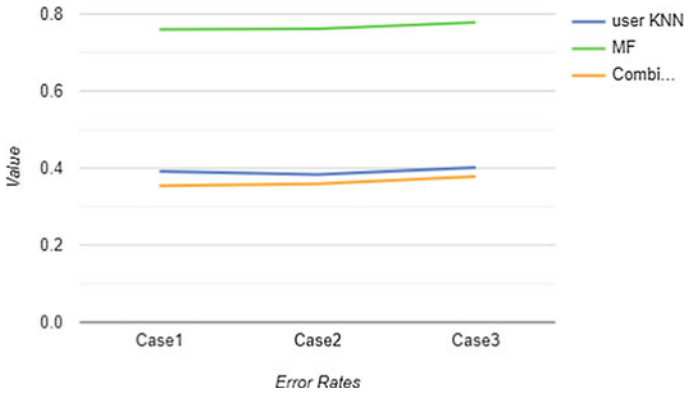

Fig. 3 Comparison of error rates in various test cases

We also find that matrix factorization has the least accuracy and highest error rate among all the models used. User KNN as well as the combined model have error rates in a common range.

We have further compared the root mean square errors of the respective test cases (Fig. 3).

Further, we have demonstrated a song recommendation method in Python which is based on the genre, song, and artist name of the respective songs. The results are displayed using a single-page app. Here, we have recommended songs to the user based on the artist name selected (Fig. 4).

There are some approaches which have adopted similar algorithms for assembling their music recommendation systems, such as the approach adopted by [24], which aims at improving the general fallacies when using KNN for recommendation by assembling a new method called KNN-improved algorithm which essentially involves adding baseline algorithm as well as using mean instead of direct rating values. This successfully results in reducing the rate of error and thereby providing better recommendations. The method yielded an improved run time (approximately 4 s faster than KNN) and comparatively better results when evaluated using RMSE and MAE. The authors in [25] use a matrix factorization technique called as singular value decomposition (SVD) in order to tackle sparsity of user ratings in item-based collaborative filtering by performing dimensionality reduction on Last.fm dataset. The algorithm is applied to the user-item matrix by taking threshold values ranging from 0.1, 0.15, and so on up to 0.4. For evaluation, the threshold values were plotted against precision, and it was found that precision value of the proposed method decreased with an increase in threshold value.

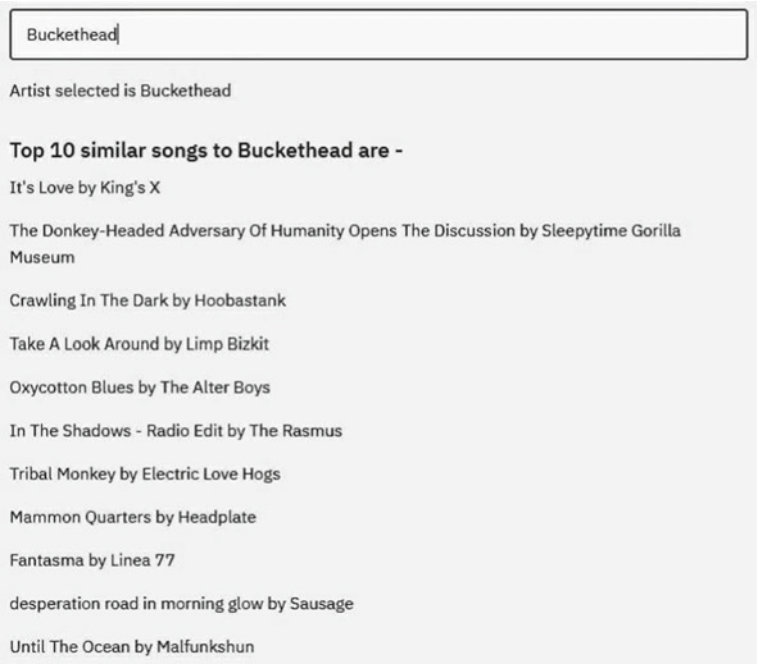

Fig. 4 Recommended songs based on artist name

5 Conclusion

Our paper is focused on two central topics—a brief review of existing methods as well the application of music recommender systems using the data science platform, RapidMiner which provides automation of machine learning tasks, portability, and functionality.

We investigate the myriad of methods used in recommender systems today based on the type of input features of data and compare the various state-of-the-art mechanisms used by the popular recommenders of Spotify, Apple Music, Pandora, and so on. Further, we also develop an application of music recommendation system focused on two tasks—rating prediction and item recommendation.

The rating prediction task is performed in RapidMiner using three operators, user K-NN, matrix factorization and a combined model using user KNN and global average. The respective performance vectors are compared to conclude that a model using combined capabilities of user KNN and global average ratings has an improved performance and lower error rate.

The song recommendation task focuses on genre-based recommendation, wherein similarities between artists and songs are computed based on the genre. The ten most similar songs are returned based on the artist or song name specified by the user.

We conclude that hybrid recommendation systems using combined models are found to perform better than single algorithm models. With the progress in computing capabilities, we hope that more research focuses on developing applications of music recommendation on data science platforms in order to help not just multinational companies but also growing businesses and startups to develop better recommendation engines that are portable and extensible.

References

1. Ivan L, Cara R (2017) Ask wonder, how many genres are there? https://askwonder.com/research/music-genres-there-ovchwa91d
2. Schedl M, Zamani H, Chen CW, Deldjoo Y, Elahi M (2018) Current challenges and visions in music recommender systems research. Int J Multimedia Inf Retrieval 7(2):95–116
3. Kamehkhosh I (2017) Advances in next-track music recommendation. Diss
4. Wikipedia contributors (2021) Recommender system. Wikipedia, the free encyclopedia. Wikipedia, the free encyclopedia, 1 July 2021. Web
5. Goyani M, Neha C (2020) A review of movie recommendation system. ELCVIA: Electron Lett Comput Vision Image Anal 19(3):18–37. https://raco.cat/index.php/ELCVIA/article/view/373942
6. Segura-Tinoco A, Benavides FA (2019) Recommender systems for LastFM. Github. https://github.com/ansegura7/RS_CF_LastFm
7. Levy M, Sandler M (2008) Learning latent semantic models for music from social tags. J New Music Res 37(2):137–150
8. Bogdanov D, Haro M, Fuhrmann F, Xambó A, Gómez E, Herrera P (2013) Semantic audio content-based music recommendation and visualization based on user preference examples. Inf Process Manage 49(1):13–33 (2013)
9. Celma O, Ramírez M, Herrera P (2005) FOAFing the music: a music recommendation system based on RSS feeds and user preferences. In: International conference on music information retrieval (ISMIR'05)
10. McFee B, Lanckriet GR (2011) Learning multi-modal similarity. J Mach Learn Res 12:491–523
11. Turnbull DR, Barrington L, Lanckriet G, Yazdani M (2009) Combining audio content and social context for semantic music discovery. In: Proceedings of the 32nd international ACMSIGIR conference on Research and development in information retrieval. ACM, pp 387–394
12. Grimaldi M, Cunningham P (2004) Experimenting with music taste prediction by user profiling. In: ACM SIGMM international workshop on multimedia information retrieval (MIR'04), pp 173–180
13. Moh Y, Orbanz P, Buhmann JM (2008) Music preference learning with partial information. In: IEEE International conferences on acoustics, speech and signal processing (ICASSP'08), pp 2021–2024
14. Barrington L, Oda R, Lanckriet G (2009) Smarter than genius? Human evaluation of music recommender systems.In: Proceedings of the 10th international conference on music information retrieval (ISMIR'09), pp 357–362
15. Herrera P, Resa Z, Sordo M (2010) Rocking around the clock eight days a week: an exploration of temporal patterns of music listening. In: ACM Conferences on recommender systems. Workshop on music recommendation and discovery (Womrad 2010), pp 7–10
16. Reddy S, Mascia J (2006) Lifetrak: music in tune with your life. In: Proceedings of the 1st ACM international workshop on human-centered multimedia (HCM), pp 25–34
17. Ignatius Moses Setiadi DR et al (2020) Comparison of SVM, KNN, and NB classifier for genre music classification based on metadata. In: 2020 international seminar on application for technology of information and communication (iSemantic), 2020, pp 12–16. https://doi.org/10.1109/iSemantic50169.2020.9234199

18. Mohamed MH, Khafagy MH, Elbeh H, Abdalla AM (2019) Sparsity and cold start recommendation system challenges solved by hybrid feedback 12:2734–2741
19. Bogdanov D, Herrera P (2012) Taking advantage of editorial metadata to recommend music. In: International symposium on computer music modeling and retrieval (CMMR'12)
20. Van den Oord A, Dieleman S, Schrauwen B (2013) Deep content-based music recommendation. Adv Neural Inf Process Syst 26; Burges C et al (ed) (2013) Neural information processing systems foundation (NIPS), vol 26, Lake Tahoe, NV, USA
21. Bertin-Mahieux T, Ellis DP, Whitman B, Lamere P (2011) The million song dataset. In: Proceedings of the 12th international conference on music information retrieval (ISMIR 2011), pp 591–596
22. Elliott GT, Tomlinson B (2006) Personalsoundtrack: context-aware playlists that adapt to user-pace. In: CHI '06: CHI '06 extended abstracts on human factors in computing systems, pp 736–741. ACM, New York, NY, USA (2006)
23. Baltrunas L, Kaminskas M, Ludwig B, Moling O, Ricci F, Lüke KH, Schwaiger R (2011) InCarMusic: context-aware music recommendations in a car. In: International conference on electronic commerce and web technologies (EC-Web). Toulouse, France
24. Li G, Zhang J (2018) Music personalized recommendation system based on improved KNN algorithm. In: 2018 IEEE 3rd conference on advanced information technology, electronic and automation control (IAEAC), 2018, pp 777–781. https://doi.org/10.1109/IAEAC.2018.8577483
25. Sunitha Reddy M, Adilakshmi T (2014) Music recommendation system based on matrix factorization technique –SVD. In: 2014 international conference on computer communication and informatics, 2014, pp 1–6. https://doi.org/10.1109/ICCCI.2014.6921744

Liveness Detection with Convolutional Neural Network Algorithm

Ronak Mundra, Avireni Srinivasulu, Cristian Ravariu, and Appasani Bhargav

Abstract Face acknowledgment is normally used in biometric approach. Face acknowledgment innovation has grown quickly lately and it is more straightforward, easy to use and advantageous contrasted with different strategies. This turning out to be more common than any time in recent memory. From face acknowledgment on your iPhone/cell phone, to confront acknowledgment for mass reconnaissance in China, face acknowledgment frameworks are being used all over. Yet, face acknowledgment frameworks are defenseless against parody assaults made by non-genuine countenances. It is a simple method to parody face acknowledgment frameworks by facial pictures, for example, representation photos. A protected framework needs liveness location to prepare for such satirizing. We have fostered a noticing framework for hostile to satirizing in face acknowledgment frameworks utilizing an essential equipment gear. We have foster arrangement of liveness discovery utilizing convolutional neural network (CNN) algorithm.

Keywords Convolutional neural network · Face detection · Facial pictures · Liveness discovery

R. Mundra
Department of Electronics and Communication Engineering, JECRC University, Jaipur, India

A. Srinivasulu (✉)
Faculty of Engineering and Technology, JECRC University, Jaipur 303905, India
e-mail: avireni@ieee.org

Faculty of Engineering and Technology, K. R. Mangalam University, Gurugram 122103, India

C. Ravariu
Faculty of Electronics ETTI, Politehnica University of Bucharest, Bucharest, Romania
e-mail: cristian.ravariu@upb.ro

A. Bhargav
School of Electronics Engineering, Kalinga Institute of Industrial Technology, Bhubaneswar, India
e-mail: bhargav.appasanifet@kiit.ac.in

© The Author(s), under exclusive license to Springer Nature Singapore Pte Ltd. 2022

A. Tripathi et al. (eds.), *Intelligent Computing Techniques for Smart Energy Systems*,
Lecture Notes in Electrical Engineering 862,
https://doi.org/10.1007/978-981-19-0252-9_37

1 Introduction

The overall population has gigantic requirement for safety efforts against parody assault. Biometrics is the quickest developing portion of such security industry. A portion of the recognizable strategies for ID are facial acknowledgment, unique mark acknowledgment, penmanship confirmation, hand math, retinal and iris scanner. Among these procedures, the one which has grown quickly lately is face acknowledgment innovation and it is more straightforward, easy to use and helpful contrasted with different strategies. Accordingly, it has been applied to different security frameworks [1–5]. Be that as it may, as a general rule, face acknowledgment calculations cannot separate "Real" face from "not real" face that will become a security issue. It is a simple method to parody face acknowledgment frameworks by facial pictures, for example, representation photos. To prepare for such caricaturing, a protected framework needs liveness recognition. The biometrics is advancement of setting up the character of an individual ward on the real time or social attributes of the person [6–10]. The meaning of biometrics in current culture has been supported by the necessity for colossal degree character the board structures whose value depends upon the exact deduction of an individual's character on the arrangement of various applications. A few instances of these applications incorporate sharing arranged PC assets, conceding admittance to atomic offices, performing distant monetary exchanges or loading up a business flight. The principle undertaking of a security framework is the confirmation of a person's personality. The essential justification this is to keep shams from getting to secured assets. General strategy for security objects are secure passwords and remarkable ID cards instruments, yet these procedures for character can point of fact be lost, hampered or might be taken hence hurt the proposed security. With the assistance of physical and typical properties of people, a biometric construction can offer more unmistakable security for a security framework.

Liveness location has been an exceptionally dynamic exploration subject in finger impression acknowledgment and iris acknowledgment networks lately. In any case, in face acknowledgment, approaches are a lot of restricted to manage this issue. This project is the demonstration of separating the component space into Real and fake one. Frauds will attempt to present an enormous many of satirize biometrics change into framework. In the assistance of liveness location, the presentation of a biometric framework will become more accurate. It is a significant and testing issue which decides the dependability of biometric framework protection from satirizing. In face acknowledgment, the standard assault techniques might be grouped into a few classes. The characterization depends on what check evidence is given to confront confirmation framework, like a taken photograph, taken face photographs, recorded video, 3-D face models with the capacities of squinting and lip moving, 3-D face models with different appearances, etc. [11–13]. Hostile to parody issue ought to be very much addressed before face acknowledgment frameworks could be broadly applied in our everyday life.

In the following area, fascinating face liveness recognition strategy is introduced. Then, at that point, a conversation is introduced referring to the benefits and inconveniences of face liveness recognition approach. At last, an outcomes and end is drawn.

2 Related Work

As the examination express that surface element of genuine and phony face are entirely unexpected. Also, accordingly, surface highlights will assist with separating the phony and a genuine face [14]. Numerous methodologies are appeared which utilized this reality. Evaluation for quality of image is a surface point methodology which expresses that all kind of genuine or satire pictures are diverse in their quality [15]. A wide range of IQA-based procedures are created by creators for show assault [16]. Other surface-based methodology is static [17] and dynamic [18].

Research article [19] proposed a solution on surface antispoofing strategy by utilizing changed DoG sifting procedure, LTP or second LBPV to separate element and afterward support vector machine is utilized in characterization. Photograph fraud informational collection NUAA is utilized in try and accomplishes great exactness result. In [20] plan a procedure for parody discovery. Firstly, SPMT is used for data of neighborhood highlights. Then, at that point TFBD is applied to remove sound system highlight of looks. After that plan a technique which consolidate scanning probe microscopy technique and execute on three informational assortments and got a nice and improved result.

In [3], Mahmood shows an instrument for static look affirmation to deal with the mocking issue. AOS-based technique gaining some colossal experiences point is used to make a scattered picture. A drawn out limit is try to remove the component of corner and internal part of pictures. Right when captured image it is look like in spoof pictures, corner are sharp also with the nose part, eyes and lips points yet evened out on rest portion of face. That is the explanation a tremendous time part is useful to devastate the corners with sharpness. In [21] author showed a new philosophy for this acknowledgment. Fetching of recuperated picture is complete in assessment and transport of Hue channel, and the clouding sway is take placed. Support vector machine is used for portrayal of authentic and non-real face [2, 22–24]. This procedure gives good quality results according to acknowledgment rate. In [22], author showed a solid 3-D model of face affirmation way good computational cost or we can say it reduce this on. The makers uses three headways first pre-treatment of 3-D yield [25–31].

3 Methodology

To keep our venture direct, the liveness finder we are working in this task will zero in on distinctive genuine countenances versus satirize faces on a screen [32–37]. To make this we first need a dataset. To construct the real or non-real dataset:

Put smart phone in selfie mode.
20–25 s short video recorded of myself strolling around.
"Again play that same 20–25-s video, this time confronting Phone toward work area where record the same while playing."
This brought about two model recordings, first for "genuine" faces after that second for "counterfeit/satirize" faces.
Finally, I applied face recognition to the two arrangements of recordings to separate individual face ROIs for the two classes.

Our dataset registry comprises of two different classes of pictures:

When video of mine face is playing on system screen at that point of time a camera focused on display screen for taking fake picture.
Real pictures of me caught from a selfie mode video recording with my smartphone.

Presently, we go with the face finder part, here we use already trained Caffe face marker to discover ROI of faces. Finding and removing ROIs of faces from our preparation dataset. The block diagram for finding face ROI from input video is shown in Fig. 1.

Since we have gotten an opportunity to survey both our underlying dataset and undertaking structure, we should perceive how we can extricate both genuine and phony face pictures from our information recordings.

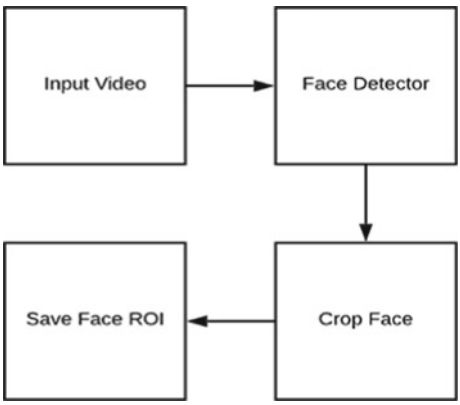

Fig. 1 Face ROI detection block model

Fig. 2 ROIs of face for real dataset

The ultimate objective of this content will fulfill by two things:

dataset/counterfeit/: Store ROIs of faces from the fake.mp4 record.
dataset/counterfeit/: Store ROIs of faces from the real.mp4 record.

Figure 2 shows the real dataset. Using original recording by our system we get this ROIs of face.

For creating fake dataset we play this recording in mobile in front of our system camera and create a new video. Using this new video we collect ROIs of face and store them as a fake dataset. ROIs of face for fake dataset is shown in Fig. 3.

By using these edges, after that we train a profound learning-put together liveness finder with respect to the images. After doing this one we have approx. 150 phony picture and 160 genuine picture dataset in our data set.

3.1 Implementing "LivenessNet"

The subsequent stage is to execute "LivenessNet", our profound studying-based liveness locator. At the center, LivenessNet is in reality a straightforward CNN.

We will be deliberately keeping this organization as shallow and with a couple of boundaries as feasible for these reasons:

To lessen the odds of over fitting on our little dataset.
To sure our project output indicator is quick, fit for running continuously (even on asset compelled gadgets, like the Raspberry Pi).

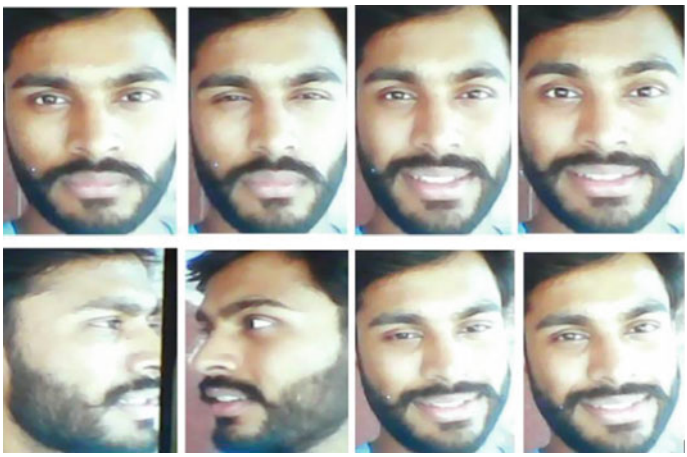

Fig. 3 ROIs of face for fake dataset

3.2 Creating Liveness Detector Training

Now, we have our all dataset of original and spoofed up images and also we have implemented LivenessNet, now we can start training of our network. To train our network, we use both data set real and spoofed as show in Fig. 2. This model consists of many of imports (Fig. 4).

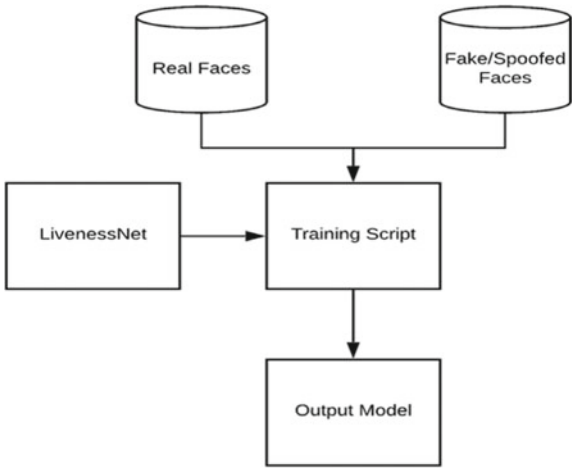

Fig. 4 Creating training model block diagram

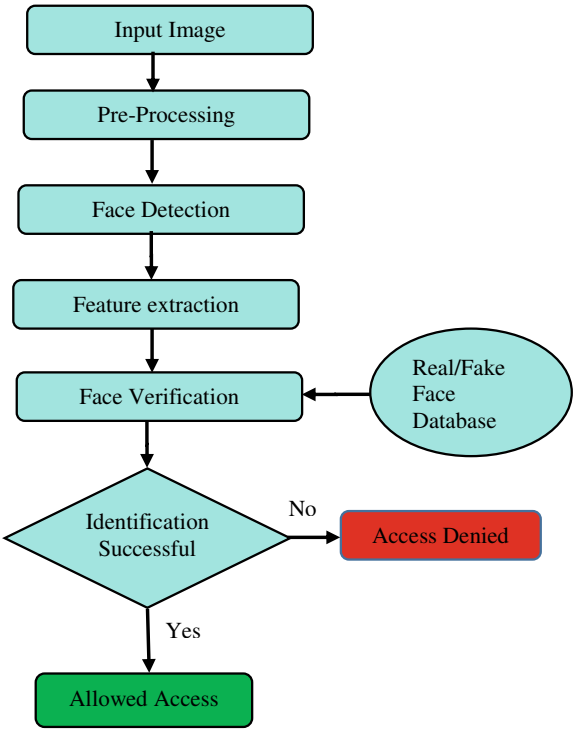

Fig. 5 System flow

Here Matplotlib: Useful for creating training plot.
LivenessNet: This we define in the last section.
train_test_split: one of scikit-learn function used for training and testing of data.

3.3 System Flow

To design liveness detection model [38–42] we create this system flow as shown in Fig. 5.

3.4 Algorithm

Step 1: Input Image and Convolution
Step 2: Pooling
Step 3: Flattening
Step 4: Full Connection

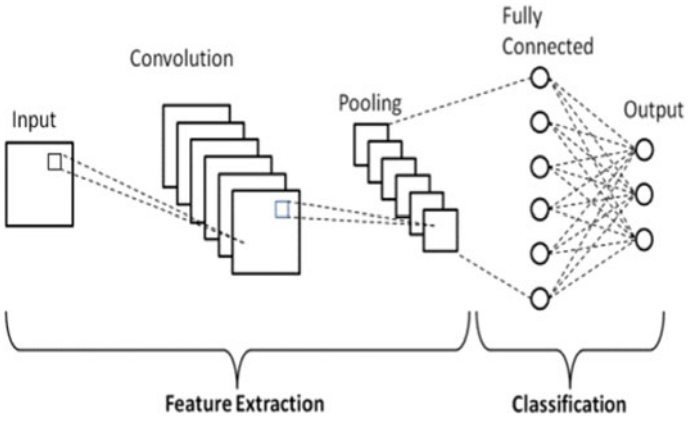

Fig. 6 CNN algorithm [15]

In the initial step of our calculation we utilized convolution activity. In this progression, we use include locators which will be utilized as neural organizations channel. In the following piece of this stage 1 will utilize Rectified Linear Unit or we can say ReLU. It will generate output directly if input side is positive or it will give 0 if our input side is negative.

In the step 2 we used pooling, this technic is used to reduce the size of the featured maps, here size is in terms of dimension.

After step 2 we get data in matrix form so in the flattening process we convert this data into one dimensional array.

Totally connected layer is simply, feed forward neural associations. Totally connected layers structure the several layers in the association. The commitment to the totally related layer is the yield from the last pooling or convolutional layer, which is smoothed and subsequently dealt with into the totally related layer. These steps are diagrammatically shown in Fig. 6.

4 Results

As effectively expressed, preparing is performed with four distinctive degrees of rate for example 50, 60–80%. Table 1 shows the accuracy of three strategies for liveness

Table 1 Accuracy rate on different level of training comparison table

Method	80% training	70% training	60% training	50% training
LBP SVN	89.96	89.91	88.98	88.69
LBP DBN	97.07	97.02	96.93	96.37
CNN	99.49	99.49	98.48	96.80

detection. This accuracy rate of LBP SVM and LBP DBN calculated [13]. The 3rd one that is convolution neural network (CNN) is used in this paper.

It is finished up by looking the table that if the level of preparing diminishes, accuracy rate of detection is additionally diminished in the past technique and yet in proposed strategy, accuracy rate is consistent for all the distinctive levels of preparing for example over 99% after 60% of training. In Fig. 7 we can see the graphical representation of accuracy rate of Table 1.

Real Time Testing Result

We test this program on real time with our data set and it gives satisfactory results. One of the demo of this results you can see in Fig. 8.

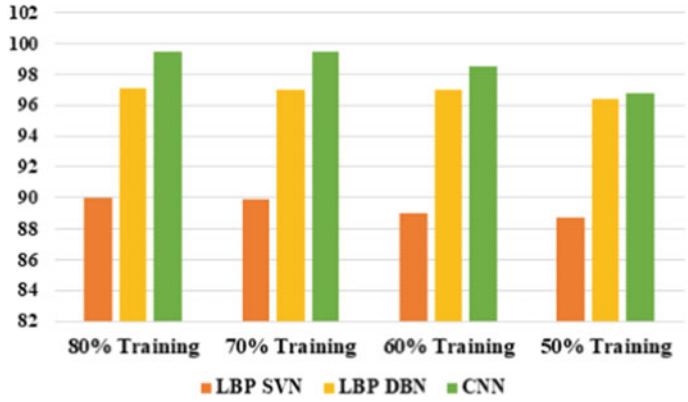

Fig. 7 Accuracy rate chart

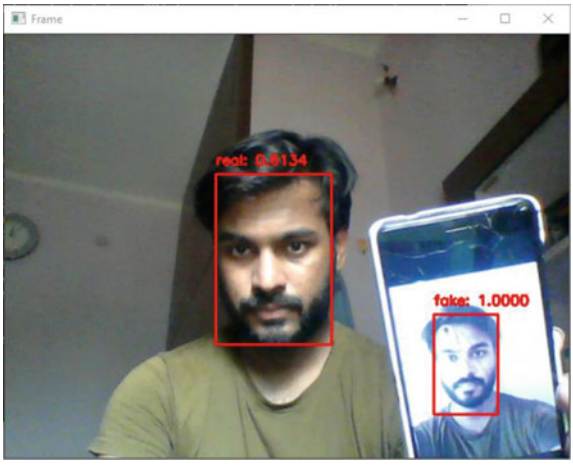

Fig. 8 Live test

5 Conclusion and Future Scope of Work

Here we showed an overwhelming and capable procedure for catching of liveness. As the significant considering convolution neural organization (CNN) approach is utilized in both part extraction and solicitation in this evaluation, this technique performs well when appeared differently in relation to other people. From the test, proposed strategy shows more than 98% distinguishing proof speed of liveness. For work in future, we will endeavor to chip away at the output of other 2 measurement or 3 measurement non-real face dataset and besides endeavor to manage cross dataset. As the significant features are taken out using significant adjusting so this is amazingly drawn out so we try to endeavor to decrease the complexity of time in face affirmation structure in future. One of the principal extensions to this work is basically total extra preparing information, and surprisingly more unequivocally, pictures/follows that are not of just me or yourself.

References

1. Amri A, A'Fifah I, Ismail AR, Zarir AA (2018) Comparative performance of deep learning and machine learning algorithms on imbalanced handwritten data. Int J Adv Comput Sci Appl 9(2):258–264
2. Jie N, Xiongzhu B, Zhong L, Yao W (2014) An improved bilinear deep belief network algorithm for image classification. In: 2014 tenth international conference on computational intelligence and security, pp 189–192. IEEE
3. Alotaibi A, Mahmood A (2016) Enhancing computer vision to detect face spoofing attack utilizing a single frame from a replay video attack using deep learning. In: 2016 international conference on optoelectronics and image processing (ICOIP), pp 1–5. IEEE
4. Shi J, Tomasi C (1994) Good features to track. In: IEEE conference on computer vision and pattern recognition, pp 593–600
5. Galbally J, Marcel S, Fierrez J (2015) Biometric antispoofing methods: a survey in face recognition. IEEE Access 2:1530–1552
6. Boulkenafet Z, Komulainen J, Hadid A (2016) Face spoofing detection using colour texture analysis. IEEE Trans Inform Forens Secur 11(8):1818–1830
7. Li Y, Po L-M, Xu X, Feng L, Yuan F (2016) Face liveness detection and recognition using Shearlet based feature descriptors. In: Proceedings of IEEE international conference on acoustics, speech and signal processing (ICASSP)
8. Zhao X, Lin Y, Heikkilä J (2018) Dynamic texture recognition using volume local binary count patterns with an application to 2D face spoofing detection. IEEE Trans Multimed 20(3)
9. Pan G, Sun L, Wu Z, Lao S (2007) Eyeblink-based anti-spoofing in face recognition from a generic webcamera. In: ICCV 2007. IEEE 11th international conference on computer vision, IEEE, pp 1–8
10. Poh N, Kittler J, Alkoot F (2012) A discriminative parametric approach to video-based score-level fusion for biometric authentication. In: 2012 21st international conference on pattern recognition (ICPR). IEEE, pp 2335–2338
11. Bao W, Li H, Li N, Jiang W (2009) A liveness detection method for face recognition based on optical flow field. In: IASP 2009. International conference on image analysis and signal processing. IEEE, pp 233–236

12. Tronci R, Muntoni D, Fadda G, Pili M, Sirena N, Murgia G, Ristori M, Roli F (2011) Fusion of multiple clues for photo-attack detection in face recognition systems. In: 2011 international joint conference on Biometrics (IJCB). IEEE, pp 1–6
13. de Freitas Pereira T, Komulainen J, Anjos A, De Martino JM, Hadid A, Pietikainen M, Marcel S (2014) Face liveness detection using dynamic texture. EURASIP J Image Video Proces 2014(1):2
14. Raheem EA, Ahmad SMS, Adnan WAW (2019) Insight on face liveness detection: a systematic literature review. Int J Electr Comput Eng 2088–8708:9
15. Pravallika P, Prasad KS (2016) SVM classification for fake biometric detection using image quality assessment: application to iris, face and palm print. In: 2016 international conference on inventive computation technologies (ICICT), vol 1, pp 1–6, IEEE.
16. Galbally J, Marcel S (2014) Face anti-spoofing based on general image quality assessment. In: 2014 22nd international conference on pattern recognition. IEEE, pp 1173–1178
17. Raheem EA, Ahmad SMS (2019) Statistical analysis of image quality measures for face liveness detection. In: 10th international conference on robotics, vision, signal processing and power applications, pp 543–549. Springer, Singapore
18. Arashloo SR, Kittler J, Christmas W (2015) Face spoofing detection based on multiple descriptor fusion using multiscale dynamic binarized statistical image features. IEEE Trans Inf Forensics Secur 10(11):2396–2407
19. Hasan MR, Mahmud SH, Li XY (2019) Face anti-spoofing using texture-based techniques and filtering methods. J Phys Conf Ser 1229(1):012044
20. Song X, Zhao X, Fang L, Lin T (2019) Discriminative representation combinations for accurate face spoofing detection. Pattern Recogn 85:220–231
21. Luan X, Wang H, Ou W, Liu L (2017) Face liveness detection with recaptured feature extraction. In: 2017 international conference on security, pattern analysis, and cybernetics (SPAC), pp 429–432. IEEE
22. Cai Y, Lei Y, Yang M, You Z, Shan S (2019) A fast and robust 3D face recognition approach based on deeply learned face representation. Neurocomputing 363:375–397
23. Chan PP, Liu W, Chen D, Yeung DS, Zhang F, Wang X, Hsu CC (2017) Face liveness detection using a flash against 2D spoofing attack. IEEE Trans Inf Forensics Secur 13(2):521–534
24. Garg S, Mittal S, Kumar P, Athavale VA (2020) DeBNet: multilayer deep network for liveness detection in face recognition system. In: 2020 7th international conference on signal processing and integrated networks (SPIN). https://doi.org/10.1109/SPIN48934.2020.9070853
25. Wen D, Han H, Jain AK (2015) Face spoof detection with image distortion analysis. IEEE Trans Inf Forensics Secur 10(4):746–761
26. https://www.upgrad.com/blog/basic-cnn-architecture/
27. Tan X, Triggs W (2010) Enhanced local texture feature sets for face recognition under difficult lighting conditions. IEEE Trans Image Process 19(6):1635–1650
28. Tirupathireddy A, Sarada M, Srinivasulu A (2021) Energy-efficient approximate adders for DSP applications. Analog Integr Circ Sig Process 107(3):649–657. https://doi.org/10.1007/s10470-020-01768-w
29. Gupta DK, Soni AK, Jha AV, Mishra SK, Bhargav A, Srinivasulu A, Bizon N, Thounthong P (2021) Hybrid gravitational-firefly algorithm based load frequency control for hydrothermal two-area system. Mathematics 9(7):712. https://doi.org/10.3390/math9070712
30. Saini JK, Srinivasulu A, Kumawat R (2019) High-performance low-power 5:2 compressor with 30 CNTFETs using 32 nm technology. Int J Sens Wirel Commun Control 9(4):462–467. https://doi.org/10.2174/2210327909666190206144601
31. Saini JK, Srinivasulu A, Kumawat R (2018) Low power—high speed magnitude comparator circuit using 12 CNFETs. In: Proceedings of the IEEE international SoC design conference, Daegu, Korea, Nov. 12–15, 2018. https://doi.org/10.1109/ISOCC.2018.8649969
32. Shirai M, Soshi T (2021) The role of bodily expression in memory representations of sadness. J Nonverbal Behav 45:367–387. https://doi.org/10.1007/s10919-021-00360-8
33. Sinclair CF, Randolph GW (2021) A thoughtful approach to IONM outcomes reporting. Curr Otorhinolaryngol Rep 9:341–344. https://doi.org/10.1007/s40136-021-00364-4

34. Kamiloğlu RG, Boateng G, Balabanova A et al (2021) Superior communication of positive emotions through nonverbal vocalisations compared to speech prosody. J Nonverbal Behav. https://doi.org/10.1007/s10919-021-00375-1
35. Van Bommel T, Merritt S, Shaffer E et al (2021) Behavioral mimicry and interaction expectations influence affect in interracial interactions. J Nonverbal Behav 45:207–239. https://doi.org/10.1007/s10919-020-00353-z
36. Farley SD (2021) Introduction to the special issue on emotional expression beyond the face: on the importance of multiple channels of communication and context. J Nonverbal Behav. https://doi.org/10.1007/s10919-021-00377-z
37. Minton AR, Mienaltowski A (2021) More than face value: context and age differences in negative emotion discrimination. J Nonverbal Behav. https://doi.org/10.1007/s10919-021-00369-z
38. Lee Y-L, Liang D, Wang W-J, Optimal online liveness fault detection for multilayer cloud computing systems. IEEE Trans Depend Secure Comput. https://doi.org/10.1109/TDSC.2021.3100680
39. Casula R et al (2021) LivDet 2021 fingerprint liveness detection competition—into the unknown. IEEE Int Joint Conf Biometr (IJCB) 2021:1–6. https://doi.org/10.1109/IJCB52358.2021.9484399
40. Purnapatra S et al (2021) Face liveness detection competition (LivDet-Face). IEEE Int Joint Confer Biometr (IJCB) 2021:1–10. https://doi.org/10.1109/IJCB52358.2021.9484359
41. Dave J, Khan A, Gupta B, Gangwar A, Suman S (2021) Human-computer interaction methodology to attain face liveness detection. In: 2021 2nd international conference for emerging technology (INCET), pp 1–4. https://doi.org/10.1109/INCET51464.2021.9456154
42. Mohamed AA, Nagah MM, Abdelmonem MG, Ahmed MY, El-Sahhar M, Ismail FH (2021) Face liveness detection using a sequential CNN technique. In: 2021 IEEE 11th annual computing and communication workshop and conference (CCWC), pp 1483–1488. https://doi.org/10.1109/CCWC51732.2021.9376030

Solar Operated Smart Elevator

G. Shilpa, Syed Sha Sayaaff, Mallari Suresh, and N. M. Suhas

Abstract In day-to-day life, elevator has become a important part. It acts as a transport device that we use every day. Elevator is used to move persons and goods in high-raise buildings. In this paper, the microcontroller AT89S52 is used to control the elevator. This paper documents the results of a microcontroller-based elevator control system. This system is controlled on the voice of any individual in order to assist disabled folks in travelling from one location to another without the assistance of others. Microcontroller is the main part of this system. This system can be used in all automation control applications like remote controllers, automatic automobiles, indicating type measuring instruments, telephone printing machines, hand-held communication devices, and many other day-to-day life products. This project can also be used for security purpose and in emergency conditions, as it is microcontroller-based. The microcontroller used in this project is used for the programming purpose for moving the elevator by storing the data and processing the data according to the user desires. This project is a human–machine communication system. Also in this project, solar power is used to reduce the consumption of electricity from mains. Using solar as alternative power source reduces the electricity bill and power that we get from grids which is largely generated from non-renewable energy source like coal, uranium, fossil fuels, etc.

Keywords Photovoltaic cells · Buck–boost converter · Speech control unit · Arduino Uno microcontroller board

1 Introduction

Lifts are an essential part of our daily lives, especially for people who live in high-rise buildings. It is also necessary in big construction buildings having more number of floors to move from one floor to another. Nowadays, it is becoming a high-status

G. Shilpa (✉) · S. Sha Sayaaff · M. Suresh · N. M. Suhas
Department of Electrical and Electronics Engineering, BMS Institute of Technology and Management, Bengaluru, India
e-mail: shilpag@bmsit.in

© The Author(s), under exclusive license to Springer Nature Singapore Pte Ltd. 2022

A. Tripathi et al. (eds.), *Intelligent Computing Techniques for Smart Energy Systems*, Lecture Notes in Electrical Engineering 862,
https://doi.org/10.1007/978-981-19-0252-9_38

symbol for the shopping malls, hospitals, hotels, colleges, which are having two or more floors. As a result, we are automating it through our project.

Speech recognition model is used to control the elevator [1]. Speech recognition model uses the speech input to control the elevator. The voice control system should understand or know the human voice as input to the speech recognition model which is known as speech recognition. In speech recognition technology, the system will identify the words, but not their meaning, spoken to the voice recognition module by any individual [2]. Speech is a fantastic and ideal way to operate the elevator.

The power used to operate the lift is generated from solar. So, the cost of electricity is reduced. The conversion of solar energy to electrical energy does not produce any products which are harmful to environment. Hence, it is environmental friendly also. During emergency condition when a temporary interruption of power supply happens, it can be compensated by the solar power converted into DC using buck–boost converter.

A study of speech recognition N [3–5] focussed on the many forms of speech recognition technologies that have been created in recent years and how they operate. The researcher has gone through numerous different types of words, speaker models, and other approaches for speech recognition systems, giving a basic knowledge of the system.

'Tutorial on system organization for voice understanding', by Reddy and Erdmann [6], covered a wide range of speech recognition concepts and the importance of understanding the distinctions between them. The study claims that voice recognition systems may be classified based on the extent of the vocabulary, style of speech, and speaker dependency.

The system employs a suitable controller, as well as a speech recognition chip for receiving voice commands, and a logical lift programme to link the AT89S52 microcontroller [7, 8]. The elevator controller is built on the microcontroller to simulate the elevator [9–11]. This paper describes a voice-activated elevator that is simple to use. The paper includes speech recognition and a programmable interface, as well as well-designed elevator software. It employs a technique known as dynamic time wrapping. It comprises of terms such as up, down, and so on. The voice recognition system, as well as the microcontroller, motor, and other components, is a significant element of this project.

2 Methodology

In this work, firstly, a motor control circuit was developed. The motor control unit can be driven in forward or reverse direction. Later, the sensor circuit for the cardboard and level board was designed. In this circuit, the phototransistor receives the signal transmitted by photo diode. Then, microcontroller circuit was developed to integrate these circuits. Lastly, the mechanical parts of the system were designed. The block diagram of the proposed system is as shown in Fig. 1.

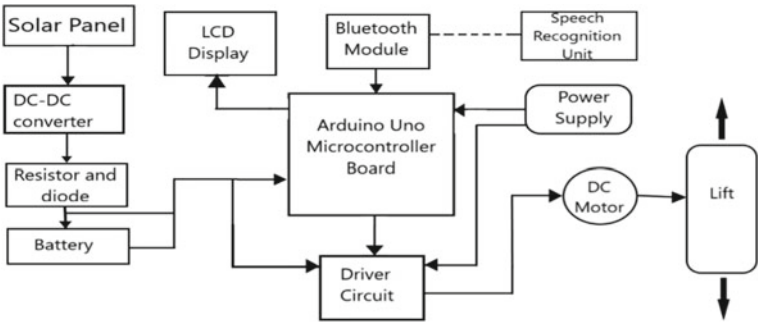

Fig. 1 Block diagram

We used Arduino apps from android phone according to the apps, we programmed in the microcontroller. Here, we have designed 1 + 2 floors. The android phone is connected in elevator. It receives the voice and send to microcontroller through the Bluetooth and the controller matching both data and move to the particular floor.

Voice recognition system is used for identification of the voice commands. Microcontroller is programmed to operate according to the given instructions. The voice recognition system is the input module to the microcontroller which takes the instructions given by the user. The controller judges whether the instruction is to take the lift upwards or to the downwards and accordingly, the switching mechanism controls the lift.

On interruption of normal power supply, an independent emergency power source supports important electrical systems. In hospitals and research laboratories, emergency power systems are established to protect people and equipment. It is also installed in data centres against the loss of data from primary electric power supply interruption. Engine-powered generators or battery-operated inverters can be used as emergency power solutions. In most commercial and industrial power systems, an engine-powered generator provides energy for emergency and backup power systems.

Diesel engines are a popular choice for generator prime movers. This is due to the inexpensive cost of diesel engines in comparison with other types of power, as well as their relative ease of application. The combustion and cooling air are the two main considerations for generator and prime mover. Also the provision for the removal of exhaust gases is also considered. In addition, fuel supply, engine maintenance, and noise reduction are also considered. A second choice will be battery-operated inverter for emergency system power. An inverter is a low-cost solution and easy installation for low-power demands.

Solar photovoltaic (PV) systems create electricity. PV systems are built to provide electricity to any sort of electrical load at any specified voltage. PV systems are made up of a series of PV modules that convert solar energy into direct current. Power conditioning equipment, energy storage devices, and electrical loads are the other

key components. The power conditioning equipment is inverter, charge, and load controllers, and energy storage device is batteries.

The power manager forces the system to pump the power generated by the PV panels to medium-sized supplementary loads such as air conditioning and ventilation systems when the battery is fully charged during peak hours of a sunny day and grid power is on, but when power is lost, connections will be switched from other supplementary loads to the emergency hospital elevator exclusively. It will relay only on power available in battery. Furthermore, if the battery is not fully charged when the power goes out, the system just powers the elevator and uses the excess energy from the panels to charge the battery pack. Other auxiliary loads must not be connected to the battery bank at night. In addition, the battery must be kept in a secure location in case of an emergency. When grid power fails, the load is provided by the battery if the SOC is greater than a minimal value.

Dual power supply is used in the smart elevator that we built for this project. The electricity is supplied from both the mains and the battery, which is charged using solar energy. The battery's power is only used as a backup source.

Solar panels turn the sun's energy into electricity. This is stored as chemical energy in the battery. This chemical energy can be converted to electrical energy by the battery and can be used to power the lift when necessary.

Buck–boost converters are DC-DC converters with output voltages that are either less than or greater than the input voltage magnitude. The fundamental goal of a buck–boost converter is to take a DC voltage input and output a different level of DC voltage, either reducing or increasing it depending on the application. In our project, the buck–boost converter takes variable DC voltage and produces constant DC voltage of required level. 3 AA sized rechargeable battery of 3.7 V is used in this prototype. These batteries will be charged by solar panel. The power is given to elevator control unit (Arduino Uno) and motor driver circuit.

The ECU is like the brain of elevator. The working process is programmed and stored in the ECU. It gives the information to motor driver circuit to operate based on the command given by user. Motor driver circuit drives the motor. It gets signals from ECU and drives the motor accordingly in either forward direction or reverse direction.

Speech control unit (SRU) takes the voice commands given by user and processes it to electrical signals. This signal is transmitted through Bluetooth, and Bluetooth module receives the signal and gives it to ECU.

A voice-controlled elevator system was designed in order to meet the project's objectives and complete the duties. The system comprises of a motion-controlled elevator prototype that has been scaled down. The elevator control unit (ECU) and the voice recognition unit are the two key units that make up the overall system's 'brain' (SRU).

The voice recognition unit is in charge of identifying and delivering passenger requests to the elevator control unit. After that, the elevator control unit organises the requests into an array and sends commands to a stepper motor to fulfil them.

Figure 2 shows a flowchart that briefly depicts the operation of the entire system. This picture will be used to discuss the overall system operation in more detail in

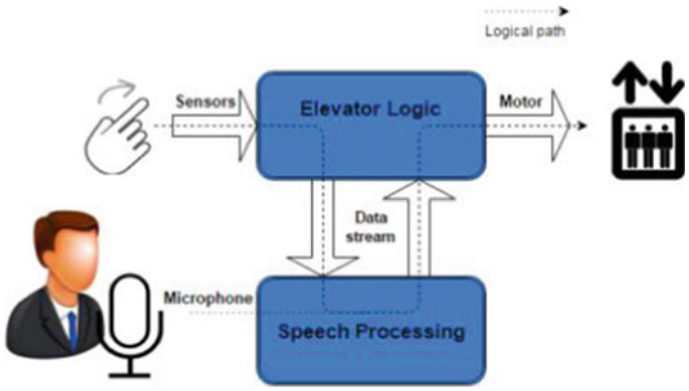

Fig. 2 Flowchart of smart system

the next sections. In terms of the downscaled prototype, design decisions have been taken.

The building has ten levels, which is thought to be sufficient for demonstrating the functionality of the speech processing and elevator control algorithms. On each storey, it was also decided not to have operable doors. Instead, two LEDs of various colours are utilised to show whether the doors are open or closed. Instructions given by the user need to be recognised and processed in the form of electrical signals so that it can be used to control the elevator. The unit which recognises the voice given by user and converts to equivalent electrical signals is the speech recognition unit.

In this prototype, we use android phone with AMR voice app to give the voice commands. The voice instruction given will be taken by the microphone in the mobile phone, and this signal is transmitted via Bluetooth to the Bluetooth module. The act of turning spoken words into text is known as speech recognition, also known as automatic voice recognition. The term 'voice recognition' is used to refer to recognition systems that must be trained to a specific speaker, as it is with most desktop recognition software. Recognizing the speaker can make it simpler to translate speech. Speech recognition technology, such as a contact centre system that can recognise arbitrary voices, can comprehend speech without being aimed at a specific speaker.

3 Proposed System

The technique we offer makes it simple for blind people to use the elevator. Thanks to the remote, the blind person will have total control over the elevator. To preserve battery life, the remote features an auto power-off feature that shuts it off after a predetermined period of time. The user receives an audio message telling them that their battery is low and that they need to charge it. Voice confirmation will also be provided for the selected floor, when the elevator arrives at that floor, and when

the elevator door opens or shuts. A relay switches to some emergency rechargeable batteries when the elevator's power runs out. The suggested solution is cost-effective since the microphone and loud speaker are combined in the remote rather than being separated. Furthermore, the entire system can be used without being connected to the Internet (i.e. no Internet is needed).

When building a prototype, it is critical to choose materials carefully in order to create a long-lasting design. In addition to ensuring that the prototype meets the performance criteria, it should be remembered that different material selections have varying effects on the environment. The prototype's main structure is made of metal, similar to that of an 'AL'. Recycling 'AL' saves 95% of the energy required to produce new metal. Given the prototype's requirements, this material choice was good from a sustainability standpoint, presuming the metal would be recycled.

Batteries are manufactured from a variety of chemicals, but one hard metal is always present. Nickel and cadmium, for example, are hazardous metals. These materials have the potential to harm both humans and the environment, and many of them are not recyclable. As a result, instead of using batteries, the system was powered by cables.

4 Working of Proposed System

The smart elevator that we have made in this project makes use of dual power supply. The power is given from both mains supply and power stored in battery by charging the battery from power generated using solar energy. The power from the battery is only used as a backup power. The solar panels convert solar energy into electrical energy. This is stored in battery as chemical energy. This chemical energy can be converted to electrical energy by the battery and can be used to power the lift when necessary. 3 AA sized rechargeable battery of 3.7 V is used in this prototype. These batteries will be charged by solar panel. The power is given to elevator control unit (Arduino Uno) and motor driver circuit. The ECU is like the brain of elevator. The working process is programmed and stored in the ECU. It gives the information to motor driver circuit to operate based on the command given by user. Motor driver circuit drives the motor. It gets signals from ECU and drives the motor accordingly in either forward direction or reverse direction. Speech control unit (SRU) takes the voice commands given by user and processes it to electrical signals. This signal is transmitted through Bluetooth, and Bluetooth module receives the signal and gives it to ECU.

Figure 3 shows the working mechanism of the smart elevator. The main component or the heart of the whole implementation is the voice recognition chip. The user entering the elevator would just give a voice command for moving up or down instead of manually pressing the switches. The voice recognition module takes the input provided by the speaker and would convert it to digital signal and in turn will be fed as an input to the microcontroller. The microcontroller will compare the input from the stored input, and if the result says to move the elevator downwards, then it

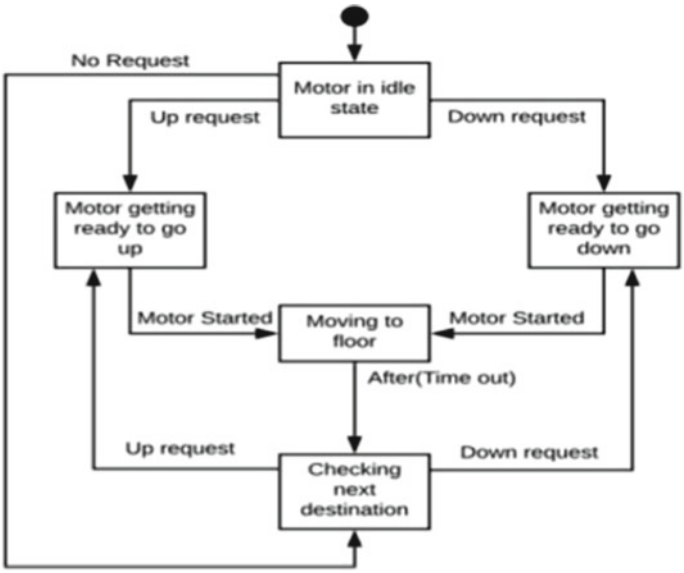

Fig. 3 Working mechanism

will accelerate the motor downwards, and if the result says to move upward, then the motor would be accelerated in upward direction, thereby leading to the movement of the lift and allowing the speaker to get off at the desired floor. The proposed system will also have an emergency switch for worst condition if the lift gets stuck.

5 Result

Before implementation of the system, we have simulated the DC-DC converter circuit. It was found that the simulation results are satisfactory as shown in Figs. 4 and 5 and practical systems work very well. As future scopes, the main controller can be re-designed in such a way so that a three-phase induction motor can be operated through a speed control circuit. A PV system with a dc-to-dc converter that uses the DC generated from the solar panel and processes this to a required DC level to cater the various DC loads. The converter works in the buck–boost mode. The converter also employed with PID controller, enhancing overall performance of the system. The simple PID (proportional, integral, and derivative) controller has been applied to a conventional buck–boost converter and tested in MATLAB Simulink environment achieving improved voltage regulation and efficiency.

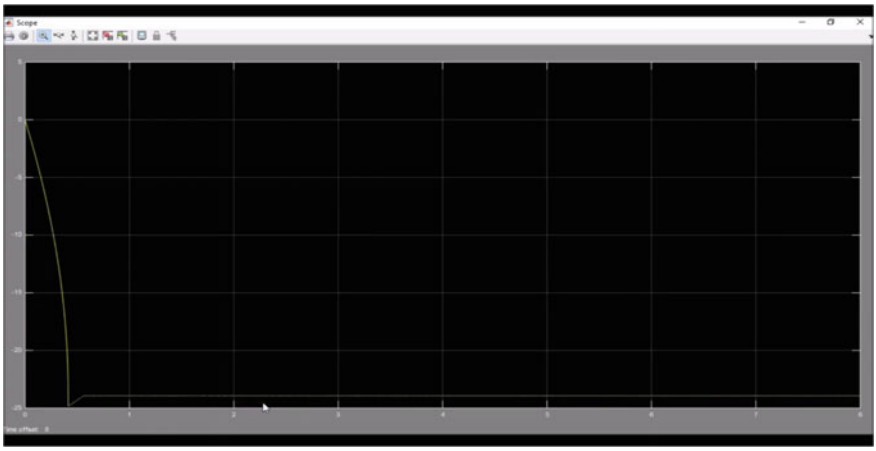

Fig. 4 Simulation of buck converter

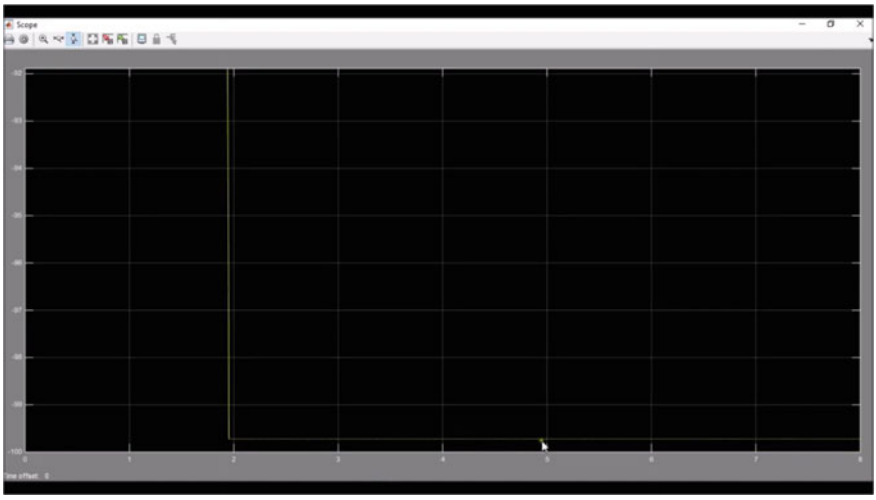

Fig. 5 Simulation of boost converter

6 Conclusion

Using an elevator simulation, this article illustrates how voice control can become a boon in everyday life in the future. Because it runs smoothly, the voice-controlled elevator is quite handy. The purpose of this research is to learn more about a voice recognition system that may be used to improve the efficiency and usability of traditional elevators for physically challenged persons. The elevator prototype is

a helpful tool for study into spoken signal recognition, computerization, and control improvements, as well as for identifying future applications in this sector.

This project functions as a mechanism for human–machine communication. Solar power also decreases the amount of electricity consumed from the grid. Using solar as alternative power source, it reduces the electricity bill and power that we get from grids is largely generated from non-renewable energy source like coal, uranium, fossil fuels, etc.

Due to their decreased sense of the world, blind and visually impaired persons have severe difficulties leading independent lives. The usage of elevators in multistorey structures is one of these issues. People who are blind or visually challenged cannot see or read the elevator keypad. Although Braille markings have made it easier for blind individuals to operate elevators, not everyone who is blind can read Braille. Elevators may be made simpler to operate for persons who are blind or visually impaired by making a few minor changes. Currently, there are several advancements in accessible elevator interfaces. The majority of today's elevators were designed with the disabled and visually impaired in mind. The elevators designed for the blind lacked voice confirmation, which would have informed the blind of the elevator's condition.

7 System Prototype

The PCB and prototype for the proposed system are depicted in the diagrams below. The solar panel is seen in Fig. 6. The LED display in the elevator is shown in Fig. 7. The Arduino circuit is shown in Fig. 8. The elevator prototype construction is shown in Fig. 9, which comprises of three levels, such as an elevator unit PCB, an elevator cabin, and sensors. The implemented circuit is shown in Fig. 10.

Blind individuals may simply utilise the elevator with the aid of our suggested technology, avoiding any embarrassing situations in front of regular people. There are two key components in the proposed system. The blind is controlled by a remote

Fig. 6 Solar panel

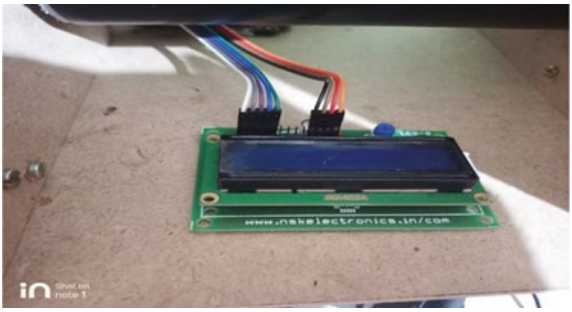

Fig. 7 LED display

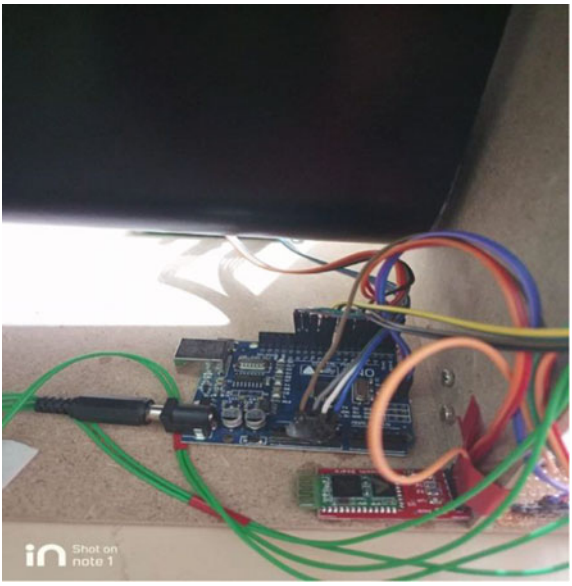

Fig. 8 Arduino board

unit, whilst the elevator cabin is controlled by an elevator unit. The remote unit includes a voice recognition module that eliminates the need for a keyboard and a text to speech module that allows the blind to make vocal confirmations. On each level, three ultrasonic sensors are positioned in front of each elevator to direct the blind to the elevator entrance. The proposed method is accurate, simple to operate, and cost-effective.

8 Upscaling to a Real-Time Elevator System

The prototype of an elevator system that was made requires a lot of changes to implement the same concept for a real elevator system. In prototype, small AA sized

Fig. 9 Elevator

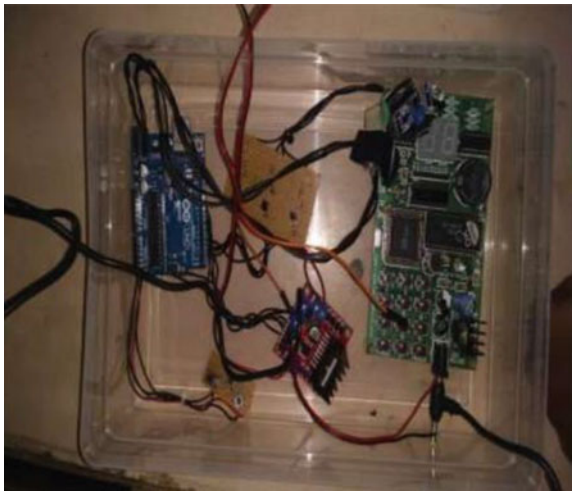

Fig. 10 Implemented circuits

batteries are used. This cannot be used to power the real elevator which carries persons and goods. For a real elevator system, large lead acid or Li-ion batteries are to be used. Since a small DC gear motor is used in the prototype, an advanced motor control was not needed to be implemented. By choosing a different motor and motor driver, a more advanced motor control needs to be implemented. With the use of an encoder, a feedback signal would also be available, allowing a PID controller to be implemented. This improvement is also crucial when aiming for the design of a real elevator system. In real elevators, large DC compound motors or 3 phase induction motors are used to move the lift.

References

1. Srilatha K, Reeshma B, Sirisha MV (2017) Automated elevator—an attentive elevator to elevate using speech recognition. IJIRCCE 9486–9490
2. Rajesh Prajapati SMJB (2016) Voice initialized elevator. Int J Electr Electron Res 4(1):154–157
3. Kaladharan N (2015) A study of speech recognition. IJIRCCE 3(9):8030–8034
4. Lee CH, Soong FK, Paliwal K (1996) An overview of speaker recognition technology. In: Automatic speech and speaker recognition: advanced topics, Kluwer Academic Publishers, Norwin
5. Johnstone A (1985) Automated speech recognition: a framework for research. EACL'85, Geneva, Switzerland, pp 239–243
6. Reddy DR, Ermann (1975) Tutorial on system organization for speech understanding. In: Speech recognition: invited papers presented at the 1974 IEEE symposium. Academic Press, pp 457–479
7. Atmel (2016) ATmega328/P data sheet [Online]. Available: http://ww1.microchip.com/downloads/en/DeviceDoc/Atmel-42735-8-bit-AVR-Microcontroller-ATmega328-328P_Summary.pdf. Accessed 2018
8. Matic N (2014) Microelectronics [Online]. Available: https://download.mikroe.com/documents/add-on-boards/click/speakup/speakup-click-manual-v100-a.pdf. Accessed 2017
9. Parallax Inc (2015) Emic 2 Text-to-Speech Module (#30016) [Online]. Available: https://www.parallax.com/sites/default/files/downloads/30016-Emic-2-Text-To-Speech-Documentation-v1.2.pdf. Accessed 2017
10. Transceiver (2016). [Online]. Available: https://www.silabs.com/documents/public/data-sheets/Si4464-63-61-60.pdf. Accessed 2016
11. Jones MP (2015) HC-SR04 user guide [Online]. Available: https://www.mpja.com/download/hc-sr04_ultrasonic_module_user_guidejohn.pdf. Accessed 2017

Monitoring of Critical Buses in Real-Time by Using PMU for 72-Bus

G. Babu Naik

Abstract This learning describes a technique for location of phasor measurement units that ensure the one-to-one care of critical buses based on the overall system's transient stability analysis. If PMUs are positioned at the buses that been considered as more vulnerable, it will monitor the phase angles at different nodes in real-time criteria, which behaves the proximity to uncertainty, the functions are defend properly. The buses are very important to monitor under the transient conditions, and also it is very difficult where to be installed PMUs, when considering various disturbances. The ideal location set with essential identified the buses from voltage stability index is determined using an ILP technique with 'equality' and also 'inequality' constraints. The main demonstrates proposed approach, and results from the 72-bus system are shown.

Keywords PMU · 72-bus system · ILP · VSI

1 Introduction

When the system is under high stress, the large interconnected nonlinear power system may go have the instabilities of systems. Such systems considerable economic cost high and lead to the system-wide shutdowns [1]. Therefore, it is very important to power system protection, operation, and proper to design under the operational reliability of electric power systems. Hence, the power system operator action provided with automatic control designed to protect or minimize the faulty caused by such outline. Over a period of time in the fast decades, the consumer demanding the power flows across the utilization of systems been growing constantly. However, the newly constructed of transmission line has been lagged due to environmental conditions and economic growth. It is generally understood in the power sector that strong power flows along transmission lines weaken the transmission lines, and that maintaining the operating system security of the power system with the effect of oscillation

G. Babu Naik (✉)
Department of Electrical and Electronics Engineering, BMS Institute of Technology and Management, Bengaluru, Karnataka, India
e-mail: babunaikg@bmsit.in

© The Author(s), under exclusive license to Springer Nature Singapore Pte Ltd. 2022

A. Tripathi et al. (eds.), *Intelligent Computing Techniques for Smart Energy Systems*, Lecture Notes in Electrical Engineering 862,
https://doi.org/10.1007/978-981-19-0252-9_39

and angle deviations causes instability. In spirit, based on the consumer demanding, the growth and new transmission lines are gradually increasing the power system operation and also very closer towards in the instabilities limiting. Under severe contingency, the system operating principle can be finding secure in the operating limits of power system network [1, 2].

The dynamic cycle operation of power system can vary over infinitely at different range of time-scale, from milliseconds to in hours. For this type of phenomena, a separate controller was designed to monitor the un-interrupted operation of electric power grid, and it contains of power transmission lines, synchronous machines, and consumer loads side. The basic controls of power flow techniques have been developed, such as protection of ultra-power system, slower-excitations, and governors' control in the past decades [3, 4]. In the previous study, most of the power system controls were constructed with local measures, but in other instances, such as when the system is significantly strained, the local measurements controls can possibly act against each other, pushing the system into cascading outages. Under this severe operation conditions, alone local measurement control cannot handle this type of security problems [1, 5–7]. There are many recent techniques have been developed of large-scale black-outs in the world wide, and black-outs point needs to have the controls for wide area. Past twenty years, there has been improved with ROM tachylogias from advances in computer and communications sciences provide the feasible and opportunity economical implementation for electric power system in wide area controls.

It is very important that placing PMUs for selected buses as to reducing the maintaining system under complete observability network either because of installation cost of communications network and also by knowing the phasor voltage and phasor currents buses emerging.

- The magnitude of voltage and angles of phasor form at the buses.
- All the branch currents phasor developing from the bus.

In the recent activity, researchers have been developed for finding such problem using reduction optimal locations by installing the PMUs so that the system gets complete observability. In this paper, Behera et al. [8–11] have been developed the minimum PMUs required through a proposed algorithm, which uses the modified technique both simulated and bisecting annealing method.

In these paper, a method is obtained to place the PMUs location, by considering the critical buses which is obtained from voltage stability index [12]. The main key point is to identified the buses under critical where to be located of PMUs during the transient condition operating the system. A ILP technique has been used as an 'equality' and as well as 'inequality' constraints to be find optimum placement of critical buses [13–17]. It will monitor the real-time data at the nodes of phase angles difference, which says the bus is instability, such conditions well defend PMUs are located at the buses which give more susceptible. The work is constraints reducing the cost of PMU, and also it is very the cost at placing the number of channels.

2 Based on Voltage Stability Index Identification of Critical Buses for 72-Bus

The proposed approach for finding the vulnerable buses consists of buses, power transmissions, etc., and read the data from that and select a line so that it will carry out the contingency analysis, performs the VSI on all l lines and find the L-index vale which will give the maximum. Arrange the buses based on merit list in descending order and group them as critical buses.

Step 1: System data to be read out the buses, power transmission lines, generators, machines, transformer, SVC, governor and excitations systems, load buses.

Step 2: Choose the appropriate power transmission lines and create disturbance for 'l' lines.

Step 3: Run the voltage stability index programme for all transmission lines.

Step 4: Collect the L-index data at all buses and hold the data corresponding to 'i' (say $i = 1$ to l).

Step 5. Calculate disturbances at each bus for $i = 1$ to get the maximum angular deviation.

Step 6: By considering the optimization technique gets the results for operability analysis using with critical buses.

A. *72-bus equivalent Indian southern grid*

72-bus system having 15 buses of generators and 37 buses of loads and buses 16–72 are load buses.

Zone 1: Buses 2, 3, 4, 5 are connected with generators.

Zone 2: Buses 1, 6, 7, 8 are connected with generators.

Zone 3: Buses 9, 10, 11, 12, 13, 14, 15 are connected with generators.

TIE-LINE: Buses 56–64 connected from zone 1 to zone 3, buses 56–60, 56–46, 58–70 connected with zone 1 to zone 2 (Fig. 1).

B. *L-index graph with full loading*

C. *L-index graphs with 10% increasing load*

By increasing the 10% load, buses 16, 38, 53, and 39 are shown in Figs. 3, 4, 5 and 6.

After increasing the 10% load at all the load buses, it has been grouped into 39 cases and the buses which give the more predictable is computed. Table 1 represents column as buses and rows show the more critical buses. The buses show most critical buses at which appear as maximum.

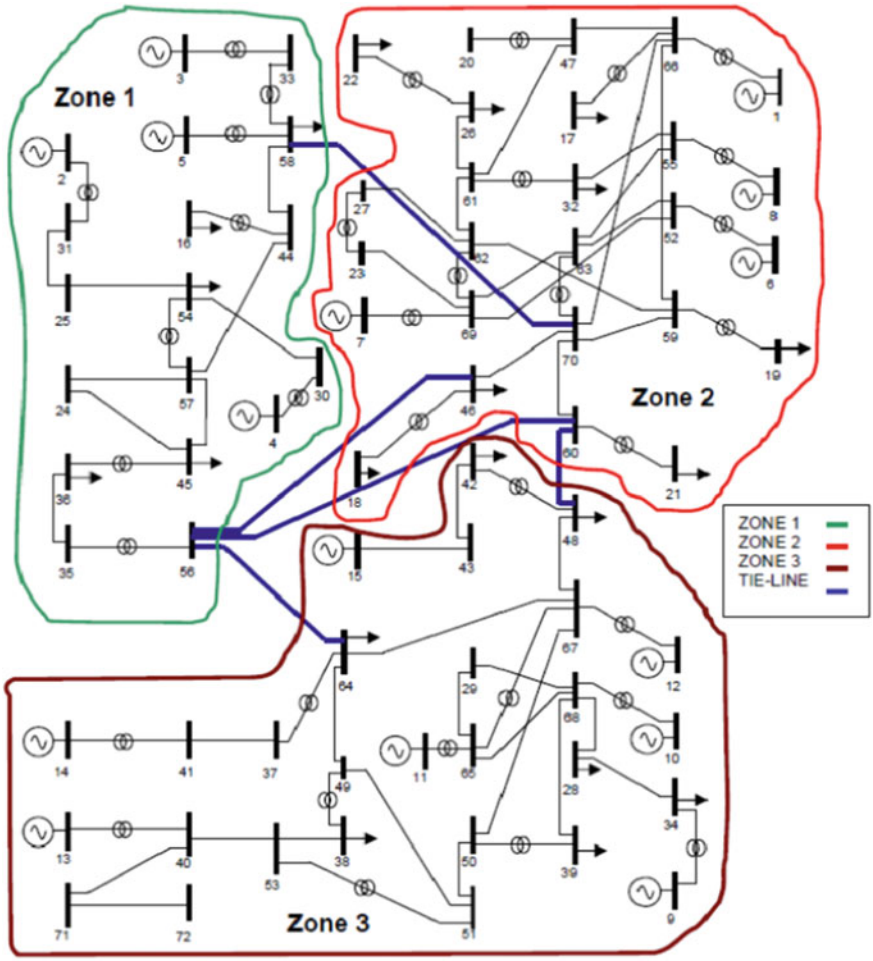

Fig. 1 The 72-bus Indian southern grid line diagram

Therefore, for the 72-bus equivalent of Indian southern grid, the most vulnerable buses considered as 38, 36, 35, and 45, respectively, in the decreasing order of vulnerability.

The most vulnerable buses are found out from the L-index, and these vulnerable buses are considered for placement of PMUs optimally.

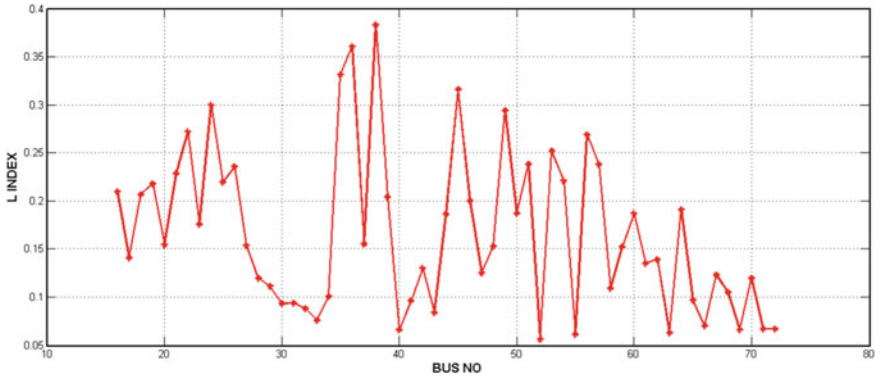

Fig. 2 L-index graph with full loading

Table 1 72-bus system of L-index group

Buses	First place	Second place	Third place	Fourth place
38	37/39	2/39	–	–
36	37/39	2/39	–	–
35	–	–	39/39	–
45	–	–	–	39/39

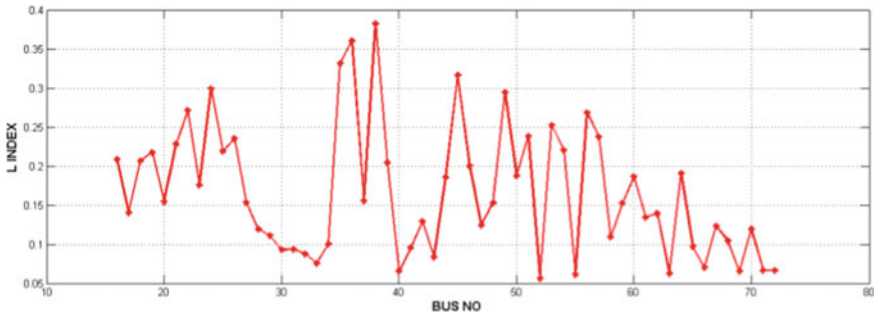

Fig. 3 The graph at bus 16 with 10%

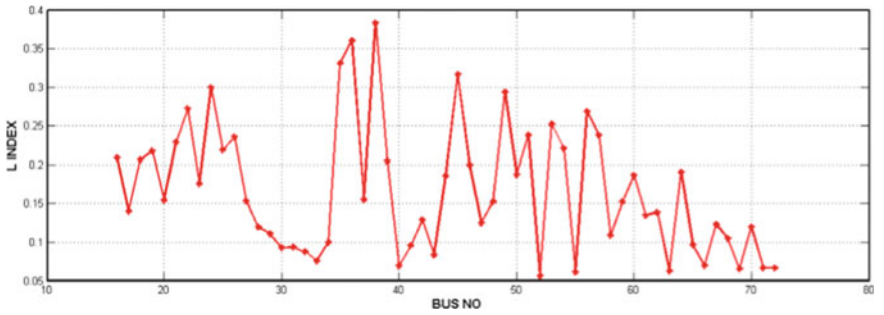

Fig. 4 The graph at bus 39 with 10%

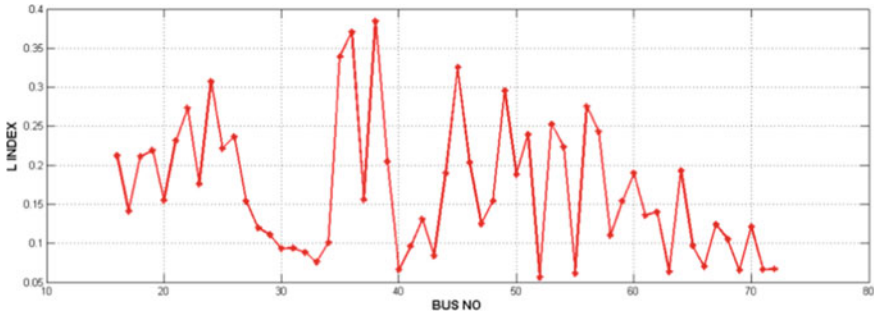

Fig. 5 The graph at bus 53 with 10%

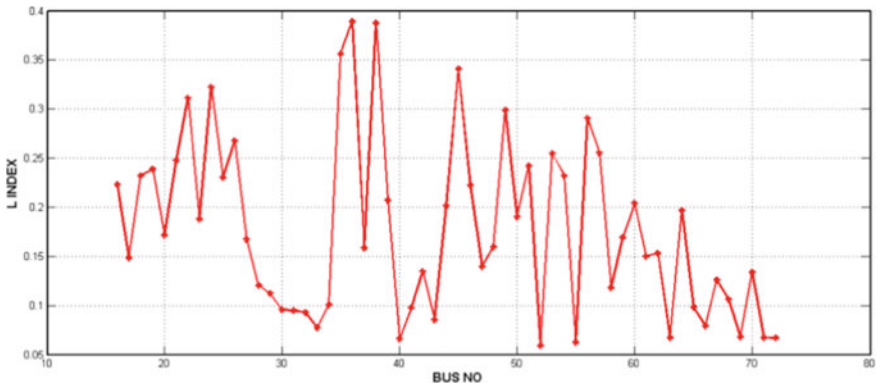

Fig. 6 The graph at bus 38 with 10%

3 Optimal PMU Placement Using Observability Analysis

The PMU is not necessary to install at the all buses, and it will measure the phase voltages, branch currents, and amplitudes at each node, so it is required suitable optimum location of PMU approach to determine for optimum set.

After placing PMU at the bus, it gives the magnitude of phasor voltages and as well as phasor currents at the bus of all incident lines. The first step of PMU placing is to identify the vulnerable buses, in power system has the impartment buses are like, when buses are connected to a heavily loaded, bus extension in the future point, and PMU already installed. This type of cases, the PMUs can be placed at chosen bus. After placing the PMU at buses, the radial buses are excluded. In connected network, the number of possible placing the PMUs reduces at the buses.

(i) *Integer Linear Programming (ILP) formulation*

The ILP formulation is explained in detail by using single-line-diagram of 72-bus shown in Fig. 1.

Let x_i be a binary choice of variable associated with buses i.

x_i is variable function, after PMU is installed at bus say i, otherwise zero. Then, minimal PMU required for the problem can be computed using the formulae as

$$\begin{aligned}&\text{Minimize } f^T x\\&\text{subject to } (Ax \geq b)\\&\text{Where } b = I^{n\times 1}\\&f = (111.....1)_{n\times 1}\\&A \text{ is the connectivity matrix}\end{aligned}$$

x_i is a binary decision variable which is been shown below.

$$x_i = \begin{cases} 1, \text{ the placed PMU is say, } i \\ 0, \text{ or else zero} \end{cases}$$

After solving the optimization technique, the placement of optimal locations minimum number of PMU required for 72-bus is 26. Table 2 talks about of PMU required at the buses.

Table 2 Optimal PMU placement for 24-bus system

Minimum no PMUs	Optimal PMU locations
26	26, 30, 31, 33, 34, 35, 40, 41, 43, 44, 46, 47, 49, 52, 55, 57, 58, 59, 60, 62, 65, 66, 67, 68, 69, 71

4 Modified ILP Formulation

The modified ILP technique which is implemented is given in below.

$$\text{Minimum} \sum_{i=1}^{n} w_i x_i$$

$$A_{\text{eq}}.X \geq b$$

$$A_{\text{eq}}.X = b_{\text{eq}}$$

w_i = the no. of branches linked to node

A = matrix of buses connected in order of $n \times n$

b = column matrix order of $n \times 1$

A_{eq} = diagonal matrix and b_{eq} = column matrix

$$A_{\text{eq}}(i, i) = \begin{cases} 1, \text{selected bus(es) } i \text{ is from vulnerability list} \\ 0, \text{otherwise} \end{cases}$$

$$b_{\text{eq}}(i, i) = \begin{cases} 1, \text{PMU is installed at bus } i \\ 0, \text{or else} \end{cases}$$

The solution to the above equations gives the solution for optimization technique for optimal locations placement of PMU taking into account placing at critical bus. The technique is tested with all four possible cases, and the PMU locations are found out with giving highest priorities to the vulnerable buses. In this, cost of all PMUs is considered to be equal irrespective of the number of connected lines to observe.

S. No	Bus category	Number of PMUs required	Location at the buses
1	38	27	26, 30, 31, 33, 34, 35, 38, 40, 41, 43, 44, 46, 47, 50, 52, 55, 57, 58, 59, 60, 62, 65, 66, 67, 68, 69, 71
2	38, 36	28	26, 30, 31, 33, 34, 35, 36, 38, 40, 41, 43, 44, 46, 47, 50, 52, 55, 57, 58, 59, 60, 62, 65, 66, 67, 68, 69, 71
3	38, 36, 35	28	26, 30, 31, 33, 34, 35, 36, 38, 40, 41, 43, 44, 45, 46, 47, 50, 52, 55, 58, 59, 60, 62, 65, 66, 67, 68, 69, 71
4	38, 36, 35, 45	26	26, 30, 31, 33, 34, 36, 38, 40, 41, 44, 46, 47, 50, 52, 55, 57, 58, 59, 60, 62, 65, 66, 67, 68, 69, 71

By considering above iteration with ILP technique, 72-bus required minimum PMU installation is ‘26’.

5 Conclusions

This paper gives the monitoring of the critical buses by placing of phasor measurement units for 72-buses has been developed. In this technique used for optimization problem done by integer linear programming is framed. The proposed approaches ensure that the system of observability completely for 72-bus system Indian southern grid.

References

1. US–Canada Power System Outage Task Force (2004) Final report on the August 14, 2003 blackout in the United States and Canada: causes and recommendations
2. Venkatasubramanian V, Li Y (2004) Analysis of the 1996 western American electric blackouts. In: Proceedings of 2004 IREP symposium bulk power dynamics and control—VI, Cortina, Italy, August 2004
3. Kundur P (1994) Power system stability and control. McGraw-Hill, New York
4. Taylor C, Erickson D, Wilson B, Martin K (2002) Wide-area stability and voltage control system (WACS) demonstration
5. U.S.–Canada Power System Outage Task Force (2003) Causes of the August 14th blackout in the United States and Canada. Interim Rep., Nov. 2003, Ch 6
6. Taylor CW, Erickson DC (1997) Recording and analyzing the July 2 cascading outage. IEEE Comput Appl Power 10:26–30
7. Baldwin TL, Mili L, Boisen MB Jr, Adapa R (1993) Power system observability with minimal Phasor measurement placement. IEEE Trans Power Syst 8(2):707–715
8. Behera S, Dev Choudhury NB, Tripathy D (2021) Brief study on applications of phasor measurement units in smartgrid technology. In: 2021 1st international conference on power electronics and energy (ICPEE), pp 1–5. https://doi.org/10.1109/ICPEE50452.2021.9358725
9. Ahmed MM, Imran K (2019) An optimal PMU placement against N-1 contingency of PMU using integer linear programming approach. Int Conf Appl Eng Math (ICAEM) 2019:127–132. https://doi.org/10.1109/ICAEM.2019.8853656
10. Matavalam ARR, Singhal A, Ajjarapu V (2020) Monitoring long term voltage instability due to distribution & transmission interaction using unbalanced μPMU & PMU measurements. IEEE Power Energy Soc General Meet (PESGM) 2020:1–1. https://doi.org/10.1109/PESGM41954.2020.9282086
11. Reis AW, Guarda FGK, Gastaldini CC (2019) Simulation of a phasor measurement unit in real time using typhoon virtual HIL. IEEE PES Innov Smart Grid Technol Conf Latin Am (ISGT Latin Am) 2019:1–5. https://doi.org/10.1109/ISGT-LA.2019.8895261
12. Alzaareer K, Saad M (2018) Real-time voltage stability monitoring in smart distribution grids. Int Conf Renew Energy Power Eng (REPE) 2018:13–17. https://doi.org/10.1109/REPE.2018.8657671
13. Alzahawi T (2018) Modified application of phasor measurement unit in voltage monitoring of power system. Third Sci Conf Electr Eng (SCEE) 2018:230–234. https://doi.org/10.1109/SCEE.2018.8682240
14. Abdelkader SM, Hatata AY, Abdelbaky MM (2017) Dynamic stability analysis of synchronous generator using phasor measurement units. Nineteenth Int Middle East Power Syst Conf (MEPCON) 2017:1416–1423. https://doi.org/10.1109/MEPCON.2017.8301369
15. Gupta AK, Verma K, Niazi KR (2017) Contingency constrained optimal placement of PMUs for wide area low frequency oscillation monitoring. In: 2017 7th international conference on power systems (ICPS), pp 579–584. https://doi.org/10.1109/ICPES.2017.8387360

16. Wu Y, Musavi M, Lerley P (2016) Synchrophasor-based monitoring of critical generator buses for transient stability. IEEE Trans Power Syst 31(1):287–295. https://doi.org/10.1109/TPWRS.2015.2395955
17. Mahipal B, Babu Naik G, Naresh Kumar Ch (2016) A novel method for determining optimal location and capacity of DG and capacitor in radial network using weight-improved particle swarm optimisation algorithm (WIPSO). In: 2019 International Journal of Advanced Research in Electrical, Electronics and Instrumentation Engineering (An ISO 3297: 2007 Certified Organization), vol 5, Issue 5

Prediction of Breast Cancer Recurrence in Five Years using Machine Learning Techniques and SHAP

I. Keren Evangeline, S. P. Angeline Kirubha, and J. Glory Precious

Abstract Cancer recurrence is the leading concern among the patients who are affected by breast cancer. Earlier detection of cancer relapse can help the clinicians in administering the right dose of treatment for the right duration of time. This can improve the prognosis of the patient and also reduce their fear regarding relapse. For this purpose, our work deals with using various machine learning (ML) models such as logistic regression, support vector machine (SVM), decision tree, and random forest to predict if a patient will have cancer relapse in 5 years. The performance of all the ML models is then compared by making use of some evaluation metrics such as C-index, accuracy, F1-score, precision, and recall. Random forest (RF) model produced the best performance when compared to all the other models. It gave a precision value of 0.75, accuracy of 0.69, recall of 0.66, C-index of 0.71, and F1-score of 0.70. Random forest model interpretation was done by using Shapley additive explanations (SHAP). This algorithm identifies the contribution given by each feature in cancer recurrence prediction by random forest model. Based on the SHAP values, the features which had high impact on model prediction were found. Features such as tumor size, mutation count, lymph nodes examined positive, age at diagnosis, Nottingham prognostic index (NPI), tumor stage, HER2 status, and cancer type detailed when they had higher values were responsible for causing cancer recurrence in 5 years according to random forest model predictions. Thus, prediction of cancer relapse helps the clinicians in administering the right treatment and improves patient prognosis.

Keywords Breast cancer recurrence prediction · SHAP · Machine learning models · Prognosis

I. Keren Evangeline · S. P. Angeline Kirubha (✉)
Department of Biomedical Engineering, SRM Institute of Science and Technology, Chennai, India
e-mail: kirubhaangeline@gmail.com

I. Keren Evangeline
e-mail: ke9123@srmist.edu.in

J. Glory Precious
Department of Electronics and Communication Engineering, SRM Institute of Science and Technology, Chennai, India
e-mail: gj8833@srmist.edu.in

© The Author(s), under exclusive license to Springer Nature Singapore Pte Ltd. 2022

A. Tripathi et al. (eds.), *Intelligent Computing Techniques for Smart Energy Systems*,
Lecture Notes in Electrical Engineering 862,
https://doi.org/10.1007/978-981-19-0252-9_40

1 Introduction

The most frequent disease observed among women is developing cancer cells in the breast area, and the mortality for this disease is mainly caused due to cancer relapse and metastasis [1]. Nearly, 30–40% of patients who experienced breast cancer had cancer relapse and among this, 10–15% died of cancer relapse or metastasis [2, 3]. Cancer recurrence or relapse is a phenomenon where cancer is not found after treatment but tends to reappear in the body after some years. Cancer may recur in the same site, it first occurred or it could even occur in other parts of the body. The reasons for cancer recurrence vary. One main reason is that trace amount of cancer cells may remain in the body even after treatment without our knowledge. Over the course of time, these cells grow and cause cancer again. This can happen after several weeks, months, or even years. Generally, recurrence may happen 1 to 20 years after treatment [4]. Hence, it is highly impossible for the doctors to predict if a patient may have a relapse. Few cancers are difficult to treat and may have a high-relapse rate. One good example is glioblastoma, which recurs in almost every patient in spite of treatment. It has a recurrence rate of almost 100% [5]. Certain cancers when treated at an initial stage have low relapse rate when compared to treatment at the last stages. The overall recurrence rate of breast cancer is 30% and patients who have ER positive breast cancer experienced a recurrence rate of 5–9% after initial treatment and maintenance therapy with letrozole or placebo during median 10.6 years [6, 7]. Breast cancer relapse can be predicted by certain features such as tumor area, tumor size, no. of lymph nodes affected, tumor stage, and other similar features. Machine learning models can predict cancer recurrence using these features with much accuracy. Machine learning is more advantageous as it can make predictions if a patient may have a relapse without the need for a biopsy or scan and saves time as well as reduce cost. Machine learning techniques have been widely used in medical field for a long time. Some of its main applications are in disease diagnosis and prediction of communicable diseases [8, 9], pulmonary hypertension disease [10], lifelong chronic diseases [11], diseases related to liver [12], heart, and other cancer diseases. The paper by Uma Ojha and Savita Goel [13] used certain evaluation metrics to compare the performance between clustering algorithms and classification algorithms in predicting cancer recurrence. They identified that classification algorithms especially support vector machine performed better when compared to clustering techniques. Roshani et al. [14] combined decision tree and association rule mining to propose a new method for data mining. They got an accuracy of 93% using fuzzy approximate reasoning for breast cancer recurrence prediction. The work by Alzu'bi et al. [15] deals with extracting key features from the medical records by using natural language processing and builds a medical dictionary. From this, breast cancer recurrence prediction was done using various machine learning techniques. OneR algorithm performed the best by giving a good balance between sensitivity and specificity. Maram et al. [16] created a multi-stage learning methodology for breast cancer relapse prediction. According to them, this method provides good performance in recurrence prediction as various techniques of classification models and

feature selection are created and merged. The main focus of this study is to predict the possibility of a patient having breast cancer relapse in 5 years using different machine learning techniques. We used the clinical and pathological features of the Molecular Taxonomy of Breast Cancer International Consortium (METABRIC) dataset for prediction. In this research work, we developed and assessed machine learning models using multiple parameters like age, cancer type, cellularity, chemotherapy, PAM50 + claudin-low subtype, ER status, cancer grade, HER2 status, hormone therapy, inferred menopausal state, lymph nodes examined positive, mutation count, Nottingham prognostic index, PR status, radio therapy, tumor size, tumor stage and whether the patient had a cancer relapse in five years to give a comprehensive and objective breast cancer recurrence prediction. Data pre-processing steps such as removal of missing data, label encoding, and feature scaling were performed on the data before using it. Four distinct machine learning models were utilized for this work, namely logistic regression, support vector machine, decision tree, and random forest. The performances of all these models were compared using certain metrics such as accuracy, F1-score, precision, recall, and C-index. Finally, the random forest model interpretation was done using Shapley additive explanations (SHAP) algorithm to determine the most important features which are responsible for breast cancer recurrence in 5 years [17]. Thus, breast cancer relapse prediction using machine learning techniques can help clinicians in better diagnosis of recurrence and give the right treatment and maintenance therapy to prevent relapse and thereby improving the prognosis of patients.

2 Methodology

Figure 1 shows the block diagram of methodology and techniques used for breast cancer recurrence prediction. Data processing is done initially on the dataset. The processed data are then trained on various machine learning (ML) models such as logistic regression, support vector machine, decision tree, and random forest for breast cancer recurrence prediction. The best model is chosen based on the performance metrics.

2.1 METABRIC Dataset

This study utilizes only the clinical and pathological features of Molecular Taxonomy of Breast Cancer International Consortium (METABRIC) dataset which is publicly made available at cBioPortal Website [18].

Eighteen features were used to train the ML models for breast cancer recurrence risk prediction. The features used for this study were age, cancer type, cellularity, chemotherapy, PAM50 + claudin-low subtype, ER status, cancer grade, HER2 status,

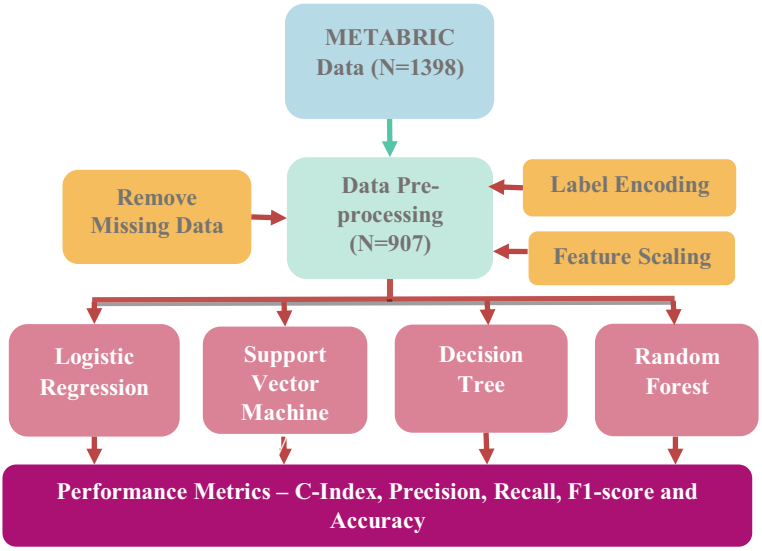

Fig. 1 Block diagram of methodology

hormone therapy, inferred menopausal state, lymph nodes examined positive, mutation count, Nottingham prognostic index, PR status, radio therapy, tumor size, tumor stage and whether the patient had a cancer relapse in five years. Figure 2 shows the count plot indicating the number of patients who had and did not have cancer relapse in five years. The number of patients who had cancer relapse in 5 years was approximately 460 patients, and the number of patients who did not have cancer recurrence within 5 years after treatment was 450 patients. From the plot, we can see that the data does not have any class imbalance.

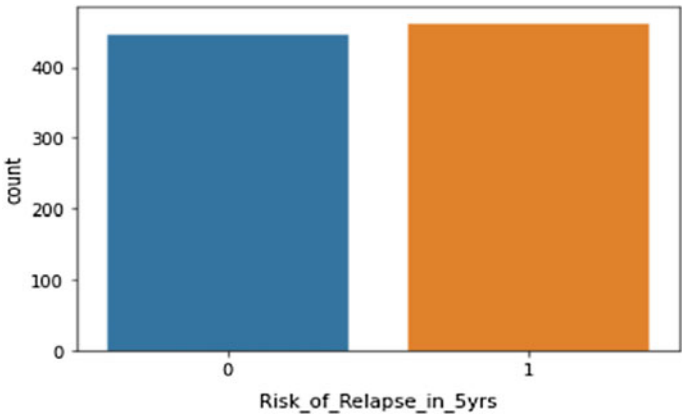

Fig. 2 Count plot of risk of relapse in five years

2.2 Data Processing

One of the prerequisites for machine learning is data processing. The ML models cannot work on raw data unless they are cleaned and processed. In this study, we have utilized data pre-processing techniques such as label encoding, feature scaling, and removal of missing or incomplete data. The METABRIC dataset consists of 1398 patient details. Out of this, only 907 patient details were available without any missing data. The rest of the data which had missing values were not considered for the study. Label encoding was then performed to convert categorical data into numerical values as machine learning models cannot work on categorical data. Finally, feature scaling was performed to normalize the range of feature values.

2.3 Machine Learning Models

Logistic Regression: Logistic regression is a statistical method which follows supervised learning and is used to detect the probabilities of the class variables. The advantage of this model is that it is easier to train and implement. Logit function is used as the function in logistic regression. This helps in determining the relationship between the features also known as the independent variable and classes known as the dependent variables by predicting the probabilities of occurrence or chance. The probability values are then converted into binary values which can be used for predictions or classifications with the help of logistic function also known as the sigmoid function. There are different categories of logistic regression models such as binary logistic regression, multinomial logistic regression, and ordinal logistic regression. For this study, we have utilized binary logistic regression model where only two dependent classes, namely patients who will have cancer recurrence in 5 years and patients who will not have cancer recurrence in 5 years.

Support Vector Machine (SVM): Support vector machine is a supervised machine learning model used for classification. The key principle of support vector machine is to identify a hyperplane in an N-dimensional space that correctly classifies the data points. Here, N is determined by the number of features present in the dataset. There are many possible hyperplanes available that could be chosen. However, in order to separate the two classes efficiently, we need to select a plane which has the maximum margin. This is nothing but the maximum distance between the points of both the classes. The advantage of maximizing the margin distance is that the future data can be classified with more accuracy. This study utilizes support vector machine with linear kernel as the training happens faster when compared to other kernels. It is also used when the data can be separated linearly and when many features are present in a dataset.

Decision Tree: Decision trees are supervised machine learning models and are non-parametric which is used for classification and regression.

They are used in decision-making for non-linear data. It appears similar to a flowchart in which each node inside constitutes a question or test on a variable asking if it is true or false. Each branch gives the outcome of the test, and each leaf denotes the label of a class. Some of the advantages in using a decision tree is that it is easy to read and discern, easy to prepare as feature scaling is not required, and less data cleaning as outliers has no significant effect on decision trees. In this study, we used decision tree for cancer relapse prediction. We set the hyperparameter maximum depth as 20 and minimum samples split as 0.5. Figure 3 shows the flowchart of the decision tree trained in this study.

Random Forest: Random forest model is based on ensemble learning technique for classification and regression. A random forest model consists of multiple decision tree model which is built during training time and it makes predictions by combining the outcomes from all the decision trees. In classification tasks, the prediction output of the random forest is the class which is chosen by most trees. The main advantage of this model is that it can be used for both continuous and categorical variables. It is an unbiased model as many decision trees are trained, and each tree is trained on the subset of the same data. In this study, we have used the grid search method for hyperparameter tuning in order to find the best combination of hyperparameters which gives the best results. Here, the number of estimators was set to 10, maximum depth as 5, and minimum samples leaf as 1. These were the best hyperparameter combinations identified by grid search method. Further, random forest model interpretation was done using Shapley additive explanations (SHAP) which uses game

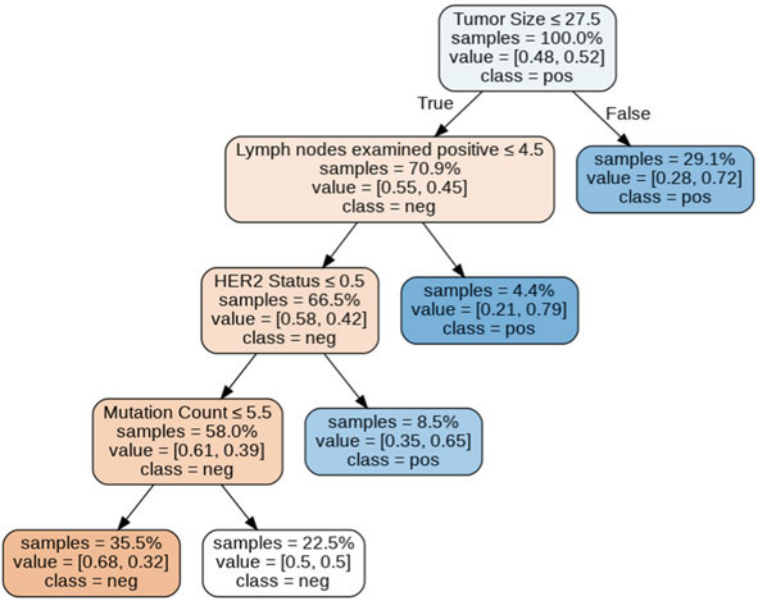

Fig. 3 Decision tree flowchart

theoretic approach to give insights into the contribution of each feature which was responsible for cancer relapse prediction.

2.4 Performance Metrics

The performance of the machine learning models is compared with the help of various evaluation metrics. The different metrics used in this study are C-index, precision, recall, F1-score, and accuracy. The C-index or concordance index is a measure of how well the model is fit which has a binary outcome. Precision is the ratio between all the correct predictions and the total positive predictions. Recall on the other hand is the ratio between the numbers of patients classified correctly to the actual positive patients. F1-score determines the balance between recall and precision. It can also be called as the weighted average between them. Accuracy could be represented as a ratio of the number of correct predictions to the total number of predictions.

3 Results and Discussion

In this proposed work, various machine learning techniques were used to determine the risk of breast cancer recurrence in five years. The machine learning algorithms were implemented using sklearn library in Python. Data pre-processing techniques such as missing data removal, feature scaling, and label encoding were initially done before feeding the input to the ML models. The Python libraries such as Pandas and NumPy were used for this process. The METABRIC dataset is split into training, validation, and test sets. Nearly, 60% of the dataset is given as input to the machine learning models for training, 20% for validation, and 20% for testing.

3.1 Evaluating the Performance of the Machine Learning Models

Table 1 shows the performance of various models such as logistic regression, support vector machine, decision tree, and random forest based on their concordance index

Table 1 C-index values for the various machine learning models

C-index	Logistic regression	SVM	Decision tree	Random forest
Train	0.73	0.67	0.69	0.83
Validation	0.61	0.56	0.58	0.63
Test	0.72	0.66	0.69	0.71

Table 2 Performance comparison of various ML models in breast cancer relapse prediction

Model	Precision	Recall	F1-score	Accuracy
Logistic regression	0.6932	0.6421	0.6667	0.6648
SVM	0.7273	0.6400	0.6809	0.6703
Decision tree	0.7386	0.6075	0.6667	0.6429
Random forest	0.7500	0.6667	0.7059	0.6978

(C-index) values. From Table 1, we can see that for the training data, the highest C-index value of 0.83 was achieved by random forest algorithm. Similarly for validation data, the highest C-index value of 0.63 was given by the random forest model. However, for the test set, logistic regression performed the best by giving a C-index value of 0.72 which is slightly better when compared to the C-index of random forest which is 0.71.

Table 2 shows the performance comparison between various machine learning models in breast cancer relapse prediction in 5 years. Random forest gives the highest value of 0.75 for precision when compared to other models. Decision tree performs the second best with a value of 0.73. Likewise, random forest gives the highest recall value of 0.66. Similarly, the model which gave the highest F1-score of 0.70 was random forest model. In terms of accuracy, random forest again performed the best giving an accuracy of 69% which is highest when compared to other machine learning models.

Figure 4 shows the confusion matrix of various ML models used in breast cancer relapse prediction. From the figure, we can see that the model which has given maximum number of true positive and true negative predictions is random forest. Similarly, random forest model gives the least number of false positive and false negative predictions.

3.2 Random Forest Model Interpretation Using Shapley Additive Explanations (SHAP)

Shapley additive explanations (SHAP) is a method that is used to explain and give insights into how the predictions are made by ML models which are too complex to be understood by humans and how the features are used to make the predictions. SHAP values quantify the additive importance of each feature and thereby explain the predictions made by the model. In order to determine which features contribute more for breast cancer recurrence in an individual, we found out the risk score predictions for each patient in the test data using the random forest model and chose the patient with the highest risk score. The SHAP values were found out for this individual. Figure 5 shows the force plot on the individual with the highest risk score and the features which contribute to the cancer relapse. From the figure, we can observe that the red sections on the left are the features which contribute mainly for the cancer

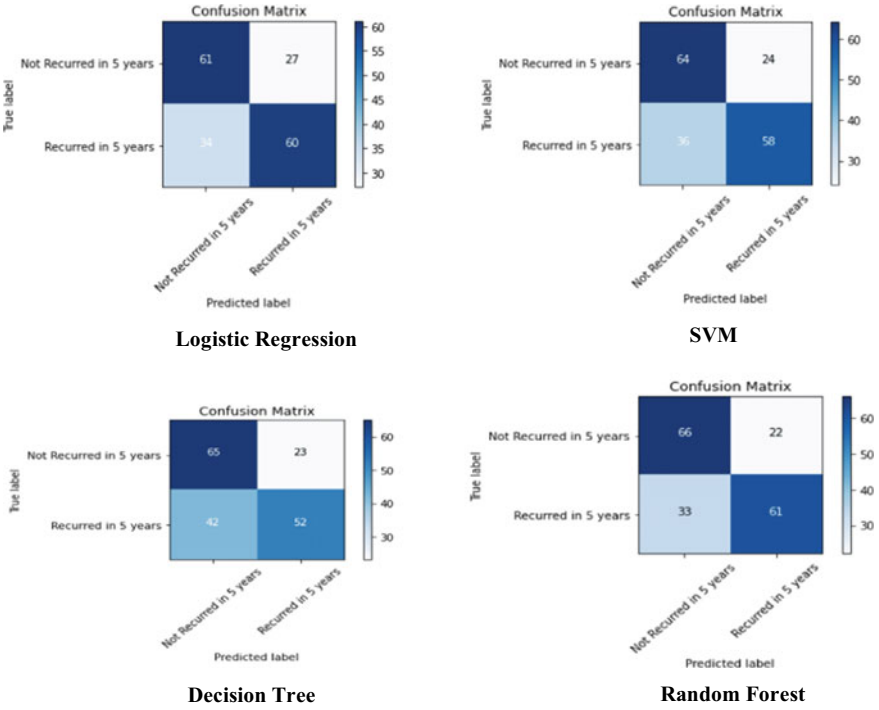

Fig. 4 Confusion matrix of various ML models used in breast cancer relapse prediction

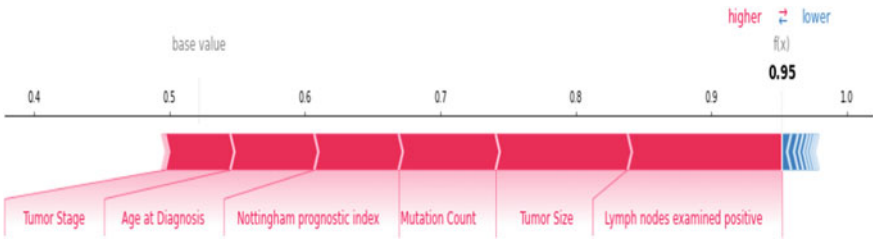

Fig. 5 Force plot showing the features which contribute to breast cancer relapse in 5 years

recurrence prediction and push the model in the positive direction. In other words, the higher the values of these features the more chances of cancer relapse in patients. The high-risk features identified by random forest for relapse prediction in an individual with a risk score of 0.95 are tumor stage, age at diagnosis, Nottingham prognostic index, mutation count, tumor size, and no. of lymph nodes examined positive. SHAP values can also be used to understand the entire test data model output. Figure 6 shows the summary plot of SHAP values for each feature on each of the test data. The figure lists out the most important features responsible for cancer relapse in

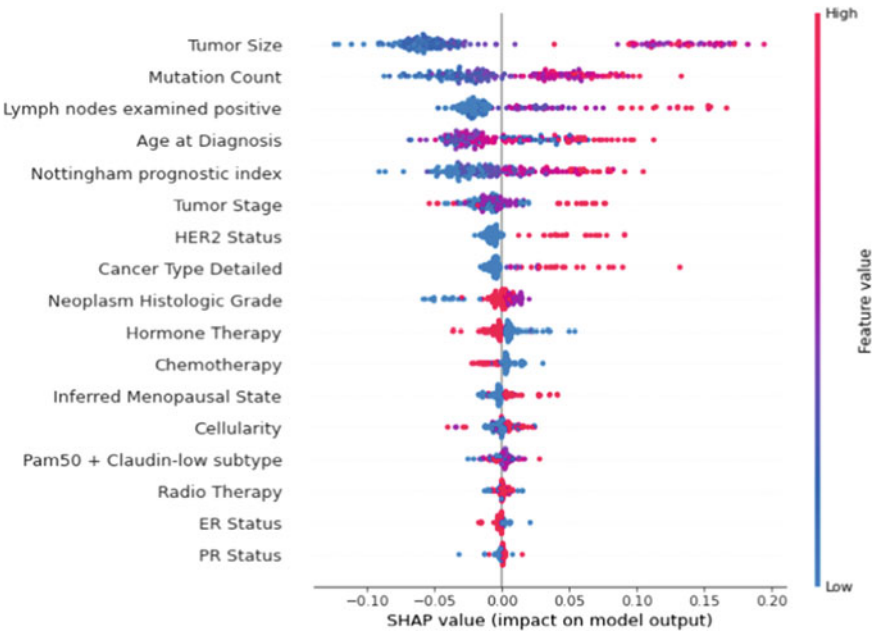

Fig. 6 Summary plot of top 17 SHAP values and its impact on model output

descending order. From the figure, we can understand that features such as tumor size, mutation count, lymph nodes examined positive, age at diagnosis, Nottingham prognostic index (NPI), tumor stage, HER2 status, and cancer type detailed are high-risk features which contribute to cancer recurrence provided they have a high value. A person who has a large tumor size, high-mutation count, more no. of lymph nodes affected, aged patients, high score of NPI, last stage of cancer, and positive HER2 status are at a very high risk to get breast cancer relapse in 5 years.

3.3 Discussion

In this study, we utilized various machine learning models such as logistic regression, SVM, decision tree, and random forest for predicting the risk of breast cancer recurrence in 5 years, and we also used SHAP algorithm for interpreting the predictions given by random forest model and also to identify the feature contribution to cancer relapse. Based on the comparison of the evaluation metrics, we can observe that logistic regression model gives the highest C-index value of 0.72 which is slightly higher than random forest which gave a value of 0.71. Random forest model gave the overall best performance for cancer recurrence prediction as it had the highest value for accuracy, F1-score, precision, and recall. However, the performance and accuracy of the model can be further increased if image features such as shape and

Table 3 Comparison of current study with the previous works

Authors	Year	Method	Performance metrics
Fu et al. [19]	2018	SVM Random forest	F1-score = 0.56 F1-score = 0.59
Haskul and Yaman [20]	2019	Random forest	Accuracy = 0.67
Mamatha et al. [21]	2019	SVM Random forest	Accuracy = 0.67 Accuracy = 0.68
Chiara et al. [22]	2020	Random forest SVM	Accuracy = 0.66 Accuracy = 0.64
Laura et al. [23]	2020	Decision tree Random forest	Accuracy = 0.63 Accuracy = 0.68
Proposed work	2021	Random forest	Accuracy = 0.69 F1-score = 0.70

texture were included for relapse prediction which was not included in this study. Table 3 shows the comparison of the current study with existing works. Since random forest performed the best using clinical and pathological features, we used SHAP algorithm on this model to find out based on which feature contribution random forest makes these predictions. Based on the SHAP values, we identified the top 17 features which have high impact on model prediction. Features such as tumor size, mutation count, lymph nodes examined positive, age at diagnosis, Nottingham prognostic index (NPI), tumor stage, HER2 status, and cancer type detailed are responsible for cancer recurrence in 5 years according to random forest model. Thus, the proposed work gives an idea about the prognosis of a patient and whether relapse of cancer will occur in 5 years following treatment.

4 Conclusion

Breast cancer is the most frequent type of cancer in women observed everywhere. Cancer relapse after treatment within 5 years can be determined by machine learning methods. Identifying the risk of cancer recurrence earlier can enable us to give the right dose of treatment for the right duration, thereby improving prognosis. This study deals with the comparison of various machine learning models for breast cancer recurrence prediction in 5 years and also in determining the feature contribution in cancer recurrence using SHAP algorithm. Among the machine learning models,

the overall best performance in prediction in terms of C-index, F1-score, precision, accuracy, and recall was given by random forest model. Future scope of this work may involve using the top features identified by SHAP as a feature selection method to re-train the models with only those features and observe the performance for cancer recurrence prediction.

References

1. Bennett KP, Demiriz A, Maclin R (2002) Exploiting unlabeled data in ensemble methods. In: Proceedings of the eighth ACM SIGKDD international conference on knowledge discovery and data mining, pp 289–296. https://doi.org/10.1145/775047.775090
2. Cheng L, Swartz MD, Zhao H, Kapadia AS, Lai D, Rowan PJ et al (2012) Hazard of recurrence among women after primary breast cancer treatment—a 10-year follow-up using data from SEER-Medicare. Cancer Epidemiol Prevent Biomark 21(5):800–809. https://doi.org/10.1158/1055-9965.EPI-11-1089
3. van den Hurk CJ, Eckel R, van de Poll-Franse LV, Coebergh JWW, Nortier JW, Hölzel D et al (2011) Unfavourable pattern of metastases in M0 breast cancer patients during 1978–2008: a population-based analysis of the Munich Cancer Registry. Breast Cancer Res Treat 128(3):795–805. https://doi.org/10.1007/s10549-011-1372-y
4. Chakradeo K, Vyawahare S, Pawar P (2019) Breast cancer recurrence prediction using machine learning. In: 2019 IEEE conference on information and communication technology, pp 1–7. IEEE. https://doi.org/10.1109/CICT48419.2019.9066248
5. Lara-Velazquez M, Al-Kharboosh R, Jeanneret S, Vazquez-Ramos C, Mahato D, Tavanaiepour D et al (2017) Advances in brain tumor surgery for glioblastoma in adults. Brain Sci 7(12):166. https://doi.org/10.3390/brainsci7120166
6. Sanz A, Del Valle ML (2016) Extending adjuvant aromatase-inhibitor therapy to 10 years. N Engl J Med 375(16):1590–1590. https://doi.org/10.1056/nejmc1610719
7. Colleoni M, Sun Z, Price KN, Karlsson P, Forbes JF, Thürlimann B et al (2016) Annual hazard rates of recurrence for breast cancer during 24 years of follow-up: results from the international breast cancer study group trials I to V. J Clin Oncol 34(9):927. https://doi.org/10.1200/JCO.2015.62.3504
8. Vinitha S, Hao Y, Hwang K, Wang Lu, Wang Li (2019) Disease prediction by machine learning over big data from healthcare communities. Comput Sci Eng 8(1). https://doi.org/10.1109/ACCESS.2017.2694446
9. Chae S, Kwon S, Lee D (2018) Predicting infectious disease using deep learning and big data. Int J Environ Res Public Health 15(8):1596. https://doi.org/10.3390/ijerph15081596
10. Dawes TJ, de Marvao A, Shi W, Fletcher T, Watson GM, Wharton J et al (2017) Machine learning of three-dimensional right ventricular motion enables outcome prediction in pulmonary hypertension: a cardiac MR imaging study. Radiology 283(2):381–390. https://doi.org/10.1148/radiol.2016161315
11. Battineni G, Sagaro GG, Chinatalapudi N, Amenta F (2020) Applications of machine learning predictive models in the chronic disease diagnosis. J Personal Med 10(2):21. https://doi.org/10.3390/jpm10020021
12. Ford E, Carroll JA, Smith HE, Scott D, Cassell JA (2016) Extracting information from the text of electronic medical records to improve case detection: a systematic review. J Am Med Inform Assoc 23(5):1007–1015. https://doi.org/10.1093/jamia/ocv180
13. Ojha U, Goel S (2017) A study on prediction of breast cancer recurrence using data mining techniques. In: 2017 7th international conference on cloud computing, data science & engineering-confluence, pp 527–530. IEEE. https://doi.org/10.1109/CONFLUENCE.2017.7943207

14. Roshani F, Turksen IB, Zarandi MF, Maftooni M (2015) Fuzzy expert system for prognosis of breast cancer recurrence. In: 2015 annual conference of the north american fuzzy information processing society (NAFIPS) held jointly with 2015 5th world conference on soft computing (WConSC), pp 1–5. IEEE. https://doi.org/10.1109/NAFIPS-WConSC.2015.7284208
15. Alzu'bi A, Najadat H, Doulat W, Al-Shari O, Zhou L (2021) Predicting the recurrence of breast cancer using machine learning algorithms. Multimed Tools Appl 80(9):13787–13800. https://doi.org/10.1007/s11042-020-10448-w
16. Alwohaibi M, Alzaqebah M, Alotaibi NM, Alzahrani AM, Zouch M (2021) A hybrid multi-stage learning technique based on brain storming optimization algorithm for breast cancer recurrence prediction. J King Saud Univ Comput Inform Sci. https://doi.org/10.1016/j.jksuci.2021.05.004
17. Lundberg SM, Lee SI (2017) A unified approach to interpreting model predictions. In: Proceedings of the 31st international conference on neural information processing systems, pp 4768–4777
18. Curtis C, Shah SP, Chin SF, Turashvili G, Rueda OM, Dunning MJ et al (2012) The genomic and transcriptomic architecture of 2,000 breast tumours reveals novel subgroups. Nature 486(7403):346–352. https://doi.org/10.1038/nature10983
19. Fu B, Liu P, Lin J, Deng L, Hu K, Zheng H (2018) Predicting invasive disease-free survival for early stage breast cancer patients using follow-up clinical data. IEEE Trans Biomed Eng 66(7):2053–2064. https://doi.org/10.1109/TBME.2018.2882867
20. Haskul M, Yaman E (2019) Comparison of different machine learning algorithms for breast cancer recurrence classification. Southeast Europe J Soft Comput 8(2). https://doi.org/10.21533/scjournal.v8i2.179
21. Yarabarla MS, Ravi LK, Sivasangari A (2019) Breast cancer prediction via machine learning. In: 2019 3rd international conference on trends in electronics and informatics (ICOEI), pp 121–124. IEEE. https://doi.org/10.1109/ICOEI.2019.8862533
22. Nicolò C, Périer C, Prague M, Bellera C, MacGrogan G, Saut O, Benzekry S (2020) Machine learning and mechanistic modeling for prediction of metastatic relapse in early-stage breast cancer. JCO Clin Cancer Inform 4:259–274. https://doi.org/10.1200/CCI.19.00133
23. Macías-García L, Martínez-Ballesteros M, Luna-Romera JM, García-Heredia JM, García-Gutiérrez J, Riquelme-Santos JC (2020) Autoencoded DNA methylation data to predict breast cancer recurrence: Machine learning models and gene-weight significance. Artif Intell Med 110:101976. https://doi.org/10.1016/j.artmed.2020.101976

Interval Modeling of Doha Water Treatment Plant

V. P. Meena, Aeshna Anand, Rohit Verma, Megha Khatri, Satyaban Behera, and V. P. Singh

Abstract Parameter variations adversely affect the performance of the system. Many systems are modeled as interval systems due to the ability to handle uncertainty. In this article, the Doha water treatment plant is modeled as an interval system. Interval modeling of desalination plant plays an important role which focuses on the construction of transfer function. Uncertainty is considered in all coefficients of the transfer function of the system for getting the interval model of the Doha water treatment plant. Further, the obtained interval models are analyzed for stability. Time domain response analysis of these parameters helps in designing and plotting control for the Doha plant.

Keywords Control · Doha system · Interval system · Modeling

1 Introduction

The rapid depletion in groundwater level and quality of running water has led to an exponential rise in demand for freshwater. This water scarcity has increased the demand for desalination plants. The desalination process is the elimination of salts from the sea or brackish water which becomes suitable for human consumption, industrial use, agriculture, etc. There are several methods used for the desalination process like solar distillation, multiple-effect distillation (MED), freeze–thaw, and wave-powered desalination. Amidst them, the leading process is reverse osmosis (RO) because of its low energy consumption and the highest efficiency [1, 2]. The RO membrane process uses high pressure to separate freshwater by rejecting salts with the aid of a semipermeable membrane [3, 4].

V. P. Meena (✉) · A. Anand · R. Verma · M. Khatri · V. P. Singh
Department of Electrical Engineering, Malaviya National Institute of Technology, Jaipur 302017, India
e-mail: vmeena1@ee.iitr.ac.in

S. Behera
Department of Information Science and Electronics, Telecommunications G.M. University Sambalpur, Sambalpur, India

© The Author(s), under exclusive license to Springer Nature Singapore Pte Ltd. 2022

A. Tripathi et al. (eds.), *Intelligent Computing Techniques for Smart Energy Systems*, Lecture Notes in Electrical Engineering 862,
https://doi.org/10.1007/978-981-19-0252-9_41

A mathematical model is required for complete analysis of the system. The nominal model is used in many cases for the same. But, there are certain limitations in the nominal model as it is only defined for certain specific operating conditions, parameter variations and does not provide much flexibility. Therefore, to get better analysis as per practical considerations, interval modeling is used. In interval modeling, finite uncertainty is considered in all coefficients of the system; thus, the coefficients vary in interval [5–10]. This method is proposed to facilitate the reduction of higher-order multi-variable systems. In many practical systems like nuclear reactor systems and cold rolling mill, interval modeling is employed.

The Doha seawater RO plant commonly known as DROP is in operation since 1984. The plant has three different membrane configuration systems, namely plate and frame (PF), hollow fiber (HF), and spiral wound (SW) systems [3, 11–15]. The Doha RO system consists of two input variables (feed pressure and pH) and two output variables (conductivity and flux). However, the performance of RO relies on the quality of the pretreatment which is crucial in case of highly saline water. The chemical dosage has to be tailored to the feed water and must be taken into account for the possible fluctuation of characteristics; otherwise, pretreatment may make the situation worse. Existing plants rely on low-level sensors and instruments to monitor the pretreatment process. On the other hand, unmanned plants suffer repetitive technical problems leading to membrane failure within few years, and the plant is then likely to be abandoned. Therefore, desalination plant must meet high standards of performance with cost-effectiveness, reliability, and operation.

A nominal model is described for DROP, and then, an interval model for the plant is developed considering 35% uncertainty in every transfer function coefficient. The structure of this paper is as follows. Section 2 includes the elucidation of the Doha Desalination Plant. Section 3 defines the interval modeling of the Doha Plant. Section 4 contains the step and impulse responses of all the transfer functions with both lower and upper limits of uncertainty. Section 5 provides the conclusion and future scope of research. This paper additionally provides the tabular descriptions of time domain specifications to support the study done.

2 Doha Desalination Plant

Doha Desalination Plant is developed in Kuwait by the Kuwait Institute of Scientific Research (KISR) [4]. It is a desalination plant that operates on the process of reverse osmosis (RO) to produce freshwater (Fig. 1).

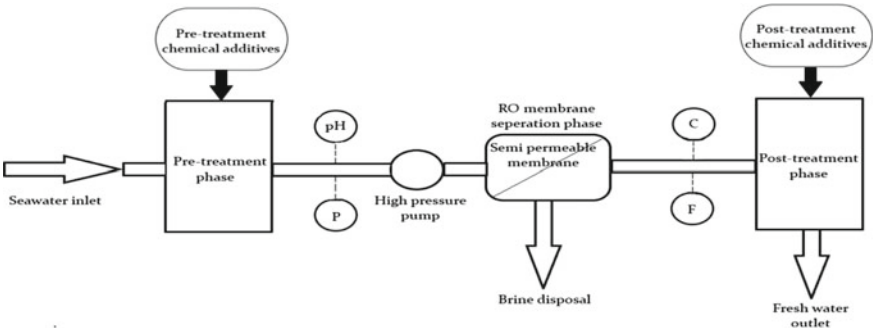

Fig. 1 Structure of Doha RO desalination plant

The process of reverse osmosis can be studied in four separate phases, i.e., 1. Pretreatment phase, 2. Water pressurization phase, 3. RO membrane separation phase, and 4. Post-treatment phase. In the pretreatment phase, the seawater or the brackish water is treated by removing suspended particles and dissolved pollutants through the appropriate use of filters and chemicals. This phase is important to prevent membrane degradation. In the water pressurization phase, a high-pressure pump is used to increase the pressure of the water as required by the membrane assembly. The range of pressure varies from 1.6 to 2.6 MPa for brackish water and 6–8 MPa for seawater. This high pressurized water passes into the RO membrane separation phase which separates freshwater from the brine solution. The concentrated brine is then removed. And the freshwater is passed for the post-treatment phase, where suitable chemicals are added as well as pH value is adjusted.

For the plant described, feed pressure (P) and pH (pH) act as input variables, and conductivity (C) and flux (F) work as output variables [16]. Thus, the system is considered as a two-input-two-output (TITO) system. The TITO system is described below as:

$$\begin{bmatrix} Y_1(s) \\ Y_2(s) \end{bmatrix} = \begin{bmatrix} T_{p11}(s) & T_{p12}(s) \\ T_{p21}(s) & T_{p22}(s) \end{bmatrix} \begin{bmatrix} U_1(s) \\ U_2(s) \end{bmatrix} \tag{1}$$

where $Y_1 = F$ (gpm), $Y_2 = C$ (μ S/cm), $U_1 = P$ (psig) and $U_2 = pH$ are flux, conductivity, feed pressure, and pH, respectively.

The transfer functions $T_{p11}(s)$, $T_{p12}(s)$, $T_{p21}(s)$ and $T_{p22}(s)$ are described as:

$$T_{p11}(s) = \frac{0.112s + 2}{3s^2 + 100s + 1000} \tag{2}$$

$$T_{p12}(s) = 0 \tag{3}$$

$$T_{p21}(s) = \frac{-178.5s - 510}{213s^2 + 700s + 1000} \tag{4}$$

$$T_{p22}(s) = \frac{-1824s - 5700}{60s^2 + 180s + 100} \tag{5}$$

3 Interval Modeling of Doha Plant

The transfer functions (2)–(5) represent the Doha Plant in form of nominal model. For these equations, considering 35% uncertainty in coefficients of the transfer function, interval model is derived. The interval transfer functions with 35% uncertainty for (2)–(5) turn out to be:

$$T_{p11}(s) = \frac{[0.0728, 0.1512]s + [1.3, 2.7]}{[1.95, 4.05]s^2 + [65, 135]s + [650, 1350]} \tag{6}$$

$$T_{p12}(s) = 0 \tag{7}$$

$$T_{p21}(s) = \frac{-[116.025, 240.975]s - [331.5, 688.5]}{[138.45, 287.55]s^2 + [455, 945]s + [650, 1350]} \tag{8}$$

$$T_{p22}(s) = \frac{-[1185.6, 2462.4]s - [3705, 7695]}{[39, 81]s^2 + [117, 243]s + [65, 135]} \tag{9}$$

4 Results and Discussion

Given below in (10)–(17) are transfer functions considering both lower as well as upper limits. Since there is no relationship between pH and flux (F), (T_{p12}) in upper as well as lower limit is considered zero.

$$T_{pL11}(s) = \frac{0.0728s + 1.3}{1.95s^2 + 65s + 650} \tag{10}$$

$$T_{pL12}(s) = 0 \tag{11}$$

$$T_{pL21}(s) = \frac{-116.025s - 331.5}{138.45s^2 + 455s + 650} \tag{12}$$

$$T_{pL22}(s) = \frac{-1185.6s - 3705}{39s^2 + 117s + 65} \tag{13}$$

$$T_{pU11}(s) = \frac{0.1512s + 2.7}{4.05s^2 + 135s + 1350} \tag{14}$$

$$T_{pU12}(s) = 0 \tag{15}$$

$$T_{pU21}(s) = \frac{-240.975s - 688.5}{287.55s^2 + 945s + 1350} \tag{16}$$

$$T_{pU22}(s) = \frac{-2462.4s - 7695}{81s^2 + 243s + 135} \tag{17}$$

The transfer functions are analyzed with time domain analysis, and all of them were found to be stable systems. Since the systems are stable, their further analysis is possible. After analysis of above transfer functions, impulse and step response plots were developed in order to obtain time domain parameters.

Given below, Figs. 2 and 3 are the plots of impulse as well as step responses of transfer function for lower and upper limits. A tabular form of time domain specifications is also generated for a clear view of time domain analysis Table 1.

It can be observed from Table 1 that the transfer function (T_{p22}) between input pH and output conductivity (C) has reached an overdamped condition, and rest of the transfer function (T_{p11}) and (T_{p21}) have underdamped response. It can also be noticed that the transfer function between input and output manifests the similar time domain response with upper and lower limits of uncertainty.

5 Conclusion

In this article, an interval system for the Doha water treatment plant is suggested by considering a fixed amount of uncertainty in every coefficient of the transfer function of the system. The acquired model successfully approximates the system. There is a possibility of the development of other interval models by considering different sets of the uncertainty of either lower bound or upper bound in all the coefficients of the transfer function for a future line of research work. Another future scope of research development can be model reduction of interval systems.

Fig. 2 Responses for lower limits

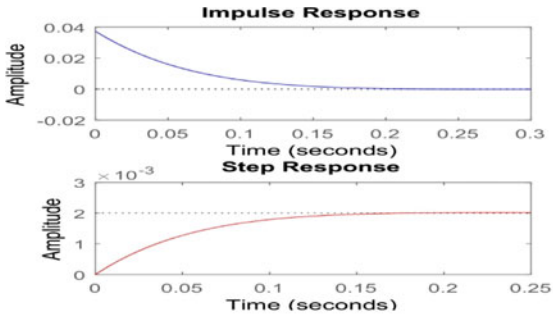

(a) Response of $T_{pL11}(s)$

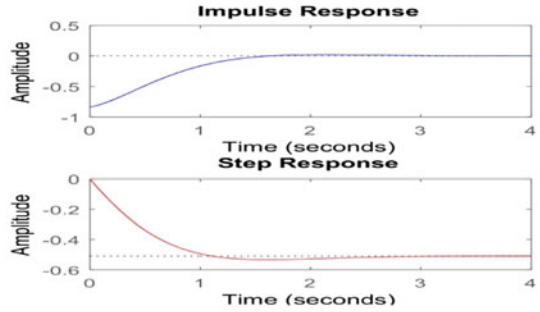

(b) Response of $T_{pL21}(s)$

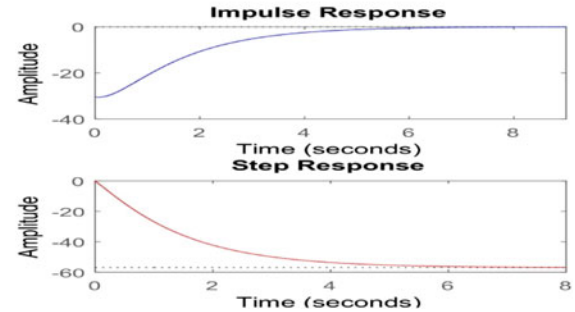

(c) Response of $T_{pL22}(s)$

Fig. 3 Responses for upper limits

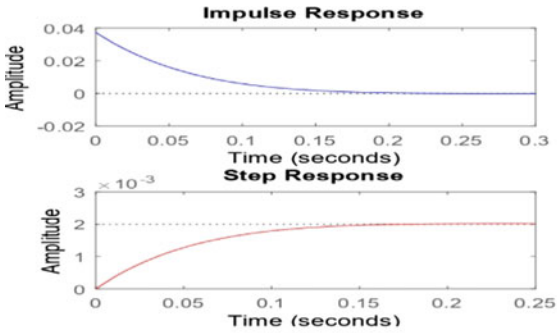

(d) Response of $T_{pU11}(s)$

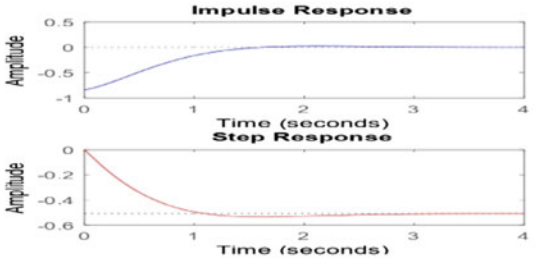

(e) Response of $T_{pU21}(s)$

(f)

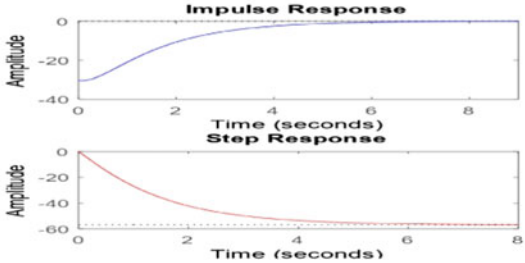

(g) Response of $T_{pU22}(s)$

Table 1 Time domain response specifications

Transfer function	Rise time (s)	Peak time (s)	Peak overshoot	Settling time (s)
$T_{pL}11$	0.0959	0.2321	0.8847	0.1459
$T_{pL}12$	n/a	n/a	n/a	n/a
$T_{pL}21$	0.7668	1.6255	4.5877	2.3682
$T_{pL}22$	3.1086	9.3171	0	5.4830
$T_{pU}11$	0.0959	0.2321	0.8847	0.1459
$T_{pU}12$	n/a	n/a	n/a	n/a
$T_{pU}21$	0.7668	1.6255	4.5877	2.3682
$T_{pU}22$	3.1086	9.3171	0	5.4830

References

1. Alatiqi IM, Ghabris AH, Ebrahim S (1989) System identification and control of reverse osmosis desalination. Desalination 75:119–140
2. Bandyopadhyay B, Ismail O, Gorez R (1994) Routh-pade approximation for interval systems. IEEE Trans Autom Control 39(12):2454–2456
3. Chodavarapu MM, Shaw B, Pratap Singh V (2020) Gwo based controller design for riverol-pilipovik water treatment plant. J Stat Manage Syst 23(2):463–470
4. Choudhary AK, Nagar SK (2018) Model order reduction of discrete-time interval system based on Mikhailov stability criterion. Int J Dyn Control 6(4):1558–1566
5. Al-Awadi F, Abdel-Jawad M (1987) Evaluation of the three post-treatment systems at doha seawater reverse osmosis plant—Kuwait. Desalination 63:109–117
6. Choudhary AK, Nagar SK (2019) Order reduction in z-domain for interval system using an arithmetic operator. Circ Syst Signal Proces 38(3):1023–1038
7. Deveerasetty KK, Nagar SK (2020) Model order reduction of interval systems using an arithmetic operation. Int J Syst Sci 51(5):886–902
8. Kumari S, Taneja R (2015) Model order reduction: An approach towards a sim- pler system design. Int J Res Appl Sci Eng Technol (IJRASET) 3:1008–1011
9. Mathur N, Meena VP, Singh VP (2021) Interval modeling of riverol-pilipovik water treatment system. In: International conference on smart grid energy systems and control
10. Vrkalovic S, Lunca E-C, Borlea I-D (2018) Model-free sliding mode and fuzzy controllers for reverse osmosis desalination plants. Int J Artif Intell 16(2):208–222
11. Meena VP, Singh VP, Barik L (2021) Kharitonov polynomials based order reduction of continuous interval systems. Circuit Syst Signal Proces 41:743–761
12. Padhy AP, Singh VP, Pattnaik S (2018) Model reduction of multi-input-multi-output discrete interval systems using gain adjustment. Int J Pure Appl Math 119(12):12721–12739
13. Prakash T, Singh VP, Singh SP, Mohanty SR (2017) Binary Jaya algorithm based optimal placement of phasor measurement units for power system observability. Energy Convers Manage 140:34–35
14. Rathore NS, Singh VP, Phuc BDH (2019) A modified controller design based on symbiotic organisms search optimization for desalination system. J Water Suppl Res Technol—AQUA 68(5):337–345
15. Rathore NS, Singh VP (2019) Whale optimisation algorithm-based controller design for reverse osmosis desalination plants. Int J Intel Eng Inform 7(1):77–88
16. Singh VP, Chauhan DPS, Singh SP, Prakash T (2017) On time moments and markov parameters of continuous interval systems. J Circ Syst Comput 26(03):1750038
17. Singh VP, Chandra D (2012) Reduction of discrete interval systems based on pole clustering and improved pade approximation: a computer-aided approach. Adv Model Optim 14(1):45–56

First Principles Study of Novel $BaSn_{1-x}In_xN_2$ (X = 0, 0.25) for Thermoelectric Applications

B. R. Bhagat, Rushikesh Pokar, and Alpa Dashora

Abstract Requirement of heat transforming devices at macro and micro levels led us to discover and study a new material $BaSnN_2$ using state-of-the-art density functional theory. Present work comprises of structural, electronic and thermoelectric properties showing exothermic nature of formation for easy synthesis and its possible application in devices utilizing waste heat. $BaSnN_2$ shows indirect band gap of 1.42 eV within generalized gradient approximation while calculated band structure shows high electron mobility with high variance in effective mass of electron and holes. High Seebeck coefficient and electrical conductivity while relatively low electronic thermal conductivity directs us towards higher thermoelectric efficiency as ZT_e tends to unity. Increase in electrical and thermal conductivity along with increasing chemical potential on either side of Fermi energy is found, while their higher values in negative chemical potential region suggests p-type doping for higher efficiency. 25% In doping in $BaSnN_2$ is also studied which worked as p-type doping and almost unaltered band gap value of pristine. Our results show $BaSnN_2$ and $BaSn_{1-x}In_xN_2$ as potential thermoelectric materials at room temperature for promising applications in thermoelectric refrigerator and generators in small-scale digital devices.

Keywords Seebeck coefficient · Electrical conductivity · Thermoelectric effect · p-type semiconductor

1 Introduction

Power generation and energy conversion utilizing waste heat have rejuvenated the interest of researchers across globe in active consideration of thermoelectric materials. Low thermal conductivity as a result of phonon anharmonicity and high valley degeneracy for high electrical conductivity are essential requirements for high efficiency. Various n, p-type doping [1–3], vacancy creation [4] and structural modification using strain and stress [5, 6] have been performed to make up the quality

B. R. Bhagat (✉) · R. Pokar · A. Dashora
Computational Material Science Laboratory, Department of Physics, The M. S. University of Baroda, Vadodara 390002, India
e-mail: bhagatbrajesh1996@gmail.com

© The Author(s), under exclusive license to Springer Nature Singapore Pte Ltd. 2022

A. Tripathi et al. (eds.), *Intelligent Computing Techniques for Smart Energy Systems*, Lecture Notes in Electrical Engineering 862,
https://doi.org/10.1007/978-981-19-0252-9_42

factor of the material for its potential applications in the mainstream energy technology. Low band gap semiconductors have shown promising results by improving the electrical conductivity as the temperature increment promotes easy minority charge carrier transfer across the band gap [7], also, increased conductivity point towards high power factor. Favourable properties for thermoelectric performance includes suppression of sharp values of Seebeck coefficient (thermopower) at higher temperature resulting in optimal carrier concentration, while interplay between a sharp peak of thermopower near Fermi energy and large electrical conductivity at high chemical potential results in high power factor for enhanced thermoelectric efficiency. Phonon scattering centre generation leading to lowering of phonon thermal conductivity has been verified to increase the figure of merit, although shortcoming regarding saturation of thermal conductivity directs us to increase power factor. Optimal carrier concentration and higher carrier mobility have found to improve the thermoelectric performance of the material.

Successful synthesis of $CuAlO_2$ along with linear variation of its power factor with temperature is presented by Park et al. [8]. Work done by Banerjee and co-workers on p-type $CuAlO_2$ thin film proclaiming high Seebeck coefficient at room temperature with enhanced thermoelectric figure of merit [9] and increased conductivity in $LaCoO_3$ on Barium doping at room temperature [10] inspired us to consider alkaline earth element-based compound at room temperature with efficient thermoelectric materials. Reduction in lattice thermal conductivity of in situ formed nanostructure and state-of-the-art ZT value nearly 1.1 for Mg_2(Si, Sn) compound display potential application of Sn in increasing efficiency in low-dimension thermoelectric materials along with its non-toxic and earth abundant elements [11]. Lamellar structure, uniaxial pressure and phonon scattering due to incorporation of In in SnSe results in the decrement of thermal conductivity to 0.48 W/μK at 615 K while increased scattering with doping concentration implies importance of anisotropic nature of material and large hole concentration [12]. Role of In-based double perovskites as thermoelectric material is also widely reported where the In atom formed states in the conduction and also fulfilled the requirement of hole doping for better thermoelectric performance in p-type semiconductor [13–15].

Considering the role of each element in the thermoelectric effect, we have proposed new material $BaSnN_2$ and computed its structural, electronic and thermoelectric properties by calculating density of states, band structure, chemical potential dependent parameters for thermoelectric effects, etc. using density functional theory. The role of In doping in $BaSnN_2$ and effect on electronic and thermoelectric properties have also been discussed.

2 Methodology

All the structural, electronic and thermoelectric properties were performed using Quantum Espresso software utilizing density functional theory [16–18] which considers Kohm-Sham equation to solve many body problems and computations of

ground-state energy using ultrasoft pseudo-potentials. Computations were carried out on the unit cell of $BaSnN_2$ with space group I-42d (#122) of tetragonal crystal system with the generalized gradient approximation (GGA) [19] treated as exchange–correlation functional.

Quasi-Newton ionic relaxation using the Broyden, Fletcher, Goldfarb, Shanno (BFGS) method was used for structural parameters optimization [16–18]. Lattice parameters were fully optimized using energy cutoff of 60 Ry and 6 × 6 × 6 Monkhorst–Pack k-point grid was used for Brillouin zone integrations with fixed convergence threshold of 10^{-6} Ry. Investigation of transport properties was carried out using BoltzTrap code [20] utilizing the Boltzmann equations considering constant relaxation time approximation (CRTA) [21].

3 Results

The optimized crystal structure (top and side view) of $BaSnN_2$ is presented in Fig. 1 a, b. After geometry optimization, optimized lattice parameters for $BaSnN_2$ are a = b = 6.058 Å, c = 7.997 Å. Optimized lattice parameters and atomic positions were further relaxed after In doping at Sn site and we found, a = b = 6.07 Å, c = 8.00 Å. Energetic stability, optimal lattice parameters and uniform bond length of 2.11 Å, 2.67 Å and 3.63 Å for Sn-N, N-Ba and Ba-Ba, respectively result in retainment for I-42d (#122) space group of tetragonal geometry. Doping of single In atom at Sn site increases the lattice parameters as a result of higher ionic radii of dopant In. All the crystal parameters for pristine and In-doped material are also presented in Table 1.

An important parameter directing towards successful synthesis of a material is its theoretical formation energy (E_{form}) which is the difference of total energy of material and energy of its individual elements. The E_{form} computed for $BaSnN_2$ in this work is −1.56 eV/f.u, which shows its formation to be exothermic and feasible in nature. After doping of In E_{form} reduces to −12.28 eV/f.u., suggests possibility of easy synthesis of doped material as well.

Figures 1 c, d comprise energy band diagram along the high symmetric direction of the Brillouin zone and total density of states (DOS) for $BaSnN_2$ and $BaSn_{0.75}In_{0.25}N_2$. An indirect band gap (E_g) of 1.42 eV between XΓ–Γ is calculated in $BaSnN_2$, while E_g increases to 1.46 eV along with shifting of Fermi energy (E_F) towards valence band on In doping. Therefore, on In doping in $BaSnN_2$, formation of p-type semiconductor implies successful acceptor doping. Large curvature of conduction band minima (CBM) implies light electrons and small curvature of valence band maxima (VBM) denotes heavy holes in our system resulting in high electron mobility leading to high variance in the effective mass of charge carriers and low value of effective mass ratio providing high charge carrier migration and low rate of recombination of electron–hole pair that improves electrical conductivity. The band curvature (VBM and CBM) shown by pristine material does not change on doping, rather E_F shifts towards occupied orbitals implying increase in hole carrier concentration which is beneficial for large phonon scattering within the material.

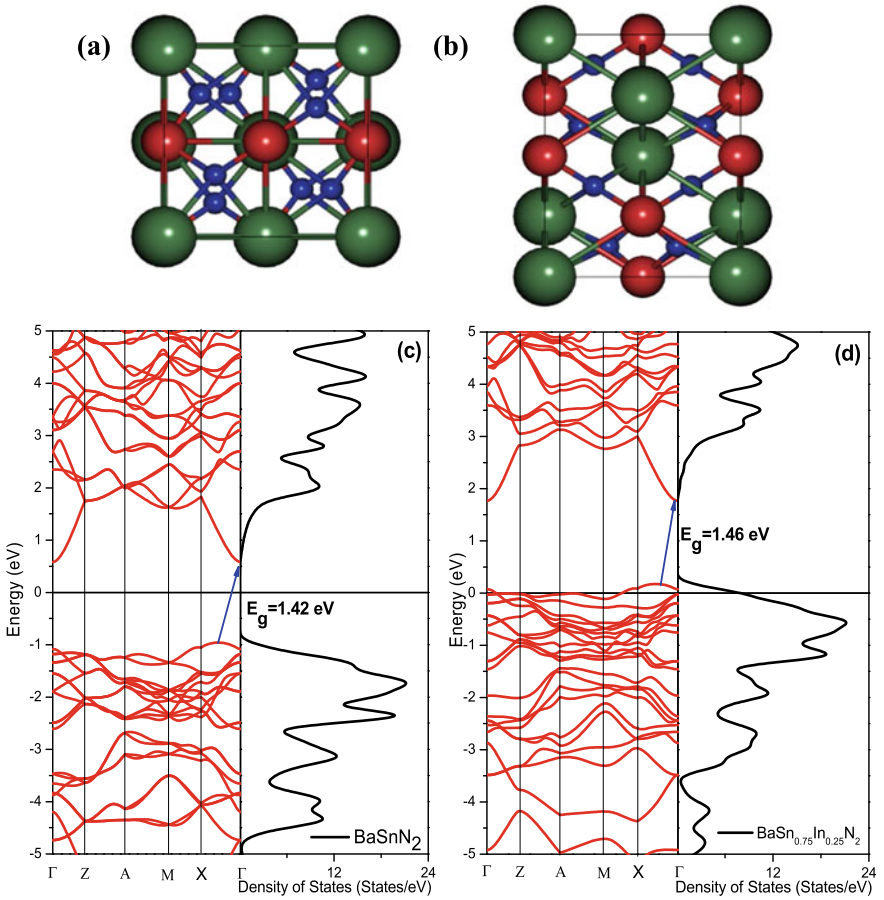

Fig. 1 **a** Top and **b** side view of $BaSnN_2$ (Ba: Green, Sn: Red, N: Blue) crystal structure along with energy band diagram and total density of states for **c** $BaSnN_2$ and **d** $BaSn_{0.75}In_{0.25}N_2$

Table 1 Optimized lattice parameter and atomic positions for $BaSnN_2$ and $BaSn_{0.75}In_{0.25}N_2$

Sample		Atomic positions			Lattice parameters (Å)	
		x	y	Z	$a = b$	c
$BaSnN_2$	Ba	0.000	0.000	0.000	6.058	7.997
	Sn	0.500	0.500	0.000		
	N	0.323	0.250	0.125		
$BaSn_{0.75}In_{0.25}N_2$	Ba	0.000	0.000	0.000	6.072	8.003
	Sn/In	0.500	0.500	0.000		
	N	0.316	0.244	0.130		

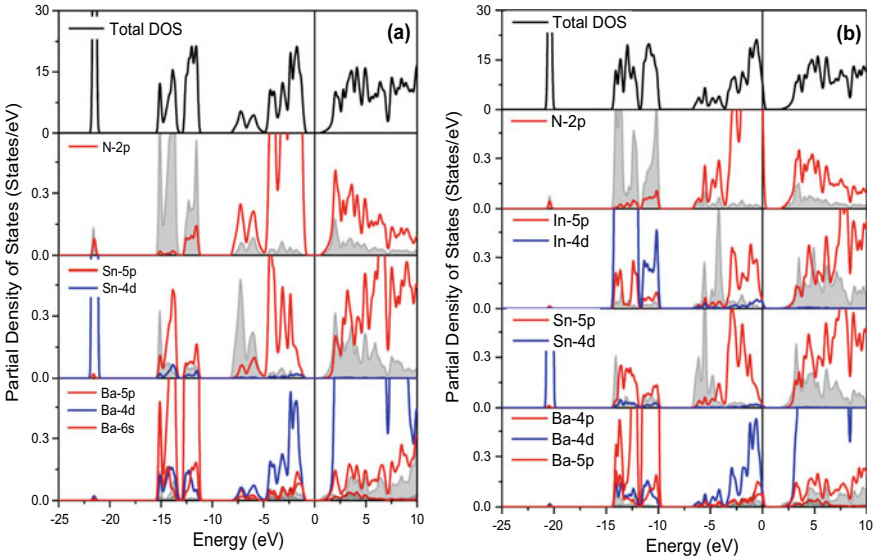

Fig. 2 Partial density of states for **a** pristine $BaSnN_2$ and **b** $BaSn_{0.75}In_{0.25}N_2$

Partial DOS of $BaSnN_2$ and $BaSn_{0.5}In_{0.25}N_2$ are presented in Fig. 2 a, b. VBM is dominated by the 2p states of N atom while CBM has major contribution of Ba-4d states while Sn-4d states show their contribution at lower energy region around − 22 eV which is clearly seen from Fig. 2a. Sn-5p states show equal contribution in VBM and CBM whereas the shaded 5 s orbitals for Sn provide major contribution in CBM. Figure 2b shows dominance of Ba in VBM and CBM, sharp DOS of N-2p states, In-5p states in occupied orbital, In-4d states are present in lower energy region, presence of In-5s states in VBM and dominance of Ba with its sharp feature in CBM explains the crucial interplay of effective mass variation and difference in electrical conductivity in either VBM or CBM for pristine and doped system for effective tuning of electronic properties based on dopant concentration. Therefore, similar positions of orbitals in the valence band and conduction band provides us multiple possibilities to utilize the material with functionalization for specific application.

Transformation of heat energy into electrical energy is known as thermoelectric effect for which analysis of primordial parameters like Seebeck coefficient (S), electrical conductivity per scattering time (σ/τ), electronic thermal conductivity per scattering time (κ/τ) and electronic figure of merit (ZT_e) along with their variation with respect to chemical potential is of utmost importance. To study the temperature dependent thermoelectric effect of novel $BaSnN_2$, the above-mentioned parameters at three different temperatures (300, 500 and 800 K) against chemical potential in a consistent range are computed and presented in Fig. 3a–d. Seebeck coefficient (S) is the ratio of voltage difference created by the movement of free electron between high temperature region and low temperature region to the temperature difference, material with majority charge carriers as electrons (n-type) has negative while with

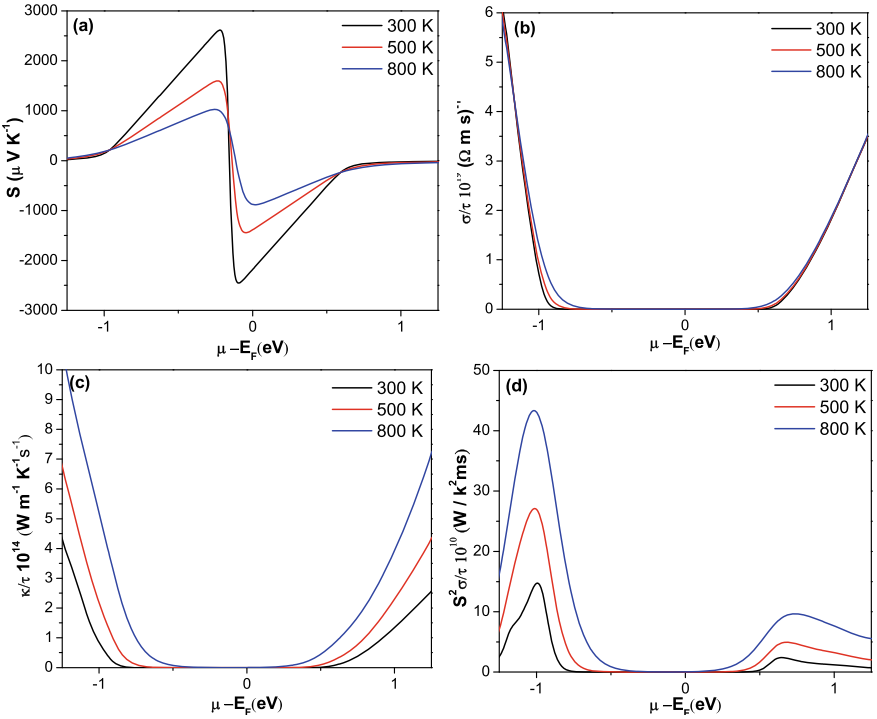

Fig. 3 Thermoelectric properties of $BaSnN_2$ within CRTA. **a** Seebeck's coefficient. **b** Electrical conductivity with respect to scattering time. **c** Electronic thermal conductivity with respect to scattering time. **d** Power factor with respect to scattering time, $S^2\sigma/\tau$ at $T = 300$, 500 and 800 K

majority charge carriers as holes (p-type) has respective positive value of S. Whereas the chemical potential determines the charge carrier concentration of the system, from Fig. 3a negative value of intrinsic Seebeck coefficient at $\mu - E_F = 0$ suggests dominance of electron in the thermoelectric transport of $BaSnN_2$. The absolute values of thermopower is 2615.12, 1597.15 and 1024.27 μ V K^{-1} at 300, 500 and 800 K, respectively established it as a good thermoelectric material.

High value of σ/τ is required to reduce Joule-heating effect in material, higher value of σ/τ in the positive region of chemical potential promotes higher electron doping and higher value of κ/τ in negative region appeals for electron acceptor doping to achieve larger phonon scattering and to reduce the thermal conductivity. Increase in the value of σ/τ and κ/τ with increase in chemical potential and similarity in the plot justifies the Wiedemann–Franz law ($\kappa = \sigma LT$ [22]; where L is the Lorentz number, σ represents the electrical conductivity, while T is the absolute temperature). Power Factor (PF) originates from S, its higher value in $\mu - E_F < 0$ shows suitability of p-type doping for further improvement of its value; therefore in the present work, we have also included In doping as an acceptor impurity. From Fig. 4a–d, after In doping, the shift of E_F towards negative chemical potential verify formation of p-type

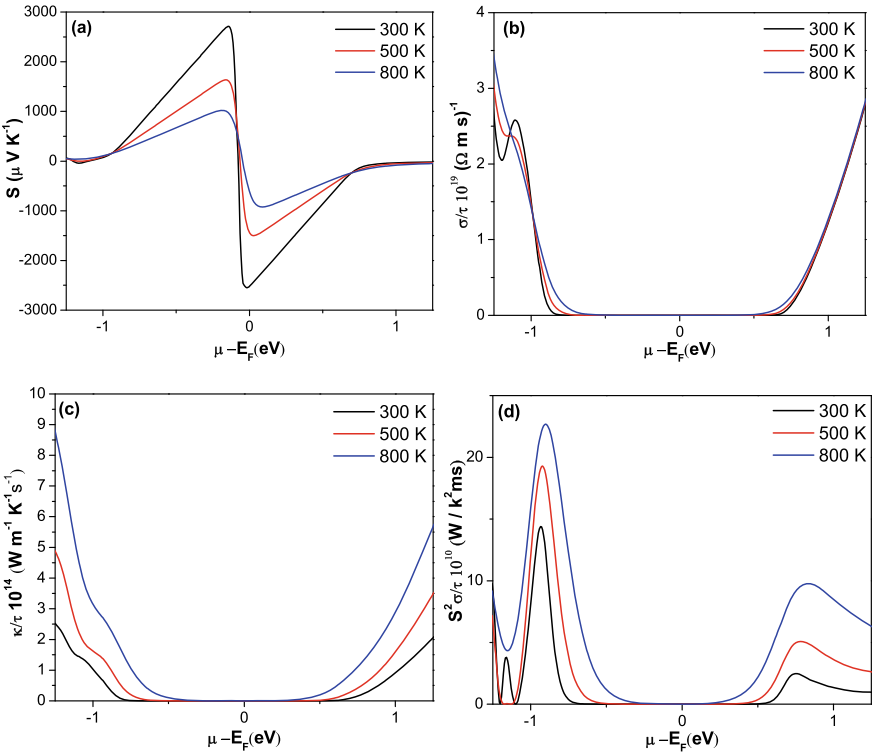

Fig. 4 Thermoelectric properties of $BaSn_{0.75}In_{0.25}N_2$ with **a** Seebeck's coefficient. **b** Electrical conductivity with respect to scattering time. **c** Electronic thermal conductivity with respect to scattering time. **d** Power factor with respect to scattering time at $T = 300$, 500 and 800 K.

semiconductor, increased value of S to 2710.10, 1633.62 and 1019.29 μ V K^{-1} at 300, 500 and 800 K, respectively justify the importance of In doping in increasing power factor. But reduction in σ/τ on either sides signifies lower electrical conductivity, while decrease in electronic κ/τ with In doping satisfies the reason of acceptor doping in pristine material. Linear relationship of temperature with κ/τ signifies its application as room temperature thermoelectric material.

Although, high electrical conductivity and high Seebeck's coefficient result in high power factor of pristine material but it does not guarantee a good ZT_e value; therefore, electronic thermal conductivity is an important parameter for accurate calculation where its low value is preferable. Here the calculated $ZT_e = 0.99$ at 300 K shown in Fig. 5 suggests its suitability in a thermoelectric device such as generators and cooler. Doping has caused reduction in power factor due to decrease in electrical conductivity but the reduction in thermal conductivity has trivially increased the ZT_e. Therefore, further investigation of phonon thermal conductivity and scattering time with carrier mobility is required for better understanding of overall thermoelectric

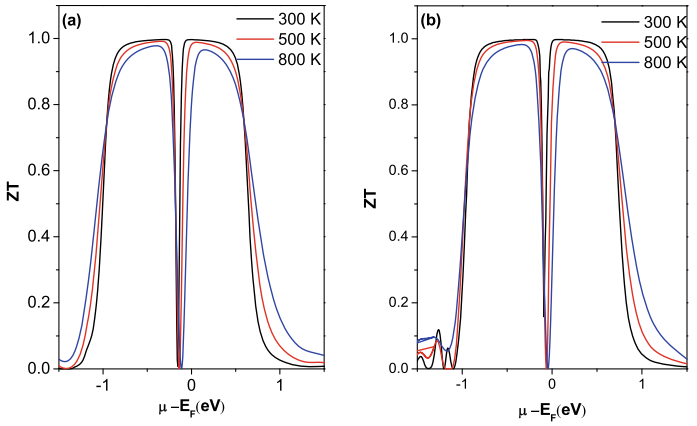

Fig. 5 Thermoelectric figure of merit (ZT_e) for **a** $BaSnN_2$ and **b** $BaSn_{0.75}In_{0.25}N_2$ with CRTA at T = 300, 500 and 800 K

efficiency and further modification in terms of improved electrical conductivity is invited.

4 Conclusions

An ab-initio study of structural, electronic and thermoelectric properties of proposed $BaSnN_2$ and $BaSn_{0.75}In_{0.25}N_2$ compounds with high negative formation energy have been undertaken. Very small change in band gap from 1.42 to 1.46 eV is reported on In doping in $BaSnN_2$ and shifting of E_F towards VB suggested In doping as p-type doping. Band curvature study shows lighter electron for higher mobility, hence larger electrical conductivity is also verified by density of states. High Seebeck coefficient and high electrical conductivity increases power factor value while high variance in charge carrier effective mass implies low rate of recombination. Whereas lower value of electronic thermal conductivity shown by this material helps in retaining the temperature difference across the surfaces. For In-doped system, high thermopower with low electronic thermal conductivity and high hole concentration results in value of ZT_e to be close to unity for pristine as well as doped system signifying higher conversion efficiency of thermal to electrical energy value at room temperature. Better value of figure of merit at higher temperature emphasizes on its applicability over large temperature range. Since, the dominance of Seebeck coefficient and electrical conductivity in negative chemical potential region indicated p-type doping; therefore, we studied acceptor dopant in the parent material and found its role in decreasing the electronic thermal conductivity as an important milestone for further modification in enhancing thermoelectric efficiency.

Acknowledgements The authors show their sincere gratitude to the University Grants Commission, India for their UGC Start-up Research grant. AD is also thankful to the University Grants Commission, India for Assistant Professorship under Faculty Recharge Programme. BRB is thankful for University Research Fellowship to The Maharaja Sayajirao University of Baroda, India.

References

1. Singh D, Shukla V, Ahuja R (2020) Optical excitations and thermoelectric properties of two-dimensional holey graphene. Phy Rev B 102(7):075444
2. Lan JL, Zhan B, Liu YC, Zheng B, Liu Y, Lin YH, Nan CW (2013) Doping for higher thermoelectric properties in p-type BiCuSeO oxyselenide. Appl Phys Lett 102(12):123905
3. Gelbstein Y, Dashevsky Z, Dariel MP (2005) High performance n-type PbTe-based materials for thermoelectric applications. Physica B: Condens Matter 363(1–4):196
4. Li W, Lin S, Zhang X, Chen Z, Xu X, Pei Y (2016) Thermoelectric properties of Cu_2SnSe_4 with intrinsic vacancy. Chem Mater 28(17):6227
5. Lv HY, Lu WJ, Shao DF, Sun YP (2014) Enhanced thermoelectric performance of phosphorene by strain-induced band convergence. Phys Rev B 90(8):085433
6. Thonhauser T, Scheidemantel TJ, Sofo JO, Badding JV, Mahan GD (2003) Thermoelectric properties of Sb_2Te_3 under pressure and uniaxial stress. Phys Rev B 68(8):085201
7. Liu Y, Lan J, Xu W, Liu Y, Pei YL, Cheng B, Liu DB, Lin YH, Zhao LD (2013) Enhanced thermoelectric performance of a BiCuSeO system via band gap tuning. Chem Commun 49(73):8075
8. Park K, Ko KY, Seo WS (2005) Thermoelectric properties of $CuAlO_2$. J Eur Ceram Soc 25(12):2219
9. Banerjee AN, Maity R, Ghosh PK, Chattopadhyay KK (2005) Thermoelectric properties and electrical characteristics of sputter-deposited p-$CuAlO_2$ thin films. Thin Solid Films 474(1–2):261
10. Muraleedharan S, Davis N, Althaf R, Singh A, Ashok AM (2021) Exploring the thermoelectric behavior of intrinsic and defect induced $LaCoO_3$ with selected alkaline earth metals. J Alloys Compd 857:157507
11. Zhang Q, He J, Zhu TJ, Zhang SN, Zhao XB, Tritt TM (2008) High figures of merit and natural nanostructures in $Mg_2Si_{0.4}Sn_{0.6}$ based thermoelectric materials. Appl Phys Lett 93(10):102109
12. Dona J, Navaneethan M, Harish S, Archana J, Muthamizhchelvan C, Hara K (2021) Synergistic effect of indium nano-inclusions to enhance interface phonon scattering in polycrystalline SnSe for thermoelectric applications. J Alloys Compd 856:157358
13. Aslam F, Sabir B, Hassan M (2021) Structural, electronic, optical, thermoelectric, and transport properties of indium-based double perovskite halides Cs_2InAgX_6 (X= Cl, Br, I) for energy applications. Appl Phys A 127(2):1
14. Gajaria TK, Dabhi SD, Jha PK (2019) Ab initio energetics and thermoelectric profiles of gallium pinictide polytypes. Sci Rep 9(1):1
15. Gajaria TK, Chodvadiya D, Jha PK (2021) Density functional theory investigation of thermal conductivity in α-CN and α-CP monolayers: Implications for thermal management of electronic devices. ACS Appl Nano Mater 4(5):4474
16. Hohenberg P, Kohn W (1964) Inhomogeneous electron gas. Phys Rev 136:B864
17. Kohn W, Sham LJ (1965) Self-consistent equations including exchange and correlation effects. Phys Rev 140:A1133
18. Giannozzi P, Baroni S, Bonini N, Calandra M, Car R, Cavazzoni C et al (2009) QUANTUM ESPRESSO: a modular and open-source software project for quantum simulations of materials. J Phys Cond Mat 21(39):395502

19. Perdew JP, Burke K, Ernzerhof M (1996) Generalized gradient approximation made simple. Phys Rev Lett 77:3865
20. Madsen GK, Singh DJ (2006) BoltzTraP. A code for calculating band-structure dependent quantities. Comput Phys Commun 175(1):67
21. Goldsmid HJ (2010) Introduction to thermoelectricity. Springer, Berlin, p 121. ISBN: 978-3-662-49256-7
22. Bejan A, Kraus AD (2003) Heat Transfer Handbook, 1. Wiley, New York

Performance and Stability Analysis of Industrial Robot Manipulator

Shailu Sachan, Harsh Goud, and Pankaj Swarnkar

Abstract Human–robot interaction (HRI) is essential in industry to the demands of technical feasibility and productivity gains in terms of quality, accuracy, dependability, and adaptability. Developing a human-like behaviour control method is one of the most difficult elements of robotics research. The dynamic nature of human responses complicates the task of a robot controller even further. This paper focuses on the development of an optimum controller for controlling a human-like robotic arm in industrial applications. The conventional technique of tuning of a PID controller is inefficient, time consuming, and has limited capabilities. A Genetic Algorithm (GA) is used to optimise the gain parameters of PID controller, with an objective function based on the Mean Square Error (MSE) as the performance index being minimised. The simulation results showcased the efficacy of GA-PID controlled industrial robot manipulator in terms of performance and stability.

Keywords Human–robot interaction (HRI) · PID controller · Genetic algorithm (GA) · Industrial robot

1 Introduction

Over the previous few decades, there has been a significant advancement in the development of robots to fulfil industrial demands for increased productivity, quality, precision, and dependability. Many industrial processes that consume a lot of energy are thought to be very efficient. To reduce energy consumption in the industry, industrial

S. Sachan (✉) · P. Swarnkar
MANIT, Bhopal, M.P, India
e-mail: sachanshailu@gmail.com

P. Swarnkar
e-mail: p_swarnkar@yahoo.co.in

H. Goud
IIIT, Nagpur, Maharashtra, India
e-mail: hgoud@iiitn.ac.in

© The Author(s), under exclusive license to Springer Nature Singapore Pte Ltd. 2022

A. Tripathi et al. (eds.), *Intelligent Computing Techniques for Smart Energy Systems*,
Lecture Notes in Electrical Engineering 862,
https://doi.org/10.1007/978-981-19-0252-9_43

robots and automation systems must be properly designed and operated [1]. Robots are employed to do dangerous, hazardous, unpleasant, and repetitive tasks.

When robots are employed in industrial applications to collaborate with humans, human–robot interaction (HRI) [2–4] has become essential owing to the demands of technical feasibility and productivity gains in terms of quality, accuracy, dependability, and adaptability. The interaction includes many modes of communication that may be broadly classified into two categories- remote interaction and proximate interaction.

Position control is used in the majority of industrial robot manipulator applications namely, spray painting, polishing spot welding, material handling, assembling, pick-and-place, product inspection and testing, etc. [5]. The position of robot must be precisely controlled for these and numerous other applications. Controlling robots is a difficult and complex task.

PID controllers are used in many sectors of industrial automation because of its simplicity and cost-effectiveness [6–8]. But conventional technique of tuning of PID controller is time consuming and poor. The stability of conventionally controlled robot is low, which is unfortunate because stability is the most important performance issue to consider when designing a robotic position control system. In order to overcome these problems, the gain parameters of robotic controller with proportional (K_P), integral (K_I), and derivative (K_D) are optimised using Genetic Algorithm (GA) that increases robustness and flexibility. GA [9–15] is an optimization approach for stochastic global heuristic search based on natural selection mechanisms.

The following are the key contributions of this paper:

(1) Modelling of industrial robot manipulator that is robotically similar to that of a human for human–robot interaction (HRI)
(2) Design an optimised GA tuned PID robot controller using Mean Square Error (MSE) as an objective function to achieve accurate and efficient motion execution.
(3) Analysis of the stability of robot performance with and without a controller.

In Sect. 2, the modelling of industrial robot manipulator is discussed. Section 3 present the GA tuned PID controlled industrial robot manipulator and simulation results are showcased in Sect. 4 along with comparative analysis followed by conclusion and references.

2 Modelling of Industrial Robot Manipulator

Modelling of industrial robot manipulator involves dynamics and kinematics. Dynamics give the relation between force and torque of the manipulator whereas movement of manipulator that is position, velocity, and acceleration is characterised in kinematics. For many years, industrial robot manipulators are widely used to perform a variety of tasks. Humans are helped by industrial robots to enhance quality,

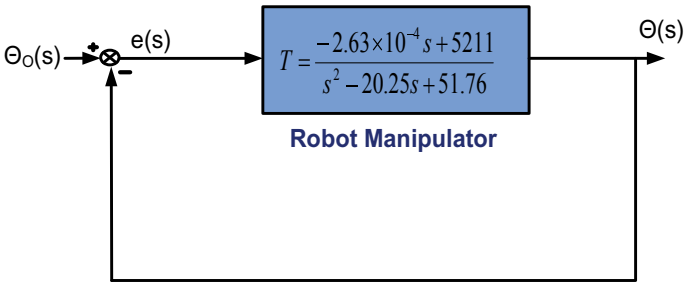

Fig. 1 Closed-loop control of human-like robot manipulator

accuracy, and technological feasibility. So, human–robot interaction (HRI) [2–4] is essential.

For successful HRI, create a conceptual framework for a human-like robotic controller for robust and behaviour-based control. Researchers studied human behaviour, to create a control strategy that is robotically similar to that of a human. The following equation can be used to represent the transfer function of the human-like robotic arm [3, 4]:

$$T = \frac{-2.63 \times 10^{-4} s + 5211}{s^2 - 20.25s + 51.76} \tag{1}$$

The closed-loop control of human-like robotic arm is shown in Fig. 1.

3 GA Tuned PID Controlled Industrial Robot Manipulator

Industrial robot manipulators are widely used in collaboration with humans to perform a wide range of tasks [2]. Where, the robot is instructed to follow a specified position trajectory and control. It is necessary to manipulate the robot's end effector in order to accomplish successful motion execution.

Stability is the most important performance issue to consider when designing a robotic position control system. Tuning of conventional robotic controller is time consuming and poor. The disadvantages of conventional controllers are overcome by using GA. GA [9–15] is an optimization approach for stochastic global adaptive search based on natural selection mechanisms. It is an iterative procedure that yields the best solution. Table 1 showed the constraints (parameters) of GA-PID control technique.

GA is used to optimise PID controller gain parameters, which include K_P, K_I, and K_D. In GA, the cost or objective function is needed to be opted such that it reduces the MSE and provides the optimum value of controller parameters [14, 15]. The objective function is denoted by:

Table 1 Parameters of GA-PID control technique

No. of iterations	50
No. of population	50
Crossover-Friction	0.8
Selection method	Stochastic uniform
Elite count	5% of population size
Crossover operator	Arithmetic
Lower Bound	[0 0 0]
Upper Bound	[100 100 100]
No. of variables to be optimised	03

$$J = \frac{1}{t}\int_0^t te^2(t)\mathrm{d}t \tag{2}$$

Figure 2 shows the flowchart of robot manipulator control using GA tuned PID controller.

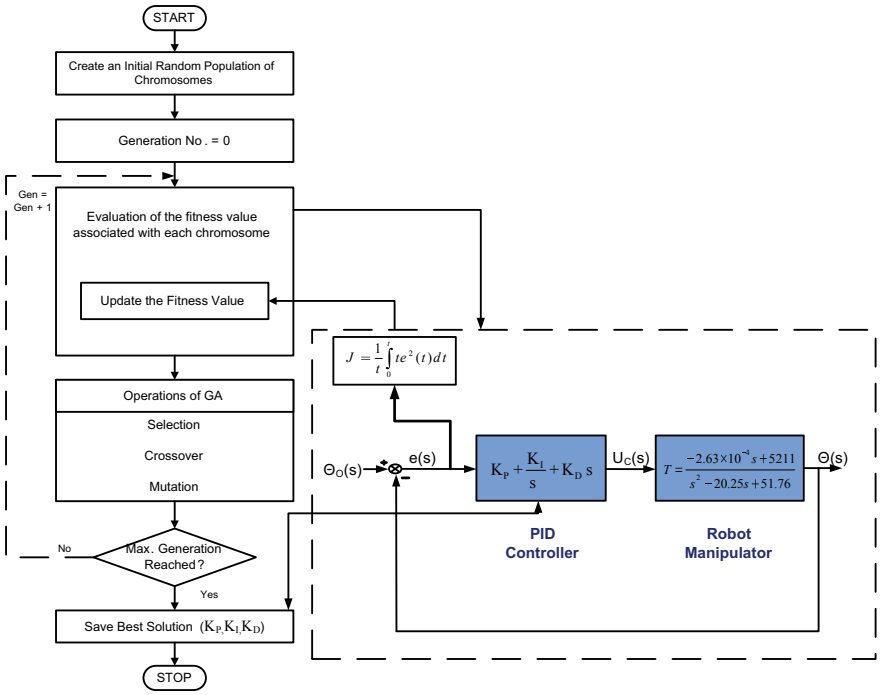

Fig. 2 Block diagram of robot manipulator controlled using GA-PID

4 Result

The position control of an industrial robot utilising GA-PID by tuning its gain parameters to achieve the best solution. The step response of robot manipulator without controller is given in Fig. 3 and with controller is given in Fig. 4. Step response with controller is highly nonlinear. The GA-PID controlled robot manipulator's response follows the input command effectively after 0.017 s having risen time 2.5035e-04 s, peak time 0.0015 s, undershoot of 0.0225%, overshoot of 73%, and the objective function value is 5.084199868849308E-5.

Figure 5 exhibits the graph between the best fitness and mean fitness for GA. It can be observed that values of best fitness and mean fitness are appeared nearby each other. Hence, presenting the optimal outcomes for the controller parameter values.

Figures 6 and 7 depict the stability analysis for a robot manipulator without and with a controller using bode plot. The industrial robot is unstable without a controller

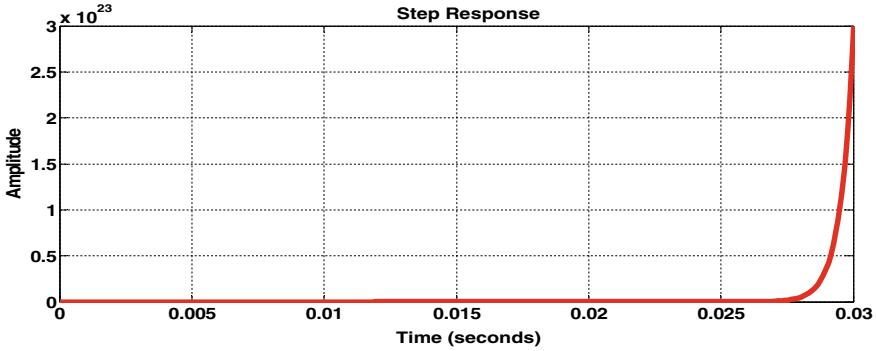

Fig. 3 Step response of robot manipulator without controller

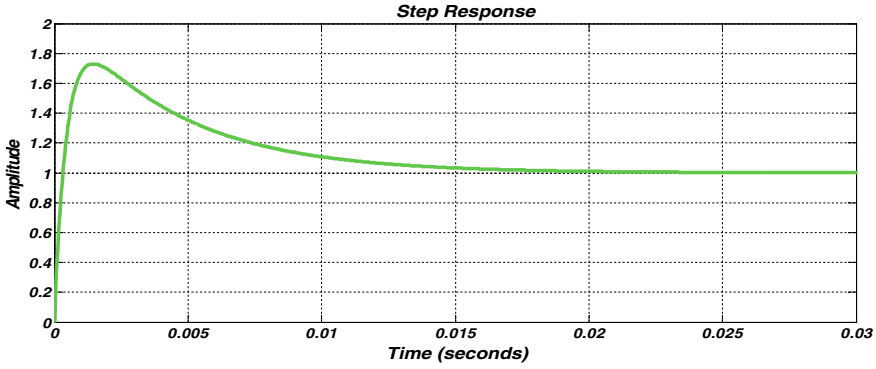

Fig. 4 Step response of robot manipulator with controller

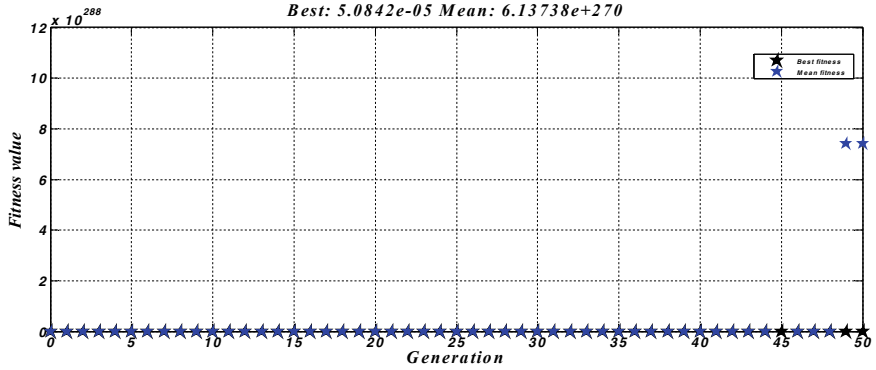

Fig. 5 Convergence of fitness for GA-PID controlled robot manipulator

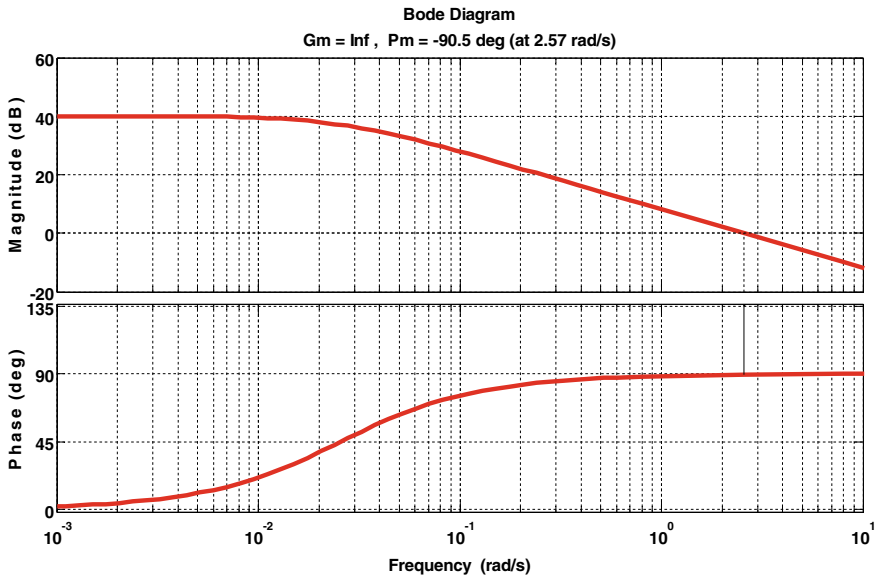

Fig. 6 Bode plot for robot manipulator without controller

because the phase margin is negative, whereas it is stable with GA-PID because both the gain margin and the phase margin are positive.

Figure 8(a) shows, the graph between the no. of children and individual which examine the selection function. Figure 8(b) shows the Best, Worst, and Mean Scores for the GA parameters during iteration.

Table 2 compares the performance and stability of the robot manipulator with and without controller.

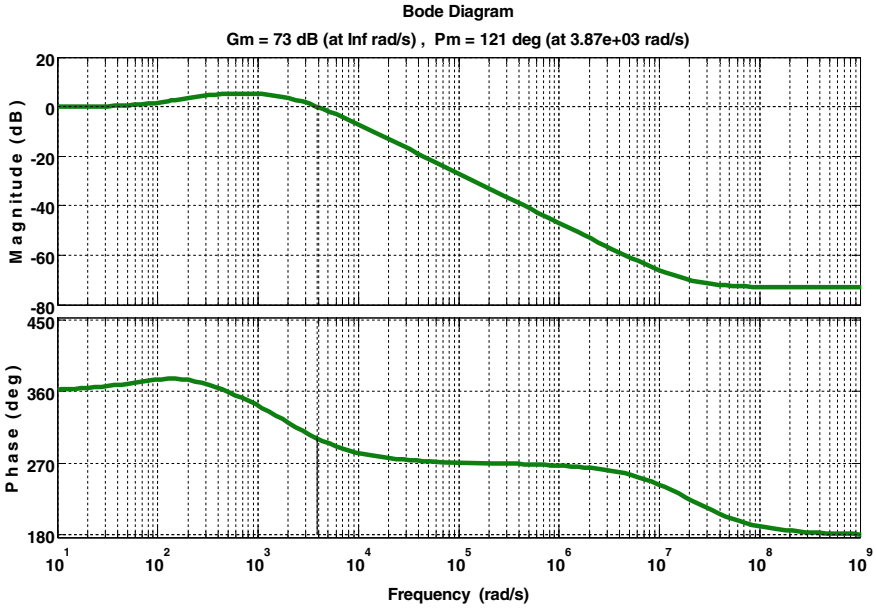

Fig. 7 Bode plot for robot manipulator with controller

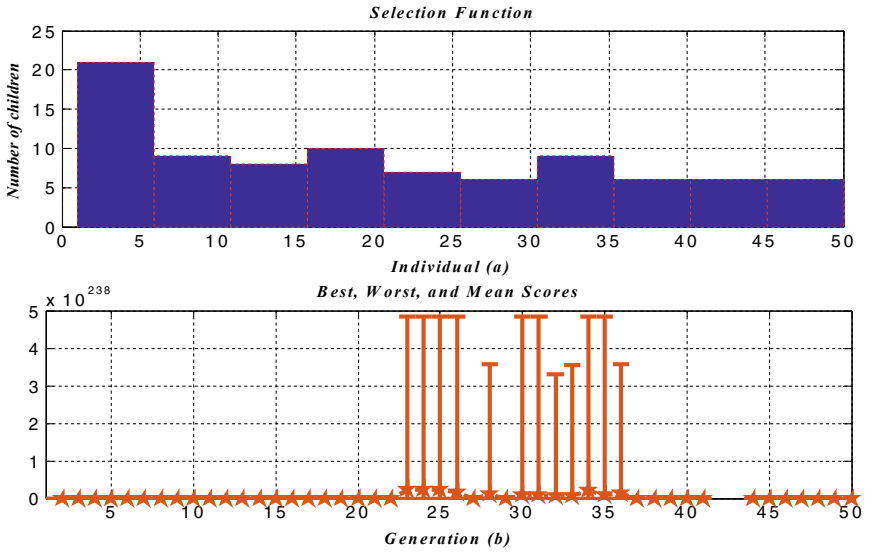

Fig. 8 Variation of GA parameters (**a**) selection function (**b**) best, worst, and mean scores

Table 2 Comparative analysis

Parameters	Without controller	Controller tuned with GA
Gain margin	∞	73 dB
Phase margin	$-80.5°$	121°
Settling time	∞	0.017 s
Stability	Unstable	Stable
Accuracy	Very poor	High

5 Conclusion

This paper concentrated on the development of an optimum controller for controlling a human-like robotic arm in industrial applications. The conventional technique of tuning of a PID controller is time consuming, poor, inefficient and has limited capabilities. Stability is the most important performance issue to consider when designing a robotic position control system. The bode plot showed that robot is highly unstable without controller. The disadvantages of conventional controllers are overcome by using GA-PID controller. It tunes the controller's parameters optimally using the MSE objective function. The mean square error is minimised to optimise the objective function. The simulation results exhibit that GA-PID controlled robots perform better and are more stable than traditional controls.

References

1. Carabin G, Wehrle E, Vidoni R (2017) A review on energy-saving optimization methods for robotic and automatic systems. Robotics
2. Neranon P, Bicker R (2016) Force/position control of robot manipulator for Human–Robot interaction. Therm Sci 20(2):S537–S548
3. Sutiphotinun T, Neranon P, Vessakosol P, Romyen A, Hiransoog C, Sookgaew J (2020) A human-inspired control strategy: a framework for seamless human-robot handovers. J Mechan Eng Res Dev 43(3):235–245
4. Neranon P, Sutiphotinun T (2021) A human-inspired control strategy for improving seamless robot-to-human handovers. Appl Sci 11:4437
5. Panomruttanarug B (2020) Position control of robotic manipulator using repetitive control based-on inverse frequency response design. Int J Control Autom Syst 18(11):2830–2841
6. Ismail HA, Ersin Y, Ertunct HM, Bingul Z (2011) PID and state feedback control of a single-link flexible joint robot manipulator. In: International conference on mechatronics, pp 409–414
7. Qureshi MS, Swarnkar P, Gupta S (2018) A supervisory on-line tuned fuzzy logic based sliding mode control for robotics: an application to surgical robots. Robot Auton Syst 109:68–85
8. Yu W (2018) PID control with intelligent compensation for exoskeleton robots. Academic Press, Mexico
9. Varma A, Sachan S, Swarnkar P, Nema S (2020) Comparative analysis of conventional and meta-heuristic algorithm based control schemes for single link robotic manipulator. In: Intelligent computing techniques for smart energy systems. Lecture Notes in Electrical Engineering, vol 607
10. The MathWorks, Inc. (2017) Matlab optimization toolbox user's guide. The MathWorks, Inc., Natick

11. Vinodha AJR (2014) Genetic algorithm based PID controller tuning approach for continuous stirred tank reactor. Adv Artif Intel 2014:1–8
12. Meena DC, Devanshu A (2017) Genetic algorithm tuned PID controller for process con-trol. In: International conference on inventive systems and control
13. Pillai RP, Jadhav SP, Patil MD (2013) Tuning of PID controllers using advanced genetic algorithm. J Adv Comput Sci Appl (IJACSA) 1–6
14. Goud H, Swarnkar P (2019) Analysis and simulation of the continuous stirred tank reactor system using genetic algorithm. In: Harmony search and nature inspired optimization algorithms. Advances in intelligent systems and computing, vol 741. https://doi.org/10.1007/978-981-13-0761-4_106
15. Goud H, Swarnkar P (2019) Investigations on metaheuristic algorithm for designing adaptive PID controller for continuous stirred tank reactor. Mapan 34:113–119. https://doi.org/10.1007/s12647-018-00300-w

Performance Evaluation of a Hybrid-MAC Protocol for Small Sensor M2M Devices

Aditi Chakraborty, Ansh Verma, Pawan Kumar Verma, and Rajesh Verma

Abstract Machine-to-machine communications are one of the reliable technologies for next generation communication systems, which is implied for enabling communication among a large number of devices without any human intervention. To facilitate the requirements of such kind of network where a huge number of devices are connected, the current versions of MAC protocols need to be upgraded to make the network more reliable, scalable, and energy efficient. In this paper, we propose an adaptive hybrid frame MAC protocol which adjusts the wait time due to transmission slots for small sensor devices by designing the frames based on the power constraint of the devices. This technique gives better results compared to the other standard existing techniques without compromising in throughput. This algorithm reduces the delay of the system as compared to the fixed size hybrid frame MAC protocol by 14%. The results are simulated in MATLAB.

Keywords Machine-to-machine communications · Hybrid frame · MAC · Adaptive · Ubiquitous

A. Chakraborty (✉) · P. K. Verma
Department of Electronics and Communication Engineering, Dr. B R Ambedkar NIT, Jalandhar, India
e-mail: aditic.ec.19@nitj.ac.in

P. K. Verma
e-mail: vermapk@nitj.ac.in

A. Verma
Department of Electronics and Communication Engineering, Shri Mata Vaishno Devi University, Katra, India
e-mail: anshvermacr754@gmail.com

R. Verma
Department of Electrical Engineering, King Khalid University, Abha, Kingdom of Saudi Arabia
e-mail: rkishor@kku.edu.sa

© The Author(s), under exclusive license to Springer Nature Singapore Pte Ltd. 2022

A. Tripathi et al. (eds.), *Intelligent Computing Techniques for Smart Energy Systems*, Lecture Notes in Electrical Engineering 862,
https://doi.org/10.1007/978-981-19-0252-9_44

1 Introduction

Some of the key requirements of M2M communications are the kind of medium access control protocols which are cost efficient can provide ubiquitous connectivity and have low complexity. That is why M2M communications find its application over a wide range [1]. Some of the research topics such as eHealth care, weather tracking, and smart homes are utilizing M2M network which mainly has a large number of small powered devices communicating through a single channel [2]. For example, smart homes, which is one of the useful applications of M2M communications, aim to integrate home automation by allowing several devices to be connected to the Internet-enable users so that they can monitor and control them remotely [3]. This smart home system uses several small powered sensor devices like smoke detector, light detector, water leakage detector, and smart thermostat. Since these devices are mainly battery powered and are unable to afford lot of power consumption for transmission, therefore, the current version of MAC protocol needs to be upgraded. The sensor devices collect information from the physical world and uplinked them at IoT server through aggregators. When data are transferred through uplink channel, the size of contention window plays an important role. Increasing contention window size may increase the delay as well as increase the power consumption of the devices. Old techniques [4] like create cluster or put the devices into sleep mode to reduce the energy utilization do not meet the requirements. TDMA which is a reservation-based MAC protocol eliminates the collisions and improves the channel utilization at high contention level. MAC protocols which are contention based such as carrier-sense multiple access with collision avoidance (CSMA/CA) are not suitable for highly dense network. For sensor networks, the best suited contention-based MAC protocol is Aloha [5] and its variations. In this paper, we propose an adaptive hybrid frame MAC protocol which merges the advantages of both the contention-based and the reservation-based techniques [6], and the time frame is adaptive in nature based on the power constraint of the devices. The contention interval uses slotted Aloha protocol, and the transmission interval uses TDMA protocol. The contribution of the paper can be summarized as below:

- Modeling an uplink-centric MAC protocol with respect to M2M network which would reduce the delay of the system by adjusting the transmission interval.
- Designing hybrid frames based on the power constraint of the devices.
- A simple computational approach which does not compromise with the throughput.

The rest of the paper is organized as follows: In Sect. 2, literature survey is presented. In Sect. 3, we describe the proposed system model and the frame structure. The proposed adaptive hybrid frame MAC protocol is described in Sect. 4. In Sect. 5, we describe the simulation results. Section 6 has the conclusion.

2 Literature Survey

Literature work [7] discusses about a MAC protocol which is energy efficient and has two steps. First step is the contention-based and reservation-based protocol for M2M network, and the second step proposes partial clustering. The result shows reduced delay. In [8], the authors suggest two techniques to improve the energy efficiency where the access probability of the users is adaptively controlled. The simulation result shows an improvement in energy efficiency. Further, [9] discusses an energy saving mode called FESM that minimizes the energy spend for retransmission. This method saves the energy consumption up to 30%. In [10], the author proposes a technique to update the M2M networks hierarchy by structuring them to carry out data transmission between terminal node and sink node in an efficient way using cluster head. This result shows reduced energy consumption by each node related to other MAC protocols. The paper work [11] proposes smart sleep protocol for M2M network in order to increase the energy efficiency. Here, clustering approach is used to balance the power consumption across the M2M network. The literature work [12] proposes Mac duty-cycling protocol where the nodes are segregated into subgroups which are disjoint, and each node has different duty-cycle configurations. This approach reduces the network delay and energy consumption.

3 System Model

Our system as shown in Fig. 1 consists of a large number of small powered sensor devices sharing a single channel. Here, nodes are represented as N_i where $i = 1; 2 \ldots n$. n is the maximum number of devices present in the network. We assume that nodes are always ready for transmission and receive hybrid time frames from the base station. In our system model, the time frames may not be equal in size. First, a device wants to send data to the *eNB* node using slotted– Aloha during contention round. The signal is received in a time slot t of *eNB* contention round successfully, if no collisions take place. The total number of time slots in contention round may vary according to the frame size.

After receiving the signal successfully, the base station executes protocol on that signal including all received signals to resolve packets. Now, the devices which are successful to send data during contention slots reserve a time slot in data transmission interval (*DTI*) to transmit data. *DTI* uses time division multiple access (TDMA) frame. The TDMA frame size may not be equal in size. Now, the unsuccessful devices will have to wait for the time δ which is described later for next contention opportunity. We assume here that the packet arrival rate for all the devices is constant and follows Poisson distribution.

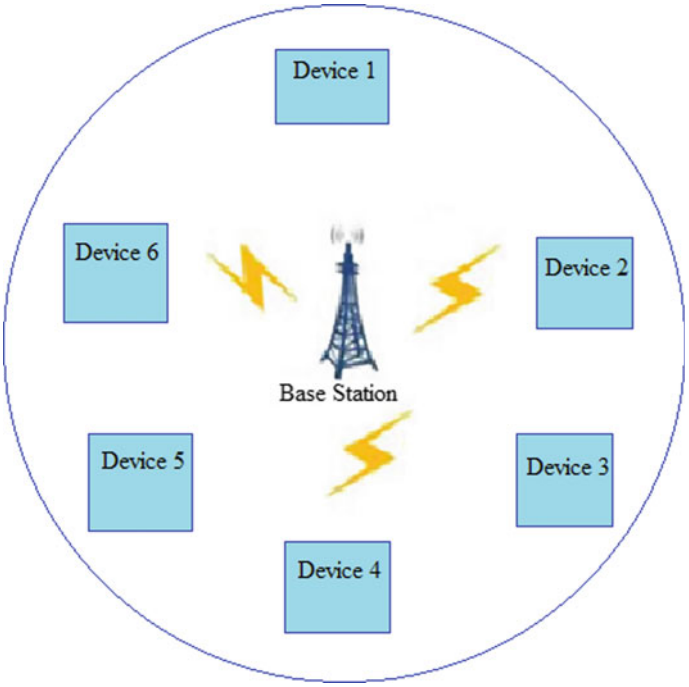

Fig. 1 Proposed system model

3.1 Frame Structure of Hybrid-MAC Protocol

Data are transmitted in M2M network frame by frame. Frames are hybrid in nature. This time frame has four different intervals such as contention notification interval (*CNI*), contention interval (*CI*), time slot announcement interval (*TAI*), and data transmission interval (*DTI*). They are described as follow:

Contention Notification Interval: All the frames start with *CNI*. In this time interval, the base station executes a message to notify all the devices within its proximity range indicating the start of the contention round. After receiving the message, the devices which have data to transmit get ready to contend during *CI.*

Contention Interval: During *CI*, the devices which have data to transmit contend to reserve a transmission slot in the *DTI*. First, the device has to send a transmission request message (REQ) to the *eNB*. If no collisions are occurred, then only the contention is considered successful. Then, the *eNB* reserves a valid time slot in the *DTI* for this device and send an acknowledgment signal. Thus, the *eNB* will send an acknowledgment signal to all the successful devices with the reserved time slot number. After receiving the acknowledgment signal ACK, the devices will stop sending the REQ message to the *eNB*. Slotted Aloha contention scheme is used here.

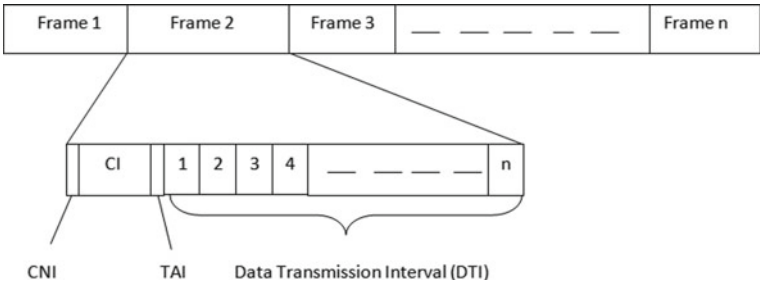

Fig. 2 Adaptive hybrid frame structure

Time slot Announcement Interval: After finishing the contention round, the *eNB* starts forwarding a massage to all the devices within its proximity range that declares the termination of the *CI* and start of the *DTI.*

Data Transmission Interval: During the transmission interval period, only, the successful selected devices are permitted to send the data packets in the reserved time slots. Slots are provided in the sequence in which devices win the contention round. TDMA mechanism is used here. The hybrid frame structure is shown in Fig. 2.

The time frames may not be in equal size.

4 Adaptive Hybrid Frame MAC Protocol

The proposed MAC protocol in this paper is mainly for small sensor M2M network. The communication is within the cell where the devices establish communication with the serving base station using a single dedicated channel. Only, uplink communication is considered here for the implementation of the protocol. Data are transmitted frame by frame. The time frame has mainly two parts: contention interval *CI* and data transmission interval *DTI*. The size of the frame plays a major role in determining the throughput of the system. Too small or too large size frame size reduces the system throughput. Again, large size frame has large data transmission interval which increases the wait time for the devices for next contention interval. This creates problem for low-powered devices as they cannot afford lot of power consumption. The proposed protocol adjusts the transmission interval delay (δ) based on the power profile of the devices and reduces the wait time for the devices for next contention interval and thus reduces the system delay without compromising in throughput. Information about the power of devices within the cell is achieved from random access channel (RACH). Based on the device power, the transmission interval is calculated using the proposed algorithm which is described later. Then, the time frame is generated. All the devices which have data to transmit first send a request message (REQ) to the base station during contention interval. The successful devices which win during the contention round reserve a time slot in transmission interval,

and all the unsuccessful devices have to wait for a delay time (δ) calculated by the proposed algorithm to contend in the next contention round.

Proposed Algorithm

Step 1: Power of the device "β" is achieved.

Step 2: Set the threshold value "θ" based on the power profile of the devices.

Step 3: Calculate $\delta = (\beta/\theta) * 100$.

Step 4: Provide contention round after interval δ.

Step 5: Return δ.

The value of the contention interval is calculated based on the value of δ.

Here, CI = (1/3) * δ.

4.1 Different Cases

Homogenous Power Devices: If the M2M network consists of the devices having same power, then the time frame will be equal in size. In that case, the choice of threshold value is important. The aim of our proposed algorithm is to reduce the transmission delay without compromising the throughput. If the threshold value is greater than the device power, then it will reduce the system throughput, but it will also reduce the data transmission interval. A better system throughput is achieved if threshold value is less than the device power. But, the lesser threshold value increases the data transmission interval. So, the choice of threshold value should be such that there remains a tradeoff between the system throughput and transmission delay. Too small and too large threshold value compared to the device power affects the system throughput and introduces more delay into the system (too small threshold value). These threshold values should be avoided to achieve an efficient system. The simulated result is shown in Sect. 5.

Heterogeneous Power Devices: If the M2M network has the devices of different power value, then some middle value of the power range should be set as threshold value. Different power values play a vital role in frame designing. Considering all the different device power in frame, designing sometimes reduce the system throughput. To achieve better system throughput, the device power should be chosen in a wise manner based on the network traffic. Simulation result is described in Sect. 5.

5 Simulation Result

We simulate the scenario on MATLAB (9.0) for 100 M2M devices. Figure 3 shows

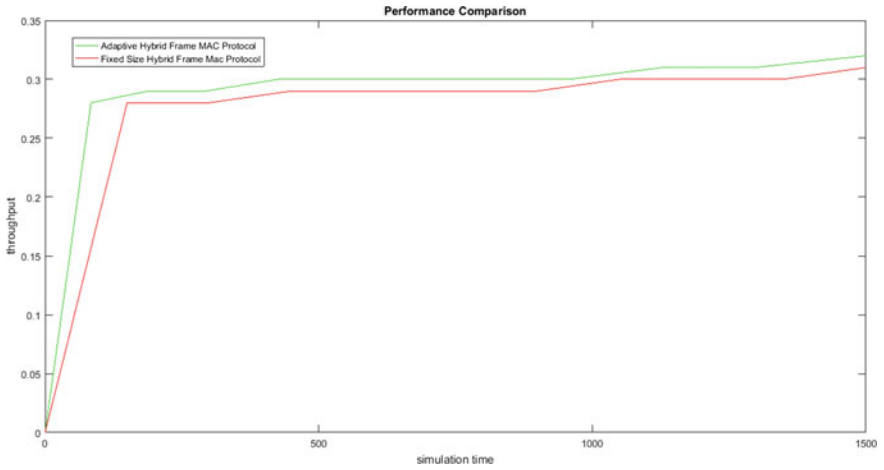

Fig. 3 Performance comparison

the performance comparison of the adaptive hybrid frame MAC protocol with fixed size hybrid frame MAC protocol in terms of throughput. The frame size of fixed size hybrid frame MAC protocol is 150 ms. The network consists of the devices whose power values remain within the range of 1–10 dbm. This comparison shows that adaptive hybrid frame MAC protocol improves the system throughput as compared to fixed size hybrid frame Mac protocol by 6.4%.

In Fig. 4, bar 1 represents the system delay due to fixed size hybrid frame MAC protocol, and bar 2 represents the system delay due to adaptive hybrid frame MAC protocol. Through simulation, we observe that adaptive hybrid frame MAC protocol

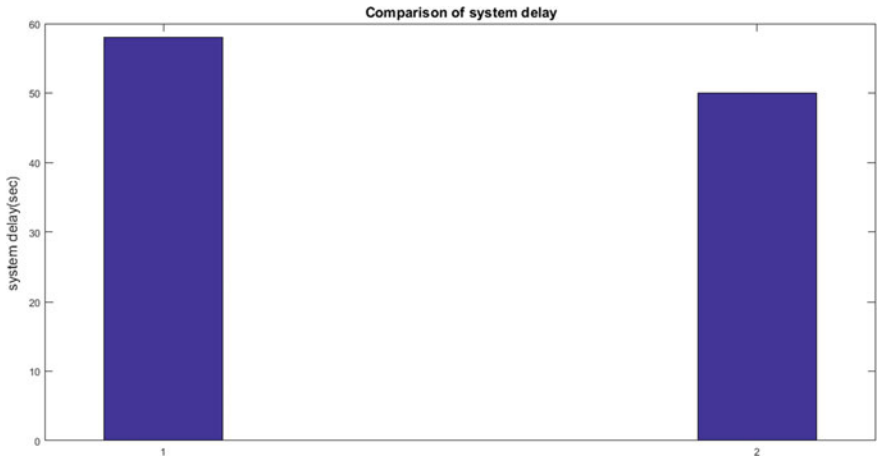

Fig. 4 Comparison of system delay

reduces the system delay by 14% as compared to the fixed size hybrid frame MAC protocol.

Figures 5 and 6 show how the choice of threshold value affects the transmission delay and the system throughput. In this case, the network consists of homogenous power devices where the power of each device is taken as 10 dbm. When the threshold value is set at 11 dbm, 13 dbm, and 15 dbm, transmission delay and system throughput both get decreased. Better system throughput is achieved, when threshold value is

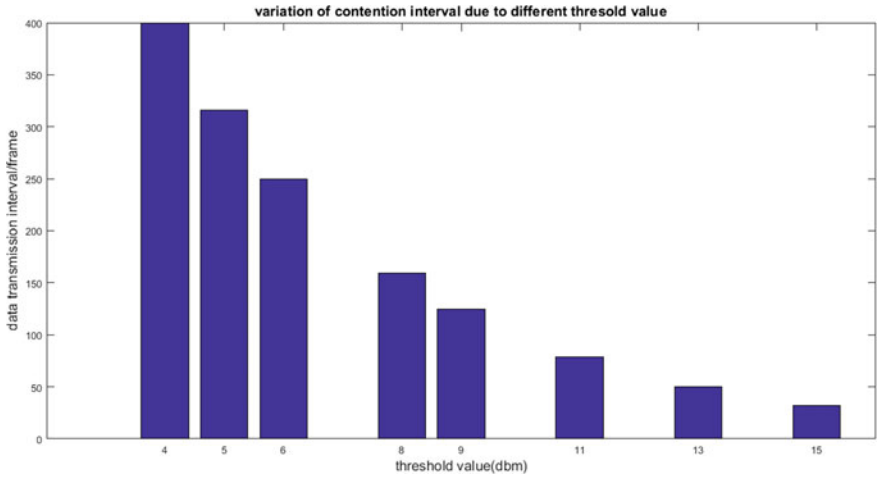

Fig. 5 Variation of data transmission delay due to different threshold value

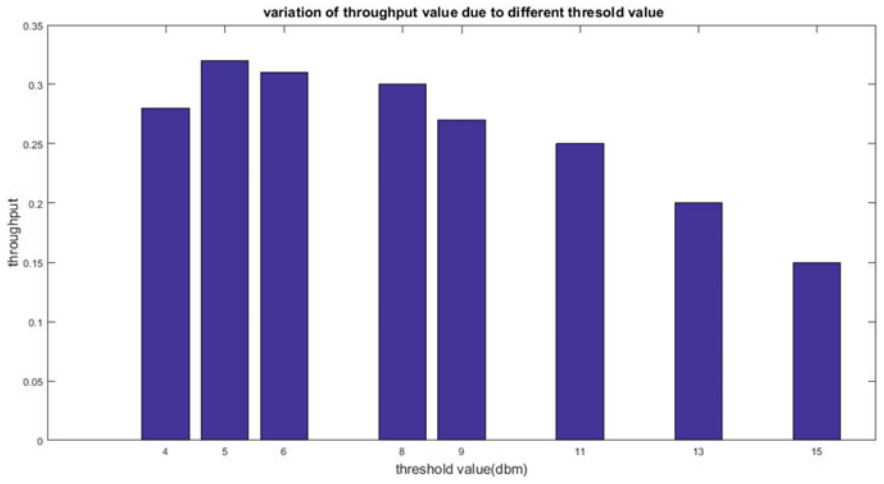

Fig. 6 Variation of throughput due to different threshold value

set at 4 dbm, 5 dbm, 6 dbm, 8 dbm, and 9 dbm, but these values introduce more transmission delay as compared to higher threshold values.

Figure 7 shows the simulation results, which compares the throughput of a homogeneous power network when threshold value is set at 8 dbm and 11 dbm, respectively. This result supports the fact that a high system throughput can be achieved when the threshold value is lesser than the device power (10 dbm) as compared to the situation, where threshold value is higher than the device power.

Figure 8 illustrates the simulation results for a heterogeneous power network in terms of throughput. The results show that if all the different power values within the

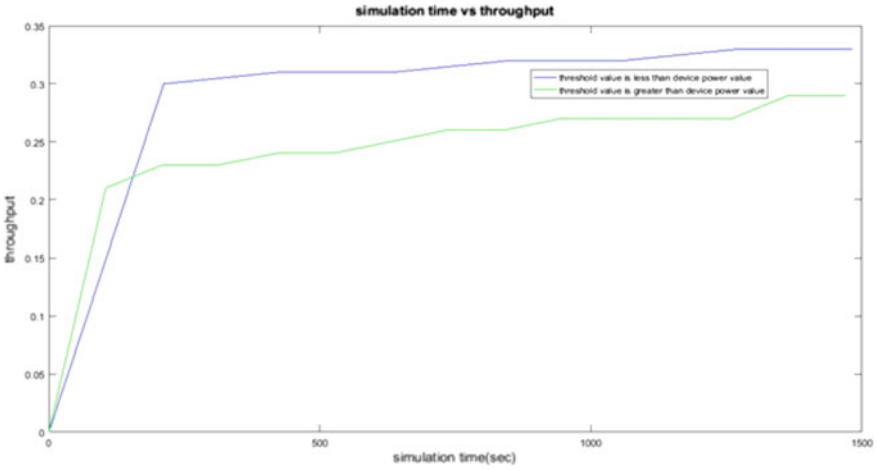

Fig. 7 Comparison of throughput for homogenous power network

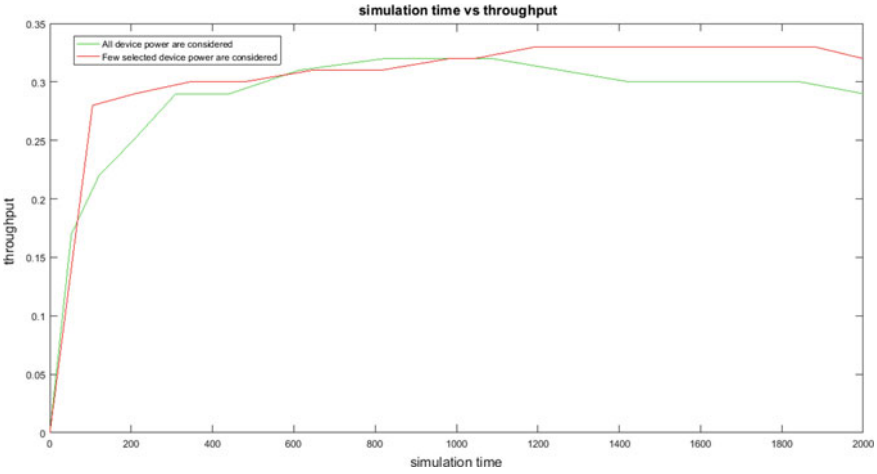

Fig. 8 Throughput comparison of heterogeneous power network

Table 1 Simulation parameters

Parameter	Value
No of device	100
Packet length	128 bits
Bit rate	512 kbps
Symbol rate	256 kbps
Time slot	1 ms
CNI	5 μs
TAI	5 μs
Service radius	100 m

power range are considered for frame designing, it will reduce the system throughput as too small and too large frames affect the system throughput. But, if some random power values are considered to design the frames based on the network traffic, it will give a better system throughput. The simulation is carried out for the power range 1–10dbm keeping the threshold value at 5 dbm.

6 Conclusion

The work in this paper focused on designing an adaptive hybrid frame which will adjust the wait time of the devices due to transmission interval based on the power profile of the devices. Also, a computational approach of the proposed method has been provided for homogenous and heterogeneous power network. MATLAB (9.0) has been used to investigate the efficiency of the proposed computational approach in terms of throughput and system delay. The simulation results have provided the idea about the right choice of the threshold value for homogenous power network to achieve high throughput and the idea about the selection of the power devices for heterogeneous power network to get better throughput.

References

1. Verma PK, Verma R et al (2016) Machine-to-Machine (M2M) communications: a survey. J Netw Comput Appl 66:83–105
2. Ali A, Shah GA, Farooq MO, Ghani U (2017) Technologies and challenges in developing machine-to-machine applications: a survey. J Netw Comput Appl 83:124–139
3. Malche T, Maheshwary P (2017) Internet of Things (IoT) for building smart home system. In: International conference on IoT in social, mobile, analytics and cloud, pp 65–70
4. Ali A, Shah GA, Arshad J (2016) Energy efficient techniques for M2M communication: a survey. J Netw Comput Appl 68:42–55
5. Munari A, Clazzer F, Liva G (2015) Multi-receiver aloha systems—a survey and new results. In: Proceedings of IEEE international conference communication workshop, pp 2018–2114

6. Verma PK et al (2016) A novel hybrid medium access control protocol for inter-M2M communications. J Netw Comput Appl 75:77–88
7. Rahimian S, Noori M, Ardakani M (2016) An energy-efficient adaptive frameless ALOHA protocol. EURASIP J Wirel Commun Network 186
8. Zhao Y, Yilmaz ONC, Larmo A (2015) Optimizing M2M energy efficiency in IEEE 802.11ah. In: Proceedings of IEEE Globecom Workshops, pp 1–6
9. Park I, Kim D, Har D (2015) MAC achieving low latency and energy efficiency in hierarchical M2M networks with clustered nodes. IEEE Sens J 15:1657–1661
10. Al-Kaseem BR, Al-Raweshidy HS (2016) Energy efficient MAC protocol with smart sleep scheduling for cluster-based M2M networks. In: Proceedings ofinternational conference on information communication and management, pp 227–232
11. Beaudaux J, Gallais A, Noel T (2013) Heterogeneous MAC duty-cycling for energy-efficient Internet of Things deployments. Netw Sci 3:54–62
12. Yilmaz ONC, Hämäläinen J, Hamalainen S (2011) Self-optimization of random access channel in 3rd generation partnership project long term evolution. Wiley Wirel Commun Mobile Comput 11:1507–1517

Converting Braille Symbol and Words to Voice

Ritwick Bhattacharya, Harish Sharma, Sandeep Chaurasia, and Satpal Singh Kushwaha

Abstract Braille system is there for almost a century in English language. The six-dot pattern is being used for describing a lot of syllables in the English dictionary like the alphabets and many words and phrases. There are many works, which has been done to help blind people to read and write and able to communicate with a person who is totally able to read and write. But there are very few instances where the text input of a blind person is being converted into voice. So, in this paper, we have presented a model to solve this issue using neural network with 97% accuracy.

Keywords Braille script · Neural Network · Character Segmentation

1 Introduction

Braille started originally not as a reading and writing script for the blind but as a secret code language devised by a French army general named Charles Barbier. It was used by him as a code language to communicate with Napoleon Bonaparte and other troops during battlefield because they did not want to allow their enemies to learn about the messages they wanted to give between each other, and it became popular among the troops as it did not use any kind of lights nor any kind of sound that would allow the opposite army to know any kind of message is being passed [1, 2].

Before the war, Charles Barbier learned about a system of communicating between troops, which used a grid system of rows and columns, in which the message was passed by switching ON and OFF the lights in the rows and columns. This system was called as Polybius square, named after a famous Greek historian, Polybius. So, keeping this idea in his mind, he started to create a system of sign language, which would use characters shaped inside a square. This was named sonography by Charles

R. Bhattacharya · H. Sharma · S. Chaurasia (✉) · S. S. Kushwaha
Department of Computer Science and Engineering, Manipal University Jaipur, Jaipur, India
e-mail: sandeep.chaurasia@jaipur.manipal.edu

S. S. Kushwaha
e-mail: satpal.singh@jaipur.manipal.edu

© The Author(s), under exclusive license to Springer Nature Singapore Pte Ltd. 2022

A. Tripathi et al. (eds.), *Intelligent Computing Techniques for Smart Energy Systems*,
Lecture Notes in Electrical Engineering 862,
https://doi.org/10.1007/978-981-19-0252-9_45

Barbier. But to write a message in this system, a user had to make paper cuttings with any tool they had (mostly used was knife as it was available with almost all the soldiers). This type of scripting was called as night writing, and initially all the symbols in it were for French as it was being used in the French army. But when he went to propose this idea to his higher ranks, they disapproved it saying it was not practical and was not accurate [1, 2].

Even after getting rejected, he never gave up on night writing. So, he started to cover up the comebacks of the system, and he presented this new and advanced version of night writing to the first blind school in the world named as Royal Institute for Blind Youths, which was located in Paris. Here, Barbier started to teach young blind children how they can use the night writing to communicate between each other and how they can use any stylus like apparatus that can make markings which could make impressions on a paper, which can be touched and felt by any person. But the problem with this system was that it can be only used for words. It did not contain any kinds of punctuation symbols, which also caused issues while writing French words and sentences. One of the students over there took this system and started to modify it in such a way that all letters and punctuations can be written and is easy to understand for any blind person reading it by touching. His name was Louis Braille, and he took another nine years to perfect the script. Louis Braille was born in 1809, and he became blind by the age of 5 due to accident and infection. He was more determined for this system because he did not want any blind people fall back in front of a normal person in terms of education [1, 2].

After successful modification, Braille system for writing and reading was created, but not before Braille's death, this system became officially recognized in the year of 1854. After few years, the system of Braille reached in Great Britain in 1861, but it never was officially accepted before 1918 [1, 2].

2 Methodology

2.1 Use-Case

Let us assume that three possible individuals can use this application as a means of bidirectional communication. All of these individuals have different traits, so instead of mentioning them using their traits it would be easier if the individuals were listed along with their traits. They are listed below:

- A has no problem in seeing or speaking.
- B can speak properly but not see.
- C cannot see properly and not speak.

Based on these three individuals, if any two of them are to take part in a two-way communication, then three use cases are possible. All these cases will be briefed below discussing about the conditions required for this application to work, whether

the application would work at all or not, and if not, then what can be done to ensure the application works.

The first case is when A and B communicate. Here A can talk to B, but A can write to B, but for A to understand what B wants to write, A needs to know something about Braille scripture which he can use to communicate what he wants to say to B so that A can read the translation and understand that B wants to say [3–6].

The second case is when A and C communicate. Here C cannot understand what A wants to say, but if C wants to say something, then he/she needs to know Braille language which the application can convert into text or audio for A to understand and vice versa [3–6].

The third case is if B and C want to communicate. Requirement is that B as well as C is required to know the Braille of a common language so that they both can communicate through Braille scriptures that could be printed on special printer made for Braille characters [3–6].

The suggested system by Sarkar and Das [4] comprises a Braille writer keyboard, a physically refreshable Braille display (named SPARSHA), a remote communication mechanism through SMS and a text audio output system.

Shahbaz et al. [5] created a system that takes input from a Braille keyboard and creates voice as well as the ability to read documents. Braille slate is made up of tiny dots that are arranged in cells. A cell is made up of six dots that fit between the fingers and are grouped into two three-dot segments. Each cell corresponds to a letter, a word, a combination of letters, a numeric or an accent mark. The major four dots are used to shape the underlying ten letters of the letters in order (1, 2, 4 and 5). The following ten letters are formed by including a speck 3, and the final six letters are formed by adding a spot 6. Complement is handled by its own unique dot pattern, which is typically seen in the cell's lowest third. Regardless of the letter set, the Braille code connects multiple compressions, which are Braille cells that can address a group of letters or the complete word.

Khajwali et al. [7] developed a method that uses the Raspberry Pi to transform any Braille character into a sound that is similar to the character in any language. However, there are some optical Braille recognizers that can recognize characters and turn them into text in any natural language in the world. Any product that can convert text to voice can be taken a step further and used for voice conversion. It will allow anyone who does not know Braille to communicate with a blind person using text and speech through the use of software.

S. Kurlekar et al. presented a device that captures pictures and converts them into audio output (Speech) using OCR and text-to-speech synthesis. The Raspberry Pi is used to convert printed documents into text files, and the PyTesseract library and Python programming are used again. Google's text-to-speech (gTTS) and the Python programming language are used to process and transform text files into audio output (speech).

3 Working Model

3.1 Preprocessing the Text

The Braille input is preprocessed in the same way that any picture is preprocessed before being used in a machine learning model, i.e.,

1. Converting into grayscale image
   (a) The average of R, G, B value of an image is taken, and the average value is being called grayscale value of the image [5–7].
2. Applying segmentation algorithm (here its binary thresholding and Otsu thresholding)
   (a) Each pixel of an image is replaced by a black pixel if $I\{i, j\} < T$, where $I\{i, j\}$ is image intensity and T is some fixed constant [8, 9].
   (b) The Otsu algorithm makes the work much more efficient and accurate as compared to another algorithm [10].
   (c) Here, a mix of both binary and Otsu has been used to increase the accuracy and efficiency of the model.
3. Removing Noise from image
   Noises are the unnecessary disturbances that are present in the image that may cause issue in image reading. There are many techniques to remove noise from the image like: trade-off, Chroma and luminance noise separation, linear smoothing filters, anisotropic diffusion, nonlinear filters, wavelet transformation, statistical methods, block-matching algorithms, shrinkage fields, and deep learning.
   (a) For this, we have used blurring, which is a type of nonlinear filtering to remove noise from the image [7, 11].
   (b) Blurring can be defined as a technique where pixels which can be defined as "outlier" is removed. It is also defined as a "low-pass" filter, i.e., which only removes noise and does not change the main image.
   (c) A blur is a very common operation we need to perform before other tasks such as edge detection.
4. Conversion into binary image
   (a) The image is then converted in a form where the pixels only contain RGB value either as black (0, 0, 0) or white (255, 255, 255) in the pixel value.
   (b) The names black-and-white, monochrome, or monochromatic are often used for this concept.
   (c) It helps the model to understand a picture much better and efficiently.
   (d) Increasing the efficiency as well as accuracy.

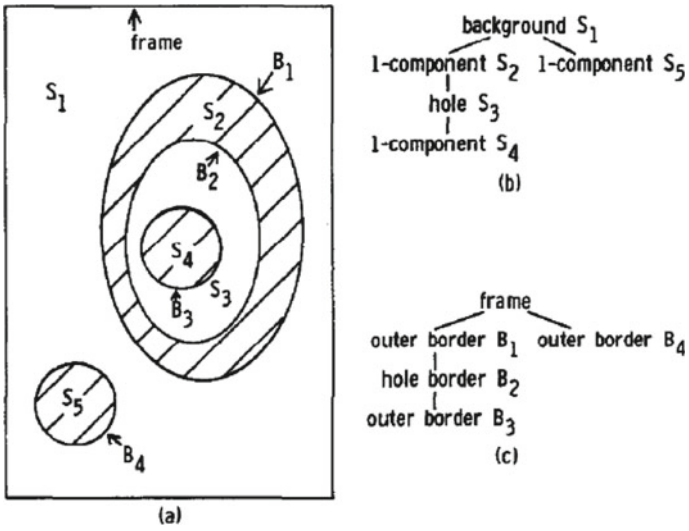

Fig. 1 Basic explanation given by Satoshi Suzuki of contouring algorithm in 1985 [12]

3.2 Contouring

Contours can be defined as the process of joining points, which are continuous in nature and have same characteristics. It is mainly used while doing object detection and shape analysis. Contours can be extracted from the binary image which was obtained from the preprocessing step. In this, we have used contouring technique given by Satoshi Suzuki [12].

The algorithm is already defined in the OpenCV library, so we do not have to create another file for getting its functionality in the model (Fig. 1).

3.3 Character Segmentation

Character segmentation is defined as the process how we are able to define an individual character out of the image which has been processed using grayscale and noise reduction [13]. The character segmentation in this is based basically on basic mathematic model made using the basic concepts of matrices.

This can be also made much more complex and powerful using artificial neural networks (ANN), but while using neural networks, it showed a significant problem [14].

The following steps were used to execute the segmentation.

i. Calculate the mean radius and diameter of each dot in each Braille character using the contours.

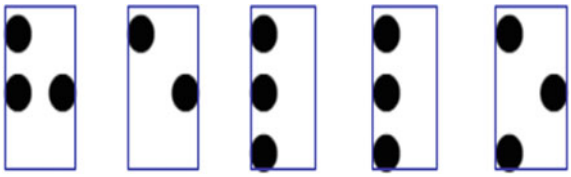

Fig. 2 Example of segmentation

ii. Using the radius and diameter, find the center point of all dots in each Braille characters.
iii. Using the radius and diameter, find the center point of all dots in each Braille characters.
iv. With the X and Y points, find all possible Braille characters as 3×2 matrix [8].
v. Get each Braille character bounding rectangle coordinates with the bounding rectangle coordinates, each Braille character can be segmented.

With each Braille character segmented as separate images, we can do simple image processing to convert the image to a 3×2 matrix, and this matrix can be converted to vector with single dimension. Each combination of such vectors will represent a character in English; thus, a sentence can be constructed (Fig. 2).

Then, this English character is passed through voice APIs for the conversion into voice, which would give English syllable as the output of the given Braille symbol or directly passing all the characters after processing into voice APIs that would give the word as voice output.

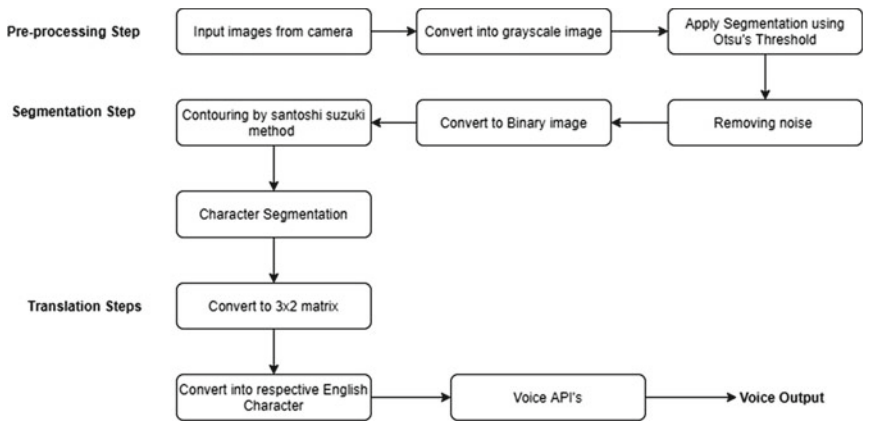

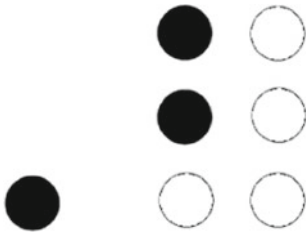

Fig. 3 Capital B is shown with a dot ahead of the character symbol

3.4 Formulas Used

- OTSU thresholding:

$$\sigma_w^2(t) = w_0(t)\sigma_0^2(t) + w_1(t)\sigma_1^2(t)$$

where w_0 and w_1 are defined as probable occurrence of two classes separated by a threshold t and $\sigma_0^2(t)$ and $\sigma_1^2(t)$ are variances of these two classes [10].

3.5 Limitation of the System

The meaning of the symbol may/may not actually be defined in the code. Some of them are mentioned below:

- There may be issues in understanding the capital letters because of the symbol of capital uses a dot before the particular character.
- It may not work with any language which is not defined in the source code, i.e., symbol for a character in a particular language may be different from other language (as depicted in Fig. 3).
- The space between two characters may be large enough that could make reading of character tough for the machine on which it is working.
- There may be errors when neural networks are been used for training for code segmentation may be because of error in dataset which is been used for training.
- The mapping of the characters may not be correct in the code, which may lead to wrong interpretation of the character symbol.
- The API for the voice may/may not work perfectly, causing delay or wrong output [15–18].
- Do not confuse the full form of API. It stands for "application programming interface" [15–18].
- The short form, "i.e.," is for "that is", and, "e.g.," is for "for example".

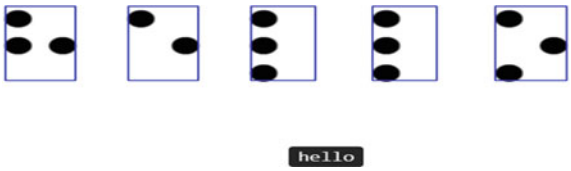

Fig. 4 Conversion of word hello from Braille to English characters

4 Conclusion and Results

We were able to do segregation and recognition of Braille characters in real time with conversion into text without any delay. The time taken to do this is almost equivalent to many artificial neural networks present at this time. The time complexity of this process is also equivalent to a neural network [19, 20].

The Braille recognition can be also done on low-powered device as it can be converted to a web-based application, and process is being done on a server-based back-end processing and also due to this program does not use any kind of neural networks [19, 20]. The accuracy of this model is approximately at par with any neural network which is close to 97% [19, 20]. The voice for the given character and word is working but causing latency due to reading characters in a loop [19, 20] (Fig. 4).

References

1. Kent-Teach.com Blog. https://www.kent-teach.com/Blog/post/2018/01/04/a-brief-history-of-braille-world-braille-day.aspx
2. Roth GA, Elizabeth F (2011) The invention of Braille. Am J Publ Health 101(3): 454–454
3. Chaitanya J, Salman, Raj, Syeda (2019) E-Braille: A Study aid for visual impared. Int J Res Eng Sci Manag 2(2) (2019)
4. Sarkar R, Das S (2012) Analysis of different Braille devices for implementing a cost-effective and portable Braille system for the visually impaired people. Int. J Comput Appl 60(9):1–5. https://doi.org/10.5120/9717-3073
5. Shahbaz AK, Shakir HM, Jameel A (2014) Blind aid: a self-learning braille system for visually impaired. Int J Eng Res Gener Sci 2(4) (2014). ISSN 2091-2730
6. Sadato N, Alvaro P, Jordan G, Marie-Pierre D, Vicente I, Mark H (1998) Neural networks for Braille reading by the blind. Brain J Neurol 121(7):1213–1229
7. Khajavali K, Jaya Kumar D, Nandakishore (2019) Electronic Braille alphabet reader for multilanguage. Int J Recent Technol Eng (IJRTE) 8(4). ISSN: 2277-3878
8. M Abadi (2016) TensorFlow: learning functions at scale. In: Proceedings of the 21st ACM SIGPLAN international conference on functional programming
9. Girshick R (2015) Fast r-cnn. In: Proceedings of the IEEE international conference on computer vision, pp. 1440–1448
10. Otsu N (1979) A threshold selection method from gray-level histograms. IEEE Trans Syst Man Cybern 9(1):62–66
11. Antonacopoulos A, Bridson D (2004) A robust Braille recognition system. In: International Workshop on Document Analysis Systems. Springer, Berlin, pp 533–545
12. Suzuki S (1985) Topological structural analysis of digitized binary images by border following. Comput Vis Graph Image Process 30(1):32–46

13. Yin J, Wang L, Li J (2010) The research on paper-mediated Braille automatic recognition method. In: 5th International conference on frontier of computer science and technology, pp 619–624. https://doi.org/10.1109/FCST.2010.95
14. Dennis HK (1998) Review of text-to-speech conversion for English. J Acoust Soc Am 82:737
15. Rupanagudi, Rao S, Huddar S, Bhat VG, Patil S, Bhaskar MK (2014) Novel methodology for Kannada Braille to speech translation using image processing on FPGA. In: International conference on advances in electrical engineering (ICAEE), pp 1–6. IEEE
16. Hanumanthappa M, Vishwanath VM (2016) Optical Braille recognition and its correspondence in the conversion of Braille script to text—a literature review. In: International conference on computation system and information technology for sustainable solutions (CSITSS), pp 297–301. IEEE
17. Padmavathi S, Manojna KSS, Sphoorthy Reddy S, Meenakshy D (2013) Conversion of braille to text in English, Hindi and Tamil languages. arXiv preprint arXiv:1307.2997
18. Vyas HA, Virparia PV (2021) Template-based transliteration of Braille character to Gujarati Text—The application. In: Rising threats in expert applications and solutions. Springer, Singapore, pp 437–446
19. Kurlekar S (2020) Reading device for blind people using Python, OCR and GTTS. Int J Sci Eng Appl 9(04), 49–52. ISSN: 2319-7560
20. Kishore, Krishna K, Prudhvi G, Naveen M (2017) Braille script to voice conversion. In: International conference on computing methodologies and communication (ICCMC), pp 1080–1082. IEEE

Exploring Security Threats and Attacks in Software-defined Networks

Gaurav Prasad, Devi Prasad Sharma, and R. Jaya Krishna

Abstract In the new era, software-defined networking (SDN) addresses the issue which exists in traditional or the conventional networks. So, it is one of the important areas in the field of networking which has lot of scope in near future. The SDN implementation identifies separation of data and control plane which has a new layer, i.e. abstraction layer which is called as controller. Although new architecture overcomes major problems or issues in traditional network but introduces new security issues which may be result in exploiting the vulnerabilities to perform different attacks. In this paper, we discuss the need for SDN and difference with traditional network, architecture, and possible applications of SDN. Secondly, we list out possible threats and discuss in detail different security attacks and analyze it to identify their cause. Furthur, we identify most important security attribute which has to be preserved to overcome most of the attacks. Finally, conclude with possible future work in this direction to mitigate these identified attacks.

Keywords Software-defined networks · Security · Security attacks · Security threats

G. Prasad (✉) · D. P. Sharma · R. J. Krishna
School of Computing and Information Technology, Manipal University Jaipur, Jaipur, Rajasthan, India
e-mail: gaurav.prasad@jaipur.manipal.edu

D. P. Sharma
e-mail: deviprasad.sharma@jaipur.manipal.edu

R. J. Krishna
e-mail: jaya.krishna@jaipur.manipal.edu

© The Author(s), under exclusive license to Springer Nature Singapore Pte Ltd. 2022

A. Tripathi et al. (eds.), *Intelligent Computing Techniques for Smart Energy Systems*, Lecture Notes in Electrical Engineering 862,
https://doi.org/10.1007/978-981-19-0252-9_46

1 Introduction

The rapid growth of technology and need of the same with respect to business around the globe has forced the need of growth in the area of communication through Internet. This requires technologies for networking to manage resource efficiently and provide scalability. Further, this has increased the complexity of conventional or the traditional network [1]. Moreover, their management has been very difficult task for the network administrators. The shortage of skill set or skilled professionals required with technical expertise has been one of the big issues which is very much concerned for present scenario. For example, in the current scenario, network contains different devices, technologies like wireless, virtualization which is uses command-based interfaces and also has specific formats with respect to different vendors. Further, proper documentation of manuals related to configuring these devices is also an issue. Further, handling of these different devices in dynamic environment requires in depth knowledge of concepts. Lack of these knowledge may result in unexpected situations [2]. These points clearly show the challenges in managing traditional network which is heterogeneous and in large scale.

To overcome these issues, wherein, the process of setting up and configuring the devices has to be rapidly done which requires improvement and use of new innovative ideas to enhance and improving the network architecture has led to evolution of software-defined networks (SDNs). The concept of SDN as an platform started since 2000 with different technologies. This technology allows efficient and effective management of network which may be homogeneous or heterogeneous network. The limitations in traditional network are that once the policies are implemented during implementation of devices, it cannot be changed in coming days, i.e. the flexibility on configuring dynamically is not possible whereas it is possible in SDN platform.

The Fig. 1 in which a topology given shows the difference between the traditional network (TCP/IP model) and the SDN network.

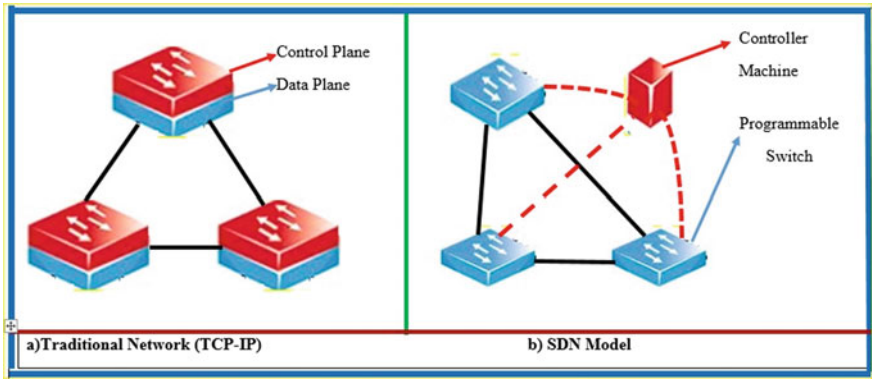

Fig. 1 Difference between traditional and SDN

The paper has Sect. 2 explains the architecture of SDN and discusses the existing application and future scope of application in different domain and also about the challenges in it. Section 3 discusses of about security threats, security attributes, and different security attacks in different layers of SDN and also lists out different causes of security attacks.

2 SDN Architecture and Applications

Architecture: SDN architecture has emerged with wide variety of application, wherein the functionality of network devices is managed by centralized controller. The idea is to remove the intelligence of the devices or nodes through data and control plane separation [3]. The structure is shown in the Fig. 2.

Infrastructure/Data Layer: Layer composes of network components or devices like switches, routers, and network access points. This represent the data plane, i.e. the duty of this is to forward the data packets. Control Layer: As the name suggests this layer has the responsibility to deal with traffic flow, i.e. take decision on the routing the packets, dropping, and forwarding through programming. The south-based API is the interface of control layer with the infrastructure layer as shown in the Fig. 2. Application Layer: This layer deals with the applications developed related to business logic. This layer deals with firewall, intrusion prevention, intrusion detection, and also virtualization. It uses north-based API to communicate with control layer as shown in the Fig. 2.

Applications of SDN

The concept of SDN has lot of applications and services in different domains out of which few very important domains, where SDN is applied are listed out.

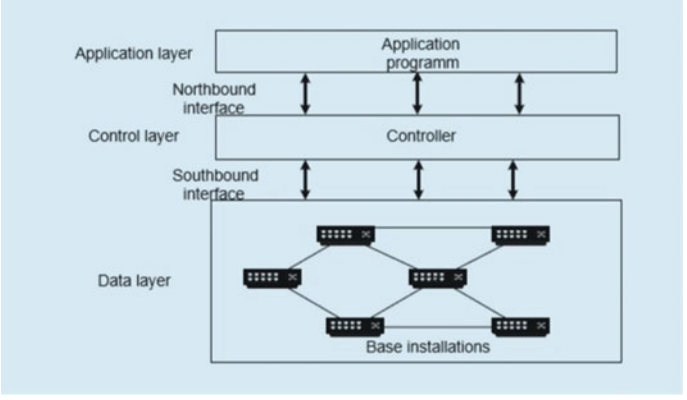

Fig. 2 Architecture of SDN

Monitoring and Measurement: Network management task is very important task in maintaining the network and even in upgradation of the network, wherein it is done by measuring the traffic flow in the network. This task is usually done by using existing custom-based hardware which has specific task of collection of data flow or traffic and analyzing it. This can be replaced by existing SDC-based open flow switched which can have rules and priority matches and appropriate algorithms for doing in the same task of monitoring and measuring the traffic which will reduce the overhead of using dedicated device which is done in traditional network [4]. Security: Enterprise network deals with security in reactive way and also depends on each security of each node and also the middle box which becomes complex as it requires communication between systems and protocols leading to the in appropriate behaviour and delayed response to different attacks. To overcome this, it requires mechanisms in network layer which can have remedy related to access control. By using the concept of SDN, we can have dynamic control access policies, i.e. use of programmable switches to handle data flow in lower layers. It can enforce high-level security based on the higher-level security [5]. Cloud: Nowadays, most of the applications are hosted in cloud environment which in turn requires virtualization environment for implementation. The advancement of virtualization has led to higher complexity and dynamicity of data centre which requires proper utilization of network resources for network management. The concept of SDN supports these features that suits virtualization environments [6]. Middleware: The performance of middleware is crucial to provide services like performance, security, and policy enforcement. This will make sure the data flow is in proper desired way which is manually done and based on the expertise. To improve this, SDN gives promising results using the concept of resource management, packet modification, and policy enforcement [7]. Optical: Distributed application around the globe requires huge transfer of data which is challenging task. This requires proper utilization of resources including packet switching and circuit switching. Wide area network which deals with this scenario requires quick reconfiguring the devices including optical devices which gives way to manage traffic in better manner. The advancement of SDN and concept of dividing the data and control plane can be applied to WAN, i.e. generalized multiprotocol label switching can integrated with data plane which give rises to new framework for developing intelligent network applications [8].

Challenges

The concept of SDN has many advantage but has different challenges. The SDN has many applications but also introduces different challenges which has to be addressed. Security, scalability, trust, policy frame work, performance, and placement of controller are few such challenges.

3 Security Threats and Attacks

Security Threats: Any network in practical terms should provide properties which are very important for network to function properly which may not be directly related to security but such may result in new security threats concerns [9] which are listed below. Forwarding: A switch in any network should be able to forward information to all the hosts which are connected to it based on the configuration. Loop Free: Any network which has multiple nodes or devices which may form loops which should not result in forwarding loops in forwarding table. Redundancy on Links: In case of multiple links amongst multiple nodes, it has to ensure that data transmission can happen in all links, and the network topology should remain unchanged if network goes down. Device Redundancy: All though a node goes done or failure in one node does not affect the working of the remaining nodes which is referred as availability. E. Scalability: The management of network should be manageable with less overhead even though the network expands or result in large network.

Security Attributes: ITU-T X.800 [10] has discussed and identified the five security services which has to be provided based the layers which are listed below with definition. Confidentiality: Confidentiality is a property in which the content of the data is not revealed to third party, i.e. sharing the data with the intended user only. Integrity: This is a property through in which the end receiver will be able to identify whether the received data are been tampered or altered. Availability: It is the property wherein the intended user has to get the service or able to access the functionality of the system or application. Authentication: Authentication is a process where the user proves his/her claim, i.e. user has some credentials to prove his identity to the system or application. Non-repudiation: It is a property in which the transactions done by the entity will not be in state of denial of his transactions done. Authorization: This basically deals with access levels or privilege levels of the user. In this, the constraint of usage on resources or objects is based on security level or privilege. Accounting: This property deals with logging of information which helps in non-repudiation process. Anonymity deals with the protecting the identity of user with respect to the external world. However, most of the security threats and vulnerabilities are based on confidentiality, integrity, and availability (CIA) [11]. The above mentioned attribute is also applicable to the SDN environment also.

Security Attacks: The topmost layer is the application layer where all the applications lie or where the business logic exists. Based on the application, the underlying layers are configured, i.e. the application which is to be implemented based on the policies, directs the control plane to identify the flow rules which is communicated through northbound API. The possible security attacks with respect to this layer are as follows.

Malicious application: To provide greater flexibility and scalability of the application, it requires SDN implementation. For this to happen, the control layer has to identify proper flow table which has to be implemented in data plane. In this scenario, the rate of success depends upon the trust between devices, i.e. switched, nodes, routers, and access points with the controller. However, if a malicious application takes part with the genuine application, wherein the malicious application has

role in formation of flow tables leads to a scenario which will damage the SDN implementation on large extent [12]. Hence, external applications pose a greater threat in SDN implementation. Malware like virus, Trojan worm can perform these attacks effecting the SDN, resulting in massive damage. These types of attacks deals with vulnerabilities related to coarse granularity, which can be resolved using role-based authentication techniques. Authorized Authentication: The northbound API deals with interaction between application layer and the control layer. However, the trust between them is major concern. The trust purely depends on whether the application is secured in terms of attacks, i.e. the vulnerabilities in application cab lead into a situation wherein attacker will generate flow rules which are malicious. Moreover, the access control should ensure whether application is allowed to take part in the process of generating the flow table rules [12]. It should ensure that through application, control layer is fully exposed to attacks. Further not only flow tables, it may change many things like deployment strategy, perform denial of service, stealing of data, and many more. Though, this attack cannot be mitigated but can be minimized having separate kernel and application module. Flow Rules Conflict: SDN implementation has open-source applications which pose challenges for configuration management and may lead to effect flow rules and the security policies. This may lead to a state which will cause network crashes. The best way to overcome is to have reduce flexibility in generating flow rules by using technique, wherein we compare the existing flow rules and inserted flow rules [13].

Northbound interface: The methods of authentication and authorization in SDN applications are diverse and constantly updating, hence trust between the application and control layer is very big issue. Moreover, its openness and ability to programme the northbound interface can be exploited by attackers to perform attack [14]. So, there is a need to have standardization of this which can overcome this security issue. Control Layer: The control layer plays a crucial role in SDN implementation which controls the entire network. Any attacker able to compromise this layer will result unpredictable damage to the network. Some of possible attacks are given below. Denial of Service (DoS/DDoS) Attacks: As the name suggests any action which leads into the state which reduces the availability of service is termed as DoS attack. In this type of attack, attackers generate large number of illegal access resulting in overloading the system which will lead to situation wherein legitimate users are not able to access the service. The attackers here will craft huge number of packets for which flow table will not have entry which will be forwarded to controller for framing the rules [15]. In this situation, it will overload the controller which may result in crashing or delay in the flow table rules, thereby denying the service to legitimate user. Hijacked Controller: In this type of attack, attacker compromises the controller then rejects the request of the genuine user. The attacker may use any method, it may be physical or logical way [15]. Though application layer logic drives the creation of flow table, but if underlying control is hijacked then lead to unpredictable damage. It is majorly due to centralized control of SDN and be mitigated by having distributed approach of controllers. Poor Controller Deployment: The major security issue is because of the controller. The implementation of SDN should be such a way that controller will not be overloaded. It is purely the scenario of single point failure. So

if the controllers are not deployed properly, it has drastic effect on the network. This will also lead to privacy issue and policy conflict will affect the firewall policies.

Southbound interface: This interface deals with transferring the flow table from control to data layer. So the communication has to be secure or else attacker may get to know the details of flow rule updation based on which he can perform attacks. The technique of securing this channel is major challenge [16].

The Data Layer: The layer deals with actual devices which include switches, routers, and other devices which deals with processing, discarding, and forwarding the packets. Some of possible attacks are given. Authentication: The possible attack is with respect to the vulnerability that is the lack of trust between devices and the controller. Forged network flow can be generated by a malicious switch in which data theft and also can discard the genuine packets which will compromise with respect to integrity and availability [16]. Further, the malicious switch can connect with controller which can induce its effect on the generation of flow table. Side Channel Attacks: The attack can be used by an attacker to get network-related information, although it will not directly affect the SDN. The attacker can gather information related to network like flow table by using this attack [17]. This is of high concern, because SDN will be having confidential and private data of the user. By using this type of attack may lead to data leakage problems. Further, attacks like denial of service attack (Dos/DDoS attack) may not directly affect but effect the security attributes such as confidentiality, integrity, privacy, authentication which can be used by attacker to perform further attacks.

Cause of Security Attacks: To overcome these attacks, it is very important to know the cause of these in SDN platform. Table 1 gives the details of the cause with attacks, its corresponding layers, and security attributes related to it.

4 Conclusion

The basic idea in SDN is to separate the data plane and control plane which has brought huge change in the field of networking which enables rapid application development implementation which is the need of the hour. The latest technologies such as data centres, cloud, optical communication, enterprise network, and Internet of things are been using SDN environment for implementation. Although SDN has improved the performance, it has introduced many challenges which includes security also. The paper focuses on the security challenges in implementation keeping in mind of security attributes and has discussed in detail about the threats and possible attacks with respect to the different layers of SDN. Finally, the root cause of these attacks is identified which will help the research community in identifying mitigation techniques to overcome these attacks.

Table 1 Cause of security attacks with respect to different layers

Layer	Security Issue	Cause						
		SDN architecture	Access con trol	Encryption	Malicious attack	Configuration	Soft war e	Communication technology
Application layer	Malicious application	Yes		Yes	yes		Yes	
	Authorized authentication		Yes	Yes		Yes	Yes	
	Flow rules conflict	Yes						
Northbound	Interface standardization	Yes					Yes	
	Trust/weak authentication/authorization		Yes	Yes	Yes		Yes	
	Malicious applications			Yes	Yes		Yes	
Control layer	DoS/DDoS attacks		Yes			Yes	Yes	Yes
	Hijacked/Rogue/controller			Yes		Yes	Yes	
	Controller deployment	Yes				Yes		Yes
Southbound	Communication security			Yes				Yes
	Eavesdropping/spoofed communications		Yes	Yes				Yes
	Application isolation	Yes				Yes		
Data layer	Authorized authentication		Yes	Yes				
	legality and consistency of flow rules		Yes			Yes		
	DoS/DDoS/side channel attacks	Yes			Yes			Yes

References

1. Han T et al (2020) A comprehensive survey of security threats and their mitigation techniques for next generation SDN controllers. Concurr Comput Pract Exp 32(16):e5300, Aug 2020. https://doi.org/10.1002/cpe.5300
2. Correa Chica JC, Imbachi JC, Botero Vega JF (2020) Security in SDN: A comprehensive survey. J Netw Comput Appl 159:102595, 01 June 2020, Academic Press. https://doi.org/10.1016/j.jnca.2020.102595
3. Hu F, Hao Q, Bao K (2014) A survey on software-defined network and open flow: From concept to implementation. IEEE Commun Surv Tuts 16(4):2181–2206, 4th Quart. 2014
4. Rahouti M, Xiong K, Xin Y (2021) Secure software-defined networking communication systems for smart cities: current status, challenges, and trends. IEEE Access 9:12083–12113. https://doi.org/10.1109/ACCESS.2020.3047996
5. Adami D, Martini B, Gharbaoui M, Castoldi P, Antichi G, Giordano S (2013) Effective resource control strategies using open flow in cloud data center. In: 2013 IFIP/IEEE international symposium on integrated network management (IM 2013), pp 568–574
6. Zhao G, Xu H, Fan J, Huang L, Qiao C (2021) Achieving fine-grained flow management through hybrid rule placement in SDNs. IEEE Trans Parallel Distrib Syst 32(3):728–742, 1 Mar 2021. https://doi.org/10.1109/TPDS.2020.3030630
7. Simeonidou D, Nejabati R, Azodolmolky S (2011) Enabling the future optical internet with open flow: a paradigm shift in providing intelligent optical network services. In: 2011 13th international conference on transparent optical networks, pp 1–4. https://doi.org/10.1109/ICTON.2011.5970832
8. Information Technology—Open Systems Interconnection—Basic Reference Model: The Basic Model, ISO/IEC Standard 7498-1: 1994 (1994)
9. Abdou A, van Oorschot PC, Wan T (2018) Comparative analysis of control plane security of SDN and conventional networks. In: IEEE communications surveys and tutorials, vol. 20(4), Fourth quarter 2018, pp 3542–3559. https://doi.org/10.1109/COMST.2018.2839348
10. International Telegraph and Telephone Consultative Committee (1991) ITUT X.800: Security architecture for open systems interconnection for CCITT applications. Data Commun Netw OSI Secur Struct Appl (1991)
11. Cui H et al. (2017) Authentication mechanism for network applications in SDN environments. In: Proceeding 20th IEEE international symposium wireless personal multimedia communications 2017, pp 1–5
12. Fu Z, Li J (2019) High speed regular expression matching engine with fast pre- processing. China Commun 16(2):177188
13. John W, Kern A, Kind M et al (2017) Split architecture: SDN for the carrier domain. IEEE Commun Mag 52(10):146–152
14. Spooner J, Zhu SY (2016) A review of solutions for SDN-exclusive security issues. Int J Adv Comput Sci Appl 7(8):113–122
15. Wu K, Liang J, Lee SC et al (2018) Efficient and consistent flow update for software defined networks. IEEE J Sel Areas Commun 36(3):411421
16. Bin BY, Zou D, Yu S et al (2016) Defending against flow table overloading attack in software-defined networks. IEEE Trans Serv Comput 12(2):1–13
17. Wu K, Liang J, Lee SC et al. (2018) Efficient and consistent flow update for software defined networks. IEEE J Sel Areas Commun 36(3):411421

Optimized Control Function with Estimation of System Parameters Against Attack for Networked Control System

Brijraj Singh Solanki, Renu Kumawat, and Seshadhri Srinivasan

Abstract Networked control systems (NCS) are prevalent in industrial and other applications due to digitization in industrial controls. While digitization provides more flexibility and key enabler for many novel applications, the system becomes vulnerable to attack (e.g., eavesdropping). This paper focuses on computing optimal system parameters to identify malicious attack in NCS. To identify the attack, system performance metrics such as overshoot, peak time, rise time, and optimal policy iterations are used. As computing optimal parameters considering the performance metrics is a challenging task, different evolutionary computation approaches such as particle swarm optimization (PSO), genetic algorithm (GA), and backtracking search optimization (BSA) are used. With the optimal system parameters computed using GA, PSO, and BSA performance metrics: rise time, overshoot, and policy iterations were optimizing the overall system performance while being subjected to attacks. Our results demonstrate that for the problem and example considered, the PSO computed optimal parameters are more accurate.

Keywords Networked control system (NCS) · Genetic algorithm (GA) · Denial-of-service (DoS) attack · Backtracking search optimization algorithm (BSA) · Packet loss · Particle swarm optimization (PSO)

1 Introduction to NCS

The networked control systems [1] are defined as where components coupled tightly through real-time communication system. In the networked system, the measured signal traveled from sensor to controller via communication network and after computation of control signal to actuator through real-time communication network. The recent applications of NCSs are in medical field, critical infrastructure, robotics,

B. S. Solanki · R. Kumawat (✉)
Manipal University Jaipur, Jaipur, India
e-mail: renu.kumawat@jaipur.manipal.edu

S. Srinivasan
Kalasalingam Academy of Research and Education, Srivilliputhur, Tamil Nadu, India

© The Author(s), under exclusive license to Springer Nature Singapore Pte Ltd. 2022

A. Tripathi et al. (eds.), *Intelligent Computing Techniques for Smart Energy Systems*, Lecture Notes in Electrical Engineering 862,
https://doi.org/10.1007/978-981-19-0252-9_47

process industries, defense system, space craft etc. The goal of networked system is to transmit the critical information faithfully to maintain the performance and stability. The malicious attacks designed by attacker may be introduced to degrade the performance of the NCS.

Some of well-known attacks reported in literatures are Stuxnet worm, Davis-Besse nuclear power plant attack, cyber-attack on a Ukraine power plant, electric grid attack, Maroochy service attack, attack on German Steel Mill, etc. [2–5].

The attacks may be of denial of service (DoS) and service-degradation (SD) attacks which are designed as per the specific information collected from eavesdropping or other means. By introducing aforementioned attack, system may be raised to margin of instability, causing the performance degradation or halting the control system. So it is important to secure the physical process and transmission medium by adopting security policies and protocols. As far as concerned, the attacks are designed based on compromised system knowledge acquired through eavesdropping, so in this paper through optimization of cost function, system parameters are estimated. To demonstrate an effectiveness of the compromised system, an optimization process is described to identify such systems, which is the key contribution of the paper. Herein, particle swarm optimization, genetic algorithm, and backtracking optimization algorithm are used to find the optimized coefficient of plant and controller transfer function.

Next part of paper describes the following sections in detail: the detailed literature review process is discussed in Sect. 2. Section 3 illustrates the problem identification including process of parameter assessment employing optimization algorithm. The simulation results for problem with optimized coefficients are presented in Sect. 4. Finally, the concluding remarks and future scope of works are discussed in Sect. 5.

2 Related Literature Work

In this section, different types of attacks and factors are discussed which may degrade the control performance and stability. The denial-of-service (DoS) and service-degradation (SD) attack may be launched in either direction of traveling of signal through communication network [6]. Herein, system is estimated by using the system identification tool and BSA algorithm. The author presented an exponential stability and receding-horizon control law to show the stability and performance improvement [7, 8]. To evaluate the performance index for NCS undergone DoS attack, an event-triggered-control system is developed adopting switching rules [1]. Moreover, false data injection (FDI) attack is employed to evaluate the stability using Kalman filter-based predictive control approach for output tracking control problem [9, 10]. Further, random switching controller is developed to identify the system identification attacks in NCS. The designed controller obeys the control function based on switching rules [11]. The improved NCS stability condition against attack with linear quadratic Gaussian, Kalman filtering along with proportional-integral derivative control action is studied in [12].

In [13], performance index improvement in power system is represented by defining the stability conditions using linear matrix inequalities (LMIs) and Wirtinger-based integral inequality with delay bound subjected to DoS attack. Furthermore, various attacks are discussed [14] in cyber-physical system (CPS) along with linear quadratic function to show improved performance. The system can be identified by extracting the information related to input and output to control system [15, 16]. Based on the designed estimated system, the attacker can develop the intended attacks. In [17], neural network (NN) method employed to detect the introduction of anomaly in CPS and shown efficacy of the improved system.

The hash-based message authentication code and symmetric key encryption methodology are used to protect the NCS against DoS and SD attacks in CPS. It has shown the improved performance parameters against such attacks [18]. In [19], author discussed the maximum allowed DoS attack which can be introduced in NCS by defining suitable stability conditions with Lyapunov function. The switched Luenberger observer theory adopted to design an observer-based switching controller which can detect the covert attack in the NCS [20]. Here, designed system uses LMI tool and convex programming which has shown the effectiveness of system. Another attack defined as time delay attack [21] draws the system toward instability. The cryptography free time delay switch design approach provided the upgraded stability with such attacks. Furthermore, type of genetic algorithm used to calculate the gain of controller which improve the performance of CPS by maximizing the jitter margin [22].

The robust controller is designed based on the graph theoretic and system theoretic approach to investigate the attack which may be unidentifiable and undetectable in the system. Herein, designed method showed the improved performance and robustness [23]. The hidden and overt pattern attack are the terms discussed to elaborate the attack consequences on NCS [24]. Such attacks degrade the stability and performance of system by changing the energy cost control function.

The measured sensor data is secured by employing the dynamic watermarking to faithfully transmitting the measured signal/data over the communication network. Author discussed that detection of unwanted signal into system can be made through this schemes [25]. Furthermore, for improving the dynamic response of system, the suitable asymptotical-stability condition evaluated using LMIs and Lyapunov–Krasovskii approach. Author discussed that performance can be maintained within limits with the designed event-based adaptive controller under uncertainty conditions, i.e., bandwidth constraints and attack [26, 27]. Author discussed the quantization and DoS attack for event-triggered system by designing controller [28].

The effect due to denial of service and packet loss is studied to design optimal controller which compensate the effects induced due to attacks [29–32]. Author used networked-predictive control (NPC) algorithm for designing such controller. The stability of the proposed method for wireless networked control systems (WNCS) calculated and validated using intrusion detection system [33].

The wormhole attack is performed by collecting the information or signals which transmit over the network through breaching the communication networked nodes. The author designed decentralized approach for the recognition of attack [34]. For

Table 1 List of attacks

Attacks	Method used by attacker	References
StuxNet worm attack on a nuclear power plant (2010)	PLC code modifications to send false control signal	[2]
Australia's Maroochy water services (2000)	Infiltrate the SCADA system to manipulate the code executed	[3]
Cyber-attack on a Ukraine power plant (2016)	SCADA Hijacking	[4]
German Steel Mill cyber- attack	PLC code modification in system	[5]
Denial-of-service (DoS)	Inducing jitter, data loss and false data injection	[6, 8, 13, 28]
Service degradation	System identification approach	[6]
Cyber-physical intelligence (CPI)	Gather information by eavesdropping	[6]
Denial-of-service attack/replay attack	Packet loss/false data injection	[6, 9, 19, 36]
Covert attacks	PLC code modification/injects the false control commands	[2, 6, 20]

protecting the data, which may be infected by the injection of attacks, traveling through communication network, author designed time-varying coding matrices. Such design resists an agent to gather information and to avoid launching an intended attack by estimation of data [35].

In literature, it has been observed that system performance may be corrupted by introduction of the designed intended attacks. Here, covert agent is able to design the intended attack, if having the system-specific knowledge. The agent may get information about the process by eavesdropping and other means. In this study, for compromising the process and plant, an optimization process is adopted to compute the coefficients and parameters of NCSs. Here, compromised system may be used for degrading the system performance with designed attack based on knowledge acquired. Some of the well-known attacks as reported in literature are shown in Table 1.

3 Defining of Problem Statement

3.1 Design of the NCS with Attacker

Basically, an attacker may interfere in either direction of stream of closed-loop control for collection of information traveling through communication network. The representation of breaching NCS network by attacker is shown in Fig. 1. The sampled signal by sensor traveled through communication channel to controller, and after computation of control signal, it is directed to actuator through network. So while

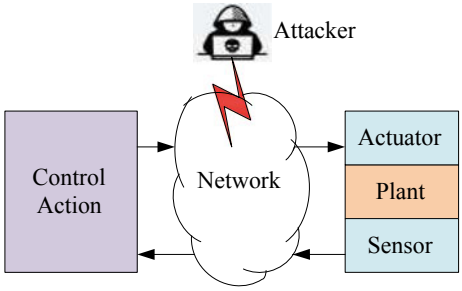

Fig. 1 Information collection by attacker in NCS

communicating through network, signal may be interfere by attacker to get critical information of networked system to launch an intended attack. The plant under consideration is linear time invariant.

3.2 Process of Estimation of System Parameters

The sensor sampled response is transmitted to controller over the communication channel, and control signal calculated by controller is directed toward the actuator over the same network. As shown in Fig. 1, it can be inferred that it is needed to secure the data and communication channel from the point of view of attackers. The attacker, based on the information access through breaching the network and/or eavesdropping or other means, is able to synthesize the intended attack. The attacker may design DoS and SD attack to degrade or compromise the system.

For designing attacks, attacker may perform the following steps to estimate the coefficient of plant and controller transfer function.

- Step-1: Attacker acquires the knowledge about the NCS by eavesdropping process.
- Step-2: After acquiring system knowledge, attacker defines the cost function based on actual system.
- Step-3: Try to minimize the defined cost function for getting the optimized coefficient of plant and controller transfer functions using optimization algorithms.
- Step-4: Based on the optimized coefficient, attacker is able to design attacks to degrade the system performance and stability.

The attacker may design the following different forms of attacks based on the estimated optimized coefficients of plant and controller transfer function as shown in Table 1.

3.3 *Optimized Parameter Identification by Optimization Algorithms*

The information can be accessed through breaching the network and/or eavesdropping or other means able to synthesize the intended attack. The designed attack introduced to degrade or compromised the system. Herein, it is preferred that system can be compromised if controller and plant coefficients are perfectly known.

In this sequence, an optimization algorithm such as PSO, BSA, or GA is employed to compute the coefficients of plant and controller transfer function. The coefficients of controller and plant are estimated through minimization of cost function. Here, in optimization process, the number of variables is six.

For the estimation of controller and plant transfer function coefficients, genetic algorithm is employed. The genetic algorithm follows the principle of genetic reproduction behavior. In the process of finding optimized coefficients using GA, the population size chosen is 50, maximum iteration is 100 with search space [−10 10]. The elite counts are 0.05 times population size, and crossover fractions are taken as 0.8. The basic flowchart used for finding optimized coefficient using GA is shown in Fig. 2.

The optimized solutions are also determined by swarm-based metaheuristic optimization algorithm PSO with given search space to the problem. Herein, population size is 50, maximum iteration is 100 with search space [−10, 10]. The approach to find global best solution is shown in Fig. 3.

In PSO, each particle i assigns its best position and swarm best position in dimension u by using the velocity $v_{iu}(t+1)$ and position $x_{iu}(t+1)$ update rule as given below [37]

$$v_{iu}(t+1) = w * v_{iu}(t) + r_1 * k_1 * (p_{iu}(t) - x_{iu}(t)) + r_2 * k_2 * (g_u(t) - x_{iu}(t)) \quad (1)$$

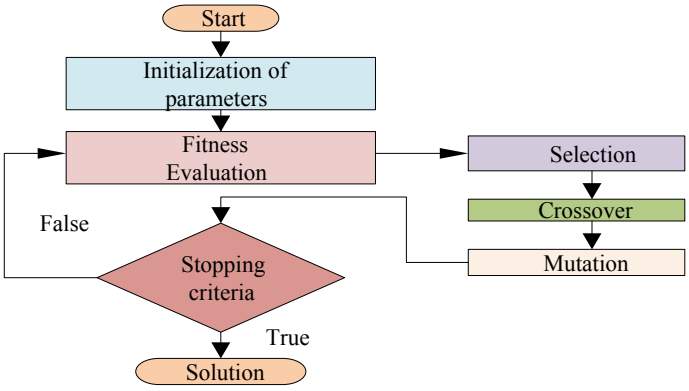

Fig. 2 Flowchart for coefficient optimization using GA

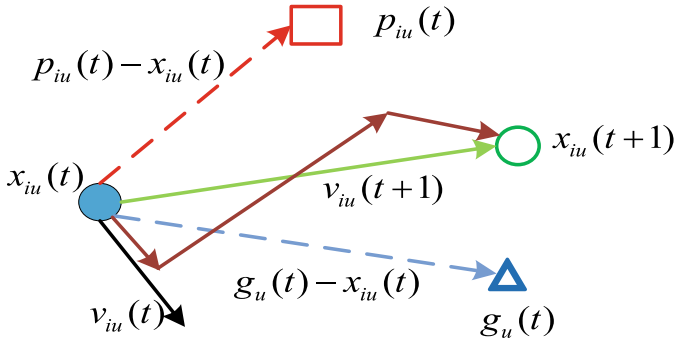

Fig. 3 Process of coefficient optimization using PSO

$$x_{iu}(t+1) = x_{iu}(t) + v_{iu}(t+1) \tag{2}$$

where $x_{iu}(t)$ is position vector, $g_u(t)$ is global best position, and $p_{iu}(t)$ is best position of ith particle. Herein, w is inertial coefficient, which is used to control number of particles remembering previous velocity. The k_1, k_2 are acceleration coefficients which controls the number of particles moving toward its best position, and swarm best position and $r_1, r_2 \in (0, 1)$ are random variables.

For solution of real-valued numerical problem, based on optimization principle, an evolutionary algorithm called BSA is also used herein [38]. The BSA computes the global minimizer for the given problem. In the process of finding optimized coefficients using BSA, the population size chosen is 50, maximum iteration is 1000 with search space [−10 10]. The basic flowchart of BSA for solving real-valued problem is shown in Fig. 4.

3.4 Designing of Controller Parameters

The role of control action is to make the system performance with prescribed limits. Here, in this section, proportional-integral (PI) control action is used to design the parameters of controller using the optimization process. The following form of PI control action is defined as

$$G_c(s) = P_c + I_c \frac{1}{s} \tag{3}$$

where $G_c(s)$ is controller gain, P_c is proportional control action, I_c is integral control action. The integral-time absolute-error (ITAE) is considered as performance measure which defines the cost function for the given problem as shown in (4).

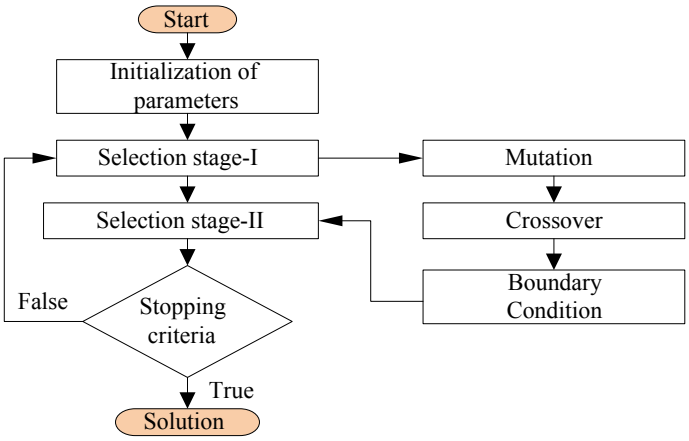

Fig. 4 Flowchart of coefficient optimization using BSA

The minimization of ITAE reduces the errors into control system by adjustment of parameters.

The ITAE minimization limits the initial errors by reducing the rise time and also decreases the overshoot and settling time to limit small errors persisting for long period of time.

$$J_{\text{ITAE}} = \int_0^t t \,.|e(t)|.dt \tag{4}$$

where J_{ITAE} integral-time absolute-error which is representing the cost function for the given problem, $|e(t)|$ is absolute value of errors representing the difference of reference value and sensor measurement.

4 Performance Metrics Based on Optimized Coefficients

This section presents the different performance metrics used to define stable control system. These metrics estimated through the determination of optimized coefficient of plant and controller transfer function employing optimization tool GA, PSO, and BSA. For computation of the performance metrics, MATLAB Simulink and Control System tool box are used. The DC motor is considered as plant, and PI control action is used as formation of controller.

The plant $G_p(s)$ and controller $G_c(s)$ transfer function in the form of coefficients of NCS in Laplace domain is represented as

$$G_p(s) = \frac{g_1 s + g_2}{s^2 - g_3 s + g_4} \quad G_c(s) = k_p + \frac{k_i}{s} \tag{5}$$

The plant coefficients g_1, g_2, g_3 and controller coefficient k_p, k_i are computed using the optimization process. Based on the optimized coefficient computed from optimization process, various performance metrics are computed for NCS as shown in Table 2. The overshoot, rise time, cost function, settling time, and peak time are considered as performance measures for control system.

This section presents the various performance metrics that are plotted graphically to show estimation of system parameters for designing an intended attack to degrade the performance and stability of NCS. It is seen, from Fig. 5, that based on the optimized coefficients of plant and controller, the rise time for GA, PSO, and BSA are 0.0412, 0.0220, and 0.0249 s, respectively.

From Fig. 5, it is concluded that PSO performs better in obtaining the optimized coefficients. From Fig. 6, it is noted that the settling time for GA, PSO, and BSA are 0.073, 0.0391, and 0.0438 s, respectively. So in this sequence, it is inferred that the PSO performs better than GA and BSA. The overshoot for GA, PSO, and BSA are 0.13, 0.62, and 4.05%, respectively. So it can be verified from Fig. 7 that overshoot is less for GA compared to other optimization algorithm.

Table 2 Performance metrics

Parameters	Algorithms		
	GA	PSO	BSA
Rise time	0.0412	0.0220	0.0249
Settling time	0.0734	0.0391	0.0438
Overshoot	0.0013	0.0062	0.0405
Peak time	0.1980	0.1055	0.0783
Cost function	3.5896e−04	1.2282e−04	5.6808e−04

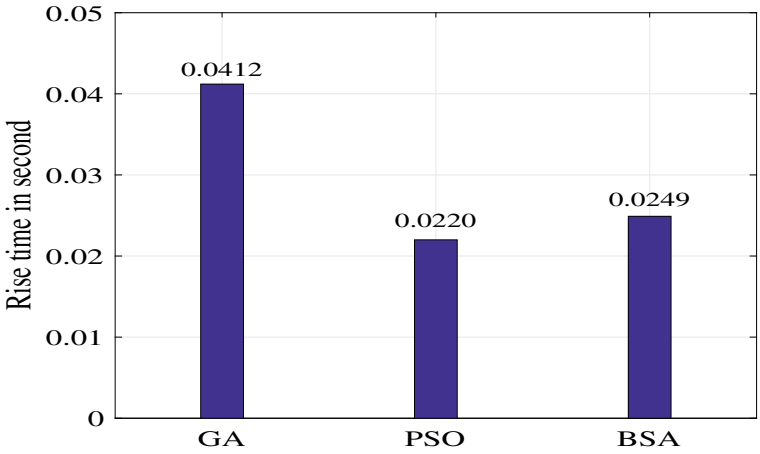

Fig. 5 Rise time in second

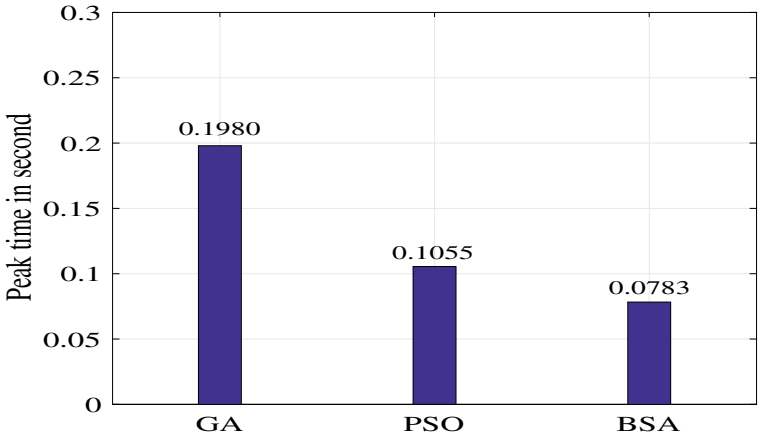

Fig. 6 Settling time in second

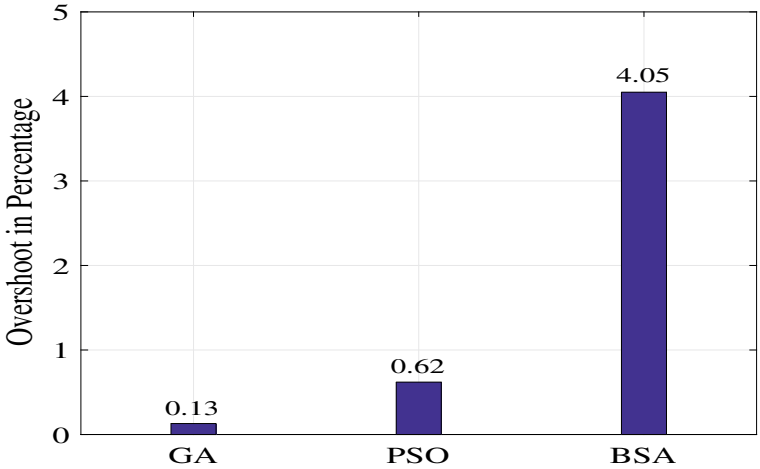

Fig. 7 Overshoot in percentage

Similarly the peak time for GA, PSO, and BSA are 0.1980, 0.1055, and 0.0783 s, respectively, as can be seen in Fig. 8. It is shown that peak time less in BSA compared to other algorithms but is of the same order. Finally, the cost functions are evaluated to verify the reduction of ITAE values so that error can be minimized in the NCS. The values of cost functions for GA, PSO, and BSA are 3.5896e−04, 1.2282e−04, and 5.6808e-04, respectively. From Fig. 9, it is deduced that value of cost function for PSO is less compared to GA and BSA. So PSO performs better than GA and BSA.

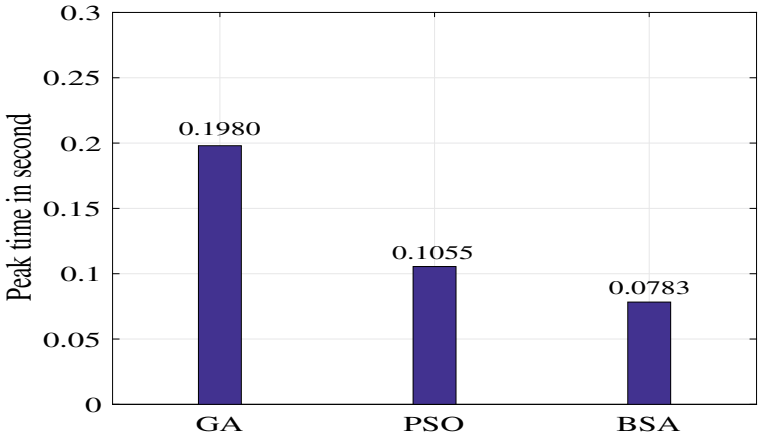

Fig. 8 Peak time in second

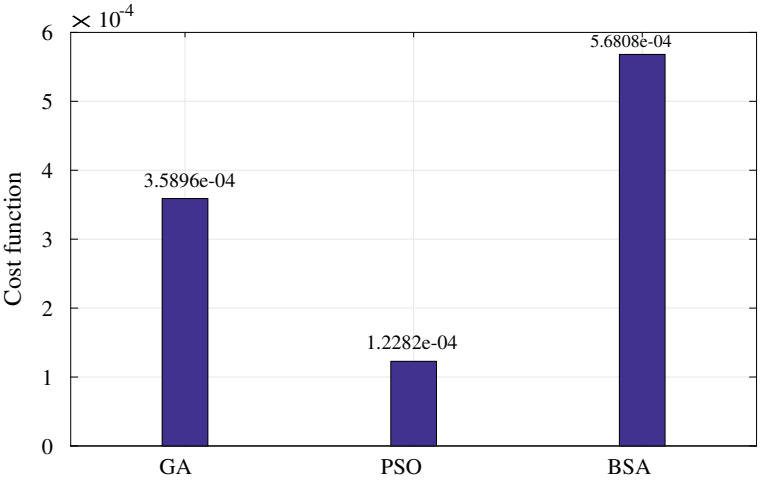

Fig. 9 Cost function

5 Conclusion and Future Work

In this section, final conclusive remarks over the computed optimized coefficients for plant and controller transfer function are presented. Herein, for computing the optimized coefficients of controller and plant BSA, PSO, GA algorithms are used. The numerical simulations are performed for the computed coefficients of plant as DC motor and PI controller. The obtained coefficients are used to show performance

of NCS in terms of performance metrics such as overshoot, rise time, cost function, settling time, and peak time. The numerical simulation part is carried out on MATLAB Simulink and control system tool box.

It is seen, from Fig. 5, that based on the optimized coefficients of plant and controller, the rise time for GA, PSO, and BSA are 0.0412, 0.0220 and 0.0249 s, respectively. From Fig. 6, it is noted the settling time for GA, PSO, and BSA are 0.073, 0.0391, and 0.0438 s, respectively. The overshoot for GA, PSO, and BSA are 0.13, 0.62, and 4.05%, respectively. Similarly, the peak time for GA, PSO, and BSA are 0.1980, 0.1055, and 0.0783 s, respectively, as can be seen in Fig. 8. The values of cost functions for GA, PSO, and BSA are 3.5896e−04, 1.2282e−04, and 5.6808e−04, respectively. From Fig. 9, it is deduced that value of cost function for PSO is less compared to GA and BSA. So based on the observation and computation of various performance metrics, it is concluded that PSO performs better than GA and BSA in calculating the optimized coefficients.

In future scope of work, it is indeed important to secure the NCS from intended intrusion and uncertainties that may be launched by attacker based on the system knowledge gathered through eavesdropping process. The extraction of critical information, when signal transmitting through communication network, can be hampered by designing security policies and protocols.

References

1. Zhao N, Shi P, Xing W, Chambers J (2020) Observer-based event-triggered approach for stochastic networked control systems under Denial of service attacks. IEEE Trans Control Netw Syst 65(9):3943–3949
2. Hou F, Sun J (2017) Covert attacks against output tracking control of cyber-physical systems. In: IECON 2017-43rd annual conference of the IEEE industrial electronics society, pp 5743–5748
3. Sayfayn N, Madnick S (2017) Cybersafety analysis of the maroochy shire sewage spill cybersafety analysis of the maroochy shire sewage spill (Preliminary Draft) (May), pp 1–29
4. Assante M (2016) Analysis of the cyber attack on the Ukrainian power grid. SANS Ind Control Syst Secur Blog 1–26 (2016)
5. Pajic M, Weimer J, Bezzo N, Sokolsky O, Pappas GJ, Lee I (2017) Design and Implementation of attack-resilient cyberphysical systems: with a focus on attack-resilient state estimators. IEEE Control Syst 37(2):66–81
6. De Sá AO, Carmo LFRDC, Machado RCS (2017) Covert attacks in cyber-physical control systems. IEEE Trans Ind Inf 13(4):1641–1651
7. Zhu M, Martinez S (2014) On the performance analysis of resilient networked control systems under replay attacks. IEEE Trans Automat Contr 59(3):804–808
8. Miao KL, Zhu JW, Zhang WA (2018) Distributed guaranteed cost control of networked interconnected systems under denial-of-service attacks: a switched system approach. In: 2018 33rd youth academic annual conference of Chinese association of automation (YAC), pp 911–915
9. Pang ZH, Liu GP, Zhou D, Hou F, Sun D (2016) Two-channel false data injection attacks against output tracking control of networked systems. IEEE Trans Ind Electron 63(5):3242–3251
10. Wu G, Sun J, Chen J (2018) Optimal data injection attacks in cyber-physical systems. IEEE Trans Cybern 48(12):3302–3312
11. De Sa AO, Carmo LFRDC, Machado RCS (2017) Use of switching controllers for mitigation of active identification attacks in networked control systems. In: Proceeding of the 2017

IEEE 15th international conference on dependable, autonomic and secure computing, 15th international conference on pervasive intelligence and computing, 3rd international conference on big data intelligence and computing and cyber science and technology congress (DASC/PiCom/DataCom/CyberSciTech), vol. 2018 Janua, pp 257–262
12. Solanki BS, Renu K, Srinivasan S (2019) Stability and security analysis with identification of attack on industrial networked control system: an overview. Internetworking Indones J 11(2):3–8
13. Cao R, Wu J, Long C, Li S (2015) Stability analysis for networked control systems under denial-of-service attacks. Proceeding of the IEEE conference on decision and control, vol. 54rd IEEE(Cdc), pp 7476–7481
14. Chen Y, Kar S, Moura JMF (2018) Optimal attack strategies subject to detection constraints against cyber-physical systems. IEEE Trans Control Netw Syst 5(3):1157–1168
15. Naung Y, Schagin A, Oo HL, Ye KZ, Khaing ZM (2018) Implementation of data driven control system of DC motor by using system identification process. In: Proceeding of the 2018 IEEE conference of Russian young researchers in electrical and electronic engineering (EIConRus), vol. 2018, pp 1801–1804
16. Solanki BS, Kumawat R, Srinivasan S (2021) An impact of different uncertainties and attacks on the performance metrics and stability of industrial control system. Commun Intel Syst 557–574
17. Goh J, Adepu S, Tan M, Lee ZS (2017) Anomaly detection in cyber physical systems using recurrent neural networks. In: Proceeding of the IEEE international symposium on high assurance systems engineering (HASE), pp 140–145
18. Jithish J, Sankaran S (2018) Securing networked control systems: Modeling attacks and defenses. In: 2017 IEEE International Conference on Consumer Electronics-Asia (ICCE-Asia, vol. 2018-Janua, pp 7–11
19. Zhang J, Peng C, Masroor S, Sun H, Chai L (2016) Stability analysis of networked control systems with denial-of-service attacks. In: 2016 UKACC 11th international conference on control (CONTROL)
20. Schellenberger C, Zhang P (2018) Detection of covert attacks on cyber-physical systems by extending the system dynamics with an auxiliary system. In: 2017 IEEE 56th annual conference on decision and control (CDC), vol. 2018-Janua(Cdc) pp 1374–1379
21. Sargolzaei A, Yen KK, Abdelghani MN, Sargolzaei S, Carbunar B (2017) Resilient design of networked control systems under time delay switch attacks, application in smart grid. IEEE Access 5:15901–15912
22. Balasubramaniyan S, Srinivasan S, Buonopane F, Subathra B, Vain J, Ramaswamy S (2016) Design and verification of cyber-physical systems using truetime, evolutionary optimization and UPPAAL. Microprocess Microsyst 42:37–48
23. Pasqualetti F, Dorfler F, Bullo F (2013) Attack detection and identification in cyber-physical systems. IEEE Trans Automat Contr 58(11):2715–2729
24. Zhang Y, Chen C, He J (2019) DoS attack on networked control system: from the viewpoint on communication-control cost. In: Proceeding of the 2019 Chinese automation congress (CAC), pp 5695–5700
25. Satchidanandan B, Kumar PR (2017) Dynamic watermarking: active defense of networked cyber-physical systems. Proc IEEE 105(2):219–240
26. Tang X, Li T, Cong S, Qian W (2019) Event-triggered adaptive control for networked control systems under two stochastic cyber-attacks. In: Proceeding of the 31st Chinese control Decision *conferences CCDC 2019*, pp 170–175
27. Sun J, Chen J (2019) Networked predictive control for linear systems with communication delay in the feedback channel. Stab Control Appl Time-Delay Syst July, pp 315–331
28. Hu S, Zhou Y, Chen X, Ma Y (2018) H ∞ controller design of event-triggered networked control systems under quantization and denial-of-service attacks. In: Chinese control conference CCC, vol. 2018-July, pp 6338–6343
29. Xiang C, Qiu L, Pan J, Zhang B, Yang R (2020) Predictive feedback control based on DoS attacks network control system. In: IEEE International Conferences Control Automation ICCA, vol. 2020-Oct, pp 1189–1192

30. Wang ZW, Gao HH (2015) Linear quadratic optimal control of networked control system. In: Proceeding of the 2015 27th Chinese control decision conference CCDC 2015, 61263003, pp 2177–2182
31. Pang ZH, Liu GP (2012) Design and implementation of secure networked predictive control systems under deception attacks. IEEE Trans Control Syst Technol 20(5):1334–1342
32. Xia Y, Chen J, Zhou L (2007) Networked control systems with different control inputs. In: Proceeding of the 26th Chinese control conference CCC 2007 (6), 539–543
33. Al-Dabbagh AW, Li Y, Chen T (2018) An intrusion detection system for cyber attacks in wireless networked control systems. IEEE Trans Circuits Syst II Express Briefs, 65(8):1049–1053
34. Padmanabhan J, Manickavasagam V (2017) Scalable and distributed detection analysis on wormhole links in wireless sensor networks for networked systems. IEEE Access 6:1753–1763
35. Miao F, Zhu Q, Pajic M, Pappas GJ (2017) Coding schemes for securing cyber-physical systems against stealthy data injection attacks. IEEE Trans Control Netw Syst 4(1):106–117
36. Hou F, Sun J (2017) Fasle data injection attacks in cyber-physical systems based on inaccurate model. In: Proceeding of the IECON 2017-43rd annual conference of the IEEE industrial electronics society, vol. 2017-Janua, pp 5791–5796
37. Shi Y, Eberhart RC (1999) Empirical study of particle swarm optimization. In: Proceedings of the 1999 congress on evolutionary computation-CEC 1999, vol. 3, pp 1945–1950
38. Civicioglu P (2013) Backtracking search optimization algorithm for numerical optimization problems. Appl Math Comput 219(15):8121–8144

Study of Magnetic Properties of 2D vdW Ferromagnets $Fe_3(Si/Sn)Te_2$ and Mn_3SiTe_2 towards Potential Spintronics Applications

Rushikesh Pokar and Alpa Dashora

Abstract Recently, the surge of 2D vdW ferromagnetic materials such as Fe_3GeTe_2, $Cr_2Ge_2Te_6$, and CrI_3 due to their itinerant long-range ferromagnetic order down to single atomic layer has opened up new possibilities of designing similar materials for their applications in spintronics. Density functional theory calculations allow to design and tailor materials without the expense of experiments, which is greatly beneficial in screening out the suitable materials. Therefore, we have explored magnetic properties of Fe_3(Si, Sn)Te_2 and Mn_3SiTe_2 using spin polarized density functional theory as embedded in QUANTUM ESPRESSO code. In our calculations, we have included van der Waals (vdW) interaction. In the present work, all the studied materials show shrinkage in the size of unit cell after including vdW interactions. Toward magnetic properties, Fe_3SiTe_2 shows negative value spin polarization while Fe_3SnTe_2 and Mn_3SiTe_2 show positive spin polarization. Total spin magnetic moments of Fe_3SiTe_2, Fe_3SnTe_2, and Mn_3SiTe_2 are 5.57, 6.51, and 4.01 μ_B/f.u. which are comparable to well-studied material Fe_3GeTe_2 (6.31 μ_B/f.u.). Our research provides the first step in exploring these novel 2D vdW materials for understanding their magnetic properties further for spintronic application.

Keywords 2D vdW ferromagnets · Density functional theory · Spintronics

1 Introduction

Recently, discovery of two-dimensional (2D) van der Waals (vdW) ferromagnetic materials have spawned a new field of interest among physicists to search new materials for room temperature spintronic applications due to their rich magneto-electric and magneto-optic and magnetotransport properties. The search of such materials is driven by high Curie temperature (T_c), high (≈100%) spin polarization factor and long-range magnetic order. From a wide variety of magnetic materials, only few have been found to have intrinsic magnetism in 2D down to a few atomic layers. Among

R. Pokar (✉) · A. Dashora
Computational Material Science Laboratory, Department of Physics, The M. S. University of Baroda, Vadodara 390002, India
e-mail: rushikesh.p-phyphd@msubaroda.ac.in

© The Author(s), under exclusive license to Springer Nature Singapore Pte Ltd. 2022

A. Tripathi et al. (eds.), *Intelligent Computing Techniques for Smart Energy Systems*, Lecture Notes in Electrical Engineering 862,
https://doi.org/10.1007/978-981-19-0252-9_48

all Fe_3GeTe_2, CrI_3, and $Cr_2Ge_2Te_6$ have proved to be good 2D vdW ferromagnets where Fe_3GeTe_2 is a metal and later two are insulator and semiconductor, respectively. T_c of up to 224.5 K is reported for Fe_3GeTe_2 [1] which is highest among all the known 2D vdW ferromagnets. T_c is observed to be decreasing upon Fe deficiency and Co doping [2, 3]. Ionic gating has shown to be a good strategy for increasing the T_c [4]. Density functional theory (DFT) calculations have predicted some high T_c materials like VS_2-WS_2 (487 K) and VS_2-MoS_2 (485 K) vdW heterostructures [5], $NiCl_3$ (400 K) [6], Cr_2C (300 K) [7], and $CrGeTe_2$ (314 K) [8]. Unfortunately, it turns out that these materials show much lower T_c than the calculated values when synthesized [9, 10]. Tunneling magnetoresistance (TMR) is observed in a three-layer system of an insulator sandwiched by ferromagnetic layers, TMR ratio shows the difference between the probabilities of current tunneling through the insulating layer for different orientations of the magnetization in ferromagnetic layers. Fe_3GeTe_2-graphene and Fe_3GeTe_2-hexagonal boron nitride heterojunctions show huge values of TMR ratio of 3621% and 6256%, respectively [11] validating their use in magneto-switching devices. TMR ratio of merely 100% has also been reported for $Cr_2Ge_2Te_6$ [12]. In non-centrosymmetric materials, Dzyaloshinskii-Moriya interaction emerges upon crystal inversion symmetry breaking due to which topological spin textures are observed commonly known as skyrmions. Many groups have observed these kinds of magnetic skyrmions in Fe_3GeTe_2 and its heterostructures with various other materials [13–16]. Skyrmions may be used as a unit magnetic storage bit hence existence of skyrmions in Fe_3GeTe_2 and its family is important for their application in next generation magnetic data storage devices. Perpendicular magnetic anisotropy can be used along with spin–orbit torque by adding a heavy metal layer next to the magnetic layer to tune the magnetization of 2D vdW magnets [17]. In fact, the presence of large magnetic anisotropy energy (MAE) in 2D vdW ferromagnets is responsible for long-range ferromagnetic order even at finite temperatures [18]. Park et al. [19] have successfully increased the MAE of Fe_3GeTe_2 by 30% through hole doping. Gweon et al. [20] has observed an interesting thickness dependence of exchange bias in oxidized Fe_3GeTe_2 system owing to weak interlayer magnetic coupling which was not reported for traditional thin film systems. Weak interlayer coupling of any vdW compound plays an important role in its application and in tuning various properties like reducing the size of the device, different stacking configurations of adjacent layers and mechanical flexibility of the material. It is also possible to modulate the properties of 2D vdW magnets by targeting these materials with light source. Femtosecond laser pulse has been used for optical doping in Fe_3GeTe_2 which results in room temperature (300 K) T_c, drastic change in MAE and tuning magnetization [18]. Similarly, focused ion beam has been used to change the domain phase of Fe_3GeTe_2 microstructures from out-of-plane to in-plane through a process known as patterning [21]. Calculations show that $CrGeTe_2$ ($T_c = 106$ K) [22] is the only member of $CrXTe_2$ and TMPX3 (TM = transition metal, X = chalcogens) families with ferromagnetic order in its unstrained monolayer. However, its perpendicular magnetic anisotropy (PMA) energy is two orders of magnitude smaller than Fe_3GeTe_2 [23]. Later, $Cr_2Ge_2Te_6$ was observed to have long-range FM ordering in monolayer [22].

A rather small T_c of bi- and trilayer $Cr_2Ge_2Te_6$ is increased to ~41 K through application of a very small field of 0.075 T by opening the spin-wave excitation gap [24]. CrX_3 family with X = Cl, Br, and I has Curie temperature of 66, 86 and 107 K, respectively which is further increased by hole doping [25]. Most studies are focused on CrI_3 because of highest magnetization in the family. CrI_3 is particularly interesting due to its layer-dependent magnetic ordering. More recent studies have shown very high T_c 2D magnetic materials like VSe_2 (300 K) [26], Co_2S_2 (404 K) [27], and Co_2Se_3 (600 K) [28]. From which VSe_2 has been found to be nonmagnetic from new experimental results.

In summary, 2D vdW ferromagnets and in particular, Fe_3GeTe_2 system shows remarkable magneto-electric and spintronic properties with relatively high T_c and MAE. More studies have confirmed the suitability of Fe_3GeTe_2 for hydrogen evolution reaction [29] and oxygen evolution reaction [30] spanning the field of possible application for such 2D systems. Despite the fact that Fe_3GeTe_2, $Cr_2Ge_2Te_6$, and CrI_3 have proven to be good start in research of the ideal room temperature 2D vdW ferromagnet, further search for such novel materials is hindered. Only other material in Fe_3GeTe_2 family which has been reported is Ni_3GeTe_2 showing temperature independent paramagnetism [3, 31]. Even though MBE has proved to be good synthesis method for producing high T_c materials, the fall back of the method is that it is very expensive. Conventionally, Fe_3GeTe_2 crystals have been grown using direct vapor transport or chemical vapor transport which are much simpler and inexpensive methods.

Hence, due to lack of exploration and expensive synthesis method for high T_c, we continue our search for novel 2D vdW ferromagnetic materials from Fe_3GeTe_2 family. In this paper, we explore a novel Fe_3SiTe_2 for preliminary magnetic properties using density functional theory. In order to understand the factors that play role in determining the origin of magnetism in such materials, we have substituted magnetic atom Fe with Mn, and in different case, we replaced Si with Sn and calculated structural, electronic, and magnetic properties of Fe_3SiTe_2, Fe_3SnTe_2, and Mn_3SiTe_2 materials and hereafter presented as Tm_3XTe_2 where Tm: transition metals Fe, Mn; X: Si, Sn.

2 Methodology

We have utilized DFT implemented in QUANTUM ESPRESSO code [32] which uses pseudopotential method to solve Kohn–Sham equations [33, 34]. Kinetic energy cutoff for the plane wave basis set was set to be 816 eV, while cutoff for charge density was set to be 8160 eV. Monkhorst–Pack mesh of $8 \times 8 \times 6$ was used for unit cells of Fe_3SiTe_2, Fe_3SnTe_2, and Mn_3SiTe_2. All the considered structures were geometrically optimized till the Hellmann–Feynman forces acting on each atom were smaller than 1 meV/Å^{-1}. Following states have been treated as valence states in pseudopotential calculation: Fe: $4s^1\ 3d^7$, Mn: $3s^2\ 3p^6\ 4s^2\ 3d^5$, Si: $3s^2\ 3p^2$, Sn: $5s^2\ 5p^2\ 4d^{10}$, and Te: $5s^2\ 5d^1\ 5p^3$. The exchange–correlation functional is solved within the constraints of

PBE-GGA functional [35]. We have also included vdW interaction in our calculations in the form of Grimme-D2 correction [36] which considers the following form for pairwise interaction: $-C_6/r^6$, where r is the distance between two atoms forming the pair and C_6 is a constant.

3 Results and Discussion

The side view of the studied bulk structures Tm_3XTe_2 is shown in Fig. 1a and b. Tm_3XTe_2 forms a hexagonal structure with space symmetry group P63/mmc (#194) [30] and the inversion symmetry point lies at the space between the layers. There are two Tm atoms located at different inequivalent Wyckoff sites. There are two formula units of Tm_3XTe_2 in one unit cell situated one above other with AB stacking, where first layer is rotated by 180° about the out-of-plane axis with respect to the other. Here, single layer of Tm_3XTe_2 is made of five sublayers. Two Te atoms form top most and bottom most layers, four Tm(1) atoms make second and other four similar Tm(1) atoms make the fourth layer of the structure. The middle layer (i.e., third layer) contains Tm(2) atom and a X atom. Inequivalent Tm atoms and X atoms form Tm_3X substructure which contains a hexagonal network built from Tm(2)-X as shown in Fig. 1b. This Tm_3X layer is sandwiched between two Te layers. Valency of different atoms in Tm_3XTe_2 are $Tm^{3+}(1)$, $Tm^{2+}(2)$, X^{4-} and Te^{2-} where each Te atom is bound to three Tm(1) and one Tm(2) atoms. A triagonal pyramid is formed by one Te and three Tm(1) atoms. There exists a vdW interaction between two successive Te layers.

The calculated lattice parameters ($a = b$ and c), c/a ratio, interlayer distance, and formation energy is shown in Table 1. There are no reports of Fe_3SiTe_2, Fe_3SnTe_2,

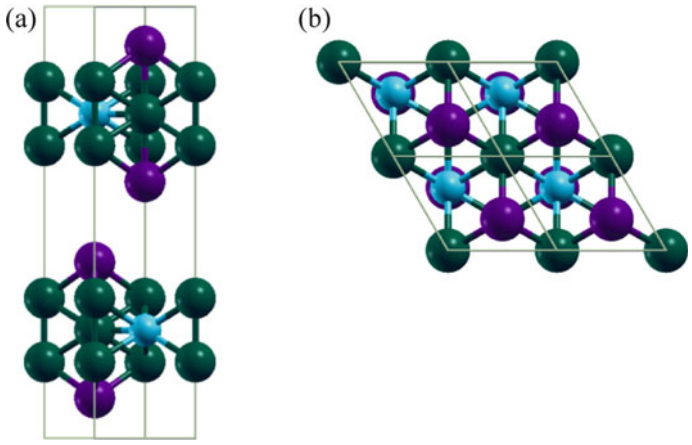

Fig. 1 Crystal structure of Tm_3XTe_2 **(a)** side view, **(b)** top view. Green: Fe/Mn atoms, Purple: Te atoms, Blue: Si/Sn atoms

Table 1 Optimized lattice parameters ($a = b$ and c), c/a ratio, interlayer distance, and formation energy of Fe_3SiTe_2, Fe_3SnTe_2, and Mn_3SiTe_2 with and without vdW correction

Compound	Lattice parameters (Å)	c/a	Interlayer distance (Å)	E_{form} (eV/f.u.)
Fe_3SiTe_2	$a = 3.87$, $c = 17.04$	4.39	4.03	−2.72
Fe_3SiTe_2–vdW	$a = 3.83$, $c = 16.48$	4.29	3.79	−4.72
Fe_3SnTe_2	$a = 4.16$, $c = 16.68$	4.00	4.08	−1.58
Fe_3SnTe_2–vdW	$a = 4.11$, $c = 16.05$	3.90	3.79	−3.68
Mn_3SiTe_2	$a = 3.91$, $c = 17.34$	4.43	4.26	−4.42
Mn_3SiTe_2–vdW	$a = 3.87$, $c = 16.67$	4.30	3.82	−6.38

and Mn_3SiTe_2 compounds as per our best knowledge; hence, we don't have any data to compare our lattice parameters with; however, all the calculated lattice parameters show similar range of values with those reported for Fe_3GeTe_2 and Ni_3GeTe_2 [2, 11, 31]. We found that after the inclusion of vdW interaction in our calculations, both lattice parameters '*a*' and '*c*' decrease, but decrease in '*c*' is more prominent than '*a*,' resulting in smaller *c*/*a* ratios for Tm_3XTe_2-vdW compounds. Interlayer distance is defined as the distance between top Te atom of one layer of Tm_3XTe_2 and bottom Te atom of the other layer. It is found that this interlayer distance also systematically decreases upon inclusion of vdW interaction acting between two successive Te layers for all the compounds under study. It is clear that the structure of unit cell in terms of *c*/*a* ratio is more sensitive to the change of Si atom; similarly, interlayer spacing shows a small change upon replacing Si but results in significant change when Fe was replaced by Mn.

Formation energy (E_{form}) represents the energy that will be either absorbed or released during synthesis. Negative value of formation energy validates the stability of the compound. The formula of formation energy is given as below, where E_{form} is formation energy of compound Tm_3XTe_2, $E_{Tm_3XTe_2}$ is half of the total energy of Tm_3XTe_2 compound (as unit cell comprises of two formula unit), $E_{Tm/X/Te}$ is energy per atom of Tm/X/Te. Our calculated value of E_{form} for all the compounds are negative showing the possibility of experimental synthesis of the compounds. Stronger binding between the adjacent Te layers and reduction of *c*/*a* ratio due to vdW correction results in decrease of formation energy. This decrease in formation energy has been observed to be almost ~2.0 eV in all the compounds we have studied. We observe that Mn_3SiTe_2 is the most stable compounds among all with E_{form} value of −6.38 eV/f.u.

$$E_{form}(Tm_3XTe_2) = E_{Tm_3XTe_2} - 3(E_{Tm}) - E_X - 2(E_{Te}) \quad (1)$$

To investigate the electronic and magnetic properties, we have calculated the spin polarized total density of states (TDOS) for Fe_3SiTe_2, Fe_3SnTe_2, and Mn_3SiTe_2 with and without vdW and presented in Fig. 2a–c. From TDOS, it is clear that all three compounds are metallic in nature, but asymmetricity of TDOS in spin-up and spin-down channel shows magnetic nature of the studied compounds. Inclusion

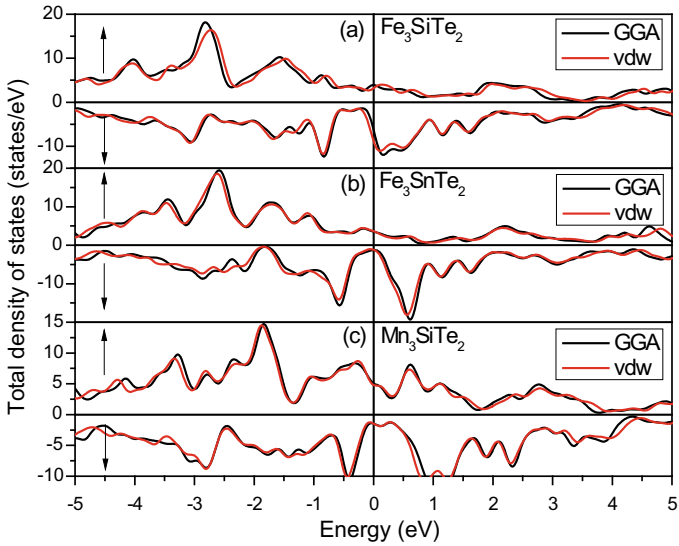

Fig. 2 Total density of states of **(a)** Fe_3SiTe_2 without vdW, **(b)** Fe_3SiTe_2 with vdW, **(c)** Fe_3SnTe_2 without vdW, **(b)** Fe_3SnTe_2 with vdW, **(a)** Mn_3SiTe_2 without vdW, **(b)** Mn_3SiTe_2 with vdW

of vdW interaction does not seem to affect TDOS too much. Visible changes are observed within energy range of −2 to −5 eV for all the compounds. Spin polarization (SP) is calculated using Eq. 2, where $n^{\uparrow}(E_f)$ and $n^{\downarrow}(E_f)$ are DOS at Fermi level (E_F) in spin-up and spin-down channels, respectively. SP represents the population difference between spin-up and spin-down channels and is an important deciding parameter for applicability of a material in spin injection devices. Even though TDOS of Fe_3SiTe_2 does not show much change due to vdW interaction, but due to the change in DOS around E_F, SP changes from −22.56 to −46.86% with inclusion of vdW. Values of SP of all the compounds are also mentioned in Table 2. We note that only Fe_3SiTe_2 shows negative value of SP. Fe_3SnTe_2 and Mn_3SiTe_2 show very small

Table 2 Spin magnetic moments, atomic magnetic moments of Fe and Mn atoms, and spin polarization factor with and without van der Waals correction

Compound	Spin magnetic moment (μB/f.u.)	Spin magnetic moment (μB/atom)		Spin polarization factor SP (%)
		Fe/Mn(1)	Fe/Mn(2)	
Fe_3SiTe_2	5.97	2.24	1.47	−22.56
Fe_3SiTe_2–vdW	5.57	2.08	1.42	−46.86
Fe_3SnTe_2	6.53	2.54	1.53	47.88
Fe_3SnTe_2–vdW	6.51	2.49	1.55	51.33
Mn_3SiTe_2	4.03	2.07	−0.09	55.63
Mn_3SiTe_2–vdW	4.01	1.98	0.04	53.64

changes in their SP value before and after the inclusion of vdW interaction.

$$\mathrm{SP} = \frac{n^{\uparrow}(E_f) - n^{\downarrow}(E_f)}{n^{\uparrow}(E_f) + n^{\downarrow}(E_f)} \tag{2}$$

In Fig. 3a–c, we have presented the spin polarized partial density of states (PDOS) for Fe_3SiTe_2, Fe_3SnTe_2, and Mn_3SiTe_2 with vdW correction. Origin of magnetic

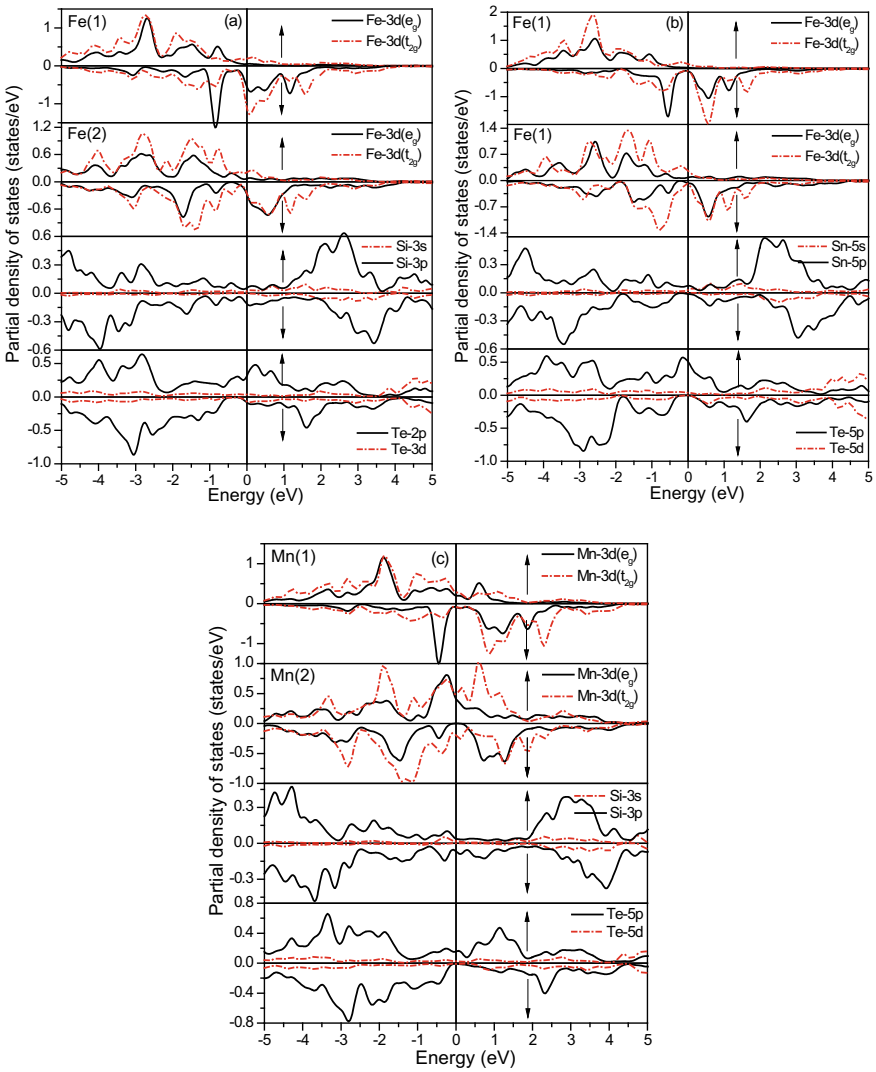

Fig. 3 Spin-dependent partial density of states of **(a)** Fe_3SiTe_2, **(b)** Fe_3SnTe_2, and **(c)** Mn_3SiTe_2

moment in transition metals is explained by exchange splitting of 3d orbitals due to crystal field. PDOS of all three compounds reveal that there is a large exchange splitting of 3d states in 3d-e_g and 3d-t_{2g} states of Tm atoms which gives rise to large spin magnetic moments associated with Fe and Mn atoms. Even though Tm(1) and Tm(2) are same elements, smaller exchange splitting for Tm(2) relative to Tm(1) results in observed different values of spin magnetic moment for these two atoms. This difference in two atoms of the same species is due to different crystal fields in which they exist.

In case of Fe_3SiTe_2, 3d-e_g, and 3d-t_{2g} states of both Fe(1) and Fe(2) atoms do not play any role in spin-up conduction region while in case of spin-down, high DOS are present around the E_F and in lower conduction region. This shows the high magnetic moment at Fe(1) and Fe(2) atoms. In case of Fe_3SnTe_2, the spin-down states of 3d-e_g and 3d-t_{2g} shifts toward higher energy as compared to Fe_3SiTe_2, and reverse the direction of SP. This may be due to the Fe-3d and Sn-5p orbital interaction.

Overall, Tm-3d states have DOS around E_F while 3p (5p) states of Si (Sn) and 5p states of Te atoms have DOS which is in general farther away from E_F. PDOS shown in Fig. 3a, c show that Si-3p states and Sn-5p states are similar for both compounds and gives similar character to the PDOS of Fe_3SiTe_2 and Fe_3SnTe_2, except the intensities at E_F which gives the change in SP.

As the Te atom does not show any magnetic moment (Table 2), but shows major contribution in deciding SP. The contribution of Te atom 5d electrons are very low while Te-5p states show very high spin polarization ratio, particularly in Fe_3SnTe_2 and Mn_3SiTe_2 the Te-5p states show 100% SP. Absence of Te-5p and 5d states in a small region of spin-down channel is also observed in Fe_3SiTe_2, but position of E_F at slightly higher energy level does not produce 100% spin polarization for these states.

In PDOS, for Fe_3SnTe_2 and Mn_3SiTe_2, we see that all the states have smaller contribution of spin-down state compared to spin-up state resulting in a positive spin polarization factor, while in Fe_3SiTe_2 spin-down channel has smaller contribution from all the states except Fe-3d, but higher intensity of Fe-3d states gives rise to the negative spin polarization factor. From the PDOS analysis, we conclude that Tm_3SnTe_3 can be made half-metallic upon suitable choice of Tm since Sn and Te already show very insignificant DOS contribution in spin-down channel.

Tm atoms contribute the most in total magnetic moment in all cases. Fe(1) and Fe(2) both show highest magnetic moment values of 2.49 and 1.55 μ_B/atom, respectively, in Fe_3SnTe_2, leads to ferromagnetic interaction between these two kinds of atoms. One of the contributing reason for larger magnetic moment of Tm(1) atom relative to Tm(2) atom is explained in the discussion of PDOS, the other reason is their different valencies. Previous studies for Fe_3GeTe_2 have also observed similar results [28, 36]. May et al. [2] have reported the ratio of magnetic moments between Fe(1) and Fe(2) atoms in $Fe_{2.9}GeTe_2$ to be 1.25 at 1.5 K. Our non-vdW calculations show the ratios to be 1.52 and 1.69 for Fe_3SiTe_2 and Fe_3SnTe_2 which decreased to 1.46 and 1.61 after inclusion of vdW correction. Spin magnetic moment residing on Si, Sn, and Te atoms is insignificantly small and negative showing antiferromagnetic nature of interaction between Si/Sn, Te, and with Tm atom. Total spin magnetic moments

of Fe_3SiTe_2, Fe_3SnTe_2, and Mn_3SiTe_2 without vdW correction are 5.97 μ_B/f.u., 6.53 μ_B/f.u. and 4.03 μ_B/f.u., respectively. Total spin magnetic moment of only Fe_3SiTe_2 is affected significantly due to vdW correction. Upon including vdW corrections in our spin polarized calculations, we observed that atomic magnetic moment per atom for Tm(1) atom reduces resulting in a drop of total magnetic moment of all the compounds since Tm(1) contribute the most in total magnetic moment. Spin magnetic moment residing on Mn(2) atom is much smaller and negative in value for Mn_3SiTe_2 when vdW is not included; however, upon incorporation of van der Waals interaction the magnetic moment residing on Mn(2) atom becomes positive but still has much smaller value compared to that of Fe(2) in Fe_3SiTe_2, Fe_3SnTe_2. SP factor representing the purity of spin current is also shown in Table 2 for vdW and without vdW cases. Our spin polarized calculations reveal that negative spin polarization factor of Fe_3SiTe_2 changes to positive when Fe and Si atoms are replaced one at a time by Mn and Sn as shown in Table 2. As discussed above, spin polarization factor is mostly unaffected by vdW correction except Fe_3SiTe_2.

4 Conclusions

Our calculations suggest that Fe_3SiTe_2, Fe_3SnTe_2, and Mn_3SiTe_2 have negative formation energies proving that they are stable and possibility of their experimental synthesis are feasible. Interlayer distance and c/a ratio are more sensitive to the replacement of Tm and X atoms, respectively. vdW interaction causes the shrinkage of unit cell, c/a ratio, and decrease of Te–Te interlayer spacing for all the systems that we have considered. All the structural parameters (a, c, c/a, interlayer distance, and formation energy) follow same trend for the three compounds under study with or without vdW correction. However, no effect of vdW interaction is observed on magnetic moments and spin polarization factor of Fe_3SnTe_2 and Mn_3SiTe_2 but shows 6.70% and 107.71% of change in total magnetic moment and spin polarization for Fe_3SiTe_2. Compounds Fe_3SiTe_2, Fe_3SnTe_2, and Mn_3SiTe_2 show that the major contribution in total magnetic moment is due to the Tm(1) site. Fe_3SiTe_2, Fe_3SnTe_2 compounds show higher values of magnetic moments per Fe atoms than Fe_3GeTe_2. We have observed very small magnetic moment on Mn(2) site in Mn_3SiTe_2 origin of which needs to be further explored. From partial density of states of Fe_3SnTe_2, we conclude that Fe_3SnTe_2 has Fermi level lying within a the forbidden region in spin-down channel of Sn and Te, therefore replacing Fe with suitable element is a key to designing a new half-ferromagnetic material.

Acknowledgements The authors show their sincere gratitude to the University grant commission, India for their UGC Start-up Research grant. AD is also thankful to University Grants Commission, India for Assistant Professorship under Faculty Recharge Programme.

References

1. Alghamdi M, Lohmann M, Li J, Jothi PR, Shao Q, Aldosary M, Su T, Fokwa BP, Shi J (2019) Highly efficient spin–orbit torque and switching of layered ferromagnet Fe_3GeTe_2. Nano Lett 19(7):4400–4405
2. May AF, Calder S, Cantoni C, Cao H, McGuire MA (2016) Magnetic structure and phase stability of the van der Waals bonded ferromagnet $Fe_{3-x}GeTe_2$. Phy Rev B 93(1):014411
3. Chowdhury RR, DuttaGupta S, Patra C, Tretiakov OA, Sharma S, Fukami S, Ohno H, Singh RP (2021) Unconventional hall effect and its variation with Co-doping in van der Waals Fe_3GeTe_2. Sci Rep 11(1):1–10
4. Deng Y, Yu Y, Song Y, Zhang J, Wang NZ, Sun Z, Yi Y, Wu YZ, Wu S, Zhu J, Wang J (2018) Gate-tunable room-temperature ferromagnetism in two-dimensional Fe_3GeTe_2. Nature 563(7729):94–99
5. Du J, Xia C, Xiong W, Wang T, Jia Y, Li J (2017) Two-dimensional transition-metal dichalcogenides-based ferromagnetic van der Waals heterostructures. Nanoscale 9(44):17585–17592
6. He J, Li X, Lyu P, Nachtigall P (2017) Near-room-temperature Chern insulator and Dirac spin-gapless semiconductor: nickel chloride monolayer. Nanoscale 9(6):2246–2252
7. Si C, Zhou J, Sun Z (2015) Half-metallic ferromagnetism and surface functionalization-induced metal–insulator transition in graphene-like two-dimensional Cr_2C crystals. ACS Appl Mater Interfaces 7(31):17510–17515
8. Zhu Y, Kong X, Rhone TD, Guo H (2018) Systematic search for two-dimensional ferromagnetic materials. Phys Rev Mater 2(8):081001
9. Bonilla M, Kolekar S, Ma Y, Diaz HC, Kalappattil V, Das R, Eggers T, Gutierrez HR, Phan MH, Batzill M (2018) Strong room-temperature ferromagnetism in VSe_2 monolayers on van der Waals substrates. Nat Nanotechnol 13(4):289–293
10. O'Hara DJ, Zhu T, Trout AH, Ahmed AS, Luo YK, Lee CH, Brenner MR, Rajan S, Gupta JA, McComb DW, Kawakami RK (2018) Room temperature intrinsic ferromagnetism in epitaxial manganese selenide films in the monolayer limit. Nano Lett 18(5):3125–3131
11. Li X, Lu JT, Zhang J, You L, Su Y, Tsymbal EY (2019) Spin-dependent transport in van der Waals magnetic tunnel junctions with Fe_3GeTe_2 electrodes. Nano Lett 19(8):5133–5139
12. Escolar J, Peimyoo N, Craciun MF, Fernandez HA, Russo S, Barnes MD, Withers F (2019) Anisotropic magnetoconductance and Coulomb blockade in defect engineered $Cr_2Ge_2Te_6$ van der Waals heterostructures. Phy Rev B 100(5):054420
13. Meijer MJ, Lucassen J, Duine RA, Swagten HJ, Koopmans B, Lavrijsen R, Guimarães MH (2020) Chiral spin spirals at the surface of the van der waals ferromagnet Fe_3GeTe_2. Nano Lett 20(12):8563–8568
14. Park TE, Peng L, Liang J, Hallal A, Zhang X, Kim SJ, Song KM, Kim K, Weigand M, Schütz G, Finizio S (2019) Observation of magnetic skyrmion crystals in a van der Waals ferromagnet Fe_3GeTe_2. arXiv preprint: 1907.01425
15. Yang M, Li Q, Chopdekar RV, Dhall R, Turner J, Carlström JD, Ophus C, Klewe C, Shafer P, N'Diaye AT, Choi JW (2020) Creation of skyrmions in van der Waals ferromagnet Fe_3GeTe_2 on (Co/Pd)n superlattice. Sci Adv 6(36):5157
16. Wu Y, Zhang S, Zhang J, Wang W, Zhu YL, Hu J, Yin G, Wong K, Fang C, Wan C, Han X (2020) Néel-type skyrmion in WTe_2/Fe_3GeTe_2 van der Waals heterostructure. Nat Commun 11(1):1–6
17. Wang X, Tang J, Xia X, He C, Zhang J, Liu Y, Wan C, Fang C, Guo C, Yang W, Guang Y (2019) Current-driven magnetization switching in a van der Waals ferromagnet Fe_3GeTe_2. Sci Adv 5(8):8904
18. Liu B, Liu S, Yang L, Chen Z, Zhang E, Li Z, Wu J, Ruan X, Xiu F, Liu W, He L (2020) Light-tunable ferromagnetism in atomically thin Fe_3GeTe_2 driven by femtosecond laser pulse. Phys Rev Lett 125(26):267205

19. Park SY, Kim DS, Liu Y, Hwang J, Kim Y, Kim W, Kim JY, Petrovic C, Hwang C, Mo SK, Kim HJ (2019) Controlling the magnetic anisotropy of the van der Waals ferromagnet Fe_3GeTe_2 through hole doping. Nano Lett 20(1):95–100
20. Gweon HK, Lee SY, Kwon HY, Jeong J, Chang HJ, Kim KW, Qiu ZQ, Ryu H, Jang C, Choi JW (2021) Exchange bias in weakly interlayer-coupled van der Waals magnet Fe_3GeTe_2. Nano Lett 21(4):1672–1678
21. Li Q, Yang M, Gong C, Chopdekar RV, N'Diaye AT, Turner J, Chen G, Scholl A, Shafer P, Arenholz E, Schmid AK (2018) Patterning-induced ferromagnetism of Fe_3GeTe_2 van der Waals materials beyond room temperature. Nano Lett 18(9):5974–5980
22. Sivadas N, Daniels MW, Swendsen RH, Okamoto S, Xiao D (2015) Magnetic ground state of semiconducting transition-metal trichalcogenide monolayers. Phy Rev B 91(23):235425
23. Zhang W, Wong PKJ, Zhu R, Wee AT (2019) Van der Waals magnets: wonder building blocks for two-dimensional spintronics? InfoMat 1(4):479–495
24. Gong C, Li L, Li Z, Ji H, Stern A, Xia Y, Cao T, Bao W, Wang C, Wang Y, Qiu ZQ (2017) Discovery of intrinsic ferromagnetism in two-dimensional van der Waals crystals. Nature 546(7657):265–269
25. Liu J, Sun Q, Kawazoe Y, Jena P (2016) Exfoliating biocompatible ferromagnetic Cr-trihalide monolayers. Phys Chem Chem Phys 18(13):8777–8784
26. Coelho PM, Nguyen Cong K, Bonilla M, Kolekar S, Phan MH, Avila J, Asensio MC, Oleynik II, Batzill M (2019) Charge density wave state suppresses ferromagnetic ordering in VSe_2 monolayers. J Phys Chem C 123(22):14089–14096
27. Zhang Y, Pang J, Zhang M, Gu X, Huang L (2017) Two-dimensional Co_2S_2 monolayer with robust ferromagnetism. Sci Rep 7(1):1–8
28. Lv P, Tang G, Yang C, Deng J, Liu Y, Wang X, Wang X, Hong J (2018) Half-metallicity in two-dimensional Co_2Se_3 monolayer with superior mechanical flexibility. *2D* mater *5*(4):045026
29. Rezaie AA, Lee E, Luong D, Yapo JA, Fokwa BP (2021) Abundant active sites on the basal plane and edges of layered van der Waals Fe_3GeTe_2 for highly efficient hydrogen evolution. ACS Mater Lett 3(4):313–319
30. Zhao Y, Gu J, Chen Z (2019) Oxygen evolution reaction on 2D ferromagnetic Fe_3GeTe_2: boosting the reactivity by the self-reduction of surface hydroxyl. Adv Funct Mater 29(44):1904782
31. Deiseroth HJ, Aleksandrov K, Reiner C, Kienle L, Kremer RK (2006) Fe_3GeTe_2 and Ni_3GeTe_2–two new layered transition-metal compounds: crystal structures, HRTEM investigations, and magnetic and electrical properties. Eur J Inorg Chem 8:1561–1567
32. Giannozzi P, Baroni S, Bonini N, Calandra M, Car R, Cavazzoni C et al (2009) QUANTUM ESPRESSO: a modular and open-source software project for quantum simulations of materials. J Phys Cond Mat 21(39):395502
33. Hohenberg P, Kohn W (1964) Inhomogeneous electron gas. Phys Rev 136:B864
34. Kohn W, Sham LJ (1965) Self-consistent equations including exchange and correlation effects. Phys Rev 140:A1133
35. Perdew JP, Burke K, Ernzerhof M (1996) Generalized gradient approximation made simple. Phys Rev Lett 77:3865
36. Grimme S (2006) Semiempirical GGA-type density functional constructed with a long-range dispersion correction. J Comput Chem 27(15):1787–1799

Design and Implementation of the Electric Bicycle with Efficient Controller

Sandeep Gupta, Saurav Poonia, Tarun Varshney, Raju Kumar Swami, and Ashish Shrivastava

Abstract The paper's main goal is to design a practical yet highly customizable electric bicycle. As the number of automobiles on the road worldwide rises at an alarming rate each year, the world's reliance on oil-based fuel has become almost unrestrained. Increased usage of nonrenewable fossil fuels causes environmental issues such as the "greenhouse effect," health issues for city dwellers, and concerns about fuel supply stability. To wean ourselves off of our reliance on oil, a large amount of money is being invested in the creation of electric vehicles (EVs) that could be mass-produced. This paper examines the design of electric bicycles. The goal of this research is to figure out how to make a basic, low-cost electronic bicycle with two-way driving control. Electric cycles are the finest development in our ever congested world to provide an easy solution to daily commute woes. They are not only save a lot of fuel and keep the environment clean but also help you develop good health with little pedal exercise during your commute.

Keywords BLDC hub motor · Controller · Battery · Charger · Accelerator

S. Gupta (✉) · S. Poonia
Department of Electrical Engineering, JECRC University, Jaipur, India
e-mail: jecsandeep@gmail.com

T. Varshney
Department of Electrical Electronics and Communication Engineering, SET, SHARDA UNIVERSITY, Greater Noida, India
e-mail: tarun.varshney@sharda.ac.in

R. K. Swami
EE Department, Pacific University, Udaipur, India

A. Shrivastava
Electrical Department, Manipal University Jaipur, Jaipur, India
e-mail: ashish.shrivastava@jaipur.manipal.edu

© The Author(s), under exclusive license to Springer Nature Singapore Pte Ltd. 2022

A. Tripathi et al. (eds.), *Intelligent Computing Techniques for Smart Energy Systems*, Lecture Notes in Electrical Engineering 862,
https://doi.org/10.1007/978-981-19-0252-9_49

1 Introduction

A car that runs on electricity rather than using a conventional internal-combustion engine is referred to as an electric vehicle (EV). Even when the electricity used to power your EV comes from renewable energy sources like wind, solar, hydro, and nuclear power, your vehicle is still capable of significant reductions in gaseous emissions. The e-bicycle has mainly five parts: the hub motor, controller, convertor, accelerator, and battery [1]. The main function of the controller is to control the function of the hub motor. The motor controller is a microcontroller-based system that uses feedback to control a three-phase BLDC motor [2].

A three-phase motor consists of a permanent rotor and a stator split into three phases. Three-phase motors are used because they are efficient, durable, and deliver constant power throughout each cycle. The drawback is a larger, more complicated controller. With a DC motor, only, two field-effect transistors (FETs) are needed to drive the motor and provide regeneration [3, 4]. The three-phase switcher block will be three FET half-bridges, one bridge for each phase of the motor. Each half-bridge corresponds to a stator winding and allows current to flow into and out of the motor. The gate drive block will be the circuit that takes a TTL level pulse with a modulated waveform for driving the FETs. The power supply block is a switching regulator that converts the 48-V battery to 12 V. The 12-V line will be created using a buck switching regulator and will be used to power the microcontroller and the signal conditioning circuitry.

The current challenges with e-bicycles include the battery's short service life and frequent replacement, the battery's long storage and charging time, the battery's limited charging and discharging times, and inadequate contact, among others. As a result, the battery is the most important component determining e-bicycle performance and quality, as well as the most significant stumbling block to e-bicycle development. Many countries with advanced science and technology have been investing in the research and development of new electric bicycle batteries, such as high-power nickel cadmium, zinc nickel, nickel hydrogen, lithium polymer, and fuel cells, in recent years. In Japan, Europe, and America, nickel–hydrogen batteries are commonly utilized, as are lithium-ion/lithium-polymer batteries [4–6]. Many Chinese research institutes are also working on new e-bicycle batteries, but traditional lead–acid batteries are still used in around 95 percent of e-bicycles. However, due to the lead–acid batteries' limited life, they will need to be replaced in roughly a year [7]. Furthermore, when the electric bicycle is starting, speeding up, facing headwind, or loading, the battery must provide dozens of amperes of current to drive the motor in a short period of time, which is difficult to achieve with a lead–acid battery. And such a large current will cause damage to the battery, reducing battery life, and mileage significantly. The bicycle paddle and the battery are coupled to drive the electric bicycle in this article, and the dual power supply connection is created suitably. The control strategy is created based on the characteristics of the

electric bicycle motor drive. The control approach may effectively increase the electric bicycle's performance, lengthen the battery's service life, and has a promising commercial future.

Electric bicycles are becoming an increasingly appealing choice for commuters who live reasonably near to work or who are seeking a less expensive alternative to powered alternatives. With advancements in battery and motor technology, the speed and range of e-bicycles have increased proportionately. A number of components can be used in an e-bicycle, depending on the intended cost and complexity of the design. A battery and cycle paddle are used to provide a dual power supply system for the electric bicycle in this research paper. The double-source connection mode is designed with a controller. For consistent power, the best working state prevents the battery from being impacted and extends the battery life.

2 E-Bicycle Component Details with Basic Concept

If you own bicycle lights driven by a dynamo, you already own an electric bicycle! Consider this: By pumping your legs up and down on the pedals, you create rotation in the wheels. A small dynamo (generator) positioned on the rear tire generates a very small amount of electricity that illuminates the back safety lamp in the dark. Now imagine, you could reverse this process. What if you replaced the bulb with a huge battery? The battery generated a constant electric current, which drove the dynamo in reverse, spinning it around like an electric motor. As the dynamo/motor turned, it rotated the tire and propelled the bicycle forward without the assistance of your pedaling, as shown in Fig. 1 [8, 9].

The main components which are used for designing the "electric bicycle" are given below with their ratings as shown in Fig. 2:

1. Hub Motor, 2. Controller, 3. Battery, 4. Accelerators, 5. Charger

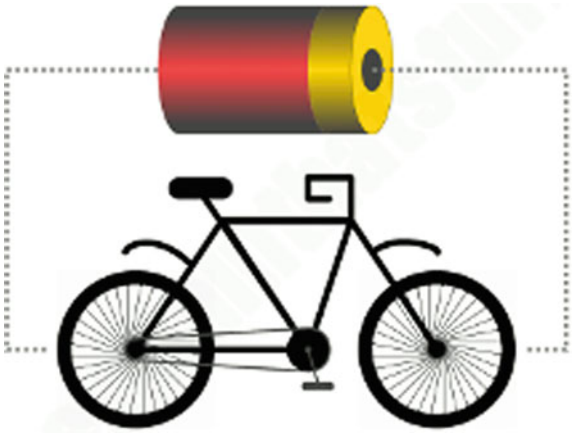

Fig. 1 Basic concept of the electric bicycle

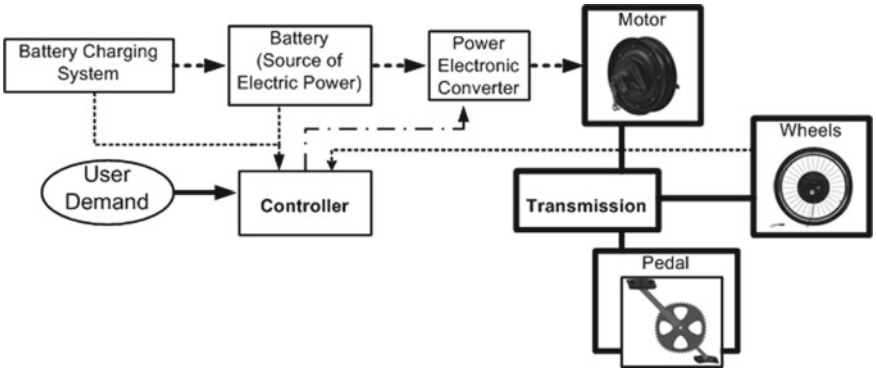

Fig. 2 Block diagram of e-bicycle

3 Hub Motor for the E-Bicycle

The motor of the e-Bicycle is a permanent magnet DC type with a nominal power of 800 W as shown in Fig. 3. The motor constants had to be determined by measurements because there was no data sheet available. Measurements have been made with a blocked motor at constant speed with variable load. An idle curve has been recorded, and a rundown test has been conducted. Hub motor parameters are such as:- Rated Power: 350 W/800 W, Size: 16 inch, Rated Current: 7 A, Rated Voltage: 48 V/60 V, Material: Aluminum alloy, Coil Material: Copper wire, The Power Properties: DC, Structure and Installation Method: 1 MB.

The features of the 800 brushless e-bicycle DC hub motor are high torque, light weight, high efficiency, low noise, long working life, and high efficiency ($\geq$78%) as shown in Table 1.

Fig. 3 Schematic diagram of hub motor

Table 1 Technical parameters of brushless e-bicycle DC hub motor [8]

Voltage	Current	Power	Speed	Size	Brake style
48 V/60 V	1.0 A	350 W/800 W	420 ± 10 rpm/460 ± 10 rpm	16 inch	Disk drum

3.1 Guidelines for the Hub Motor Installation:

If you don't have a bicycle stand, you may securely install your rear wheel by using the handlebars and seat of your bicycle to support it in the position shown. Follow these instructions to maintain the protection of your bicycle:

Step 1. Take off the original front wheel.
Step 2. Position the hub motor such that the disk brake is on the left side of the bicycle and the electric wires are on the right while facing forward.
Step 2. The disk rotor can be removed from the hub if the bicycle does not have disk brakes. By removing the disk, the internal workings of the hub may be seen through the bolt holes. Bolts and tiny washers must be used to fill the holes.
Step 4. If the axle cannot be slipped into the groove in your fork without difficulty, a tiny bit of filing may be required.
Step 5. The hub motor axles should be ground flat on two edges to 10 mm, and your bicycle dropout holes should be 10 mm wide as well, allowing the motor to slip into position.
Step 6. If your axle does not fit into the dropouts, you will need to use a file to a) expand the dropout slot and/or b) file down the axle flats so that the axle fits snuggly into the dropouts.
Step 7. "Note: Only expand enough for a snug fit when filing is necessary."
Step 8. After verifying that the axle is seated deeply and snuggly in the dropout slots, attach the axle to the fork with the washers, lock washer, and axle nuts.
Step 9. The axle nuts must then be tightened since the motor's torque is transmitted to the bicycle frame via the axle flats and axle nut.
Step 10. Double-check that the nut on your axle is securely fastened and that all parts are flat against the fork.

4 Controller and Battery Installation

The electric bicycle controller is one of the most important components of an electric bicycle; it controls the motor's speed, start, and stop. It is wired to all the other electrical components, including the battery, motor, throttle (accelerator), display (speedometer), PAS, and any other speed sensors that may be present. Principal chips (microcontrollers) and secondary components (resistors, sensors, MOSFET, etc.) make up a controller. The PWM generating network, AD device, power circuit,

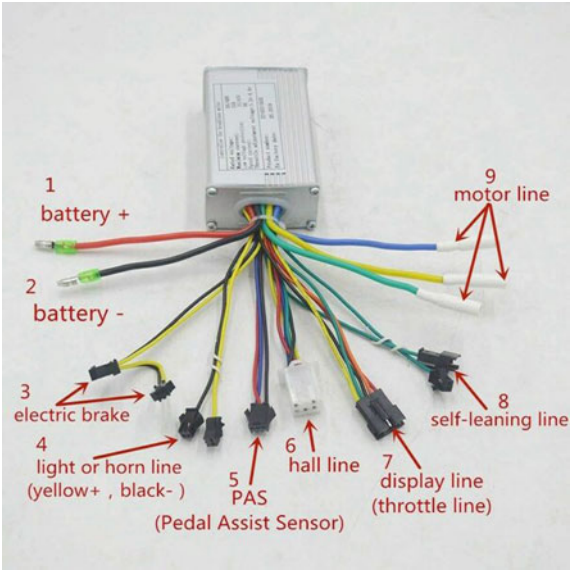

Fig. 4 Different wires and connection of the controller

power device driver circuit, signal acquisition and processing circuit, over-current and under-voltage protection circuit, and signal acquisition and processing circuit are all found inside the controller.

The controller for a 350-W, 48-V brushless DC (BLDC) motor used to power an electric bicycle microcontroller unit (MCU) and accompanying circuitry to execute driving control, regenerative braking, and fault protection is described in this application note. The source code for this application note may be found in the Application Sample Libraries section under Z8 Encore! MC Applications Code Library.

The controller delivers the working voltage to the external device through the power circuit after attaching the battery, such as the switch +5 V, the headlamp + 5 V, and so on, as shown in Fig. 4. Based on the input from the throttle or PAS, the PWM generates a matching pulse waveform for the MOSFET driving circuit [10, 11]. To regulate the motor speed, the MOSFET drive circuit controls the MOSFET circuit's turn-on and turn-off as shown in Table 2. When the voltage is lower than the controller set value, the under-voltage circuit protects the battery from draining, and the PWM circuit stops the output. The over-current safety circuit prevents the controller, battery, and motor from operating at higher currents. The overall controller working is shown in Fig. 5 for the e-bicycle.

The following are the primary characteristics of the high-torque design:

(a) Commutation of hall sensors.
(b) Measurement of motor speed.
(c) The motor speed can be adjusted with a potentiometer.
(d) Precise speed management thanks to closed-loop speed control.
(e) Over-voltage, over-current, and heat protection logic are all included.

Table 2 Functions of different MOSFET connections

Items	Function
6 MOSFET	Power, power within, manual/automatic curls, dial gear/point thee speed, speeding, anti-theft, e-abs brakes, overload protection, anti-speed protection, meter, high/low-level brake, customized functions are available
9, 12, 15, 18 MOSFET	Power, reverse, manual/automatic cruse, dial gear/point thee speed, speeding, anti-theft, E-abs brakes, overload protection, anti-speed protection, meter, high/low level brake, customized functions are available
24 MOSFET	Reverse, manual/automatic curls, high level brake, dial gear thee speed

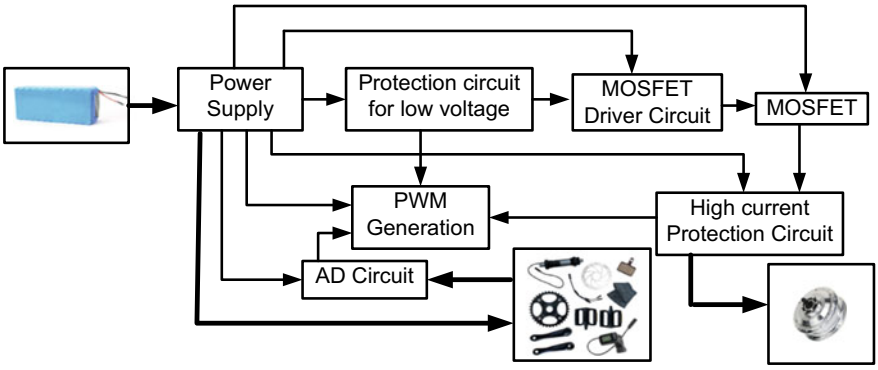

Fig. 5 Block diagram for the controller working

4.1 Battery

A battery is a type of electrical element that generates electrical potential as a result of chemical reactions [12, 13]. Each electrochemical process has a maximum potential difference between two electrodes at which it may generate an electric potential difference. The battery cells are the devices in which these electrochemical processes occur to generate a finite electric potential difference. A series connection of many cells is required to provide the appropriate electric potential difference across the battery terminals. Thus, a battery may be defined as a collection of many cells, each of which is referred to as a cell [14].

Here, four dry cell batteries of 12 V/20 AMP are used. The batteries are connected in parallel to take a 48v supply for the hub motor. The batteries are placed in the battery box which is attached to the chassis. The connection of the batteries in series and parallel is given below as shown in Fig. 6.

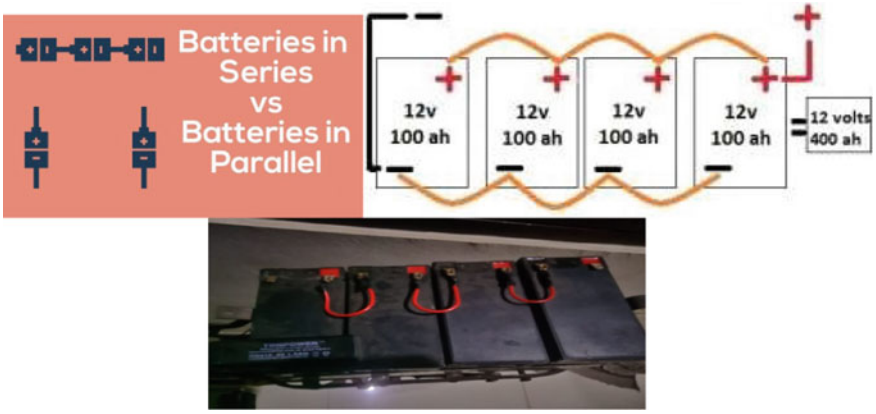

Fig. 6 Series and parallel battery connection

4.2 Charging the Battery and LED Battery Life Indicator

(a) The battery can be charged at any time, regardless of whether the battery is completely depleted or not. When the battery is completely depleted, the LED and display will turn off automatically.

(b) Before connecting the charger and turning it on, confirm that the battery switch is in the on position. When the battery is low on charge, the orange LED illuminates, and the internal fan spins. When the charge is complete, the LED light changes to green, and the fan turns off. A depleted battery will take approximately five hours to fully charge.

(c) If the charger is activated while the battery switch is deactivated. If the charger is not attached to the battery, the charger light will illuminate green, suggesting a fake full charge. Once the charger has turned green, it must be switched off and on again to reset. Because the manufacturer's battery is charging in the "on" position, we recommend that you turn off your throttle switch or separate your battery from the system to prevent your bicycle from taking off on you while charging.

(d) When the battery is connected to your rig and turned on, the middle of the meter will be at the "F" point. When the battery is low, then the middle will be at point "E." The charger of the 48v battery will indicate a red light when the battery is charging; otherwise, a green light will glow when the battery is fully charged.

5 Accelerator and Charger for the E-Bicycle

The accelerator is used for increasing or decreasing the speed of the motor. The function of the accelerator is controlled by the controller. The supply is given to the

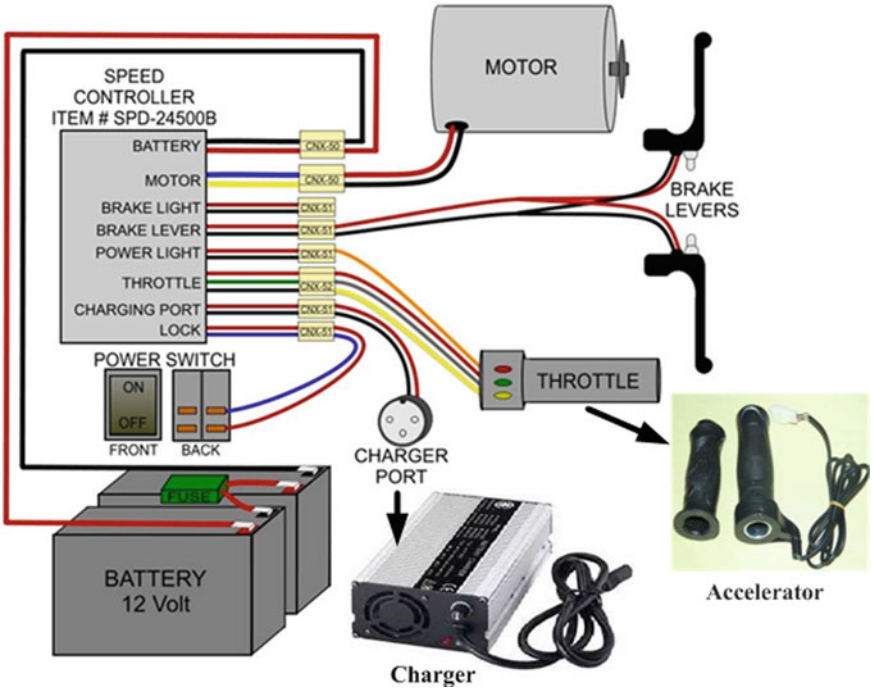

Fig. 7 Working connections for the e-bicycle

all parts of the e-bicycle by switching ON as shown in Fig. 7. When switch is ON, the supply comes into the accelerator also. As we rotate the handle of the accelerator, then, supply is given to the hub motor for running.

The charger is used for charging the battery. The 48v charger is used for charging the battery. Some characteristics of the charger are given below:

a. Reduce the dehydration of the battery, the hydration of the KELEN charger is only 1/3–1/2 compared to the normal charger.
b. Remove the sulphuration effectively pattern car KELEN positive and negative pulse charge protects the battery effectively when it is charging and makes the battery throughout to maintain good condition.
c. Equalizing charge controls the unbalance of the time batteries effectively and controls the vicious circle of batteries which are backward.

5.1 Functions

The temperature compensation along with temperature change, the charger can change the charge voltage automatically and thoroughly settle the battery charges incompletely in winter and overcharged in summer [8, 13]. We use an advanced

multiple protection control circuit to cease the overcharging problem for the batteries. Low-voltage protection guards against charging of bad and old or not matching batteries. Overheat protection ensure the charger is safe under high temperature conditions (note the charger is not allowed to work for a long time under high temperature conditions). Misconnection protects guards against damage to chargers when they misconnect accidentally. Short-circuit protection guards against damage to the charger, while the circuit is a short circuit. The LED light will bright one when it is charging to show the capacity of the batteries. The function of waterproofing the crust is used in the design of waterproofing to protect the charger when it is working.

5.2 Silent Features of the Electric Bicycle Designing

1. We replaced the front wheel of the cycle with a hub motor wheel.
2. We chose the front wheel for replacement because we wanted there to be two running modes, i.e., PEDAL RUN and MOTOR RUN.
3. The battery box is made by welding to support/fix batteries.
4. We mounted a dynamo on the back seat stand.
5. The rotor part of the dynamo is attached to a cycle tire.
6. The LED light is connected to dynamo terminals to show the usage.
7. A small battery (4 V) is also connected to the dynamo to store the produced power by dynamo.
8. The controller is mounted on the front wheel cover.
9. Next, the connections were connected.
10. The connections included a controller connected to the hub motor, throttle, and batteries by means of wire connection.
11. All the remaining parts, like the throttle, head light, and horn, are assembled. The final output is shown in Fig. 8.

Fig. 8 Final output: E-bicycle with low costing

6 Conclusion

Today's oil prices are high with fast consumption rates. Therefore, research and development need to be done to curb consumption. The deficiency and the price of oil are the major problems of this generation. To overcome this problem, we have to try our best ourselves to make an e-bicycle. The e-bicycle runs with the help of electricity or a 48-V DC supply. There is no use of oil like petrol. So, a person travels on this bicycle without causing air and sound pollution. So, this bicycle will provide a better environment for the next generation. In the e-bicycle, there is much to describe; because in an e-bicycle, after the completion of 4 to 6 h of charging, it travels only 20 to 25 km. The full-charged battery travels 45 to 50 km when only one person is riding it. The converter and controller are doing their work properly. The lights, indicators, and horns, etc., also give good performance. The working of the e-bicycle is quite good. The hub motor is running smoothly and giving better performance. The overall result of the e-bicycle is good.

References

1. Xiao D, Liu X, Du W, Wang J, He T (2012) Application of topology optimization to design an electric bicycle main frame. Struct Multi Optim 46(6):913–929
2. Somchaiwong N, Ponglangka W (2006) Regenerative power control for electric bicycle. In: 2006 IEEE SICE-ICASE international joint conference, pp 4362–4365
3. Cheng Y, Hu C (1999) MOSFET modeling and BSIM3 user's guide. Springer Science & Business Media
4. Bhardwaj R, Gupta S (2021) Evolutionary progress of the electric car market with future directions. In: Latest trends in renewable energy technologies, lecture notes in electrical engineering, vol. 760. Springer, Berlin, pp 315–321
5. Dimitrov V (2018) Overview of the ways to design an electric bicycle. In: 2018 IX IEEE national conference with international participation (ELECTRONICA), pp 1–4
6. Salmeron-Manzano E, Manzano-Agugliaro F (2018) The electric bicycle: worldwide research trends. Energies 11(7):1894
7. Liang C-Y, Lin W-H, Chang B (2006) Applying fuzzy logic control to an electric bicycle. In: First IEEE international conference on innovative computing, information and control-volume I (ICICIC'06), vol. 1, pp 513–516
8. Morchin WC, Oman H (2006) Electric bicycles: a guide to design and use. vol. 8. Electric Bicycle Manual
9. Keseev VP (2020) Electric bicycle design experiences and riding costs. In: 2020 7th IEEE international conference on energy efficiency and agricultural engineering (EE & AE), pp 1–4
10. Williams RK, Darwish MN, Blanchard RA, Siemieniec R, Rutter P, Kawaguchi Y (2017) The trench power MOSFET: Part I—History, technology, and prospects. IEEE Trans Electron Devices 64(3):674–691
11. Pham TT, Rouger N, Masante C, Chicot G, Udrea F, Eon D, Gheeraert E, Pernot J (2017) Deep depletion concept for diamond MOSFET. Appl Phys Lett 111(17), pp 173503
12. Pellitteri F, Campagna N, Castiglia V, Damiano A, Miceli R (2020) Design, implementation and experimental results of an inductive power transfer system for electric bicycle wireless charging. IET Renew Power Gener 14(15):2908–2915

13. Hung NB, Lim O (2020) A review of history, development, design and research of electric bicycles. Appl Energy 260:114323 (2020)
14. Zheng Y, Dai R, Zhou Z (2019) Design of torque system for electric bicycle based on fuzzy PID. J Eng 23:8710–8714

Ab-Initio Investigation of Electronic and Magnetic Properties of 2D Mn Doped Mo_2NT_2 (T: O/F)

Kishan H. Mali, B. R. Bhagat, and Alpa Dashora

Abstract Over increasing demand of 2D materials with high Curie temperature above room temperature has motivated us to work on 2D MXenes that can exhibit scalable magnetic properties using density functional theory. In the present work, we have studied structural, electronic and magnetic properties of pristine and Mn doped Mo_2NT_2 with oxygen and fluorine termination groups (T). Pristine Mo_2NT_2 is found to be nonmagnetic-metallic in nature. Enhancement in magnetic properties is observed due to doping of Mn. Magnetic moment of Mn d-orbital shows large exchange splitting as observed from partial density of states which induces spin polarization in the layer of Mo_2NT_2. Fluorine terminated Mo_2N with doping of Mn shows better spin polarization factor as compared to oxygen termination. Increasing concentration of Mn into Mo_2NF_2 may results to spin polarization factor about 9.4% due to interlayer arrangement of Mn at neighboring sites via substitution of Mo atoms. Contribution of Mo d-orbital can be minimized in minority spin channels by intralayer configuration of Mn within Mo_2NT_2 MXene enhancing its spin polarization up to 92.1% that can be used as next generation 2D spintronic material.

Keywords Spin polarization · 2D spintronics · MXenes

1 Introduction

The uninterrupted downscaling of the physical dimensions of charge-based electronic device with an enormous demand for more robust, energy-efficient digital devices has boosted the spintronic field by discovering two-dimensional (2D) magnetic materials. A strong cooperation between the spintronic field and 2D materials has given rise to a new field known as 2D spintronics. 2D spintronics has its own new challenges and opportunities such as scalability, ambient stability, interface-induced magnetic phenomena, electric field induced control over magnetic properties, etc. Recently discovered 2D systems are so far nonmagnetic in nature. One of the important

K. H. Mali (✉) · B. R. Bhagat · A. Dashora
Computational Material Science Laboratory, Department of Physics, The M. S. University of Baroda, Vadodara 390002, India

© The Author(s), under exclusive license to Springer Nature Singapore Pte Ltd. 2022

A. Tripathi et al. (eds.), *Intelligent Computing Techniques for Smart Energy Systems*, Lecture Notes in Electrical Engineering 862,
https://doi.org/10.1007/978-981-19-0252-9_50

requirements for 2D spintronics field is discovery of intrinsic magnetism for the applications like memory storage, spin polarize carrier injection devices, spin valve, spin filter, magnetic sensors, spin-based field effect transistors, nano-medicine and quantum computation.

The spontaneous breaking of time reversal symmetry along with an ordered arrangement of magnetic moments are trademarks of magnetism. In magnetic materials specific relative orientation of neighboring spins and also thought exchange couplings plays key role governing the long range interaction. At absolute zero temperatures long range magnetic moment orientation could extend up to macroscopic length scales but at finite temperature this thermal energy starts overcoming this exchange interaction by misaligning magnetic moment orientations. When we move toward 2D systems from bulk, dimensionality plays crucial role deciding effect of thermal energies over the critical behavior of many body systems. In one dimensional systems, long range order of magnetic moments survives at absolute temperatures while in case of three-dimensional (3D) systems this long range order occurs at finite temperatures also known as curie temperature for ferromagnetic ordering. While situation for the 2D systems is bit complex due to determination of long rang ordering on physical parameters of system such as magnetic anisotropy of the system. Thermal energy at finite Curie temperatures excites large Magnon modes suppressing the expectation value of collective spin. When number of layers start increases will reduce Magnon density states near excitation gap, which will require further higher temperature, ensuring sufficient population of excitations to destroy the long range magnetic order [1].

Newly found intrinsic magnetic materials with positive interlayer and intralayer exchange coupling in semiconducting (CrI_3, $CrBr_3$, $Cr_2Ge_2Te_6$) and metallic (Fe_3GeTe_2, VSe_2) 2D materials have given deep insight to understand the magnetic behavior [2]. Huang et al. [3] observed supressed magnetization due to metamagnetic effect and ferromagnetic ordering in trilayer and monolayer CrI_3. While magnetic ordering in bilayer CrI_3 can be switched from antiferromagnetic to ferromagnetic by magneto-electric response near the critical field [4]. $Cr_2Ge_2Te_6$ is a nearly ideal two-dimensional Heisenberg ferromagnet and could be good option for studying fundamental spin behavior [1]. Itinerant ferromagnetism with out-of-plane magneto-crystalline anisotropy is come across in monolayer Fe_3GeTe_2 [5]. Several two-dimensional van der Waals (vdW) layered structures such as graphene, MoS_2, show remarkable electronic properties but no significant magnetic properties are observed. To bring such materials in the 2D spintronics inspires to extrinsically induce magnetism using different approaches: (a) Defect engineering (vacancies, adatoms, grain boundaries, edge modification) (b) adding magnetic elements by substitution or interaction (c) by magnetic proximity effect (2D materials are placed in contact of magnetic substrates). Apart from this, one important advancement in past few years revealing manipulation of magnetic moment via spin polarized current and external field (electric field, magnetic field and photonic field) [5, 6].

In this line, recently discovered new family of early transition metal carbide and nitride known as MXenes with excellent electronic and multifaceted structural properties are also explored. MXene is layered structure with hexagonal class having

common formula $M_{n+1}X_nT_x$ ($n = 1$–3) where, M is early transition metals, X is C and/or N, T is surface termination groups such as –F, –O, –OH, –Cl. This termination group attaches with MXene structure while selective chemical etching of its bulk counterpart (MAX phase). Khazaei et al. [7] found Cr_2CF_2, $Cr_2C(OH)_2$, Cr_2NF_2 and Cr_2NO_2 having ferromagnetic ground state. Most of the MXenes having quite strong covalent bond between M-X and M-T, and nonmagnetic in nature. But intrinsic magnetism is observed in bare Ti_2C and Ti_2N MXenes [8]. Uniform biaxial strain on M_2C (M = Hf, Nb, Sc, Ta, Ti, V, Zr) MXenes induces magnetism by nonmagnetic to ferromagnetic phase transition [9]. Whereas Ti_2C and Zr_2C found exhibiting magnetic moment without applying strain [8]. Apart from the strain, doping in Sc_2CT_2 by Ti, V induces weak magnetism and Cr, Mn induces magnetic moment of approximately 2.1 μ_B/unit cell [10].

Spin orbit coupling and covalent bonding in 2D materials provides strong magnetic anisotropy by symmetry breaking resulting energetically favorable orientation of magnetic moments. In this work, we have studied electronic and magnetic properties of pristine Mo_2NT_2 (surface termination group T = O/F) MXene. The primary reason behind considering transition metal nitride as part of study is its robust ferromagnetic ground state as compared to transition metal carbide due to extra electron which leads to excess density of states at Fermi level [11]. Further, we have doped Mo_2NT_2 with Mn in order to understand role of magnetic species to enhance its electronic and magnetic properties that could be next step toward the field of 2D spintronics.

2 Methodology

In this study structural, electronic and magnetic properties of pristine and doped Mo_2NT_2 is studied using density functional theory (DFT) as embodied in open-source code QUANTUM ESPRESSO [12] using the plane wave and pseudopotential method. All the properties are calculated considering the 2 × 2 × 1 supercell of Mo_2NT_2 with generalized gradient approximation (GGA) [13] as exchange–correlation functional and ultra-soft pseudopotential with scalar relativistic correction. In order to optimize and calculate electronic structure plane wave energy cutoff of 90 Ry and charge density cutoff of 900 Ry is used. Supercell is optimized with spin polarization till force in the structure reduces below threshold of 10^{-3} eV/Å using 6 × 6 × 1 Monkhorst k-point grid. We have also considered grimme-d3 [14] correction to incorporate vdW interaction for calculation of total energy of the systems. We have given vacuum of about 25.7 Å between consecutive periodic unit cell to consider it as layered flack structure. To calculate electronic structure using 13 × 13 × 1 Monkhorst k-point grid is used for Brillouin zone integration with smearing of 0.01 eV in order to have correct ground state with this k-point sampling.

3 Results and Discussion

The surface termination group binds to the surface of MXene during the selective etching of MXene flakes from its bulk phase, changing its electronic and magnetic properties drastically. In the present work, we have considered the Mo_2NT_2 MXenes with two different surface termination groups –O and –F. Pristine Mo_2NT_2 has N atom layer sandwich between the Mo atomic layers with symmetric distribution of T-atoms on either side of the structure as seen in Fig. 1a–b. To induced magnetism in Mo_2NF_2, we have doped Mn with weight percent concentration about 5.8% ($Mo_{1.75}Mn_{0.25}NF_2$)

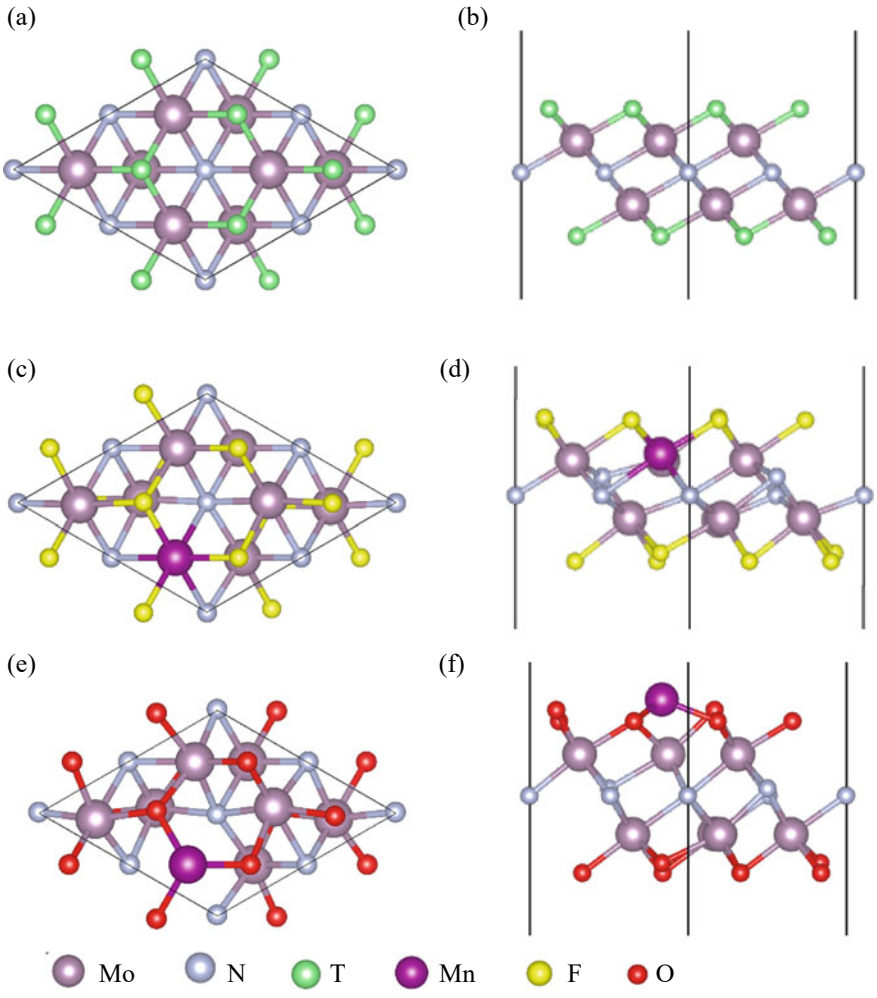

Fig. 1 Optimized (**a**) Top and (**b**) side view of Mo_2NT_2, (**c**) Top and (**d**) side view of Mn doped Mo_2NF_2, (**e**) Top and (**f**) side view of Mn doped Mo_2NO_2

and 12.3% ($Mo_{1.50}Mn_{0.50}NF_2$). For higher Mn doping ($Mo_{1.50}Mn_{0.50}NF_2$), we have considered two different doping named as site-1 and site-2. $Mo_{1.50}Mn_{0.50}NF_2$ (site-1) has both Mn atoms situated at neighboring site of different layer (interlayer) and $Mo_{1.50}Mn_{0.50}NF_2$ (site-2) has both Mn atoms within similar layer (intralayer). In case of Mo_2NO_2, Mn is doped with weight percent concentration about 6.0%. All the optimized crystal structures of Mn doped Mo_2NT_2 are presented in Fig. 1c–f.

Thickness of the Mo_2NT_2 after optimization is found about 4.48 Å and 4.16 Å approximately for –F and –O termination, respectively. Thickness of Mo_2NF_2 reduces after doping of Mn atom locally near the doping site about 0.1-0.2 Å. While in case of Mo_2NO_2 thickness increases due to doping of the Mn. This local distortion in MXene layer can also be confirmed via analysis of average bond length of doped MXene comparing with its pristine structure as shown in Table 1.

Change in lattice parameter observed while doping of Mn into Mo_2NF_2 is within 1%. While in case of Mn doping in Mo_2NO_2, Mn atom moves toward surface side and binds with –O atom leaving its initial site reducing the lattice parameter about 7% as shown in side view of Fig. 1f. In order to understand the favorable doping site, we have computed doping energy (E_{doping}) required to dope Mn atom via substitution of Mo atoms of MXene. Doping energy is calculated as:

$$E_{\text{doping;Mn}} = \left[E_{Mo_{2-x}Mn_xNT_2} - E_{Mo_2NT_2} + \mu(\text{Mo}) - \mu(\text{Mn})\right] \tag{1}$$

$E_{Mo_{2-x}Mn_xNT_2}$ and $E_{Mo_2NT_2}$ are total energy of doped and pristine Mo_2NT_2, respectively while μ(Mo) and μ(Mn) is chemical potential of Mo and Mn, respectively. Chemical potential of Mo is evaluated from its common form MoS_2 using formula:

$$\mu(\text{Mo}) = [E(MoS_2) - 2\mu(S)] \tag{2}$$

where $E(MoS_2)$ is total energy of MoS_2 compound and $\mu(S)$ is chemical potential of sulfur is calculated from its common form orthorhombic alpha sulfur which contain S_8 ring structure. Chemical potential of Mn is calculated from MnO_2 using formula:

$$\mu(\text{Mn}) = [E(MnO_2) - 2\mu(O)] \tag{3}$$

where $E(MnO_2)$ is total energy of MnO_2 and μ(O) is chemical potential of oxygen. To evaluate chemical potential, we need to consider the correction to total energy of O_2 molecule to avoid over binding due to GGA functional [15]. So, chemical potential of oxygen $\mu(O)$ can be calculated using formula,

$$\mu(O) = [E(O_2) - E_{\text{corr}}]/2 \tag{4}$$

Here, $E(O_2)$ is calculated total energy of oxygen molecule and E_{corr} is correction term in order to avoid over binding of molecule. E_{corr} term was found 1.02 eV in accordance with experimental atomization energy [15]. Calculated doping energy of different MXenes was found negative showing exothermic nature of reaction to

Table 1 Lattice parameters, bond length and doping energy of doped and pristine Mo_2NT_2 MXenes

MXenes	Lattice parameter a (Å)	Average bond length (Å)					Doping energy E_{doping} (eV)
		Mo–N	Mo–T	Mo–Mn	Mn–T	Mn–N	
Mo_2NF_2	6.534	2.098	2.304	–	–	–	–
Mo_2NO_2	6.298	2.097	2.091	–	–	–	–
$Mo_{1.75}Mn_{0.25}NF_2$	6.482	2.110	2.250	2.877	2.179	2.319	−2.126
$Mo_{1.75}Mn_{0.25}NO_2$	5.854	2.138	2.060	–	1.910	–	−2.690
$Mo_{1.50}Mn_{0.50}NF_2$ (site-1)	6.527	2.089	2.228	2.700	2.374	2.124	−2.966
$Mo_{1.50}Mn_{0.50}NF_2$ (site-2)	6.550	2.079	2.244	2.772	2.284	2.190	−3.179

Mn doped Mo_2NT_2 as shown in Table 1. All the doping sites of Mo is equivalent in pristine Mo_2NT_2 due to its symmetric structure. So, $Mo_{1.75}Mn_{0.25}NT_2$ shows more negative doping energy with T = O as compared to T = F irrespective of Mo site. For higher concentration doping, intralayer (site-2) doping of Mn is more suitable as compared to interlayer (site-1) doping in Mo_2NF_2 as shown in Table 1.

To study electronic and magnetic properties of Mn doped Mo_2NT_2, spin polarized total density of states (DOS) are calculated as shown in Fig. 2. As per Fig. 2a, b, pristine Mo_2NT_2 found to be nonmagnetic metal with both termination groups since it shows identical DOS in spin-up and spin-down channels. $Mo_{1.75}Mn_{0.25}NF_2$ has metallic nature along with net spin polarization due to contribution of spin-up channel while with same Mn doping and O termination, $Mo_{1.75}Mn_{0.25}NO_2$ also shows metallic behavior along with very low spin polarization as seen in Fig. 2c–d. Higher concentration of Mn in case of F-termination is also found metallic. But its spin polarization depends mainly on relative interacting site of Mn within MXene structure. In case of $Mo_{1.5}Mn_{0.5}NF_2$ (site-2), high spin polarization due to low DOS at E_F in spin-down channel is reported. While in case where both Mn atoms lies at different layer neighboring sites (interlayer) resulting to compensating partial spin polarization in $Mo_{1.5}Mn_{0.5}NF_2$(site-1) [Fig. 2e–f].

Further, partial spin polarized DOS are also calculated to understand the role of each atomic sites as shown in Fig. 3a–f. In case of Mo_2NT_2 (for T = O and F), at E_F the major contribution comes due to the 4d orbital of Mo. Doping of Mn into Mo_2NF_2 has shown shifting of Mn occupied 3d states of spin-up to the unoccupied states in spin-down (Fig. 3c). This shifting observed in Mn in -F terminated case is more prominent due to sharp peak at −1.8 eV as compared to −O terminated case. Local magnetic moment of Mn leads to non-compensated distribution of partial DOS for nonmagnetic species (Mo, N, F) by breaking time reversal symmetry. $Mo_{1.75}Mn_{0.25}NF_2$ shows noticeable net spin polarization in Mo species. But in case of $Mo_{1.75}Mn_{0.25}NO_2$ significant spin polarization is observed in O species instead of Mo because after optimization magnetic species Mn moves on surface attaching with O. In case of higher concentration of Mn in $Mo_{1.50}Mn_{0.50}NF_2$, both the configuration has large shifting of occupied Mn-3d-states of spin-up channel to unoccupied spin-down channel. Relative arrangement of Mn in layer of MXene leads to totally reverse effects in spin-down channel at Fermi energy effecting directly on spin polarization. Intralayer configuration of Mn in $Mo_{1.5}Mn_{0.5}NF_2$ shows vanishing contribution of d-orbital of Mo at E_F as shown in Fig. 3f.

One of the important key parameter for good magnetic materials is spin polarization factor (SP). 100% spin polarization means half metallic material allowing fully spin polarized current within material. Spin polarization factor can be found using formula,

$$\mathrm{SP} = \frac{n_{\uparrow}(E_f) - n_{\downarrow}(E_f)}{n_{\uparrow}(E_f) + n_{\downarrow}(E_f)} \tag{5}$$

where $n_{\uparrow}(E_f)$ and $n_{\downarrow}(E_f)$ are DOS at E_F.

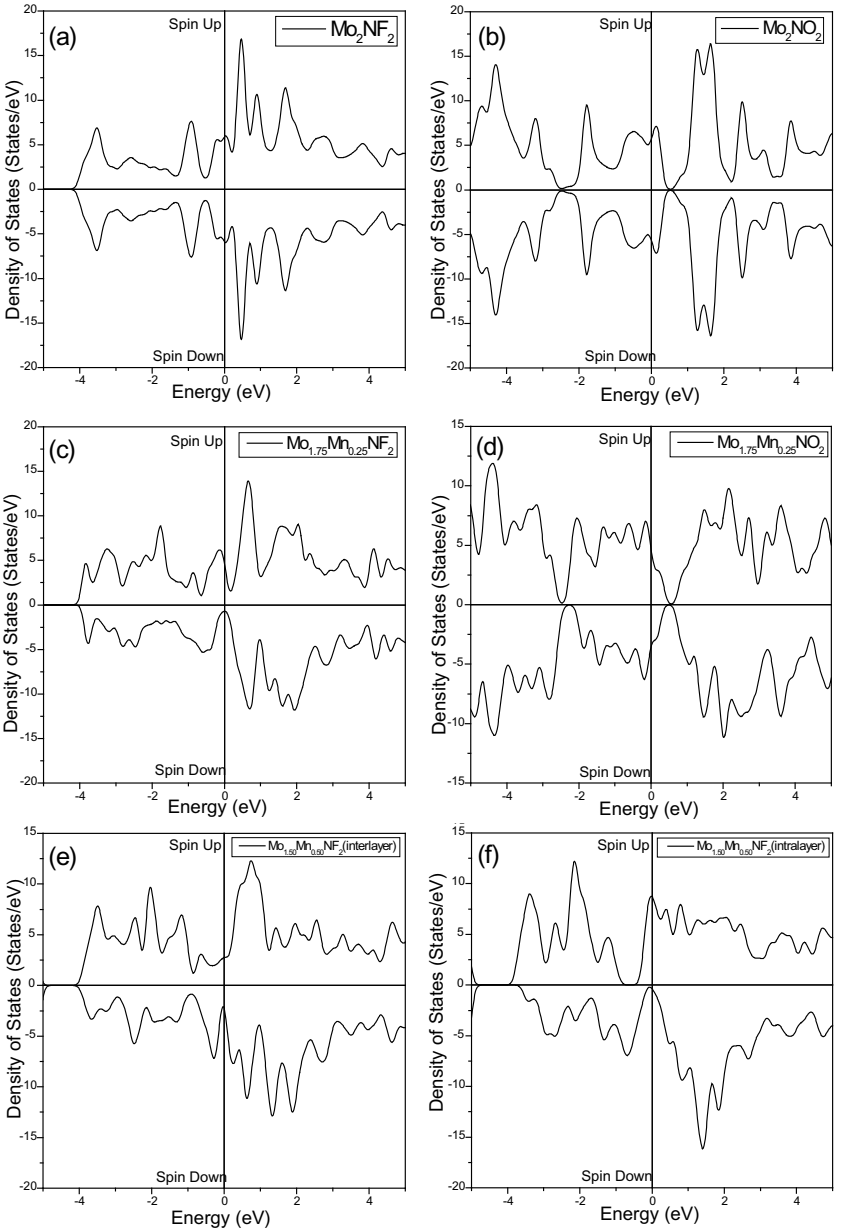

Fig. 2 Calculated DOS for pristine (**a**–**b**) and Mn doped (**c**–**f**) MXenes

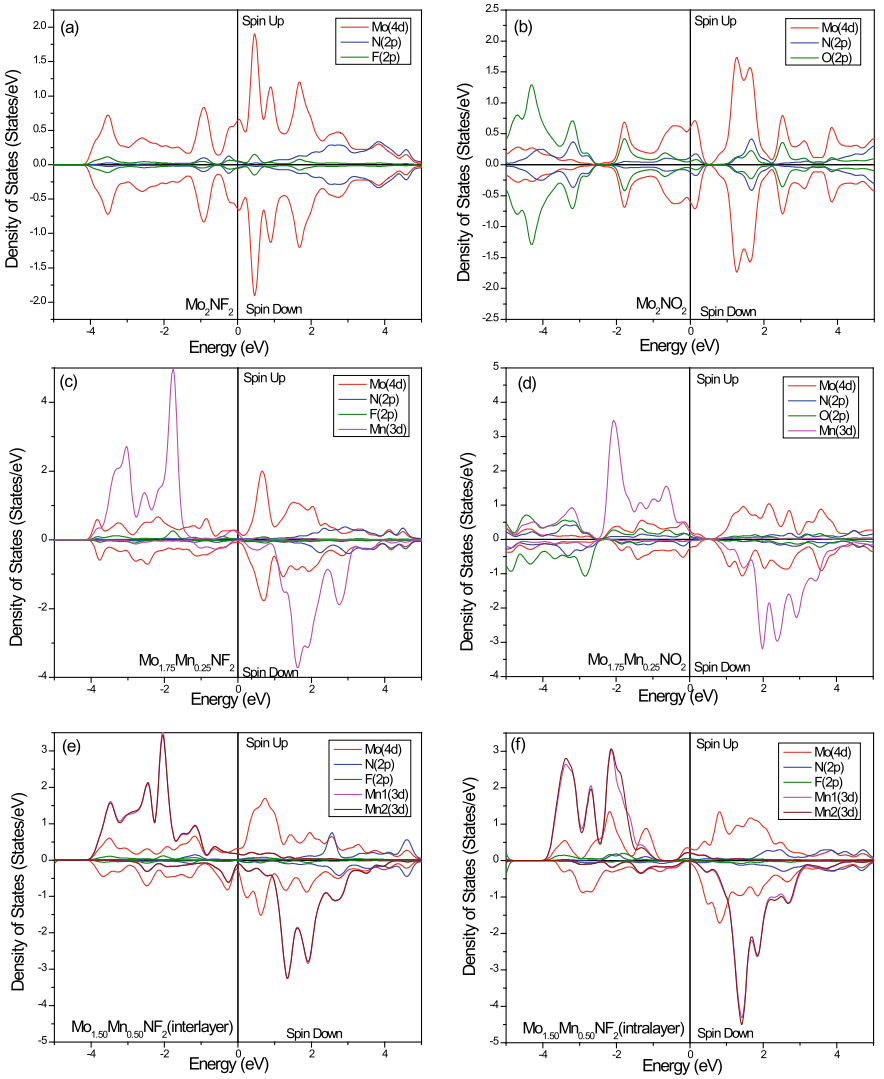

Fig. 3 Calculated partial DOS for pristine (**a**–**b**) and Mn doped (**c**–**f**) MXenes

$Mo_{1.50}Mn_{0.50}NF_2$ (site-2) shows highest total magnetization 1.49 μ_B/f.u. as compared to other MXenes with spin polarization factor 92.1% as shown in Table 2. The main contribution of total magnetization per unit cell is coming from Mn dopant atom. But, contribution of Mo in spin polarization is major at E_F compared to termination groups in pristine and doped Mo_2NT_2 as shown in Fig. 3a–f. From the DOS analysis, it is seen that in all the studied MXenes, to obtain high spin polarization, contribution of Mo 4d-orbital in spin-down channel at E_F should be minimum. As in case of $Mo_{1.50}Mn_{0.50}NF_2$ (site-2) intralayer dopant Mn causes minimization

Table 2 Total magnetization, magnetic moment of atoms and spin polarization factor in pristine and Mn doped Mo_2NT_2

MXenes	Magnetic moment M (μ_B/atom)			Total magnetization (μ_B/f.u.)	Spin polarization factor SP (%)
	M_{Mo}	M_{Mn1}	M_{Mn2}		
Mo_2NF_2	0.00	–	–	0.00	0.0
Mo_2NO_2	0.00	–	–	0.00	0.0
$Mo_{1.75}Mn_{0.25}NF_2$	0.06	3.91	–	1.16	73.4
$Mo_{1.75}Mn_{0.25}NO_2$	0.03	3.62	–	1.17	14.5
$Mo_{1.50}Mn_{0.50}NF_2$ (site-1)	−0.17	3.43	3.42	1.48	9.4
$Mo_{1.50}Mn_{0.50}NF_2$ (site-2)	0.19	3.76	3.77	1.49	92.1

of partial DOS of Mo-4d states at E_F. While, in case of interlayer doping of Mn in $Mo_{1.50}Mn_{0.50}NF_2$ (site-1) increases partial DOS of Mo at E_F hence reducing spin polarization. Reduced spin polarization was observed as a result of Mn atom capturing toward the surface side, leaving their initial location in $Mo_{1.75}Mn_{0.25}NO_2$. Magnetic moment for Mo atom in all cases found very small. While magnetic moment of doped Mn is larger in –F terminated case as compared to –O terminated Mo_2NT_2 as shown in Table 2.

4 Conclusion

Structural, electronic and magnetic properties of Mn doped Mo_2NT_2 are studied with O- and F-termination groups. Pristine Mo_2NT_2 is found to be nonmagnetic metallic in nature. Doping of Mn in Mo_2NT_2 leads to local distortion in layer enhancing its magnetic properties. O terminated Mo_2NT_2 shows more stable doping configuration as compared to F-termination. While in case of F-terminated Mo_2NF_2, intralayer interacting Mn doping is favorable as compared to interlayer doping. While doping of Mn induces magnetism by breaking time reversal symmetry. Mn doped Mo_2NT_2 relatively shows poor magnetic spin polarization due to Mn capturing at surface side by O termination. F-terminated Mo_2NT_2 elevates the spin polarization by lowering the density of states of the minority spin channel at E_F. Intralayer Mn doped MXene [$Mo_{1.50}Mn_{0.50}NF_2$ (site-2)] is reported with excellent magnetic spin polarization about 92.1% which can be used as potential magnetic 2D spintronic material.

Acknowledgements The authors show their sincere gratitude to the University grant commission, India for UGC Start-up grant. AD is also thankful to University Grants Commission, India for Assistant Professorship under Faculty Recharge Program.

References

1. Gong C, Li L, Li Z, Ji H, Stern A, Xia Y, Cao T, Bao W, Wang C, Wang Y, Qiu ZQ (2017) Discovery of intrinsic ferromagnetism in two-dimensional van der Waals crystals. Nature 546(7657):265
2. Gibertini M, Koperski M, Morpurgo AF, Novoselov KS (2019) Magnetic 2D materials and heterostructures. Nat Nanotechnol 14(5):408
3. Huang B, Clark G, Navarro-Moratalla E, Klein DR, Cheng R, Seyler KL, Zhong D, Schmidgall E, McGuire MA, Cobden DH, Yao W (2017) Layer-dependent ferromagnetism in a van der Waals crystal down to the monolayer limit. Nature 546(7657):270
4. Jiang S, Shan J, Mak KF (2018) Electric-field switching of two-dimensional van der Waals magnets. Nat Mater 17(5):406
5. Deng Y, Yu Y, Song Y, Zhang J, Wang NZ, Sun Z, Yi Y, Wu YZ, Wu S, Zhu J, Wang J (2018) Gate-tunable room-temperature ferromagnetism in two-dimensional Fe_3GeTe_2. Nature 563(7729):94
6. Bader SD, Parkin SSP (2010) Spintronics. Annu Rev Condens Matter Phys 1(1):71
7. Khazaei M, Arai M, Sasaki T, Chung CY, Venkataramanan NS, Estili M, Sakka Y, Kawazoe Y (2013) Novel electronic and magnetic properties of two-dimensional transition metal carbides and nitrides. Adv Funct Mater 23(17):2185
8. Gao G, Ding G, Li J, Yao K, Wu M, Qian M (2016) Monolayer MXenes: promising half-metals and spin gapless semiconductors. Nanoscale 8(16):8986
9. Zhao S, Kang W, Xue J (2014) Manipulation of electronic and magnetic properties of M_2C (M= Hf, Nb, Sc, Ta, Ti, V, Zr) monolayer by applying mechanical strains. Appl Phys Lett 104(13):133106
10. Yang J, Luo X, Zhang S, Chen L (2016) Investigation of magnetic and electronic properties of transition metal doped Sc_2CT_2 (T= O, OH or F) using a first principles study. Phys Chem Chem Phys 18(18):12914
11. Stoner EC (1938) Collective electron ferronmagnetism. In: Proceedings of the royal society of London. Series A. Math Phys Sci 165(922):372
12. Giannozzi P, Baroni S, Bonini N, Calandra M, Car R, Cavazzoni C, Ceresoli D, Chiarotti GL, Cococcioni M, Dabo I, Dal Corso A (2009) QUANTUM ESPRESSO: a modular and open-source software project for quantum simulations of materials. J Condens Matter Phys 21(39):395502
13. Perdew JP, Burke K, Ernzerhof M (1996) Generalized gradient approximation made simple. Phys Rev Lett 77(18):3865
14. Grimme S (2006) Semiempirical GGA-type density functional constructed with a long-range dispersion correction. J Comput Chem 27(15):1787
15. Gebhardt J, Rappe AM (2018) Doping of BiFeO3: A comprehensive study on substitutional doping. Phys Rev B 98(12):125202

Correlative Study of Compositional and Bioelectric Parameters Using Multi-Frequency Bioelectrical Impedance Analysis (MFBIA)

Shiva Sharma, Neha Singh, Anupama Chaudhary, and Manisha Rastogi

Abstract Assessment of human body composition is one of the important factors to identify physiological anomalies and health risks since several decades. Evidences related to the age associated alterations in the human body composition measured as bioelectrical impedance are highly sparse. The present study aims to evaluate the bioelectrical impedance and anthropometric changes in different ages (18–50 yrs) male candidates and to identify the correlation in bioelectrical impedance and measured variables, if any. Bioelectrical impedance was measured using multi-frequency body impedance analysis BIA (MFBIA) and the outcomes were recorded as the impedance, resistance, reactance, and phase angle on passing an alternating current (<1 mA) at multiple frequencies (5, 50, 100, and 200 K Hz) in succession. The present study outcomes demonstrated no statistically significant association between impedance recorded at multiple frequencies and anthropometric variables.

Keywords Bioelectric impedance · Aging · Male · Anthropometric and BMI

1 Introduction

Variations in body composition and its association with age is an established phenomenon. These variations can be at cellular, tissue, and organ or at whole body level. Previous studies reported the correlation of these compositional changes with the help of bioelectrical impedance in human and animal tissues [1, 2]. However, there are several techniques available to measure these age associated compositional changes in the human body including Hydro-densitometry, Air displacement plethysmography (ADP)/Bod Pod, Hydrometry, Dual Energy X-ray, skinfold method, Near infrared method, and anthropometric. No single method can fulfill all the criteria for

S. Sharma · A. Chaudhary · M. Rastogi (✉)
Department of Biomedical Engineering, School of Biological Engineering and Sciences, Shobhit Institute of Engineering and Technology (Deemed to be University), Meerut, India
e-mail: manisha.rastogi@shobhituniversity.ac.in

N. Singh
Department of Electronics and Communication Engineering, Manipal University Jaipur, Jaipur, India

© The Author(s), under exclusive license to Springer Nature Singapore Pte Ltd. 2022

A. Tripathi et al. (eds.), *Intelligent Computing Techniques for Smart Energy Systems*, Lecture Notes in Electrical Engineering 862,
https://doi.org/10.1007/978-981-19-0252-9_51

ideal body composition measurement as it requires methods and statistical approach to quantify each of the major components at five levels (elemental, cellular, tissue, organ, and whole body) [3, 4].

Multi-frequency bioelectrical impedance analyzer (MFBIA) comes as anon-invasive, precise, consistent, portable, inexpensive, easy to use, safe and quick technique to evaluate these compositional changes. MFBIA is a simple painless procedure where low voltage alternating current of 100 μA to 1 mA (approx. 800 μA) of high frequency is applied to the body and its resistance or the impedance measured by the help of ohm's law. Here the body is considered as a series of cylinders and resistance of body is proportional to the length of the cylinder while inversely proportional to the cross-sectional area. Therefore, resistance and the length, determines the volume of cylinder. Assuming that the current flows through the path of least resistance (water), then the volume determined gives the content of body water [5, 6].

MFBIA measures the impedance of body at multiple frequencies 5, 50, 100, and 200 kHz [7]. Variation in measured electrical impedance may be associated with the age that is not clearly understood. Therefore, the aim of this study is to understand the age associated bioelectrical changes in human body. The study also intends to identify the association between the bioelectrical impedance at different frequency and anthropometric variables if any.

2 Methodology

2.1 Participants

This pilot study was carried out with the prior approval of Institutional Ethical Committee, School of Biological Engineering and Life Sciences, Shobhit Institute of Engineering and Technology (Deemed to be University), Meerut. Consented healthy male candidates aged between (18–50 yrs.) were recruited in this study. A total number of 450 candidates were approached for the study. Out of them 78 male candidates recruited based upon the inclusion criteria (healthy, nonsmoking, not taking any kind of medication). **Group1** includes 26 males of 21–30 yrs.; **Group 2** had 26 males of 31–40 yrs.; **Group 3** includes 26 males of 41–50 yrs.; overall seventy eight candidates participated in the study.

2.2 Demographic

Several demographic parameters recorded before analysis. Age, height, weight were recorded parameters from each participants as these are the basic input parameters for the analytical system Quad Scan 4000 MFBIA. Body Mass Index (BMI) calculatory parameters based on input. Anthropometric measurements viz. height (cm), weight

(kg), were recorded as per the guidelines suggested by Jelliffe [8]. The height was measured using anthropometric rod to nearest 0.1 cm. The subjects were weighed on portable platform weighing balance to nearest 0.5 kg with ordinary clothes. A non-flexible tape was used to measure the waist and hip circumference. The measurements were made to nearest 0.1 cm.

2.3 Analysis of Bioelectrical Impedance

All measurements were performed after the subjects had fasted for 8 h. The subjects were weighed in standardized light clothes and without shoes on a platform manual scale balance. BIA measurements were carried out with the subject lying in a supine position on a flat, nonconductive bed by using a multi-frequency tetrapolar electrode system (Bodystat QuadScan 4000; Bodystat, Douglas, United Kingdom). Two electrodes were placed on the right wrist with one just proximal to the third metacarpophalangeal joint (positive) and one on the wrist next to the ulnar head (negative). Two electrodes were placed on the right ankle with one just proximal to the third metatarsophalangeal joint (positive) and one between the medial and lateral malleoli (negative). Multi-frequency (5, 50, 100, and 200 kHz) currents were introduced from the positive leads and traveled throughout the body to the negative leads. The flow of current through the body (impedance) is dependent on the frequency applied. At low frequencies, the current cannot bridge the cellular membrane and will pass predominantly through the extra-cellular space. At higher frequencies, penetration of the cell membrane occurs and the current is conducted by both the extra-cellular and intra-cellular spaces.

2.4 Statistical Analysis

Data is presented as mean ± SD, P-values were calculated by the ANOVA at a significance level of less than 0.05. Correlation analysis was conducted using Pearson's correlation test.

3 Results and Discussion

Table 1 represents the measured demographic variables among different groups. Average age of group 1 male was (25.615 ± 3.305); group 2 (33.769 ± 2.006); group 3 (43.308 ± 3.301). **Anthropometric parameters,** average height of the group1-3 participants was between 164.538 ± 2.961 to 170.462 ± 6.778 cm; average weight was 59.662 ± 10.228 to 74.454 ± 16.096 kg; average BMI was 20.623 ± 3.51

Table 1 Demographic and anthropometric variables

Variables	Group 1 Mean ± SD (Max, Min)	Group 2 Mean ± SD (Max, Min)	Group 3 Mean ± SD (Max, Min)	P value
AGE	24.769 ± 2.488	33.769 ± 2.006 (31, 38)	43.308 ± 3.301 (40, 50)	< 0.00001
HEIGHT	170.154 ± 4.86	170.462 ± 6.778 (162, 182)	164.538 ± 2.961 (162, 170)	0.00802
WEIGHT	59.662 ± 10.228	74.454 ± 16.096 (56, 105)	69.769 ± 6.723 (58, 82)	0.008549
BMI	20.623 ± 3.51	25.392 ± 3.762 (20.1, 31.7)	25.831 ± 3.158 (20.8, 31.2)	0.00071

to 25.831 ± 3.158. All variable (age, height, weight, and BMI) were significantly different among group1-3 participants.

Results for compositional analysis indicated all three groups are non-obese and healthy as the BMI ranging in between 20 and 25. BMI value of group 2 and group 3 is at almost boarder line that may due to age associated changes [9]. Hayes et al. 2015 indicated changes in BMI are strongly age-dependent changes [10]. Meeuwsen et al. 2010 reported same type of findings and represented a progressive increase in BMI with aging and plateaued between 40 and 70 years in men therefore significant changes with age [11].

In bioelectrical impedance analysis, impedance at 5 kHz was significantly different in all three groups. However impedance at 50, 100, and 200 kHz was not significantly different in between group1-3. Impedance at 5, 50, 100, and 200 kHz was found in order of G1 > G3 > G2 (Table 2).

According to Stroud et al. [12] and Baumgartner et al. [13] impedance is frequency dependent phenomenon that changes within a conductor with the permissibility of an AC current. Amount of the impedance directly associated with two vectors resistance (R) and reactance (Xc) [12, 13]. Yamada et al. 2014 reported changes in bioelectrical impedance and resistance are associated with the compositional variation in the human body [14]. Young (1990) also reported a direct influence of these compositional changes on the bioelectrical parameters of human body. Here, we can hypothesize considerable changes in fat percentage in the G1, G2, and G3 leading the significant variation in impedance at 5 kHz frequency [15]. Baumgartner et al. [13] also indicated the adipose tissue affected the impedance outcome [13].

Overall results for correlation analysis indicating insignificant positive and negative correlation of impedance at 5, 50, 100, and 200 kHz with age, height, weight, and BMI as shown in Fig. 1. In group 1 negative but insignificant correlation was found between impedance at different frequency and weight, BMI and height however age was positively associated. In group 2 and group 3 all variables were negatively associated with impedance at different frequencies. No such relationship was described by the previous studies.

4 Conclusion

Overall this study shows **bio**electrical impedance and anthropometric parameters (weight, height, and BMI) are age associated variables. However no significant correlation was identified in these variables with impedance to evaluate this control trial need to be carry out.

Table 2 Results for bioelectrical impedance analysis

Variable	Group 1 Mean ± SD (Max, Min)	Group 2 Mean ± SD (Max, Min)	Group 3 Mean ± SD (Max, Min)	P value
IMPED5K	721.3854 ± 91.536 (679, 797)	654.077 4 ± 78.72 (609, 674)	656.154 ± 52.594 (652, 663)	0.048538
IMPED 50 K	627.846 4 ± 86.522 (594, 693)	569.385 4 ± 71.236 (532, 587)	574 4 ± 52.954 (567, 599)	0.082121
IMPED 100 K	595.077 4 ± 83.266 (563, 654)	538.923 4 ± 67.452 (501, 555)	543.923 4 ± 53.211 (535, 577)	0.085778
IMPED 200 K	571.846 4 ± 78.953 (541, 624)	519.462 4 ± 64.297 (479, 532)	525.308 4 ± 53.344 (513, 559)	0.102151

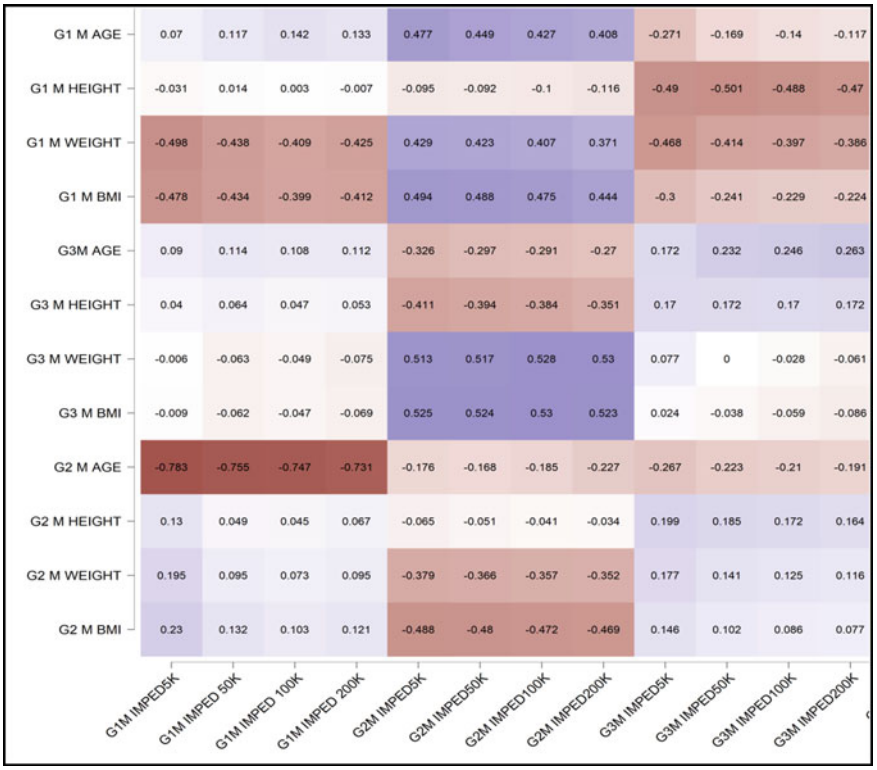

Fig. 1 Correlation analysis

References

1. Chumlea WC, Guo SS (1994) Bioelectrical impedance and body composition: present status and future directions. Nutr Rev 52(4):123–131
2. Lukaski HC (1987) Methods for the assessment of human body composition: traditional and new. Am J Clin Nutr 46(4):537–556
3. Goswami PN, Munna K (2007) Bioelectrical impedance analysis: phase angle-an independent predictive health marker and its clinical applications. In: 3rd Kuala Lumpur international conference on biomedical engineering 2006 2007. Springer, Berlin, pp 321–324
4. Smye SW, Sutcliffe J, Pitt E (1993) A comparison of four commercial systems used to measure whole-body electrical impedance. Physiol Meas 14(4):473
5. Ryde SJ, Thomas DW, Birks JL, Ali PA, Saunders NH, Al-Zeibak S, Morgan WD (1993) Assessment of body fat: a comparison of techniques. In: Human body composition 1993. Springer, Boston, MA, pp 59–62
6. Ward LC (2019) Bioelectrical impedance analysis for body composition assessment: reflections on accuracy, clinical utility, and standardisation. Eur J Clin Nutr 73(2):194–199
7. Moonen HP, van Zanten FJ, Driessen L, de Smet V, Slingerland-Boot R, Mensink M, van Zanten AR, van Zanten (2021) AR Association of bioelectric impedance analysis body composition and disease severity in COVID-19 hospital ward and ICU patients: The BIAC-19 study. Clin Nutr 40(4):2328–2336

8. Jelliffe DB (1996) World health organization the assessment of the nutritional status of the community (with special reference to field surveys in developing regions of the world. World Health Organization
9. https://www.euro.who.int/en/health-topics/disease-prevention/nutrition/a-healthy-lifestyle/body-mass-index-bmi
10. Hayes A, Gearon E, Backholer K, Bauman A, Peeters A (2015) Age-specific changes in BMI and BMI distribution among Australian adults using cross-sectional surveys from 1980 to 2008. Int J Obes 39(8):1209–1216
11. Meeuwsen S, Horgan GW, Elia M (2010) The relationship between BMI and percent body fat, measured by bioelectrical impedance, in a large adult sample is curvilinear and influenced by age and sex. Clin Nutr 29(5):560–566
12. Stroud DB, Cornish BH, Thomas BJ, Ward LC (1995) The use of cole-cole plots to compare two multi-frequencybioimpedance instruments. Clin Nutr 14(5):307–311
13. Baumgartner RN, Ross R, Heymsfield SB (1998) Does adipose tissue influence bioelectric impedance in obese men and women? J Appl Physiol 84(1):257–262
14. Yamada Y, Ikenaga M, Takeda N, Morimura K, Miyoshi N, Kiyonaga A, Kimura M, Higaki Y, Tanaka H (2014) Estimation of thigh muscle cross-sectional area by single-and multifrequency segmental bioelectrical impedance analysis in the elderly. J Appl Physiol 116(2):176–182
15. Young VR, Marchini JS, Cortiella J (1990) Assessment of protein nutritional status. J Nutr 1990 Nov 1;120(suppl_11):1496–502

Accurate Estimation for Stability of Slope and Partition Over Old Underground Coal Workings Using Regression-Based Algorithms

Kumar Dorthi, Anil Kumar, and Karra Ram Chandar

Abstract Numerical modeling simulation has found to be best solution for predicting slope and partition stability over old underground coal workings. But it has taken huge time to complete a single simulation model. In this regard, machine learning-based framework is used to predict the stability of old galleries. A case study is taken up in opencast mine and simulation is carried out using numerical model and machine learning-based framework. Framework has shown an overall accuracy of 94–95% for different slope and partition stability. Framework shows a speedup of 2366× against numerical simulator.

Keywords Numerical modeling · Machine learning · Slope · Partition · Opencast mine · Support vector regression

1 Introduction

Various techniques are being tried in India's opencast coal mines to improve coal production. Converting ancient underground coal mines to opencast mines is one of them which can be seen in Fig. 1. However, the conversion process generates slope and partition failures, resulting in equipment damage and, in some cases, death. Prediction of slope and partition stability is necessary to avoid failures [9, 10].

K. Dorthi (✉)
Department of Computer Science and Engineering, Kakatiya Institute of Technology & Science, Warangal, Telangana, India
e-mail: drkumar.cse@kitsw.ac.in

A. Kumar
Department of Computer Science and Engineering, Nitte Meenakshi Institute of Technology, Bangalore, Karnataka, India
e-mail: anil.kumar@nmit.ac.in

K. R. Chandar
Department of Mining Engineering, National Institute of Technology Karnataka, Mangaluru, Karnataka, India

© The Author(s), under exclusive license to Springer Nature Singapore Pte Ltd. 2022

A. Tripathi et al. (eds.), *Intelligent Computing Techniques for Smart Energy Systems*, Lecture Notes in Electrical Engineering 862,
https://doi.org/10.1007/978-981-19-0252-9_52

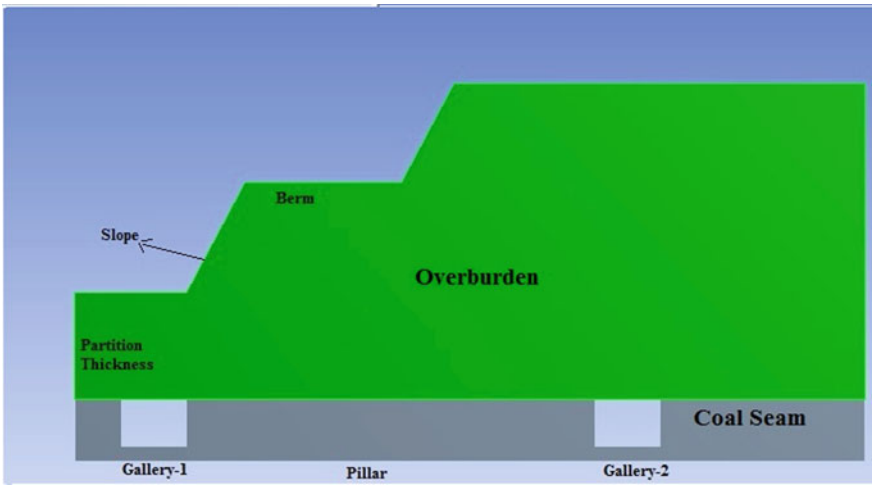

Fig. 1 Schematic diagram of old underground coal workings

There are many approaches to predict slope and partition stability, but numerical modeling has found to be the best method in the field of mining engineering. Numerical modeling has wide applications in engineering geology, hydrogeology, rock mechanics, and slope stability study of opencast mines [2]. The capacity to simulate the nonlinear, non-homogeneous, and anisotropic nature of rock strata has led to their extensive application [1].

The major contribution of our work is proposing a machine learning (ML) framework which can be used to simulate the opencast mine field conditions based on numerical simulation of field data. In this paper, ML-based framework is used to predict the slope and partition stability over old underground coal workings based on numerical data.

The following is how the paper is organized: Sect. 2 reviews related research, Sect. 3 describes the ML framework, Sect. 4 presents scientific results, and Sect. 5 brings the paper to a conclusion.

2 Case Study

To estimate the slope and partition stability of a major opencast mine in Telangana, India, a case study was conducted which can be seen in Fig. 2. ANSYS Workbench software tool was used to develop the models by simulating the field conditions. Input parameters like rock properties, bench configuration, and old gallery dimensions for modeling were collected during field visits. The geometrical dimensions such as partition thickness, gallery width, gallery height, pillar width, berm width, and slope angle were considered for this study. The 3D model created in ANSYS workbench is shown in Fig. 3.

Fig. 2 A view of opencast mine in south India

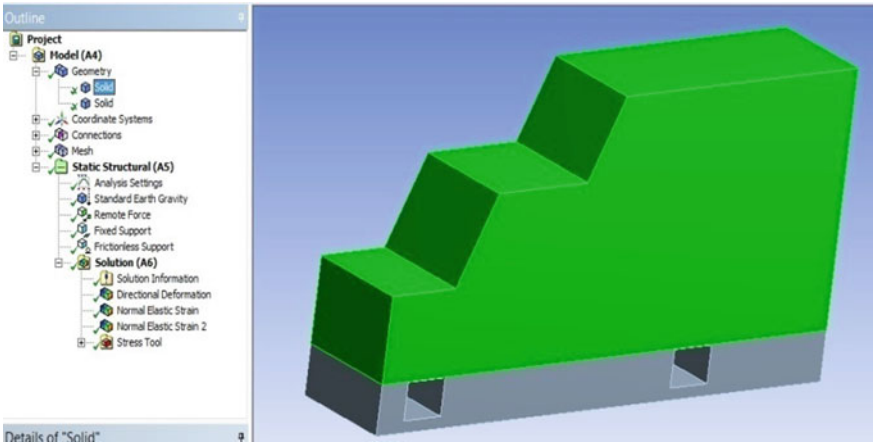

Fig. 3 3D model in ANSYS

3 Numerical Modeling

The impact of geometric dimensions, rock characteristics, and external pressure on the stability of old underground galleries was investigated using numerical modeling under mining field circumstances. The geometric dimensions are gallery width, gallery height, pillar width, partition thickness, slope angle, and berm width. Rock properties are density, compressive strength of sandstone, and coal. External load includes the load of shovel and dumper combination. Vertical deformation was observed at the surface centers ('R' and 'S') over old galleries and roof centers ('P' and 'Q') of gallery1 and gallery2 which an be observed in Fig. 4.

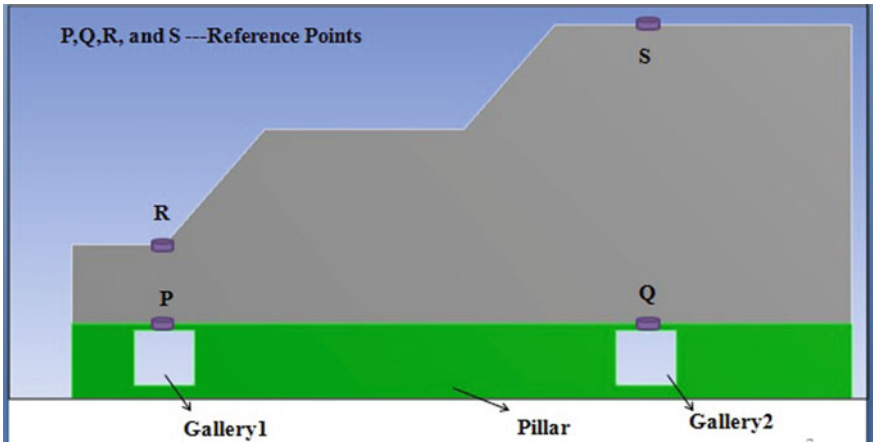

Fig. 4 Reference points for output in the model

Geometrical dimensions included gallery widths of 3.0 m, 3.6 m, 4.2 m, and 4.8 m were considered as per Reg. No. 111 of CMR—2017. Pillar widths were considered with respect to the gallery width and incremented by 1 m. Gallery height values were ranging from 2.4 to 3.4 m with an increment of 0.2 m. Partition thickness was considered from 4 to 12 m with increment of 2 m. Berm width of 5–10 m with an increment of 1 m was considered. Slope angle of 50°−75° with an increment of 5° was considered. The above parameters were varied by keeping other parameters such as rock properties and external load as constant. Multi-colored output results from ANSYS for the partition thickness of 4 m is shown in Fig. 5. The results of directional deformation for different partition thicknesses over gallery 1 and gallery 2, when the gallery width is 4.2 m, gallery height is ranging from 2.4 to 3.4 m, slope

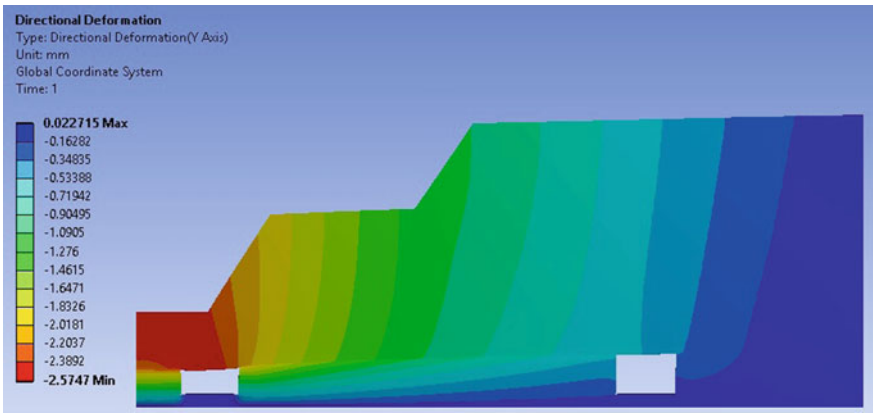

Fig. 5 A Vertical deformation contours over old galleries for partition thickness of 4m

angle is 550, berm width is 5 m, and pillar widths are about 30.5 m, 31.5 m, and 32.5 m, are given in Tables 1 and 2. In total, 12,960 models were developed by varying different parameters.

4 Machine Learning Framework

Machine learning (ML) framework is developed to assess and predict the stability of slope over old underground galleries. The overview of the ML framework is shown in Fig. 6.

The ML framework is depicted in Fig. 6 as an overview and step-by-step process, with all procedures divided into two phases. There is no dataset available in this area. Hence, ANASYS simulator is used to generate the reference data. The framework is divided into two phases training and testing phase. In training phase, various configurations has been given to ASASYS simulator to generate the datasets. Later, feature extraction is performed on the data and the pre-processed data is divided into training and testing data. In our work, the dataset is divided 50:50 ratio, 50% data for training and remaining 50% for testing.

Several generalized linear regression methods, including as lasso, lassolars, larsCV, Bayesian-ridge, linear, ridge, elastic-net, and support vector regression (SVR) using linear, radial basis function (RBF), and polynomial kernels, were tested while developing the framework. All trained algorithms are fine-tuned until they produce the least amount of error. The ML framework was built using the algorithm that produced the least amount of error. In this study, we used the SVR algorithm to predict values since it produced the least amount of error when compared to the other algorithms.

In ϵ-SVR, ϵ stands for insensitive loss function, which is utilized to solve the quadratic optimization problem. Despite the fact that the value of $epsilon$ must be supplied before the SVR model can be trained, most problems make predicting the value of ϵ challenging. To get around this restriction, $upsilon$-SVR [8] is used, where υ specifies a lower bound on the number of support vectors and a higher bound on the fraction of training samples. The kernels used in the framework are '*linear*,' '*polynomial*,' and '*radial basis function(RBF)*' [3–7].

Both linear and nonlinear data may be analyzed using RBF. C, which controls the trade-off between margin and size of slack variables, and '*gamma*', which is the kernel coefficient for '*RBF*' and '*linear*,' are two more SVR parameters. To fit data to the training dataset, more levels of the '*gamma*' algorithm are utilized. '*RBF*' and '*linear*' kernels were used to illustrate the method's effectiveness.

ML framework experiments were used to evaluate various combinations of ($epsilon$, C, $gamma$) and ($upsilon$, C, $gamma$). The algorithm with the lowest error rate was taken into consideration.

Table 1 Variation in directional deformation at points 'P' and 'R' of gallery 1 for gallery width of 4.2 m

Partition thickness (m) above gallery1	Pillar width (m)	Deformation (mm) at different gallery heights (m) and gallery width = 4.2 m											
		Roof center of gallery 1 (Point Q)						Surface center of gallery 1 (Point S)					
		2.4	2.6	2.8	3	3.2	3.4	2.4	2.6	2.8	3	3.2	3.4
4	30.5	2.12	2.16	2.2	2.24	2.28	2.32	2.45	2.49	2.53	2.57	2.61	2.65
	31.5	2.04	2.08	2.12	2.16	2.2	2.24	2.37	2.41	2.45	2.49	2.53	2.57
	32.5	1.96	2	2.04	2.08	2.12	2.16	2.29	2.33	2.37	2.41	2.45	2.49
6	30.5	1.81	1.85	1.89	1.93	1.97	2.01	2.14	2.18	2.22	2.26	2.3	2.34
	31.5	1.73	1.77	1.81	1.85	1.89	1.93	2.06	2.1	2.14	2.18	2.22	2.26
	32.5	1.65	1.69	1.73	1.77	1.81	1.85	1.98	2.02	2.06	2.1	2.14	2.18
8	30.5	1.69	1.73	1.77	1.81	1.85	1.89	2.02	2.06	2.1	2.14	2.18	2.22
	31.5	1.61	1.65	1.69	1.73	1.77	1.81	1.94	1.98	2.02	2.06	2.1	2.14
	32.5	1.53	1.57	1.61	1.65	1.69	1.73	1.86	1.9	1.94	1.98	2.02	2.06
10	30.5	1.61	1.65	1.69	1.73	1.77	1.81	1.94	1.98	2.02	2.06	2.1	2.14
	31.5	1.53	1.57	1.61	1.65	1.69	1.73	1.86	1.9	1.94	1.98	2.02	2.06
	32.5	1.45	1.49	1.53	1.57	1.61	1.65	1.78	1.82	1.86	1.9	1.94	1.98
12	30.5	1.57	1.61	1.65	1.69	1.73	1.77	1.9	1.94	1.98	2.02	2.06	2.1
	31.5	1.49	1.53	1.57	1.61	1.65	1.69	1.82	1.86	1.9	1.94	1.98	2.02
	32.5	1.41	1.45	1.49	1.53	1.57	1.61	1.74	1.78	1.82	1.86	1.9	1.94

Table 2 Variation in directional deformation at points 'P' and 'R' of gallery2 for gallery width of 4.2m

Partition thickness (m) above gallery2	Pillar width (m)	Deformation (mm) at different gallery heights (m) and gallery width = 4.2 m											
		Roof center of gallery 2 (Point Q)						Surface center of gallery2 (Point S)					
		2.4	2.6	2.8	3	3.2	3.4	2.4	2.6	2.8	3	3.2	3.4
4	30.5	1.32	1.36	1.4	1.44	1.48	1.52	1.55	1.59	1.63	1.67	1.71	1.75
	31.5	1.24	1.28	1.32	1.36	1.4	1.44	1.47	1.51	1.55	1.59	1.63	1.67
	32.5	1.16	1.2	1.24	1.28	1.32	1.36	1.39	1.43	1.47	1.51	1.55	1.59
6	30.5	1.01	1.05	1.09	1.13	1.17	1.21	1.24	1.28	1.32	1.36	1.4	1.44
	31.5	0.93	0.97	1.01	1.05	1.09	1.13	1.16	1.2	1.24	1.28	1.32	1.36
	32.5	0.85	0.89	0.93	0.97	1.01	1.05	1.08	1.12	1.16	1.2	1.24	1.28
8	30.5	0.89	0.93	0.97	1.01	1.05	1.09	1.12	1.16	1.2	1.24	1.28	1.32
	31.5	0.81	0.85	0.89	0.93	0.97	1.01	1.04	1.08	1.12	1.16	1.2	1.24
	32.5	0.73	0.77	0.81	0.85	0.89	0.93	0.96	1	1.04	1.08	1.12	1.16
10	30.5	0.81	0.85	0.89	0.93	0.97	1.01	1.04	1.08	1.12	1.16	1.2	1.24
	31.5	0.73	0.77	0.81	0.85	0.89	0.93	0.96	1	1.04	1.08	1.12	1.16
	32.5	0.65	0.69	0.73	0.77	0.81	0.85	0.88	0.92	0.96	1	1.04	1.08
12	30.5	0.77	0.81	0.85	0.89	0.93	0.97	1	1.04	1.08	1.12	1.16	1.2
	31.5	0.69	0.73	0.77	0.81	0.85	0.89	0.92	0.96	1	1.04	1.08	1.12
	32.5	0.61	0.65	0.69	0.73	0.77	0.81	0.84	0.88	0.92	0.96	1	1.04

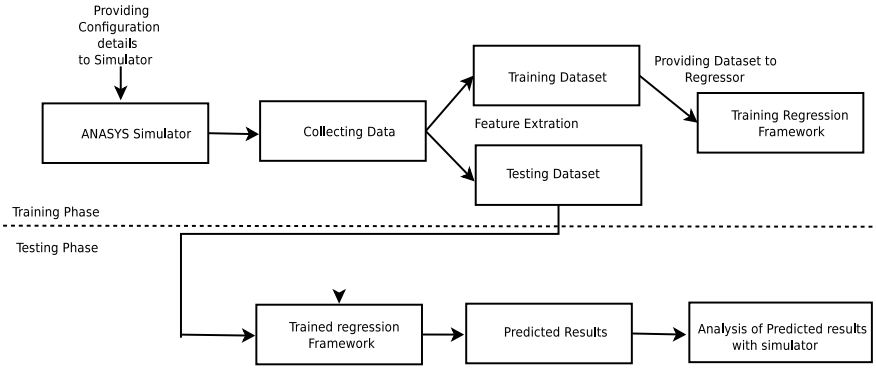

Fig. 6 Overview of machine learning framework

5 Results and Discussion

5.1 Experimental Results

Slope and partition stability over old galleries is assessed using machine learning and numerical modeling. Numerical modeling is one of the best approach to simulate mining field conditions but takes more time to compute a module. In total of 20,960 models were simulated to assess the slope stability of old galleries using numerical modeling approach. Machine learning approach is used to not only reduce the time to simulate the model but also given accurate results. The accuracy of ML frame work is evaluated using mean square error (MSE) against ANSYS results. MSE is given as follows:

$$MSE = \frac{1}{l} \sum_{i=1}^{l} (a_i - a_i^*)^2$$

where a_i is the actual value, a_i^* is the predicted value and 'l' is the number of data points.

5.2 Runtime Comparison

We have conducted all the experiments using the system configuration with I5 processor and 8GB RAM. The total time consumed for ANSYS software to give results of numerical simulation model is around 120sec. But machine learning framework predicted the same results in 0.02 s as shown in Table 3. The proposed ML framework has shown a speed up of 2336x against ANSYS work bench simulator for a single sample.

Table 3 Mean square errors of machine learning framework

Partition thickness (m) above gallery1	Pillar width (m)	Roof center of gallery 1 (Point P)						Surface center of gallery 1 (Point R)					
		2.4	2.6	2.8	3.0	3.2	3.4	2.4	2.6	2.8	3.0	3.2	3.4
8	30.5	0.0036	0.0035	0.0036	0.0033	0.0037	0.0036	0.004	0.0041	0.0036	0.0034	0.0032	0.003
	31.5												
	32.5												
10	30.5												
	31.5												
	32.5												

6 Conclusion

The slope and partition stability are predicted using a machine learning framework that takes into account several locations. The support vector regression approach was used to develop the framework. In this work, we used two well-known SVR variants: *epsilon*-SVR and *upsilon*-SVR. SVR's '*linear*,' '*RBF*,' and '*polynomial*' kernels were used to verify the datasets. That kernel was chosen from among those that produced the least amount of error. Different slope and partition stability are predicted by the proposed framework. For the parameters studied, framework had an overall accuracy of 94–95%. In terms of execution time, the ML framework differs from the traditional ANSYS simulator. The error rate was less than 5%, with a speedup of 2366× when compared to the ANSYS simulator.

References

1. Harrison J (2001) Engineering rock mechanics part 2: illustrative worked examples. Hutching WK (2015) Finding the Paleoindian spearthrower: quantitative evidence for mechanically-assisted propulsion of lithic armatures during the North American Paleoindian Period. J Archeol Sci 55:34–41
2. Jing L (2003) A review of techniques, advances and outstanding issues in numerical modelling for rock mechanics and rock engineering. Int J Rock Mech Min Sci 40(3):283–353
3. Kumar A, Talawar B (2018) Machine learning based framework to predict performance evaluation of on-chip networks. In: 2018 Eleventh international conference on contemporary computing (IC3). IEEE, pp 1–6
4. Kumar A, Talawar B (2019) Accurate router level estimation of network-on-chip architectures using learning algorithms. In: 2019 International conference on smart systems and inventive technology (ICSSIT). IEEE, pp 746–751
5. Kumar A, Talawar B (2019) Floorplan based performance estimation of network-on-chips using regression techniques. In: 2019 IEEE 5th international conference for convergence in technology (I2CT). IEEE, pp 1–6
6. Kumar A, Talawar B (2019) A support vector regression-based approach to predict the performance of 2d & 3d on-chip communication architectures. In: 2019 International conference on smart systems and inventive technology (ICSSIT). IEEE, pp 35–39
7. Kumar A, Talawar B (2020) Upm-noc: learning based framework to predict performance parameters of mesh architecture in on-chip networks. In: Kalam A, Niazi KR, Soni A, Siddiqui SA, Mundra A (eds) Intelligent computing techniques for smart energy systems. Springer, Singapore, pp 723–733
8. Schölkopf B, Smola AJ, Williamson RC, Bartlett PL (2000) New support vector algorithms. Neural Comput 12(5):1207–1245
9. Singh T, Singh D (1992) Prediction of instability of slopes in an opencast mine over old surface and underground workings. Int J Surface Min Reclam Environ 6(2):81–89
10. Watters RJ, Finn D, Coulthard J (1989) Pit slope instability problems induced by disused underground mine workings. In: Symposium on engineering geology and geotechnical engineering, vol 25, pp 101–106

A DFT Study for Analyzing Opto-electronic Behavior of $ZnCN_2$

Hansraj Karwasara, Karina Khan, Amit Soni, K. C. Bhamu, Jagrati Sahariya, and Ushma Ahuja

Abstract We obtained optoelectronic properties of wide band gap semiconductor ternary chalcopyrite $ZnCN_2$ through density functional theory, which is executed in the Wien2k package. The full-potential linearized augmented plane wave method is utilized to sort out the equation of Kohn_Sham. The optoelectronic properties are computed by choosing exchange-correlational potential named as generalized gradient approximation in order to yield good results. The computed results ratified the compound $ZnCN_2$ having direct band gap of 1.94 eV, and its prominent intensity is in range 3–5 eV revealed through absorption spectra which supports its availability in optoelectronic applications.

Keywords Chalcopyrite semiconductor · Optoelectronic · DFT · PBE-GGA

1 Introduction

Energy is the basic need for humans' survival and their development, and the most part of energy is fulfilling through fossil fuels like coal and petroleum etc., but the fossil fuels are limited in nature, so we have to concentrate on its alternates. Renewable energy can reduce burden on fossil fuels, and it is beneficial in combating the

H. Karwasara · K. Khan
Department of Physics, Manipal University Jaipur, Jaipur, Rajasthan 303007, India

A. Soni (✉)
Department of Electrical Engineering, Manipal University Jaipur, Jaipur, Rajasthan 303007, India
e-mail: amitsoni_17@yahoo.co.in

K. C. Bhamu
Department of Physics, Gramin Mahila P.G. College, Sikar, Rajasthan 332024, India

J. Sahariya
Department of Physics, National Institute of Technology, Uttarakhand, Srinagar (Garhwal), Uttarakhand 246174, India

U. Ahuja
Department of Electrical Engineering, NMIMS, Mukesh Patel School of Technology Management and Engineering, Mumbai 400056, India

© The Author(s), under exclusive license to Springer Nature Singapore Pte Ltd. 2022

A. Tripathi et al. (eds.), *Intelligent Computing Techniques for Smart Energy Systems*, Lecture Notes in Electrical Engineering 862,
https://doi.org/10.1007/978-981-19-0252-9_53

climate changes. Renewable energy can generate through sun, air, water etc. Availability of these sources are enormous and not harmful for the environment as well [1]. Solar energy has wide energy capacity to fulfill the need of world's energy demand, and by using solar energy, we can achieve sustainable development goals. Scientists are working on solar cells since nineteenth century and continuously try to improving its efficiency [2–4]. The ternary chalcopyrite semiconductors belong to II-IV-V2 group are lattice analog of zinc blende structure and showing same semiconductor behavior. The compounds belong to this group are widely acceptable for researchers due to their remarkable properties such as non-toxicity, abundance, stiffness, and thermal stability, make these compounds available for optoelectronic [1, 5, 6]. The phosphide, arsenide, and carbonitrides belong to the II-IV-V2 group showing versatile applications in electric, magnetic, thermoelectric, and optical field due to their diversity in their band gaps [7–9]. The carbonitrides crystals II-CN_2 exist in orthorhombic as well as in tetragonal structure, and both of its structures are showing different properties and are stable at room temperature. The tetragonal form of II-CN_2 can be used in solar cells due to their hardness and also possess semiconducting properties as their band gap ranges up to 1.4–5 eV [10]. For explaining the electronic behavior and energy framework of II-CN_2, theoretical study has been performed by using density functional theory (DFT) [10–15]. One of the materials from II-CN_2 is $ZnCN_2$ which is used in medicine, DC batteries, and catalysis. Cubic phase of zinc cyanide, i.e., $Zn(CN)_2$ shows negative thermal expansion so it can be used in optoelectronic devices, fuel cells, and thermoelectric conversion system [16]. $ZnCN_2$ has high thermal and chemical properties which make it suitable for luminescent host material [17]. ZnCN2 is also useful to reduce corrosion process of metals in different fields and water-oxidation photo-catalyst for Li-ion batteries [18]. Due to direct band gap and its suitable optoelectronic properties, $ZnCN_2$ would be used to enhance the performance of optoelectronic circuit. Crystalline, electronic, and vibrational structures of $ZnCN_2$ were calculated using CRYSTAL14 software [15]. This work aims to simulating the optoelectronic properties of compound $ZnCN_2$ using Wien2k code of DFT.

2 Computational Details

The theoretical tool Wien2k package is used for obtaining crystal structure, lattice symmetry, electronic, and optical properties of $ZnCN_2$. To sort out the Kohn-Sham equation, we preferred the full-potential linearized augmented plane wave method (FP-LAPW method) [19, 20].

To proceed the calculations, firstly, we have done the optimization of tetragonal chalcopyrite $ZnCN_2$ crystal by taking generalized gradient approximation (GGA) exchange correlation functional through which we get the crystal constant, atomic positions Zn (0, 0, 0); C (0, 0, 0.5); and N (0.29, 0.25, 0.125) having the space group. The value of radii of muffin tin are 1.88, 1.47, and 1.54 of Zn, C, and N, respectively. The PBE-GGA potential method is used for obtaining electronic and

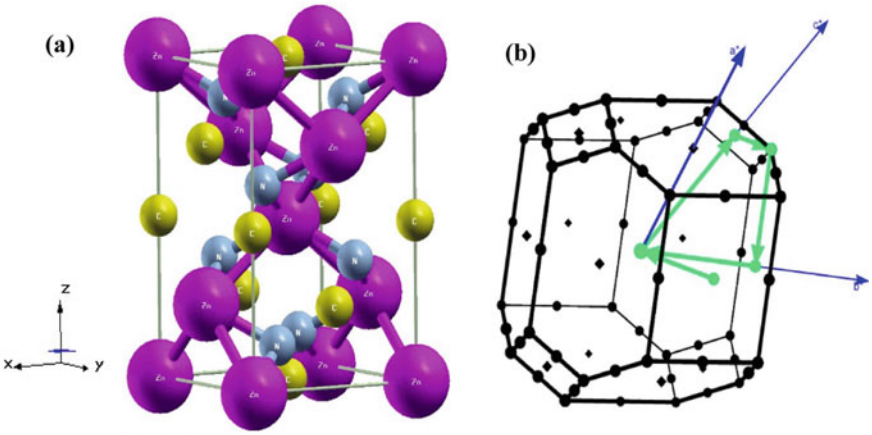

Fig. 1 **a** Crystal structure, **b** Brillouin zone of $ZnCN_2$

optical properties. The additional input values such as RMT Kmax, number of k points, Gmax, lmax, and energy are fixed to 7, 1000, 12, 10, and -6 Ry, respectively. The structure of crystal of $ZnCN_2$ is represented in Fig. 1 along with the Brillouin zone which is used to show the crystal along high symmetry direction.

3 Results and Discussion

To put the focus on the electronic properties, we explain these through the band structure and density of states (DOS) which include total and partial DOS that are computed through the PBE-GGA.

The band structure, which is shown in Fig. 2, tells us about the semiconductor nature of $ZnCN_2$ as its calculated band gap is 1.94 eV, in which the fermi energy level is 0 eV. Also, this compound having direct band gap nature because its highest point of valence band and lowest point of conduction band lies at same I′-I′ k point. The value of obtained band gap is highest than the previously quoted band gap which is about 0.84 eV; it is arises due to use of different type of theoretical tools [10]. The different color bands shown in the energy band structure present the different energy level along with the position of electrons and also their transitions from valence to conduction band.

Figure 3 depicted DOS spectra of $ZnCN_2$ which gives more explanation of electronic property by the mixing of different hybridization state of the Zn, C, and N. It also describes the formation of bands, number of electrons per unit volume, and energy. The energy band gap is also calculated and confirmed by DOS spectra is 1.94 eV. The fermi energy is set at 0 eV, but the valence bands lie after a little gap from fermi energy. The band arises near fermi energy is due to the ‘d’ state of Zn and ‘p’ state of N, and valence band −8 to −6 eV is due to the mixing of ‘s’ state

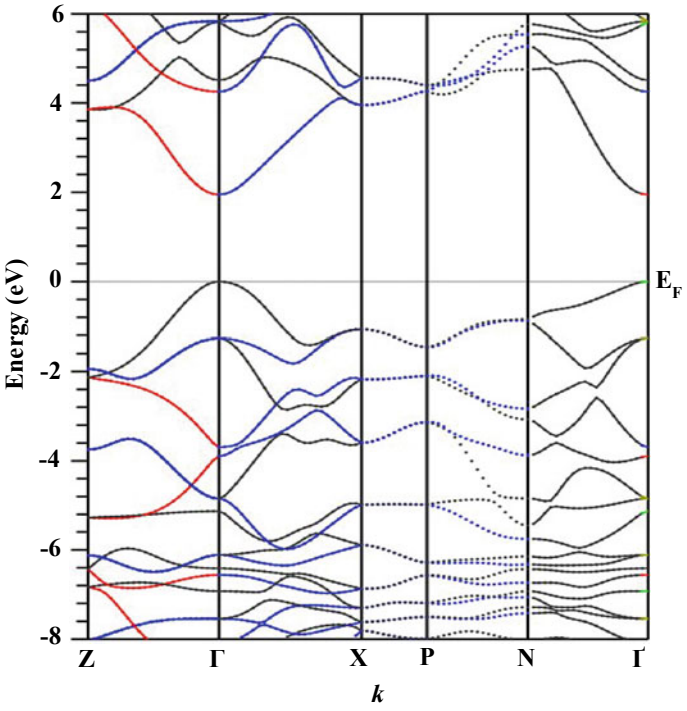

Fig. 2 Energy band structure of $ZnCN_2$

of Zn, C, and N. The main contribution in conduction band due to the mixing of 's' and 'p' state of C and N. It shows the valence band existed from −8 to 0 eV, and conduction band is from 1.94 to 6 eV.

The optical response of $ZnCN_2$ is explained through the optical spectra by using exchange-correlational functional PBE-GGA. The real and imaginary dielectric tensor spectra in Fig. 4a, b through the real dielectric tensor spectra which is used to obtained the degree of polarization through the of $ZnCN_2$ at zero frequency is 4.80, and peak arises in Fig. 4b at 7.37 eV shows the transition of electrons from the valence to conduction band.

Figure 5a indicates the absorption coefficient of the complete optical nature of compound, and it shows the intensity lies in the range of 3–5 eV. The value of integrated absorption coefficient (IAC) for $ZnCN_2$ is 9.5548 ($\times 10^4$ eV/cm). Figure 5b, c shows the reflectivity spectra and refractivity spectra which is used to tell about the surface of the material. The absolute value of reflectivity and refractivity is 0.13 and 4.84. And, we can see through the optical spectra that the parallel component and perpendicular component do not match with each other; hence, the compound is showing the anisotropic nature and prove its utility in optoelectronic applications.

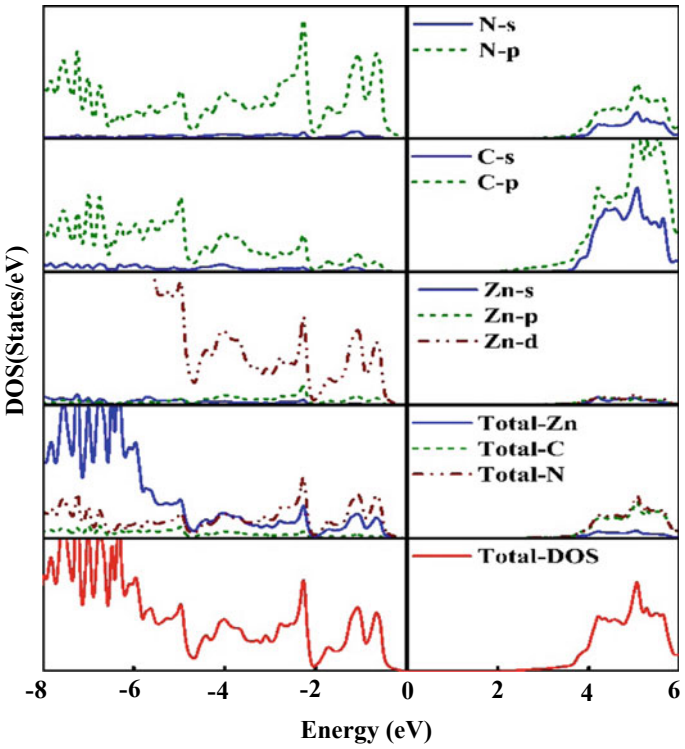

Fig. 3 Density of state (DOS) of $ZnCN_2$

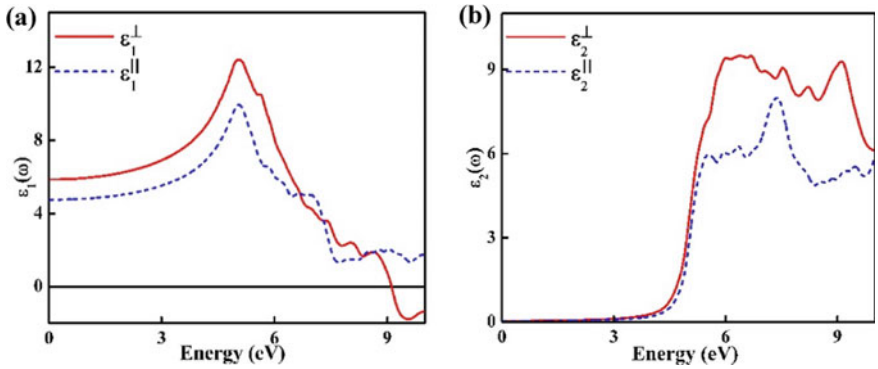

Fig. 4 **a** Real dielectric tensor spectra, **b** imaginary dielectric tensor spectra of $ZnCN_2$

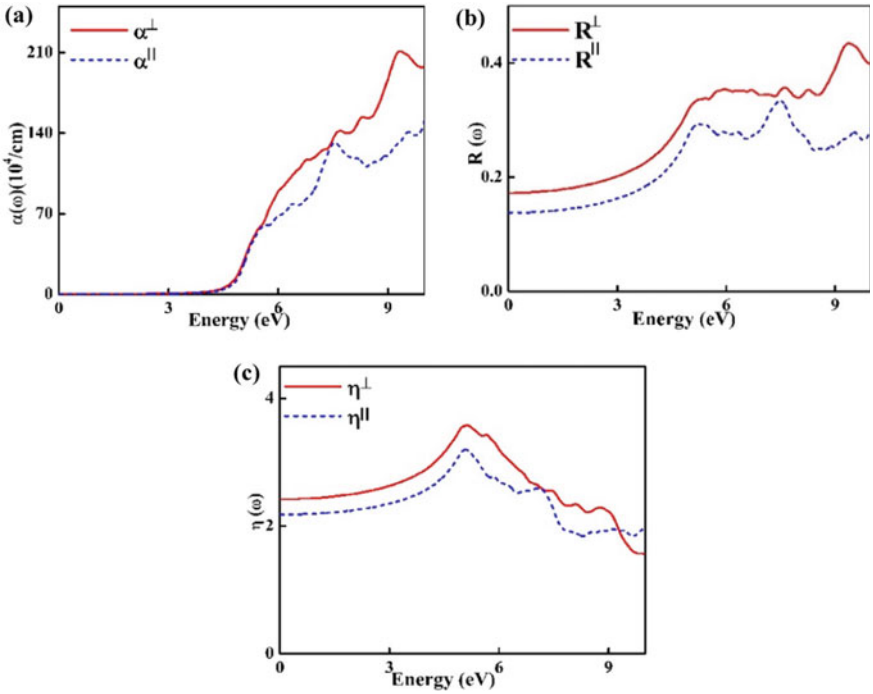

Fig. 5 **a** Absorption spectra, **b** reflectivity spectra, **c** refractivity spectra of $ZnCN_2$

4 Conclusion

By using FP-LAPW method, material properties of $ZnCN_2$ are investigated. The calculations of optical and electronic properties are done by utilizing by PBE- GGA. The electronic spectra showed that $ZnCN_2$ have wide direct band gap and is semiconductor in nature. The optical spectra confirm the anisotropic behavior of compound, and absorption spectra confirms the suitability of $ZnCN_2$ for optoelectronic devices.

Acknowledgements The Wien2k code is used in this work which is provided by Prof. P. Blaha, so we all authors showing a sincere gratitude to him. This work is funded by DST-SERB, New Delhi (India), vide grant number EMR/2017/005534. Also thanks to Manipal University Jaipur for all the support.

References

1. Khan K, Gaur A, Ahuja U, Soni A, Sahariya J (2020) Density functional investigations to study effect of M = (Ge, Sn) doping on opto-electronic response of ZnSi(1–x)MxP2. Optik 208:164570. https://doi.org/10.1016/j.ijleo.2020.164570

2. Luque A (2011) Will we exceed 50% efficiency in photovoltaics? J Appl Phys 110:031301. https://doi.org/10.1063/1.3600702
3. Bennacer H, Berrah S, Boukortt A, Ziane MI (2015) Electronic and optical properties of GaInX2 (X=As, P) from first principles study. Indian J Pure Appl Phys (IJPAP) 53:181–189
4. Bennacer H, Boukortt A, Meskine S, Hadjab M, Ziane MI, Zaoui A (2018) First principles investigation of optoelectronic properties of ZnXP2 (X = Si, Ge) lattice matched with silicon for tandem solar cells applications using the mBJ exchange potential. Optik 159:229–244. https://doi.org/10.1016/j.ijleo.2018.01.079
5. Kizaki H, Morikawa Y (2018) First-principles study of ZnSnAs2-based dilute magnetic semiconductors. Jpn J Appl Phys 57:020306. https://doi.org/10.7567/JJAP.57.020306
6. Kumar P, Soni A, Bhamu KC, Sahariya J (2017) Optoelectronic behavioral study of defect-chalcopyrite semiconductors XGa2Te4 (X=Zn, Cd). Mater Res Bull 86:131–138. https://doi.org/10.1016/j.materresbull.2016.10.012
7. Lavrentyev AA, Gabrelian BV, Shkumat PN, Nikiforov IY, Parasyuk OV, Khizhun OY (2015) The electronic structure of defect chalcopyrite CdGa2Se4 as determined from first principles calculations and X-ray spectroscopy studies. J Struct Chem 56:492–496. https://doi.org/10.1134/S0022476615030154
8. Zhu C, Verozubova GA, Mironov YP, Lei Z, Song L, Ma T, Okunev AO, Yang C (2016) Two-temperature synthesis of non-linear optical compound CdGeAs2. J Cryst Growth 455:129–135. https://doi.org/10.1016/j.jcrysgro.2016.09.057
9. Yu T, Wang S, Zhang X, Li C, Qiao J, Jia N, Han B, Xia S-Q, Tao X (2019) MnSiP2: a new mid-IR ternary phosphide with strong SHG effect and ultrabroad transparency range. Chem Mater 31:2010–2018. https://doi.org/10.1021/acs.chemmater.8b05015
10. Basalaev YM, Basalaeva OG, Sidorova AV (2020) A first-principles simulation of electronic structure of MCN2 crystals (M = Be, Mg, Ca, Zn, Cd, Hg). J Struct Chem 61:337–343. https://doi.org/10.1134/S0022476620030014
11. Suh C, Rajan K (2004) Combinatorial design of semiconductor chemistry for bandgap engineering: "virtual" combinatorial experimentation. Appl Surf Sci 223:148–158. https://doi.org/10.1016/S0169-4332(03)00918-8
12. Anatoly L, Gabrel'yan B, Nikiforov I (1998) X-ray spectra and electronic structure of several ternary chalcogenides and their solid solutions. J Struct Chem 39:884–889. https://doi.org/10.1007/BF02903598
13. Gou H-Y, Gao F-M, Zhang J-W, Li Z-P (2011) Structural transition, dielectric and bonding properties of BeCN 2. Chin Phys B 20:016201. https://doi.org/10.1088/1674-1056/20/1/016201
14. Yan H, Wei Q, Chang S, Guo P (2011) Ab initio study of ultra-incompressible ternary BeCN2 polymorph. J Phys Chem Solids 72:667–672. https://doi.org/10.1016/j.jpcs.2011.02.013
15. Basalaev YM, Emelyanova AM, Sidorova AV (2018) Crystalline, electronic, and vibrational structures of zinc cyanides. J Struct Chem 59:1761–1767. https://doi.org/10.1134/S0022476618080012
16. Ding P, Liang EJ, Jia Y, Du ZY (2008) Electronic structure, bonding and phonon modes in the negative thermal expansion materials of Cd(CN)2and Zn(CN)2. J Phys Condens Matter 20:275224. https://doi.org/10.1088/0953-8984/20/27/275224
17. de Rohello EL, Bour F, Suffren Y, Merdrignac-Conanec O, Guillou O, Cheviré F (2021) Synthesis and photoluminescence properties of Mn2+ doped ZnCN2 phosphors. Open Ceramics 7:100157. https://doi.org/10.1016/j.oceram.2021.100157
18. Zhao W, Pan J, Huang F (2018) Nonaqueous synthesis of metal cyanamide semiconductor nanocrystals for photocatalytic water oxidation. Chem Commun 54:1575–1578. https://doi.org/10.1039/C7CC09699B
19. Blaha P, Schwarz K, Tran F, Laskowski R, Madsen GKH, Marks LD (2020) WIEN2k: an APW+lo program for calculating the properties of solids. J Chem Phys 152:074101. https://doi.org/10.1063/1.5143061
20. Zada Z, Laref A, Murtaza G, Zeb A, Yar A (2019) First-principles calculations of electronic and magnetic properties of XMn2Y2 (X = Ca, Sr; Y = Sb, Bi) compounds. Int J Mod Phys B 33:1950199. https://doi.org/10.1142/S0217979219501996

Dynamic Electricity Pricing by Modified Levenberg-Marquardt Backpropagation (LMBP) Algorithm

Anirban Majumdar, Gurpinder Singh, Anil Swarnkar, Nikhil Gupta, and K. R. Niazi

Abstract Dynamic pricing is a pricing technique in which companies set extremely flexible costs for products or services based on customer demands. Dynamic pricing is famous because of its capacity to boost a company's revenue. Day-ahead electricity pricing is an important technique for producers of electricity, by which the grid stability can be improved by energy procurement price. In this paper, a novel technique of demand-side management (DSM) has been used to design individual price policies, where each and every end customer receives a separate electricity pricing scheme. This is designed to incentivize demand management in order to optimally manage flexible demands. A general artificial neural network-based stochastic process for consumer's power demand has been made to minimize the mean electricity price paid by the users. The projected pricing in Manchester's ISO New England market was calculated using MATLAB Software's ANN fitting tool. Hourly historical data of temperature, electrical load, and natural gas price from the ISO New England market were utilized in the forecasts. The artificial neural network (ANN) was trained on hourly data from 2004 to 2007 and evaluated on out-of-sample data in 2008. The simulation results revealed extremely accurate day-ahead estimates with very small amount of price forecasting error.

Keywords Artificial neural network (ANN) · Day-ahead electricity price forecasting (DEPF) · Demand-side management (DSM) · Levenberg–Marquardt backpropagation (LMBP)

1 Introduction

Price of electricity is a key issue in market competition, and high-quality short-term electricity price forecasting, particularly day-ahead electricity price forecasting

A. Majumdar (✉) · G. Singh · A. Swarnkar · N. Gupta · K. R. Niazi
Malaviya National Institute of Technology, Jaipur, India
e-mail: 2019pes5196@mnit.ac.in

G. Singh
e-mail: 2019ree9142@mnit.ac.in

© The Author(s), under exclusive license to Springer Nature Singapore Pte Ltd. 2022

A. Tripathi et al. (eds.), *Intelligent Computing Techniques for Smart Energy Systems*,
Lecture Notes in Electrical Engineering 862,
https://doi.org/10.1007/978-981-19-0252-9_54

(DEPF), is critical due to its cost-effective function in allowing all market participants to make rational decisions during market business activities. Recent energy networks are intended to maintain high-quality standards while delivering a consistent and dependable supply to fulfill the rising diversity of demand [1, 2].

The demand for improved short-term price forecasting methodologies has grown as wholesale power markets have deregulated. Short-term projections range from a few minutes to roughly a week in advance. These are helpful for short term or spot trade, as well as shipment. The day-ahead market is the subject of this research. Different academics have tried a variety of price predicting techniques with various degrees of success [1, 2].

Smart grid technologies are continually evolving and developing in order to meet these complex problems. Smart grid technology implementation confronts several obstacles, including optimizing distributed generation (DG) capacity, transmission and distribution (T&D) systems, and energy storage techniques [1–3].

In the energy industry, price forecasting is critical; it aids an independent generator in determining the best bidding patterns and establishing bilateral contracts. The many electrical businesses, in general, have required predict future electricity prices since their profitability is dependent on them. Because of the volatile nature of energy market prices, supply and demand-side managers face several challenges in the day-ahead power market. Knowing the previous information about energy market price changes may provide power suppliers an advantage in their short-term projection of their reasonable offerings. Furthermore, it assists power suppliers in establishing their bidding methods in order to maximize their profit on a large scale [2, 3].

With the current contributing factor that contributes to rising power costs, an appropriate estimation tool would be useful in assisting consumers in estimating prices based on previous data. They will have enough time to research the current state of the power market and plan their buy accordingly [4].

Demand-side management, on the other hand, has to be aware of market pricing changes and variances in order to establish short-term operational planning. As a result, price forecasting in the energy market has grown in interest in recent times [4].

This study compares and contrasts the training strategies for artificial neural networks created for the aim of forecasting short-term power costs. To analyze the training techniques, the training error, the number of iterations required reach the target error, and the capacity to generalize after training are utilized [4].

The approaches analyzed are as follows: Levenberg–Marquardt BP (LMBP) algorithm trained with backpropagation and feed-forward network trained with genetic algorithm. Based on the basic concept of backpropagation, a more efficient training algorithm of LMBP method is proposed.

2 Literature Review

The strategy of adjusting price over time is known as dynamic pricing. Dynamic pricing, in the context of electricity, is a technique for deciding how electricity tariffs change over time, with time being customized to the electrical load. Customer's behavior to change power usage might be influenced by dynamic electricity pricing. The average consumption behavior is to move power demand from one period to another, causing the peak load to occur at a time when electricity demand is typically low. Making a proper plan for using household appliances may help you save a lot of money on your energy bills.

Time of use (TOU), critical peak pricing (CPP), and real-time pricing (RTP) are three well-known dynamic pricing schemes in the energy industry. Peak rebate time (PRT) is one of the other initiatives.

2.1 Time of Use (TOU)

The objective of time-of-use tariffs is to better align energy users' bills with the real cost of production. Most utilities adjust household power tariffs once or twice a year at the moment. This rate, which is represented in dollars or cents per kilowatt-hour ($/kWh), is meant to cover the total cost of generating the power that users consume [5, 6].

The cost of power at a utility, on the other hand, varies during the day for a variety of reasons. Historically, as the demand for energy rises during the day, the cost of generating that electricity rises as well. Residential users have little visibility into how the cost of power climbs and decreases each day without a time-varying electricity tariff [5, 6].

Some utilities bill consumers are using time-of-use rates, which are a form of power pricing. Customers pay various rates per kilowatt-hour (kWh) of power they use depending on when they use it under a TOU tariff. Pricing varies depending on the time of day, as well as the day of the week (weekend or weekday) and the season.

TOU rates are distinguished by pricing differences between "peak" and "off-peak" hours; some rates additionally have other price periods in between.

Both residential and business clients may be subject to TOU tariffs. The exact specifications of a customer's TOU rate will be determined by the electric utility's individual rate plan [1–4, 7].

2.2 Real-Time Pricing (RTP)

Real-time pricing, is well-known technique of dynamic pricing, is a system in which the per-kWh charge changes every hour based on the utility's current cost of production. Retail energy costs are higher at peak hours than during shoulder and off-peak times under real-time pricing because peaking facilities are more costly to operate than base-load plants. Customers earn higher peak rates when supplying power into the grid at peak hours when combined with net metering. The client is most likely purchasing electricity from the grid during off-peak hours, albeit at a cheaper off-peak cost [8, 9].

In smart grid systems, the real-time pricing (RTP) scheme is an excellent way to alter the power balance between supply and demand. In the energy business, this strategy has a significant influence on user behavior, system operation, and overall grid management [8, 9].

Real-time pricing (RTP) has been called the wave of the future and a reasonable reaction to competition, among other things. In principle, it allows utilities to deliver effective pricing signals to their consumers, allowing them to control loads, save costs, and optimize profits. As a result, it might be a beneficial approach for utilities to boost competitiveness and promote customer retention and growth [1–4, 7].

2.3 Critical Peak Pricing (CPP)

Critical peak pricing (CPP) offers customers with timely information about energy costs, particularly during peak energy consumption periods. This information aids in making more precise judgments about energy usage efficiency. The CPP gives consumers more precise information about energy costs, especially during peak energy usage periods, so they may make more informed decisions about their power consumption. While power prices are higher during CPP events, the CPP rate is low at all other times. This distinction allows consumers to better analyze and perhaps lower their overall annual energy costs.

Critical peak pricing is a tariff option that reduces load on particular days in order to balance demand and supply. On these limited days, the power tariff is raised, but on non-constrained/normal days, the tariff is reduced. Customers are notified (usually a day ahead of time) that the day is a key peak day on certain limited days. Customers will have the option of either limiting or lowering their use or paying the crucial peak day prices as a result of this. The critical peak day pricing allows consumers to save money on their overall power bill by curtailing, reducing, or shifting their electricity use during CPP days [5, 6, 10, 11].

2.4 Peak Rebate Time (PRT)

It is a program that pays members who save energy on days when a "peak event" is announced. When you use a lot of electricity, it costs more. This is because more electricity is required to maintain the system on days when demand is high. This extra electricity is usually derived from inefficient and expensive resources. By having users voluntarily limit usage during peak events, customers are able to avoid purchasing power from higher-cost resources [6].

2.5 Dynamic and Customized Pricing

The research presented in this study looked to represent the time-varying cost of delivering power, dynamic pricing results in differing power prices at different periods of every day and year. However, due to growing demand, utilities will be forced to purchase electric energy industry to fulfill their short and medium demands. Because the method is spread, both the utility and the end consumer gain from it. The goal of this endeavor is unique in comparison to previous programs; nonetheless, end users with a main goal of cost reduction are not given precedence [12, 13].

On the other side, if capacity is expanded over a certain threshold, the customer can profit from renewable energy. The authors solve this challenge by employing a reinforcement learning technique that requires no prior information of either the consumer or the business. Utility companies, on the other hand, can employ DP to help stabilize the power grid [5, 11].

3 Load Types

The loads are classified into the following groups depended on their power demand and rated power: such that [d_l, c_l, mr_l] (i) discrete load (d_l), (ii) continuous load (c_l), and (iii) must run load (mr_l). The EMC is in charge of controlling the d_l and c_l working cycles, respectively. To maximize user comfort, the mr_l does not participate in the scheduling process. These loads are seen as being turned on according to the need of the users. Due to their adaptability, d_l duty cycles may be changed throughout operating time. In other words, consumers can tolerate delays caused by differences in appliance start times. *cl*, on the other hand, cannot be switched off when in action. Because once these loads are switched on, they complete their duty cycles. Figure 1 depicts the load demand for each load. The specifications of how these loads are functioning are explained further below [1, 8, 9].

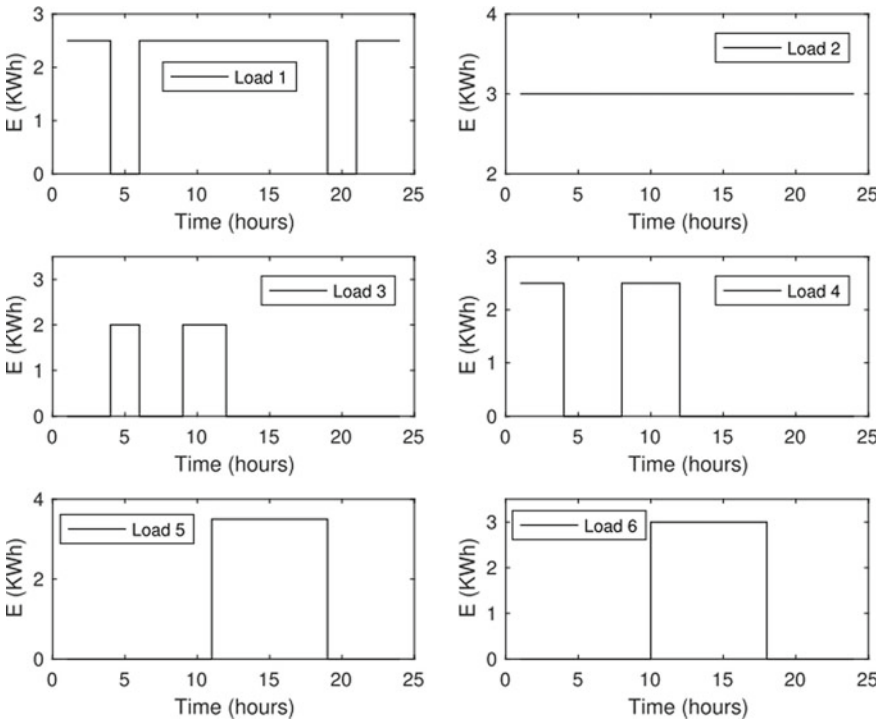

Fig. 1 Day profile of energy demand

3.1 Must Run Load (MR_L)

m_{rl} does not participate in the DR program; thus, it is not planned at that period. Although as seen in Fig. 1, this load has set scheduling intervals of 24 h. As a result, it is required that these loads require a constant source of electricity to complete the needed work within the specified time frame. E_{mrl} and $\wp_{mr}$ stand for the energy demand and power rating of mr_l, correspondingly [8, 9]. The following equation is used to compute mr_l's total energy consumption

$$E_{mrl(t)} = \sum_{mrl} \sum_{t \in T} \left(\wp_{mr(t)} \times \beta_{mrl(t)} \right)$$

where β_{mrl} stands for the TURNON/TURN OFF status of m_{rl}

$$\mathrm{B}_{mrl} = \begin{cases} 1 & \text{when the load is turned on} \\ 0 & \text{when the load is turned off} \end{cases}$$

3.2 Discrete Load (D_L)

It is supposed that d_l's power consumption may be shifted from one time slot to another in order to lower total costs. In other words, this load is different implementations, and its usual operation can be relocated or modified at any moment, independent of the time intervals defined by the user. This guarantees the lowest possible energy consumption price, but customer satisfaction in cases of scheduling delay must be sacrificed. E_{dl} is a representation of d_l's power usage [9, 12]. If $\wp_{dl}$ stands for d_l's power rating, the total energy demand is computed as follows:

$$E_{dl(t)} = \sum_{dl} \sum_{t \in T} \left(\wp_{dl(t)} \times \beta_{dl(t)} \right)$$

where β_{dl} stands for the TURN ON/TURN OFF status of d_l

$$\mathrm{B}_{dl} = \begin{cases} 1 & \text{when the load is turned on} \\ 0 & \text{when the load is turned off} \end{cases}$$

3.3 Continuous Load (C_L)

It is supposed that unlike d_l, the power consumption of c_l may be scheduled; nevertheless, once planned, regular operations cannot be disrupted. If a load requires 5 kW of electricity, for example, the scheduling algorithm meets the need by changing the schedules the demand in different slots depending on lowest cost intervals. Customers, on the other hand, must endure longer scheduling delays [9, 12]. When compared to other forms of load, this load would contribute immensely to more optimized results

$$E_{cl(t)} = \sum_{cl} \sum_{t \in T} (\wp_{cl(t)} \times \beta_{cl(t)})$$

where β_{cl} shows the state of c_l and can be stated as follows:

$$\mathrm{B}_{cl} = \begin{cases} 1 & \text{when the load is turned on} \\ 0 & \text{when the load is turned off} \end{cases}$$

$$E_{u(t)} = \sum_{cl} \sum_{t \in T} \left(E_{mrl(t)} + E_{dl(t)} + E_{cl(t)} \right)$$

Table 1 Power usage of appliances and duty cycles

Load type	Loads	Duty cycle (h)	Energy consumption (kW)
mr_l	Load 1	20	2.5
	Load 2	24	3
c_l	Load 3	5	2
	Load 4	7	2.5
d_l	Load 5	8	3.5
	Load 6	8	3

However, because of a lack of understanding of variations in consumer load demand, it is difficult to apply. Similarly, pricing variations make it harder for customers to manage their loads. Dynamic pricing is a pricing approach in which companies set highly robust costs for business will depend on market demand. Dynamic pricing is famous because of its capacity to boost a company's revenue. China, Japan, and Korea are three Asian nations that popularized the use of dynamic pricing in the electrical sector [12, 13].

4 Artificial Neural Network for Price Forecasting

Neural networks are made up of basic pieces called neuron that operate together in a parallel manner. A neuron is a data processing component that is essential for a neural network's functionality. The neuron model is made up of three fundamental components. Firstly, there is an adder for summation of the input signals. Secondly, there is an activation function to limit the magnitude of the output of a neuron. ANN techniques are highly inspired by the biological nervous systems. Artificial neural network is made to perform an adjustment of a particular function by changing the weights of the variables of connection between the elements. Figure 2 is showing the pictorial representation of ANN algorithm. In price forecasting, many input pairs are needed to design the model of neural network.

ANN is designed between a data collection of numeric inputs and a collection of numeric goals in fitting problems. A two-layer feed-forward network with sigmoid hidden neurons and linear output neurons make up the neural network matching tool. Given consistent input and enough neurons in its hidden layer, it can suit multi-dimensional mapping problems arbitrarily well. The Levenberg–Marquardt backpropagation method is used to train the neural network.

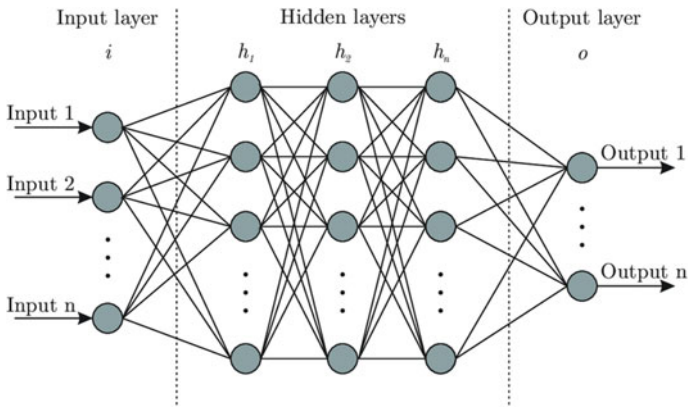

Fig. 2 Multilayer model of artificial neural network

4.1 Backpropagation Algorithm

For classification and optimization problems, artificial neural networks have been widely explored. The designed algorithm for multilayer neural networks is back-propagation. In this technique, the slope from the summation of the squared errors with respect to the individual variables weightage is adjusted by the following toward the negative direction. This is an implementation of recursiveness of the chain rule for the derivatives. This is old-fashioned technique; because by this algorithm, the curvature of the loss is not eliminated properly, and this algorithm works only on the basis of gradient descent [14–18].

$F(w)$ is the performance index.

$$F(w) = e^T e$$

where $w = [w_1, w_2, \ldots, w_N]$ depicts of all weightages of the variables of the network, e is the representation of error vector showing the errors for each and every designed examples. The chronology to implement the backpropagation algorithm is given below:

1. *Initialize each and every weightage* (w_l) *by putting a small random values*
2. *Unless the termination condition is achieved, it must be done for each training example* $< (x_l, \ldots, x_n), t >$ (t *is the required output*)
   (a) *Input the time* $(x_l, \ldots, x_n)$ *to the network and calculate the network outputs* O_k
   (b) *For every output layer k,* $\delta_k = O_k(l - O_k)(t_k - O_k)$
   (c) *For every hidden layer h,* $\delta_h = O_h(1 - O_h) \sum_k w_{h,k}\delta_k$
   (d) *For every network variable weightage, do* $w_{i,j} = w_{i,j} + \Delta w_{i,j}$ *where* $\Delta w_{i,j} = \eta \delta_j x_{i,j}$

η is the rate of learning, which is described by the customers. The algorithm will converge to its desired value when the slope will be lesser than the predetermined value of the minimum error value [14–18].

4.2 Levenberg–Marquardt Algorithm

Levenberg–Marquardt (LM) technique is a curve fitting mechanism which is a compilation of two famous algorithms named Newton–Raphson algorithm and the gradient descent mechanism. It is used to calculate the nonlinear equations. The Levenberg–Marquardt (LM) mechanism is an iterative technique that figures out the least of a multivariable function which is expressed by the summation of square of the nonlinear functions having real value. In present, it is a proper method for problems having minimum squares in the nonlinear equation. When the present evaluation is very different from the actual values, the mechanism works as a steepest descent algorithm: slow, but confirmed to be converged in desired value. When the present evaluation is closer to the desired values, it works as a Gauss–Newton algorithm [14–18].

Designing the LM method, the increase of weights Δw can be calculated as follows:

$$\Delta w = [J^T(w)J(w) + \mu I]^{-1} J^T(w)e$$

$J(w)$ is the Jacobian matrix,

$J^T(w)J(w)$ is the Hessian matrix,

I is the identity matrix,

μ is the update rate of learning, depends on the outcome,

β is the decay rate (0–1).

The normal LM designing method can be described in the following steps:

Initialize the weightages and the value of μ.

1. *Calculate the summation of the squared errors for all the inputs* $F(w)$.
2. *Until the termination condition is met, do*

   (a) *Calculate (2) to get the increase of the weightages of* Δw.

   (b) *Using* $w + \Delta w$ *as the trial* w *and judge IF trial* $F(w) < F(w)$ *in step (2) THEN*

   $w = w + \Delta w, \mu = \mu\beta$

   Go back to step (2)

   ELSE, $\mu = \mu/\beta$.

   Go back to step (a)

END IF

This is quite similar with BP mechanism; the LM mechanism is converged when the value of the slope is lesser than some predefined value. When $\mu = 0$, the mechanism becomes Gauss–Newton algorithm. When $\mu = 1$, then, LM mechanism works like the steepest decent algorithm. The values are adjusted each and every iteration to set the convergence [14–18].

5 Performance Evaluation

The ANN models' projections have been compared to those of alternative approaches in order to assess their performance. For this aim, there are a variety of alternatives. The mean absolute percentage error (MAPE) is a popular approach for evaluating price predicting effectiveness [19, 20]. This is how the mean average percent error is defined:

The percentage error (PE) is defined as:

$$\mathrm{PE} = \frac{(X_{\text{forecasted}} - X_{\text{actual}})}{X_{\text{actual}}} \times 100\%$$

The value of is *APE*: $\mathrm{APE} = |\mathrm{PE}|$

The *MAPE* is calculated as

$$\mathrm{MAPE} = \frac{1}{N} \sum_{i=1}^{N} (\mathrm{APE}_i)$$

where

$X_{\text{forecasted}}$: the forecasted value of price.

X_{actual}: the original value of price.

N: no. of designed data.

6 Results and Discussion

6.1 Proposed Artificial Neural Network Model

MATLAB SIMULINK software has been used here to develop an artificial neural network model, by which the forecasting of load and price have been done properly. By using this MATLAB program, a mathematical model is going to be developed

using previous data of Manchester city in England. After creating the mathematical model, the model is tested by comparing the data forecasted by this model and an actual data of the same Manchester. At the end, the percentage error has also been calculated from the comparison of forecasted and actual data sheet. Then, the efficiency of the mathematical model has been figured out. In this model, there are one input layer, two hidden layers, and one output layer. Input layer is consisted of historical pricing data and system load. In this paper, the Levenberg–Marquardt BP (LMBP) approach is utilized instead of the traditional backpropagation (BP) approach for artificial neural network training to get a proper boost in the time of convergence.

6.2 Simulation Results

In this paper, the mathematical model has one input layer, two hidden layers, and one output layer. The hidden layer consists of total 48 neurons which are chosen in such a way, it gives lesser percentage error. A datasheet of load and price Manchester city from the year 2004 to 2007 has been used from ISO ENGLAND Web site is the input of this ANN model. The mathematical model has been compared with the original load data of the year 2008 of the same city. Figure 3 shows a comparison between forecasted data and actual data for the entire year. The 2nd part of the graph depicts the percentage error between data for each hour of the day in 2008.

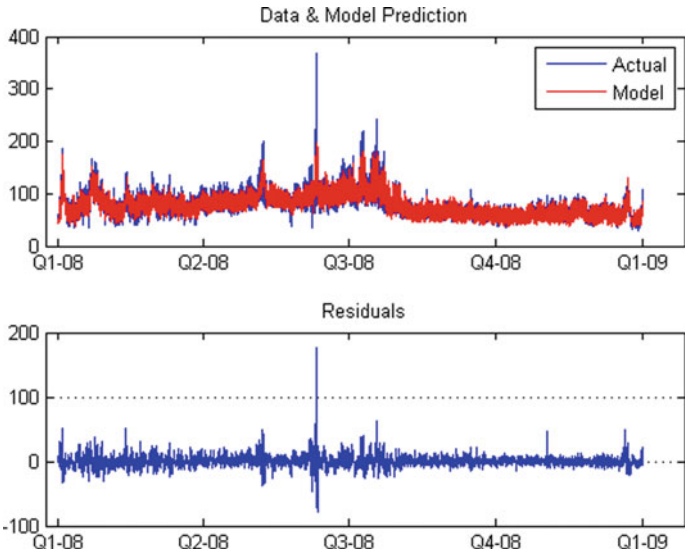

Fig. 3 Yearly comparison of forecast price and actual price

From this graph, it is shown that the mean average error (MAE) is almost $6.03, and the value of daily peak MAPE is approximate 6.54%. The value of the mean average percent error (MAPE) of this model has come around 7.41%. It is clearly visible that in the year 2008, the maximum error can be found almost around in the 21st hour of the day. It has also been figured out that the least error has been found more or less for the 14th hour of the day.

Figure 4 is showing the comparison between forecasted data and actual data of different months of 2008. Along with the comparison, MAPE is shown for each and every month so that efficiency of this model can be checked.

In Fig. 4, it shows that the two weekly comparison between the forecasted and actual data. There it is shown that the forecasted curve has almost followed the actual curve. Therefore, it shows the accuracy of the ANN mathematical model proposed in this paper. In Fig. 4, the residuals between the actual and forecasted curve have been converted to MAPE. The MAPE for every two weeks throughout the entire year 2008 has been deducted, and the average value of the mean average percent error (MAPE) for the entire year 2008 is calculated, which is around 7.411%. The first 4 week's comparison curve and the MAPE have been shown in Fig. 4.

In the 1st part of Fig. 4, the comparison curve between forecasted and actual data from January 1st, 2008 to January 14th, 2008 has been shown, and it is clearly visible that the MAPE for the 1st two weeks is almost 11.63% which is higher than the average value of MAPE for entire year by a little amount. Therefore, the MAPE for entire year 2008 has been deducted by taking two weeks per slot. As the average value of MAPE is 7.411%, it can be said easily that the ANN model proposed in this paper is around 92.589% accurately forecasted the price, which is quite high.

For the goal of finding the best value, the quantity of neurons in the hidden layer (n), can be ranged from 1 to 50. Due to the random nature of weights initialization, each training procedure with a given n is repeated 50 times to obtain the optimal MAPE, after which the average MAPE, lowest MAPE, and maximum MAPE for each and every value of n are calculated. The optimum solution has been found for the neuron number 48 in the hidden layer.

The suggested system comes to a conclusion, based on the findings of the proposed model. The experimental findings demonstrate that the predicted results are quite accurate. When there isn't a lot of variation between each hour and day, these findings are collected. With regard to the England electricity market, this paper is an attempt to research and analyze market pricing in the day-ahead market.

Table 2 is showing the mean average percent error (MAPE) of the entire year taking two weeks per slot. From this Table 2, the value of the average mean average percent error (MAPE) can be easily evaluated, which is approximately 7.411%.

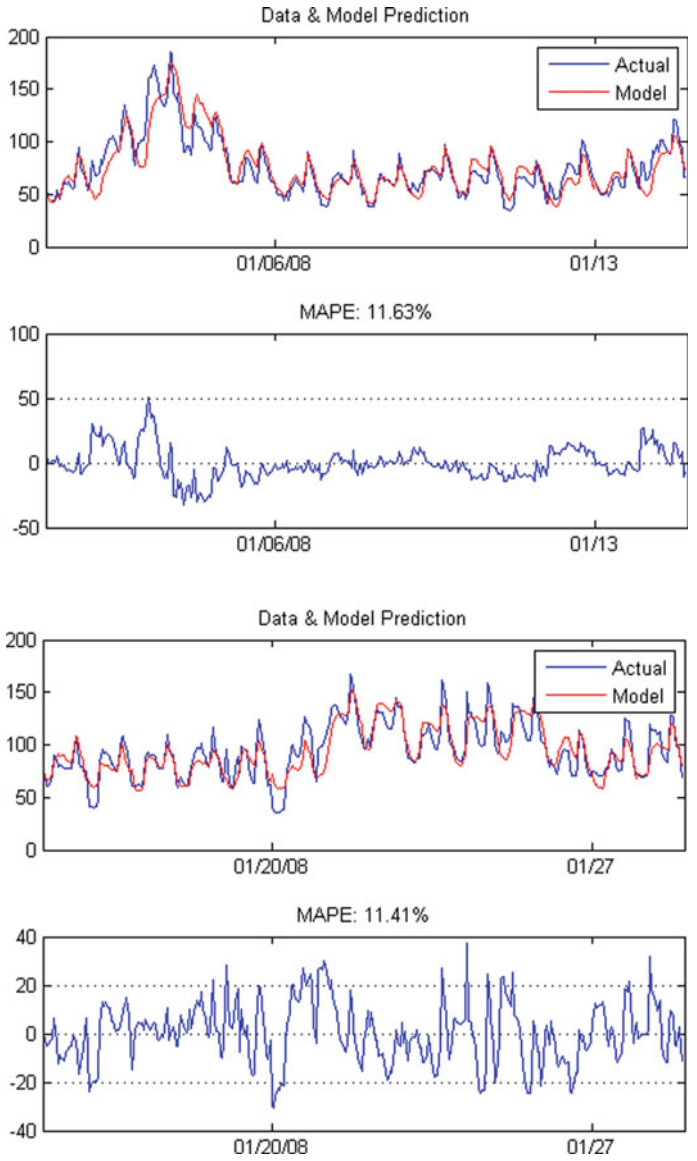

Fig. 4 Comparison of forecasted and actual price along with mean average percent error (MAPE) for first 4 weeks of the year in the test set

Table 2 Mean average percent error (MAPE) of entire year taking two weeks per slot

Date from	To date	MAPE (%)
01/01/2008	14/01/2008	11.63
15/01/2008	28/01/2008	11.41
29/01/2008	10/02/2008	9.19
11/02/2008	24/02/2008	9.63
25/02/2008	09/03/2008	8.24
10/03/2008	23/03/2008	6.91
24/03/2008	06/04/2008	6.17
07/04/2008	20/04/2008	4.66
21/04/2008	04/05/2008	5.95
05/05/2008	18/05/2008	7.46
19/05/2008	01/06/2008	6.20
02/06/2008	15/06/2008	13.93
16/06/2008	29/06/2008	5.86
30/06/2008	13/07/2008	7.40
14/07/2008	27/07/2008	7.93
28/07/2008	10/08/2008	6.62
11/08/2008	24/08/2008	5.79
25/08/2008	07/09/2008	6.54
08/09/2008	21/09/2008	6.90
22/09/2008	05/10/2008	5.40
06/10/2008	19/10/2008	5.84
20/10/2008	02/11/2008	5.35
03/11/2008	16/11/2008	5.14
17/11/2008	30/11/2008	4.90
01/12/2008	14/12/2008	6.37
15/12/2008	28/12/2008	11.28

7 Conclusion

In this paper, artificial neural network Levenberg–Marquardt BP (LMBP) method has been used to estimate forecasting of load and price, i.e., the day-ahead predictions of energy market characteristics throughout a week. Hourly historical data of temperature, electrical load, and natural gas price from 2004 to 2007 of the ISO New England market were utilized in the forecasts to train the artificial neural network was developed on hourly data and tested with the sample data from 2008. The simulation results were accurate with a little error in the day-ahead estimates of load and price prediction. To get further improvement, the number of hidden layers should be increased. It can be noted that by using this technique, the forecasted price has an average mean percent error of 7.411%. It has been shown that the proposed

technique for price forecasting provides better results than using the conventional backpropagation technique.

Acknowledgements This paper is supported by the associate professor of Department of Electrical Engineering, Malaviya National Institute of Technology, Jaipur, Rajasthan **Dr. Anil Swarnkar**.

References

1. Rasheed M, Qureshi M, Javaid N, Alquthami T (2020) Dynamic pricing mechanism with the integration of renewable energy source in smart grid. IEEE Trans Smart Grid 8
2. Singh G, Swarnkar A, Gupta N, Niazi KR (2020) A review of scheduling techniques and communication protocols for smart homes capable of implementing demand response. In: Intelligent computing techniques for smart energy systems, pp 505–513
3. Hung Y-C, Michailidis G (2019) Modeling and optimization of time-of use electricity pricing systems. IEEE Trans Smart Grid 10(4):4116–4127
4. Sahay K, Tripathi MM (2013) Day ahead hourly load and price forecast in ISO New England market using ANN. IEEE Trans Smart Grid
5. Huang H, Li H, Mishra Y (2015) Modeling dynamic demand response using monte Carlo simulation and interval mathematics for boundary estimation. IEEE Trans Smart Grid 6(6)
6. Chen W, Qiu F, Chai Q (2021) Customized critical peak rebate pricing mechanism for virtual power plants. IEEE Trans Sustain Energy
7. Jayasurya S, Kumar V (2012) Smart grid infrastructure for efficient power consumption using real time pricing algorithm and distributed algorithm. IEEE Trans Smart Grid
8. Gibo N, Kikuma T, Takenaka K, Hatano R, Yamamoto N (2009) Estimation method of load type and capacity by using starting load characteristics. In: 2009 IEEE/PES power systems conference and exposition, 24 Apr 2009
9. Wu J, Huang Y, Gao W, Schulz N (2006) Power system load modeling in virtual test bed. In: 2006 IEEE power engineering society general meeting, 16 Oct 2006
10. Papadaskalopoulos D, Fatouros P, Strbac G (2018) Addressing demand response concentration under dynamic pricing. IEEE Trans Power Syst 13(2):688–694
11. Niu C, Zheng Z, Wu F, Tang S, Chen G (2020) Online pricing with reserve price constraint for personal data markets. IEEE Trans Power Syst
12. Wang J, Yang L, Ma Y, Wang J, Tolbert L, Wang F, Tomsovic K (2016) Static and dynamic power system load emulation in a converter-based reconfigurable power grid emulator. IEEE Trans Power Electron 31(4)
13. Shiri A, Afshar M, Rahimi-Kian A, Maham B (2015) Electricity price forecasting using support vector machines by considering oil and natural gas price impacts. In: 2015 IEEE international conference on smart energy grid engineering (SEGE), 12 Nov 2015
14. Tang Q, Gu D (2009) Day-ahead electricity prices forecasting using artificial neural networks. In: 2009 IEEE international conference on smart energy grid engineering (SEGE), 12 Nov 2009
15. Nargale KK, Patil SB (2016) Day ahead price forecasting in deregulated electricity market using artificial neural network. In: 2016 International conference on energy efficient technologies for sustainability (ICEETS), 06 Oct 2016
16. Chogumaira EN, Student Member, IEEE, Hiyama T, Senior Member, IEEE (2009) Training artificial neural networks for shortterm electricity price forecasting. In: 2009 Transmission & distribution conference & exposition: Asia and Pacific, 18 Dec 2009
17. Pourdaryaei A, Mokhlis H, Illias H, Kaboli HS. Ang S (2019) Hybrid ANN and artificial cooperative search algorithm to forecast short-term electricity price in de-regulated electricity market. IEEE Access 7

18. Jia-li T, Yi-jun L, Fang-sheng W (2010) Levenberg-Marquardt neural network for gear fault diagnosis. In: 2010 International conference on networking and digital society, 07 June 2010
19. Shahid A (2018) Smart grid integration of renewable energy systems. In: 2018 7th International conference on renewable energy research and applications (ICRERA), 10 Dec 2018
20. Bhalshankar S, Thorat C (2017) Integration of smart grid with renewable energy for energy demand management: Puducherry case study. In: 2016 International conference on signal processing, communication, power and embedded system (SCOPES), 26 June 2017
21. Zhou M, Li X, Li G (2008) Approach on pricing electricity for large consumers based on hedonic price model. In: 2008 Third international conference on electric utility deregulation and restructuring and power technologies, 16 May 2008
22. Dunbar A, Tagliaferri F, Viola IM, Harrison GP (2014) The impact of electricity price forecast accuracy on the optimality of storage revenue. In: 3rd Renewable power generation conference (RPG 2014), 22 Dec 2014
23. Gao G, Lo K, Lu N (2017) Risk assessment due to electricity price forecast uncertainty in UK electricity market. In: 2017 52nd international universities power engineering conference (UPEC), 21 Dec 2017
24. Javedani S, Rasul E, Hisyam L, Maqsood M (2016) A hybrid model based on differential fuzzy logic relationships and imperialist competitive algorithm for stock market forecasting. Appl Soft Comput 40:132–149
25. Chen-Yin K (2016) Does the vector error correction model perform better than others in forecasting stock price? An application of residual income valuation theory. Econ Model 52:772–789
26. Salim L, Mounir B (2015) Intelligent ensemble forecasting system of stock market fluctuations based on symetric and asymetric wavelet functions. Fluctuat Noise Lett 14(4)
27. Lin Z, Yingmin J (2016) Neural network-based adaptive consensus tracking control for multi-agent systems under actuator faults. Int J Syst Sci 47(8):1931–1942
28. Toly C, Yu-Cheng W (2016) Estimating simulation workload in cloud manufacturing using a classifying artificial neural network ensemble approach. Robot Comput-Integr Manuf 38:42–51
29. Nikolic S, Antic D, Milojkovic M, Milovanovic M, Mitic D (2016) Application of neural networks with orthogonal activation functions in control of dynamical systems. Int J Electron 103(4):667–685
30. Schofield L, Mark D, Steven H (2016) Radiometric calibration of a dual-wavelength terrestrial laser scanner using neural networks. Remote Sens Lett 7(4):299–308
31. Jose L, Laura L, Chrisina J (2016) An empirical study of neural network-based audience response technology in a human anatomy course for pharmacy students. J Med Syst 40(4)
32. Chengyang W, Yoshihiko N (2015) Volatility forecast of stock indices by model averaging using high-frequency data. Int Rev Econ Finance 40:324–337
33. Mandi R, Reza A, Mohammad A (2015) Stock price forecasting for companies listed on Tehran stock exchange using multivariate adaptive regression splines model and semi-parametric splines technique. Phys A-Stat Mech Appl 438:625–633
34. Soman S, Zareipour H, Malik O, Mandal P (2010) A review of wind power and wind speed forecasting methods with different time horizons. North American power symposium, pp 1–8, Sept 2010, ISBN: 978-1-4244-8046-3
35. Haque A, Mandal P, Meng J, Kaye M, Chang L (2012) A new strategy for wind speed forecasting using hybrid intelligent models. In: IEEE Canadian conference on electrical and computer engineering, pp l–4, 29 Apr 2012–02 May 2012, ISSN: 0840 7789, ISBN: 978-1-4673-1431-2
36. Tao H, Srivastava A, Pineda R, Mandal P (2012) Wind power generation impact on electricity price in ERCOT, San Diago, CA, pp 1–7, July 2012, ISSN: 1944-9925, ISBN: 978-1-4673-2727-5
37. Haque A, Mandal P, Meng J, Srivastava A, Tseng T, Senjyu T (2012) A novel hybrid approach based on wavelet transform and fuzzy ARTMAP network for predicting wind farm power production. Annual meeting on industrial applications society, pp 1–8, Oct 2012, ISSN: 0197 2618, ISBN: 978-1-4673-0330-9

38. Manda IP (2014) Application of an artificial neural network to study the transient stability of an alternator connected to infinite bus. In: 1ST international conference on non conventional energy, pp 224–227, Jan 2014, ISBN: 978–1–4799–3339-6
39. Goude Y, Nadellec R, Kong N (2014) Local short and middle term electricity load forecasting with Semi parametric additive models. IEEE Trans Smart Grid 5(1):440–446. ISSN: 1949-3053
40. Zareipour H, Cañizares C, Bhattacharya K (2010) Economic impact of electricity market price forecasting errors: a demand side analysis. IEEE Trans Power Syst 25(1):254–262. ISSN: 0885-8950
41. Yun Z, Quan Z, Caixin S, Shaolan L, Yuming L, Yang S (2008) RBF neural network and ANFIS based short term load forecasting approach in real time price environment. IEEE Trans Power Syst 23(3):853–858. ISSN: 0885-8950
42. Liang R, Cheng C (2002) Short-term load forecasting by a neuro-fuzzy based approach. Electr Power Energy Syst 24(2):103–111
43. Rixing H, Chongqing K, Qing X (2000) System marginal price forecasting in electricity market. Automat Electr Power Syst 24(22):9–12
44. Fei J, Feng Z (2003) Application of fuzzy neural network to power system short-term load forecast. Control Theory Appl 22(8):23–26
45. Guo L, Xiangming F, Fuying G (2002) Forecasting, market—clearing price in Zhejiang generation market using neural network. Automat Electr Power Syst 26(9):49–52
46. Nogales FJ, Contreras J, Conejo AJ et al (2006) Forecasting next-day electricity prices by time series models. IEEE Trans Power Syst 17(2)
47. Shehle G (1996) Price based operation in an auction market structure. EEE Trans Power Syst 11(4):1770–1777
48. Bunn DW (2000) Forecasting loads and prices in competitive power markets. Proc IEEE 88(2):163–169
49. Sun W, Lu J, Meng M (2006) Application of time series based SVM model on next-day electricity price forecasting under deregulated power market. In: Proceedings of the fifth international conference on machine learning and cybernetics, pp 13–16
50. Zhao J, Dong Z, Li X, Wong K (2007) A framework for electricity price spike analysis with advanced data mining methods. IEEE Trans Power Syst 22(1)
51. Szkuta B, Sanabria L, Dillon T (1999) Electricity price short-term forecasting using artificial neural networks. IEEE Trans Power Syst 14(3):851–857

Outlier Detection and Clustering of household's Electrical Load Profiles

Gurpinder Singh, Anil Swarnkar, Nikhil Gupta, and K. R. Niazi

Abstract The concept of data analysis exit in the literature theoretically for years. However, rapidly increasing technology has facilitated the practical implementation also. However, the data science field has excelled to its limits in various fields, but still, a lot of scope for research exists in data analysis for a power system. As each field has salient features, the power system also has its own salient features and complexities. One of such complexity is dealt with in this paper, i.e., outliers detection from residential customers' electrical load profile. Due to salient features of residential customers' load profiles, most of the algorithm results in false detection. In this paper, a novel approach to detect outliers dedicated to residential customers load profiles is proposed. After outlier detection, the clustering of different consumer's profiles is done using k-means clustering. Each cluster is represented with a class representative profile to reduce the computation burden of the aggregator and extract better high-grade information from it.

Keywords Outlier detection · Outliers in power system · Residential customer's load profile analysis · Data analysis in power system · Data-driven demand side management · K-means clustering

1 Introduction

With rapidly growing rate of smart meter's (SM) installation, by the end of 2020, 107 million SMs were deployed in the U.S. itself [1]. A single information about load consumption for 15 min is of about 10 kilobytes [2] and in a year about 35,000 readings are recorded. Therefore, single meter will generate about 350 megabytes and 100 million SMs will generate about 35 petabytes of data in a year. The amount of data is huge with the huge concealed potential. This residential data has its own unique features and complexities [3]. Therefore, it requires special modifications in

G. Singh (✉) · A. Swarnkar · N. Gupta · K. R. Niazi
Malaviya National Institute of Technology, Jaipur, India
e-mail: 2017pes5202@mnit.ac.in; 2019ree9142@mnit.ac.in

© The Author(s), under exclusive license to Springer Nature Singapore Pte Ltd. 2022

A. Tripathi et al. (eds.), *Intelligent Computing Techniques for Smart Energy Systems*,
Lecture Notes in Electrical Engineering 862,
https://doi.org/10.1007/978-981-19-0252-9_55

existing algorithms for data analysis. One of such a problem is outlier detection from residential data.

Outliers are basically the data points which exist in data as a noise or error [4]. Outlier detection is the foremost step to be done before fitting any model. There are many techniques exits in literature for outlier detection. However, major techniques assume the data to be normally distributed and are not suitable for residential customer's load profile dataset. The residential customers load consumption profile (RCLP) have various salient features due to which, most existing methods give a high fault detection rate. RCLP requires a dedicated algorithm for outlier detection, which considers the salient features of RCLP.

There exist various techniques in literature for outlier detection like p-test [5], quantile regression [6], regression forest [7], etc. The dedicated literature for outlier detection from RCLP is very little. In [8], the authors have proposed the density-based outlier detection but it was for based load detection. Work in [8], is detection of baseload's outlier detection, instead of outlier detection from RCLP. In [9], the identification model has been proposed for outliers in behavior detection of the residential customer. Work in [9] is based on SVM model, and can be used for outlier detection of RCLP.

Training a model with the data containing outlier will not be an efficient model. After cleaning data, the later part of the paper performs clustering of RCLP using the K-means algorithm. Due to large volume and high diversity of the RCLP it becomes necessary to cluster them into groups. As using the aggregated data will lead to masking of information that might be crucial for the program. To form an efficient program the data should be clustered first into groups and then the group representative profiles should be detected. These group representative profiles should be analyzed or treated as input for various programs for better results.

Clustering customer into segmentations is the basis for the many major analyses to increase revenue. Like any industry to increase benefit data analysis like customer targeting, behavior analysis, flexibility calculation, etc. are also important for the power industry. Data analysis especially for demand side management and nearly emerging load of EVs [10], is a research field for various researchers like [8, 11–16]. For analyzing data, it is extremely important to cluster the data first, for a better sight in data and minimize the computation burden. There exists a lot of literature on clustering the customers on the basis of load profiles of the customers [17–22]. The major methods in clustering are basically divided into four major categories, i.e., density [23], hierarchical-based [24], grid-based [25], and partitioning-based [26]. Selection of clustering technique, majorly dependent on objective of analysis and selection of number of clusters requires optimization [27]. Most of the research prefers k-means clustering to cluster RCLP [17, 28–30]. In this paper, the RCLP are clustered using k-means clustering, with the elbow method for selecting number of clusters.

The first part of the paper will discuss the novel outlier detection technique and later part will contain clustering of the profiles. Section 2 will discuss various salient features of RCLP, Sect. 3 will discuss the outlier detection technique, Sect. 4 will discuss the clustering of RCLP and Sects. 5 and 6 are result and conclusion sections,

respectively. The dataset utilized in this paper is released by the national renewable energy laboratory of the U.S. department [31]. The dataset contains the load consumption data of 200 households with a resolution of 10 min.

2 Salient Features of RCLP

Most of the outlier detection techniques are based on the assumption that the data is normally distributed and the data point lies a particular distance away from 1.5 times of the third quartile, is considered to be an outlier as shown in Fig. 1. Figure 1 shows the box of a household's daily load consumption for a month from the dataset used.

Figure 1 shows various outliers, but these are just suspicious points and it is not necessarily outliers. This is due to the fact that RCLP salient features, which are as follows:

- Does not follow normal distribution as shown in Fig. 2, which is an assumption for various popular outlier detection techniques. Hence, increase complexities in outlier detection.
- There are wide range of appliances in a household and the higher rating appliances are used seldomly. These points are highly vulnerable for false detection as an outlier.

Figure 2 shows the box plot of a household for one month and it points out various data points as an outlier on the basis of interquartile range. However, all these points are not outliers for an electrical load data for a residential customer.

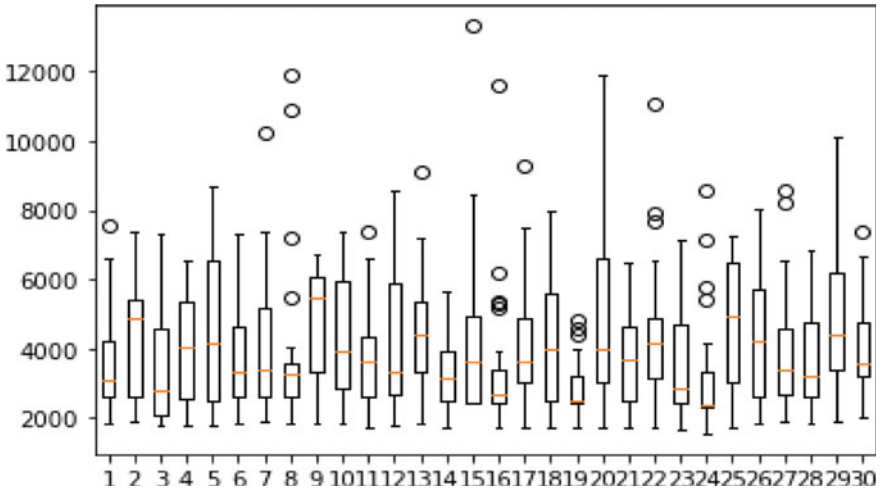

Fig. 1 Box plot for a household's daily load consumption for a month

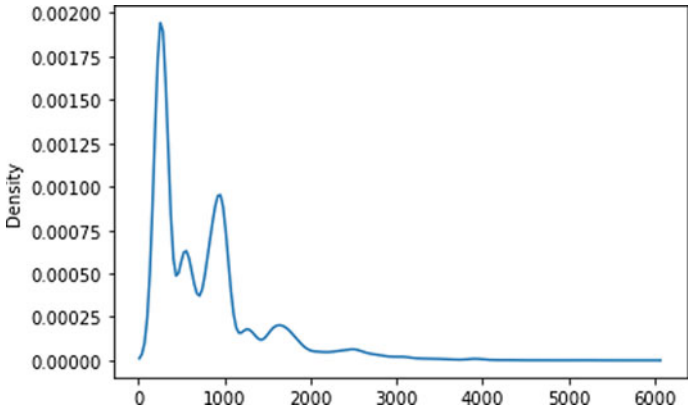

Fig. 2 Density plot of a house for 1 year

These suspicious points should be analyzed in relation to density of these points and variance of the data distribution. Behavior analysis should be conducted and compared with these points. Due to the salient features of the data distribution of a residential consumer, a novel technique for outlier detection has been proposed in the next section.

3 Outlier Detection Methodology

Firstly, all the given vectors are identified,

$$
\begin{aligned}
X_{td} &= [x_{1d}, x_{2d}, x_{3d}, x_{4d}, \ldots, x_{(k-1)d}, x_{kd}] \\
M_{id} &= [m_{1d}, m_{2d}, m_{3d}, m_{4d}, \ldots, m_{(k-1)\mathrm{d}}, m_{kd}] \\
\mathrm{Max}_d &= [mx_1, mx_2, mx_3, mx_4, \ldots, mx_{(k-1)\mathrm{d}}, mx_k] \\
\mathrm{Std}_d &= [std_1, std_2, std_3, std_4, \ldots, std_{(D-1)\mathrm{d}}, std_D]
\end{aligned}
$$

where

Xtd is the load points at t time period and d day,

M_{id} is the vector of suspicious points with the criteria, $1.5 * Q3$,

$Q3$, is 3rd interquartile range, i.e., 75% of data distribution,

Max$d$ is the vector of max points of each d day,

Std$d$ is the vector of standard deviation of each d day.

After identifying the four vectors, the three types of distances should be calculated and distance vectors should be formed (Figs. 3, 4 and 5):

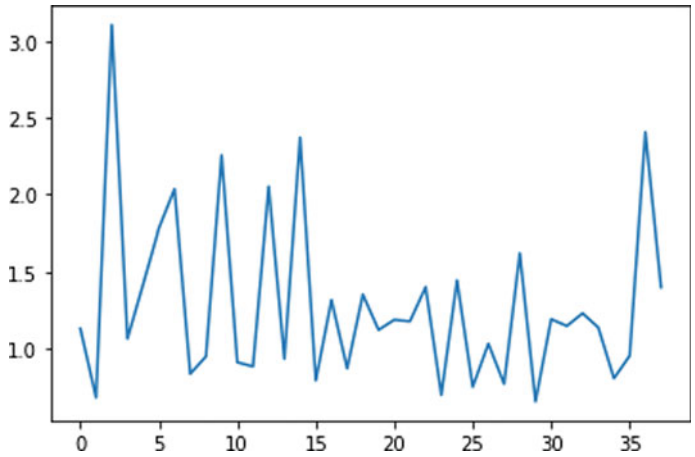

Fig. 3 Relative distance of suspicious points from the mean of that day (ω_{id})

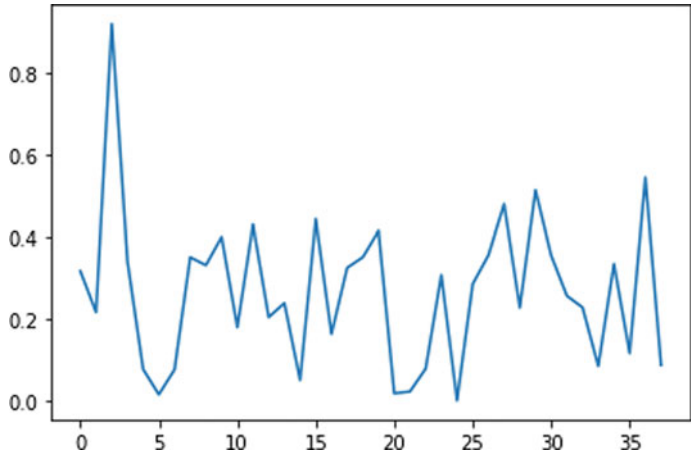

Fig. 4 Relative distance of suspicious points from the max of that day (τid)

1. Distance of suspicious points from the mean load consumption of that day (ω_{id}).

$$\omega_{id} = \frac{\text{abs}|m_{id} - X_{td}|}{\overline{X_{td}}}$$

2. Distance of suspicious points from the mean max load consumption that month (τ_{id})

$$\tau_{id} = \frac{|m_{id} - \max_d|}{\overline{\max_d}}$$

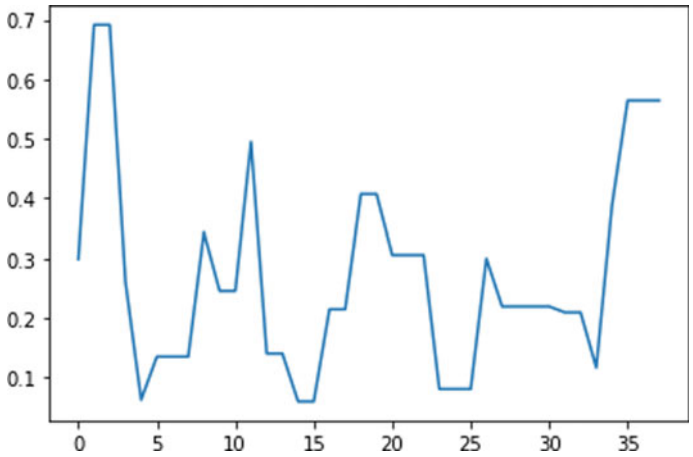

Fig. 5 Relative distance of std of that day from the mean of monthly std (σ_{id})

3. Distance of that day's standard deviation from the mean standard deviation of that month (σ_{id}).

$$\sigma_{id} = \frac{|\text{std}_d - \overline{\text{std}}|}{\overline{\text{std}}}$$

These distances are on their own relative scale, for better comparison all the distances should be normalized between 0 and 1.

Figure 6 shows the standardized distances, using these distances the outliers can easily be identified. Now, utilizing the standardized distances a point value (D) should be calculated and a *Threshold* is decided.

$$D = \frac{\alpha * \omega_{id} + \beta * \sigma_{id} + \gamma * \tau_{id}}{3}$$

$$\text{Threshold} = D * \delta$$

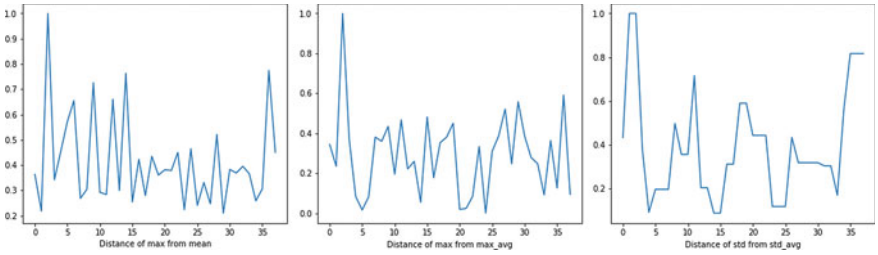

Fig. 6 Standardized distances of corresponding distance vectors

where α, β, γ are the weights for the standardized distance and δ is *Threshold* deciding factor. In this paper, the values of the weights are considered as follow.

$$\alpha = 1.2, \beta = 1, \gamma = 1, \delta = 1.5$$

If the value of D is greater than *Threshold* than the point will be considered as outlier otherwise the point will be considered and a normal data point or an equipment which is rarely used and have high rating.

4 Clustering

After cleaning the data, it is ready for clustering stage. The monthly avg data is considered as the variations of weather can be considered. The clusters are formed for the month of January for 200 households. Figure 7 shows the raw data after cleaning.

The very first step for k-means clustering is to decide the number of clusters. In this paper, elbow method is implemented for finding the optimal number of clusters. In elbow method the clustering is performed in an iterative manner, starting with 1 cluster and noting the sum of square error corresponding to it. Then, similarly clustering is performed with 2 number of clusters and sum of square error is noted corresponding to it and so on. Then the sum of square error is plotted against the number of clusters. It will form an elbow like graph and the number of clusters corresponding to which the elbow is formed is considered as optimal number of clusters. As increasing number of clusters more than that value will not decrease the error to a significant value. In this case, as seen in Fig. 8 the number of clusters should be 4.

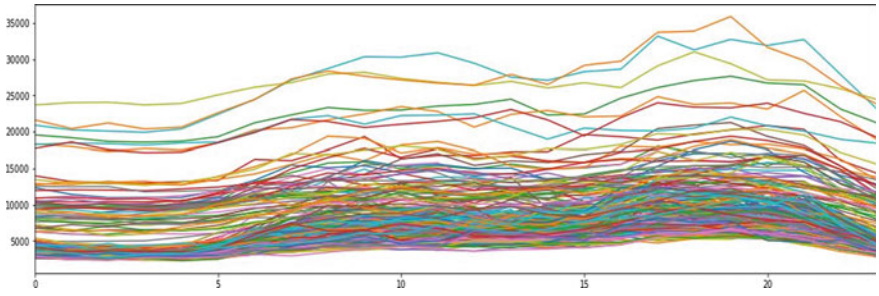

Fig. 7 Monthly (January) avg. consumption of 200 households after removing outliers

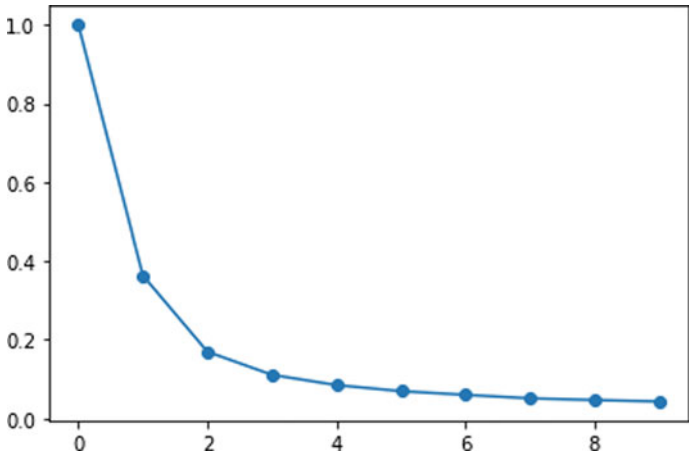

Fig. 8 Plot of standardized sum of square versus number of clusters

5 Results

In cleaning phase, the proposed outlier detection technique is utilized on the given dataset to find outliers. Figure 9 shows the point distance (D) on the load consumption of household 1.

As it can be seen that only two points are identified as outliers, however factors sensitivity and threshold level can be changed by varying weights. Here with given weights the threshold is 0.5484. Any point above the threshold will consider as an outlier. Similarly, the outliers are removed from all the 200 households in the given dataset.

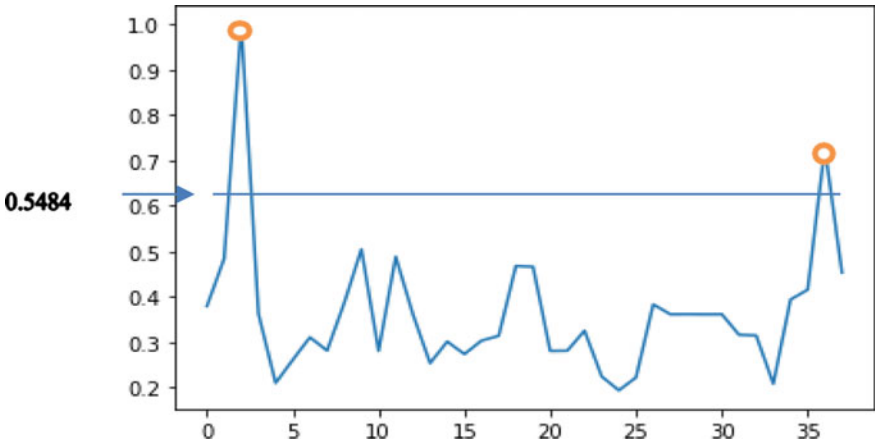

Fig. 9 Point distance with threshold 0.5484

Then the cleaned data is used for clustering with the 4 number of clusters. Figure 10 shows the different clusters.

Figure 10 shows 4 clusters which contains 200 households and 4 class representative profiles. If the class representative profiles can be used for analysis of 200 households. Figure 11 shows the class representative profiles.

Here, the class representatives can be analyzed to extract features like:

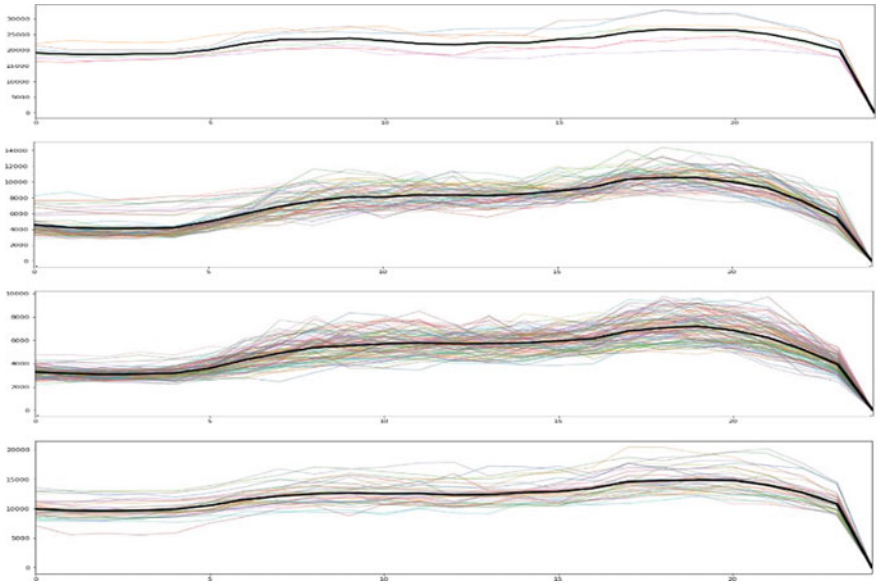

Fig. 10 Load profiles of all the 200 households clustered into 4 clusters

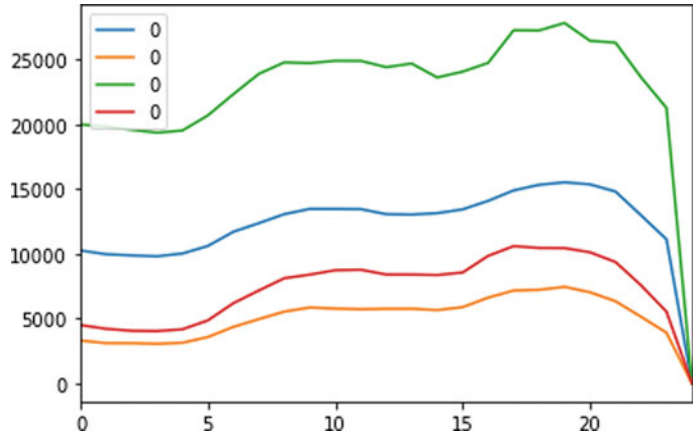

Fig. 11 Class representative for month of January for 200 households

- Most revenue generating households
- Maximum density cluster
- Minimum density cluster
- Time of peak and valley of a cluster.

6 Conclusion

For any analysis of load profiles of residential customers, the preprocessing stage is very important for accurate results. But due to salient features of RCLPs, it requires the dedicated techniques for data preprocessing. Therefore, for outlier detection a novel methodology has been proposed and it has been seen that the proposed method has pointed out two outliers from the data of household 1. Whereas, quantile approach was suggesting 32 outliers. All 32 points are not outliers, they could the rarely operated high rated equipment. As the proposed method has successfully pointed out the outliers only, as it considered the behavior of the customer also.

After cleaning the data clustering of RCLPs is performed. Where, first the optimal number of clusters are identified, i.e., 4, using elbow method. Then 200 customers are clustered into 4 clusters, using k-means clustering. The 4 clusters can be represented with the class representative profiles. Therefore 200 load profiles can be replaced efficiently with 4 profiles without making any important information. The 4 profiles distinctively represent the features of different households. It will reduce computation burden and made it possible to identify the target customers for different schemes.

This work can be further extended by considering more sensitive behavior analysis for outlier detection. Different customers with different weather sensitivity should be grouped first and similarly multi-stage clustering can be performed.

References

1. https://www.tdworld.com/grid-innovations/smart-grid/arti-cle/21120206/smart-meter-deployment-projected-to-reach-107-million-as-of-yearend-2020
2. The Data Impact of Smart Metering, https://www.ibi.com/blog/james-cot-ton/16610/
3. Sun M, Konstantelos I, Strbac G (2017) C-Vine copula mixture model for clustering of residential electrical load pattern data. IEEE Trans Power Syst 32:2382–2393
4. Ben-Gal I (2005) Outlier detection. Data mining and knowledge discovery handbook, pp 131–146
5. Bagdonavičius V, Petkevičius L (2020) Multiple outlier detection tests for parametric models. Mathematics 8:2156
6. Cho H, Kim Y, Jung HJ, Lee S-W, Lee JW (2008) OutlierD: an R package for outlier detection using quantile regression on mass spectrometry data. Bioinformatics 24:882–884
7. Zhang J, Zulkernine M (2006) Anomaly based network intrusion detection with unsupervised outlier detection. IEEE Int Conf Commun 5:2388–2393
8. Liang H, Ma J, Sun R, Du Y (2020) A data-driven approach for targeting residential customers for energy efficiency programs. IEEE Trans Smart Grid 11:1229–1238

9. Nizar AH, Dong ZY (2009) Identification and detection of electricity customer behaviour irregularities. In: 2009 IEEE/PES power systems conference and exposition, PSCE 2009
10. Vashisth S, Kumar Agrawal P, Gupta N, Naizi KR, Swarnkar A (2020) PEV traffic-based planning attributes for fast charging stations. In: 2020 IEEE 17th India council international conference, INDICON 2020
11. Holyhead JC, Ramchurn SD, Rogers A (2015) Consumer targeting in residential demand response programmes. In: Proceedings of the 2015 ACM sixth international conference on future energy systems
12. Kwac J, Rajagopal R (2013) Demand response targeting using big data analytics. In: Proceedings 2013 IEEE international conference on big data, big data 2013, pp 683–690
13. Kwac J, Rajagopal R (2016) Data-driven targeting of customers for demand response. IEEE Trans Smart Grid 7:2199–2207
14. Zhou D, Balandat M, Tomlin C (2016) Residential demand response targeting using machine learning with observational data. In: 2016 IEEE 55th conference on decision and control, CDC 2016, pp 6663–6668
15. Siebert LC, Aoki AR, Fernandes TSP, Lambert-Torres G (2019) Customer targeting optimization system for price-based demand response programs. Int Trans Electr Energy Syst 29:e2709
16. Smith BA, Wong J, Rajagopal R (2012) A simple way to use interval data to segment residential customers for energy efficiency and demand response program targeting. ACEEE Sum Study Ener Effic Buil
17. Alvarez MAZ, Agbossou K, Cardenas A, Kelouwani S, Boulon L (2020) Demand response strategy applied to residential electric water heaters using dynamic programming and k-means clustering. IEEE Trans Sustain Energy 11:524–533
18. Silva C, Faria P, Vale Z (2019) Discussing different clustering methods for the aggregation of demand response and distributed generation. In: Proceedings of the 2018 IEEE symposium series on computational intelligence, SSCI 2018, pp 1645–1650
19. Chelmis C, Kolte J, Prasanna VK (2015) Big data analytics for demand response: clustering over space and time. In: Proceedings 2015 IEEE international conference on big data, IEEE Big Data 2015, pp 2223–2232
20. Lin S, Li F, Tian E, Fu Y, Li D (2019) Clustering load profiles for demand response applications. IEEE Trans Smart Grid 10:1599–1607
21. Maigha, Crow ML (2014) Clustering-based methodology for optimal residential time of use design structure. In: 2014 North American power symposium, NAPS 2014
22. Chaweewat P, Singh JG, Ongsakul W (2019) A two stages pattern recognition for time-of-use customers based on behavior analytic by using Gaussian mixture models and k-mean clustering: a case study of PEA, Thailand. In: Proceedings of the conference on the industrial and commercial use of energy, ICUE
23. Sander J (2010) Density-based clustering. In: Sammut C, Webb GI (eds) Encyclopedia of machine learning. Springer, Boston, pp 270–273
24. Zhong S, Tam KS (2015) Hierarchical classification of load profiles based on their characteristic attributes in frequency domain. IEEE Trans Power Syst
25. Wang W, Yang J, Muntz R et al (1997) STING: a statistical information grid approach to spatial data mining. In: VLDB, pp 186–195
26. Partion-based, https://www.semanticscholar.org/paper/Partition-Based-Clus-tering-Using-Constraint-Grossi-Guns/ae2578788685e47534020452c0c8b65548570179/figure/0
27. Singh G, Swarnkar A, Gupta N, Niazi KR (2020) A review of scheduling techniques and communication protocols for smart homes capable of implementing demand response. Lect Notes Electr Eng 607:505–513. https://doi.org/10.1007/978-981-15-0214-9_54
28. Mahmoudi-Kohan N, Moghaddam MP, Bidaki SM (2009) Evaluating performance of WFA K-means and modified follow the leader methods for clustering load curves. In: 2009 IEEE/PES power systems conference and exposition, PSCE 2009. https://doi.org/10.1109/PSCE.2009.4840115

29. Zhi-qiang WBD, Deng-hui ZAI (2010) Application of k-means algorithm based on effective index to identifying bad data of the power system. Northeast Electric Power Technol 3
30. Hartigan A, Wong MA (1979) A K-means clustering algorithm. J R Stat Soc
31. Impact of uncoordinated plug-in electric vehicle charging on residential power demand—supplementary data. NREL data catalog, https://data.nrel.gov/submissions/69. Last accessed 2021/07/30

Anomaly Detection in Short-Term Load Forecasting

Rinit Rakesh, Gurpinder Singh, Anil Swarnkar, Nikhil Gupta, and K. R. Niazi

Abstract Load forecasting refers to the prediction of load behavior for the future. As the accurate forecasting is the foundation for various planning, programs, etc. Therefore, there is a necessity to increase the accuracy of the forecasted load. In this work, firstly a day ahead, hourly load is forecasted. A polynomial regression method has been proposed and is compared with linear regression. The error associated with the forecasted load dataset is evaluated. Then, the anomaly or the fallacy in the calculated load dataset is evaluated. An anomaly detection equation using statistical parameters has also been proposed.

1 Introduction

1.1 General

The term load forecasting refers to the estimation of load consumption in upcoming given time period. Precise prediction facilitates the electrical utility in numerous services like unit commitment demand response, price estimation, ancillary services, etc. [1]. The accuracy of a forecast is crucial to any electric utility, since it determines the timing and characteristics of major system addition. The load forecasting is categorized into three parts on temporal basis, i.e., short-term, medium-term, load-term.

Short-term load forecasting is mainly done for the operations to be done one daily basis such as to know sufficient producing capability, for preserving the specified spinning reserve, to trade in electricity market, ancillary services, etc.

The maintenance, scheduling, coordination of load dispatch is mainly the goal of medium-term load forecast, which is executed for the term of every week to a year.

R. Rakesh (✉) · G. Singh · A. Swarnkar · N. Gupta · K. R. Niazi
Malaviya National Institute of Technology, Jaipur, India
e-mail: 2019pes5224@mnit.ac.in

G. Singh
e-mail: 2017pes5202@mnit.ac.in

© The Author(s), under exclusive license to Springer Nature Singapore Pte Ltd. 2022

A. Tripathi et al. (eds.), *Intelligent Computing Techniques for Smart Energy Systems*, Lecture Notes in Electrical Engineering 862,
https://doi.org/10.1007/978-981-19-0252-9_56

The long-term forecasting is performed for one-five years earlier so as to plot the future growth of technology capability, input into a settlement for electricity interchange with neighboring utilities, etc.

1.2 Background

Load prediction helps an electrical utility to form necessary decisions almost every field like participating in energy market, demand side management, and infrastructure development, etc. The predictive values are necessary for the suppliers, ISOs, financial utilities, and alternative members associated with the energy sector.

In power industries pre-monsoon maintenance is done and the prediction of future loads can help the make important amendments during the maintenance. Short-term load forecast can ease the appraisal, which can help to anticipate the burden on the system. The system operators use the load forecasting end results as a foundation of off-line network evaluation to decide if the system is vulnerable to faults and outages. If so, corrective moves must be prepared, together with the load shedding, power purchases and bringing peaking units on line. The distribution system is directly involved as the sink to the power supplied through the consumer's demand of power. So, to deal with power supply demand mismatch, the only option is to plan for the distribution system considering forecasted load.

2 Literature Survey

2.1 Overview

The recent years had seen various trends in the financial status, migration, per capita income, standards of living [2]. This has led to greater consumption in electricity. Many African nations had seen great upsurge in tourists, the travels vlogs and Internet has boomed the hospitality sector which demand higher electrical energy and hence energy predictive studies have a gained pace [3]. The notion of balance to meet demands has become significant across many nations. Within the last decades, short-run load forecast algorithms are wide studied [4, 5]. The key forecast models can be divided into 3 categories: ancient, machine-learning, and artificial intelligent models. The normal models studied and used contain fast computing speed and strength [6]. Some common ones embrace regression toward the mean [7, 8] and automobiles regressive integrated moving average (ARIMA) [9, 10]. Others, like exponential smoothing [11] and multiple regressions toward the mean [12, 13], have conjointly attracted the interests of relevant researchers. In managing the linear forecast downside, these models provide effective measure effective results of learning the qualitative relationship between prediction parameters and its influencing factors. But,

these models are not always competent in indirect issues like relationship between weather and cargo, which can be confusing issues. For examples, ARIMA has difficulty in choosing the upcoming order in 2 processes automobile regressive (AR) and moving average (MA), etc. Regression is that the one in all most commonly used applied mathematics techniques. For this study the presented technique offers the model connecting various terms to be taken as independent, the final evaluation is considered as the outcome considering these factors. Statistic has found applications over the years in domains as financial studies, accounts, government organizations, elections, nevertheless as in this project. Auto regressive integrated moving average with exogenous variables (ARIMAX) uses classical statistic method.

2.2 Different Approaches to Load Forecasting

Same Day Approach
This is done by looking out at the historical knowledge for any day with a similar characteristics, like, climate and calendar variables, span (if vacation or any auspicious day) with reference to a particular time of interest. Prior available information is often utilized in linear combination or regression to create an analytic thinking.

Regression-based Approach
In this approach previously known terms are used to calculate the unknown term. The independent variables are first considered because these are the first ones to have an influence on results. In electricity statement, the dependent, variable is sometimes demand of the electricity as a result of it depends on production that on the opposite hand depends on the independent variables. Free terms are associated with climatic situations, like hot or cold conditions, wetness or air motion in the region.

Continual Hour Approach
The sequence of information usually at serial uniform periods is utilized in the working by the aid of statistical analysis. The idea here is to makes an attempt to try and grasp the sample of the information and look for the continual occasions supported the future occasions. This is usually worked for a short quantity into the lasting period.

Artificial Neural Network
Artificial neural network is a purposeful unit of deep learning. It imitates the conduct of human brain to carry out its tasks. It takes sample data analyze it and when a similar data is fed into it, the previous data patterns are utilized to crack the pattern and to finally acquire results. Neural networks are made from neurons, those shape the premise which techniques the network and have a layered structure. Each neuron is related to a numerical value referred to as bias.

Support Vector Machines
The primary capability of support vector machines is to do classification. In support vector machines, linear functions are trained to produce linear call boundaries in the new area. It may be used for each category and regression problem. It makes use of kernels and can be better at functioning than taking a hyper plane which was earlier used for classification.

2.3 Factors Affecting Short-term Load Forecasting

Time Factor
The crucial component in predicting load is the examination of time. Round the clock in a day the sunlight hours varies, which contribute to heat, which decide the usage of equipments like fans, coolers, and air conditioners. Common notion on across the middle of the night is that the load demand is predominately ruled by family activities and lighting.

Climatic Conditions
Load sample significantly relies upon at the Weather Factors, environmental circumstance because the climatic situations immediately impacts the kinds of system used. For example in the wintry weather there may be excessive utilization of electrical equipment that can heat the home, during summer cooling is needed and in rainy season as India is agricultural hub the water deliver is needed and the water garage is imperative. All those elements make contributions to the improved call for energy and consequently are critical on this study. The commitment of electrical units is largely affected by the climate situations, how warm or cold it is.

Wealth and Economy
Money can be the great motivator as well the greatest constraint. If the per capita income of any city is high then the usage of electricity will be high, the more gadgets can be used. If we compare a port city and a landlocked city there can be vast differences in level of income activities, which creates differences in demand. In cyber cities like Bengaluru and Pune the demand is high as the computers are part and parcel of lives. In the places with high agricultural activities load demand is high during irrigation season.

2.4 Data Concern

The researchers have given consideration to the parameters which follow reactive load pattern. The truth of the matter is that to know the electricity demand with utmost precision is a far reality even for the big players of the industry. It is so because the

instantaneous information can be diluted because of the meter malfunction, communication failures and instrumentation outages and the precision is lost, so a pin point value is hard to record. Also, there are arbitrary interruptions which add to the aforementioned issue. There are chances of cyber-attacks which can further reduce the reliability of the acquired information.

There are various scheduling techniques or algorithms available in literature. In this section rule-based, training-based artificial intelligence (AI) techniques, heuristic, meta-heuristic, based approaches for scheduling demand response are discussed.

3 Methodology

3.1 Test System Dataset

The maximum latest load records can also additionally be gathered after many hours or can also take number of days. The instrument error, lack of proper links and electrical failure, so the initial errors can also be in addition cleansed via the load agreement technique after a few days as well. The data has been collected from Independent System Operator New England (ISO-NE). This has been the raw ingredient for this study. ISO-NE more than one region, however, to simplify our task we carried out the observation primarily based totally on system (ISO-NE). ISO-NE serves the six states in the north-eastern United States together with Connecticut, Massachusetts, Maine, New Hampshire, Rhode Island, and Vermont. Weather is incorporated in records. In this work dry bulb temperature in step with hour has been taken into consideration. A dry bulb temperature, additionally called air temperature, is the degree of temperature through a thermometer which has been freely uncovered to air, however it have not an impact on of radiation and moisture. Other records parameters consist of day, weekend, and month.

3.2 Regression Analysis

Regression evaluation can be an extensively used method for load forecasting. In the multivariate evaluation framework, demand calculation is normally dealt with due to the fact the variable, even as the climate and date variables are dealt. The parameters of this study are typically foreseen the aid of the least rectangular approach. Multiple linear regression can be a method it is maximum often used while numerous variables are known, and a reaction is predicted. This approach is used to clarify a link among one continuous variable and no less than independent variable. The vanilla version can be a linear regression version that can be proposed with the intention to reduce

the error. Our aim is the calculation of load using the regression analysis. For these two different objective functions have been chosen.

3.3 Objective Functions

A.

$$E(\text{load}) = b_0 + b_1(\text{month}) + b_2(\text{day}) + b_3(\text{weekend}) + b_4(\text{hour}) + b_5(\text{temperature})$$

This is a linear function which is considering only the linear variation of four different parameters to get load demand. LHS is the energy demand (in MW), which are required to calculate. The coefficients $b0$, $b1$, $b2$, $b3$, $b4$, and $b5$ are calculated using linear regression. These gives the idea as to what changes would occur in the left hand side of equation (A), as the changes occurs on the right hand side of the same equation. Each coefficient estimates the change in the mean response per unit increase in their respective independent variable, for instant $b1$ for per unit change in month value. If the month variable is increased by 1 and other variables remain the same, then load is decreased/increased (depending upon the sign of calculated value of $b1$ by regression analysis) by about $b1$ times on average. Day variable ranges from 1 to 31 depending upon the day of the month. Weekend variable is from 1 to 52, the first week starting from January is termed as 1, the weekend variable becomes 2 for the next week and so on. The hour variable ranges from 1 to 24, starting from 1 at midnight 12 and counting in increasing order till 24. The temperature is the dry bulb temperature and was measured in Celsius, only the magnitude is used for calculation. Let us call this method I.

B.

$$\begin{aligned} E(\text{load}) = {} & b_0 + b_1(\text{month}) + b_2(\text{day}) + b_3(\text{weekend}) \\ & + b_4(\text{temperature}) + b_5(\text{hour}) + b_6(\text{weekend})(\text{hour}) \\ & + b_7(\text{temperature})(\text{hour}) + b_8(\text{temperature})^2(\text{hour}) \\ & + b_9(\text{temperature})^3(\text{hour}) + b_{10}(\text{temperature})^2(\text{month}) \\ & + b_{11}(\text{temperature})^3(\text{hour}) \end{aligned}$$

The 2nd function mentioned above was chosen to get better results. The error to be reduced and hence, increased efficiency. This is a polynomial regression method equation. Here, linear trend with quadratic, cubic, and nonlinear trends are employed.

Let us term this method II. The selection of variable is similar to that in the previous case. In this case a total of 17,543, observation points were employed.

3.4 Benchmarking the Models of Load Forecasting

The one hour ahead forecasting to be done using the two aforementioned methods. Here we make use of the mean percentage error in order to check the merit of our prediction. It is calculated by first calculating error, then the error percentage with respect to actual load and the taking the mean of errors around 24 h. The steps are mentioned as follows:

First we will calculate the error:

$$\text{Error} = \text{Actual load demand} - \text{Calculated load demand}.$$

Then the percentage error is calculated:

$$\frac{\text{Actual load demand} - \text{Calculated load demand}}{\text{Actual load demand}} \times 100$$

After this the mean percentage error is calculated:

$$\frac{\%\text{error1} + \%\text{error2} + \%\text{error3} + \cdots + \%\text{error24}}{24}$$

In this analysis we have taken the calculated value of 24 h. The above error analysis is to be done for both the functions separately. Then we can evaluate the functions on the basis of merit, i.e., which has lesser error. The analysis is mentioned in the results section in tabular form.

The two methods are also tested on statistical parameter. Here, we have used a term known as standard error is used. Essentially the values of coefficients are calculated using the regression analysis, in the evaluation of these values there can be some statistical error as well. So, standard error which defines the precision to which the regression coefficients are calculated is the parameter also mentioned in the results section. The standard error values when falls within the 5% range of calculated coefficients value, then the calculation is supposed to reliable.

3.5 Anomaly Identification

The mean and the standard deviations of the observations are gathered, and are given by the symbols and σ, respectively. After this the electricity requirement is calculated for each hour and the load demand values which are outside the interval $[\mu - k\sigma, \mu$

$+ k\sigma]$ are termed to be anomalies, where k is the threshold and is predefined. In our analysis k is taken as 1.15. This way we can check the stealthy data present in the load values. This method enables us to have a better monitoring by omitting the bad data which can be otherwise present in the forecast.

If the anomaly detection shows that the calculated load values are within specified range then the prediction is perfect. Along with predicting load values our task here is to also check if the load values are correct or not.

4 Results and Discussion

4.1 Load Calculation

The test dataset had 17,543 observations. It included month, day, weekend, hour, and temperature as the independent variables while the load to be calculated was the dependent variable. These were then used to perform the linear regression and the values of regression coefficients were calculated. These calculated coefficients were then put in objective function and the load was calculated. Along with the load values the standard errors are also mentioned. Standard errors were under the permissible limits, therefore it can be inferred that the calculated coefficient values are validated on statistical grounds.

The coefficients for month, day, weekend, hour, and temperature are evaluated using the calculated using regression analysis

$$E(\text{load}) = b_0 + b_1(\text{month}) + b_2(\text{day}) + b_3(\text{weekend}) + b_4(\text{hour}) + b_5(\text{temperature})$$

This is a linear function which is considering only the linear variation of the four distinct parameters.

The standard error describes the precision with which the regression coefficients are calculated. The values of standard error are within 5% range in the regression analysis. Then the values of load are calculated using the first optimization function. The values of coefficients are put in the optimization function which gives the load values. The calculated load values and the actual load values at different times (load duration curve) are depicted in Figs. 1 and 2.

The discrete load values for every hour are plotted in Figs. 1 and 2.

The actual load values are marked by * symbol, the calculated values are plotted discretely and are joined by a smooth line also referred to as regression line. The load duration curve is plotted for Sunday (weekend day) as well as Monday (week day). Now second method is used for load prediction as depicted in Fig. 3.

$$E(\text{load}) = b_0 + b_1(\text{month}) + b_2(\text{day}) + b_3(\text{weekend}) + b_4(\text{temperature}) + b_5(\text{hour}) + b_6(\text{weekend})(\text{hour})$$

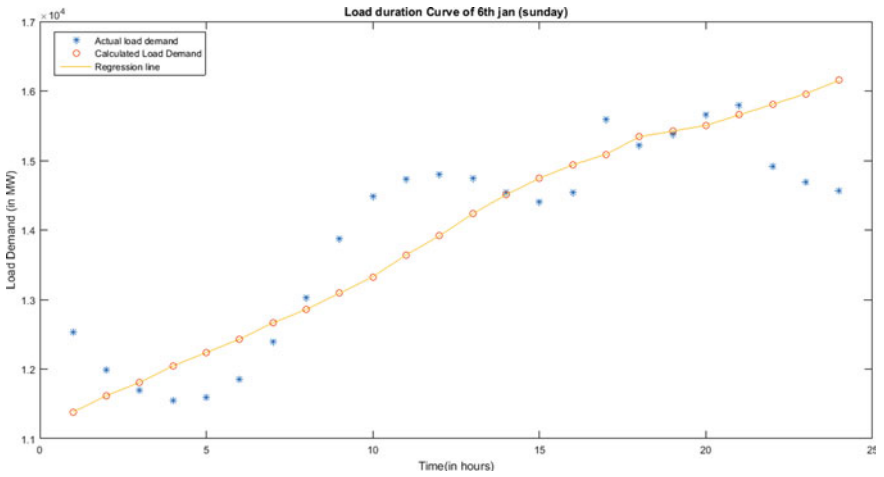

Fig. 1 Load curve for predicted and actual load for a time interval of 24 h using the method I for 6th January

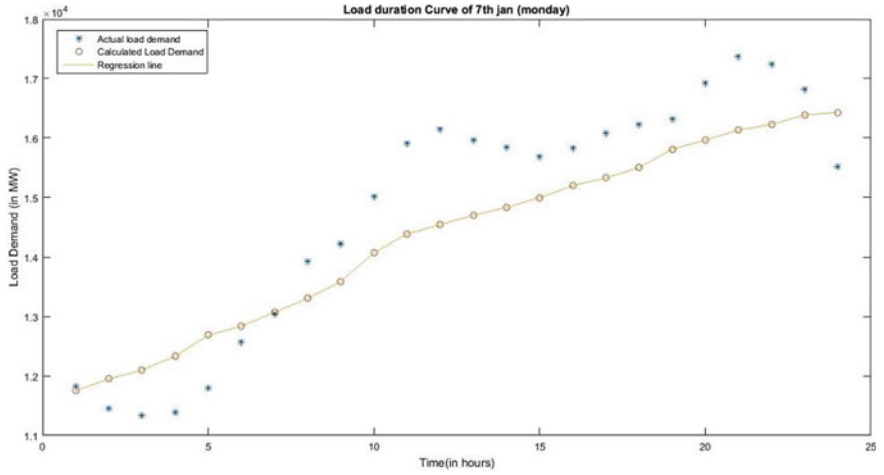

Fig. 2 Load curve for predicted and actual load for a time interval of 24 h using the method I for 7th January

$$+ b_7(\text{temperature})(\text{hour}) + b_8(\text{temperature})^2(\text{hour})$$
$$+ b_9(\text{temperature})^3(\text{hour}) + b_{10}(\text{temperature})^2(\text{month})$$
$$+ b_{11}(\text{temperature})^3(\text{hour}).$$

The load duration curve depicts the load calculation using the method II as depicted in Fig. 4.

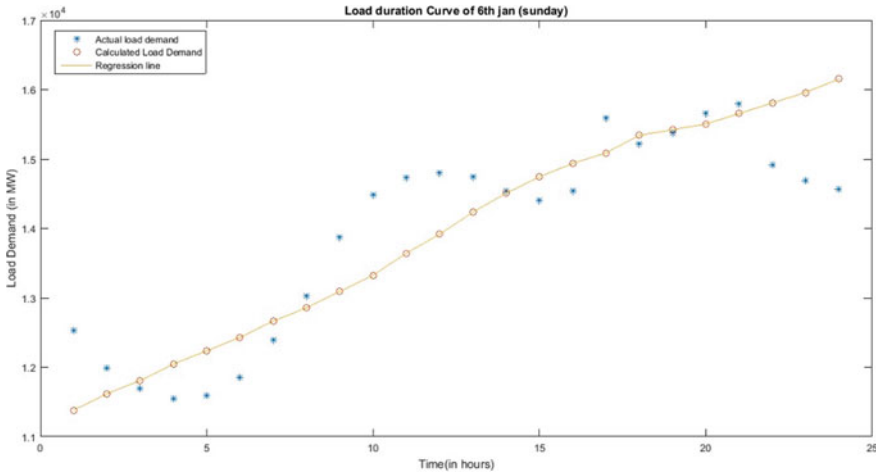

Fig. 3 Load curve for predicted and actual load for a time interval of 24 h using Method II for 6th January

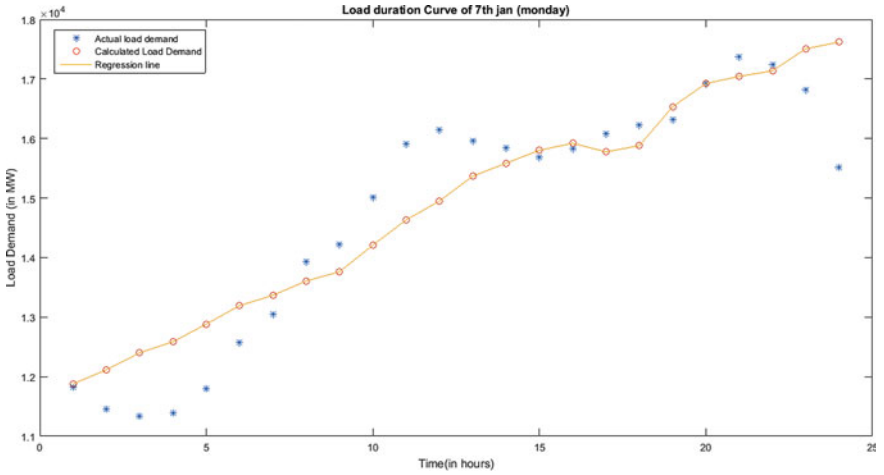

Fig. 4 Load curve for predicted and actual load for a time interval of 24 h using Method II for 7th January

Here, nonlinear terms are also introduced. The temperature function is given the great consideration as the electricity usage is heavily governed by temperature variations. Here the cubic, quadratic as well as linear variations of temperature value are considered because of which additional coefficients are introduced in the function. This becomes a polynomial function and along with linear nonlinear trend is analyzed. The deviation of the calculated values from the actual can be analyzed using the error. It is depicted in the next section.

Table 1 Percentage mean error in case of Method I

Method I	Percentage mean error
6th January	7.11
7th January	9.73
Average of the two	8.42

Table 2 Percentage mean error in case of Method II

Method II	Percentage mean error
6th January	8.04
7th January	8.52
Average of the two	8.28

4.2 Error Calculation

- To calculate error we take the difference between actual and calculated values.
- Error = Actual load demand − Calculated load demand

$$\%\text{Error} = \frac{\text{Actual load demand} - \text{Calculated load demand}}{\text{Actual load demand}} \times 100$$

- % Mean error:

Using the above formulas error is calculated, the %mean error for both the cases is shown in Tables 1 and 2.

The percentage mean errors are calculated for both the methods on both the days and their average is also evaluated.

As it is evident that the percentage mean error is higher in case of Method I, thus the prediction of load in Method II can be inferred to be more reliable.

4.3 Anomaly Detection

The anomaly detection can be done by setting a range under which the load predicted can be termed valid and if found breaching this limit the observed value can be declared stealthy. There is anomaly in load values if it falls out of following range:

$[\mu - k\sigma, \mu + k\sigma]$, μ is the mean of calculated load values, σ is the standard deviation and k is threshold taken to be 1.15. For this primary step is the calculation of mean and standard deviation, it is calculated and shown in Tables 3 and 4 for the two methods, respectively.

Using the above information and putting the threshold $k = 1.15$, the permissible range can be set. The range with upper and lower limits is depicted in Tables 5 and 6.

Now it can be checked which values are in the range and which are out of range.

This is checked for 24 discrete hours of both days. This has been shown by Table 7.

Table 3 Statistical parameters in case of Method I

Method I	6th January	7th January
Mean	13,927.49	13,942.89
Standard deviation	1503.128	1273.256

Table 4 Statistical parameters in case of Method II

Method II	6th January	7th January
Mean	14,396.40	14,716.12
Standard deviation	1407.263	1539.074

Table 5 Permissible load value range using Method I

Method I	Upper limit	Lower limit
6th January	15,656.08	12,198.89
7th January	15,407.13	12,478.65

Table 6 Permissible load value range using Method II

Method II	Upper limit	Lower limit
6th January	16,014.76	12,778.05
7th January	16,321.28	12,486.19

This shows that the regression analysis showed some data which is beyond permissible limit. By anomaly detection we can check for such calculated forecasted results. This proves handy in order to have a complete method where along with forecasting we are able to check for error and presence of unwanted data can be traced.

5 Conclusion

In this work, two different models for load forecasting were proposed. One concerned only linear variations in variables while the other one included nonlinear variables as well. The statistical validity of both the methods was checked and then their deviation from actual load values was calculated. The 2nd method which used polynomial regression came meritorious, on the account of lesser error.

Then the detection for stealthy data was done using statistical parameters the average of acquired observations and the dispersion of individual record from this term. After checking for the presence of the observations which breached the specified

Table 7 The calculated values which breached limits

	6th January	7th January
Method I	4	4
Method II	2	4

limit, to evaluate the presence of anomaly, polynomial regression method has lesser anomalies. It can be inferred that the polynomial regression method can be used to forecast.

References

1. Xiu J, Yui M (2014) Real-time anomaly detection for very short-term load forecasting. J Mod Power Syst Clean Energy
2. Singh G, Swarnkar A, Gupta N, Niazi KR (2020) A review of scheduling techniques and communication protocols for smart homes capable of implementing demand response. Intell Comput Tech Smart Energy Syst 505–513
3. Hong T, Pinson P, Fan S (2014) Global energy forecasting competition 2012. Int J Forecast 30(2):357–363
4. AlamaniotisIkonomopoulos A, Tsoukalas LH (2012) Evolutionary multiobjective optimization of kernel-based very short-term load forecasting. IEEE Trans Power System 27(3):1477–1484
5. Guan C, Luh PB, Michel LD (2013) Very short-term load forecasting: wavelet neural networks with data pre-filtering. IEEE Trans Power Syst 28(1):30–41
6. Luo C, Hong T, Fang SC (2018) Benchmarking robustness of load forecasting models under data integrity attacks. Int J For 34(1):89–104
7. Huang SJ, Shih KR (2003) Short term load forecasting via ARMA model identification including non-Gaussian process consideration. IEEE Trans Power Syst 18:673–679
8. Cheng J, Li W, Lau A (2010) Automated load curve data cleansing in power systems. IEEE Trans Smart Grid 1(2):213
9. Mandal P, Tomonobu S, Naomitsu U, Toshihisa F (2006) A neural network based several hours ahead electric load forecasting using similar days approach. Int J Electr
10. Charytoniuk W, Chen MS, Van Olinda P (1998) Nonparametric regression based short-term load forecasting. IEEE Trans Power Syst 13:725–730
11. Short Term load forecasting using time series modelling with peak load estimation capability. IEEE Trans Power Syst 16(3)
12. Park DC, El-Sharkawi, Marks II RJ, Atlas LE, Damborg MJ (1991) Electric load forecasting using an artificial neural network. IEEE Trans Power Eng 6:442–449
13. Kandil MS, El-Debeiky SM, Senior Member, IEEE, Hasanien NE (2002) Long-term load forecasting for fast developing utility using a knowledge-based expert system

Comparative Study of Islanding Detection Techniques of Microgrid for Solar PV as Distribution Generator

Vikas Panchal, Anil Swarnkar, Nikhil Gupta, and K. R. Niazi

Abstract Islanding is one of the major aspect of microgrid that has a direct effect on grid operation. If islanding is detected then microgrid needs to be isolated from main grid. Solar PV's are most likely to integrate with grid as these are mostly used for distribution generation at residential and commercial areas. This paper presents various types of islanding detection schemes of microgrid and these schemes are analyzed for grid connected with solar PV as distribution generation. A tabulated comparison of various islanding schemes is presented and their advantages and limitations are discussed.

Keywords Islanding detection methods · Non-detection zone · Distribution generation

1 Introduction

Distribution generation (DG) in simplest view is outlined as generation at load end [1], it can be an autonomous structure or part of a microgrid. The DG practices are increasing rapidly due to rise in energy demand and ability of DG unit to compensate that demand [2]. From past decade the cost of solar panel is constantly decreasing with increase in their efficiency also India has location benefit to receive ample amount of sunlight throughout year. Easy installation, low maintenance and other perks makes it suitable to use solar PV as DG source [3, 4].

A microgrid typically consists of various distributed generation units operating in two modes either connected to grid or independent (Islanded mode) [5, 6]. Generally microgrid operates in grid connected mode as it increases reliability and resiliency in specific areas where critical load is present (e.g. medical, military base, etc.) while islanded mode finds application in remote areas. Microgrids are one stop solution for many problems but it also struggles with various skillful problems are one of the major problem with microgrid is islanding.

V. Panchal (✉) · A. Swarnkar · N. Gupta · K. R. Niazi
Malaviya National Institute of Technology, Jaipur, India
e-mail: 2020ree9549@mnit.ac.in

© The Author(s), under exclusive license to Springer Nature Singapore Pte Ltd. 2022

A. Tripathi et al. (eds.), *Intelligent Computing Techniques for Smart Energy Systems*,
Lecture Notes in Electrical Engineering 862,
https://doi.org/10.1007/978-981-19-0252-9_57

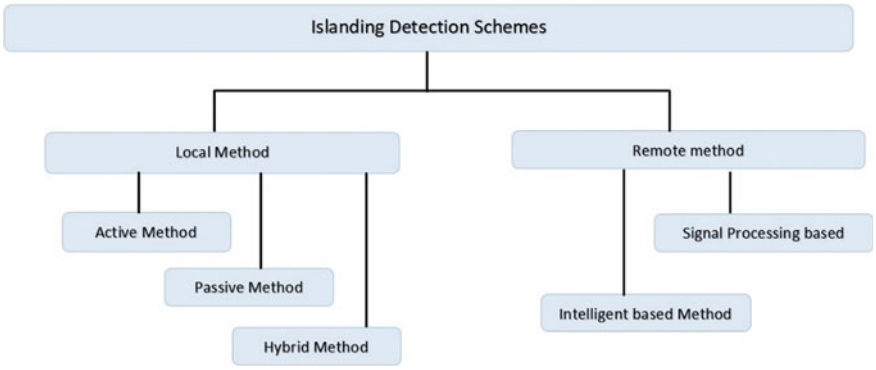

Fig. 1 Classification of islanding detection schemes

Microgrid islanding is a procedure in which the main grid is isolated through the load and then supply is carried out only by DG unit [7]. Islanding can be done intentionally or unintentionally, although intentional islanding is done during maintenance by disconnecting a part of unit from main grid. During intentional islanding is done considering that the load of isolated area matches the capacity of DG so that no disturbance occurs in power quality [8]. Unintentional islanding occurs because of fault in main distribution system, during unintentional islanding the DG dissociate solely from the main grid and connects with critical load present in its vicinity forming the island. The problem associated with unintentional islanding is that in almost all the cases the load does not match with the DG source capacity and islanding cannot be made. Due to this mismatch the power quality voltage balance and frequency deteriorate abruptly which makes islanding detection an important aspect of microgrid operation. There are various islanding examination methods till now are based on several parameters Fig. 1. All these methods comprises their own merits and demerits, this paper depicts various islanding detection techniques in detail their classification, detailed study and presented a comparative analysis of various methods based upon suitability to grid connected photovoltaic system (GCPVS).

2 Anti-islanding Standards

Table 1 presents the various international standards recommended by IEEE under IEEE STD 929-2000 for “Utility interface of photovoltaic”.

Table 1 Anti-islanding standards

Parameters/standards	Q_F (quality factor)	t (detection time)	f (frequency range)	V (voltage range)
IEEE (1547–2003)	1	$t < 2$ s	59.3–60.5 Hz	0.88–1.10
IEEE (929-2000)	2.5	$t < 2$ s	59.3–60.5 Hz	0.88–1.10
UL 1741	<1.8	$t < 2$ s	59.3–60.5 Hz	0.88–1.10
IEC-62116	1	$t < 2$ s	fo− 1.5 Hz ≤ f and f ≤ fo + 1.5 Hz	0.88–1.15

3 Review of Islanding Methods:

Islanding detection methods detects the islanding situation when electrical parameters crosses a predefined threshold value and triggers the inverter to halt the supply of loads. IDMs are broadly classified as local IDMs and remote IDMs. These are further classified as active, passive, modified passive, hybrid method as local IDMs and signal processing-based, communication-based and intelligent-based methods in remote IDM as shown in Fig. 1.

3.1 Active IDMs

In active method of islanding detection a small disturbance signal is introduced into the DG output to detect the possible condition of islanding [9, 10]. Under normal steady state condition the effect of these disturbance is negligible but when the system is in islanding condition the disturbance brings significant variation in the system parameter as such to trigger the relays, as shown in Fig. 2. Active methods are simple, robust but tends to cause harmonic disturbance due to injection of disturbance signal and may deteriorate the power quality as well but it has an advantage of having a small Zone of none-detection (ZND).

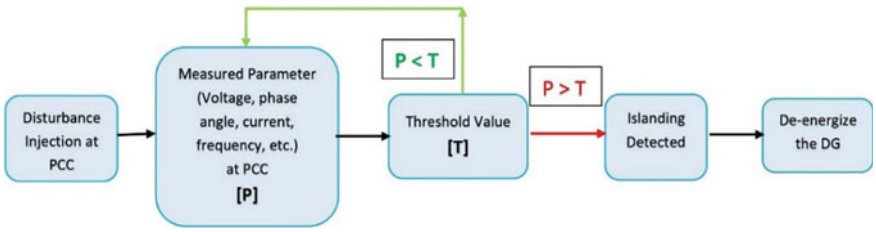

Fig. 2 Active islanding detection scheme

3.1.1 Impedance Measurement (IM) IDMs

DC converters have constant impedance at high frequency but a significant variation in the impedance can be seen in harmonic resistance of the system after islanding [11]. This variation can be computed from voltage and current measurements and islanding in the system is detected. In this IDM, a low amplitude signal is dispensed, and it is detected with high speed. The method holds a limitation due to complex threshold selection however IM method possess a small NDZ.

3.1.2 Active Frequency Drift (AFD)

In AFD method a small disturbance is introduced in current waveform of the inverter, this has no effect on the voltage and frequency waveform due to grid stability but a zero crossing of voltage occurs when the main grid is abrupt it will give rise to phase error within inverter current and output voltage causing a frequency drift in inverters output current [12]. This frequency drift causes further zero crossing until it tends to exceed the voltage frequency from its threshold limit and in turn detecting islanding condition. This technique can be readily implemented but it comprises significant NDZ.

3.1.3 Sandia Frequency Shift (SFS)

This method introduces positive current feedback in the system that increases the harvest current of the inverter. As system was connected to the main utility, minor change tries to put the system out of frequency range but the control of the grid holds the system in stability. When the microgrid is islanded then the control action is no longer present and this deviation if crosses threshold value then islanding is detected [13]. The frequency of output current increases during islanding and is does not affect any parameter during grid connected mode (As shown by Eq. 1)

$$C_f = C_{fo} + k\left(F_a - F_{\text{grid}}\right) \tag{1}$$

where C_{fo} = fraction when frequency error is zero, k = accelerating factor which improves the speed of detection technique, F_a = frequency of voltage at point of common coupling and F_{grid} = frequency at the grid.

3.1.4 Sandia Voltage Shift (SVS)

The islanding detection in SVS method is done by comparing voltage amplitude variation with threshold value. A positive feedback generates through voltage amplitude at PCC, there may be slight effect on the system it is grid connected which can be

neglected but when the system is islanded then the voltage drop becomes significant enough to be detected by relays and a tripping signal is generated to cease the operation [13–15]. Developed by "Sandia National Laboratory, USA" this technique is considered as most efficient IDM.

3.1.5 Slip Mode Frequency Shift (SMFS)

This technique provides positive feedback generally present in the frequency and phase angle of the inverter. Beneath the normal operation, frequency of the voltage is constant at PCC but after islanding even a little distress of frequency creates phase error and since the feedback in SMFS is positive that's why phase angle error increases until it reaches steady state point. If the steady state frequency point crosses its predefined range then it relays shut down of the inverter [16, 17]. It can be shown in Eq. 2.

$$\theta \text{sms} = \theta m \sin\left(\frac{\pi}{2}\frac{f - fg}{fm}\right) \tag{2}$$

where "f" = inverter frequency, "fg" = nominal grid frequency and θm and "fm" = SMFS parameters.

3.2 *Passive IDMs*

Passive IDMs are constructed on the basis of continuous monitoring of various electrical parameters like voltage, current, frequency, impedance or power, etc. for islanding detection [9]. These parameters are monitored (one or more) by PCC or at the DG terminals and then compared with the standard value, if the variation in these parameter crosses threshold value then then relay sense it and trips the main breaker as shown in Fig. 3. Passive IDMs have an asset of cost effectiveness and fast operation with comprehensive power quality of the system which remains unaffected. Although

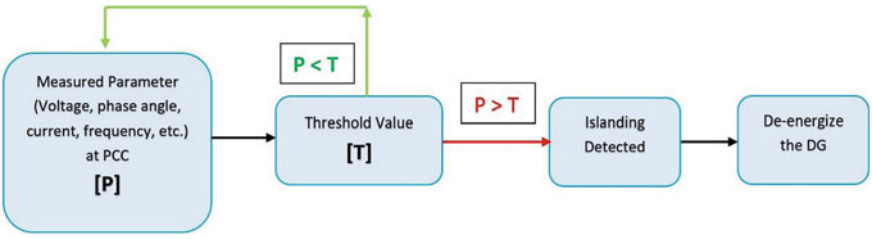

Fig. 3 Passive islanding detection scheme

passive methods have ample of NDZ and the threshold selection is also complex but still these methods are used because of its simple and easy implementation. Various types of passive IDMs are described below.

3.2.1 Over/Under Voltage and/or Frequency (OUV/OUF)

The voltage and/or frequency is incessantly measured at PCC in this islanding detection technique and when the measured value crosses the predefined value then the DG and the main grid connection is obstructed [18]. Although some time delay is provided by the system owing to the sudden rise/fall in voltage/frequency as it may be caused due to change in connected load [19]. If the variation is due to connected load then the grid will interact with the DG link and supply/take excess power from the unit and the normal condition is restored which is not in the case if it is islanded as if unit is islanded then the parameters keeps deviating from normal.

3.2.2 Rate of Change of Frequency (ROCOF)

It is referred as passive islanding detection technique which is totally based on frequency measurement. In this the rate change of frequency (Δf) is measured (at PCC) as per Eq. 3 given below [20] and the DG unit will be disconnected if Δf exceeds threshold value.

$$\frac{df(n)}{dt} = \frac{f(tn) - f(tn - \Delta t)}{\Delta t} \tag{3}$$

where $f(t_n)$ is frequency of current sample, $f(tn - \Delta t)$ is frequency of sample just before current sample and Δt is the time interval. This method considers the mismatch between load and generation which have a direct effect on frequency. ROCOF is fast method as contrast to OUV/OUF and is unaffected by minimal power mismatches [21].

3.2.3 Phase Jump Detection (PJD)

This technology of island detection utilizes phase difference within voltage and current as crucial parameters as to detect islanding [22]. If the phase difference within voltage and current of an inverter harvest process crosses prescribed limit then islanding is detected [23]. Under islanding operation of the harvested current of the inverter remains same but the voltage swings its path creating a new path for inverter voltage causing phase error. If this error is more than prescribed limit then relay trips the DG from grid. PJD IDM is immune to transients and power quality but suffers from large NDZ.

3.3 Hybrid Method

This method of islanding detection takes the asset of active and passive methods to produce fast and reliable operation with improved NDZ [24, 25]. Active and passive both IDM have limitations, active methods are reliable but effects power quality and passive methods are cheap but are relatively unreliable. Hybrid methods are designed to take perks of both methods [26]. In hybrid method to monitor the system passive method is employed while in the event of islanding the active method it is referred to confirm islanding. This is done as passive method does not affect power quality so under the normal condition these can be used while in the event of islanding the control shifts are used in active methods. As active methods have less NDZ which will avoid undetected islanding condition.

3.4 Remote Method

The remote techniques uses signal processing techniques and communication infrastructure for islanding detection which is implemented between the utility grid and DG [27]. In this method of islanding detection the information of the live parameters is collected by communication channel and sent to tripping switch. Remote scheme offers negligible NDZ and are high reliable as contrast to active or passive IDMs. The main discrimination of this technique is higher cost, complex installations and implementation [28]. Remote IDMs includes Power Line Communication (PLC), Supervisory Control and Data Acquisition (SCADA) and transfer trip methods.

3.4.1 Signal Processing (SP)

The signal processing-based methods implemented as to prevail the drawbacks of existing methods [29]. These techniques are capable to differentiate islanding and non-islanding events precisely even in low power imbalance. The signal processing method permits the extraction of hidden attributes of the deliberated signals as such to observe the islanding condition [30]. Artificial intelligent (AI) classifies uses these extracted hidden attributes as input to discriminate the islanding and non-islanding conditions. SP supported islanding sensing schemes use time domain—frequency domain supported schemes to improve the speed while minimizing NDZ. These methods limitation of high installation cost and sometime turns out to be financially inefficient.

3.4.2 Intelligent IDMs

Intelligent IDM uses diverse intelligent classifiers and data mining methods to detect islanding [31]. These methods do not necessitate threshold selection and can be considered as extension to signal processing-based methods. In intelligent IDM various data mining techniques and intelligent classifiers used to detect islanding. Commonly, intelligent methods are combined with SP techniques these include artificial neural network (ANN), probabilistic neural network (PNN), fuzzy logic (FL) and decision tree (DT). These techniques are capable of handling pattern recognition which conventional approaches cannot handle and thus efficiently islanding detection. These methods have best performance than other techniques but suffers from large computational burdens [32] in view of existence of various training and testing methods.

4 Islanding Detection Methods for Grid Connected Photovoltaic Systems (GCPVS)

The selection of method for islanding detection depends on place of installation, also to improve the performance some modification and improvement is provided as per the installed location. Below are some of the novel islanding detection techniques described with special reference to GCPVS.

1. **Two level islanding detection method** [33]:

In this criteria of islanding detection is ideal for GCPVS, firstly rate alteration of output voltage (ROCOV) is calculated and then disruption is inserted in the duty cycle of converter (DC/DC) if this value exceeds the threshold. This deviates the system operating point's away from maximum power point (MPP) condition and remains under islanding condition and there is significant reduction in voltage and active power of the system but if that system is non-islanding then variation of atleast one of these variable is near-zero that's why the ROCOV and rate of change of power (ROCOP) coefficient is usually measured in the second state. Hardware-in-the-loop (HIL) simulation technique is used for testing using two PV power plants. Results shows precise islanding classification, small NDZ and self-standing threshold determination without affecting the power quality. Also after islanding identification it provides fast MPP restoration.

2. **New voltage feedback-based islanding detection method** [34]:

This method islanding detection is based on active IDM, the paper proposes voltage feedback type IDM for GCPVS-based microgrid. In this algorithm, a disruption is injected in d-axis reference current of inverter consistently equal to the deviation of output voltage. This reference current modifies the active power output and consequently voltage at PCC. The testing is conducted using MATLAB/Simulink under standard conditions defined by IEEE standards on two large scale GCPVS.

3. **Maximum Power Point Tracking Injection Method** [35]:

This method of the paper signifies islanding detection by introducing disturbance in maximum power point (MPPT) algorithm. Under normal condition the voltage is balanced or varies on permissible limits but when absolute deviation overstep permissible limits then then operating point shifts from MPP. This shift of operating point causes reduction in the power output and accordingly a significant voltage drop is seen in islanding. This algorithm is designed to restore MPP after islanding classification which makes it suitable for critical loads connected to microgrid. The method is tested for a sample network with two GCPVS including actual relays in HIL and the produced results shows accurate detection with negligible NDZ.

4. **Inverter-based distribution generation techniques** [36]:

This is the passive islanding detection technique, considered ideal for inverter-based PV generation. This method uses two parameters for analyzing the system, first is the rate of change of voltage (ROCOV) while second is the ratio of current and voltage magnitude (VOI). Both the parameters detects all events at PCC and differentiate islanding and non-islanding condition. It has a decentralized control operation and the design is simple and robust.

5. **Method based on harmonic impedance measurement** [37]:

The conventional IDMs using reactive power or frequency and phase quantities are not suitable on DC grid as these grid does not transmit reactive power or frequency and phase. At present most of the IDMs proposed for DC/DC converters are based on active power injection which are not suitable for multi-photovoltaic (PV) DC system. Multi-photovoltaic system may lead to detection failure due to synchronization problem with converter injection. This paper suggests passive IDM for the system by using impedance as measuring quantity for multi -PV DC microgrid. The resistance of DC converters is invariant at high frequency and changes significantly after islanding this change is measured for islanding detection.

5 Comparison of Various IDMs for PV

Table 2 depicts scrutiny of various islanding detection methods based on solar photovoltaic as distribution generator as described in Sect. 5 along with some more methods.

Table 2 Comparison of various IDM for PV

References	Type	Ideal for	Based on (parameters)	Testing	Features	Islanding detection (ms)
[33]	Active	GCPVS	ROCOV, ROCOP	HIL with 2 PV Plants	• Self-standing threshold determination • Unaffected power quality • Simple and inexpensive structure • Automatic MPP restoration	<510
[20]	Active	GCPVS	Voltage feedback MPPT tracking	HIL with GCPVS	• Power quality unaffected • No false tripping • Small NDZ • Inexpensive	200–300
[21]	Passive	Inverter-based DG	ROCOV, Ratio of voltage and current magnitude	MATLAB/Simulink	• Compatible with existing network infrastructure • Decentralized operation	<2000
[22]	Active	DC microgrid	Harmonic impedance	MATLAB/Simulink	• DC/DC converter is used injection equipment avoiding additional injection equipment	<500
[38]	Passive	Inverter-based	Probabilistic neural network	DigSilent Power Factorys software	• 100% accuracy	200–210

(continued)

Table 2 (continued)

References	Type	Ideal for	Based on (parameters)	Testing	Features	Islanding detection (ms)
[39]	Hybrid	Inverter-based	SFS and ROCOF	MATLAB/Simulink based on IEEE 1547 and UL1741 anti-islanding test	• Improved system power quality • Small NDZ	<1500
[40]	Signal processing	GCPVS	WT	MATLAB/Simulink	• Improved islanding detection	3–8 cycles
[41]	Signal processing	GCPVS	ST, WT	IEEE 30-bus system	• Effective performance in presence of harmonics as well	20–30
[42]	Signal processing	Generalized	WT, NN	MATLAB/Simulink	• Considerable reduction of NDZ	<50

6 Recommendation and Future Trends

Based on extensive analysis of various islanding detection methods it has been observed that SP-based IDMs are most feasible method of islanding detection. SP-based methods have effortless, precise and robust operation, efficient at all operating conditions and less computational burden then intelligent-based IDMs considering all these factors it is concluded that SP methods are convenient choice for islanding detection. There is scope of improvement in SP-based techniques in near future to further reduce the computational speed and also the cost of installation. Also it is observed that hybrid IDM holds enough potential for the scope of improvement and are likely to become more convenient option in near future.

7 Conclusion

In this paper profuse methods for island detection of microgrid are stockpiled with special reference to active solar photovoltaic system as distribution generation is presented in detail. Various islanding detection criteria are scrutinized in detail along with their merits and demerits. Some methods specially designed for solar PV as DG unit are also discussed and their comparison is presented. Thorough study of literature review is done and it has been observed that SP-based methods are the most suitable methods for islanding detection for PV-based DG due to their good response time, high accuracy and reliability.

References

1. Radwan AAA, Mohamed YARI (2012) Assessment and mitigation of interaction dynamics in hybrid AC/DC distribution generation systems. IEEE Trans Smart Grid 3:1382–1393
2. Mahmud MA, Hossain MJ, Pota HR (2011) Analysis of voltage rise effect on distribution network with distributed generation. IFAC Proc 44:14796–14801
3. Wijeratne WMPU, Yang RJ, Too E, Wakefield R (2019) Design and development of distributed solar PV systems: Do the current tools work? Sustain Cities Soc 45:553–578
4. Singh G, Swarnkar A, Gupta N, Niazi KR (2020) A review of scheduling techniques and communication protocols for smart homes capable of implementing demand response. Lect Notes Electr Eng 607:505–513
5. Shuai Z, Sun Y, Shen ZJ, Tian W, Tu C, Li Y, Yin X (2016) Microgrid stability: classification and a review. Renew Sustain Energy Rev 58:167–179
6. Martin-Martínez F, Sánchez-Miralles A, Rivier M (2016) A literature review of microgrids: a functional layer based classification. Renew Sustain Energy Rev 62:1133–1153
7. Lopes JAP, Moreira CL, Madureira AG (2006) Defining control strategies for microgrids islanded operation. IEEE Trans Power Syst 21:916–924
8. Katiraei F, Iravani MR, Lehn PW (2005) Micro-grid autonomous operation during and subsequent to islanding process. IEEE Trans Power Deliv 20:248–257
9. Reigosa D, Briz F, Charro CB, Garcia P, Guerrero JM (2012) Active islanding detection using high-frequency signal injection. IEEE Trans Ind Appl 48:1588–1597

10. Verma V, Jain S (2017) Active islanding detection method for grid and DG failure in a community microgrid application. In: IEEE international conference on power electronics, drives and energy systems, PEDES 2016, 1–5 Jan 2016
11. Papadimitriou CN, Kleftakis VA, Hatziargyriou ND (2015) A novel islanding detection method for microgrids based on variable impedance insertion. Electr Power Syst Res 121:58–66
12. Ropp ME, Begovic M, Rohatgi A (1999) Analysis and performance assessment of the active frequency drift method of islanding prevention. IEEE Trans Energy Convers 14:810–816
13. Zeineldin HH, Kennedy S (2009) Sandia frequency-shift parameter selection to eliminate nondetection zones. IEEE Trans Power Deliv 24:486–487
14. Wang X, Freitas W, Xu W, Dinavahi V (2007) Impact of DG interface controls on the Sandia frequency shift antiislanding method. IEEE Trans Energy Convers 22:792–794
15. Vahedi H, Karrari M (2013) Adaptive fuzzy Sandia frequency-shift method for islanding protection of inverter-based distributed generation. IEEE Trans Power Deliv 28:84–92
16. Mohammadpour B, Pahlevaninezhad M, Kaviri SM, Jain P (2016) A new slip mode frequency shift islanding detection method for single phase grid connected inverters. In: 2016 IEEE 7th international symposium on power electronics for distributed generation systems, PEDG 2016
17. Akhlaghi S, Akhlaghi A, Ghadimi AA (2016) Performance analysis of the Slip mode frequency shift islanding detection method under different inverter interface control strategies. 2016 IEEE power energy conference on Illinois, PECI 2016
18. Admasie S, Bukhari SBA, Haider R, Gush T, Kim CH (2019) A passive islanding detection scheme using variational mode decomposition-based mode singular entropy for integrated microgrids. Electr Power Syst Res 177:105983
19. Makkieh A, Florida-James A, Tzelepis D, Emhemed A, Burt G, Strachan S, Junyent-Ferre A (2019) Assessment of passive islanding detection methods for DC microgrids. IET Conf Publ 2019
20. Reddy CR, Reddy KH (2018) A passive islanding detection method for neutral point clamped multilevel inverter based distributed generation using rate of change of frequency analysis. Int J Electr Comput Eng 8:1967–1976
21. Jahdi S, Lai LL (2011) DG islanding operation detection methods in combination of harmonics protection schemes. IEEE PES Innov Smart Grid Technol Conf Eur
22. Xie X, Huang C, Li D (2020) A new passive islanding detection approach considering the dynamic behavior of load in microgrid. Int J Electr Power Energy Syst 117:105619
23. Somalwar RS, Shinde DA, Kadwane SG (2018) Comparative analysis of ripple-based passive islanding detection techniques for single-phase micro-grid system. In: Proceedings of 2018 IEEE international conference on power electronics, drives and energy systems, PEDES 2018
24. Loh PC, Li D, Chai YK, Blaabjerg F (2013) Autonomous operation of hybrid microgrid with ac and dc subgrids. IEEE Trans Power Electron 28:2214–2223
25. Liu J, Hossain MJ, Lu J, Rafi FHM, Li H (2018) A hybrid AC/DC microgrid control system based on a virtual synchronous generator for smooth transient performances. Electr Power Syst Res 162:169–182
26. Eghtedarpour N, Farjah E (2014) Power control and management in a hybrid AC/DC microgrid. IEEE Trans Smart Grid 5:1494–1505
27. Khamis A, Shareef H, Bizkevelci E, Khatib T (2013) A review of islanding detection techniques for renewable distributed generation systems. Renew Sustain Energy Rev 28:483–493
28. Wang W, Kliber J, Zhang G, Xu W, Howell B, Palladino T (2007) A power line signaling based scheme for anti-islanding protection of distributed generators—Part II: field test results. IEEE Trans Power Deliv 22:1767–1772
29. Hubana T (2020) Artificial intelligence based station protection concept for medium voltage microgrids. In: 2020 19th international symposium on INFOTEH-JAHORINA, INFOTEH 2020—Proceedings
30. Raza S, Mokhlis H, Arof H, Laghari JA, Wang L (2015) Application of signal processing techniques for islanding detection of distributed generation in distribution network: a review. Energy Convers Manag 96:613–624

31. Menezes TS, Fernandes RAS, Coury DV (2020) Intelligent islanding detection with grid topology adaptation and minimum non-detection zone. Electr Power Syst Res 187:106470
32. Heidari M, Seifossadat G, Razaz M (2013) Application of decision tree and discrete wavelet transform for an optimized intelligent-based islanding detection method in distributed systems with distributed generations. Renew Sustain Energy Rev 27:525–532
33. Bakhshi-Jafarabadi R, Sadeh J, de Chavez JJ, Popov M (2021) Two-level islanding detection method for grid-connected photovoltaic system-based microgrid with small non-detection zone. IEEE Trans Smart Grid 12:1063–1072
34. Bakhshi-Jafarabadi R, Sadeh J (2020) New voltage feedback-based islanding detection method for grid-connected photovoltaic systems of microgrid with zero non-detection zone. IET Renew Power Gener 14:1710–1719
35. Bakhshi-Jafarabadi R, Sadeh J, Popov M (2021) Maximum power point tracking injection method for islanding detection of grid-connected photovoltaic systems in microgrid. IEEE Trans Power Deliv 36:168–179
36. Karimi M, Farshad M, Hong Q, Laaksonen H, Kauhaniemi K (2021) An islanding detection technique for inverter-based distributed generation in microgrids. Energies 14
37. Ke J, Zhengxuan Z, Qijuan Z, Zhe Y, Tianshu B (2019) Islanding detection method of multi-port photovoltaic DC micro grid based on harmonic impedance measurement. IET Renew Power Gener 13:2604–2611
38. Khamis A, Shareef H, Mohamed A, Bizkevelci E (2015) Islanding detection in a distributed generation integrated power system using phase space technique and probabilistic neural network. Neurocomputing 148:587–599
39. Khodaparastan M, Vahedi H, Khazaeli F, Oraee H (2017) A novel hybrid islanding detection method for inverter-based DGs using SFS and ROCOF. IEEE Trans Power Deliv 32:2162–2170
40. Kim IS (2016) Islanding detection technique using wavelet energy in grid-connected PV system. Int J Electron 103:1381–1396
41. Mohanty SR, Kishor N, Ray PK, Catalao JPS (2015) Comparative study of advanced signal processing techniques for islanding detection in a hybrid distributed generation system. IEEE Trans Sustain Energy 6:122–131
42. Shahryari E, Nooshyar M, Sobhani B (2019) International Journal of Ambient Energy Combination of neural network and wavelet transform for islanding detection of distributed generation in a small-scale network Combination of neural network and wavelet transform for islanding detection of distributed generation in a small-scale network. Int J Ambient Energy 40:263–273

A Computational Investigation of the Optoelectronic Characteristics of Chalcopyrite $HgCP_2$

Karina Khan, Aditi Gaur, Ushma Ahuja, Amit Soni, and Jagrati Sahariya

Abstract The theoretical tool based on density functional theory has been used to explore optoelectronic characteristics of ternary chalcopyrite $HgCP_2$ that is executed in Wien2k code. For obtaining the solution of Kohn–Sham equation, we have adopted FP-LAPW method, and entire computations are done by utilizing optimized lattice parameters that are obtained through PBE-GGA (generalized gradient approximation). Electronic properties are computed through energy band and density of state spectra by using TB-mBJ exchange-correlational potential, which yields 0.77 eV band gap of $HgCP_2$. The optical analyzations are done by using spectra of absorption coefficient, complex dielectric tensor, reflection, and refraction. Through these spectra, we observed that the value of absolute reflectivity is lower and the value of absorption coefficient is higher which indicate that the material exhibits optoelectronic properties.

Keywords Absorption coefficient · Chalcopyrites · DFT · Optoelectronic applications

1 Introduction

Today's world leads toward the modernization for the development of the individual as well as for whole nation, which needs the new technologies that require energy to establish. And currently, the energy system is majorly depending on fossil fuels

K. Khan
Department of Physics, Manipal University Jaipur, Jaipur 303007, India

A. Gaur · A. Soni (✉)
Department of Electrical Engineering, Manipal University Jaipur, Jaipur 303007, India
e-mail: amitsoni_17@yahoo.co.in

U. Ahuja
Department of Electrical Engineering, NMIMS, Mukesh Patel School of Technology Management and Engineering, Mumbai 400056, Maharashtra, India

J. Sahariya
Department of Physic, NIT Uttrakhand, Srinagar 246174, Uttarakhand, India

© The Author(s), under exclusive license to Springer Nature Singapore Pte Ltd. 2022

A. Tripathi et al. (eds.), *Intelligent Computing Techniques for Smart Energy Systems*, Lecture Notes in Electrical Engineering 862,
https://doi.org/10.1007/978-981-19-0252-9_58

(petroleum, coal, gas) whose present availability on earth is sufficient, but it will not long-lasting as these fossil fuels take nearly hundreds of years of manufacture. Along with the exhaustible nature of fossil fuels, their non-eco-friendly nature also become the sedative issue globally, so it is better to switch on the renewable energy source (wind, air, solar) rather than the non-renewable sources [1–5]. So the scientific community mainly focus on to harvest the renewable source into its useful form in a proper way that its harvesting takes low cost and favorable for environment. Among all the renewable energies, the energy we get from the sun is very vast, cleanest, and its harvesting cost is comparatively low [6, 7], and the photovoltaic modules are used to convert the solar energy into its usable form such as electrical energy either directly or indirectly [8]. Along with conversion of energy, a solar cell must produce good efficiency; the material used in solar cell must be non-toxic and having optimum band gap. The II-IV-V_2 ternary chalcopyrites have fascinated the researchers for investigation due to their wide applications in the optoelectronic devices. There are large number of compounds that belong to this group and having large variation in their band gap facilitates them in numbers of fields: optoelectronic, thermoelectric, magnetic, photonic, spintronic etc. [9–13]. The phosphides of the group II-IV-V_2 are having structural symmetry with binary III-P semiconductors; these compounds are perfect for the photo electrochemical applications. These phosphides are made up to such type materials which have good natural abundance also having properties of direct and indirect band gap semiconductors with higher charge carrier mobility. These phosphides are thermally stable and possess larger second harmonic generation coefficient, so can be used as harmonic oscillators [14–18]. The electronic behavior of $HgAX_2$ (A = C, Si, Ge, Sn; X = N, P, As, Sb) has been reported along with the chemical bonding by Basalaev et al. [19–21]; they have calculated the band gaps ($HgCP_2$ = 1.05 eV) of these compounds by using energy band structure which are plotted by using CRYSTAL package. In addition, it has been reported by authors that this compound can be used in optical data storage devices, detectors for infrared radiations, and Bragg's reflector.

2 Details of Computations

This paper is based on the computation of structure-based optoelectronic properties of ternary chalcopyrite $HgCP_2$ by using theoretical tool named as Wien2k code, which is rooted on the concept of DFT, and by adopting full potential linearized augmented plane wave method (FP-LAPW)is ingurgitate to get the basis set [22–24]. In this work, we have used two exchange-correlational functional: PBE-GGA: Perdew Burke Ernzerhof-generalized gradient approximation and TB-mBJ: Tran-Blaha modified Becke Johnson potential for computing structural and optoelectronic properties, respectively [25]. We have used the mesh 10 × 10 × 10 k points in order to achieve accuracy in the results. In addition, the value l_{max}, G_{max}, RMT K_{max} and energy cut-off is set to 10, 12, 7, and −6 Ry. First, we have taken the lattice parameter of tetragonal $HgCP_2$ (space group:122(I $4\bar{2}$d)) from the previously

reported literature [19]. Then, we performed the volume optimization by using PBE-GGA exchange-correlational functional, plot is depicted in Fig. 1 which yield the optimized parameters $a = b = 5.3824$ Å; c= 9.1845 Å with Wyckoff positions (0, 0, 0); (0, 0.5, 0.5) and (0.326, 0.25, 0.125) of Hg, C, and P, respectively, and the value of absolute energy is obtained through Fig. 1 is −815,536.186057 Ry. The crystal structure of $HgCP_2$ is presented in Fig. 2 along with the Brillouin Zone, which presented this structure in highly symmetry direction.

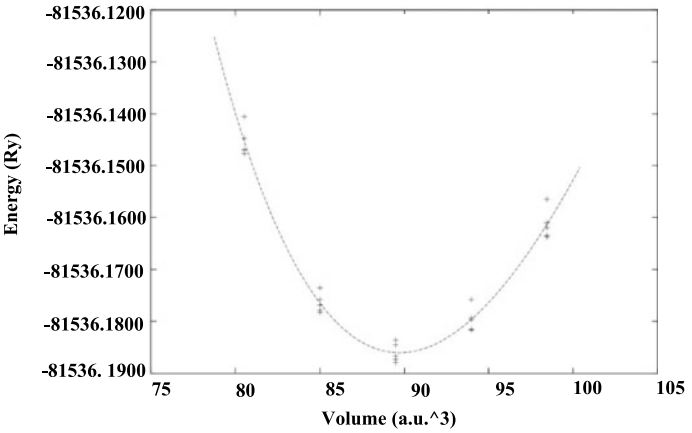

Fig. 1 Energy versus volume optimization curve of $HgCP_2$

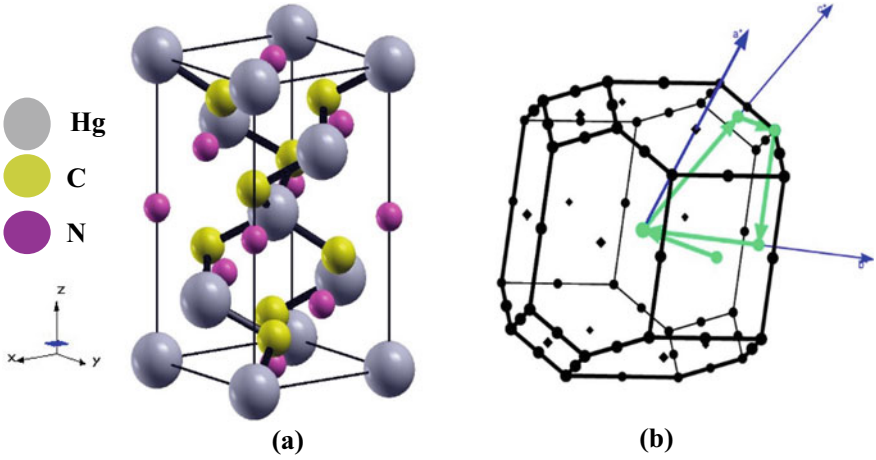

Fig. 2 **(a)** Crystal structure. **(b)** Brillouin zone of $HgCP_2$

3 Results and Discussion

3.1 Electronic Properties

The exchange–correlation potential: TB-mBJ is used for computing electronic response of $HgCP_2$ through the electronic band structure, which is depicted in Fig. 3, and through this structure, we estimate the energy gap of compound that depicts the nature of the compound as well. In Fig. 3, the zero electron-volt is chosen as fermi energy level, and the energy gap between the lowest point of valence and highest point of conduction band gives the band gap of the compound. The compound $HgCP_2$ exhibits direct band gap, as it is evident through the band structure (Fig. 3) that valence band maximum (VBM) and conduction band minimum(CBM) both located at the same momentum point. The band gap of this compound is 0.77 eV and its comparison with other reported work is given in Table 1. The different color bands in electronic band structure is used to tell the position of electron and their transitions as well.

We further explain the electronic properties by using the density of states (DOS) spectra, which is plotted, by using TB-mBJ potential. The fermi energy is set at zero electron volt through which is used to calculate the band gap at 0.77 eV. The valence band is not present just after the fermi energy level; it is situated at little gap. The DOS spectra of HgCP2 is presented in Fig. 4.The DOS spectra is used to explain the energy distribution among the electrons in different energy level, and in this DOS

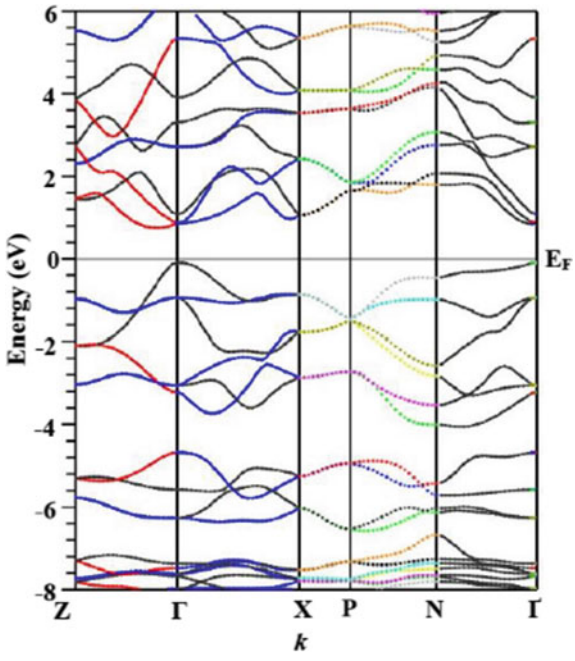

Fig. 3 Energy band spectra of $HgCP_2$

Table 1 Band gap (eV) comparison with other similar compounds

Compound	Band gap (eV)
$HgCP_2$	0.77[a], 1.04 eV[b]
$HgCN_2$	2.70[b], 0.54[c]
$HgCAs_2$	0.41[b]
$HgCSb_2$	0.47[b]

[a] Our work, [b] [19], [c] [19]

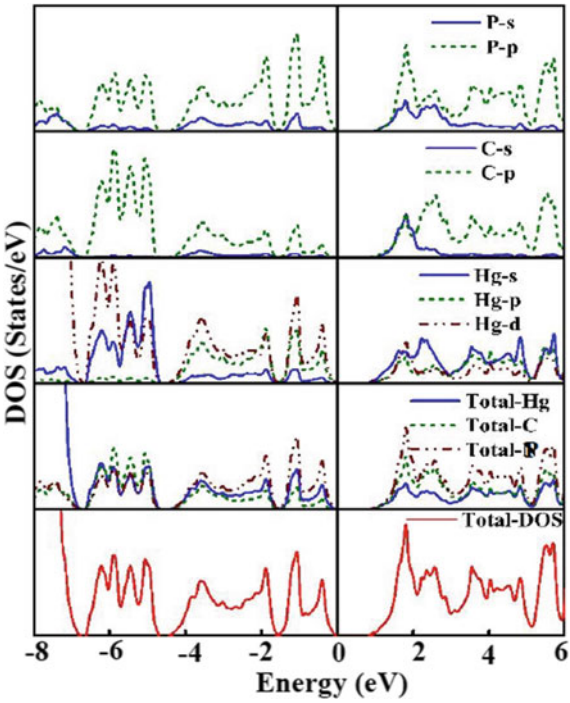

Fig. 4 DOS spectra of $HgCP_2$

spectra, three band regions are formed: core, valence, and conduction which lie at −8 to 5.6 eV; −5.6 to 0 eV, and 0.77–6 eV, respectively. The hybridization state of 'p' of C and P devote the maximum contribution in the core region. The bands in the valence region arise mostly due to d-energy state of Hg atom and p-energy state of P atom. The major contribution of 's' and 'p' state of P in conduction band region. Most of the bands overlapped each other which indicate their covalent bonding.

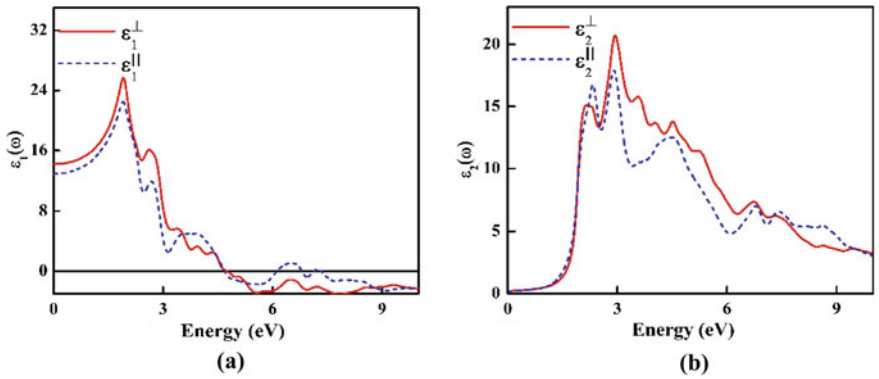

Fig. 5 **a** Real dielectric tensor spectra. **b** Imaginary dielectric tensor spectra of $HgCP_2$

3.2 Optical Properties

The optical parameters, which are generated due to mobility and recombination of electrons with respect time, are most important for the explanation of the utility of the compound in the optoelectronic applications. In this portion, we explain the optical properties of the HgCP2 by using optical spectra up to 10 eV, which are computed through TB-mBJ potential.

In Fig. 5a, b, we explain dielectric tensor spectra of real and imaginary components that explain through the wave vector. The real dielectric tensor is useful for obtaining energy storage and polarization, and we obtained the absolute value of = 12. In addition, the peaks at 2.33 and 2.911 eV arise in imaginary dielectric tensor are used to explain the transition of electrons from VB to CB and attenuation of the electromagnetic waves.

Figure 6a represents the spectra of the absorption coefficient of $HgCP_2$; this spectrum is used to tell us about the amount of energy absorbed by the material and in which range of electromagnetic spectrum its intensity falls. Moreover, through the absorption spectra, we found that most of the intensity fall in 3–5 eV range that belongs to the visible spectra region. The computed value the integrated absorption coefficient (IAC) is 228.74 ($\times 10^4$ eV/cm). The absorption of the material also depends on the surface where the light incidents, and this factor is determined through the reflectivity and refractivity optical parameters that are spectra as shown in Fig. 6b–c. These two parameter tell about the transparency and roughness of the material. The absolute values of reflection and refraction are 0.31 and 3.5, respectively. The $HgCP_2$ compound has a partial anisotropic nature as it can be seen through the optical spectra that their parallel and perpendicular components coincide only in the low energy range.

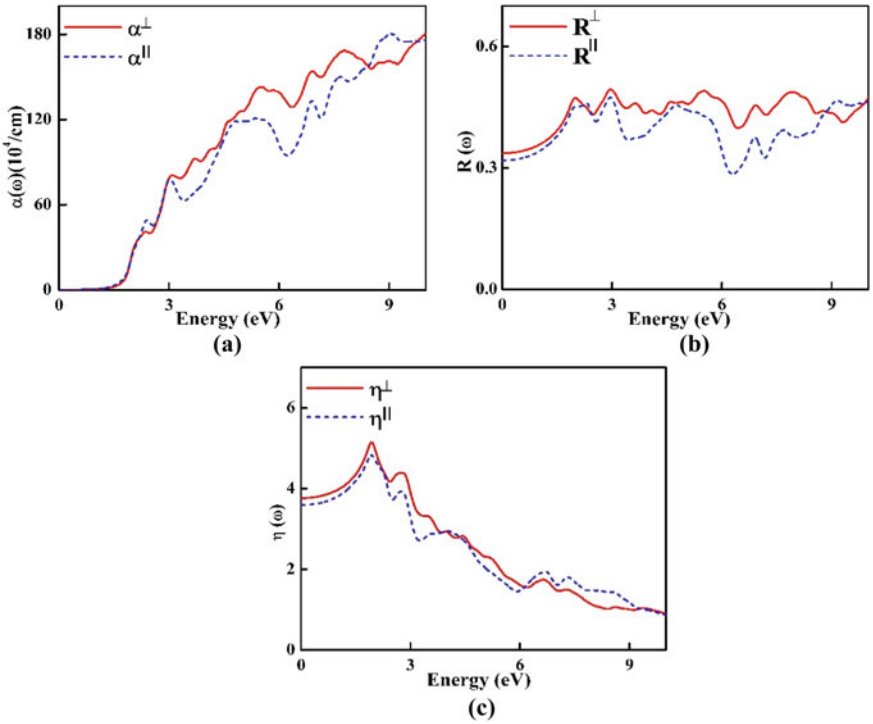

Fig. 6 Spectra of **(a)** absorption **(b)** reflectivity, and **(c)** refractivity of $HgCP_2$

4 Conclusion

In the summary, we come to conclusion that after studying the optoelectronic characteristics of $HgCP_2$ by using DFT embodied in Wein2k package with FP-LAPW method, this can be utilized well in the optoelectronic applications. As we found through energy band diagram and DOS spectra that $HgCP_2$ has semiconductor nature with direct energy gap. Moreover, the optical behavior confirms that the $HgCP_2$ has partial isotropic nature, and notable intensity is observed in the visible spectra region.

Acknowledgements We highly presenting our gratitude toward the Prof. Peter Blaha for providing the tool Wein2k code for all computational work. Authors are thankful to Manipal University Jaipur for providing work place. Financial support is provided through DST-SERB, New Delhi (India), vide grant number EMR/2017/005534.

References

1. Lund H (2007) Renewable energy strategies for sustainable development. Energy 16:912–919

2. York R, Bell EB (2019) Energy transitions or additions?: why a transition from fossil fuels requires more than the growth of renewable energy. Ene Res Soc Sci 51:40–43
3. Abas N, Kalair A, Khan N (2015) Review of fossil fuels and future energy technologies. Futures 69:31–49
4. Kåberger T (2018) Progress of renewable electricity replacing fossil fuels. Glo Ene Int 1:48–52
5. Forsberg CW (2009) Sustainability by combining nuclear, fossil, and renewable energy sources. Prog Nuc Ene 51:192–200
6. Harjanne A, Korhonen J (2019) Abandoning the concept of renewable energy. Energy Policy 127:330–340
7. Liu J (2019) China's renewable energy law and policy: a critical review. Renew Sust Ener Rev 99:212–219
8. Zhong ZW, Song B, Lo PE (2011) LCAs of a polycrystalline photovoltaic module and a wind turbine. Renew Ener 36:2227–2237
9. Shaposhnikov VL, Krivosheeva AV, Borisenko VE (2012) Ab initio modeling of the structural, electronic, and optical properties of $A^{II}B^{IV}C^{V}_2$ semiconductors. Phys Rev B 85:205201-1–205209
10. Rud VY, Rud YV, Terukov EI (2016) Polarization studies of the photoelectric properties of II–IV–V2-semiconductor-compound–electrolyte systems. J Opt Tech 83:275–278
11. Boukabrine F, Chiker, Miloua F et al (2016) Combined theoretical studies of the optical characteristics of II-IV-V_2 semiconductor thin films. Opt Mat 54:200–206
12. Pandey M, Kuhar K, Jacobsen KW (2017) II–IV–V_2 and III–III–V_2 polytypes as light absorbers for single junction and tandem photovoltaic devices. J Phys Chem C 33:17780–17786
13. He G, Rozahun I, Li Z et al (2019) Size effect and identified superior functional units enhancing second harmonic generation responses on the II-IV-V2 type nonlinear optical crystals. Chem Phy 518:101–106
14. Oumelaz F, Nemiri O, Boumaza A et al (2017) Theoretical investigation of the structural stabilities, optoelectronic properties and thermodynamic characteristics of GaP_xSb_{1-x} ternary alloys. Ind J Phys 92:705–714
15. Lee S, Fahrenkrug E, Maldonado S (2015) Synthesis of photoactive $ZnSnP_2$ semiconductor nanowires. J Mater Res 30:2170–2178
16. Gautam R, Singh P, Sharma S et al (2015) Structural, electronic, optical, elastic and thermal properties of $CdSnP_2$ with the application in solar cell devices. Mat Sci Semi Proc 31:493–500
17. Chen J, Lin C, Peng G et al (2019) $BaGe_2Pn_2$ (Pn = P, As): Two congruent-melting non-chalcopyrite pnictides as mid- and far-infrared nonlinear optical materials exhibiting large second harmonic generation effects. Chem Mater 31:10170–10177
18. Gani A, Cheref O, Ghezali M et al (2020) Mechanical stability and optoelectronic behavior of $BeXP_2$ (X=Si and Ge) chalcopyrite. Chin J Phys 64:174–182
19. Basalaev Y, Basalaeva M (2020) Simulation of electronic structures of Hg–IV–V_2 compounds. J Struc Chem 61:1007–1016
20. Basalaev Y, Basalaeva M, Duginova EB et al (2020) Electronic structure of pnictides $HgCX_2$. J Struc Chem 61:1839–1844
21. Basalaev Y, Basalaeva OG, Sidorova AV (2020) A first-principles simulation of electronic structure of MCN_2 Crystals (M = Be, Mg, Ca, Zn, Cd, Hg). J Struc Chem 61:337–343
22. Blaha P, Schwarz K, Tran F et al (2020) WIEN2k: an APW+lo program for calculating the properties of solids. J Chem Phys 152:074101
23. Sahariya J (2017) Structural and optical investigations of $ZnGa_2X_4$ (X = S, Se) compounds for solar photovoltaic applications. Mat Chem Phy 199:257–264
24. Perdew JP, Wang Y (1992) Accurate and simple analytic representation of the electron-gas correlation energy. Phys Rev 45:13244–13249
25. Rauch T, Miguel AL, Botti S (2020) Local modified Becke-Johnson exchange-correlation potential for interfaces, surfaces, and two-dimensional materials. J Chem Theory Comp 16:2654–2660

Performance Analysis of Model Reduction Techniques Applied to High Order Systems

Apoorv Srivastava, Asha Rani, and Jyoti Yadav

Abstract This paper focuses on the analysis of different model order reduction methods and control of the reduced order systems. Higher order systems are difficult to control and analyze, due to the complex calculations. Therefore, in this work, different methods are used to reduce the model order with an objective that characteristics of reduced order system are same as the original system. The analysis of reduced and original system is carried out based on different performance measures. Further, the technique is applied for control of high-order systems. The results reveal that balanced truncation of state space, shows the best performance for the problem under consideration.

Keywords MOR · Controller · Approximation · Original system · Reduced order system · Model order reduction · SVD · HVD

1 Introduction

There are several model order reduction (MOR) techniques which are used to obtain reduced order modal which are developed in early stages. There are constant modification and improvement in these techniques. Some new techniques are also developed. The most common technique for MOR is Routh approximation [1]. The Routh approximation method reported in the literature is based on the alpha and beta parameters. The proposed method also has the advantage of always delivering a stable lower-order model if the original higher order system is stable.

Direct and balanced truncation method [2–4] is also very popular. In direct truncation method, we just eliminate higher order terms. Varricchio [2] proposed a model

A. Srivastava (✉) · A. Rani · J. Yadav
NSUT, New Delhi, India
e-mail: apoorvsri99@gmail.com

A. Rani
e-mail: asha.rani@nsut.ac.in

J. Yadav
e-mail: jyoti.yadav@nsut.ac.in

© The Author(s), under exclusive license to Springer Nature Singapore Pte Ltd. 2022

A. Tripathi et al. (eds.), *Intelligent Computing Techniques for Smart Energy Systems*,
Lecture Notes in Electrical Engineering 862,
https://doi.org/10.1007/978-981-19-0252-9_59

order reductions, a combination of modal and balanced truncation approaches is used. A stopping criterion based on spectral energy principles is also proposed to efficiently integrate these strategies. Prajapati [3] discussed a numerical method to deal with the resulting matrix exponential functions and Lyapunov equations which are used for solving low-rank approximations. The rational Krylov subspace methods are the scheme's key tool. The eigenvalue decay and numerical rank of Lyapunov equation solutions are also taken into account. When compared to ordinary balanced truncation, the numerical rank of the Lyapunov solutions in time-limited balanced truncation can be identical. Kürschner [4] used factor division and balanced truncation methods to find the most accurate reduced order modal.

Mikhailov stability criterion is widely used method which is based on frequency domain analysis. Nagar [5] introduced two separate algorithms which were integrated with the Mikhailov stability criterion's property.

The reduced order denominator polynomial is derived using the described method, and the numerator polynomials are computed using two alternative methods. The importance of the provided algorithms in the numerical examples justifies their uniqueness.

State space methods are also quite popular for MOR as they use matrices for calculation. Ha compares balanced truncation and modal truncation, two well-known model reduction strategies [6]. The comparison is based on the error-bound equations given for a specific class of systems in this paper. A numerical example is used to show the comparison. Interval systems are also used in industrial applications because of their dynamic coefficients. Deveerasetty [7] derived the reduced order model for interval system. The proposed method generates stable reduced order models, while retaining the zeroth order interval time moment.

Apart from standard methods, some AI-based methods are also reported in literature. Cuckoo search optimization-based [8] reduced order systems is proposed which shows better performance than other order reduction techniques. After obtaining reduced order model, there is also need to design an efficient controller. VGD Rayudu [9] designed a PID controller for a large-order system which was constructed using a reduced order concept. By comparing the step responses of the original and lower-order models, the effectiveness of the recommended strategy may be established. The suggested technique's performance is evaluated using step responses and performance indices. Kumbasar [10] proposed a fuzzy-based controller for second-order interval system, which is more robust than other controllers due to well-defined rules. These methods are applied in various fields such as in gas turbine [11], in power system [12], in robotics [13], in magnetic field [14], and in wind farm [15]. The literature survey reveals that model order reduction is important area of research, and there is a large scope of improvement in the performance of reduced models. Therefore, in this work, different model order reduction techniques are analyzed, and reduced order system is controlled using PID controller.

2 Model Reduction Techniques

There are many techniques available to reduce model order, some are based on time domain and others on frequency domain analysis.

Let G_n be very high-order system defined by Eq. (1).

$$G_n(s) = \frac{N(s)}{D(s)} = \frac{a_o + a_1 s + a_2 s^2 + \ldots a_{n-1} s^{n-1}}{b_o + b_1 s + b_2 s^2 + \ldots b_n s^n} \tag{1}$$

MOR techniques are used to get reduced order model R_k which is defined by Eq. (2)

$$R_k(s) = \frac{N(s)}{D(s)} = \frac{c_o + c_1 s + c_2 s^2 + \ldots c_{k-1} s^{k-1}}{d_o + d_1 s + d_2 s^2 + \ldots d_k s^k} \tag{2}$$

The major goal is to implement the kth order reduced model while keeping the important characteristics of the original high-order system.

2.1 Pade's Approximation

Pade's approximation is one of the widely used techniques in model order reduction [16]. It compares the fraction with a polynomial for finding the coefficients, but it requires complex calculations and is less efficient.

2.2 Direct Truncation

It is one of the easiest methods and is the most suitable for some class of polynomials [17]. In this method, the unwanted coefficients are directly eliminated for obtaining reduced order model. The DC gain is made equal to the original system for the purpose.

2.3 Stability State Equation

This approach is based on canceling poles and zeros [18]. The transfer function's numerator and denominator are separated into odd and even sections. Since lower magnitude poles or zeros are more dominating than bigger magnitude poles or zeros, they are rejected to reduce the order of stability equations.

2.4 Routh Approximation

Routh table is the most common method for checking stability of the system. This method is based on Routh table [19]. Two different tables for numerator and denominator are made which is called α and β tables and used for model reduction.

2.4.1 V. Krishnamurthy Approach

V. Krishnamurthy also suggested a very easy approach based on Routh table [20]. In this method, entire row of Routh table is eliminated to find the reduced order model.

2.5 Mikhailov Stability Criteria

Mikhailov stability criteria is also an accurate method for model order reduction. It is based on frequency response of transfer function [21]. This method is used only for denominator polynomial. The denominator polynomial is divided into real and imaginary parts, and then, higher frequency elements are eliminated.

2.6 Mixed Methods

All above methods are good, but improved model reduction may be achieved using hybrid techniques to find numerator and denominator polynomial [9]. In this work, denominator polynomial is obtained using Mikhailov stability, and numerator polynomial is obtained by modified Pade approximation. The suggested method may provide good results as it contains the advantages of two methods.

2.7 Balanced Truncation of State Space Model

The classical methods discussed above can be very lengthy and difficult to work, if the system order is too high. Therefore, state space model technique is used for very high model. This is achieved by state space transformation to obtain the reduced order matrix. Most commonly used methods for the purpose are singular values decomposition (SVD) and Hankel value decomposition (HVD) [22, 23].

3 Results and Discussion

In this work, a high-order transfer function is considered as experimental model whose order is reduced using different model reduction techniques. The considered transfer function is defined by Eq. (3). The different model reduction methods are used to reduce this transfer function into second order. Step response and ISE and IAE performance indices are calculated for quantitative analysis. All simulations are done in MATLAB R2019a on AMD Ryzen 5 PC.

$$G(s) = \frac{s^5 + 8s^4 + 20s^3 + 16s^2 + 3s + 2}{s^6 + 18.3s^5 + 102.4s^4 + 209.5s^3 + 155.9s^2 + 33.6s + 2} \tag{3}$$

$$\text{ISE} = \int_0^\infty [y(t) - y_r(t)]^2 \mathrm{d}t \tag{4}$$

$$\text{IAE} = \int_0^\infty [y(t) - y_r(t)] \mathrm{d}t \tag{5}$$

where $y(t)$ and $y_r(t)$ denote the original and reduced order systems' step responses, respectively.

3.1 Model Order Reduction

All model order reductions techniques discussed in section II are tested, so as to find the best method for reduction of order with low calculation complexities. The second-order transfer obtained using different methods are given in Table 1.

Table 1 Reduced order transfer function obtained from different methods

Method	Reduced order transfer function
Pade approximation	$\frac{0.0313s+0.01233}{s^2+0.22s+0.01233}$
Direct truncation	$\frac{3s+2}{155.9s^2+33.6s+2}$
Stability state equation	$\frac{3s+2}{154.5s^2+33.4s+2}$
Routh approximation	$\frac{1.127s+0.1558}{s^2+0.234s+0.1392}$
V. Krishnamurthy approach	$\frac{0.312s+2}{137.1s^2+30.59s+2}$
Mixed method	$\frac{3s+2}{155.0388s^2+33.565s+2}$
SVD	$\frac{0.04051s+0.003558}{s^2+0.08066s+0.004026}$
HVD	$\frac{0.1164s^2+0.002129s+0.01791}{s^2+0.2759s+0.01791}$

The step response of reduced order models is shown in Fig. 1, and the quantitative analysis of the performance is given in Table 2. It is observed from the results that HVD gives very good results because it uses the concept of balanced truncation. The mixed methods are preferred as they have advantages of different methods. It is also noted that HVD gives the best results, but it generates semi-proper transfer function which has its own drawback. It is also revealed that frequency response-based methods provide more efficient results than time domain methods; thus, Mihailov and stability state methods show good performance as compared to Pade's and Routh which are time domain methods.

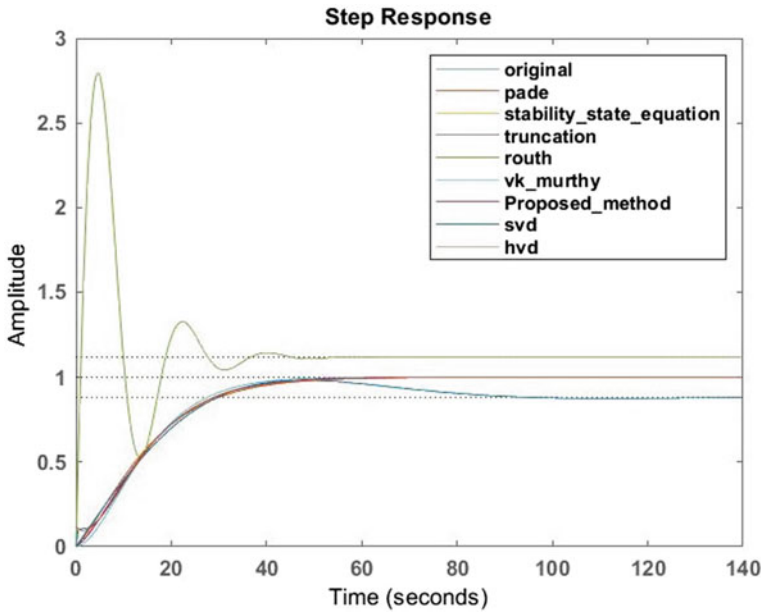

Fig. 1 Step response obtained from all techniques

Table 2 Performance comparison

Method	ISE	IAE
Stability state equation	2.1666	3.5667
Pade	2.1112	3.6555
Direct truncation	2.1733	3.5789
Routh	4.2781	3.2175
V. Kmurthy method	2.1786	3.6694
Hybrid method	2.3576	3.5907
SVD	0.5844	0.5844
HVD	0.0029	0.1362

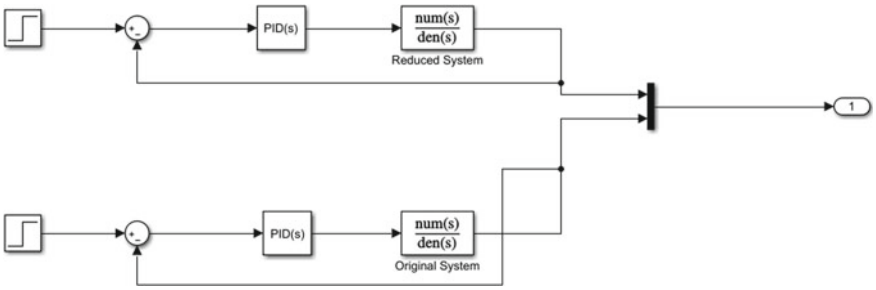

Fig. 2 Simulink model for controller design

Table 3 PID parameters

Method	K_P	K_I	K_D
Mixed method	28.644	0.1671	1.1386
SVD	0.8352	0.1239	0
HVD	0.8352	0.1239	0

3.2 Controller Design

The next step after model reduction is to design a controller for reduced order system. Therefore, PID controller, shown in Fig. 2, is designed for the reduced system, and controller is also used for the original system. The PID parameters are obtained using trial and error approach (Table 3).

The controller performance is shown in Fig. 3. It is observed from the results that mixed method shows high transient oscillations, but after some time, it converges to desired output. Initial oscillations are due to the very high order of the original system which takes some time to reach steady state.

It is revealed from the reduced order model results that HVD is the best method for model order reduction and controller also shows the best performance. It is also revealed that order reduction does not show the initial oscillations in controller response.

3.3 Model Order Reduction Application

Some very high-order real systems are also considered in this work, and the order is reduced by model order reduction technique. As HVD gives good results, so this method is used to reduce order of high order real systems. The ninth order Boiler system used by Zhao and Sinha [24] is considered in this work for model order reduction using HVD method.

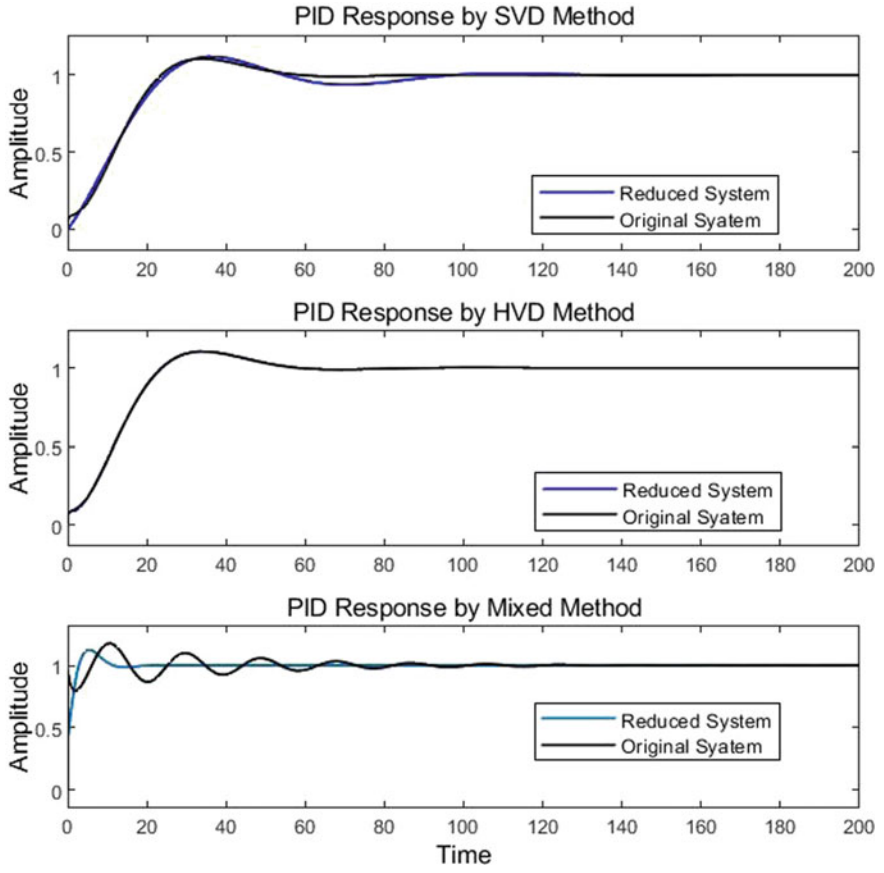

Fig. 3 PID response for mixed method

$$A = \begin{bmatrix} -0.9 & 0 & 0 & 0 & 0 & 0 & 0 & 0 & 0 \\ 0 & -4.4 & 0 & 0 & 0 & 0 & 0 & 0 & 0 \\ 0 & 0 & -10.2 & 571.5 & 0 & 0 & 0 & 0 & 0 \\ 0 & 0 & -571 & -10.2 & 0 & 0 & 0 & 0 & 0 \\ 0 & 0 & 0 & 0 & -10.9 & 0 & 0 & 0 & 0 \\ 0 & 0 & 0 & 0 & 0 & -15.2 & 11.6 & 0 & 0 \\ 0 & 0 & 0 & 0 & 0 & -11.6 & -15.2 & 0 & 0 \\ 0 & 0 & 0 & 0 & 0 & 0 & 0 & -89.8 & 0 \\ 0 & 0 & 0 & 0 & 0 & 0 & 0 & 0 & -503 \end{bmatrix}$$

$$B = \begin{bmatrix} -4.336 \\ -3.691 \\ 10.14 \\ -1.612 \\ 16.63 \\ -242.5 \\ -14.26 \\ 13.67 \\ 82.19 \end{bmatrix}$$

$$C = \begin{bmatrix} -0.4 & -0.7 & 0 & 0.2 & -0.8 & -0.7 & 0.5 & -0.2 & -0.08 \end{bmatrix}$$

After reduction, reduced state space model obtained is

$$a = \begin{bmatrix} -1.581 & -3.984 \\ -3.531 & -22.02 \end{bmatrix} \quad b = \begin{bmatrix} -4.605 & -16.94 \end{bmatrix}$$

$$c = \begin{bmatrix} -3.936 \\ -15.21 \end{bmatrix} \quad d = \begin{bmatrix} -1.349 \end{bmatrix}$$

$$A = \begin{bmatrix} -0.5 & 0 & 0.30 & 0 & 0 & 0 & 0 & 0 & 0 & 0.16 \\ -0.04 & 0 & -0.03 & 0 & 0 & 0 & 0 & 0 & 0 & 0 \\ 0 & 314.2 & 0 & 0 & 0 & 0 & 0 & 0 & 0 & 0 \\ 9.55 & 0 & -0.86 & -20 & 0 & 0 & 0 & 0 & 0 & 0 \\ 0 & 0 & 0 & 0 & -1 & 0 & 0 & 0 & 0.04 & -0.03 \\ -0.19 & 10.87 & -0.16 & 0 & 0 & -10.8 & 0 & 0 & 0 & 0 \\ -0.93 & 51.98 & -0.79 & 0 & 0 & -41.1 & -10.8 & 0 & 0 & 0 \\ -0.93 & 51.98 & -0.79 & 0 & 0 & -41.1 & -10.8 & -0.1 & 0 & 0 \\ 0 & 0 & 0 & 0 & -100 & -100 & 0 & 1000 & -20 & 0 \\ 0 & 0 & 0 & 0 & 0 & 0 & 0 & 0 & 1.05 & -0.82 \end{bmatrix}$$

$$B = \begin{bmatrix} 0 & 0 \\ 0 & 0.0926 \\ 0 & 0 \\ 0 & 0 \\ 0 & 0 \\ 0 & 0.4428 \\ 0 & 2.118 \\ 0 & 2.118 \\ 1000 & 0 \\ 0 & 0 \end{bmatrix}$$

$$C = \begin{bmatrix} 0 & 0 & 1 & 0 & 0 & 0 & 0 & 0 & 0 & 0 \\ 0.4777 & 0 & -0.0433 & 0 & 0 & 0 & 0 & 0 & 0 & 0 \end{bmatrix}$$

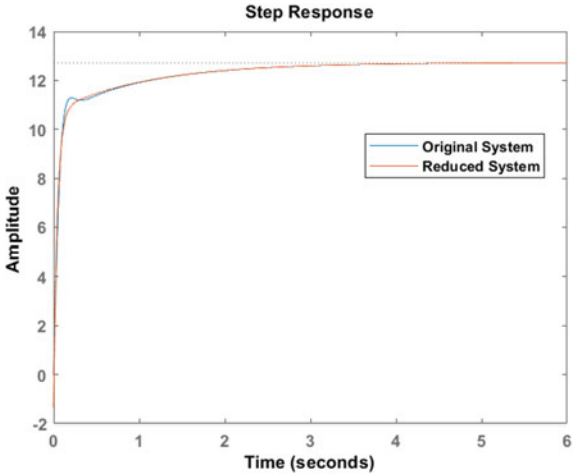

Fig. 4 Step response of boiler system

After reducing it with HVD method, it becomes

$$a = \begin{bmatrix} -0.7397 & 3.366 \\ -3.672 & 1.075 \end{bmatrix} \quad b = \begin{bmatrix} -0.2293 & 0.7008 \\ -0.03542 & -0.3832 \end{bmatrix}$$

$$c = \begin{bmatrix} -6.971 & 10.69 \\ 0.5785 & -0.08818 \end{bmatrix} \quad d = \begin{bmatrix} -9.23 & -0.5362 \\ 3.858 & 0.2644 \end{bmatrix}$$

Another considered system is a practical power system which is a multi-input multi-output tenth order system taken from literature [25]. It consists of a $3 - \Phi$ synchronous generator, with an automatic excitation control system.

The step response of original and reduced order systems for the two applications is shown in Figs. 4 and 5, respectively. It is observed from the results that reduced order systems show almost similar characteristics as that of original systems and can replace the high order system. It is also observed that model reduction adds a feed-forward matrix 'd' to the system which was missing in original system. However, it is inferred from the above analysis that reduced order systems may be used for analysis and controller design of high-order systems.

4 Conclusion

Different classical approaches were tried, and it is found that mixed method is best for model order reduction. When second-order reduced model is derived from sixth order original system by using Mihalov Criteria and Pade approximation, it is found that reduced order system response is matching with original system with some

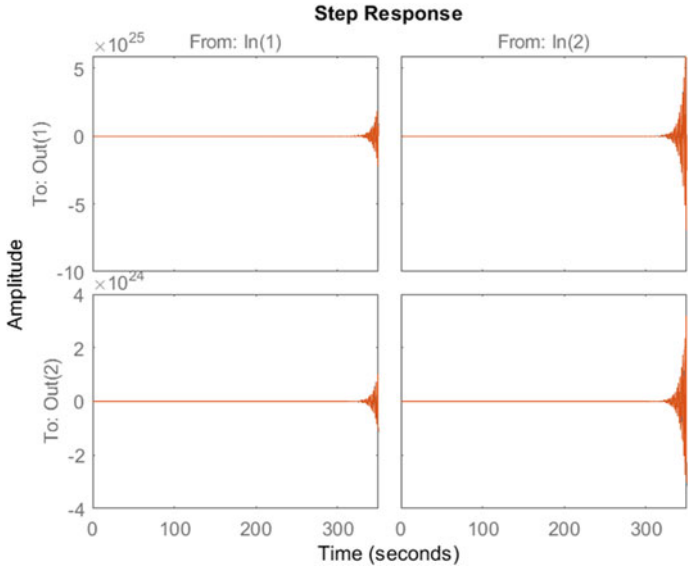

Fig. 5 Step response of power system

negligible deviation. Performance measures of both the system are also calculated, and it is found that reduced system has nearby performance.

For higher system, classical approach is somewhat very lengthy and difficult; therefore, state space-based truncation using SVD and HVD are also performed. It is seen that HVD is the best method and gives very impressive results.

PID controller is also design for reduced system. When these parameters are verified with original system, we found that response is the same. In this way, it is shown that controller for higher order systems can be designed with the help of reduced order systems.

References

1. Prajapati A, Prasad R (2018) Order reduction of linear dynamic systems by improved routh approximation method. IETE J Res 65(5):702–715
2. Varricchio S, Freitas F, Martins N (2015) Hybrid modal-balanced truncation method based on power system transfer function energy concepts. IET Gener Transm Distrib 9(11):1186–1194
3. Prajapati A, Prasad R (2018) Model order reduction by using the balanced truncation and factor division methods. IETE J Res 65(6):827–842
4. Kürschner P (2018) Balanced truncation model order reduction in limited time intervals for large systems. Adv Comput Math 44(6):1821–1844
5. Choudhary A, Nagar S (2018) Model order reduction of discrete-time interval system based on Mikhailov stability criterion. Int J Dyn Control 6(4):1558–1566

6. Ha M, Chu M, Sreeram V (2015) Comparison between balanced truncation and modal truncation techniques for linear state-space symmetric systems. IET Control Theory Appl 9(6):900–904
7. Kumar Deveerasetty K, Nagar S (2020) Model order reduction of interval systems using an arithmetic operation. Int J Syst Sci 51(5):886–902
8. Narwal A, Prasad B (2015) A novel order reduction approach for LTI systems using Cuckoo search optimization and stability equation. IETE J Res 62(2):154–163
9. Prajapati A, Rayudu V, Sikander A, Prasad R (2020) A new technique for the reduced-order modelling of linear dynamic systems and design of controller. Circ Syst Sign Process 39(10):4849–4867
10. Kumbasar T (2016) Robust stability analysis and systematic design of single-input interval Type-2 fuzzy logic controllers. IEEE Trans Fuzzy Syst 24(3):675–694
11. Mohamed Iqbal M, Sarumathi S, Jothi K, Brindadevi A (2018) Model order reduction of heavy duty gas turbine power plants with field test parameters. Int Trans Electr Energy Syst 29(2):e2703
12. Ramirez A et al (2016) Application of balanced realizations for model-order reduction of dynamic power system equivalents. IEEE Trans Power Deliv 31(5):2304–2312
13. Goury O, Duriez C (2018) Fast, generic, and reliable control and simulation of soft robots using model order reduction. IEEE Trans Rob 34(6):1565–1576
14. Kirschneck M, Rixen D, Polinder H (2014) Model reduction methods for magnetic fields based on modal analysis. IEEE Trans Magn 50(11):1–4
15. Ali H, Kunjumuhammed L, Pal B, Adamczyk A, Vershinin K (2019) Model order reduction of wind farms: linear approach. IEEE Trans Sustain Energy 10(3):1194–1205
16. Shamash Y (1974) Stable reduced-order models using Padé-type approximations. IEEE Trans Autom Control 19(5):615–616
17. Moore B (1981) Principal component analysis in linear systems: Controllability, observability, and model reduction. IEEE Trans Autom Control 26(1):17–32
18. Chen T, Chang C, Han K (1979) Reduction of transfer functions by the stability-equation method. J Franklin Inst 308(4):389–404
19. Langholz G, Feinmesser D (1978) Model reduction by Routh approximations. Int J Syst Sci 9(5):493–496
20. Krishnamurthy V, Seshadri V (1978) Model reduction using the Routh stability criterion. IEEE Trans Autom Control 23(4):729–731
21. Stojic M, Siljak D (1965) Generalization of Hurwitz, Nyquist, and Mikhailov stability criteria. IEEE Trans Autom Control 10(3):250–254
22. Klema V, Laub A (1980) The singular value decomposition: its computation and some applications. IEEE Trans Autom Control 25(2):164–176
23. Patil P, Patil M (2011) Model order reduction of high order LTI system using balanced truncation approximation. In: 2011 international conference on process automation, control and computing
24. Zhao G, Sinha N (1883) Model selection in aggregated models, pp 209–216
25. Anderson P, Fouad A (2003) Power system control and stability. IEEE Press, Piscataway

Numerical Simulation and Analytical Modelling of C8-BTBT-C8 Organic Transistor and Analysis of Semiconductor Thickness

Shubham Dadhich, A. D. D. Dwivedi, and Garima Mathur

Abstract Thin film devices have pervasive presence role in applause emerging and conventional technologies. This paper presents TCAD modelling of 2,7-dioctyl{1}benzothieno{3,2-b}{1}benzothiophene (C8-BTBT-C8) OTFT. The model is based on defect description and charge recombination. The model consists of band gap modelling and deep and tail density of state (DOS). The model is examined with experimental data, and the performance parameter is also compared. Using this verified model, the systematic study of the active layer thickness is also performed in this work.

OTFT · C8 BTBT · p-type Organic semiconductor · DOS · T-CAD Modeling

1 Introduction

Organic thin film transistors (OTFTs) are promising basic element for next-generation electronic devices due to pliability and easy fabrication process [1]. Improvement of OTFT performance and development of high-quality organic semiconductor (OSC) material have a wide scope [2]. The effective and low-cost realization still required academia and industrial efforts. The efforts will deliver an entire value-added chain to organic electronics. The future market of several billion Euros is estimated for flexible electronics [3, 4]. The competition for implementation into marketable product is significantly high. This could be seen at considerable expenses for research. On the other hand, it has a strong commitment to the global economy. The biocompatibility and biodegradability [5] qualities also open an era for medical science innovation. The next-generation electronics will bring exciting new applications such as foldable display, electronics textiles [6], wearable bio-sensor for monitoring human health [7]. The organic electronics will also extend functionality

S. Dadhich (✉) · G. Mathur
Department of Electrical and Electronics Engineering, Poornima University Jaipur, Vidhani, India
e-mail: saytoshubham@gmail.com

A. D. D. Dwivedi
School of Electronics Engineering, VIT University Vellore, Vellore, India

© The Author(s), under exclusive license to Springer Nature Singapore Pte Ltd. 2022

A. Tripathi et al. (eds.), *Intelligent Computing Techniques for Smart Energy Systems*,
Lecture Notes in Electrical Engineering 862,
https://doi.org/10.1007/978-981-19-0252-9_60

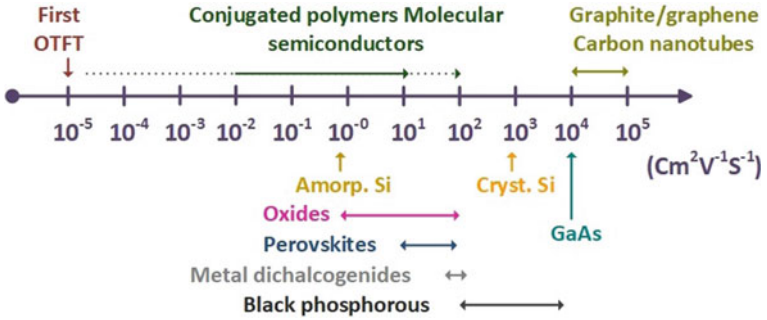

Fig. 1 Comparison of numerous semiconductor device technology

of robot and unmanned air vehicles through energy conservation and lightweight devices. It will also be a revolution for solar cell and optoelectronics [8]. So, it indicates that for device development and implication the semiconductor characteristics-based TCAD model is required. It also contributes in improving device performance and understanding device operation. After it, a compact model is required for designing circuit from OTFT. The review ceased that the developing model should have (a) congruous behaviour, (b) sufficient input parameter variable, (c) upgradable, (d) structural symmetry, (e) conversable, (f) modulable for bad experimental data.

The OSC is yet at development face. The device performance can be measured from mostly seven parameters (Table 3). The charge carrier mobility $\mu\left(\mathrm{cm}^2\ \mathrm{V}^{-1}\ \mathrm{s}^{-1}\right)$ is one of them for evaluating performance. The higher μ enables fast switching $(fT - Hz)$ of the circuit. It belongs to circuit performance and speed. In Fig. 1, the comparison of numerous semiconductor device technology is shown. To improve the mobility and performance, some surface modification is attempted [9]. Exposure to gas or light modifies supramolecular structures of OSC, and it changes the condition for charge transport. The efforts are made continuously to improve mobility for higher switching speed. The charge transportation channel develops at the interface layer between the OSC and dielectric. So, the characteristics of OSC/dielectric interface traps affect the device performance. A self-assembled monolayer was also implemented in [10] to reduce traps. In our previous work [11], the surface modification was also done on P3HT TFT. So, to study the device performance and dependency of all these effects on scalable parameters we need a TCAD model. Here, we present TCAD model for C-8 BTBT organic semiconductor transistors.

2 3-D Device Model

The model incorporates fundamental device physics. The SILVACO ATLAS [12] is used to parameterize all the phenomena. It simulates the model by applying Maxwell's laws on mesh points and solves the Poisson equation for charge boundary

conditions. Thus, AC and DC both transient models could be defined by ATLAS. The numerical values are solved by three methods (a) GUMMEL, (b) NEWTON and (c) BLOCK. For the lengthy calculation, the NEWTON is suitable and mostly conversable. This also solves quadratic convergence and strongly coupled equations.

2.1 Semiconductor Parameter Mapping

The device operation depends on semiconductor properties. The 2,7-dioctyl{1}benzothieno{3,2-b}{1}benzothiophene (C8-BTBT-C8) has sigma (σ), pi (π) bonds. The weak pi (π) bond's electron comes from the 'p' orbital that is far from nuclei. In the series of alternative sigma, pi bonds become shorter than regular length. So, these π-electrons become free to move molecule to molecule. Thus, pi bond electrons' localization and delocalization start the conduction in OSC film. The sequence of anti-bonding and bonding creates a forbidden energy gap. Thus, the band gap could be calculated by the distribution of molecules and the mean of energy gap (Fig. 2).

These molecules could be in different arrangements at the time of spin coating or thermal evaporation. Two possibilities are shown in Fig. 3. The chain stacking exhibits better permeances and charge mobility.

A free charge molecular [13] model is described by minimum elements described by quotative approach. Insulator, conductor and semiconductor are built of linear chain of carbon. Assuming a sequence of N atoms having distance d, so the chain length becomes $(N-1)d$, for large number of 'N' it is Nd (approximately). According

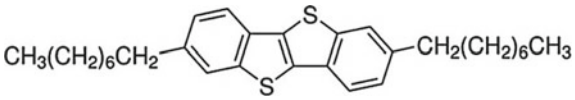

Fig. 2 C8-BTBT-C8 chemical structure [4]

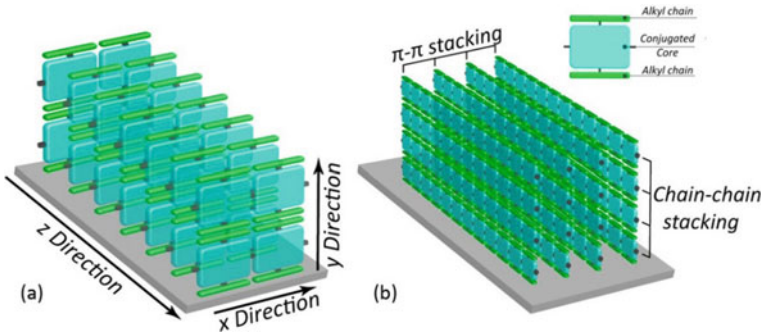

Fig. 3 Two types of molecular arrangement along channel **a** opposite than channel direction, **b** along with channel

to quantum mechanics:

$$E_n = n^2h^2/8m(\mathrm{Nd})^2, \text{ with } n = 1, 2, 3\ldots \tag{1}$$

where m is electron mass, h is Planck's figure, n is quantum numeral.

Assume that pi bond e^- comes from 'N' p-orbitals with two e^- per molecule. The highest occupied molecular orbital (HOMO) energy becomes Eq. (2), and least unoccupied molecular orbital (LUMO) energy becomes Eq. (3).

$$E(\mathrm{HOMO}) = (N/2)^2h^2/8m(\mathrm{Nd})^2 \tag{2}$$

$$E(\mathrm{LUMO}) = (N/2+1)^2h^2/8m(\mathrm{Nd})^2 \tag{3}$$

So, energy required for exciting an electron is Eq. (4).

$$\begin{aligned} E_{g0} &= E(\mathrm{LUMO}) - E(\mathrm{HOMO}) \\ &= (N+1)h^2/8m(\mathrm{Nd})^2 \approx \left[h^2/8md^2\right]/N \text{ for large } N \end{aligned} \tag{4}$$

OSCs usually have a broad range of band gap (1–4 eV) [2]. Usually, semiconductor to be oxide for p-type molecular doping and reduction is significant to n-type molecular doping. The metal (S/D) is connected to semiconductor to ignite the charge carrier. Thus, metal work function plays an important role to energize the charge transporter [14]. So, it should match the HOMO energy level for p-type OSC. The electron affinity (χ) of C8-BTBT is 1.4 eV, and work of the function (Φ_s) is 4.3 eV. The ionized energy of C8-BTBT is 5.8 eV [15], which is nearby the gold work function (Φ_M) 5.5 eV. So, the gold contacts are very suitable for this OSC.

The energy band gap of a material can be defined by a mathematical function of a dependent variable. The band gap depends on temperature also. The higher temperature increases the average valence band energy, and it shows an exponential effect at high electric field. The low energy band gap increases the current amount at the same input voltage, and it increases temperature again. But under 5 voltage, there is not enough electric field that compounds the chain. Here in Eq. (5), the energy band gap is formulated with four variables. E_{G_α} and E_{G_β} are fitting parameters, and E_{G300} is an experimental band gap at 300 K (3.32 eV) [16] at ideal conditions. The ΔE_g is formulated for higher doping concentration through oxidation. This function can totally represent the band gap of C8-BTBT.

$$E_g(T_L) = E_{G300} + E_{G_\alpha}\left[\frac{300^2}{300 + E_{G_\beta}} - \frac{T_L^2}{T_L + E_{G_\beta}}\right] + \Delta E_g \tag{5}$$

$$\Delta E_g = -\zeta_c\left[\frac{\varepsilon_s^5}{N}\left(m_0 + \zeta_B * T^2\frac{\varepsilon_s}{N}\right)\right]^{-\frac{1}{4}} \tag{6}$$

Table 1 Semiconductor band gap parameter

Parameter	Value	Units
E_{G300} [16]	3.32	eV
E_{G_α}	3.85×10^{-4}	eV/K
E_{G_β}	565	K
ζ_c	3.1×10^{-5}	eV $cm^{-3/4}$
ζ_B	2.9×10^{12}	$cm^{-3}K^{-2}$
N	2×10^{17}	cm^{-3}
ε_s	3.6	(ratio)

Equation (6) correction of higher doping also depends on semiconductor dielectric ε_s. The m_0 is mass of electrons at static condition $\left(9.11 \times 10^{-31}\ \text{kg}\right)$. The ζ_B and ζ_c are fitting parameters. The N is doping concentration. The values are shown in Table 1.

2.2 Density of State (DOS)

In theoretical perspective, both charges move in OSC film. But in most semiconductors only single type of charge moves [17]. Thus, only one type of charge is injected by contacts and it could be trapped. Due to the large energy band gap, the thermal charge generation is weaker. So, most of the time one charge carrier per molecule is assumed. That total density of state is often equal to concentration of the molecules $(10^{20} - 10^{21})$.

$$g_{TA}(E) = N_{TA}\exp\left[\frac{E - E_c}{W_{TA}}\right] \tag{7}$$

$$g_{GA}(E) = N_{GA}\exp\left[-\left[\frac{E_{GA} - E}{W_{GA}}\right]^2\right] \tag{8}$$

For exponential tail distribution, N_{TA} consists of edge intercept densities and WTA constitutes characteristic decay energy. Similarly for Gaussian distribution, N_{GA} represents total density of state, W_{GA} is about decay energy attribute, and E_{GD} is about apex energy distribution. Similarly, it is also described for donor [18].

The charge recombination also depends on DOS. The net generation/recombination is identical for both negative and positive charge carriers. This theory is upgraded to Shockley–Read–Hall [19] with DOS parameters.

$$R_{n,p} = \int_{E_V}^{E_C} \left(\frac{v_n v_p \sigma_{TAE}\sigma_{TAH}\left(np - n_i^2\right)g_{TA}(E)}{v_n\sigma_{TAE}\left(n + n_i \exp\left[\frac{E-E_i}{kT}\right]\right) + v_p\sigma_{TAH}\left(p + n_i \exp\left[\frac{E_i-E}{kT}\right]\right)} \right.$$

Table 2 DOS parameter for C8-BTBT

Pa	Values	Unit	Pa	Values	Unit
NTA	2.0×10^{15}	cm^{-3}/eV	σ_{TDE}	1.0×10^{-14}	cm^2
NGA	3.6×10^{15}	cm^{-3}/eV	σ_{GAE}	3.0×10^{-16}	cm^2
NTD	1.0×10^{14}	cm^{-3}/eV	σ_{GDE}	1.2×10^{-14}	cm^2
NGD	2.2×10^{14}	cm^{-3}/eV	σ_{TAH}	2.5×10^{-14}	cm^2
EGA	3.0	eV	σ_{TDH}	1.5×10^{-16}	cm^2
EGD	2.1	eV	σ_{GAH}	3.5×10^{-14}	cm^2
σ_{TAE}	2.0×10^{-16}	cm^2	σ_{GDH}	1.2×10^{-16}	cm^2

$$
\begin{aligned}
&+ \frac{v_n v_p\, \sigma_{TGAE}\, \sigma_{GAH} \left(np - n_i^2\right) g_{GA}(E)}{v_n \sigma_{GAE} \left(n + n_i \exp\left[\frac{E-E_i}{kT}\right]\right) + v_p\, \sigma_{GAH} \left(p + n_i \exp\left[\frac{E_i-E}{kT}\right]\right)} \\
&+ \frac{v_n v_p\, \sigma_{TGAE}\, \sigma_{GAH} \left(np - n_i^2\right) g_{GA}(E)}{v_n \sigma_{GAE} \left(n + n_i \exp\left[\frac{E-E_i}{kT}\right]\right) + v_p\, \sigma_{GAH} \left(p + n_i \exp\left[\frac{E_i-E}{kT}\right]\right)} \\
&+ \frac{v_n v_p\, \sigma_{TDE}\, \sigma_{TDH} \left(np - n_i^2\right) g_{TD}(E)}{v_n \sigma_{TDE} \left(n + n_i \exp\left[\frac{E-E_i}{kT}\right]\right) + v_p \sigma_{TDH} \left(p + n_i \exp\left[\frac{E_i-E_T}{kT}\right)\right.} \\
&+ \frac{v_n v_p \sigma_{GDE}\, \sigma_{GDH} \left(np - n_i^2\right) g_{GD}(E)}{v_n \sigma_{GDE} \left(n + n_i \exp\left[\frac{E-E_i}{kT}\right]\right) + v_p \sigma_{GDH} \left(p + n_i \exp\left[\frac{E_i-E}{kT}\right]\right)} \Bigg) \mathrm{d}E \qquad (9)
\end{aligned}
$$

Here, σ is the width of distribution, subscript T stands for tail, G stands for Gaussian, A stands for acceptor, D stands for donor, and H,E stand for hole and electron. 'n_i' stands for intrinsic concentration of charge carriers. The n and p are DOS for electrons and holes in the corresponding band. 'v_n' and 'v_p' are electron and hole average thermal velocity, respectively [14] (Table 2).

3 Simulation Set-Up

Since the organized cost of experimental study of any technology is higher and it includes a lot of time, TCAD becomes a very important platform to examine any technology. The development and optimization of semiconductor processes required a study to implement at device level. It also provides GUI that reduces the time for understanding and generalizing the fundamentals. In [20], Qijing Wang et al. done an experiment on C8-BTBT-C8 with different dielectric layers. The bottom gate bottom contact structure (BGBC) structure is fabricated. The performance is compared with AlO_x and HfO_2 dielectric. The substrate was supposed to silicon; it can be flexible substrate, i.e., ITO. But highly doped silicon acts as a gate electrode in the device. The HfO_2 dielectric offers low voltage characteristics more stable than AlO_X which

gave high voltage characteristics. It concludes that low dielectric material performs better in low voltage range.

At first, the structure was defined in deckbuild ATLAS Silvaco [12]. Then, the organic (C8 BTBT) material in ATLAS was added with the semiconductor material parameters. ATLAS simulated the band gap and DOS and stores temporary log and str files. The charge flow amount is calculated by charge transport model. In this work, the drift–diffusion model [21] was modified that calculates drain current. It depends upon generation and recombination of charge. The charge density is calculated by Eq. (10) for electrons and Eq. (11) for holes (Fig. 4).

$$\vec{J}_n = qn\mu_n \vec{E}_n + qD_n \nabla n \tag{10}$$

$$\vec{J}_p = qp\mu_p \vec{E}_p - qD_p \nabla p \tag{11}$$

where

$$\vec{E}_n = -\nabla\left(\psi + \frac{kT}{q}\ln n_{ie}\right); \vec{E}_p = -\nabla\left(\psi - \frac{kT}{q}\ln n_{ie}\right) \tag{12}$$

$$D_n = \frac{kT}{q}\mu_n; D_p = \frac{kT}{q}\mu_p \tag{13}$$

$\vec{J}_n$ is the current density, μ_n is mobility of electron, $\vec{E}_n$is electric field, and 'q' is the charge of an electron. The 'n' and 'p' are Boltzmann approximation for electron and hole. The 'ψ' is the electrostatic potential between the source and drain (S/D). 'n_{ie}' is the intrinsic concentration of charge carriers. The total current is $\vec{J}_n + \vec{J}_p$ in the semiconductor.

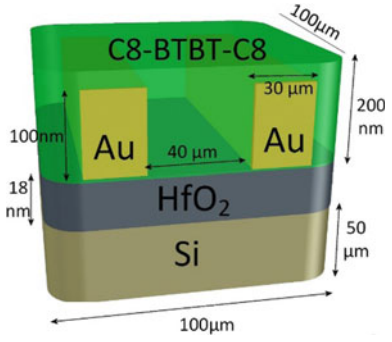

Fig. 4 Structure and dimensions of C8-BTBT OTFT [20]

4 Verification and Result and Discussion

The simulation was performed, and I_{DS} vs V_{GS} and I_{DS} vs V_{DS} characteristics were generated. As can be seen from Fig. 5, simulated outputs are very close to those of experimental. The I_{DS} versus V_{GS} was simulated at three V_{DS} voltage points, but in Fig. 5 it is shown at only −4 voltage point on logarithmic scale. In this figure, we can see the threshold voltage of about −1.55 V. All the model parameters provide good results with reasonable match of curve fitting. This model is deferred from the conventional transport model. Because in OSC higher than 150 K, the charge transportation could not be explained by the former theory. The small difference between experimental and simulated $I_{DS} - V_{DS}$ is because of the high doping effect that starts early current flow in the semiconductor layer. The experimental curve also showed instability on high values of voltage range. The Qijing Wang et al. also

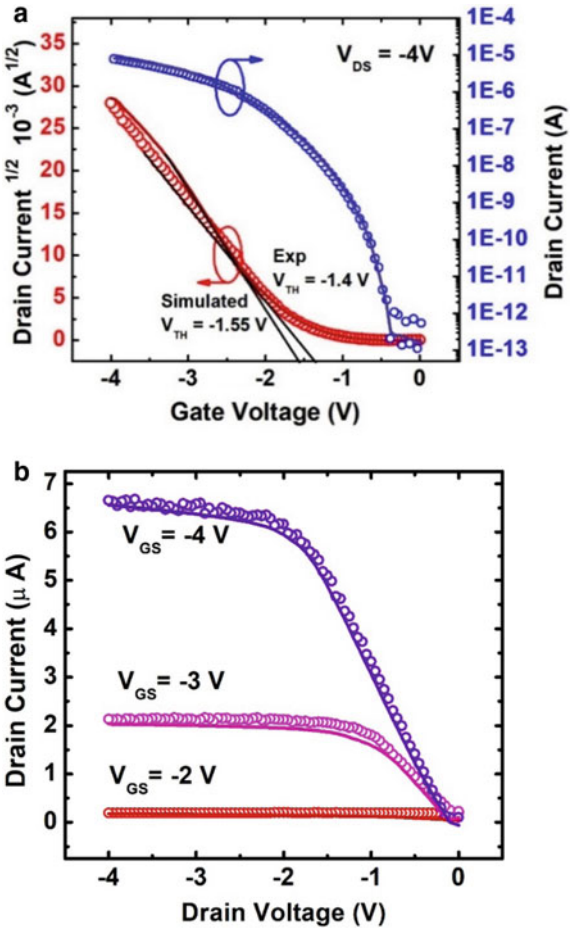

Fig. 5 **a** Comparison of simulated and experimental data [20] of I_{DS} versus V_{GS}. **b** Comparison of simulated and experimental data [20] of I_{DS} versus V_{DS}

Table 3 Performance parameter comparison of simulated versus experimental

Parameters	Formula	Experimental values	Simulated values	Unit
Capacitance per unit area (C_{ox})	$C_{OX} = \frac{\varepsilon_{OX}}{T_{OX}}$	0.37	0.39	$\mu F/cm^2$
Threshold voltage (V_t)	Graphically extracted	1.4	1.55	volt
Trans-conductance (G_m)	$G_m = \frac{\partial I_{DS}}{\partial V_{GS}}$	1×10^{-8}	5.82×10^{-9}	siemens
Mobility in linear region (μ_{lin}) (at $V_{GS} = -2V$)	$\mu_{LIN} = \frac{LG_M}{WC_{OX}V_{DS}}$	2.7×10^{-5}	1.6×10^{-5}	$cm^2/V-s$
Mobility in saturation region (μ_{sat}) (at $V_{GS} = -3.5V$)	$\mu_{SAT} = \frac{2L}{WC_{OX}}\left(\frac{d\sqrt{I_{DS}}}{dV_G}\right)^2$	2.62×10^{-2}	3.11×10^{-2}	$cm^2/V-s$
Sub-threshold slope (SS)	$SS = \left(\frac{d\log(I_{DS})}{dV_{GS}} \mid \max\right)^{-1}$	0.087	0.075	Volt/decade
On–off ratio	I_{on}/I_{off}	10^5	10^5	(ratio)

observe that HfO_2 dielectric is favourable for low voltage. But more efforts should be done to improve HfO_2-based organic transistor performance. We also analyse the effect of semiconductor (C8 BTBT) thickness on device performance.

The device performance is evaluated on the base of these seven performance parameters. These are extracted from standard formulas and also used in many research papers [11, 22–24]. The threshold voltage is extracted from graphical method. In linear regime, the ratio of changing I_{DS} and V_{DS} is called transconductance and with the help of this value the mobility of total charges is calculated. The sub-threshold slope defines the minimum gate voltage to change the drain current in order of one decade (10^1) (Table 3).

5 Analyse the Effect of Semiconductor Thickness

The developed model is well examined with experimental data for C8-BTBT. The channel layer thickness plays a vital role in conduction and device performance. In the set-up, we want to deeply study for channel thickness. In this structure, the 200 nm thickness is varied from 100 to 500 nm. In Fig. 6, it can clearly see that current density in lower order thickness is high at equal input voltage points because the charge conjunction is increasing. But the effects are not linearly proportional because in OSC the charge carriers are limited. Near about $x = 10$, the current is negligible, and

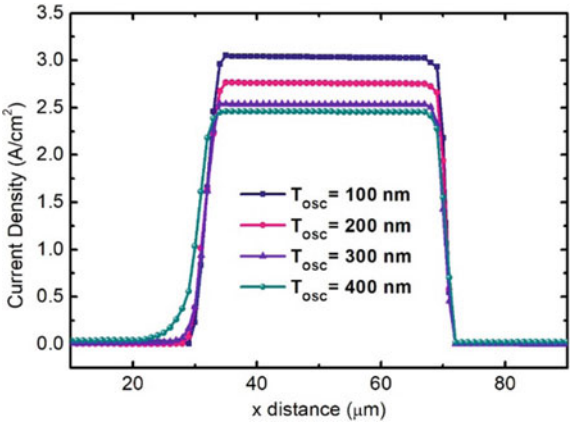

Fig. 6 Effect of channel thickness on current density

little current flows due to minor charge carriers. The charge accumulation forming is away from the dielectric surface because of dipoles near the insulator surface. The high electric density also shifts the accumulation layer; in the result, the trap becomes reduced and current flow is increased. In the bottom gate top contact structure, the capacitance increases when the channel thickness increases because the dielectric constant also increases.

The performance parameter of the study is also shown in Table 4. The linear mobility is increased when thickness decreases because the horizontal electric filed ignites the charge fast and current density also increases. But due to less charge, the threshold voltage is raised. Same for dielectric, the reduced thickness increases the charge accumulation and in the result the mobility is raised. Reduced channel and dielectric thickness increase the response, so sub-threshold voltage is decreased; i.e., less voltage is required to change one decade current. The on-to-off ratio is significantly increased. But in case of dielectric thickness variation, the on–off ratio is not so much changed because with the increment of maximum current due to thin dielectric leakage current also increases. So, the total on–off ratio is almost same.

Table 4 Effect of thickness scaling on performance parameters

Thickness scaling	Variation in performance parameters			
	μ_{lin}	V_t	SS,	$I_{on}/_{off}$
OSC 200–100 nm	22% ↑	22% ↑	45% ↓	4×10^1
				times ↑
Dielectric 36–18 nm	18% ↑	19% ↑	23% ↓	1.5
				times ↑

6 Conclusion

We discussed noteworthy attributes of the organic semiconductor and flexible device market. The polymer conduction theory is discussed for energy band gap. It is also tailored for C8-BTBT OSC devices and verified from experimental comparison. The density of state is discussed and charge recombination described after it. The developed model is easily conversable, and simulated data is reasonably matched with experimental data. It is observed that the OSC thickness has critical behaviour for TFT performance. The model is useful to improve device performance.

7 Future Scope

In this work, we develop the TCAD model to study the C8-BTBT OSC device. It depends on physical behaviour and conduction phenomenon. The compact model for the same can be developed for implementing the circuit of this OTFT. We also work for an ANN-based model for calculation of I–V characteristics. At the fabrication end, device performance could be optimized by varying OSC thickness and placement of molecule. The OTFT has huge possibilities for real electronic devices.

Acknowledgements The authors are thankful to the DST, Government of India, for Early Career Research Award (ECRA) for Project No. ECR/2017/000179. Mr. Shubham Dadhich (PhD. Scholar at Poornima University) is thankful for receiving Junior Research Fellowship (JRF) under this project.

References

1. Guo X et al (2017) Current status and opportunities of organic thin-film transistor technologies. IEEE Trans Electron Devices 64(5):1906–1921
2. Zschieschang U, Klauk H (2019) Organic transistors on paper: a brief review. J Mater Chem C 7(19):5522–5533
3. Corzo D, Tostado-Blázquez G, Baran D (2020) Flexible electronics: status, challenges and opportunities. Front Electron 1:1–13
4. Sawada T et al (2020) Correlation between the static and dynamic responses of organic single-crystal field-effect transistors. Nat Commun 11(1)
5. Shen H, Di CA, Zhu D (2017) Organic transistor for bioelectronic applications. Science China Chem 60(4):437–449
6. Louris E, Stefanakis D, Priniotakis G, Van Langenhove L, Tassis D (2017) Optimization of cylindrical textile organic field effect transistors using TCAD simulation tool. IOP Conf Ser Mater Sci Eng 254(16)
7. Zhu M, Ali MU, Zou C, Xie W, Li S, Meng H (2021) Tactile and temperature sensors based on organic transistors: towards e-skin fabrication. Front Phys 16(1):1–13
8. Sánchez-Vergara ME, Hamui L, Habib SG (2019) New approaches in flexible organic field-effect transistors (FETs) using InClPc. Materials (Basel) 12(10)
9. Liu J et al (2015) High mobility emissive organic semiconductor. Nat Commun 6:0–7

10. Leonardi F, Casalini S, Albonetti C, Kovtun A, Liscio A, Biscarini F (2015) Charge-injection organic gauges to detect dopamine down to the nanomolar scale. IEEE Trans Electron Devices 62(12):4251–4257
11. Dadhich S, Dwivedi ADD, Singh AK (2021) Fabrication, characterization, numerical simulation and compact modeling of P3HT based organic thin film transistors. J Semicond 42(7):0–13
12. Software DS (1998) ATLAS user's manual. II:567–1000
13. Heeger A, MacDiarmid AG, Shirakawa H (2000) The Nobel Prize in chemistry, 2000: conductive polymers, stock. Sweden R Swedish Acad Sci 1–16
14. Dwivedi ADD, Jain SK, Dwivedi RD, Dadhich S (2019) Numerical simulation and compact modeling of low voltage pentacene based OTFTs. J Sci Adv Mater Devices 4(4):561–567
15. Sanda S et al (2019) Effect of non-chlorinated solvents on the enhancement of field-effect mobility in dioctylbenzothienobenzothiophene-based top-gate organic transistors processed by spin coating. Org Electron 69:181–189
16. Moh AM, Khoo PL, Sasaki K, Watase S, Shinagawa T, Izaki M (2018) Growth and characteristics of C8-BTBT layer on C-sapphire substrate by thermal evaporation. Phys Status Solidi Appl Mater Sci 215(11):1–5
17. Rolin C, Kang E, Lee JH, Borghs G, Heremans P, Genoe J (2017) Charge carrier mobility in thin films of organic semiconductors by the gated van der Pauw method. Nat Commun 8
18. Dev Dhar Dwivedi A, Kumar Jain S, Dhar Dwivedi R, Dadhich S (2020) Numerical simulation and compact modeling of thin film transistors for future flexible electronics. Hybrid Nanomater Flex Electron Mater 1–16
19. Goudon T, Miljanović V, Schmeiser C (2007) On the shockley-read-hall model: generation-recombination in semiconductors. SIAM J Appl Math 67(4):1183–1201
20. Wang Q et al (2017) Low-voltage, high-performance organic field-effect transistors based on 2D crystalline molecular semiconductors. Sci Rep 7(1):1–8
21. Model AH (2007) Hopping and drift–diffusion currents in organic, vol 5, pp 830–833
22. Han Y et al (2018) Anion-induced N-doping of naphthalenediimide polymer semiconductor in organic thin-film transistors. npj Flex Electron 2(1)
23. Dhar Dwivedi AD, Jain SK, Dadhich S (2019) Numerical simulation-based comparative study of P3HT-based top contact and bottom contact OTFTs. J Electron Des Technol 27–32
24. Dadhich S, Dhar Dwivedi AD, Mathur G (2021) Surface charge based modeling of TIPS Pentacene TFT. In: 8th international conference on smart computing & communications (ICSCC)

Security-Focused Mathematical Model for Voice Over Wireless Sensor Network

Rohit Mathur and Tarun Kumar Dubey

Abstract This work makes an attempt to facilitate the design of voice over wireless sensor network applications. After an extensive literature survey, it was observed that there is a dire need to develop a mechanism that may assist researchers and developers in designing voice over wireless sensor network application. The proposed theory is based on the ITU-T's narrowband E-model and previously developed theories for voice over Internet protocol and wireless sensor networks. The originally proposed equation of delay is further modified by updating the parameter pertaining to delay associated with the network.

Keywords Zigbee · ITU-T · E-model · WSN · VoWSN · Delay · Mathematical modeling

1 Introduction

Wireless sensor network (WSN) is a subcategory of data networks belonging to infrastructure-less networks [1]. WSN was conceptualized for sensing and reporting environmental parameters. The network element used for sensing and reporting these environmental parameters is referred to as WSN node or mote [2]. Depending upon the target application's requirements, WSN nodes are equipped with a microcontroller unit for all the required processing-related task, memory unit for storage of both code and data, sensors with relevant signal conditioning unit for properly sensing the desired environmental parameters, and communication unit for data transmission between the nodes [3]. WSN-based sensor nodes employ transceivers working at industrial, scientific, and medical (ISM) band frequencies [4]. The most popular is the 2.4 GHz frequency band [5]. Additionally, the nodes may have multimedia sensors

R. Mathur (✉) · T. K. Dubey
Manipal University Jaipur, Jaipur, India
e-mail: rohit.mathur@jaipur.manipal.edu

T. K. Dubey
e-mail: tarunkumar.dubey@jaipur.manipal.edu

© The Author(s), under exclusive license to Springer Nature Singapore Pte Ltd. 2022

A. Tripathi et al. (eds.), *Intelligent Computing Techniques for Smart Energy Systems*,
Lecture Notes in Electrical Engineering 862,
https://doi.org/10.1007/978-981-19-0252-9_61

like camera and microphone [6], power generation unit, mobility management unit [7], and at times Global Positioning System (GPS) unit [8] for localization.

WSN has been reported useful in numerous complex applications like

(i) Domestic applications

- monitoring of road traffic [9]
- agriculture [10]
- real-time voice communication applications [11]

(ii) Military applications

- underwater intrusion detection application [12]
- detecting metal mines [13].

A lot of work in the form of simulation studies [14] and practical implementations [15–17] has been reported in the currently available literature.

The deployment of the nodes depends upon the application scenario. Therefore, the deployment may be planned or unplanned. Though the planned deployment is preferred over unplanned deployment [18].

After the deployment, the nodes themselves search for their neighbor nodes and constitute the most suitable network topology. WSN primarily relies on three topologies, namely star topology, tree topology, and mesh topology, Fig. 1. The preferred topology is the mesh topology, wherein every WSN node is connected to at least two of its neighbor nodes constituting the interconnections between the WSN nodes [19]. This type of topology is advantageous in hostile environments in which connections

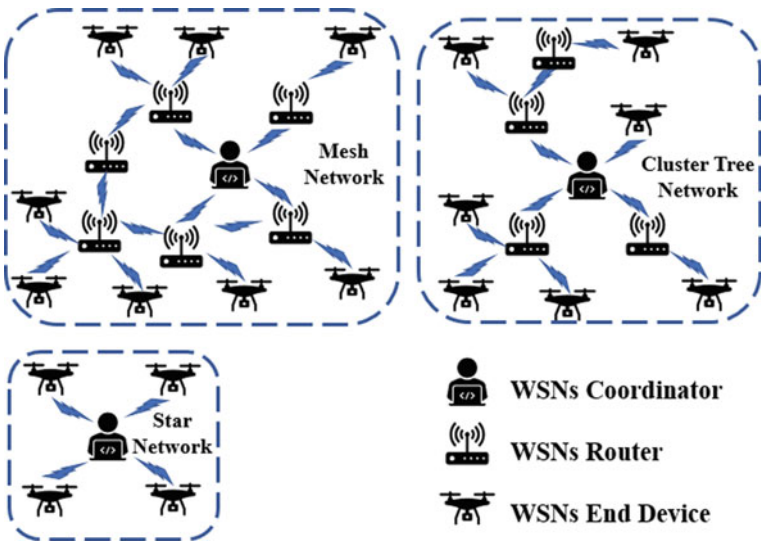

Fig. 1 Wireless sensor network topologies

may be easily broken. If a connection is broken in this topology, at least one substitute path is available for carrying the communication.

As mentioned earlier, WSN was developed to sustain low-cost applications, with constraints of low data rates, limited computational capability, and restricted use of onboard power. WSN was not originally intended for use in voice communication over WSN (VoWSN) applications [20, 21].

A review of previously developed voice over WSN (VoWSN) is presented in Sect. 2. Section 3 presents the proposed mathematical model followed by discussion and conclusion presented in Sect. 4.

2 Related Work

The capability of Zigbee to sustain audio streaming over WSN was explored in [19]. Wherein researchers experimented with the queue size so as to optimize network performance, their experiments revealed that modifying queue size does assist in supporting VoWSN.

Authors in [15] had a noble objective of providing telephony services in the rural area. They choose an area of 2–3 km^2 in Ahupe village, near Mumbai, India. The testing was carried out for 18 h over 3 days with the intention to maximize the coverage of indoor and outdoor to a maximum of two hops. They reported a source to destination latency < 120 ms, average packet loss percentage < 2%, and a MOS of 3.6. The implementation was carried out with the help of TelosB motes and indigenously developed handset, gateway, and lightweight time division multiple access (TDMA)-based medium access control (LiT MAC) protocol. A survey of previously done research is presented in Table 1.

Table 1 Survey of previous research focusing on developing VoWSN application

Ref. no.	Target application	Standard frequency band/s used	Implementation mechanism	Max. Hop count	Topology
[15]	Telephony services	IEEE 802.15.4 and GSM	Hardware	3	Tree
[22]	Full-duplex voice over IP (VoIP) and half-duplex push-to-talk (PTT)	IEEE 802.15.4	NS-2	3	Linear configuration
[23]	Push-to-talk application	IEEE 802.15.4	Hardware	3	In-line
[24]	Voice communication	IEEE 802.15.4	NS-2	240	Not specified

Researchers in their scholarly work investigated [23] the feasibility of push-to-talk application. The investigation was employed using Zigbee compliant commercially available off-the-shelf (COTS) hardware. The investigation method focused on enhancing the quality of service (QoS) of voice communication. The experiments were designed to observe the effects of compression algorithm for voice encoding and unicast and broadcast addressing on quality of audio received at the receiver and power consumption. The conclusion was that the voice streaming applications over low-range wireless personal area networks (LR-WPANs) is possible but with a limitation of a few hops. The major constraints reported in the literature, that influenced the voice quality of such implementation were, packet loss and delay.

Researchers in their scholarly work reported 2-way voice communication over sensor networks employing Firefly platform [25]. The platform uses time division multiple access (TDMA)-based scheduling with a 2.4 GHz IEEE 802.15.4 and Zigbee compliant off-the-shelf RF transceivers. It was reported that 24 ms per-hop deterministic latency across 8 hops was observed. They analyzed mean opinion score (MOS) for voice communication across 4 hops only. Reported MOSs using different sampling and encoding mechanisms were of the range fair and poor with constraint of low packet loss. They developed this for deployment in coal mines.

Another indigenous work targeting emergency speech calls was reported in [26] with the ultimate goal of supporting speech communication by protecting the perceptually important packets. The implementation was made using UTMOST nodes, which employed the CC1101 transceiver that works on the 915 MHz, frequency band. The reported mechanism was not only successful in conserving network bandwidth and energy, but was also successful in achieving good speech quality across three hops.

3 Proposed Mathematical System Design Model

All the aforementioned implementations had a different approach for implementation and therefore had different results in terms of maximum achieved number of hops, one-way time delay, packet loss percentage, and MOS. The biggest hurdle is that there was no widely accepted mechanism which would assist researchers and developers in designing VoWSNs application.

The initial scholarly work based on ITU-T's E-model was reported for voice over IP (VoIP) application in [21]. E-model defines a computational mathematical transmission rating algorithm. It was originally defined for telephony services, to assist transmission planners in transmission planning. The objective behind defining this model was to reduce time consumed in planning and testing end-to-end conversational quality. The narrowband (NB) E-model was defined for 300–3400 Hz. The model encompasses effects of vital parameters ranging from signal-to-noise ratio to equipment impairments. The output of the E-model algorithm is the scalar user satisfaction factor known as the rating factor (R). Each of the constituent components is further divided into relevant impairments.

Following the footsteps, a modified mechanism is presented based on the updated, 2015, ITU-T's NB E-model. Not all the parameters of the updated E-model are relevant to our theme and therefore are not discussed further. Inquisitive readers are suggested to refer [27] for more details. The value of R as defined in updated E-model is presented as Eq. (1).

$$R = R_o - I_s - I_d - I_{e-\text{eff}} + A \tag{1}$$

where

R_o represents signal-to-noise ratio component

I_s represents combination of all impairments which occur more or less simultaneously with the voice signal

I_d represents impairments caused by delay

$I_{e-\text{eff}}$ represents effective equipment impairment

A represents compensation of impairment.

An estimated mean opinion score (MOS) (as per updated document, 2015 [27]) for the conversational situation in the scale 1–5 can be obtained from the R-factor using Eq. 2. Also, the relation between R-value and user satisfaction is as per Table 2.

$$\begin{aligned} &\text{For } R < 0 : \text{MOS}_{\text{CQE}} = 1 \\ \text{For } 0 < R < 100 :&\text{MOS}_{\text{CQE}} = 1 + 0.035R + R * (R - 60) * (100 - R) * 7 * 10^{-6} \\ &\text{For } R > 100 :\text{MOS}_{\text{CQE}} = 4.5 \end{aligned} \tag{2}$$

Researchers in [21] neglected constituent component I_s and A. To clarify this decision, they stated that the impairments quantified under I_s, none of which are relevant to packet transport, and A has default value of zero abiding by the same logic. The modified relation incorporating default values is mentioned in [27], and aforementioned assumption came out to be, as mentioned in Eq. (3),

Table 2 Relation between R-value and user satisfaction

R-value (lower limit)	MOS (lower limit)	User satisfaction
90	4.34	Very satisfied
80	4.03	Satisfied
70	3.60	Some users dissatisfied
60	3.10	Many users dissatisfied
50	2.58	Nearly all users dissatisfied

$$R = 93.2 - I_d - I_e \tag{3}$$

Further, they [21] expanded the term I_d and I_e using appropriate graphical tool and came up with equations for the same. Since our focus is only on I_d, the relevant equation from original work is presented in Eq. (4).

$$I_d = 0.024d + 0.11 * (d - 177.3) * H(d - 177.3) \tag{4}$$

where

$d = d_{\text{codec}} + d_{\text{de-jitter\_buffer}} + d_{\text{network}}$ represents overall one-way mouth-to-ear delay

d_{codec} represents the algorithmic and packetization delay

$d_{\text{de-jitter\_buffer}}$ represents delay associated with de-jitter buffer functioning.

d_{network} represents transit delay

$$H(x), \text{ Heavyside function}$$
$$H(x) = 0 \text{ if } x < 0, \text{ else}$$
$$H(x) = 1 \text{ for } x \geqslant 0$$

Looking at most of the application scenarios [11], security aspect is not as an integral part of design and development phase or considered as a regular feature in WSNs. Thus, security aspect in most of the proposed implementations is considered as an add-on feature. But it is an essential feature in our opinion.

As per the observations of the above equations, it is important to highlight that no constituent components of Eq. (4) cater to the delay incurred due to security measures adopted by the wirelessly connected network nodes during runtime.

Results of studies show [28] that the delay incurred in these evaluations is of the same order as other delays, thus making it significant. Therefore, it is proposed to modify the above-stated parameter of d_{network} with addition of another delay component, namely d_{sec} which encompasses the overall network delay. Thus, the modified proposed equation of d_{network} comes out to be as represented in Eq. (5).

$$d_{\text{network}} = d_{\text{net}} + d_{\text{sec}} \tag{5}$$

where

d_{net} represents other delays associated with one-way transit

d_{sec} represents time consumed by security mechanism.

4 Conclusion

The presented work modified the originally proposed method developed for voice over IP for Zigbee-based VoWSNs implementation. The aforementioned modifications are aimed in assisting designers in taking intelligent decisions pertaining to practical implementation. Thus, by utilizing the aforementioned mechanism the design problem will not be just a hit and trial but a calculated expectation, which will in turn help developers develop solutions more appropriately.

The ITU-T's E-model pertaining to narrowband was updated in 2015. The inputs from the same are incorporated. Specifically, the default value of R in [21] was taken as 94.2, and we have proposed to use the updated value of 93.2.

The originally proposed equation of d is further modified by updating the parameter d_{network}, with the most significant crucial parameters like maximum possible number of nodes, time consumed by security aspect delay.

References

1. Kim B-S, Park H, Kim KH, Godfrey D, Kim K-I (2017) A survey on real-time communications in wireless sensor networks. Wirel Commun Mob Comput 2017:1–14
2. Rashid B, Rehmani MH (2016) Applications of wireless sensor networks for urban areas: a survey. J Netw Comput Appl 60:192–219,
3. Estrin D, Girod L, Pottie G, Srivastava M (2001) Instrumenting the world with wireless sensor networks. In: Proceedings of IEEE international conference on acoustics, speech, and signal processing, vol 4, pp 2033–2036
4. Hlaing Y, Maung Maung NA (2020) Hybrid time synchronization for ZigBee networks: an empirical approach. In: 2020 17th international conference on electrical engineering/electronics, computer, telecommunications and information technology (ECTI-CON), pp 376–379
5. Bricker G, Harris D (2007) Getting started with XBee RF modules
6. Yick J, Mukherjee B, Ghosal D (2008) Wireless sensor network survey. Comput Netw 52(12):2292–2330
7. Jung MK, Lee JH, Cho SH (2013) A design of data storage using voice over sensor network(VoSN) systems. In: Proceedings of third world congress on information and communication technologies (WICT 2013), pp 343–346
8. Singh N (2016) Literature survey on wireless sensor network. Int J Eng Comput Sci 5(8):17544–17548
9. Kafi MA, Challal Y, Djenouri D, Doudou M, Bouabdallah A, Badache N (2013) A study of wireless sensor networks for urban traffic monitoring: applications and architectures. Procedia Comput Sci 19:617–626
10. Ojha T, Misra S, Singh N (2015) Wireless sensor networks for agriculture: the state-of-the-art in practice and future challenges. Comput Electron Agric 118:66–84
11. Mathur R, Chouhan DN, Dubey TK (2020) An overview of application scenarios of voice over wireless sensor networks. Smart Innov Syst Technol 141(1):587–593
12. Liu L, Zhang N, Liu Y (2015) Topology control models and solutions for signal irregularity in mobile underwater wireless sensor networks. J Netw Comput Appl 51:68–90
13. Ahmad R, Singh A, Muzamil R, Beg MS, Ahamed J (2015) Use of WSN for detection of metal landmines using unmanned vehicle. In: Proceedings of international conference on computing for sustainable global development, INDIACom 2015, pp 50–55

14. Rekha G, Adhikary Y, Shrinivasan L (2016) Modeling and simulation of voice communication over ad hoc network for search and rescue operations. In: 2016 international conference on inventive computation technologies (ICICT), pp 1–6
15. Gabale V, Patani J, Mehta R, Kalyanaraman R, Raman B (2012) Building a low cost low power wireless network to enable voice communication in developing regions. ACM SIGMOBILE Mob Comput Commun Rev 16(2):2–15
16. Li H (2015) HD2UB: a voice communication system for underground mine monitoring. In: Proceedings of the 5th international conference on computer engineering and networks—PoS (CENet2015), pp 1–7
17. Song HY, Cho SH (2011) Performances of IEEE 802.15.4 unslottedCSMA-CA for voice communications. In: Proceedings of 17th Asia-Pacific conference on communications, APCC 2011, pp 151–156
18. Zhang Q, Li J, Rong J, Xu W, He J (2011) Application of WSN in precision forestry. In: Proceedings of 10th international conference on electronic measurement and instruments, ICEMI 2011, vol 4, pp 320–323
19. Abdulhussien SA, Ibrahim SK (2020) Effects of wireless sensor network topology on response time. In: 2020 international conference on electrical, communication, and computer engineering (ICECCE), pp 1–5
20. Alsaif O, Saleh I, Ali D (2019) Evaluating the performance of nodes mobility for zigbee wireless sensor network. ICCISTA 2019—IEEE international conference on computing and information science and technology and their applications, pp 4–8
21. Cole RG, Rosenbluth JH (2001) Voice over IP performance monitoring. ACM SIGCOMM Comput Commun Rev 31(2):9–24
22. Wang C, Sohraby K, Jana R, Ji L, Daneshmand M (2008) Voice communications over zigbee networks. IEEE Commun Mag 46(1):121–127
23. Brunelli D, Teodorani L (2008) Improving audio streaming over multi-hop ZigBee networks. In: Proceedings of IEEE symposium on computers and communications, pp 31–36
24. Choi E, Hur Y, Huh J, Nam Y, Yoo D, Choi W (2008) Simulation and implementation of voice-over-IEEE 802.15.4 LR-WPAN. In: Proceedings of international conference on consumer electronics, pp 1–2
25. Mangharam R, Rowe A, Rajkumar R, Suzuki R (2006) Voice over sensor networks. In: 2006 27th IEEE international real-time systems symposium (RTSS'06), pp 291–302
26. Petracca M, Litovsky G, Rinotti A, Tacca M, De Martin JC, Fumagalli A (2009) Perceptual based voice multi-hop transmission over wireless sensor networks. In: Proceedings of IEEE symposium on computers and communications, pp 19–24
27. ITU (2015) The E-model, A computational model for use in transmission planning: ITU-T recommendation G.107
28. Mathur R, Chouhan DN, Dubey TK (2018) A comparative study of trust based security mechanisms for wireless sensor networks. In: Proceedings of international conference on optical & wireless technologies (OWT 2018), pp 52–55

Profit Maximization of a Micro-grid with Renewable Generation Using Smart Household Management Systems

Dileep Kumar Jareda, Gurpinder Singh, Anil Swarnkar, Nikhil Gupta, and K. R. Niazi

Abstract In recent year, growth in electric power demand, electricity production cost and emission of greenhouse gases have increased rapidly. As a result, a special emphasis on distributed generation is needed. The best way to solve the problem is to develop distributed generation, primarily from renewable energy resources. These tools are placed close to the residence in order to produce a few kilowatts. Besides several benefits, there are major challenges in its management and optimal use. These challenges have become one of the main concerns for researchers. In this paper, an innovative model is proposed for strategic energy management to facilitate demand response. Its aim is to improve the efficiency of households that include generation units such as wind turbines, solar panels, storage units and uncontrollable or controllable loads. This optimization management's main goal is to maximize micro-grid profitability for 24 h a day. The cumulative effect of this model shows that the benefit of the micro-grid has greatly improved.

Keywords Demand response (DR) · Distribution generation (DG) · Smart energy management system (SEMS) · Energy storage system (ESS) · And micro-grid

1 Introduction

Modern power distribution systems are facing problems like high power losses, poor power quality, peak power demand, limited power transfer capability of line and high carbon emission. Demand-side management refers to initiatives and technologies that encourage consumers to optimize their energy uses and shifting the load pattern. Demand response is defined as reduction in consumers' electricity

D. K. Jareda (✉) · G. Singh · A. Swarnkar · N. Gupta · K. R. Niazi
Malaviya National Institute of Technology, Jaipur, India
e-mail: 2019pes5013@mnit.ac.in

G. Singh
e-mail: 2017pes5202@mnit.ac.in

K. R. Niazi
e-mail: krn152001@yahoo.co.in

© The Author(s), under exclusive license to Springer Nature Singapore Pte Ltd. 2022

A. Tripathi et al. (eds.), *Intelligent Computing Techniques for Smart Energy Systems*, Lecture Notes in Electrical Engineering 862,
https://doi.org/10.1007/978-981-19-0252-9_62

consumption in line with changing energy costs or using the encouraging factors which provided by electrical distributions company [1]. There are various methods for implementing demand response program; two main classifications are incentive base demand response and price base demand response. Incentive-based program provides the incentives for the curtailment or load shifting. In most of these programs, an agreement has been signed with the customers who are willing to participate in demand response programs, but if they do not act according to the agreement, there are various penalties.

In price-based programs, dynamic pricing is provided to the consumer. This pricing scheme provided in advance such that the pricing during the peak hours is high and low during off-peak hours. Such a type of demand response program will motivate the consumer to change consumption pattern to minimize the electricity bill. The concept of demand response is not just limited to evidentiary loads. It can be applied on the commercial and industrial consumers for reducing the peak in load curve. Both utility and consumers are benefited by demand response adopting the optimal scheduling of their load.

2 Literature Survey

The studies of micro-grids have been of interest for many researchers. As article [2] was to improve the load transfer method and alter the energy consumption patterns of smart homes. Consumer demand is controlled using a pricing scheme like day-ahead basis and real-time basis. A typical model is highlighted for balancing load during off-peak hours. The system is set up to operate demand response (DR) actions with consistency indices in the pricing scheme over duration of time [3]. The results revealed that it is likely to lower the cost of energy for patrons while also improving their health. This is accomplished by delivering a well-coordinated program. The author of article [4] recommends using an action-based heuristic dynamic programming (ADHDP) approach to solve the residential energy scheduling problem in order to improve the electricity efficiency of a residential micro-grid. The results indicate that the system lowers the cost of electricity energy usage while also helping to improve load balancing.

Demand response in micro-grid: The micro-grid covering of electrical energy sources and various loads that is usually linked to homes and synchronous with macro-grid or the conventional grid, but these can cut off from grid which interconnected and operate alone in "island mode". Micro-grids improve supply security within the micro-grid area and can supply emergency power by controlling between isolate and connected modes in this method. An off-grid application is referred to as an independent, stand-alone or isolated micro-grid. The energy generation system near consumer is economical, where power transmission and distribution by larger centralized energy resource are far away, and they provide a rural electrification option for remote locations. The micro-grids can provide the safety of being fortified

against harsh climate and disaster using obviating the need to maintain or replace large possessions and miles of ground cables and infrastructure in the aftermath of such an event. Scheduled safeguarding, poor energy quality, problems in the locality grid or financial reasons may cause a micro-grid to switch between these two modes. Micro-grids enable the combination of renewable resources such as solar, wind and battery storage without needing an increased infrastructure of national distribution system by altering power. To increase efficiency, economics and robustness, modern optimization approaches can be integrated into the micro-grid energy management system.

In [5], the authors developed a market-based droop management strategy that promoted the generation price as well as the cost of participating customers in a demand management program. The findings indicate management methodology reduced the overall cost of production [6] for intelligent housing buildings. The primary aim of this algorithm has reduced electrical energy costs. An energy storage system (battery) has been developed by study [7] to increase income. A home energy management system with solar panels and battery system was investigated in the study [8]. A fuel cell as storage was used like an energy carrier for utilized isolate mode in research [9]. An energy managing approach has used in this study to control renewable generation sources inside smart household. The fuzzy control logic was developed to this purpose and created in MATLAB. The authors of article [10] aimed to improve the electrical energy efficiency of a household micro-grid by developing an (ADHDP) technique for solving the housing energy arrangement difficulty. The results revealed that the scheme lowers the cost of energy usage while also improving load balancing. The variability of the energy generation with demand management is identified as a critical dispute in the long-term sustainability of power supply resources in study [11]. In [12] created a cost-dependent droop control approach depending on power generation cost and participating customers cost in a demand-side management program. The droop control method was found to have the lowest generation expense. In article [13], a residential energy management system is suggested. The key goal of this scheme is to reduce energy price while keeping the overall energy demand within certain variables like as the operation of loads and the use of renewable sources.

3 System Modal

The considered micro-structure grids integrated wind turbine, solar panels, battery storages system and the connected loads to the AC bus. The losses are assumed to be zero at the micro-grid junction of bus bars (Fig. 1).

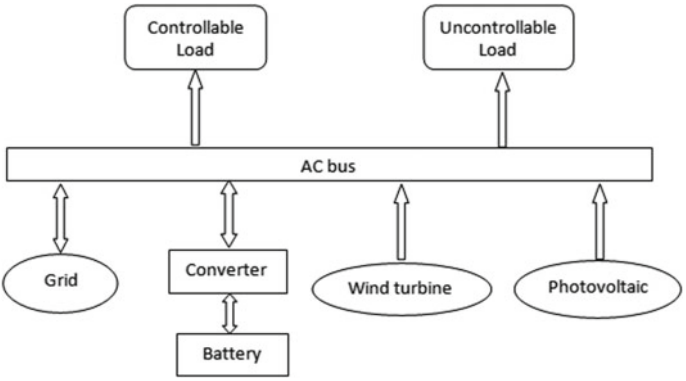

Fig. 1 Diagram of a micro-gird layout

4 Objective Function

An objective function that identifies the micro-operation grid's strategy is required in order to produce an ideal operation program. The function's goal is to maximize profit by analyzing all of the operation's requirements as revenue minus cost. This function is used to boost micro-grid's profit. Load supplying, generator contribution rate, storage system and power exchange are all resolved. Regardless of how renewable units behave, all generated energy is injected into the micro-grid bus, whether it is on or off mode.

The overall representation of objective function is

$$F = \text{maximize} \sum_{t=1}^{24} [\text{revenue}(t) - \text{cost}(t)]$$

The objective is to increase the profit of micro-grid which is revenue minus cost; this profit is calculated in every hour of the day.

The micro-grid earnings are as follows:

i. Selling of electrical energy to the main grid
ii. Selling of electrical energy to uncontrollable load
iii. Electrical energy selling to controllable load
iv. Electrical energy selling to light loads.

The micro-grid's costs are as follows:

i. The cost of purchase energy from grid
ii. The cost of energy saving in the battery
iii. The cost of solar unit generation
iv. The cost of wind unit generation.

The objective function is represented by maximizing of this following equation

$$\sum_{t=1}^{24}\{[P^{s}_{\text{grid}}(t).\rho^{s}_{\text{grid}}(t) + P_{\text{load}}(t).\rho_{\text{load}}(t)] - [P^{p}_{\text{grid}}(t).\rho^{p}_{\text{grid}}(t) + C_{\text{bat}}(t)]\}$$

where

$P^{s}_{\text{grid}}(t)$ = power selling to grid by micro-grid.

$\rho^{s}_{\text{grid}}(t)$ = cost of selling power to grid.

$P_{\text{load}}(t)$ = sold power to load by micro-grid.

$\rho_{\text{load}}(t)$ = price of sold power to grid.

$P^{p}_{\text{grid}}(t)$ = purchase power from grid.

$\rho^{s}_{\text{grid}}(t)$ = cost of purchase of power from grid.

$C_{\text{bat}}(t)$ = charge and discharge energy cost.

Constraints

In the power balance, total power supplied from all sources like grid, discharging of energy storage system, PV production and wind production is equal to the power consumed by the household appliances, energy storage system and selling power to grid.

$$P^{\max}_{\text{load}}(t) < P^{\max}_{\text{grid}}(t) \tag{1}$$

Here, $P^{\max}_{\text{load}}(t)$ = Maximum energy exchanged between grid and load.

$P^{\max}_{\text{grid}}(t)$ = Maximum energy generated by grid.

The power balance equation is given by

$$P_{\text{load}}(t) + P^{s}_{\text{grid}}(t) = P_{\text{pv}}(t) + P_{\text{w}}(t) + P_{\text{bat}}(t) + P^{p}_{\text{grid}}(t) \tag{2}$$

where $P^{s}_{\text{grid}}(t)$ = power selling to grid by micro-grid at time slot t.

$P_{\text{load}}(t)$ = sold electrical energy to load at time slot t.

$P_{\text{pv}}(t)$ = power generation by solar radiation at time slot t.

$P_{\text{w}}(t)$ = wind power generation at time slot t.

$P_{\text{bat}}(t)$ = power storage in battery at time slot t.

$P^{p}_{\text{grid}}(t)$ = power purchase from grid by micro-grid at time slot t.

4.1 Model of Energy Storage System (ESS)

The minimum and maximum state of charge limits are taken into account while modeling the charging and discharging of energy storage systems. This energy storage system presents for the all-time slot. The system charges sources in low-price period and discharges in high-price period.

Power used of ESS in household appliances is given by:

$$P_t^{\mathrm{ESS},u} = P_t^{\mathrm{ESS},d}.\mathrm{DE}_{\mathrm{ESS}} \tag{3}$$

where $\mathrm{DE}_{\mathrm{ESS}}$ = Discharging efficiency of the ESS in kilowatt per time duration.

Power consumed by ESS in charging process at time slot t is given by:

$$P_t^{\mathrm{ESS},c.} = \mathrm{CR}_{\mathrm{ESS}}.b_t^{\mathrm{ESS}} \tag{4}$$

$\mathrm{CR}_{\mathrm{ESS}}$ = Charging rate of the ESS in kilowatt per time interval.

b_t^{ESS} = Binary variable. 1 if ESS is charging during period t, 0 else.

Discharging power of ESS at time slot t is given by:

$$P_t^{\mathrm{ESS},d} = \mathrm{DR}_{\mathrm{ESS}}.(1 - b_t^{\mathrm{ESS}}) \tag{5}$$

$\mathrm{DR}_{\mathrm{ESS}}$ = Discharging rate of the ESS.

State of charge equation for ESS is given by:

$$\mathrm{SOC}_t^{\mathrm{ESS}} = \mathrm{SOC}_{t-1}^{\mathrm{ESS}} + \mathrm{CE}_{\mathrm{ESS}}.P_t^{\mathrm{ESS},c} - P_t^{\mathrm{ESS},d} \tag{6}$$

At starting

$$\mathrm{SOC}_t^{\mathrm{ESS}} = \mathrm{SOC}_t^{\mathrm{ESS}i} \tag{7}$$

$\mathrm{SOC}_t^{\mathrm{ESS}i}$ = Initial state of charge in energy storage system

$$\mathrm{SOC}_t^{\mathrm{ESS}} \geq \mathrm{SOC}^{\min} \tag{8}$$

$$\mathrm{SOC}_t^{\mathrm{ESS}} \leq \mathrm{SOC}^{\max} \tag{9}$$

$\mathrm{SOC}^{\min}$ = Minimum allowed state of charge of the ESS (kWh).

$\mathrm{SOC}^{\max}$ = Maximum allowed state of charge of the ESS (kWh).

$\mathrm{SOC}_t^{\mathrm{ESS}}$ = Current state of charge of the ESS (kWh).

Equation (3) represents the fact that the actual power supplied by the energy storage system is used to fulfill some part of household demand. Constraints in

Eqs. (4) and (5) set charging and discharging power limit on energy storage system. These equations also represent the fact that charging and discharging together cannot be done in same time slot. If charging of energy storage system is considered, then put b_t^{ESS} is 1 and automatically the discharging power of energy storage system will be zero or vice versa. Equation (6) represents the current state of charge at any time interval in energy storage system. In the current, starting state of charge is equal to the initial state of charge represented by Eq. (7). Equation (8) imposes the minimum discharging limit on energy storage system. It prevents from deep discharging. Equation (9) represents maximum allowed state of charge of battery as storage system.

Figures 2 and 3 show predicted power (KW) of solar generation and wind turbine power generation during whole day. Figure 4 shows the renewable generation and

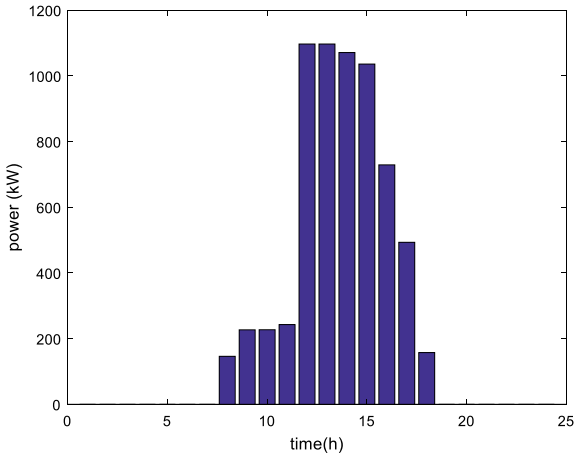

Fig. 2 Predicted solar power generation

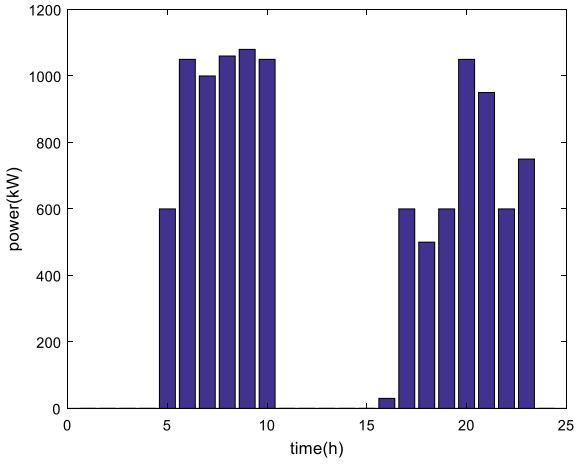

Fig. 3 Predicted wind power generation

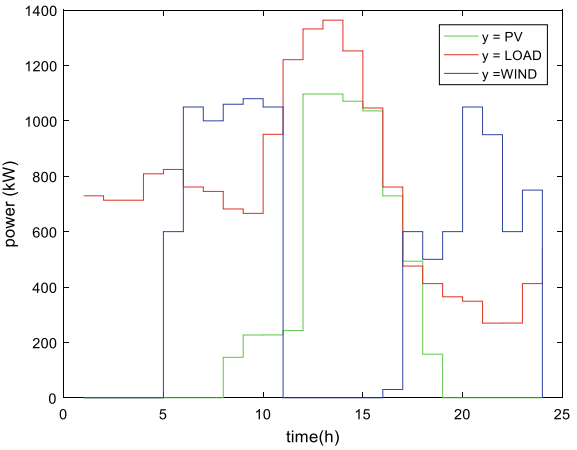

Fig. 4 Renewable power generation and load profile

total load profile of appliances throughout the 24 h in a day. The demand of consumers is shown in red graph of this figure.

5 Results

From the given load profile of the consumer [14], it has been assumed that washing machine and dishwasher are operated by home energy management system. Figure 5 represents number of controllable devices operating in a particular hour and the energy generated by micro-grid without demand management. These appliances are operated for short duration of time but consume a large amount of energy. Operation of these appliances results a peak in load profile as shown in Fig. 6.

So, it is necessary to manage the operation of these devices. Therefore, an energy management system is proposed in this paper. The EMS helps in implementing demand response [16]. Figure 7 represents the controllable devices operated with demand response management. For this purpose, the operating hours of controllable

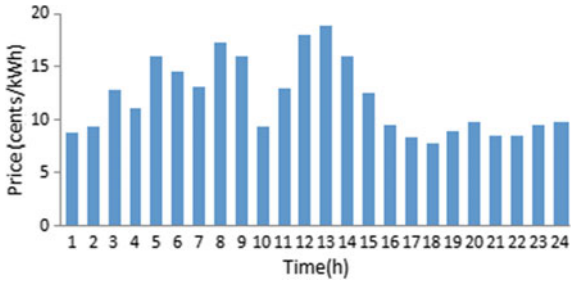

Fig. 5 Predicted price of electrical energy market

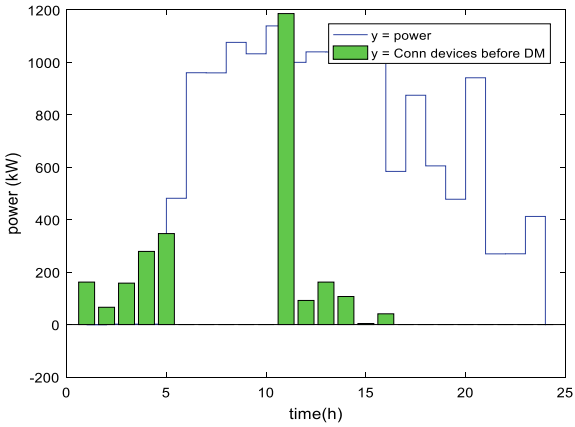

Fig. 6 Power consumption of shiftable appliances before demand-side management [15]

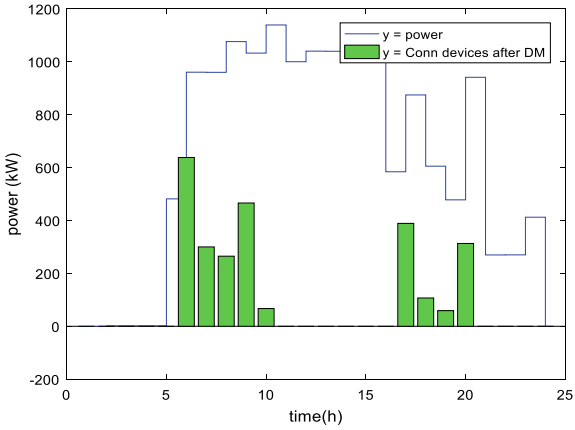

Fig. 7 Power consumption of shiftable appliances after demand-side management

loads are managed to obtain maximum utilization of renewable energy generated by micro-grid. Particle swarm optimization is used for this reason.

It is observed that after demand management, the power generated by renewable resources is excessive compared to the demand [17]. Therefore, the residual power can be used for charging the energy storage system and can also be sold it to the grid. Load profile before and after demand management is shown in Fig. 8. In this figure, green curve represents renewable power generation [18]. The red curve represents load profile before demand management, and blue curve represents the load profile after algorithm for demand management is implemented. It observed that numbers of peaks are reduced after demand management program and the resultant demand closely follows the desired load profile.

This signifies the optimum utilization of renewable energy resources and increases profit of micro-grid to 7004 cents. The energy storage system consists of a battery with maximum battery capacity 10.86 kWh. The battery is charged and discharged

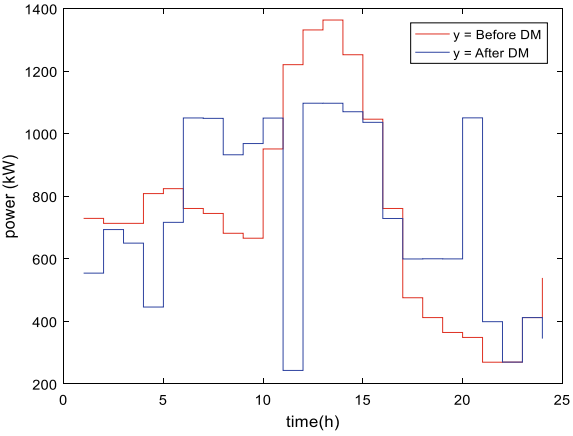

Fig. 8 Load profile before and after demand-side management

as per objective function to maximize profit. Figure 9 demonstrates the change in battery states over an entire day, where positive axis represents charging and negative axis represents discharging [19].

Figure 10 shows below selling power to grid and purchasing power from grid. The negative sign means power is purchased from grid, and positive sign means power is sold to grid. Before demand-side management 1am to 5 duration, there is no renewable power, but demand is presented continuously and at 11 am; less renewable power is available compared to demand. So in this duration, power is purchased from grid. It has shown that after demand management, less power was purchased from gird compared to before demand management. So cost of purchasing extra power has been reduced when controllable load is managed.

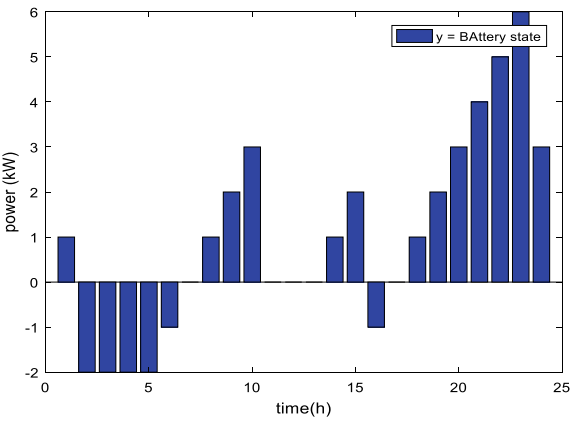

Fig. 9 Change in battery states over entire day

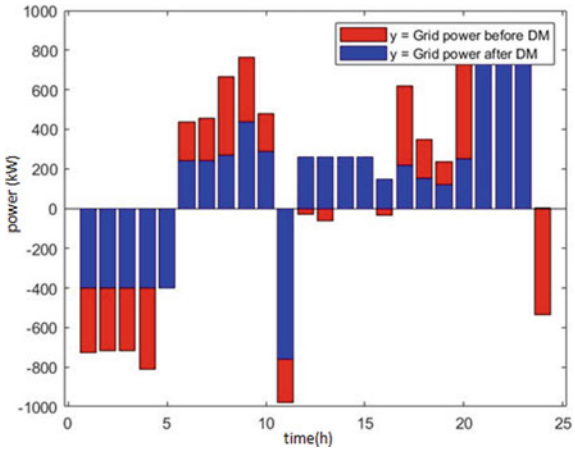

Fig. 10 Grid power before and after demand-side management

6 Conclusion

In this paper, a new smart energy management system for household load with battery as storage capability is proposed. The battery storage and renewable resource are used in this paper to increase profit of a micro-grid. It is observed that the profit of micro-grid has been increased 12.9% after implementation of demand-side management. The reason is that the operating hours of controllable devices are managed in such a manner that energy generated by micro-grid is utilized to the maximum extent. Several cases were examined by considering the PV generation, wind power generation and energy storage system with and without demand-side management. The home energy management systems shift the shiftable appliances in low-price period for minimizing the energy consumption in high-price period. It noticed that with demand response management, the maximum devices are operated in the peak hours of energy generation by micro-grid. Therefore, it increases the overall profit of micro-grid.

References

1. Eid C, Koliou E, Valles M et al (2016) Time-based pricing and electricity demand response: existing barriers and next steps. Util Policy 40:15–25
2. Khalid A, Javaid N, Guaraní M et al (2018) Towards dynamic coordination among home appliances using multi-objective energy optimization for demand side management in smart buildings. IEEE Access 6:19509–19529
3. Hakimi SM, Saadatmandi M, Shafie-khah M, Catalão JPS (2019) Smart household management systems with renewable generation to increase the operation profit of a micro-grid. IET Smart Grid. https://doi.org/10.1049/iet-stg.2018.0299
4. Rahim H, Khalid A, Javaid N et al (2018) Efficient smart buildings using coordination among appliances generating large data. IEEE Access 6(6):34670–34690

5. Hu J, Xu Y, WaiCheng K et al (2018) A model predictive control strategy of PV-battery microgrid under variable power generations and load conditions. Appl Energy 221(4):195–203
6. Manna D, Goswami SK, Chattopadhyay PK (2017) Droop control for micro-grid operations including generation cost and demand side management. CSEE J Power Energy Syst 3(3):232–242
7. Arun SL, Selvan MP (2018) Intelligent residential energy management system for dynamic demand response in smart buildings. IEEE Syst J 12(2):1329–1340
8. Wu X, Hu X, Teng Y et al (2018) Optimal integration of a hybrid solar-battery power source into smart home micro-grid with plug-in electric vehicle. J Power Sources 363(5):277–283
9. Zhou L, Zhang Y, Lin X et al (2018) Optimal sizing of PV and BESS for a smart household considering different price mechanisms. IEEE Access 6(6):41050–41059
10. Bagherian A, Moghaddas Tafreshi SM (2009) A developed energy management system for a microgrid in the competitive electricity market. Power Tech Conf Bucharest 1–6
11. Wang Y, Liang H, Dinavahi V (2019) Parallel stochastic programming for energy storage management in smart grid with probabilistic renewable generation and load models. IET Renew Power Gener 13(3):774–784
12. Zaibi M, Champenois G, Roboam X et al (2016) Smart power management of a hybrid photovoltaic/wind stand-alone system coupling battery storage and hydraulic network. Math Comput Simul 146(5):210–228
13. Chang TP (2010) Estimation of wind energy potential using different probability density functions. Appl Energy 88(1):1848–1856
14. Electrical Energy Price (2016). Available at http://www.bahaye_bargh.tavanir.org/
15. Oviedo RM, Fan Z, Gurus S et al (2014) A residential PHEV load coordination mechanism with renewable sources in smart grids. Electra Power Energy Syst 55(4):511–521
16. Liu D, Xu Y, Wei Q et al (2018) Residential energy scheduling for variable weather solar energy based on adaptive dynamic programming. IEEE/CAA J Autos Sonic 5(4):36–46
17. Lokeshgupta B, Sivasubramani S (2018) Cooperative game theory approach for multi-objective home energy management with renewable energy integration. IET Smart Grid 2(2):34–41
18. Solar Panel (2016) Available http://shangde.fanyacdn.com/imglibs/files/stp270_wemmc4_270_265_260
19. Atia R, Yamada N (2016) Sizing and analysis of renewable energy and battery systems in residential micro-grids. IEEE Trans Smart Grid 7(2):1204–1213

Energy and Area Efficient Binary-to-Gray Code Converter

Deepika Bansal, Shubham Srivastava, Katyayani Chauhan, and Peeyush Garg

Abstract With the rising requirement of handheld and portable devices, low-power and area-efficient circuits are prime concern for nanoscale devices. Binary-to-gray code converter is employed in various applications such as communication systems and processors. XOR gates have been significantly improved to enhance the performance of binary-to-gray code converter. The work proposes an idea to improve the efficiency of the 4-input binary-to-gray code converter with modification of transmission gate configuration. Binary-to-gray code conversion has been analyzed for existing and modified circuits using 45 nm CMOS technology. Simulation result shows the improvement in power consumption and delay by 28 and 40%.

Keywords Transmission gate · Power dissipation · Binary-to-gray code converter · CMOS technology · GDI

1 Introduction

Requirement of advanced electronic devices and efficient circuits has been raised the development of VLSI circuits with high packaging density [1]. In recent times, high-performance and area-efficient technologies are the major emerging part for designers. Power dissipation and the speed of a circuit have become an important considerations for nanoscale devices. The overall reduction in power consumption and power management is the main challenge with shrinking technology over the years [2]. Logic gates are used in most electronic circuits.

The work shows the circuit improvement of the binary-to-gray code (BGC) converter to enhance the efficiency and effective area by the use of the very popular transmission gate (TG) technique [3]. Code converters are commonly used circuits

D. Bansal · S. Srivastava · K. Chauhan
Department of Electronic and Communication Engineering, Manipal University Jaipur, Jaipur 303007, Rajasthan, India
e-mail: deepika.bansal@jaipur.manipal.edu

P. Garg (✉)
Department of Electrical Engineering, Manipal University Jaipur, Jaipur 303007, Rajasthan, India
e-mail: Peeyush.garg@jaipur.manipal.edu

© The Author(s), under exclusive license to Springer Nature Singapore Pte Ltd. 2022

A. Tripathi et al. (eds.), *Intelligent Computing Techniques for Smart Energy Systems*, Lecture Notes in Electrical Engineering 862,
https://doi.org/10.1007/978-981-19-0252-9_63

in digital systems, which can also be modified to reduce the hardware requirements [4].

Conversion of binary stream into gray code is needed for few applications such as digital communication, genetic algorithm, and mathematical puzzles [5]. However, code conversion is also needed in sensors to deliver the information in gray code. The most important application of gray code is analog signal to digital signal converter to minimise errors and decrease the occurrence of "Hamming Walls" (an undesirable state) in genetic algorithms.

In binary code, the data is represented by the combination of 0's and 1's, and then digital circuits are used to convert the signal from one type of code to another [6]. Previous research shows that various XOR gate configurations have been implemented to reduce the power and delay in a circuit [7, 8]. But the only drawback is that they require a large area with a large number of transistors. The useful technique from the other designs is pass transistor logic because of their small node capacitance that gives high speed and reduced number of transistors that gives less power dissipation at the cost of voltage drop [9]. Other technologies demonstrate low power dissipation, which is the reversible logic at the cost of higher transistor count. The GDI-based XOR gate has been designed as a low-power device[10, 11].

XOR gate is a vital part of many modern designs of complex digital circuits [12]. In this work, XOR modules have been developed for binary-to-gray code converter. BGC converter has been designed and compared with published circuits.

According to research analysis, the proposed BGC converter shows better results than conventional circuits in every aspect.

2 Proposed Circuit

The work proposes the BGC converter circuit using XOR gate as a key module. XOR gate is the basic building block in various circuits, especially arithmetic circuits. A new design of XOR gate has been proposed using TG configuration. It occupies less area compared to existing XOR gates as well as less power with smaller delay. The strength of a signal is measured by how closely it approximates an ideal voltage source.

The proposed circuit is a modified version of TG represented as the XOR module in Fig. 1. The major advantage of TG configuration is low power dissipation because of pulse-operated gates. It also avoids the use of supply voltage and reduce the delay but occupies large area due to placement of both transistors. As nMOS transistor produces good 0 condition and vice versa pMOS always passes good 1 condition. Proposed XOR module as in Fig. 1 has been designed using only seven transistors. The proposed configuration provides better results in terms of full swing, low power dissipation, improved delay and a smaller number of transistors as compared to published work. The modified TG configuration is using three transistors only in the XOR module, where two pMOS and one nMOS are displayed in Fig. 1.

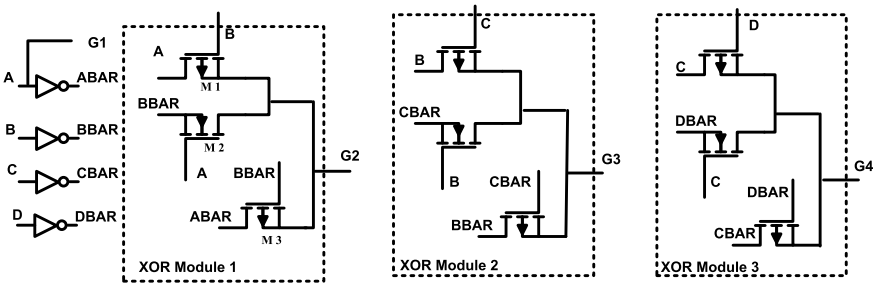

Fig. 1 Proposed circuit of 4-input binary-to-gray code converter

The operation of the proposed XOR module 1 is as follows: When both inputs of XOR gate are connected to a low level, then only M1 pMOS is in ON condition. Hence, it produces a low level at XOR module output G2. In the next case, if both inputs are powered with logic high, then M2 and M3 both MOSFETs are in active mode (ON condition) and it passes the low level at XOR output node.

In the further case, inputs A and B are connected to low and high levels, respectively. Again, M3 pMOS is in working condition, which passes the high logic at the XOR output node. For the last case, if inputs A and B are powered with high and low levels respectively, then M1 and M2 MOSFETs are in ON condition. Therefore, output possesses high logic at the output node.

The BGC converter circuit is displayed in Fig. 1, where three modules of the proposed XOR gate have been used. A 4-input binary-to-gray code converter has been implemented by 17 transistors only. The BGC converter has four input and four output nodes. The proposed BGC dissipates less power, and it requires less area using the modified TG configuration. Figure 2 shows the timing analysis of the 4-input binary-to-gray code converter. The timing diagram in Fig. 2 depicts the correct output levels for all the input combinations and produces full swing.

3 Simulation and Result Analysis

All published and proposed circuits are analyzed by the Synopsys HSPICE simulator using 45 nm CMOS technology. All simulations have been done for 1 V supply voltage and 1fF load capacitance at room temperature. Table 1 shows performance analysis of existing and proposed XOR gates using 45 nm CMOS technology. Multiple XOR gates have been simulated for various parameters such as delay, transistor count, dynamic and static power consumption and PDP.

Aim of the work is designing the efficient binary-to-gray code converter. As XOR is a key module of BGC converter, XOR circuits are analyzed first to check the performance for all parameters as displayed in Table 1. According to the simulation

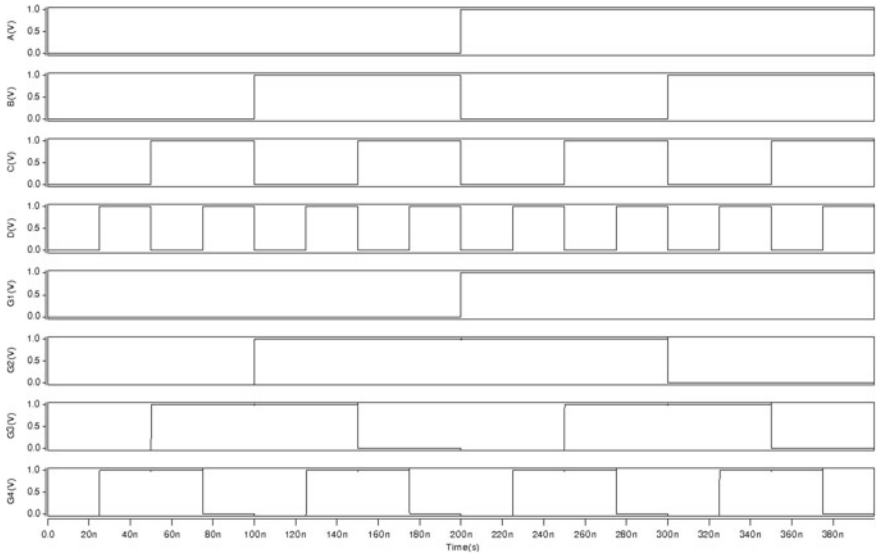

Fig. 2 Timing analysis of 4-input binary-to-gray code converter

Table 1 Performance analysis of existing and proposed XOR gate using 45 nm COMS technology

Design configurations	Number of transistors	Static power consumption (pW)	Dynamic power consumption (nW)	Delay (ps)	PDP (aJ)
TG XOR [3]	8	17.6932	20.3510	37.0602	75.42
GDI XOR [9]	6	22.4399	16.8621	33.4550	56.41
6TXOR [4]	6	16.7854	21.5584	38.7973	83.64
6TXOR [7]	6	16.7854	15.9926	45.0075	71.98
Proposed TG XOR	7	16.5871	17.2659	30.4810	52.64

results as mentioned in Table 1, the proposed circuit produces a lower leakage current, improved delay and better PDP compared to the other designs.

Figure 3 shows the dynamic and static power analysis of 4-input BGC converter using 45 nm CMOS technology. In the analysis, five circuits have been designed to validate the circuit's functionality and characteristics. The line graph shows the static power analysis, whereas bar graph depicts dynamic power consumption of BGC converter. It is very clear in Fig. 3 that proposed BGC converter consumes less power compared to other designs. Now technology wants least power-consuming circuits; the proposed circuit is a way forward in that direction.

Figure 4 demonstrates the comparative analysis of published and proposed converter circuits for delay and PDP. It is observed that the proposed circuit improves the delay and PDP as shown in Fig. 4. Line graph and bar graph depict delay and PDP

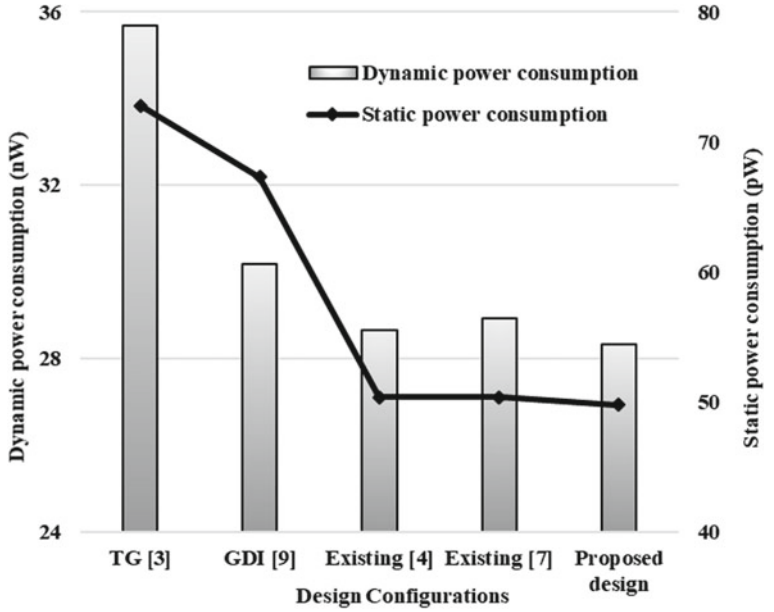

Fig. 3 Power analysis of 4-input BGC converter using 45 nm CMOS technology

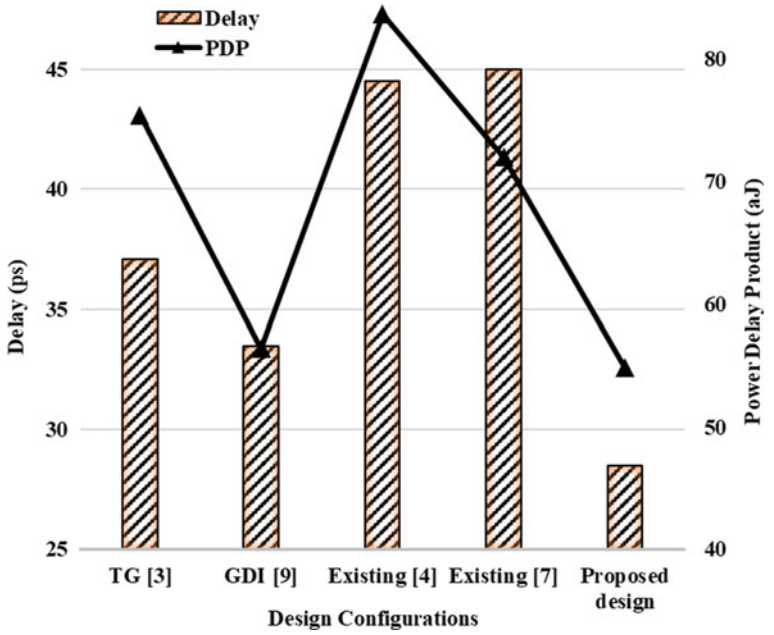

Fig. 4 Delay analysis of 4-input BGC converter using 45 nm CMOS technology

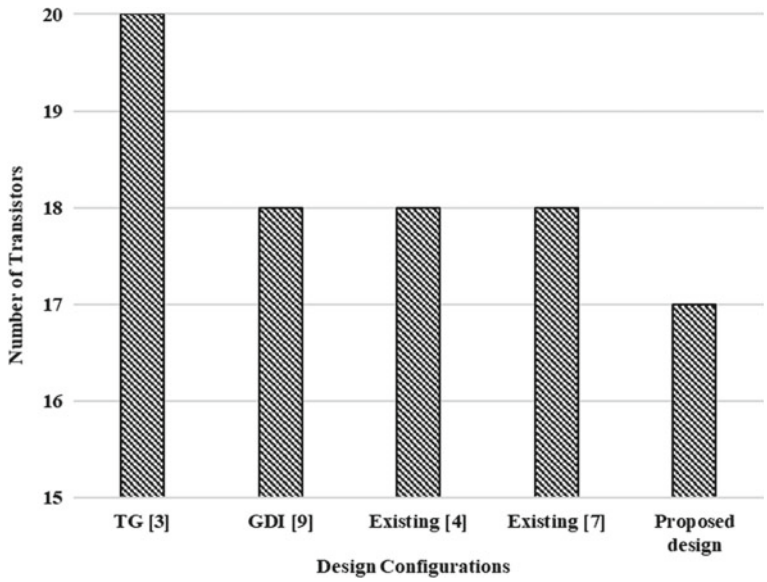

Fig. 5 Transistor count of various design configurations for 4-input BGC converter

analysis, respectively, for BGC converter. The proposed design improves the speed of the circuit which is the main advantage for devices. The overall performance of the proposed converter has been improved over the other published work.

Transistor count of BGC converter circuit is available for various design configurations in Fig. 5. The proposed circuit is having 17 transistors, and it achieved lowest PDP as demonstrated in Fig. 4. Due to having less transistor count, the circuit has a lesser area as compared to other circuits.

Supply voltage directly depends on the performance of the digital circuits. It is noted that as supply voltage decreases, leakage current also decreases, but delay increases and the speed reduces. Figure 6 shows performance analysis of the proposed converter with supply varied from 1 to 0.5 V. The power consumption rapidly decreases as there is a decrement in supply voltage but PDP improves. Simulation results determine the improvement in performance with the state-of-the-art design.

4 Conclusions

In this article, binary-to-gray code converter has been improved for various applications. Simulation results prove the efficiency of the proposed circuit over the other cited work using 45 nm CMOS technology at room temperature. Significance of the article is improvement in the performance of BGC converter. Circuit analyses demonstrate the improvement in all constraints such as power, speed and transistor

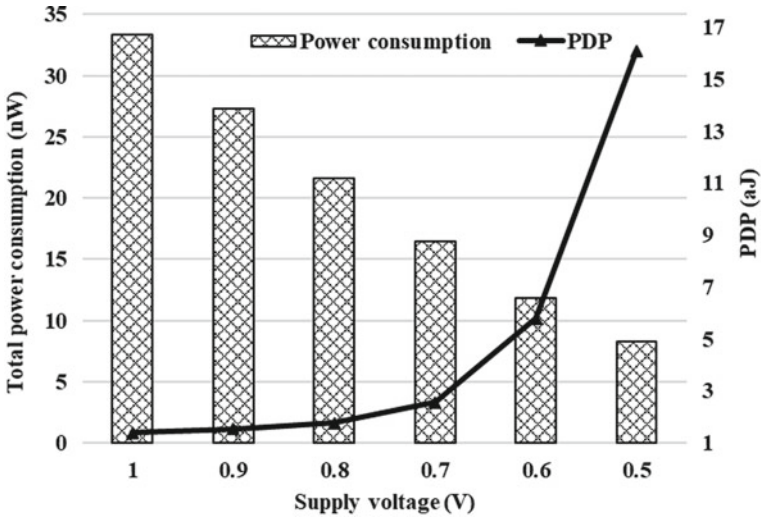

Fig. 6 Total power consumption and PDP analysis of the proposed circuit for supply voltage variation

count. The proposed converter shows a total power reduction of 28% as compared to the transmission gate using 1fF load capacitance. Moreover, the proposed circuit is especially suitable for all XOR-based application design logic with lower power and delay. Comparative analysis shows the better performance of proposed converter over the existing work.

References

1. Aguirre-Hernandez M, Linares-Aranda M (2010) CMOS full-adders for energy-efficient arithmetic applications. IEEE Trans Very Large Scale Integr Syst 19(4):718–721
2. Naseri H, Timarchi S (2018) Low-power and fast full adder by exploring new XOR and XNOR gates. IEEE Trans Very Large Scale Integr Syst 26(8). https://doi.org/10.1109/TVLSI.2018.2820999
3. Kang S-M, Leblebici Y (2003) CMOS digital integrated circuits. Tata McGraw-Hill Education
4. Ahmad N, Rezaul Hasan SM (2013) Low-power compact composite field AES S-Box/Inv S-Box design in 65 nm CMOS using Novel XOR Gate. Integr VLSI J 46(4):333–344. https://doi.org/10.1016/j.vlsi.2012.06.002
5. Rathor VS, Khandelwal S, Akashe S (2014) Domino logic topologies of OR gate with variable threshold voltage keeper. IOSRJVSP 4(4):16–22
6. Anand RK (2015) High performance binary to gray code converter using transmission GATE. 2(1):116–119
7. Stabile A, Liberali V, Calligaro C (2008) Design of a rad-hard library of digital cells for space applications. In: Proceedings of 15th IEEE international new circuits and systems conference. ICECS 2008, no. August, pp 149–152. https://doi.org/10.1109/ICECS.2008.4674813

8. Bui HT, Wang Y, Jiang Y (2002) Design and analysis of low-power 10-transistor full adders using novel XOR-XNOR gates. IEEE Trans Circuits Syst II Analog Digit Signal Process 49(1):25–30
9. Bansal D, Nagar BC, Singh BP, Kumar A (2020) A new keeper domino logic based full adder for high-speed arithmetic circuits. Micro Nanosyst 13(2):223–232. https://doi.org/10.2174/1876402912999200723153358
10. Shoba M, Nakkeeran R (2016) GDI based full adders for energy efficient arithmetic applications. Eng Sci Technol Int J 19(1):485–496. https://doi.org/10.1016/j.jestch.2015.09.006
11. Nishad AK, Chandel R (2011) Analysis of low power high performance XOR gate using GDI technique. In: Proceedings of 2011 international conference on computational intelligence, communication systems and networks, CICN 2011, pp 187–191. https://doi.org/10.1109/CICN.2011.37
12. Bansal D, Singh BP, Kumar A (2015) A novel low power keeper technique for pseudo domino logic. In: 2015 IEEE international conference on electronics, computing and communication technologies (CONECCT), pp 1–6. https://doi.org/10.1109/CONECCT.2015.7383865

Risks of Data Breaches and Mitigating Controls in Financial Sector

Mudit Chaturvedi, Shilpa Sharma, and Gulrej Ahmed

Abstract In today's technological age, where new inventions are happening everywhere, its side effects are also increasing day by day. All over the world, all the work being done in all the fields is based on the processing of data in some form or the other. There are basically three stages of data; the first is the storage of the data, the second is the movement of the data, and the third is the processing of the data through a tool or technology for a particular type of work. Security of data is essential in all the three stages, so that the basic principles of security, i.e., confidence, integrity and availability can be maintained. This paper presents a view on the financial loss due to data breach and preventive safeguards in the financial sector.

Keywords Cyber security · Data breach · Risk · Risk impact · Data in rest · Data in transit · Data in process

1 Introduction

With the increasing use of technology in the financial sector, people have been able to do all banking related tasks like money transfer, balance check, passbook, deposit, etc. Many other facilities are easily accessible through Internet, mobile and computer sitting at home. However, these facilities have made the entire confidential information related to the person's banking available in the market [1]. Today all the works like writing, sending, receiving, image, fax or processing of data are done through computers, mobiles, etc. The transfer of data from one place to another is also done

M. Chaturvedi (✉) · G. Ahmed
Department of Computer and Communication Engineering, Manipal University Jaipur, Jaipur, India
e-mail: mudit09chaturvedi@gmail.com

G. Ahmed
e-mail: gulrej.ahmed@jaipur.manipal.edu

S. Sharma
Department of Computer Applications, Manipal University Jaipur, Jaipur, India
e-mail: shilpa.sharma@jaipur.manipal.edu

© The Author(s), under exclusive license to Springer Nature Singapore Pte Ltd. 2022

A. Tripathi et al. (eds.), *Intelligent Computing Techniques for Smart Energy Systems*, Lecture Notes in Electrical Engineering 862,
https://doi.org/10.1007/978-981-19-0252-9_64

through computers and various devices connected to the computer. Therefore, not only the security of the data, but the devices in which there is availability of data and the devices through which the data is transferred from place to place, or is processed, the security of all is essential [2].

- Data created by computer.
- Data written on a paper sent by fax, scanned copy and image.
- Data received through network.
- Data stored in computers, disks and micro-film.
- Data held on and printed out.
- Data transmitted across networks [3].
- Data shared through different applications like email, web, etc.

For the security of the data, it is essential that all the devices being used, such as computers, mobiles, servers, hard disks, etc., where the data is either kept or from where the data is transferred in any form is protected. It has to be noted that safety is always based on standards [4]. The guidelines related to data security are published from time to time by various governing bodies, regulatory bodies and banking institutes, and all financial units should follow the guidelines word by word and monitor the sensitivity and awareness of the subject in their employee's timely manner. The compliance of the standards related to the security of the data should be checked regularly by independent auditor and do compliance as per the recommendation [5].

2 Terms in Used

Data: A representation of information, knowledge, facts, concepts, or instructions which are being prepared in a formalized manner, and is processed, in a computer system or computer network, and may be in any form printouts magnetic or optical storage media, punched cards, tapes or stored internally in the memory of the computer;

(Sect. 2(o) in the Information Technology Act, 2000).

Data breach: A data breach is an incident in which confidential and sensitive, or any protected data is illegally accessed or disclosed without permission [6]. This issue can involve theft or loss of sensitive information such as social security number, financial data, health records, business data, private data, personal identifiable information, password, or anything which isn't supposed to be available publically. Data breach can be intentional or accidental and often thrives in environments without proper security measures [7].

Security means

- **Protection of**: Information, equipment, devices, computer resource, communication device and information stored therein

- **From**: Unauthorized access, use, disclosure, disruption, modification or destruction.
- **Through**: The technologies, processes and practices
- **To**: Ensure preservation of confidentiality, integrity and availability.

(Sect. 2(nb) in the Information Technology Act, 2000).

Types of data according to their states

Data in rest: When data is kept in a computer resources, i.e., availability of data in hard disk, pendrive, server, card, disk, cloud, etc. [8].

Data in transit: The movement of data from one place to another when data is called through an application, tool, algorithm [9].

Data in process: When data is used for a specific task, to modify its form through a specific instruction, to perform any task related to it, to verify or to make a decision [10].

All the activities that take place in all the fields and all over the world are based on the processing of data directly and in direct. It can be easily understood by this example as every work done by man is done by processing the old information on the related subject available in his mind, his experience, gained and gathered knowledge on different parameters! In the same way, all the work is done by the processing of data, in which computer resources are used [11].

The increasing use of technology in the recent few years has brought all the data into digital form and has made easy access to the data by hackers. Technology is being increasingly used by people, but they do not have knowledge of the various standards used [12].

We can easily understand the growing threat of data breach by Table 1 (Fig. 1).

If we see in Table 2, we can easily understand that not only in India but all over the world hacking cases are increasing day by day. On analyzing the table, you will find that there is no case of loss of any kind of data due to natural disaster; most of the cases have happened due to the company's poor security control, hacking and lack of insider access control. All the data breach cases that happen in the financial sector have a direct impact on the creditworthiness of the financial institution but also on the account holder. Therefore, it is necessary to take important steps related to this. In the above array, 1 out of 40 data breach cases are accidental published, all other cases are related to hacking and poor security (Figs. 2 and 3).

As it is clear from Tables 1 and 2 that data breach is a significant risk. As technology has been promoted, in that proportion the correct instructions for its use have not been disseminated to the people. Most of the people are still unaware of the security and value of data. For the security of data, we have to pay attention that the security of data can be not only logically, but we should also pay attention to physical security [13–17].

Table 1 Data breach cases in India

S. No.	Year	Records breached	Name of the reported organization	Method
1	May, 2021	4.5 million	Air India data breach	Poor security
2	May, 2021	190,000	CAT applicants' personal details	Hacked
3	Apr, 2021	180 million	Domino's India pizza orders	Inside job
4	Apr, 2021	All	All Upstox customers passwords	Hacked
5	Apr, 2021	60 lakh	Facebook	Hacked
6	Mar,2021	10 crore	MOBIKWIK	Inside job
7	Feb, 2021	5,00,000	Indian police personnel	Hacked
8	Jan, 2021	1500	COVID-19 test results of Indian patients	Poor security
9	Jan, 2021	35 million	User data from Juspay	Hacked
10	Oct, 2020	20 million	BigBasket user data	Hacked
11	May, 2020	22 million	Unacademy	Poor security
12	Mar, 2020	5.2 million	Marriot Hotel	Hacked
13	Aug, 2019	68 lakh	Patients and doctors records	Hacked
14	Apr, 2019	10 Crore	JustDial	Inside job
15	Jan, 2019	3 million	SBI	Hacked
16	2019	2093	RBI (Case more than 1 Lakh rupees fraud)	Poor security
17	2018	968	RBI (Case more than 1 Lakh rupees fraud)	Poor security
18	2017	2095	RBI (Case more than 1 Lakh rupees fraud)	Poor security
19	2016	1343	RBI (Case more than 1 Lakh rupees fraud)	Poor security

The main reasons described for a data breach can be classified as follows:

1. **Physical security**: There is an important part in the security of data, in which all those devices are protected from theft, damage, alter, natural disaster, etc.
2. **Logical security**: It is a very important part in the security of data, in which the maximum possibility of theft of data occurs in such ways which are difficult to detect easily and the status of data remains the same in devices like computers, etc. [18].

As of now there are many possibilities of data breach, some can be grouped together according to their nature, mainly classified as following.

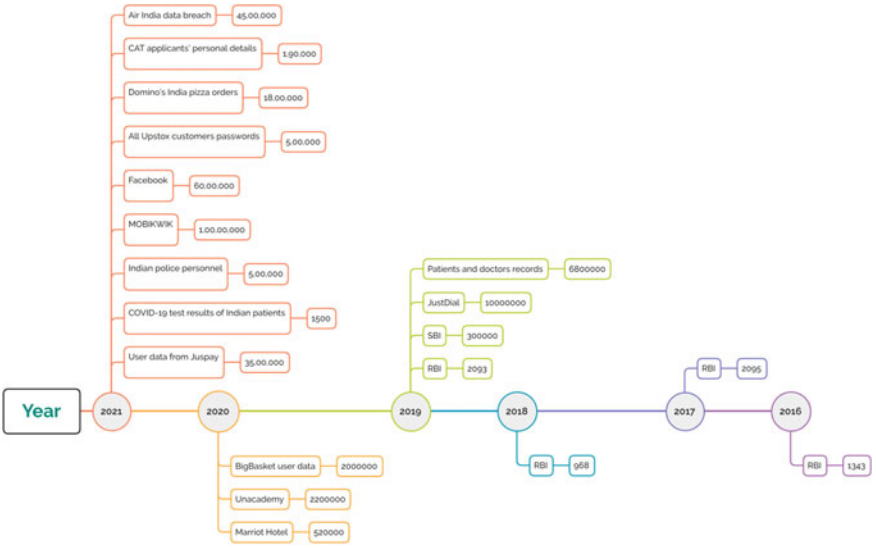

Fig. 1 Data breach cases in different domain in India

2.1 Risk from Data Breach in Financial Sector

The As you have seen in Table 3 that there are innumerable cases of data breach not only in India but all over the world and in all domains, which directly harm the customer and the organization. In today's time, data is a very important component for all the organization, and the whole business depends on the processing of data [19–21]. There are various types of penalties and punishments for the loss of data in all areas, but in the financial sector, the direct loss of data breach falls on the customer with immediate effect. The theft of data in the financial sector leads to the loss of the earned money of the life of the customer, in which many times the person is unable to take care of himself and the person dies. Therefore, the security of data in all areas should be as per the stated standards, and it should be followed especially in the financial sector [22–24].

So if we calculate the risk:

$$\text{Risk} = \text{Likelihood} \times \text{Impact}$$

If the facts mentioned in the above list are assessed, then we will find that most of the data breaches have happened through poor security, hacking and interim members of the company, etc. which depends on the organization's policy, procedure and the awareness of the people working [25]. The impact of a financial data breach that occurs due to lack of logical security guideline stated and non-adherence to any security framework is displayed as theft of number of records. If you multiply these two, then the value of risk can be easily calculated. If the methods that are suitable

Table 2 Globally data breach cases in financial sector

S. No.	Year	Records breached	Name of the reported organization	Method
1	TD Ameritrade	2021	200,000	Lost/stolen media
2	Now: Pensions	2020	30,000	Rogue contractor
3	Unknown agency (believed to be tied to United States Census Bureau)	2020	200,000,000	Accidentally published
4	Capital one	2019	106,000,000	Unsecured S3 bucket
5	Desjardins	2019	2,900,000	Inside job
6	Westpac	2019	98,000	Hacked
7	First American Corporation	2019	885,000,000	Poor security
8	Equifax	2017	163,119,000	Poor security
9	Central Coast Credit Union	2016	60,000	Hacked
10	Internal Revenue Service	2015	720,000	Hacked
11	Scottrade	2015	4,600,000	Hacked
12	European Central Bank	2014	800,000	Hacked
13	JP Morgan Chase	2014	76,000,000	Hacked
14	Korea Credit Bureau	2014	20,000,000	Inside job
15	NASDAQ	2014	Unknown	Hacked
16	Citigroup	2013	150,000	Poor security
17	Global payments	2012	7,000,000	Hacked
18	Iranian banks (three: Saderat, Eghtesad Novin and Saman)	2012	30,00,000	Hacked
19	Massive American business hack, including 7-Eleven and Nasdaq	2012	160,000,000	Hacked
20	TD Bank	2012	260,000	Hacked
21	Citigroup	2011	360,083	Hacked
22	Countrywide Financial Corp	2011	2,500,000	Inside job
23	Morgan Stanley Smith Barney	2011	34,000	Lost/stolen media

(continued)

Table 2 (continued)

S. No.	Year	Records breached	Name of the reported organization	Method
24	Educational Credit Management Corporation	2010	3,300,000	Lost/stolen media
25	Federal Reserve Bank of Cleveland	2010	400,000	Hacked
26	JP Morgan Chase	2010	2,600,000	Lost/stolen media
27	CheckFree Corporation	2009	5,000,000	Hacked
28	Heartland	2009	130,000,000	Hacked
29	The Bank of New York Mellon	2008	12,500,000	Lost/stolen media
30	Data Processors International, (MasterCard, Visa, Discover Financial Services and American Express)	2008	8,000,000	Hacked
31	RBS Worldpay	2008	1,500,000	Hacked
32	Compass Bank	2007	1,000,000	Inside job
33	Fidelity National Information Services	2007	8,500,000	Inside job
34	TD Ameritrade	2007	6,300,000	Hacked
35	Countrywide Financial Corp	2006	2,600,000	Inside job
36	Mitsubishi Tokyo UFJ Bank	2006	960,000	Intentionally lost
37	Automatic data processing	2005	125,000	Poor security
38	Bank of America	2005	1,200,000	Lost/stolen media
39	Card Systems Solutions Inc., (Master Card, Visa, Discover Financial Services and American Express)	2005	40,000,000	Hacked
40	Citigroup	2005	3,900,000	Lost/stolen media

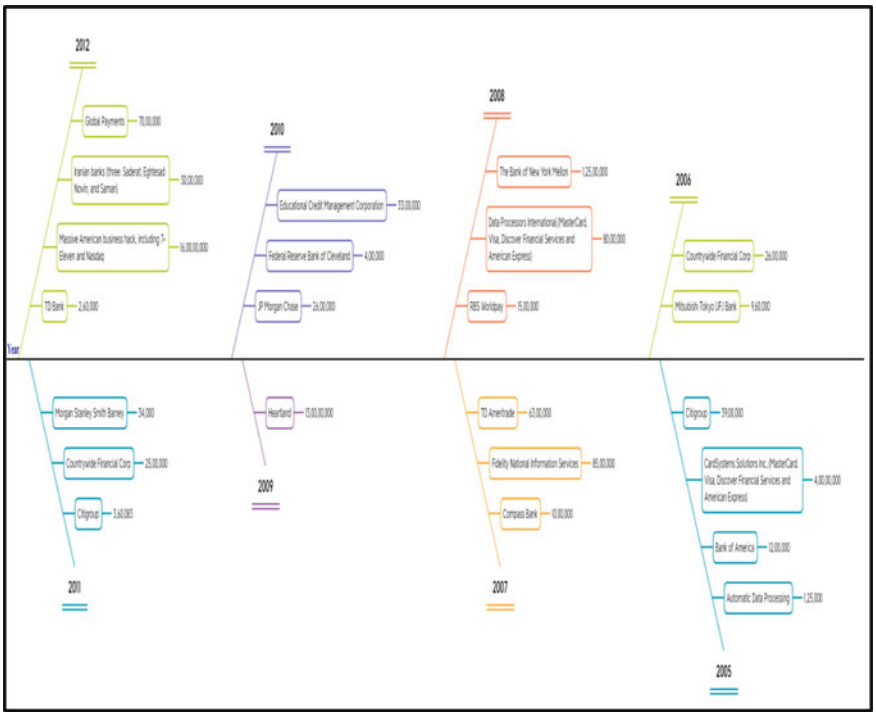

Fig. 2 Global data breach cases in financial sector globally, 2005–2012

for data breach are indicated on the basis of their probability, then according to the globally available data, we will find that 70 to 80 percent of the cases are due to lack of internal security mechanism in the organization and the employee is not aware of the data protection. Due to this, most of the data frauds happen.

If taking an average we assume that 75 out of 100 data breach cases in a financial institution are due to lack of logical security, then it can easily be concluded that the probability of a logical security breach is high. The impact of the financial data breach directly hit the customer's deposits, bank credit and additional penalties on the bank; hence, its impact is also high. Therefore, according to the rule of risk calculation, the multiple of probability of vulnerability (Likelihood) and high impact value will show high risk [26].

$$\text{Risk} = \text{High(Likelihood value)} \times \text{High(Impact value)} = \text{High(Risk)}$$

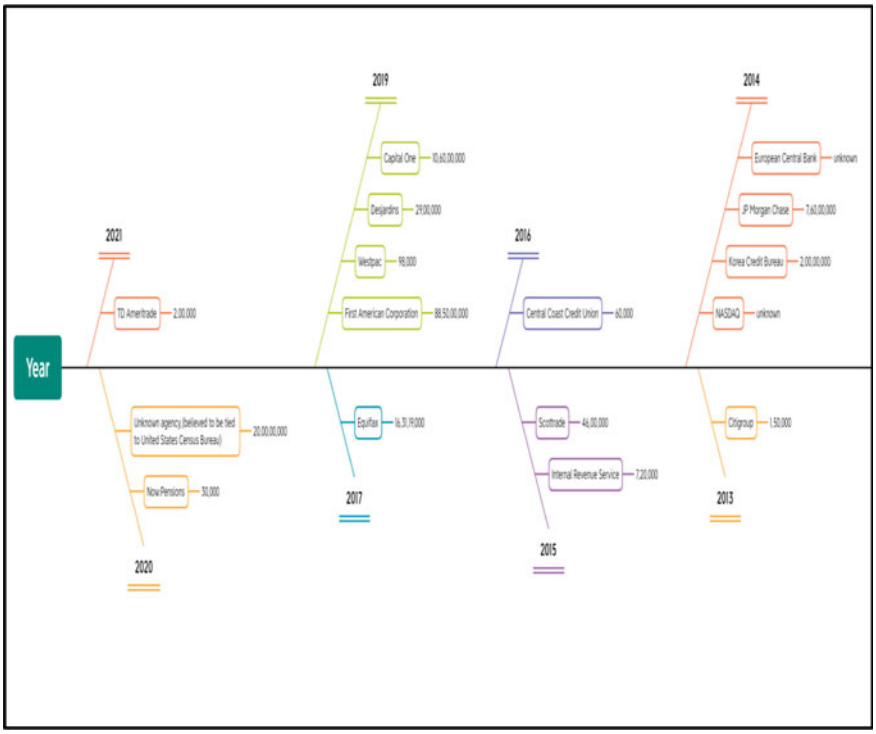

Fig. 3 Global data breach cases in financial sector globally, 2013–2021

Table 3 Reasons of data breach

S. No.	Physical security	Logical security	
1	Physical theft of a data-carrying device	Old, unpatched security vulnerabilities	Application vulnerabilities
2	Natural disaster: flood, fire, lightening	Human error	Unauthorized use
3	No access control, water leakage	Insider misuse	Social engineering
4	Physical actions open port, no proper cabling	Weak and stolen credentials	Criminal hacking Malware

3 Proposed Solution

A risk assessment and risk mitigation plan should be done in every organization. The risk assessment in the organization should be updated from time to time so that new risks can be identified and added, and the risk mitigation plans can be prepared. In order to do risk assessment in the organization, the company should implement a

standard security framework recommended by any relevant regulatory bodies for the security of the data [27]. The security of every organization is based on three things.

1. **Policy**: The organization should make a policy related to every work going on in the organization using a standard, which should be approved through the board member and all the members of the organization should be made aware of the policy

   Every organization should make the above-mentioned documented policy to protect the data, and those policies should be approved by the organization management. The organization should communicate all these policies to its employees and check them from time to time through audit, monitoring tools, etc.
2. **Technology**: All the technologies used in the organization such as firewall, computer, server, etc. should all be properly configured, and all the instructions approved by the technical institutions should be followed in their use (Tables 4, 5 and 6).

In the security of data, it is necessary to protect not only computer laptop devices but also all the devices connected in the network through which the transfer of data takes place. Every organization should keep all the equipment installed by their premises up to date, check them regularly, get their proper maintenance method and document manual from the concerned vendor. In case of any problem, immediately contact the service provider and get it fixed immediately. Information related to the proper maintenance and installation of devices is made available by

Table 4 Documented as per business requirements and relevant laws and regulations

Information security policy	
1	Documented management direction for information security
2	Documented information security roles and responsibilities
3	Documented segregation of duties
4	Mobile device and teleworking policy
5	Human resource security policy to check all IT credential prior to employment, during employment, termination and change of employment
6	Asset management policy
7	Access control policy, user access management policy
8	Cryptography and data encryption policy
9	Physical and environment security policy
10	Operational security policy
11	Communication security policy
12	System acquisition, development and maintenance policy
13	Supplier relationship policy
14	Incident management policy
15	Business continuity management plan

Table 5 Secure technology

Secure configuration of devices	
1	Firewall
2	Data leak prevention
3	Router
4	Switch
5	Server
6	Antivirus
7	Operating system [not pirated]
8	Administrator account
9	Wireless devices
10	Media handling
11	Active directory

Table 6 Training and testing

Cyber security awareness	
1	Cyber law
2	Safe use of technology
3	Do's and don'ts in daily work
4	Different cyber fraud and modus operandi
5	Regular competence check

many organizations from time to time. Many government organizations and international standard organizations issue information related to the new shortcomings in the devices according to their model, i.e., zero-day vulnerability. Therefore, all the devices should be protected according to the prescribed standards.

Training and awareness: Through training, all the members of the organization should be made aware of the increasing cybercrime and their methods day by day. Teach them the correct use of the technology used by them in the organization so that data breach can be prevented.

Even after the security of the policy, procedure and technology, the organization should continuously conduct cyber awareness training of its employees. Make them aware of the increasing cybercrime in different ways and the measures to avoid them. The organization should pay attention to how all the employees have spelled cyber security-related awareness in their work and make them aware of the policies and procedures of the organization.

Apart from all this, the organization should get audit done by independent auditor once in a year or whenever the organization changes or updates its IT infrastructure, so that the application policy, procedures, technical equipment and work done by the people in the organization should be investigated and necessary corrective steps can be taken up [28].

If work is done properly on the above-mentioned three topics in the organization and they are updated and checked from time to time, then the risk coming in the organization can be reduced to a great extent. Data breaches that occur through hacking, poor security and interim employees can be addressed through this.

4 Conclusion

In today's time, data is an important element of or every organization, and there are many laws related to the protection of data exist like GDPR, HIPAA, PCI-DSS, DPA, etc. Data security is an important topic in many countries, and there is a provision of heavy penalty on such organization which do not implement this law effectively. The security of financial data is also important because today all the business and transactions are done through online means, if an organization cannot protect its customer information properly, then that customer will become an easy target for hacker, and he suffers by the penalty of poor security control of the organization by losing his deposit. The organization should adhere to the security standard and should continuously monitor it through tools.

References

1. Alhazmi OH, Malaiya YK (2008) Application of vulnerability discovery models to major operating systems. IEEE Trans Reliab 57:14–22
2. Ponemon Institute (2013) 2013 Cost of Data Breach Study: The US Sponsored by Symantec. Available online: http://www.symantec.com/content/en/us/about/media/pdfs/b-cost-of-a-data-breach-us-report-2013.en-us.pdf. Accessed on 30 Mar 2021
3. Algarni AM, Malaiya YK (2016) A consolidated approach for estimation of data security breach costs. In: Proceedings of the 2016 2nd international conference on information management (ICIM), London, UK, 7–8 May 2016
4. Layton R, Watters PA (2014) (2014) A methodology for estimating the tangible cost of data breaches. J Inf Secur Appl 19:321–330
5. Thapa C, Camtepe S (2021) Precision health data: requirements, challenges and existing techniques for data security and privacy. Comput Biol Med 129:104130
6. Ponemon Institute (2020) 2020 Cost of Data Breach Study: The US. Sponsored by IBM. Cost of a Data Breach Report 2020|IBM. Available online: https://www.ibm.com/security/digital-assets/cost-data-breach-report/. Accessed on 30 Mar 2021
7. Westland JC (2020) The information content of Sarbanes-Oxley in predicting security breaches. Comput Secur 90:101687
8. Da Veiga A, Astakhova LV, Botha A, Herselman M (2020) Defining organizational information security culture—Perspectives from academia and industry. Comput Secur 92:101713
9. Diesch R, Pfaff M, Krcmar H (2020) A comprehensive model of information security factors for decision-makers. Comput Secur 92:101747
10. Iannacone MD, Bridges RA (2020) Quantifiable & comparable evaluations of cyber defensive capabilities: a survey & novel, unified approach. Comput Secur 96:101907
11. Romanosky S (2016) Examining the costs and causes of cyber incidents. J Cybersecur 2(121):135

12. Gay S (2017) Strategic news bundling and privacy breach disclosures. J Cybersecur 3:91–108
13. Sun H, Xu M, Zhao P (2020) Modeling malicious hacking data breach risks. N Am Actuar J 2020:1–19
14. Ogonji MM, Okeyo G, Wafula JM (2020) A survey on privacy and security of Internet of Things. Comput Sci Rev 38:100312
15. Jouini M, Rabai LBA, Khedri R (2020) A quantitative assessment of security risks based on a multifaceted classification approach. Int J Inf Secur 2020:1–18
16. Park JY, Huh EN (2020) A cost-optimization scheme using security vulnerability measurement for efficient security enhancement. J Inf Process Syst 16:61–82
17. Li K, Tong Z, Liu X, Zhang J, Tong S (2020) Quantitative assessment and driving force analysis of vegetation drought risk to climate change: Methodology and application in Northeast China. Agric For Meteorol 282:107865
18. Fusco F, Allocca V, Coda S, Cusano D, Tufano R, De Vita P (2020) Quantitative assessment of specific vulnerability to nitrate pollution of shallow alluvial aquifers by process-based and empirical approaches. Water 12:269
19. HIPAA (2019) Data breach barometer report shows the massive increase in exposed healthcare records. HIPAA J. Available online: https://www.hipaajournal.com/2019-data-breach-barometer-report-shows-massive-increase-in-exposed-healthcare-records/. Accessed on 30 Mar 2021
20. Forgerock (2019) Consumer Data Breach Report 2019: Personally identifiable information targeted in breaches that impact billions of records; Forgerock Breach Report 2019; Forgerock: San Francisco, CA, USA
21. Aziz MMA, Sadat MN, Alhadidi D, Wang S, Jiang X, Brown CL, Mohammed N (2019) Privacy-preserving techniques of genomic data-a survey. Brief Bioinform 20:887–895
22. Jacobs J (2021) Analyzing Ponemon cost of data breach. Data Driven Secur. 2014, 11, 5. Available online: http://datadrivensecurity.info/blog/posts/2014/Dec/ponemon/. Accessed on 30 Mar 2021
23. Team, Verizon RISK (2015) 2015 data breach investigations report. Available online: http://www.verizonenterprise.com/DBIR/2015/. Accessed on 30 Mar 2021
24. Weiss NE, Miller RS (2015) The target and other financial data breaches: frequently asked questions congressional research service. Available online: https://fas.org/sgp/crs/misc/R43496.pdf. Accessed on 30 Mar 2021
25. Target Reports Fourth Quarter and Full-Year 2014 Earnings. Available online: http://investors.target.com. Accessed on 30 Mar 2021
26. Target Reports Fourth Quarter and Full-Year 2015 Earnings. Available online: http://investors.target.com/phoenix.zhtml?c=65 828&p=irol-newsArticle&ID=2142619. Accessed on 30 Mar 2021
27. TechRepublic (2015) Data breaches may cost less than the security to prevent them. Available online: http://www.techrepublic.com/article/data-breaches-may-cost-less-than-the-security-to-prevent-them/. Accessed on 30 Mar 2021
28. PYMNTS (2015) How much did the target, home depot breaches really cost. Available online: http://www.pymnts.com/news/2015/target-home-depot-reveal-full-breach-costs/. Accessed on 30 Mar 2021

Battery Energy Management for Community Microgrid

Divya Mathur, Neeraj Kanwar, and Sunil Kumar Goyal

Abstract Community microgrid is implemented in existing electricity grid to mitigate greenhouse effect and meet changing climate change-related disturbance. The energy management system is the key element of community microgrid with battery storage system, wind, and solar farms. The grid transaction is calculated with proposed battery energy management. The overall cost of the power flow of community microgrid with utility grid per hour is estimated in this paper. The net cost of energy is reduced over a period of 24 h by using the proposed battery energy management scheme.

Keywords Community microgrid · Energy management · Battery management · Renewable integration

1 Introduction

The deployment of renewable energy resources (RESs) has been increasing extensively day by day, to mitigate the greenhouse gas emission in atmosphere, and to meet climate change-related disturbances. With the increase in the penetration of RESs, the more challenges occur at the distribution networks due to bidirectional flow of power. These problems can be minimized by converting centralized distribution network control into distributed control over many areas called microgrid. A microgrid is a set of interconnected loads and distributed resources that act as a single entity and operate independently from grid [1]. It can operate as a grid-tied mode or islanded mode. However, microgrid has some operational issues due to uncertain power generation of RESs, variable nature of load demand and electricity

D. Mathur · N. Kanwar (✉) · S. K. Goyal
Department of Electrical Engineering, Manipal University Jaipur, Jaipur, Rajasthan, India
e-mail: nk12.mnit@gmail.com

D. Mathur
e-mail: divya.199209604@muj.manipal.edu

S. K. Goyal
e-mail: sunilkumar.goyal@jaipur.manipal.edu

© The Author(s), under exclusive license to Springer Nature Singapore Pte Ltd. 2022

A. Tripathi et al. (eds.), *Intelligent Computing Techniques for Smart Energy Systems*,
Lecture Notes in Electrical Engineering 862,
https://doi.org/10.1007/978-981-19-0252-9_65

pricing, etc. Therefore, an efficient energy management is a requirement for optimal operation of microgrid.

Community microgrid is a type of microgrid which acts as a independent controllable entity with respect to main grid and having its defined electrical boundaries [2]. Energy storage is considered as an integral part of microgrid. It helps to obtain a stable operation of microgrid as well as cope up the uncertain power generation of RESs and variable load demand. However, battery charging/discharging depends on load available on the system at any particular time. The life cycle of energy storage directly depends on its charging and discharging. With increase in number of charging and discharging cycles of a battery, its lifecycle decreases. Therefore, it requires replacement and add an extra cost on microgrid that is additional to other mandatory costs of microgrid.

Several approaches have been used in literature for battery energy management [3, 4]. However, a very few works are available in literature to solve battery energy management by considering degradation cost of battery. In this paper, a battery energy management scheme is proposed to reduce the net cost of grid transaction in consideration of its degradation cost. The proposed methodology has been applied on a community microgrid, and simulation results are presented.

2 Proposed Model

2.1 A Community Microgrid

A model of community microgrid is considered in this paper, for efficient battery storage management with optimum community electricity cost. A remotely located area with availability of solar and wind power is considered as residential load with maximum demand of 36 kWh. The installed capacity of solar and wind farms is 40 kW and 25 kW, respectively. The microgrid under consideration is capable to work in both islanded and grid-connected modes [5]. A controlling unit, i.e., energy management unit (EMU) is connected with microgrid, which takes care of electric power flow corresponding to instant generation and load demand in network, as shown in Fig. 1.

The power generation through solar and wind farms, SOC of battery, instant price of electricity, and load profile is the input parameters of EMU, which controls the flow of power with utility grid and generates the reference command signal for charging/discharging of battery. The reference command for charging/discharging of battery for power exchange with grid is generated through input parameters of EMU. The battery system connected with microgrid is used to maintain power supply and fulfill power demand of household. During low electricity price, the battery should be charged from grid, while during high pricing, it can be charged from renewable energy sources (RESs). This will lead to increase in charging/discharging cycles and thus reduce battery lifespan [6].

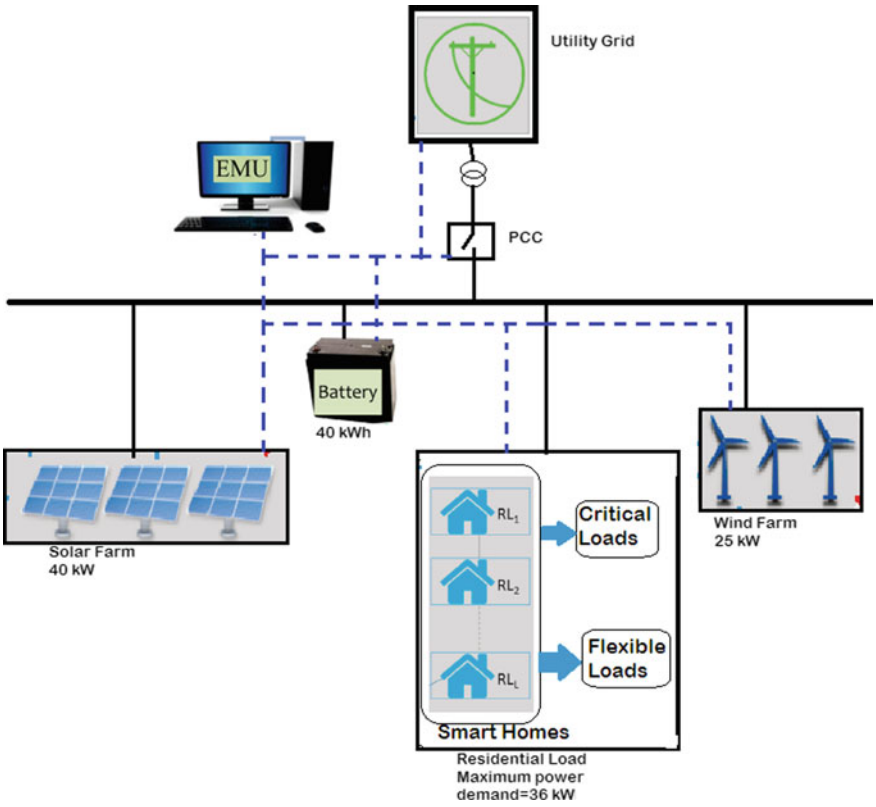

Fig. 1 Community microgrid

2.2 Solar Generators

A solar generator is an array of solar photovoltaic panels connected with an inverter and control unit. The covered area of solar generator is considered as 200 m^2. The maximum power and conversion efficiency of solar generator are 4 kW and 18%, respectively. Its capacity is dependent on size of PV array and solar irradiation (I) [7]. The solar PV output can be calculated as

$$P_{\mathrm{SPV}} = \eta_{\mathrm{solar}} \times A \times I(1 - 0.005(t_0 - 25)) \tag{1}$$

where η_{solar} and A are the % efficiency and PV panel area in m^2, respectively, and t_o indicates environment temperature (°C). The hourly solar irradiation and wind velocity are shown in Figs. 2 and 3, respectively.

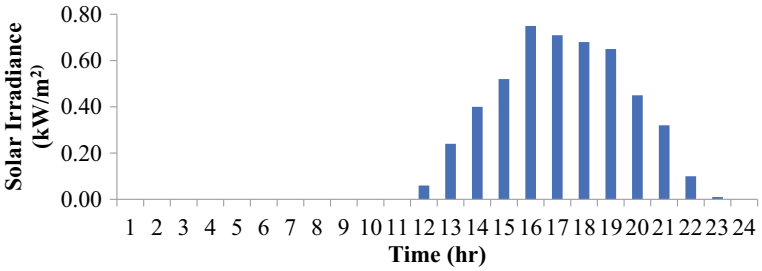

Fig. 2 Solar irradiation over 24 h horizon

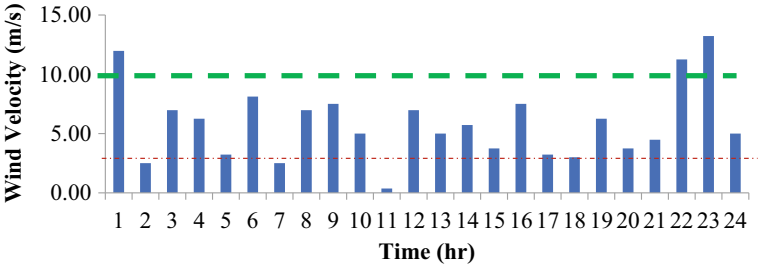

Fig. 3 Wind velocity over 24 h horizon

2.3 Wind Turbines

The wind generator power output power is obtained using following function which depends upon its wind speed and the rated power. The power output of wind turbine depends upon the wind velocity, v (m/s) as denoted by following relation [8]:

$$P_{\mathrm{WT}} = \eta_{\mathrm{wind}} \times \begin{cases} 0; & \text{if } v_3 \leq v \text{ or } v \geq v_1 \\ P_m \times \frac{v^2 - v_1^2}{v_2^2 - v_1^2}; & \text{if } v_1 \leq v \leq v_2 \\ P_m; & \text{if } v_2 \leq v \leq v_3 \end{cases} \tag{2}$$

where P_m is the rated electrical power considered to be 25 kW; v_1 is the cut-in wind speed considered to be 3 m/s; v_2 is the rated wind speed considered to be 10 m/s; and v_3 is the cut-off wind speed considered to be 25 m/s; η_{wind} is the wind generator efficiency considered to be 95%. The hourly representation of wind velocity over 24 h is shown in Fig. 2

2.4 Battery Storage System

The EMU manages the battery storage system to lower the electricity price and reduce the effect of uncertain behavior of RESs. The EMU sends the command signals for optimal operation of battery, depending upon battery energy level, electricity price, power generation, and load demands. The battery will be charged from grid when generation is lower than load, and if at the state of discharging, it will act as another source for fulfilling load. Similarly, battery will charge from RES if the generation is higher than load. The limits are imposed on the command signals for prolonging the battery lifetime as

$$\mathrm{SOC}_{\min} < \mathrm{SOC}(t) < \mathrm{SOC}_{\max} \tag{3}$$

where $\mathrm{SOC}_{\max}$ and $\mathrm{SOC}_{\min}$ are the maximum and minimum values of state of charge for battery. The $\mathrm{SOC}_{\min}$ is taken as 20% while the $\mathrm{SOC}_{\max}$ as 90% of full SOC. Alternatively, the battery energy levels B_{L} can be represented as [9]:

$$B_{\mathrm{L}}(t) = B_{\mathrm{L}}(t-1) \pm \text{Charging/Discharging Rate} \tag{4}$$

It is assumed that the charging/discharging rate varies between +4 and −4 kWh keeping maximum/minimum battery energy level at 36/7.2 kWh.

2.5 Loads

In this paper, hourly variations in a residential load are considered in a time step of 1 h [10] which is as shown in the Table.1. The maximum load demand is considered to be 36 kW covering all the important household equipment.

2.6 Electric Grid Utility

Electricity can be purchased or sell to grid utility according to the availability of renewable power at each hour. Generally, buying electricity at high price is avoided. In this paper, buying and selling rates are kept same for simplicity and are shown in Table 1. The real-time electricity price is varying with time corresponding to electricity market [11].

Table 1 Hourly variation of power demand (kW) and electricity price ($/kWh)

Time	Power demand (kW)	Battery command signal	Electricity price ($/kWh)	Time	Power demand (kW)	Battery command signal	Electricity price ($/kWh)
1	10	0	0.175	13	21.25	−2.6	0.325
2	9	2.55	0.125	14	25	−2.4	0.275
3	8	4	0.14	15	25	−2.3	0.29
4	12.5	4	0.175	16	22.5	−1.9	0.3
5	13	3.5	0.225	17	25	−1.8	0.35
6	13	3.5	0.3	18	32.5	−2.6	0.36
7	20	0.7	0.3	19	30	−2.3	0.375
8	17.5	−0.5	0.3625	20	34	−3.6	0.38
9	12	−0.6	0.3125	21	18	−1.8	0.25
10	12	−1.25	0.3	22	17.5	0	0.225
11	12.5	−2	0.3	23	12	3.5	0.175
12	12.6	−2	0.3375	24	15	4	0.125

3 Results

The modeled grid-connected community microgrid is considered for the minimization of community electricity cost and maintaining power balance. The grid-connected microgrid optimally utilizes the renewable power for feeding the load power demand with the use of battery energy storage. The solar and wind power generation are shown in Fig. 4.

The battery energy control with respect to the real-time electricity price (RTP) is prime goal in this paper. The initial battery level for first hour is assumed to be known. Due to limits of battery energy SOC, the maximum level of battery is taken to be 36 kWh. If the generated power is lesser than the power demand, then the battery will be discharged, but if battery level is not enough, then power will be purchased from main grid. Similarly, at the time of low power demands, the battery will be charged

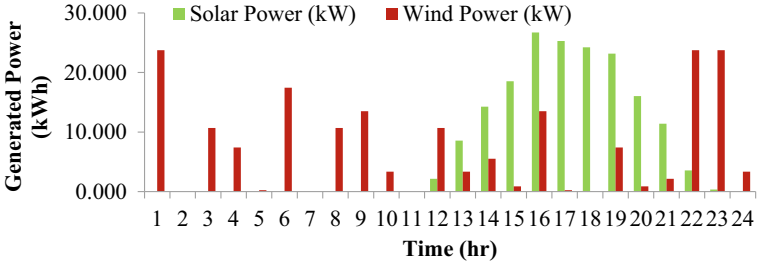

Fig. 4 Renewable power generation connected with microgrid

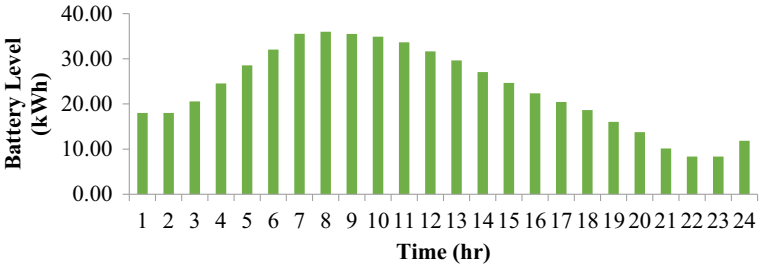

Fig. 5 Hourly representation of battery level

from excess power, but if it is not required, then the power will be sold to grid. This increases the charging/discharging cycles of battery and thus decreases the lifespan of battery. Therefore, it is necessary to reduce the unwanted non-profitable cycles to increase battery lifespan. The battery level during charging and discharging at each hour is obtained by Eq. (4) and shown in Fig. 5.

The battery charging/discharging level assumed here is at its minimum/maximum limits, i.e., 7.2/36 kWh to increase the lifespan of the battery. The hourly battery level as shown in Fig. 5 is used to estimate the overall energy cost for feeding the load at each hour. The total renewable energy generation through solar and wind farms, load, battery level, and total cost is presented in Fig. 6. It is observed that the load is feed by the renewable energy first, and unsupplied load is taken from the battery and utility grid in case of power deficit. However, the surplus generated power is used to charge the battery and feed to the grid. The energy cost is increased due to either more power demand or more energy price for the said duration. Figure 7 presents the relation between hourly power demand from/to grid and energy cost for variable energy pricing. The total energy cost incurred two components, i.e., cost of power imbalance between load and renewable energy generation and cost for charging/discharging of battery. In Fig. 8, positive values represent the payable amount to the grid, and negative values show the earnings of the community by selling the power to the grid.

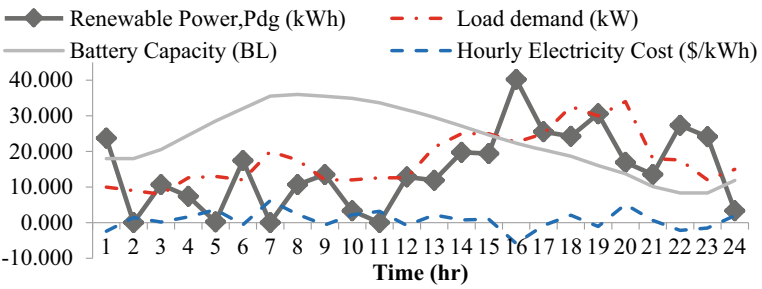

Fig. 6 Optimum energy cost with battery and renewable power generation

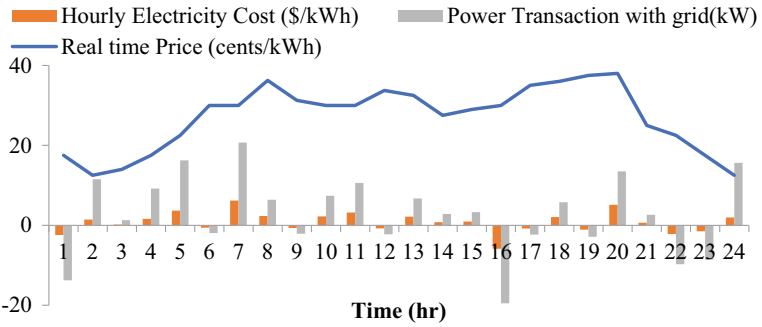

Fig. 7 Hourly power exchange and cost to community microgrid

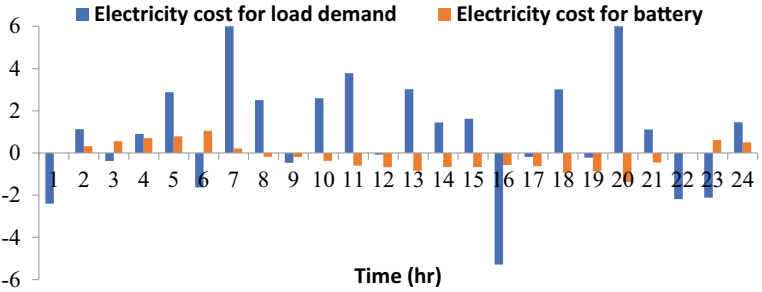

Fig. 8 Net cost for load power demand and battery charging/discharging

4 Conclusions

This paper presented battery energy management for a community microgrid. Community microgrid has been modeled using solar photovoltaic system and wind energy-based renewable energy sources including energy storage. Optimal energy management has been obtained in community microgrid with minimum charging and discharging cycles of energy storage system. It has been seen from obtained results that electricity costs of the community microgrid are reduced with proposed methodology. The result shows that whenever the electricity price is higher, battery discharge to complete load demand. It reduces the power borrowed from the utility grid. On the other hand, battery charges whenever the renewable generation is higher and sells power to the grid. The reason for reduction in electricity cost is less charging/discharging cycles which generate promising results.

References

1. Platt G, Berry A, Cornforth D (2012) What role for microgrids? (Chapter 8). In: Smart grid. Academic Press, Boston, pp 185–207
2. Mathur D, Kanwar N, Goyal SK (2020) Impact of electric vehicles on community microgrid. AIP Conf Proc 2294(1):040010
3. Xu B et al (2017) Factoring the cycle aging cost of batteries participating in electricity markets, vol 8950 no c, pp 1–12
4. Venayagamoorthy GK et al (2016) for a Smart Microgrid. IEEE Trans Neural Netw Learn Syst 27(8):1643–1656
5. Khooban MH, Niknam T, Shasadeghi M (2017) Load frequency control in microgrids based on a stochastic non-integer controller, vol. 3029, no. c, pp 1–9
6. Vetter J, Nov P, Wagner MR, Veit C (2005) Ageing mechanisms in lithium-ion batteries vol 147, pp 269–281
7. Hong Y, Beltran AA, Paglinawan AC (2018) A robust design of maximum power point tracking using Taguchi method for stand-alone PV system. Appl Energy 211(2017):50–63
8. Salameh ZM (1994) Optimum photovoltaic array size for a hybrid wind/PV system, vol 9, no 3, pp 482–488
9. Hossain A, Roy H, Squartini S, Zaman F, Muttaqi KM (2019) Energy management of community microgrids considering degradation cost of battery. J Energy Storage 22(September 2018):257–269
10. Fuselli D et al (2013) Electrical power and energy systems action dependent heuristic dynamic programming for home energy resource scheduling. Int J Electr Power Energy Syst 48:148–160
11. Steriotis K, Tsaousoglou G, Efthymiopoulos N, Makris P, Varvarigos EM (2018) A novel behavioral real time pricing scheme for the active energy consumers participation in emerging flexibility markets. Sustain Energy Grids Netw 16:14–27

First principle Investigation of the Electronic properties of $SrGe_{1-x}Sn_xP_2$

Aditi Gaur, Karina Khan, Amit Soni, Alpa Dashora, and Jagrati Sahariya

Abstract Solar cell forms an essential part of the renewable form of energy, and thus, several advancements in the field are being made to make it feasible, affordable and most importantly efficient. The new innovation is the intermediate band solar cells (IBSCs) which provide an efficiency around 60% which is just double the efficiency of single-junction ordinary solar cell. In this paper, we have presented the comparative electronic and structural analysis of $SrGeP_2$ and $SrGe_{0.5}Sn_{0.5}P_2$. The exchange correlation adopted for the investigation is Tran-Blaha modified Becke Johnson functional, and the bandgap calculated for $SrGeP_2$ and $SrGe_{0.5}Sn_{0.5}P_2$ is 0.20 eV and 0.9928 eV and 1.16 eV and 0.772 eV, respectively. The nature of bandgap is observed to be indirect. We have also made the observation that the incorporation of Sn in the sample has yielded an enhanced intermediate band formation providing low cost and efficient solution for solar cells. The sample thus has shown promising capabilities in the optoelectronic field as the intermediate band solar cells.

Keywords Absorption · Band structure · Chalcopyrite · Dielectric tensor · Intermediate bandgap solar cell · Optoelectronic

1 Introduction

The future of renewable energy is shaped by the existence of affordable, clean, reliable and scalable solution, i.e., solar cells aiding in the potential growth of energy requirement [1]. Within the power systems, the growth of solar photovoltaic technology can

A. Gaur · A. Soni (✉)
Department of Electrical Engineering, Manipal University Jaipur, Jaipur 303007, India
e-mail: amit.soni@jaipur.manipal.edu

K. Khan
Department of Physics, Manipal University Jaipur, Jaipur 303007, India

A. Dashora
Department of Physics, The M. S. University of Baroda, Vadodara 390002, India

J. Sahariya
Department of Physics, NIT Uttarakhand, Uttarakhand 246174, India

© The Author(s), under exclusive license to Springer Nature Singapore Pte Ltd. 2022

A. Tripathi et al. (eds.), *Intelligent Computing Techniques for Smart Energy Systems*,
Lecture Notes in Electrical Engineering 862,
https://doi.org/10.1007/978-981-19-0252-9_66

be seen since a decade in past. In 2014, several countries have seen considerable amount of progressive advancement along with renewable power sources development. The main advancement in the journey of photovoltaics is to focus on their efficiency. Among these photovoltaic sources of energy, i.e., conventional solar cells (monocrystalline), polycrystalline solar cells and thin film solar panels, the recent efficiency of monocrystalline that has been quoted is 22.4% in the practical research domain.

Intermediate bandgap solar cells (IBSCs) are the new advancement in solar cell category that offers high output voltage along with large photon generated current. Their working goes in a manner that the presence of partially filled energy band within the forbidden band gap of a semiconductor is responsible for its operation. In such materials, the transition is shown from valence band (VB) to intermediate band (IB) and then further from intermediate band to conduction band (CB). A single-gap solar cell in comparison to IB solar cells is not able to supply a greater voltage as compared to lowest photon energy absorbed. IB solar cells on the other hand offer to supply a high photo voltage by the absorbance of photons of two sub-bandgap thus producing an electron of high energy [2].

Chalcopyrite compounds are found to be the primary copper sulfide which exists as the most suitable copper mineral structurally in the form of tetragonal face centered lattice. Wide range of band gap energies has been found in the copper (Cu) chalcopyrites system [Cu(In, Ga, Al)(Se, S)$_2$] ranging from 1.04 eV [$CuInSe_2$] to 2.4 eV [$CuGaS_2$] and 2.7 eV [$CuAlS_2$], offering coverage to almost the major part of visible spectrum [3]. The direct nature of band gap in these compounds is the reason that all these compounds are suitable for photovoltaic thin film-based absorber materials and in other optoelectronic applications.

Ternary chalcopyrite compounds in recent years have found to be studied theoretically and practically. The studied cases are presented in following manner: in a work done by Gani et al. [4], first principle investigation based on electronic, structural, optical and elastic characteristics of Be-based ternary chalcopyrite compounds, i.e., BeX(=Si, Ge)P_2. The study was carried out in VASP computational model. In another work accomplished by Fahad et al. [5] the characteristically existing properties of BeA(=Si, Ge, Sn)Z(P, As) have been researched and studied based on the first principle density functional theory methodology. Ziani et al. [6] in their work have described the first principle-based investigation of $BeSiPn_2$ (Pn = P, As) based on their thermoelectric and electronic study which has been given. The material has thus been shown promising thermoelectric capabilities. In a research work [7] performed by Basalaev and Gordienko, Wannier functions and chemical bonding in the Be-based ternary chalcopyrites have been studied with the compound constituting of Be–X–P_2, where X = C, Si, Ge, Sn. Basalaev and Gordienko have studied many features of Be–X–P_2, (where X = C, Si, Ge, Sn) using Quantum Espresso based on DFT methodology [8]. In a research work accomplished by Xiao et al. [9], the first principles-based investigation of $MgYZ_2$ (where Y = Si, Ge, Sn and Z = P, As) is done. Among them, $MgGeP_2$ and $MgSiAs_2$ are found out to be possessing approximately larger band gaps and larger static SHG coefficients which are believed to be potentially good for mid-IR NLO application. In a work by Kocak and Ciftci [10], the

core understanding of electronic, structural, elastic and optical properties has been explored for the three Mg-based ternary chalcopyrite semiconductors, with the use of first-principles calculations density functional theory scheme. A combined work depicting novel properties of Ca/$SrSiP_2$ [11] chalcopyrites based on full potential linear augmented plane wave (FP-LAPW) methodology. The reported direct energy gap for both the compounds $CaSiP_2$ and $SrSiP_2$ is 0.97 eV and 0.22 eV, respectively. The optical properties of II–IV–V_2 (with II being occupied by Be, Mg, Zn, Cd; IV being occupied by Si, Ge, Sn and V being occupied by P, As) have been studied using VASP model depicting their applicability in field of optoelectronics [12].

In this research work, we have studied the effect of Sn atom on $SrGeP_2$ compound and studied its characterizing properties. The structural description and electronic analysis have been accomplished during the research. The presenting flow of this paper goes in following manner: Sect. 2 contains *Computational details,* Sect. 3 contains *Structural details,* Sect. 4 contains *Electronic details* and final section beholds the *Discussion* and *Conclusion.*

2 Computational Details

In this work, we have undertaken tetragonal structure of $SrGeP_2$ and then doped it with 'Sn' at 'Ge' site forming $SrGe_{0.5}Sn_{0.5}P_2$.This is done in order to observe effect of Sn on the electronic structure, investigated in the form of band structure and density of states (DOS). The investigation on the above mentioned sample is carried out in Wien2k model embodied on the framework of first principle linear augmented plane wave (FP-LAPW). The methodology followed is based on computational technique to get the basic detailing of a particular sample through input of appropriate parameters and the predefined code accordingly works in computing the properties of materials. Computational details followed in the investigation are space group, input lattice parameters ($a = b \neq c$; $\alpha = \beta = \gamma = 90°$), R_{MT}-K_{MAX}, l_{max}, G_{max} values, followed by number of k points which provide a better computational speed and accurate calculations of plots obtained. Space group provides an insight into the symmetry group in a 3D space. A more specific explanation of k points presents sampling points in the first Brillouin zone for the system. It represents a specific reciprocal space which lies close to the origin (0, 0, 0). The value of k points taken for $SrGeP_2$ is 1000 and for $SrGe_{0.5}Sn_{0.5}P_2$ is 500 with k-mesh being calculated as 10*10*10 and 9*9*5. The work of k-mesh is to sample first Brillouin zone, and the latter part is inversely proportional to unit cell's size. The radius of muffin tin (RMT) sphere dimensions for each element has been set as Sr = 2.5, Ge = 2.5, P = 2.11 and Sn = 2.5; according to these values, the code utilizes the spherical harmonics and they must not touch. A larger unit cell in one direction corresponds to a Brillouin zone with narrow edge and vice-versa [13]. The resultant depicts that lesser k points are required for a narrow edge of the Brillouin zone compared to a longer edge regarding same sampling density.

$R_{mt}*K_{max}$ value of a system accounts as a strong indicator of quality for a particular element's basis set. The value of $R_{mt}*K_{max}$ can be left unchanged for most of the times in case supercell or modified structure. The $R_{mt}*K_{max}$ for $SrGeP_2$ is 8 and for $SrGe_{0.5}Sn_{0.5}P_2$ is also kept as 8. The value of l_{max} and G_{max} remains same for both the systems, i.e., 10 and 12.

Kohn–Sham density functional scheme's exchange correlation potential is the difference between potential of Fermi (the one appearing in 1 electron Schrodinger equation's square root of electron density) and the Pauli potential [20], given as:

$$\nu_{XC}(z) = \nu_F(z) - \nu_P(z) \tag{1}$$

The exchange correlation used for our theoretical investigation is Tran-Blaha modified Becke Johnson (TB-mBJ). TB-mBJ is reported to offer highly exact value of bandgaps suitably for semiconductors and also insulators [14]. It functions for both classical sp-type semiconductors and strongly interrelated transition metal (TM) samples. TB-mBJ works efficiently in offering distinctly accurate band structure of particular samples along with electron density and magnetic moment. This potential provides cheaper and much better quantitative predictive power in comparison to expensive methodologies. It is believed to offer almost closely relative bandgaps for theoretical investigations and the experimental values.

3 Structural Details

The structural details of our investigation involve the parameters like originating space group, structure formation and the alterations that occur due to the insertion of impurity element in the system. Our system chosen for the study is $SrGeP_2$, which is believed to be a novel discovery in terms of chalcopyrite material existing in tetragonal form. The tetragonal structure exists in the form of 122-I42d space group. In the pure system, the elements are arranged in a cuboidal-shaped cell with top and bottom layers containing the Sr (Strontium) atoms in all respective corners. Sr atoms share a single bonded connection with P (Phosphorous) atoms and the Ge (Germanium) atoms are placed in the interspatial zones and center of top and bottom layers. With 50% doping of Sn at Ge site in the unit cell, we get a #3 numbered P2 space group, i.e., primitive monoclinic and only 4 Sr atoms forming single bond with P, 2 gray-colored Sn (Tin) atoms can be seen on two of the lateral faces. So basically, we can see the deduction in number of Sr, Ge and P atoms after in the transition of tetragonal to monoclinic structure. These depictions can be observed in Fig. 1a, b.

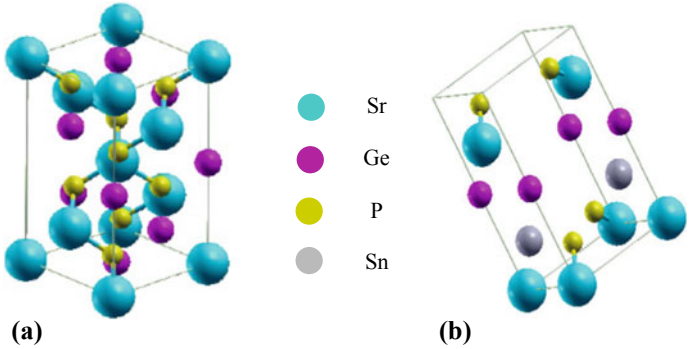

Fig. 1 **a** $SrGeP_2$ tetragonal-based structure (#122, I42d); **b** $SrGe_{0.5}Sn_{0.5}P_2$ primitive monoclinic-based structure (#3, P2)

4 Electronic Details

The electronic details of our pure and doped system are explained through band structure and density of states plot. The band structure of a sample is the diagrammatic approach to describe the nature of a sample whether it is metallic, semiconductor or insulator. This is accomplished through the measure of bandgap and their type whether direct or indirect in nature. So basically, band structure is the depiction of different energy levels of the electrons present within it. These help in creating the image of quantum mechanical wave functions of electrons present in the periodic lattice structure of an atom [15]. Such conceptual basis helps in the formation of band theory which in turn provides an in depth knowledge of the solid's physical properties such as resistivity, optical absorption and dielectric tensor.

We have doped $SrGeP_2$ with 50% of Sn at Ge site; this doping has caused a unique feature of intermediate band solar cells. The residual energy ranges which are not occupied by any bands are termed as bandgaps. The calculated band gaps formed for $SrGeP_2$ are at 0.20 and 0.9928 eV and for $SrGe_{0.5}Sn_{0.5}P_2$, bandgaps with slight increment have formed at 1.16 and 0.772 eV. By introducing Sn in the system $SrGeP_2$, the effect of intermediate bands can be observed. Figure 2a, b depicts the formation of intermediate bands in both pure and doped $SrGeP_2$.

The nature of bandgap is indirect for pure and doped both the systems as depicted. So, the minimum energy difference between the valence and conduction band is present at two different momentum points. Here in both pure and doped compounds, the transition has taken place from valence band (VB) to intermediate band (IB) and then from IB to conduction band (CB). For a basic briefing, the transition can be explained in following manner: with peak A at −0.01 eV, peak B at 0.01 eV and peak C at 2.00 eV for Fig. 3a and with peak A at −0.02 eV, peak B at 0.05 eV, peak C 1.99 eV and peak D 3.00 eV for Fig. 3b. In Fig. 3b, we can also observe the amount of bands near Fermi energy has increased in doped compound in comparison to the pure $SrGeP_2$ which has got one band near Fermi. Thus, we can also observe

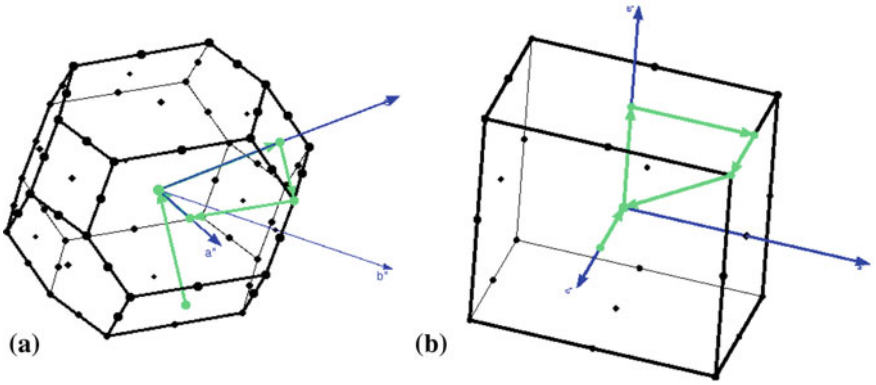

Fig. 2 **a** Brillouin zone for $SrGeP_2$; **b** Brillouin zone for $SrGe_{0.5}Sn_{0.5}P_2$

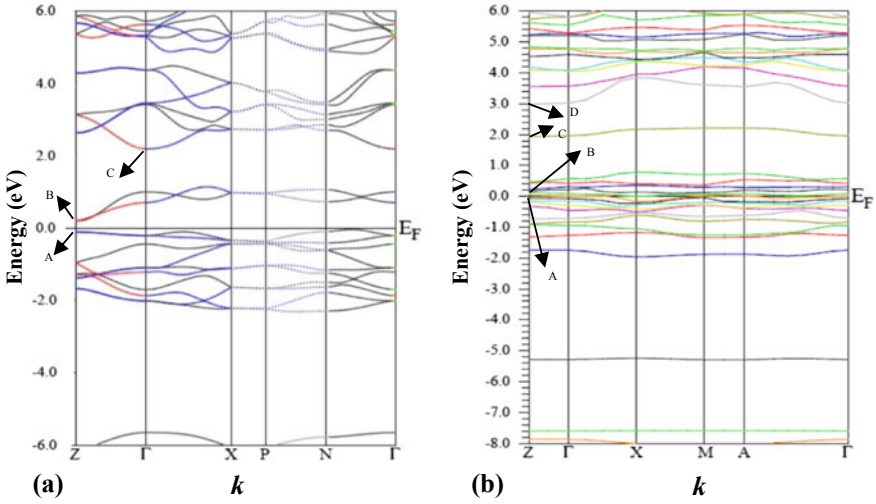

Fig. 3 **a** Band structure depiction for $SrGeP_2$; **b** Band structure depiction for $SrGe_{0.5}Sn_{0.5}P_2$

the plot between Energy axis and high symmetrical Brillouin points termed as *k*. For the tetragonal structure the *k* points are Z, Γ, X, P, N, Γ and after doping they got changed into Z, Γ, X, M, A, Γ.

The density of states (DOS) calculated in Wien2k is a representation of bands of energy at different levels arising from the atomic orbitals. It is built by the calculations undertaken in DFT. It is also basically an insight into the electronic structure of a sample. It is believed to be an essential factor in condensed matter physics, defining properties of the system [16]. DOS is an interpretation of the actual transition probability of number of states present in initial and final energies. Unlike band structure which provides only the information of bands at high symmetrical directions, DOS

provides the information across the entire Brillouin zone. The band plot and DOS plot are correlated to each other explaining the energy gap and different orbital effect with respect to the bands at different k points.

In Fig. 4a, density of states for $SrGeP_2$ is depicted which describes the major contributions through a particular atomic orbital. It means for $SrGeP_2$, the major contributions are shown by 5*s* in case of Sr; 4*p* in case of Ge and 3*p* in case of P. On further introducing Sn in $SrGeP_2$, the major contribution is observed by 5*p* orbitals. Figure 4b represents the DOS of $SrGe_{0.5}Sn_{0.5}P_2$ with each atom showcasing its atomic orbitals.

The bandgap values of other chalcopyrite compounds have been shown in Table 1 with the comparison to the existing compound $SrGeP_2$ and $SrGe_{0.5}Sn_{0.5}P_2$.

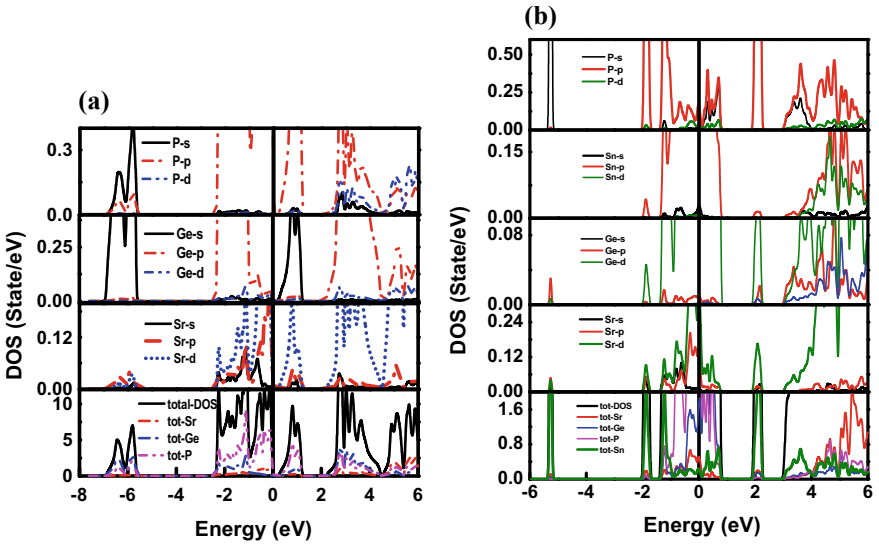

Fig. 4 **a** DOS plot for $SrGeP_2$; **b** DOS plot for $SrGe_{0.5}Sn_{0.5}P_2$

Table 1 Energy gap values for different chalcopyrite compounds

Compound name	Energy gap (eV)
$MgGeP_2$ (reported)	2.15 [17]
$MgGeN_2$ (reported)	3.43 [18]
$SrGeN_2$ (reported)	3.82 [19]
P doped $SrGeN_2$ (reported)	2.71 [19]
$SrGeP_2$ (present work)	0.20 and 0.9928
Sn doped $SrGeP_2$ (present work)	1.16 and 0.772

5 Discussion and Conclusion

In the concluding part of our investigation, we would highlight the effect of doping that has caused intermediate band solar cells (IBSCs). The IBSCs own a unique feature of enhancing the efficiency of solar cells by offering large amount of photo-generated current meanwhile maintaining high output voltage. By doping a small amount of Sn into the unit cell of $SrGeP_2$, we introduced the IB feature in a solar cell. The TB-mBJ exchange correlation functional has been adopted to perform our theoretical calculations. We have compared the band gap results through band structure and DOS and have observed enhanced intermediate bandgap effect in our system. Also, there has been a shift in the Fermi energy of the compound toward the valence band after doping since it is a p-type material. Larger doping quantity of Sn might introduce larger density states at Fermi energy. The nature of bandgap determined from the band structure plot is characterized as indirect energy gap. More such impurities can be investigated to see its positive or negative effect on the intermediate bandgap. The electronic analysis of $SrGeP_2$ and $SrGe_{0.5}Sn_{0.5}P_2$ showcases the suitability of this compound in optoelectronic applications. Also, we can quote with our research that II-A group-based compounds show bandgap more nearer to the solar cell eligibility as it goes down the group from Mg toward Sr.

Acknowledgements This theoretical investigation has been supported by the DST-SERB Project under grant number EMR/2017/005534. We express our gratitude to Prof. P. Blaha for giving us the useful DFT tool Wien2k. Also, we would like to express our heartfelt gratitude to Manipal University Jaipur for providing us with useful and necessary resources to complete plenty such theoretical investigations.

References

1. Gul M, Kotak Y, Muneer T (2016) Review on recent trend of solar photovoltaic technology. Energy Explor Exploit 34:485–526. https://doi.org/10.1177/0144598716650552
2. Luque A, Martí A, Stanley C (2012) Understanding intermediate-band solar cells. Nature Photon 6:146–152. https://doi.org/10.1038/nphoton.2012.1
3. Rau U, Schock HW (2012) Cu(In,Ga)Se2 thin-film solar cells. In: Practical handbook of photovoltaics fundamentals and applications, 2nd edn, pp 323–371. https://doi.org/10.1016/B978-0-12-385934-1.00010-6
4. Gani A et al (2020) Mechanical stability and optoelectronic behavior of BeXP2 (X=Si and Ge) chalcopyrite. Chin J Phys Taipei 64:1–21
5. Fahad S, Murtaza G, Ouahrani T et al (2015) Structural, elastic, electronic, bonding, and optical properties of BeAZ2 (A= Si, Ge, Sn; Z= P, As) chalcopyrites. J Alloys Compd 1–36
6. Ziani NS, Seddik T, Abdelkader B et al (2019) First principles investigations of electronic and thermoelectric properties of BeSiPn2 (Pn = P, As) chalcopyrite compounds. Solid State Commun 302:1–8 (2019)
7. Basalaev Y, Gordienko AB (2021) Wannier functions and chemical bonding in compounds Be–Iv–P2 (Iv = C, Si, Ge, Sn) with chalcopyrite structure. J Struct Chem 62:817–823
8. Basalaev Y, Gordienko A (2020) B: electron structure of Be–IV–P2 crystals with a chalcopyrite lattice. Phys Solid State 62:2016–2023

9. Xiao J, Zhu S, Zhao B et al (2018) Computational assessment of promising mid-infrared nonlinear optical materials Mg–IV–V2 (IV = Si, Ge, Sn; V = P, As): a first-principles study. Mater Res Exp 5:035907
10. Kocak B, Ciftci YO (2016) Determination of the basic physical properties of semiconductor chalcopyrite type $MgSnT_2$ (T = P, As, Sb) from first-principles calculations. J Mater Res 31:1518–1531
11. Tahirunnisa SR, Banu IB (2018) Optical properties of novel ASiP2 (A=Ca, Sr) chalcopyrites: first principle study. Appl Phys A 124:1–7
12. Shaposhnikov VL, Krivosheeva AV, Borisenko VE (2012) Ab initio modeling of the structural, electronic, and optical properties of $A^{II}B^{IV}C^{V}{}_2$ semiconductors. Phys Rev B 85:205201
13. Cottenier S (2002)–(2013) Density functional theory and the family of (L)APW-methods: a step-by-step introduction, 2nd edn. ISBN 978-90-807215-1-7. Freely available at http://www.wien2k.at/reg%20user/textbooks
14. Koller D, Tran F, Blaha P (2011) Merits and limits of the modified Becke-Johnson exchange potential. Phys Rev B 83:195134. https://doi.org/10.1103/PhysRevB.83.195134
15. Ashcroft N, Mermin ND, Band structure of selected metals, solid state physics, pp 283–310. ISBN 0-03-083993-9
16. Yeo BC, Kim D, Kim C, Han SS (2019) Pattern learning electron density of states. Sci Rep 9. https://www.nature.com/articles/s41598-019-42277-9
17. Kocak B, Ciftci Y (2016) Ab-initio calculations of semiconductor MgGeP2 and MgGeAs2. Mater Res Bull 77
18. Rasander M et al (2017) Structure and lattice dynamics of the wide band gap semiconductors MgSiN2 and MgGeN2. J Appl Phys 122:085705
19. Gaur A et al (2021) The optoelectronic property analysis of P doped SrGeN2: a first principle calculation for solar cell compound. J Phys Conf Ser 1849:012025
20. Staroverov VN, Ospadov E (2019) State of the art of molecular electronic structure computations: correlation methods, Basis Sets More Adv Quantum Chem 79:201–219. https://doi.org/10.1016/bs.aiq.2019.04.002

Setting up Local Private Smart Grids with Data Collection Sensors for Scientific Experiments using MQTT and Node-Red

Mohammed Almshari, Adil O. Khadidos, Georgios Tsaramirsis, Fazal Qudus Khan, Alaa Khadidos, Iordanis K. Giannopoulos, Assimakis K. Leros, Dimitris Piromalis, and Mahipal Bukya

Abstract Smart grids are popular areas of research as they are an essential component of smart cities, smart homes, IoT, and other popular research areas. Scientific experiments in smart grids may be conducted by researchers who may have limited experience in the field or limited budget or come from different disciplines. This paper is aimed for such a research audience as it demonstrates in some detail and with simple steps, how a small size private smart grid can be installed using low cost, widely available hardware and software. The paper proposes the use of Sonoff POW 2 smart switches, with either windows PC or single board computers such as Raspberry Pi to host the MQTT servers and Node-Red, offering a simple, low-cost but yet effective solution for conducting scientific experiments.

Keywords Smart grid · Local smart grid · Power consumption · IoT · Smart home · Smart plugs · Raspberry Pi · Sonoff POW 2 · MQTT · Node-Red

M. Almshari (✉) · A. O. Khadidos · F. Q. Khan
Department of Information Technology, Faculty of Computing and IT, King Abdulaziz University, Jeddah, Saudi Arabia
e-mail: malmshari0002@stu.kau.edu.sa

G. Tsaramirsis
Abu Dhabi Women's Campus, Higher Colleges of Technology, Abu Dhabi, UAE

A. Khadidos
Department of Information Systems, Faculty of Computing and IT, King Abdulaziz University, Jeddah, Saudi Arabia

I. K. Giannopoulos · A. K. Leros
Department of Information and Communication Systems Engineering, University of Aegean, Samos, Greece

D. Piromalis
Department of Electrical and Electronic Engineering, University of West Attica, Athens, Greece

M. Bukya
Department of Electrical Engineering, Manipal University Jaipur, Jaipur, India

© The Author(s), under exclusive license to Springer Nature Singapore Pte Ltd. 2022

A. Tripathi et al. (eds.), *Intelligent Computing Techniques for Smart Energy Systems*, Lecture Notes in Electrical Engineering 862,
https://doi.org/10.1007/978-981-19-0252-9_67

1 Introduction

Smart grid is an interconnected electricity network capable of advanced monitoring and control of individual nodes and segments. It consists of sensors that include smart meters and possibly, wireless communication, and even artificial intelligence and provides constant feedback with consumption information such as power consumption, peak usage, etc., to the control center [1]. Smart grids are a main component of smart cities as they enable reliable and optimized power supply to the various buildings [2], with the potential of maximizing the profits and increasing customer's satisfaction [3]. Smart grids support algorithms for detecting and responding to the voltage issues within a smart grid [4]. They can use optimization techniques such as load balancing, rules, and regulations for optimization [5] and even save the extra power to batteries so it can be used in case of a power shortage [6].

At a local level such as a smart house, the smart grid connects various electricity consumption devices via smart plugs, enabling advanced electricity metering, monitoring, and management. Smart grid sensors, such as smart plugs, allow us to measure the power consumption of the electric devices connected to them, almost in real time. This leads to a number of benefits such as information about the actual power consumption of individual devices and hence cost of usage calculation, identification of electricity theft, and other monitoring-related advantages. Power outages in homes can be prevented by applying smart grids meters that know the maximum threshold enabling prediction and generating cautions to the home users in case of overload [7]. Additionally, smart plugs give the ability to control the connected devices by switching them ON and OFF. This can be manually, or based on a time schedule or even automatically from a computer, based on some computational logic (e.g., if no more employees are in the building, switch OFF all lights). Utilizing and managing the devices at the smart home can reduce the monthly costs, for example, cleaning machines, water heating, air conditioners, kitchen devices, home lights, and all devices that can be totally managed by the smart plugs [8]. Smart plugs can also be controlled remotely via the Internet, which gives great flexibility, but it also introduces some security threads. However, standard security, such as authentication and authorization, data integrity on the connections, and cryptography, is applied protecting these devices from unauthorized access and other possible attacks [9–15].

Smart grids and local area smart grids are an ongoing area of research. However, having access to a smart grid may not be possible for many researchers. On the other hand, simulations may not be capable of realistically simulating some scenarios. This work demonstrates, step by step, how to set up a low-cost, highly accurate, and low latency feedback (1s) local smart grid.

The proposed approach is using the low-cost smart switches sensors, with the option to connect them to other sensors in a tree-like structure. However, the total power (W), current (I), and voltage (V) of the children nodes must not exceed the maximum capacity of the parent node. All of these sensors are connected via a local Wi-Fi to a local or Internet-based Message Queue Telemetry Transport (MQTT) server. The users can monitor and control the sensors via the MQTT server.

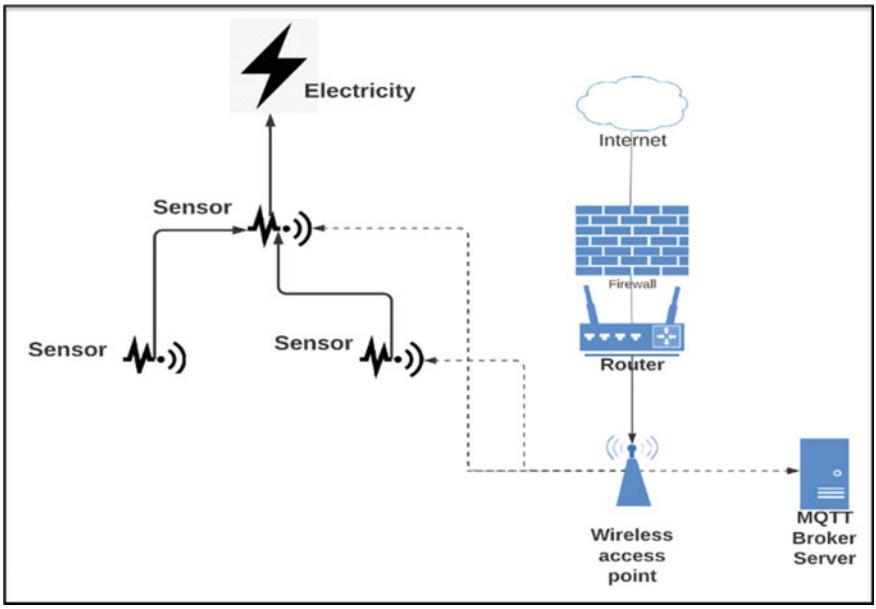

Fig. 1 Architecture of the proposed solution

Researchers can install required custom software applications to the MQTT server host. Figure 1 shows an overview of the proposed approach.

While there various smart switch sensors, in the proposed approach, we used the Sonoff POW R2. A Raspberry Pi 4, which is used as the MQTT server. In this paper, we show how to set up the various devices (e.g., flash the Sonoff sensors) as well as how to set up the smart grid.

This paper is structured as follows: Sect. 2 describes the related work. Section 3 explains the installation of the MQTT server and Node-Red. Section 4 explains how to set up the smart switches. Section 5 explains the setting up of Node-Red. Section 6 summarizes this work and provides direction for future research.

2 Related Work

This section discusses the state of the art in smart grid data collection. Researchers in [16] used a private local small size smart grid for collecting power consumption data of desktop computers in order to determine if they have been infected by a virus or not. They used Sonoff POW 2 sensors connected to a Raspberry Pi that was hosting an MQTT server. Node-Red was used to develop the monitoring and control application. While relevant to this work, it was not clear how the proposed approach could have been generalized to include different types of experiments as

it was focused on information security. Bazenkov et al. [17] proposed a method for incentive power consumption data collection from smart grid sensors using smart meters connected via low-power wide area network (LoRa) to MQTT server. Their proposal was capable of visualizing the power consumption data in 2D and 3D. The main difference with the current proposal is that this proposal focuses more on local private smart grids at a smaller scale. Jui-sheng and Ngoc-Tri in [18] proposed a system for analyzing the power consumption of the home buildings. In their work, they installed a local smart grid in a residential house. Their data were acquired from smart meters connected to the local Wi-Fi that were reporting to an Internet-based database. While they provided some information for how the local smart grid was set up, their work mainly focused on the analysis of the data for power purposes. Aparna and Sudeep in [19] proposed a model for smart grid within the context of smart cities and discussed the future of secure smart grid. They included a case study that included secure data collection, but it was described at a high level. A secure data collection scheme has been presented by Croce et al. [20]. They set up a peer-to-peer network and collected power consumption data from multiple connected buildings. Their work focused mainly on consumer's privacy. Kumar et al. in [21] tested the security of smart power consumption meters via two experiments. His work includes data collection, but they presented little information for how their experiments were conducted and did not include sufficient information for how they can be duplicated. Uludag et al. [22] proposed a protocol for data collection from the smart grid power consumption sensors. They utilized secure communication over the Internet and cloud technologies for storing the collected data. Their work focused on the communication protocols and not the actual smart grid.

The differences between the state of the art of this work are summarized in Table 1.

Table 1 Comparison with similar work

Paper reference number	Area	Detailed smart grid setup	Detailed explanation of data collection process	MQTT/server location	Data collection rate	Private use?	Dataset?
16	Very small	No	No	Local	1 s	Yes	Yes
17	Large/public	No	No	Remote	NA	No	Yes
20	Large/public	No	No	Local	No	No	Yes
21	Local/small	No	No	Local	No	No	No
19	Medium	No	No	Remote	1 s	Yes	Yes
18	Local/small	No	No	Remote	No	Yes	No
22	Large/public	No	No	Remote	No	Yes	No
This paper	Local small/very small	Yes	Yes	Local/remote	1 s/variable (±)	Yes	No

As it can be seen from Table 1, the proposed approach is not only the only one that details how to set up a local private smart grid but also it allows variable data collection rate of even less than 1s. In the proposed approach, the MQTT can be local or in a remote location. Finally, the proposed approach is the only one that supports a small or very small grid network. Very small grids can be ideal for some small-scale scientific experiments as they offer a controlled environment that is less prone to unexpected errors and anomalies.

3 Installing the MQTT Server and Node-Red

The MQTT protocol was developed by IBM in the 1990s, and it was used for the sensors of the satellites at that time. MQTT is a lightweight protocol with low latency for securely exchanging encrypted communication messages, it is considered as the standard for IoT communication [23], and this is why it was adopted in this proposal. The MQTT broker server will be responsible for monitor and control of the smart switches, and hence, all of them must have a direct connection with the MQTT server. Depending on the nature of the target experiment, the MQTT server can be installed in different ways and devices. This proposal gives a number of options for hosting the MQTT broker server. It can be installed on a physical or virtual PC or a single board computer such as Raspberry Pi.

3.1 Installing on a PC

Installation of MQTT broker on a local computer is possible by downloading the Mosquitto MQTT broker from [12] a Mosquitto MQTT broker executable installation file. After the installation is complete, Open Command prompt as administrator and type “mosquitto install” command to complete the installation. Once the setup is complete, you can run the mosquitto MQTT broker by typing the command “net start mosquitto”.

As an alternative, the MQTT can be installed on a virtual machine such as Microsoft Azure virtual machine [24] or other alternatives. Once the virtual machine is installed, download the Mosquitto MQTT broker in the virtual machine and follow the process described above.

3.2 Installing on a Single Board Computer

There are multiple single board computers widely available in the market. Raspberry Pi is one of the most popular single board computers that support Mosquitto MQTT server. Using a Raspberry Pi as a MQTT broker server is a popular option due to its

low-cost, small size and low-energy consumption attributes. The Mosquitto MQTT broker server can be installed using the commands below:

```
> apt-get install mosquito.
```

```
> apt-key add mosquitto-repo.gpg.key
```

```
> apt-get update
```

```
> apt-get install mosquitto-clients
```

The next step is to install an application called Node-Red that will enable the direct connection between the smart switches (e.g., SONOFF POW R2) and the MQTT server.

3.3 Installing Node-Red

Node-Red is an IBM product and popular visual programming tool, used for IoT application development [25]. The Node-Red application will be responsible for interfacing with the smart switches for monitor and control purposes. The Node-Red application will also be responsible for storing the data to a database or cloud or a local file. Similar to Mosquitto MQTT server, Node-Red can be installed on a desktop (see Sect. 3.3.1) or a single board computer (see Sect. 3.3.2). In order to simplify the process, we propose the installation of Node-Red in the same computer with the Mosquitto MQTT server.

3.3.1 Installing Node-Red on a Windows PC

Node-Red can be installed on a windows PC by following the steps below:

1. Install the packages of Node.js in your computer from the official Node.js Web site [25].
2. Open Command prompt and install Node-Red by executing the following:

```
> npm install -g –unsafe-perm Node-RED.
```

3. Once the Node-Red has been installed, open it by executing the following command in command prompt:

```
>Node-red
```

4. Once the Node-Red is running, start using it by opening the browser.

```
>http://localhost:1880.
```

3.3.2 Installing Node-Red on a Single Board Computer

Node-Red can be installed on a single board computer, as an alternative to installing it to a desktop by following the steps below.

Simply running the following command in the terminal will download the packages and run the scripts:

```
> bash < (curl -sL https://raw.githubusercontent.com/node-red/linux-installers/master/deb/update nodejs-and-nodered).
```

The script will do the following:

(1) Remove all old versions of Node-Red if they exist.
(2) Install the latest version of Node.js.
(3) Download and install the latest version of Node-Red.
(4) Installation of packages that are optional and can be used for supporting extra functions of Node-Red.

Upon completion of the installation of the MQTT server and Node-Red, the researchers must set up the smart switches prior to connecting them with the rest of the smart grid.

4 Setting up the Smart Switches

There are multiple options for smart switches for monitor and control. They vary in terms of cost, size, durability, operating environment, power output, data reporting, and response time. All of the above should be considered before selecting the best smart switch for the target experiment. If, for example, the experiment is underwater or in very high/low temperatures, then an appropriate device must be selected.

4.1 Wiring the Sonoff Smart Switches

In our example, we focus on a very small smart grid, e.g., in a room with small temperature variations and low-energy consumption requirements: voltage range: 90–50 V AC, max current: 16A, and max power 3500 W. For this, we used the Sonoff Pow R2 smart switches because they fit this operational profile at a very low cost or less than 15 USD. Figure 2 shows the selected smart power switch.

Table 2 shows the mapping for each pin.

As it can be seen from Fig. 2 and Table 2, starting from left to right, the first slot and the fifth or sixth are used for supplying power to the device that will be controlled. Please note that in AC, there is no + or -. Ideally, one of the grounds (slot 2, slot 3) should also be connected to the device to be controlled. The fourth slot and either fifth or sixth slot, together with one of the grounds, should be connected to the corresponding slots of the power supply.

4.2 Flashing the SONOFF Firmware with Espurna

In order to use the Sonoff smart switch with the MQTT technology the default firmware of the SONOFF sensor must change to Espurna. The Espurna firmware has the following capabilities:

- Controlling Wi-Fi settings and ability to switch to access point mode.
- Ability to change the function of the SONOFF button and choose any action you need when you click the button.
- Enable Message Queuing Telemetry Transport (MQTT) standard for messages transfer between the devices.
- Make a schedule for sensor operation

Fig. 2 Sonoff POW 2 smart switch

Table 2 USB-TTL cable mapping with SONOFF Pow R2

Wiring between USB-TTL and SONOFF	
USB-TTL	SONOFF Pow R2
GND	GND
VCC	VDD
TXD	ERX
RXD	ETX

- Integration with many cloud services.
- Espurna can support many sensors similar to SONOFF Pow R2.

The following requirements must be met before flashing a sensor with Espurna.

- SONOFF POW R2 sensor
- USB to TTL cable (FT232)
- Esp tool
- Electric plug and socket.

The sensors can be flashed by following the steps below:

(1) Make sure electricity is disconnected from the SONOFF sensor.
(2) Connect the USB to the computer.
(3) Convert SONOFF to flash mode by disconnecting the USB, then connect again and keep pressing the button for 2–4 s.
(4) Download latest espurna firmware based on your sensor model, from [26].
(5) Extract the firmware package to a folder in your computer.
(6) Open Command prompt (CMD).
(7) Type the following command, change the values to your COM port number and Espurna version:

```
> (esptool.exe -vv -cd nodemcu -cb 11,500 -cp COMx -ca oxooooo -cf espurna -x.x.x-ithead-sonoff-powr2)
```

Then you will notice the executable file will start the firmware update. The LED will blink, and the new Wi-Fi access point name of the sensor will be changed to "Espurna".

(8) Connect to the new Espurna Wi-Fi network.
(9) Open your Web browser and type the below address to access the sensor page: 192.168.4.1.

The default login information including username and password will be mentioned in the above link which is by default "admin".

(10) Set up your MQTT addresses to match the MQTT broker server settings.

Once the new firmware has been installed to the sensors, the researchers can use Node-Red for their custom experiments.

5 Setting up Node-Red

To start using the Node-Red, the following steps must be followed:

(1) Open terminal
(2) If Node-Red is installed on a Raspberry Pi, start the service by typing

```
>Node-RED-start
```

If Node-Red is installed on a Windows PC, start the service by typing

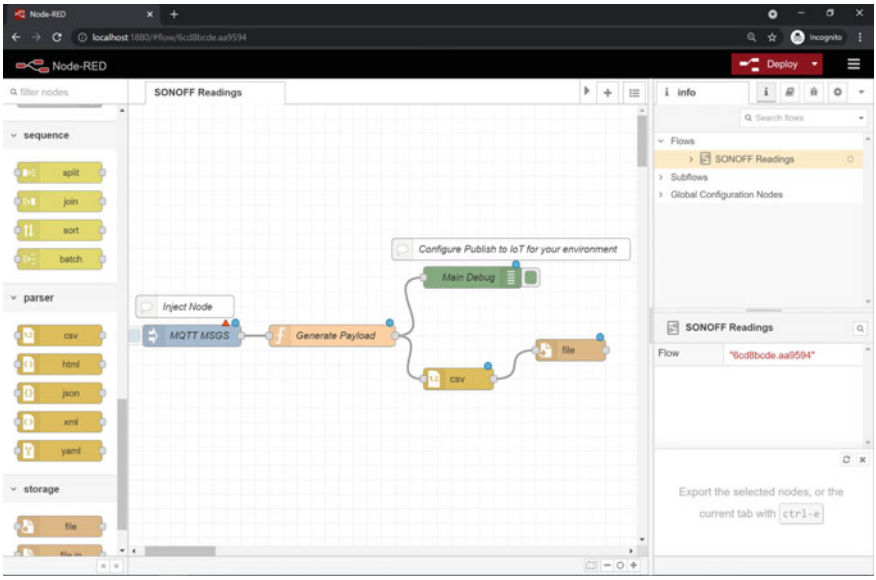

Fig. 3 Node-red

>Node-RED

Please note the Node-Red will run as a background process.

(3) To open the Node-Red editor to add the ports and setup the MQTT settings.
(4) Open the browser and type the following URL: http://localhost:1880.

The Node-Red editor can be seen in Fig. 3.

Here the users can choose MQTT inputs and add output files for the datasets and other control functions. The menu on the left side contains all the nodes needed for the connectivity. The input node must be selected to take the readings from sensors through the MQTT broker. All the readings can be stored in popular formats such as CSV format by using the CSV node, file output, and the target path. Once data collection is completed, the files from each sensor will be located in the selected folders. Node-Red is a powerful, simple-to-use tool that in conjunction with the proposed setup can accommodate most types of experiments.

6 Conclusion

In this paper, we have explained step-by-step process for setting up a smart grid with data collection capabilities. In this work, we proposed the use of Windows PC or

Raspberry Pi single board computers for installing the MQTT broker server as well as the Node-Red service and editor for designing and executing custom experiments. The Sonoff Pow 2 smart switches were used as example smart switches. The smart switches wiring and flashing processes were also explained. The main limitation of this paper is that due to space limitation, it only detailed the use of Sonoff devices, which is a good but not the only option. Future work can include more sensors and setups as well as few case studies.

References

1. Huh J-H, Otgonchimeg S, Seo K (2016) Advanced metering infrastructure design and test bed experiment using intelligent agents: focusing on the PLC network base technology for smart grid system. J Supercomput 72(5):1862–1877
2. La QD, Chan YWE, Soong B-H (2016) Power management of intelligent buildings facilitated by smart grid: a market approach. IEEE Trans Smart Grid 7(3):1389–1400
3. Maharjan S, Zhu Q, Zhang Y, Gjessing S, Basar T (2016) Demand response management in the smart grid in a large population regime. IEEE Trans Smart Grid 7(1):189–199
4. Yen SW, Morris S, Ezra MA, Huat TJ (2019) Effect of smart meter data collection frequency in an early detection of shorter-duration voltage anomalies in smart grids. Int J Electr Power Energy Syst 109:1–8
5. Fan D, Ren Y, Feng Q, Liu Y, Wang Z, Lin J (2021) Restoration of smart grids: current status, challenges, and opportunities. Renew Sustain Energy Rev 143:110909. https://doi.org/10.1016/j.rser.2021
6. Zame KK, Brehm CA, Nitica AT, Richard CL, Schweitzer GD III (2018) Smart grid and energy storage: policy recommendations. Renew Sustain Energy Rev 82:1646–1654
7. Bayindir R, Colak I, Fulli G, Demirtas K (2016) Smart grid technologies and applications. Renew Sustain Energy Rev 66:499–516. https://doi.org/10.1016/j.rser.2016
8. Ustun TS, Hussain SS (2019) A review of cybersecurity issues in smartgrid communication networks. In: 2019 international conference on power electronics, control and automation (ICPECA), New Delhi, India, Nov 2019
9. Alamaniotis M, Bourbakis N, Tsoukalas LH (2019) Enhancing privacy of electricity consumption in smart cities through morphing of anticipated demand pattern utilizing self-elasticity and genetic algorithms. Sustain Cities Soc 46:101426
10. Talaat M, Alsayyari AS, Alblawi A, Hatata AY (2020) Hybrid-cloud-based data processing for power system monitoring in smart grids. Sustain Cities Soc 55:102049
11. Marinakis V, Karakosta C, Doukas H, Androulaki S, Psarras J (2013) A building automation and control tool for remote and real time monitoring of energy consumption. Sustain Cities Soc 6:11–15
12. MQTT, IBM Developer. https://developer.ibm.com/components/mqtt/. Accessed 13 Mar 2021
13. Kumar N, Mishra VM, Kumar A (2020) Smart grid security with AES hardware chip. Int J Inf Technol 12(1):49–55
14. Das L, Munikoti S, Natarajan B, Srinivasan B (2020) Measuring smart grid resilience: Methods, challenges and opportunities. Renew Sustain Energy Rev 130:109918. https://doi.org/10.1016/j.rser.2020
15. Giannopoulos IK, Leros AK, Leros AP, Tsaramirsis G, Alassafi MO (2021) Real-time adaptive stochastic control of smart grid data traffic for security purposes. In: Sustainable cities and society, vol 63. Elsevier
16. Almshari M, Tsaramirsis G, Khadidos AO, Buhari SM, Khan FQ, Khadidos AO (2020) Detection of potentially compromised computer nodes and clusters connected on a smart grid, using power consumption data. Sensors 20(18):5075

17. Bazenkov NI et al (2019) Intensive data collection system for smart grid and smart building research. In: 2019 1st international conference on control systems, mathematical modelling, automation and energy efficiency (SUMMA), Lipetsk, Russia
18. Chou J-S, Ngo N-T (2016) Smart grid data analytics framework for increasing energy savings in residential buildings. Autom Constr 72:247–257
19. Kumari A, Tanwar S (2020) Secure data analytics for smart grid systems in a sustainable smart city: challenges, solutions, and future directions. Sustain Comput Inform Syst 28:100427
20. Croce D, Giuliano F, Tinnirello I, Giarré L (2020) Privacy-preserving overgrid: secure data collection for the smart grid. Sensors 20(8):2249
21. Kumar S, Kumar H, Gunnam GR (2019) Security integrity of data collection from smart electric meter under a cyber attack. In: 2019 2nd international conference on data intelligence and security (ICDIS), South Padre Island, TX, USA
22. Uludag S, Lui K-S, Ren W, Nahrstedt K (2016) Secure and scalable data collection with time minimization in the smart grid. IEEE Trans Smart Grid 7(1):43–54
23. Saha K et al (2018) A low cost remote controlled underwater rover using rasp- berry Pi. In: 2018 IEEE 8th annual computing and communication workshop and conference (CCWC), Las Vegas, NV, 2018, pp 769–772
24. Microsoft Azure. https://azure.microsoft.com/en-us/. Accessed 31 July 2021
25. Node-RED. https://nodered.org. Accessed 13 Mar 2021
26. X. Pérez, xoseperez/espurna. https://github.com/xoseperez/espurna. Accessed 13 Mar 2021

Security Considerations and Network Parameters in WSN

Vivek Sharma and Devershi Pallavi Bhatt

Abstract Wireless sensor networks (WSN) are attracting researchers. Recent advancements in electronics and wireless communications prompted the world for crating cost efficient, multifunctional, small in size, inexpensive, dynamic, and smart sensors. For such networks, deploying specially in scarce areas provides extensive benefits. With advanced applications and deployment of such network, one major thing to be concerned is security issues within WSN. Currently, there are a large number of opportunities within the research in WSN Security, and many advancements have already been proposed in this certain area. This paper firstly presents the explored complications in security of WSNs; after that, the required security constraints in WSN; then, we have listed type of the attacks and persistent threats within WSNs. We have also reviewed security mechanisms proposed by current research works, and at the end, we have discussed parameters which are necessary to address while considering the threats and attacks related to WSN.

Keywords WSN, Security · Localization · Layer wise security · Ad hoc architecture

1 Introduction

WSN needs good security mechanism as it may interact with sensitive data, and it is more error prone as compared to other wireless networks because it is a form of collaborative wireless network to monitor events without any human interaction; also, it should act as an auto or self-configurable, ad hoc manner and self-organizing, which means without human interaction or human intervention. We need to understand the specific kind of attacks because Wireless sensor network is referred as heterogeneous system, which comprise of a range varying from dozens to hundreds or thousands of

V. Sharma · D. P. Bhatt (✉)
Manipal University Jaipur, Jaipur, India
e-mail: devershipallavi.bhatt@jaipur.manipal.edu

V. Sharma
e-mail: vivek.sharma@jaipur.manipal.edu

© The Author(s), under exclusive license to Springer Nature Singapore Pte Ltd. 2022

A. Tripathi et al. (eds.), *Intelligent Computing Techniques for Smart Energy Systems*,
Lecture Notes in Electrical Engineering 862,
https://doi.org/10.1007/978-981-19-0252-9_68

low-power, self-organizing, low-cost sensor nodes using a wireless media [1]. These nodes are built and deployed to observe environmental, surroundings or physical conditions of area, to measure or sense motion, temperature, vibration, visuals, sound, pressure, pollutants, humidity etc.

1.1 Obstacles in WSN Security

Wireless sensor network has many obstacles compared to the traditional wireless networks [2]

Limited Resources: The resources available for the desired functionalities of a network play a vital role in performance of that network and related applications. In case of WSN, resources are limited because the sensor nodes are the only components of network (apart from base stations), and we cannot provide a lot of resources due to size constraints of sensor nodes, provided that these nodes run on a limited source of power and limited computation power.

Cost: WSN must be low cost because there are hundreds, or thousands, of tiny sensor nodes that are placed which work on battery, and it is today's demand to implement WSN that it should has low price so that it can be used in such great numbers and cover larger geographical area.

Energy (Power): Energy is a constraint as the sensor networks are based on ad hoc networks which work on battery, and these sensor nodes cannot be recharged or replaced easily after they are deployed in sensor network [3].

Memory: Sensor nodes contain limited memory, in which node has to keep many types of information like location so that it can identify its own position and sends the data or routing information to other sensor nodes, so designing of the security algorithms should aim to consume less memory.

Imprecise Data Transfer: Routing in WSN is typically packet-based and connectionless; also, it is unreliable if compared with connection-oriented architecture. Packet may get damaged or lost due to many reasons like channel error, low power, environmental reasons, or high congested areas. Furthermore, data packet loss may raise unfavorable events in unreliable or connectionless wireless communication channels [4].

Network Inconsistencies: Due to the broadcasting nature of WSN (using proactive protocols), it can make the network unreliable even if the channel is reliable. If packets collide in between the transfers in channels, they can accidentally lose their data, which results in failure of the data transfer.

Mobility: If the sensor network's nodes are mobile and not static, then there is a huge challenge in locating the correct node and sending the data to it because WSN topology changes time to time.

Physical Attack: Often, the sensor network is deployed in such a place where the nodes are vulnerable to adversaries like physical damage due to bad weather or any other mischievous activities caused by culprits and so on; thus, it makes the sensor network prone to physical attacks.

Fig. 1 Challenges in WSN

Distributed Network: As there is no centralized system, sensor nodes (sender) send their data generally in two manners; reactive and proactive. So sender broadcasts data to all or some neighboring nodes, and if in middle of the communication some attacker places an unauthorized node, then the information can be delivered in attacker's hand.

2 Security objectives in WSN

A wireless sensor network may be a special sort of network. It is almost like the standard network in some aspects and also unique in its own way. Therefore, we will consider the necessity of security in typical network encompasses in WSN also in some aspects [5]:

Confidentiality of Data: The information that is contained in nodes ought to be guarded its privacy. In several applications, security of information is incredibly necessary because of sensitivity of information, for example distribution of public keys, private keys (Fig. 1).

Integrity: While considering confidentiality, we mean protection of the data against stealing. But this does not mean that now data is completely safe because the attacker may manipulate, alter, or damage the data by adding few erroneous portion

Fig. 2 Security Objectives in WSN

or facts within data of a packet. It is important to maintain the data's originality (as it was while sending or at its origin), i.e., integrity of information.

Updated Data: Updation of data means that the old data is not repeated or previously sent information is not replayed. It is vital when shared key techniques are used. Shared key required to be modified over time. This takes its due time to update a shared key and let it apply to whole network [6]. Meanwhile, the attacker can deploy a replay attack. As a answer to this problem, timer can be introduced into a packet to make sure freshness of the information.

Self-Organization: Unlike most other wireless networks, wireless sensor networks are ad hoc networks that require the implementation of every sensor node in the network and the ability to self-heal under various conditions. At different points in time, WSN has different topologies [7]. Those inherent characteristics pose a significant challenge to the security of wireless sensor networks. An efficient technique for public key distribution is also required for cryptography (public-key). If a sensor network lacks self-organization, the harm caused by an physical attack or the environment can result in significant data loss or topological damages (Fig. 2).

Availability: Classical security mechanisms or encryption methods will not function in a wireless sensor network since they are maintained by a central point system, which is not present in most wireless sensor networks [8]. Even though WSN is a distributed system, a different methodology is required for the following reasons:

(a) Energy: Information is no longer provided if the battery power has run out, and there is no more sufficient energy. (b) Computation: Standard encryption algorithms offer additional computation, resulting in even more energy consumption. (c) Ad hoc nature: Because WSNs are ad hoc in nature, different methodology is required for them.

Secure Localization: WSN depends on the way that every node in the network will find another sensor node precisely and automatically. But any attacker can intrude and control insecure area location's data by conveying bogus messages, replaying signals and so forth. For these, distinct strategies have been proposed to secure the information in the WSN. We will discuss shortly some of these methods, which are specially proposed for WSNs only [9].

3 Various Categories of Attacks in WSNs

Two main types of attacks are there in WSN: one type is attack on the security procedures, and another type is attack on the routing process. WSNs are particularly vulnerable to a number of attacks as discussed below [2, 10]:

Denial of Service (DoS): In DoS, an attacker may destroy a network's capability of providing its desired functioning by trying to exhaust the resources available to the victim network by sending a lot of extra packets which can participate as an authorized entity to use the resources of network. DoS attack may distort the work of basic four layers: (i) de-synchronization and malicious flooding at the transport layer, (ii) misdirection, black holes, and negligence at the network layer, (iii) exhaustion and collision at the data-link layer, (iv) jamming at the physical layer.

Attack during Data Transfer: in this type of attacks of WSN, the information is spoofed, altered, replayed, and ends up inconsistent. Wireless communication leads to eavesdropping as an attacker will observe the data in the traffic flow, and leads to interfere, interrupt, and modify packets obtained from sensing nodes maliciously. WSN usually have short-distance communications and low power is required, but attacks may cause high computing process leading to power wastage and can engage a large number of nodes in this power consuming process of malicious signals.

Blackhole/Greyhole/Sinkhole Attack: These attacks are quite similar to each other with a range of differences purpose, procedure, or intention of attacks. One or more than one malicious node is placed in the network by an attacker, and it consumes, steals, destroys, and drops the data packets from the network. This affects the network topology, and these malicious nodes spread malicious packets disrupting the flooding-based protocol. If the malicious node entered once in the network, it participates silently in the network and able to do various malicious processing on the packets passing through them.

Sybil Attack: Whenever the WSN operates in a distributed way and task is distributed between all nodes to be completed, the intruder or malicious node node can attack and use the identities of other legitimate nodes to pretend to be more than one node. Such type of attacks is known as a Sybil Attack. Peer-to-peer and decentral-

Table 1 Threats and possible solutions in WSNs

Attack description	Layer affected	Security violation	Suggestions
Traffic analysis	Data link layer	Integrity	Time diversity, Error correction code
Sybil	Network layer	Confidentiality	Authentication, encryption
DoS	Transport layer	Availability	Reduce false alarms
Jamming	Physical layer	Availability	Spread spectrum
Eavesdropping	Physical layer	Integrity	Fake packet generation
HELLO flood	Network layer	Availability	Authentication, forwarding, multipath multi base station data, packet grouping
Blackhole/Wormhole	Network layer	Availability, confidentiality, integrity	Multiplexing paths, authentication, clock synchronization, detection malicious node, accurate location verification
Malicious node	Application layer	Availability, confidentiality, integrity	Monitoring, authentication
Node capturing	Physical layer	Confidentiality, integrity	Encryption, authentication, monitoring, resiliency

ized networks are especially vulnerable to such attacks. It is not so easy to protect networks from these kind attack, but as a possible strategy, WSN can deploy efficient protocols which can monitor to prevent the Sybil attack in network up to a certain level.

HELLO flood attack: This attack is considered as spoofing, where the attacker nodes use HELLO packets for creating problems of resource exhaustion, such as power consumption, processing wastage, and false channel utilization in the network. This occurs in high radio transmission range and sends HELLO packets to a large number of nodes within the network due to the Omni directional communication.

Wormhole Attack: Wormhole attack in WSN is very common as this may happen at initial level when nodes start finding information of neighbor nodes. Information is captured at one location and sent to next location using tunnels. These type of attack instances happen in between or in the path of the two legitimate nodes which are located at distance of a few hops (Table 1).

4 Discussion on Security Model

Here, it is seen that Sybil, wormhole, sinkhole, and DoS attacks may affect the secure functioning of WSN. We have to keep this in mind that WSN is not like other wireless networks and it has special characteristics of its own. So, before recommending any new approach, following points (areas) are to be considered [11]:

Models of Sensor Networks: It is to study and consider the framework of WSN like number of nodes, mobility of nodes, probability of node failure, properties of nodes, number of static nodes, number of moving nodes, presence of base station, distance between nodes, environmental conditions around network etc.

Traditional Routing techniques: It is to consider that the traditional routing techniques with unique global ID are feasible or not with WSN, processing, memory, communication requirement is to be considered in WSN.

Wireless Sensor Networks as Information gathering networks: It implies that the WSN model makes assumptions or study the information about the environmental condition and make it an information and then pass it. It is itself defines the special nature of sensor nodes (agents) which is not directly related to problem in hand [12].

New Routing and Transport protocols: New transport mechanism is to be introduced which will focus on energy efficiency according to the heterogeneous nature of WSN. Once the new transport protocols are made for WSN, it will not be limit to WSN but it may be used for many other networks would also be benefited by these mechanisms or protocols [13]. If we talk about routing protocols then traditional methods needs much energy and computation due to maintaining and updating routing tables so, it is needed to introduce some new routing protocols which are tailored for ultra low energy and with realistic assumption about the topology change and number of nodes in the network [14]. Many protocols are already available for exclusive WSN but most of them need improvement because most of them are based on static topology and smaller network and if topologies are changing frequently and the network size increases to hundreds or thousands then these techniques would not work (Fig. 3).

Secure Localization: Various methods have been proposed for secure localization in the WSN. Here, we discuss some of the methods proposed for WSN:

SeRLoc (Secure Range-Independent Localization): SeRLoc is distributed, resource-efficient,, and range-free localization method, and there is no communication is required between nodes for position discovery. This is a proper algorithm which is strong and robust for wormhole and Sybil attacks and sensor-compromising attacks.

Beacon Suite: A Beacon set is used to identify malicious signals, detection of malicious beacon nodes, identification of replayed signals, prevention of false detections, and at the end for withdrawing of malicious nodes out of the network [15].

SPINE: SPINE stands for secure positioning in sensor networks, and it is a distance-based positioning system. It provides verification of the position and secure computation in mobile sensor devices within the network.

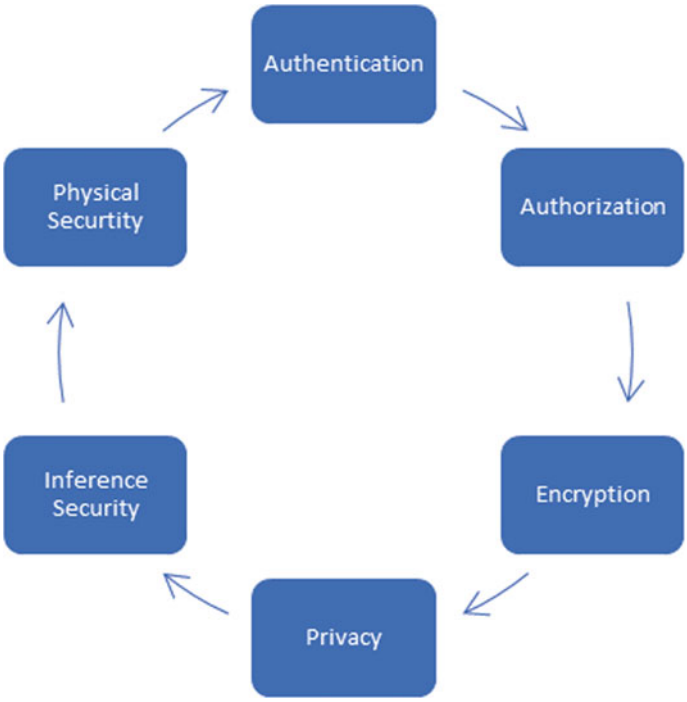

Fig. 3 Components of the security models

HiRLoc: It is higher-resolution range-independent localization technique. HiRLoc compels sensor nodes to find their respective locations with no direct communications with another nodes.

Encryption: Encryption was developed before origination of the computers when this art was developed to consist ways of distorting the information being conveyed, to make it available to authorized recipients only. In computer era, cryptographic algorithms are made of methods that translate encrypted data in plain data and also vice versa. For this purpose, cryptographic keys are used, and only a person or program with key can decode the original information. While most of the cryptography algorithms are in public domain now, so making an algorithm public, give an exposure to researchers and enthusiastic cryptanalysts, and it makes stronger or solid version of it finally. Encryption provides us with confidentiality and integrity of authentication.

Basic notations: Plaintext P id the original data. C is ciphertext, i.e., the outcome of an encryption process, which is not readable by human. E is an encryption algorithm. Here, E(P) = C means that we apply an encryption process E to the plaintext P to produce the ciphertext C.

D is a decryption algorithm. Here, D(C) = P means that we apply a decryption process D to the ciphertext C to reproduce the plaintext P.

It also employs that D(E(P)) = P and E(D(C)) = C.

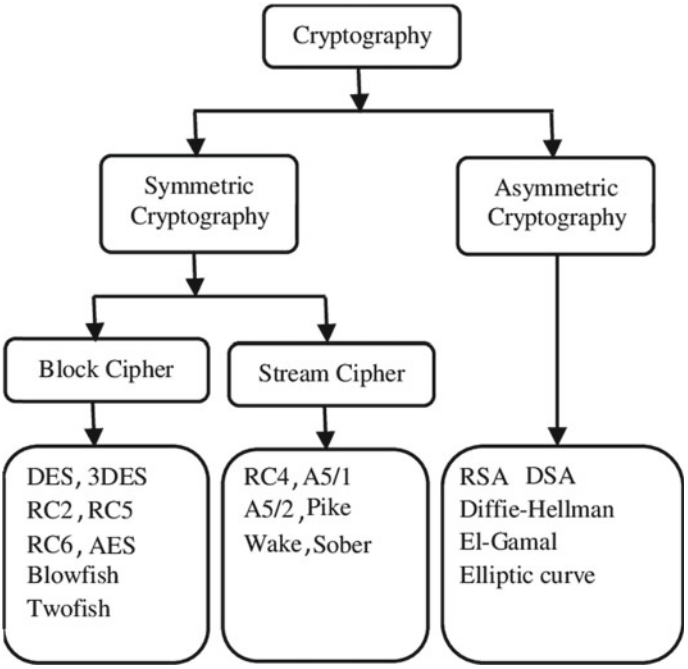

Fig. 4 Classification of encryption algorithms

Most of the present encryption procedures are categorized as asymmetric or symmetric according to the keys used. If same confidential key is used for both encoding and decoding, then its symmetric; otherwise, it will be considered asymmetric. When two different public and private keys are used at sender and receiver ends, one is for the encryption process and another for the decryption procedure.

Symmetric encryption algorithms again can be divided into subcategories as stream and block. Stream encryption algorithms encrypt the information in byte-by-byte manner, or even it can be a bit-by-bit procedure also. Streaming algorithm need not to store the data in the memory or buffer of the system, so loosely, we can say that it is safer compared to block ones, because no piece of information is present in system without encryption. Block encryption algorithms encrypt a set of data block by block (many bytes at a time). Here, the term block implies a definite group of bytes those are encoded or encrypted using a secret key at one go. Public key procedures are made by using mathematical methods and are not based only on substitution and permutation as used in symmetric encryption. A secured platform is given by the asymmetric encryption to transfer sensitive information between two remote ends, and it assures security in the field of growing wireless communication digital information exchange applications.

RSA: RSA is an asymmetric encryption algorithm which is commonly used for securing the data during transmission. for sake of explaining the working of encryp-

tion, we will discuss RSA algorithm's working: for encoding of data of sender takes two prime numbers p and q, and then calculates value of:

$N = p * q$; and

F(N) = (p − 1)*(q − 1)

Sender also selects two integers e and d such that:

e*d = 1 mod F(N)

Sender publishes a pair (N, e). Sender's encryption function is:

$E(P) = P^e \bmod N$

We assume that plaintext is somehow encoded using integers mod N.

Here, decryption function is: $D(C) = C^d \bmod N$; Where for each P mod N;

$D(C) = D(P^e) = P^{e*d} = P^{F(N)} = P$.

But then to compute d from e and N, at receiver end, one needs N, which is not available, and this makes secure encryption (Fig. 4).

4.1 Mathematical Formulation for Various Network Parameters

Remaining Energy: The sensor nodes in WSN are installed and deployed with limited initial energy. But while functioning, a node loses its energy and after certain time, energy level drops by time and the node might not function as required. The nodes with low energy (below a certain threshold) do not participate in communication, and these are called dead nodes. Therefore, remaining energy of a node in particular is an essential parameter for clustering. Remaining energy $\mathbf{E_r}$ for a node can be computed by taking difference of initially assigned energy $\mathbf{E_i}$ of a node and $\mathbf{E_x}$ energy spent by that node. $\mathbf{E_r}$ for a node can be represented by the given equation:

$$E_r = E_i - E_x \tag{1}$$

$\mathbf{E_x}$ again can be composed of two factors: one is $\mathbf{E_f}$, energy spent for legitimate functioning of a node, and another is ε, energy spent due to some attack, error, or fault in the system. $E_x = E_f + \varepsilon$ where $E_x > \varepsilon > 0$

For the whole network, $\mathbf{E_{r\_network}}$ is mentioned as aggregated remaining energy at any instance, and it can be seen as sum of remaining energy of all alive nodes. If we denote the total number of nodes alive at time t in the network as N_a, and k denotes the serial number of a node, then we can represent total remaining energy in network by given equation:

$$E_{r\_network} = \sum_{k=1}^{Na} E_{ik} - E_{fk} - \varepsilon_k \tag{2}$$

When we separate the error part as $\varepsilon_{\mathbf{total}}$, the total energy spent in error, we can rewrite this equation as mentioned below:

$$E_{r\_\text{network}} = \left(\sum_{k=1}^{Na} E_k^i - E_k^f\right) - \varepsilon_{\text{total}} \tag{3}$$

If the node energy is regulated according to the need, and error part is reduced to as lower as possible, the level of the performance of network can be enhanced in terms of energy consumption.

Mobility of nodes: It is an important property of nodes in ad hoc networks. Deployed sensor nodes may frequently roam around the places in the network randomly. The mobile nodes with low mobility are capable of creating more stable clusters, as these nodes can connect to each other for a longer duration in comparison of nodes with high mobility. Thus, node's mobility $\mathbf{M_k}$ may contribute as a parameter which can be represented using following equation:

$$M_k = \frac{1}{T}\sum_{t=1}^{T} \sqrt{\left(X_{k,t+1} - X_{k,t}\right)^2 + \left(Y_{k,t+1} - Y_{k,t}\right)} \tag{4}$$

where, $\mathbf{X_{k,t}}$ and $\mathbf{Y_{k,t}}$ are the coordinates of node **k** at instance **t**, and $\mathbf{X_{k,t+1}}$ and $\mathbf{Y_{k,t+1}}$ are the coordinates of node **k** at instance **t+1** in a two-dimensional pane and **T** is the run time of network.

If we consider the average mobility of all nodes inside a cluster or whole network, the degree of mobility can be used as a metric of overall movement inside any cluster or network. For whole network, this metric can be taken as average of mobility of all alive nodes.

$$M_{\text{Network}} = \frac{1}{Na}\sum_{k=1}^{Na} (M_k) \tag{5}$$

If the value of $\mathbf{M}_{network}$ increases, it causes a significant drop in stability of clusters in network because nodes can go out of range of signal range of cluster heads due to high degree of mobility.

Weightage: All the parameters defined for various metrics are scaled on different scales, so normalization of all parameters is required to get an acceptable weight for a node in process of choosing fittest or optimum nodes eligible for becoming cluster heads, and it requires a combination of these parameters. For this, a weight is required to be computed by a process in which all the parameters are scaled on a similar scale. Thus, we prepare a list of fittest nodes by calculating weights. During weight calculation, for the scaling of the node performance parameters into a similar scale; there some factors are constructed. While calculating the weights, in general practice, the sum of all factors is kept 1, and the range of the weights is kept between range of 0 and 1.

$$W_k = w_1 * c_1 + w_2 * c_2 + w_3 * c_3 + \cdots + w_m * c_m \tag{6}$$

where $\mathbf{W_k}$ is the weight of a node k, $\mathbf{w_1, w_2, \ldots w_n}$ are weightage of various individual parameters and $\mathbf{c_1, c_2, \ldots c_m}$ are different scaling coefficients.

5 Conclusion

This paper outlined some of the available attacks and threats which are associated attacks and threats which are associated with wireless sensor network like Sybil, wormhole, sinkhole, DoS attack while information transition etc. Also, we have reached to the conclusion that by using traditional approaches of general wireless network would not fully address the issues related to wireless sensor networks security due to WSN ad hoc architecture, limited energy, limited power, and topological changes etc. So, it is recommended researchers should happen to design some new protocols, approaches, mechanisms, or models which are exclusively made after understanding the special threats for which wireless sensor network is prone.

References

1. Aliti K, Sevrani (2019) A security model for Wireless Sensor Networks. In: 2019 42nd International convention on information and communication technology, electronics and microelectronics (MIPRO), pp 1165–1168
2. Kaur R, Sandhu K (2021) A study on security attacks in wireless sensor network. In: 2021 International conference on advance computing and innovative technologies in engineering (ICACITE), pp 850–855
3. Sharma S, Yadav A, Panchal M, Vyavahare PD (2019) Classification of security attacks in WSNs and possible countermeasures: a survey. In: 2019 IEEE International conference on advanced networks and telecommunications systems (ANTS), pp 1–6
4. Zahid MN (2020) Security issues and challenges in RFID, wireless sensor network and optical communication networks and solutions. In: 2020 IEEE 3rd International conference of safe production and informatization (IICSPI), pp 592–599
5. Ovasapyan T, Moskvin D (2020) Security provision in WSN on the basis of the adaptive behavior of nodes. In: 2020 Fourth world conference on smart trends in systems, security and sustainability (WorldS4), pp 81–85
6. Jilani SA, Koner C, Nandi S (2020) Security in wireless sensor networks: attacks and evasion. In: 2020 National conference on emerging trends on sustainable technology and engineering applications (NCETSTEA), pp 1–5
7. Bhola J, Soni S, Cheema GK (2019) Recent trends for security applications in wireless sensor networks—a technical review. In: 6th International conference on computing for sustainable global development, pp 707–712
8. Nandi GS, Pereira D, Vigil M, Moraes R, Morales AS, Araújo G (2019) Security in wireless sensor networks: a formal verification of protocols. In: 2019 IEEE 17th International conference on industrial informatics (INDIN), pp 425–431
9. Kumar R, Tripathi SR (2020) A review on security in wireless sensor network. In: 2020 International conference on emerging smart computing and informatics (ESCI), pp 304–308
10. Butun I, Morgera SD, Sankar R (2014) A survey of intrusion detection systems in wireless sensor networks. IEEE Commun Surv Tutor 16(1):266–282. https://doi.org/10.1109/surv.2013.050113.00191

11. Liu W, Chen H, Chen M (2012) A survey of wireless sensor networks. World Automation Congress, pp 305–307
12. Almheiri SM, Alqamzi HS (2013) Data link layer security protocols in wireless sensor networks: a survey. In: 10th IEEE International conference on networking, sensing and control (ICNSC), pp 312–317
13. Islam W, Shen X, Wang (2012) Security and privacy considerations for wireless sensor networks in smart home environments. In: Proceedings of the 2012 IEEE 16th International conference on computer supported cooperative work in design (CSCWD), pp 626–633
14. Raza AA, Romman MF, Qureshi (2019) Security issues in wireless sensor network broadcast authentication. In: 2019 2nd International conference on new trends in computing sciences (ICTCS), pp 1–7
15. Indira K, Sakthi U (2019) Security issues, countermeasures and dynamic queue scheduling for SDWSN. In: 2019 2nd International conference on signal processing and communication (ICSPC), pp 79–82

Dual-Port 8T SRAM Cell Design with Shorted Gate FinFET for Leakage Reduction and Improved Stability

Chusen Duari and Shilpi Birla

Abstract Since the CMOS technology has reached to nanometer regime to meet the increasing demand of smarter and faster device, CMOS circuits have to face various short channel effects and variation in process parameters leading to degradation in performance and reliability. CMOS SRAM is one of the major circuits which degrades its performance due to short channel effects. To address this issue, in this paper, we proposed a novel static random-access memory cell with reduced leakage and improved stability using FinFET technology. In our design, we have shorted both the gates of the FinFET devices to apply a common biasing voltage. The cell is designed with FinFET logic, and results are compared with the conventional 6T FinFET cell in terms of leakage and stability at 22 nm technology node using HSPICE. The results show significant improvements in leakage and stability in comparison with the conventional SRAM cell and offer a good trade-off at sub-nanometer technology node.

Keywords FinFET · SRAM · Leakage current · SNM

1 Introduction

The increasing demand of smarter portable devices with high functionalities, lighter weight, and lower power consumption, the semiconductor industry is scaling down the technology to sub-nanometer scale to meet the above requirements. Static random-access memory is one of the most popular choices in various smart devices as embedded memory [1]. Consequently, in present state-of-the-art processors, the SRAM array occupies a considerable amount of die area within the chip [2]. The CMOS-based SRAM cell suffers various short channel effects and variation in

C. Duari (✉) · S. Birla
Department of Electronics and Communication Engineering, Manipal University Jaipur, Jaipur 303007, India
e-mail: chusen.duari@jaipur.manipal.edu

S. Birla
e-mail: shilpi.birla@jaipur.manipal.edu

© The Author(s), under exclusive license to Springer Nature Singapore Pte Ltd. 2022

A. Tripathi et al. (eds.), *Intelligent Computing Techniques for Smart Energy Systems*, Lecture Notes in Electrical Engineering 862,
https://doi.org/10.1007/978-981-19-0252-9_69

process parameters which results in adverse effect like increase in leakage, degradation of stability, and hence reliability of the memory array [3]. One of the most attractive choices to replace traditional planar CMOS technology is FinFET transistor structure because of its better gate controllability and scalability [4]. Even though new device structures like junctionless transistor [5], hybrid III–V tunnel FET, [6] etc., are proposed for sub-20 nm regime but due to established FinFET fabrication technology are still preferred. The FinFET devices have gates on both sides of fin which can be isolated electrically to apply independent biasing or can be connected together to apply common biasing voltage [7]. In independent-gate mode of operation, one gate can be used to switch the transistor ON/OFF, and the other gate can be used to control the threshold voltage for better controllability of channel area. This gives static and dynamic performance controllability which provides the designers more flexibility [1, 4, 8]. In [9], authors used independent word lines which were connected to two independent gates of each access transistor to enhance stability of SRAM cell. In [10], independent-gate FinFET has been successfully fabricated with reduced leakage. The conventional 6T SRAM cell is much susceptible to consistency issues and process variations. In this work, we propose a novel 8T SRAM cell designed with shorted gate FinFET technology with improved leakage and stability. The rest of the paper is organized as follows. Various leakage mechanisms and short channel effects in CMOS design are discussed in Sect. 2. In Sect. 3, a brief review of FinFET devices and technology is discussed. In Sect. 4, we explain about 6T SRAM. Proposed techniques have been discussed in Sect. 5. Analysis and simulation result have been reported in Sect. 6.

2 Leakage Currents in Scaled Technologies

There are six leakage mechanisms that contribute to the total static power dissipation in nanoscaled CMOS technologies [11]. These six leakage mechanisms are as follows:

Reverse bias junction current: This current flows from the source or drain to substrate through the reverse biased PN junction diodes formed by source and drain with the substrate when the transistor is in both ON and OFF [9]. These parasitic diodes are in reverse biased when the terminals are at high voltages [11]. This current can be expressed as shown in Eq. (1) [12].

$$I_{\text{sub}} = \mu_0 C_{\text{ox}} \frac{W_{\text{eff}}}{L_{\text{eff}}} V_{\text{T}}^2 e^{1.8} \tag{1}$$

Subthreshold or weak inversion current: This leakage current flows due to the minority carriers diffusing through substrate from the drain to source region when the gate to source voltage is less than the transistor threshold voltage, i.e., when the transistor is in weak inversion region. The dependence of subthreshold leakage

current on various parameters can be modeled [13] by Eq. (2) as shown below:

$$I_{\text{sub}} = \mu_0 C_{\text{ox}} \frac{W_{\text{eff}}}{L_{\text{eff}}} V_{\text{T}}^2 e^{1.8} \exp\left(\frac{V_{\text{gs}} - V_{\text{th}}}{n V_{\text{T}}}\right) \cdot \left(1 - \exp\left(\frac{-V_{\text{ds}}}{V_{\text{T}}}\right)\right) \tag{2}$$

where μ_0 is the carrier mobility, C_{ox} is the gate oxide capacitance per unit area, W_{eff} and L_{eff} denote the transistor effective width and length, $V_{\text{T}} = kT/q$ is the thermal voltage at temperature T, 'n' is the subthreshold swing coefficient of the transistor, V_{gs} is the gate to source voltage of the transistor, Vth is the threshold voltage, and V_{ds} is the drain to source voltage of the transistor [14].

Oxide tunneling current: Due to high electric field and low oxide thickness, tunneling of electrons occurs through and into the gate which results in considerable amount of current flows from the gate terminal to the substrate. Direct tunneling current is significant for low oxide thickness. At technology, node lower than 45 nm effect of this current is severe. NMOS device is more effected than the PMOS device with this current, typically by one order of magnitude with identical oxide thickness and Vdd [15].

Hot carrier injection current: This current occurs due to the injection of hot carrier because of high electric field experienced in the gate drain overlapping region. Due to high electric field, electron acquires sufficient energy to overcome the barrier potential to cross the insulating oxides and reach to the gate terminal.

Gate-induced drain leakage (GIDL) current: GIDL current occurs due to flow of minority carrier formed due to the strong electric field in the gate oxide region. When the oxide thickness is scaled down, high electric field is generated across the oxide even a small voltage is applied to the drain region which causes the generation of electron–hole pair in the drain gate overlapped region. This current becomes more noticeable when drain voltage is higher.

The channel punch through current: Because of the close proximity of source and drain region, this current results in scaled CMOS. When the channel length is reduced to a certain extent, the depletion regions formed by source and drain with the body come in contact which results in a conducting path and punch through current flows in the bulk, and this occurs in OFF state.

3 FinFET Device and Technology

The FinFET device is one of the most common and emerging choices among the recent new device architectures that are proposed to overcome the issues observed in CMOS devices in sub-nanometer regime because of its improved control over the channel due to multiple gates and compatible fabrication process [7, 16]. The better

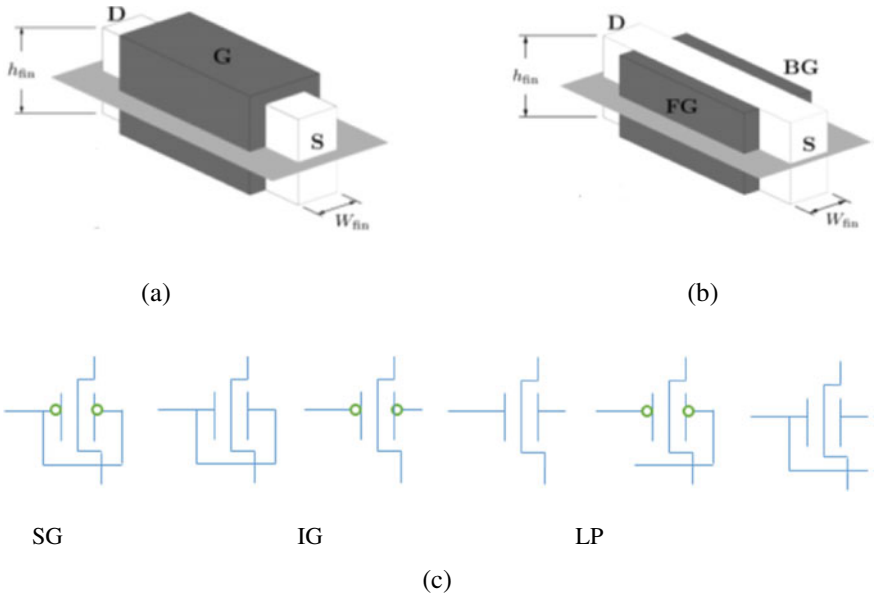

Fig. 1 Geometrical structure of FinFET [9]

gate controllability results in a reduction of source–drain leakage and short channel effects [4, 17, 18]. FinFET devices also exhibit better electrostatic properties [19].

The FinFET comprises a thin silicon body; its width is denoted by W_{fin}, wrapped around by poly-silicon gate. Figure 1 shows the schematic diagram of FinFET devices in two different flavors. The space between the source and drain is defined as fin length, L_{fin}, and h_{fin} denotes the fin height. Figure 1a depicts a shorted gate (SG) FinFET in which two gates are tied together. Figure 1b shows an independent-gate (IG) FinFET in which the top portion of the gate region is etched out to form a double gate, which can be biased separately. Two gates are controlled independently; the IG FinFET exhibits more design flexibility. In general, FinFET has been used in three different modes: (i) SG, (ii) low power (LP), here the back gate is connected to reverse body bias voltage to reduce leakage, and (iii) IG mode, where independent signals are being applied to drive the gates. Figure 1c shows the symbols of FinFET in different modes.

4 6T SRAM Cell

SRAM cells perform three different functions, viz read, write, and hold a bit. All these operations are essential in designing SRAM cell. In each operation, different parts of SRAM architecture are activated. Several SRAM cells have been suggested by a different researcher with different aspects of their application. The common 6T

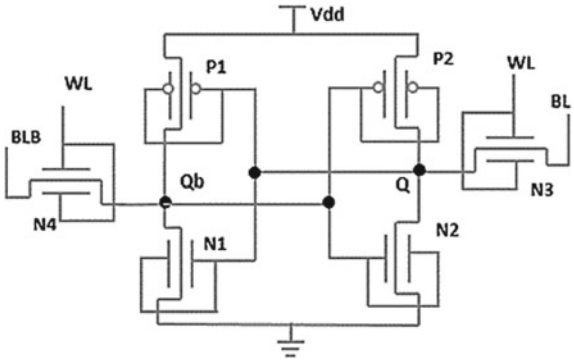

Fig. 2 Circuit diagram of 6T FinFET SRAM cell [8]

SRAM cell, which is most frequently used with FinFET logic, is shown in Fig. 2. This 1-bit memory cell is derived from CMOS SRAM cell which consists of the simple cross-coupled inverter formed by transistors P1, P2, N1, and N2, which acts as a simple latch circuit having two stable states. The data stored in the internal nodes Q and Qb of the memory cell can be interpreted as logic '1' or '0' depending on the state of the two stable states. The data stored in the internal nodes can be accessed through two access transistors N3 and N4 via bitlines BL and BLB. During a write operation, the bitline BL will be pre-charged to logic '1' or '0'. The access transistors which act as a switch are controlled by word line 'WL' which is kept high during read and write operations. During retention mode, this word line has kept a logic low, and thereby the access transistors act as an open switch.

5 The Proposed 8T SRAM Cell

The conventional 6T transistor suffers read destruction problem when the voltage at zero storing node exceeds the threshold voltage of the opposite inverter [20]. Because of this, the stability of the cell also degrades. In write operation, the activity factor increases due to discharging of bitline pairs [21]. In this proposed novel cell topology, we have used single ended write operation to reduce the activity factor of discharging both the bitlines during write operation. Optimal transistor sizing ensures the stability of the cell at various supply voltages. The schematic of the designed cell is given in Fig. 3. A separate control signal to the access transistors provides the facility to use it as dual-port memory. The cell uses a transmission gate as access transistor to achieve full swing of bitline voltage and hence enhances the stability. The proposed 8T SRAM cell depends on the principle of cutting off the feedback connection between the left and write inverter, before a write operation. To accomplish the feedback connection and disconnection, an NMOS (N5) is used. The circuits are simulated at supply voltage ranging from 0.9 to 0.5 V at 22 nm technology node.

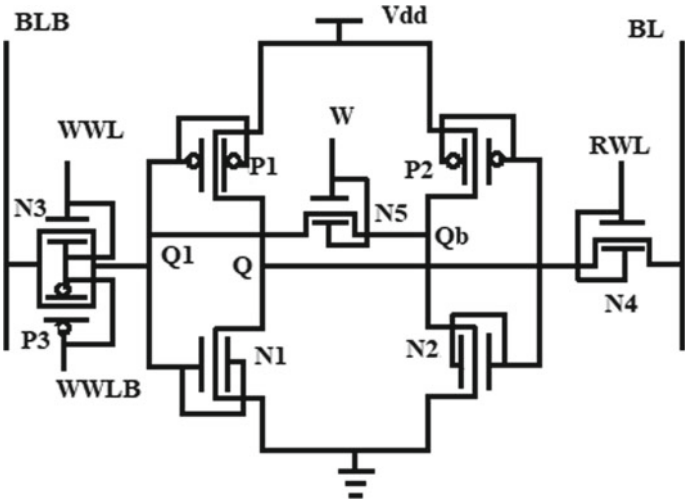

Fig. 3 Circuit diagram of proposed 8T FinFET SRAM cell

5.1 Read Operation

During data reading, the bitline 'BL' is pre-charged to logic '1' and transistor N4 is turned ON by asserting the signals 'RWL' and 'WWL' high while 'WWLB' is de-asserted. Thus, the access transistor 'N4' acts as a closed switch to provide a discharging path for the bitline through 'N1'. Discharging of bitline signifies that the content stored in the node is '0'; otherwise, it is '1'.

5.2 Write Operation

At starting of write operation, the feedback connection is cut off by turning OFF the transistor 'N5' through the control signal 'W'. During a write operation, the transmission gate is activated by applying suitable voltage to the signals 'WWL' and 'WWLB' to make the access transistors 'ON' and provide a connecting path from the bitline 'BLB' to the respective data storing node and keeping 'RWL' signal de-asserted. 'BLB' line carries complement of the input data to be written into the cell node. Transistors 'N3' and 'P3' will be 'ON', while transistor 'N5' will be kept 'OFF'. Transmission gate transfers the data from 'BLB' line to 'Q1' which will drive the left inverter, and transistor 'P1' and 'N1', to develop 'Q', the cell data. Similarly, 'Q' drives right inverter, and 'P2' and 'N2', to develop 'Qb' which equals to 'Q1' if data is '0' and slightly higher than 'Q1' if data is '1'. Then, transmission gate is turned OFF, and 'N5' is turned ON to reconnect the feedback link between the two inverters to stabilize the new data. Both the bitlines are pre-charged to logic high.

In this scheme, 'BLB' is kept high for writing '0'. To store '1' in the cell, 'BLB' is discharged to '0' with comparable power consumption to the conventional 6T cell. To store a '0' in the cell, there is no need to discharge 'BLB'; hence, the activity factor of discharging bitline is less than 1 and depends on the percentage of writing '1'.

5.3 Stability Analysis

Stability is measured by estimating the static noise margin for read, write, and hold operations. This is the measure of the maximum noise signal that can be tolerated without flipping the stored bit. Butterfly curve is used to estimate these noise margins. The square with a maximum length that can be embedded in the curve measures the noise margin.

6 Simulation Results

In this paper, a novel 8T SRAM cell designed with FinFET logic has been proposed, and performance is compared with existing 6T SRAM cells. The total static leakage power for 6T SRAM cell and the proposed SRAM cell at various supply voltages have been evaluated using HSPICE simulation tool, and the result is given in Table 1. Leakage power and stability results have been discussed in the following section. Noise margin for retention and access modes is being calculated using butterfly curves.

Table 1 shows the leakage power for the SRAM cells, viz 6T and 8T cells at varying supply voltages, and 8T SRAM cell has improved leakage power consumption in comparison to 6T SRAM cell.

Table 1 Comparative analysis of leakage power at different supply voltages

Supply voltage (V)	6T_SRAM (nW) [8]	8T_SRAM (nW)
0.9	89.77	16.52
0.85	62.56	14.46
0.8	41.63	10.28
0.75	26.16	6.34
0.7	15.33	2.76
0.65	8.26	1.46
0.6	4.06	0.98
0.55	1.83	0. 46
0.5	0.76	0.32

Hold static noise margin (HSNM), read static noise margin (RSNM), and write static noise margin (WSNM) for 6T and 8T SRAM are being calculated for various supply voltages from 0.5 V to 0.9 V. Figure 4 shows the butterfly curve for HSNM at 0.8 V. The values of HSNM for 6T and 8T are 288 mV and 320 mV at 0.8 V supply voltage, respectively. RSNM is also calculated for the same supply voltage range using butterfly curve. The butterfly curves for RSNM are shown in Fig. 5. The values for the same are 108 mV and 120 mV, respectively, for 6T and 8T SRAM cells at 0.8 V supply voltage. The butterfly curve for WSNM calculated at 0.8 V supply voltage is shown in Fig. 6. The values obtained for the same are 194 mV and 224 mV, respectively, for 6T and 8T SRAM cells at 0.8 V supply voltage. Figure 7a–c shows the comparison of HSNM, RSNM, and WSNM, respectively, at different supply voltages between the two SRAM cells. The proposed cell shows significant improvement in noise margin at all supply voltages.

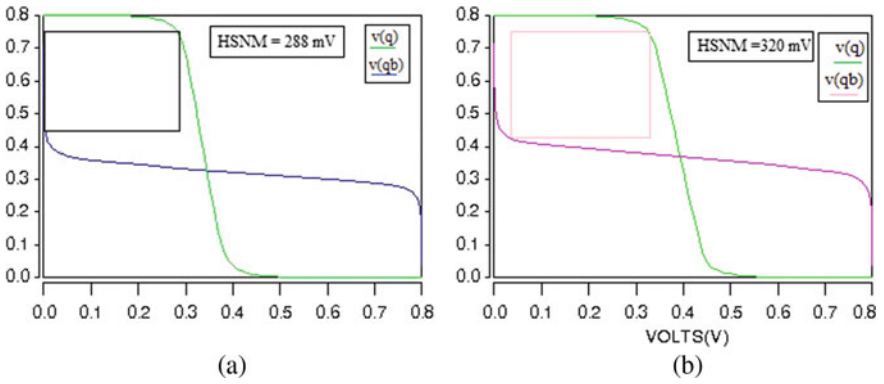

Fig. 4 Butterfly curve for HSNM at 0.8 V, **a** 6**T** SRAM cell, **b** 8T SRAM cell

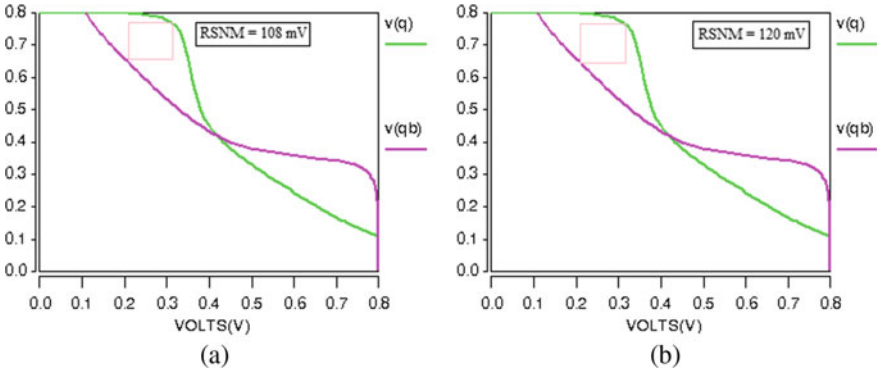

Fig. 5 Butterfly curve for RSNM at 0.8 V, **a** 6**T** SRAM cell, **b** 8T SRAM cell

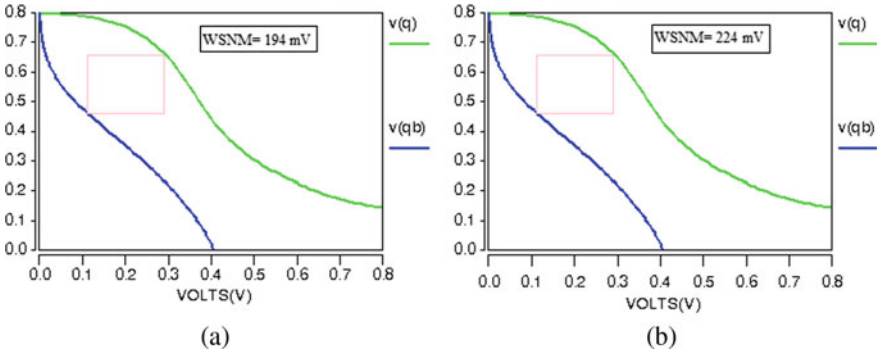

Fig. 6 Butterfly curve for WSNM at 0.8 V, **a** 6**T** SRAM cell, **b** 8T SRAM cell

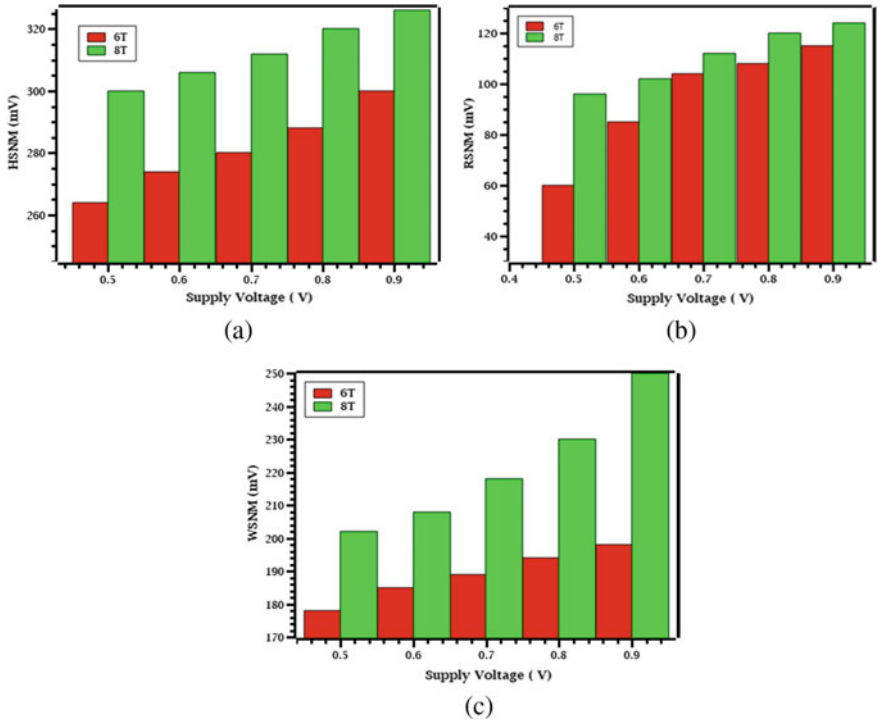

Fig. 7 Comparison of stability of the SRAM cells: **a** HSNM, **b** RSNM, **c** WSNM

7 Conclusions

In this paper, a novel power-efficient dual-port 8T SRAM bit cell structure with combined gate FinFET has been proposed. Stability for retention, read, and write

mode operations is improved by 1.11×, 1.12×, and 1.15×, respectively, in comparison with the existing 6T cell at 22-nm technology node at 0.8 V supply voltage. The static leakage power during a write operation is also reduced by 77% compared to the existing 6T cell topology at 0.8 V supply voltage. The proposed memory cell can be useful for low-voltage low-power embedded memory design.

References

1. Oh TW, Jeong H, Kang K, Park J, Yang Y, Jung S-O (2017) Power-gated 9T SRAM cell for low-energy operation. IEEE Trans Very Large Scale Integr Syst 25(3):1183–1187. https://doi.org/10.1109/TVLSI.2016.2623601
2. Pilo H, Barwin C, Braceras G, Browning C, Lamphier S, Towler F (2007) An SRAM design in 65-nm technology node featuring read and write-assist circuits to expand operating voltage. IEEE J Solid-State Circuits. https://doi.org/10.1109/JSSC.2007.892153
3. Kawasaki H et al (2009) Challenges and solutions of FinFET integration in an SRAM cell and a logic circuit for 22 nm node and beyond. In: 2009 IEEE international electron devices meeting (IEDM), Dec 2009, pp 1–4. https://doi.org/10.1109/IEDM.2009.5424366
4. Gupta SK, Roy K (2013) Device-circuit co-optimization for robust design of FinFET-based SRAMs. IEEE Des Test. https://doi.org/10.1109/MDAT.2013.2266394
5. Bora N, Das P, Subadar R (2016) An analytical universal model for symmetric double gate junctionless transistors. J Nano-Electron Phys 8(2). https://doi.org/10.21272/jnep.8(2).02003
6. Bora N (2021) An approach for drain current modeling including quantum mechanical effects for a DMDG junctionless field effect nanowire transistor. SILICON. https://doi.org/10.1007/s12633-021-01282-2
7. Mishra P, Muttreja A, Jha NK (2011) FinFET circuit design. In: Nanoelectronic circuit design, 2011
8. Duari C, Birla S, Singh AK (2020) A dual port 8T SRAM cell using FinFET and CMOS logic for leakage reduction and enhanced read and write stability. J Integr Circ Syst 15(2):1–7. https://doi.org/10.29292/jics.v15i2.140
9. Salahuddin SM, Kursun V, Jiao H (2015) Finfet sram cells with asymmetrical bitline access transistors for enhanced read stability. Trans Electr Electron Mater. https://doi.org/10.4313/TEEM.2015.16.6.293
10. Ma K et al (2014) Independently-controlled-gate FinFET 6T SRAM cell design for leakage current reduction and enhanced read access speed. In: 2014 IEEE computer society annual symposium on VLSI, Jul 2014, pp 296–301. https://doi.org/10.1109/ISVLSI.2014.25
11. Roy K, Mukhopadhyay S, Mahmoodi-Meimand H (2003) Leakage current mechanisms and leakage reduction techniques in deep-submicrometer CMOS circuits. Proc IEEE. https://doi.org/10.1109/JPROC.2002.808156
12. Abbas Z, Olivieri M (2014) Impact of technology scaling on leakage power in nano-scale bulk CMOS digital standard cells. Microelectron J. https://doi.org/10.1016/j.mejo.2013.10.013
13. Kim T-H, Liu J, Keane J, Kim CH (2007) A high-density subthreshold SRAM with data-independent bitline leakage and virtual ground replica scheme. In: 2007 IEEE international solid-state circuits conference. Digest of technical papers, Feb. 2007, pp 330–606. https://doi.org/10.1109/ISSCC.2007.373428
14. Lorenzo R, Chaudhury S (2017) Review of circuit level leakage minimization techniques in CMOS VLSI circuits. IETE Technical Review (Institution of Electronics and Telecommunication Engineers, India). 2017. https://doi.org/10.1080/02564602.2016.1162116
15. Kim CH, Roy K (2002) Dynamic Vt SRAM: a leakage tolerant cache memory for low voltage microprocessors, 2002. https://doi.org/10.1109/lpe.2002.146748

16. Mishra P, Jha NK (2010) Low-power FinFET circuit synthesis using surface orientation optimization. In: 2010 design, automation and test in Europe conference and exhibition (DATE 2010), Mar 2010, pp 311–314. https://doi.org/10.1109/DATE.2010.5457187
17. Gupta SK, Kulkarni JP, Roy K (2013) Tri-mode independent gate finfet-based sram with pass-gate feedback: technology-circuit co-design for enhanced cell stability. IEEE Trans Electron Dev. https://doi.org/10.1109/TED.2013.2283235
18. Duari C, Birla S, Singh AK (2021) A 4 × 4 8T-SRAM array with single-ended read and differential write scheme for low voltage applications. Semicond Sci Technol. https://doi.org/10.1088/1361-6641/abf7d3
19. Lawrence B, Rubia J (2015) Review of Fin FET technology and circuit design challenges, 2015
20. Wen L, Li Z, Li Y (2013) Single-ended, robust 8T SRAM cell for low-voltage operation. Microelectronics J. https://doi.org/10.1016/j.mejo.2013.04.007
21. Pasandi G, Fakhraie SM (2013) A new sub-threshold 7T SRAM cell design with capability of bit-interleaving in 90 nm CMOS, 2013. https://doi.org/10.1109/IranianCEE.2013.6599738

Structural and Optical Characteristics of Boron Doped $CuGaSe_2$ Chalcopyrite

Shikha Sharma, Karina Khan, Amit Soni, and Jagrati Sahariya

Abstract In this paper, we discussed the structural and optoelectronic properties of boron-doped chalcopyrite's $CuGaSe_2$ to explore their utility as a photovoltaic material. The structural, optical, and electronic properties of 12.5% B doped in $CuGaSe_2$ are determined by using DFT approach which is based on the Wien2k code. The first principle investigation has been performed by considering the most accurate Tran-Blaha modified Becke Johnson exchange potential. $CuGaSe_2$ supercell constructed of a $2 \times 2 \times 2$ dimension. The electronic properties of $CuGa_{0.875}B_{0.125}Se_2$ are investigated by analyzing its energy band structure and density of states. Our investigation represents that the $CuGa_{0.875}B_{0.125}Se_2$ have direct band gap nature with band gap value of 0.82 eV. The optical properties of $CuGa_{0.875}B_{0.125}Se_2$ are explained through some parameters like dielectric function, absorption coefficient, reflectivity, and refraction.

Keywords Density functional theory · Optical properties · Super cell

1 Introduction

Since the earth is suffering from the energy crisis from the last few years and currently it is one of the leading issues and increasing rapidly as on increasing the world's demands [1]. Solar energy is a huge source of renewable energy, and it is a clean source of energy and used for the generation of electricity [2, 3]. Now a days the researchers emphasize on finding a efficient material used in solar cell for the maximum utilization of solar energy. A renewable energy resource is a key

S. Sharma · K. Khan
Department of Physics, Manipal University Jaipur, Jaipur, Rajasthan 303007, India

A. Soni (✉)
Department of Electrical Engineering, Manipal University Jaipur, Jaipur, Rajasthan 303007, India
e-mail: amitsoni_17@yahoo.co.in

J. Sahariya
Department of Physics, National Institute of Technology, Uttarakhand, Srinagar (Garhwal) 246174, India

© The Author(s), under exclusive license to Springer Nature Singapore Pte Ltd. 2022

A. Tripathi et al. (eds.), *Intelligent Computing Techniques for Smart Energy Systems*,
Lecture Notes in Electrical Engineering 862,
https://doi.org/10.1007/978-981-19-0252-9_70

source for photovoltaic technology. Several research works have proved that the main energy source for the future is solar photovoltaic energy conversion. Solar energy exhibits inexhaustible, renewable characteristics. Chalcopyrite compounds are investigated currently due to their various optoelectronic applications such as light-emitting diodes, and solar cells. [4, 5]. In the past decades, I-III-VI_2 types of chalcopyrite compounds have been paid a lot of attention as their exhibit the property of a good absorber for the solar cell [6, 7]. The ternary semiconductor copper gallium diselenide $CuGaSe_2$ is composed of the group I-III-VI_2 family and is applicable as a good absorber layer for solar material. $CuGaSe_2$ belongs to this favorable chalcopyrite compound because of its wide band gap and high value of optical absorption coefficient. This compound has almost all the qualities required for solar cells. The material used in photovoltaic is considered on the basis of its band gap value, electronic and optical properties. There are various theoretical and experimental studies based on structural and optoelectronic properties of pure and doped $CuGaSe_2$ thin film. In experimental studies, Koteski et al. [8] have been presented a study on Ge doping on $CuGaSe_2$. Ishizuka et al. [9] have been investigated the effects of post-deposition treatment of light and heavy alkali-halide on $CuGaSe_2$ thin-film solar cells. Kikuchi et al. [10] have been investigated Ga_2O_3/$CuGaSe_2$ hetero-junction for visible light sensors. Ishizuka et al. [11] have been synthesized $CuGaSe_2$, polycrystalline thin films which are used as top cells in tandem structure for photovoltaic devices. Weiss et al. [12] have been prepared precursor Ag-doped $CuGaSe_2$ for thin-film solar cells and observed that as optical properties completely changed and its radiative transmission occurred at 1.61 eV. Theodoropoulou et al. [13] have been studied the properties of germanium-doped $CuGaSe_2$ films by Raman spectroscopy. Ullah et al. [14] have been prepared $CuGaSe_2$ polycrystalline thin-film absorber by electrodeposition process for photovoltaic applications. Rusu et al. [15] have been investigated the $CuGaSe_2$ thin-film transport properties as a function of the absorber composition. In theoretical studies, Bikerouin et al. [16] have investigated the effect of lattice deformation on electronic and optical properties of $CuGaSe_2$ by implementing ab-initio calculations. Dergal et al. [17] studied the structural and optoelectronic properties of 3d transition metals-substituted $CuGaSe_2$ through the first principle method. Xue et al. [18] have been carried out the $CuGaSe_2$ up to 100 GPa based on density functional theory. Khan et al. [19] reveal the impact properties of aluminum-doped $CuGaSe_2$ thin-film flexible solar cells through a DFT study, and the obtained band gap value is 1.27 eV. Fan et al. [20] has been studied the Sn-doped $CuGaSe_2$ thin films, structural and optical characteristics for solar cell by VSAP method. Present work for investigation of properties of boron-doped $CuGaSe_2$ is inspired from Khan et al. work [21].

2 Computational Details

In this section, firstly we investigated the structural properties and then calculated the optoelectronic properties of B-doped $CuGaSe_2$ by using a first-principles theory

based on the density functional theory under the theoretical simulation process that executed in the wein2k code [22]. Density functional theory is generally used for the calculation of electronic structure of system containing many atoms or a complex system. It is based on the theory of electron density. Here, wein2k code used for the solution of Kohn–Sham DFT equations with high level of accuracy. It provides useful results for the study of various materials. Firstly, supercell is derived from the tetragonal $CuGaSe_2$ structure and then the dilution proposed here, on substituting B atom in a Ga atom position inside a $CuGaSe_2$ supercell. We computed 12.5% dilutions of the B dopants inside the $CuGaSe_2$. For calculation supercells of size 16, 16 and 16 atom cells were carried out. Calculations and densities of states (DOS and PDOS) for boron dilution on host compound were carried out using the DFT wein2k code. For this purpose, we have taken the lattice constant $a = b = 5.596$Å, c = 11.004 Å from the already reported work et al. [23]. By using the standard structure of $CuGaSe_2$, we constructed a super cell of dimension $2 \times 2 \times 2$, which alter the structure into monoclinic B-base centered having 5(C2) space group. The lattice structure of B-doped $CuGaSe_2$ along with the Brillouin zone is presented in Fig. 1a–b. For the achieving the maximum accuracy in the calculations, we also consider some other parameters as an input, $R_{MT} \times K_{MAX} = 5$, k points = 100, G_{max} = -12 and $l_{max} = 10$. For the separation of the core and valence states, consider value of energy is –6.00 Ry. The atomic positions are set as Cu (0, 0, 0); Ga (0.5, 0.5, 0.0), and Se (0.25, 0.25, 0.125).

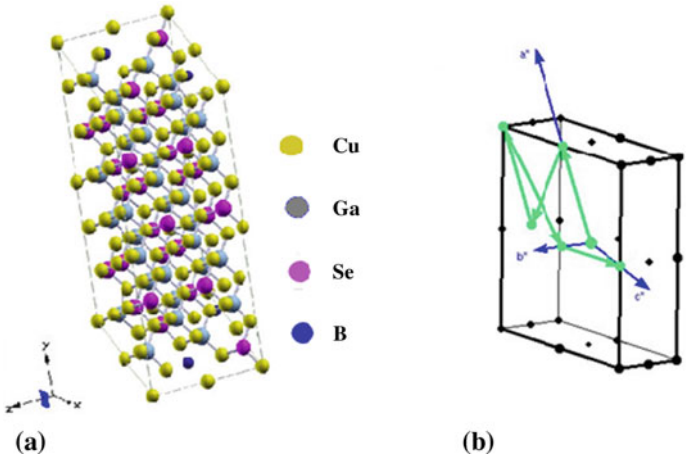

Fig. 1 $CuGa_{0.875}B_{0.125}Se_2$, **a** lattice structure and **b** Brillouin zone

3 Results and Discussion

3.1 Electronic Properties

The physical characteristics of a material depend mainly on their electronic structures. So in this section, we have calculated the electronic band structure, band gap and density of states spectra for the $CuGa_{0.875}B_{0.125}Se_2$ compound using TB-mBJ exchange–correlation potential. Here in Fig. 2 for the first Brillouin zone, we plotted the energy band structure along the highly symmetry momentum points G → B → C → E → V → Z and their coordinates are (0,0,0); (0.5,0,0); (-0,-0.5,-0.5); (0.5,0.5,-0.5); (0,0.5,0); (0,0,0.5), respectively. As illustrated in Fig. 2, the Fermi energy level is at 0 eV, and the observed energy band gap, i.e., gap between the maximum of valence band and minimum of conduction band is 0.82 eV. This band gap value proves that $CuGa_{0.875}B_{0.125}Se_2$ compound is semiconductor in nature. We observed from our band structure calculations that the valance band maxima and the conduction band minima both lies at G-Z, *k* points which confirmed its direct band gap nature. The evaluated energy band gap value for $CuGa_{0.875}B_{0.125}Se_2$ is 0.82 eV. Hence, we can say that $CuGa_{0.875}B_{0.125}Se_2$ is a semiconductor compound having direct band gap nature. In Table 1, there is a comparison between band gap values of different-different-doped elements.

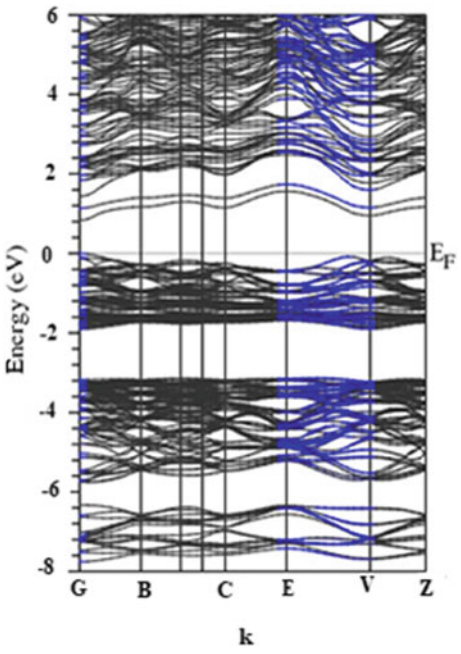

Fig. 2 Electronic band structure of $CuGa_{0.875}B_{0.125}Se_2$ by using the TB-mBJ

Table 1 Band gaps in the chalcopyrite compound $CuGaSe_2$ with and without doping

$CuGaSe_2$	Band gap (eV)
Pure	1.16[23]
Al-doping	1.27[19]
Si-doping	2.21[17]
Ge-doping	1.89[17]
Sn-doping	1.86[17]
Ag-doping	1.61[12]
B-doping (our work)	0.82

The DOS spectra are used for the explanation of the energy distribution of occupied electrons at each energy level, which depict the formation of band. For the explanation of the distribution of energy of occupied electrons at each energy level, we lay the DOS spectra, in Fig. 3 for the description of the band formation.

From Fig. 3, we observed that three bands are forms from the energy value -8 to 6 electron volt. The first band, i.e., core band, lies from nearly -8 eV to 3.18 eV, the second band is valance band -2.13 eV to 0 eV, and the last band is conduction band from 0.82 to 6 eV. In valence band, state '*d*' and '*s*' of Cu and Ga contribute,

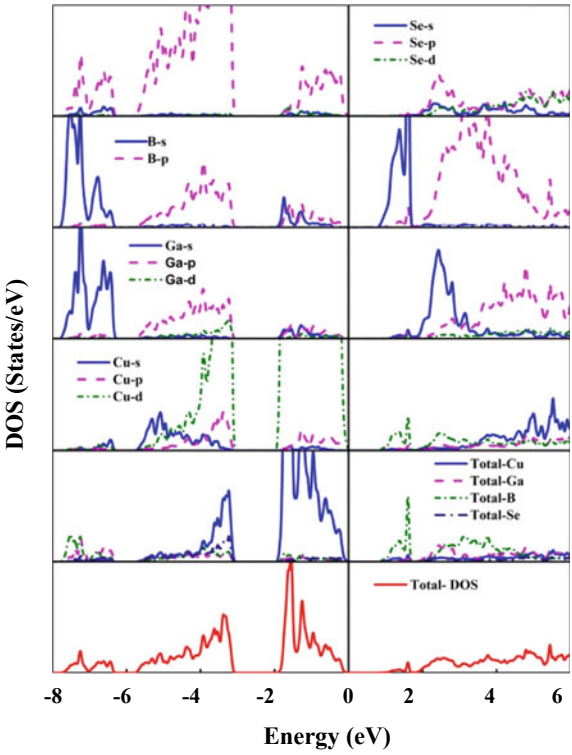

Fig. 3 Density of state spectra of $CuGa_{0.875}B_{0.125}Se_2$

and in core band, contribution is of '*p*' and '*s*' state of B and Se. The gap between the valence band and conduction band is equivalent to the observed band gap that calculated from Fig. 2. The achieved band gap of $CuGa_{0.875}B_{0.125}Se_2$ semiconductor depicts that the compound is acceptable for the photovoltaic applications.

3.2 Optical Properties

In this section, we explored the complete optical behavior of $CuGa_{0.875}B_{0.125}Se_2$ to investigate its utility for the optoelectronic applications. The plotting of the curve for dielectric tensor, absorption, reflection, and refraction has been done for the illustration of the optical properties of $CuGa_{0.875}B_{0.125}Se_2$ which are represented in Figs. 4a, b, 5 and 6. The calculation of optical properties of compounds requires detail study of frequency-dependent complex dielectric function ε (ω). It has two components,

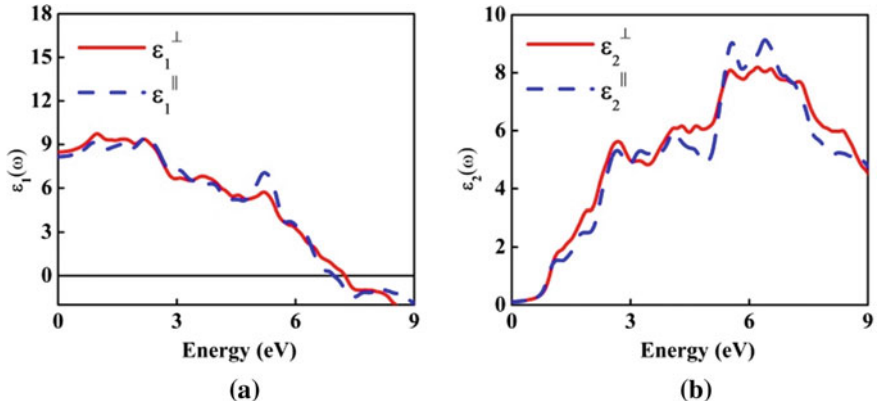

Fig. 4 **a** Real and, **b** imaginary dielectric tensor spectra of $CuGa_{0.875}B_{0.125}Se_2$

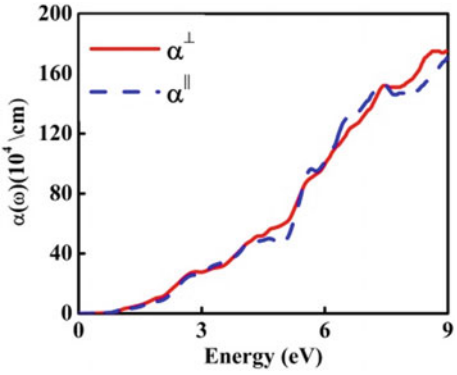

Fig. 5 Absorption spectra of $CuGa_{0.875}B_{0.125}Se_2$

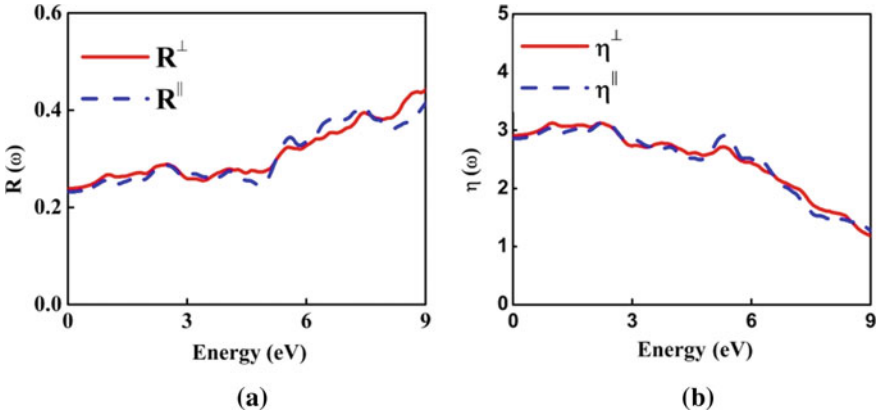

Fig. 6 **a** Reflectivity spectra, **b** refractivity spectra of $CuGa_{0.875}B_{0.125}Se_2$

perpendicular component and parallel component. We have selected mBJ calculations for investigating the optical behavior of $CuGa_{0.875}B_{0.125}Se_2$ compound since it is the more accurate one. In Fig. 4a, b the real and imaginary components of dielectric tensor ε (ω) are plotted for analyzing its variation with energy of the electromagnetic radiation. Figure 4b represents the imaginary part of dielectric function ε_2 (ω), and its imaginary part 'ε_2 (ω)' is helps to understand the transitions that occurs between occupied and unoccupied state.

The optical characteristics of compounds are important for show casing the compound for optoelectronic devices. Here, we explain the optical response of any material by using complex dielectric function, absorption coefficient, reflectivity, and refraction produce by the compound. The obtained absolute value of real dielectric tensor spectra at 0 eV is 6.13. The peaks (2.93, 4.5, 6.16 and 7.07 eV) appear in imaginary dielectric tensor spectra which describes the transition of free electron from valence to conduction band. Figure 5 represents the spectra of absorption coefficient which is used to explain about the extent of absorption of material for the incident photon, and the calculated value of integrated absorption coefficient is 113 ($\times 10^4$ eV/cm). Figure 6a, b represents the reflectivity and refractivity spectra of the $CuGa_{0.875}B_{0.125}Se_2$ compound, and their values are at 0 eV is 3.85 and 7.21, respectively. Hence, we concluded that these calculated values make the compound $CuGa_{0.875}B_{0.125}Se_2$ suitable for optoelectronic applications.

4 Conclusion

In this paper, the electronic and optical properties of $CuGa_{0.875}B_{0.125}Se_2$ are calculated through theoretical simulation DFT which operated in Wien2k package. The energy band gap, its structure, density of states (DOS) spectra, and optical properties

calculations are performed by using TB-mBJ exchange_correlation functional for attaining more accuracy in band gap value. The obtained value of band gap from band structure signed that $CuGa_{0.875}B_{0.125}Se_2$ exhibits a semiconductor nature. The optical spectra certify the anisotropic nature. The absorption spectra prove the utility of compound for optoelectronic devices, and DOS spectra reveal its direct band gap nature.

Acknowledgements We all are very grateful to Prof. P. Blaha Vienna University Group for providing the WIEN2K code. We are also thankful to DST-SERB, New Delhi, (India) for grant number EMR/2017/005534. Also thankful to Manipal University Jaipur, India, for their support.

References

1. Bhamu KC, Soni A, Sahariya J (2018) Revealing optoelectronic and transport properties of potential perovskites Cs_2PdX_6 (X= Cl, Br) -A probe from density functional theory. Sol Energy 162:336–343
2. Rabaia MKH, Abdelkareem MA et al (2021) Environmental impacts of solar energy sytems. A Rev Sci Total Env 754:(1)41989–1-18
3. Llanos M, Yeakni R et al (2020) Alternatives assessment of perovskite solar cell materials and their methods of fabrication. Renew Sustain Energy Rev 133(110207):1–7
4. Nuese CJ (1977) III-V alloys for optoelectronic applications. J Electr Mater 6(3):253–293
5. Robinson W, Han R et al (2020) Wide band gap chalcogenide semiconductors. Chem Rev 120(9):4007–4055
6. Contreras MA, Egaas B et al (1999) Progress towards 20% efficiency in Cu (In, Ga)S_e2 polycrystalline thin-film solar cells. Prog Photovoltaics Res Appl 7:311–316
7. Ramanathan K, Contreras MA et al (2003) Properties of 19.2% efficiency $ZnO/CdS/CuInGaSe_2$ thin-film solar cells. Prog Photovoltaics Res Appl 11(4):225–230 (2003)
8. Koteski V, Doka S, Hofstetter J et al (2010) Germanium doping of wider band-gap $CuGaSe_2$ chalcopyrite: local and electronic structure. Phys Rev B 81:24521 3
9. Ishizuka S, Taguchi N, Nishinaga J et al (2020) A comparative study of the effects of light and heavy alkali-halide postdeposition treatment on $CuGaSe_2$ and Cu(In, Ga)S_e2 thin-film solar cell. Sol Energy 211:1092–1101
10. Kikuchi K, Imura S, Miyakawa K et al (2014) Electrical and optical properties of $Ga_2O_3/CuGaSe_2$ heterojunction photoconductors. Thin Solid Films 550:635–637
11. Ishizuka S, Fons PJ et al (2020) Polycrystalline $CuGaSe_2$ thin film growth and photovoltaic devices fabricated on alkali-free and alkali-containing substrates. J Crystal Growth 532:125407
12. Weiss T, Birkholz M, Saad M et al (1999) Ag doped CuGaSe2 as precursor for thin film solar cells. J Crystal Growth 198(199):1190–1195
13. Theodoropoulou S, Papadimitriou D, Doka S et al (2007) Structural properties of Ge doped $CuGaSe_2$ films studied by Raman and photoluminescence spectroscopy. Thin Solid Films 515:5904–5908
14. Ullah S, Mollar M, Mari B et al (2016) Electrodeposition of $CuGaSe_2$ and $CuGaS_2$ thin films for photovoltaic applications. J Solid State Electrochem 20:2251–2257
15. Rusu M, Bar M, Lehmann S et al (2011) Transport properties of $CuGaSe_2$ based thin film solar cells as a function of the absorber composition. Thin Solid Films 519:7304–7307
16. Bikeroui M, Balli M, Farkous M et al (2020) The effect of lattice deformation on electronic and optical properties of $CuGaSe_2$ by implementing ab-initio calculations. Thin solid film 696:1–9

17. Dergal M, Faraoun HI, Mahmoudi A (2017) First principles study on structural, electroni and optical properties of 3d transition metals-substituted $CuGaSe_2$. Optik 135:346–352
18. Xue HT, Tang FL, Jianglu W et al (2013) First-principles investigation of structural phase transitions and electronic properties of $CuGaSe_2$ up to 100 GPa. Comput Mater Sci 67:21–26
19. Khan K, Gaur A, Soni A, Sahariya J (2020) Revealing the impact of aluminum doping on opto-electronic properties of $CuGaSe_2$ thin films flexible solar cells—A DFT study. AIP Conf Proc 2294:030004 (2020)
20. Fan W, Yao H et al (2020) Structural and optical characteristics of Sn-doped $CuGaSe_2$ thin films as a new intermediate band material for high-efficiency solar cells. AIP Adv 10(065031):1–6
21. Khan K, Gaur A, Soni A, Sahariya J, Ahuja U (2021) A probing study on the optoelectronic properties of flexible-thin film $CuGa_{0.89}B_{0.11}Se_2$- a DFT approach. In: International conference. Lecture notes in electrical engineering FLEXEV, Springer (2021)
22. Blaha P, Schwarz K, Madsen GKH, Kvasnicka D, Luitz J (2020) J Chem Phys 152:074101-1-30 (2020)
23. Soni A, Dashora A et al (2011) Electronic and optical modeling of solar cell compounds $CuGaSe_2$ and $CuInSe_2$. J Electron Mater 40, Article no 2197

Author Index

© The Editor(s) (if applicable) and The Author(s), under exclusive license to Springer Nature Singapore Pte Ltd. 2022

A. Tripathi et al. (eds.), *Intelligent Computing Techniques for Smart Energy Systems*, Lecture Notes in Electrical Engineering 862,
https://doi.org/10.1007/978-981-19-0252-9